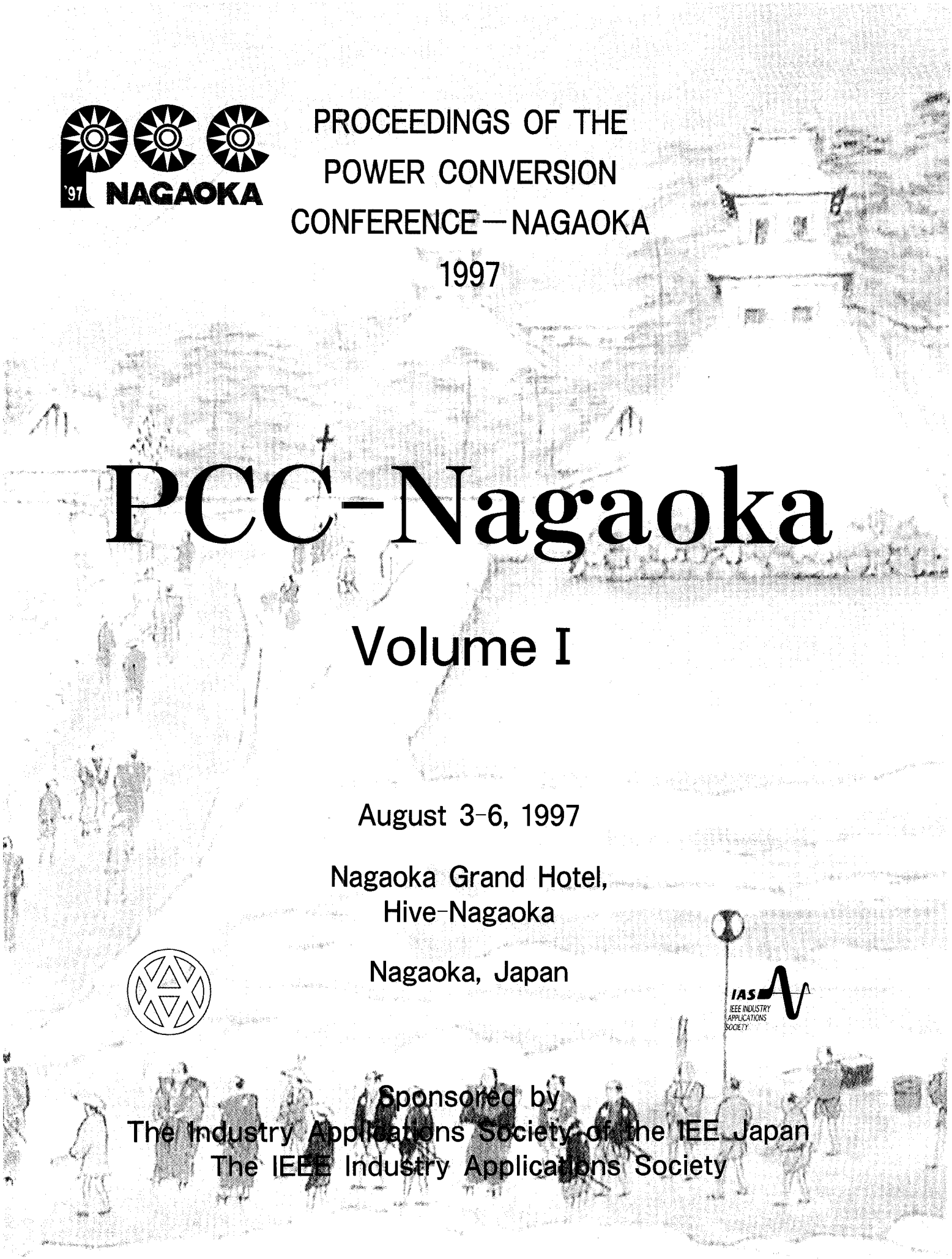

PROCEEDINGS OF THE
POWER CONVERSION
CONFERENCE — NAGAOKA
1997

PCC-Nagaoka

Volume I

August 3-6, 1997

Nagaoka Grand Hotel,
Hive-Nagaoka

Nagaoka, Japan

Sponsored by
The Industry Applications Society of the IEE Japan
The IEEE Industry Applications Society

IEEE 97TH8266

Proceedings of the Power Conversion Conference-Nagaoka 1997

Volume I

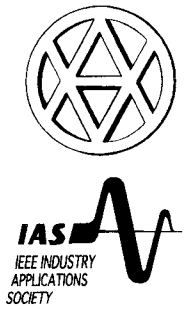

sponsored by

the Industry Applications Society of the IEE Japan

and

the IEEE Industry Applications Society

in cooperation with

the IEEE Industrial Electronics Society,
the IEEE Power Electronics Society,
IEEE Tokyo Section,
Japan Society for Power Electronics,
the Illuminating Engineering Institute of Japan,
the Society of Instrument and Control Engineers,
the Institute of Electrical Installation Engineers of Japan,
the Institute of System, Control and Information Engineers,
the Institute of Electronics, Information and Communication Engineers

IEEE Catalog Number 97TH8266

IEEE Catalog Number:	97TH8266
ISBN SoftboundEdition:	0-7803-3823-5
MicroficheEdition:	0-7803-3824-3
Library of Congress Number:	97-70237

ORGANIZING COMMITTEE

Chairperson: **Akira Nabae** *Tokyo Institute of Polytechnics*
Investigator: **Masao Yano** *Toyo University*
Secretary: **Isao Takahashi** *Nagaoka University of Technology*

Eisuke Masada
University of Tokyo

Tadashi Fukao
Tokyo Institute of Technology

Akeshi Maeda
Tokyo Denki University

Takayoshi Nakano
Shibaura Institute of Technology

Rokuya Ishii
Yokohama National University

Koji Iwata
Chube University

Takamasa Hori
Mie University

Toru Maruhashi
Kobe University

Sakutaro Nonaka
Kinki University

Takeichi Sakurai
Tokyo Electric Power Co.

Taizo Hasegawa
Kansai Electric Power Co.

Isamu Kobayashi
Chubu Electric Power Co.

Minoru Morikuni
Tohoku Electric Power Co.

Hiromasa Higasa
Shikoku Research Institute Inc.

Hisashi Ooi
Electric Power Development Co., Ltd.

Naoe Kawakami
Hitachi Ltd.

Sumio Kobayashi
Toshiba Corp.

Kazuya Furukawa
Mitsubishi Electric Co.

Akira Takai
Fuji Electric Co., Ltd.

Masaaki Obana
Meidensya Co.

Takashi Koga
Toyo Electric Mfg.

Koichi Hirano
Yaskawa Electric Corp.

Jun Nishidai
Nissin Electric Co.

Keisuke Fujisaki
Nippon Steel Corp.

Hironori Shimizu
Shinko Electric Co.

Kozo Hiyoshi
Sharp Corp.

Sinya Tanaka
Sanken Electric Co.

Yoshihiro Sekino
Sanyo Denki Co., Ltd.

Hisatoshi Goshima
Origin Electric Co.

Atsuo Nagai
Nippon Seiki Corp., Ltd.

Masaru Wasaki
TDK Corp.

Tatsuo Naito
JAPAN STORAGE BATTERY Co., Ltd.

Kiyotaka Ikawa
Yuasa Corp.

Toshiaki Sasaki
Railway Tech. Research Institute

Akihiro Tabata
SHINDENGEN Electric Mfg. Co., Ltd.

Kikuji Tsuneyoshi
Mitsubishi Heavy Industries Ltd.

Naotake Kumagai
Mitsubishi Motors Corp.

Tsuneo Kume
Yaskawa Electric Corp.

Masashi Mizoguchi
NETUREN Co., Ltd.

Toru Hirano
Daikin Industries, Ltd.

ADVISORS

Seizaburo Hiura
Mayor of Nagaoka

T. A. Lipo
University of Wisconsin -Madison

B. K. Bose
University of Tennessee

P. C. Sen
Queen's University

K. R. Heumann
Technische Universitat Berlin

F. Profumo
Politecnico di Torino

Jijum Wu
Xian Power Electronic Research Institute

Young-Moon Hwang
Pusan National University

Junichi Nishizawa
Tohoku University

Koosuke Harada
Kumamoto Institute of Technology

Fumio Harashima
University of Tokyo

Yasuzo Uchida
Nagaoka University of Technology

Ichiro Nagata
Hitachi Ltd.

Keiji Nishijima
Toshiba Corp.

Toshio Suzuki
Mitsubishi Electric Co.

Kunihiko Sawa
Fuji Electric Co., Ltd.

Takashi Hirayama
Meidensya Co.

Sumio Nagabuchi
Toyo Electric Mfg.

Rikihiro Madarame
NEMIC-LAMDA K.K.

STEERING COMMITTEE

Chairperson: **Isao Takahashi** *Nagaoka University of Technology*
Co-Chairperson: **Ryuichi Shimada** *Tokyo Institute of Technology*
Secretary: **Kiyoshi Ohishi** *Nagaoka University of Technology*

Tung-Hai Chin
Sophia University

Kouki Matsuse
Meiji University

Gunji Kimura
Tokyo Metropolitan University

Toshimasa Haneyoshi
Tokyo Denki University

Yoichi Hori
University of Tokyo

Kenzo Kamiyama
Utsunomiya University

Shigeru Okuma
Nagoya University

Nobuyuki Matsui
Nagoya Institute of Technology

Katsunori Taniguchi
Osaka Institute of Technology

Yoji Takeda
University of Osaka Prefecture

Atsuo Kawamura
Yokohama National University

Yasuo Haga
Nagaoka National College of Technology

Keiichi Tsuchida
Nagaoka National College of Technology

Seiji Kondo
Nagaoka University of Technology

Toshihiko Noguchi
Nagaoka University of Technology

Itatu Ando
Nagaoka University of Technology

Kazuo Saito
Nagaoka University of Technology

Susumu Horiuchi
Tokyo Electric Power Co.

Seiichi Muroyama
NTT Interdisciplinary Research Lab.

Mitsuyuki Hombu
Hitachi Ltd.

Suzuo Saito
Toshiba Corp.

Ryohei Uchida
Mitsubishi Electric Co.

Kouetsu Fujita
Fuji Electric Co., Ltd.

Yasuo Kataoka
Meidensya Co.

Ichiro Miyashita
Toyo Electric Mfg.

Junji Hirai
Yaskawa Electric Corp.

Yuichi Sakuragawa
NEMIC-LAMDA K.K.

Takayuki Uchida
Society of Electric Vehicle

Kunio Ishibashi
IEE of Japan

TECHNICAL PROGRAM COMMITTEE

Chairperson: **Ryuichi Shimada** *Tokyo Institute of Technology*
Co-Chairperson: **Deepakraj M Divan** *University of Wisconsin*
Secretary: **Seiji Kondo** *Nagaoka University of Technology*
Secretary: **Yukihiko Sato** *Tokyo Institute of Technology*

Akagi, Hirofumi
Okayama University

Ando, Itaru
Nagaoka University of Technology

Buja, Giuseppe
University of Padova

Chiba, Akira
Science University of Tokyo

Choi, Jae-Ho
Chungbuk National University

Dawson, Francis P.
University of Toronto

Ehsani, Mehrdad
Texas A&M University

Fujita, Hideki
Chubu Electric Power Co.

Fujita, Kouetsu
Fuji Electric Corporate Research and Development Ltd.

Fukuda, Shoji
Hokkaido University

Hayashi, Yoichi
Aoyama Gakuin University

Heumann, Klemens
Technische Universitat Berlin

Holtz, Joachim
Wuppertal University

Hombu, Mitsuyuki
Hitachi Ltd.

Hwang, Young Moon
Busan National University

Ikeda, Haruo
Railway Technical Research Institute

Irie, Hisaichi
Osaka Electro-Communication University

Ise, Toshifumi
Osaka University

Ishida, Muneaki
Mie University

Ishikawa, Tadao
Central Research Institute of Electric Power Industry

Ito, Youichi
Sanken Electric Co., Ltd.

Itoh, Yuzo
Hokkaido University

Iwakane, Takanobu
Yaskawa Electric Corp.

Iwata, Makoto
Sanken Electric Co., Ltd.

Jahns, Thomas M.
Massachusetts Institute of Technology

Jinzenji, Toshimasa
Sanyo Denki Co.

Kanmachi, Toshiyuki
Sendai National College of Technology

Kataoka, Yasuo
Meidensha Co.

Kaushik, Rajashekara
Delphi Energy & Engneering

Kawamura, Atsuo
Yokohama National University

Kaynak, Okyay
Bogazici University

Kim, Moon Hwan
Korea Electrotechnology Research Institute

Kitano, Jun-ichi
Central Japan Railway Co.

Koyama, Masato
Mitsubishi Electric Corp.

Kubota, Hisao
Meiji University

Kuroki, Kazuo
Fuji Electric Corporate Research and Development Ltd.

Lorenz, Robert D.
University of Wisconsin - Madison

Matsuda, Yasuo
Hitachi Ltd.

Matsui, Keiju
Chubu University

Matsui, Mikihiko
Tokyo Institute of Polytechnics

Matsui, Nobuyuki
Nagoya Institute of Technology

Matsuo, Hirofumi
Nagasaki University

Matsuse, Kouki
Meiji University

Miki, Ichiro
Meiji University

Miyashita, Kunio
Hitachi Ltd.

Morimoto, Masayuki
Mitsubishi Heavy Industries Ltd.

Morimoto, Sigeo
Osaka Prefecture University

Murai, Yoshihiro
Gifu University

Naitoh, Haruo
Toshiba Corp.

Nakagawa, Toshiko
Tokyo Denki University

Nakajima, Tatsuhito
Tokyo Electric Power Co.

Nakaoka, Mutsuo
Yamaguchi University

Nishikata, Shoji
Tokyo Denki University

Ogasawara, Satoshi
Okayama University

Ogata, Tsutomu
NTT Integrated Information & Energy Systems Laboratories

Ogihara, Yoshiya
Nisshin Electronic Co., Ltd.

Oguchi, Kuniomi
Ibaraki University

Ohishi, Kiyoshi
Nagaoka University of Technology

Ohmae, Tsutomu
Hitachi Ltd.

Ohnishi, Kohei
Keio University

Ohshima, Masaaki
Tokyo Electric Power Co.

Ohyama, Kazunobu
Daikin Industries Ltd.

Okuma, Shigeru
Nagoya University

Panda, Sanjib Kumar
National University of Singapore

Peng, Fang-Zheng
Oak Ridge National Lab.

Rahman, M.A.
Memorial University of Newfoundland

Rajagopalan, Venkatachari
Universite du Quebec

Rashid, Muhammad H.
Indiana-Purdue University

Sakui, Masaaki
Toyama University

Schroeder, Dierk
Technishe Universitat Munchen

Sen, Paresh C.
Queen's University

Senjyu, Tomonobu,
University of the Ryukyus

Shimizu, Toshihisa
Tokyo Metropolitan University

Su, Guijia
Sanken Electric Co., Ltd.

Sugimoto, Hidehiko
Fukui University

Sul, Seung-Ki
Seoul National University

Tadakuma, Susumu
Chiba Institute of Technology

Takahara, Eimei
Toshiba Corp.

Takahashi, Isao
Nagaoka University of Technology

Takeda, Yoji
Osaka Prefecture University

Tamura, Yoshiaki
Toshiba Corp.

Tanaka, Shigeru
Toshiba Corp.

Tanaka, Toshihiko
The Polytechnic University, Japan

Taniguchi, Katsunori
Osaka Institute of Technology

Terashima, Masayuki
Meidensha Co.

Uceda, Javier
Universidad Politecnica de Madrid

Uchida, Ryohei
Mitsubishi Electric Corp.

Umita, Hidetoshi
Fuji Electric Corporate Research and Development Ltd.

Van Wyk, J.D.
Rand Afrikaans University

Vas, Peter
University of Aberdeen

Watanabe, Hiroshi
Tokyo Metropolitan Institute of Technology

Yanase, Takao
Fuji Electric Corporate Reserach and Development Ltd.

TABLE OF CONTENTS

Volume I :

O1 Electric Vehicle

O2 Traction Systems

O3 Induction Motor Control (1)

O4 Induction Motor Control (2)

O5 Permanent Magnet Motor Control

O6 Active Power Filter

O7 Utility Network Applications (1)

O8 PWM (1)

O9 PWM (2)

O10 Soft Switching (1)

O11 Power Supply Systems

O12 Simulation of Power Converter Systems (1)

O13 Simulation of Power Converter Systems (2)

O14 Modeling and Analysis of PE System (1)

O15 Control and Applications (1)

O16 Motion Control and Soft Computing

Volume II :

P1 Induction Motor Control (3)

P2 Induction Motor Control (4)

P3 Motor Control Technology

P4 New Synchronous Motors and Their Control

P5 Utility Network Applications (2)

P6 PWM (3)

P7 Soft Switching (2)

P8 Modeling and Analysis of PE System (2)

P9 Measurement and Control

P10 Control and Applications (2)

P11 Industrial Applications

AUTHORS INDEX

Traction Control of Electric Vehicle based on the Estimation of Road Surface Condition

- Basic Experimental Results using the Test EV "UOT Electric March" -

Yoichi Hori, Yasushi Toyoda and Yoshimasa Tsuruoka
Department of Electrical Engineering, University of Tokyo, 7-3-1 Hongo, Bunkyo, Tokyo, 113 Japan
Phone: +81-3-3812-2111 ext 7680, Fax: +81-3-5800-3865
E-mail: hori@kaya.t.u-tokyo.ac.jp, Homepage: http://www.kaya.t.u-tokyo.ac.jp/

Abstract- The most distinct advantage of electric vehicle is in its quick and precise torque generation. We propose two novel traction control techniques of electric vehicle, i.e., the model following control and the optimal slip ratio control. Their effectiveness is demonstrated by using the test vehicle "UOT Electric March".

I. Introduction

Recently a lot of electric vehicles (EV) have been developed to solve environment and energy problems caused by the use of internal combustion engine vehicles (ICV). Some of them already have enough performance in practical use. However, they have not yet utilized the most remarkable advantage of EV. Electric motor torque can be controlled much more quickly and precisely than that of internal combustion engine. Adhesion characteristics between tire and road surface are greatly affected by the control of traction motor. This means that the vehicle stability and safety can be improved by motor torque control. If we can use special low drag tires with smaller energy loss, the range of one battery charge will be drastically expanded.

In this paper, we will propose the novel traction control techniques, which can be firstly realized only by utilizing electric motor's quick torque response. They are the model following control and the optimal slip ratio control. By using a newly developed test vehicle "UOT Electric March", we will show some successful experimental results. In order to achieve the best control performance, the estimation method of road surface condition is proposed and its realizability is shown also by real experiments

II. State-Of-The-Art Of Traction Control

Traction control is the control to suppress tire slip when the vehicle is running, for example, on icy road by controlling the traction force and to improve the driving and cornering performances mainly in acceleration.

We should consider two forces acting on the vehicle body, i.e., the driving (longitudinal) and side (lateral) forces. As depicted in Fig.1, these forces depend on the slip ratio λ. λ is defined by eq.(1), where V_w and V are the wheel and vehicle speeds.

$$\lambda = (V_w - V) / V_w \qquad (1)$$

The side force takes its maximum value when λ=0 and becomes smaller for bigger λ. If λ increases by sudden decrease of road friction, the side force gets smaller drastically. This causes serious problems: drift-out in front wheel driven cars, spin in rear wheel driven cars, and drift-out with rotation in four wheel driven cars. Such a loss of cornering force is extremely dangerous. The average traction force is also decreased.

Traction control can be classified into following two steps:

(1) **longitudinal control**, for example, the adhesion improvement to prevent slip. This is done by controlling the traction force, and

(2) **lateral control**, for example, the yaw control to keep the yaw motion to be zero. This is done mainly by controlling the steering angle.

For the lateral control, the steering angle of the front wheels is the absolutely dominant control input. Such a technique is already well developed for ICV and the results can be applied to EV. For this reason, in this paper, we focus our discussion into (1) **longitudinal control**.

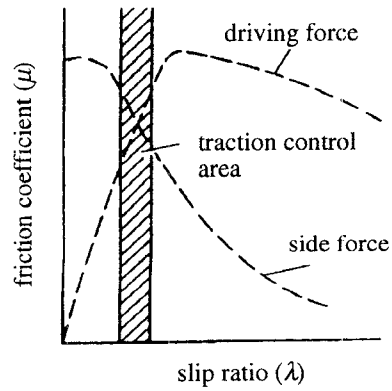

Fig.1. Characteristics of driving and lateral forces

0-7803-3823-5/97/$10.00© 1997 IEEE

To realize the effective traction control system, we need a sophisticated mechanism quickly to reduce the excessive driving torque. In ICV, this is realized mainly by the following three techniques.

(1) **engine control:** Engine torque itself is suppressed. To reduce air supply is the basic technique, but for quicker response, advanced techniques like fuel-cut and spark timing shift are used together.

(2) **brake control:** Wheel rotation itself can be stopped by braking. This method has quicker response than the engine control. Independent control of left and right tires is effective for μ-split braking. Brake control should be used together with the engine control because brake parts often have thermal problem.

(3) **mission control:** Driving torque of the slipping tire is transferred to the non-slipping tire. This technique is effective for μ-split road. As the total torque can not be reduced, mission control technique should be applied together with the engine control.

TABLE I summarizes the advantages and disadvantages of these techniques.

TABLE I
COMPARISON OF TRACTION CONTROLS FOR ICV

	control-lability	response	cost	operation feeling	total
engine control	○	△	◎	△	○
brake control	○	◎	◎	×	△
mission control	△	×	◎	△	×
engine + mission controls	○	△	○	△	△
engine + brake controls	◎	◎	○	○	◎

III. ADVANTAGE OF ELECTRIC VEHICLE

Electric Vehicle has great advantages as followings for realization of high performance traction control.

(1) **low cost**: Above mentioned techniques for ICV need additional costly hardware, e.g., throttle and brake actuators. EV does not need anything more. Traction control can be realized only by software. Low cost "basic car" can have high performance traction control.

(2) **quick response**: In ICV, more than 200[ms] are needed to open the throttle actuator. The actual response time is much longer because the mechanical delay is included. In contrast, the response time of electric motor torque is less than 10[ms].

(3) **easy controller design**: In ICV, unknown strong non-linearity lies in the transfer characteristics from the control input (for example, air valve angle to engine, oil pressure of brake system, etc.) to the generated torque. This makes it difficult to construct a mathematical model for controller design. In EV, by applying simple current control, the generated torque is exactly proportional to the torque command.

IV. MODEL FOLLOWING CONTROL

In this paper, we propose two control strategies: one is the **model following control (MFC)**, and another is the **optimal slip ratio control**. MFC is the starting point of our research project of "Control of Electric Vehicle" and its basic feasibility is demonstrated here by real experiment.

A. Principle of MFC

Fig.2 shows the block diagram of the model following control. I_{com} is the current command proportional to the acceleration pedal angle. ω is the rotational speed of the driving shaft. ω increases drastically when the tire slips. Vehicle dynamics including tire characteristics and road surface friction are very complicated, but if we introduce the slip ratio λ, the vehicle body can be seen as one inertia system having the equivalent inertia moment of

$$J = J_w + Mr^2(1-\lambda) \qquad (2)$$

Here, J_w , M and r are the shaft inertia moment, vehicle weight and tire radius. Eq.(2) means that, when slip occurs, the vehicle seems lighter. Therefore, we use the following inertia moment with λ=0 in the reference model.

$$J_{model} = J_w + Mr^2 \qquad (3)$$

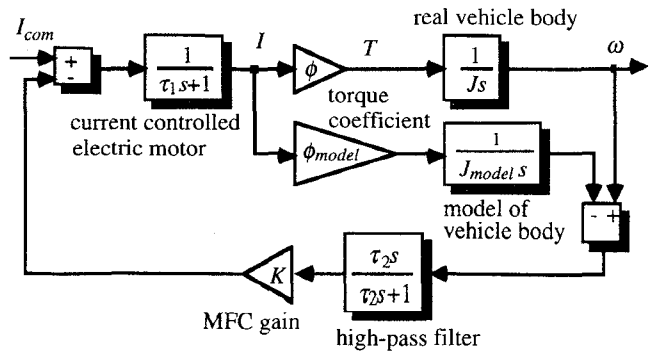

Fig.2. Block diagram of MFC

When there is no slip, actual J is almost equal to J_{model}. Any signal is not generated from MFC controller. If the tire slips, the actual wheel speed ω increases immediately. The model wheel speed does not increase. By feeding back the speed difference to the motor current command, the

actual motor torque is reduced quickly and it induces re-adhesion.

This control function is needed only in relatively higher frequency region, we used a high pass filter on the feedback pass. In actual implementation, two high pass filters are inserted before taking the difference between actual and model speeds to avoid the offset problem of integrator.

B. Experimental Result of MFC

Fig.3 shows the slip experiment using UOT Electric March. We used iron plates as slippery road surface. Water is scattered to reduce the friction coefficient. The vehicle is accelerated by the constant current command of 300[A]. The feedback gain K in Fig.2 is 30. The front wheels are on the slippery area between t=1.25[s] and 1.7[s].

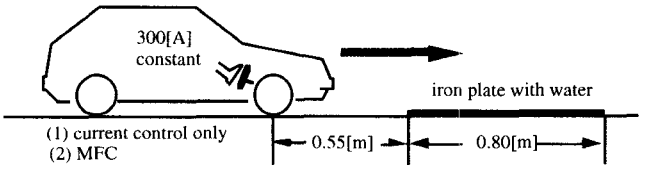

Fig.3. Slip experiment

Experimental results are given in Fig.4. We can see that MFC can reduce the motor current effectively when the vehicle goes onto the slippery area, and then the slip ratio is kept much lower comparing to the current control only. Some vibration seen in the current waveform in Fig.4(a) should be suppressed in the future.

V. Optimal Slip Ratio Control

The model following control is a very rough approach although it has been shown that the motor control is really effective for adhesion improvement. If we want more exactly to regulate the slip ratio within the desired range, more precise approach is needed. Fig.5 shows the idea of the optimal slip ratio control developed from this viewpoint. When the optimal slip ratio is decided by the road condition estimator, the slip ratio controller receives the command and realizes it.

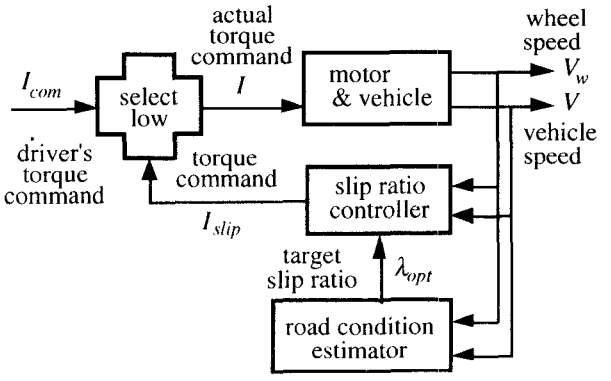

Fig.5. Block diagram of the optimal slip ratio controller

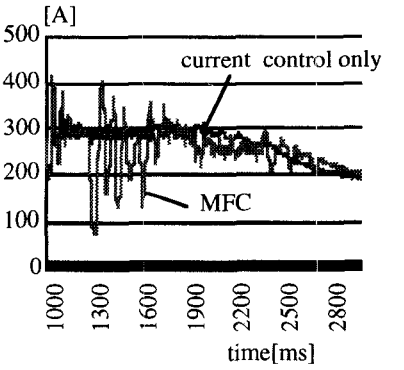

(a) motor current

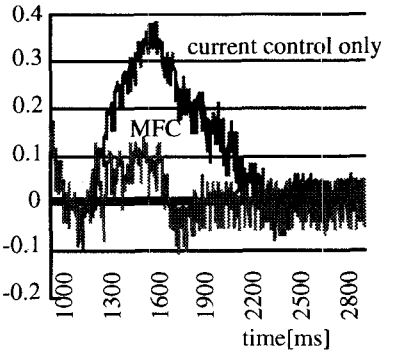

(b) slip ratio

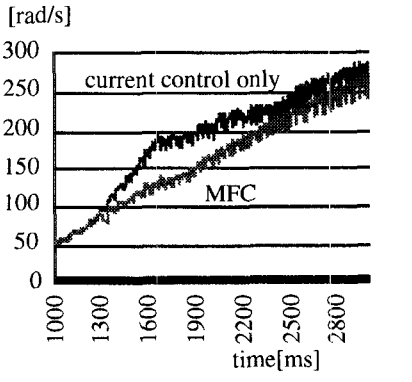

(c) wheel speed

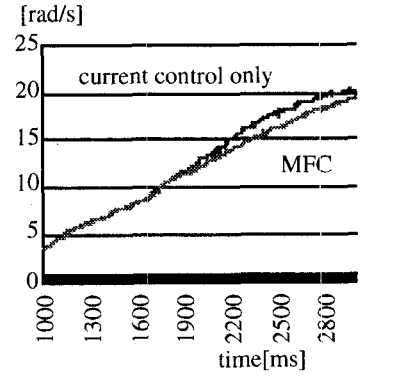

(d) vehicle speed

Fig.4. Experimental results of MFC

A. Vehicle Model

We assume that the two motor torques and friction forces are same in left and right, and that the rolling and air frictions are small enough. In Fig.6, the kinematic equations of the wheel and vehicle take the forms of

$$(F_m - F_d)\frac{1}{M_w s} = V_w \tag{4}$$

and

$$F_d \frac{1}{Ms} = V \tag{5}$$

where,

F_m : motor torque (force equivalent)
F_d : friction force
M_w : wheel inertia (mass equivalent)
M : vehicle weight

The friction force between the road and wheel is given by

$$F_d = N\,\mu(\lambda) \tag{6}$$

where N is the vertical force given by $N = Mg$.

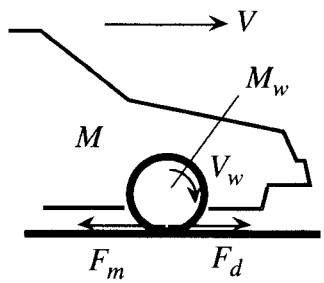

Fig.6. Vehicle model.

From eq.(1), the following perturbation system is derived.

$$\Delta\lambda = \frac{\partial\lambda}{\partial V}\Delta V + \frac{\partial\lambda}{\partial V_w}\Delta V_w$$
$$= -\frac{1}{V_{w0}}\Delta V + \frac{V_0}{V_{w0}^2}\Delta V_w \tag{7}$$

where V_{w0} and V_0 are the wheel and vehicle speeds at the operational point. The friction force is represented using a, the gradient of μ–λ curve, as

$$\Delta\mu = a\,\Delta\lambda \tag{8}$$

By combining eqs.(7) and (8) with the perturbed forms of eqs. (4) and (5), the transfer function from the motor torque to the slip ratio is finally given by

$$\frac{\Delta\lambda}{\Delta F_m} = \frac{1}{Na}\,\frac{M(1-\lambda)}{M_w + M(1-\lambda)}\,\frac{1}{1+\tau s} \tag{9}$$

where the time constant τ is given by eq.(10) which is proportional to the wheel speed V_{w0}.

$$\tau = \frac{1}{Na}\,\frac{MM_wV_{w0}}{M_w + M(1-\lambda)} \tag{10}$$

The typical value of τ in our experimental vehicle is 150~200[ms] when a=1 and the vehicle speed is around 10[km/h]. Note that a can be negative in the right-hand side of the peak point of μ–λ curve.

B. Design of Slip Ratio Controller

We used a simple P&I controller with a variable gain as the slip ratio controller given by eq.(11). Its nominator compensates for the pole of eq.(9). The integral gain is constant and the proportional gain is proportional to the vehicle speed.

$$K\frac{1+\tau s}{s} \tag{11}$$

Finally, the transfer function from the slip ratio command to the actual slip ratio becomes

$$\frac{\Delta\lambda}{\Delta\lambda^*} = \frac{1}{1 + Na\,\dfrac{M_w + M(1-\lambda)}{M(1-\lambda)}\,\dfrac{1}{K}\,s} \tag{12}$$

If λ<<1, this is a simple first order delay characteristics with a time constant which can be adjusted by K. Here, we put this response time 50~100[ms].

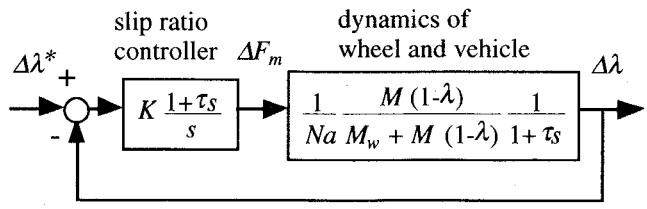

Fig.7. Slip ratio controller

Fig.8 shows the nominal slip ratio used in the slip ratio controller. We defined it by a=1. The point of a=1 is located just in left side of the peak and is stable. Both of the longitudinal and lateral forces are kept still high.

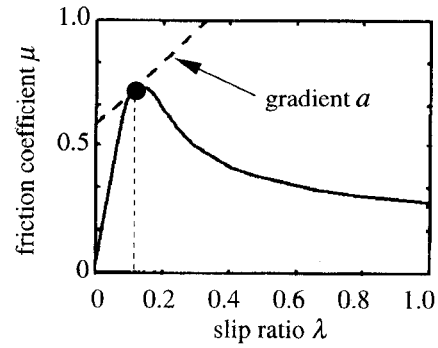

Fig.8. Nominal slip ratio is given by a=1.

C. Robustness to Parameter Variation

Because the actual system parameters change widely, we should investigate the robustness of the slip ratio controller. Fig.9 draws the root locus to the continuous change of K and a.

From the figure, we can see that the roots move to the left half plane when the controller gain K increases. It is interesting that this controller stabilizes the system even when actual a is negative, although the roots move to unstable region.

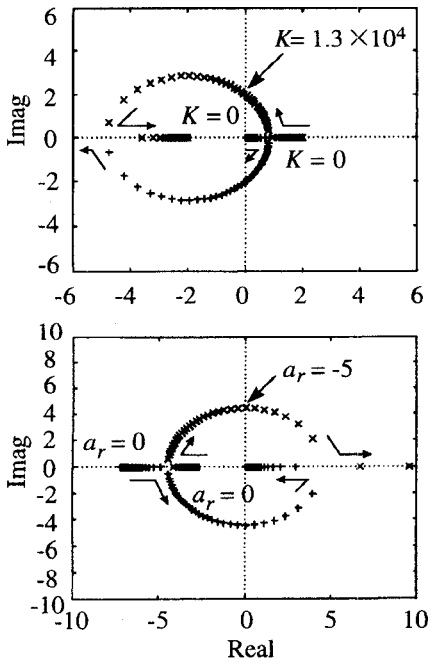

Fig.9. Root locus against parameter variation

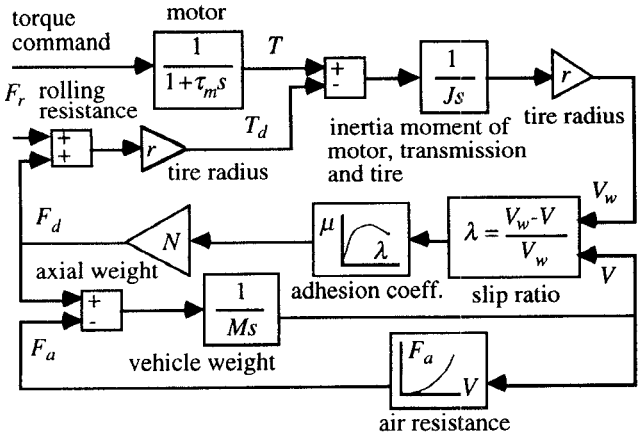

Fig.10 Vehicle model used in the simulation

D. Simulation of Slip Ratio Control

Fig.10 shows the vehicle model we used in the simulation. T represents the motor torque and r the total gear ratio of the drive train. F_d represents the summation of traction force transferred to the contact point of tire and road surface. It is the product of traction coefficient μ and $N=Mg$, the vertical load on the contact point. μ is defined as a function of λ (slip), which is given by the measured curve shown in Fig.11.

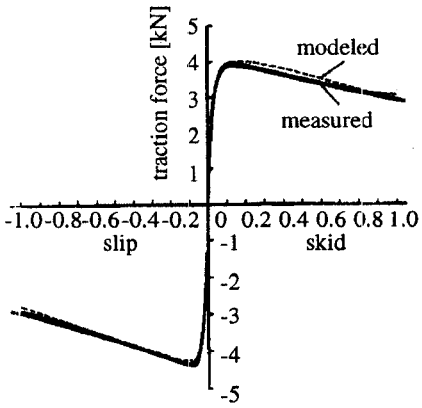

Fig.11. μ–λ characteristics used in the simulation

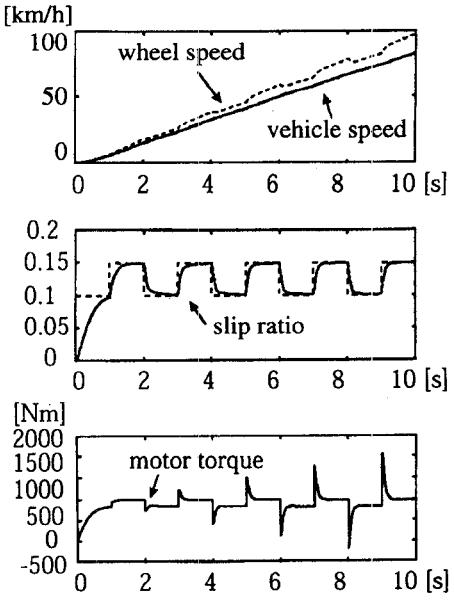

Fig.12 Simulation of the slip ratio control

Fig.12 is the simulation result. The response time of the slip ratio controller is set to be 100[ms]. We can see good response characteristics.

E. Experimental Results of Slip Ratio Control

Fig.13 shows the experimental results of the slip ratio control using the laboratory-made experimental electric vehicle "UOT Electric March". Here the response time is 50[ms] and the target slip ratio is 0.1 in Fig.13(a) and is changed stepwise from 0.3 to 0.1 in Fig.13(b).

Basically we can see fairly good performances but there are some problems. First, the actual value of a was much smaller than the nominal value: 1. This made the response

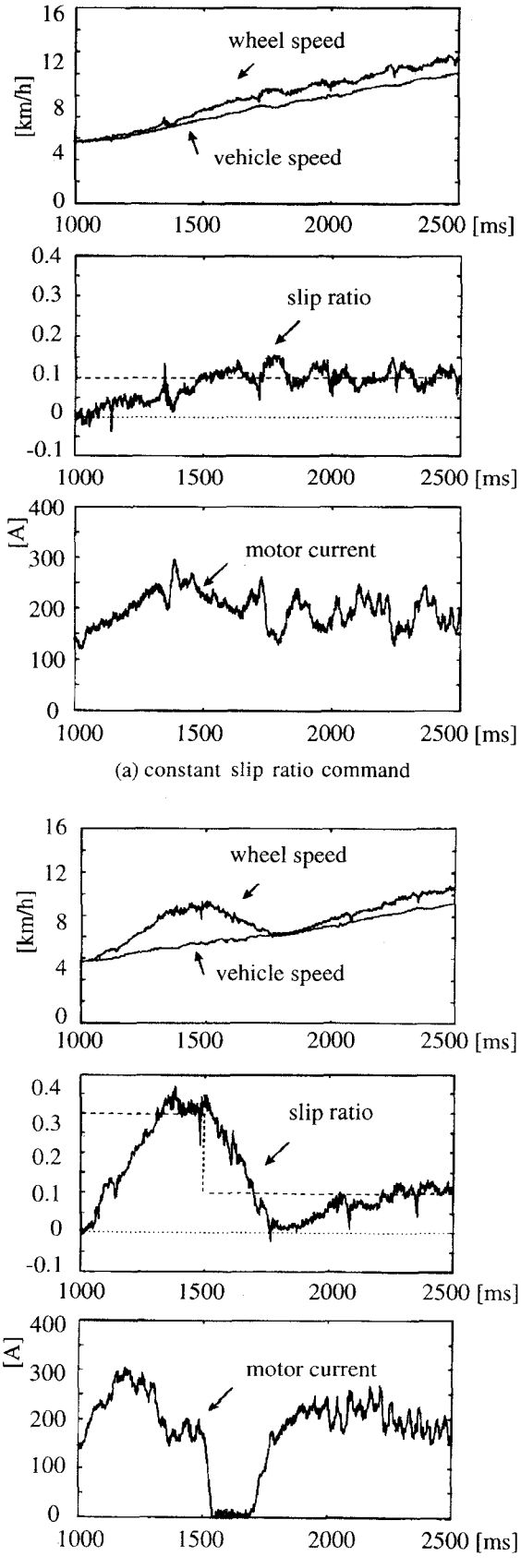

(a) constant slip ratio command

(b) changing slip ratio command

Fig.13. Experimental results of the slip ratio control

time longer than the designed value. Next, in Fig.13(b), we see an undershoot to the slip ratio command of 0.1. This is because the motor controller we used is just an 1-quadrant chopper, who can not absorb the motor current.

VI. Estimation Of Road Condition

In the previous chapter, we showed effective slip ratio control. Next problem is how to give the optimal slip ratio to the slip ratio controller.

We showed the relation between the slip ratio λ and the friction coefficient μ in Figs.1 and 11, but it varies very widely according to road surface condition as shown in Fig.14. It is clear that the slip ratio where the friction force takes its maximum value vary according to road condition. This means that road condition should be estimated relatively quickly for commanding the optimal slip ration to the slip ratio control.

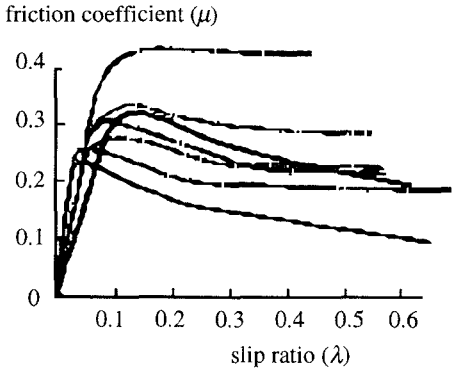

Fig.14. Various Road Condition.
(Actual explanation of each curves is omitted.)

To know the road surface condition, we should estimate the friction coefficient. If we can measure the vehicle speed directly by using non-driven wheel, the friction coefficient μ can be obtained by eq.(13) based on eqs.(3) and (4).

$$\mu = \frac{M}{N}\frac{dV}{dt} \tag{13}$$

When the vehicle speed can not be measured directly, we can estimate μ based on eq.(14).

$$\mu = \frac{1}{N}\left(F_m - M_w \frac{dV_w}{dt}\right) \tag{14}$$

In our case, we can use both of these two methods. Fig.15 shows the estimation result of μ-λ curve of dry asphalt road when no slip control is active. At the point around λ=0.08, the gradient a of μ-λ curve is about 1.

Fig.16 shows the estimation results on wet iron surface under the slip ratio control proposed in the previous chapter. Here, the optimal slip ratio is smaller than 0.05.

It is also noticed that, in our experiment shown in Fig.13(a), the actual gradient of μ-λ curve at λ=0.1 was almost -1. We can see that the slip ratio controller is effective even when the operation point is unstable, but, in this case, we should have commanded a lower slip ratio.

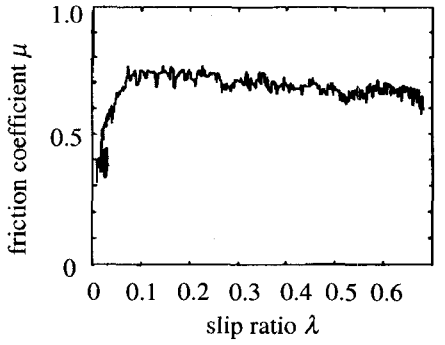

Fig.15. Estimation result of μ-λ curve of dry asphalt road

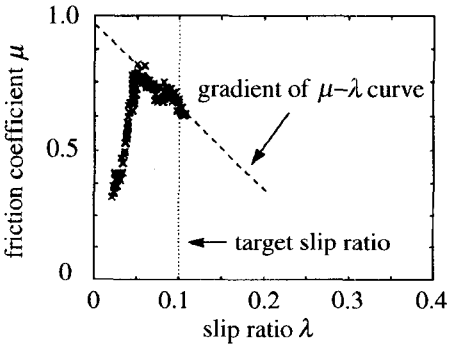

Fig.16. Estimation result of μ-λ curve of wet iron plate under the slip ratio control

VII. Conclusion

We are proposing a new field of "Motion Control of Electric Vehicle". EV is a very interesting object combining electrical and mechanical engineering fields from the view point of motion control. As an example, we proposed advanced adhesion control utilizing quick and precise torque response of electric motor.

We proposed the Model Following Control and the Optimal Slip Ratio Control. We confirmed that MFC can reduce its torque quickly when the motor speed is suddenly increased by tire slip. Next, we showed that the optimal slip ratio control has more advanced performance. Such kinds of quick controls are firstly realized only in electric vehicles. It is clearly shown that relatively precise control theory can work well in actual experiments.

Advanced adhesion control is helpful for lateral control like yaw disturbance attenuation. This is because the proposed optimal slip ratio control keeps the tire slip within the small region where both of the longitudinal and lateral adhesion coefficients are still high enough.

Acknowledgement

The authors would like to express their sincere thanks to Mr. Furuya in Kansai Electric Power Company for his big work on Electric March when he was a graduate student in Hori Laboratory. They also thank Mr. Uchida and Mr. Yamazaki for their help in manufacturing of the vehicle.

References

[1] M.Ito and K. Isoda, "The Present and Future Trends of Traction Control System", Jidosha-Gijutsu, Vol.46, No.2, pp.32-37, 1992. (in Japanese)

[2] K. Ise, et. al., "The 'Lexus' Traction Control (TRAC) System", SAE Paper 900212, 1990.

[3] J. Ackermann, "Yaw Disturbance Attenuation by Robust Decoupling of Car Steering", 13th IFAC World Congress, 8b-01-1, pp.1-6, 1996.

[4] Y. Wang and M. Nagai, "Integrated Control of Four-Wheel-Steer and Yaw Moment to Improve Dynamic Stability Margin", Proc. 35th IEEE-CDC, pp.1783-1784, 1996.

[5] C. Liu and H. Peng, "Road Friction Coefficient Estimation for Vehicle Path Prediction", Vehicle System Dynamics Supplement 25, pp.413-425, Swets & Zeitlinger, 1996.

[6] A. Daiss and U. Kiencke, "Estimation of Tyre Slip during combined Cornering and Braking Observer Supported Fuzzy Estimation", 13the IFAC World Congress, 8b-02-2, pp.41-46, 1996.

[7] Hideo Sakai, "Tire Engineering", Grand-Prix Pub. Co. , 1987. (in Japanese)

[8] S. Yamazaki, T. Fujikawa and I. Yamaguchi, "A Study on Braking and Driving Properties of Automotive Tires", Transactions of the Society of Automotive Engineers of Japan, Vol.23, No.2, pp.97-102, 1992.

[9] T.Furuya, Y.Toyoda and Y.Hori, "Implementation of Advanced Adhesion Control for Electric Vehicle", Proc. IEEE Workshop on Advanced Motion Control, AMC-Mie'96, Vol.2, pp.430-435, 1996.

Appendix

Configuration of UOT Electric March

We developed a real test electric vehicle "UOT Electric March (Todai Sangatsu Go)" seen in Fig.A-1. It is a so-called convert car, whose IC engine is replaced by an electric motor.

The front two wheels are driven by a 19[kW] series-wound DC motor through a 5 speed manual transmission and a differential gear. The 1-quadrant DC chopper supplies power to the motor. Its current limit is 400[A] and can produce maximum torque over 100[Nm], which is enough to perform the slip experiment. Current and speed sensors are also implemented. To detect the vehicle speed, a speed sensor is implemented in the rear wheel.

TABLE A-I
SPECIFICATION OF UOT ELECTRIC MARCH

Conversion Base	Nissan March (Micra)
size	3785×1560×1395[mm]
weight	900[kg](batteries included)
Motor	Advanced D.C. Motors, Inc.
type	DC series wound
rated power (@120V)	19[kW](1hr.), 32[kW](5min.)
size/weight	ϕ 232, length 397[mm], 65[kg]
Controller	Curtis Instruments, Inc.
type	MOSFET PWM Chopper
operating frequency	15[kHz]
rated voltage/current	120[V]/400[A]
Battery	Japan Storage Battery Co.,Ltd. GTX-130E41L
type	lead acid
voltage/capacity	72[V]/92[Ah](5hr)
weight	27.5[kg]×6
CPU	PC9801NS/T (386SL, 20MHz)
weight	3.2[kg]
A/D and D/A converters	12bit, 8ch / 12bit, 2ch

Fig.A-2 shows the control system of the vehicle and TABLE A-I gives its specification. We use a note-type personal computer to realize the torque control. It not only executes the control algorithm and puts out the voltage command to the chopper, but also reads, shows and records the sensor data. As the control algorithm is written by software (C-language), we can easily investigate various control strategies.

Fig.A-3 shows the basic experimental results of the current controller.

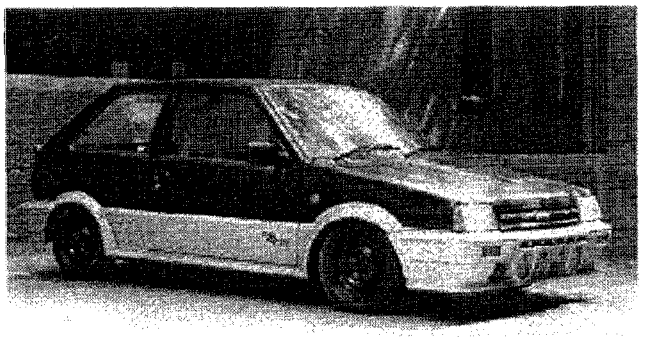

Fig.A-1 UOT Electric March (Todai Sangatsu Go)

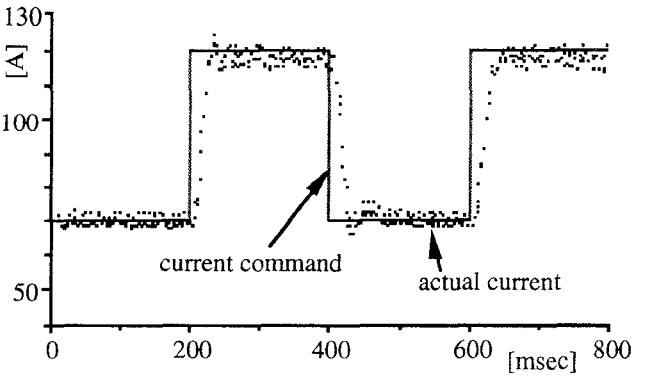

Fig.A-3. Basic experiment on the current response

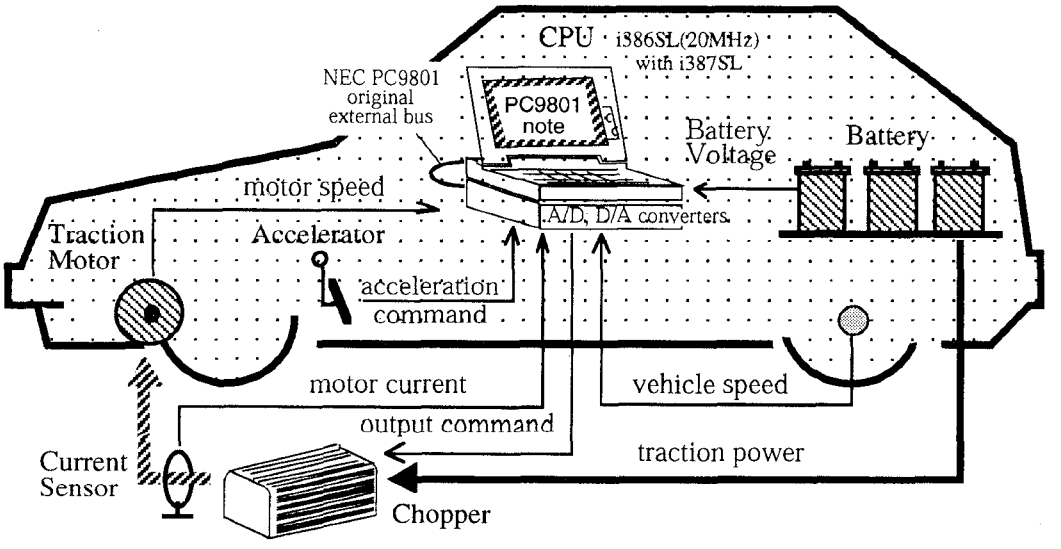

Fig.A-2 Configuration of UOT Electric March

A High Performance Drive System for Electric Vehicle

Yoshinobu Sato, Kouetsu Fujita, Takao Yanase, Shigenori Kinoshita, *Kenji Endo

Fuji Electric Corporate R&D , Ltd.
1,Fuji-machi, Hino 191 ,Japan
Fax: +81-0425-86-9665 , Phone: +81-0425-1102

*Fuji Electric Corporate R&D , Ltd.
1-1 Tanabe-shinden, Kawasaki-ku
Kawasaki, Kanagawa 210, Japan

Abstract – **We have developed a high performance drive system which has satisfied high efficiency, small size and high productively. The traction motor is a simple structure with a cylindrical magnet using a silicone glue. And for the field weakening control, the optimal Xd is realized. To minimize a current, the torque control method without the voltage margin is adopted. And the PWM control method which uses the voltage of a battery effectively is also adopted.**

In this paper, details of the optimal design of a permanent magnet motor and control techniques are explained, and specifications of the system and testing results are described.

I . INTRODUCTION

In recent years, as the measures of the environment problem, the development of the electric vehicle (EV) is extensively done. For drive system, there are some requirements, high efficiency, small size, wide constant power operation range and low cost.

To improve system efficiency, the permanent magnet synchronous motor as a traction motor has been applied. The field weakening control for a wide constant power control operation with the permanent magnet motor has been used. It is known that the air gap flux can be weakened by the d-axis current (Id) and the operation range of the field weakening control depends on the armature reactance (Xd) [1]-[4].

In case of a surface permanent magnet motor (SPM) with a cylindrical magnet is used as a traction motor, it is necessary to give considerations with Id and Xd for the field weakening control.

The SPM has no saliency, and the Id doesn't contribute to the output torque. So it is need to minimize the Id for the improvement of the system efficiency.

And the cylindrical magnet needs a certain thickness to secure enough strength and to prevent demagnetization. The permeability of the magnet is as same as the air. So the effective air gap is wide and the Xd is small. Therefore it isn't easy for the operation range of the field weakening control to become wide.

In this paper, we describe the optimal design of the motor and the control methods for a drive system.

II . THE FEATURES OF THE DRIVE SYSTEM

We have developed a high performance drive system with a traction motor and an inverter.

The appearance of the drive system is shown in Fig.1 and the specifications are shown in table 1. The efficiency map of the drive system is shown in Fig.2.

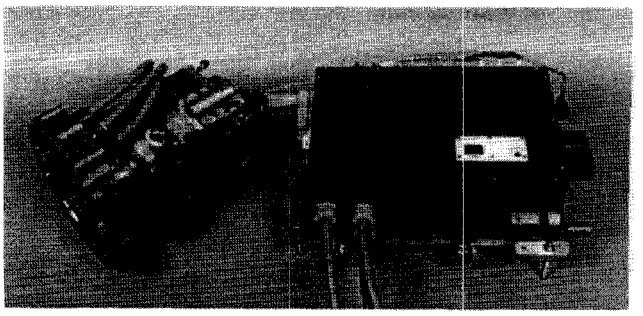

Fig.1. The appearance of the drive system.

TABLE I
SPECIFICATIONS OF DRIVE SYSTEM

MOTOR		
Max. Output (kW)		60
Rated Output (kW)		36
Max. Torque (N·m)		180
Rated Torque (N·m)		108
Max. Speed (r/min)		13,000
Rated Speed (r/min)		3,400
Size	(mm)	ϕ 220×324
Mass	(kg)	40
INVERTER		
Device		IGBT (600V, 400A)
Switching Frequency (kHz)		10
Input Voltage (V)		288~336
Max. Output Current RMS (A)		240

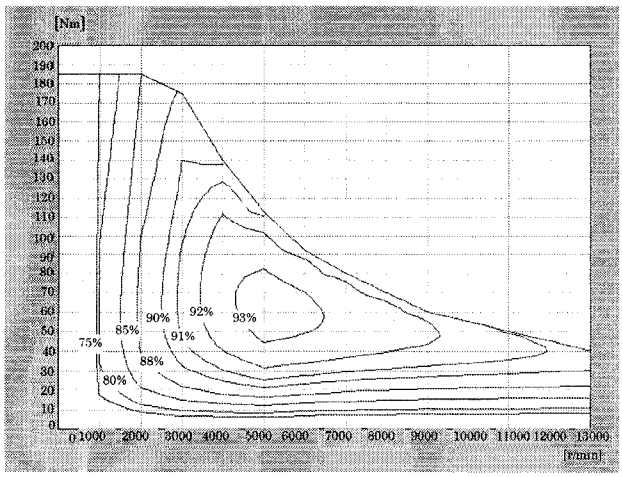

Fig.2. The system efficiency map.

III. Optimal Design of The Motor

A cylindrical magnet in the SPM is usually glued to the rotor surface and further is reinforced with using a binding system against a centrifugal force.

To withstand a centrifugal force by the strength of the magnet itself, the magnet with the high mechanical strength is adopted. To fix the magnet and to buffer against the difference of the thermal expansion between the magnet and the rotor core, a silicone glue is adopted. So we have developed the simple motor structure without a binding system. The structure of the motor is shown in Fig.3. No use of the binding system increases the magnetic density at the air gap, and the size of the motor becomes small.

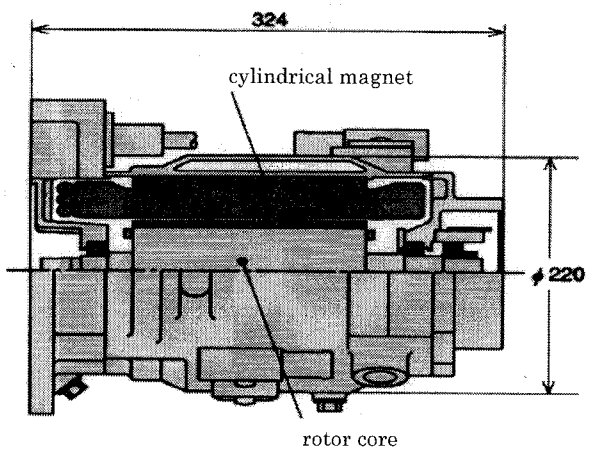

Fig.3. The structure of the motor.

The Xd should be designed with depending on the magnetic flux (ϕ_m) to use the field weakening control in the wide operation range. So we consider the components of Xd not only to meet the Xd but also to decrease losses and to make the size of motor small.

The Xd is composed armature reaction reactance (Xad) and armature leakage reactance (Xl). When the Xad is large, the magnet becomes easy to be demagnetized and to be overheated by carrier losses. So it is desired to make the Xad small and the Xl large for the meeting the Xd. The former is accomplished with the increasing the number of poles and the latter is also accomplished with the extending slot depth.

IV. Control System for The Motor

The block diagram of the control system is shown in Fig.4. The features of the control system are the torque control method and the PWM control method. These control methods make a current minimum in all the operation ranges to improve the efficiency of the drive system.

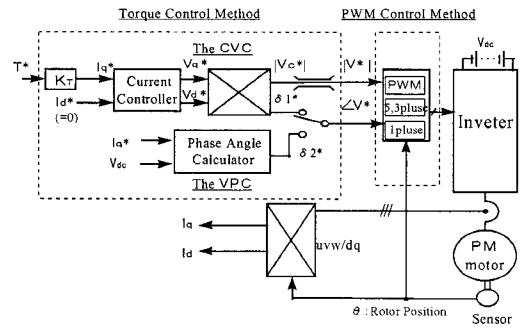

Fig.4. The block diagram of the control system.

A. Torque Control Method

The torque control method calculates the output voltage command vector (V*) from the torque command (τ^*) and consists of the current vector control (CVC) and the voltage phase control (VPC). And these controls are used properly in response to the operation condition.

The phasor diagram of the torque control is shown in Fig.5. The semicircle line shows the maximum fundamental voltage of the inverter (Vmax).

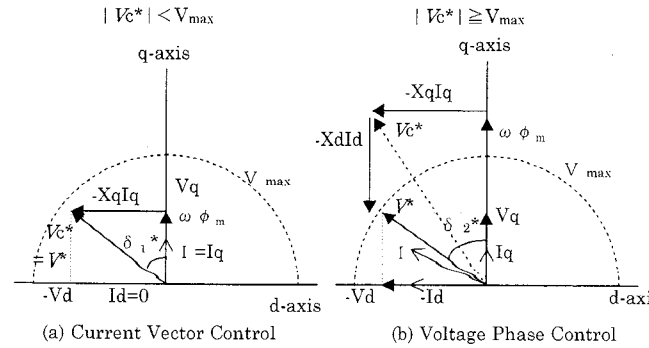

Fig.5. Phasor diagram of the torque control.

The CVC keeps the d-axis current zero (Id=0) to become maximum the ratio of a torque to a current and maintains the q-axis current (Iq) depending on the torque command. So the voltage command

vector (V*) is equal to the CVC voltage vector (Vc*) calculated at the current controller shown in Fig.4. The amplitude of the Vc* (|Vc*|) and the phase of the Vc* (δ_1*) are calculated.

$$\tau^* = P \cdot \phi_m I q^* \quad (1)$$

$$\begin{bmatrix} Vd^* \\ Vq^* \end{bmatrix} = \begin{bmatrix} R & -Xq \\ Xd & R \end{bmatrix} \begin{bmatrix} I d^* \\ I q^* \end{bmatrix} + \begin{bmatrix} 0 \\ \omega \phi_m \end{bmatrix} \quad (2)$$

$$|Vc^*| = \sqrt{Vd^{*2} + Vq^{*2}} \quad (3)$$

$$\delta_1^* = Tan^{-1}\left(Vd^*/Vq^*\right) \quad (4)$$

When PI regulators are used for a current controller, so as not to be saturated for integrators, a voltage margin about 10% of the maximum output voltage is usually needed.

To make this voltage margin unnecessary, P regulators are used for the current controller. A steady-state error in the P regulators is decreased with using the compensators for terms of the EMF and impedance drops.

The VPC always keeps the amplitude of the voltage command vector (|V*|) as same as the Vmax. And as the phase of the voltage command vector (∠ V*), the VPC phase (δ_2*) is calculated at the phase angle calculator shown in Fig.4 and as follows.

$$\delta_2^* = Sin^{-1}\left(\frac{Vd^*}{V_{max}}\right) = Sin^{-1}\left(\frac{-Xq\, I q^*}{V_{max}}\right) \quad (5)$$

$$Vq = V_{max} Cos\ (\delta_2^*) \quad (6)$$

The d-axis voltage (Vd) outputs preferential to maintain the Iq depending on the torque command.

The output torque is controlled with only using ∠ V*, by the delay of the measuring of the rotor angle and the calculating of the V*, the angle errors reduce the output torque linearity especially at high speed. Therefore, the ∠ V* is compensated depending on the motor speed.

Making-up the voltage difference between the EMF and the q-axis voltage (Vq) (6), the Id becomes minimum automatically. So It is not necessary to calculate the d-axis current command in response to the operating situation with load and speed, and a copper loss is decreased.

The judgment of the switching-over of the CVC and the VPC goes in comparing the Vmax and the |Vc*|.

At low speed, the |Vc*| is smaller than the Vmax, the CVC is used for the torque control.

As the motor speed rises and the |Vc*| is larger than or equal the Vmax, the torque control method is switched over from the CVC to the VPC. The |V*| is limited to the Vmax. And as the ∠ V*, the δ_2* is used instead of the δ_1* as shown in Fig.4.

As using the P regulators in the current controller, there is no problem of the saturation for the regulators. So the transition from the VPC to the CVC is also smooth.

As the battery voltage (V_{dc}) is changed, the torque control methods are also switched properly, because of the Vmax is adjusted in response to the V_{dc}.

The characteristic of torque when switching-over from the CVC to the VPC is shown in Fig.6.

There is no change of torque before and after the transition. It shows that the transition of the torque control methods is smooth.

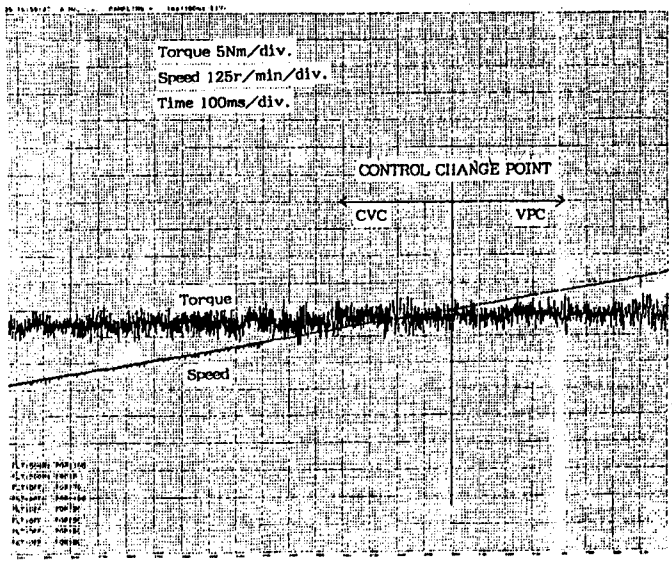

Fig.6. The characteristic of torque when switching-over form the CVC to the VPC.

B. PWM Control Method

The relationship between the |V*| and the output voltage is shown Fig.7.

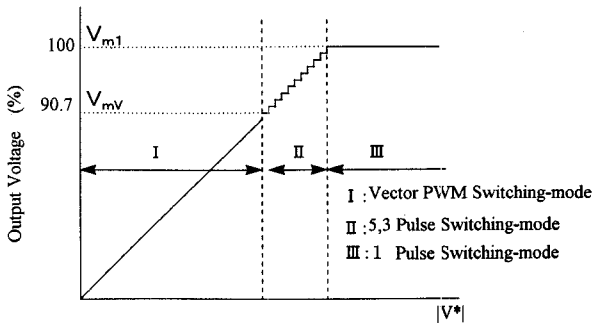

Fig.7. Relationship between the |V*| and the output voltage.

The features of the PWM control method is using the vector PWM switching-mode which has no low order harmonics and the 1 pulse switching-mode which is the maximum fundamental voltage of the voltage-fed inverter.

The fundamental voltage of the 1 pulse switching-mode (V_{m1}) and the maximum fundamental voltage of the vector PWM switching-mode (V_{mv}) are given as follows.

$$V_{m1} = \left(\sqrt{6}/\pi\right) V_{dc} \quad (=100\%) \qquad (7)$$

$$V_{mv} = \left(1/\sqrt{2}\right) V_{dc} \quad (90.7\%) \qquad (8)$$

To interpolate the output voltage value between the vector PWM switching-mode and the 1 pulse switching-mode, the 5,3 pulse switching-mode is also used.

The output voltage using the 1 pulse switching-mode, can be 10% increased compared with only using the vector PWM switching-mode. And the Id and the switching number of time are decreased. So this PWM control method has an greatly effect in the increase of the system efficiency with decreasing the copper loss and the switching loss.

But, the 1 pulse switching-mode has some problems which are caused by the harmonics. The high frequency components are inhibited with the impedance of the motor winding. So the 1 pulse switching-mode should be used at high speed when the influence of harmonics is enough decreased .

The current waveform and the values of output torque with using the vector PWM switching-mode and 1 pulse switching-mode are shown in Fig.8.

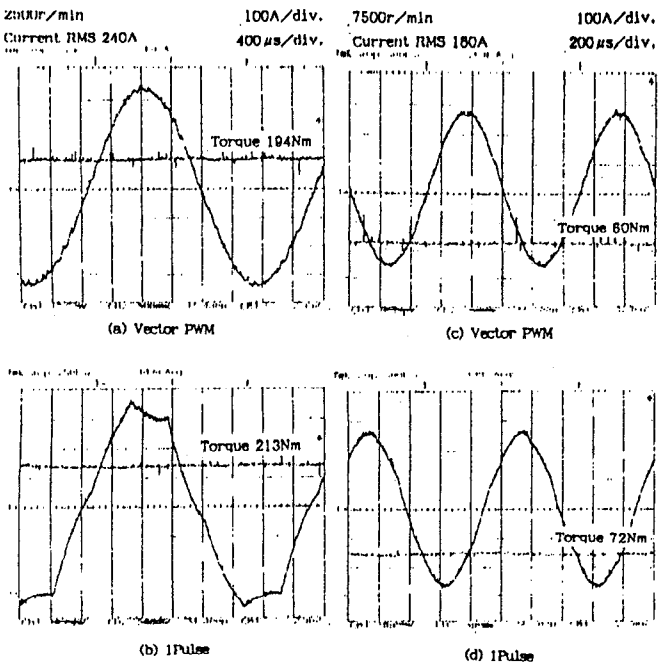

Fig.8. Oscillographs of current waveform and output torque.

At the low speed (2,500r/min), the output torque of the 1 pulse switching-mode is increasing by 10%, but a lot of harmonics are contained in the current.

At the high speed (7,500r/min), the output torque of the 1 pulse switching-mode is increasing by 20%, and the current waveform of the 1 pulse switching-mode is approximately equal to the vector PWM.

Using this PWM control method, it confirmed an increase with 5% of system efficiency at high speed compared with using only the vector PWM switching-mode.

These data about the PWM control method are measured with another motor (max. speed 8000r/min, max. output 60kW, 16 poles)

V. CONCLUSION

In this paper, the high performance drive system for electric vehicle is introduced.

As using the high performance cylindrical magnet and fixing with the silicone glue, the simple rotor structure is realized without a bind. And the number of the poles and the slot shape are designed for the optimal Xd which is required from the field weakening control to operate wide constant power speed range.

To minimize a current in all the operation ranges, two torque control methods are adopted. At low speed, the current vector control keeps d-axis current zero, and at high speed, the voltage phase control automatically minimizes the d-axis current for the field weakening control. And the 1 pulse switching-mode which outputs the maximum fundamental voltage in the voltage-fed inverter is also adopted to use the voltage of battery effectively and to decrease the switching loss.

By combining above these techniques, the drive system for EV with maximum speed 13,000 r/min, maximum output 60kW, maximum system efficiency over 93% is developed and the performance is confirmed by the experiment.

REFERENCE

[1] S. Morimoto, Y. Takeda, T. Hirasa, K.Taniguchi, "Expansion of Operating Limits for Permanent Magnet Motor by Current Vector Control Considering Inverter Capacity," IEEE Trans. Ind. Appl.,vol.26, pp. 866-871, Sep./Oct. 1990.

[2] T. Jahns, "Flux-Weakening Regime Operation of an Interior Permanent-Magnet Synchronous Motor Drive," IEEE Trans. Ind. Appl. vol. 23, pp. 681-689, July/Aug. 1987.

[3] B. K. Bose, " A High-Performance Inverter-Fed Drive System of an Interior Permanent Magnet Synchronous Machine," IEEE Trans. Ind. Appl., vol. 24, pp. 987-997, Nov./Dec. 1988

[4] Y. Takeda, S. Morimoto, K.Ohyama, A. Yamagiwa, "Comparison of Control Characteristics of Permanent Magnet Synchronous Motor with Several Rotor Configuration," Transaction of I.E.E. JAPAN, vol. 114-D, No.6,1994

Energy Saving Vector Control Strategies for Electric Vehicle Motor Drives

Sadegh Vaez,
V. I. John, Senior Member IEEE,
Department of Electrical & Computer Engineering,
Queen's University, Kingston, ON, Canada, K7L3N6

M. A. Rahman, Fellow IEEE,
Faculty of Engineering & Applied Science,
Memorial University of Newfoundland,
St. John's, NF, Canada, A1B3X5

Abstract—**The applications of different energy saving vector control strategies to motor drives used in the electric vehicle (EV) are studied. The performance of an interior permanent magnet (IPM) motor drive under an off-line energy saving control over a typical EV driving cycle is presented. Discussing the difficulties and limitations of the off-line, and currently available on-line energy saving methods, an advanced on-line energy saving control strategy is proposed for EV applications. The strategy is based on an adaptive current vector control. The performance of an IPM motor drive under the proposed control strategy is evaluated experimentally. Test results are given to prove the validity of this strategy for energy saving in the motor drive.**

I. INTRODUCTION

A renewed interest in the electric vehicle (EV) has been revived in recent years which seems to be more serious and more fruitful than ever before [1]. Almost all major car makers all over the word have programs on the EV in hand and a number of major improvements like fast battery charging techniques, high power high efficiency, light weight motors and controllers have been reported [2]-[5]. The mass production and market entry have also been initiated recently. However, there are major obstacles yet to be overcome before there will be public acceptance. The EV range is not sufficient and the performance can not compete with the one easily obtained by internal combustion engine cars. The EV range and performance greatly depend on the battery and on the efficiency of propulsion system. The interior permanent magnet (IPM) motors have shown to perform well in EV propulsion systems due to their potential high efficiency, low weight and small size [6]. However their efficiency does not remain high under the varying operating conditions as required in EV applications. A dedicated control strategy is needed to maintain maximum efficiency (minimum loss) and save energy [7].

Two energy saving control strategies are studied here for IPM motor drives and their performances are evaluated based on the requirements of EVs. It is shown that the off-line method is fast and provides smooth operation of the motor drive. However it needs a detailed machine model and suffers from parameter dependency. On the other hand drawbacks and limitations of on-line energy saving methods, as presented in the literature, prevent their applications in EV motor drives.

In this paper a new on-line adaptive energy saving control strategy is proposed which is suitable for EV applications. The proposed strategy is implemented on a DSP board and applied to an experimental IPM motor drive to confirm its ability to save the available energy in the EV battery and extend the range of EV.

II. MACHINE MODEL

Assuming sinusoidal voltage, current and flux, an IPM motor in steady state can be represented by a d-q axis equivalent circuit in the synchronously rotating reference frame as shown in Fig. 1. The conventional notations are used for the presentation of model variables and parameters

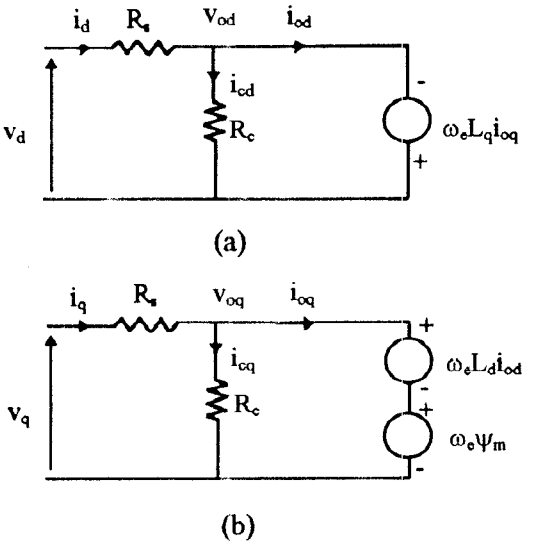

Fig. 1. Equivalent circuit of an IPM motor in synchronously rotating reference frame, (a) d-axis circuit, (b) q-axis circuit.

as defined in the Appendix. According to Fig. 1 the voltage equations are presented in terms of i_{oq} and i_{od}, the torque producing components of q- and d-axis stator currents i_q and i_d respectively, as follows:

$$v_d = R_s i_{od} + \left(\frac{R_s}{R_c} - 1\right)\omega_e L_q i_{oq} \quad (1)$$

$$v_q = R_s i_{oq} + \left(\frac{R_s}{R_c} + 1\right)\omega_e L_d i_{od} + \left(\frac{R_s}{R_c} + 1\right)\omega_e \psi_m \quad (2)$$

Also by referring to Fig. 1 the following current equations can be written:

$$i_q = i_{oq} + i_{cq}, \tag{3}$$

$$i_{cd} = -\frac{\omega_e L_q i_{oq}}{R_c}, \tag{4}$$

$$i_{cq} = \frac{\omega_e(\psi_m + L_d i_{od})}{R_c}. \tag{5}$$

The developed torque is given by:

$$T_e = \frac{3}{2} i_{oq} P[\psi_m + (L_d - L_q) i_{od}]. \tag{6}$$

II. Analysis of Motor Loss

Motor loss consists of several components among them the electrical loss plays the most important role. The motor efficiency can be improved if the electrical loss reduces. In this section the formulation of electrical loss, the condition under which the electrical is minimized and the effects of parameter variations are discussed.

A. Formulation of Electrical Loss

Referring to the machine model presented above, the motor electrical loss W_E as a combination of copper loss and iron loss can be found as:

$$W_E = \frac{3}{2} R_s (i_d^2 + i_q^2) + \frac{3}{2} R_c (i_{cd}^2 + i_{cq}^2). \tag{7}$$

where the first term is the motor copper loss and the second term is the motor iron loss. At a specific value of the motor speed and load, and assuming constant motor parameters, it can be shown that the electrical loss is a convex function of d-axis component of stator current i_d. This is done by substituting all the current components in (7) in terms of i_d and then plotting W_E versus i_d. However the calculations are quite lengthy and cumbersome except numerical calculations are employed or a software with the capability of analytical computation is used. A simpler approach is to represent the electrical loss in terms of i_{od}. In this case (3)-(6) are used to calculate all the current components in (7) in terms of i_{od}, the motor speed and torque [7]. At a specific operating point, where the motor speed and torque are constant, W_E is a function of one variable only i.e. i_{od}. This function is depicted in Fig. 2 by a dashed line. The shape of W_E versus i_{od} stems from the fact that the stator current versus i_{od} in permanent magnet synchronous motors is a V-shaped curve. The optimal value of i_{od} corresponding to a minimum W_E can be found by solving the derivative of W_E with respect to i_{od} [7].

B. Parameter Variations

In general the motor parameters vary over wide ranges depending on the operating conditions and the ambient temperature. In many IPM motors these variations are dominant due to the motor construction [8]. In particular L_q, L_d and magnet flux are affected by saturation. R_s changes due to a temperature rise. R_c varies depending on the motor speed, and also due to the saturation in the iron bridges between rotor magnets. These variations affect the motor characteristics and performance including the minimum loss operation. A way of accounting for parameter variations is to model motor parameters in terms of motor variables e.g. stator current components. The relevant relations expressing L_q, L_d and magnet flux as functions of i_{od} and i_{oq} can be found by experimental measurements. R_c can also be presented as a function of motor frequency to reflect both components of iron loss i.e. hysteresis loss and eddy current loss.

Using variable parameters in the equivalent circuit of Fig. 1, it is still possible to model W_E as a function of i_{od} only and find out the optimal value of i_{od}. The lengthy calculations carried out by the use of a commercial software featuring symbolic calculations are not shown here. However, the functions representing variable parameters and the motor electrical loss with these variations are presented.

Iron loss consists of eddy current loss and hysteresis loss. A constant iron loss resistance, R_c in Fig. 1, can represent the eddy current loss rather accurately but it is not a good representative for the hysteresis loss. The true value of R_c is difficult to obtain, However, an approximation of R_c as a function of motor frequency can be found which models both components of iron loss as [9]:

$$R_c = R_{cn} \frac{K + 1/f_n}{K + 1/f} \tag{8}$$

where R_{cn} is the value of R_c at the rated speed, f is the motor electrical frequency, f_n is the rated motor frequency and K is a constant. W_E versus i_{od} for machine #1 (see Appendix for the motor data) is depicted in Fig. 2 with R_c as in (8) by a solid line and with constant $R_c=R_{cn}$ by a dashed line. It can be seen that the optimal values of i_{od} are quite different. W_E is also depicted in Fig. 2 with elevated $R_s=2R_{sn}$ by a doted line where R_{sn} is the nominal value of stator resistance. The minimum value of W_E shifts towards a less negative value of i_{od} due to an increase in the copper loss when R_s increases. The increase in R_s is caused by different factors including a rise in the ambient temperature.

Magnetic saturation is also a major source of parameter variations. Saturation depends on the motor design. For machines with high energy permanent magnets and small air gap, as in modern IPM motors, the effects of saturation are significant [8]. Saturation in general tends to reduce

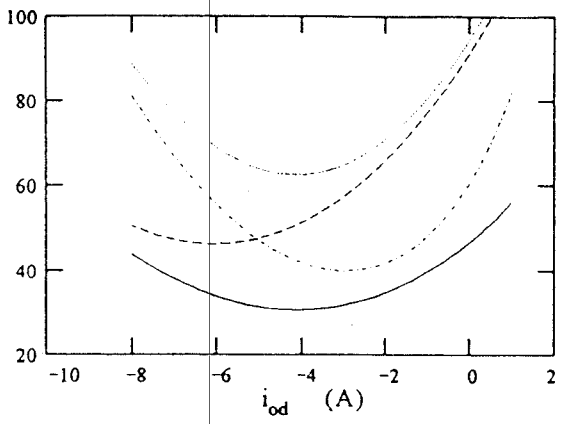

Fig. 2. Electrical loss (Watts) versus i_{od} for machine #1; constant parameters (dashed), variable R_c (solid), $R_s=2R_{sn}$ (dotted), variable parameters (dot-dashed).

machine inductances and the magnet flux. Saturation is due to the flux produced by the stator current. Therefore it can be considered in the d-q axis equivalent circuit by substituting constant inductance L_q and L_d and magnet flux by functions of stator current components [8]. In IPM motors saturation mainly occurs on the q-axis. Therefore here only L_q is modeled as a function of i_{oq} by the following equation:

$$L_q = L_q^0(1 - Ji_{oq}) \qquad (9)$$

where L_q^0 is the value of L_q at $i_{oq}=0$ and J is a constant representing the strength of saturation. Having L_q at the rated operating point, L_{qn}, from the motor data in the Appendix, and assuming that L_q varies between $2L_{qn}$ and $1/2\ L_{qn}$ as suggested in [7]. L_q^0 and J are found as 45.56 mH and 0.077 respectively. It is assumed that the minimum and maximum values of L_q occur at $i_{oq}=0$ A and $i_{oq}=13$ A respectively. Substituting i_{oq} in terms of i_{od} into (9) and then substituting the result into the loss equation results in W_E with saturation as a function of i_{od}.

By using (8), (9) and $R_s=2R_{sn}$ the effects of simultaneous variation of parameters on W_E can be considered. W_E versus i_{od} with variable parameters is shown in Fig. 2 by a dotted line where L_q, R_c and R_s in (7) are replaced by (8), (9) and $2R_{sn}$. It is evident that the combination of changes in different motor parameters adds to the difference between the values of optimal i_{od} with and without parameter variations. The important implication of these results is the fact that the optimal value of i_{od} is greatly parameter dependent. A further consideration confirms however, that the parameter dependency is minimal when the motor works under the rated values of speed and torque.

IV. Off-Line Energy Saving Strategy

An off-line current vector control can be applied to IPM motors to achieve energy saving [7]. In this method the stator current components are controlled in such a way that the d-axis current is at its optimal value all the time. The optimal values of i_d and the corresponding values of i_q are calculated off-Line for many operating points. The calculations are based on the procedure presented in the previous section. The motor electrical loss is formulated in terms of i_d by using the motor equivalent circuit of Fig. 1. Solving the derivative of this loss with respect to i_d at each operating point (a specific motor speed and load) gives the optimal value of i_d. Having this optimal current and the motor torque, the corresponding i_q can be found from (6) [7]. In practice the optimal values of i_d and the corresponding values of i_q for many values of motor speed are stored in a memory as a look-up table. The look-up table gives an output (optimal i_d corresponding to a minimum motor loss) in response to a pair of inputs i.e. motor speed and i_q command. The latter signal in turn is the output of the speed controller. The out put from the look-up table in conjunction with the speed controller output, i.e. the d- and q-axis current commands respectively, are applied to the motor current controllers. In this way the energy saving operation of the motor is ensured at every operating point.

Here the off-line energy saving strategy is applied to motor #1. The off-line calculations for finding the optimal values of i_d are done numerically. The motor performance under the off-line strategy is studied by simulation over a typical electric vehicle driving cycle. The following assumptions are made in the simulation:

i) the losses other than motor electrical loss are not considered.

ii) the driving cycle used is J227a-D schedule consisting of 28 seconds of acceleration period from stop to a maximum speed followed by 50 seconds of cruising at the maximum speed, 10 seconds of coasting and 9 seconds of braking. There is also an idle period of 25 seconds at the end of the driving cycle.

iii) the tractive force needed for an EV is scaled down to be compatible with the motor rating. The motor torque during acceleration followed by a constant torque equal to 25% of the rated torque during cruising is shown in Fig. 3. The optimal values of i_d corresponding to the same torque profile are also shown in Fig. 3. Torque during coasting is zero and during braking is negative.

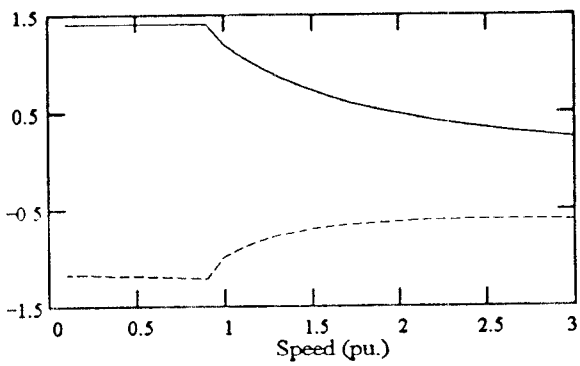

Fig. 3. Torque (pu.) solid, and i_{od} (pu.) dashed versus motor speed.

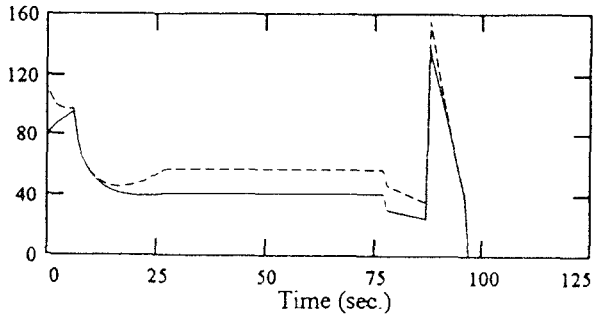

Fig. 4. Motor electrical loss under off-line energy saving control strategy over J227a-D electric vehicle driving cycle; with (solid), and without (dashed) parameter variations.

Fig. 4 shows the motor electrical loss over the entire driving cycle in two cases. In both cases W_E is calculated based on the variable motor parameters as described in the previous section to resemble the actual situation. However, the dashed line shows W_E for case 1 where the off-line computation of the optimal i_d is carried out based on a machine model with constant parameters. Whereas the solid line corresponds to the case 2 where the optimal values of i_d are calculated based on a varying parameter model. It is evident that the case 1 does not give a minimum loss operation. As a result not much energy is saved. On the other hand the case 2 shows a substantial energy saving due to a reduced W_E.

In spite of the advantages of case 2 the design and implementation of this case face some difficulties in practice. In fact developing a variable parameter model for the calculation of optimal i_d values is complicated due to the extensive measurement and modeling needed. This task becomes more difficult in the situation where some motor parameters have multiple dependencies. For instance R_c may depend on both motor frequency and i_d. Therefore it is concluded that an off-line energy saving control strategy is not suitable for motors with parameter variations working under wide range of operating conditions as in an EV.

V. On-Line Energy Saving Strategy

In on-line energy saving strategy, in contrast to the off-line approach, the optimum value of control variable corresponding to a minimum loss is found by an on-line search. A common practice in energy saving control of induction machines is to apply a step change to a control variable e.g. the motor flux or d-axis component of stator current. Then wait for some time, long enough for the motor to pass the subsequent transient and come to a fairly steady state situation. Then compare the input power values before and after the change made in the control variable. If the power reduces, another step is applied to the control variable in the same direction. Otherwise the second step is applied in the opposite direction. This procedure continues until a step change in the control variable does not change the input power. This means that a minimum input power has been obtained. The motor output power is kept constant during the search by a regulator. This strategy seems very attractive since it does not need a system loss model. Furthermore the motor parameter variations are taken into account naturally resulting in more energy saving. The strategy is successfully applied to induction and synchronous motor drives resulting different degrees of energy saving depending on the motor operating condition [10]-[14].

In spite of these features an important deficiency of on-line approach, when applied to high performance applications, is a long search time it takes to reach the minimum input power [10]-[14]. In many applications with frequent changes in operating conditions (speed and load), e.g. electric vehicles, the steady state period is short and there is not enough time to reach a minimum input power condition. This is because the search for an optimum value of the control variable starts only after the machine reaches an steady state. During transient states, when the operating point is changing, the reduction in input power cannot be used as a criterion for energy saving. Even if the steady state period permits finding of the minimum input power, some energy is lost during a long search time. If the transient state is repeated frequently as in an EV, the total energy saving may not be significant.

The long search time is mainly caused by the stepwise change of the control variable and the sluggish response of the regulator responsible for maintaining the output power. Avoiding the stepwise change of control variable eliminates the relatively long transient after each step and subsequent wait period between steps resulting a faster and smoother energy saving operation.

Here an on-line energy saving strategy is proposed for IPM motor drives in which the stepwise change of control variable, the d-axis current command i_d^*, is replaced by a contiguous adjustment of i_d^* towards its optimal value. A linear pattern of change for i_d^* with respect to time is considered. The control variable therefore follows a ramp trajectory until it reaches the optimal i_d^*. Also a new method is used for determining the changes in the input power. The inverter DC input power, P_{DC}, is monitored continuously inside a moving time window. Therefore as i_d^* varies contiguously the reduction in input power is determined at each instance by the difference between the two values at the beginning and at the end of the window.

A current vector control is designed based on the above concept and applied to a 1 hp, 4-pole, 3-phase, rare earth IPM motor. The motor specifications (Motor #2) are found in the Appendix. The control system is implemented using a TMS320C31 DSP based control board and undergoes extensive experimental tests. Details of the design and implementation are not elaborated here. However, the control system performance is described by referring to the experimental results presented in Fig. 5. During the transient state when the speed error is large the energy

saving control is off and the motor works under an original i_d resulting a desirable dynamics. Once the steady state speed reaches, the direction of change in d-axis current command i_d^* by which the input power is reduced is detected as shown in Fig. 4 (a)-(b). This is done by monitoring the input power variation in response to continuous change of i_d^* for a short period of time. Then i_d^* varies in the same direction towards its optimal value resulting a reduction in the input power towards a minimum input power as in Fig. 5 (c). The optimal value of i_d^* in this experiment is about zero due to saturation in rotor bridges between magnets. In contrast to other on-line energy saving methods the reduction in P_{DC} is fast and smooth due to a continuos pattern of i_d^*. The minimum input power is determined when the change in P_{DC} during a short interval falls below a limit. At this point the input power becomes flat meaning that a further change in i_d^* does not have a noticeable effect on the input power. A new mode of operation starts next in which i_d^* varies in a triangular manner by changing i_d^* for short periods in opposite directions repeatedly. This ensures an energy saving operation if the motor operating point changes slowly.

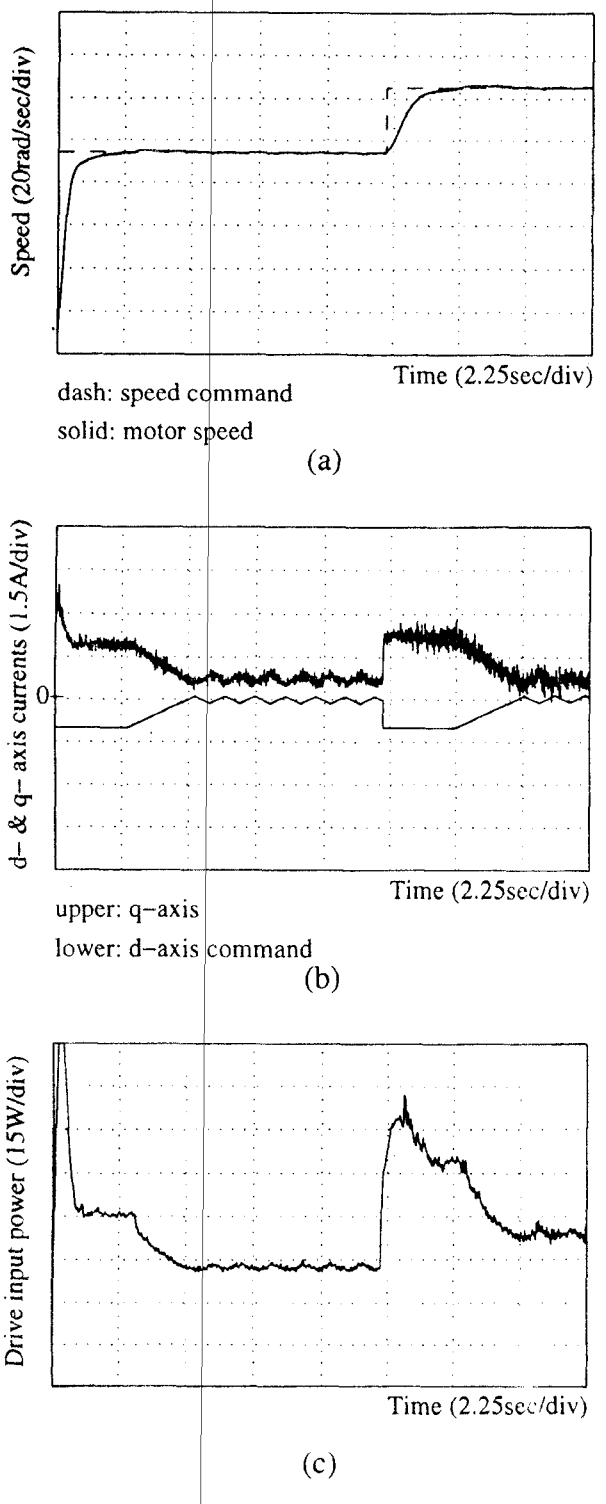

Fig. 5. Experimental results of the drive performance under the proposed on-line energy saving control strategy, (a) speed response, (b) current components, (c) drive DC input power.

A nonlinear speed compensator keeps the motor speed virtually unchanged in spite of the change in the reluctance torque caused by the change in i_d^*. This is done by increasing the effective speed error signal, applied to a PI speed controller, depending on the amount of change in i_d^*. The higher the change in i_d^* the higher is the effective speed error signal. This results in an output of the speed controller, i_q^*, which is affected by changes in i_d^*. Therefore the change in the reluctance torque caused by i_d^* is compensated by the change in the magnet torque caused by i_q^*. Therefore the total motor torque and thus the motor speed remain constant.

In the case of a rapid change in the speed signal caused by a change in the speed command (or motor load), the energy saving mode is terminated and the original d-axis current command is restored. This provides a desirable transient state. Once a new steady state is obtained the energy saving control becomes active again and a new minimum input power is achieved in a short time as seen in Fig. 5 (a)-(c). This ensures the validity of the proposed on-line energy saving contro strategy for EV applications.

VI. CONCLUSIONS

The loss analysis of IPM motors shows that a maximum energy saving point or a minimum loss condition can be achieved by current vector control. Under this condition, the variations in motor parameters substantially affect the motor loss resulting a non-minimum loss operation. Therefore an off-line energy saving control strategy, which depends strongly on motor parameters, may results in no energy saving due to the variation in the optimal value of i_d^* caused by parameter variations.

On the other hand existing on-line energy saving methods may not be fast enough for EV applications where the operating condition changes frequently.

The proposed on-line energy saving control strategy with the continuos pattern of change in i_d^*, instead of a stepwise change, in conjunction with a nonlinear speed controller overcomes the problem. This results in a fast and smooth

energy saving operation suitable for many applications including electric vehicles.

ACKNOWLEDGMENT

The first author gratefully acknowledges the assistance of the central office of Jahad Daneshgahi, Tehran, Iran during the preparation of final manuscript.

REFERENCES

[1] C. C. Chan, "An overview of electric vehicle technology," IEEE Power Eng. Review, pp. 9-14, Feb. 1992,.
[2] US Government Printing Office, "Status of Domestic electric vehicle development," 1993.
[3] OECD document, "Electric vehicle technology," 1993.
[4] M. Fukino, et al., "Development of an electric concept vehicle with a super quick charging system," Electric and Hybrid Vehicle technology, SAE, pp. 25-32, 1992.
[5] K. Faust, et al. "Introduction to BWM-E1," Electric and Hybrid Vehicle Technology, SAE, pp. 33-40, 1992
[6] B. K. Bose, "A microprocessor-based control and simulation of an advanced IPM synchronous machine drive system for electric vehicle propulsion," IEEE Trans., IE-35 pp. 574-559, Nov. 1988.
[7] S. Morimoto, et al. "Loss minimization control of permanent magnet synchronous motor drives," IEEE Trans., IE-41, pp. 511-517, Oct. 1994.
[8] P. H. Millor, "Estimation of parameters and performance of rare earth permanent magnet motors avoiding measurement of load angle," IEE Proc., Part B, Vol. 138, pp. 322-330, Nov. 1991.
[9] H. G. Kim, et al., "Optimal efficiency drive of a current source inverter fed induction motor by flux control," IEEE Trans., IA-20, pp.1453-59, 1984.
[10] D. S. Kirschen, et al., "On-line efficiency optimization of a variable frequency induction motor drive," IEEE Trans., IA-21, pp. 610-616, 1985.
[11] G. Kim, et al., "Control of induction motors for both high dynamic performance and high efficiency," IEEE Trans., IE-39, pp. 323-333, Aug. 1992
[12] G. C. D. Sousa, et al., "Fuzzy logic based on-line efficiency optimization control of an indirect vector-controlled induction motor drives," IEEE Trans., IE-42, pp. 192-198, April 1995.
[13] J. G. Cleland, et al., "Design of an efficiency optimization controller for inverter-fed AC induction motors," Proc. IAS-95, pp. 16-21.
[14] R. S. Colby, and D. W. Novotny, "An efficiency optimizing permanent magnet synchronous motor drive," IEEE Trans., IA-23, pp. 462-469, 1988.

APPENDIX

Motor Specifications

	Motor #1	Motor #2
Rated speed, rpm	2000	1800
Rated torque, Nm	1.67	3.96
Rated current, A	5	3
No. of pole pairs P	2	2
Stator resistance per phase R_s, Ω	0.54	1.93
Iron loss resistance R_c, Ω	240 (R_{cn})	330
D-axis inductance L_d, H	0.00872	0.04244
Q-axis inductance L_q, H	0.02278 (L_{qn})	0.07957
Magnet flux ψ_m, Wb	0.08794	0.314

Driving Characteristics of Anti-Directional-Twin-Rotary Motor on Electric Vehicle Simulator

Nobukazu Hoshi* Kantaro Yoshimoto Atsuo Kawamura**

Dept. of Electric. and Electro. Eng.
Ibaraki University
4-12-1 Nakanarusawa-cho, Hitachi-city
Ibaraki 316 JAPAN
E-mail: * star@ee.ibaraki.ac.jp

Dept. of Elec. and Comp. Eng.
Yokohama National University
79-5 Tokiwadai, Hodogaya-ku
Yokohama 240 JAPAN
E-mail: ** kawamura@kawalab.dnj.ynu.ac.jp

Abstract— **An Anti-Directional-Twin-Rotary Motor (ADTR-motor for abbreviation) were tested on an Electric Vehicle (EV for abbreviation) simulator, which behaves as if the ADTR-motor were installed in an EV, and was driven in the EV driving conditions. The ADTR-motor has the novel motor structure suitable for EV drives, in which the stator in the conventional motor was reformed to be movable, and the stator (outer rotor) rotates in the anti-direction of a rotor in the conventional motor(inner rotor). Several motor structures of ADTR-motor are considerable; permanent magnet (pm for abbreviation) type, induction motor (im for abbreviation) type and so on.**

In this paper, a driving characteristics of a pm type ADTR-motor on the EV simulator was measured and compared with the computer simulations using an EV simulator model.

I. Introduction

Recently, many engineers and researchers have been studied and investigated concerning electric vehicles(EV for abbreviation) for the environmental protection and a solution of the energy problem, and also, as a new future vehicle. There are many research fields regarding the electric vehicles, for example components of EV–battery, controller, motor and so on, and a novel powertrain such as hybrid drive. As the driving motor for EV, some new motors have been proposed, for example the in-wheel motor[1],and the anti-directional-twin-rotary motor(ADTR-motor for abbreviation)[2], [3]. The ADTR-motor has two rotors, one of which is a rotor (inner rotor) in the conventional motor, and the other of which is a stator (outer rotor) in the conventional motor [4]. Thus both rotors rotate in the anti-directions. Several motors are considerable for the ADTR-motor structure, for example, induction motor, brushless dc motor and so on. When an ADTR-motor drive is employed for the EV power train, one of the rotor direction is reversed by a reversing gear, and both wheels rotate at the same direction. Then, the ADTR-motor drive propels the two of the wheels of EV without a differential gear, and the torque of both wheels are automatically balanced. Only one pair of motor-inverter is required for this scheme.

The fundamental characteristics of im and pm type ADTR-motor have been reported in [2], [3], [5], [6]. In these papers, the inertia of both rotors are different in the prototype ADTR-motor. Then, the transient responses of the inner and the outer rotor are a little different.

In this paper, an EV simulator was constructed, in which the load torque was controlled as if the ADTR-motor were installed in the actual car and the car ran at the various conditions. Also, the transient characteristics of ADTR-motor was simulated using the four-mass model[7], [2], [3] and the EV model. Moreover, an prototype of pm type ADTR-motor was tested in the EV simulator.

II. Basic Characteristics of Anti-Directional-Twin-Rotary motor

A. Structure

Fig. 1 shows the illustration of a pm type ADTR-motor. ADTR-motor has two rotors, one of which is a rotor (inner rotor) in the conventional motor, and the other of which is a stator (outer rotor) in the conventional motor. The electricity is supplied through the slip ring to the outer rotor. Each rotor is independently supported by bearings, and independently rotates. The both rotors torque are automatically balanced in the structure in Fig. 1 [2], [3].

Some powertrains are considerable using the ADTR-motor. Fig. 2 is some of the powertrains using ADTR-motor. A reversing gear is necessary in Fig. 2(a), however the differential gearless power train can be constructed only with one pair of motor-inverter. A center differential gear is required in the four wheel drive of the conventional gasoline powered car. A center differential gearless powertrain in Fig. 2(b) or differential

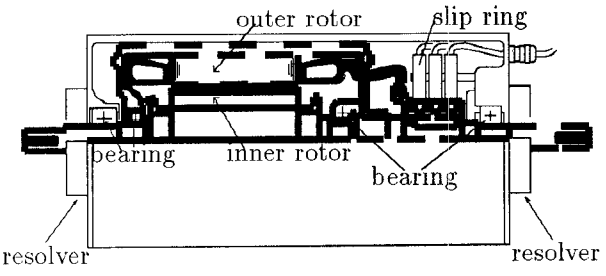

Fig. 1. Illustration of ADTR-motor

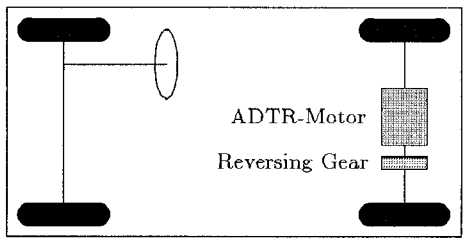

(a) 1 motor differential gearless 2WD

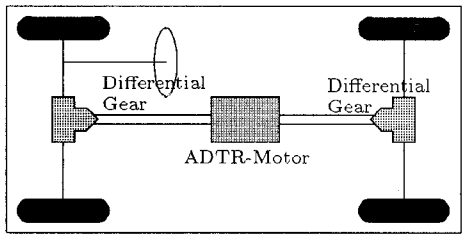

(b) 1 motor center differential gearless 4WD

Fig. 2. EV power trains using ADTR-motor

gearless powertrain of the four wheel drive could be also constructed using one or two of an ADTR-motor.

Several motor structures of ADTR-motor are considerable; pm type, im type and so on. In this paper, a prototype spm(surface mount pm) type ADTR-motor was tested on the EV simulator and driving characteristics were analyzed by the computer simulations considering EV driving conditions. The rating and parameters of the prototype spm type ADTR-motor are shown in Table I.

B. Basic Characteristics

The speed response and the torque response of the both rotors of spm type ADTR-motor were measured using the equipment as shown in Fig. 3. The rotor speeds were measured by tachometers attached to the dc motors, which were connected to the both sides of ADTR-motor as loads. The torque was measured by torque meters, which are located between the rotors and the dc motors.

In the fundamental characteristics measurements, the

TABLE I
RATING AND PARAMETERS OF THE SPM TYPE ADTR-MOTOR

Rated Output	1.8 (kW)
Rated Torque	5.73 (N-m)
Rated Speed	3000 (rpm)
Rated Current	5.15 (A)
Pole Number	6
Induced Voltage Constant K_E	34.56 (mV/rpm/phase)
Torque Constant K_t	1.11 (N-m/A)
Armature Resistance R_a	0.21 (Ω/phase at 20°C)
Armature Inductance L_a	1.0 (mH at 20°C)

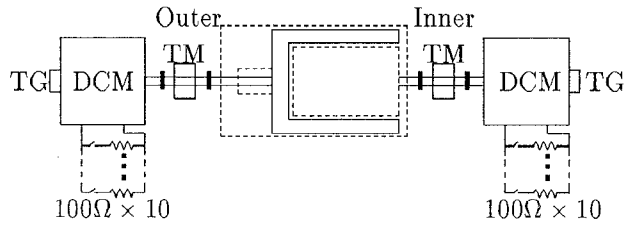

Fig. 3. PM Type ADTR-motor Driving System for Experiment

dc motors were used as generators, and the induced voltage of them was consumed by resistor banks as the loads. The load could be varied by changing the resistance.

Fig. 4 shows the speed response of the spm type ADTR-motor when the motor starts and stops. In this experiment, the d-axis voltage and the q-axis voltage were maintained constant.

The inner rotor motor speed increased faster than the outer rotor. The reason is that the inertia of the inner motor is less than that of the outer rotor in case of the structure in Fig. 1.

Fig. 5 (a) and (b) are the speed response and the torque response of the each rotor in spm type ADTR-motor under the torque control. Both responses were measured under the condition that after the steady-state speed is obtained, suddenly the outer rotor-side load was removed, and again connected. This experiment correspond to that one side wheel is suddenly slipped and recovered on an actual EV. The torque is step-wise changed, but soon balanced. This result shows that the ADTR-motor has the function of the differential gear.

Now, an EV simulator was constructed to study the effects for the inertia difference of the ADTR-motor when actual EV was propelled using ADTR-motor. In the EV simulator, the torque of the dc motors in Fig. 3 was controlled using the EV model.

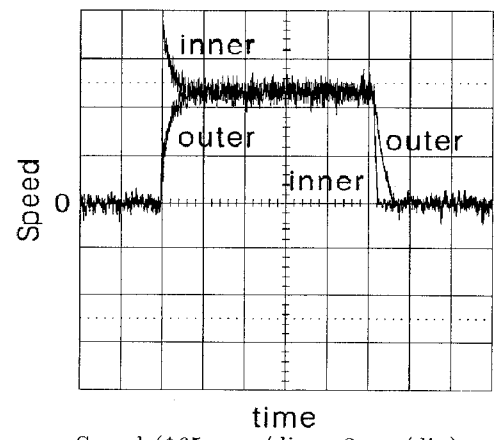

Speed (↑65 rpm/div,→2 sec/div)

Fig. 4. Transient Response without Torque Control (Starting and Stopping)

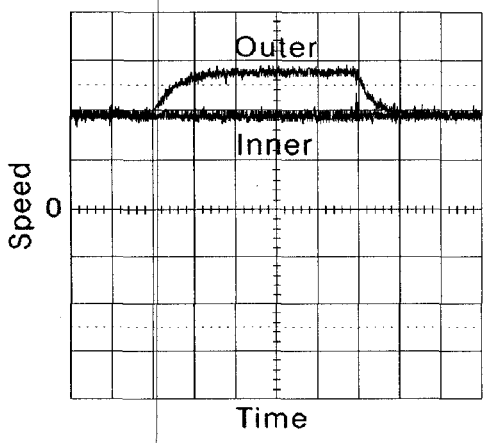

(a) Speed (↑65 rpm/div,→2 sec/div)

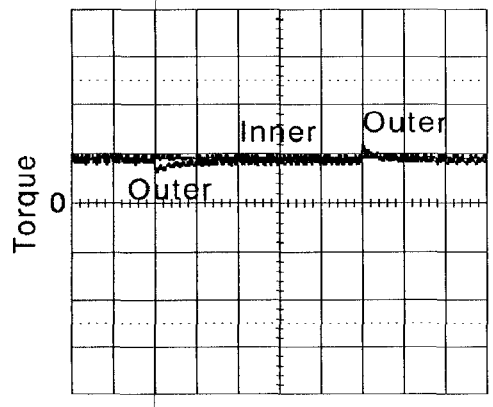

(b) Torque (↑ 0.196 Nm/div,→2 sec/div)

Fig. 5. Transient Response with Torque Control (Load Change)

III. Electric Vehicle Simulator(EV Simulator)

A. EV driving model using the ADTR-motor

At first, the EV model was considered before construction of the EV simulator. The motion equations for the vehicle body and one of the rotor are given as follows;

$$J\frac{d\omega}{dt} = T_e - Fr_w - B\omega \tag{1}$$

$$M\frac{dv}{dt} = F - F_R \tag{2}$$

$$F = \mu(s)Mg \tag{3}$$

where,

r_w	:	Radius of wheel
M	:	Total weight of the vehicle
T_e	:	Torque
g	:	Gravity accelerator constant
v	:	Vehicle speed
J	:	Inertia of Tire
μ	:	Friction coefficient between the wheel and road
B	:	Friction coefficient between the shaft and bearing
F	:	Thrust force
F_R	:	Road resistance force
ω	:	Rotor speed,

where, the load resistance force F_R is assumed to consist of the aerodynamics resistance, which is expressed as the next equation.

$$F_R = \frac{C_d S v^2}{16} \tag{4}$$

C_d is the air drag coefficient, and S is the front projection area.

Now, the friction coefficient μ is varied as a function of the speed difference between the vehicle and the wheel. Also, the friction coefficient μ is changed by the road condition; for example, driving in the rainy road or the fine road. On the EV simulator, this situation was simulated by changing the μ−slip curve. The speed difference s(slip speed) between the wheel and the vehicle is expressed as follows.

$$s = r_w\omega - v \tag{5}$$

In this paper, the road condition is not changed. The μ is approximated as (6) for simplification. Fig. 6 shows μ−slip curve obtained from (6).

$$\mu = \begin{cases} -(exp(0.54s) - exp(1.22s)) \\ \qquad\qquad (s \le 0) \\ exp(-0.54s) - exp(-1.22s) \\ \qquad\qquad (s > 0) \end{cases} \tag{6}$$

Fig. 7 shows the EV simulator model for the ADTR-motor drive in equations(1)-(6). The meshed part in

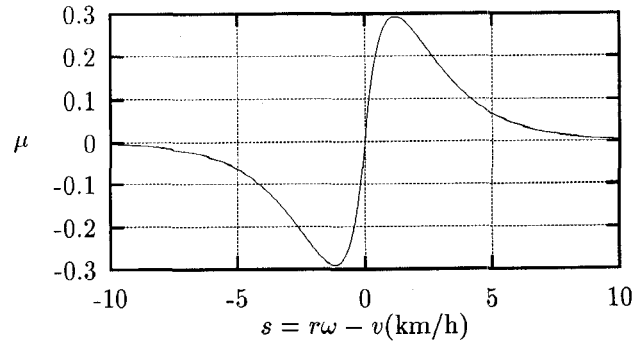

Fig. 6. Friction coefficient vs. slip

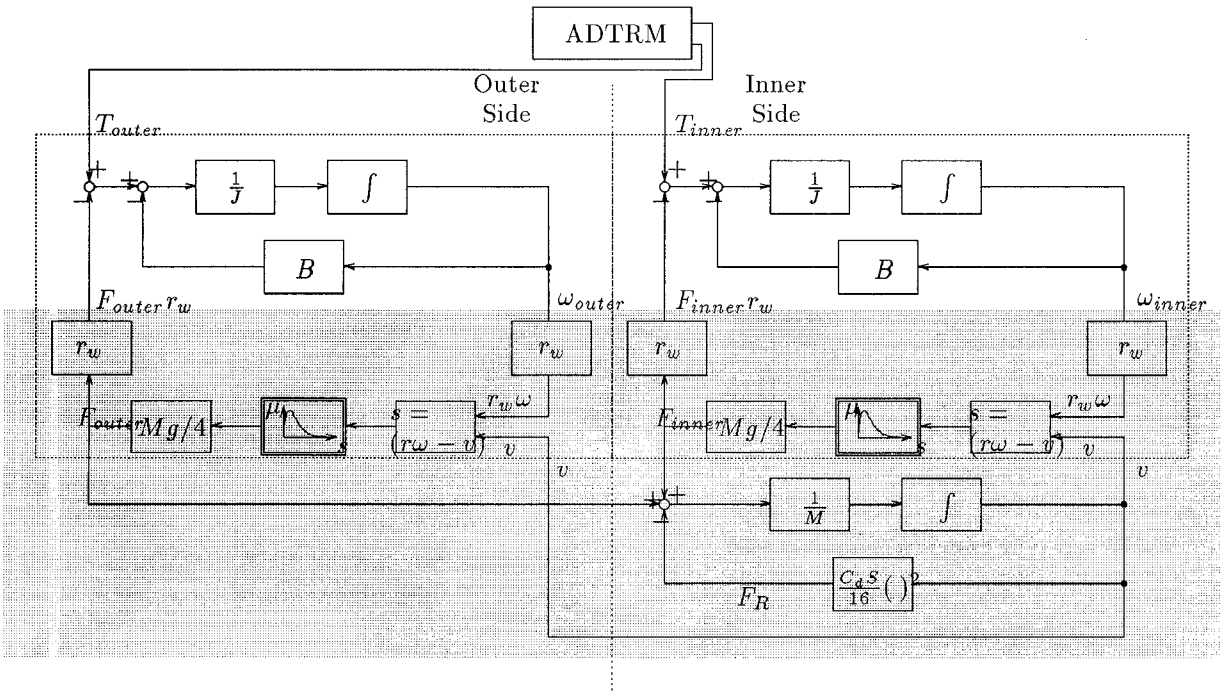

Fig. 7. EV simulator model

the figure is the EV simulator.

B. Algorithm of EV simulator and Realization

In the EV simulator, the following algorithm is computed.

1. The slip speed in (5) is calculated from the rotor speed and the vehicle speed.
2. The friction coefficient is calculated from the slip speed in (6), and the thrust force F is computed in (3).
3. The torque of the dc motor is adjusted to equal to the thrust force Fr_w. This is converted to the equivalent dc motor current reference.
4. The vehicle speed v is calculated in (2).

The hardware of the EV simulator is shown in Fig. 8. The motor torque is adjusted by the current regulators, using a power amplifier. The current reference in Fig. 8 is calculated by a personal computer(PC for abbreviation). The rotor speed is obtained through A/D converter. Then, PC calculates the thrust force(or current reference) following the above algorithm or in Fig. 7. Then, the current reference is output through the D/A converter to the current controller, which consists of analogue operation amplifiers and power amplifiers. Table II shows the hardware specification of the EV simulator.

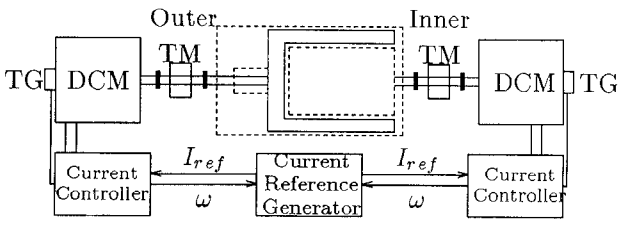

Fig. 8. EV simulator

C. Computer simulations

The transient response of ADTR-motor could be analyzed and simulated using the EV model in (1)–(6) with the four-mass model[7], [2], [3].

Fig. 9 is the simulated transient response of each rotor speed and the vehicle speed using the EV model in (1)–(6), when the motor starts. Table III shows the parameters for computer simulations. The response was

TABLE II
THE SPECIFICATION OF EV SIMULATOR

PC	NEC PC9821Xe10 CPU 486DX 100MHz		
A/D & D/A board	ADTEK AB98–57B		
	A/D	resolution	12bit
		conversion time	45μs
	D/A	resolution	12bit
		settling time	40μs
power amplifier	TAKASAGO BWS40–15		
current sensor	Nana electronics SR-13AP		

TABLE III

PARAMETERS FOR THE SIMULATIONS

J	2.0×10^{-4} (N· m· sec^2)
J_{outer}	1.5×10^{-3} (N· m· sec^2)
J_{inner}	5.0×10^{-4} (N· m· sec^2)
r_w	0.32 (m)
M	1500/2.0 (kg)
C_d	0.2
g	9.8 (N/m)
μ	$0.01\times s$
B	1.0×10^{-3}
S	1.55/2.0 (m^2)
F_R	$C_dSv^2g/16.0$
T_{ref}	100.0 (N)

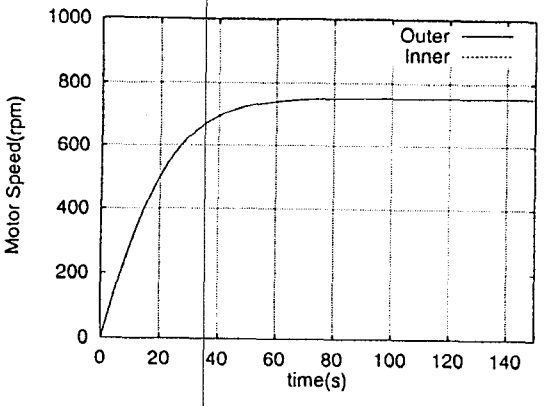

(a) Motor speed

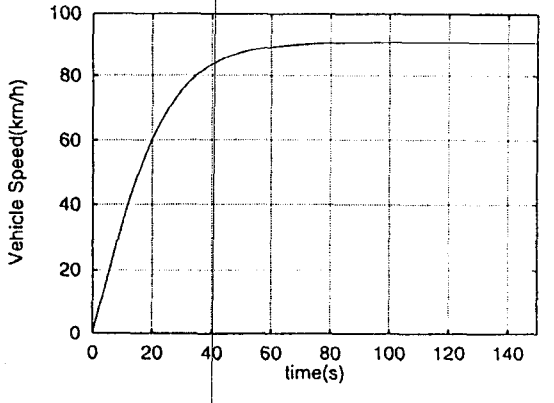

(b) Vehicle speed

Fig. 9. Simulated Transient Response using EV model(Computer simulations)

simulated under the torque control condition.

Although the inertia of the both rotor are different, the both wheel speeds increase almost equally. The reason is that the inertia difference between both rotors is less than the vehicle inertia.

TABLE IV

PARAMETERS FOR THE EXPERIMENTS

Total Weight(M)	500(kg)
Radius of wheels(r)	0.2(m)
Air drag coefficient (C_d)	0.1
Front area projection(S)	1.55(m^2)
Sampling period of EV simulator	100(μs)
Torque reference of ADTR-motor	8.28(N)

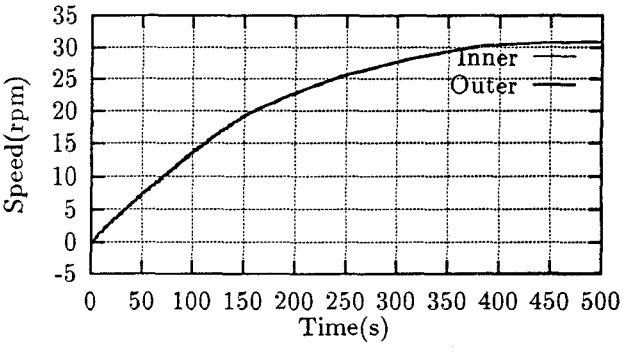

(a) Motor speed

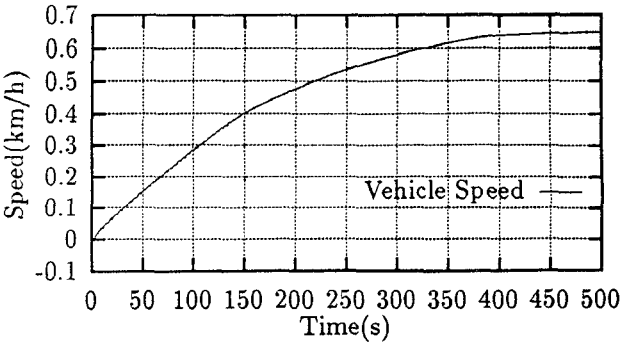

(b) Vehicle speed

Fig. 10. Transient response on EV simulator(Experiments)

IV. EXPERIMENTS

In general, EV is driven under the torque control. Accordingly, the ADTR-motor was driven under the torque control in the experiments. The transient response of the pm type ADTR-motor on the EV simulator is shown in Fig. 10. Table IV shows the parameters of the EV simulator for the experiments. In Fig. 10, inner and outer rotor speeds were increased almost in same manner, although there was a little vibration. Also, the vehicle speed was accelerated as the rotor speeds increased. The causes of the vibration may be that the sampling time of the system is not small enough for the friction coefficient calculation at

the present facilities.

V. Conclusion

In this paper, the EV simulator was constructed to analyze and verify the characteristics of the ADTR-motor when it was installed in EV. The characteristics of the reaction between the wheel, the road, and the vehicle speed, were simulated using simplified differential equations and non-linear equations in (1)–(6). The elementary characteristics of this simulator was verified by the simulated starting of the vehicle. Through experiments, the inner and the outer rotor speeds were increased as if the ADTR-motor were installed in the actual vehicle. Due to the limited facility, there is a little oscillation in the measured rotor speeds.

In the future works, the transient characteristics will be tested using this simulator such as the slip condition, and a traction control will be developed.

References

[1] M. Terashima, T. Ashikaga, T. Mizuno, T. Yamamoto, K. Natori, and N. Fujiwara, "AC Drive System with 4 In-Wheel-Motor for High Performance Electric Vehicle," *IEE of Japan Trans.D*, vol. 114, no. 1, pp. 33–41, 1994. (in Japanese).

[2] A. Kawamura, T. Yokoyama, and T. Kume, "Drive characteristics of anti-directional-twin-rotary motor drive for electrical vehicles," *IEE of Japan Trans.D*, vol. 115, no. 1, pp. 31–37, 1995. (in Japanese).

[3] A. Kawamura, N. Hoshi, T. W. Kim, T. Yokoyama, and T. Kume, "Analysis of anti-directional-twin-rotary motor drive characteristics for electrical vehicles," *IEEE Trans. on Industrial Electronics*, vol. 44, no. 1, pp. 64–70, 1997.

[4] T. Yokoyama and A. Kawamura, "Characteristics of ADTR-motor for electric vehicles," in *IEE of Japan IAS Meeting*, 1993. (in Japanese).

[5] N. Hoshi and A. Kawamura, "Experimental Discussion on the Permanent Magnet Type Anti-Directional-Twin-Rotary Motor Drive for Electric Vehicle," in *4nd IEEE international Workshop on Advanced Motion Control*, pp. 425–429, 1996.

[6] N. Hoshi and A. Kawamura, "Transient Characteristics of Permanent Magnet Type Anti-Directional-Twin-Rotary Motor under Torque Control," in *IEE of Japan IAS Meeting*, pp. 19–20, 1996. (in Japanese).

[7] A. Kawamura, T. Yokoyama, and T. Kume, "Anti-directional-twin-rotary motor drive for electrical vehicles," in *IEEE IAS Annual Meeting*, pp. 453–462, 1994.

[8] T. Furuya, Y. Toyoda, and Y. Hori, "Implementation of Advanced Adhesion Control for Electric Vehicle," in *4nd IEEE international Workshop on Advanced Motion Control*, pp. 430–435, 1996.

A Control Method of An Inverter-Fed Six-Phase Pole Change Induction Motor for Electric Vehicles

Masato Mori Takayuki Mizuno Tadashi Ashikaga Isao Matsuda
Meidensha Corporation
Nishibiwajima-cho,Nishikasugai-gun,Aichi 452, JAPAN
Fax:+81-52-509-1399, Phone:+81-52-509-1353
E-mail : mori-mas@honsha.meidensha.co.jp

Abstract — **In attempt to further improve a constant power operation properties of an induction motor (IM) , we have developed a six-phase pole change IM (six-phase PCIM) . The six-phase PCIM can further expand a constant power operation range without increasing the volume and current of an IM. The pole change can be carried out smoothly without the torque fluctuation by the technique of controlling the currents of two modes (4-pole and 8- pole) independently. The characteristics of the proposed system are shown through the simulations and experimental results. Furthermore, the acceleration characteristics of the prototype electric vehicle (EV) mounted a six-phase PCIM is shown.**

I. INTRODUCTION

In recent years, the research and development of EV has been promoted because of environmental problems, etc. One of the characteristics of the EV drive system is a drive train that eliminates the transmission by using the wide range speed controllability of the motor. Therefore, the motor for EV must generate a high torque at low speed ranges, and must have a wide range of constant power operation. And the motor must be compact, lightweight, and easy to service and then it must have a sturdy structure. An IM has a sturdy structure, and with vector control, high torque operation at low speed ranges and a wide range of constant power operation are relatively easy. Thus, an IM is considered as a motor that can satisfy the requirements for the EV motor.

In large EV applications such as trucks, however, a large torque is required even at high speed ranges. So a wider range of constant power operation is required to eliminate the transmission, and a larger size of IM must be applied. Therefore, configuring a drive system that eliminates the transmission is difficult. To resolve this problem, the authors have proposed the six-phase PCIM that further improves the operation characteristics of an IM for EV, and also its analysis method [1] , [2] . The six-phase PCIM uses a new drive method that a single winding PCIM with the number of poles ratio 2:1 is run with a six-phase inverter (six-phase INV) . The difference in motor characteristics caused by the dissimilarity in the number of poles is used to achieve a further increased constant power operation range without increasing the motor size or current. The number of poles is changed by controlling the winding voltage (current) phase and frequency with a six-phase INV, so the mechanical contactor conventionally used to change the connection is no longer required. In addition, the intermittent torque is eliminated at the pole change, and continuous torque control is possible. So the six-phase PCIM further enlarges the application range of the drive system that uses the features of the EV that it does not require transmission. And the six-phase PCIM is extremely effective when the operation performance is a priority at high speeds.

In this paper, the authors will briefly explain the operation theory of the six-phase PCIM, and will show that the vector control is possible by using the six-phase tensor-transformed rotational d-q axis proposed in [2] . Furthermore, the authors will propose a control method that suppresses the transient torque fluctuation that greatly affects the comfort of riding in EV at the pole change. And it will be shown that the validity through simulations, experiments and vehicle mounted tests.

II. OPERATION THEORY OF PCIM FOR EV [1]

Generally, the maximum torque during constant power operation of an IM driven with an INV changes in inverse proportion to the square of the speed when the INV's output voltage is constant. On the other hand, the required torque of the load changes in inverse proportion to the speed. So when the maximum torque corresponds to the load's required torque as shown with the 8-pole torque curve in Fig.1, the operation limit is reached. To increase the constant power operation range, an IM must be designed with a large maximum torque, or with a low rated voltage at the base speed. However, in these cases, the size of an IM will increase, or the current will increase and it will cause the inverter capacity to increase. A method to resolve this problem is the six-phase PCIM that uses the single winding pole change method. If the six-phase PCIM has the number of poles ratio of 2:1, any number of poles can be handled. So, the 4/8 pole used for the prototype will be used in this paper.

When the layout and connection of one phase of the six-phase PCIM are as shown in Fig.2, if a current is flowed as shown in Fig.2 (a) , it will function as 8-pole. However, if the current flows as shown in Fig.2 (b) , it will function as 4-pole. In this case, if the six-phase PCIM is operated at the same voltage and speed, the maximum torque of the 4-pole operation will be approximately twice that of the 8-pole operation. Because of this, if the number of poles is changed at the speed

0-7803-3823-5/97/$10.00© 1997 IEEE

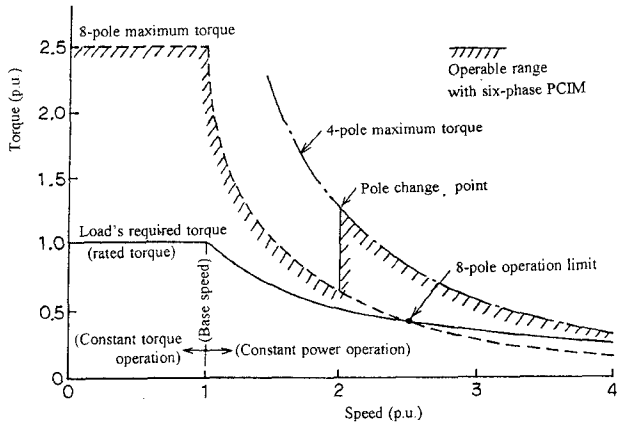

Fig.1. Torque characteristics of the six-phase PCIM at constant power operation.

shown in Fig.1, an allowance will be generated in the maximum torque of an IM in respect to the load's required torque. And a constant power operation over a wider range than the 8-pole operation will be possible. To use the 4-pole operation in the six-phase winding shown in Fig.3, the voltage must be applied to create a flux so that the opposing windings have different poles. The voltage of each phase ($va1$ to $vf1$) is obtained with (1). To use 8-pole, the phase voltage ($va2$ to $vf2$) obtained with (2) must be applied to create a flux so that the opposing windings have the same poles. Where, $v1m$, $\omega 1$, $\phi 1$: maximum phase voltage value, angular frequency, phase angle during 4-pole operation. $v2m$, $\omega 2$, $\phi 2$: maximum phase voltage value, angular frequency, phase angle during 8-pole operation.

$$
\begin{aligned}
va1 &= v1m\cos(\omega 1t+\phi 1)\\
vb1 &= v1m\cos(\omega 1t+\phi 1-\pi/3)\\
vc1 &= v1m\cos(\omega 1t+\phi 1-2\pi/3)\\
vd1 &= v1m\cos(\omega 1t+\phi 1-3\pi/3)\\
ve1 &= v1m\cos(\omega 1t+\phi 1-4\pi/3)\\
vf1 &= v1m\cos(\omega 1t+\phi 1-5\pi/3)
\end{aligned}
\qquad (1)
$$

$$
\begin{aligned}
va2 &= v2m\cos(\omega 2t+\phi 2)\\
vb2 &= v2m\cos(\omega 2t+\phi 2-2\pi/3)\\
vc2 &= v2m\cos(\omega 2t+\phi 2-4\pi/3)\\
vd2 &= v2m\cos(\omega 2t+\phi 2)\\
ve2 &= v2m\cos(\omega 2t+\phi 2-2\pi/3)\\
vf2 &= v2m\cos(\omega 2t+\phi 2-4\pi/3)
\end{aligned}
\qquad (2)
$$

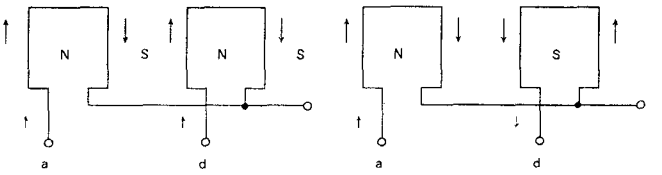

(a) 8-pole excitation (b) 4-pole excitation

Fig.2. Principle of the six-phase PCIM (for only one pair of poles)

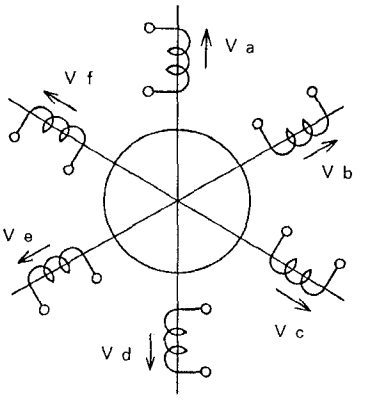

Fig.3. Winding model of the six-phase PCIM.

III. Application of Vector Control on Six-phase PCIM

A. Six-phase PCIM Voltage Equation

Coordinate transformation is carried out by using the six-phase tensor-transformed rotational d-q axis that is a combination of the single angle d-q axis (coordinate axis for the 4-pole) and the double angle d-q axis (coordinate axis for the 8-pole) proposed in [2]. According to the analysis by using the six-phase tensor-transformed rotational d-q axis, the voltage equation (3) for the 4-pole on the single angle d-q axis is obtained, and the voltage equation (4) for the 8-pole on the double angle d-q axis is obtained. Where Rs: primary resistance, Ls: primary inductance, Msr: magnetizing inductance, Rr: secondary resistance, Lr: secondary inductance, p: differential operator, vd, vq: d-q axis voltage, id, iq: d-q axis current, ω: angular frequency, ωs: slip angular frequency. And the parameters for the 4-pole motor have the suffix "1," and the parameters for the 8-pole motor have the suffix "2."

$$
\begin{bmatrix} vds1 \\ vqs1 \\ 0 \\ 0 \end{bmatrix} = \begin{bmatrix} Rs1+Ls1p & -\omega 1Ls1 & Msr1p & -\omega 1Msr1 \\ \omega 1Ls1 & Rs1+Ls1p & \omega 1Msr1 & Msr1p \\ Msr1p & -\omega s1Msr1 & Rr1+Lr1p & -\omega s1Lr1 \\ \omega s1Msr1 & Msr1p & \omega s1Lr1 & Rr1+Lr1p \end{bmatrix} \begin{bmatrix} ids1 \\ iqs1 \\ idr1 \\ idr1 \end{bmatrix} \qquad (3)
$$

$$
\begin{bmatrix} vds2 \\ vqs2 \\ 0 \\ 0 \end{bmatrix} = \begin{bmatrix} Rs2+Ls2p & -\omega 2Ls2 & Msr2p & -\omega 2Msr2 \\ \omega 2Ls2 & Rs2+Ls2p & \omega 2Msr2 & Msr2p \\ Msr2p & -\omega s2Msr2 & Rr2+Lr2p & -\omega s2Lr2 \\ \omega s2Msr2 & Msr2p & \omega s2Lr2 & Rr2+Lr2p \end{bmatrix} \begin{bmatrix} ids2 \\ iqs2 \\ idr2 \\ idr2 \end{bmatrix} \qquad (4)
$$

Each is independent and non-interfering, and the 4-pole torque $T1$ is expressed with (5) and the 8-pole torque $T2$ with (6) . The composite torque T is obtained with (7) . Where, $P1$ and $P2$ are the number of pole pairs of 4-pole and 8-pole.

$$T1 = P1Msr\,(idr1iqs1 - iqr1ids1) \quad (5)$$
$$T2 = P2Msr\,(idr2iqs2 - iqr2ids2) \quad (6)$$
$$T = T1 + T2 \quad (7)$$

B. Configuration of Vector Control System

The 4-pole and 8-pole can be handled independently. So if constant values are used for the d axis (exciting) currents $ids1$ and $ids2$ and the slip angular frequencies $\omega s1$ and $\omega s2$ with (8) and (9) are used, indirect vector control for each pole is independently possible. The torque during vector control is expressed with (10) by (5) to (7) , and torque control in proportion to each pole's q axis (torque) current $iqs1$ and $iqs2$ is possible. With this, operation control of 4-pole or 8-pole is independently possible. And 4-pole and 8-pole simultaneous control is possible too.

$$\omega s1 = (iqs1 / ids1) \cdot (1 / \tau r1) \quad (8)$$
$$\omega s2 = (iqs2 / ids2) \cdot (1 / \tau r2) \quad (9)$$
$$T = P1\,(Msr^2 / Lr1)\,ids \cdot 1iqs1 + P2\,(Msr^2 / Lr2)\,ids2 \cdot iqs2 \quad (10)$$

The matrix that transforms the six-phase tensor-transformed rotational d-q axis voltage into a six-phase voltage is expressed with (11) , and on the other hand, the matrix that transforms the six-phase current into the six-phase tensor-transformed rotational d-q axis is expressed with (12) . Where, ids: exciting current, iqs: torque current, vds, vqs: d-q axis voltage, $ia \sim if$: six-phase AC current, $va \sim vf$: six-phase AC phase voltage, θ: rotor position angle. And the suffixes "1" and "2" indicate the 4-pole motor and 8-pole motor respectively.

The configuration diagram of this control system is shown in Fig.4. The d-q axis currents of each pole are obtained from the six-phase current by using the coordinate transformation given in (12) to control the current independently for each pole at "Current control 1,2" of Fig.4. The voltage command value obtained here is transformed into the six phase by using (11) to carry out vector control independently for the 8-pole and 4-pole. The pole change point lies on a constant power control range, and the pole change is carried out at the point that the six-phase PCIM speed corresponds to the pole change speed (approximately double the base speed) . If the speed is lower than the pole change speed, the 4-pole side current command is set as zero, and only the 8-pole side current command is applied for 8-pole operation. If the speed is higher, the motor is run with only 4-pole. While changing the number of poles, the current command for both modes is applied to carry out 8-pole and 4-pole simultaneous operation so as to suppress the fluctuation of the torque. The pole change method is described in the next section.

IV. Pole Change Method [3], [4]

With the method being proposed, the number of poles are changed by controlling the voltage (current) phase and frequency of each winding with the six-phase INV. Therefore, the two modes can be operated simultaneously, and the number of poles can be changed continuously. So the control that suppresses the torque fluctuation when the number of poles is changed is possible. Here the torque fluctuation suppression method is described.

Assuming that the mode is being changed from 8-pole to 4-pole (when increasing the speed) , the simplest change method is to lower the 8-pole current command in a step, and to raise the 4-pole current command in a step. However, in this case, a large torque fluctuation will be generated due to the residual flux of the 8-pole and the starting lag of the 4-pole flux. To prevent this, the 8-pole flux must be sufficiently attenuated before the 4-pole current command is gradually increased. But in this case, the torque will be intermittent. With proposed method, both modes are operated simultaneously. The 8-pole current command is gradually lowered with an exponential function, and at the same time, the 4-pole current command is increased to supplement the drop in the 8-pole torque. This allows the torque fluctuation to be suppressed. The control method is shown below.

$$\begin{bmatrix} va \\ vb \\ vc \\ vd \\ ve \\ vf \end{bmatrix} = \frac{1}{\sqrt{3}} \times \begin{bmatrix} \cos\theta 1 & -\sin\theta 1 & \cos\theta 2 & -\sin\theta 2 \\ \cos(\theta 1-\pi/3) & -\sin(\theta 1-\pi/3) & \cos(\theta 2-2\pi/3) & -\sin(\theta 2-2\pi/3) \\ \cos(\theta 1-2\pi/3) & -\sin(\theta 1-2\pi/3) & \cos(\theta 2-4\pi/3) & -\sin(\theta 2-4\pi/3) \\ \cos(\theta 1-3\pi/3) & -\sin(\theta 1-3\pi/3) & \cos\theta 2 & -\sin\theta 2 \\ \cos(\theta 1-4\pi/3) & -\sin(\theta 1-4\pi/3) & \cos(\theta 2-2\pi/3) & -\sin(\theta 2-2\pi/3) \\ \cos(\theta 1-5\pi/3) & -\sin(\theta 1-5\pi/3) & \cos(\theta 2-4\pi/3) & -\sin(\theta 2-4\pi/3) \end{bmatrix} \begin{bmatrix} vds1 \\ vqs1 \\ vds2 \\ vqs2 \end{bmatrix} \quad (11)$$

$$\begin{bmatrix} ids1 \\ iqs1 \\ ids2 \\ iqs2 \end{bmatrix} = \frac{1}{\sqrt{3}} \times \begin{bmatrix} \cos\theta 1 & \cos(\theta 1-\pi/3) & \cos(\theta 1-2\pi/3) & \cos(\theta 1-3\pi/3) & \cos(\theta 1-4\pi/3) & \cos(\theta 1-5\pi/3) \\ -\sin\theta 1 & -\sin(\theta 1-\pi/3) & -\sin(\theta 1-2\pi/3) & -\sin(\theta 1-3\pi/3) & -\sin(\theta 1-4\pi/3) & -\sin(\theta 1-5\pi/3) \\ \cos\theta 2 & \cos(\theta 2-2\pi/3) & \cos(\theta 2-4\pi/3) & \cos\theta 2 & \cos(\theta 2-2\pi/3) & \cos(\theta 2-4\pi/3) \\ -\sin\theta 2 & -\sin(\theta 2-2\pi/3) & -\sin(\theta 2-4\pi/3) & -\sin\theta 2 & -\sin(\theta 2-2\pi/3) & -\sin(\theta 2-4\pi/3) \end{bmatrix} \begin{bmatrix} ia \\ ib \\ ic \\ id \\ ie \\ if \end{bmatrix} \quad (12)$$

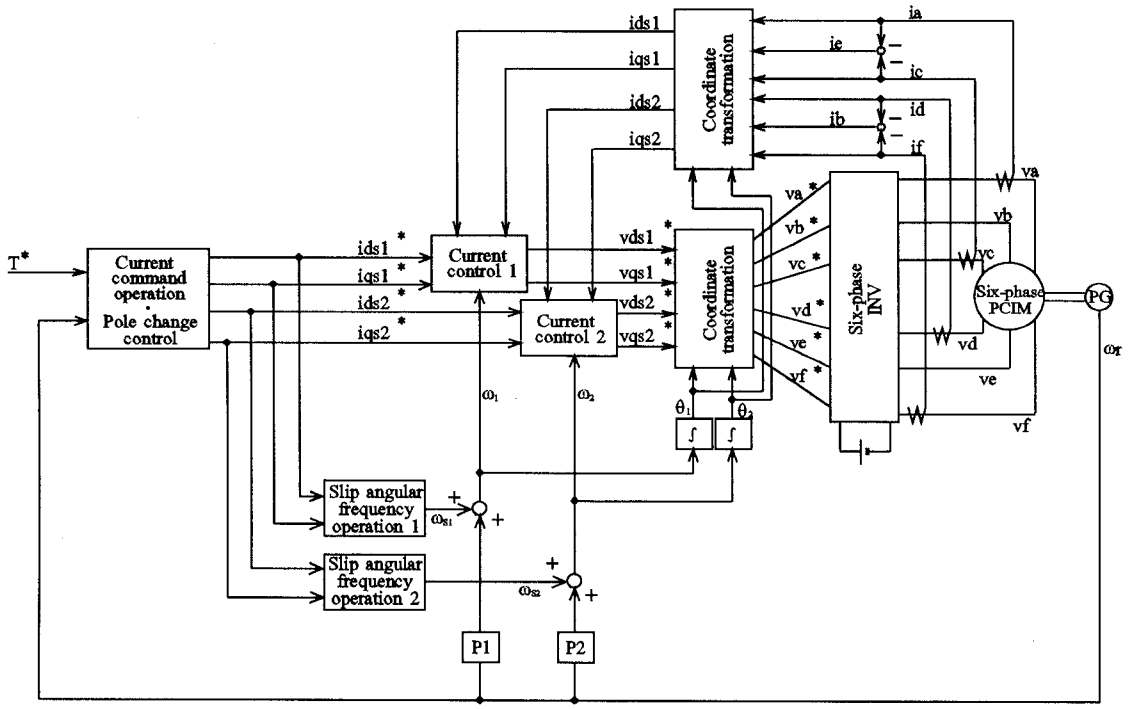

Fig.4. Configuration diagram of the six-phase PCIM control system.

A. 4-Pole Side

The response of the 4-pole secondary flux $\lambda r1$ has a secondary time constant $\tau r1$ lag in respect to the exciting current. Thus, $ids1^*$ is applied in a step to the rated value, and the torque current command $iqs1^*$ is increased with the first lag shown in (13) having the change time constant $\tau ch1$ ($\geqq \tau r1$) that is equivalent to or larger than $\tau r1$.

$$iqs1^* = iqs1^* \times \{1 - \exp(-t / \tau ch1)\} \quad (13)$$

B. 8-Pole Side

To make sure that the secondary flux $\lambda r2$ can follow the changes in the exciting current command, the exciting current command $ids2^*$ and torque current command $iqs2^*$ are decreased with the exponential function indicated with (14) and (15) having the change time constant $\tau ch2$ ($\geqq \tau r2$) that is equivalent to or larger than a secondary time constant of the 8-pole $\tau r2$.

$$ids2^* = ids2^* \times \exp(-t / \tau ch2) \quad (14)$$
$$iqs2^* = iqs2^* \times \exp(-t / \tau ch2) \quad (15)$$

However, as a 8-pole secondary time constant $\tau r2$ is smaller than a 4-pole $\tau r1$, the change time constant $\tau ch1$, $\tau ch2$ are dominated by $\tau r1$. And the minimum value of the exciting current is limited to 20% of the rated value so as to stabilize the control. The condition for completion of the pole change is the point when the 4-pole side torque current command value increases to 90%. And, the pole change is completed with the 8-pole side current command value as zero, and then 4-pole single operation is started. The change from 4-pole to 8-pole (when decreasing the speed) is the above operation in reverse. This pole change control is carried out at "current command operation, pole change control" of Fig.4. And the block diagram is shown in Fig.5.

In this pole change operation, the torque fluctuation amount and line-to-line voltage waveform change during the pole change process due to the setting value of the change time constant. Thus, this setting is important. In particular, the line-to-line voltage during the pole change operation becomes the composite voltage waveform of the 4-pole and 8-pole, and the voltage peak value becomes higher than the 8-pole single operation. So it must be suppressed to within the range that can be output by the INV. This voltage rise amount and torque fluctuation amount have a trade-off relation, and the change time constant is determined by the simulation results shown in the next section. In addition, considering the response of

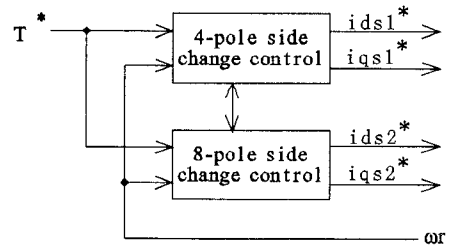

Fig.5. Current command operation, pole change control section.

the secondary flux in respect to the exciting current, it is difficult to set the change time constant to a value lower than the secondary time constant of each pole. So the secondary time constant value of the 4-pole side having the larger time constant is used as the standard.

V. Simulation and Experimental Results

A. Prototype Motor Rating And Parameters

The prototype motor rating and parameters are shown in Table I. And a view of the six-phase PCIM is shown in Fig.6.

B. Experimental Results at Both Modes Simultaneous Operation

The torque, while 4-pole and 8-pole are operated simultaneously, is the composite torque of both modes as obtained with (10). The experimental results using the actual motor are shown in Fig.7. Fig.7 (a) shows phase voltage, current and torque waveform for the 4-pole single operation at a speed of 3600 rpm and torque command of 28%. Fig.7 (b) shows the case for the 8-pole single operation (torque command 72%). Fig.7 (c) shows the waveform during 4-pole and 8-pole simultaneous operation at a torque command of 28% and 72% respectively. From Fig.7 (c), it can be seen that the both modes' voltage (current) is superposed on, and that the torque matches the value obtained by adding both modes' torque. It can also be seen that there is no torque

TABLE I

RATING OF THE PROTOTYPE MOTOR (AT 120 Hz / 240 Hz)

Maximum power	45 kW	Base speed	2500 rpm
Number of poles	4 / 8	Pole change speed	3600 rpm
Maximum voltage	150 V	Maximum speed	10000 rpm
Primary resistance	R_{s1} / R_{s2} (W)		0.0380 / 0.0380
Secondary resistance	R_{r1} / R_{r2} (W)		0.0120 / 0.0150
Primary inductance	L_{s1} / L_{s2} (mH)		4.7036 / 1.3459
Secondary inductance	L_{r1} / L_{r2} (mH)		4.6834 / 1.3225
Magnetizing inductance	M_{sr1} / M_{sr2} (mH)		4.6229 / 1.2495
Secondary time constant	τ_{r1} / τ_{r2} (sec)		0.3903 / 0.0882

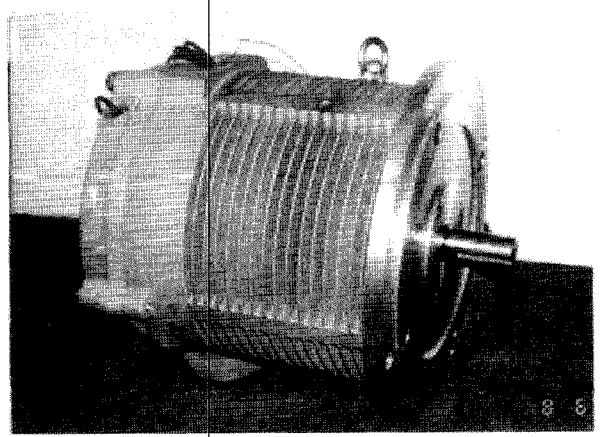

Fig.6. The six-phase PCIM.

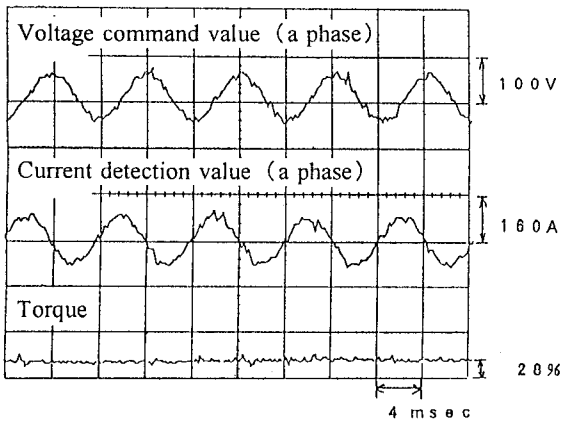

Fig.7. (a) Characteristics at 4-pole single operation.

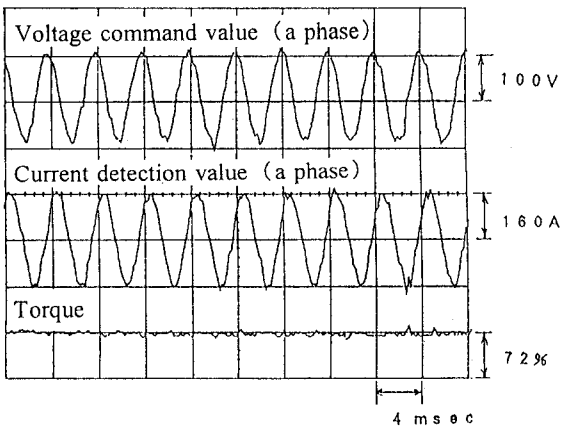

Fig.7. (b) Characteristics at 8-pole single operation.

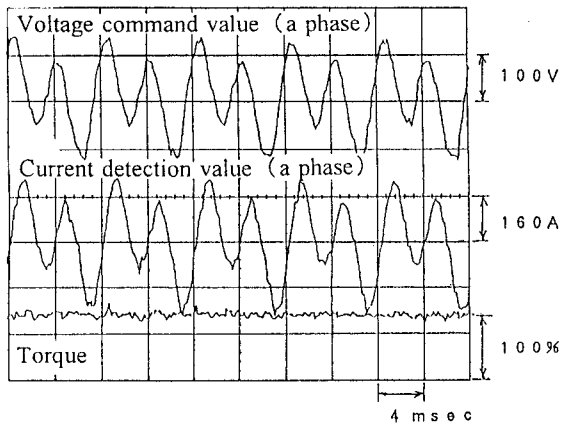

Fig.7. (c) Characteristics at 4-pole and 8-pole simultaneous operation.

pulsation. From these results, it can be confirmed that torque control independently for each pole and simultaneously for both modes are possible with this control system.

C. Simulation Results of Pole Change Control

The simulation results of the torque and line-to-line voltage when changing from 8-pole to 4-pole at a speed of 3600 rpm and the maximum output are shown in Fig.8.

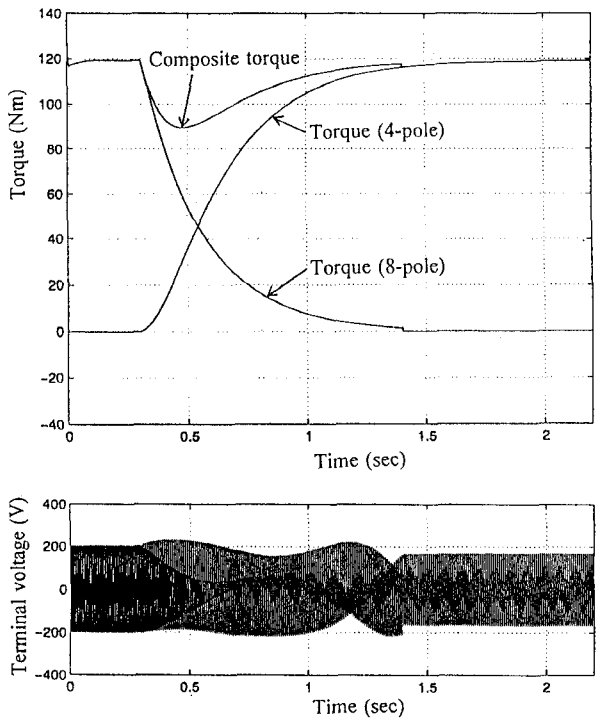

Fig.8. Simulation results of pole change characteristics at $\tau ch1 = \tau ch2 = \tau r1$.

This figure shows the case when the change time constant is set to the 4-pole secondary time constant value ($\tau ch1$, $\tau ch2 = \tau r1$) . At the time t = 0.3 sec, the operation changes from the 8-pole single operation to the 8/4-pole simultaneous operation, and the 4-pole single operation is started at t = 1.4 sec. The torque drops about 25% for a maximum torque during pole change, but the fluctuation is relatively small, and the waveform is smooth. The line-to-line voltage during pole change is the composite of both modes' voltage, and "undulation" occurs due to the difference in frequency. However, the peak value is 230 V at the maximum, and is suppressed to an approximately 10% increase compared to the 208 V for 8-pole operation.

D. Comparison of Experimental Results and Simulation Results

Fig.9 shows the feedback exciting current of each pole ($ids1$, $ids2$) , the feedback torque current ($iqs1$, $iqs2$) , the c-phase current waveform, and the torque when the number of poles are changed with the actual motor at the same conditions as the simulation in Fig.8. The torque drops approximately 33%, and is slightly larger than the simulation results. However, the general waveform approximately corresponds to the simulation results. The d-q axis currents of each pole are also operated according to the commanded value. It is believed that the motor's secondary time constant error is the cause of the slightly larger torque drop than the simulation results.

From the above results, a six-phase PCIM control system with no intermittent torque can be structured, although there is a slight torque fluctuation at the pole

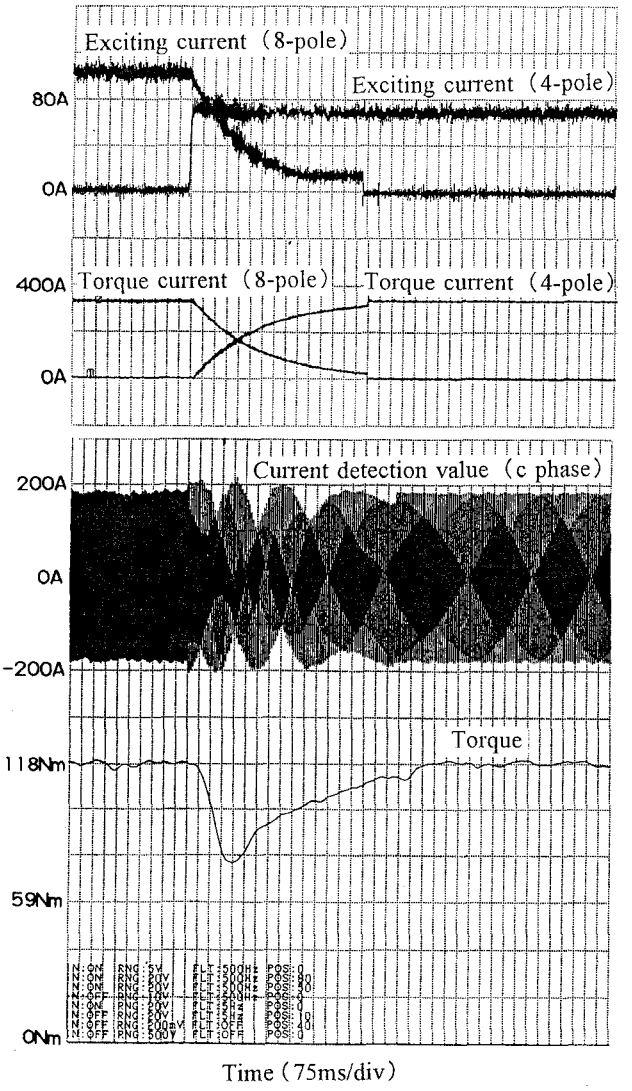

Fig.9. Characteristics of pole change operation at 8-pole to 4-pole.

change. And it is assumed that this system can be applied for EV drive use.

VI. Results of Vehicle Mounted Test

To investigate the effect of the torque fluctuation generated when the number of poles is changed on the comfort of the ride, a prototype EV mounted the proposed six-phase PCIM was manufactured and evaluated. This prototype EV was a modified gasoline engine vehicle with a 4-step manual transmission. And a view of the prototype EV is shown in Fig.10. The data obtained by accelerating from the stopped state to 4680 rpm with the fully opened accelerator and the transmission fixed at 2nd gear is shown in Fig.11. The number of poles was automatically changed at 3600 rpm. A slight speed fluctuation was observed at this time, but it can be seen that the acceleration is smooth. The adverse effect of this speed fluctuation on the comfort of the drive is almost nil, and thus is not considered as a problem for the practical

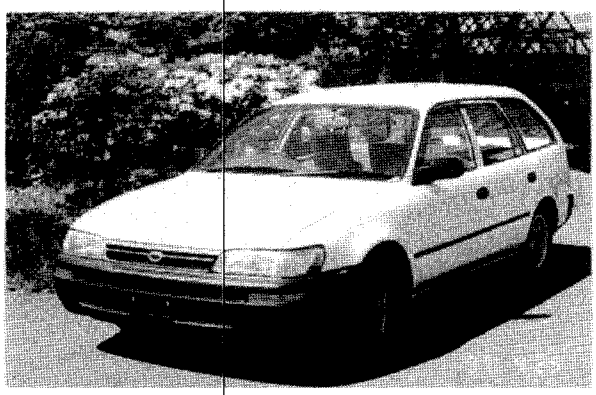

Fig.10. The prototype EV.

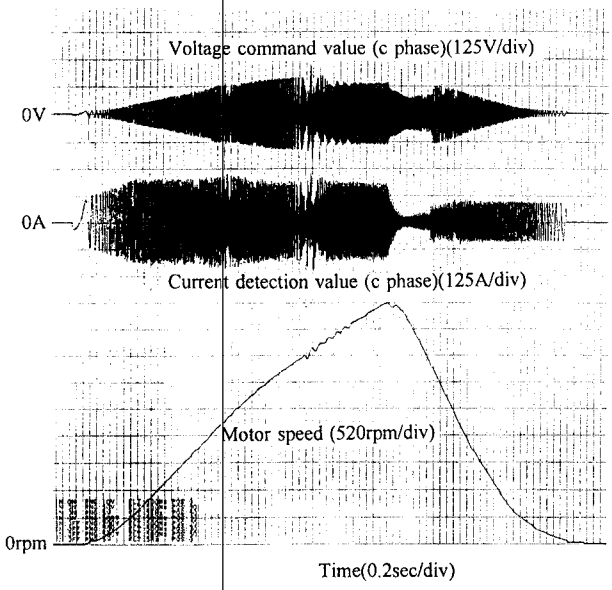

Fig.11. Acceleration characteristics of the prototype EV.

use. Almost no shock was felt by the driver at the pole change. Thus, it is believed that this system has a sufficient performance for practical applications.

VII. Conclusion

The vector control system for controlling the torque and the control method for suppressing the torque fluctuation at the pole change with the six-phase PCIM for EV have been proposed. The six-phase PCIM allows the constant power operation range to be increased. And the validity has been indicated through simulations, experiments and vehicle mounted tests. The results are as follows:

i) By transforming the six-phase current of the six-phase PCIM into the six-phase tensor-transformed rotational d-q axis, vector control of each pole is independently possible. Through the experiment using the six-phase INV, it was confirmed that the torque is the sum of each pole's torque, and that each pole can be independently controlled.

ii) As a pole change method that eliminates the intermittent torque at the pole change, a method to control the 4-pole and 8-pole simultaneously to increase /decrease the current of each pole with an exponential function to suppress the torque fluctuation and continuously change the number of poles was proposed. And the effectiveness was confirmed through simulations and experiments.

iii) A travel test using an EV mounted the six-phase PCIM was carried out. As a result, it was found that the torque fluctuation at the pole change did not adversely affect the comfort of the ride. And it was confirmed that there were no problems for the practical application. The shock caused by the pole change was hardly felt by the driver.

From the above results, it is believed that the proposed six-phase PCIM control system can resolve the intermittent torque problem, which was a barrier to applying the pole change method to EV, at the pole change, and that this system can be applied to EV drive system.

Acknowledgment

The authors would like to thank Professor Kazuo Tsuboi of the Chubu University, and his research assistants for their guidance and cooperation in this research.

References

[1] T.Mizuno, K.Tsuboi, I.Hirotsuka, S.Suzuki, I.matsuda, and T.Kobayashi, "Basic Principle and Maximum Torque Characteristics of A Six-Phase Pole Change Induction Motor for Electric vehicles," T.IEE Japan, Vol.116-D, No.3, pp.256-264, March 1996.

[2] T.Mizuno, K.Tsuboi, I.Hirotsuka, S.Suzuki, T.Ashikaga, and I.Matsuda, "Transient Performance Analysys of A Six-Phase Pole Change Induction Motor for Electric Vehicles," T.IEE Japan, Vol.116-D, No.11, pp.1116-1125, November 1996.

[3] M.Mori, K.Nagayama, T.Mizuno, T.Ashikaga, and I.matsuda, "Development of an Inverter-Fed Six-Phase Pole Change Induction Motor for Electric Vehicles," in National Convention Record of The I.E.E.Japan, No.872, March 1996.

[4] T.Ashikaga, T.Mizuno, M.Mori, K.Nagayama, I.matsuda, and M.Date, "A Control Method of an Inverter-Fed Six-Phase Pole Change Induction Motor for Electric Vehicles," T.IEE Japan, Vol.117-D, No.6, June 1997.

[5] M.Mori, Y.Kido, T.Mizuno, T.Ashikaga, I.matsuda, And T.Kobayashi, "Development of an Inverter-Fed Six-Phase Pole Change Induction Motor for Electric Vehicles," in Symposium Proceedings of The EVS-13, Vol.2, pp.511-517, October 1996.

[6] K.Tsuboi, T.Mizuno, I.Hirotsuka, S.Suzuki, K.Matsui, and I.matsuda, "Maximum Torque Characteristics of a Six-Phase Pole Change Induction Motor for Electric Vehicles," in National Convention Record of The I.E.E.Japan, No.972, 1995.

[7] T.Mizuno, I.matsuda, K.Tsuboi, I.Hirotsuka, and S.Suzuki, "An Examination of Winding Method and Magnetomotive Force of Six-Phase Pole Change Induction Motor for Electric Vehicles," in National Convention Record of The I.E.E.Japan, No.973, 1995.

[8] S.Suzuki, K.Tsuboi, I.Hirotsuka, T.Mizuno, and I.matsuda, "Experimental Study of Stray Load Loss of Pole Change Induction Motor for Electric Vehicle," in National Convention Record of The I.E.E.Japan-IAS Society, No.T-11, 1995.

High Performance Design of an Interior Permanent Magnet Synchronous Reluctance Motor for Electric Vehicles

Shinichiro Kawano, Hiroshi Murakami, Noriyoshi Nishiyama,
Yasufumi Ikkai, Yukio Honda and Toshiro Higaki
Motor Engineering Research Laboratory, Motor Company, Matsushita Electric Industrial Co., Ltd.
7-1-1 Morofuku, Daito, Osaka 574, JAPAN
Fax: +81-720-70-3158, Phone: +81-720-70-3080
E-mail: kawano@mot.mei.co.jp

Abstract - We have examined the optimum rotor design of an Interior Permanent Magnet motor (IPM motor) for Electric Vehicles. By using double-layer magnets embeded into the rotor with the layers separated in the direction of the rotor radius, we have been able to construct a rotor that takes greatest advantage of reluctance torque, resulting in a 10 percent torque increase over the conventional IPM motor, which uses only a single-layer of magnets in the rotor.

I. INTRODUCTION

In the past few years, worldwide awareness of environmental problems has grown dramatically, and tremendous interest has grown in developing non-polluting Electric Vehicles (EV). Fig. 1 shows the motor requirements of EV. The desired characteristics are high efficient, high torque and a wide operating range. In recent years, IPM using the field weakening control is paid to great attention as a motor which satisfies this demand[1-4].

For this study, we examined an IPM motor for use in an EV. The IPM motor has permanent magnets inside the rotor, and we compared performance characteristics depending on rotor configuration.

The q-axis inductance of the IPM motor is greater than the d-axis inductance, because the magnets of the IPM motor are embeded inside the rotor. As a result, reluctance torque can be used in addition to magnetic torque, giving bright promise for a high efficiency motor. However, many points remain unresolved in determining the optimum ratio for utilizing magnetic torque and reluctance torque.

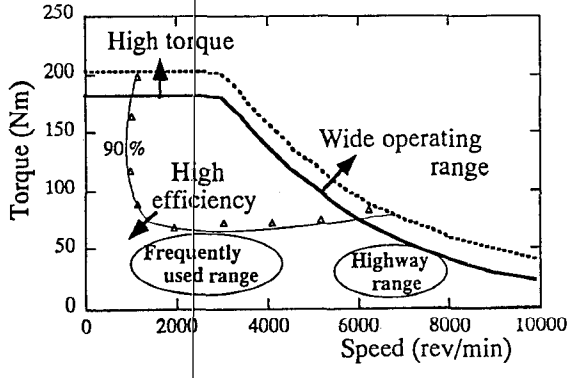

Fig. 1 Motor requirements of EV.

We examined the differences in motor characteristics depending on how the magnets were embeded in. For this comparison, we set conditions so that the volume of magnets remained constant, and we used both computer simulation and experiments.

As a result, we were able to develop an IPM motor with double-layer magnets. This motor produces 10 percent greater torque than the conventional single-layer magnet IPM operating on the same current.

II. THE OPTIMUM ROTOR CONFIGRATION

The output torque T of the IPM motor is represented as

$$T = P\left\{\phi_a i_q + \left(L_q - L_d\right) i_d i_q\right\} = P\left\{\phi_a I_a \cos\beta + \frac{1}{2}\left(L_q - L_d\right) I_a^2 \sin 2\beta\right\}. \quad (1)$$

where, ϕ_a: flux-linkage expressed on the d-q coordinates, i_d, i_q: d- and q-axis components of armature current, $I_a : \sqrt{i_q^2 + i_d^2}$, L_d, L_q: d- and q-axis inductance, β: leading angle of armature current from the q-axis, R_a: armature resistance per phase, V_a: motor terminal voltage and P:the number of pole pairs.

Next, the voltage equation is as follows:

$$V_a^2 = \left(R_a i_d - \omega L_q i_q\right)^2 + \left(R_a i_q + \omega L_d i_d + \omega \phi_a\right)^2 \quad (2)$$

The first term of Eq. (1) is the magnet torque generated by the permanent magnets. The second term is the reluctance torque occurring from the difference between the d- and q-axis inductance. Under the condition that magnet volume is remained constant, flux-linkage ϕ_a is roughly the same. This means to increase the torque with the same current I_a, we must increase the difference between the d- and q-axis inductance L_q-L_d. However, when the difference increased, according to Eq. (2) voltage saturation occurs at more low speed. At this point, we can make a wide-range motor drive by effectively using the field weakening control method.

0-7803-3823-5/97/$10.00© 1997 IEEE

To display the maximum motor characteristics using weak field control, it is necessary to create a design that gains a balance between reluctance torque generated from rotor saliency and magnet torque from the permanent magnets. The motor characteristics depends on the machine parameter ϕ_a, L_q and L_d [5]. It is important that the optimum machine parameters are selected in order to obtain the desired output characteristics of EV motor. Below, we would discuss the optimum values of machine parameter.

Table 1 shows the calculation parameters. We simulated the speed vs. Torque characteristics using the maximum torque and the field weakening control[4]. Fig.2 shows the results of a simulation to determine how motor characteristics change in the parameters of magnetic flux, q-axis inductance, and d-axis inductance. Through simulation, we found that increasing the q-axis inductance 10 percent without increasing the magnetic flux or d-axis inductance is effective in increasing the maximum output torque and broadening the constant-power operating region.

Table 1 Calculation parameters.

	Type 1	Type 2	Type 3	Type 4
Magnetic flux linkage: ϕ_a	1	1.1	1	1
q-axis inductance: L_q	1	1	1.1	1
d-axis inductance: L_d	1	1	1	0.9

(p.u.)

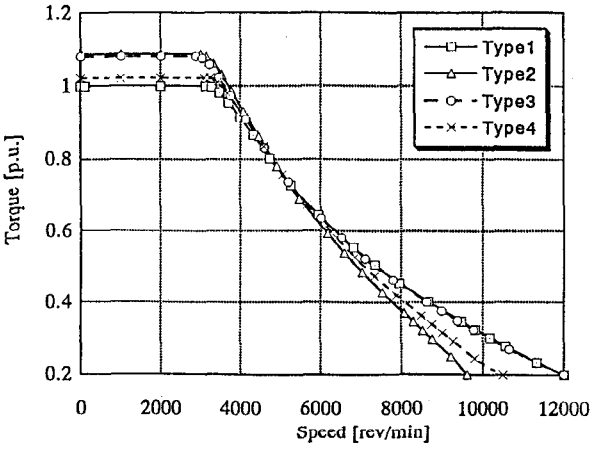

Fig. 2 Calculation results of a simulation.

We decided to use a FEM(Finite Element Method) simulation to examine the effect on d- and q-axis inductance caused by changing the number of magnet layers inside the rotor[6]. Fig.3 shows four types of IPM rotor configurations used in this analysis. Type (a) is a Single-layer IPM rotor, type (b) is a double-layer IPM, type (c) is a three layer, and type (d) is a ten-layer IPM rotor.

The volume of magnets is the same in each. In the single- layer rotor, each pole consists of a single magnet, and the magnet thickness is the greatest of the four types. But to maintain the same magnet volume, increasing the number of magnet layers results in decreasing the magnet thickness. The other primary factors(for example, outer diameter of the rotor, air gap between rotor and stator, and stack length and stator specifications) are all remain the same.

Fig. 4 shows the results of this analysis. Increasing the number of magnet layers reduces the d-axis inductance L_d. On the other hand, the q-axis inductance L_q is increased by adding more magnet layers. This means that increasing the magnet layers increases L_q-L_d. This results in a greater reluctance torque generated in response to more magnet layers. However, the value shows little increase when using more magnet layers than three. As more magnet layers are used, the width of flux path on the q-axis becomes smaller between each layer. This causes the magnetic saturation on the q- axis and little increase of L_q. Considering the increased cost of more layers, the optimum rotor configuration is a double layered magnet IPM motor.

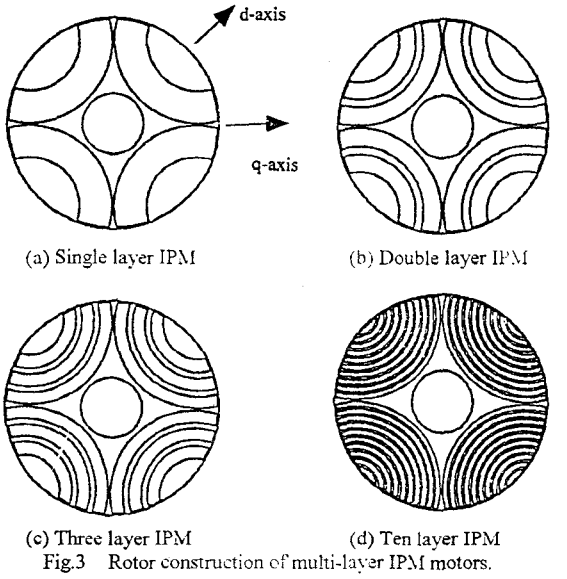

Fig.3 Rotor construction of multi-layer IPM motors.

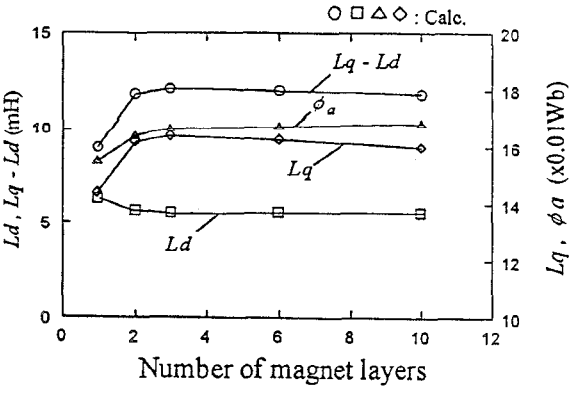

Fig. 4 L_d, L_q, L_q -L_d and ϕ_a vs. Number of magnet layers.

III. SPECIFICATION OF A PROTOTYPE MOTOR

Fig. 5 shows a cross section diagram of the rotor core for the prototype motors constructed based on this simulation. Table 2 shows the motor specifications. We constructed both a single layer and a double layer IPM to compare performance. Separating the embedded magnets lengthwise at the rotor radius in the double layer IPM created a q-axis magnet torque flux path. By adjusting the dimensions of this path, the magnet flux can be controlled using the magnets and q-axis inductance.

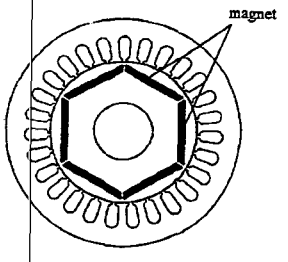

(a) Single layer IPM motor.

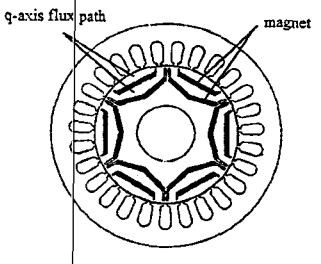

(b) Double layer IPM motor.

Fig. 5 Prototype motor configuration.

Table 2. Motor Specifications.

3 phase / 6 poles / 27 slots
Rotor O.D. : 135.6 mm
Stator O.D. : 220.0 mm
Stack Length : 135.0 mm
Rated Voltage : 288V
Maximum Current : 250A
Maximum Power : 50 kW
Magnet : Br = 1.1 T, iHc = 1990 kA/m

IV. RESULTS AND DISCUSSIONS

A. Inductance and Torque Simulation

The d-axis inductance L_d and q-axis inductance L_q of the prototype IPM motor were calculated using FEM analysis and actual measurements. Fig. 6 shows the results. The actual measurements are somewhat higher than the calculated results, but they are within 6 percent margin of error, and both rotor showed the same tendencies.

The d-axis inductance L_d decreases in response to increasing d-axis current i_d. However the difference between the two types of rotors is slight.

The q-axis inductance L_q tends to decrease as q-axis current i_q increases. Also the influence of magnetic saturation appears clearly. The value of q-axis inductance L_q is greatest in the double-layer IPM. Fig. 7 shows a flux distribution diagram of the magnetic flux when q-axis current i_q is applied. In comparing the two types, the single-layer magnet rotor has a flux path only along the magnet surfaces, but the double-layer magnet rotor also has flux paths between the two magnet layers in addition to smaller magnet surfaces. Because of this, L_q is greater with the double-layer magnets than with the single-layer. Also, q-axis inductance L_q is more easily influenced by magnetic saturation, so L_q decreases as the q-axis current increases. When designing the IPM motor, it is essential to fully consider the magnetic saturation of q-axis inductance L_q.

Fig. 8 shows results of torque simulation. The maximum torque of the double-layer rotor is 10 percent higher torque than the single-layer IPM.

With these results, we were able to confirm that the inductance difference L_q-L_d relating to the occurrence of reluctance torque is greater in the double-layer IPM.

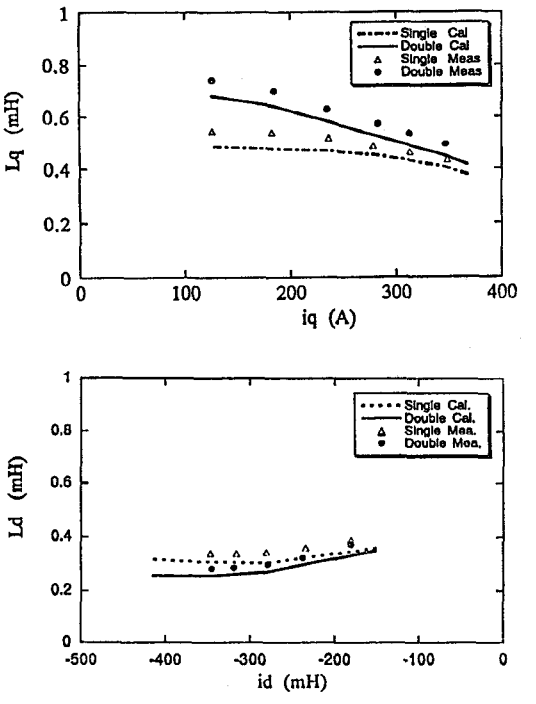

Fig. 6 The Calculated and measured L_q and L_d of the prototype motor.

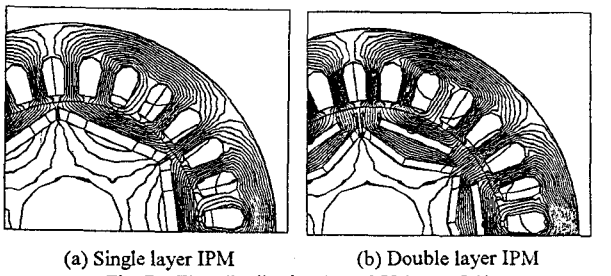

(a) Single layer IPM (b) Double layer IPM

Fig. 7 Flux distribution (i_q = 250A, i_d = 0A).

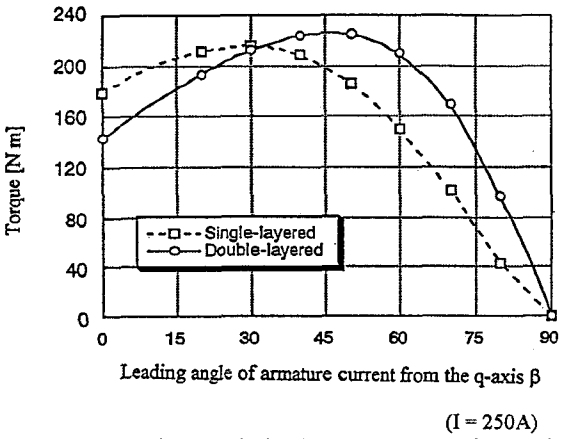

(I = 250A)

Fig. 8 Comparison of calculated torque vs. current phase angle.

B. Motor performance Characteristics

Fig. 9 shows the comparison of Torque vs. Speed characteristic of the prototype IPM motors. We were able to confirm that the double-layer IPM had 10 percent higher torque in the constant torque region. This is because the reluctance torque was increased by separating the magnets into two layers in the double layered IPM.

However, in the constant output power region, the performance characteristics remained approximately the same by using the field weakening control.

Fig. 10 shows a comparison of the efficiency of both types. Because the torque is higher in the double-layer IPM using the same current as the single-layer IPM, the copper loss is reduced. This causes the efficiency curve range is expanded at 90 percent. Also, over 97 percent peak motor efficiency was achieved.

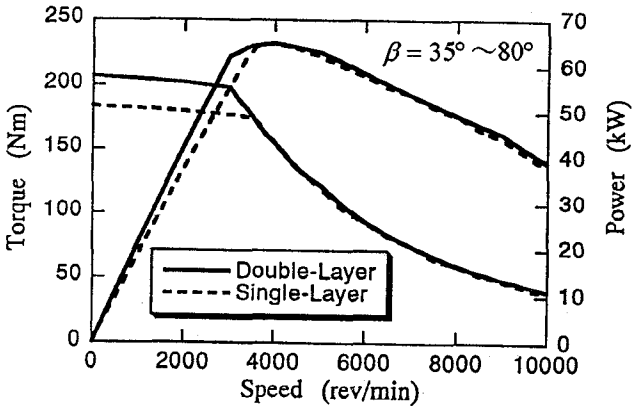

Fig. 9 Comparison of torque and power vs. speed characteristic.

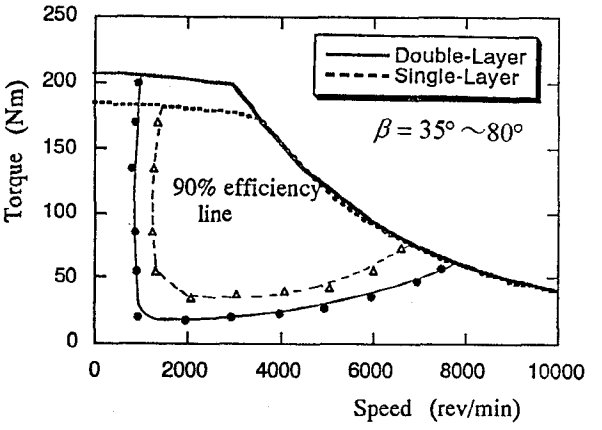

Fig. 10 Efficiency curve of the prototype motors.

V. CONCLUSIONS

This paper presented what is the suitable rotor configuration for the IPM motor for electric vehicle . We also examined what rotor shape yields the maximum reluctance torque with the condition that the magnet volume remained the same. The double-layer IPM motor increases q-axis inductance L_q by 10% over the single-layer IPM. As a result of efficiently utilizing the reluctance torque in the double-layer IPM, motor torque was increased by 10 percent, and the high efficiency drive range was increased by 10 percent compared to the single-layer motor.

REFFERENCES

[1] Jahns,T.M., "Flux-weakening regime operation of an interior permanent magnet synchronous motor drive", IEEE Trans. Ind. Appl., Vol.23, pp.681-689, 1987

[2] B.K.Bose, "A high-performance inverter-fed drive system of an interior permanent magnet synchronous machine", IEEE Trans. Ind. Appl., Vol.24, pp.987-997, Nov./Dec. 1988

[3] R.Schiferl, T.A.Lipo, "Power Capability of Salient pole Permanent Magnet Synchronous Motors in Variable Speed Drive Applications", IEEE Trans. Ind. Appl., Vol-23,pp.23-31,1988

[4] S.Morimoto, Y.Takeda, T.Hirasa, K.Taniguchi, "Expansion of Operating Limits for Permanent Magnet Motor by Current Vector Control Considering Inverter Capacity", IEEE Trans. Ind. Appl., Vol.26, No.5, pp.866-871, Sep./Oct. 1990

[5] W L Soong, T.J.E. Miller, "Field-weakening performance of brushless synchronous AC motor Drive" IEEE Proc. Electr. Power Appl., Vol.141, N0.6, Nov.1994

[6] Y.Honda, H.Murakami, K.Narazaki, T.Higaki, Y.Takeda, S.Morimoto, "Performance of a Double-Layered Interior Permanent Magnet Synchronous Motor", Speedam 96 Symposium on Power Electronics, Industrial Drives, Power Quality, Traction systems A4-33-39 Capri(Italy), 5-7 June 1996

Development of Power Supply System for Yamanashi Maglev Test Line

Haruo Ikeda, Shigeo Kaga (Railway Technical Research Institute)
Yutaka Osada, Jun-ichi Kitano (Central Japan Railway Company)
Kenji Ito, Yasuyosi Mugiya, Hideo Ito (Toshiba Corporation)
Kazuya Tutumi (Hitachi Corporation),

Abstract — The electric power supply system of north part for Yamanasi Maglev Test Line, is composed of the power receiving system, the drive control system, the power conversion system and the feeding system. This Test Line system employs a linear synchronous motor with primary side on ground which consist of the superconducting magnets aboard the vehicle and the armature coil on the ground. The 3-phase ac current which synchronizes with the vehicle speed is supplied to the armature coils. Therefore, the PWM inverter with a rating of 38MVA is installed and some experiment data at coil-loaded is obtained. This paper gives an outline of the electric power supply system and some experiment data.

I. INTRODUCTION

The superconducting magnetic levitation system employs a linear synchronous motor with primary side on ground which consists of the superconducting magnets aboard the vehicle and the armature coils on the ground. The 3-phase ac current which synchronizes with the vehicle speed is supplied to the armature coils.

The power supply system supplies electric power for driving the vehicle according to the running pattern from the drive control system.

This paper gives an outline of the electric power supply system which has been developed for the driving facility of north part of Yamanasi Maglev Test Line.

II. POWER SUPPLY SYSTEM

Fig.1 shows an outline of the power supply system of Yamanashi Maglev Test Line.

The power supply system comprises the power receiving system, the drive control system, the power conversion system and the feeding system.

The drive control system controls the speed of the vehicle and the stop position according to the running pattern ordered from the traffic control system.

The power conversion system converts the power into a variable frequency and a variable voltage, and supplies the ground armature coils with the power through the feeder and section switchgear.

The power conversion system receives electric power at 154kV and converts it into the frequency (0-56.6Hz) and into voltage (0-22kV) corresponding to the operation of maglev trains.

The feeding system is a triplex feeding system, so the power conversion system consists of three inverter units. The propulsion coils are installed on both sides of the guideway. The coil group which is called a 'section', is connected to one inverter unit.

The section s on both sides of the track are laid out with half section overlap. In this configuration , even if one of the inverter units fails, the other two continue to operate the vehicle.

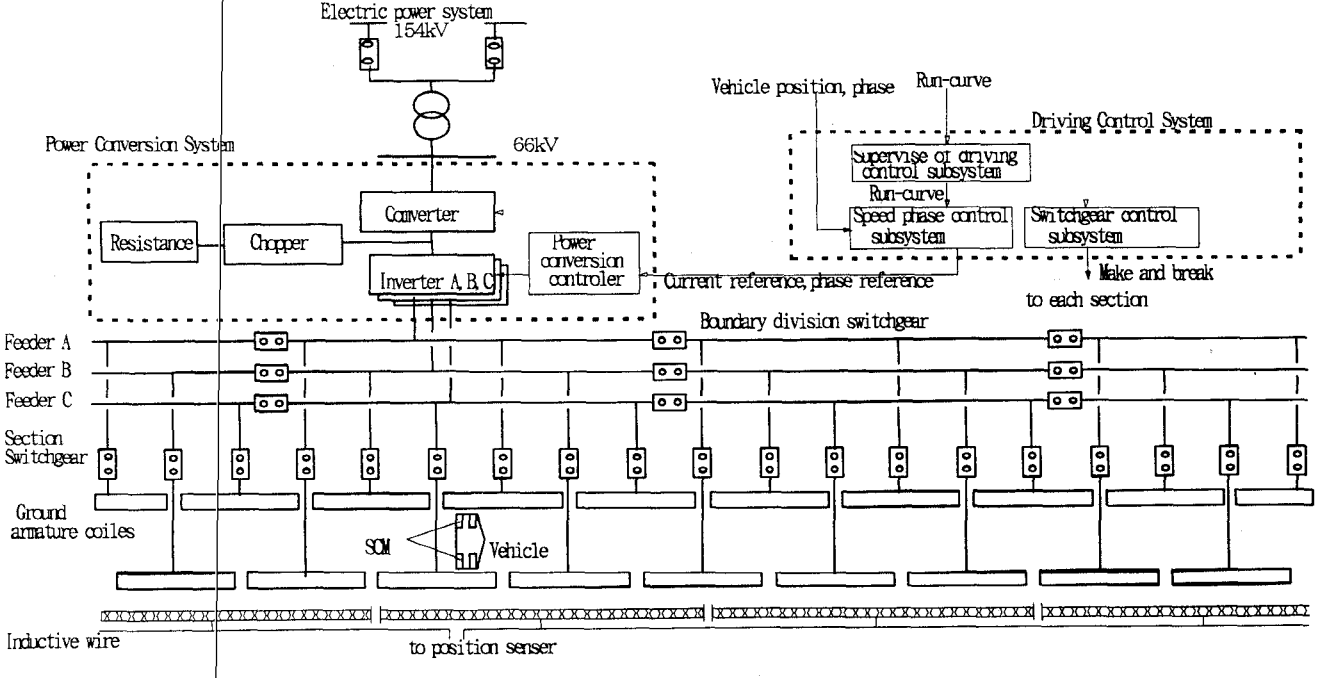

Fig.1 Power supply control system of Yamanashi Maglev Test Line

0-7803-3823-5/97/$10.00© 1997 IEEE

Ⅲ. DRIVE CONTROL SYSTEM

The drive control system is composed of the supervisor of the driving control subsystem, the speed phase control subsystem, and the switchgear control subsystem.

A. Supervisor of the driving control subsystem

The supervisor of the driving control subsystem is responsible for mode setting and start-stop control of the subsystem of the speed phase control and of the switchgear control. Additionally, this subsystem provides the man-machine interface and monitors the test data and the journal.

B. Speed phase control subsystem

The speed phase control subsystem is composed of the speed reference generation unit, the speed control unit, and the phase synchronization control unit.

1) Speed reference generation unit

Traffic control system instructs a run curve to the drive control system before the vehicle begins to run. When this run-curve is received, the speed reference generation unit produces a continuous position-speed curve that the vehicle should follow.

The speed reference generation unit reads the speed instruction value one by one corresponding to the vehicle position coming from the running pattern table and transmits them to the tracking control unit.

The block diagram of the speed reference generation unit is shown in Fig.2.

2) Speed control unit

The speed control unit issues the current command to the power conversion device as the speed instruction value corresponding to a real speed of the vehicle.

Thecurrent command gives output at a rate of 10ms cycle. The block diagram of the speed control unit is shown in Fig.3.

3) Phase synchronization control unit

The phase synchronization control unit operates the phase reference from the vehicle position and the phase signal from the position detection device, and outputs this reference to the electric power conversion device.

The phase synchronization control unit corrects the delay and the phase delay by a signal interface and an internal processing in a phase advancing correction process. The block diagram of phase synchronization control unit is shown in Fig.4.

C. Switchgear control subsystem

The switchgear control subsystem does the making and breaking control of the section switchgear so that the ground armature coils feed power to the output of inverter only in the section where a vehicle exists.

When the vehicle moves from one section to another section, the switchgear control subsystem controls to start and stop the inverter when the vehicle comes to an adequate position.

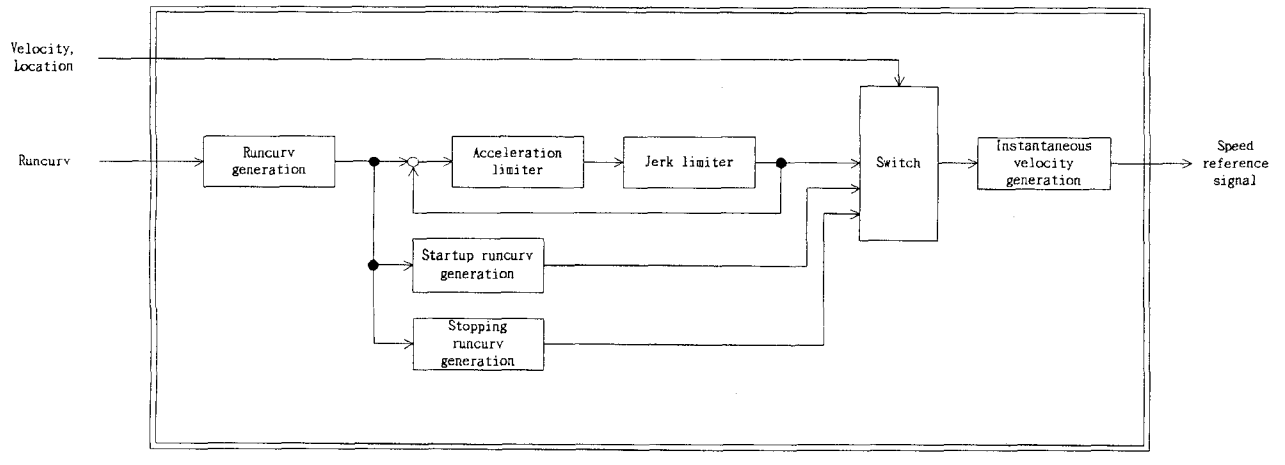

Fig.2 BlockDIagram of the speed reference generation unit

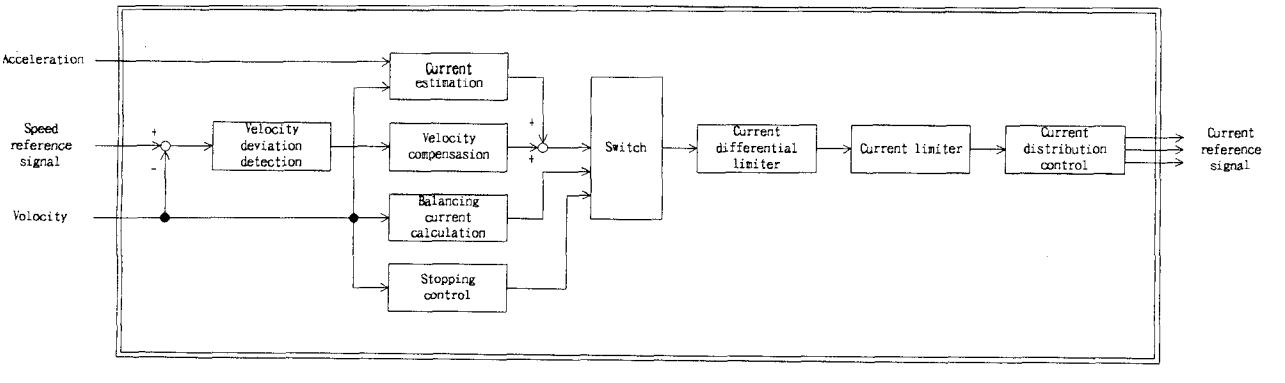

Fig.3 BlockDIagram of the speed control unit

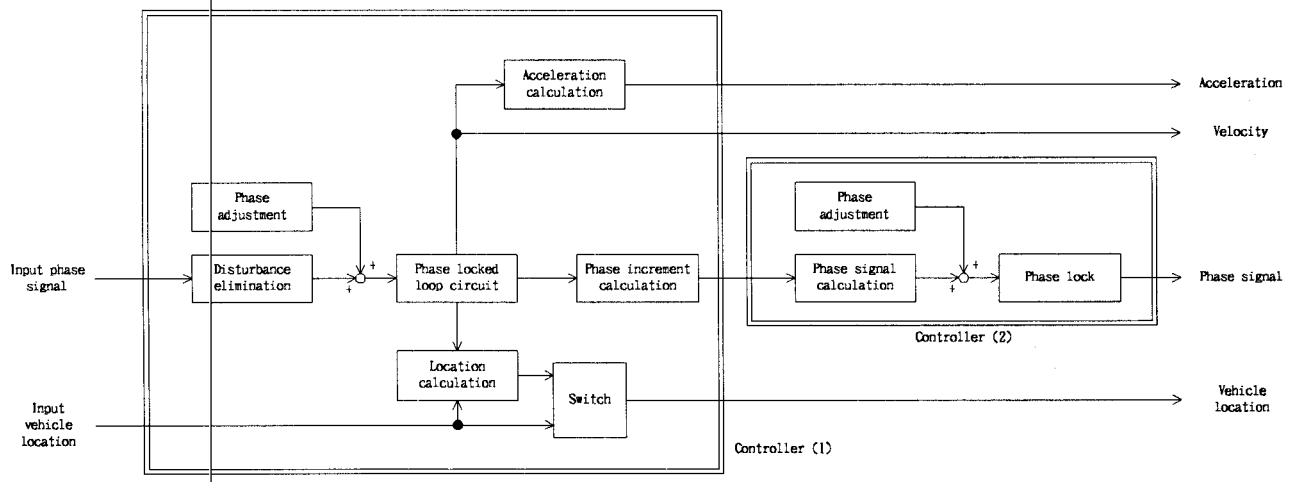

Fig.4 BlockDIagram of the phase synchronization control unit

IV. EQUIPMENT COMPOSITION OF ELECTRIC POWER CONVERSION SYSTEM

The electric power conversion system is composed of the converter, the inverter and the chopper, as illustrated in Fig.5.

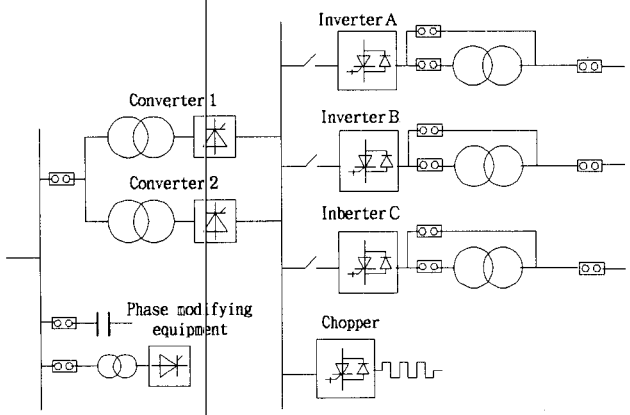

Fig.5 Power conversion system

Fig.6 Power conversion Substation

A. Converter

The converter has a large capacity of 69MW and drives the thyristor rectifier of 24-pulse type in parallel.

The filter and the phase modifying equipment of 50MVA are installed to suppress a higher harmonic and a reactive power fluctuation in the power supply system.

Table 1. Specification of converter

Rated output capacity	69MW
Rated output current	10,000A
Rated direct current input voltage	±3,450V
Main circuit composition	3-phase bridge× 2steps × 2parallel
Element used	6,000V-2,5000A-light triggered thyristor
Element composition	2S1P×6-arms × 8-bridges

B. Inverter

1) Main circuit composition

The inverter is composed of three aspects in single phase bridge, four steps of the pulse width modulation and connects cascade in four steps with the output transformer. Since the core of the output transformer is saturated in the low speed section , the inverter drives in the cascade connection of 1 step in a half bridge and 3 steps in a full bridge. It drives in the cascade connection of four steps in a full bridge in the high-speed area. This main circuit change is done with four composition switches.

When the half bridge is operated, a balancer reactor is installed between these arms to operate in parallel with two arms.

When a direct current is included in the output voltage, the core of the output transformer does a dc magnetization. Therefore, the dc-magnetization preventing control is controlled by using the current of pilot reactors which are connected with the winding of the output transformer in parallel.

2) PWM frequency

The PWM frequency is 500Hz. A phase of each unit inverter carrier is shifted every 45 degrees. The equivalent PWM frequency in the output current is 4kHz.

3) Transformer dc magnetization preventing control

The inverter output transformer is dc-magnetized when the dc components are produced in the inverter output voltage.

Therefore, we detect the flux of the inverter

transformer by a reactor current, called a pilot reactor, connected in parallel with the primary winding. The dc magnetization is detected by calculating the difference between the peak pilot reactor current in positive cycles of output current and that in negative cycles of output current. The inverter output voltage is compensated to cancel the dc magnetization.

4) EMF compensation

We have adopted compensation for the EMF voltage drop to prevent current fluctuation. EMF compensation values are calculated from the inverter output voltage referenced and the detected values of inverter output currents.

Table 2. Specification of PWM inverter

Rated output capacity	38MVA
Rated output current	960A
Rated output frequency	56.6Hz
Rated direct current input voltage	±3,450V
Main circuit composition	Single phase bridge× 3-phases × 4 steps
Control method	Pulse width modulation
Rated modulation frequency	500Hz
Element used	4,500V-3,000A-GTO thyristor
Element composition	4S1P×4 arms × 3-phase ×4 steps

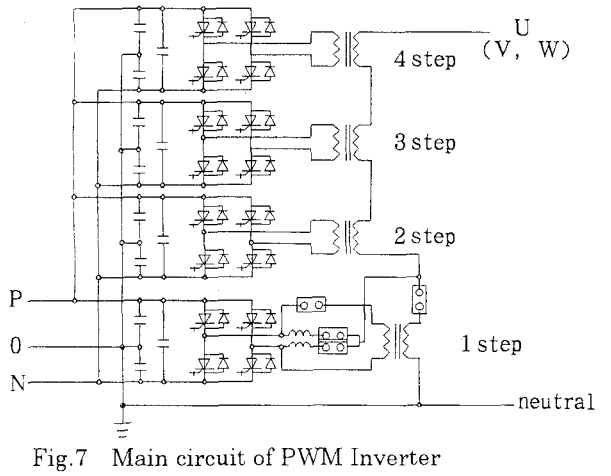

Fig.7 Main circuit of PWM Inverter

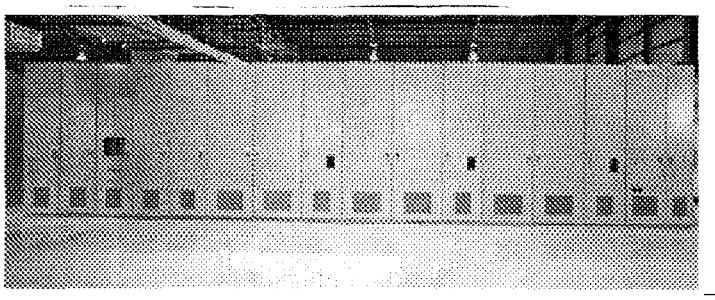

Fig.8 External appearance of inverter

C. Chopper

The chopper is a device to consume the regenerative electric power from the vehicle by the resistor for the regenerative braking. The chopper is composed of five units in parallel to improve reliability. Even if one unit breaks down in parallel, the rest in parallel continue to operate.

When the converter before the inverter is operated is in no-load-condition, this chopper consumes the electric power for the stabilization of the dc voltage control.

Table 3. Specification of chopper

Rated output capacity	19MW
Rated direct current input voltage	±3,550V A
Rated chopping frequency	300Hz
Main circuit composition	5 parallels
Control method	Pulse width modulation

V. COOPERATIVE OPERATE OF ELECTRIC POWER SUPPLY SYSTEM

Thyristor converter should flow several percent of the rated current to avoid the interruption current under no load. The chopper operates with this load.

When the converter is under light load, the converter operates with only half of four of eight bridges.

Moreover, when the inverter supplies the electric power and the converter load increases, the chopper is stopped.

Thus, it is necessary to operate the inverter , the converter and the chopper according to the load. These devices have each electric power characteristic and are operated independently of each other.

Fig.9 shows the chopper operating characteristic.

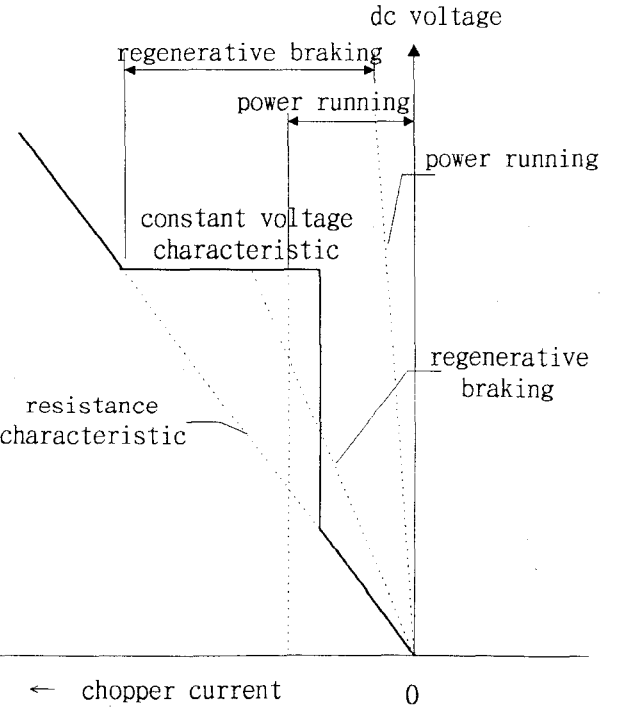

Fig.9 Chopper drive characteristic

VI. TEST RESULTS AT THE COIL LOAD

Figure 10 shows the operating characteristics of the inverter at the coil load.

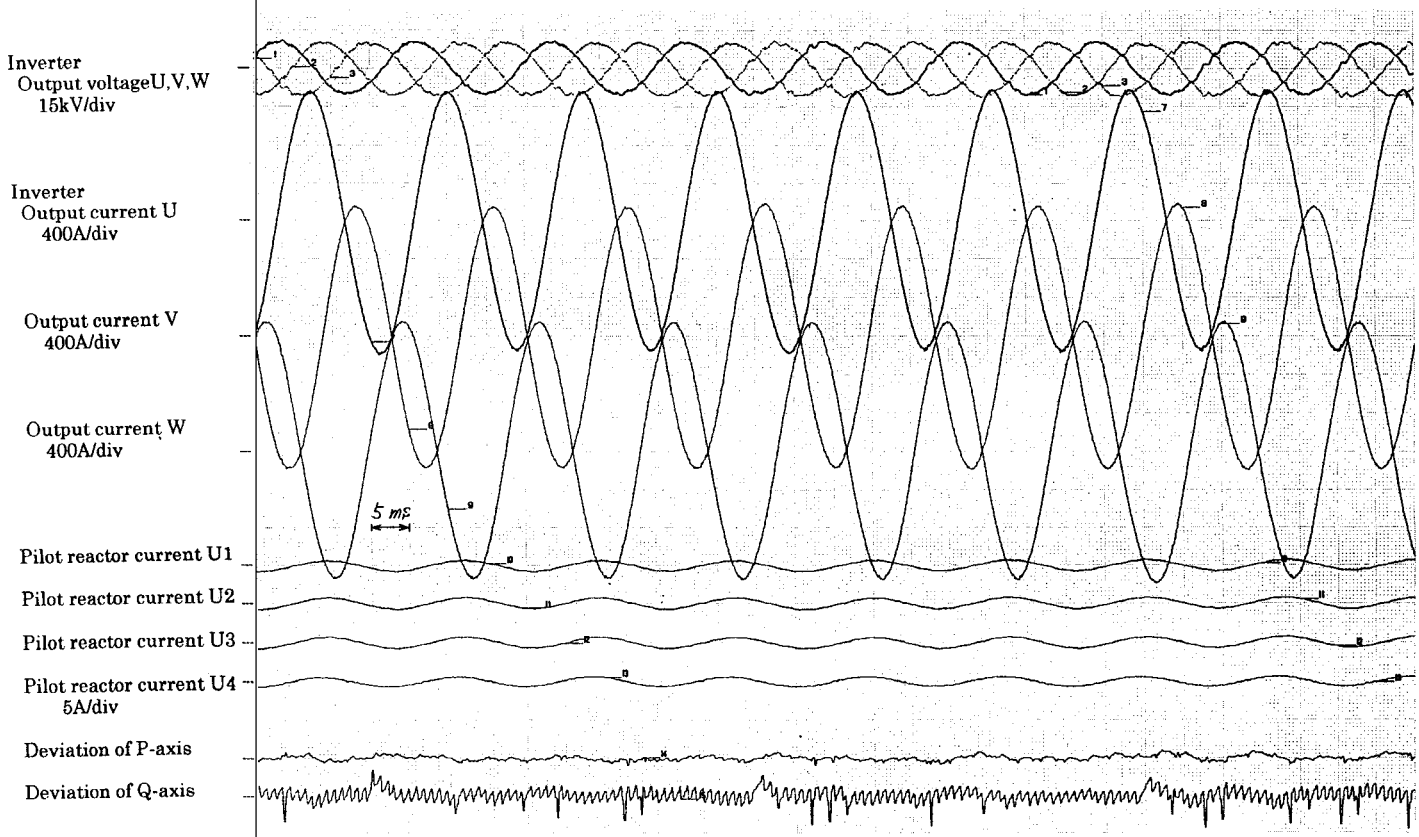

Fig.10 Operating characteristics of inverter

VII. CONCLUSIONS

The power supply system of north line for Yamanashi maglev test line is completed and was able to give the characteristic which it is demanded at first. A first target high-speed run is scheduled with further tuning of the control system in the running tests.

This inverter was manufactured by the financial support from the governmend.

REFERENCES

[1] H.Ikeda,S.Kaga,K.Iwasige,J.Kitano,H,Kikuti,et al., "A 38MVA PWM inverter for Yamanasi Test Track",Proceedings of 1993 National Convention Record I.E.E. Japan,March,1993

[2] H.Ikeda,H.Ohtsuki,J.Kitano,Y.Osada,N.Katoh, N.Morishima,H.Aizawa., "Power Supply System for Superconducting Magnetic Levitation System." 1993

[3] J.Kitano,K.Inden,H.Ikeda,T.Nakashima,S.Koike, Y.Mugiya,H.Ishii,H.Sogihara, "Development of the Drive Control System for Yamanashi MAGLEV Test Line", Proceedings of 1997 National Convention Record I.E.E. Japan,Janualy,1997

Harmonics Control of the 20MVA PWM Inverter Fed LSM Drive System for the Yamanashi Maglev Test Line

Yusuke Yamauchi Hiroaki Tanitsu Jun-ichi Kitano
Central Japan Railway Company
1-6-6 Yaesu, Chuo-ku, Tokyo 103, JAPAN

Shigeo Kaga
Railway Technical Research Institute
2-8-38, Hikari-cho, Kokubunji, 185, JAPAN

Yoshihiro Tagami Yoshinori Otsuka Naoki Morishima
Mitsubishi Electric Corp.
1-1-2 Wadasaki-cho, Hyogo-ku, Kobe, 652, JAPAN

Abstract- **This paper deals with harmonics control of the 20MVA PWM inverter fed LSM drive system for the Yamanashi Maglev Test Line in Japan.**

Contents are following:

(1) To maintain a current control performance, compensate the resonant characteristics of the LSM load with the HP-filter.

(2) Develop the novel PWM control method, to reduce the lowest and/or second order carrier harmonics caused by asymmetrical PWM multiplication.

(3) Reduction of the inductive interference caused by zero sequence harmonics with the common-mode reactor.

1. INTRODUCTION

At Yamanashi maglev test line in Japan, the running tests are conducting since April 3 1997. At this test line, 2 groups of power conversion systems are required, because 2 vehicles are operated at the same time. The power conversion system for the southern line driving a vehicle of 3 sections consists of a 33MW GTO PWM converter and three 20MVA GTO VVVF PWM inverters[2]. The specification of this inverter is shown in Table 1.

Table 1 Specification of the Inverter

Capacity	20MVA
DC Voltage	5250V
AC Voltage	11kV
AC Current	1015A
Frequency	0～46.3(Rating f=41.2Hz)
Connection	Full-Bridge×3stages×3φ
Bridge arm	3S-1P-4A(4.5kV-4kA GTO)
Carrier	Asynchronous 300Hz

Compare with the conventional ac motor drive system, this system has some particular characteristics. For example, this system is to take charge of the LSM coils with long feeder cable, to have very large capacity and to generate very low frequency.

In this paper, we describe three problems caused by these characteristics, the solutions of them and the results of these solutions.

2. HP-FILTER FOR EQUALIZING LSM LOAD IMPEDANCE

The load impedance of LSM with long feeder cable (10 to 20km) has some resonant peaks in the audio frequency. Such resonant peaks affect the current control performance and stability.

To examine the characteristic of this load impedance, we simulated step response of this load circuit assumed single phase model as shown in Fig.1-(1).

The result is shown in Fig.2-(1). As in Fig.2-(1), about 2kHz ripples add on the ramp wave. So, this load impedance has remarkable resonant peak around 2kHz.

In the high frequency operation (described later), this inverter generates around the 6th (full-bridge×3stage) order carrier harmonics, 1800Hz. These harmonics may resonate with this load circuit.

Therefore, we decided to install the HP-filter tuned to compensate the resonant characteristics of this load circuit at the output of the inverter as shown in Fig.1-(2).

We simulated step response of the load circuit with this HP-filter again.

The result is shown in Fig.2-(2). As in Fig.2-(2), the ripples are almost suppressed.

0-7803-3823-5/97/$10.00© 1997 IEEE

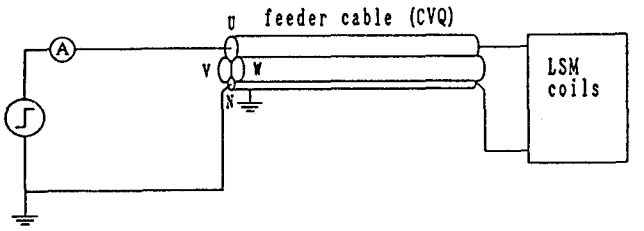

Fig.1-(1) LSM model circuit assumed single phase

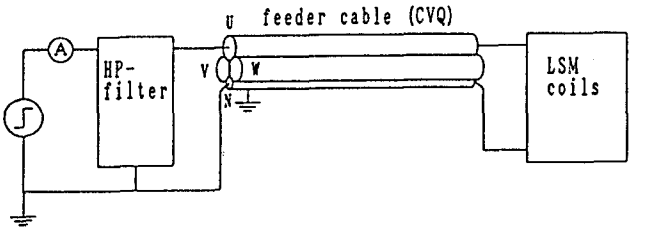

Fig.1-(2) LSM model circuit assumed single phase with HP-filter

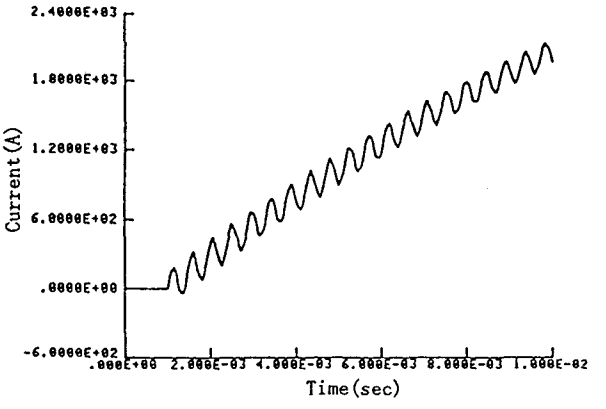

Fig.2-(1) Step response of model circuit

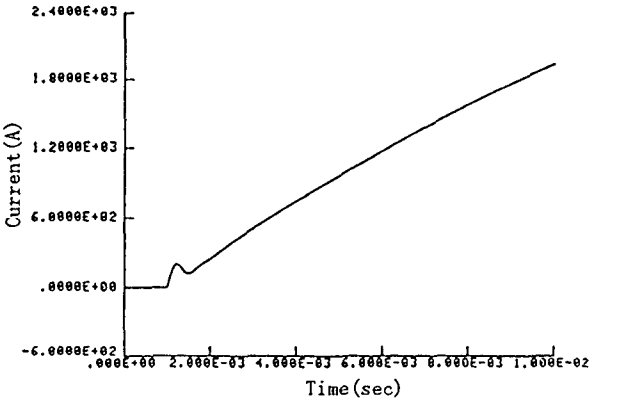

Fig.2-(2) Step response of model circuit with HP-filter

3. Ripple Reduction Control

For this inverter, the number of composed full-bridges are 3 per 1 phase and series connected GTOs are 3 as shown in Fig.3. In the high frequency operation, the construction switch SWH1,SWH2 are close and SWL1,SWL2 are open. In this operation, the inverter construction is symmetric so that the harmonics around the carrier frequency are suppressed by the conventional PWM multiplication with carrier phase shift.

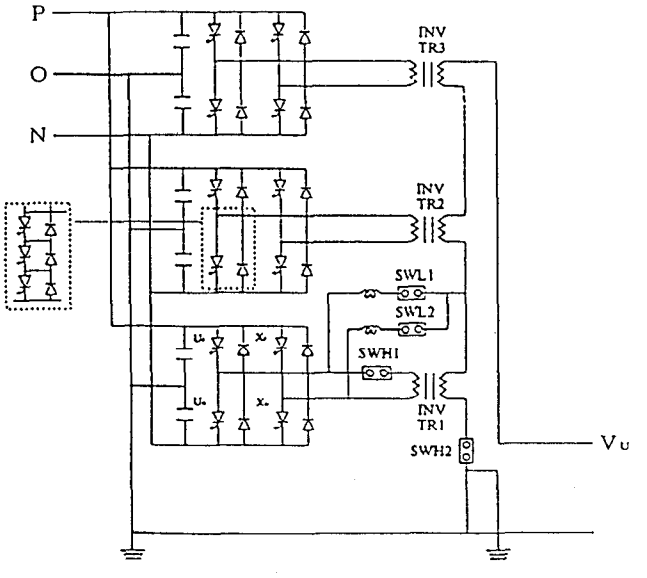

Fig.3 Circuit configuration of inverter

In the low frequency operation, the construction of the inverter is changed as SWH1,SWH2 are open and SWL1,SWL2 are closed and the 1st step inverter is operated as half-bridge. The half-bridge shares the output voltage less than its saturate level and the full-bridges share the rest to minimize the flux of the transformer. Fig.4 shows the each shared voltage in the low frequency operation.

When the 1st step inverter is fully shared the dc part of the output voltage and the other full-bridge inverters are shared the other part (the B area on Fig.4), the harmonics around the second order carrier frequency caused by the full-bridge

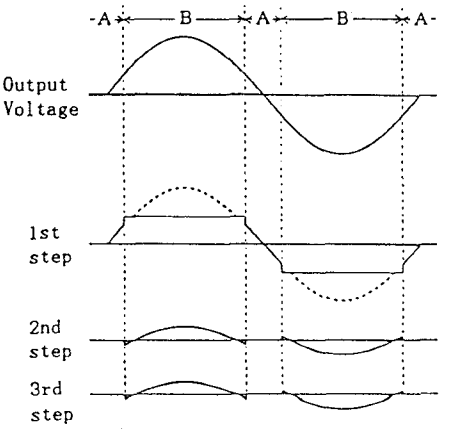

Fig.4 The share of voltage in the low frequency operation

inverter with carrier phase shift. But when the half-bridge is shared all of the output voltage (the A area on Fig.4), the harmonics around the carrier frequency caused by the half-bridge come to the surface.

So that, the novel PWM control called "Ripple Reduction Control" is developed[1].

In this control, the full-bridges act as a kind of an active filter and the harmonics around the lowest and/or second order carrier frequency caused by the half-bridge is suppressed.

Here, we describe about the ripple reduction control using only the 2nd step full-bridge inverter. Fig.5 shows the idea of this control, where S1 is the carrier wave of the 1st step inverter, C1 is the modulating signal, V1 is the output voltage of the 1st step inverter. The output voltage of 2nd step full-bridge inverter V2 is made to cancel the one of the carrier harmonic components of the V1. In addition, V2 is made to be that the average of V2 for one cycle of the carrier frequency is zero. Thus, the harmonics around the lowest order carrier frequency fc(=300Hz) is suppressed.

In similar ways, the ripple reduction control using the 2nd and 3rd step full-bridges suppress the harmonics around the lowest and second order carrier frequency fc(=300Hz) and 2fc(=600Hz).

Fig.6 shows the measured frequency spectrum of the output voltage in voltage-generate mode (3,790V 20Hz) without the ripple reduction control (Fig.6-(1)), with it using only the 2nd step full-bridge (Fig.6-(2)) and with it using the 2nd and 3rd step full-bridges (Fig.6-(3)).

As shown in Fig.6-(1), the harmonics around the lowest and second order carrier frequency fc(=300Hz) and 2fc (=600Hz) appear. As shown in Fig.6-(2), the harmonics around the fc disappear. As shown in Fig.6-(3), the harmonics around the fc and 2fc disappear.

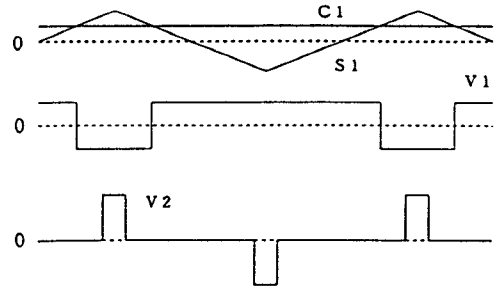

Fig.5 Ripple reduction control

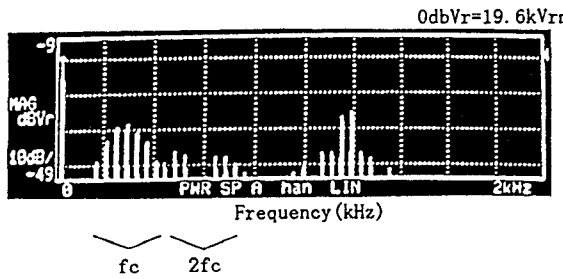

Fig.6-(1) Spectrum of output voltage without ripple reduction control

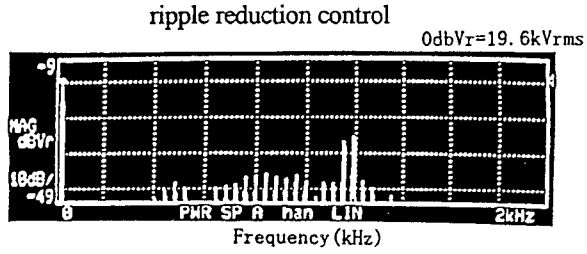

Fig.6-(2) Spectrum of output voltage with ripple reduction control using 2nd step inverter

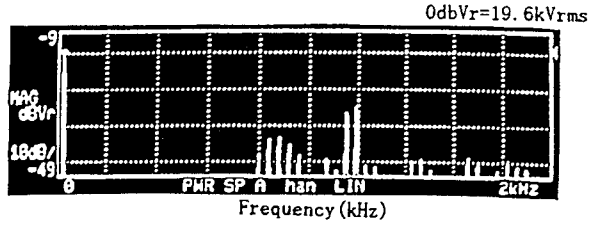

Fig.6(3) Spectrum of output voltage with ripple reduction control using 2nd and 3rd step inverter

4. Common-mode Reactor

The zero sequence harmonics of the inverter with long feeder cable like the Yamanashi Maglev Test Line may cause the inductive interference on the telecommunication line nearby.

So that, the common-mode reactor(X=2pu, m=0.99) is installed at the output of the inverter. The reactor has large common-mode impedance but the rating at the fundamental frequency is only 1%.

To verify the performance of this reactor and to decide the parameters, we simulated by the model of this circuit as shown in Fig.7, where Ig is the ground current as represent of inductive interference.

Fig.8 shows the calculated waveforms and the frequency spectrum of Ig without and with the common-mode reactor. (INV output: 30Hz, 1015A)

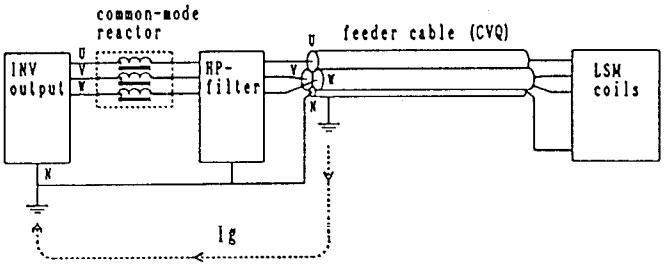

Fig.7 LSM model circuit with the common-mode reactor

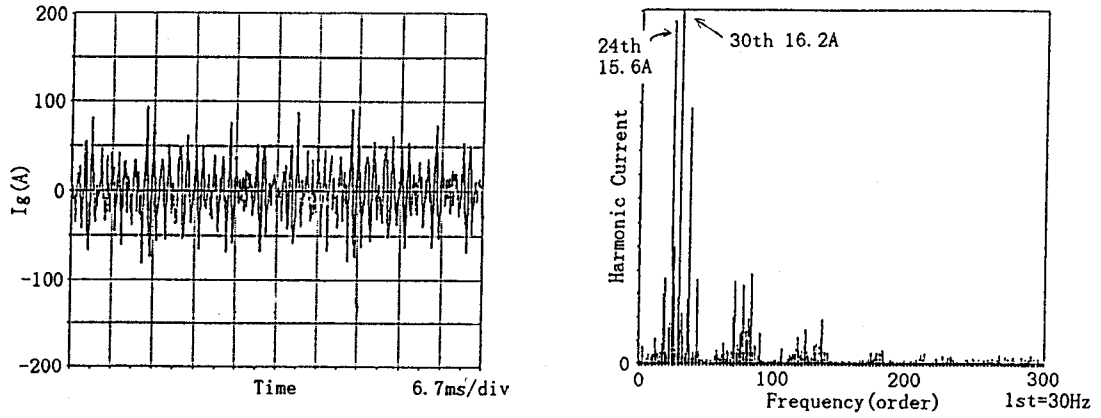

Fig.8-(1) Waveform and spectrum of ground current without the common-mode reactor

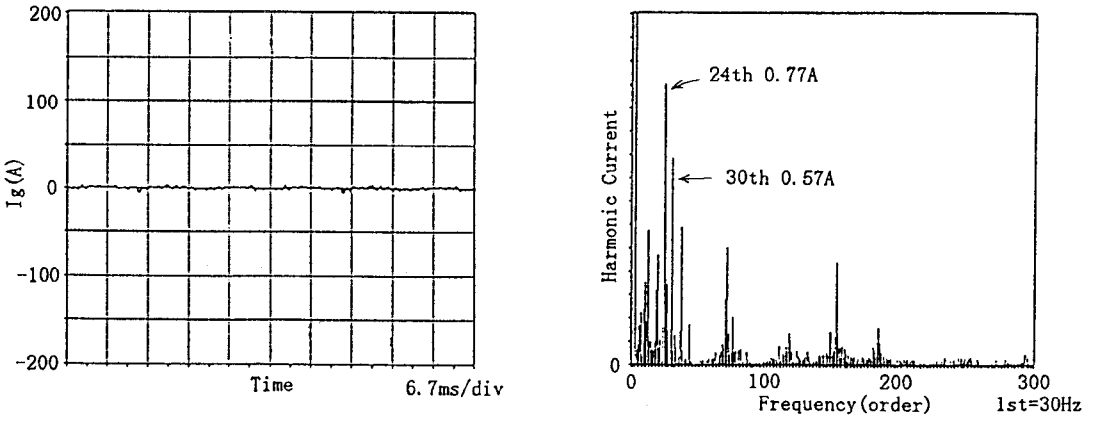

Fig.8-(2) Waveform and spectrum of ground current with the common-mode reactor

As shown in Fig.8, the noises are clearly suppressed.

The results of equivalent interference current Jp that is calculated from harmonics 300 to 3200 Hz are shown in Table 2. As in Table 2, the Jp is suppressed to less than 5% with the common-mode reactor.

Table 2 The equivalent interference current Jp

without reactor	Jp=24.9A
with reactor	Jp=1.16A
	300～3200Hz

5. Conclusion

We have installed the HP-filter at the output of the inverter to equalize the load impedance of LSM with long feeder cable. We have developed the novel PWM control called "Ripple Reduction Control" to suppress the harmonics in low frequency operation and confirmed the effect of this control. We have installed the common-mode reactor at output of the inverter to suppress the zero sequence harmonics of the inverter.

We will continue to verify the effects of these harmonics controls at real-load operation during the magnetic levitation test.

Part of this work is financially supported by the Japanese Government.

References

[1] Morishima, et al., "Current Waveform Improvement in Multiple PWM Inverter for Maglev Drive," Proceedings of 26th Symposium on Cybernetics for Railway Applications, pp.646-650, February 1990(in Japanese)

[2] J.Kitano, et al., "PWM Converter and Inverter System for Yamanashi Maglev Test Line," Proceedings of 14th International Conference on Magnetically Levitated Systems (MAGLEV'95 Bremen), pp.239-243, November 1995

Optimization of Readhesion Control of Shinkansen Trains with Wheel-Rail Adhesion Prediction

Tomoki WATANABE, Akihiro YAMANAKA, Toshio HIROSE, Katsuyoshi HOSH, Shigeru NAKAMURA

Railway Technical Research Institute
2-8-38, Hikari, Kokubunji, Tokyo 185, Japan
Fax: +81-425-73-7259, Phone: +81-425-73-7284
E-mail: tomowata@rtri.or.jp

East Japan Railway Company
2-10-1, Yuurakuchou, Chiyoda, Tokyo, 100 JAPAN
Fax: +81-3-3217-0258, Phone: +81-3-3217-0256

***Abstract*-We propose a new practical readhesion control for electric railway vehicles with three phase drive. The control circuit won't promote wheelslip/slide pehnomenon when it occurs, and the torque is slightly reduced. The former is achieved by using the lowest axle velocity of all as a frequency reference of inverters feeding asynchronous traction motors. The latter is realized by an accurate slip/slide velocity detection. By running tests with a protptype Shinkansen train "STAR 21" of "East Japan Railway", we succeeded to utilize as high traction force as possible under any wheel-rail conditions, with the introduction of wheel-rail adhesion prediction.**

I . INTRODUCTION

When three phase traction was applied first to electric railway vehicles, many people expected higher adhesion performance than that in the case of d.c. traction, because of the steep torque/velocity characteristics peculiar to asynchronous motors. It is proved, however, that to accomplish it satisfactorily we have some questions to be solved. Railway companies require optimal readheive characteristics adapted to each application such as commuter trains, limited express electric multiple units, locomotives, etc.

We investigated readhesion characteristics and control of electric motor vehicles theoretically and practically. Theoretically we proposed Slip Velocity Feedback Torque Control with which we can get good readhesion characteristics by introducing two control parameters (feedback gain and electric time constant) assuming that wheel slip velocities can be measured precisely [1,2].

If we succeed in getting a train velocity and making an inverter frequency by using it, a greater slip than slip frequency of the motors cannot occur. And the smaller the slip velocity is, the more easily we can make the wheel readhere. To get good readhesion characteristics we think that detection of wheel velocities is very important.

We made running tests using STAR21 Shinkansen Train. At first step we could keep slip velocities at low values such as 1-2km/h, in comparison with 10km/h of conventional anti-slip control. Then we experienced reiteration of slip-readhesion when adhesion force was much lower than the tractive effort. To cope with this phenomenon we introduced adhesion prediction. We succeeded in avoiding slip-readhesion reiteration and in utilizing as high adhesion force as possible.

II . AUTOMATIOC CURRENT CONTROL SPURS WHEEL SLIP

When the three phase drive with PWM inverter and asynchronous motors was first introduced for railway application, running tests have proved that a slip of one axle provokes slips of other axles in the case of 1C4M (one PWM inverter feeds 4 traction motors of one motor coach) and of an automatic current control that is dominant in emus with three phase traction. We think it is because traction motor current of a slipping axle decreases and the current order(i.e. slip frequency) increases due to the Automatic Current Regulator (ACR) which raises the torques of the traction motors of adhering wheels and stimulates slips. As soon as all axles corresponding to one inverter begin to slip, the reference speed is lost, which accelerates slips compounded with the effect of the automatic current regulator[3,4]. So slip detection and readhesion control have become inevitable and much effort has been done to improve the readhesive characteristics of electric motor vehicles[3,5,6].

III . HOW TO GET ACCURATE WHEEL VELOCITIES

Conventional way to detect train velocity is to calculate pulses of a speed sensor installed at one end of the wheel axle or traction motor axle. In railway application usually it is very difficult to realise a sensor with as many pulses per rotation as the encoder has in other industrial applications. So we have used an average pulse width calculating method since several years ago [7,8]. We think use of this method is inevitable for detection of small slips and readhesion control. From our experience we propose the calculation in Table 1. It can

Table 1. Method of velocity/acceleration calcuration for anti-slip/slide detection

Velocity	average pulse width calculation of pulses in a sampling time sampling time: 100ms timer of pulse width counting: 100kHz renewal of velocity: every 25ms
acceleration	calculate from velocity difference btw. latest one and one 100ms before

0-7803-3823-5/97/$10.00© 1997 IEEE

be proved that errors of calculated acceleration become minimum when time interval of acceleration equals to that of velocity calculation.

Ⅳ. SLIP VELOCITY CONTROL

Slip velocity control that keeps slip velocity at the reference value is described in [9, 10]. In this case the reference slip velocity is given as a linear function of vehicle velocity and the slip velocity controller is formed by feeding back a real value of slip velocity. They state that step response time of torque must be very fast such as 5ms, so a field-oriented control of traction motors is needed[11]. The reference slip velocity is obtained real-time by searching for an optimal slip velocity[11, 12, 13, 14].

We intend to solve the problem of adding readhesion characteristics to all torque-controllable electric motor vehicles more easily and propose the following method.

(1)From test results analysis we always get maximum adhesion force with wheel slip velocity smaller than 1-2km/h. So we propose to keep slip/slide velocity within these values.

(2)We get axle velocities with above mentioned method. Here we call a minimum/maximum value of 4 or more axle velocities in time of powering/braking a pseudo train velocity (or a reference velocity) and the difference of axle velocity from pseudo train velocity a pseudo slip velocity.

(3)We detect a small pseudo slip/slide velocity using the threshold level of within 1km/h for example.

(4)Then we reduce the torque of the relevant traction motor. The current reduction takes place in steps proportional to the pseudo slip of the axle.

Our proposed readhesion control has the following advantages.

(1)Detection of small slip/slide minimizes torque reduction required for readhesion.

(2)By detection of small slip and prevention of large slip we can avoid losing a train velocity :the reference velocity follows well the train velocity.

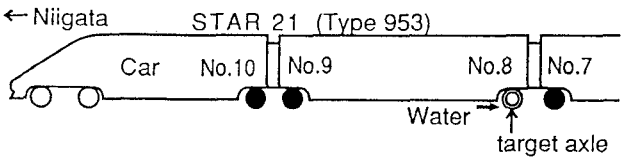

Fig2. Tested vehicles of STAR21 train

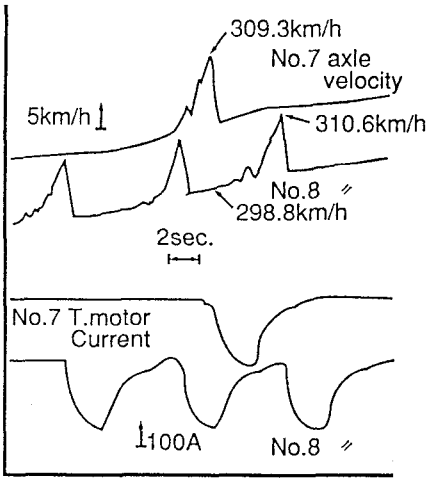

Fig 3. Running test results of STAR21 (DEC. 8th '93)

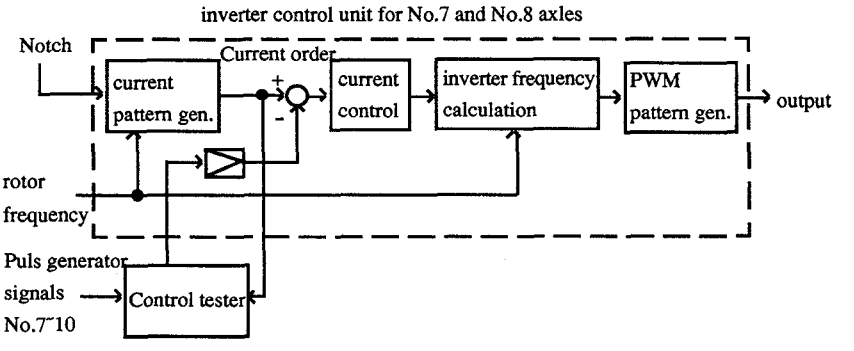

Fig 4. Control tester and inverter control unit

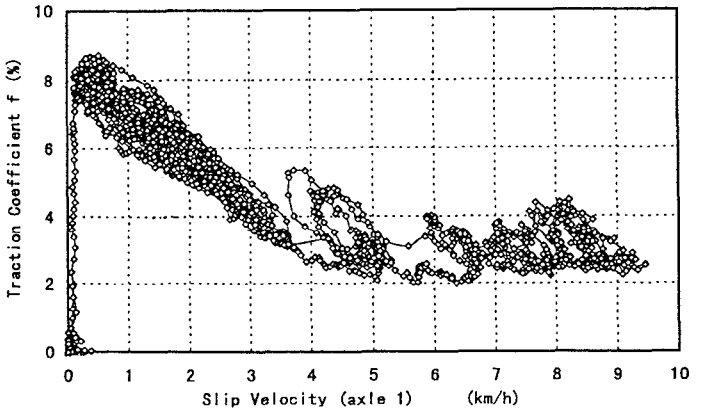

Fig 1. An example of traction coeffient of shinkansen train (powering, water spayed on rail)

Table 2. Comparison of Control of inverter and control tester

controller of the inverter No.7,9,10 axle	control tester (our proposal) No.8 axle
short time velocity detection (5ms) and filtering	velocity detection using 100ms interval renewal every 25ms
current reduction flollowing fixed pattern	current reduction in accordance with slip velocity and acceleration

(3)This practical method of readhesion control can apply both conventional slip frequency control and vector control. Because slip phenomena do not change so fast if we succeed in keeping slip velocity at a small value.

(4)Almost all electric motor vehicles have ACR that substantially aggravates readhesion characteristics. We recommend such a design that control circuit does not promote slip/slide phenomena when slip/slide occurs. But it is not necessary, because the following running test was performed without changing the Automatic Current Regulator and we got good results.

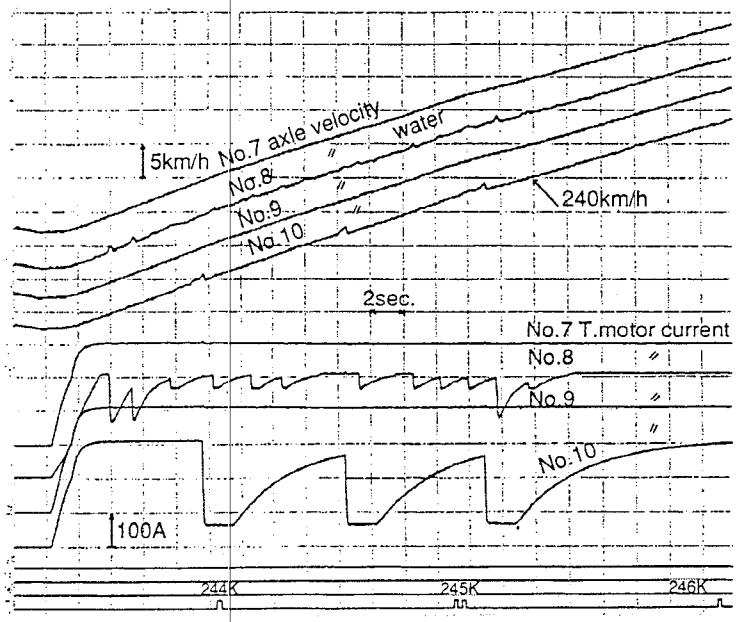

Fig 5. First step test results of STAR21(control applied to 8th wheel)

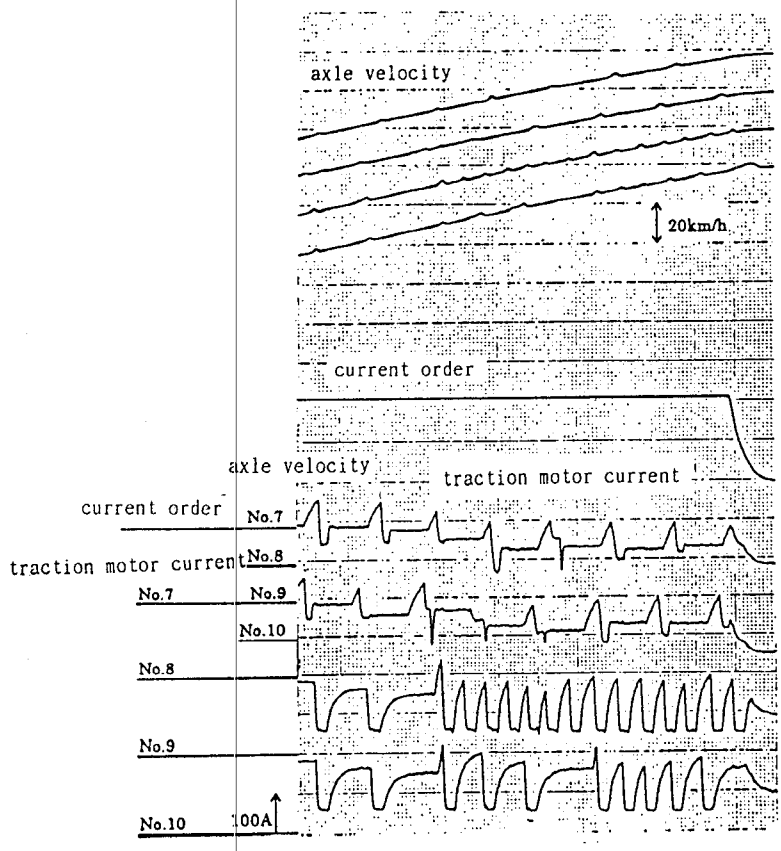

Fig 6. Test results of STAR21

(Readhesion control with adhesion prediction applied to 7th and 8th axles)

V. TEST RESULTS WITH STAR21 SHINKANSEN TRAIN

We performed running tests with STAR21 Shinkansen train. At first step we measured axle velocities of STAR21 with water spayed on rail. From Fig.3 we can see relative large slips and large traction motor current reductions.

To make on-board optimization process faster we installed a "Control Tester" between master controller and controller of inverter. The control tester detects wheel slip and issues the current reducing order to the controller of the inverter. Control parameter can be changed directly from a keyboard of the control tester.

No.8 axle of Fig 3 shows a result of running tests of proposed readhesion control in 1994. We succeeded in keeping both smaller slip and higher traction motor current than in the conventional case of the controller of the inverter(No.10 axle).

However, we found that frequent repetition of slip-readhesion and large fluctuaion of traction motors occur at bad wheel-rail condition or when adhesion force is much lower than the tractive effort determined by traction motor current.

We introduced a learning control using adhesion prediction. Difference in force between tractive effort and adhesion force(=traction force) causes acceleration of axle. So adhesion force fa can be predicted by

$$fa = ft - K * \alpha$$

ft : tractive effort

K : constant (rotational inertia)

α : axle acceleration

No.7, 8 axle of Fig 6 shows a test result of our new proposal. We succeed in stopping slip-readhesion reiteration and in keeping traction motor current much more stable.

new proposal

controller of the inverter

VI. CONCLUSIONS

As a practical method of readhesion control for electric motor vehicles with three phase drive, we recommended such a design that control circuit does

not promote slip/slide phenomena of wheel when a slip/ slide occurs, by using an Automatic Current Regulator which does not respond to traction motor velocity variation due to slip, and by using the lowest velocity of all motor axles as a reference frequency value of inverters feedig asynchronous traction motors. And we propose detection of a small pseudo slip, a slight reduction of traction motor current in time of the detection and online adhesion prediction. Running tests results show the effectiveness of our proposed readhesion control.

VII. REFERENCE

[1] Watanabe,T.,Ogasa,M.:Improvement of readhesive chracteristics of electric motor vehicles by Slip Velocity Feedback Torque Control, Speedam, pp.373-378, 1992, Positano

[2]T.Watanabe,M.Ogasa:Realization of Anti-slip/slide Control in Railway Motor Vehicles by Slip Velocity Feedback Torque Control, EPE'93, Vol.6,pp.156-161, Aahen

[3] Aburaya,K.:Technical trend of inverter controlled electric vehicles, Denkisha no Kagaku, Vol.43, No.2,p.15,1990(in Japanese)

[4]T.Watanabe,M.Ogasa,S.Ohe:Improvement of Re-adhesive Characteristics of Electric Motor Vehicles, STECH'93,pp.243-247, Yokohama

[5] Yasukawa,S.,Ohe,S.:A study on Re-adhesion Control for the Inverter Controlled Motor Vehicle by Simulation,National conv.rec.IEEJ-IAS,6,1990(in Japanese)

[6] Nakazawa,H.,Kikuchi,T.:VVVF inverter control equipment of series 05 of Tozai line of TRTA, Denkisha no Kagaku,Vol.44,No.12,pp.13-20,.1991(in Japanese)

[7] Watanabe,T. :Precise Detection of Train Velocity, National conv. rec. IEEJ-IAS,12, 1989 (in Japanese)

[8] Watanabe,T.,Komoto,Y.:Automatic Split and Combine System of the Shinkansen train, CCCT'89 (IFAC),pp.123-129,Paris

[9] Weinhardt,M.:Erkenntnisse und Maßnahmen zur Hochausnutzung des Kraftschlusses auf modernen Triebfahrzeugen,AET,42,pp.119-144, 1987

[10] Köck,F.,Weinhardt,M.:Tractive effort and wheel slip control of locomotive type 120,10th World Congress on Automatic Control (IFAC), Vol.3,pp.259-267

[11] Buscher,M.,Pfeiffer,R.,Schwarz,H-J.: Radschlupf-regelung für Drehstromlokomotiven, Elektrisehe Bahnen,Vol.91,No.5, pp.163-178, 1993

[12] Vogel,U.:Untersuchung eines Verfahrens zur Hochausnutzung des Rad-Schiene-Kraftschlusses bei Triebfahrzeugen,Elektrische Bahnen,Vol.89,No.10, pp.285-292,1991

[13] Vogel,U.:Auwendung eines Verfahvens zur Hochausnutzung des Rad-Schiene-Kraftschlusses auf ein Digitalrechnermodell der Lokomotive Baureihe 120, Elektrische Bahnen,Vol.90,No.12,pp.359-365,1992

[14] Körber,J. et al:Die Weiterentwicklung der Leistungs- und Steuerungselektronik gemäß den Anforderungen des modernen Schienenverkehrs,ZEV Glases.Ann Vol. 114, No.11/12,pp.503-511, 1990

[15] Kimura,A.,Nakamura,K.:Study on the Stabilization of Control Systems for Induction Moter Driver Rolling Stock,T.IEE Japan,Vol.110-D, No.3, pp.291-298,1990 (in Japanese)

Improvement of Re-adhesion for Commuter Trains with Vector Control Traction Inverter

Author Name

Ikuo Yasuoka, Takuma Henmi, Yooske Nakazawa, Ikuya Aoyama

Drive Systems Department,Fuchu Works,Toshiba Corporation

1 Toshiba-cho, Fuchu-shi,Tokyo, 183, Japan

Fax: +81-423-40-8044 Phone: +81-423-33-2378

Abstract - We developed a re-adhesion control algorithm of traction inverter system with vector control for commuter trains.

The re-adhesion algorithm consists of creep control, estimated traction force control, oscillation suppress control and all wheel slip suppression control.

As the result of the running test with new control, the adhesion performance was improved by more than 20% and passenger comfort was greatly improved, regardless of the conditions of the rail, gradient and kind of rolling stock.

I . Introduction

The individual axle control traction system ,in which each traction motor for a commuter train is independently controlled by one inverter , has been proposed [1]. This system is suitable for re-adhesion control , because each inverter can independently reduce its own motor torque according to the slipping condition of the wheel . Therefore, the reduction of the total torque of the train can be minimized.

This technology made it possible to reduce the number of motor cars to trailer cars for a train formation, and the percentage of number of motor cars can be reduced to be less than fifty percent in some cases.

Accordingly, the each motor power is increased, and the traction force and expected adhesion coefficient of each drive axle should be also increased. That means average adhesion under wet rail condition, such as in rainy days, should be kept at higher grade ,otherwise there will be large effects on the accelerating performance of the train system

Moreover ,when the number of traction motors is small because of short train formation, and the rail condition is poor because of slopes and tunnels, the accelerating performance will fully depends on its re-adhesion control ability by simultaneous slipping of some motors.

This paper describes development and test results of the creep control with speed observer .This system applies vector control for guide torque responses, and performs good re-adhesion. The concept of this control and the contents of the algorithm used for it are also described.

II . Concept for re-adhesion control

The traction inverter circuits for individual control of the motors on commuter trains are shown in Fig. 1.

The maximum power of each induction motor is 220 kW , and the expected adhesion coefficient is 17 to 20% depending on the rail conditions.

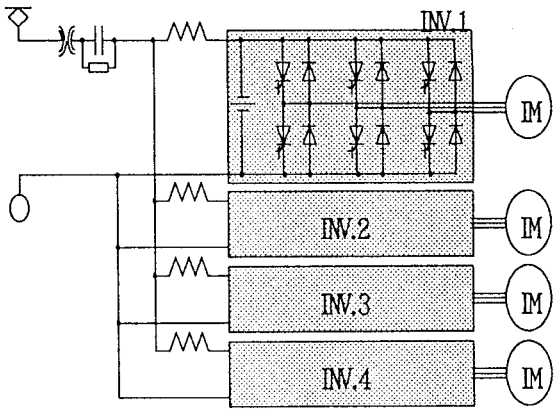

Fig. 1 Traction inverter circuits

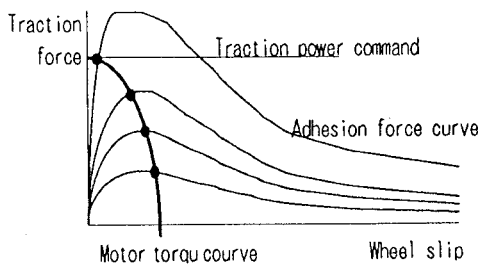

Fig. 2 Traction force between wheel and rail

0-7803-3823-5/97/$10.00© 1997 IEEE

In the conventional cases, traction inverters are controlled by the rotor slip frequency method, that is, the value of Voltage/Frequency and the motor current are control to be constant.

Since the secondary magnetic flux phase of the motor is not directly controlled in this method, it takes nearly 100 ms to settle the transient condition. This makes it difficult to control the motor torque quickly. It is necessary to obtain the optimum tractive power when the rotor slip changes sharply, because of the characteristics of the traction transmitted from the wheels to the rails and the slip ratio shown in Fig. 2. That is, even if the re-adhesion control speed would be increased, the actual torque cannot follow it. To overcome this problem, stepped control is employed to judge slip by watching acceleration the change rate of the wheel speed and reducing the motor current as shown in Fig. 3.

If the vector control described in the referenced paper [2] and shown in Fig. 4 is employed, the response time of the motor torque to the re-adhesion reference value becomes as short as 10 ms. The difference of these systems in step response is shown in Fig. 5.

Since a quick response is obtained by this method, the torque on the wet rail can be controlled continuously in the creep range in Fig. 2.

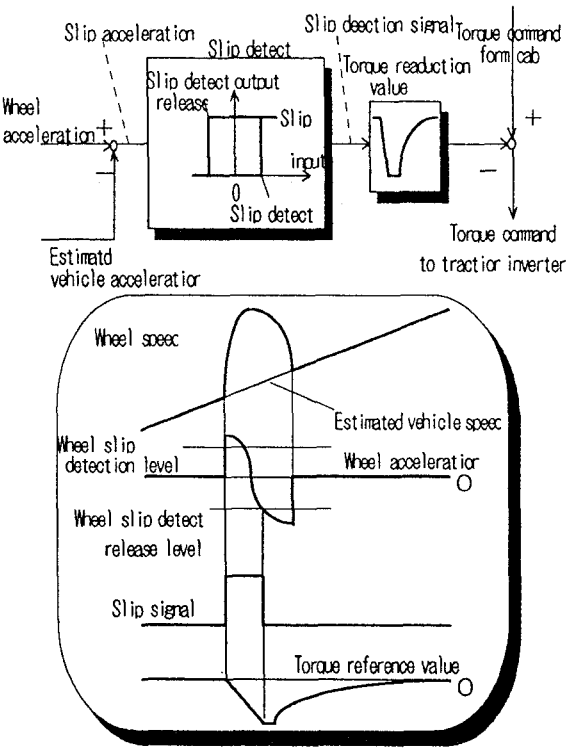

Fig. 3 Acceleration detector

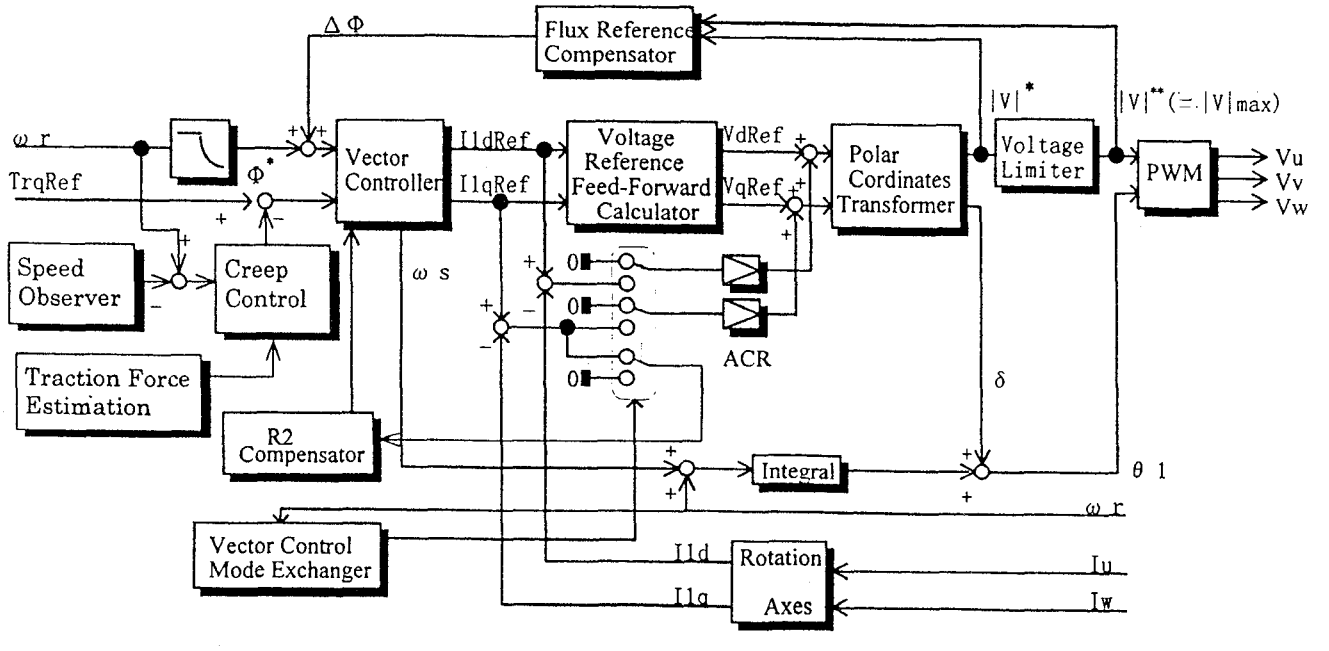

Fig. 4 Vector control for electric cars

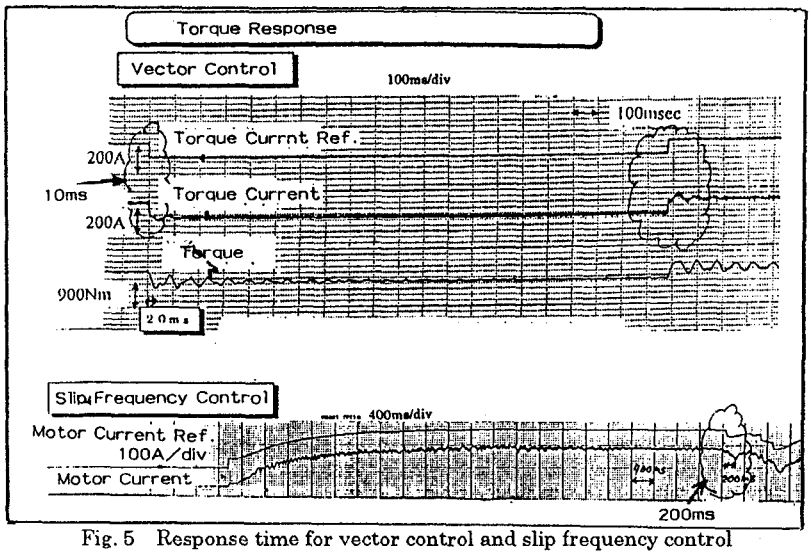

Fig. 5 Response time for vector control and slip frequency control

The re-adhesion algorithm for implementing this method is the speed observer type of creep control. The concept of this control is shown in Fig. 6.

The slip speed and torque with changes of the adhesion coefficient simulated by this method are shown in Fig. 7. In this figure, results of the conventional rotor slip frequency control method are also shown for comparison. By the proposed control system, the maximum usable tractive power reaches approximately equal to the motor torque, according to the slip ratio under the adhesion limit in the creep range. The conventional control system , however, repeats so-called slip and re-adhesion in the slip range.

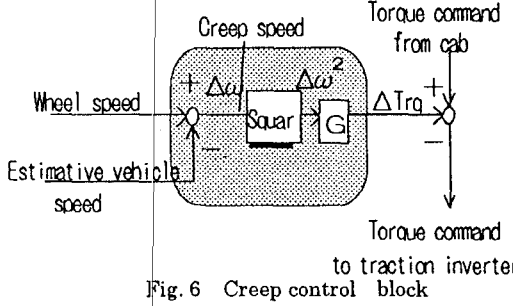

Fig. 6 Creep control block

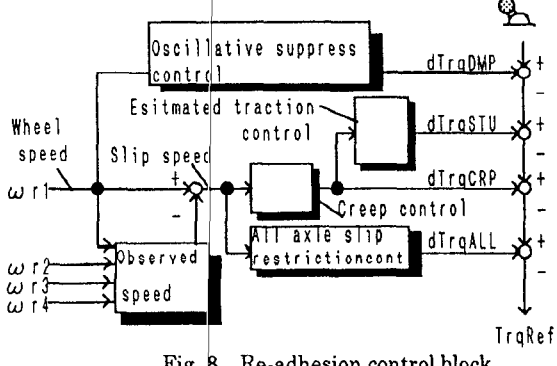

Fig. 8 Re-adhesion control block

III. Function of creep control with speed observer

The details of the creep control with speed observer and its concept , as shown in Fig. 8, are explained below.

The general configuration of the re-adhesion control implemented here is shown in Fig. 8. The overall control consists of creep control, estimated traction force control, oscillation suppress control , all wheel slip suppression control. The operation principle and configuration of each control function are explained below. The method used to solve the problems that occurred in the field running test is also explained.

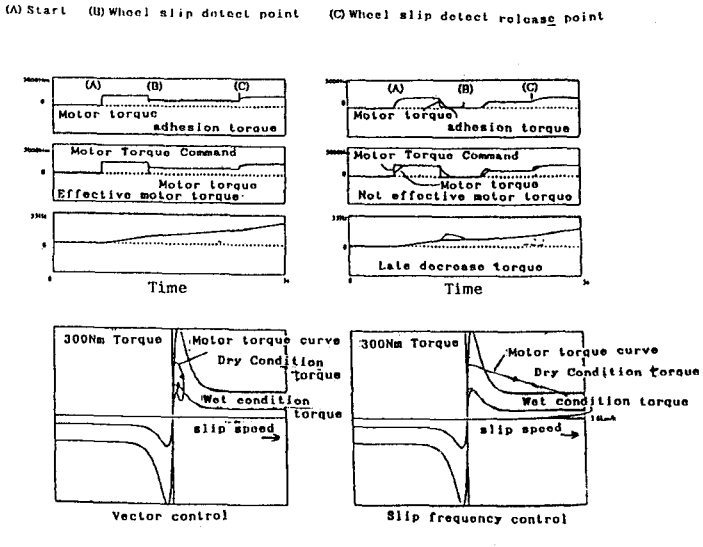

fig.7 Simulation result

A. Speed observer

Detection of the slip speed is essential to the creep control. We call the slip speed is as the difference between the wheel speed and vehicle speed. The wheel speed can be conventionally measured with a motor shaft speed sensor. A vehicle speed sensor , however, cannot easily be installed in the conventional systems, and it is required to estimate from several motor shaft sensor signals.

Since four motors are installed within a motor car, the individual control system estimates the vehicle speed from the respective speeds of those motors. The vehicle speed is estimated on the basis of the lowest speed of the four motors (in the powering mode), considering the inertia of the vehicle.

Block of estimation of vehicle speed is shown in fig. 9 and vehicle speed data is shown in fig. 10.

B. Estimation of traction force control

When the adhesion force is evenly lowered through the track, for example by rainy condition, the slip control can be stabilized by lowering the torque command in advance, as is known from experience. The question in this case is how much the torque command should be lowered. When creep control is applied, the motor torque automatically move to the balanced point with the adhesion force of the rail, thus the adhesion force on the rail can be estimated. In the estimated traction force control, the torque is determined , in advance , according to the torque reduction by creep control.

Running test data are shown in Fig. 15.

C. All axle slip suppress control

Since the vehicle speed is estimated from the four wheel axles, if all of those axles slip at the same time on a rainy day, for example, then the estimated vehicle speed gradually deviates from the true speed.

All axle slip is suppressed by detecting it. and lowering the torque properly. The sign used to detect all axle slip is the fact that the slip speed does not become zero for a certain period. When this is detected, the torque is reduced slightly according to a set reference value. Since the motor torque and adhesion torque are almost balanced with each other by the creep control, the slip speed can be set to zero by lowering the torque slightly. As a result, all axle slip, by which the vehicle speed is lost, can be minimized.

D. Oscillation suppress

If the response of the creep control is increased so that the motor torque follows the change of the rail condition, the bogies drive system resonate at about 10 Hz, and passenger is uncomfortable and the average transmitted torque is reduced because of the oscillation of the torque and bogie.

This oscillation can be reduced even in the high response mode of the creep control by detecting the oscillation of the motor speed compensating (lead and lag is shown in fig.12), and lowering the torque .

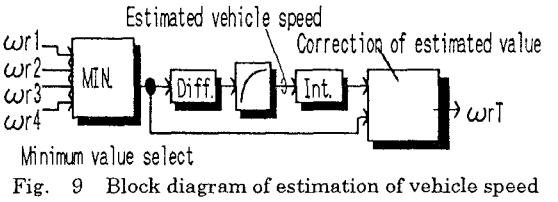

Fig. 9 Block diagram of estimation of vehicle speed

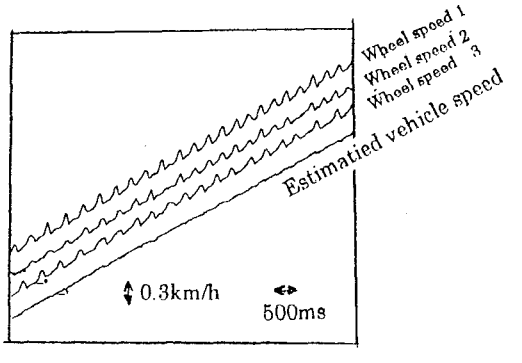

Fig. 10 Estimation of vehicle speed

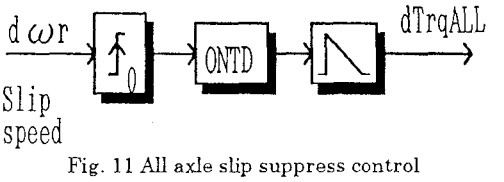

Fig. 11 All axle slip suppress control

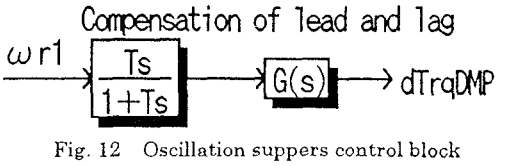

Fig. 12 Oscillation suppers control block

E. Optimization of creep control

The motor torque for the creep control must be set so that it follows the maximum values of adhesion torque. We did not have suitable data, however, at what slip speed the maximum torque was obtained.
Therefore, measurement was took place the relationship between the slip speed and traction force by changing the motor torque for the creep control as shown in Fig. 13.

An example measurement result is shown in Fig. 14. According to this figure, the traction force becomes maximum value when the slip speed is 0.1 ~ 0.3 km/h.

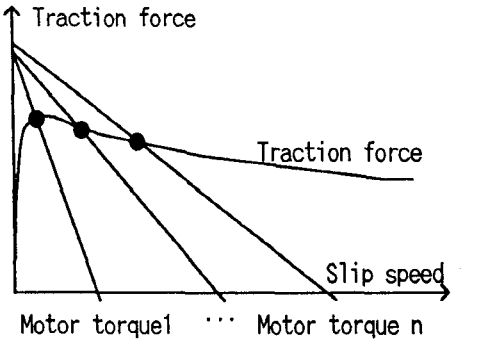

Fig. 13 Slip speed and traction force

IV. Confirmation of effects by field running test of actual cars

We tested the creep control with speed observers which uses vector control by actual train. Simultaneously conventional slip frequency control by detection of motor wheel acceleration is also tested by the same train for comparison.

As shown in Table 1, the control result in two cases for different cars and tracks are compared.
Typical running test data applying the vector control and the slip frequency control obtained with water sprayed rails on a gradient are shown in Fig.16 and Fig.17 respectively.
The results of adhesion performance evaluation are shown in Table 1.

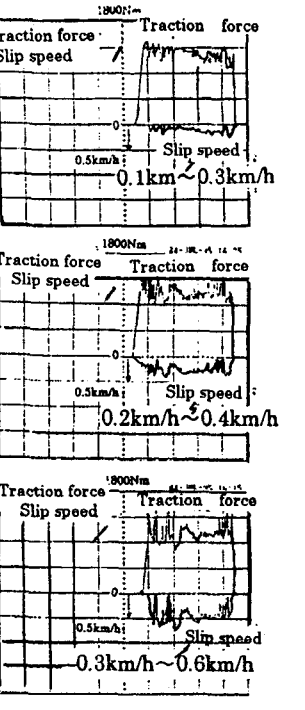

Fig. 14 Traction force and Slip speed

V. Conclusions

The developed re-adhesion control has the following effects.
The adhesion performance is improved by about 20%.
Continuous control in the creep range becomes possible.
Oscillating torque fluctuation caused by wheel slip and re-adhesion control during acceleration, is reduced to nearly half.

We expect that the vector control for electric cars is the most suitable control method for traction inverters . The speed observer type creep control, proposed in this paper will replace the conventional control method.

REFERENCES

[1] I.Aoyama,A.Nishio,I.Yasuoka, and E.Takahara,"The individual-Axle-Control (IAC) Traction System for Electric Railcars",Proc. IPEC-Yokohama '95,pp801-806,1995
[2] Y. Nakazawa, S. Toda, I. Yasuoka ,and Dr. H. Naito,"One-Pulse PWM Mode Vector Control for Traction Drives", IEEE Work Shop on Power Electronics in Transportation, pp135-141, 1996

Table 1 The result of running test

test case	Expected adhesion coefficient	Motor current in dry condition	Average acceleration dry condition	Water splashing rate	slip speed	Gradient in %	Average motor current in wet condition	Average acceleration wet condition	Forward and backward movement in wet state
VC1 SFC1	21% 21%	175A 175A	1.3 km/h/s 1.3 km/h/s	1.5 l/min.	0.4～0.7km/h 7～8km/h	3.5	120A 95A	0.91km/h/s 0.84km/h/s	-------- 0.08g
VC2 SFC2	18% 18%	140A 140A	2.3 km/h/s 2.3 km/h/s	3 .0 l/min.	0.7～1.0km/h ----------	level	120A 100A	2.07km/h/s 1.94km/h/s	0.03g 0.08g

VC1,VC2 : Vectrol control SFC1 ,SFC2: Slip frequency control

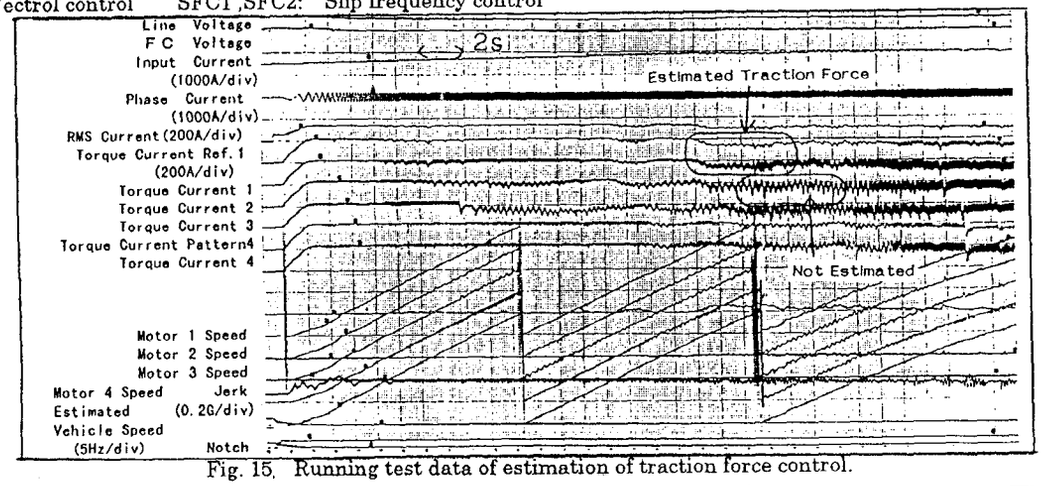

Fig. 15. Running test data of estimation of traction force control.

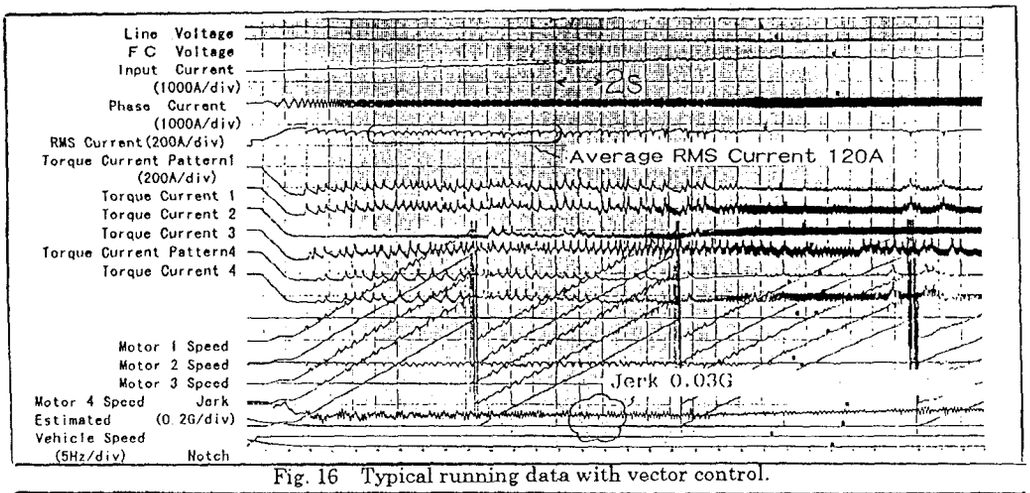

Fig. 16 Typical running data with vector control.

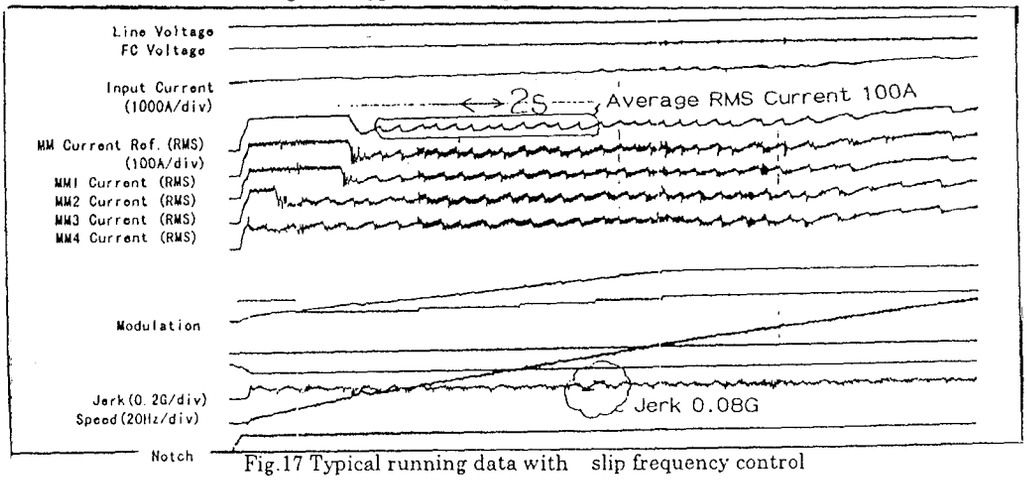

Fig.17 Typical running data with slip frequency control

Harmonic Compensator for 50-Hz Fed AC Railway Vehicles

Masamichi Ogasa
Railway Technical Research Institute
2-8-38 Hikari-cho, Kokubunji 185, JAPAN
Fax: +81-425-73-7259, Phone: +81-425-73-7284
E-mail: ogasa@rtri.or.jp

Jens Onno Krah & Joachim Holtz
University-Wuppertal
42097 Wuppertal, GERMANY

Abstract ------ AC railway vehicles controlled by PWM line side converters inject harmonic current into the feeding overhead line. This causes problems such as resonance expansions which produce misfunctions or overcurrents at sub stations and electromagnetic interference with signalling systems. Normal active filters only shift the harmonic frequencies to a higher range. A novel harmonic compensator produces an exact counter mmf of which in the main transformer main flux is then sinusoidal. Experimental results from a small model of a Japanese AC railway vehicle are described. Especially the 3-4kHz frequency range that coincides with the signalling band harmonic currents are quite well suppressed. From the result, this novel compensating method appears promising for any 50Hz fed PWM controlled AC railway traction system.

1. Introduction

From the point of low energy consumption and maintenance free, PWM controlled AC traction system has been introduced in railway vehicles. Usually line side single phase PWM converters are used to produce DC voltage necessary for the 3 phase PWM inverters to drive 3 phase induction motors for traction. And to make mmf in main transformer near sinusoidal, the secondary windings are divided to 4 stages for examples and of course each winding has a PWM converter which converts AC voltage to higher DC voltage. These converters are operated at different PWM phase angles. But from the principle of switching, it is inevitable to occur harmonic flux. This makes primary current containing high frequency harmonics caused by the PWM switching.

The harmonic currents cause many problems. Resonances with feeder line inductance L and capacitance C between feeder line and earth, harmonic current occured by line side converters may get amplified more than 10 times as large as the original, at the sub statiotions. This overcurrent has a possibility to burn out condensors in the sub stations. Electromagnetic interference for the signalling system has a danger to fail the train control signals like positions, or speed.

2. Suppresion of PWM Converters Harmonics by Various Methods

There are many different methods to suppress the harmonic currents.

To avoid big amplitude of the harmonic currents, the converters are operated with different PWM phase angles. But from the principle of switching, it is inevitable to produce harmonic flux components in the transformer.

The easiest solution is to use harmonic passive filter composed by series inductor, relatively big capacitor and damping resistor. But this method has problems that the weight will be quite big. Should the resonance condition change, the harmonics elimination effect is lost.

Using three level converters is another solution. The effective switching frequency is then doubled, and the individual voltage steps of the switching are reduced to one half. But the penalty is that the number of power semiconductor devices doubles. There remains still higher frequency harmonics, and the cost and the complexity increase.

Another proposal is adaptive PWM modulation. The prevailing resonance conditions in the line are identified in a real-time process. This method needs a good identification.

Active Filter installation is a further choice. A PWM converters operates at a very high frequency range, forming part of the closed loop control system with the fundamental load current or voltages as the reference. This method transfers the harmonics of the traction converter to a higher frequency range, which is determined by the switching rate of the compensating converter.

To overcome these problems, a novel method has been proposed, which eliminates the undesired converter harmonics completely[1]. The principle used here is

0-7803-3823-5/97/$10.00© 1997 IEEE

feedforward waveform compensation. The compensator can be designed as an addition to the power conversion system of an existing AC vehicle with main transformer and PWM converters.

Experiment have been presented in[1] using 16 $^{2/3}$Hz supply. This paper describes the experimental results for a small model of Japanese AC railway vehicles using 50Hz feeding frequency which means 3 times larger than that in Germany. It opens the possibility to apply this novel method to any 50Hz fed PWM controlled AC railway vehicle.

3. Configuration of Shinkansen EMU

In the actual vehicles, for example, the configuration of the "Star21(type 952)" test train is shown in Fig. 1. This series train uses 4 PWM converters and 2 DC link voltage circuits, and each DC link has 4 pararell induction motors, which means eight traction motors for one main transformer. Secondary side of the transformer is divided into 4 windings for traction and one winding for service power supply such as internal lighting, air conditioning, and control circuits. The total power is 3,080kW, and the line voltage is 25kV, 50Hz.

Four pararell converters are operated at the different PWM angles as 0, 90, 22.5, 112.5 degrees in order to avoid signalling frequeny interference, while in general, it will be supposed to be 0, 90, 45, 135 degrees. Under the 0, 90, 45, 135 degrees PWM phase differnce condition, the equivalent traction converter voltage, defined as a sum of the switching functions like +1, 0, -1, is shown in Fig. 2. Fig. 2 shows a 9 stepped ac waveform Ut, acting as the counter emf of the traction converters to the line voltage. The number of the step changes in accordance with the amplitude reference of PWM wave production. The number of PWM pulses in a synchronized period is 9, which makes subharmonics both side around 50Hz * 9 pulses * 2 = 900Hz on the mmf in main transformer. 2 converters operated at the same time with 0 and 90 degrees PWM switching angles eliminate this frequency but emit subharmonics at both sides around the double frequency, 1,800Hz. Furthermore, four PWM converters operated at 0, 90, 45, 135 degrees emit subharmonics at both sides around 3,600Hz.

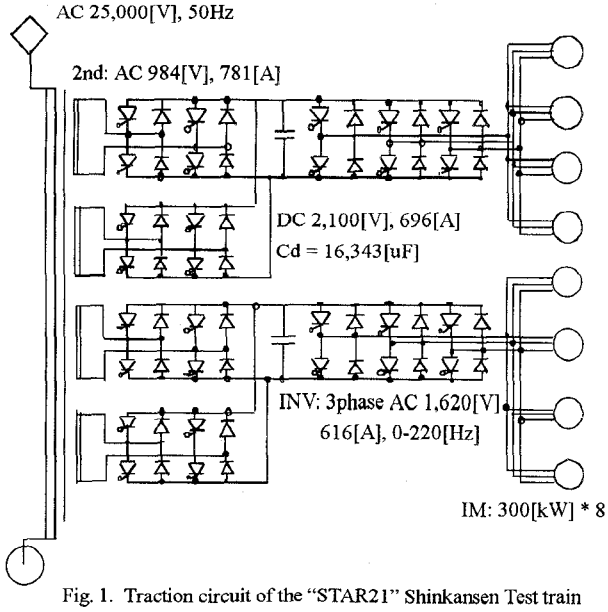

Fig. 1. Traction circuit of the "STAR21" Shinkansen Test train

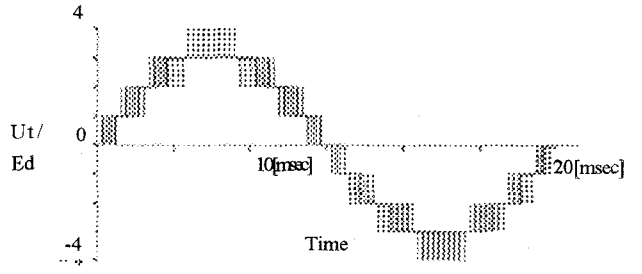

Fig. 2. Equivalent traction converter voltage

4. Harmonic Compensation by Counter MMF Superposition Method

From the above consideration, the harmonic compensator has to emit the counter voltage against the value of the subtract the sinusoidal voltage from the equivalent voltage. The novel concept of the harmonic compensator eliminates the distortion of the line current by injecting the inverse of the harmonic current waveform into an auxiliary winding of the main transformer. The harmonic compensator must produce the oppsite waveform which is subtracted fundamental sinusoidal wave from the sum of the switching function. This waveform is shown in Fig. 3.

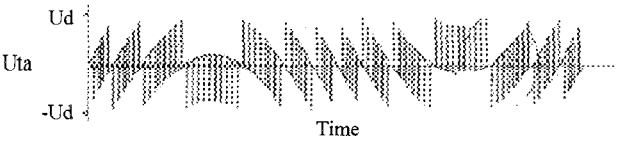

Fig .3. Compensating voltage from harmonic compensator

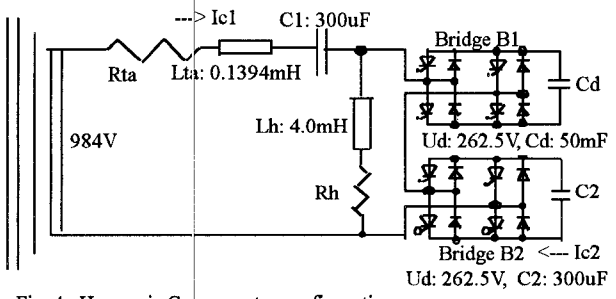

Fig. 4. Harmonic Compensator configuration
(Phisical values are determined by Computer simulation)

To realize the harmonic compensation voltage, the compensator circuit is configurated like Fig. 4. This compensation voltage can be decomposed into a pulsed rectangular waveform Ub1 and a piecewise sinusoidal voltage Ub2, shown in Fig. 5. Bridge B2 is switched as shwon in Fig. 6, from which the particular voltage and current waveforms result.

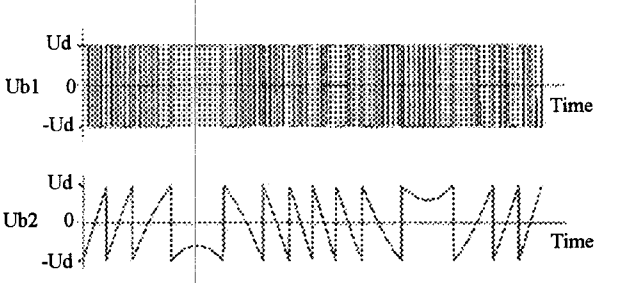

Fig. 5. Decomposed Compensator Voltage

5. Control of Harmonic Compensator

The practical implementation of the compensator control is based only on the feedforward switching and not event-orirnted, in order to avoid the pulse displacement by the parameter changes on the capacitors. The control opertaion is described below:

The basic switching pattern of bridge B1 is derived from the switching sequence of the traction converters.

The bridge B2 switching pattern is based on the calculation from the nominal sinusoidal reference waveform for the PWM converters.

The switchin pattern is shown in Fig. 7.

6. Design of the Harmonic Compensator

The most important design problem is how to set the system parameters like leakage inductance of the transformer winding for the harmonic compensator. The capacitances C1, Cd and C2. C1 and C2 are selected as the same, and

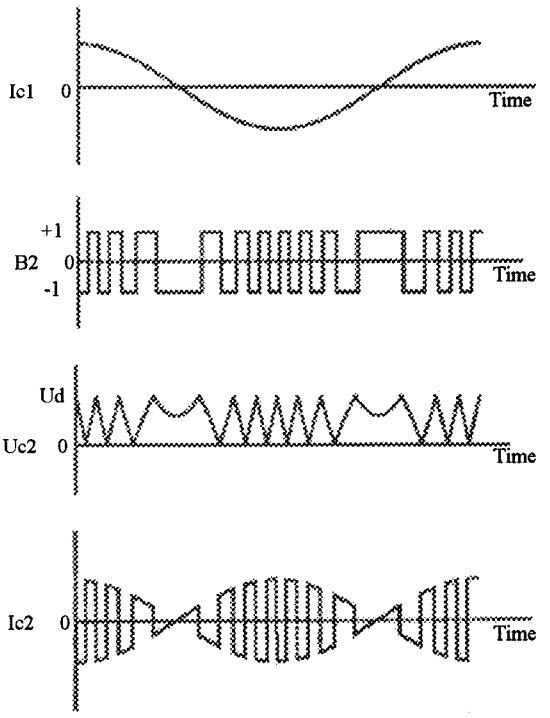

Fig. 6. Bridge B2 switching timing and voltage, current (one period)

Cd is relatively big.

Other parameters are choosen based on a numerical simulation on the computer.

From this simulation the parameters are set as below:

C1 = C2 = 300[μF], Cd = 50[mF],
Lt = 0.1394[mH], Lh = 4.0[mH], Rh = 0.5[ohm]

7. Configuration of the Experimental System

In order to prove to the possibilty to apply the method to AC railway vehicles using 50Hz feeding frequency which means 3 times larger than that in Germany, the experiment system was produced by ourselves. As we cannot test the whole power ciucuits same as the real vehicles, a small model experiment system was made.

The ratio is 1/10 voltage and 1/50 current, which means 5/1 impedances and 1/500 electric power. Fig. 8 shows the configuration of the experimental system. Parameters are calculated from the result of the simulation.

The control components are:

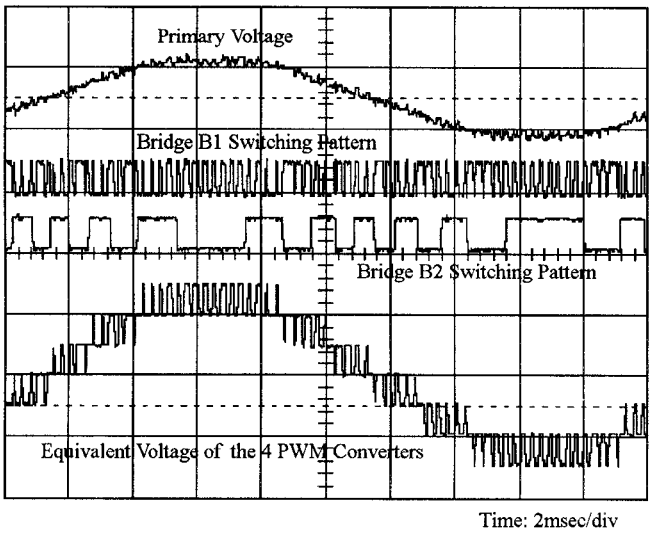

Fig. 7. Measured switching pattern of 2 bridges in the harmonic compensator and the equivalent voltage of the 4 PWM converters

CPU board(Pentium 90MHz) on the IBM PC
Bus changer from ISA_bus
I/O interface(12bit A/D, 12bit D/A, FIFO, variable INTERRUPT with 10MHz clock)
Gate_drivers
Bridge Circuit with 1200V-25A IGBTs, without Snubbers

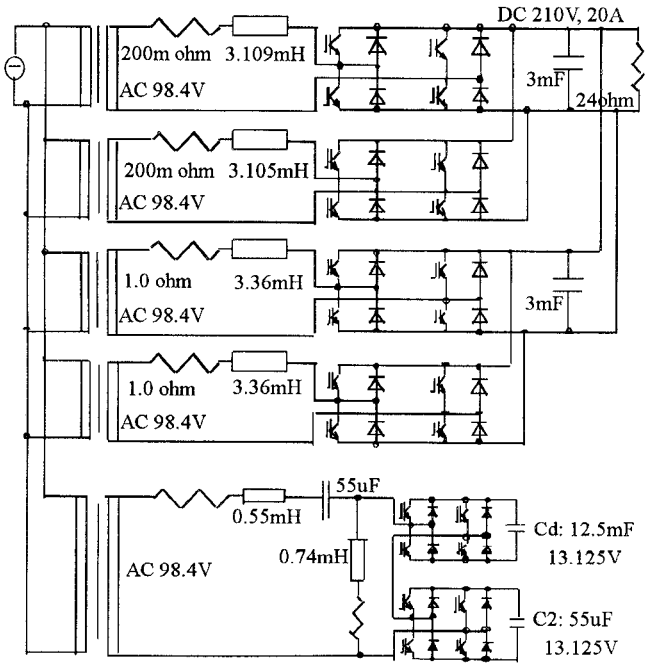

Fig .8. Configuration of experimental system

Control sequence(by software) is:

Interrupt in every 200[μsec] and read the data such as voltage and current
Synchronization by software PLL
Amplitude and Phase detection by DFT for the fundamental frequency
Regulation of DC voltage and AC phase between voltage and current by PI_compensation
PWM amplitude and phase setting
PWM timing calculation by Newton Method
Timing calculation by software sorting and set the compensation data(timing and switching function) to pararell FIFOs

In this implementaion, timing calcurations of B2 are completely feedforward method and not event-orientd, while the former method[1] is event-oriented based on measuring the voltage of C2. Event-oriented method shows to compensate the amplitude displacement by the changing load conditions, but the penalty appears in the switching frequency of the compensator itself because the switching timing displacement with the equivalent converter voltage occurs enevitably. This completely feed forward switching employed here is derived from the amplitude of the PLL synchronized sinusoidal signal by the step of 1/8 maximum values.

This method does not require measuring the capacitor voltages Ucd and Uc2.

A compromise had to be made in the design of the experimental set-up since the equivalent of a single five-winding transformer was not available. Instead, there were five separate transformers used, as shown in Fig. 8. A cancellation of the harmonic flux componets cannot be achieved in this arrangement. Also, the electrical data of the four transformers were not identical. More specifically: they did not have the required value of leakage inductance. As an improvement, additional inductors were inserted in series to the secondary winding as shown in Fig. 8. Nevertheless, the requierd symmetry was not suffucient obtained.

8. Experimental Result

The experimental results were compared in the time domain and frequency domain, both without and with harmonic compensator.

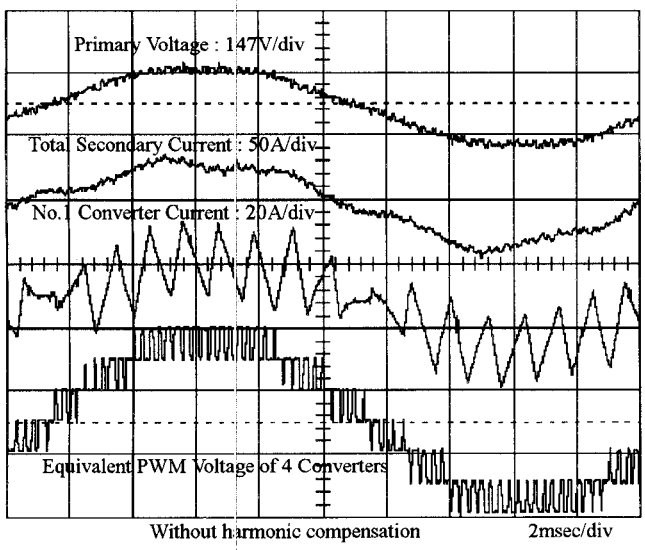

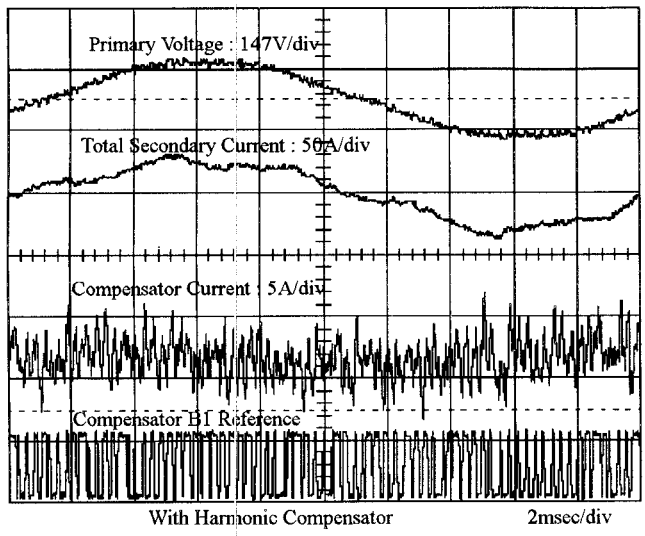

Fig .9. Waveforms before and after compensation, experimental result

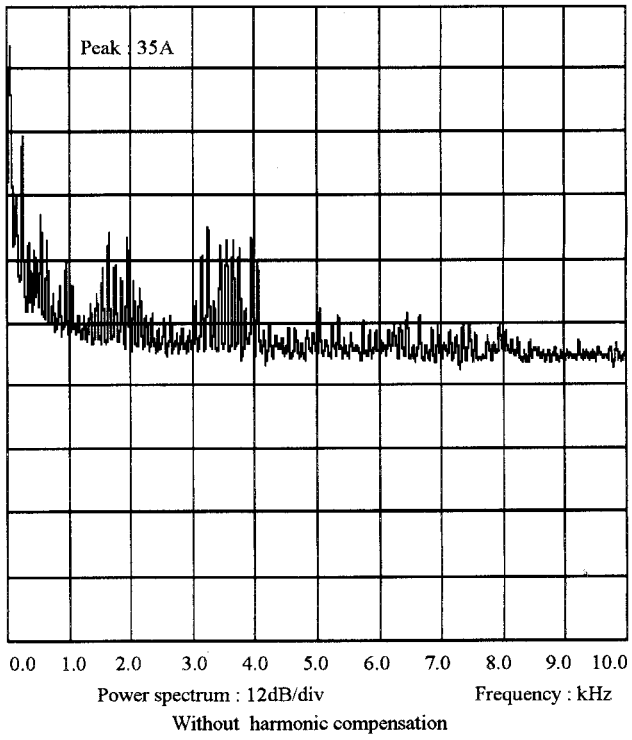

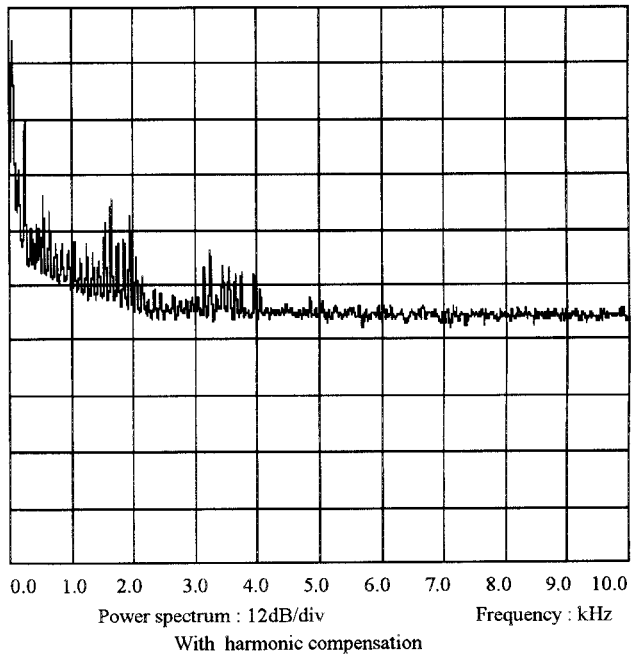

Fig. 10. Power spectrum of total secondary current experimental result

Especially the current harmonics in the signalling band 3-4kHz are marvellously reduced by about 10dB. The performance is shown in Fig. 9 and Fig. 10.

Moreover, above 4kHz frequency, the power spectrum density is decreased and there are no more harmonics by the switching, while the harmonics by switching in the higher frequency increase usually by normal active filters. This point is quite important and specific for this type of harmonic compensator.

The result could have been much better if the main transformer used in the experiments were adequately designed. This point was discussed in Section 7.

Another degradation of quality of the experimental results is owed to some design problem of the current control system of the converter unit. Unnecessary noise was generated by the current controlers, and the current waveforms could not reach a complete steady-state. This noise generates additional current harmonics in the frequency range from 0 - 1 kHz.

9. Important Design Issues

From the result of the experiment, the most important point is that the four leakage inductances of the main transformer must be the same in good accuracy.

In order to realize the complete compensaion, it is quite important to make four leakage inductance of each transformer precisely the same.

In Figure 10, without and with compensator seems to have the same spectrum in the lower frequency, around 0.9kHz sideband harmonics and around 1.8kHz sideband harmonics. They still remain because of the unbalance of the leakage inductances in the four main transformers, and because separate transformers were used instead of a single transformer as described in Section 7. As a cosequence, the harmonic spectrum of the equivalent line current of the traction system exhibits imperfect harmonic cancellation.

Due to the deiciencies of the main transformer used in the experiment, the best combination in tuning the four leakage inductances resulted in the waveforms shown in Fig. 9.

The unbalance of the leakage inductances causes the distortion of the total current of the four converters, which reduces the compensating effect even if the compensator operates at exact timing of its switching instants.

So the above harmonics spectrum is expected to improve significance by a good choice of the values of the leakage inductances.

10. Conclusion

Experimental proof of the performance of the novel harmonic compensator was given.

The scale down model of Japanese AC railway vehicles using 50Hz feeding frequency which means 3 times larger than that in Germany is built from the parameter consideration based on the numerical simulation.

The control method of the harmonic compensator is completely feedforward and not event-driven.

Experimental results show especially 3-4kHz for signalling band harmonic current is quite well suppressed as over 10dB.

The point to apply this method lies on the well choosen leakage inductances of the main transformer. Of such procedures are made, the harmonic compensation effect will be much the better, as the former result for 16 2/3Hz like 30dB in [1].

From the result, this novel compensating method has a great possibility to be applied on to any 50Hz fed PWM controlled AC railway vehicle with the attention to the smoothing of the leakage inductances in the main transformer.

Acknowledgement

I gratefully thanks to Prof.Dr.Holtz and Dr.Krah for their advice given during the research work, and also thanks to all the members in Electric Machines Drive Laboratory in the University of Wuppertal for all the kindness during my 2 years' stay in Germany.

Reference

[1] J.O.Krah and J.Holtz, "Total Compensation of Line-Side Switching Harmonics in Converter-Fed AC Locomotives", *IEEE Transactions on Industry Applications*, Vol.31, No.6, Nov./Dec. 1995, pp.1264 -1273.

Permanent Magnet Synchronous Motor Control System for Railway Vehicle Traction and Its Advantages

Keiichirou Kondou Kouichi Matsuoka
Railway Technical Research Institute
2-8-38, Hikari-cho, Kokubunji-shi, Tokyo 185, JAPAN
Fax : +81-425-73-7259, Phone : +81-425-73-7287
E-mail : kkondou@rtri.or.jp kmatsu@rtri.or.jp

Abstract — In this paper we report our results about a permanent magnet synchronous motor control system for railway vehicle traction. First we show the details of the system structure, second how to design the ACR system and its characteristics, third an example of application of our assumed system and lastly we introduce test results and the advantages of our system from the viewpoint of vehicle traction.

I. INTRODUCTION

In the field of railway vehicle traction, direct drive tractions motor without any gears are expected not only to eliminate noise and maintenance problem but also to improve curve running performance with the center of gravity placed lower [1] . As the direct drive motor to be put into practice, we choose a PMSM or permanent magnet synchronous motor which has the advantages of downsizing and simple arrangement on the bogie [2] .

There has never been a precedent of permanent magnet synchronous motors being used for railway vehicle traction. For practical use of permanent magnet synchronous traction motors we must also study a novel and appropriate drive system. At first we began with constructing the system structure and reached a conclusion that a voltage source inverter with a view to downsizing on-board, a resolver for detection of rotating angle with a view to stabilizing against any disturbance, and vector control for precise and instantaneous torque control are to be adopted [3] .

Under the current control system of vector control of PMSM an electromotive force (e.m.f) compensation is usually adopted to prevent interference between d-axis current and q-axis current and e.m.f. caused by PM field flux with a view to more precise and fast torque control [4] . On the other hand 1` pulse modulation or fundamental modulation is alway s adopted to raise the maximum output voltage, but in this modulation, delay of voltage output and harmonics of current are increased. If real currents are fed back for compensation of interference of both currents there is a possibility of disturbing the current control stability. To cope with this problem we proposed feed-forward compensation with use of reference currents. With this compensation we can obtain a one-order delay system from reference currents to real currents theoretically.

Compared to the conventional V/F-slip frequency controlled asynchronous motor drive for vehicle traction in Japan, some differences are implemented in our suggested PMSM drive system i.e. precise velocity calculation with a resolver, certain field flux by permanent magnet and precise torque control due to vector control. These items provide some advantages from the viewpoint of vehicle traction control.

II. VECTOR CONTROL THEORY FOR PMSM

A. Basic Equations of PMSM

On the d-q coordinates which are the oriented to the rotating field flux, the voltage and current formula is expressed by (1) .

$$\begin{bmatrix} v_d \\ v_q \end{bmatrix} = \begin{bmatrix} r_m + sL_d & -\omega L_q \\ \omega L_d & r_m + sL_d \end{bmatrix} \begin{bmatrix} i_d \\ i_q \end{bmatrix} + \begin{bmatrix} 0 \\ \omega \Phi_f \end{bmatrix} . \quad (1)$$

Here v_d and v_q are the d-axis voltage and q-axis voltage, i_d and i_q are the d-axis current and q-axis current, L_d and L_q are d-axis inductance and q-axis inductance, r_m is the amateur winding resistance and Φ_f is the permanent magnet field flux.

The PMSM torque T_m is composed of the intersected flux vector and current vector as (2) .

$$T_m = p\left\{\Phi_f + \left(L_d - L_q\right) i_d\right\} i_q . \quad (2)$$

Assuming a cylindrical PMSM, we can set $L_d \fallingdotseq L_q$ and express T_m by equation (3) from (2) .

$$T_m = p\Phi_f i_q . \quad (3)$$

The PMSM terminal voltage V_m is expressed by (4) assuming steady state and neglecting resistance voltage drop.

$$V_m = \omega \sqrt{\left(-L_q i_q\right)^2 + \left(L_d i_d + \Phi_f\right)^2} . \quad (4)$$

B. Torque and Voltage Control Method

In accordance with vehicle performance characteristics reference torque T_m^* and reference terminal voltage V_m^* shown in Fig. 1 are determined. To make T_m and V_m coincide with T_m^* and V_m^*, i_d and i_q should be controlled according to (3) and (4) . In this case reference d-axis

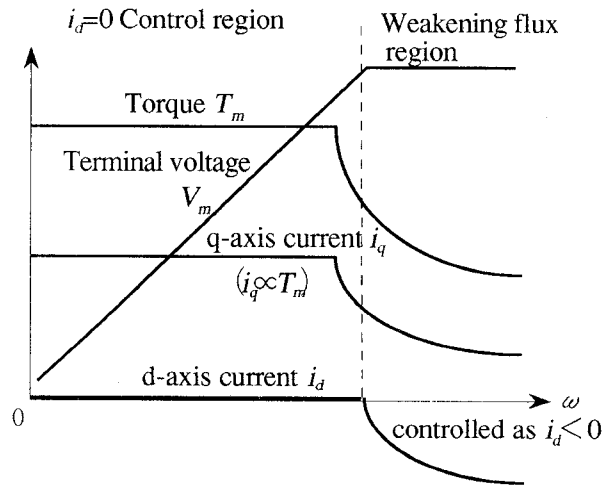

Fig. 1. Velocity vs.torque,current and voltage characteristic

currents i_d^* and i_q^* areexpressed in Fig. 1

B. Construction of Current Regulation System.

1) Basic concept of current control [5] : *In* (1) non-diagonal elements of impedance matrix express amateur reactance voltage which causes interference between i_d and i_q and the second terms on right side express electrical motive force by permanent magnet flux which performs as a disturbance on current control.

To cope with this problem, feed-forward compensation is adopted, which depresses amateur reactance voltage and e.m.f. and the errors between real currents and reference currents will be regulated by feed-back compensation with PI compensator. Fig. 2 shows our proposed current control system.

2) Design of ACR compensator : From the current control system in Fig. 2 reference voltage vector $v^*= [v_d^* \ v_q^*]^T$ is expressed in (5) .

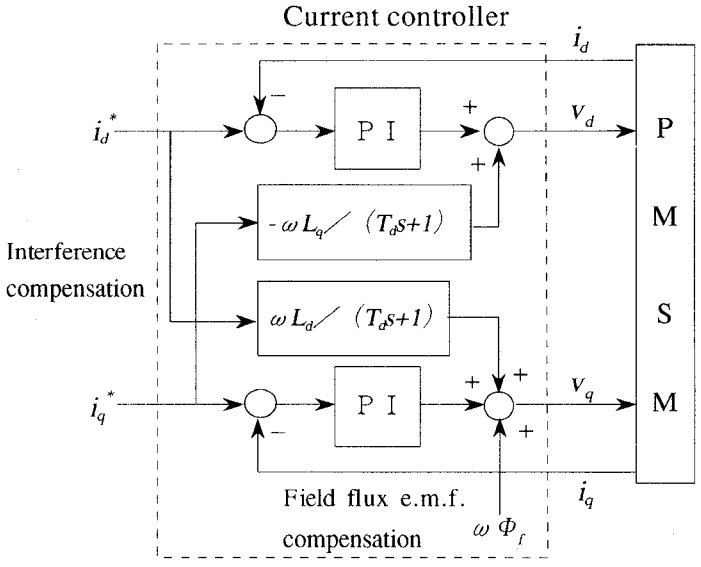

Fig. 2 . Block diagram of current control system

$$\begin{bmatrix} v_d^* \\ v_q^* \end{bmatrix} = \begin{bmatrix} G_{PId}(s)\left(i_d^* - i_d\right) & -\omega L_q /(1+sT_d) \\ \omega L_d /(1+sT_d) & G_{PIq}(s)\left(i_q^* - i_q\right) \end{bmatrix} + \begin{bmatrix} 0 \\ \omega\Phi_f \end{bmatrix}. \quad (5)$$

Here we assume current regulation can be perfectly achieved and the real current vector $i= [i_d \ i_q]^T$ can be controlled in one-order delay with time constant T_d as input of reference current vector $i^*= [i_d^* \ i_q^*]^T$. This assumption gives the following equation :

$$\begin{bmatrix} i_d \\ i_d \end{bmatrix} = \begin{bmatrix} 1/(1+sT_d) & 0 \\ 0 & 1/(1+sT_d) \end{bmatrix} \begin{bmatrix} i_d^* \\ i_q^* \end{bmatrix}. \quad (6)$$

If we can neglect the effect of microprocessor performing time and any voltage error with PWM, the real voltage vector $v= [v_d \ v_q]^T$ is regarded coincident to $v^*= [v_d^* \ v_q^*]^T$. With this assumption and relation expressed by (6) which is based on (5) , we express $v= [v_d \ v_q]^T$ as follows :

$$\begin{bmatrix} v_d \\ v_q \end{bmatrix} = \begin{bmatrix} sT_d G_{PId}(s) & -\omega L_q \\ \omega L_d & sT_d G_{PIq}(s) \end{bmatrix} \begin{bmatrix} i_d \\ i_q \end{bmatrix} + \begin{bmatrix} 0 \\ \omega\Phi_f \end{bmatrix}. \quad (7)$$

Voltage vector in (7) is given to PMSM model equation (1) as input voltage and we obtain an equation related to the PI compensators G_{PId} (s) and G_{PIq} (s) as

$$\begin{bmatrix} r_m + sL_d - sT_d G_{PId}(s) & 0 \\ 0 & r_m + sL_q - sT_d G_{PIq}(s) \end{bmatrix} \begin{bmatrix} i_d \\ i_q \end{bmatrix} = \begin{bmatrix} 0 \\ 0 \end{bmatrix}. \quad (8)$$

From this equation the PI compensators G_{PId} (s) and G_{PIq} (s) should be expressed as follows to always realize equation (8) :

$$G_{PId}(s) = \frac{r_m}{sT_d} + \frac{L_d}{T_d}. \quad (9)$$

$$G_{PIq}(s) = \frac{r_m}{sT_d} + \frac{L_q}{T_d}. \quad (10)$$

In this way ACR gains can be designed theoretically and current step response is expected to be a one-order delay system.

III. CONTROL SYSTEM FOR PERMANENT MAGNET SYNCHRONOUS MOTOR

Here we describe the control system for a permanent magnet synchronous motor which is studied in the abovementioned text.

A. An Example of Main Traction Circuit.

Fig. 3 shows an example of a main traction circuit for a DC power-fed electrical multiple unit. A voltage source inverter is suitable for on-board traction because only one simple power converter is required to convert DC to AVAF AC. Each inverter must feed and control each traction motor to perform self control. An IGBT is suitable for a three-level inverter of this capacity. With use of the three-level inverter there are less harmonics of input and output of the inverter than in the case of the two-level inverter. In addition, an adjustable voltage output will be available even at the synchronized 1` pulse (fundamental switching) mode.

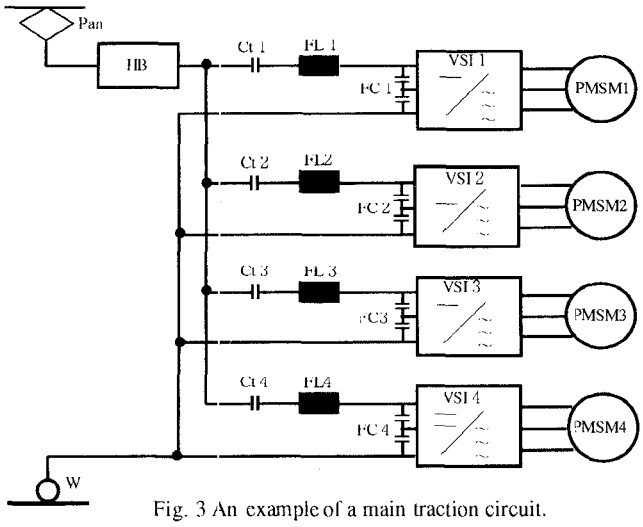

Fig. 3 An example of a main traction circuit.

B. Structure of Control System

Fig. 4 shows an actual structure of a trial manufactured control system. Command values of

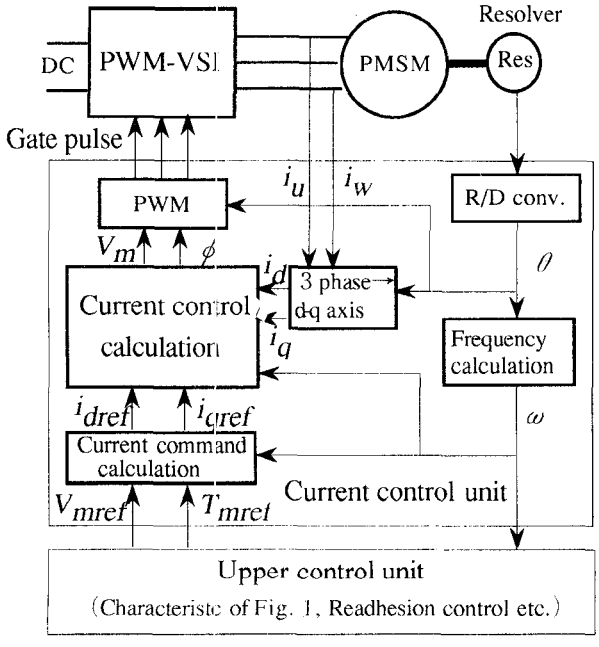

Fig. 4 The structure of control system

current of d-axis and q-axis are given as a function of velocity as shown for example in Fig. 1. Currents are controlled by the current control system described in Fig. 2. PWM control performs an asynchronous sinusoidal-trapezoidal modulation in the range from start-up to middle speed and a synchronous 1` pulse modulation in the range of higher velocities after reaching the limit of output voltage. The rotating angle of the rotor is detected by the resolver and its processing unit called the R/D converter. Rotating velocity can be obtained by a differential of the detected rotor angle value. All of the functions except R/D and PWM are performed by software.

IV. TEST RESULTS

We conducted the tests by use of an actually manufactured 420kVA IGBT three level-inverter which includes the control system as mentioned above to make sure that our suggested PMSM control system has the basic function of railway vehicle traction. Results shown here are obtained at the test site feeding 1500V DC line voltage.

1) *Continuous Acceleration and Deceleration Tests* : In Fig. 5 we show results of test using 80kW trial manufactured PMSM and DC generator as a load. According to this result we can recognize that the control is smoothly performed in any speed range.

2) Repowering Characteristics : In Fig. 6 we show the result of repowering test under the same conditions as in Fig. 5. It can be confirmed that operation of the inverter can be restarted without any problem under the condition of an e.m.f generated.

In the test results :

I_U : current of phase u
I_d^* : reference value of d-axis current
I_q : reference value of d-axis current
I_d : d-axis current
I_q : q-axis current
α : modulation issue
I_{FL} : current of filter inductance
V_{FC} : voltage of filter capacitor
ω_r : mechanical rotor angle velocity
T_m : real torque

V. MERITS OF PMSM CONTROL SYSTEM IN VEHICLE TRACTION

A. Merits of the PMSM Control System

In the conventional V/F-slip frequency-controlled asynchronous motor traction, rms current regulation with slip frequency and detecting rotating velocity with pulse sensors of less than 100 pulse/r have been usual in Japan. This ordinary control method resulted from its simple structure and low performance of

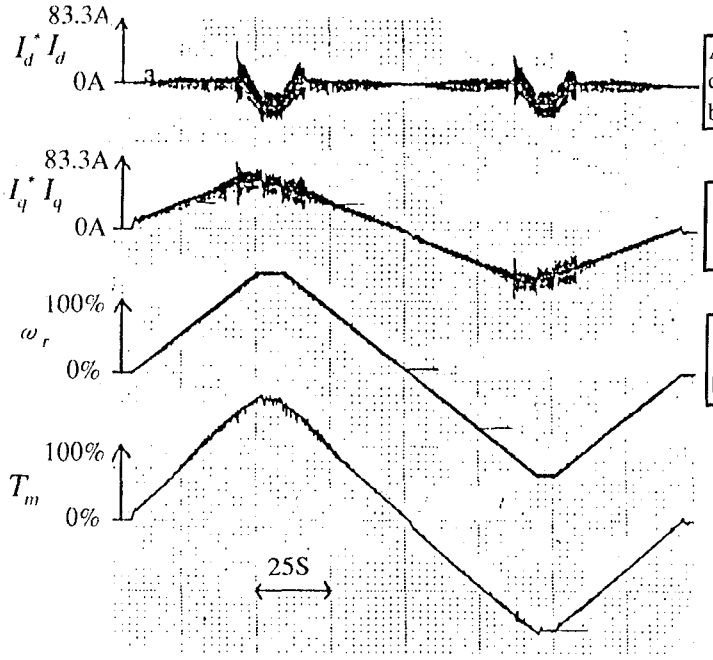

Fig. 5. Continuous acceleration and deceleration test.

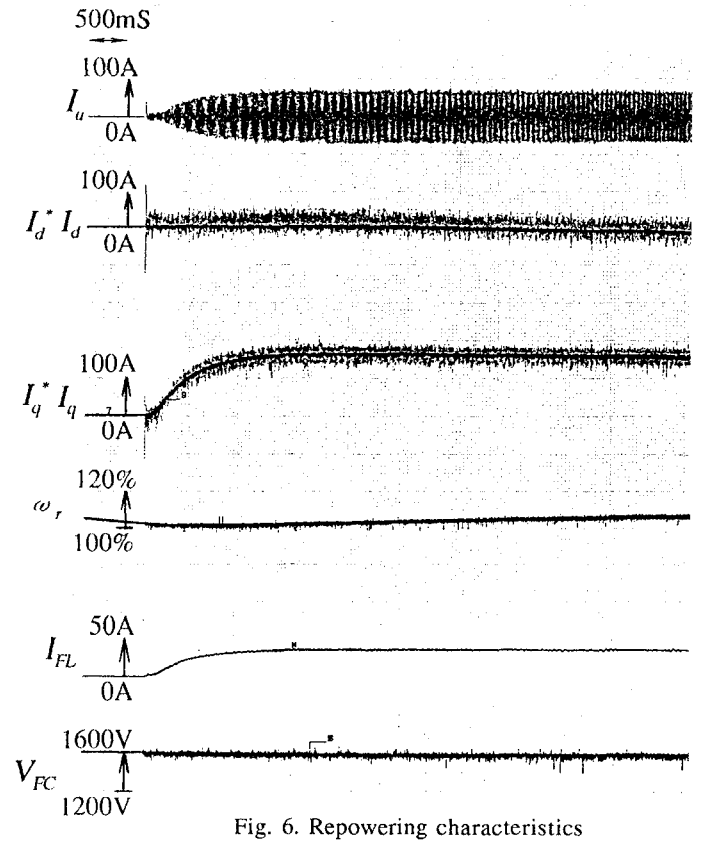

Fig. 6. Repowering characteristics

microprocessor in those days. In this system precise torque control is not expected with rms current control due to a long secondary time constant of the asynchronous motor. It is principally difficult to detect precise rotating velocity due to few teeth of the pulse sensor, especially at the low speed range.

Unlike this ordinary asynchronous motor drive system there are particular advantages in our PMSM drive system as follows :

· precise and instantaneous torque control by vector control.

· precise and continuous velocity calculation by use of rotating angle detected by the resolver even at low speed range.

· certainly established field flux by PM.

These advantages are favorable from the viewpoint of vehicle traction, as shown in Fig. 7.

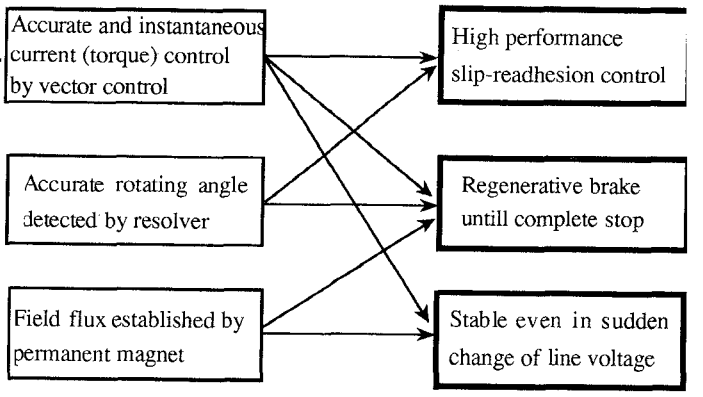

Fig. 7. Advantages of the PMSM control system in railway vehicle traction

In case of wheel slip/skid, quick detection is essential and it can be confirmed by the use of a resolver. After detecting slip/skid precise torque control is required to effectively utilize the adhesion force. By use of vector control it is easy to control torque precisely and quickly.

From the viewpoint of saving power consumption in train operation and wearing of brake equipment a regenerative brake should be available even in the very low speed range. In an ordinary asynchronous motor drive system with pulse sensors it is difficult to detect low speed precisely. By use of a PMSM drive system it is easy to detect low speed due to continuous and precise rotor angle detection. In addition PMSM vector control can make it easy to control torque, coupled with mechanical brakes in halting the vehicle.

Line voltage of electrical railway tends to vary within a wide range and suddenly compared with usual power sources for industrial applications. The drive system for railway vehicle traction must be stable under such situations. The ordinary asynchronous motor drive system is originally unstable and it is already reported that a damping control loop should be added to the slip frequency control loop to cope with this problem [6] . Sudden change of input voltage in the asynchronous motor disturbs the exciting current to fluctuate main flux, but input voltage in the PMSM does not affect field flux due to the use of permanent magnets. In addition vector control realizes instantaneous current control. For these reasons our suggested PMSM control system is expected to stabilize even a sudden change of line voltage.

B. Test results

As mentioned above our suggested PMSM drive

system has some advantages. We conducted an extended test in addition to basic tests to confirm its advantages.

Tests except for regenerative braking in the range of 0 speed are executed at sites not on-board. But the regenerative test is done elsewhere in combination with the bogie in the rolling stock test facility to utilize inertia load.

1) Step Response of Current : In Fig. 8 we show a current step response waveform which is obtained by use of a trial-manufactured 80kW permanent magnet synchronous motor and a DC generator as a load. We could confirm that instantaneous and precise current (torque) control is performed by vector control.

2) Regenerative Braking in the Range of 0 Speed : In Fig. 9 we show test results which are obtained by use of a trial manufactured 90kW permanent magnet synchronous motor and a fly wheel as an inertia load. According to this test result, regenerative braking is effective even in the range of 0 speed and we confirm the possibility of stopping the vehicle without any mechanical brakes.

3) Response to Sudden Change of Line Voltage : In Fig. 10 we show test results of response to sudden change of line voltage which is obtained by use of a trial manufactured 90kW permanent magnet synchronous motor and a flywheel. According to this result, we can recognize that our suggested control system can immediately suppress vibration of current and can be stable without any special damping control loop.

VI. CONCLUSIONS

In this paper we have described an outline of a control system of a permanent magnet synchronous motor for railway vehicle traction of which we are now pursuing research and development. In addition we cited its merits together with test results.

The contents of this paper are as follows :

1) We started with deciding the system structure and finally adopted the voltage source inverter as a power converter for drive, the resolver-R/D system for field flux detection, and vector control for precise and quick torque control.

2) In the current regulation system feed-forward e.m.f. compensation with one-order delay is thought out in order to suppress interference of i_d and i_q in consideration of 1` pulse mode in voltage source inverter.

3) We showed a theoretical designing method of PI compensators with one-order delay feed-forward compensation.

4) We showed a tests results of basic function and recognized that system is satisfactory enough to be utilized for vehicle traction.

5) We recognized some advantages of our suggested PMSM drive system from a viewpoint of vehicle traction

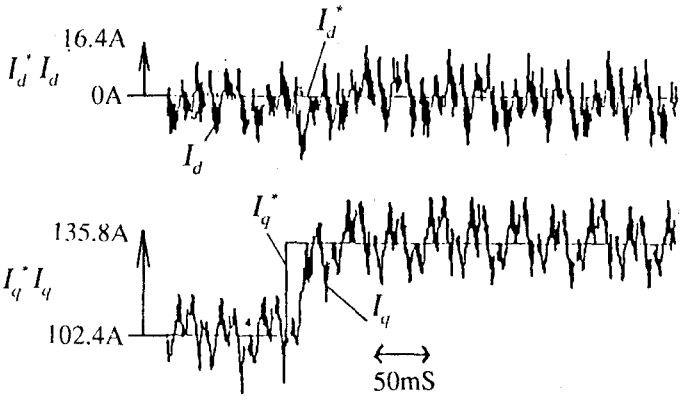

Fig. 8. Step response of current.

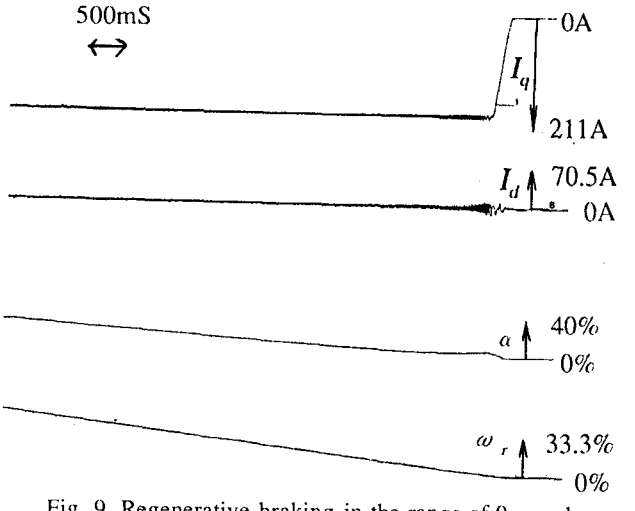

Fig. 9. Regenerative braking in the range of 0 speed.

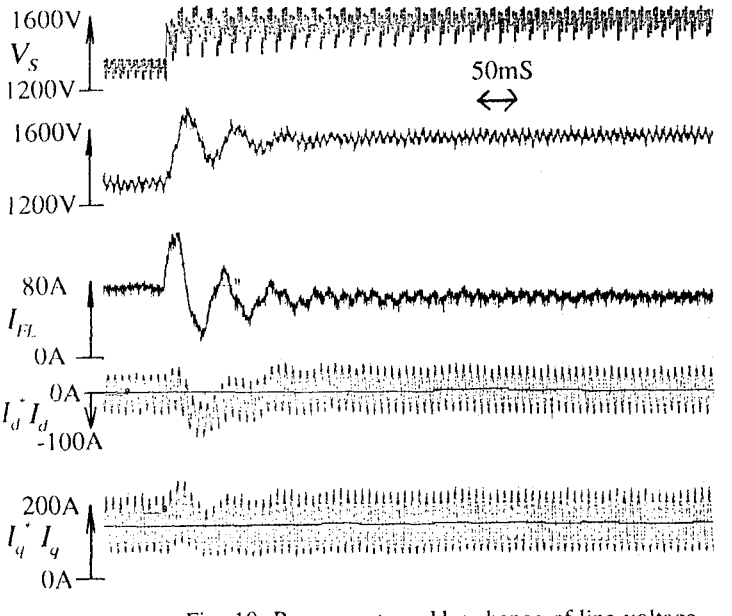

Fig. 10. Response to sudden change of line voltage.

over the ordinary asynchronous motor drive system.
6) In order to clarify the advantages of the PMSM drive system we enforced some tests and confirmed them.

Through the investigation as mentioned in this paper , we ensure that a PMSM drive system can bring railway companies some benefits in saving operation cost and offering the customers high quality service.

Now we have other tests waiting, for example tests of slip adhesion control and on-board tests on actual lines. We will proceed with them in near future.

REFERENCES

[1] K. Matsuoka, K. Kondou, et, "Conception of NEXT250 (Narrow gauge EXpress Train for 250km/h) and Investigation of the Wheel-in Motor" (in Japanese) in Proceedings of the 1993 NATIONAL CONVENTIONAL RECORD I.E.E. JAPAN-INDUSTRY APPLICATION SOCIETY-, pp509-514 (1993)

[2] K. Matsuoka, K. kondou, et, "Development of Wheel-in Permanent Magnet Synchronous Motor for Railway Vehicle Traction" (in Japanese) , Technical Meeting on Transportation and Electric Railway of I.E.E. Japan, TER95-19 (1995) .

[3] K. Kondou, K. Matsuoka, et al. "Drive System of Permanent Magnet Synchronous Motor for Railway Vehicle Traction" (in Japanese) , Technical Meeting on Transportation and Electric Railway of I.E.E. Japan, TER95-20 (1995) .

[4] K. Kondou, K. Matsuoka, et al, "E.m.f Compensation Method in Control of Permanent Magnet Synchronous Motor for Railway Vehicle Traction" (in Japanese) , Technical Meeting on Rotating Machine of I.E.E. Japan, RM95-94 (1995) .

[5] K. Kondou, K. Matsuoka, "Speed Electrical Motive Force Compensation in Current Control of Permanent Magnet Synchronous Motor for Railway Vehicle Traction," (in Japanese) in Proceedings of the 1995 NATIONAL CONVENTIONAL RECORD I.E.E JAPAN-INDUSTRY APPLICATION SOCIETY-,pp241-244 (1995)

[6] A. Kimura, K. Nakamura, "Study on the Stability of Control Systems for Induction Motor Driven Rolling Stock" Trans. I.E.E. Japan, Vol. 110-D, No. 3, pp.291-300, Mar. 1990.

Position Estimation in Induction Machines Utilizing Rotor Bar Slot Harmonics and Carrier Frequency Signal Injection

M.W. Degner†, R.D. Lorenz‡

†Dept. of Mech. Engr.
University of Wisconsin-Madison
1513 University Avenue
Madison, WI 53706, USA
Tel: 608-262-0556 Fax: 608-265-2316
Email: degner@cae.wisc.edu

‡Dept. of Mech. Engr. and Dept. of Elec. & Comp. Engr.
University of Wisconsin-Madison
1513 University Avenue
Madison, WI 53706, USA
Tel: 608-262-5343 Fax: 608-265-2316
Email: Lorenz@engr.wisc.edu

Abstract - **This paper presents a simple and robust way of utilizing harmonic saliencies for the estimation of rotor position. A carrier frequency voltage excitation is used to produce a carrier frequency current which contains the desired spatial information. A closed-loop, tracking observer is then used to estimate the rotor position. Due to its reliance on a spatial saliency and carrier frequency signal injection, the technique is very robust over a wide speed range, including low and zero speed.**

I. INTRODUCTION

The cost and reliability advantages of eliminating mechanical sensors and cabling for the measurement of position, velocity, and flux has led to a lot of research into what is commonly termed "sensorless" or "self-sensing" control of ac machines. The goal of this research is to estimate the rotor position or flux angle using the power leads of the machine, without separate position, velocity, or flux transducers. Many of these methods depend on the fundamental excitation of the machine and speed dependent phenomenon (back emf), causing them to ultimately fail at low and zero speed [1 - 4].

Several researchers [5 - 21] have developed methods to estimate rotor position or flux angle which rely on a spatial saliency being present in the machine. These methods can be divided into two major groups: 1) those that use the fundamental excitation to estimate the rotor position or flux angle [5 - 10], and 2) those that use a separate excitation signal from the fundamental excitation to estimate the rotor position or flux angle [11 - 21]. The reliance on the fundamental excitation ultimately causes the methods in group one to fail at low and zero speed due to low signal levels, signal to noise ratio, and lack of spectral separation between the signal with the spatial information and the fundamental excitation. The methods in group two do not suffer from these same problems at low and zero speed since they do not rely on the fundamental excitation for their estimation. Instead they rely on a separate, known test or carrier signal to extract the spatial information.

This paper will extend the technique presented in [15 - 21] to the estimation of rotor position in machines with a harmonic saliency. This paper will systematically look at the differences caused by using a harmonic saliency for the estimation of rotor position. The techniques developed in this paper will then be applied to an induction motor to estimate its rotor angle using the saliency created by the rotor bar slots.

II. SALIENT AC MACHINE MODEL

At high frequency a polyphase, ac machine can be modeled as shown in (1).

$$v_{qds} \cong j\,\omega_c\,L_{\sigma s}\,i_{qds} \tag{1}$$

$$\text{where } L_{\sigma s} = \left(L_s - \frac{L_m^2}{L_r}\right)$$

When a saliency is present in the machine the stator transient inductance is no longer constant and instead becomes a function of the rotor position. In the stationary reference frame the stator transient inductance matrix can be represented as shown in (2).

$$L_{\sigma s} = \begin{bmatrix} \Sigma L_{\sigma s} + \Delta L_{\sigma s}\cos(h\ \theta_r) & -\Delta L_{\sigma s}\sin(h\theta_r) \\ -\Delta L_{\sigma s}\sin(h\theta_r) & \Sigma L_{\sigma s} - \Delta L_{\sigma s}\cos(h\ \theta_r) \end{bmatrix} \tag{2}$$

Where $\Sigma L_{\sigma s}$ is the average stator transient inductance, $\Delta L_{\sigma s}$ is the differential stator transient inductance caused by the saliency, h is the harmonic number of the saliency and can be positive or negative, and θ_r is the rotor position in electrical degrees.

III. CARRIER SIGNAL INJECTION

The estimation of rotor position at low and zero speed requires a persistent excitation in the machine. One way of providing this persistent excitation is through the injection of a carrier signal in addition to the fundamental excitation [15 - 21]. One of the simplest forms of carrier signal injection is the injection of a balanced three phase voltage [15-18, 20, 21]. This type of carrier signal injection will produce a voltage vector which rotates at the carrier frequency, (3).

$$v^s_{qds\_c} = \begin{bmatrix} v^s_{qs\_c} \\ v^s_{ds\_c} \end{bmatrix} = V_{sc}\begin{bmatrix} \cos(\omega_c t) \\ -\sin(\omega_c t) \end{bmatrix}$$

$$= V_{sc}\, e^{j\omega_c t} \tag{3}$$

The carrier signal excitation can be injected on top of the fundamental excitation using a pulsewidth modulated, voltage source inverter (PWM-VSI) as shown in Figure 1.

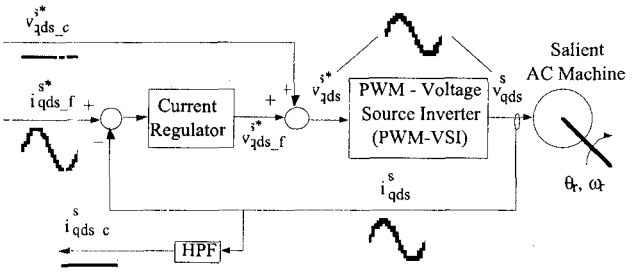

Figure 1: Injection of Carrier Signal Excitation using a PWM-VSI

When a salient machine, with an stator transient inductance modeled by (2), is excited with a carrier signal voltage excitation, carrier signal currents will be induced equal to (4).

$$i^s_{qds\_c} = \begin{bmatrix} i^s_{qs\_c} \\ i^s_{ds\_c} \end{bmatrix}$$

$$= I_{cp}\begin{bmatrix} \sin(\omega_c t) \\ \cos(\omega_c t) \end{bmatrix} - I_{cn}\begin{bmatrix} \sin(h\theta_r - \omega_c t) \\ \cos(h\theta_r - \omega_c t) \end{bmatrix}$$

$$= -j\, I_{cp}\, e^{j\omega_c t} + j\, I_{cn}\, e^{j(h\theta_r - \omega_c t)} \qquad (4)$$

where $$I_{cp} = \frac{V_{sc}}{\omega_c\left(\Sigma L_{\sigma s}^2 - \Delta L_{\sigma s}^2\right)}\Sigma L_{\sigma s}$$

$$I_{cn} = \frac{V_{sc}}{\omega_c\left(\Sigma L_{\sigma s}^2 - \Delta L_{\sigma s}^2\right)}\Delta L_{\sigma s}$$

The carrier signal current can be seen to consist of two components.

1) A positive sequence component relative to the carrier signal voltage which contains no spatial information. This positive sequence component is proportional to the average stator transient inductance.
2) A negative sequence component relative to the carrier signal voltage which contains spatial information in its phase. This negative sequence component is proportional to the differential stator transient inductance.

Because there are two distinct components to the carrier signal current and only one of them contains any spatial information, it is desirable to filter off the component which contains no spatial information.

IV. SYNCHRONOUS REFERENCE FRAME FILTERING

Since the two components of the carrier signal current rotate in opposite directions, it is relatively easy to filter off the component with no spatial information. Transforming the carrier signal current to a reference frame synchronous with the positive sequence component causes the positive sequence component to become a dc value. A simple high-pass filter can then be used to totally filter off the positive sequence component. The implementation of this positive sequence carrier signal synchronous reference frame high-pass filter is shown in Figure 2.

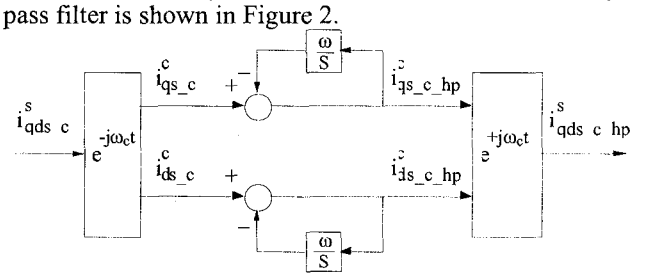

Figure 2: Positive Sequence Carrier Signal Synchronous Reference Frame High-pass Filter

Because the signal which is being filtered off is a dc value the order and the bandwidth of the filter do not have to be very high to achieve adequate filtering.

It is also possible to implement the synchronous reference frame filtering in a stationary reference frame as shown in Figure 3. In the stationary reference frame the filter is a linear system if the carrier frequency is constant.

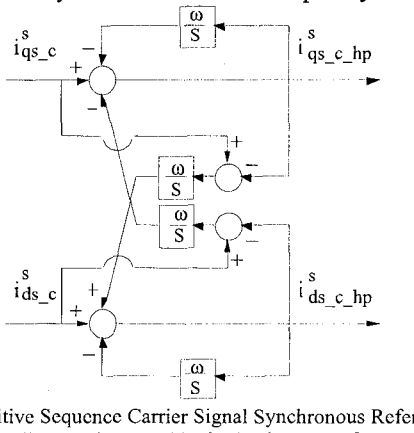

Figure 3: Positive Sequence Carrier Signal Synchronous Reference Frame High-pass Filter Implemented in the Stationary Reference Frame

The synchronous reference frame filters can also be used to filter off the fundamental component of the stator current. Filtering the fundamental component in this way is a little more complex than using a stationary reference frame high-pass filter. This increased complexity has to be traded off with the improved filtering provided by the synchronous reference frame high-pass filter.

V. ROTOR POSITION ESTIMATION

With the fundamental excitation and the positive sequence component of the carrier signal current filtered off, it is possible to extract the spatial information contained in the phase of the negative sequence component of the carrier signal current using the tracking observer shown in Figure 4.

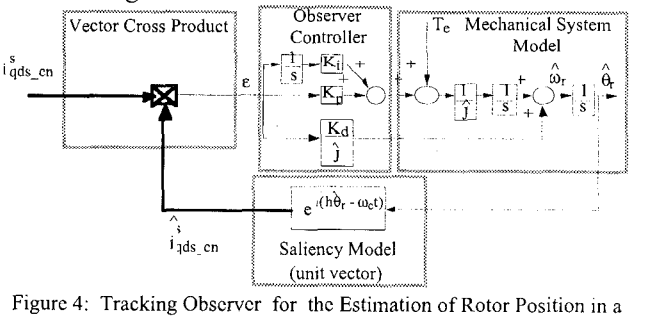

Figure 4: Tracking Observer for the Estimation of Rotor Position in a Machine with a Harmonic Saliency

The error signal, which forces the estimated rotor position to track the actual rotor position, is formed by taking the vector cross-product between an estimated and measured negative sequence carrier signal current vector, (5).

$$\varepsilon = \hat{i}^{s}_{qds\_c} \times i^{s}_{qds\_c} = I_{cn} \sin(h\,(\theta_r - \hat{\theta}_r)) \qquad (5)$$

The estimated negative sequence carrier signal current vector is formed from a model of the saliency. It is not important for the estimated vector to accurately model the magnitude of the measured negative sequence carrier signal current vector because the spatial information is contained in its phase, not its magnitude. The reliance on only the phase of the negative sequence carrier signal current vector is important because it makes the estimation independent of any machine parameters which may vary. The simplest form for an estimated negative sequence carrier signal current vector is an unit vector as shown in Figure 4.

The use of a harmonic saliency for the estimation of rotor position affects the tracking observer in several ways. First the harmonic number of the saliency scales the estimated position error. This scaling of the estimated position error is shown in (6) with the assumption of a small estimated position error.

$$\varepsilon \approx I_{cn}\, h\,(\theta_r - \hat{\theta}_r) \qquad (6)$$

The scaling of the estimated position error must be accounted for in the calculation of the tracking observer gain. A second way a harmonic saliency affects the estimation is by increasing the number of stable operating points that the observer may operate about. For a saliency with a period equal to the pole pitch of the machine, h = P/2, the number of stable operating points is equal to the number of poles. For a harmonic saliency the number of stable operating points is equal to the number of pole pairs times the harmonic number. This increase in the number of stable operating points increases the effective resolution of the rotor position estimate.

VI. EXPERIMENTAL RESULTS USING ROTOR BAR SLOT HARMONICS

The saliency model and position estimation technique described in the previous sections was implemented using a Motorola 56000 dsp on an induction motor with the parameters shown in Table 1. The switching frequency of the inverter and the sample rate of the dsp were synchronized at 10 kHz. All control and estimation calculations were performed at this 10 kHz sample rate.

The saliency in the machine was caused by the rotor bar slots. The machine had a somewhat unique construction in that the rotor slots were not skewed. This caused the machine to have a increased saliency due to the rotor bar slots than would normally be seen in a skewed rotor design. The stator transient inductance for this machine can be modeled using (2) with h = 14, (6).

$$L_{\sigma s} = \begin{bmatrix} \Sigma L_{\sigma s} + \Delta L_{\sigma s}\cos(14\ \theta_r) & -\Delta L_{\sigma s}\sin(14\theta_r) \\ -\Delta L_{\sigma s}\sin(14\theta_r) & \Sigma L_{\sigma s} - \Delta L_{\sigma s}\cos(14\ \theta_r) \end{bmatrix} \qquad (6)$$

TABLE 1 – Motor Paramters

Parameter	Value
r_s	0.0135 Ω
r_r	0.0140 Ω
L_{ls}	0.065 mH
L_{lr}	0.078 mH
L_m	0.530 mH
$\Sigma L_{\sigma s}$	0.133 mH
$\Delta L_{\sigma s}$	0.016 mH
rated speed	450 rpm
rated torque	4.82 N m
rated current	120 A
poles	4
stator slots	24
rotor slots	28
dc bus voltage	12 V

The rotor position estimate was obtained by exciting the machine with a balanced 3 phase carrier signal voltage vector. The magnitude of the carrier signal voltage vector was set equal to 15% of the dc bus voltage with a carrier frequency of 1 kHz. This resulted in carrier signal currents which could be modeled using (7).

$$i^{s}_{qds\_c} = -j\, I_{cp}\, e^{j\omega_c t} + j\, I_{cn}\, e^{j(14\,\theta_r - \omega_c t)} \qquad (7)$$

where I_{cp} = 1.02 A (1% of rated current), and I_{cn} = 0.147 A (0.1% of rated current).

The estimated rotor position was used to implement an indirect field oriented torque controller on the test machine. Figure 5 shows an overlay of the estimated and measured rotor positions while the test motor produced a constant torque of 1.5 N m (31% of rated) and the dynamometer, which was under speed control, went through a speed trajectory from 0 rpm to –5 rpm to 5 rpm back to 0 rpm.

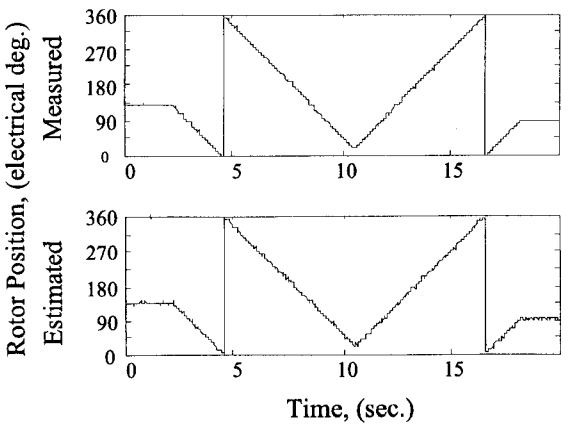

Figure 5: Overlay of Estimated and Measured Rotor Position for Steps in the Rotor Speed (0 rpm to –5 rpm to 5 rpm to 0 rpm)

Figure 6 shows an overlay of the estimated and measured rotor position for the exact same conditions as Figure 5 except that the dynamometer speed trajectory was changed to 0 rpm to –50 rpm to 50 rpm back 0 rpm.

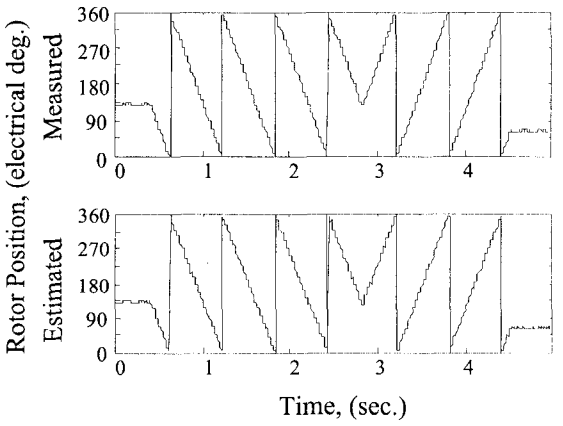

Figure 6: Overlay of Estimated and Measured Rotor Position for Steps in the Rotor Speed (0 rpm to –50 rpm to 50 rpm to 0 rpm)

Figures 5 and 6 show very clearly that the estimation technique is capable of sustained operation at low and zero speed. The estimated rotor position tracks the measured rotor position very accurately through speed transients and at zero speed. Experimental results for higher speeds were not included since the rotor position estimate does not degrade as the speed increases and the low speed operation was felt to be of the most importance.

VII. CONCLUSIONS

– The estimation of rotor position or flux angle independent of operating point, including low and zero speeds, requires that the estimation technique not be dependent on the rotor speed or fundamental excitation. This results in two conclusions: 1) a trackable spatial saliency must be present in the machine, and 2) persistent excitation must be provided to the machine in addition to the fundamental excitation, e.g. carrier frequency excitation.

– A balanced, 3 phase, carrier signal voltage excitation induces both a positive and negative sequence component of the carrier signal current in a machine with saliencies.

– All of the spatial information is contained in the negative sequence component of the carrier signal current. The positive sequence component of the carrier signal current contains no spatial information and can be filtered off using a synchronous reference frame high-pass filter.

– The model of the saliency used in the tracking observer has to accurately model the phase, not the magnitude, of the saliency present in the machine. This makes the estimation independent of any machine parameters which may vary.

– The use of a harmonic saliency increases the effective resolution of the rotor position estimate.

– Induction motors may have parasitic spatial saliencies present which can be used for rotor position estimation without modification to the machine.

ACKNOWLEDGEMENT

The authors wish to acknowledge the financial support and motivation provided by the Ford Motor Company and the Wisconsin Electric Machines and Power Electronics Consortium (WEMPEC) of the University of Wisconsin – Madison.

REFERENCES

[1] Schauder, C., "Adaptive Speed Identification for Vector Control of Induction Motors without Rotational Transducers", *Proc. IEEE-IAS 1989 Annual Meeting*, San Diego, CA, October, 1989, pp.493-499.

[2] Tajima, H. and Hori, Y., "Speed Sensorless Field-Orientation Control of the Induction Machine", *Proc. IEEE-IAS 1991 Annual Meeting, October 1991*, pp. 385-391, and *IEEE Trans. on Ind. Appl.*, Vol. 29, No. 1, Jan./Feb. 1993, pp. 175-180.

[3] Jansen, P.L. and Lorenz, R.D., "A Physically Insightful Approach to the Design and Accuracy Assessment of Flux Observers for Field Oriented Induction Machine Drives", *IEEE Trans. on Ind. Appl.*, Vol. 30, No. 1, Jan./Feb. 1994, pp. 101-110.

[4] Jansen, P.L. and Lorenz, R.D., "Accuracy Limitations of Velocity and Flux Estimation in Direct Field Oriented Induction Machines", *Proc. EPE Conf.*, Brighton, UK, September 1993, pp. 312-318.

[5] M. Ishida and K. Iwata, "A New Slip Frequency Detector of an Induction Motor Utilizing Rotor Slot Harmonics", *Proc. of the International Semiconductor Power Conversion Conference*, 1982, pp. 408-415.

[6] M. Ishida and K. Iwata, "Steady-state Characteristics of a Torque and Speed Control System of an Induction Motor Utilizing Rotor Slot Harmonics for Slip Frequency Sensing", *IEEE Transactions on Power Electronics*, Vol. PE-2, No. 3, July 1987, pp. 257-263.

[7] Zinger, D.S., Lipo, T.A., and Novotny, D.W., "Using Induction Motor Stator Windings to Extract Speed Information", *Proc. of IEEE-IAS 1989 Ann. Mtg.*, San Diego, CA, Oct., 1989, pp. 213-218.

[8] J. Jiang and J. Holtz, "High Dynamic Speed Sensorless AC Drive with On Line Model Parameter Tuning for Steady-state Accuracy", *IEEE Trans. on Industrial Electronics*, vol 44, no. 2, April 1997.

[9] Cuzner, R.M., Lorenz, R.D., and Novotny, D.W., "Application of Non-Linear Observers for Rotor Position Detection on an Induction Motor Using Machine Voltages and Currents", *Proc. IEEE-IAS 1990 Annual Meeting*, October 1990.

[10] Ferrah, A., Bradley, K.G., and Asher G.M., "Sensorless Speed Detection of Inverter Fed Induction Motors using Rotor Slot Harmonics and Fast Fourier Transform", *PESC*, 1992, pp. 280-286.

[11] Schroedl, M., "Operation of the PM Synchronous Machine Without a Mechanical Sensor", *Proc. Int. Conf. on Power Electronics and Variable Speed Drives*, IEE, London, July 1990, pp. 51-56.

[12] Schroedl, M., "Sensorless Control of Induction Motors at Low Speed and Standstill", *Proc. ICEM*, Boston, MA, Aug. 1990, pp. 863-867.

[13] Schroedl, M., Hennerbichler, D., and Wolbank, T.M., "Induction Motor Drive for Electric Vehicles without Speed- and Position Sensors", *Proc. EPE Conf.*, Brighton, UK, Sept. 1993, pp. 271-275.

[14] Schroedl, M.., and R.S. Wieser, "Induction Motor Drive for in Locomotives", in *5th European Power Electronics (EPE) Conf. Rec.*, Vol 3., Sevilla, Spain, Sept. 19-21, 1995, pp. 62-67.

[15] Jansen. P.L., The Integration of State Estimation, Control, and Design for Induction Machines, Ph.D. Dissertation, Dept. of Electrical and Computer Engineering, University of Wisconsin-Madison, 1993.

[16] Jansen, P.L. and Lorenz, R.D., "Transducerless Position and Velocity Estimation in Induction and Salient AC Machines", *Proc. IEEE-IAS 1994 Annual Meeting*, Denver, CO, Oct. 1994 and IEEE Trans. on Ind. Appl., Vol. 31, No. 2, March/April 1995, pp. 240-247.

[17] Jansen, P.L., Corley, M.J., Lorenz, R.D., "Flux, Position, and Velocity Estimation in AC Machines at Zero Speed via Tracking of High Frequency Saliencies", in *5th European Power Electronics Conf. Rec.*, Vol 3., Sevilla, Spain, Sept. 19-21, 1995, pp. 154-160.

[18] Jansen, P.L., and Lorenz, R.D., "Transducerless Field Orientation Concepts Employing Saturation-Induced Saliencies in Induction Machines", *Proc. IEEE-IAS 1995 Annual Meeting*, Orlando, FL, Oct. 9-13, 1995, pp. .174-181, and IEEE, IAS Transactions , vol 32, no. 6, Nov/dec 1996.

[19] Corley, M.J., and Lorenz, R.D., "Rotor Position and Velocity Estimation for a Permanent Magnet Synchronous Machine at Standstill and High Speeds," *Proc. IEEE-IAS 1996 Annual Meeting*, San Diego, CA, October 5-10, 1996, pp. 36-41.

[20] Lorenz, R.D., "Self-Sensing Methods Wide Bandwidth Position & Velocity Sensing at Any Speed, incl. Zero", Tutorial Notes for "Sensorless Control of AC Machines", *Proc. IEEE-IAS 1996 Annual Meeting*, San Diego, CA, October 5-10, 1996

[21] Cilia, J., Asher, G.M., and Bradley, K., "Sensorless Position Detection for Vector Controlled Induction Motor Drives Using an Asymmetric Outer-Section Cage", *Proc. IEEE-IAS 1996 Annual Meeting*, San Diego, CA, October 5-10, 1996, pp. 286-292.

Sensorless Speed Estimation based on Primary and Secondary Resistance Estimation and Output Voltage Compensation of Induction Motor

Kan Akatsu* Atsuo Kawamura**

Dept. of Elec. and Comp. Eng.
Yokohama National University
79–5 Tokiwadai, Hodogaya-ku
Yokohama 240 JAPAN
E-mail: * aka@kawalab.dnj.ynu.ac.jp
E-mail: ** kawamura@kawalab.dnj.ynu.ac.jp

Abstract— **In the very low speed region, it is difficult to estimate the rotor speed of the induction motor, because the machine parameter (especially R_2) has strong influence to the speed estimation. It is known that the simultaneous estimation of the speed and R_2 is impossible. In this paper proposed are the R_2 estimation in the transient state without adding any additional signal to the stator current, and the output voltage compensation without the voltage sensors. The R_1 is estimated from the instantaneous reactive power.**

I. Introduction

Recently, the research concerning the speed sensorless algorithm of the induction motor has been much focused and progressed. But the speed sensorless estimation in the low speed is difficult due to the following problems.

1. R_1 and R_2 variations
2. output voltage error in the inverter
3. drift-offset error in the flux integration
4. speed oscillation due to nonlinear friction-load characteristics in the very low speed

In [1] the above problems (3) and (4) were solved by estimation of the slip frequency, and (1) and (2) were manually adjusted, and the speed of 5[rpm] was achieved by the proposed slip frequency estimation.

This paper proposes the online solution for the problem (1) and (2). It is known that the simultaneous estimation of the rotor speed and R_2 under the field oriented control (i.e. the secondary flux is constant) is impossible [2]. Thus in [3] another signal was added to the stator current, and the secondary flux is a little oscillated. Thus, this algorithm made the actual speed oscillation under the indirect vector control. As a result, the low speed estimation under this algorithm was very difficult.

In this paper we propose

- R_2 is estimated by the least mean square algorithm under the transient states without adding any signal to the stator current.
- R_1 is estimated based on the instantaneous reactive power [4].
- The inverter output voltage error due to the dead time and voltage drops of the switching devices are calculated by estimating the real inverter output voltage from the measured stator current.

II. Sensorless Speed Estimation Algorithm[1]

The following differential equations fixed on the synchronously rotating reference frame (d-q) are assumed.

$$\begin{bmatrix} \vec{v_1} \\ 0 \end{bmatrix} = \begin{bmatrix} (R_1 + pL_1)I + \omega L_1 J & * \\ pL_m I + \omega_s L_m J & \\ * & pL_m I + \omega L_m J \\ & (R_2 + pL_2)I + \omega_s L_2 J \end{bmatrix} \begin{bmatrix} \vec{i_1} \\ \vec{i_2} \end{bmatrix} \quad (1)$$

where

$$I = \begin{bmatrix} 1 & 0 \\ 0 & 1 \end{bmatrix}, J = \begin{bmatrix} 0 & -1 \\ 1 & 0 \end{bmatrix} \quad (2)$$

All symbols are listed in the appendix.

Making the outer-product of the second row of (1) and $\vec{\Phi}_2$, and solving for ω_s produces,

$$\omega_s = R_2 \frac{\vec{i_2} \times \vec{\Phi}_2}{\vec{\Phi}_2 \times J\vec{\Phi}_2} + \frac{p\vec{\Phi}_2 \times \vec{\Phi}_2}{\vec{\Phi}_2 \times J\vec{\Phi}_2} \quad (3)$$

In (3), the secondary flux $\vec{\Phi}_2$ and the secondary current $\vec{i_2}$ are replaced with the estimated values $\hat{\vec{\Phi}}_2$ and $\hat{\vec{i}}_2$, as follows.

$$\hat{\vec{\Phi}}_{1s} = \int (\vec{v_{1s}}^* - R_1 \vec{i}_{1s}) dt \quad (4)$$

$$\hat{\vec{i}}_{2s} = \frac{1}{L_m}(\hat{\vec{\Phi}}_{1s} - L_1 \vec{i_{1s}}) \quad (5)$$

$$\hat{\vec{\Phi}}_{2s} = L_m \vec{i}_{1s} + L_2 \hat{\vec{i}}_{2s} \quad (6)$$

$$\hat{\vec{i}}_2 = Rot(\theta) \cdot \hat{\vec{i}}_{2s} \quad (7)$$

$$\hat{\vec{\Phi}}_2 = Rot(\theta) \cdot \hat{\vec{\Phi}}_{2s} \quad (8)$$

0-7803-3823-5/97/$10.00© 1997 IEEE

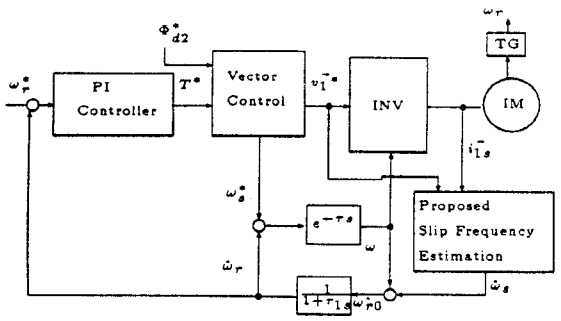

Fig. 1. block diagram

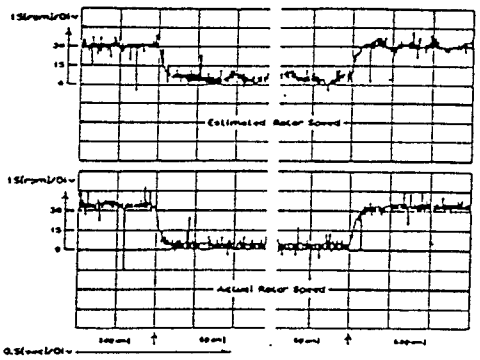

(30[rpm] → 5[rpm] 5[rpm] → 30[rpm]).

Fig. 2. experiment (ω_r and $\hat{\omega}_r$)

where

$$Rot(\theta) = \begin{bmatrix} \cos\theta & \sin\theta \\ -\sin\theta & \cos\theta \end{bmatrix} \tag{9}$$

$$\theta = \int \omega dt \tag{10}$$

In the all equations, the variable with the subscription "s" mean on the stationary reference frame, and the variable with "*" means a command reference. In this algorithm[1], the voltage is replaced with voltage command reference $\vec{v}_{1s}^{*}$.

The slip frequency estimation $\hat{\omega}_s$ and the rotor angular velocity estimation $\hat{\omega}_r$ are made as follows.

$$\hat{\omega}_s = R_2 \frac{\hat{\vec{i}}_2 \times \hat{\vec{\Phi}}_2}{\hat{\vec{\Phi}}_2 \times J\hat{\vec{\Phi}}_2} + \frac{p\hat{\vec{\Phi}}_2 \times \hat{\vec{\Phi}}_2}{\hat{\vec{\Phi}}_2 \times J\hat{\vec{\Phi}}_2} \tag{11}$$

$$\hat{\omega}_r = \omega - \hat{\omega}_s \tag{12}$$

where ω is the electrical angular velocity.

The second term of the right sides in (11) is a transient term. In the low speed range, the steady state operation is not always maintained due to the mechanical instability such as nonlinear friction-load characteristics and spatial harmonics caused by the stator slots. Thus, this transient term is very important.

The integration in (4) produce a problem of a dc offset component in the very low speed region. This problem was avoided by using the digital integration. Fig.1 shows the block diagram of the sensorless speed estimation algorithm, and Fig.2 shows experimental results. This algorithm made 5[rpm] estimation possible by the manual voltage compensation and R_1 and R_2 adjustment.

III. R_2 Estimation

A. *influence of R_2 variation*

From (11) it is obvious that the R_2 variation makes much influence to the speed estimation. Fig.3 and Fig.4 show the relationship between the variation of R_2 and the estimation error of the slip frequency. From Fig.3 and Fig.4 it is obvious that the change of R_2 has much influence to the speed estimation in the low speed under the 100[rpm].

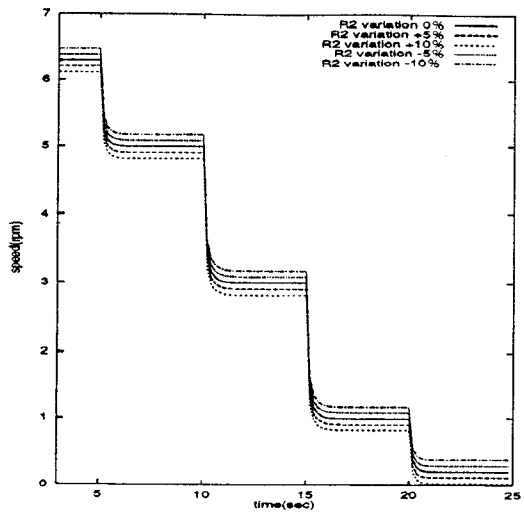

Fig. 3. the variation of R_2 and the estimation of the slip frequency

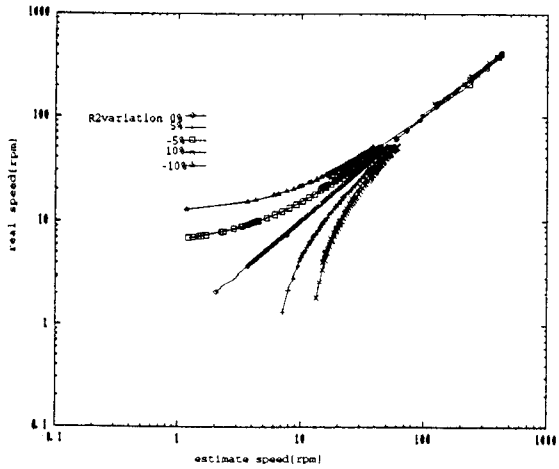

Fig. 4. the variation of R_2 and estimation error of the slip frequency (log scale)

B. algorithm of R_2 estimation

Though we need to estimate R_2 in the low speed, it is impossible to estimate R_2 and the speed at the same time under the field oriented control in case the secondary flux is constant [2].

Dividing the second row of (1) to d-q components, and canceling ω_s produces R_2 [5].

$$\hat{R}_2 = -\frac{p\hat{\vec{\Phi}}_2 \cdot \hat{\vec{\Phi}}_2}{\hat{\vec{i}}_2 \cdot \hat{\vec{\Phi}}_2} \tag{13}$$

This equation is zero if $\vec{\Phi}_2$ is constant, thus in[3] a small alternating current is added to i_{1d}^* and $\vec{\Phi}_2$ is fluctuated. As a result R_2 estimation is possible in (13). But in the slip frequency control type vector control (indirect control), this alternating current makes oscillation to the real speed. Fig.5 and Fig.6 show the estimation of R_2 and slip frequency when the alternating current (about 5%) is superimposed to the secondary flux (the real value of R_2 is 0.285Ω).

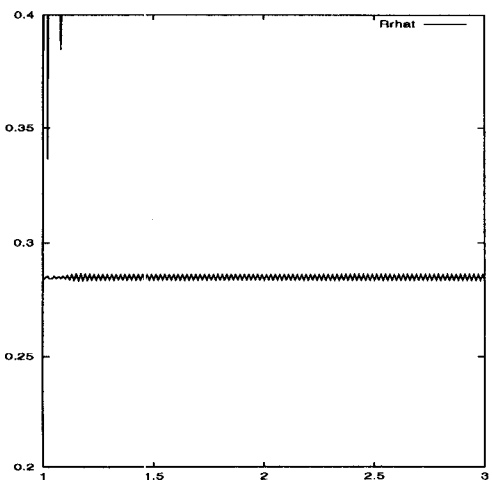

Fig. 5. The estimated R_2 when the alternating current (x axis:time[sec],y axis:$\hat{R}_r$[Ω])

It is cleared that the estimation of R_2 without any additional signal to the stator current is required for the algorithm in (11). In this paper R_2 is estimated through the speed transient, because the secondary flux is not exactly constant in this period. The proposed least mean square algorithm is as follows.

$$\hat{R}_2[N+1] = \hat{R}_2[N] + k[N+1](b[N+1] - a[N+1]\hat{R}_2[N]) \tag{14}$$

$$k[N+1] = \begin{cases} \frac{P[N]a[N+1]}{\rho + a^2[N+1]P[N]} & b[N] \neq 0 \\ 0 & b[N] = 0 \end{cases} \tag{15}$$

$$P[N+1] = (1 - k[N+1]a[N+1])P[N]\frac{1}{\rho} \tag{16}$$

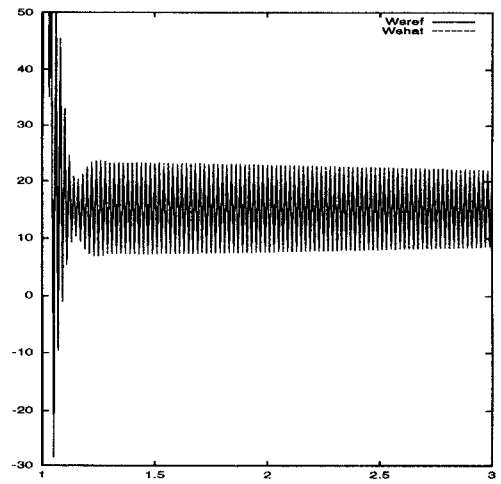

Fig. 6. slip frequency when the ac current is added to the stator current for the estimation of R_2 (x axis:Speed[rad/sec],y axis:time[sec])

where

$$a[N] = \hat{\vec{i}}_2 \cdot \hat{\vec{\Phi}}_2 \tag{17}$$

$$b[N] = p\hat{\vec{\Phi}}_2 \cdot \hat{\vec{\Phi}}_2 \tag{18}$$

$$\rho : \textit{a forgetting factor}$$

The advantages of this algorithm are

- it is not required to add any alternating current to the stator current.
- the low pass filter is not needed.

The disadvantages are

- R_2 can not be estimated in the steady state.

However usually R_2 changes slowly, thus it will not be a problem if the speed of the motor changes frequently. This algorithm is useful for the Electric Vehicle (EV) application, because the speed of EV often changes.

In the transient state, R_2 is obtained from (14). In the steady state, the $\hat{R}_2$ become zero. Fig.7 shows R_2,$\hat{R}_2$ and ω_r, $\hat{\omega}_r$ when the rotor speed changes. Fig.7 indicates that the true R_2 is obtained only after the speed of the motor changes.

IV. R_1 Estimation

From (4) it is expected that the R_1 variation makes the estimation error of the primary flux $\hat{\vec{\Phi}}_1$ and it leads to the estimation error of the rotor speed $\hat{\omega}_r$. The outer product of the first row of (1) and $\vec{i}_{1s}$ yields the instantaneous reactive power(Q), and it does not have the term R_1. This algorithm does not require the voltage if the primary voltage $\vec{v}_{1s}$ is replaced with the command voltage reference $\vec{v}_{1s}^*$.

The Q and $|\hat{\vec{\Phi}}_2|$ are expressed as follows [4].

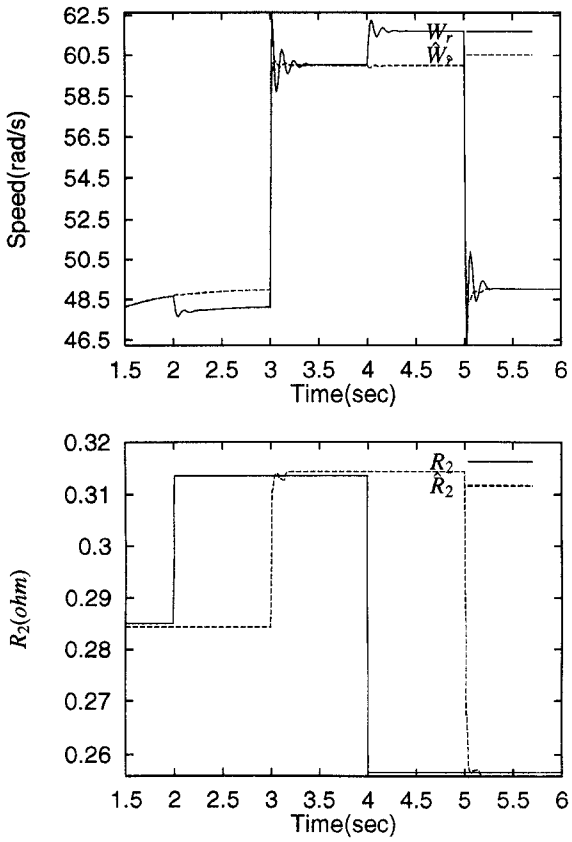

Fig. 7. $\hat{R}_2$ *and* $\hat{\omega}_r$

$$|\vec{\Phi}_2|^2 = L_2(\frac{Q}{\omega} - \frac{L_1L_2 - L_m^2}{L_m}|\vec{i_{1s}}|^2) \quad (19)$$

$$Q = \vec{i_{1s}} \times \vec{v_{1s}^*} \quad (20)$$

R_1 is adjusted so that the norms of (8) and (19) become the same.

Fig.8 shows R_1 and $\hat{R}_1$, and Fig.9 shows ω_r and $\hat{\omega}_r$ when the R_1 changes at t=2 and 6 seconds.

From those figures, it is observed that the estimate values becomes equal to the real ones in the steady state.

V. Output Voltage Compensation

The output voltage of the inverter is usually less than the voltage reference due to the voltage drop of the switching devices. Also when the speed is very low, the voltages become very low, and the actual voltage is less than the voltage command due to the transient phenomena of the switching devices. The mismatching of the actual voltage and the voltage command produces an error in (4), which causes the speed estimation error in (11).

Fig.10 shows the actual and estimated rotor speed when the inverter has a 10% voltage drop from the voltage reference.

Thus the voltage error should be estimated without a voltage sensor. On the synchronously rotating reference frame, $|\hat{V}|$ is graphically obtained using only from the

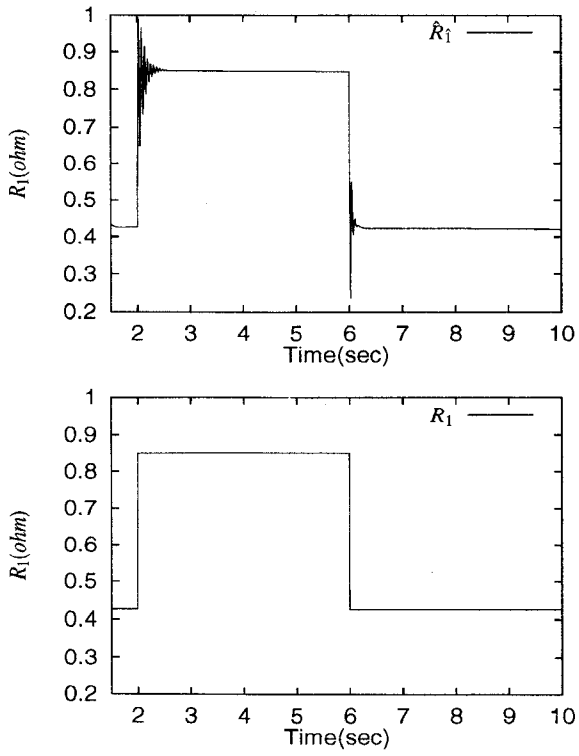

Fig. 8. R_1 and $\hat{R}_1$

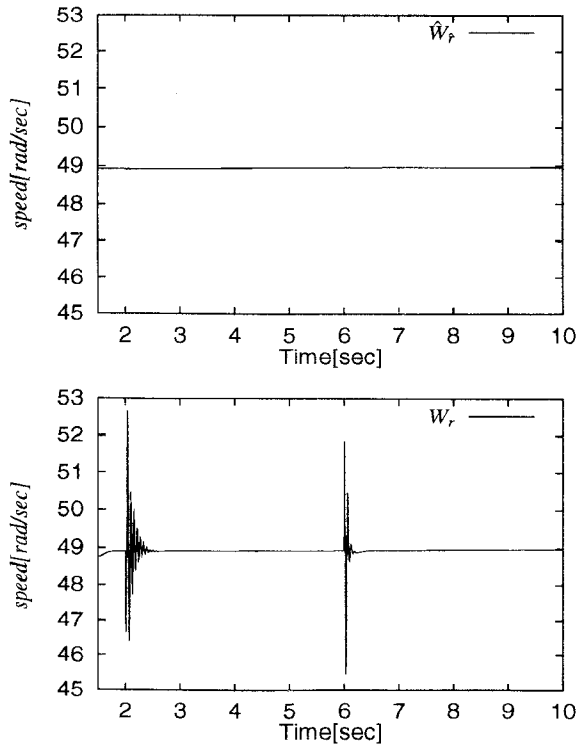

Fig. 9. ω_r and $\hat{\omega}_r$

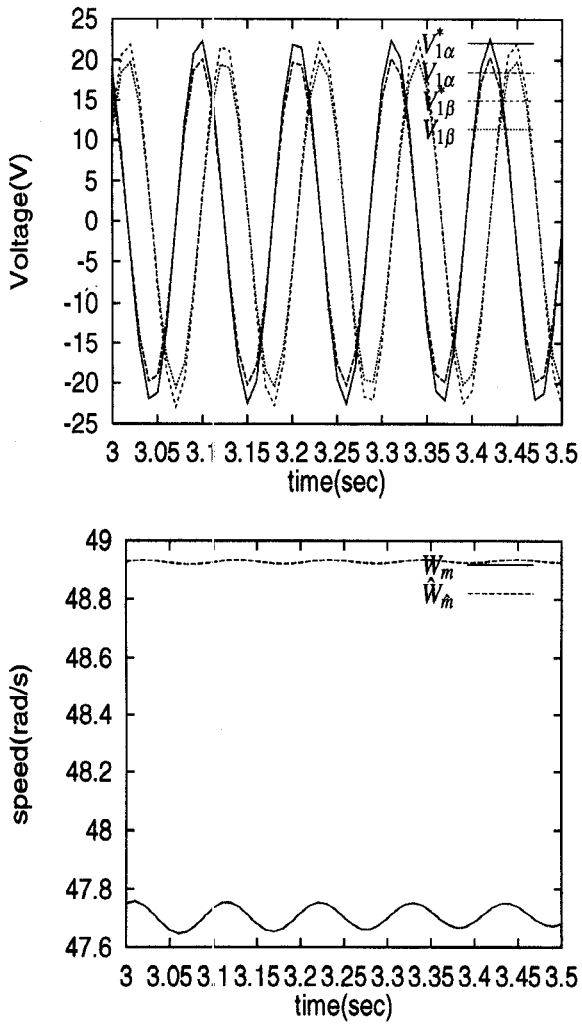

Fig. 10. the rotor speed estimation error caused by the voltage offset : (upper) the stator voltage waveforms, (lower) speed

stator informations, as shown in Fig.11, if the parameters in the stator side are correct. $|\hat{V}|$ becomes [6],

$$|\hat{V}| = (\omega L_1 i_{1d} + R_s i_{1q})\cos(\delta) - (R_s i_{1d} - \omega \frac{L_1 L_2 - L_m^2}{L_2} i_{1q})\sin(\delta) \quad (21)$$

$$\delta = \tan^{-1} \frac{-R_s i_{1d} + \omega \frac{L_1 L_2 - L_m^2}{L_2} i_{1q}}{\omega L_1 i_{1d} + R_s i_{1q}} \quad (22)$$

The norm of the compensated voltage reference $|V^*_{comp}|$ and its d-q components V^*_{compd} and V^*_{compq} are expressed as follows,

$$|V^*_{comp}| = |V^*| + \int (|V^*| - |\hat{V}|)dt \quad (23)$$

$$V^*_{compd} = |V^*_{comp}|\cos(\delta_0) \quad (24)$$

$$V^*_{compq} = |V^*_{comp}|\sin(\delta_0) \quad (25)$$

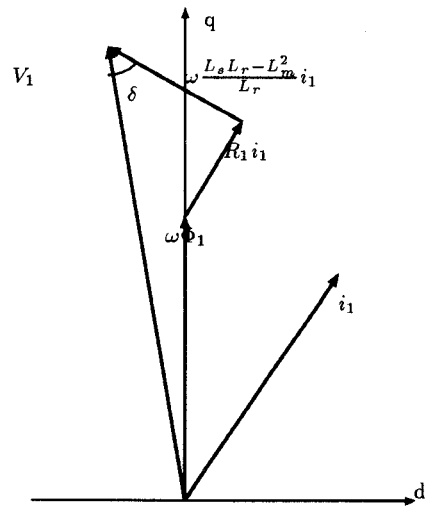

Fig. 11. Output voltage vector

where

$$|V^*| = \sqrt{v^{*2}_{1d} + v^{*2}_{1q}} \quad (26)$$

$$\delta_0 = \tan^{-1} \frac{v^*_{1q}}{v^*_{1d}} \quad (27)$$

Fig.12 shows a block diagram for the output voltage compensation.

Fig.13 shows digital simulations of $|\hat{V}|$, $|V^*|$ and $|V^*_{comp}|$, ω_r and $\hat{\omega}_r$ when there is 3% voltage drop of the inverter. The voltage compensation started at t = 12 (sec). The compensated voltage reference V^*_{comp} became a little larger, and $|\hat{V}|$ was converged to $|V^*|$.

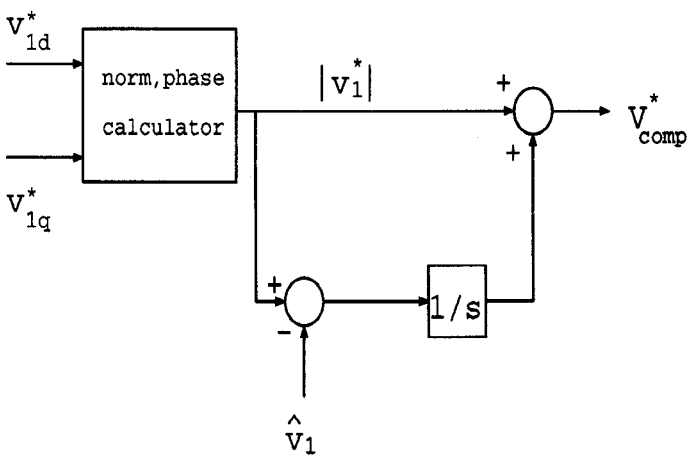

Fig. 12. block diagram for output voltage compensation

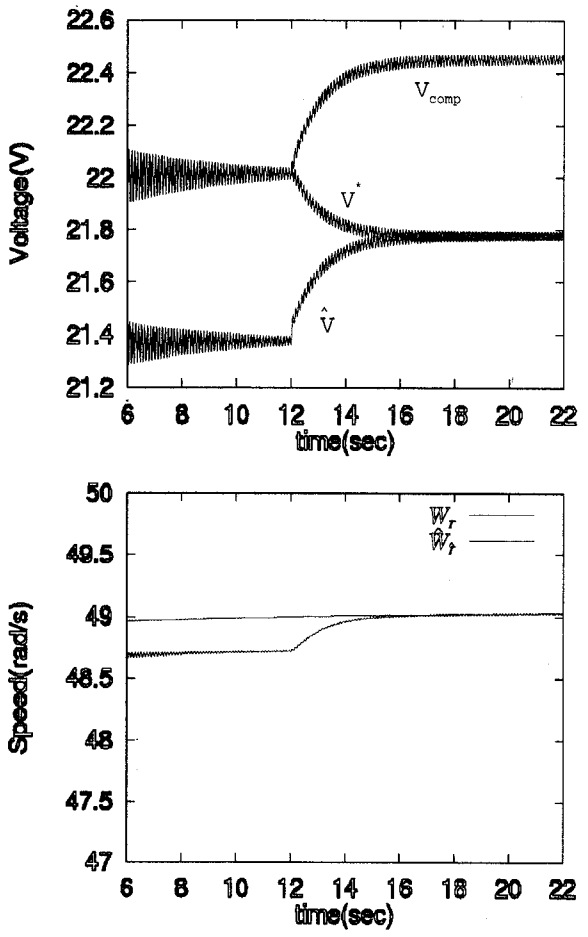

Fig. 13. $|\hat{V}|, |V^*| and |V_{comp}|$(upper), ω_r and $\hat{\omega_r}$ (lower)

VI. Conclusions

In this paper, the following are presented.

- R_2 is estimated by the LMS algorithm when the rotor speed is in the transient.
- R_1 is estimated from the instantaneous reactive power.
- The inverter output voltage is adjusted by the output voltage compensation.

These compensations seem to be effective for the very low rotor speed estimation. However there is a problem that the inverter voltage compensation and R_1 estimation can not be used at the same times. Because the algorithm of the inverter voltage compensation uses the R_1, and the algorithm of R_1 estimation uses the command voltage reference v_{1s}^*. R_1 and v_{1s}^* can not be simultaneously obtained in the proposed algorithm. This will be solved in future.

Appendix

R_1, R_2	:	stator and rotor resistance
L_1, L_2	:	stator and rotor self inductance
L_m	:	mutual inductance
ω_s	:	slip frequency
ω_r	:	rotor angular velocity
i_1, i_2	:	primary and secondary current
Φ_1	:	primary flux $(L_1 i_1 + L_m i_2)$
Φ_2	:	secondary flux $(L_m i_1 + L_2 i_2)$
p	:	derivative operator (d/dt)
$\vec{\Phi_2} \times J\vec{\Phi_2}$	$\triangleq$	$\Phi_{2d}^2 + \Phi_{2q}^2$
$\vec{i_2} \times \vec{\Phi_2}$	$\triangleq$	$i_{2d}\Phi_{2q} - i_{2q}\Phi_{2d}$
$p\vec{\Phi_2} \times \vec{\Phi_2}$	$\triangleq$	$p\Phi_{2d}\Phi_{2q} - p\Phi_{2q}\Phi_{2d}$
$p\vec{\Phi_2} \cdot \vec{\Phi_2}$	$\triangleq$	$p\Phi_{2d}\Phi_{2d} + p\Phi_{2q}\Phi_{2q}$
$\vec{i_2} \cdot \vec{\Phi_2}$	$\triangleq$	$i_{2d}\Phi_{2d} + i_{2q}\Phi_{2q}$

References

[1] T.W Kim and A.Kawamura. Sensorless slip frequency edtimation of inducion motor in the very low speed region. *IEE Japan Trans 116-D No.6*, pp. 644 – 650, 1996.

[2] S.Shinnaka. A unified analysis on simultaneous identification of velocity and rotor resistance of induction motor. *IEE of Japan Trans 113-D No.12 (in Japanese)*, pp. 1483 – 1484, 1993.

[3] H.Kubota and K.Matsuse. Speed sensorless field oriented control of induction motor with rotor resistance adaption. In *IEEE IAS Annual Meeteing*, pp. 414–418, 1993.

[4] T.Kamimachi and I.Takahashi. Primary resistance compensation for sensoress speed control of an induction motor. In *JIASC (in Japanese) Vol.3*, pp. 213 – 214, 1996.

[5] T.Kamimachi and I.Takahashi. Sensorless control of an induction motor with no influence of secondary resistance variation. pp. 408 – 413, 1993.

[6] T.Okuyama, N.Fujimoto, and H.Fujii. Simplified vector control system without speed and voltage sensors. *IEE Japan Trans 110-D No.5(in Japanese)*, pp. 477 – 486, 1990.

[7] I.Miyashita and Y.Ohmori. Speed sensorless high-speed torque and speed control of induction motor based on instataneous spatial vector theory. In *IPEC-Tokyo*, pp. 1144 – 1151, 1990.

Sensorless Vector-Controlled Induction Motor Drive System with Rotor Resistance Estimation Using Parallel Processing with Floating Point DSP

Teodor Pana
Technical University of Cluj-Napoca, Dept. of Electrical Drives and Robots,
3400, Cluj-Napoca, P.O. Box 1-99, ROMANIA
Fax: +40-64-192055;
E-mail:pana@utcluj.ro

Abstract-**The paper deals with the aspects related to simultaneous rotor speed estimation and rotor resistance identification in field-oriented induction motor systems using only the induction motor model. A statistical based computing algorithm is proposed in order to avoid the division by zero. Three basic algorithms have been considered in order to establish the optimum solution. The study of the speed and rotor resistance estimator has been performed together with a Gopinath flux observer. Hence, the rotor flux, rotor speed and resistance have been estimated using only the electrical feedback magnitudes of the motor: the stator voltages and currents. The estimated rotor resistance is applied to the input of the flux observer and voltage compensator blocks. In order to evaluate the performances of the proposed method, a multiprocessor based simulation, using floating point DSP, has been performed.**

I. INTRODUCTION

This paper deals with the aspects related to simultaneous rotor speed estimation and rotor resistance identification in field-oriented induction motor systems, which allows speed and rotor resistance estimation using only the induction motor model. Hence, the control of the induction motor could be achieved without the use of special estimating strategies, such as Kalman filters, Fuzzy estimators, neural networks etc.

A statistical based computing algorithm is proposed in order to avoid the division by zero. Three basic algorithms have been considered in order to establish the optimum solution. The study of the speed and rotor resistance estimator has been performed together with a Gopinath flux observer. Hence, the rotor flux, rotor speed and resistance have been estimated using only the electrical feedback magnitudes of the motor: the stator voltages and currents. Two cases have been considered: the sensorless vector control without rotor resistance feedback loop (based on the immunity of the Gopinath flux observer to the variation of the rotor resistance) and the vector control with rotor resistance feedback loop. The simulation results prove the simplicity and the performance of the estimator based only on the electromagnetic phenomena inside the motor.

II. THE SPEED AND ROTOR RESISTANCE PRINCIPLE

As it is already known, the most difficult aspects concerning the implementation of the electrical drive systems based on the field-orientation theory, are in relation with rotor flux components, speed and rotor resistance estimation. It has been already proved that simultaneous identification of the rotor resistance and the rotor speed is possible only when the rotor flux is time-variant [12]. If the model of the induction motor is considered, the rotor speed and rotor resistance can be expressed as follows:

$$R_r = \frac{\psi_{rd}\dot{\psi}_{rd} + \psi_{rq}\dot{\psi}_{rq}}{-\left(i_{rd}\psi_{rd} + i_{rq}\psi_{rq}\right)}$$
$$\omega_r = \frac{i_{rq}\dot{\psi}_{rd} - i_{rd}\dot{\psi}_{rq}}{-\left(i_{rd}\psi_{rd} + i_{rq}\psi_{rq}\right)} \quad (1)$$

From the rotor equation of the induction motor, the modulus variation of the rotor flux phasor is deduced:

$$\frac{d}{dt}\left\|\psi_r\right\|^2 = 2[\psi_{rd} \quad \psi_{rq}]\begin{bmatrix}-R_r i_{rd} - \omega_r\psi_{rq}\\ -R_r i_{rq} + \omega_r\psi_{rd}\end{bmatrix} = \quad (2)$$
$$= -2R_r[\psi_{rd}i_{rd} + \psi_{rq}i_{rq}]$$

or

$$\frac{d}{dt}\left\|\psi_r\right\|^2 = -2R_r[\psi_r]^T[i_r]\,. \quad (3)$$

As equation (2) shows, if the modulus of the rotor flux is kept constant, the following relation results:

$$\psi_{rd}i_{rd} + \psi_{rq}i_{rq} = 0 \quad (4)$$

At this point, some preliminary conclusions might be considered:

- if the modulus of the rotor flux is kept strictly constant, the denominators in expressions from (1) are always zero; consequently, in order to estimate the rotor speed and resistance, the rotor flux must be time-variant [12]. This comes in contradiction with the basic principle of the vector control of induction motor;

0-7803-3823-5/97/$10.00© 1997 IEEE

•even if the rotor flux is time variant, the shape of the denominator is wavy and hence division by zero periodically appears in the computation of the estimated magnitudes from (1).

The principle of the rotor speed and rotor resistance estimation is shown in Fig. 1. The nominators and the denominator of (1) are calculated. At each iteration, these components are used by the Fixed Trace Block to determinate the instantaneous speed and rotor resistance values, using a statistic algorithm, in order to avoid the division by zero.

III. THE STATISTIC ALGORITHMS

The difficulties in implementing relations (1) on digital computing devices, derive from the dividing by zero operation. It has also to be pointed out two more aspects that make this operation more complicated:

•the richness of the rotor speed signal, especially at low values;

•the speed profiles, that vary from one application to another, including the frequency and duration of speed variations;

Three types of identification algorithms were taken into consideration [4]:

•The Least Square Method (LS);
•The Recursive Least Square Method (RLS);
•The Fixed Trace Method.

Taking into account the reasons enumerated above, and also the simulation results, we consider that only the Fixed Trace Method could be applied for the speed and rotor resistance estimation. It is, in fact, an improved version of the recursive least square one, based on the following recursive expressions:

$$\hat{\theta}[m] = \hat{\theta}[m-1] - \frac{P[m-1]x[m]}{\lambda + P[m-1](x(m))^2}\left(\hat{\theta}[m-1]x[m] - y[m]\right)$$

$$P[m] = \frac{P[m-1]}{\lambda + P[m-1](x(m))^2} \tag{5}$$

where

$$\hat{\theta}[m] = \frac{y[m]}{x[m]} \tag{6}$$

Here θ could be either R_r or ω_r from (1). λ is the forgetting factor of the exponential window. As λ is constant in the RLS method, it is variable in the fixed trace one, in accordance with the variation of the estimated value and is given by the following expression:

$$\lambda = \frac{1}{1+\gamma(x[m])^2} \tag{7}$$

The variable forgetting factor is obtained by fixing the trace of the gain matrix P:

$$tr(P[m]) = tr(P[0]) = \gamma > 0 \tag{8}$$

The recursive form for the fixed trace algorithm used in the estimation is expressed by the following relation:

$$\hat{\theta}[m] = \hat{\theta}[m-1] - \frac{P[0]x[m]}{1 + P[0](x[m])^2}\left(\hat{\theta}[m-1]x[m] - y[m]\right) \tag{9}$$

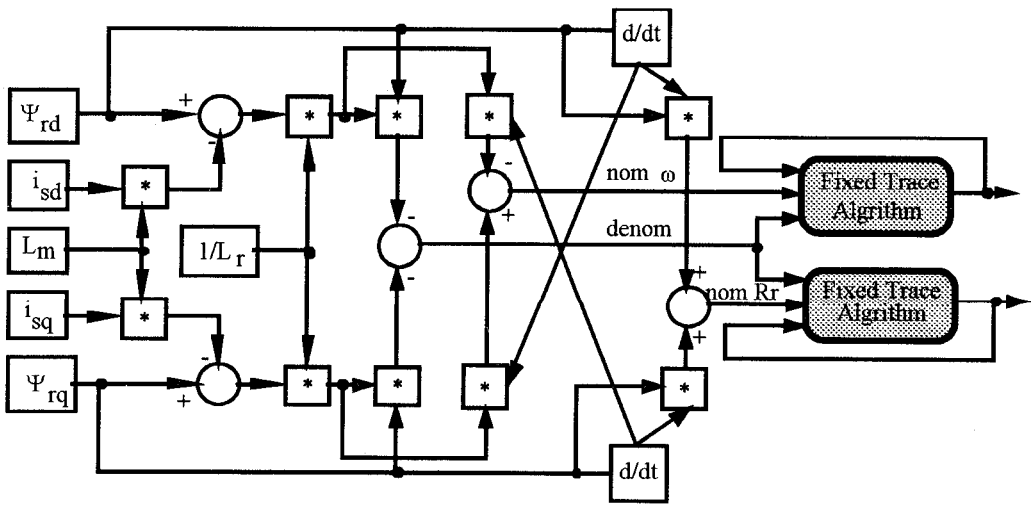

Fig. 1. The principle of simultaneous speed and rotor resistance estimation.

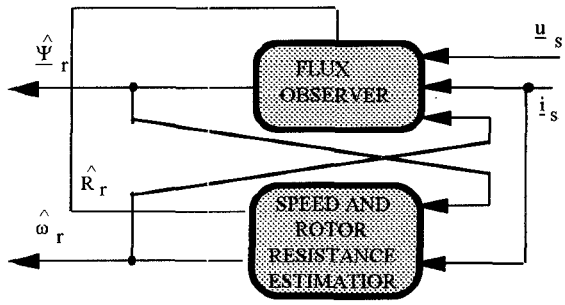

ig. 2. The speed and rotor resistance estimation assembly.

IV. THE FIELD-ORIENTED INDUCTION MOTOR DRIVE SYSTEM

The speed and rotor resistance estimator was simulated as a component block of the field-oriented induction motor drive shown in Fig. 3. Only the stator currents and voltages of the induction motor have been considered as feedback magnitudes. The Gopinath reduced order flux observer (presented in detail in [2] and [3]) was used to estimate the rotor flux components [2,3]. The influence of the poles allocation of the flux observer was also taken into consideration, through the k coefficient. The poles allocation of the flux observer was designed in order to obtain duplicate poles on the real axis, which guarantees the flux estimation with unity damping factor [2,3]. The pole allocation is performed real time, according to the instantaneous rotor speed and rotor resistance, estimated by the proposed speed and rotor resistance estimator. According to α and β, the gain coefficients g_a and g_b are calculated.

The analytical structure of the rotor flux -speed and resistance estimation assembly in Fig. 2. From the Fig. 2 one can notice that the outputs of each estimator is at the same time input for the other one. With other words the two estimators have embedded feedback loops.

In Fig. 3 the field-oriented induction motor drive system is presented. The estimated rotor resistance is also used in the computation of the voltage commands, by the voltage compensation block.

It has been already proved that the modulus of the rotor flux must be time-variant in order to keep the denominator of relations (1) at nonzero values. Some authors consider that the ripples caused by the non-sinusoidal PWM voltage supply could avoid the permanent division by zero [5].

Good results have been reported also using a low frequency sinusoidal signal summed to the constant flux reference one [7,8]. The simulations proved that using the variation of the rotor flux modulus with 5%, satisfactory results have been obtained.

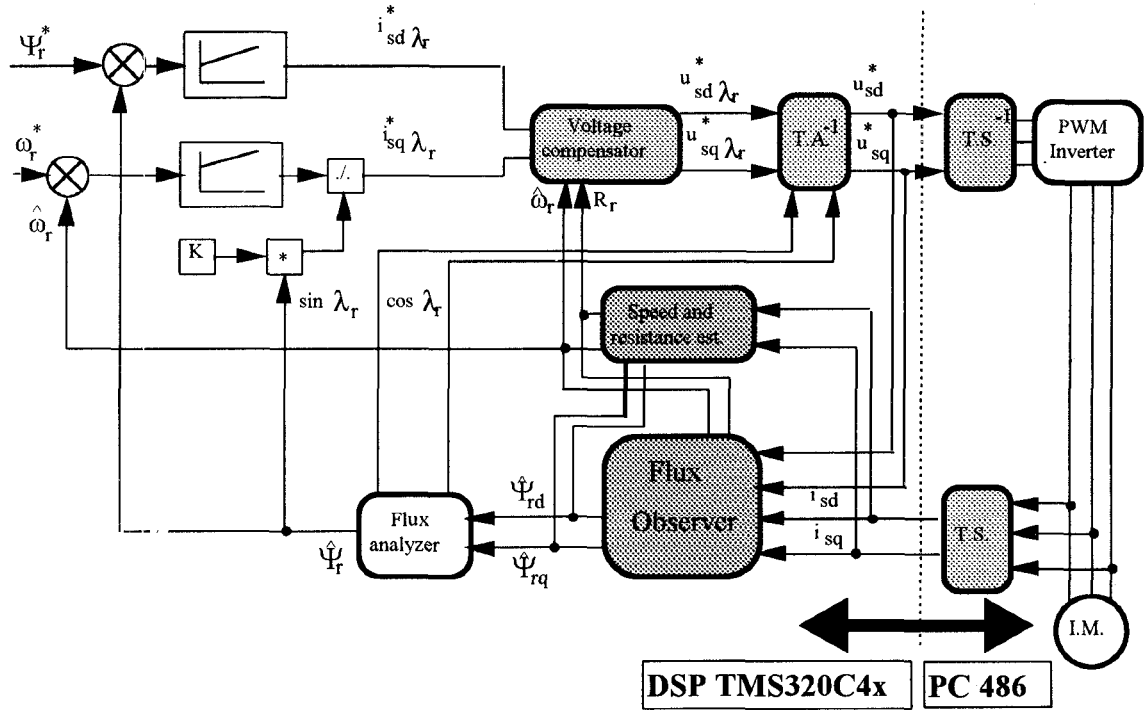

Fig. 3. The field-oriented induction motor drive system.

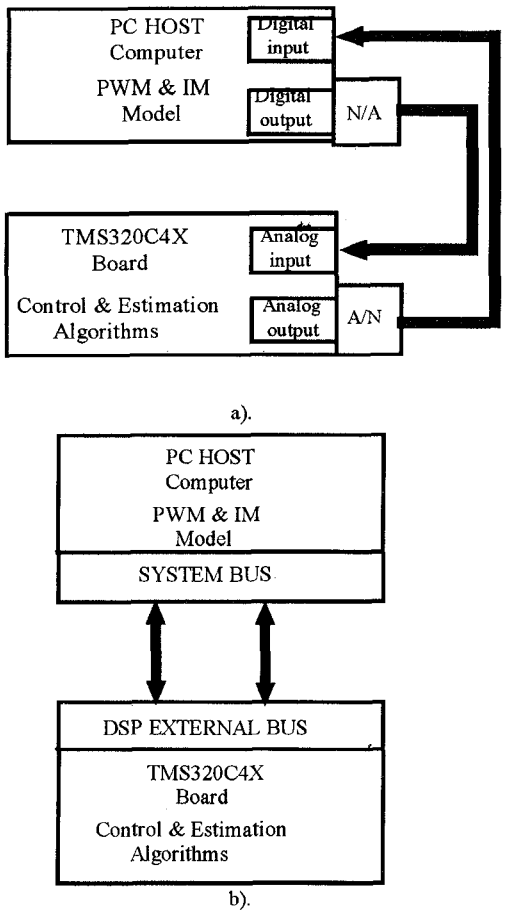

Fig. 4. The structure of the bi-processor real-time simulation assembly.

V. REAL-TIME SIMULATION USING A MULTI-PROCESSOR STRUCTURE BASED ON TMS320C40

In order to test the performances of the proposed sensorless drive system, a real time simulation using a multi- processor computer assembly, based on a floating point digital signal processor network (TMS320C40) has been performed, as shown in Fig. 4 a and b. Fig. 4 a shows the structure with analogic feed-back loop, while Fig. 4b shows the structure which uses the on-line real-time dialogue between the DSP board and the host computer, performed at the beginning and at the end of each sample time. Consequently, the vector-control algorithm, as well as the flux, rotor speed and rotor resistance estimation ones have been implemented on a TMS320C40 based network, using C programming language. At this stage, in order to simulate as close as possible the real working conditions, the model of the induction motor have been implemented on the host computer. Consequently, using a 2 TMS320C40 DSP assembly, the computing time is strongly shorten. In case of TMS320C40 DSP family, the processor intercommunication takes place simultaneous with the tasks execution. The task distribution between the host computer and the DSP network is shown in Fig. 5. In case a) the conversion time (which cannot be neglected in fast applications) is also taken into consideration. In both cases an initial deviation of 0.3Ω between the secondary resistance as parameters for the flux estimator and voltage compensator and the real rotor resistance of the motor (1.47Ω) has been considered. A simple time about 150 microseconds has been used.

Fig. 6 shows the estimated magnitudes when the field-oriented system has been excited with a reversal reference input. It has to be pointed out the influence of the k parameter of the flux observer on the performance of the whole system. In fact k controls the compensation of the flux estimation error, caused by the deviation of the rotor resistance with the temperature [2,3]. This rate could now be minimized (by choosing a small k), because of the estimation of the instantaneous rotor resistance.

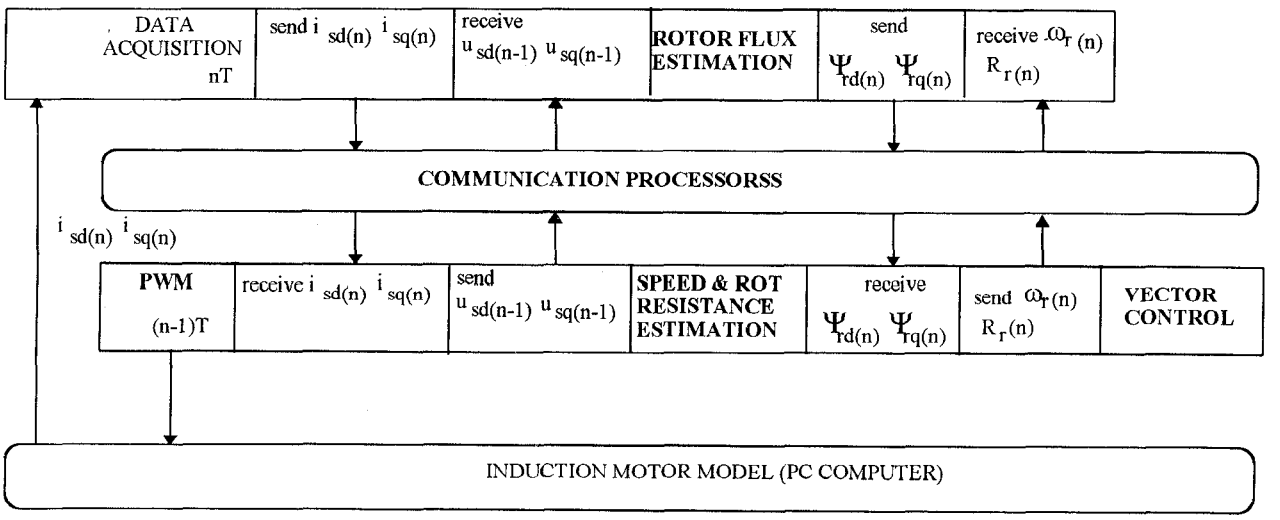

Fig. 5. The real-time simmulation tasks distribution diagram.

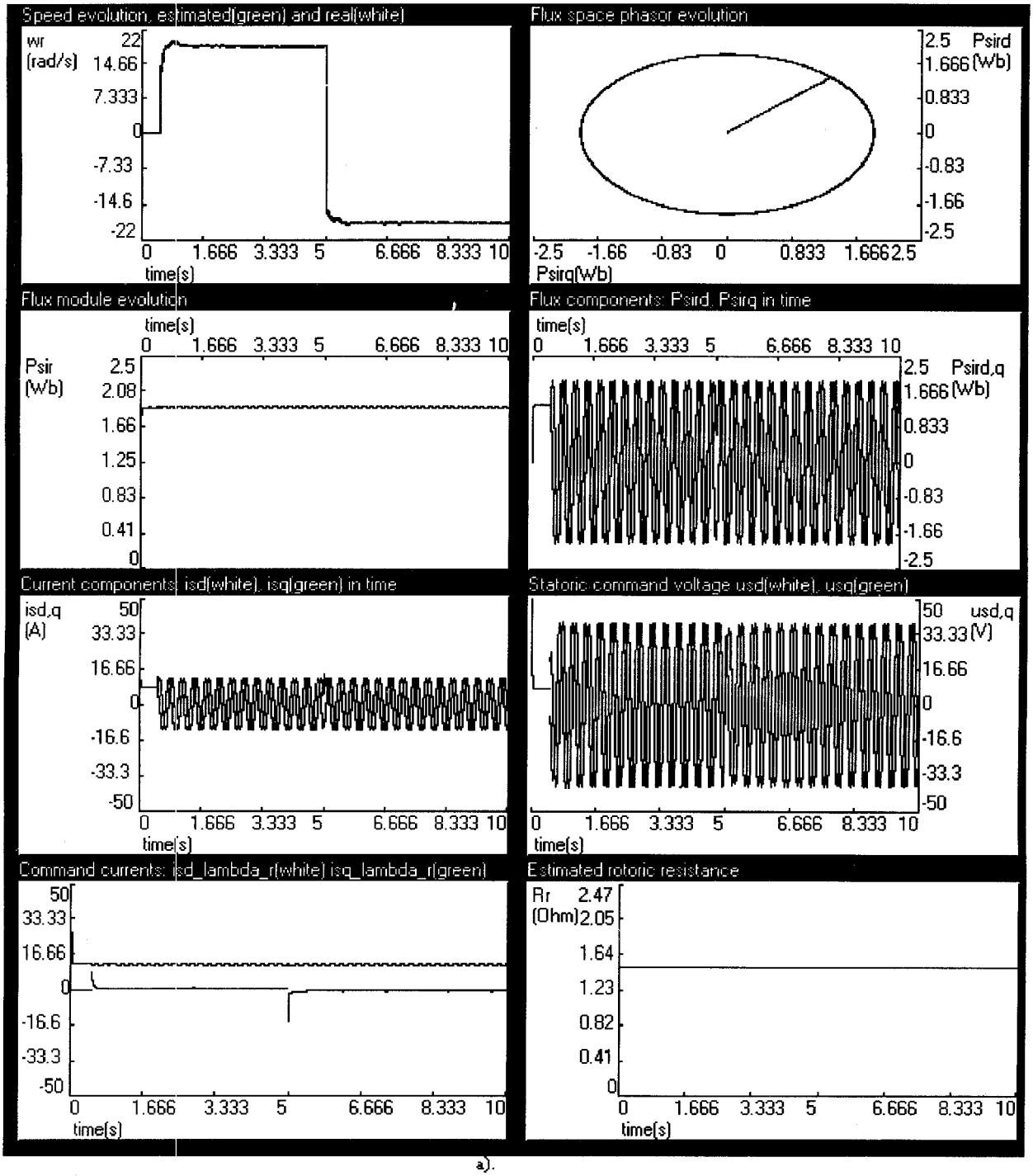

a).

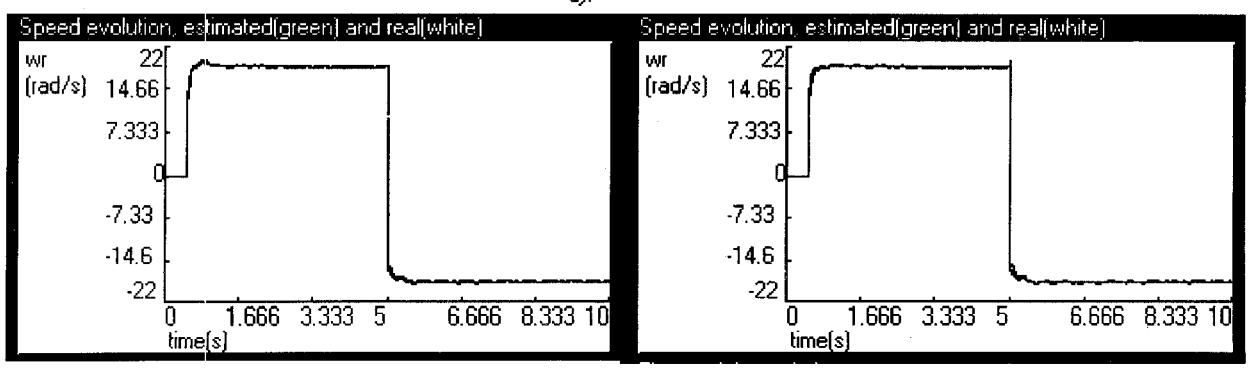

f=5Hz.

b).

f=2Hz.

Fig. 6. Real-time simulation results, using the multi-processor TMS320C4x-PC486 system
a). General results.
b). The influence of the frequency of the superimposed sinusoidal flux reference input on the speed estimation.

VI. CONCLUSIONS

The results which have been obtained using the simultaneous rotor speed estimation and rotor resistance identification encouraged us in further research. It also can be concluded that the only reliable statistical algorithm in order to avoid the division by zero is the fixed trace method. This algorithm assures the best results in both rapid and slow speed variations and also the smallest estimation errors for both rotor speed and resistance.

As Fig. 6 shows, the performances of the drive system are influenced by the amplitude and the frequency of the superimposed sinusoidal component of the rotor flux reference input. This could be subject also for further research.

ACKNOWLEDGMENT

The authors would like to express their acknowledgment to Prof. Yoichi Hori for his guidance and all kinds of wise advice.

REFERENCES

[1] Saroj Biswas, Henry Sendaula, Thomas Caro, "Self Tunning Vector Control for Induction Motors" *Proceedings of IECON'89 Annual Conference of IEEE Industrial Electronics Society, Philadelphia, USA,* 1989, pp. 276-280.

[2] Y. Hori, V. Cotter and Y. Kaya. A Novel, "Induction Machine Flux Observer and its Application to a High Performance AC Drive System" *10th IFAC World Congress, 1987, Pergamon Press* , 1987, pp. 363-368,.

[3] Y. Hori, and T. Umeno, "Robust Flux Observer Based Field Orientation (FOFO) Controller: Its Theoretical Development on the Complex Number System and Implementation Using DSP" *Proceedings of the 11th IFAC World Congress, Tallinn,* 1990, pp. 499-504.

[4] Yoichi. Hori, "Robust and Adaptive Control of a Servomotor using Low Precision Shaft Encoder" *Proceedings of IEEE IECON'93 Conference,, Hawaii,* 1993, pp. 1-6.

[5] T. Kanmachi, I. Takahashi, "Sensor-less Speed Control of An Induction Motor with No Influence of Secondary Resistance Variation" *Proc. of IEEE IAS Annual Meeting,* 1994, pp. 408-413.

[6] Arpad Kelemen and Maria Imecs, "Vector Control of Induction Machines Drives" *OMIKK Publisher, Budapest,* 1992.

[7] Kubota, H., Matsuse, K., and Nakano, T, "DSP-Based Speed Adaptive Flux Observer of Induction Motor" *IEEE Transactions on Industry Applications*, Vol. 29, No.2, pp. 344-348.

[8] Kubota H., Matsuse, K., and Nakano, T, "New Adaptive Flux Observer of Induction Motor for Wide Speed Range Motor Drives" *Conf. Rec.. 1990, IEEE IECON'90,* 1990, pp.921-926.

[9] T. Pana and Y. Hori, "A MATLAB Toolbox for Field-Oriented Induction Motor Systems Design" *Proc. of 1994 Japan USA Symphosium on Flexible Automation, Kobe, Japan,* 1994, pp. 1203-1210.

[10]. T. Pana, Y. Hori, "Simultaneous Speed Estimation and Rotor Flux Identification for Sensorless Induction Motor Drives," *Japan Industry Applications Society Conference, JIASC'94, 1994, Ehimae, Japan,* 1994, pp 135-140.

[11] Teodor Pana, " Model Based Speed and Rotor Resistance Estimation for Sensorless Vector-Controlled Induction Motor Drives Using Floating Point DSP", *Proc. of 1996 4th International Workshop on Advanced Motion Control, Mie, Japan,* 1996, pp. 168-173.

[12] Shinji Shinnaka, "A Unified Analysis on Simultaneous Identification of Velocity and Rotor resistance of Induction Motors" *The Transactions of The Institute of Electrical Engineers of Japan*, Vol 113-D, No.12, 1993, pp.1483-1484.

A Speed-Sensorless IM Drive with Modified Decoupling Control

Somboon Sangwongwanich Surapong Suwankawin
Dept. of Electrical Eng., Chulalongkorn University
Payatai, Bangkok 10330, Thailand
Tel. +662-2186550 Fax. +662-2518991 e-mail : somboona@netserv.chula.ac.th

Abstract The popular speed-sensorless drive of current-controlled type has several disadvantages. It needs current loop of high bandwidth which causes complexity in the implementation hardware/software, and requires a dedicated high speed DSP. The structure of sped-sensorless inverters is also not compatible with the general purpose V/F inverters of volatge type. To overcome such problems, we will develop a new sensorless drive based on decoupling control and an adaptive full-order observer. Our new sensorless drive differs from the existing sensorless drive in the following points : (I) speed estimation is based on rigorous control theory, and is well analyzed, (II) a modified decoupling control is introduced with which the torque control performance is improved, and (III) decoupling control is integrated with the adaptive observer to reduce complexity of the whole system.

1. Introduction

Most of speed-sensorless induction motor (IM) drives, nowadays, have been developed from the basic concept of the conventional vector control, and thus usually work by controlling the stator current with a current-controlled inverter[1][2]. These sensorless drives of current-controlled type have several disadvantages:

I) current loop of high bandwidth is needed, which causes complexity in the implementation hardware/software, and requires a dedicated high speed DSP,
II) their structure is not compatible with the general purpose V/F inverters (voltage-controlled type) which shares the largest market in the industry, and
III) stator voltage sensing is difficult if the hysteresis current control is used.

On the contrary, a sensorless drive based on decoupling control can overcome such problems because

I) it controls the stator voltage generated by a PWM inverter with no current loop,
II) it can be looked as an improved V/F inverter, and
III) the voltage command in the controller can be used instead of detecting the real voltage.

In this paper, we will develop a new sensorless drive based on decoupling control and an adaptive full-order observer. Our new sensorless drive differs from the existing sensorless drive [3] in the following points :

- speed estimation is based on rigorous control theory, and is well analyzed,
- a modified decoupling control is introduced with which the torque control performance is improved, and
- decoupling control is integrated with the adaptive observer to reduce complexity of the whole system.

In the following, we will first derive the modified decoupling control, and then explain about the speed and flux estimation with a full-order observer. A simple guideline for the proposed decoupling control will also be discussed. Finally, simulation and experimental results will be given to confirm our theoretical conclusion.

2. Decoupling Control with Stator Voltage

Firstly, we will breifly show the model of an induction motor expressed both on stator frame and rotor flux frame. These models will in the sequel be used to derive the new decoupling control and the adaptive full-order observer.

2.1 Model of IM on d-q axis of stator frame

The dynamic model of IM viewed from stator frame is given by equations (1) and (2).

$$\frac{d\vec{i}_s}{dt} = A11\vec{i}_s + A12\vec{i}_o + B1\vec{v}_s \tag{1}$$

$$\frac{d\vec{i}_o}{dt} = A21\vec{i}_s + A22\vec{i}_o \tag{2}$$

where in

$$A_{11} = -\left(R_s + R_r M^2 / L_r^2\right) / \sigma L_s \bullet I$$

$$A_{12} = -A_{22} * M^2 / \sigma L_s L_r \qquad B_1 = 1/\sigma L_s$$

$$A_{21} = (R_r / L_r) \bullet I \quad A_{22} = -(R_r / L_r) \bullet I + p\omega_m \bullet J$$

$$I = \begin{bmatrix} 1 & 0 \\ 0 & 1 \end{bmatrix} \quad J = \begin{bmatrix} 0 & 1 \\ -1 & 0 \end{bmatrix}, \quad \sigma = 1 - M^2 / LsLr$$

$\vec{v}_s$: stator voltage vector $\vec{i}_s$: stator current vector
$\vec{i}_o$: rotor flux magnetizing current vector
R_s: stator resistance R_r: rotor resistance
L_s: stator self-inductance L_r: rotor self-inductance
M: mutual inductance, $\omega_m = d\theta_m / dt$: rotor speed
p : numbers of pole pairs

2.1 Model of IM on d-q axis of rotor flux frame

As our aim is to control flux and torque of the motor, it is, therefore, more convenient to transform the

above IM's model onto the rotor flux frame, and we obtain the following model:

Stator dynamic :

$$R_s i_{sd} + \sigma L_s \frac{d i_{sd}}{dt} = \omega \sigma L_s i_{sq} - \frac{M^2}{L_r^2} R_r (i_{sd} - i_o) + v_{sd} \tag{3}$$

$$R_s i_{sq} + \sigma L_s \frac{d i_{sq}}{dt} = -\omega L_s i_{sd} + \frac{M^2}{L_r} \omega (i_{sd} - i_o) + v_{sq} \tag{4}$$

Rotor dynamic :

$$R_r i_o + L_r \frac{d i_o}{dt} = R_r i_{sd} \tag{5}$$

$$\frac{d\theta}{dt} = \omega = p\omega_m + \omega_s = p\omega_m + R_r i_{sq} / L_r i_o \tag{6}$$

$$\vec{i}_s = \begin{bmatrix} i_{sd} \\ i_{sq} \end{bmatrix} \quad \vec{v}_s = \begin{bmatrix} v_{sd} \\ v_{sq} \end{bmatrix} \quad \vec{i}_o = \begin{bmatrix} i_o \\ 0 \end{bmatrix} \tag{7}$$

where i_{sd}, i_{sq}, v_{sd}, v_{sq} are the d and q components of the stator current and voltage, and i_o is the rotor flux magnetizing current.

2.3 Conventional decoupling control

Decouling control for IM has been previously introduced in [4], [5], using the following relations:

$$v_{sd} = u_{sd} - \omega \sigma L_s i_{sq}^* \qquad (u_{sd}=Rs\, i_{sd}^*) \tag{8}$$

$$v_{sq} = u_{sq} + \omega L_s i_{sd}^* \qquad (u_{sq}=Rs\, i_{sq}^*) \tag{9}$$

where '*' denotes the commanded value. What the decoupling control does is just compensating the induced voltage coupling across the d-q axes. However, this conventional decouling control ignores the stator dynamic, and thus is imperfect. To acheive a complete decoupling stator dynamic we have to use the following compensating voltage instead:

$$v_{sq} = u_{sq} + \hat{\omega} L_s \hat{i}_{sd} - \frac{M^2}{L_r} \hat{\omega} (\hat{i}_{sd} - \hat{i}_o) \tag{10}$$

$$v_{sd} = u_{sd} - \hat{\omega} \sigma L_s \hat{i}_{sq} + \frac{M^2}{L_r^2} R_r (\hat{i}_{sd} - \hat{i}_o) \tag{11}$$

where '^' denotes the estimated value. With the above decoupling control (10) and (11), the decoupled stator dynamic becomes :

$$R_s i_{sd} + \sigma L_s \frac{d i_{sd}}{dt} = u_{sd} \tag{12}$$

$$R_s i_{sq} + \sigma L_s \frac{d i_{sq}}{dt} = u_{sq} \tag{13}$$

which is very simple. It should be noted that the decoupling control does not change the rotor dynamic. As such, the decoupling voltage can be calculated from the rotor quatities $(\hat{\omega}, \hat{i}_0)$ estimated from equations (5) and (6) together with the estimated current $(\hat{i}_{sd}, \hat{i}_{sq})$ calculated from the decouple dynamic (12) and (13).

2.4 Modified decoupling control

However, in reality, the estimated current and flux always contain some errors which may be caused by speed estimation error during a transient response or by parameter variations. The aforementioned decoupling control is purely feed forward and cannot be expected to handle this kind of errors. Therefore, it is natural to modify the decoupling control voltage by adding a feedback term Ke as :

$$v_{sd} = u_{sd} - \omega \sigma L_s \hat{i}_{sq} + \frac{M^2}{L_r^2} R_r (\hat{i}_{sd} - \hat{i}_o) + [Ke]_d \tag{14}$$

$$v_{sq} = u_{sq} + \omega L_s \hat{i}_{sd} - \frac{M^2}{L_r} \omega (\hat{i}_{sd} - \hat{i}_o) + [Ke]_q \tag{15}$$

wherein the current error $e = \hat{\vec{i}}_s - \vec{i}_s$. It will be shown in later section how to select a suitable feedback gain K to overcome the effect of speed estimation error during transient. We can conclude that the main features of the modified decoupling control are that :

- complete decoupling flux/torque current control is achieved even during transient,
- stator dynamic is simple, and
- current error feedback can suppress speed/parameter error.

3. Speed and Flux Estimation

To implement the decoupling control according to equations (14) and (15), we need to know the rotor quatities including the rotor speed. In the conventional decoupling control, this information is obtained from the IM's decoupled model as given by equations (5), (6), (12) and (13). In this paper, we will use an adaptive full-order observer instead of the model to estimate the required information. The reason is that with the observer we can improve the stability and sensitivity of the estimation.

3.1 Adaptive full-order observer on stator frame

From the linear model (1) and (2), we can build an adaptive observer as shown in equations (16) - (18) [2], [6]-[8] .

$$\frac{d\hat{\vec{i}}_s}{dt} = A_{11} \hat{\vec{i}}_s + \hat{A}_{21} \hat{\vec{i}}_o + B_1 \vec{v}_s - H_1' (\hat{\vec{i}}_s - \vec{i}_s) \tag{16}$$

$$\frac{d\hat{i}_o}{dt} = A_{21} \hat{\vec{i}}_s + \hat{A}_{22} \hat{\vec{i}}_o - [H_2' / M] * (\hat{\vec{i}}_s - \vec{i}_s) \tag{17}$$

$$A_{12} = -\hat{A}_{22} * M^2 / \sigma L_s L_r$$

$$\hat{A}_{22} = -\left(R_r / L_r\right) \bullet I + p\hat{\omega}_m \bullet J$$

$$\hat{\omega}_m = (k_p + k_I \int dt)\, w^T e \qquad k_p, k_I > 0 \tag{18}$$

$$w = J pM \hat{i}_o \quad e = \hat{i}_s - i_s$$

where H_1' and H_2' are the feedback gains of the observer. The rotor speed is estimated through the adaptive PI gain (k_p, k_I) by projecting the current error onto the q-axis of the estimated rotor flux frame.

3.2 Adaptive full-order observer on rotor flux frame

In order to merge the observer with the decoupling control on the rotor flux frame, we will, therefore, express the adaptive observer on the rotor flux frame as:

$$R_s \hat{i}_{sd} + \sigma L_s \frac{d\hat{i}_{sd}}{dt} = \omega\sigma L_s \hat{i}_{sq} - \frac{M^2}{L_r^2} R_r (\hat{i}_{sd} - \hat{i}_o) + v_{sd} - \sigma L_s [H_1' e]_d \tag{19}$$

$$R_s \hat{i}_{sq} + \sigma L_s \frac{d\hat{i}_{sq}}{dt} = -\omega L_s \hat{i}_{sd} + \frac{M^2}{L_r} \omega (\hat{i}_{sd} - \hat{i}_o) + v_{sq} - \frac{M}{L_r} [H_2' e]_q - \sigma L_s [H_1' e]_q \tag{20}$$

$$R_r \hat{i}_o + L_r \frac{d\hat{i}_o}{dt} = R_r (\hat{i}_{sd} - \frac{L_r}{R_r M} [H_2' e]_d) \tag{21}$$

$$\frac{d\theta}{dt} = \omega = p\hat{\omega}_m + \omega_s = p\hat{\omega}_m + \frac{R_r}{L_r} (\hat{i}_{sq} - \frac{L_r}{R_r M} [H_2' e]_q) / \hat{i}_o \tag{22}$$

$$\hat{\omega}_m = (k_p + k_I \int dt)\, [\hat{i}_{sq} - i_{sq}] * pM\hat{i}_o \tag{23}$$

where $[]_d$, $[]_q$ denote the d and q components, respectively. It should be noted that the rotor speed is estimated through the torque current error similar to the method in [3]. Main features of this adaptive observer are that:

- estimation characteristics can be rigorously analyzed via linear control theory[6]-[9], and
- since it uses the same model as that of the decoupling control, that same model can be shared by both.

4. Integration of decoupling control and adaptive observer

Now we are going to merge the decoupling control with the adaptive observer. Firstly, when the adaptive observer is used together with the modified decoupling control, the resultant stator dynamic of the observer is found to be :

$$R_s \hat{i}_{sd} + \sigma L_s \frac{d\hat{i}_{sd}}{dt} = u_{sd} + [Ke]_d - \sigma L_s [H_1' e]_d \tag{24}$$

$$R_s \hat{i}_{sq} + \sigma L_s \frac{d\hat{i}_{sq}}{dt} = u_{sq} + [Ke]_q - \sigma L_s [H_1' e]_q - \frac{M^2}{L_r} [H_2' e]_q \tag{25}$$

The rotor flux dynamic is unchanged, and is still given by equations (21) and (22). Based on the relations (14), (15) of decoupling control, the resultant dynamics (equations (21), (22), (24), and (25)), and speed estimator (23), we can integrate the decoupling control together with the adaptive observer as shown in Fig. 1.

5. Selection of Feedback Gain K

Even though the speed estimator can track any constant real rotor speed without steady-state error, it do exhibits a transient estimation error against the ramp response of speed during acceleration/deceleration. For simplicity we will assume that

$$H_1' = h_1' * I, \quad H_2' = h_3' * I, \quad , K = k * I \tag{26}$$

and consider that the speed estimation error during transient is approximately a step function. From the estimation error system shown in Fig. 2, this transient error can be then calculated as :

$$\Delta\omega_m = \omega_m - \hat{\omega}_m = \lim_{s\to 0} s \times \frac{R}{s^2} \times \frac{1}{1 + (-C^2)\, G_{22}'(s)\, (K_P + K_I / s)} = \frac{R}{-C^2\, G_{22}'(s)\big|_{s=0}\, K_I} \tag{27}$$

where $G_{22}'(s)\big|_{s=0} \approx \frac{-1}{Rr * Ls / M - h_3'}$, $C = pM\hat{i}_o$ (28)

and R is the acceleration/deceleration rate (see [9] for detail derivation). This error can be suppressed by using a large K_I gain, but there is a limit. This transient speed error will disturb the decoupling control beause the decoupling voltage compensation will be then incorrect, especially the q-axis back e.m.f. which depends mainly on the estimated flux frequency or the estimated rotor speed. As a consequence, the torque current and motor torque will not follow the command as is expected. The amplitude of rotor flux is, however, quite insensitve to this error because of its slow response. Simulation result shown in Fig. 3 clearly indicates this phenomena. The generated torque during acceleration/deceleration is lowered by nearly 20%. To improve the torque control capability, we must know how current error feedback affects the estimated flux frequency which is the most important factor. From the block diagram shown in Fig. 2, it can be

derived that the torque current error caused by the speed estimation error is given by :

$$[e]_q = \hat{i}_{sq} - i_{sq} = -pM\hat{i}_o * G'_{22}(s)\Big|_{s=0} * \Delta\omega_m \approx \frac{pM\hat{i}_o}{Rr * Ls/M - h_3'} * \Delta\omega_m \quad (29)$$

which means that the torque current error depends roughly on the feedback gain h'_3 (H_2') only. Next we have to consider how the torque current command is compensated by the feedback gains H_1', H_2' and K. Since the decoupled stator dynamic is very fast, it can be neglected for simplicity. From the block diagram in Fig. 1, we can see that

$$\hat{i}_{sq} = i_{sq} * + \frac{1}{Rs}[Ke]_q - \frac{M}{Lr * Rs}[H_2' e]_q - \frac{\sigma L_s}{Rs}[H_1' e]_q \quad (30)$$

In addition to the above compensating terms (the last three terms), the slip equation in the rotor flux dynamic also contains the compensating term of $\frac{Lr}{M * Rr}[H_2' e]_q$. As a result, the net compensating frequency for the flux frequency will be given by :

$$\omega_c = (Rr / Lr\, i_o) * \{\frac{1}{Rs}[Ke]_q - \frac{M}{Lr * Rs}[1 + \frac{M^2 Rs}{Lr^2 * Rr}][H_2' e]_q - \frac{\sigma L_s}{Rs}[H_1' e]_q\} \quad (31)$$

For the decoupling voltage to be correct, it is necessary that

$$\omega_c = p\Delta\omega_m \quad (32)$$

By substituing the relations (26), (29) and (31) into equation (32), the necessary condition for complete compensation of flux frequency becomes

$$\{\frac{k}{Rs} - \frac{M}{LrRs}[1 + \frac{M^2 Rs}{Lr^2 Rr}]h_3' - \frac{\sigma L_s}{Rs}h_1'\} * \frac{Rr * M / Lr}{Rr * Ls/M - h_3'} = 1 \quad (33)$$

This is the condition which is important in design. Normally, we have to design the feedback gains H_1', H_2' so as to stabilize the speed estimation, especially in the low speed region with regenerative loads [9]. Therefore, to achieve a good decoupling control we must select the feedback gain K to satisfy the relation (33). We will verify this conclusion by simulation carried out under the same condition as that of Fig. 3, but with error feedback.

CASE I : $H_1' = H_2' = 0, K = Rs * I$

Using these gains, the flux frequency will be almost completely compensated. And from the simulation result shown in Fig. 4, it is clearly seen that the generated torque follows the torque command very well compared to that in Fig. 3. We can also see that the speed estimation error characteristic, which is governed by the feedback gain of the observer, remains unchanged. This means that we can improve the torque control performance independently with the speed estimation characteristic.

CASE II: $H_1' = 0, H_2' = -0.25Rs * I, K = 0.84Rs * I$

In this case, by using the observer gain H_2' , we slow down the estimation response to improve the stability as can be seen from the increasing of speed error during transient in Fig. 5. However, we still have a good torque control performance owing to the feedback gain K.

6. Implementation and Experimental Results

The new decoupling control sensorless drive is implemented using a RISC microcontroller SH7032 as shown in Fig. 6. The timing diagram of the software module is given in Fig. 7. The sampling time is fixed at 500μsec. The stator voltage command is used instead of the real one, and the effect of dead time is also compensated. The stator current is detected synchronously at the beginning of each period of the space-vector PWM pattern. Experimental result at speed reversal from 1420 to -1420 rpm is shown in Fig. 8, and it can be seen that the performance of the decoupling sensorless drive is comparable to that of the vector control with sensor.

7. Conclusion

In this paper, we have proposed a new sensorless drive based on a modified decoupling control. The complexity of the whole system is minimized by integrating harmonously the decoupling control with the adaptive observer. The current error feedback in modified decoupling control improves the torque control characteristic if its feedback gain is appropriately designed. Owing to its simple structure, the proposed sensorless drive can be implemented easily, and its feasibility is also shown by simulation and experiment.

Appendix

Motor's parameters:

Rs = 1.84 [Ohm], Rr = 0.885 [Ohm]
Ls = 131 [mH], Lr = M = 120 [mH], p=2

References

[1] J. Holtz, Speed Estimation and Sensorless Control of AC Drives, Proc. of IEEE/IECON'93, 1993, pp. 649-654.

[2] H. Kubota et al., Direct Field Oriented Control of Induction Motor Without Speed-Sensor, Trans. of IEE Japan, Vol. 111-D, No. 11, 1991, pp. 954-960.

[3] T. Okuyama et al., Vector Control Scheme of Induction Motor Without Speed and Voltage Sensors, Trans. of IEE Japan, Vol. 107-D, No. 2, 1987, pp. 191-198.

[4] K. Ohnishi et. al., Decoupling Control of Secondary Flux and Secondary Current in Induction Motor Drive With Controlled Voltage Source and Its Comparison

With Volts/Hertz Control, IEEE Trans. on Ind. Appl., Vol. IA-21, No. 1, 1985, pp. 241-247.

[5] F. Harashima et al., Multimicroprocessor-Based Control System for Quick Response Induction Motor Drive, IEEE Trans. on Ind. Appl., Vol. IA-2, No. 4, 1985, pp. 602-609.

[6] S. Sangwongwanich, Speed-Sensorless Vector Control of Induction Motors - Stability Analysis and Realization-, Proc. of IPEC-Yokohama, Vol. 1, 1995, pp. 310-315.

[7] S. Suwankawin, and S. Sangwongwanich, Stability Analysis of Speed-Sensorless Vector Control System, Proc. of ICPE, Korea, 1995, pp. 403-408.

[8] S. Sangwongwanich, Speed-Sensorless Induction Motor Drive Systems- Structure and Stability-, Proc. of PEMC'96, Hungary, 1996, pp. 78-85.

[9] S. Suwankawin, and S. Sangwongwanich, Stability Anaysis and Design Guidelines for A Speed-Sensorless Induction Motor Drive, PCC-Nagaoka, 1997, (to be appeared).

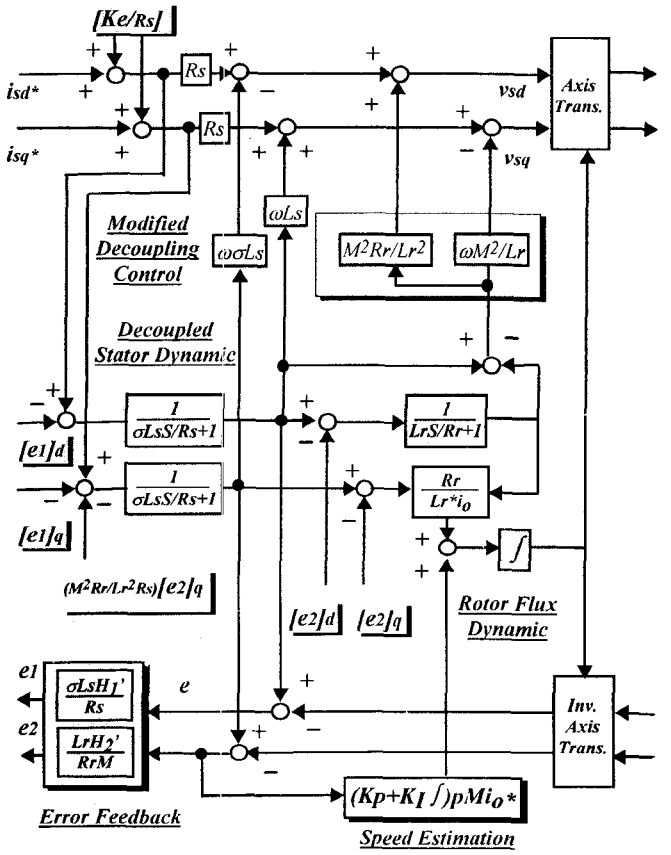

Fig. 1 Block diagram of sensorless drive with modified decoupling control

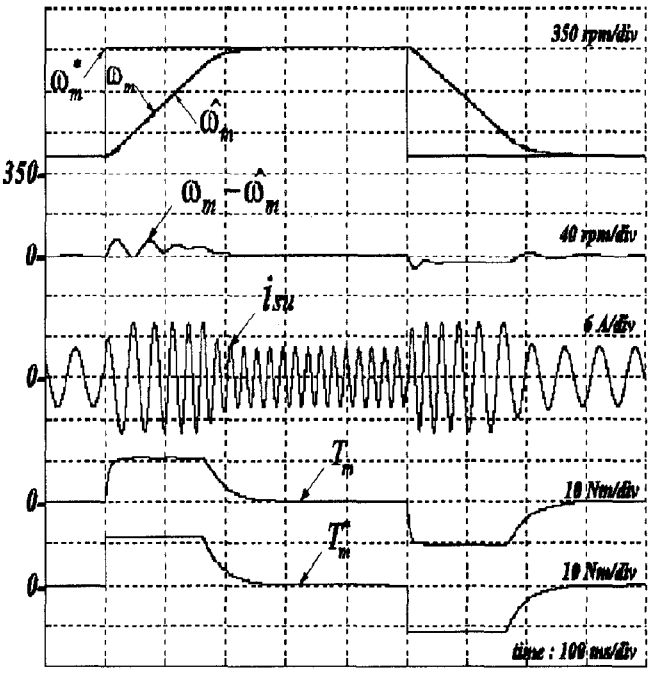

Fig. 3 Simulation result at acceleration/deceleration (no feedback)

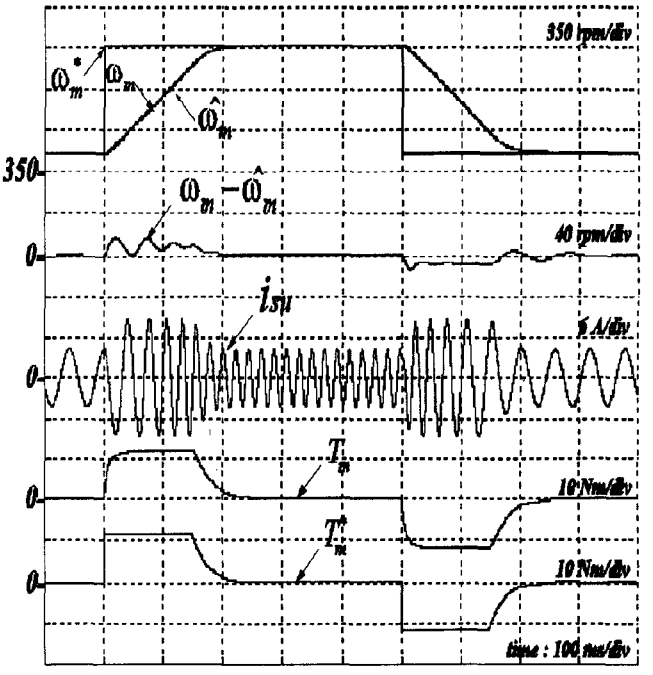

Fig. 4 Simulation result with modified decoupling control (I) (observer with no feedback)

$$H_1' = H_2' = 0, K = Rs * I$$

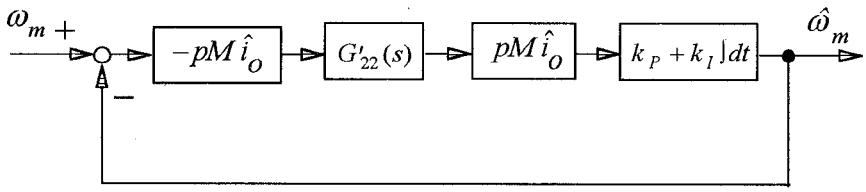

Fig. 2 Estimation error in adaptive observer

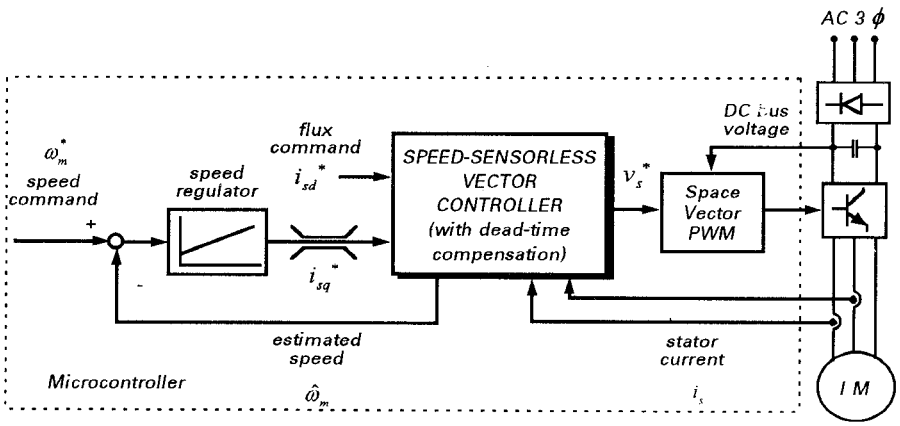

Fig. 6 Block diagram of experimental setup

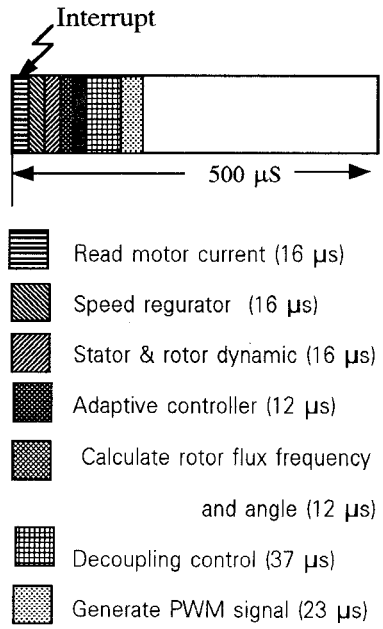

Fig. 7 Timing diagram of software module

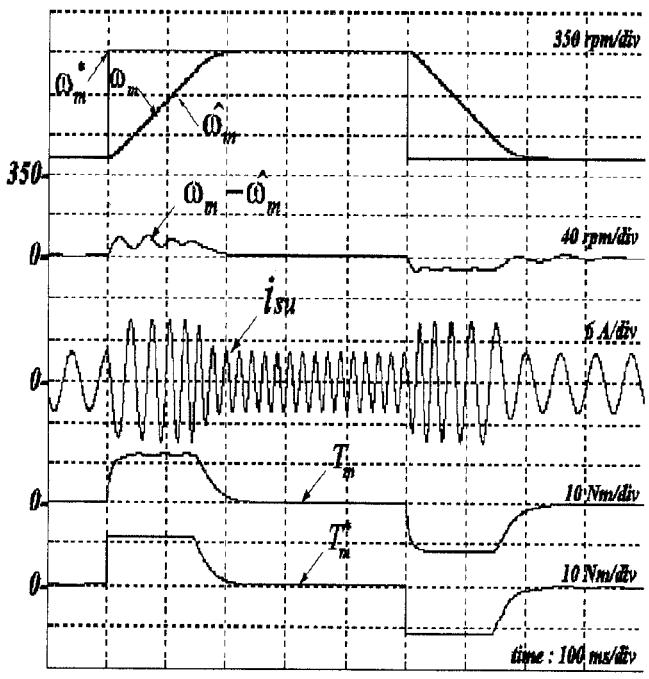

Fig. 5 Simulation result with modified decoupling control (II) (observer with feedback)

$$H_1' = 0, H_2' = -0.25Rs * I, K = 0.84Rs * I$$

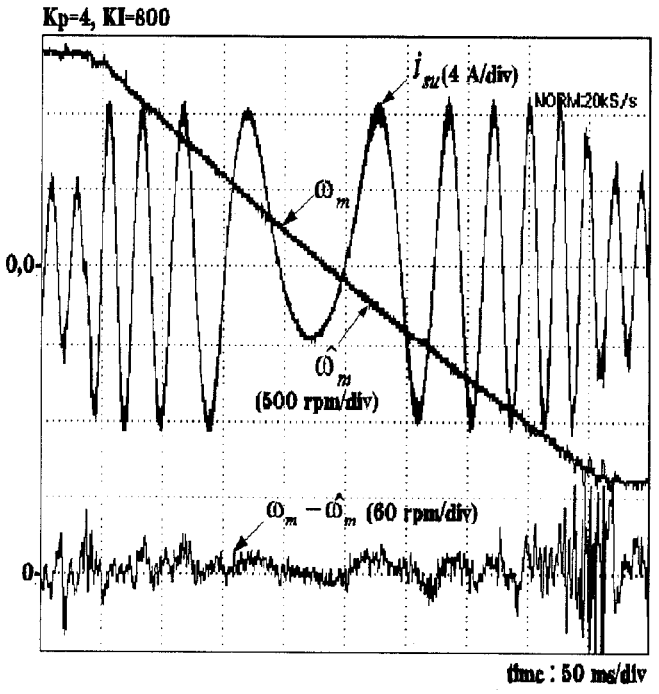

Fig. 8 Experimental result at speed reversal

Sensorless Speed Control of an Induction Motor with No Influence of Resistance Variation

Toshiyuki Kanmachi

Sendai National College of Technology
1, Kitahara, Aoba-ku, Sendai 989-31, JAPAN
Phone: +81-22-392-4761
Fax: +81-22-392-3359
E-mail: kanmachi@cc.sendai-ct.ac.jp

Isao Takahashi

Nagaoka University of Technology
1603-1, Kamitomioka, Nagaoka, 940-21, JAPAN
Phone: +81-258-47-9515
Fax: +81-258-47-9500
E-mail: taki@voscc.nagaokaut.ac.jp

Abstract — **Many speed sensorless vector control systems of induction motors have been developed. However, the speed control characteristics are affected by machine temperature variations, because these methods use the primary and the secondary resistance value to estimate the rotor speed.**

This paper describes method of the primary and the secondary resistance estimation for speed sensorless control systems. The primary resistance estimation uses the secondary flux which is calculated by the instantaneous reactive power. On the other hands, the secondary resistance is directly calculated by the line voltage and the current without speed sensors. This method makes possible on the PWM inverter fed induction motor. By combining these two methods, the speed control characteristic is robust to the machine temperature variations. The feasibility of these methods was verified by some simulation and experimental results. In the tested system, the compensation of the primary and the secondary resistance mismatching is achieved.

I. INTRODUCTION

The speed sensorless vector control systems of an induction motor have been developed and applied in the industrial drives.[1][2][3] These systems, which have economic advantage and high performance, are required in several applications. However, there are two problems in the performance of the speed sensorless vector control systems. First, the estimation of the primary and the secondary flux are difficult in the low speed region.[4] The performance of the torque and the speed are affected by this problem. The second, the accuracy of speed control is influenced by mismatched motor parameters, used in the speed estimation, the primary and the secondary resistance.[5]

Some identification methods of the secondary resistance without speed sensors have been proposed.[6][7] In these methods based on the adaptive identification system, the secondary resistance in the controller can be converged to the correct value with long time constant. We already had proposed a directly identification method of the secondary resistance.[8][9] In this method, the secondary resistance is calculated quickly by only using the instantaneous terminal voltage and the line current without speed sensors.

On the other hand, the sensorless vector control system with no influence of the primary resistance had been proposed.[10] In this system, the rotor speed is estimated by using the reactive power, and it is robust to the primary resistance.

In this paper, the primary resistance identification method using the reactive power is proposed.[11] This method can be applied to existing speed sensorless control system. Additionally, by combining to the above secondary resistance calculation method, the sensorless speed control system will be free from the machine temperature variations.

II. PRIMARY RESISTANCE IDENTIFICATION

Fig.1 illustrates the equivalent circuit of an induction motor. Base on this circuit, the characteristics equations are expressed as (1).

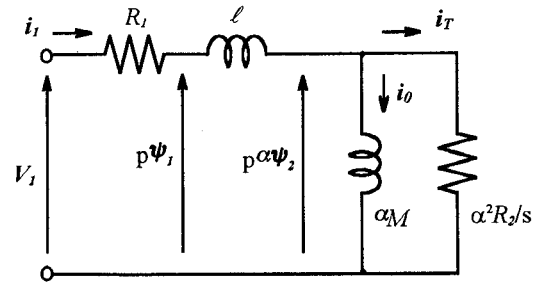

Fig.1. Equivalent circuit of induction motor.

$$\begin{bmatrix} v_{1d} \\ v_{2d} \\ 0 \\ 0 \end{bmatrix} = \begin{bmatrix} R_1+\mathrm{p}\ell & 0 & \mathrm{p}\alpha & 0 \\ 0 & R_1+\mathrm{p}\ell & 0 & \mathrm{p}\alpha \\ -\alpha R_2 & 0 & \mathrm{p}+R_2/L_2 & \omega_m \\ 0 & -\alpha R_2 & -\omega_m & p+R_2/L_2 \end{bmatrix} \begin{bmatrix} i_{1d} \\ i_{1q} \\ \psi_{2d} \\ \psi_{2q} \end{bmatrix} \quad (1)$$

where R_1 and R_2 are the primary and the secondary resistance; L_1 and L_2 are the primary and the secondary self-inductance; M is the mutual inductance; ω_m is the rotor speed; p represents d/dt; α is equal to M/L_2; ℓ is equal to $L_1-\alpha M$. The secondary flux $\alpha\psi_{2d}$, $\alpha\psi_{2q}$ are obtained to solve the first and the second lows of (1) as

$$\alpha\psi_{2d} = \int (v_{1d} - R_1 i_{1d})\,\mathrm{dt} - \ell i_{1d} = \psi_{1d} - \ell i_{1d}$$

$$\alpha\psi_{2q} = \int (v_{1q} - R_1 i_{1q})\,\mathrm{dt} - \ell i_{1q} = \psi_{1q} - \ell i_{1q}. \quad (2)$$

$$|\alpha\boldsymbol{\psi}_2|^2 = (\alpha\psi_{2d})^2 + (\alpha\psi_{2q})^2. \quad (3)$$

These equations mean that the secondary flux can be directly calculated from the primary voltage and the primary current with considering of the voltage drop at R_1 and the leakage flux. The accuracy of these equations are affected by R_1 variations.

On the other hand, the reactive power q, which is calculated by (4), means the energy on the mutual inductance and the leakage inductance.

$$q = i_{1d} v_{1q} - i_{1q} v_{1d}. \quad (4)$$

The exciting current of the secondary flux I_0 is calculated using q as

$$I_0 = \sqrt{q/(\omega_0 \alpha M) - \ell I_1^2/(\alpha M)} \quad (5)$$

where ω_0 is the angular speed of the secondary flux vector. On the steady state, ω_0 approximates to the angular speed of the primary current ω_1, therefore the amplitude of the secondary flux is estimated as follows;

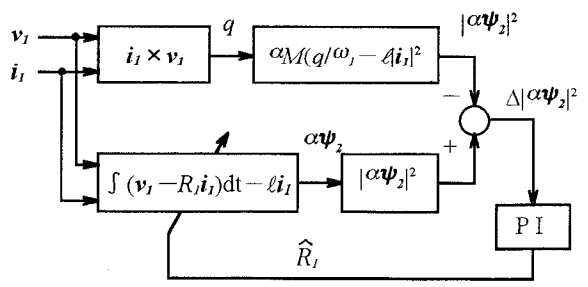

Fig.2. Adaptive identification system of primary resistance.

$$|\alpha\boldsymbol{\psi}_2|^2 = \alpha M(q/\omega_1 - \ell I_1^2). \quad (6)$$

Since (6) does not involve R_1, the accuracy is robust to R_1 variation.

Fig.2 illustrates the adaptive identification algorithm of $\hat{R}_1$, where (6) is the reference model and (3) is the adjustable model. The error between the secondary flux of these model is used to drive the PI adaption mechanism which generates $\hat{R}_1$ for the adjustable model.

Fig.3 shows the simulation results of the proposed identification method. The nominal value of the primary resistance is equal to 0.53(Ω), and the initial value of $\hat{R}_1$ in the adjustable model is 50(%) of the nominal value. The secondary flux of (3) converges to the value of (6) within 2 (sec). The primary resistance adjustment from the initial value to the correct one is verified from fig.3.

Fig.4 shows $\hat{R}_1$ identification errors of the proposed method with the mismatching of the mutual inductance αM. The accuracy of the secondary flux calculation of (6) is affected directly by αM mismatching. Therefore, the mismatch of αM will be a serious problem for this method.

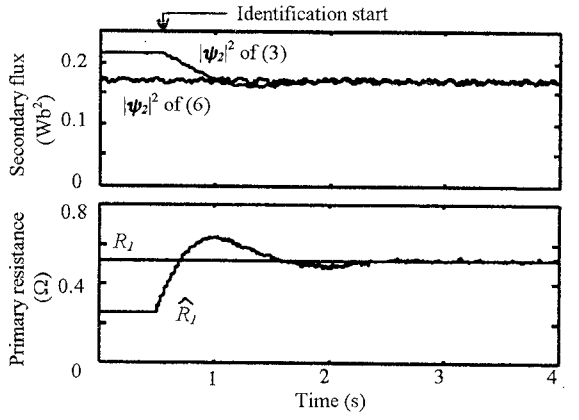

Fig.3. Simulation result of primary resistance identification.

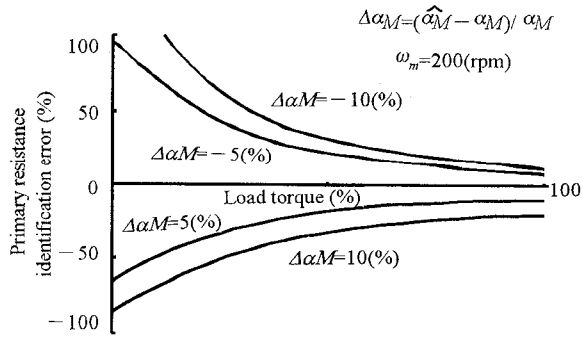

Fig.4. Primary resistance identification error for mutual inductance mismatching.

As can be seen in Fig.4, the minimum $\hat{R}_1$ identification error at the rated load is $\pm$ 17(%) with $\pm$ 10(%) mismatching of αM.

Fig.5. shows the identification errors of $\hat{R}_1$ with mismatched the leakage inductance ℓ. The leakage flux is enough smaller than the secondary flux. Then, the influence of the leakage inductance mismatching to the proposed method can be ignored. The maximum identification error at rated load is $\pm$1.4(%) for $\pm$10(%) mismatching of ℓ.

III. SECONDARY RESISTANCE ESTIMATION

Solving respectively the third and the fourth low of (1), the secondary resistance is obtained as (7).

$$\hat{R}_2 = (\mathrm{p}\psi_{2d}L_2 + \omega_m\psi_{2q}L_2) / (Mi_{1d} - \psi_{2d})$$
$$\hat{R}_2 = (\mathrm{p}\psi_{2q}L_2 - \omega_m\psi_{2d}L_2) / (Mi_{1q} - \psi_{2q}) \qquad (7)$$

These equations demand the value of the rotor speed ω_m which is not able to detect on the speed sensorless drives. Therefore, we can not calculate these equations independently. By considering (7) are simultaneous equations, the secondary resistance can be calculated as (8) to eliminate ω_m;

$$\hat{R}_2 = \frac{-\alpha\psi_{2d}\,\mathrm{p}\alpha\psi_{2q} - \alpha\psi_{2q}\,\mathrm{p}\alpha\psi_{2d}}{(\alpha\psi_{2d} - \alpha Mi_{1d})\alpha\psi_{2d} + (\alpha\psi_{2q} - \alpha Mi_{1q})\alpha\psi_{2q}} L_2$$
$$= \frac{-\boldsymbol{\psi}_2 \cdot \mathrm{p}\boldsymbol{\psi}_2}{(\boldsymbol{\psi}_2 - Mi_1)\cdot\boldsymbol{\psi}_2} L_2 = -\frac{1}{2}\frac{\mathrm{p}(|\boldsymbol{\psi}_2|^2)}{i_2\cdot\boldsymbol{\psi}_2}. \qquad (8)$$

This equation means that the secondary resistance is calculated by the inner product of $\alpha\boldsymbol{\psi}_2$, $\boldsymbol{i}_2$ and dividing $\mathrm{p}(|\alpha\boldsymbol{\psi}_2|^2)$ by $\boldsymbol{i}_2\,\boldsymbol{\psi}_2$.

When the secondary flux is represented by the amplitude $|\boldsymbol{\psi}_2|$ and the phase angle θ_2 as (9), the differential vector of the secondary flux $\mathrm{p}\boldsymbol{\psi}_2$ is calculated as (10).

$$\boldsymbol{\psi}_2 = |\boldsymbol{\psi}_2| \exp(\mathrm{j}\theta_2) \qquad (9)$$
$$\mathrm{p}\boldsymbol{\psi}_2 = \mathrm{j}(\mathrm{p}\theta_2)\,|\boldsymbol{\psi}_2| \exp(\mathrm{j}\theta_2) + \mathrm{p}|\boldsymbol{\psi}_2| \exp(\mathrm{j}\theta_2) \qquad (10)$$

If the secondary flux has no ripples, the second term of (10) is equal to zero, and the phase angle between the vectors $\boldsymbol{\psi}_2$ and $\mathrm{p}\boldsymbol{\psi}_2$ becomes to $\pi/2$. Therefore, the numerator of (8) goes to zero. Additionally, the denominator of (8) which is expressed by the differential value of the secondary flux amplitude is equal to zero. Then, it is impossible to calculate the secondary resistance. However, the PWM inverter makes the flux ripples and assures the possibility of the $\hat{R}_2$ calculation.

Fig.6 shows the simulation results of the secondary resistance estimation. The induction motor, R_2 is equal to 1(Ω), is fed by the PWM inverter and the rotor speed is kept at 1500(rpm) under rated load. It illustrates that the numerator and the denominator are not always equal to zero and the R_2 estimation is possible. However, there are momentary zero cross points in the denominator and the numerator which makes impossible to divide. Therefore, the estimation of R_2 must be avoided near these zero cross points.

Fig.7 illustrated the R_2 estimation block diagram. It can calculate R_2 directly and instantly from the instantaneous primary voltage and current. However, when the value of denominator is small at neighboring the zero cross points, there is possibility that the calculation error of division become increase. The calculated R_2 is averaged by a LPF to suppress the calculation error at neighboring zero cross

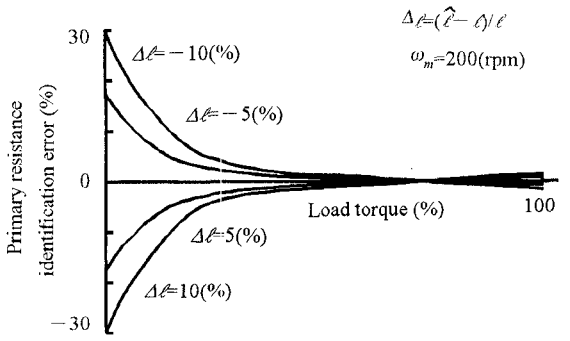

Fig.5. Primary resistance identification error for leakage inductance mismatching.

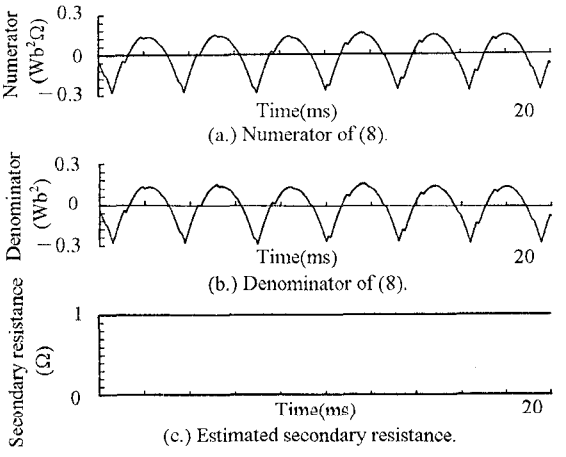

Fig.6. Simulation results of secondary resistance estimation.

points. The time constant of the LPF, which removes the ripple frequency components, is enough shorter than the time constant of R_2 variation. Therefore, the influence of the LPF to $\hat{R}_2$ estimation's dynamics is small, and the rotor speed estimation is almost not affected.

Fig.8 shows the $\hat{R}_2$ estimation errors with the mismatching of αM. The mismatching of αM makes error in the secondary current calculation of (8). However, the numerator of (8) is not affected by αM mismatching, then the $\hat{R}_2$ estimation error is small. The maximum error is equal to -4(%) at 10(%) mismatching in αM.

Fig.9 shows the $\hat{R}_2$ estimation errors of (8) with mismatching of ℓ. The secondary flux ripples, which are used in the secondary resistance estimation, depends on greatly the leakage inductance. Therefore, $\hat{R}_2$ estimation is highly sensitive to the mismatching of ℓ. As shown in Fig.9, the maximum $\hat{R}_2$ estimation error is ± 140(%) with ± 10(%) mismatching in ℓ.

IV. System Configuration

Fig.10 illustrates the sensorless speed control system of an induction motor based on DSP(TMS320C25) applying the proposed $\hat{R}_1$ and $\hat{R}_2$ identification methods. On the steady state, assuming ω_0 is equal to the inverter frequency reference ω_1*, the rotor speed $\hat{\omega}_m$ is estimated as

$$\hat{\omega}_m = \omega_0 - \hat{\omega}_S = \omega_1^* - R_2 T/|\psi_2|^2 \qquad (11)$$

where T is the generated torque, which can be calculated by

$$T = \psi_{1d} i_{1q} - \psi_{1q} i_{1d} . \qquad (12)$$

The estimated speed is fed back and compared with the speed reference ω_m*. The error between these value is used to drive the PI controller which generate the inverter frequency reference ω_1*. The sign of ω_1* gives direction of the rotation (F/B), and the amplitude makes Run/Stop (R/S) command which decides the voltage and the

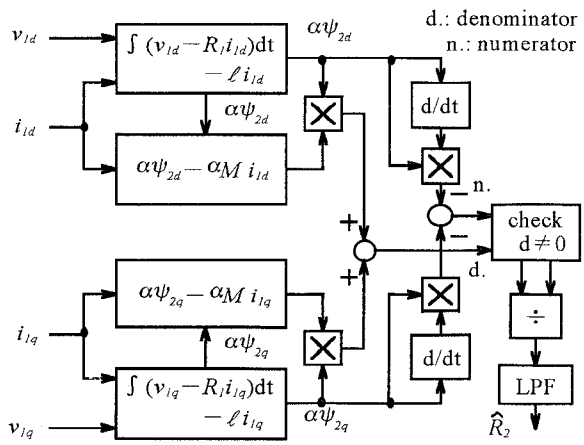

Fig.7. Secondary resistance identification block diagram.

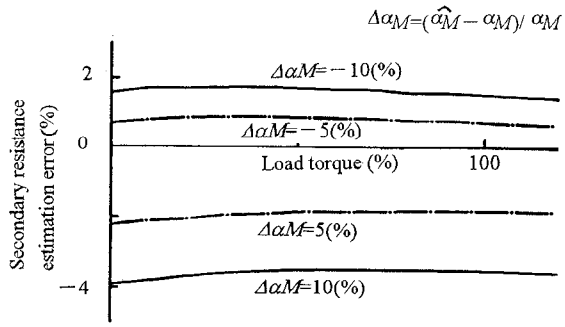

Fig.8. Secondary resistance estimation error for mutual inductance mismatching.

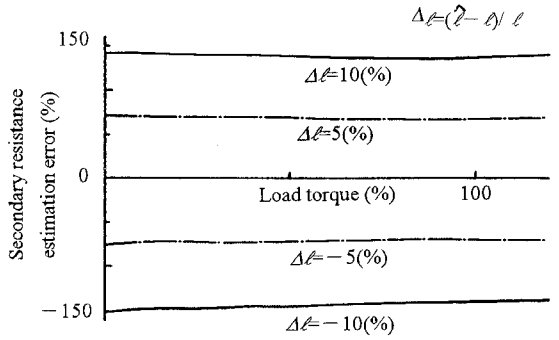

Fig.9. Secondary resistance estimation error for leakage inductance mismatching.

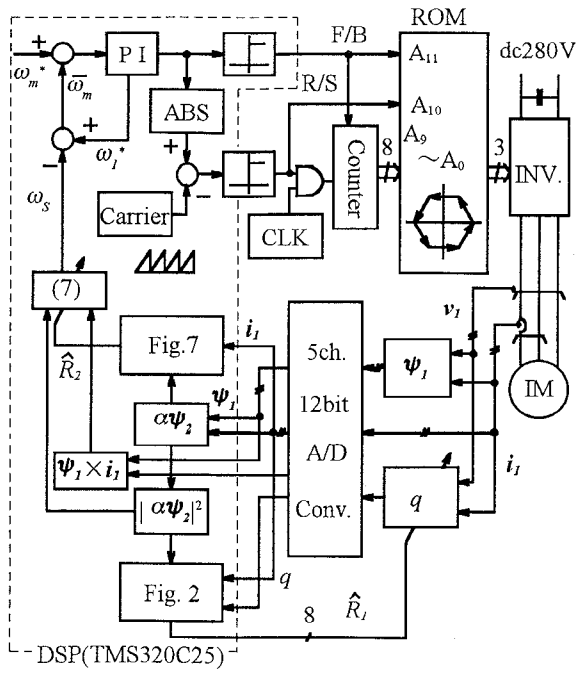

Fig.10. Configuration of speed control system.

frequency of the PWM inverter. The PWM inverter drives the induction motor with hexagonal primary flux locus to produce large flux ripples. The secondary resistance calculation will be assured by these flux ripples.

To estimate $\hat{R}_1$, $\hat{R}_2$ and the rotor speed $\hat{\omega}_m$, the primary voltage and the primary current must be detected. In this system, the primary flux in (2) and the reactive power in (4) are calculated by some analogue circuits.

Fig.11 illustrated the calculation circuits of the primary flux ψ_1 and the reactive power q. The primary flux is calculated by the integration circuits using the ultra-low offset voltage amplifiers, and $\hat{R}_1$ in (2) can be varied to estimated value in Fig.2 by the 8bits multiplying D/A converters. The reactive power is calculated by the analogue multipliers and averaged by LPF. By using the analogue circuits, the error due to the sampling cycles and the quantization is reduced.

The calculated ψ_1, q and the primary current are detected by 12bits A/D converters, and used to estimate $\hat{R}_1$ and $\hat{R}_2$ in Fig.2 and Fig.7. By using these estimated values of $\hat{R}_1$ and $\hat{R}_2$, the rotor speed estimation in (11) is not affected by the variations of R_1 and R_2. The speed estimation and control with the compensation of R_1 and R_2 are carried out on DSP. The calculation time is about 105(μs), and the sampling frequency is fixed at 4.88(kHz).

V. Experimental Results

Table 1 shows the rating and motor parameters of the induction motor using in the experiments. The tested machine is coupled to a 2(kW) dc machine.

Fig.12 shows the primary resistance identification result which is independent of the secondary resistance calculation. The induction motor is driven under the rated load torque and the speed reference is 200(rpm). The initial value of the estimated $\hat{R}_1$ is 50(%) of the nominal value, and the speed control error which is caused by the mismatching of $\hat{R}_1$ is 24(rpm). The estimated $\hat{R}_1$ converges to the nominal value within 3(s), and the speed control error is reduced to 1(rpm). The identification error of $\hat{R}_1$ is −2(%). The dynamics of $\hat{R}_1$ convergence which depends on the PI adaptation mechanism is enough to compensate the machine temperature variations.

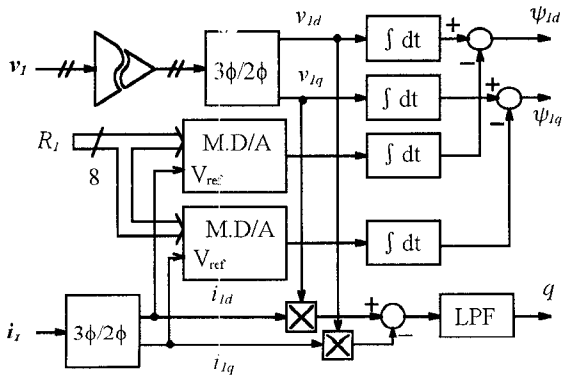

Fig.11. Block diagram of analog circuit.

Fig.13 shows the secondary estimation result. The speed reference is 200(rpm) and the load torque is rated value. The primary resistance is fixed at nominal value. The estimated $\hat{R}_2$ converges from initial value, which is 30(%) of the nominal value, to the correct one. The converging time which is caused by the LPF is about 1.5(s). It is enough shorter than the time constant of the machine temperature variations. The speed control error is reduced from 74(rpm) to 4(rpm). The calculation error of $\hat{R}_2$ is about 5(%).

Figure 14 shows the speed control characteristics with both compensations of the primary and the secondary resistance. The initial values of each resistance are 50(%) of the nominal values. When the induction motor is controlled without $\hat{R}_1$ and $\hat{R}_2$ estimation on the rated torque, the speed control error is 63(rpm). After beginning the estimation of $\hat{R}_1$ and $\hat{R}_2$, each values converge to the suitable value within 3(s). It reduces the speed control error from 63(rpm) to 1(rpm). The estimation errors of each resistance are under 3(%). This result shows that the simultaneous estimations of $\hat{R}_1$, $\hat{R}_2$ and $\hat{\omega}_m$ are possible on the speed sensorless drive system.

VI. Conclusions

In this paper, the primary and the secondary resistance estimation methods of an induction motor are described. They can use for speed sensorless control and compensate the machine temperature variation. The conclusions are summarized as follows:

1)By using the reactive power, the primary resistance is estimated on the adaptive identification system within 2(%) error.

2)By using the flux ripples, the secondary resistance estimation without speed sensors is possible. The accuracy

Table.1. Parameters of induction motor.

1.5kW Induction motor			
200V, 55Hz, 4poles			
Primary resistance	R_1:	0.53	Ω
Secondary resistance	R_2:	0.51	Ω
Mutual inductance	αM:	54.3	mH
Leakage inductance	ℓ:	3.19	mH

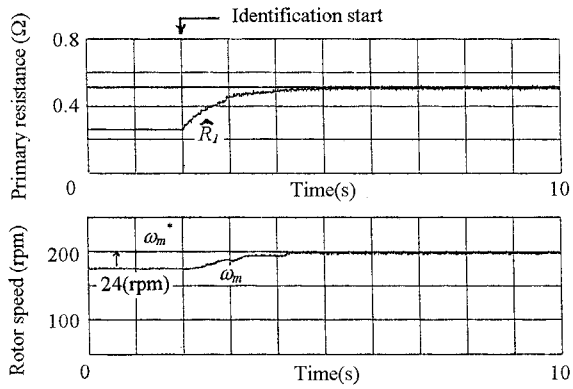

Fig.12. Experimental result of primary resistance compensation.

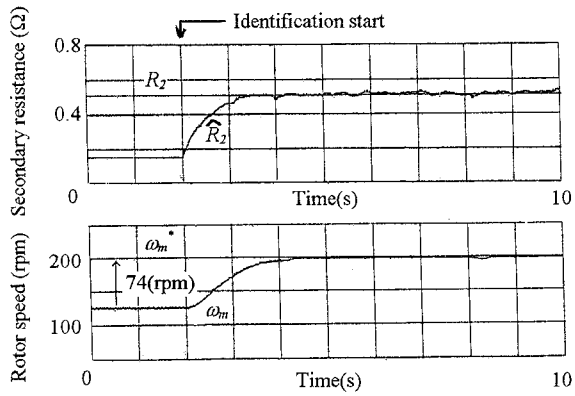

Fig.13. Experimental result of secondary resistance compensation.

of the secondary resistance calculation is obtained within 5(%).

3)In this paper, proposed estimation methods of $\hat{R}_1$ and $\hat{R}_2$ are combined and applied to the simple speed sensorless drive. The mismatching of $\hat{R}_1$ and $\hat{R}_2$ are compensated by these methods, and the speed control error caused by the mismatching is reduced from 63(rpm) to 1(rpm).

4)The accuracy of the proposed primary resistance estimation method is affected by the mismatching of the mutual inductance, and the secondary resistance estimation is highly sensitive to the leakage inductance.

5)By using the analogue circuits to calculate the primary flux and the reactive power, the detection error caused by the sampling cycles is reduced.

ACKNOWLEDGMENT

The authors would like to express their appreciation to Mr. I. Miyashita of Toyo Electric Co. Ltd. and Power Electronics Laboratory members of Nagaoka University of Technology.

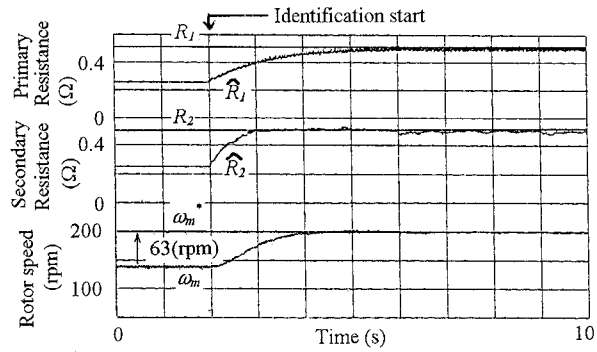

Fig.14. Primary and secondary resistance compensation.

REFERENCES

[1] C.Schauder, "Adaptive Speed Identification For Vector Control Of Induction Motors Without Rotational Transducers," in *Conf. Rec. of the IEEE IAS Annual Meeting*, 1989, pp. 493-499.

[2] U.Baader, M.Depenbrock, "Direct Self Control of Inverter-Fed Induction Machine, A Basis for Speed Control without Speed Measurement," in *Conf. Rec. of the IEEE IAS Annual Meeting*, 1989, pp. 486-492.

[3] Y.R.Kim, S.K.Sul, M.H.Park, "Speed Sensorless Vector Control of an Induction Motor Using an Extended Kalman Filter," in *Conf. Rec. of the IEEE IAS Annual Meeting*, 1992, pp. 594-598.

[4] P.L.Jansen, R.D.Lorenze, "Transducerless Position and Velocity Estimation in Induction and Salient AC Machines," in *Conf. Rec. of the IEEE IAS Annual Meeting*, 1994, pp. 488-495.

[5] T.Ohtani, "A New Method of Torque Control Free From Motor Parameter Variation in Induction Motor Drives," in *Conf. Rec. of the IEEE IAS Annual Meeting*, 1986, pp.203-209.

[6] I.Miyashita, H.Fujikawa, Y.Ohmori, "Speed Sensor less Instantaneous Vector Control with Identification of Secondary Resistance," in *Conf. Rec. of the IEE Japan IAS Annual Meeting*, 1991, pp.130-135.

[7] H.Kubota, K.Matsuse, "Speed Sensorless Field Oriented Control of Induction Motor with Rotor Resistance Adaption," in *Conf. Rec. of the IEEE IAS Annual Meeting*, 1993, pp.414-418.

[8] T.Kanmachi, I.Takahashi, "Sensor-less Speed Control of Induction Motor with No Influence of Secondary Resistance Variation," in *Conf. Rec. of the IEEE IAS Annual Meeting*, 1993, pp.408-413.

[9] T.Kanmachi, I.Takahashi, "A Secondary Resistance Calculation Method for Sensor-less Speed Control of an Induction Motor," in *Proceedings of the IPEC-Yokohama*, 1995, pp.1671-1676.

[10] F.Z.Peng, T.Fukao, J.S.Lai, "Low-Speed Performance of Robust Identification Using Instantaneous Reactive Power for Tacholess Vector Control of Induction Motor," in *Conf. Rec. of the IEEE IAS Annual Meeting*, 1994, pp.509-514.

[11] T.Kanmachi, I.Takahashi, "Primary Resistance Compensation for Sensorless Speed Control of an Induction Motor," in *National Convention Record IEE Japan-IAS*, 1996, Vol.3, pp.213-214.

An Auto-Tuning Method for Vector Controlled Induction Motor Drives Considering Stator Core Loss

Hiroaki Yamamoto, Kohji Tanaka, and Ichiro Miki
Department of Electrical Engineering, Meiji University
1-1-1, Higashimita, Tama-ku, Kawasaki 214, JAPAN
Phone: +81-44-934-7295 Fax: +81-44-934-7909
E-mail: miki@isc.meiji.ac.jp

Abstract – This paper presents an auto-tuning method for the indirect vector controlled induction motor drives for the start up. The tuning algorithm is based on the rotor flux behavior of the induction motor for a stepwise torque command. An effect of the stator core loss of the induction motor, which appears in the transient motor terminal voltage caused by the undesirable rotor flux variation, is taken into account when the tuning is implemented. This method can tune the accurate inverse of the rotor time constant. Simulation results of the laboratory model system verify the validity of the proposed auto-tuning method.

I . INTRODUCTION

Vector control system of an induction motor is widely applied to a field of industry applications. The control performance of this system depends on the accuracy of the identified electrical motor parameters. In particular, the slip gain K_s defined as the inverse of the rotor time constant considerably affects the motor control performance [1]. These parameters can be calculated from the results of no-load and locked rotor tests of the induction motor. However, these values are different from the actual motor operating parameters. Therefore, it may be difficult to obtain a high performance when these parameters are used to constitute the vector control system. To overcome this problem, we have presented the auto-tuning method for the vector controlled induction motor drive system for the start up [2],[3]. However, the effect of core loss is neglected in these papers. The stator core loss must be considered to obtain the higher control performance when the tuning is implemented [4].

This paper presents an auto-tuning method for vector controlled induction motor drives considering stator core loss. First, effects of stator core loss on the tuning are discussed based on the circuit equation of the induction motor considering stator core loss. Next, a tuning algorithm is made up based on examination results. Finally, this algorithm is implemented in the simulation model drive system, and the accuracy of tuning results are discussed.

II . EQUATION OF INDUCTION MOTOR

Based on the assumption that core loss occurs due to the eddy current of the stator [5], the equations of an induction motor and rotor flux in the synchronously rotating d-q reference frame are given as

$$\begin{bmatrix} V_{ds} \\ V_{qs} \\ 0 \\ 0 \end{bmatrix} = \begin{bmatrix} R_s + R_m + L_s p & -\omega_0 L_s + (R_m/\omega_0)p \\ \omega_0 L_s - (R_m/\omega_0)p & R_s + R_m + L_s p \\ sR_m + Mp & -\omega_s M + (R_m/\omega_0)p \\ \omega_s M - (R_m/\omega_0)p & sR_m + Mp \end{bmatrix} *$$

$$* \begin{bmatrix} R_m + Mp & -\omega_0 M + (R_m/\omega_0)p \\ \omega_0 M - (R_m/\omega_0)p & R_m + Mp \\ R_r + sR_m + L_r p & -\omega_s L_r + (R_m/\omega_0)p \\ \omega_s L_r - (R_m/\omega_0)p & R_r + sR_m + L_r p \end{bmatrix} \begin{bmatrix} i_{ds} \\ i_{qs} \\ i_{dr} \\ i_{qr} \end{bmatrix} \quad (1)$$

$$\lambda_{dr} = L_r i_{dr} + M i_{ds} + (R_m/\omega_0)(i_{qs} + i_{qr}) \quad (2)$$

$$\lambda_{qr} = L_r i_{qr} + M i_{qs} - (R_m/\omega_0)(i_{ds} + i_{dr}), \quad (3)$$

where

p	differential operation
i_{ds} , i_{qs}	d-axis and q-axis stator currents
λ_{dr} , λ_{qr}	d-axis and q-axis rotor interlinked fluxes
V_{ds} , V_{qs}	d-axis and q-axis voltages
R_s , R_r	stator and rotor resistances
L_s , L_r	stator and rotor self-inductances
M	mutual inductance
q	number of pole pairs
ω_0	angular velocity of power source
ω_r	mechanical rotor angular velocity
ω_s	slip angular velocity

0-7803-3823-5/97/$10.00© 1997 IEEE

R_m equivalent stator core loss resistance.

In (1), (2), and (3), the terms including R_m/ω_0 exist. The effect of these terms is considerably smaller than that of any other term. However, the detailed effect of these terms on tuning is under discussion. In this study, these terms are neglected for simplicity. Therefore, (2) and (3) are rewritten as (4) and (5), respectively. Furthermore, from (4), (5), and (1), (6) is obtained.

$$\lambda_{dr} = L_r i_{dr} + M i_{ds} \tag{4}$$

$$\lambda_{qr} = L_r i_{qr} + M i_{qs} \tag{5}$$

$$\begin{bmatrix} V_{ds} \\ V_{qs} \\ 0 \\ 0 \end{bmatrix} = \begin{bmatrix} R_s + R_m + L_\sigma p & -\omega_0 L_\sigma \\ \omega_0 L_\sigma & R_s + R_m + L_\sigma p \\ \frac{-MR_r}{L_r} + (1 - \frac{M}{L_r})sR_m & 0 \\ 0 & \frac{-MR_r}{L_r} + (1 - \frac{M}{L_r})sR_m \end{bmatrix} *$$

$$* \begin{bmatrix} \frac{M}{L_r}p & -\frac{\omega_0 M}{L_r} \\ \frac{\omega_0 M}{L_r} & \frac{M}{L_r}p \\ \frac{(R_r + sR_m)}{L_r} + p & -\omega_s \\ \omega_s & \frac{(R_r + sR_m)}{L_r} + p \end{bmatrix} \begin{bmatrix} i_{ds} \\ i_{qs} \\ \lambda_{dr} \\ \lambda_{qr} \end{bmatrix} + \begin{bmatrix} R_m i_{dr} \\ R_m i_{qr} \\ 0 \\ 0 \end{bmatrix} \tag{6}$$

where

$$L_\sigma = \left(L_s L_r - M^2\right)/L_r \tag{7}$$

III. Effect of Stator Core Loss

Fig.1 shows the tuning signals used in this study. In this figure, time t_{2n-1} and t_{2n} show the time to start interval B and A, respectively. The tuning algorithm is based on the rotor flux behavior of the induction motor for the tuning signals shown in this figure. However, it is difficult to directly measure the rotor flux, so the transient terminal voltage caused by the variation of the rotor flux in interval A is noticed instead. Since pi_{ds}^* and i_{qs}^* equal zero in interval A, the stator d-axis voltage equation in interval A can be obtained from the first, third and fourth rows of (6) as follows:

$$V_{ds} = \left(R_s + R_m(f)\right)I_{ds}^* + R_m(f)I_{dr}(t_{2n})e^{-\frac{R_r}{L_r}t}$$

$$-\frac{M}{L_r}e^{-\frac{R_r}{L_r}t}\left\{\frac{R_r}{L_r}\left(\lambda_{dr}(t_{2n}) - MI_{ds}^*\right) + q\omega_r\lambda_{qr}(t_{2n})\right\}$$

$$= R_s I_{ds}^* + \Delta V_{ds} \tag{8}$$

$$\Delta V_{ds} = R_m(f)I_{ds}^* + R_m(f)I_{dr}(t_{2n})e^{-\frac{R_r}{L_r}t} + \Delta V_{ds}' \tag{9}$$

$$\Delta V_{ds}' = -\frac{M}{L_r}e^{-\frac{R_r}{L_r}t}\left\{\frac{R_r}{L_r}\left(\lambda_{dr}(t_{2n}) - MI_{ds}^*\right) + q\omega_r\lambda_{qr}(t_{2n})\right\}, \tag{10}$$

where f is a frequency of the power source, I_{ds}^* is the commanded exciting current value, and $R_m(f)$ shows that the stator core loss is a function of the frequency.

In this study, since the vector control scheme uses a reference frame in which the rotor flux vector always remains in phase with the d-axis, the constraint is

$$\lambda_r = \lambda_{dr} = MI_{ds}^*. \tag{11}$$

Therefore, when the slip gain K_s has an accurate value, ΔV_{ds} is rewritten as follows:

$$\Delta V_{ds} = R_m(f)I_{ds}^*. \tag{12}$$

Fig.2 shows the response of V_{ds} when K_s has the accurate value under the condition considering stator core loss. The

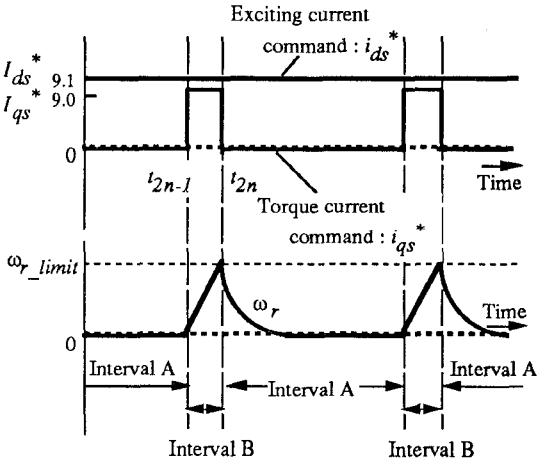

Fig.1. Tuning signals.

part of oblique lines in this figure shows the voltage drop of $R_m(f)I_{ds}$*. The tuning method which neglects the effect of the stator core loss has already been published [3]. In this paper, it is assumed that ΔV_{ds} equals zero if K_s has the accurate value. However, as is obvious from the above discussion, this assumption in the conventional method contains theoretical error. The effect of the stator core loss appears in the motor terminal voltage.

Fig.3 shows the response of V_{ds} when the tuning has completed using conventional method. Comparing Fig.2 with Fig.3, these response wave forms of V_{ds} are obviously different each other. If the K_s obtained by the conventional method has the accurate value, the wave form shown in Fig.3 must be the same as that in Fig.2. Therefore, as seen from this, it is obvious that the accurate K_s has not been obtained using the conventional method.

IV. Principle of Tuning Method

As mentioned previously, the slip gain K_s obtained by the conventional method contains error theoretically. Therefore,

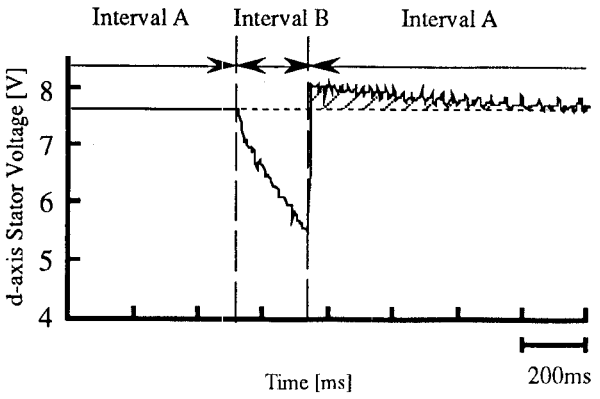

Fig.2. Response of V_{ds} when K_s has the accurate value.

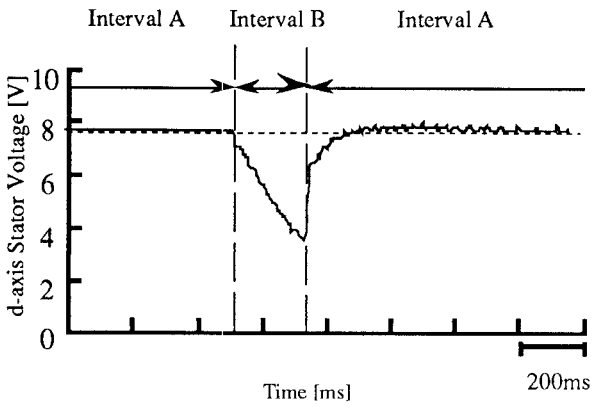

Fig.3. Response of V_{ds} when tuning has completed.

a new auto-tuning method taking the effect of stator core loss into consideration is discussed here. First, we define the new characteristic value ΔV_{ds_k} as follows:

$$V_{ds} = \left(R_s + R_m(f)\right)I_{ds}^{*} + \Delta V_{ds\_k} \tag{13}$$

$$\Delta V_{ds\_k} = R_m(f)I_{dr}(t_{2n})e^{-\frac{R_r t}{L_r}} + \Delta V_{ds}', \tag{14}$$

where $\Delta V_{ds}'$ is the same as (10).

In above equations, ΔV_{ds_k} appears in the motor terminal voltage when K_s has an inaccurate value. If K_s has the accurate one, ΔV_{ds_k} equals zero because the constraint for vector control given by (11) is satisfied.

Comparing the absolute value of the integration of the first term with that of the second term in (14), the value of the first term is smaller than the other, and therefore the sign of ΔV_{ds_k} depends on the sign of $\Delta V_{ds}'$. Fig.4(a) and (b) show the comparison between the absolute value of the integration of the first term and that of the second term in (14).

The relationship between K_s and ΔV_{ds_k} equals the relationship between K_s and $\Delta V_{ds}'$ [3]. Table 1 shows this relationship.

Consequently, we can accurately tune K_s using the relationship shown in Table 1.

V. Tuning of Motor Parameters

The accurate K_s can be obtained utilizing the results shown in Table 1. However, it is necessary to know R_s and $R_m(f)$ because V_{ds} required to compute ΔV_{ds_k} contains these terms.

A. Stator Core Loss Resistance

As mentioned previously, Stator core loss is a function of frequency, and can be assumed to vary linearly with $\omega_0^{1.6}$ [6] as follows:

$$R_m(f) = K\omega_0^{1.6} = K(2\pi f)^{1.6}, \tag{15}$$

where K is a coefficient.

From the above equation, K is

$$K = R_m(f)/\omega_0^{1.6} = R_m(f)/(2\pi f)^{1.6}. \tag{16}$$

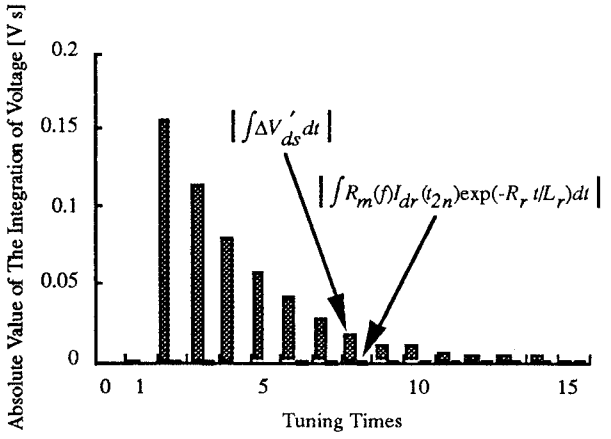

(a) General view from the beginning of tuning to the end.

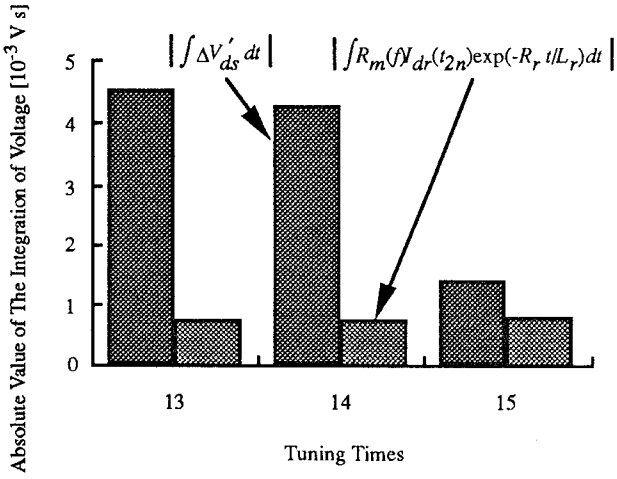

(b) Expanded view of a part of Fig.4 (a).

Fig.4. Absolute values of the integration of voltages.

Table 1. Relationship between K_s and V_{ds_k}.

	ΔV_{ds_k}
$K_s < R_r / L_r$	-
$K_s = R_r / L_r$	0
$K_s > R_r / L_r$	+

When the rotor flux is in the steady state in interval A, the following equation can be obtained from (13).

$$V_{ds} = (R_s + R_m(f)) I_{ds}^* \tag{17}$$

Accordingly, $R_m(f)$ can be obtained as follows:

$$R_m(f) = (V_{ds} - R_s I_{ds}^*) / I_{ds}^* . \tag{18}$$

The data of V_{ds} and ω_0 are simultaneously sampled at several hundred points on the frequency. From (16) and (18) using these data, we can obtain values of K at these points. We use the average value of these values as the coefficient K after this. From the above procedure, K is given and $R_m(f)$ can be computed by (15).

Fig.5 shows the response of V_{ds} when $K_s < R_r / L_r$. In this figure, the time to sample the data necessary for the implementation of the tuning is also shown. In interval A, the sample of the data V_{ds} and ω_0 is started when the rotor flux is in the steady state.

B. Stator Resistance

From (13), when the rotor flux is in the steady state in interval A, R_s can be obtained as follows:

$$R_s = \{V_{ds} - R_m(f) I_{ds}^*\} / I_{ds}^* . \tag{19}$$

In the first interval A, the frequency is zero because the torque current has been zero and the rotor has been at a standstill. Therefore, the stator core loss is also zero ($R_m(f)$=0), and Rs can be easily obtained by (19). After the first tuning, $R_m(f)$ can be computed as described before, and R_s can be obtained by using (15) and (19) . As we compute R_s repeatedly in interval A, we use the average value of these values as R_s .

C. Slip Gain

Slip gain K_s can be tuned using the relationship shown in Table 1. Since ΔV_{ds_k} has ripples , K_s is tuned using the following value F which is the integration of ΔV_{ds_k}.

$$F = \int_{t_{2n}}^{t_{2n}+\tau} \Delta V_{ds\_k} dt \tag{20}$$

where τ is the time of integration.

Next, we define the following equation to tune K_s.

$$K_s(n+1) = \alpha K_s(n) \tag{21}$$

where n is the number of times of tuning, and α is the gain factor defined as

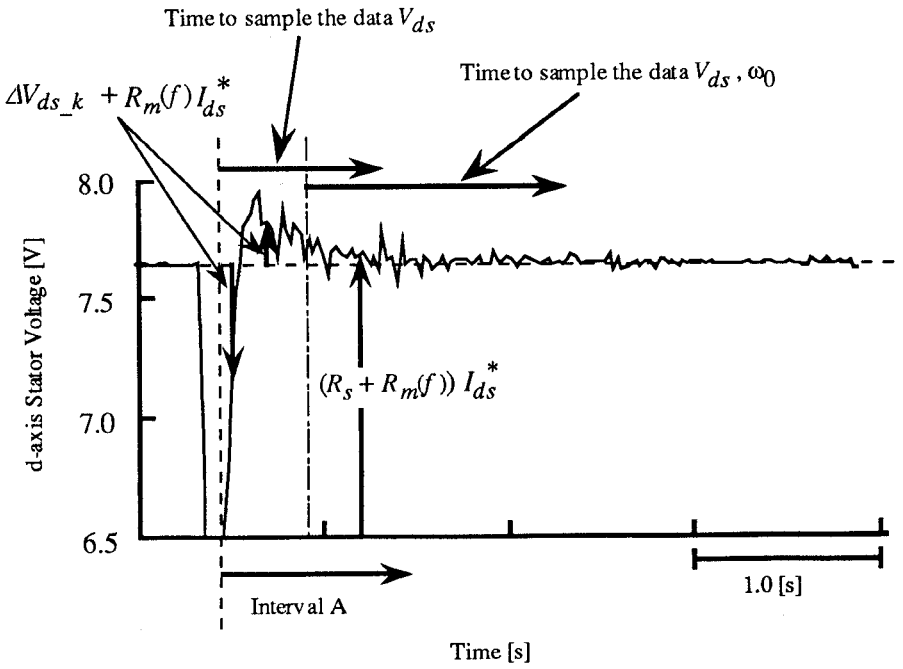

Fig.5. Response of V_{ds} ($K_s < R_r / L_r$).

$$\alpha = N^{-F}, \qquad (22)$$

where $N > 1$.

From (22) and Table 1, the relationship between F and α can be obtained as shown in Table 2. Therefore, K_s can be tuned using (20), (21), (22), and the relationship shown in Table 2. Fig.6 shows the algorithm of this auto-tuning.

VI. Simulation Results

Simulation has been carried out using the drive system with 0.75kW, 100V, 7.6A, 4–pole, 50Hz induction motor. Fig.7 shows the block diagram of this vector controlled induction motor drive system including the proposed auto-tuning system. In this simulation, the initial slip gain $K_s(0)$ is set to 10.71 obtained from the result of the conventional method. Table 3 shows the tuning results. According to the results, R_s is accurately obtained, and K_s obtained by the proposed method agrees well with the set value.

Consequently, the validity of the proposed auto-tuning method has been verified.

Table 2. Relationship between F and α.

	F	α
$K_s < R_r / L_r$	−	$\alpha > 1$
$K_s = R_r / L_r$	0	$\alpha = 1$
$K_s > R_r / L_r$	+	$0 < \alpha < 1$

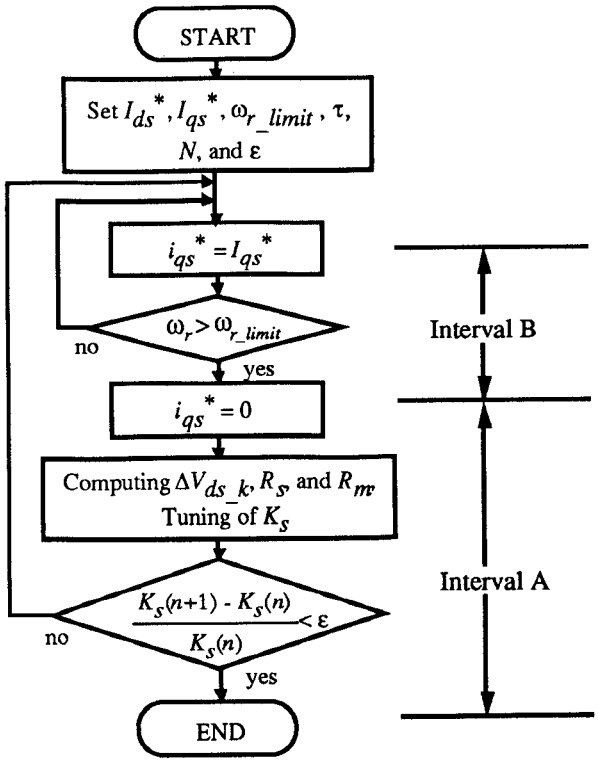

Fig. 6. Algorithm of auto-tuning.

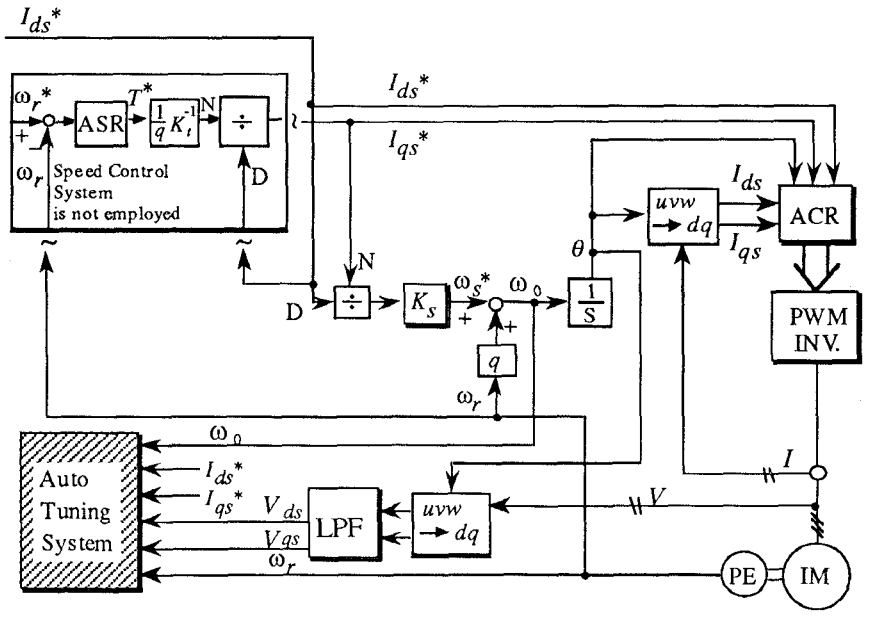

Fig. 7. Block diagram of indirect vector control system

Table 3. Tuning results

	proposed method	conventional method	set values
R_s [Ω]	0.840	0.840	0.840
K_s	13.29	10.71	13.28

VII. Conclusion

An auto-tuning method for the vector controlled induction motor drives considering the stator core loss of the motor has been studied. The effect of the stator core loss, as well as the effect of the slip gain, appears in the motor terminal voltage. In this method, the tuning algorithm is based on this terminal voltage response caused by the undesirable rotor flux variation. The drive system using the proposed method is simulated, and it is confirmed that the slip gain obtained by this method agrees well with the set value.

References

[1] R.D.Lorenz, "Tuning of Field-Oriented Induction Motor Controllers for High-Performance Applications", IEEE Trans. Ind. Appl., pp.293-297, Mar./Apr. 1986

[2] M.Akiyama, I.Miki, "Auto-tuning method for vector control of induction motor with emphasis on variation of secondary flux", speedam conference ,Taormina Italy, pp.209-214, 1994

[3] M.Akiyama, K.Kobayashi, I.Miki & M.A.El-sharkawi, "Auto-Tuning Method for Vector Controlled Induction Motor Drives", Trans. IEE Japan, Vol.116-D, No.8, pp844-851, 1996

[4] M.Iwata, S.Itoh, K.Morita and T.Ohno, "Influence of Stator Core Loss in a Speed Sensorless Vector Control Based on Rotor Induced Voltage Estimation", IEE Japan, Vol.4, No.908, pp.302-303, 1996

[5] T.Mizuno, J.Takayama, T.Ichioka & M.Terashima, "Decoupling Control Method of Induction Motors Taking Stator Core Loss into Consideration", Trans. IEE Japan, Vol.109-D, No.11, pp.841-848, 1989

[6] J.Takayama, T.Mizuno, M.Date, T.Ichioka, "Relationship between Vector-Control of Induction Motor Taking Stator Core-Loss into Consideration and Equivalent Circuit", IEE Japan -Industry Applications Society -, No.55, pp.206-209, 1992

High - Torque and High - Efficiency Control in Induction Motor Drives

Lishi WANG, Hirohito FUNATO, Kenzo KAMIYAMA
Department of Electrical and Electronic Engineering
Utsunomiya University
2753 Ishii-cho, Utsunomiya-shi, Tochigi-ken, 321, JAPAN
Fax: +81(JPN)-28-689-6089, Phone: +81(JPN)-28-689-6089
E-mail: t9756@cc.utsunomiya-u.ac.jp

Abstract - **The induction motor used in the industrial application has been generally controlled based on Vector Controlled Induction Motors (VCIM) to obtain well dynamic torque response and high-efficiency performance. In this paper, the authors present a simple control method which maximizes the motor efficiency under any load condition and also propose a simple high-efficiency and high-torque control system. The characteristics of the torque and efficiency are demonstrated using this system through simulations.**

I. INTRODUCTION

Until now, since an induction motor is structurally stronger, less expensive, energy savings and is suitable for widely constant output operations which can be easily realized controlling the motor flux level, therefore, the induction motor (IM) is suitable for industrial applications and electric vehicle drives. However, there is a new problem of driving IMs, the core loss increases at the light load torque region, resulting in worsening the motor efficiency. And a torque or speed of a motor far from rated values may cause a efficiency drop. For this reason, a high efficiency system is required, which can be realized by keeping a balance between the losses, in particular for iron and copper losses. A good machine design dictates that the operation around the rated operating condition corresponds to a high- efficiency operating point.

From the viewpoint of the energy savings , it is required that the industrial drive system must be equipped with a torque controller having high response along with an efficiency controller. Recently, many control systems have been reported to improve the efficiency of IMs by adjusting the magnetizing current according to the load torque [1] [7]. Since the magnetizing current of an induction motor is changed due to the energy saving, at the same time, the speed and torque control are performed using the slip frequency type vector control, the speed response and the torque response are worsen because of a limited torque current when torque disturbance changes significantly. Thus, simultaneous realization of the high-torque and the high-efficiency control methods is expected.

This paper describes a simple control method that maximizes the efficiency of the vector controlled IM under any load torque. A simple control system achieving high-torque response is also presented. In this system, magnetizing current is changed to reduce the core loss, and it is possible to control the motor torque stably and accurately by keeping a desirable ratio of the magnetizing current to the torque current with the controller. Finally, the simulation results are demonstrated.

II. HIGH- EFFICIENCY CONTROL METHOD

The efficiency maximizing theory that improves the efficiency at light load ranges of IM during conventional vector control is as follows. The key to solve the problem of maxi- mizing the IM efficiency is to minimizes copper and iron losses. Fig.1 represents a equivalent circuit in $\gamma\ \delta$ generalized coordinates with a vector controlled IM considering core loss.

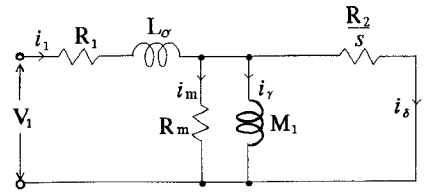

Fig.1 Equivalent circuit of a vector controlled IM considering core loss.

where L_σ : leakage inductance, M_1: mutual inductance s : slip
R_m : equivalent core loss resistance, R_2: secondary resistance

The total loss L_t generated in the motor can be expressed by (1) according to torque current i_δ and magnetizing current i_γ .[1]

$$\begin{aligned} L_t &= R_1 i_1^2 + R_2 i_\delta^2 + R_m i_m^2 + L_m \\ &= (R_1 + M^2 R_2 / L_2^2)\, i_\delta^2 + (R_1 + M R_m / L_2)\, i_\gamma^2 + \\ &\quad 2[R_m R_1 i_\gamma i_\delta / (\omega_1 M)] + L_m \end{aligned} \tag{1}$$

The equivalent core loss resistance R_m changes according to the rotor speed ω_r, when the R_m can be assumed as (2)

$$R_m = R_{mo} \times (\omega_r / \omega_b)^{1.6} \tag{2}$$

where R_{mo} : core loss resistance, ω_b : base speed,

machine loss is considere by $L_m = K_m \omega_r^2$.

Considering these relationships, the motor output P_{out} and the efficiency of motor is expressed as follows,

$$P_{out} = \omega_r T$$

$$\eta = \frac{P_{out}}{P_{out} + L_t} \times 100\ (\%) \qquad (3)$$

In order to keep the efficiency of the motor to maximum even in steady and transient states, the ratio of the magnetizing current i_γ to the torque current i_δ must always be kept at a desirable value which makes the total loss generated in the motor. So the maximum efficiency of motor can be accomplished over any load state. Since the secondary magnetic flux can be assumed by detecting the γ -coordinate component , the torque of motor is expressed by (4)

$$T = 3pM i_\gamma i_\delta \qquad (4)$$

By appling the value to (1), consider that the ratio betweem the torque current and magnetizing current K. Therefor, by solving for K minizing total loss through $dL_t / dK = 0$, the solution is shown by (5).

$$K = \sqrt{(R_1 + MR_m / L_2) / (R_1 + M^2 R_2 / L_2^2)} \qquad (5)$$

Thus, the torque current and magnetizing current according to the given torque reference can be obtained from (4), (5).

Moreover, the control which maximizes efficiency under a given load can be realized through relatively simple calculations. So the speed control system of induction motors using high- efficiency control is shown by Fig.2 . However, due to the problems of magnetic saturation and the stability of control, the control range of magnetizing current has to be limited. As a result, the response of the motor torque deteriorates and then stability becomes worse in transient states. The performance characteristics are shown by Fig.3.

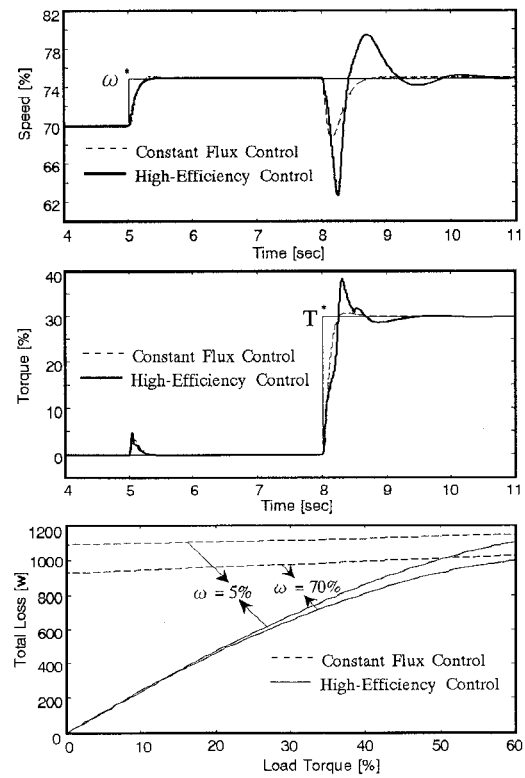

Fig.3 Characteristics of loss and response of speed and torque.

III. Proposed High-Efficiency Control Method

When a existing high-efficiency control is applied, in order to improve the motor torque response and stability in transient states, a new high-efficiency control method is proposed by Fig.4, here, torque controller is designed by PI.

A. Principle of Control

In this paper, the torque control is performed, based on the slip frequency type vector control.

The fundamental control conditions for the slip type vector control are derived from (6) regarding the secondary

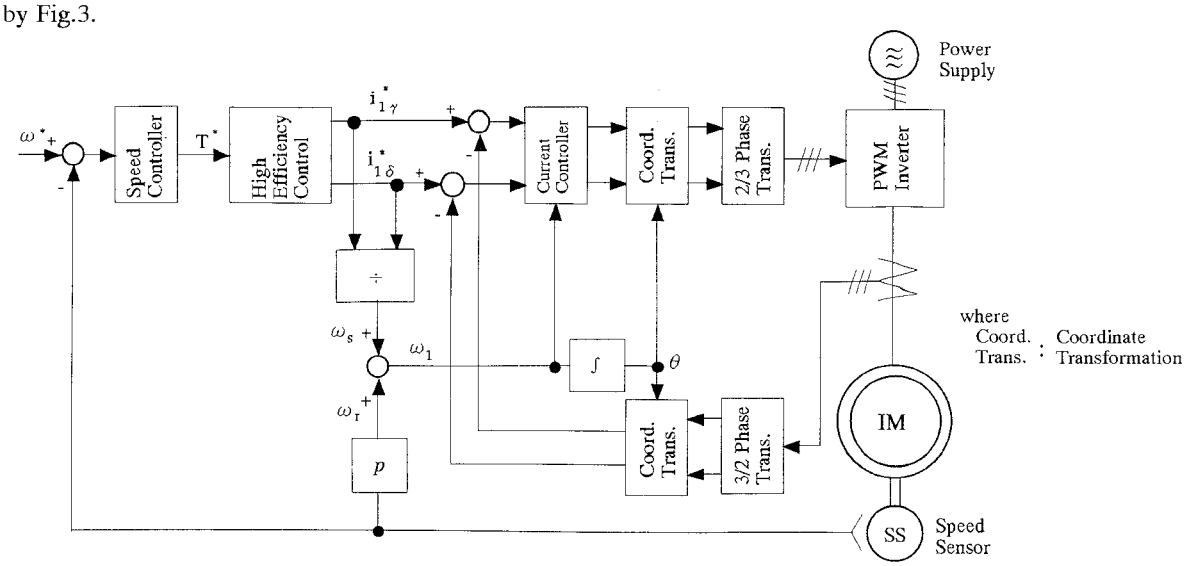

Fig.2 Block diagram of speed control system with existing high-efficiency control.

magnetic flux equations using the γ - δ coordinates.

$$\left.\begin{aligned}\phi_{2\gamma} &= M i_{1\gamma} + L_2 i_{2\gamma} + \frac{R_m}{\omega}(i_{1\delta} + i_{2\delta}) \\ \phi_{2\delta} &= M i_{1\delta} + L_2 i_{2\delta} + \frac{R_m}{\omega}(i_{1\gamma} + i_{2\gamma})\end{aligned}\right\} \quad (6)$$

ω : motor electric angular speed

Here, if the δ coordinate component of the secondery magnetic flux is kept zero, the calculation of the motor torque can be expressed by (4) in the γ - δ coordinates, and determining the operating value of the slip angular frequecy can also be given by (7).

$$\omega_s = \frac{i_\delta}{T_2 i_\gamma} \quad (7)$$

$T_2 = L_2 / R_2$

T_2 : secondary time constant

Here, the change variation the secondary resistance R_2 caused from temperature is not considered. By this system, the torque control with the high-efficiency control can feedback an assumed motor torque calculated using the secondary magnetic flux and the torque current component detected from current sensors of the primary currents, then, the desirable torque current reference can be determined on the basis of the torque controller and high efficiency controller. Moreover, the high-efficiency of motor in the steady and transient states can be obtained by the ratio of the magnetizing current i_γ to the torque current i_δ, because this ratio always be kept at a desirable value which makes the total loss generated in the drive system. Due to the loss of the converter is not considered here, Fig.5 shows a comparison of efficiency between the constant flux control and the high- efficiency control.

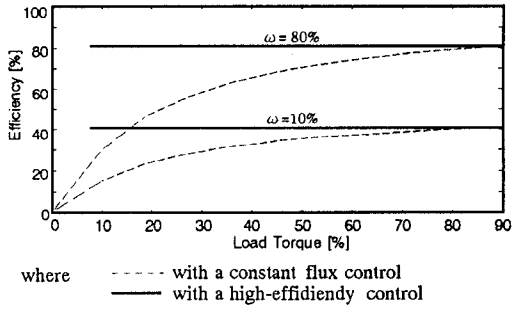

Fig.5 Efficiency with and without a high-efficiency control.

B. Simulation results

An exsiting high-efficiency control (without a torque controller) and a proposed method (with a torque controller) are shown by Fig. 6 and Fig.7.

Fig.6 shows the characteristics when the low speed and light load torque are applied to the motor. Fig.7 shows the characteristics when the high speed and lightload torque are applied to the motor.

It is demonstrated by simulations that the motor can generate the output torque quickly, stably, and accurately using the torque cotroller and also high-efficiency control was obtained by proposed method.

TABLE 1
SPECIFICATIONS OF INDUCTION MOTOR

maximum output	30kw
number of poles	4
maximum voltage	300V
base velocity	650rpm
maximum velocity	1850rpm
primary resistance R_1	0.120 Ω
secondary resistance R_2	0.072 Ω
core loss resistance R_{mo}	0.012 Ω
leakage inductance $L\sigma$	2.693mH
mutual inductance M_1	26.807mH

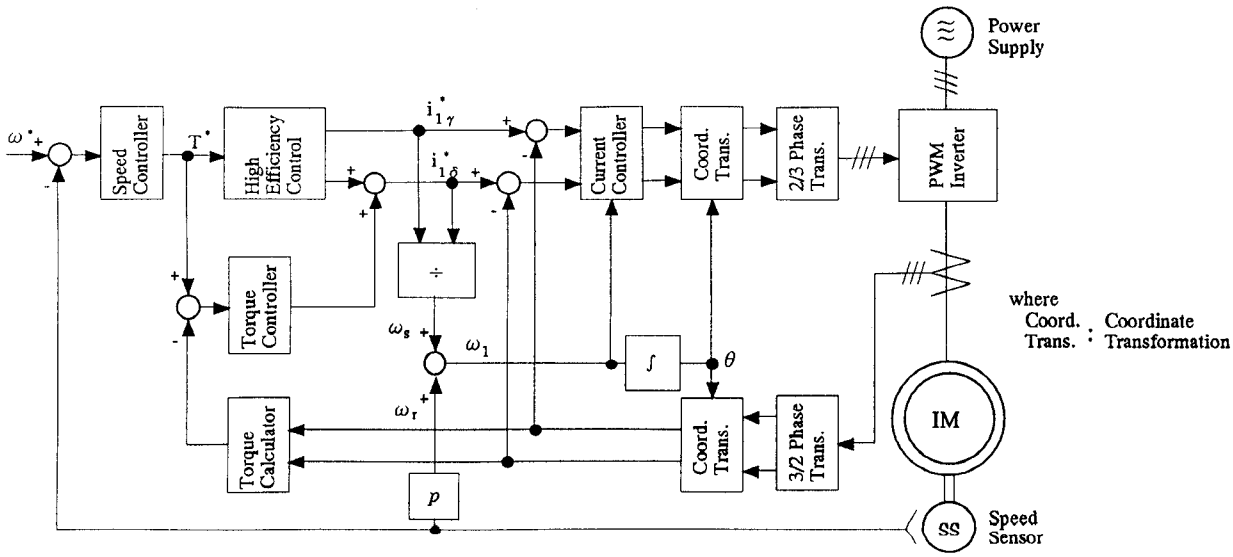

Fig.4 Block diagram of a speed control system with the proposed high-efficiency control.

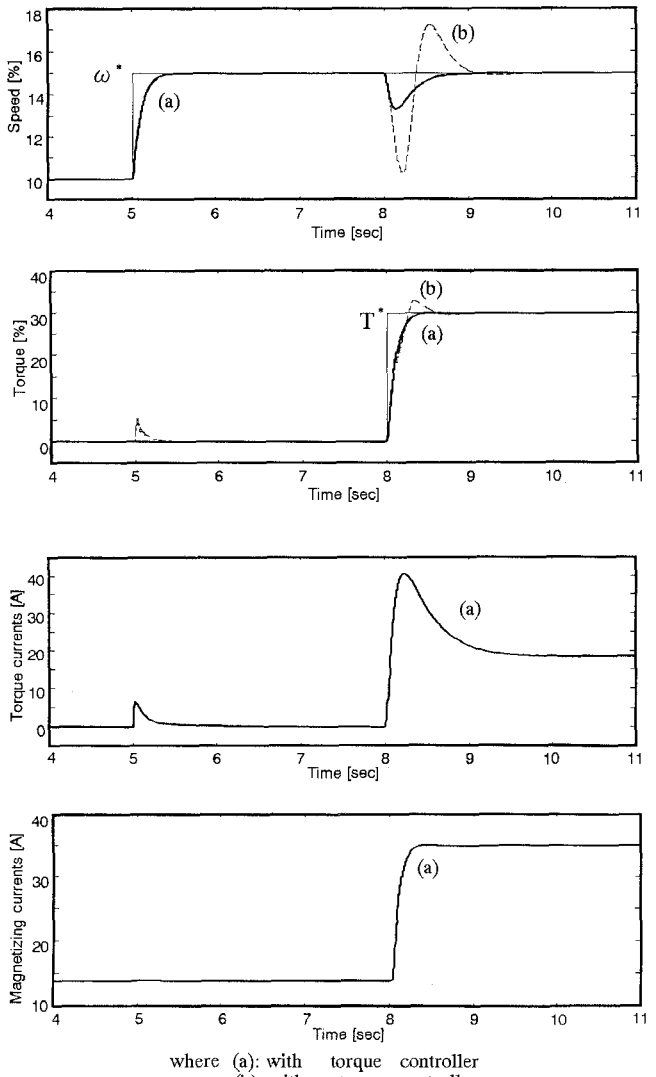

Fig.6 Response when speed reference is10% and load is 30%.

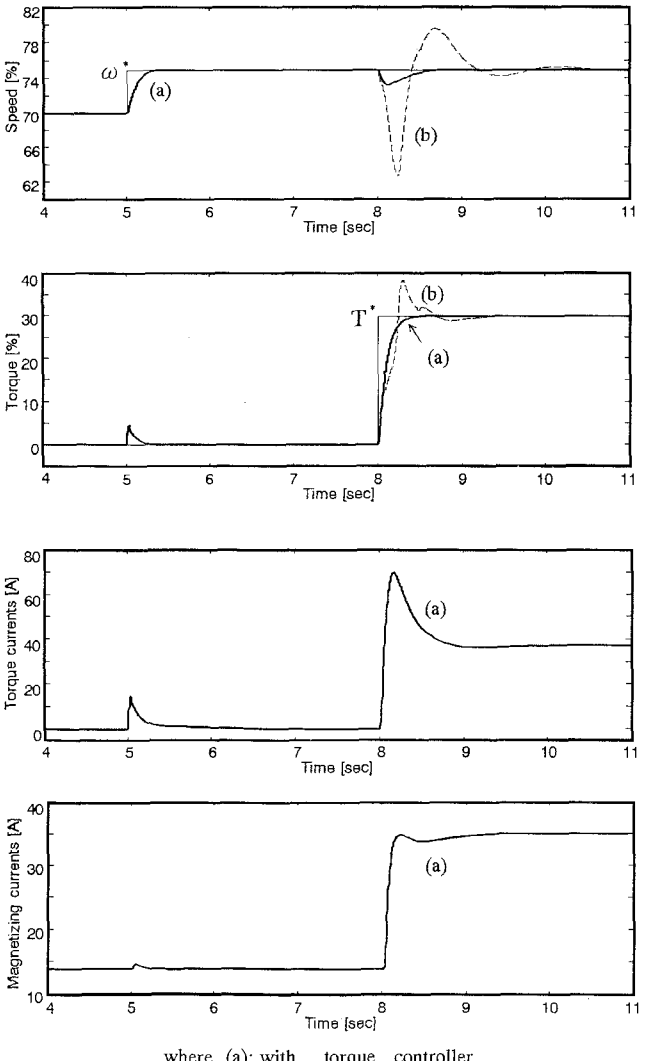

Fig.7 Response when speed reference is70% and load is 30%.

IV. Conclusions

This paper proposed a simple speed control method with a torque controller suitable for industrial applications and electric vehicles. It could make it possible to stably, accurately and efficiently generate the motor torque. Several results were obtained through the theoretical consideration and the simulations.

(1) The torque controller can be simply equiped with a conventional vector control scheme.

(2) The torque controller generates the torque deviation which turns to be an additional torque current reference so that the assumed torque agrees with the torque reference using the secondary magnetic flux estimated from the detected magnetizing current.

References

[1] Nobuyoshi Mutoh, "A Torque Controller suitable for Electric Vehicles", IPEC-Yokohama'95, pp.1089-1095, 1995.

[2] Alexander Kusko, " Control Means for Minimization of Losses in AC and DC Motor Drives ", IEEE Trans. Ind. Appl.,vol.IA-19, pp.561-570, July/August 1983.

[3] M.Azizur Rahman and Ruifeng Qin, " A Permanent Magnet Hysteresis Hybird Synchronous Motor for Electric Vehicles ", IEEE Trans. Ind. Elec., vol.44, pp.46-53, February 1997.

[4] Mehrdad Ehsani and Khwaja M. Rahman, " Propulsion System Design of Electric and Hybrid Vehicles ", IEEE Trans. Ind. Elec. vol.44, pp.46-53, February 1997.

[5] Kenji Yamada and katsuyuki Watanbe, " An Efficiency Maximizing Induction Motor Drive System for Transmissionless Electric Vehicle ", IEVS-13 Osaka, JAPAN, 1996.

[6] Hirohisa Yamamura and Hiroshi Katada, "AC Drive System for Electric Vehicles ", Hitachi Review, vol.44, No.3, 1995.

[7] G.O. Garcia and J.C. Mendes Luis, " Fast Efficiency Maximizer for Adjustable Speed Induction Motor drive ", IECON'92, pp.37, November 9-13 1992.

[8] Hisao Kubota and kouki Matsuse, " Compensation for core loss of adaptive flux observer based field oriented induction motor drives ", IECON'92, pp.67, November 9-13 1992.

[9] T.Ohmae, T.Sukegawa and K.kamiyama, " Application trends in AC motor drives ", IECON'92, pp.31, November 9-13 1992.

Vector Control of an Induction Motor for the Field Weakening Region with Tuning of the Magnetizing Inductance

D. H. Choi* M. H. Shin* T. K. Lee S. B. Cho*** D. S. Hyun***

*Dept. of Electrical Eng., Hanyang University
Seongdong-ku, Seoul, 133-791, KOREA
Phone : +82-2-290-0341, Fax : +82-2-297-1569
Email : dshyun@hyunp1.hanyang.ac.kr

** Dept. of Control & Instrumentation of Eng.
Ansung National Univ.

***Dept. of Electric
Doowon Technical College

Abstract - **Above base speed, the flux level must be reduced in inverse proportion to the actual rotor speed. Then the magnetizing inductance is varied by rotor flux reference. In this region, if there is incorrect magnetizing inductance value in the vector controller, it is difficult to properly obtain the magnetizing current and the decoupling terms. The improper magnetizing current decreases the voltage margin, so that makes torque response unstable. Also, improper decoupling terms make voltage reference incorrect. The torques in the stator and rotor flux reference frame have been calculated. If the magnetizing inductance is correct, two torque values are same. Therefore, if two values are different, the controller has different magnetizing inductance from that of the actual motor. This paper presents the new tuning scheme of the magnetizing inductance by comparing two torque values. Those rotor time constant tuning and magnetizing inductance tuning scheme make the vector control system properly operating on the wide speed range. Especially, the improved system performance in the field weakening region by applying this scheme is illustrated. Computer simulation and experimental results demonstrate the efficacy of the proposed scheme.**

I. INTRODUCTION

For the operation of the spindle drive, traction, electric vehicle and so on, there is the necessity of the control scheme for field weakening region, above base speed. In this region the increased speed voltage makes the voltage margin reduced, then deterioration of the torque response is unavoidable. For vector control system of an induction motor, the control algorithm needs parameters of the motor that are obtained from manufacturer or several machine tests. But parameters change from initial value according to the operating condition, therefore the primary factor of the performance degradation is the variation of parameters [1],[2]. In case of indirect vector control, the controller requires correct slip constant that includes the rotor time constant. The rotor time constant is composed of the rotor resistance and the rotor inductance, the former is varied with temperature and the latter with the flux level. The variation of the rotor time constant makes the entire system performance deteriorated. The tuning of the rotor time constant has been studied during decades. The scheme used Model Reference Adaptive Control(MRAC) that directly control the slip constant using the difference between torque model and real torque has been proposed. But the initial parameters that established the torque model must be correctly calculated [3]. In spite of the constant flux level is maintained for fast torque response. Above base speed, the flux level must decreased, then the dynamic performance of the controller is deteriorated. Therefore, the improvement of the system performance and the maximum torque operation has been studied [4]-[8]. The conventional method that is to vary the rotor flux reference in proportion to the inverse of the rotor speed has the limitation that caused by the neglecting the dynamics of the rotor circuit. To solve this problem, the modeling of the rotor circuit to predict the induced flux transient was suggested. The flux calculation correct the slip gain and command the correct field current. But the machine model is complicated because of need of the correct parameters that are inductance ratios, stator resistance, and derivatives of stator currents [4]. In state space model, the torque constant is determined by rotor flux and the rotor time constant. Therefore the rotor flux observer that obtains the rotor flux and determine the rotor time constant was suggested. This method requires motor parameters and needs the consideration of the dynamic interaction of flux, slip, and voltage margin [5]. From MRAC [3], the tuning scheme that doesn't need the initial parameters was suggested [6]. The maximum torque operation method using limits of the current and the voltage in which the proper stator current vector and base speed are selected was suggested. Unfortunately, that includes several inner control loops and the implementation is complicate [7]. A stator flux controller was proposed as an alternate to the indirect rotor flux controller. This direct control is less sensitive to parameter variation and does not require velocity or position feedback. However in constant torque region, the controller is affected by the variation of the stator resistance and the system performance is deteriorated compared with indirect controller [9],[10]. In field weakening region, the flux reference is reduced, then the magnetizing inductance increase. In this paper, the variation of the magnetizing inductance and the effect of that are demonstrated. And the tuning algorithms of the magnetizing inductance and the rotor time constant are proposed.

0-7803-3823-5/97/$10.00© 1997 IEEE

II. VARIATION OF THE MAGNETIZING INDUCTANCE

In field-weakening operation, because of the power limit, the flux reference must be decreased inversely proportional to the rotor speed. If the flux reference is decreased on the B-H curve, the operating point moves toward the origin. Therefore, the magnetizing inductance, the slope of B-H curve, is increased [11],[12].

The aspect of the variation of the magnetizing inductance to the flux reference is shown in Fig. 1.

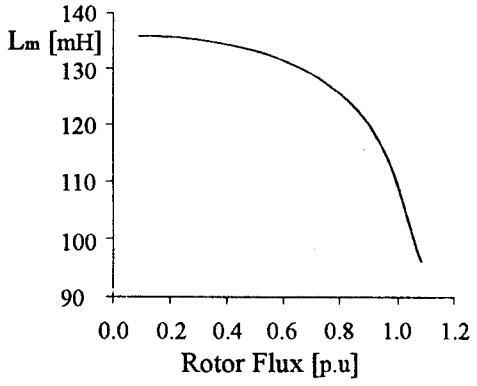

Fig. 1. Variation of the magnetizing inductance.

In Fig. 1, as the speed is increased, the flux reference is decreased and the magnetizing inductance is increased.

III. EFFECT TO THE SYSTEM PERFORMANCE

To be short, the effects of the varying magnetizing inductance is subdivided by three :

- *The establishment of the magnetizing current*
- *The variation of the decoupling terms*
- *The error of the rotor-flux position information*

In case of the magnetizing inductance of actual motor(L_m) is lager than the magnetizing inductance of controller(L_m*), the magnetizing current reference that is obtained by dividing the flux reference by the magnetizing inductance($i_{ds}^* = \lambda_{ref}^* / L_m^*$) is larger than that of actual magnetizing current. So, the motor is overexcited.

To confirm this over-excitation problem, the stator voltage equation developed two-phase form(d-q axis) is followed.

$$V_{ds} = (R_s + \sigma L_s p) i_{ds} + \frac{L_m}{L_r} p\lambda_{dr} - \omega_e (\sigma L_s i_{qs} + \frac{L_m}{L_r} \lambda_{qr}) \quad (1\text{-a})$$

$$V_{qs} = (R_s + \sigma L_s p) i_{qs} + \frac{L_m}{L_r} p\lambda_{qr} + \omega_e (\sigma L_s i_{ds} + \frac{L_m}{L_r} \lambda_{dr}) \quad (1\text{-b})$$

In steady state,

$$p\lambda_{dr} = i_{dr} = \lambda_{qr} = 0 \quad (2)$$

The substitution of steady state condition(2) into the stator voltage equation(1) and simplification of the resulting equations produces both the familiar voltage equations.

$$V_{ds} = (R_s + \sigma L_s p) i_{ds} - \omega_e \sigma L_s i_{qs} \quad (3\text{-a})$$

$$V_{qs} = (R_s + \sigma L_s p) i_{qs} + \omega_e L_s i_{ds} \quad (3\text{-b})$$

where, $\sigma = 1 - \frac{L_m^2}{L_s L_r}$

First, if the magnetizing current(i_{ds}) is actually increased and actual motor magnetizing inductance(L_m) is increased, the latter term of Eq. (3-b) is increased considerably because the rotor speed is very high. Therefore, the voltage margin that is known as the derivative of torque component current(pi_{qs}) is so reduced and it is difficult to control torque smoothly. Second, decoupling terms ,that are the latter terms of the right side in Eq. (3) for decoupling control, are wrong determined. Therefore, gating signal into inverter controller is incorrect, and inverter can't operate properly. Third, the position information of rotor flux is extremely important for indirect vector control system. That information needs rotor time constant and rotor time constant is closely related to the magnetizing inductance in field weakening operation. If the controller has incorrect magnetizing inductance value, the fatal error in system performance is unavoidable.

Therefore, following tuning scheme of the magnetizing inductance is presented.

IV. PROPOSED TUNING ALGORITHM OF THE MAGNETIZING INDUCTANCE

The torque in stationary reference frame and that in rotating reference frame are calculated. The former doesn't include the magnetizing inductance and the latter includes that.

♦ *Torque in stator flux reference frame*

$$T_e = \frac{3}{2}\frac{P}{2} \lambda_{\alpha\beta s} \times i_{\alpha\beta s} = k(\lambda_{\alpha s} i_{\beta s} - \lambda_{\beta s} i_{\alpha s}) \quad (4)$$

where, $k = \frac{3}{2}\frac{P}{2}$

In Eq. (4), using following Eq. (5), stator flux is obtained.

$$\lambda_{\alpha s} = \int (V_{\alpha s} - R_s i_{\alpha s}) dt \quad (5\text{-a})$$

$$\lambda_{\beta s} = \int (V_{\beta s} - R_s i_{\beta s}) dt \quad (5\text{-b})$$

The parameter in Eq. (5) is only the stator resistance. But, in high speed range the stator resistance can be neglected because of high speed emf. Therefore, the torque in stationary reference frame (Eq. (4)) is not affected by the variation of parameters and doesn't have the establishment error of the magnetizing inductance.

- *Torque in rotor flux reference frame*

$$T_e = \frac{3}{2}\frac{P}{2}\frac{L_m}{L_r}\lambda_{dr} i_{qs} = k\frac{L_m^2}{L_r} i_{ds} i_{qs} \approx k L_m i_{ds} i_{qs} \quad (6)$$

where, $k = \frac{3}{2}\frac{P}{2}$

Because it is assumed that $L_m/L_r \approx 1$, the torque in rotating reference frame is affected so much by the magnetizing inductance.

In field weakening region, the voltage margin is so small that the actual torque-component current(i_{qs}) can't follow the reference of that (i_{qs}^*).

If the actual magnetizing inductance is increased, the establishment error of magnetizing current(i_{ds}) limits the torque-component current(i_{qs}). Therefore, the torque in Eq. (6) is severely affected by the error of the magnetizing inductance.

The difference between the torque in stationary reference frame and that in rotating reference frame is confirmed as the error of the magnetizing inductance.

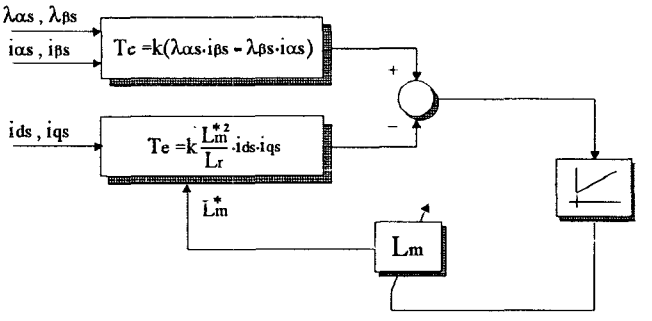

Fig. 2. Tuning scheme of the magnetizing inductance.

As shown in Fig. 2, in case of the flux reference is varied in field weakening region and the magnetizing inductance is increased, the tuning scheme is implemented in form of PI controller which has the input, that is the difference between two torque values.

V. PRECONDITION OF THE PROPOSED SCHEME

But, the torque in Eq. (6) has precondition that the rotor flux in quadrature axis must be zero, i.e. the controller must have exact rotor time constant.

The rotor time constant is mainly affected by the rotor resistance in constant torque region but is affected by not so much the rotor resistance as the magnetizing inductance in field weakening region.

Above all, it is necessary that the tuning scheme of the rotor time constant available in whole speed range.

VI. TUNING ALGORITHM OF THE ROTOR TIME CONSTANT

If the rotor time constant is established correctly, the tangent torque angle in stationary and rotating reference frame are same.

Two tangent values are calculated following equations.

$$\tan\delta^e = \frac{i_{qs}}{i_{ds}} = \omega_{sl}^* T_r^* \quad (7)$$

$$\tan\delta^s = \frac{\lambda_{\alpha r} i_{\beta s} - \lambda_{\beta r} i_{\alpha s}}{\lambda_{\alpha r} i_{\alpha s} + \lambda_{\beta r} i_{\beta s}} \quad (8)$$

The tuning process is followed.

$\tan\delta^e < \tan\delta^s \rightarrow T_r^*$ is increased

$\tan\delta^e > \tan\delta^s \rightarrow T_r^*$ is decreased

$\tan\delta^e = \tan\delta^s \rightarrow T_r^*$ is correctly established

The tuning scheme of the rotor time constant is shown in Fig. 3. By using this scheme the controller has the correct rotor time constant in whole speed range.

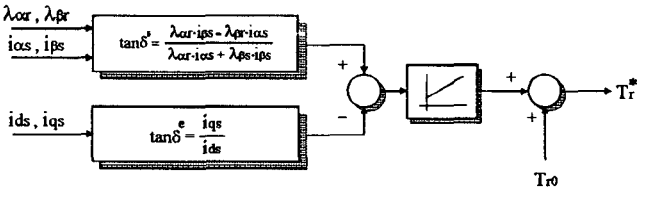

Fig. 3. Tuning scheme of the rotor time constant.

VII. PROPOSED SCHEME WITH TWO TUNING ALGORITHMS

However, in spite of the correct time constant if the controller has improper magnetizing inductance, the voltage margin is decreased severely.

Following simulation result shows the variation of the voltage margin to the rotor speed.

In Fig. 4, the base speed is *1500[rpm]* and the flux reference starts to decreased at *1500[rpm]*.

The Lm is the constant value like that in the constant torque region, but the Lm* is adjusted value that increases according to the decrease of the flux reference. The adjustment of the magnetizing inductance according to the rotor speed makes voltage margin sufficient.

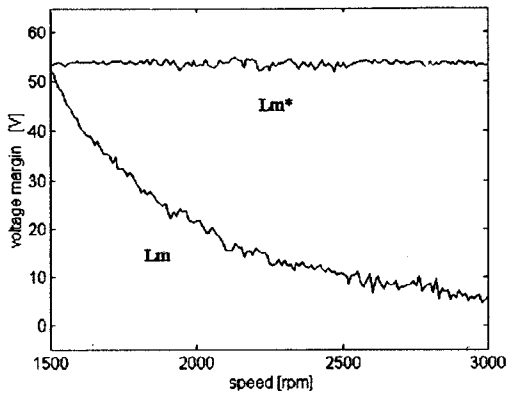

Fig. 4. Voltage margin to the rotor speed(*10rpm* interval).
Lm : not considering the variation
Lm* : considering the variation

The proper establishment of the magnetizing inductance yields the fast torque response and the correct *q*-axis current. Two tuning schemes of the rotor time constant and the magnetizing inductance have been applied simultaneously. The flow chart is followed, Fig. 5.

First, the rotor time constant has been correctly established by upper tuning scheme and the tuning scheme of the magnetizing inductance is operated. When adjusting the magnetizing inductance, the rotor time constant in the controller is varied. Therefore two scheme is operated simultaneously. The tuning process is finished when the error of the magnetizing inductance is converged to zero.

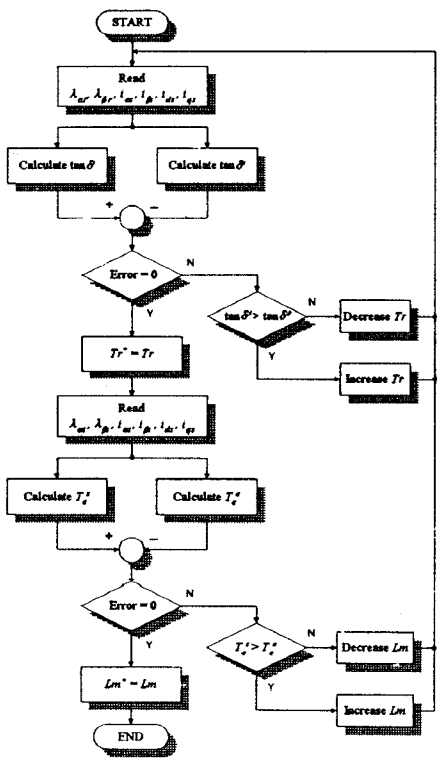

Fig. 5. Flow chart of tuning schemes.

The proposed entire block diagram of the proposed scheme is followed.

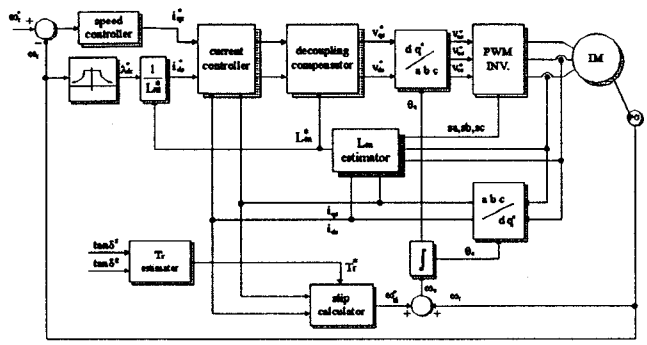

Fig. 6. Proposed block diagram.

As mentioned above, the tuned magnetizing inductance is applied the magnetizing current block and the decoupling block.

VIII. SIMULATION AND EXPERIMENTAL RESULTS

The simulation results are shown in Fig. 7, 8, and 9.

This tuning schemes of parameters are well performed any speed reference and any torque reference.

Fig. 7, Fig. 8, and Fig. 9 are simulation results when *2000[rpm], 2[Nm], 3[Nm]*, and *3000[rpm], 3[Nm]* respectively.

After tuning of the rotor time constant, the two torque values are different that is the establishment error of the magnetizing inductance.

The torque in stationary reference frame is not affected by the variation of the magnetizing inductance. As the difference between two values has diminished, the magnetizing inductance has been being correctly established. Therefore, actual q-axis voltage margin has been sufficiently large and the q-axis stator current, torque component current, has become stable.

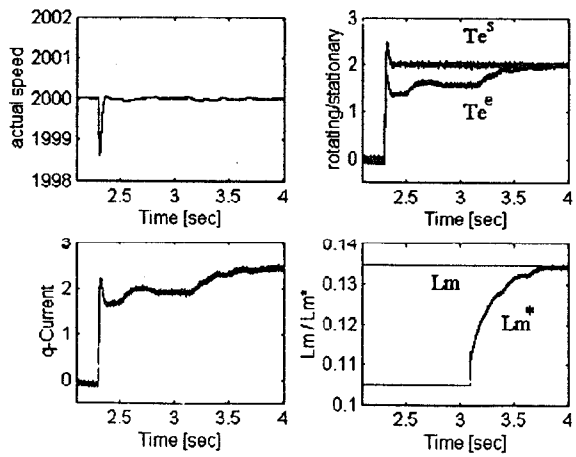

Fig. 7. Simulation results (2000[rpm], 2[Nm]).

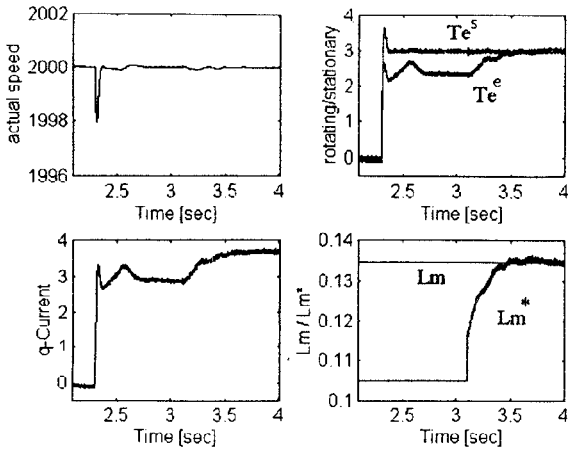

Fig. 8. Simulation results (2000[rpm], 3[Nm]).

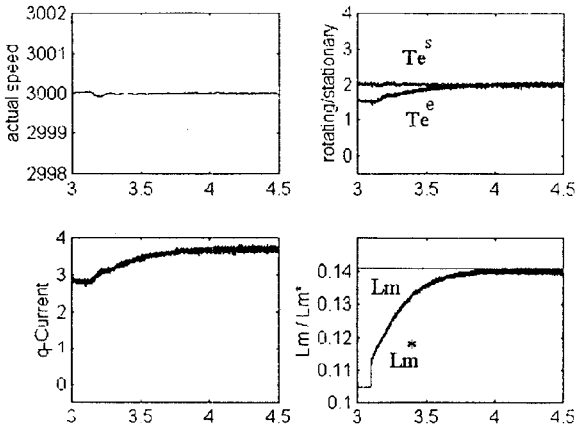

Fig. 9. Simulation results (3000[rpm], 2[Nm]).

To demonstrate the operation and the performance of the proposed control scheme, an induction motor with *5kVA IGBT* inverter was investigated.

Parameters of the drive are presented in Table 1.

Unit	Parameter	Value
Inverter	DC link voltage	300 [V]
	switching frequency	10 [kHz]
Motor	rated power	2.2 [Kw]
	stator resistance	1.26 [Ω]
	rotor resistance	1.28 [Ω]
	magnetizing inductance	112 [mH]
	# of pole pairs	2

Table 1. Inverter and motor capacity.

The main CPU of the drive is *TMS320C31* and the sampling time of the current controller and the speed controller are *100 [μs], 1 [ms]* respectively.

Fig. 10, 11 show the actual speed, the flux-component current, the reference and actual value of the torque-component current when the drive is operated from *0[rpm]* to *3000[rpm]* with the *1250[rpm]*, base speed. Fig. 10 demonstrates the conventional scheme and Fig. 11 does the proposed scheme.

In the conventional scheme, the drive can't operate properly according to the variation of the magnetizing inductance. Therefore, the flux-component current is larger than that of the proposed scheme in the field-weakening region. In the proposed scheme, the drive is well operated according to the variation of that. The flux-component current is smaller than that of the conventional scheme. Therefore, the decoupling term of the q-axis stator voltage is decreased, and voltage margin is enlarged. Increased voltage margin makes speed response faster than that of the conventional scheme.

When the base speed is *1500[rpm]*, the waveforms are shown in Fig. 12, 13. Fig. 14 shows the difference between speed waveforms.

The magnetizing inductance has varied from 112[mH] to about 140[mH] and considering that variation, the speed characteristics improves about 30%.

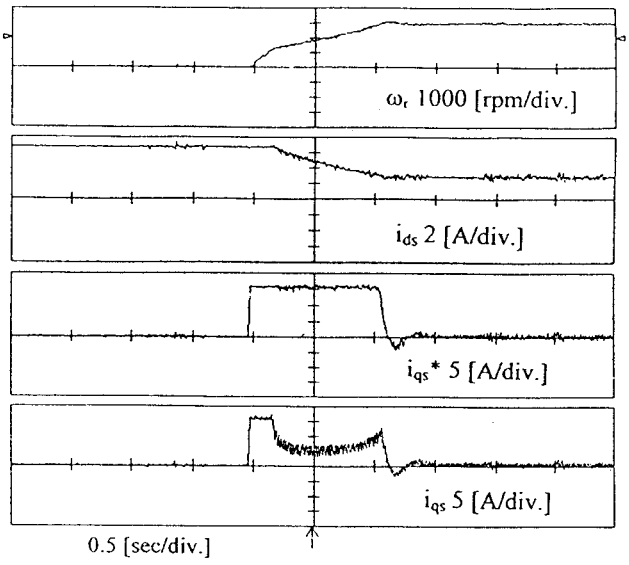

Fig. 10. Experimental results of the conventional scheme (0[rpm]~3000[rpm]).

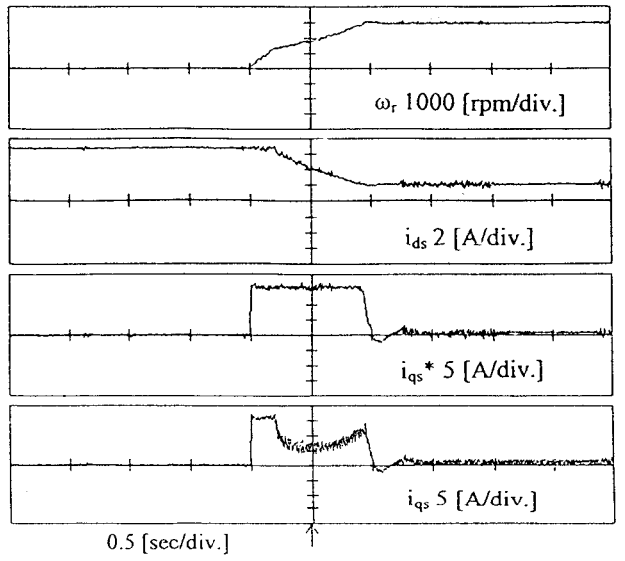

Fig. 11. Experimental results of the proposed scheme (0[rpm]~3000[rpm]).

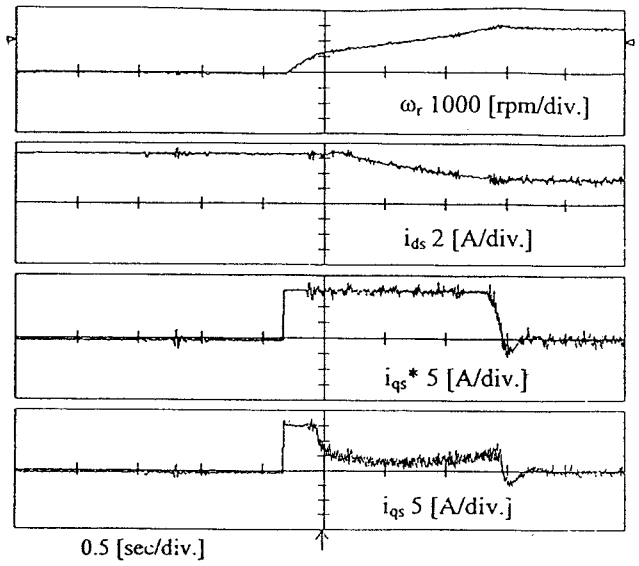

Fig. 12. Experimental results of the conventional scheme (0[rpm]~3000[rpm]).

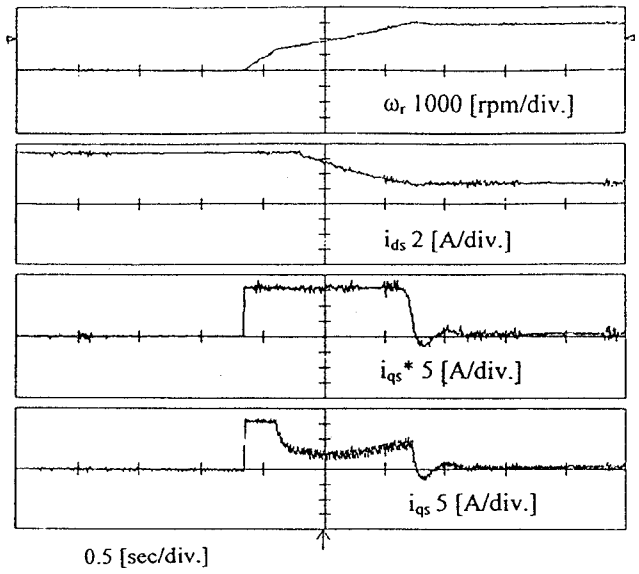

Fig. 13. Experimental results of the proposed scheme (0[rpm]~3000[rpm]).

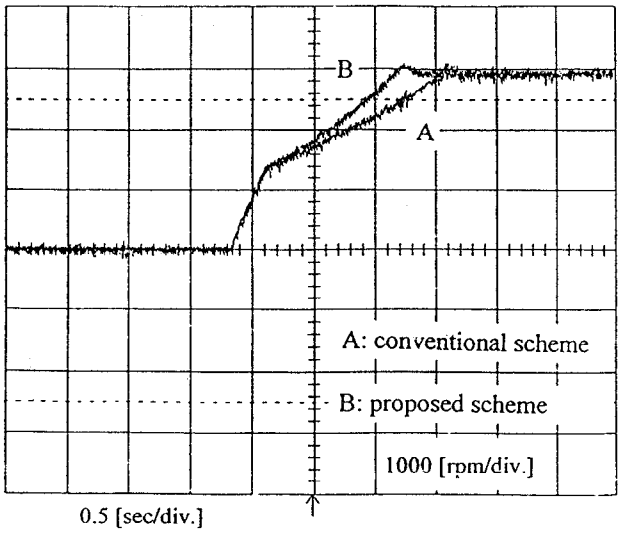

Fig. 14. Speed comparison between conventional and proposed scheme.

IX. CONCLUSION

In vector control system, the parameter variation deteriorates the system dynamics. Especially, the rotor time constant is seriously affected the position information of the rotor flux and the overall system dynamics relies absolutely on the rotor time constant in the indirect vector control system. In the field weakening region, the magnetizing inductance is affected the voltage margin and the speed characteristics.

In this paper, using the tangent torque angles in stationary frame and in rotating frame, the rotor time constant is established correctly in the whole speed range. In the field weakening region, using the torque values in the stator flux frame and in the rotor flux frame, the magnetizing inductance is tuned properly.

Therefore, two tuning schemes make the system dynamics improved.

REFERENCE

[1] F. Blaschke, "The Principle of Field Orientation as applied to the New Transvector Closed Loop Control System for Rotating Machines," *Siemens Rev.*, Vol. 39, no. 5, pp. 217-220, 1972.

[2] K. Ohnishi, H. Suzuki, and K. Miyachi, "Decoupling Control of Secondary Flux and Secondary Current in Induction Motor Drive with Controlled Voltage Source and its comparison with Volts/Hertz," *Conf. Rec. Annu. Meet. IEEE Ind. Appl. Soc.*, pp. 678-685, 1982.

[3] R. D. Lorenz, D. B. Lawson, "A Simplified Approach to Continuous, On-line Tuning of Field Oriented Induction Machine Drives," *Conf. Rec. Annu. Meet. IEEE Ind. Appl. Soc.*, pp. 444-449, 1988.

[4] R. Jotten, H. Schierling, "Control of the Induction Machine in the Field Weakening Range," *Proc. IFAC* pp. 297-304, 1983.

[5] R. D. Lorenz, D. B. Lawson, "Flux and Torque Decoupling Control for Field Weakened Operation of Field Oriented Induction Machine Drives," *IEEE-Trans. Ind. App.*, Vol. 26, No.2, pp. 290-295, 1990.

[6] R. J. Kerkman, T. M. Rowan, D. Leggate, "Indirect Field-Oriented Control of an Induction Motor in the Field-Weakening Region," *IEEE-Trans. Ind. App.*, Vol. 28, No.4, pp. 850-857, 1992.

[7] S. H. Kim, S. K. Sul, "Maximum Torque Control of an Induction Machine in the Field Weakening Region," *IEEE-Trans. Ind. App.*, Vol. 31, No.4, pp. 787-794, 1995.

[8] A. Bunte et al, "Field Weakening of Induction Motors In a Very Wide Region with Regard to Parameter Uncertainties," *PESC Conf. Rec.*, pp. 944-950, 1996.

[9] X. Xu, R. D. Doncker, D. W. Novotny, "Stator Flux Orientation Control of Induction Machine in the Field Weakening Region," *Conf. Rec. Annu. Meet. IEEE Ind. Appl. Soc.*, pp. 437-443, 1988.

[10] X. Xu, D. W. Novotny, "Selection of the Flux Reference for Induction Machine Drives in the Field Weakening Region," *IEEE-Trans. Ind. App.*, Vol. 28, No.6, pp. 1353-1358, 1992.

[11] K. Matsuse, H. Kubota, "Deadbeat Flux Level Control of High Power Saturated Induction Servo Motor Using Rotor Flux Observer," *Conf. Rec. Annu. Meet. IEEE Ind. Appl. Soc.*, pp. 409-414, 1991.

[12] N. R. Klaes, "Parameter Identification of an Induction Machine with Regard to Dependencies on Saturation," *IEEE-Trans. Ind. App.*, Vol. 29, No.6, pp. 1135-1140, 1993.

[13] X. Xu, R. D. Doncker, D. W. Novotny, "A Stator Flux Oriented Induction Machine Drive," *PESC Conf. Rec.*, pp. 870-876, 1988.

[14] S. B. Cho, D. S. Hyun, "A Robust Indirect Vector Control for the Rotor Time Constant Variation of Induction Machines," *IEEE IECON*, Vol. 2, pp. 1240-1245, 1996.

Precise Torque Control of Induction Motor with On-Line Parameter Identification in Consideration of Core Loss

Toshihiko Noguchi [1], Paiboon Nakmahachalasint [2], and Narin Watanakul [2]

[1] : Nagaoka University of Technology
1603-1 Kamitomioka, Nagaoka 940-21, JAPAN
Phone : +81-258-46-6000, Fax : +81-258-46-6506
E-mail : omom@voscc.nagaokaut.ac.jp

[2] : Thammasat University
Khlong-Luang, Pathum-Thani 12121, THAILAND
Phone : +66-2-516-4551, Fax : +66-2-516-0974
E-mail : paiboon@ipied.tu.ac.th

Abstract — **This paper describes improved torque control of an induction motor. The control is based on direct field orientation with a rotor flux simulator, and motor parameters in the simulator are estimated by a robust identifier with no sensitivity to the stator resistance. Owing to model mismatch in the controller caused by the equivalent core loss resistance, however, both the field orientation and the parameter identification cannot be carried out perfectly, which results in degradation of torque control performance. In order to improve accuracy of the output torque, the proposed system employs a modified machine model taking the core loss into consideration. Consequently, it has been verified through computer simulations that the technique achieves high precision in torque control within a few percent errors.**

I. Introduction

The principle of field-oriented control has inherently been derived on the assumption that no core loss is in the induction motor model. In recent years, some papers have reported that the core loss detrimentally affects the field orientation, especially torque control accuracy, unless the core loss are taken into consideration [1]-[3]. However, there have probably been few reports that dealt with direct field-oriented control (flux-feedback field orientation) with on-line identification of the motor parameters incorporating the core loss. In order to achieve highly precise torque control by the direct field orientation, it is substantial to comprehensively modify not only the field-oriented controller but also the parameter identifier by taking the core loss into consideration. This paper describes a quite simplified technique for improvement of torque control accuracy which is based on the above modified system, and shows possibility of reducing the output torque error down to less than a few percent through computer simulations.

II. Basic Concept of Direct Field-Oriented Control and Parameter Identification

Fig. 1 and 2 show schematic diagrams of the direct field-oriented controller and the on-line parameter identifier respectively [4]. The direct field orientation is performed on the basis of the following equations :

$$\boldsymbol{i}_{1dq}{}^{*} = i_{1d}{}^{*} + \mathrm{j}i_{1q}{}^{*} = G_{AFR}\left\{|\psi_2|^{*} - |\hat{\psi}_2|\right\} + \mathrm{j}\frac{L_{22}}{M}\frac{T^{*}}{|\psi_2|^{*}}, \quad (1)$$

$$\hat{\boldsymbol{\psi}}_{2\alpha\beta} = \frac{\hat{M}}{1+(\mathrm{p}-\mathrm{j}\omega_m)\hat{\tau}_2}\boldsymbol{i}_{1\alpha\beta}, \quad (2)$$

$$\hat{\boldsymbol{i}}_{1dq} = \frac{\overline{\hat{\boldsymbol{\psi}}_{2\alpha\beta}}}{|\hat{\psi}_2|}\boldsymbol{i}_{1\alpha\beta} \text{ and} \quad (3)$$

$$\boldsymbol{v}_{1\alpha\beta}{}^{*} = \frac{\hat{\boldsymbol{\psi}}_{2\alpha\beta}}{|\hat{\psi}_2|}\boldsymbol{v}_{1dq}{}^{*}, \quad (4)$$

where the motor variables and parameters are defined as follows :

$\boldsymbol{i}_1$: stator current vector,
$\boldsymbol{v}_1$: stator voltage vector,
$\boldsymbol{\psi}_2$: rotor flux vector,
T : output torque,
ω_m : rotor speed,
τ_2 : rotor time constant,
L_{22} : rotor inductance,
M : magnetizing inductance,
ℓ : leakage inductance,

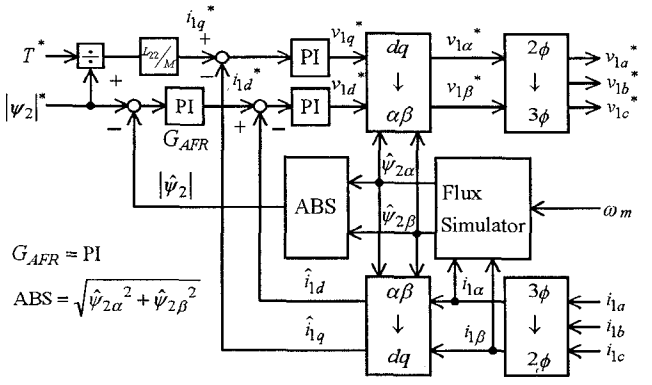

(a) Current controller.

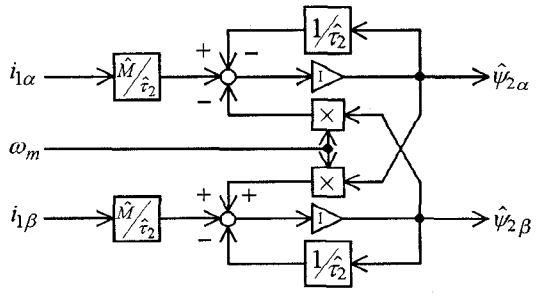

(b) Rotor flux simulator.

Fig. 1. Basic configuration of direct field-oriented controller.

G_{AFR} : transfer function (PI) of flux regulator,

p : differential operator,

j : imaginary unit,

x^* : command value of x,

$\hat{x}$: estimated value of x,

$\overline{x}$: complex conjugate of x,

$|x|$: amplitude of x,

$\alpha\beta$: vector on stator ($\alpha-\beta$) coordinates, and

dq : vector on rotor flux ($d-q$) coordinates.

The first equation is regarded as a feedforward block which determines amplitudes of the d-axis and q-axis components of the stator current command. The d-axis current command is obtained from an output of the PI controller with respect to an amplitude of the rotor flux, while the q-axis current command is directly calculated from the torque command. On the other hand, the second equation is a feedback block with respect to the rotor flux, which gives an estimated value of the flux using the motor model with the parameters in order to perform coordinate transformations described by (3) and (4).

The parameter identifier shown in Fig. 2 is based on a model reference adaptive system, which tunes the magnetizing inductance at no load and the rotor time

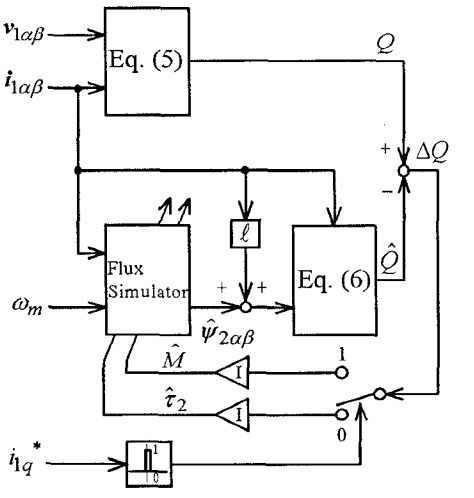

Fig. 2. Parameter identifier with robustness to stator resistance.

constant at loaded condition in the flux simulator by taking advantage of instantaneous reactive power. The instantaneous reactive power which is calculated by the following equation is used as a reference model :

$$Q = \mathrm{Im}\left(\boldsymbol{v}_{1\alpha\beta}\overline{\boldsymbol{i}_{1\alpha\beta}}\right). \tag{5}$$

On the other hand, the following equation gives a mathematical model of the instantaneous reactive power with respect to the estimated rotor flux and the stator current :

$$\hat{Q} = \mathrm{Im}\left(\frac{M}{L_{22}}\mathrm{p}\hat{\boldsymbol{\psi}}_{2\alpha\beta}\overline{\boldsymbol{i}_{1\alpha\beta}} + \ell\mathrm{p}\boldsymbol{i}_{1\alpha\beta}\overline{\boldsymbol{i}_{1\alpha\beta}}\right). \tag{6}$$

Since both of the above equations have no influence of the stator resistance, the configuration of Fig. 2 enables the identifier to achieve robust estimation of the motor parameters in (2) against the stator resistance. The core loss in the induction motor, however, has not been incorporated in the control and identification algorithms described above. Owing to the model mismatch caused by the core loss, both the field orientation and the parameter identification cannot be carried out perfectly, which results in degradation of torque control accuracy.

III. Equivalent Core Loss Resistance and Its Influence on Torque Control

A. Experimental Measurement of Motor Parameters

Since the core loss of the motor has been taken into consideration in neither the control nor the identification, the output torque error of not a few percent can probably remain owing to the model mismatch on the field

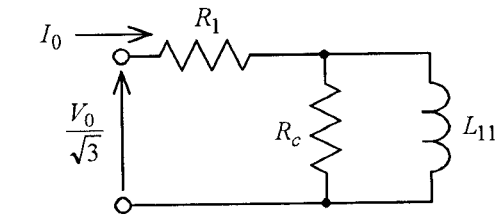

(a) Equivalent circuit at no load.

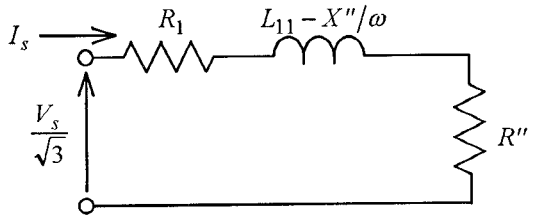

(b) Equivalent circuit with rotor locked.

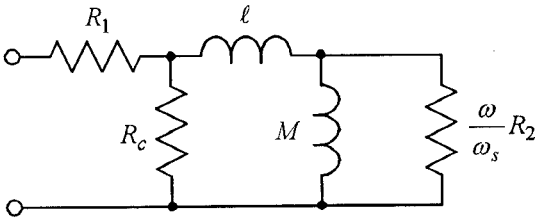

(c) Whole equivalent circuit of induction motor.

Fig. 3. Equivalent circuits of induction motor.

orientation. In the section, measurements of the motor parameters are briefly reviewed to clarify some assumptions in the following discussion [5]. The measurements are conducted according to three kinds of experimental tests as usual, dc excitation test, no load test, and lock test. The stator resistance is measured with ease by exciting the motor with a dc voltage source. When the no load test is conducted, several parameters are calculated according to the equivalent circuit shown in Fig. 3(a). In the figure, a resistance which equivalently acts as a dissipater of the core loss is connected in parallel with the stator inductance. The equivalent core loss resistance and the stator inductance can be calculated by the following process :

$$R_c = \frac{R'^2 + X'^2}{R'}, \text{ and} \tag{7a}$$

$$L_{11} = \frac{R'^2 + X'^2}{\omega X'}, \tag{7b}$$

where the intermediate parameters R' and X' are obtained by :

$$R' = \frac{P_0 - P_m}{3I_0^2} - R_1, \text{ and } X' = \sqrt{\frac{V_0^2}{3I_0^2} - \left(\frac{P_0 - P_m}{3I_0^2}\right)^2}.$$

In the above calculation, the motor variables and parameters are defined as follows :

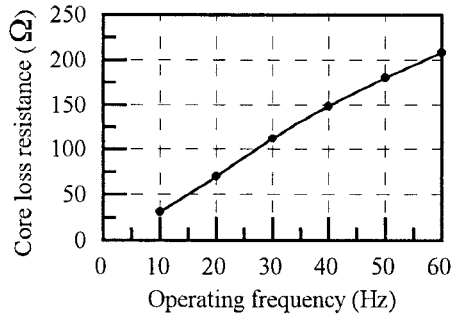

(a) Characteristic for test motor A.

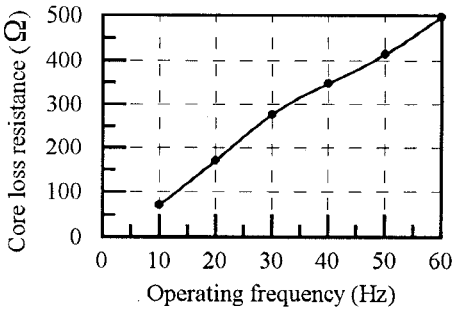

(b) Characteristic for test motor B.

Fig. 4. Characteristics of equivalent core loss resistance.

V_0 : stator terminal voltage (rms) at no load,

I_0 : stator line current (rms) at no load,

P_0 : dissipated power at no load,

P_m : mechanical power loss at no load,

ω : operating angular frequency,

R_1 : stator resistance,

R_c : equivalent core loss resistance, and

L_{11} : stator inductance.

The lock test is subsequently conducted on the basis of the equivalent circuit shown in Fig. 3(b). The rotor resistance, the magnetizing inductance and the leakage inductance are calculated by the following process :

$$R_2 = R''\left(\frac{R''^2 + X''^2}{X''^2}\right), \tag{8a}$$

$$M = \frac{X''}{\omega}\left(\frac{R''^2 + X''^2}{X''^2}\right), \text{ and} \tag{8b}$$

$$\ell = L_{11} - M, \tag{8c}$$

where R'' and X'' are obtained by :

$$R'' = \frac{P_s}{3I_s^2} - R_1, \text{ and } X'' = \omega L_{11} - \sqrt{\frac{V_s^2}{3I_s^2} - \left(\frac{P_s}{3I_s^2}\right)^2}.$$

The variables and the parameters are defined as follows :

V_s : stator terminal voltage (rms) with rotor locked,

I_s : stator line current (rms) with rotor locked,

P_s : dissipated power with rotor locked, and

R_2 : rotor resistance.

TABLE I SPECIFICATIONS OF TEST MOTORS

	Test Motor A	Test Motor B
Rated Power (kW)	1.5	1.5
Rated Torque (Nm)	8.63	10.1
Rated Voltage (V)	180	200
Rated Current (A)	8.1	6.8
Rated Frequency (Hz)	55	50
Rated Speed (rpm)	—	1420
Number of Poles	4	4

Consequently, the equivalent circuit of the induction motor on the whole can be drawn as shown in Fig. 3(c). It should be noted that the leakage inductance on the rotor side has been equivalently canceled out and automatically converted to the stator side when the calculation processes described above are taken.

Fig. 4 shows characteristics of the equivalent core loss resistance which have been measured on the basis of the method. Two kinds of induction motors of which specifications are shown in TABLE I have been tested. In order to make the measurements as accurate as possible, a precise VVVF analog power amplifier which is able to generate pure sinusoidal waveforms has been used. Although the value of the resistance is known to be proportional to the operating frequency to the 1.6 power, the results can be approximated as linear proportional functions of the operating frequency within the range of less than 60Hz. On the assumption, the equivalent core loss resistance is written as follows using a coefficient k_c :

$$R_c \approx k_c \omega . \tag{9}$$

B. Torque control performance without compensation

Fig. 5 shows a characteristic of the control error against the output torque obtained by computer simulations. In the simulations, a model of the test motor A in which the equivalent core loss resistance had been incorporated was employed as a controlled object (cf. Appendix). When the motor is controlled by the system shown in Fig. 1 and 2, which has not introduced the core loss compensation, the error raises up to 7% as the output torque increases. It can be found that the core loss brings not only insufficient output torque but also non-linearity in torque control. The output torque error should be avoided for the applications which require accurate pressure or tension control such as plastic forming or winding machinery. In what follows, a simplified method to overcome the problem is described.

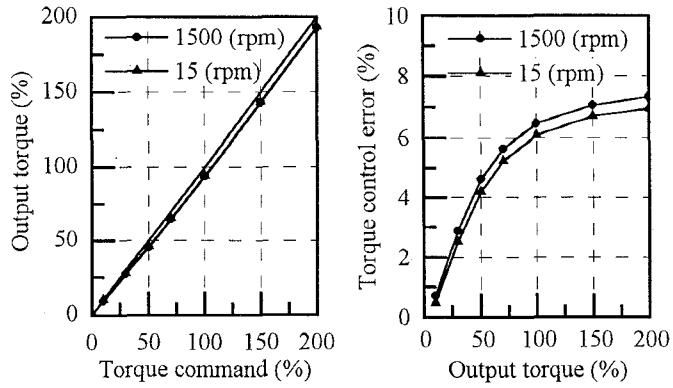

Fig. 5. Characteristic of torque control without core loss compensation.

IV. IMPROVED TORQUE CONTROL IN CONSIDERATION OF EQUIVALENT CORE LOSS RESISTANCE

A. Modified control system with core loss compensation

The direct field-oriented control system is inherently composed of two blocks, the feedforward block and the feedback block, as previously described. The feedforward block converts the torque and flux commands into the d-axis and q-axis current commands, while the feedback block estimates the rotor flux and performs the coordinate transformations to regulate the currents on the rotor flux ($d-q$) coordinates. Since both of the blocks include the motor model, the equivalent core loss resistance has to be considered for both.

In order to make the consideration simpler, it is assumed that the leakage inductance is much smaller than the magnetizing inductance and the influence of the leakage flux on the rotor circuit is negligibly small compared with the main flux in the steady-state equivalent circuit. On the assumption described here, the equivalent core loss resistance can be moved to another position which is in parallel with the magnetizing inductance in the circuit. Then it is possible to suppose that some amount of the q-axis current bypasses the equivalent core loss resistance, which probably causes insufficient torque current to the rotor circuit. Therefore, a current command which corresponds to the bypassing component should be superposed beforehand on the q-axis current command in (1). The current component i_c^* to be superposed for the core loss compensation is derived by simply dividing the steady-state induced voltage by the equivalent core loss

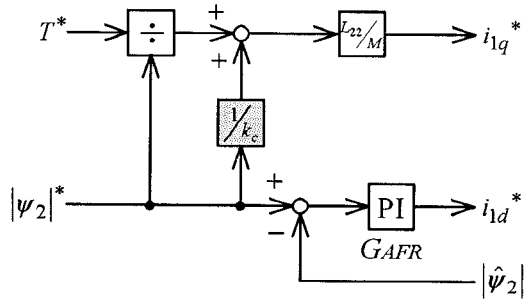

(a) Modified current command calculation block.

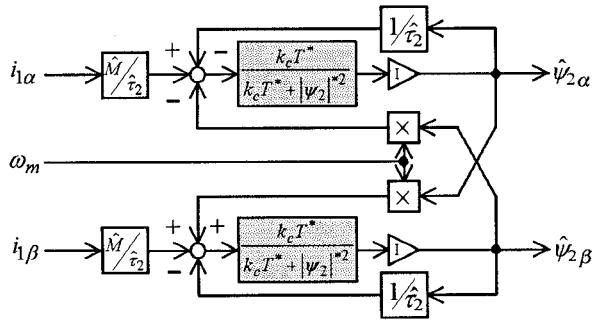

(b) Modified rotor flux simulator block.

Fig. 6. Modified field-oriented control blocks.

resistance on the rotor flux ($d-q$) coordinates as follows :

$$i_c^* = \frac{\omega \frac{L_{22}}{M}|\psi_2|^*}{R_c} = \frac{L_{22}}{M}\frac{|\psi_2|^*}{k_c}. \tag{10}$$

In the above derivation, the frequency characteristic of the equivalent core loss resistance described by (9) is utilized. Consequently, the modified q-axis current command can be obtained from (1) and (10) as :

$$i_{1q}^* = \frac{L_{22}}{M}\left(\frac{T^*}{|\psi_2|^*} + \frac{|\psi_2|^*}{k_c}\right). \tag{11}$$

It can be found that the above equation is identical with the q-axis current command in (1) when k_c is infinite. Since the equivalent core loss resistance diverges in case of the infinite k_c, this condition corresponds to the fact that no core loss has been assumed in the conventional field-oriented controller. The core loss compensation considered in the above discussion is performed on the rotor flux ($d-q$) coordinates with respect to a current amplitude. Unless the rotor flux is correctly estimated taking the core loss into consideration, the feedforward compensation on the coordinates must not be carried out properly. Therefore, it is necessary to investigate the core loss compensation for the feedback block, what is called the rotor flux simulator.

The rotor flux estimation error necessarily occurs in the simulator shown in Fig. 1(b) because of the model

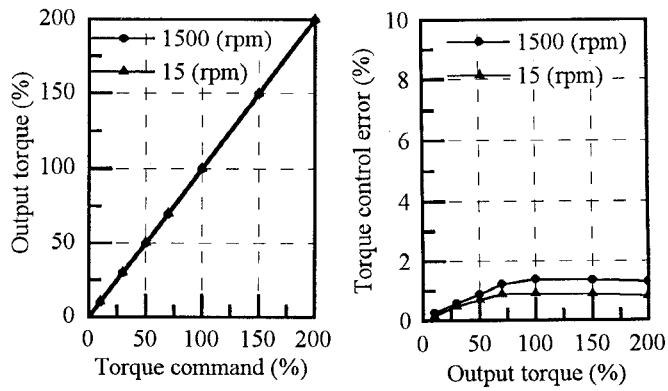

Fig. 7. Characteristic of torque control with core loss compensation.

mismatch owing to the equivalent core loss resistance. On the assumption that the equivalent core loss resistance is in parallel with the magnetizing inductance, it is considered that the resistance has influence on the rotor time constant in the simulator and the rotor time constant is changed by a ratio of $\left(i_{1q}^* + i_c^*\right)/i_{1q}^*$. Substituting i_{1q}^* of (1) and (10) into the ratio, the rotor flux simulator of (2) can be modified as follows :

$$\hat{\psi}_{2\alpha\beta} = \frac{\hat{M}}{1+(\mathrm{p}-\mathrm{j}\omega_m)\hat{\tau}_2\frac{i_{1q}^* + i_c^*}{i_{1q}^*}} i_{1\alpha\beta}$$

$$= \frac{\hat{M}}{1+(\mathrm{p}-\mathrm{j}\omega_m)\hat{\tau}_2\left(1+\frac{|\psi_2|^{*2}}{k_cT^*}\right)} i_{1\alpha\beta}. \tag{12}$$

This equation is identical with the rotor flux simulator of (2) when k_c is infinite as well as (11). Fig. 6 shows both modified blocks which correspond to (11) and (12), and only the coefficient k_c in (9) is necessary to compensate the core loss according to the figures, which can simplify the configuration of the whole control system.

By employing the modified rotor flux simulator represented by (12), the parameter identifier shown in Fig. 2 can be utilized without any modification of its configuration to estimate the motor parameters, because the core loss dose not have relation with the instantaneous reactive power.

B. Improved torque control performance

Some simulation tests have been conducted under the same condition as that of Fig. 5. in order to verify the

validity of the method. Fig. 7 shows the characteristic of the torque control error against the output torque. As shown in the figure, the error has been reduced down to less than 2%, and it is found that the error hardly increases even though the output torque is increased. It is supposed that the remaining error has been caused by a model mismatch owing to the position of the equivalent core loss resistance in the equivalent circuit. Also, in a strict sense, it should be considered that the resistance affects not only q-axis but also d-axis in the feedforward block, and the feedback block must be more complicated than what has been considered in the above discussion. However, it would be recognized that the method presented in the paper gives the direct field-oriented controller an effective and simple solution to compensate the torque control error caused by the core loss.

V. Conclusion

In the paper, a simplified precise torque control strategy of an induction motor has been described. The torque control system consists of two subsystems which should incorporate modification of the machine model by taking core loss into consideration. One is a direct field-oriented controller with a rotor flux simulator, which makes it possible to control the output torque and the rotor flux independently like a separately exited dc motor. The other is a robust parameter identifier utilizing instantaneous reactive power of the induction motor, which enables the system to compensate the parameter mismatch in the flux simulator with no sensitivity to the stator resistance. Owing to the model mismatch caused by the core loss in the motor, however, both the field orientation and the parameter identification cannot be carried out perfectly, which results in inaccurate torque control. The paper has presented a simple solution to improve the accuracy with small modifications of the feedforward and feedback blocks in the direct field-oriented controller. Consequently, quite precise torque control characteristic within 2% error has been verified through computer simulation tests, which shows possibility of reducing the output torque error effectively.

References

[1] T. Mizuno, J. Takayama, T. Ichioka, and M. Terashima, "Decoupling Control Method of Induction Motor Taking Stator Core Loss into Consideration," *IEE Japan Trans. Ind. App.* , vol. 109-D, No. 11, pp. 841-848, 1989.

[2] E. Levi, "Impact of Iron Loss on Behavior of Vector Controlled Induction Machines," *IEEE Trans. Ind. App.* , vol. 31, No. 6, pp. 1287-1296, 1995.

[3] M. Sokola, E. Levi, G. Jamieson, and D. Williams, "Representation and Compensation of Iron Loss in Rotor Flux Oriented Induction Machines," *1996 PEDES Conf. Rec. - New Delhi*, vol. 1, pp. 243-249.

[4] T. Noguchi, S. Kondo, and I. Takahashi, "Field-Oriented Control of an Induction Motor with Robust On-Line Tuning of Its Parameters," *IEEE Trans. Ind. App.* , vol. 33, No. 1, pp. 35-42, 1997.

[5] H. Nakano, H. Akagi, I. Takahashi, and A. Nabae, "A New Type Equivalent Circuit of a Induction Motor Based on the Total Linkage Flux of the Secondary Windings," *IEE Japan Trans. Power. Elec.* , vol. 103-B, No. 3, pp. 216-222, 1983.

Apendix

The induction motor which has been controlled in the computer simulations is based on the following model [1] :

$$\begin{bmatrix} \boldsymbol{v}_{1dq} \\ \mathbf{0} \end{bmatrix} = \begin{bmatrix} R_1 + R_m + \mathrm{p}L_{11} + \mathrm{j}\left(\omega L_{11} - \mathrm{p}\frac{R_m}{\omega}\right) & R_m + \mathrm{p}L_m + \mathrm{j}\left(\omega L_m - \mathrm{p}\frac{R_m}{\omega}\right) \\ \omega_s \frac{R_m}{\omega} + \mathrm{p}L_m + \mathrm{j}\left(\omega_s L_m - \mathrm{p}\frac{R_m}{\omega}\right) & R_2 + \omega_s \frac{R_m}{\omega} + \mathrm{p}L_{22} + \mathrm{j}\left(\omega_s L_{22} - \mathrm{p}\frac{R_m}{\omega}\right) \end{bmatrix} \begin{bmatrix} \boldsymbol{i}_{1dq} \\ \boldsymbol{i}_{2dq} \end{bmatrix},$$

where

$\omega_s = \omega - \omega_m$: slip angular frequency,

$R_m = \dfrac{\omega^2 M^2}{{R_c}^2 + \omega^2 M^2} R_c$: equivalent core loss resistance,

and

$L_m = \dfrac{{R_c}^2}{{R_c}^2 + \omega^2 M^2} M$: magnetizing inductance.

The resistance R_m is considered to be in series with the inductance L_m in the model described above.

Multi-Star Induction Motors fed by Voltage Source Inverters

H. Stemmler, R. Deplazes
The Swiss Federal Institute of Technology (ETH)
Power Electronics and Electrometrology Laboratory
Physikstrasse 3, CH-8092 Zurich, Switzerland
Fax: +41-1-6321212, Phone: +41-1-6325324
E-mail: deplazes@lem.ee.ethz.ch

Abstract — **This paper deals with the problems of multi-star induction motors fed by voltage source inverters. After an introduction, the structure of this drive system is described in chapter II using the example of a 3-star motor with three independent 3-phase windings in the stator which are phase shifted mechanically against each other. Based on the transient equations derived in chapter III, a control structure is proposed in chapter IV. In chapter V special attention is given to the harmonics of the inverter output currents. They can reach a high level due to the interactions of the inverters allocated to the individual 3-phase windings, which are coupled to each other magnetically. The current harmonics determine the dimensioning of the turn-off capability of the inverters. The modes of operation with sinusoidal PWM and square wave mode with fundamental switching frequency are illustrated in chapter VI and compared to normal single-star drives. Chapter VII shows how the pulse patterns can be optimized, in order to get the lowest possible current harmonics at a given inverter switching frequency and a given fundamental frequency. The paper concentrates on the motor side of the drive system.**

I. INTRODUCTION

Current source inverters feeding 2-star synchronous motors with two 3-phase windings in the stator, which are shifted mechanically against each other for 30° (el.), are state of the art for many years in the field of high power drives. Their advantages are described for example in [1] and [2].

2-star induction motors fed by *voltage* source inverters are described in the literature [3], [4] and [5]. But there are very few commercial applications, one of them in the field of traction drives in multi system locomotives [6].

This paper describes multi-star induction motors fed by voltage source inverters - using the example of a 3-star configuration. 2- and 3-star configurations will be attractive for large industrial drives and for future traction applications.

There is a big difference in behaviour between current source and voltage source fed motors: Current source inverters impress currents on the motor the wave shape of which is determined by the inverter. Voltage source inverters, however, impress the inverter-voltages on the motor. This leads to increased interactive current harmonics between the inverters of the individual stars. In chapter II of this paper the structure of 3-star motor drives is represented. Based on the transient equations, derived in chapter III, a control structure is proposed in chapter IV and the harmonics in torque and inverter output currents are calculated in chapter V. The modes of operation with sinusoidal PWM and square wave mode with fundamental switching frequency are illustrated and compared to normal single-star drives in chapter VI. Chapter VII shows how the pulse patterns can be optimized. The paper concentrates on the motor side of the drive system.

II. THE STRUCTURE OF 3-STAR MOTOR DRIVES

II.A. Configuration of motor and inverters

Figs. 1a and b show the 3-star configuration: Three 3-phase voltage source inverters feed the three, star-connected, 3-phase stator windings of the motor. The axes of the three star windings are mechanically shifted against each other by the angle Δ (el.).

Fig. 1c shows the example of a winding arrangement with $\Delta = 20°$ (el.) shift between the winding axes. For reasons of simplification fig. 1c shows a 2-pole motor with 36 slots and only one winding per slot. Typical high power traction motors have rather 4 poles (pole pair $z_p = 2$), 72 slots and a higher number of windings per slot.

II.B. Generation of the inverter output voltages

A 3-phase 3-level inverter consists of twelve turn-off power semiconductors (GTOs, IGBTs), four per phase. In fig. 1a each phase is represented by a 3-point change-over switch the output of which can be connected either to the positive pole, the zero point or the negative pole of the d.c. supply voltage.

One 3-level inverter, as shown in fig. 1a, can be regarded as an inverter which can be operated with *two* independent pulse patterns to form the resultant inverter output voltage according to the eqs. (2 ÷ 4):

The PWM switching mode is illustrated in fig. 5a and b. The 3-phase 3-level inverter output voltages $u_{.\,a,b,c}$ for each star x, y, z (eqs. (4)) are generated by the intersections of the corresponding modulation signals (index M) with two (indices I and II) triangular carrier signals (index C) according to eqs. (2).

The 3-phase sinusoidal modulation (M) signals $u_{M\,.\,a,b,c}$ for each star x, y, z determine the amplitudes $U_{F\,.}$ and the frequency $f_{1\,.}$ of the fundamental (index F) component of the inverter voltages $u_{\,.\,a,b,c}$ of the stars x, y, z.

$$U_{Fx,y,z} = m_{x,y,z} \cdot U_{dx,y,z} \text{ with } m_{x,y,z} = U_{Mx,y,z} / \hat{U}_{Cx,y,z}$$

where
$U_{Mx,y,z}$: amplitude of $u_{Mx,y,z;a,b,c}$
$\hat{U}_{Cx,y,z}$: peak value of $u_{Cx,y,z;I,II}$ (1)
$m_{x,y,z}$: modulation index $(0 \div 1)$

The triangular carrier (C) signals determine the switching frequency F of the power semiconductors. The carrier signals with index II are 180° phase shifted to the corresponding carrier signals with index I. As illustrated in fig. 5a this leads to a staggered switching sequence of the pulse patterns I and II which doubles the resultant switching frequency in the 3-level inverter output voltage and reduces the harmonics drastically [7], [8].

0-7803-3823-5/97/$10.00© 1997 IEEE

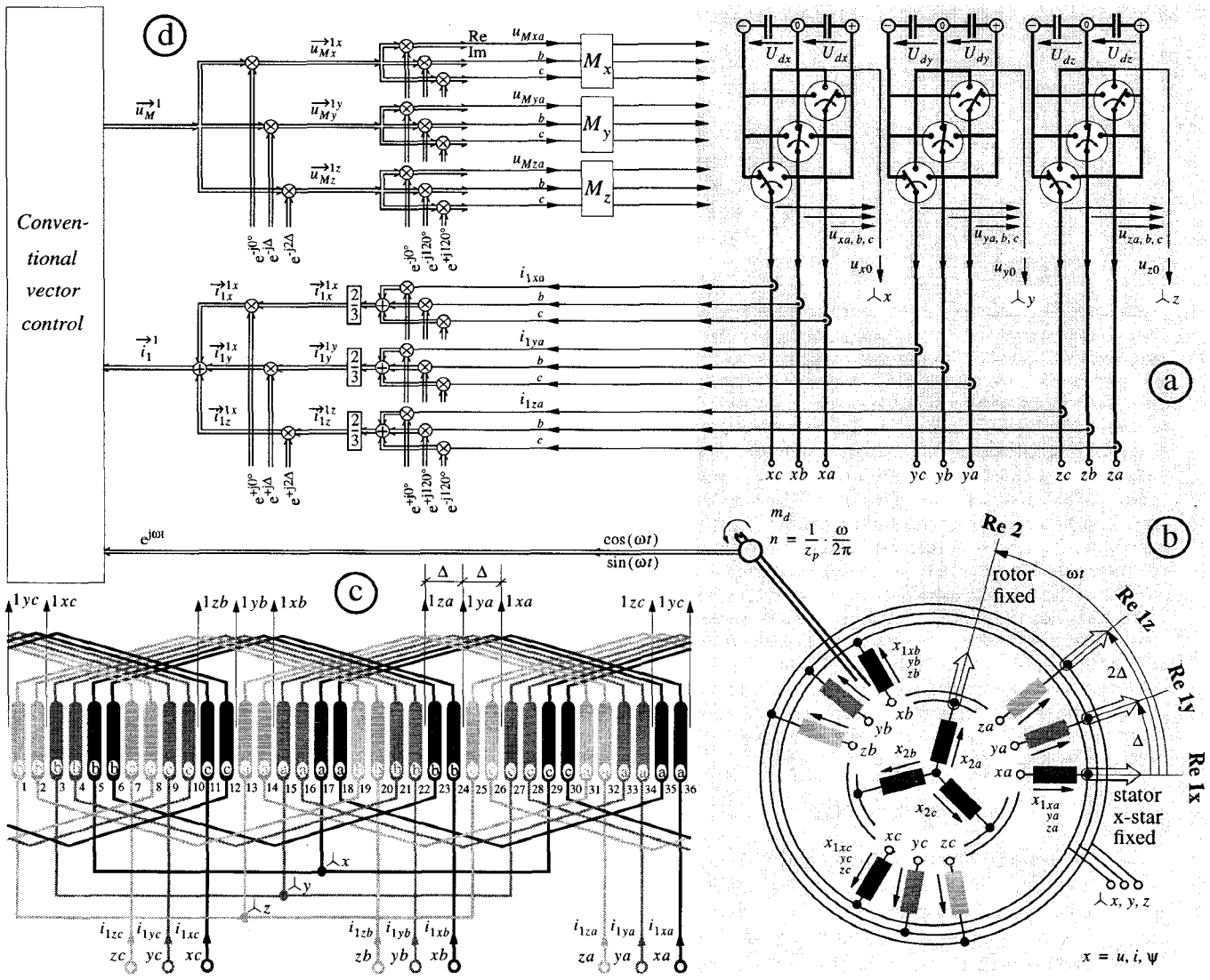

Fig. 1: Structure for 3-star motor drives and the winding diagram of a 3-star motor

The fundamental frequency switching mode (square wave mode) is illustrated in fig. 4a and b. The 3-phase 3-level inverted output voltages $u_{\ldots a,b,c}$ for each star x, y, z (eqs. (4)) are generated by two (indices I and II) modulation signals (index M) according to eqs. (3). They have fundamental frequency and switch the inverters when they cross the zero line. With a phase shift $\varphi_{I\,II}$ against each other the resultant amplitude of the fundamental component can be controlled. In figs. 4a and b this angle is $\varphi_{I\,II} = 32.8°$.

$$u_{\substack{Mxa,b,c \\ y \\ z}} - u_{\substack{Cx I \\ y \\ z}} \quad >0 \quad >0 \quad <0 \quad <0 \qquad (2)$$

$$u_{\substack{Mxa,b,c \\ y \\ z}} - u_{\substack{Cx II \\ y \\ z}} \quad >0 \quad <0 \quad >0 \quad <0$$

$$u_{\substack{Mxa,b,cI \\ y \\ z}} \quad >0 \quad >0 \quad <0 \quad <0 \qquad (3)$$

$$u_{\substack{Mxa,b,cII \\ y \\ z}} \quad >0 \quad <0 \quad >0 \quad <0$$

$$u_{\substack{xa,b,c \\ y \\ z}} \quad +U_{\substack{dx \\ y \\ z}} \quad 0 \quad 0 \quad -U_{\substack{dx \\ y \\ z}} \qquad (4)$$

In order to compensate for the mechanical angle Δ (el.) between the three star axes, the fundamental components of the inverter voltages need, of course, the corresponding phase shift Δ in time from star to star. This is also illustrated in figs. 4a, b and 5a, b.

II.C. Three phase quantities and rotating phasors

Fig. 1b contains the reference frames (real axes) which are used to transform the 3-phase quantities to rotating phasors. Table 1 eqs. (5) show, how the quantities $(x_{\ldots})$ in the three phases a,b,c $(x_{\ldots a})$, $(x_{\ldots b})$, $(x_{\ldots c})$ of each star x, y, z in the stator 1 $(x_{1x\,.})$, $(x_{1y\,.})$, $(x_{1z\,.})$ and in those in the rotor 2 $(x_{2\,.})$ are summed up geometrically $(x_{\ldots a}e^{j0°} + x_{\ldots b}e^{j120°} + x_{\ldots c}e^{-j120°})$ to form three rotating stator star phasors $(\vec{x}_{1x}^{\,\cdot})$, $(\vec{x}_{1y}^{\,\cdot})$, $(\vec{x}_{1z}^{\,\cdot})$ and a rotating rotor phasor $(\vec{x}_2^{\,\cdot})$. Each rotating stator star phasor is related to the stator fixed frame in its own star $(\vec{x}_{1x}^{\,1x})$, $(\vec{x}_{1y}^{\,1y})$, $(\vec{x}_{1z}^{\,1z})$. The rotating rotor phasor is related to its own rotor fixed frame $(\vec{x}_2^{\,2})$. In table 1 eqs. (6), all rotating phasors are related to the stator-fixed frame in the x-star. The eqs. (7) in table 1 show the inverse transformation of the star frame related rotating phasors to the 3-phase star quantities.

The voltages across the motor windings $u_{1x,y,z;a,b,c}$ (eq. (8)) differ from the inverter output voltages $u_{x,y,z;a,b,c}$ by the zero sequence components $u_{x,y,z;0}$ (eq. (9)) and have a

Table 1: Transformation and inverse transformation 3-phase quantities ↔ rotating phasors

Rotating phasors of the quantities in the	related to the fixed frames in the	$x = u \text{ or } i \text{ or } \psi$ (5)	related to the fixed frames in the	(6)
stator x-star	stator x-star	$\vec{x}_{1x}^{1x} = \frac{2}{3}\{x_{1xa}e^{j0°} + x_{1xb}e^{+j120°} + x_{1xc}e^{-j120°}\}$	stator x-star	$\vec{x}_{1x}^{1x}$
stator y-star	stator y-star	$\vec{x}_{1y}^{1y} = \frac{2}{3}\{x_{1ya}e^{j0°} + x_{1yb}e^{+j120°} + x_{1yc}e^{-j120°}\}$	stator x-star	$\vec{x}_{1y}^{1x} = \vec{x}_{1y}^{1y} \cdot e^{j\Delta}$
stator z-star	stator z-star	$\vec{x}_{1z}^{1z} = \frac{2}{3}\{x_{1za}e^{j0°} + x_{1zb}e^{+j120°} + x_{1zc}e^{-j120°}\}$	stator x-star	$\vec{x}_{1z}^{1x} = \vec{x}_{1z}^{1z} \cdot e^{j2\Delta}$
rotor	rotor	$\vec{x}_{2}^{2} = \frac{2}{3}\{x_{2a}e^{j0°} + x_{2b}e^{+j120°} + x_{2c}e^{-j120°}\}$	stator x-star	$\vec{x}_{2}^{1x} = \vec{x}_{2}^{2} \cdot e^{j\omega t}$

$$x_{1xa,b,c} = Re(\vec{x}_{1x}^{1x} e^{j0°,-j120°,+j120°}); \quad x_{1ya,b,c} = Re(\vec{x}_{1y}^{1y} e^{j0°,-j120°,+j120°}); \quad x_{1za,b,c} = Re(\vec{x}_{1z}^{1z} e^{j0°,-j120°,+j120°}) \quad (7)$$

remarcably lower harmonics content. See figs. 1a and b.

$$u_{\substack{1xa,b,c \\ y \\ z}} = u_{\substack{xa,b,c \\ y \\ z}} - u_{\substack{x0 \\ y \\ z}} \quad (8)$$

$$u_{\substack{x0 \\ y \\ z}} = (1/3)(u_{\substack{xa \\ y \\ z}} + u_{\substack{xb \\ y \\ z}} + u_{\substack{xc \\ y \\ z}}) \quad (9)$$

III. Transient Equations

Eqs. (10) in table 2 represent the transient voltage and flux linkage equations of the three stator stars and of the rotor. They are based on rotating phasors. The flux linkage equations show the interactions between the three stator stars and the rotor: The flux linkage in each of the stator stars depends on the current in the own star but also on the currents in the neighbouring stars and - of course - on the rotor current. The interaction is characterized by the mutual 3-phase inductances ($M_{\ldots}$) and the mechanical angle (Δ) between the winding axes of the neighbouring stars.

To get a better understanding of the behaviour of the 3-star motor it is useful to build the *resultant* rotating stator phasors from the rotating stator phasors of the individual stars. The resultant rotating stator phasors $\vec{u}_1^1$, $\vec{i}_1^1$ and $\vec{\psi}_1^1$ are defined according to the eqs. (11) in table 2. They are referred to the stator-fixed x-star frame. Introducing these resultant rotating stator phasors into eqs. (10) for a symmetrically built 3-star motor - according to eqs. (12) - results in eqs. (13) and finally in eqs. (14).

Comparing the eqs. (14) for the 3-star motor with the eqs. (16) for a normal one-star motor, it is interesting to note, that both have exactly the same structure. The torque equation (15) for the 3-star motor, therefore, is the same as for normal one-star motors (eq. (17)). That means: *A 3-star motor behaves like a normal one-star motor, if the resultant rotating stator phasors - defined according to eqs. (11) - are used instead of the rotating stator phasors in the individual stars.*

IV. Control Structure

The results of chapter III give the hint, how a multi-star motor has to be controlled in order to get the same results as with a normal single-star motor. See fig. 1d.

- We have to use the resultant rotating stator current phasor $\vec{i}_1^1$ - defined according to eqs. (11) in table 2 - instead of the individual star current phasors as feed back signal for the closed loop controls. Fig. 1d shows how the resultant phasor $\vec{i}_1^1$ is made up with the individual 3-phase currents $i_{1xa,b,c}$, $i_{1ya,b,c}$, and $i_{1za,b,c}$ of the three stars x, y and z by using the definitions in eqs. (5, table 1) and eqs. (11, table 2).

- We have to split up the rotating phasor $\vec{u}_M^1$ of the modulation signal at the output of the closed loop control for the modulators M_x, M_y and M_z which are allocated to the inverters of the three stars. The rotating phasor $\vec{u}_M^1$ has to be turned with the angles 0°, Δ and 2Δ for the stars x, y and z. This results in $\vec{u}_{Mx}^{1x}$, $\vec{u}_{My}^{1y}$ and $\vec{u}_{Mz}^{1z}$. Then the inverse transformation according to eqs. (7, table 1) delivers the 3-phase modulation signals $u_{Mxa,b,c}$, $u_{Mya,b,c}$ and $u_{Mza,b,c}$ for the individual star modulators. Their mode of operation is described in chapter IIB and illustrated in figs. 4a and 5a.

Systems which control the *resultant* rotating current phasor $\vec{i}_1^1$ via the *resultant* rotating modulation phasor $\vec{u}_M^1$ need star individual corrections - not shown in fig. 1d - to keep the individual star rotating current phasors $\vec{i}_{1x}^{1x}$, $\vec{i}_{1y}^{1y}$ and $\vec{i}_{1z}^{1z}$ balanced. They have to correct such deviations in the star currents which would sum up to zero in the resultant current and therefore could not be detected.

V. Harmonics

When looking at the harmonics we mainly have to focus on two aspects: harmonics in the torque and in the inverter output currents. The torque harmonics are less significant for the drive because the large inertia of the motor normally keeps their influence on the speed at a negligible level. The inverter current harmonics, however, determine the dimensioning of the turn-off capability of the inverters. They can reach a high level if the windings of the three stars are not well enough decoupled magnetically.

The relations between the rotating phasors of the voltage and current harmonics (Index H) of 3-star motors can easily be derived from the transient equations in chapter III if introducing $R_1 = 0$ and $R_2 = 0$. These resistances R_1 and R_2 in the stator and in the rotor can be neglected because the ohmic voltage drop of the current harmonics ($\vec{i}_{\ldots H} \cdot R_{\ldots}$) is always low compared to the voltage harmonics $\vec{u}_{\ldots H}$ generated by the pulsed inverters.

Introducing $R_1 = 0$, $R_2 = 0$ into the transient eqs. (13) and (14), then eliminating $\vec{i}_2^2$ and using the definitions for the leakage factors σ_{10}, σ_{12} in eqs. (21) delivers - after very

Table 2: Motor equations

Transient equations related to the respective stator star fixed frame respectively to the rotor fixed frame: (10)

$$\begin{aligned}
\vec{u}_{1x}^{1x} &= \vec{i}_{1x}^{1x} R_{1x} + \frac{d}{dt}\vec{\psi}_{1x}^{1x} & \vec{\psi}_{1x}^{1x} &= \vec{i}_{1x}^{1x} L_{1x} + \vec{i}_{1y}^{1y} e^{j\Delta} M_{1xy} + \vec{i}_{1z}^{1z} e^{j2\Delta} M_{1xz} + \vec{i}_2^2 e^{j\omega t} M_{1x2} \\
\vec{u}_{1y}^{1y} &= \vec{i}_{1y}^{1y} R_{1y} + \frac{d}{dt}\vec{\psi}_{1y}^{1y} & \vec{\psi}_{1y}^{1y} &= \vec{i}_{1y}^{1y} L_{1y} + \vec{i}_{1z}^{1z} e^{j\Delta} M_{1yz} + \vec{i}_{1x}^{1x} e^{-j\Delta} M_{1yx} + \vec{i}_2^2 e^{j\omega t} e^{-j\Delta} M_{1y2} \\
\vec{u}_{1z}^{1z} &= \vec{i}_{1z}^{1z} R_{1z} + \frac{d}{dt}\vec{\psi}_{1z}^{1z} & \vec{\psi}_{1z}^{1z} &= \vec{i}_{1z}^{1z} L_{1z} + \vec{i}_{1x}^{1x} e^{-j2\Delta} M_{1zx} + \vec{i}_{1y}^{1y} e^{-j\Delta} M_{1zy} + \vec{i}_2^2 e^{j\omega t} e^{-j2\Delta} M_{1z2} \\
0 &= \vec{i}_2^2 R_2 + \frac{d}{dt}\vec{\psi}_2^2 & \vec{\psi}_2^2 &= \vec{i}_2^2 L_2 + \vec{i}_{1x}^{1x} e^{-j\omega t} M_{21x} + \vec{i}_{1y}^{1y} e^{-j\omega t} e^{j\Delta} M_{21y} + \vec{i}_{1z}^{1z} e^{-j\omega t} e^{j2\Delta} M_{21y}
\end{aligned}$$

Transient equations related to the stator x-star fixed frame: (13)

$$\begin{aligned}
\vec{u}_{1x}^{1x} &= \vec{i}_{1x}^{1x} R_1 + \frac{d}{dt}\vec{\psi}_{1x}^{1x} & \vec{\psi}_{1x}^{1x} &= \vec{i}_{1x}^{1x} L_1 + \vec{i}_{1y}^{1y} e^{j\Delta} M_{11} + \vec{i}_{1z}^{1z} e^{j2\Delta} M_{11} + \vec{i}_2^2 e^{j\omega t} M_{12} \\
\vec{u}_{1y}^{1y} e^{j\Delta} &= \vec{i}_{1y}^{1y} e^{j\Delta} R_1 + \frac{d}{dt}\vec{\psi}_{1y}^{1y} e^{j\Delta} & \vec{\psi}_{1y}^{1y} e^{j\Delta} &= \vec{i}_{1y}^{1y} e^{j\Delta} L_1 + \vec{i}_{1z}^{1z} e^{j2\Delta} M_{11} + \vec{i}_{1x}^{1x} M_{11} + \vec{i}_2^2 e^{j\omega t} M_{12} \\
\vec{u}_{1z}^{1z} e^{j2\Delta} &= \vec{i}_{1z}^{1z} e^{j2\Delta} R_1 + \frac{d}{dt}\vec{\psi}_{1z}^{1z} e^{j2\Delta} & \vec{\psi}_{1z}^{1z} e^{j2\Delta} &= \vec{i}_{1z}^{1z} e^{j2\Delta} L_1 + \vec{i}_{1x}^{1x} M_{11} + \vec{i}_{1y}^{1y} e^{j\Delta} M_{11} + \vec{i}_2^2 e^{j\omega t} M_{12} \\
0 &= \vec{i}_2^2 e^{j\omega t} R_2 + \frac{d}{dt}\vec{\psi}_2^2 e^{j\omega t} & \vec{\psi}_2^2 e^{j\omega t} &= \vec{i}_2^2 e^{j\omega t} L_2 + \vec{i}_{1x}^{1x} M_{12} + \vec{i}_{1y}^{1y} e^{j\Delta} M_{12} + \vec{i}_{1z}^{1z} e^{j2\Delta} M_{12}
\end{aligned}$$

Resultant rotating stator phasors (11) and the definition of a symmetrically built three-star motor (12):

$$\begin{aligned}
\vec{u}_{1x}^{1x} + \vec{u}_{1y}^{1y} e^{j\Delta} + \vec{u}_{1z}^{1z} e^{j2\Delta} &= 3\vec{u}_1^1 \quad (11) \\
\vec{i}_{1x}^{1x} + \vec{i}_{1y}^{1y} e^{j\Delta} + \vec{i}_{1z}^{1z} e^{j2\Delta} &= 1\,\vec{i}_1^1 \\
\vec{\psi}_{1x}^{1x} + \vec{\psi}_{1y}^{1y} e^{j\Delta} + \vec{\psi}_{1z}^{1z} e^{j2\Delta} &= 3\vec{\psi}_1^1
\end{aligned}$$

$$\begin{aligned}
R_{1x} &= R_{1y} = R_{1z} = R_1 \quad (12) \\
L_{1x} &= L_{1y} = L_{1z} = L_1 \\
M_{1xy} &= M_{1xz} = M_{1yx} = M_{1yz} = M_{1zx} = M_{1zy} = M_{11} \\
M_{21x} &= M_{21y} = M_{21z} = M_{1x2} = M_{1y2} = M_{1z2} = M_{21} = M_{12}
\end{aligned}$$

Resultant transient equations: (14)

$$\begin{aligned}
\vec{u}_1^1 &= \vec{i}_1^1 \frac{R_1}{3} + \frac{d}{dt}\vec{\psi}_1^1 & \vec{\psi}_1^1 &= \vec{i}_1^1 (L_{10}/3 + M_{11}) + \vec{i}_2^2 e^{j\omega t} M_{12} & L_{10} &= L_1 - M_{11} \\
0 &= \vec{i}_2^2 e^{j\omega t} R_2 + \frac{d}{dt}\vec{\psi}_2^2 e^{j\omega t} & \vec{\psi}_2^2 e^{j\omega t} &= \vec{i}_2^2 e^{j\omega t} L_2 + \vec{i}_1^1 M_{12}
\end{aligned}$$

$m_d = \frac{3}{2} z_p Im(\vec{i}_1^1 \vec{\psi}_1^{1*})$ z_p : Number of pole pairs (*) : conjugate complex (15)

Transient equations of a normal one-star motor: (16)

$$\begin{aligned}
\vec{u}_1^1 &= \vec{i}_1^1 R_1 + \frac{d}{dt}\vec{\psi}_1^1 & \vec{\psi}_1^1 &= \vec{i}_1^1 L_1 + \vec{i}_2^2 e^{j\omega t} M_{12} \\
0 &= \vec{i}_2^2 e^{j\omega t} R_2 + \frac{d}{dt}\vec{\psi}_2^2 e^{j\omega t} & \vec{\psi}_2^2 e^{j\omega t} &= \vec{i}_2^2 e^{j\omega t} L_2 + \vec{i}_1^1 M_{12}
\end{aligned}$$

$m_d = \frac{3}{2} z_p Im(\vec{i}_1^1 \vec{\psi}_1^{1*})$ (17)

Transient equations for the harmonics:

$$\begin{aligned}
\vec{u}_{1xH}^{1x} &= \sigma_{10} L_1 \frac{d}{dt}\vec{i}_{1xH}^{1x} + (\sigma_{12} - \sigma_{10}) L_1 \frac{d}{dt}\vec{i}_{1H}^1 \quad (18) \\
\vec{u}_{1yH}^{1y} e^{j\Delta} &= \sigma_{10} L_1 \frac{d}{dt}\vec{i}_{1yH}^{1y} e^{j\Delta} + (\sigma_{12} - \sigma_{10}) L_1 \frac{d}{dt}\vec{i}_{1H}^1 \\
\vec{u}_{1zH}^{1z} e^{j2\Delta} &= \sigma_{10} L_1 \frac{d}{dt}\vec{i}_{1zH}^{1z} e^{j2\Delta} + (\sigma_{12} - \sigma_{10}) L_1 \frac{d}{dt}\vec{i}_{1H}^1
\end{aligned}$$

$$\vec{u}_{1H}^1 = \frac{d}{dt}\vec{\psi}_{1H}^1 \quad (19)$$

$$\vec{u}_{1H}^1 = \left[\frac{1}{3}\sigma_{10} + (\sigma_{12} - \sigma_{10})\right] L_1 \frac{d}{dt}\vec{i}_{1H}^1 \quad (20)$$

where: $L_1 = L_{10} + M_{11}$; $\sigma_{10} = L_{10}/L_1$; $\sigma_{12} = 1 - M_{12}^2/(L_1 L_2)$ (21)

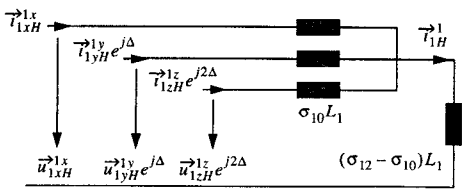

Fig. 2a: Equivalent circuit diagram for the harmonics

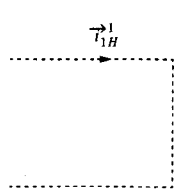

for:

$$\left|\vec{i}_{1H}^1 (\sigma_{12} - \sigma_{10}) L_1\right| << \left|\vec{i}_{1x,y,z}^{1x,y,z} \sigma_{10} L_1\right|$$

Fig. 2b: Simplified equivalent circuit diagram for the harmonics

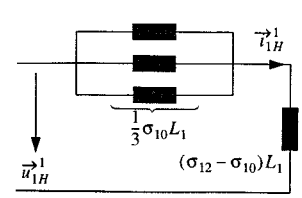

Fig. 3: Equivalent circuit diagram for the resultant harmonics

short algebraic calculations - the eqs. (18), (19) and (20) and the equivalent circuits in figs. 2 and 3, which describe the relation between the voltage and current harmonics.

$\sigma_{10}L_1$ is the stator to stator leakage inductance, which decouples the three stars. $\sigma_{12}L_1$ is the total stator to rotor leakage inductance.

The harmonics equivalent circuit in fig. 2a, which represents the eqs. (18) for the harmonics, shows: The harmonics of the rotating current phasors in each individual star $\vec{i}_{1xH}^{\,1x}$, $\vec{i}_{1yH}^{\,1y}$, $\vec{i}_{1zH}^{\,1z}$ depend on the voltage harmonics $\vec{u}_{1xH}^{\,1x}$, $\vec{u}_{1yH}^{\,1y}$, $\vec{u}_{1zH}^{\,1z}$ of the allocated inverters and are limited by the inductance $\sigma_{10}L_1 = L_{10}$ which decouples the three star windings. But they also depend on the voltage drop of the resultant rotating current phasor $\vec{i}_{1H}^{\,1}$ at the inductance $(\sigma_{12}-\sigma_{10})L_1$.

In some cases this voltage drop can be neglected. This leads to the equivalent circuit in fig 2b. This simplified equivalent circuit always delivers the worst case for the dimensioning of the turn-off capability of the power semiconductors in the inverters:

$$\begin{aligned}\vec{u}_{1xH}^{\,1x} &\approx \sigma_{10}L_1\frac{d}{dt}\vec{i}_{1xH}^{\,1x}\\ \vec{u}_{1yH}^{\,1y} &\approx \sigma_{10}L_1\frac{d}{dt}\vec{i}_{1yH}^{\,1y}\\ \vec{u}_{1zH}^{\,1z} &\approx \sigma_{10}L_1\frac{d}{dt}\vec{i}_{1zH}^{\,1z}\end{aligned} \qquad (22)$$

This simplification leads to realistic results for the example shown in fig. 4 and to too pessimistic results for the example shown in fig. 5.

Eqs. (19) and (20) and the equivalent circuit in fig. 3 give the relation between the resultant rotating phasors of the voltage, flux linkage and current harmonics $\vec{u}_{1H}^{\,1}$, $\vec{\Psi}_{1H}^{\,1}$ and $\vec{i}_{1H}^{\,1}$. The resultant rotating current phasor $\vec{i}_{1H}^{\,1}$ is determined by the resultant rotating voltage phasor $\vec{u}_{1H}^{\,1}$ and the leakage inductance $(1/3)\sigma_{10}L_1 + (\sigma_{12}-\sigma_{10})L_1$.

The *resultant* rotating phasors of the harmonics determine the torque harmonics:

$$\begin{aligned}\vec{i}_1^{\,1} &= \vec{i}_{1F}^{\,1} + \vec{i}_{1H}^{\,1} \qquad \text{F: Fundamental}\\ \vec{\Psi}_1^{\,1} &= \vec{\Psi}_{1F}^{\,1} + \vec{\Psi}_{1H}^{\,1} \qquad \text{H: Harmonics in eq. (15)} \rightarrow\\ m_d &= m_{dF} + m_{dH} = \frac{3}{2}z_p Im\left\{(\vec{i}_{1F}^{\,1} + \vec{i}_{1H}^{\,1})\cdot(\vec{\Psi}_{1F}^{\,1} + \vec{\Psi}_{1H}^{\,1})^*\right\}\end{aligned} \qquad (23)$$

VI. Illustration of Wave Shapes

The voltages and currents shown in figs. 4 and 5 are represented as per unit quantities. They are related to the dc supply voltage U_d and to the amplitude I_m of the magnetizing current. The leakage factors are assumed to be $\sigma_{10} = 6.9\%$ and $\sigma_{12} = 9.4\%$. These values are valid for the 10kW-3-star-motor, mentioned in chapter VIII. The values for high power traction motors are little bit smaller.

The fundamental frequency switching mode is illustrated in fig. 4. Fig. 4a represents the modulation signals $u_{Mx,\,y,\,z;a\,I,\,II}$ of the phases a in all three stars x, y, z. They switch the inverters when crossing the zero line generating in this way the corresponding inverter output voltages $u_{x,\,y,\,z;a}$ shown in fig. 4b. (See eqs. (3) and (4)). The voltages across the motor windings $u_{1x,\,y,\,z;a}$ in fig. 4c differ from the inverter output voltages $u_{x,\,y,\,z;a}$ in fig. 4b by the zero sequence voltages - according to eq. (8) - which are not shown in fig. 4. Fig. 4c contains also the corresponding inverter output currents $i_{1x,\,y,\,z;a}$. Currents and voltages in fig. 4c are represented with the fundamental components and the harmonics. These quantities in the phases a of the three stars x, y, z have the same shape but are phase shifted from star to star by the angle Δ - as mentioned at the end of chapter IIB. Fig. 4f represents the rotating stator phasors of the x-, y- and z-star currents $\vec{i}_{1x}^{\,1x}$, $\vec{i}_{1y}^{\,1x}$, $\vec{i}_{1z}^{\,1x}$ and of the corresponding flux linkages $\vec{\Psi}_{1x}^{\,1x}$, $\vec{\Psi}_{1y}^{\,1x}$, $\vec{\Psi}_{1z}^{\,1x}$ (left) as well as the resultant stator phasors $(1/3)\vec{i}_1^{\,1}$ and $\vec{\Psi}_1^{\,1}$ (right). The resultant rotating phasors $\vec{i}_1^{\,1}$ and $\vec{\Psi}_1^{\,1}$ - defined in eqs. (11) - generate the torque m_d (see eq. (23)), which is shown in fig. 4e. The real components $Re(\vec{i}_1^{\,1}) = i_{1g}$ and $Re(\vec{u}_1^{\,1}) = u_{1a}$ of the resultant rotating phasors $\vec{i}_1^{\,1}$ and $\vec{u}_1^{\,1}$ are shown in fig. 4d.

Fig. 4 is based on the following figures: fundamental frequency $f_1 = 50Hz$, modulation degree $m = 1.221$ ($m_{max} = 1.273$), rated current (≈ 4 times the magnetizing current I_m), angle between the winding axes of the stars x, y, z $\Delta = 20°$ (el.) (see fig. 1b and c) and phase shift between the modulation signals I and II $\varphi_{I\,II} = 32.8°$ (see figs. 4a,b).

The PWM switching mode is illustrated in fig. 5, using the same sequence of line diagrams as in fig. 4. The modulator operates with modulation signals $u_{Mx,\,y,\,z;a,\,(b,c)}$. As shown in fig. 5a they switch the inverters when crossing the carrier signals $u_{C\,.\,I,\,II}$. (See eqs. (2) and (4)).

Fig. 5 is based on the following figures: fundamental frequency $f_1 = 28.7Hz$, modulation degree $m = 0.7$, rated current (≈ 4 times the magnetizing current I_m), angle between the winding axes of the stars x, y, z $\Delta = 20°$ (el.) (see fig. 1b and c) and switching frequency $F = 230Hz$. The modulation signals $u_{Mx,\,y,\,z;a}$ are $\Delta = 20°$ phase shifted from star to star. The carrier signals $u_{C\,.\,I,\,II}$ are saw tooth-shaped and identical for all three stars.

VII. Pulse Pattern Optimization

The individual stars in a multi-star motor are coupled to each other by the relatively low stator to stator leakage inductance $\sigma_{10}L_1$ which is lower than the stator to rotor leakage inductance $\sigma_{12}L_1$ which determines the current harmonics in normal single-star motors. Multi-star motors, therefore, tend to increased current harmonics, generated by the interactions of the inverters allocated to the individual stars. Since the turn-off capability of the inverters is determined by this harmonics, they should be kept at a low level. Torque harmonics are less significant for drives because the large inertia of the motors keeps their influence on the speed at a negligible level.

The pulse pattern optimization, therefore, should aim at the lowest possible inverter current harmonics at a given switching frequency F per turn-off power semiconductor. The total harmonics distortion THD of the current can be used as a measure for the quality of the generated pulse patterns in the inverter output voltage. The THD - related to the nominal rms magnetizing current $I_m/\sqrt{2}$ - is defined in eq. (24). For a 3-star motor, four THDs can be defined: The THDs for each star $THD_{i1\,x,\,y,\,z}$ and for the resultant current THD_{i1}.

$$THD_{i1\,.} = \frac{\sqrt{\frac{1}{T}\int_0^T (i_{1\,.\,Ha,\,b,\,c})^2\,dt}}{I_m/\sqrt{2}} \qquad (24)$$

$i_{1\,.\,Ha,b,c}$: Harmonics of the phase currents.

I_m: Amplitude of the nominal magnetizing current.

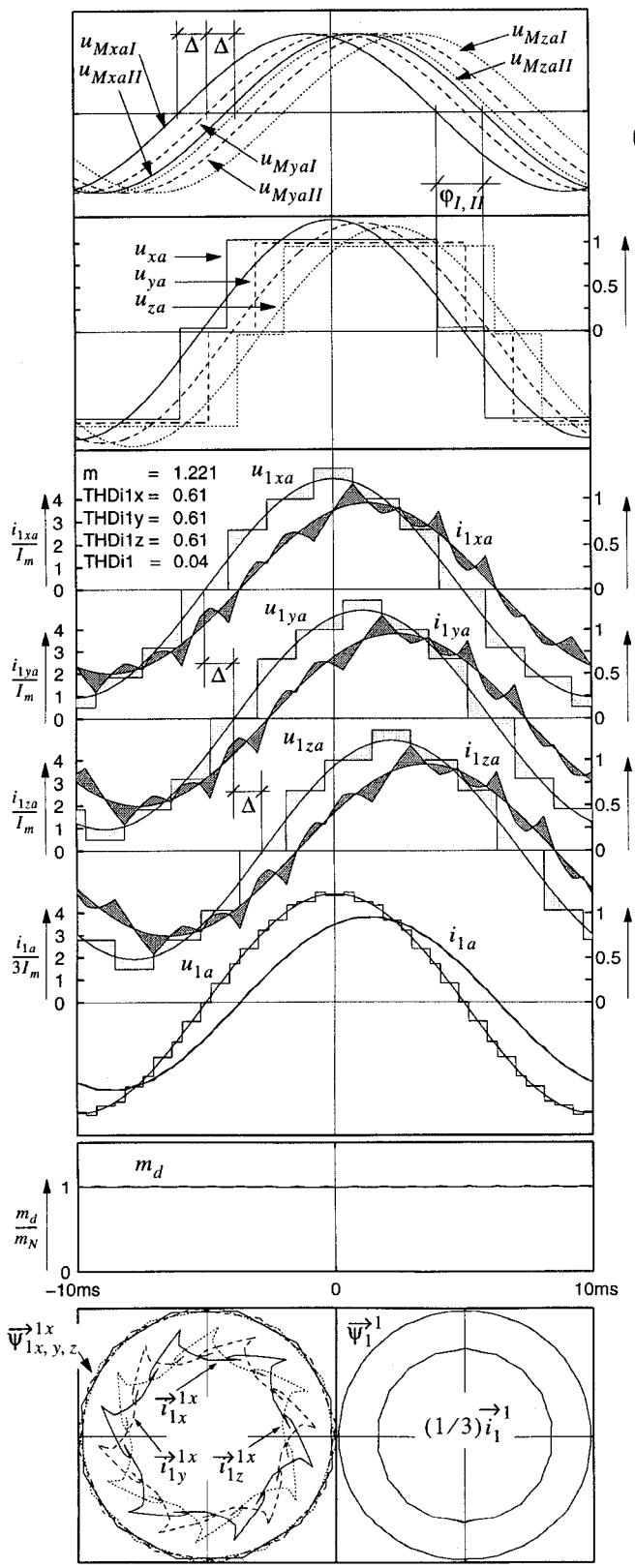

Fig. 4: Line diagrams for fundamental frequency switching mode

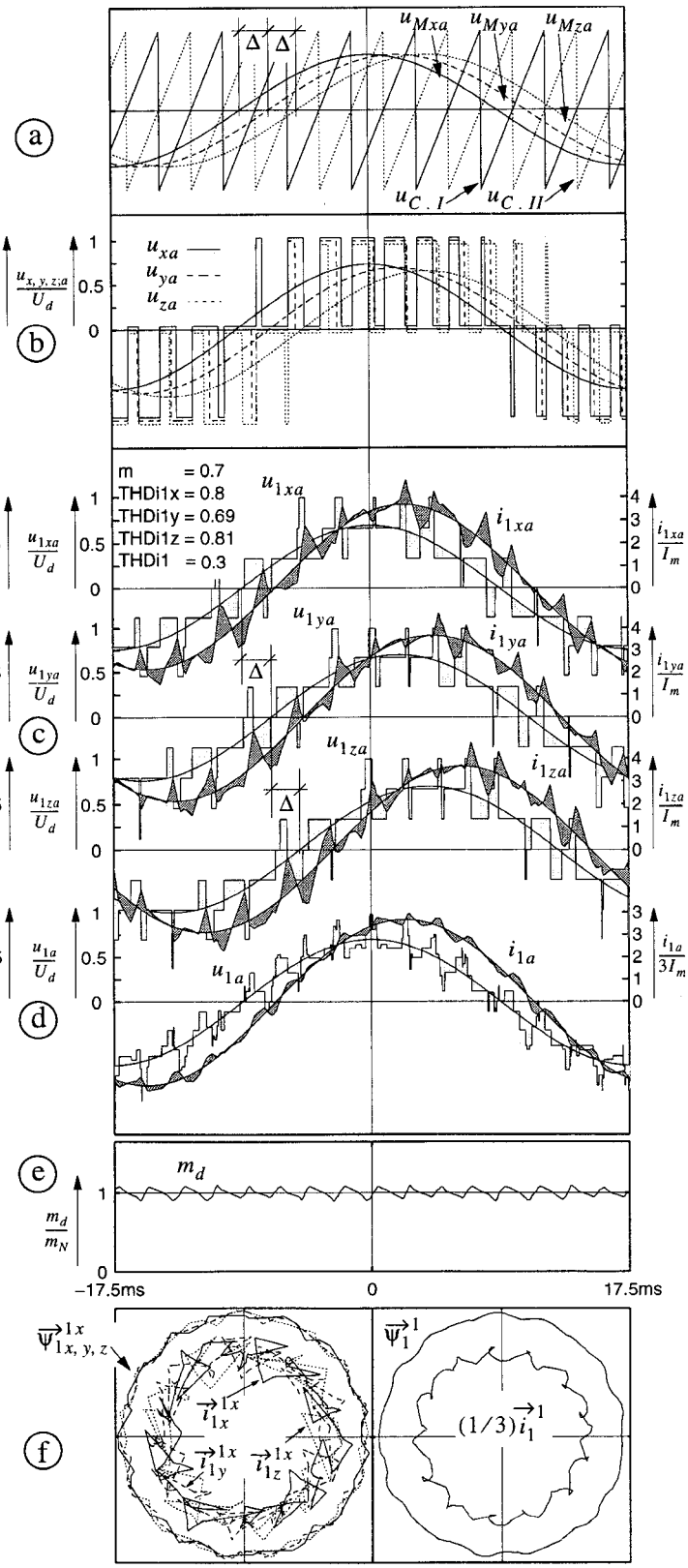

Fig. 5: Line diagrams for PWM switching mode

VII.A. Fundamental frequency switching mode

In the fundamental frequency switching mode the phase angle $\varphi_{I\,II}$ between the modulation signals $u_{M\,..\,I}$ and $u_{M\,..\,II}$ - see figs. 4a, b - is the main optimization parameter.

Fig. 6 shows the modulation index m, the $THD_{i1x,\,y,\,z}$ and THD_{i1} as a function of $\varphi_{I\,II}$ for a 3-star motor with the angle Δ = 20° between the winding axes of the three stars. For comparison fig. 6 also contains the $THD_{i1\_1\text{-}star}$ for a normal single-star motor with same power rating and, therefore, a three times higher phase current.

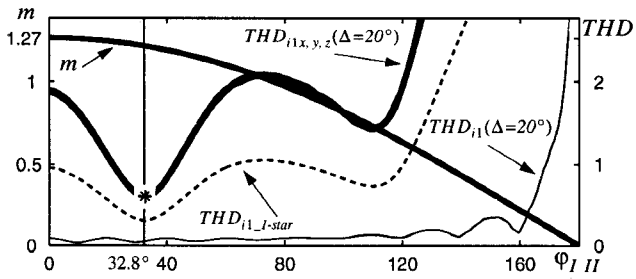

Fig. 6: Modulation degree and different THDs for a 3-star motor with $\Delta = 20°$

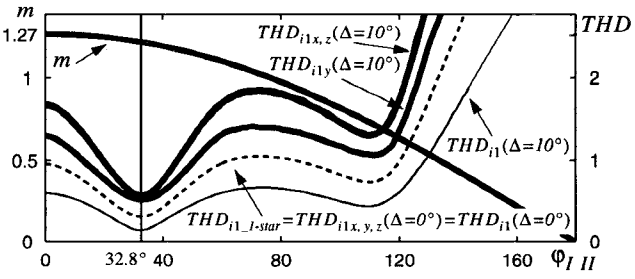

Fig. 8: Modulation degree and different THDs for a 3-star motor with $\Delta = 10°$ respectively $\Delta = 0°$

It can be seen in fig. 6 that the angle $\varphi_{I\,II} = 32.8°$ is optimal. It gives the lowest $THD_{i1x,y,z}$ at a high modulation degree $m = 1.221$ (96% of $m_{max} = 1.27$). This operation mode marked with "*" in fig. 6 is illustrated in fig. 4. Corresponding wave shapes are illustrated in fig. 7 for the angles $\varphi_{I\,II} = 0°$ and $\varphi_{I\,IIopt} = 32.8°$ for a 3-star motor and a normal single-star motor.

The influence of the second optimization parameter, the angle Δ between the three star winding axes, is shown in fig. 8. For $\Delta = 10°$ (el.) fig. 8 shows that THD_{i1y} differs from $THD_{i1x,z}$ and that THD_{i1}, responsible for the torque harmonics, is relatively high. $\Delta = 0°$, with the windings of all three stars placed in the same slot, delivers the best results: $THD_{i1x,y,z} = THD_{i1\_1\text{-}star}$. That means that the current harmonics in the three stars are as low as in a normal single-star motor. THD_{i1}, however, is relatively high compared to the cases for $\Delta = 10°$ and $20°$.

The choice of Δ, however, not only depends on the $THD_{i1x,y,z}$ of the inverter current harmonics. In cases, not explained in this paper, where the individual star windings have to be operated with different potentials, the insulation is easier to realize, if each slot contains only windings of one of the three stars. This is possible with $\Delta = 10°$ and $20°$. In the following we concentrate on $\Delta = 20°$. It gives a better winding coefficient and has only marginally higher $THD_{i1x,y,z}$ than $\Delta = 10°$.

The fundamental frequency switching mode is especially important for traction applications. Locomotives are operated in a wide speed range with field weakening at constant maximum inverter voltage.

VII.B. PWM switching mode

The carrier signals $u_{C\cdot I}$ and $u_{C\cdot II}$ used for the inverter control are 180° phase shifted against each other. Each pair, allocated to one of the three stars, can, however, also have a phase shift φ_{Cxy} and φ_{Cxz} relative to the pairs of the neighbouring stars. This is one of three parameters which can be varied in search for the optimal pulse patterns with low harmonics in the inverter currents. The other parameters are the wave shape of the triangular carrier signals, which can be varied between a symmetrical triangle and an unsymmetrical saw tooth-shaped triangle, and the mechanical angle Δ between the winding axes of the three stars.

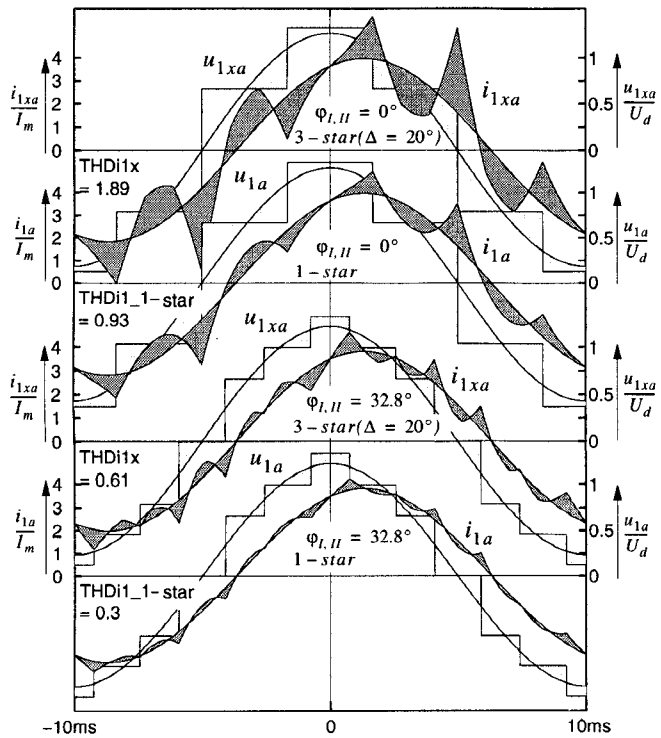

Fig. 7: A 3-star motor with $\Delta = 20°$ compared to a one-star motor using fundamental frequency switching

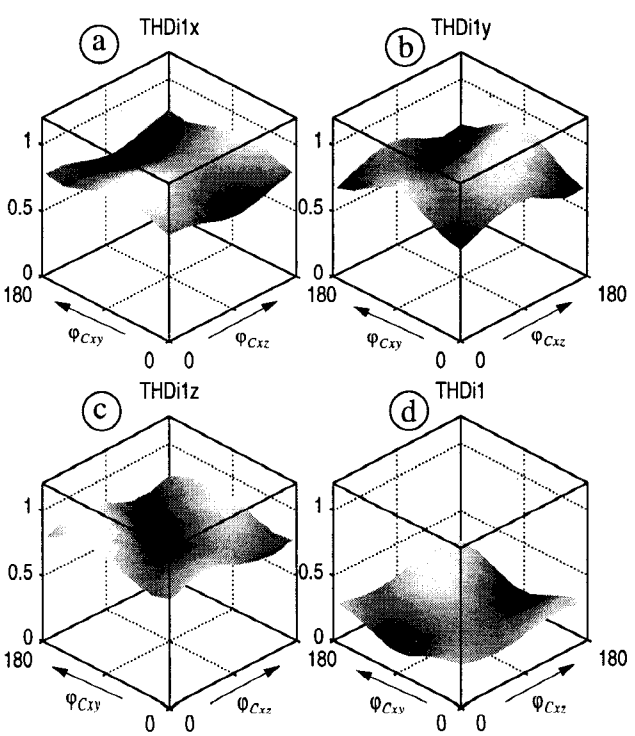

Fig. 9: Influence of the phase shifts φ_{Cxy} and φ_{Cxz} on the different THDs. Modulation degree m=0.7, Switching frequency F=230Hz, saw-tooth-carriers, $\Delta = 20°$.

The influence on the THDs caused by the phase shifts φ_{Cxy} and φ_{Cxz} between the carrier pairs of the three stars is shown in fig. 9. The THDs in fig. 9 are valid for the mechanical phase shift $\Delta = 20°$, which has been shown to be optimal (chapter VIIA) and for saw-tooth-carriers, which also have the optimal shape - as will be shown below. The THD-minimums of the three stars have slightly different values and different positions in the φ_{Cxy}-φ_{Cxz}-plane. In addition these values and positions change with the modulation degree m. The differences, however, between the values of the THD-maximums and -minimums for a given modulation degree are relatively small.

More detailed investigations showed: Using only one pair of carrier signals for all three stars - that means $\varphi_{Cxy} = \varphi_{Cxz} = 0°$ - is the optimal solution, because it is the simplest solution and because their THD-values are never far away from and in most cases close to or identical with the lowest possible THDs.

The influence of differently shaped triangular carrier signals on the THDs of the currents is shown in fig. 10. The other parameters influencing the current harmonics are kept at their optimal values: $\Delta = 20°$ for the mechanical phase shift between the three stars and $\varphi_{Cxy} = \varphi_{Cxz} = 0°$, that means only one single pair of carriers for all three stars. The meaning of the parameter A describing the wave shape of the triangular carrier signals is also illustrated in fig. 10 on the bottom. The four graphs in fig. 10 show $THD_{i1x,y,z}$ and THD_{i1} for the different wave shapes $A = 0;\ 0.25;\ 0.5;\ 0.75;\ 1$ as a function of the modulation degree $m = 0 \div 1$.

Below $m \approx 0.7$ saw tooth carriers ($A = 0$) and above $m \approx 0.9$ carriers with symmetrical triangles ($A = 1$) lead to the lowest current harmonics.

The operation modes with $m = 0.7$ and $A = 0$ which are marked with "*" in fig. 10 are illustrated in fig. 5.

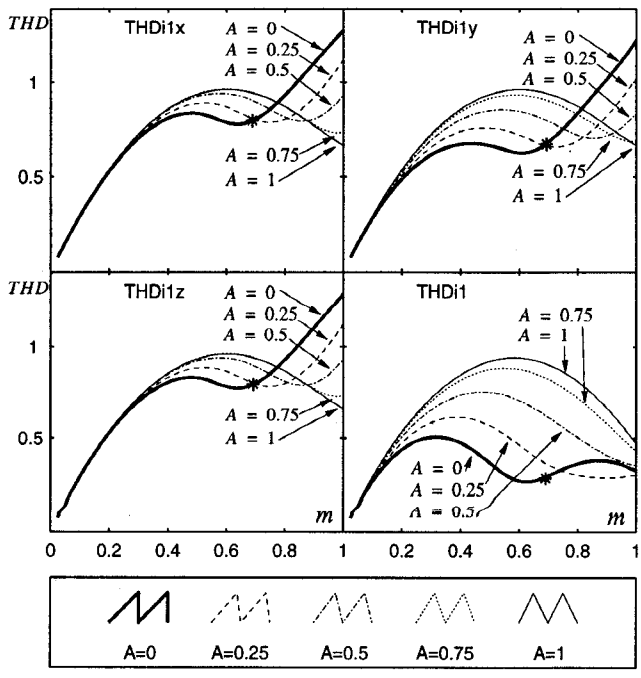

Fig. 10: Influence of differently shaped triangular carriers on the THDs. Switching frequency F = 230 Hz, $\Delta = 20°$.

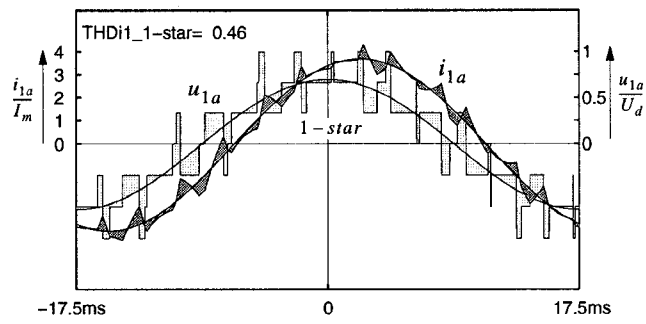

Fig. 11: Current and voltage of a single-star motor.

For comparison fig. 11 shows the motor current and voltage of a single-star motor with the same power rating in the same operation modes.

VIII. Resume

This paper deals with the problem of multi-star induction motors fed by voltage source inverters. The structure of the drive system is described and the transient motor equations are derived.

Based on these equations a control structure, using the resultant phasors of the individual star windings, is proposed.

Special attention is given to the current harmonics which can reach a high level because of the close magnetic coupling of the individual star windings. The inverter pulse patterns are optimized in order to keep the current harmonics at the lowest level, so avoiding an expensive increase in the inverter's turn-off capability.

The theoretical results are verified on a 10kW-3-star-drive. Experimental results are ready for presentation at the PCC-Nagaoka '97 conference.

IX. References

[1] E. Andersen und K. Bieniek, "Der Asynchronmotor mit drei und sechs Wicklungssträngen am stromeinprägenden Wechselrichter", Archiv für Elektrotechnik 63, 153-167, 1981.

[2] D. Roger, J. F. Brudny and F. Notelet, "Electrical drives using double-star induction machine", Speedam: Symposium on Power Electronics, Electrical Drives, Advanced Electrical Motors, Positano, Italy, 1992.

[3] R. H. Nelson and P. C. Krause, "Induction Machine Analysis for Arbitrary Displacement between Multiple Winding Sets", Annual Meeting of the IEEE Industry Applications Society, Paper 73 CHO 763-3 IA, 1973.

[4] T. A. Lipo, "A d-q Model for Six Phase Induction Machines", International Conference on Electric Machines, Athens, Greece, 1980.

[5] M. A. Abbas, R. Christen and T. M. Jahns, "Six-Phase Voltage Source Inverter Driven Induction Motor", IEEE Transactions on Industry Applications, Vol. 20, No. 5, September / October, 1984.

[6] K. H. Kettler, "Multisystem Propulsion Concept on the Basis of the Double Star Circuit", EPE '95 p. 2.159 - 2.166, Sevilla, 1995.

[7] A. Nabae, I. Takahashi and H. Akagi, "A new neutral-point-clamped PWM inverter", IEEE-Ind. Appl. Soc. (IAS) Annual Meeting, Cinci. (USA), 1980.

[8] H. Stemmler and P. Guggenbach, "Configurations of high-power voltage source inverter drives", Fifth European Conference on Power Electronics and Applications, IEE, vol. 5 p. 7 - 14, London, UK, 1993.

For Practical Use Position and Speed Sensorless Salient-Pole Brushless DC Motor Drives

Nobuyuki Kasa and Hiroshi Watanabe
Tokyo Metropolitan Institute of Technology
6-6, Ashahigaoka, Hino-City 191, JAPAN
Fax:+81-425-83-5119, Phone:+81-425-83-5111
E-mail:kasa@ecwhs2.tmit.ac.jp

Abstract— **In this paper, a practical use sensorless control drive of a salient-pole brushless DC motor is proposed. In the system, the position angle and the speed at a rotating condition are estimated basically by the model reference adaptive system (MRAS). At an initial or a starting condition, the position angle is estimated by a new AC current injection method. And at a lower speed region, the estimated position angle and the speed obtained from MRAS are corrected with a new correcting technique. The position angles and the speeds which were estimated values by MRAS and the AC current injection method are compared and corrected effectively on the correcting system. The experimental results of the estimated position angles or the speed and the variable speed control with the experimental system are shown in the paper. From these results, the proposed sensorless speed control system may be applicable to as a practical use sensorless brushless DC motor drive system.**

Keywords— **sensorless control, salient-pole brushless DC motor, MRAS, speed estimation**

I. Introduction

Usually, the rotor position of the brushless DC motor is detected by the position sensor as a rotary encoder or a resolver. An ommision of any transducer, mounted on the rotor shaft, reduces the system complexity and cost. Then the many position sensorless control systems of the brushless DC motor have been proposed. To the sensorless control methods of the cylindrical permanent magnet motors at a rotating condition, the rotor position angle and the angular speed are estimated on a stationary coordinate reference flame[1]-[3]. At zero speed, it is difficult for most principles to estimate the position angle, because the magnet does not induce any voltage. Therefore, the initial rotor position at a standstill can't be estimated with these methods for cylindrical permanent magnet motors.

On the other hand, many sensorless control methods of the salient-pole brushless DC motors are proposed[4][5]. A salient-pole brushless DC motor has the characteristic of which the winding inductance changes as a function of the position angle. In the reference [6], at a standstill and a low speed region, the rotor position angle is estimated by the measurement of the line current response for the applied rectangular pulse voltage[6]. Then, the motor is controlled with the sensorless control in a lower speed region. However, an accurate speed and the position angle estimation in a low-speed area such as immediately before positioning may be difficult.

In this paper, a practical use sensorless control drive of a salient-pole brushless DC motor is proposed. To estimate the position angle at a standstill, we adopted the previously proposed method[7]. In the system, the position angle is obtained from the detected voltages which are induced by adding sine wave slight currents. (Hereafter, it is called the current injection method.) And for a polarity distinction, we applies the method of the reference [10]. After a starting condition, we divide two speed ranges. One of them is a lower speed region from the standstill to about tens of % or less of the ratings and the other is a drive speed region from tens of % or more of the ratings up to the rated speed. The speed in the drive speed region is calculated from the error of the current of the motor based on MRAS. MRAS is fundamentally a speed identifying apparatus and the position angle signal is obtained as an integral value of the identified angular velocity. Therefore, the accurate estimation of an angular velocity and the position angle in a low-speed area becomes difficult. And the estimation of the initial position angle is impossible by MRAS.

The position angle estimating technique by the current injection method is a technique of an estimated position angle fundamentally. Therefore, the differentiated value in the time domain of the estimated position angle is the value influenced by the noises which are contained in the detected voltages. And it is difficult for the bare value to use as the speed control signal though contains a speed information. In this system, the estimated values of the position angle and the angular velocity obtained by MRAS are compared with the values obtained by the current injection method. Then the difference is corrected complimentary. In the lower speed region, the estimated value correction method by which the accuracy of estimated values are improved, is proposed. From the experimental results, the motor can be precisely controlled in the all speed region by the proposed sensorless drive system.

II. Sensorless Control Method

A. Sensorless control system

Figure 1 shows the construction of the sensorless control system of this research. The most important matter in a practicable sensorless drive method of the brushless DC motor is to be able to generate the position angle signal which can be driven within the designated ranges of the speed control. It is securing of the position angle signal by which the motor can continue rotating in the direction of specification, not to say satisfied the vector control condition as the following description eq.(1). Concretely, it is hoped for not a position angle signal faithful to the instant detection value but the position angle signal in relation of

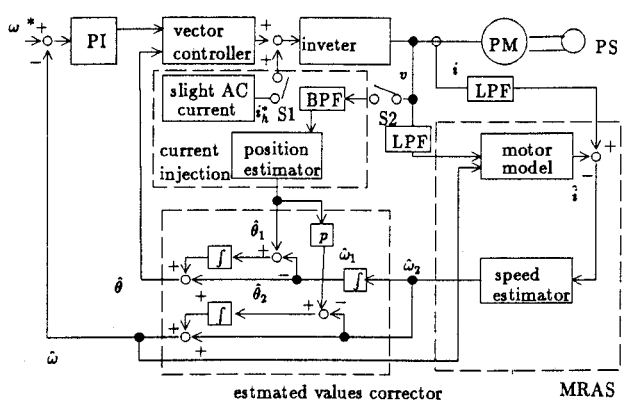

Fig. 1. Sensorless control system.

the convolution integral value of the speed signal to generate. Furthermore, to obtain the control more accurately than the same level as a DC servo motor, the speed signal can be secured in a low-speed area at the vicinity of the standstill. In addition, it is necessary to apply the position angle estimating method not to be accompanied with any vibration and the rotation of the shaft at the initial position angle estimation.

The angular velocity is calculated from the current error based on MRAS, although the system of figure 1 omitted the initial position angle estimation part. When the parameters of the motor are accurate values and the system fills the condition of the stable operation, this method can estimate high accurate angular velocity and the rotor position angle calculated as an integral value of the estimated angular velocity in the time domain. However, in a low-speed area at the vicinity of the standstill, an accurate speed estimation becomes difficult by the troublesome of the detection of the small currents and voltages and the variations of the parameters of the motor, etc. The estimated position angle by the current injection method is not affected directly by which the variation of the motor parameters. In this system, the position angle estimated by the current injection method and its differentiated value in the time domain as the angular velocity are compared with the each estimated values by MRAS. And a corrector revises the estimated values complimentary. This is shown as an estimated values corrector in figure 1.

B. Position angle estimation at standstill and lower speed region

In this section, a sensorless control method of the salient-pole brushless DC motor is presented. Figure 2 shows the analytical model of the motor. In this figure, three coordinate systems (u–v–w, α–β and d–q axes) are defined.

It is difficult to apply the estimating method at the running condition as to at a standstill condition, because at the standstill the estimated angular speed is zero and the position angle can not be calculated correctly. The some estimating methods of the position angle at a standstill are proposed[6][7][9]. On these paper, the estimating methods of the position angle are based on the winding inductance which changes as a function of the position angle. We have also proposed a new estimating method at a standstill for the salient-pole motors[7]. In this method, the position angle can be calculated by the voltages which are induced by adding sine wave slight currents to the motor windings. And the motor parameters are not used for its calculation. Then we can obtain the accurate position angle at a standstill.

On the d–q axis which rotates in phase with rotor position, the voltage equation of the salient-pole brushless DC motor is expressed as follows:

$$\begin{bmatrix} v_d \\ v_q \end{bmatrix} = \begin{bmatrix} R+pL_d & -\omega L_q \\ \omega L_d & R+pL_q \end{bmatrix} \begin{bmatrix} i_d \\ i_q \end{bmatrix} + \begin{bmatrix} 0 \\ \omega\phi_f \end{bmatrix} \quad (1)$$

where, R : stator winding resistance,
L_d, L_q : d and q axes inductances,
v_d, v_q : d and q axes voltages,
i_d, i_q : d and q axes currents,
p : differential operator $p = d/dt$,
ϕ_f : flux linkage produced by permanent magnet,
ω : angular velocity.

Eq.(1) is expressed as the next equation on the stationary coordinate system (α–β axis).

$$\begin{aligned} \begin{bmatrix} v_\alpha \\ v_\beta \end{bmatrix} &= \{R+\omega(L_d-L_q)A\} \begin{bmatrix} i_\alpha \\ i_\beta \end{bmatrix} \\ &+ \frac{1}{2}\{(L_d-L_q)B+(L_d+L_q)\}p \begin{bmatrix} i_\alpha \\ i_\beta \end{bmatrix} \\ &+ \omega\phi_f \begin{bmatrix} -\sin\theta \\ \cos\theta \end{bmatrix} \end{aligned} \quad (2)$$

where,
v_α, v_β : α and β axes voltages,
i_α, i_β : α and β axes currents,
θ : position angle,

$$A = \begin{bmatrix} -\sin 2\theta & \cos 2\theta \\ \cos 2\theta & \sin 2\theta \end{bmatrix}, \quad B = \begin{bmatrix} \cos 2\theta & \sin 2\theta \\ \sin 2\theta & -\cos 2\theta \end{bmatrix}$$

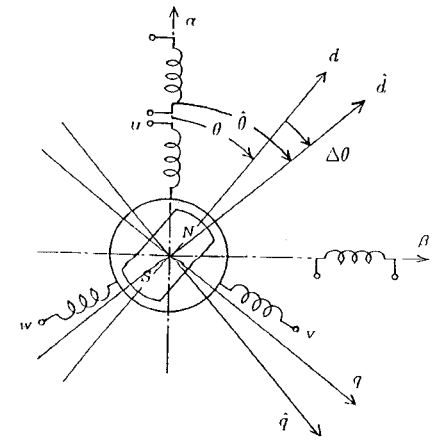

Fig. 2. Relation between rotor position and coordinates.

In a lower speed region, the AC small currents as the next equations are add to the motor currents. And these currents frequency is ω_h^* and amplitude is i_h^*.

$$\left.\begin{aligned} i_\alpha^* &= i_d^* \cos\hat{\theta} - i_q^* \sin\hat{\theta} + i_h^* \sin(\omega_h^* t) \\ i_\beta^* &= i_d^* \sin\hat{\theta} + i_q^* \cos\hat{\theta} - i_h^* \cos(\omega_h^* t) \end{aligned}\right\} \quad (3)$$

When the currents are added to the windings as eq.(3), the voltages $[v_\alpha, v_\beta]$ contain the components of the frequency ω_h^* and ω. Because the currents are slight and the interference between the motor currents and the currents for the position angle estimation can be neglected. The components of the frequency ω_h^* of the voltages are expressed as the next equation, when the voltages are detected through the band pass filters whose pass band frequency is ω_h^*.

$$\begin{aligned} \begin{bmatrix} v_\alpha \\ v_\beta \end{bmatrix} &= Ri_h^* \begin{bmatrix} \sin\omega_h^* t \\ -\cos\omega_h^* t \end{bmatrix} \\ &+ \frac{1}{2}\omega_h^*(L_d + L_q) i_h^* \begin{bmatrix} \cos\omega_h^* t \\ \sin\omega_h^* t \end{bmatrix} \\ &+ \frac{1}{2}\omega_h^* (L_d - L_q)\, i_h^* \begin{bmatrix} \cos(2\theta - \omega_h^* t) \\ \sin(2\theta - \omega_h^* t) \end{bmatrix} \end{aligned} \quad (4)$$

The winding voltages $[v_\alpha, v_\beta]$ are transformed to $[v_s, v_t]$ as the next equations with the phase angle $\omega_h^* t$ of the supply currents.

$$\begin{aligned} \begin{bmatrix} v_s \\ v_t \end{bmatrix} &= \begin{bmatrix} \cos\omega_h^* t & -\sin\omega_h^* t \\ \sin\omega_h^* t & \cos\omega_h^* t \end{bmatrix} \begin{bmatrix} v_\alpha \\ v_\beta \end{bmatrix} \\ &= Ri_h^* \begin{bmatrix} \sin 2\omega_h^* t \\ -\cos 2\omega_h^* t \end{bmatrix} \\ &+ \frac{1}{2}\omega_h^*(L_d + L_q) i_h^* \begin{bmatrix} \cos 2\omega_h^* t \\ \sin 2\omega_h^* t \end{bmatrix} \\ &+ \frac{1}{2}\omega_h^* (L_d - L_q)\, i_h^* \begin{bmatrix} \cos 2\theta \\ \sin 2\theta \end{bmatrix} \end{aligned} \quad (5)$$

In eq.(5), the right-hand side terms include the component of the frequency $2\omega_h^*$ and the DC voltages. The DC component in eq.(5) is expressed as the next equation.

$$\begin{bmatrix} v_{sd} \\ v_{td} \end{bmatrix} = \frac{1}{2}\omega_h^* (L_d - L_q)\, i_h^* \begin{bmatrix} \cos 2\theta \\ \sin 2\theta \end{bmatrix} \quad (6)$$

When the DC components $[v_{sd}, v_{td}]$ in the voltages $[v_s, v_t]$ are detected, the position angle can be calculated by

$$\hat{\theta}_1 = \frac{1}{2}\tan^{-1}\frac{v_{td}}{v_{sd}} + \frac{n\pi}{2} \quad (7)$$

- $L_d < L_q$: $n = 1, 3$
- $L_d > L_q$: $n = 0, 2$

To obtain the DC component of the voltages, they are calculated with a discreet Fourier transform.

The position angle is calculated with eq.(7) and the polarity is distinguished with a method of the applying flux saturation effects[10]. In our system, the width of the voltage pulse for the distinction of the polarity is about 10 ms.

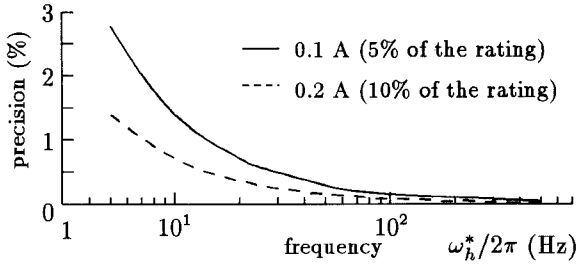

Fig. 3. Accuracy of estimated position angle.

C. Accuracy of estimated position angle

The accuracy of the detected position angle depends on the amplitude and frequency of the supply AC currents. The relation between the voltages $[v_{sd}, v_{td}]$ and the current for the detecting position angle is expressed as eq.(6). Figure 3 shows the accuracy of the estimated position angle when the frequency or the amplitude of AC currents change in our system. The accuracy of the estimated position angles depends on the resolution of the A/D converters which are used for detecting the stator voltages. When the amplitude of the AC currents is bigger and the frequency is higher, the accuracy of the detected position angle increases. However, the motor torque is influenced by the amplitude of AC currents. The amplitude of the currents is chosen in minimum value which the position angles can be detected, and the value of frequency depends on the system's sampling period. Then we selected the values of them (0.1A, 50Hz) by the results of our experiments.

D. Angular velocity estimation on rotational coordinate system

The state equation of the motor can be expressed as follows:

$$\begin{aligned} p\begin{bmatrix} i_d \\ i_q \\ \phi_d \\ \phi_q \end{bmatrix} &= \begin{bmatrix} -R/L_d & \omega L_q/L_d & 0 & -\omega/L_q \\ -\omega L_d/L_q & -R/L_q & \omega/L_d & 0 \\ 0 & 0 & 0 & 0 \\ 0 & 0 & 0 & 0 \end{bmatrix} \begin{bmatrix} i_d \\ i_q \\ \phi_d \\ \phi_q \end{bmatrix} \\ &+ \begin{bmatrix} v_d/L_d \\ v_q/L_q \\ 0 \\ 0 \end{bmatrix} \end{aligned} \quad (8)$$

where, $\phi_d = \phi_f$ and $\phi_q = 0$ are d and q axes flux linkages.

Because ω is included in eq.(8), it is a suitable state equation to identify ω. The estimated values of θ and ω denote as $\hat{\theta}$ and $\hat{\omega}$. When R, L_d, L_q are already known, the state equation of the mathematical model which uses new state variables as followings:

$$\hat{\boldsymbol{\phi}} = [\hat{\phi}_d, \hat{\phi}_q] = [\phi_f \cos\Delta\theta, \phi_f \sin\Delta\theta]$$

$$p\hat{\boldsymbol{\phi}} = p[\hat{\phi}_d, \hat{\phi}_q] = [-\Delta\omega\phi_f \sin\Delta\theta, \Delta\omega\phi_f \cos\Delta\theta]$$

where, $\Delta\theta = \theta - \hat{\theta} = \omega t - \hat{\omega} t = \Delta\omega t$
is expressed as follows:

$$p\begin{bmatrix}\hat{i}_d\\ \hat{i}_q\\ \hat{\phi}_d\\ \hat{\phi}_q\end{bmatrix}=\begin{bmatrix}-R/L_d & \hat{\omega}L_q/L_d & 0 & -\hat{\omega}/L_q\\ -\hat{\omega}L_d/L_q & -R/L_q & \hat{\omega}/L_d & 0\\ 0 & 0 & 0 & -\Delta\omega\\ 0 & 0 & \Delta\omega & 0\end{bmatrix}\begin{bmatrix}\hat{i}_d\\ \hat{i}_q\\ \hat{\phi}_d\\ \hat{\phi}_q\end{bmatrix} + \begin{bmatrix}v_d/L_d\\ v_q/L_q\\ 0\\ 0\end{bmatrix} \quad (9)$$

where, $\hat{i}_d$ and $\hat{i}_q$ are d and q axes currents of the mathematical model.

Where, the state equations of the motor and its mathematical model are determined. From eq.(8) and (9), the error of the state equations is expressed as follows:

$$p\begin{bmatrix}\epsilon_{id}\\ \epsilon_{iq}\end{bmatrix}=\begin{bmatrix}-R/L_d & \omega L_q/L_d\\ -\omega L_d/L_q & -R/L_q\end{bmatrix}\begin{bmatrix}\epsilon_{id}\\ \epsilon_{iq}\end{bmatrix} + \begin{bmatrix}0 & \Delta\omega L_q/L_d & 0 & -\Delta\omega/L_q\\ -\Delta\omega L_d/L_q & 0 & \Delta\omega/L_d & 0\\ 0 & 0 & 0 & \Delta\omega\\ 0 & 0 & -\Delta\omega & 0\end{bmatrix}\begin{bmatrix}\hat{i}_d\\ \hat{i}_q\\ \hat{\phi}_d\\ \hat{\phi}_q\end{bmatrix} \quad (10)$$

where, $\epsilon_{id} = i_d - \hat{i}_d$, $\epsilon_{iq} = i_q - \hat{i}_q$.

We adopt the adjustment rules of ω for MRAS[8]. To consider the stability of the system, the identify equation of the angular speed is obtained. These processes are shown in the reference[11]. As a result, the estimated angular speed $\hat{\omega}_2$ is identified by using a proportional and integral adjustment law as follows:

$$\hat{\omega}_2 = K_{P1}\{\hat{\omega}'\epsilon_{id} + (p + R/L)\epsilon_{iq}\}\hat{\phi}_d + K_{I1}\int_0^\tau \{\hat{\omega}'\epsilon_{id} + (p + R/L)\epsilon_{iq}\}\hat{\phi}_d dt \quad (11)$$

where K_{P1} and K_{I1} are gain constants, $\hat{\omega}'$ is $\hat{\omega}_2$ at one sampling before.

At a condition of $\Delta\theta \simeq 0$, $\Delta\theta$ is estimated from the 3rd and 4th rows of eq.(9).

$$\hat{\phi}_q/\hat{\phi}_d = \tan\Delta\theta \simeq \Delta\theta \quad (12)$$

Then, the position angle can be estimated in next equation.

$$\hat{\theta}_2 = \int_0^\tau \hat{\omega}_2 dt + \Delta\theta \quad (13)$$

E. Influence of set errors of parameters

The sensorless system is based on the condition in which the motor parameters are correct values. However, it is difficult to use the correct parameters, because the resistance is varied with the motor temperature. Then, we investigate the influence of the set errors of parameters on the system.

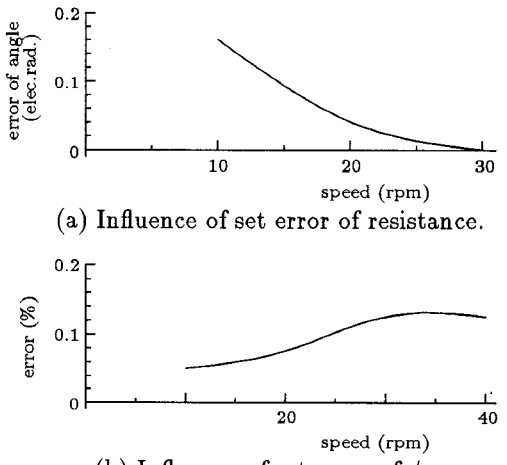

(a) Influence of set error of resistance.

(b) Influence of set error of ϕ_f.

Fig. 4. Influence of set errors of parameter.

Figure 4 (a) shows the errors between the estimated position angles and the actual ones when the values of the resistance are 1.2 times as larger as actual one. The influence of the set errors of the resistance becomes large error of the estimated position angle in a lower speed region. Figure 4 (b) shows the errors between the estimated angular speeds and the actual ones when the values of ϕ_f are 1.2 times as large as the actual one. The estimated angular speed is influenced by the set error of the ϕ_f. By analyzing on the rotating coordinate reference flame, when the motor parameters vary in a lower speed region, the estimated values are influenced seriously.

III. Corrector of Estimated Values

A. Corrector of the estimated values

Figure 5 is a flow chart by which the position angle and the angular velocity estimation and the procedure of the correction of estimated values are shown. When the initial position angle is estimated by the current injection method, the amplitude and the frequency of the currents are decided as the values not to be accompanied with the vibration or the rotation of the shaft. Estimated values are corrected in the lower speed region where accurate estimation by MRAS becomes difficult. After starting, the position angle and the angular velocity are basically estimated by MRAS. In figure 5, the right hand routine shows the estimated value correction routine, and it is called an estimated value corrector.

In the case where the frequency of the currents for the position angle estimation is larger than the frequency of the currents for the motor drive, the position angle can be accurately estimated enough by the current injection method. We call this area the lower speed region.

The estimate values corrector revises the angular velocity which is the differentiated value of the position angle estimated by the current injection method eq.(7) and the

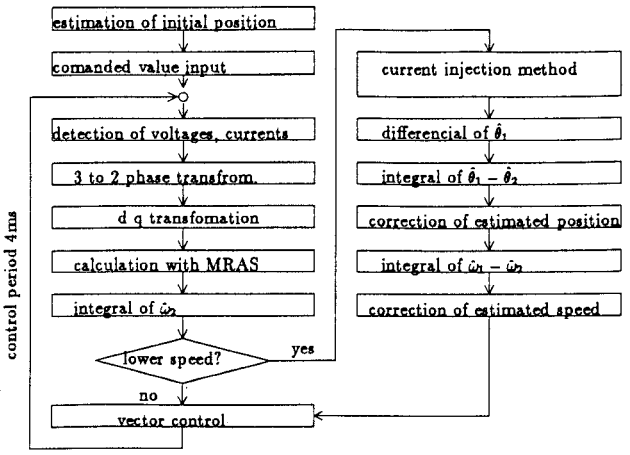

Fig. 5. flow chart of sensorless control system.

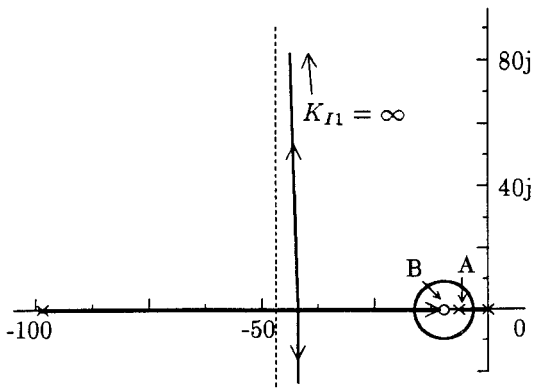

Fig. 6. Root locus of the system

angular velocity estimated by MRAS eq.(11). Then the corrector revises the position angle which is the integral value of the angular velocity estimated by MRAS and the position angle estimated by the current injection method.

$$\hat{\theta} = \hat{\theta}_2 + K_{I2}\int_0^\tau (\hat{\theta}_1 - \hat{\theta}_2)dt \qquad (14)$$

$$\hat{\omega} = \hat{\omega}_2 + K_{I3}\int_0^\tau (\hat{\omega}_1 - \hat{\omega}_2)dt \qquad (15)$$

where, K_{I2}, K_{I3} are gain constants for correcting the estimated values.

By using this corrector, not only the error by the noise but also the phase advances or the phase delay can be compensated according to the signature of the difference between $\hat{\theta}_1$ and $\hat{\theta}_2$ or $\hat{\omega}_1$ and $\hat{\omega}_2$. Therefore, we can reduce the errors which originates in the variation of the motor parameters in MRAS and the problems based on the small voltages detection.

B. Stability of the corrector

The root locus of this system is shown in figure 6. When the gain of angular velocity estimation by MRAS is enlarged, two complex root locuses go to the infinite-point of

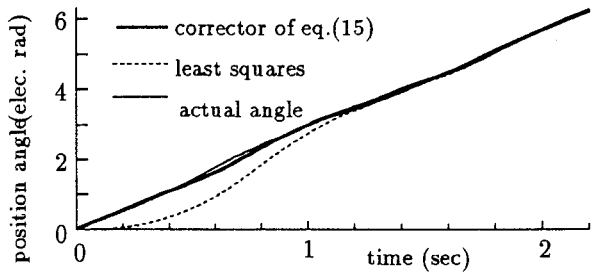

Fig. 7. Effect of error compensation.

$\pm$ 90 degrees along an asymptotic line. However, the root locus on real axis unlimitedly approaches the zero of transfer functions and it does not influence the transition characteristic after all. Therefore, the pole with the corrector is adjacent and becomes dipole with zero. Therefore, the system does not become unstable by adding the estimate values corrector to MRAS whose stability is guaranteed. In the corrector of the estimated position angle, the integrator is add to the system as figure 1 and the analyzing of stability is same as eq.(14). By adding the corrector to the system, the poles and zero are neighborhood and they become dipole.

Figure 7 shows the estimated position angle, when the motor is driven at 7 rpm. With the corrector based on eq.(14), the estimated position angles fit the actual ones. The corrector based on the method of least squares delays estimating the position angle. The corrector based on eq.(14) estimated the position angles accurately. And the position angles are estimated stably.

The gain constants of the system are $K_{P1} = 0.01$, $K_{I1} = 10$, $K_{I2} = 2$, $K_{I3} = 10$.

In the speed region which is lower than 10 rpm, the switches S1 and S2 in figure 1 are on.

In another speed region which is higher than 10 rpm, the position angle can be precisely estimated only with eq.(13), and the AC currents for estimated position angle are not added to the motor currents. Then, the switches S1 and S2 in figure 1 are off.

IV. Experimental Results

The tested motor is a 8 poles 18W salient-pole brushless DC motor, and the ratings of the motor are shown in TABLE I. The control process was implemented by a personal computer (NEC:PC-9821Xa). The calculation time of the sensorless control method is within 200 μs. The controlled period of the speed controller is 2 ms. The winding currents and the voltages are detected by A/D converters through

TABLE I
RATINGS OF TESTED MOTOR.

rated voltage	70V	R	17.3 Ω
rated current	1.53A	ϕ_f	0.27 wb
rated torque	4.0Nm	L_d	0.1649 H
rated rpm	43rpm	L_q	0.2071 H

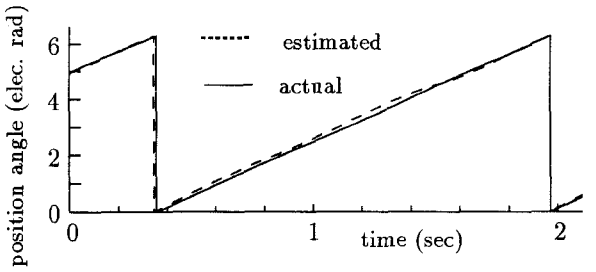

Fig. 8. Results of estimated position angles in lower speed region.

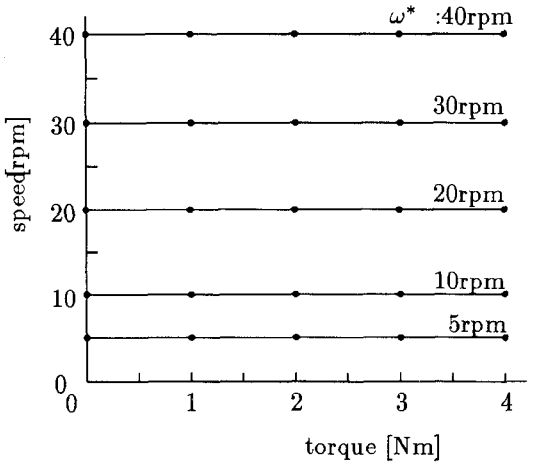

Fig. 9. Torque–speed characteristics.

the low pass filters (cut off frequency 500Hz).

Figure 8 shows the actual position angle and the estimated one in a lower speed region. In this experiment, the motor is held at the commanded value (8 rpm) by the sensorless control system. The errors between the estimated position angle and the actual one are within about 15 electrical degrees. The amplitude i_h^* and frequency ω_h^* of the currents for the position angle estimation are 0.1 A and 50 Hz.

Figure 9 shows the torque–speed characteristics by the sensorless control system. The system can control the motor in a lower speed region.

Figure 10 shows the starting condition by the sensorless control system.

Figure 11 shows an experimental result at the 4-quadrant drive condition of the tested sensorless drive system. In this case, the commanded speed −20 rpm is supplied at t=0, and after t=1s +20 rpm command is supplied to the system. The speed of the motor respond suitable fitted to

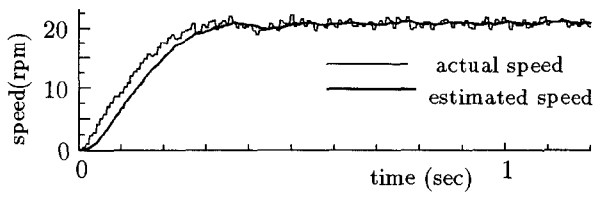

Fig. 10. Characteristics of starting condition.

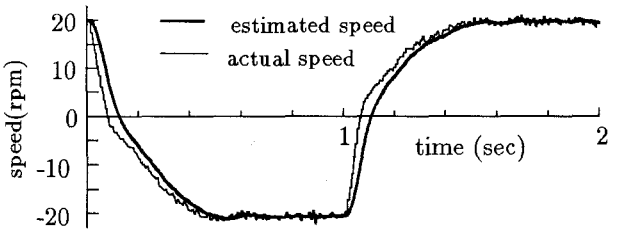

Fig. 11. 4-quadrant operation.

the commanded ones.

V. Conclusion

A practical use sensorless control drive of a salient-pole brushless DC motor is proposed. At a standstill condition, the initial position angle can be estimated without the vibration and the rotation of the shaft by adopting the current injection method. At a rotating condition, by using the estimate value corrector which is an easy composition, we can obtain the accurate estimated values stably even in a lower speed region. Hence, there are neither a rapid stopping nor a hunting motion by the turbulence of the noises which are contained in the detected voltages and currents etc. And it is possible to drive stably because the consecutive position angle signal can be obtained at any time. Therefore, the proposed method may extend the applications of sensorless brushless DC motor systems.

References

[1] G.Yang, R.Tomioka, M.Nakano and T.Chin, "Position Speed Sensorless Control of Brush-Less DC Motor Based on an Adaptive Observer," *T.IEE Japan*, Vol.113-D, No.5, 1993, pp. 579-586.

[2] M.Tomita, S.Douki and S.Ohkuma, "A Position-and-Velocity Sensorless Control for Brushless DC Motor With an Adaptive Sliding Observer," *T.IEE Japan*, Vol.115-D, No.6, 1995, pp. 765-774.

[3] T.Senjyu, T.Shimabukuro and K.Uezato, "Position Sensorless Vector Control of Cylindrical Permanent Magnet Synchronous Motors," in *Proceedings. of the IPEC-Yokohama '95*, 1995, pp 304-309.

[4] T.Takeshita and N.Matsui, "Sensorless Control and Initial Position Estimation of Salient-Pole Brushless DC Motor," in *Proceedings. of the AMC'96-MIE*, 1996, pp. 18-23.

[5] N.Matsui, "Sensorless PM Brushless DC Motor Drives," *IEEE Ind. Elec.*, vol.43, NO.2, APRIL, 1996, pp. 300-308.

[6] J.Watanabe, T.Takeshita and N.Matsui, "Low Speed Drive Including Zero-Speed for Sensorless Salient-Pole Brushless DC Motor," *National Conv. Rec. IEEJ'96*, No. 896.

[7] M.Tada, N.Kasa and H.Watanabe, "A Detecting Method of Starting Position Angle for Salient-Pole Brushless DC Motors," *T.IEE Japan*, Vol.116-D, 1996, pp. 978-979

[8] K.J.Astrom and B.Wittenmark, *Adaptive Control*, Addison-Wesley Publishing Company.

[9] K.Yamada, T.Noguchi, S.Kondou and I.Takahashi, "A Proposition of Rotor Position Estimation for Sensorless Salient PM Motor at Rest," in *Proceedings. of the JIASC'95*, No.178.

[10] H.Watanabe, H.Miyazaki and T.Fujii, "A Sensorless Detecting Strategy of Rotor Position and Speed on Permanent Magnet Synchronous Motor," *T.IEE Japan*, Vol.110-D, 1989, p1193.

[11] N.Kasa and H.Watanabe, "A Detecting Method of Position Angle at Standstill and Lower Speed Region for Salient-Pole Brushless DC Motors," in *Proceedings. of the ICIT'96* , 1996, pp. 574-578.

Fully Digital Implementation of PMSM Servo Based on A Novel Current Control Strategy

Jia Wu, Dongsheng Zhang, Yongdong Li*
Department of Electrical Engineering
Tsinghua University Beijing China 100084
Fax:8610-62562768, Phone:8610-62785520
E-mail:lyd@pwrs.eea.tsinghua.edu.cn

***Abstract*—A novel current control strategy for use in fully digital control of Permanent Magnet Synchronous Motor (PMSM) servo drive system is presented. This digital current control strategy is based on the information about three-phase current errors. There is no need to know precise motor parameters. It also requires no complex calculation such as motor counter EMF calculation. The sequence of output voltage vectors can be selected intelligently so that the number of switching is significantly minimized. The practical servo drive system adopting this current controller is designed with Intel 87C196KC as its control core part and with a third generation intelligent power module (IPM) as power switches of the inverter. Simulation and experimental results show that the practical system has satisfactory static and dynamic performance.**

I . INTRODUCTION

In recent years, permanent magnet synchronous motor (PMSM) servo drive systems are being used more and more in various high performance applications such as industrial robots, numerically controlled machine tools, and aerospace actuators. In order to eliminate the effect of the stator dynamics and control the torque directly, PMSM is usually fed by current-regulated voltage-source inverter (CR-VSI). Up to now, many current control strategies have been developed [1]-[8]. Amongst the most common are the hysteresis, ramp comparison, and predictive current control techniques. The hysteresis control technique can provide quick current response in transient state, but in steady state, the current ripple is usually large and the switching frequency varies widely [1]-[3], [6], [7]. Predictive control technique gives optimum performance in terms of steady accuracy, but requires complex calculation and the response time is relatively long [5]-[8]. Ramp comparison control technique has the advantage of preset operation frequency and producing well-defined harmonics but requires compensation to reduce the current error [1], [4], [7].

Since digital control of ac drive has many advantages such as high flexibility, simple hardware structure and excellent performance, more and more microprocessor-based controllers for ac drives are being employed with the development of microelectronics and power electronics.

In this paper, a novel simple current control strategy is presented. The output voltage vectors are selected according to the order of the values of three-phase current errors. The time durations of voltage vectors are derived from a PID regulator in each sampling period. This current control strategy can be implemented easily by software. It requires only very simple calculation. A fully digital PMSM servo drive system based on this control strategy has been designed. Simulation and experimental results of the system are given.

II . MATHEMATICAL MODEL OF PMSM

With the conventional assumptions, the basic equations of surface PMSM in the rotor reference frame are given directly as follows [8]:

$$u_d = r\,i_d + p\psi_d - \omega_r\,\psi_q \tag{1}$$

$$u_q = r\,i_q + p\psi_q + \omega_r\,\psi_d \tag{2}$$

$$\psi_d = L\,i_d + \psi_f \tag{3}$$

$$\psi_q = L\,i_q \tag{4}$$

$$J\frac{d^2\theta_r}{dt^2} + D\frac{d\theta_r}{dt} + K\theta_r = T_e - T_L \tag{5}$$

$$T_e = N_p\,(i_q\,\psi_d - i_d\,\psi_q) \tag{6}$$

The zero-i_d control method is suited for the surface PMSM, and high performance torque control can be obtained [10]. By adopting this method, the electric-magnetic torque equation (6) can be simplified as follows:

$$\begin{aligned} T_e &= N_p\,i_q\,\psi_d = N_p\,i_q\,(L\,i_d + \psi_f) \\ &= N_p\,i_q\,\psi_f \end{aligned} \tag{7}$$

From equation (7), the torque is proportional to the i_q. The reference command i_q^* is given by the speed regulator in the proposed control scheme. Therefore, the reference current components i_d^* and i_q^* in the *d-q* frame are given, the commands of three-phase instantaneous currents i_a^*, i_b^* and i_c^* in the *a*, *b* and *c* frame can be given as follows:

$$\begin{bmatrix} i_a^* \\ i_b^* \\ i_c^* \end{bmatrix} = \sqrt{\tfrac{2}{3}} \begin{bmatrix} \cos\theta_r & -\sin\theta_r \\ \cos(\theta_r - \tfrac{2}{3}\pi) & -\sin(\theta_r - \tfrac{2}{3}\pi) \\ \cos(\theta_r + \tfrac{2}{3}\pi) & \sin(\theta_r + \tfrac{2}{3}\pi) \end{bmatrix} \begin{bmatrix} 0 \\ i_q^* \end{bmatrix} \tag{8}$$

From equation (8), i_a^* ,i_b^* and i_c^* can be calculated by:

$$i_a^* = \sqrt{\frac{2}{3}} i_q^* \cos(\theta_r + \frac{\pi}{2}) \quad (9)$$

$$i_b^* = \sqrt{\frac{2}{3}} i_q^* \cos(\theta_r - \frac{\pi}{6}) \quad (10)$$

$$i_c^* = -(i_a^* + i_b^*) \quad (11)$$

Based on the above mathematical model of PMSM, simulation and control algorithm are carried out.

III . DIGITAL CURRENT CONTROLLER

Fig.1 shows the topological diagram of the circuit of PMSM fed by a voltage-source inverter (VSI). In this diagram, each leg of the inverter is made up of two power switches. There are three legs in the inverter. Conduction states of the legs are represented by three logic variables: *Sa*, *Sb* and *Sc*. When the upper switch of a leg is conducting, then *S*=1, and the conduction of the lower switch corresponds to *S*=0. There are eight effective operating states for the inverter (if no neutral is connected). They can be represented by voltage vectors *V(Sa, Sb, Sc)* as shown in Fig.2 , where *V*(0, 0, 0) and *V*(1, 1, 1) are zero voltage vectors and the other sixs are nonzero voltage vectors.

Block diagram of the proposed digital current controller is shown in Fig.3 . The function of a current controller is to force the instantaneous phase currents to follow their references. This can be accomplished by comparing the actual phase currents and the references. Proper voltage vectors and their time durations can be used to reduce the phase current errors $\Delta i = (i^* - i)$. If the current error in a phase winding is greater than zero, applying positive voltage will reduce it. On the contrary, if it is less than zero, applying negative voltage will achieve the same effect.

Because no neutral is connected in the servo drive system, there are interactions among three-phase current variations. In order to reduce phase current errors simultaneously, voltage vectors should be selected according to the order of the values of three phase current errors Δi_a ,Δi_b and Δi_c , expressed as :

$$\Delta i_L \geq \Delta i_M \geq \Delta i_N \quad (12)$$

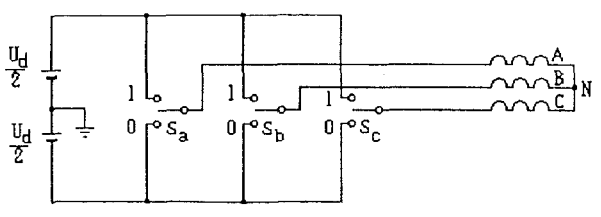

Fig. 1 Topological diagram of a PMSM fed by VSI

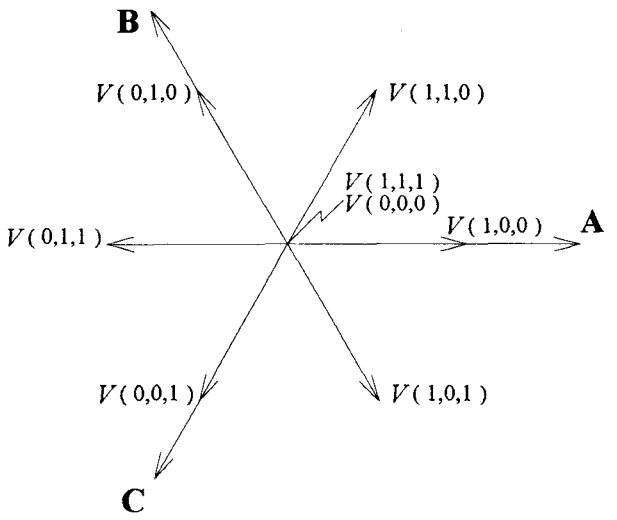

Fig. 2 Inverter voltage vectors

where Δi_L, Δi_M and Δi_N correspond to three phase current errors in value order.

In the next sampling period, conduction state of the leg corresponding to phase *L* holds "1", that is S_L=1. Conduction state of the leg corresponding to phase *N* holds "0", that is S_N=0. Conduction state of the leg corresponding to phase *M* switches from "0" to "1" or from "1" to "0". Then two nonzero voltage vectors are decided. For example, if $\Delta i_b \geq \Delta i_a \geq \Delta i_c$ in a current sampling period, then *L*=*b*, *M*=*a*, *N*=*c*. Thus *Sb*=1, *Sa*=0 or 1, *Sc*=0 in the next period. In other words, two nonzero output voltage vectors *V*(0, 1, 0) and *V*(1, 1, 0) should be chosen. If there is a time spare after the two active voltage vectors, a zero voltage vector should be selected. The sequence of the two or three voltage vectors is decided according to the preceding output voltage vector so as to minimize the number of switching (only one leg of the inverter changes conduction state when the output voltage vector varies). In the example above, if the preceding output voltage vector is *V*(0, 0, 0), then in the next sampling period the sequence of output voltage vectors should be *V*(0, 1, 0), *V*(1, 1, 0) and *V*(1, 1, 1).

Based on the error information, average phase voltage U_L and U_M corresponding to the two larger values of three phase current errors during a sampling period can be given by the PID regulator:

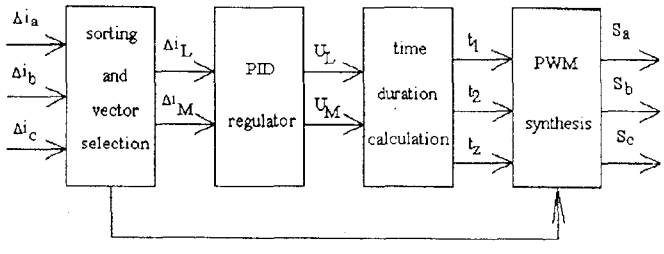

Fig. 3 Block diagram of the digital current controller

$$U_L(n) = U_L(n-1) + K_p[\Delta i_L(n) - \Delta i_L(n-1)] + K_i \Delta i_L(n) + K_d[\Delta i_L(n) - 2\Delta i_L(n-1) + \Delta i_L(n-2)] \quad (13)$$

$$U_M(n) = U_M(n-1) + K_p[\Delta i_M(n) - \Delta i_M(n-1)] + K_i \Delta i_M(n) + K_d[\Delta i_M(n) - 2\Delta i_M(n-1) + \Delta i_M(n-2)] \quad (14)$$

where $U_L(n), U_M(n), U_L(n-1)$ and $U_M(n-1)$ are the average phase voltages at n-th and (n-1)-th sampling instant respectively, and $\Delta i_L(n)$, $\Delta i_M(n)$, $\Delta i_L(n-1)$, $\Delta i_M(n-1)$, $\Delta i_L(n-2)$ and $\Delta i_M(n-2)$ are the phase current errors at n-th, (n-1)-th and (n-2)-th sampling instant respectively, K_p is the proportional coefficient, K_i is the integral coefficient and K_d is the differential coefficient of the PID regulator.

In the example mentioned above, the time durations of three voltage vectors can be derived from Fig.4. Fig.4 shows the topological diagram of PMSM windings fed by the two nonzero voltage vectors.

From Fig.4, average phase voltage U_L and U_M can also be given by:

$$U_L = (\tfrac{2}{3}U_d \cdot t_1 + \tfrac{1}{3}U_d \cdot t_2)/T \quad (15)$$

$$U_M = (\tfrac{1}{3}U_d \cdot t_1 - \tfrac{1}{3}U_d \cdot t_2)/T \quad (16)$$

Therefore time durations of the voltage vectors in the given example can be calculated as follows:

$$t_1 = T(U_L + U_M)/U_d \quad (17)$$

$$t_2 = T(U_L - 2U_M)/U_d \quad (18)$$

$$t_z = T - t_1 - t_2 \quad (19)$$

where t_1 and t_2 are the time durations of two non zero voltage vectors, t_Z is the time duration of the zero voltage vector, T is the sampling period and U_d is the dc input voltage of the inverter.

Thus, conduction states and time durations of the inverter during a sampling period can be depicted as Fig.5.

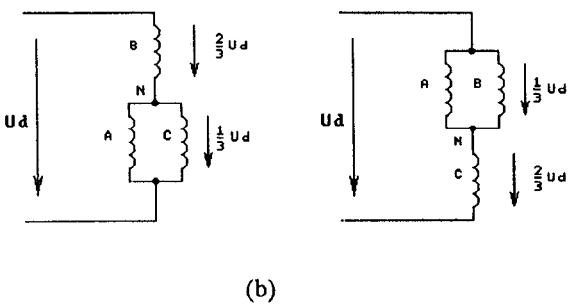

Fig. 4 Topological diagram of PMSM windings
(a) output voltage vector is $V(0, 1, 0)$
(b) output voltage vector is $V(1, 1, 0)$

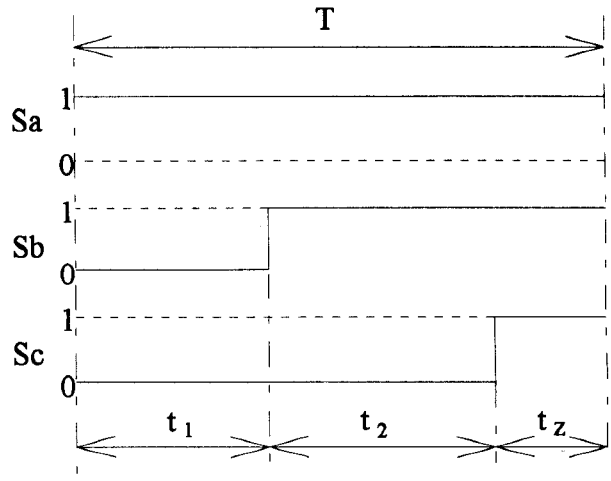

Fig. 5 Diagram of conduction states and their time durations

The output conduction states *Sa*, *Sb* and *Sc* shown as Fig.5 are used as drive signals for the inverter power switches.

Therefore this current control scheme is characterized by the simple digital implementation, optimized number of switching, constant switching frequency and no need to know accurate motor parameters.

Ⅳ. PMSM DRIVE SYSTEM CONFIGURATION

Based on the proposed current control strategy, a fully digital PMSM servo drive system has been implemented. The block diagram of this system is shown in Fig.6.

It consists of a PMSM fed by VSI, a composite position encoder mounted on the motor shaft and a fully digital controller using a high performance single chip microprocessor Intel 87C196KC to carry out speed and current closed-loop control. An incoming speed command ω_r^* is given to the microprocessor. Based on the speed information, the current command i_q^* can be derived from the speed regulator. It is then transformed to the

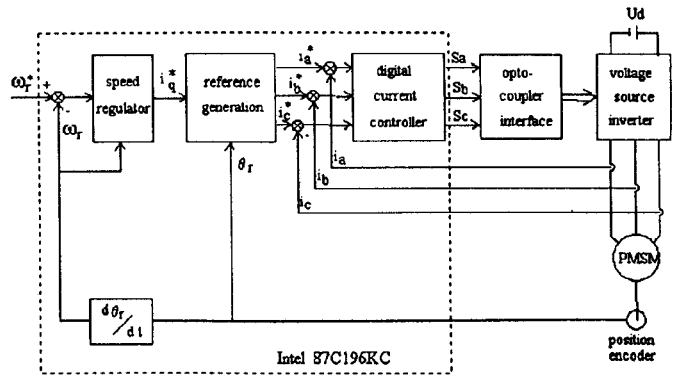

Fig. 6 Block diagram of the PMSM drive system

corresponding phase reference currents i_a^* ,i_b^* and i_c^* using the information of instantaneous rotor position. According to the phase current errors, the digital current controller selects proper voltage vectors and calculates their time durations.

Besides the regulation of motor speed and current, the measurement of rotor position and speed, PWM output, A/D conversion of phase currents are all placed on 87C196KC.

In this system, a third generation Intelligent Power Module (IPM) is used in the inverter as power switches. It integrates drive function, self-protection and self diagnostic function. Owing to this advanced power device, it only takes a little time to develop the drive and protection circuit for the inverter, and excellent performance such as low power loss, small size and high reliability of the inverter has been achieved.

V . Simulation and Experimental Results

Digital simulation for the whole servo drive system has been carried out on personal computer using C program. The parameters for the PMSM of this system are listed in the appendix. Simulation results with a sampling period of $100\mu s$ are shown as Fig.7-Fig.10. Fig.7 shows the step response at motor start from 0 rpm to the rated speed. In Fig.8 the step response at motor start from 0 rpm to 1rpm is plotted. Both of the torque ripple and speed ripple are considerable small.

Fig.9 shows the phase current in steady state operation at ω_r=3rpm. It can be observed that this system also has good dynamic and static performance at low speed even though the dc supply voltage is very high (300volts). Fig.10 shows the phase voltage and line voltage of the PMSM at ω_r=500rpm. It is noted that the number of switching is significantly minimized even compared with the improved hysteresis control scheme [3].

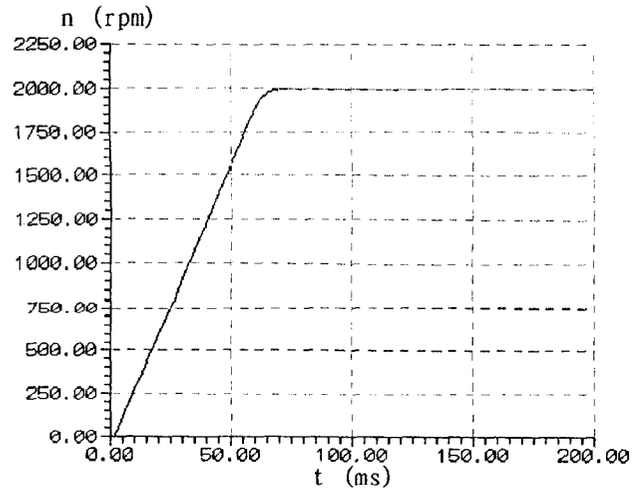

(a)

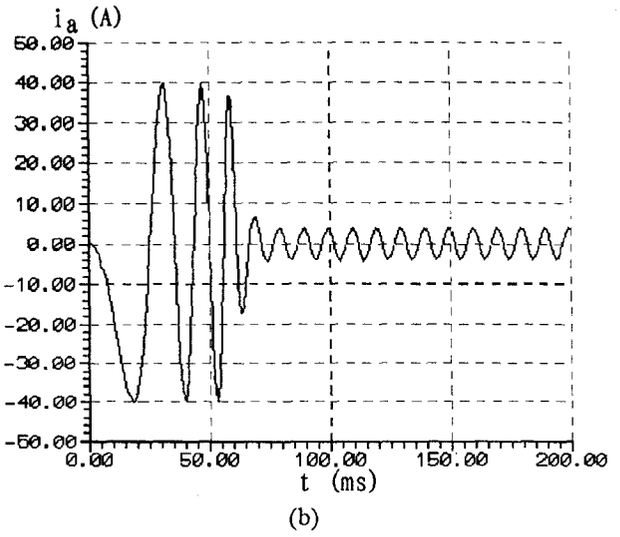

(b)

Fig. 7 Step response from 0rpm to the rated speed
(a) speed response (b) phase current response

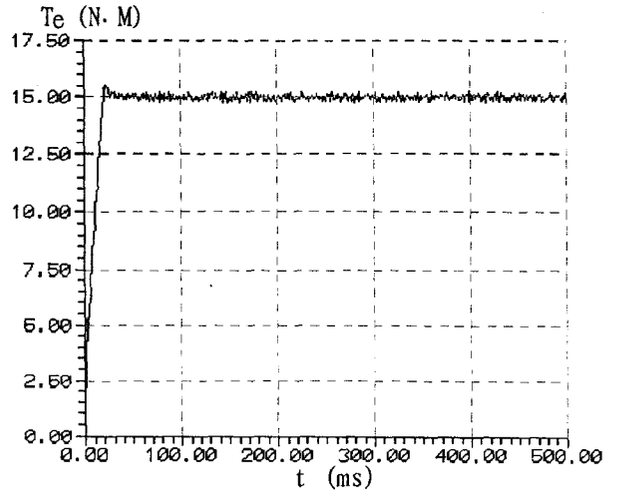

(a)

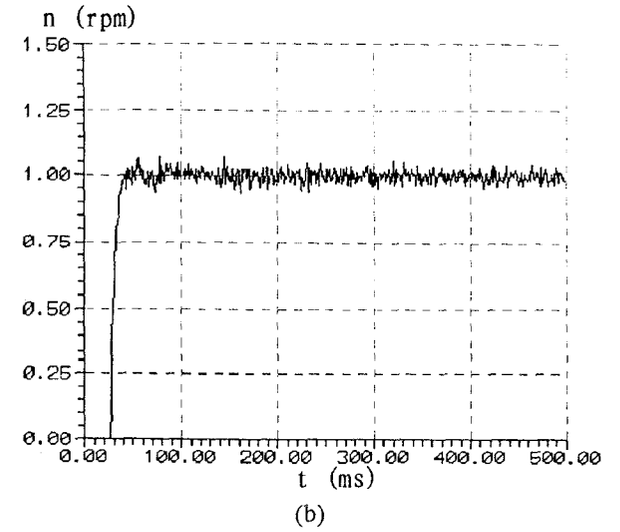

(b)

Fig. 8 Step response from 0rpm to 1rpm
(a) torque response (b) speed response

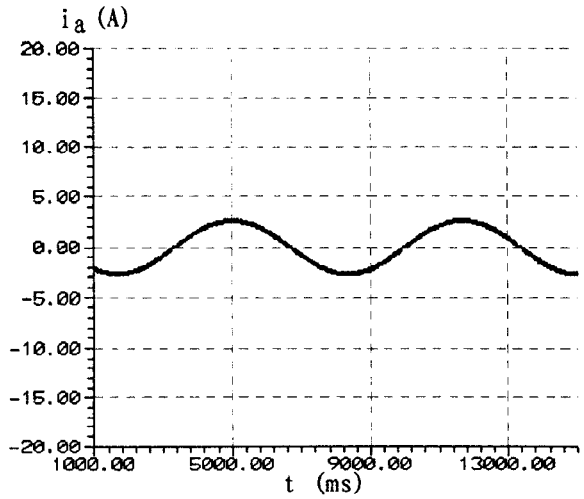

Fig. 9 Phase current waveform in steady state operation

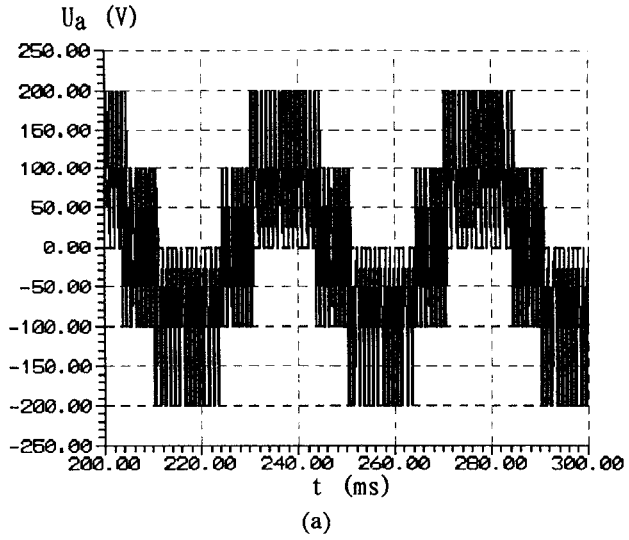

(a)

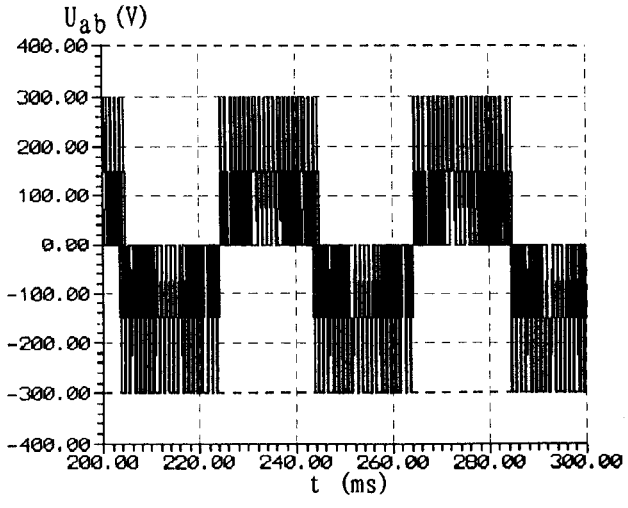

(b)

Fig. 10 Voltages of PMSM (a) phase voltage (b) line voltage

The proposed fully digital controller is tested with the practical servo drive system of PMSM. The experimental results are shown as Fig.11-Fig.13.

Fig.11 shows the phase current response to step change of reference speed from 0 rpm to 2000 rpm. Fig.12 shows the response of two phase currents in steady state

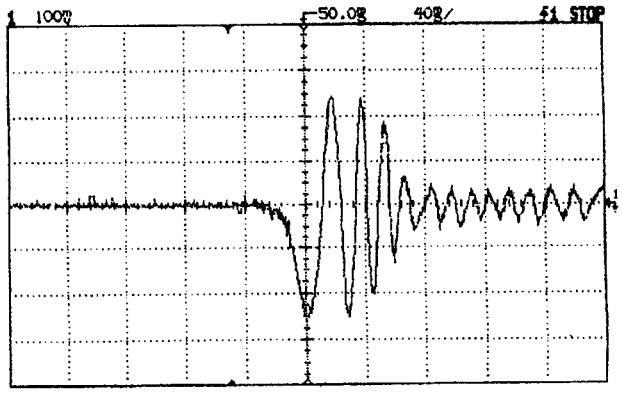

Fig. 11 Current response in one phase

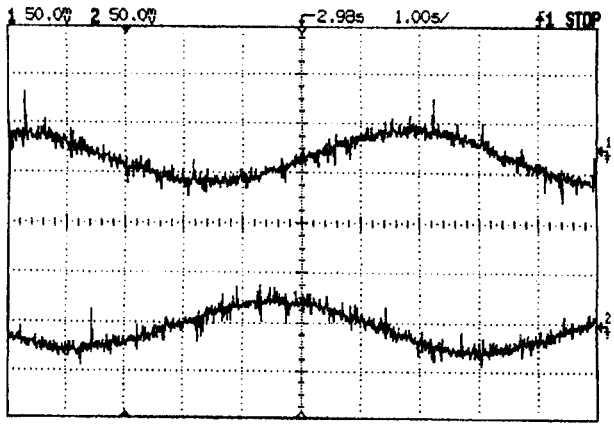

Fig. 12 Two phase currents in steady state

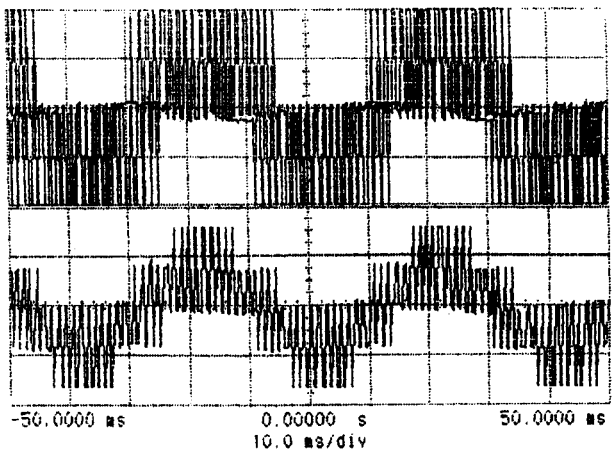

Fig. 13 Line voltage (upper) and phase voltage (lower) of PMSM

operation at ω_r=3rpm. Fig.13 shows the waveform of voltages of the PMSM at ω_r=500rpm.

The experimental results agree well with the simulation ones. It demonstrates that the practical system using the proposed control strategy can obtain satisfactory performance both in transient state and in steady state.

VI . Conclusion

A novel current control strategy has been described. It has been implemented simply all by software. No motor counter EMF calculation is required. No precise motor parameters are needed. By adjusting the sequence of two nonzero voltage vectors and a zero voltage vector (if exists) at every sampling period, the number of switching can be reduced intelligently. Digital simulation and experimental results indicate that the practical VSI-fed PMSM servo drive system adopting the proposed control strategy can achieve satisfactory performance.

Appendix

rated current:	18A
rated output torque:	$15N \cdot M$
motor parameters	
rated speed:	2000 rpm
number of poles:	6
armature resistance:	0.115Ω
armature inductance:	1mH
rotor inertia:	$J=0.0081N \cdot m \cdot s^2$
DC voltage source:	U_d=300 volts

References

[1] D. M. Brod and D. W. Novotny, "Current Control of VSI-PWM Inverters", *IEEE Trans. Ind. Appl.*, vol. IA-21, No. 4, pp. 562-570, 1985.

[2] M. L. Mazenc, C. Villanueva and J. Hector, "Study and Implementation of Hysteresis Controlled Inverter on a Permanent Magnet Synchronous Machine", *IEEE Trans. on Ind. Appl.*, vol. IA-21, No.2, pp408-413, 1985.

[3] M. P. Kazmierkowski, M. A. Dzieniakowski, and W. Sulkowski, "Novel Space Vector Based Current Controllers for PWM-Inverters", *IEEE Trans. Power Electron.*, vol. PE-6, No.1, pp158-165, 1991.

[4] T. M. Rowan and R. J. Kerkman, "A New Synchronous Current Regulator and an Analysis of Current Regulated PWM Inverters", *IEEE Trans. on Ind. Appl.*, vol. IA-22, No.4, pp678-690, 1986.

[5] A. Nabae, S. Ogasawara and H. Akagi, "A Novel-Control Scheme for Current-Controlled PWM Inverters", *IEEE Trans. Ind. Appl.*, vol. IA-22, No. 4, pp. 697-701, 1986.

[6] H. Le-Huy and L. A. Dessaint, "An Adaptive Current Scheme for PWM Synchronous Motor Drives: Analysis and Simulation", *IEEE Trans. Power Electron.*, vol. PE-4, No.4, pp486-495, 1989.

[7] R. Dhaouadi and N. Mohan, "Analysis of Current-Regulated Voltage-Source Inverters for Permanent Magnet Synchronous Motor Drives in Normal and Extended Speed Ranges", *IEEE Trans. on Energy Conversion*, vol.5, No.1, pp137-144, 1990.

[8] Zhang Xue, Li Yongdong and Yin Tong, "Fully digital control of PMSM servo drive using DSP", in Proc. PEDS Conf. Rec., 1995, pp. 287-291, vol.1.

[9] Wu Jia, "The Study of a Fully Digital Permanent Magnet Synchronous Motor Servo Drive System and Its Novel Current Control Strategy", M.S. thesis, Tsinghua Univ., 1996.

[10] S. Morimoto, Y. Takeda, and T. Hirasa, "Current Phase Control Methods for Permanent Magnet Synchronous Motors", *IEEE Trans. Power Electron.*, vol. PE-5, No.2, pp133-139, 1990.

Sensorless Starting and Low Speed Drive of Cylindrical Brushless DC Motor Using Eddy Current at Un-known Load

Mutuwo Tomita *, Hideyuki Yamaguchi ** ,
Shinji Doki *, Shigeru Okuma *

*Okuma Lab. ,Dept. of Electrical Eng., Nagoya University
Furo-cho, Chikusa-ku, Nagoya, 464-01 , Japan
Fax:+81-52-789-3140 Phone:+81-52-789-2777
E-mail : tomita@okuma.nuee.nagoya-u.ac.jp

** AICHI ELECTRIC CO.,LTD.
1, Aichi-cho, Kasugai, 486, Japan
Fax:+81-568-35-1253 Phone:+81-568-31-1111

Abstract- **A novel technique is proposed to realize starting and low speed drive of a cylindrical brushless dc motor without a position sensor at an un-known load. They have been difficult because an electro-motive force does not arise enough at the starting and at low speeds and a coil inductance is constant irrespective of rotor position. Therefore, this paper proposes to paste non-magnetic materials on the rotor surface and to measure an opened phase voltage change caused by an eddy current which flows on the non-magnetic materials. The proposed method is shown very useful by experiments.**

1 Introduction

In this paper, new starting and low speed drive method of a cylindrical brushless dc motor without a position sensor at an un-known load is proposed.

Position sensors of brushless dc motors are expensive and they need wiring and extra space. To eliminate them, many methods of the position sensorless controls of brushless dc motors have been proposed. However, starting and low speed drive of a cylindrical brushless dc motor without a position sensor at an un-known load have been difficult because an electro-motive force does not arise enough at the starting and at low speeds and a coil inductance is constant irrespective of a rotor position. Therefore, the realization has been desired.

Recently, to estimate a rotor position of the cylindrical motor at a standstill, we have proposed a simple processing of the rotor that non-magnetic materials are pasted on the rotor surface to flow eddy currents. The eddy currents make an opened phase voltage change according to the rotor position. It has been possible to estimate the rotor position at a standstill using this opened phase voltage change [1].

In this paper, in case of the motor which has the rotor proposed [1], a low speed drive method without a position sensor is proposed. The opened phase voltage changes according to the rotor position because the eddy currents flow on the non-magnetic materials. Starting and low speed drive of the cylindrical motor without a position sensor at an un-known load is realized using both the proposed method in this paper and the rotor position estimation method at the standstill which has been published [1].

We show that the proposed method is very useful by experiments.

2 Opened Phase Voltage Change caused by Eddy Current

2.1 Structure of Motor and Pasted Non-magnetic Materials

We use a cylindrical brushless dc motor shown in fig.1 which has 6 slots, intensive windings and 4 poles. The non-magnetic materials whose width is 180° at an electrical angle are pasted every 360° at an electrical angle on the rotor surface as shown in fig.1. The position of the non-magnetic material is discussed in chapter 3. The rotor position shown in fig.1 is θ_{rm} at a mechanical angle.

2.2 Change of Inductance of Coil

An inductance of the coil changes according to a rotor position because eddy currents flow on the non-magnetic materials. It can be explained using an equivalent magnetic circuit.

In fig.1, take the U-phase coil for example. If each non-magnetic material whose width is 90° at a mechanical angle is divided into 6 pieces, 3 pieces of the non-magnetic material are superimposed on the U-phase coil as shown in fig.2 when the rotor position θ_{rm} is 45° (fig.1). In the case, if the flux generates as shown in fig.2, we can get the equivalent magnetic circuit shown in fig.3 [1] [2].

0-7803-3823-5/97/$10.00© 1997 IEEE

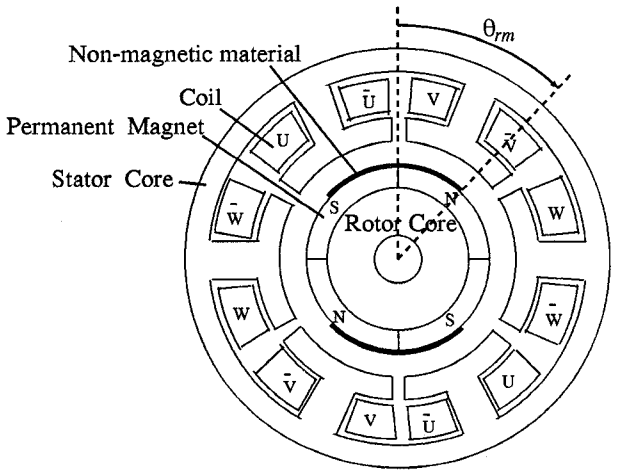

Fig. 1: Motor structure

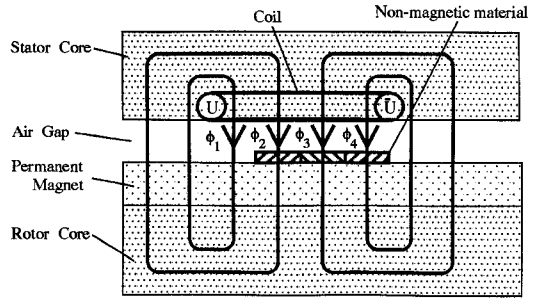

Fig. 2: Flux flow

In this equivalent magnetic circuit, we regard the non-magnetic material as a ring coil shown in fig.3. A number of the turns is equal to that of the U-phase coil. And it is assumed as N turns. Here, we assume a resistance of the ring coil as r whose number of turns is converted to that of the U-phase coil, and assume the current which flows in the ring coil as i_r [3]. We also assume a magnetic resistance of the magnetic path as R_g of the gap because the magnetic resistance of a yoke is less than that of air and is negligible. The gap mentioned is sum of the air gaps and thickness of the permanent magnet, as a magnetic conductivity of the permanent magnet is equal to that of air.

An equivalent electric circuit of the U-phase coil shown in fig.4 can be obtained from the equivalent magnetic circuit shown in fig.3 using the dual circuit theory [3].

When the coil consists of the 4 inductances in series, the resistances r are connected with each inductance in parallel as shown in fig.4, whose number is equal to that of the divided non-magnetic materials superimposed on the coil [1] [2].

As the resistances r of the ring coil is by far less than the reactances, we assume the resistances r is zero to evaluate qualitatively a change of the inductance of the coil. On the assumption, the equivalent circuit of the coil against the number of the pieces of the divided non-

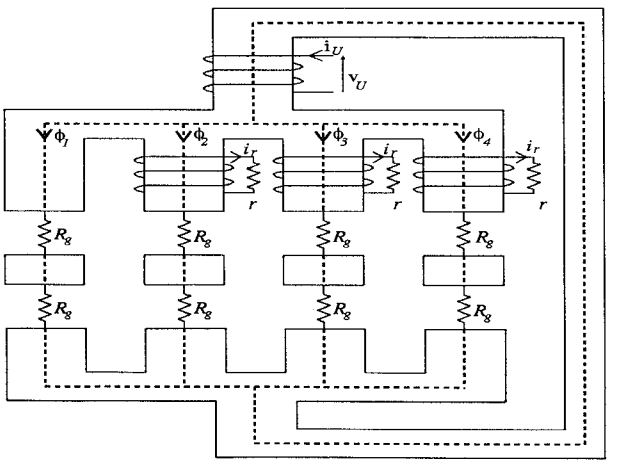

Fig. 3: Equivalent magnetic circuit (in case of the rotor position shown in fig.2)

magnetic materials superimposed on the coil is shown in fig.5 [1] [2].

From fig.5, we can see that the inductance of the coil changes according to the rotor position.

2.3 Mutual Inductance

In the preceding section, the change of the self-inductance is explained. In this section, change of the mutual inductance is described.

When the current i_U flows in the U-phase coil, the flux ϕ_U which generates in the U-phase coil is shown as follows,

$$\phi_U = \frac{L_U i_U}{N} \quad , \tag{2}$$

where

L_U: self-inductance of the U-phase coil .

We assume that the flux ϕ_U generates as shown in fig.6. A half of the flux ϕ_U is interlinked with the V-phase coil. The interlinked flux ϕ_{VU} is shown as follows,

$$\phi_{VU} = -\frac{1}{2}\phi_U \quad . \tag{3}$$

The number of turns of both the V-phase coil and W-phase coil is equal to the one of the U-phase coil and it is N. Therefore, from eqs.(2)and(3), the mutual inductance M_{VU} is shown as follows,

$$\begin{aligned} M_{VU} &= \frac{\phi_{VU} N}{i_U} \\ &= -\frac{1}{2} L_U \quad . \end{aligned} \tag{4}$$

Similarly, the inductance matrix $[L]$ is calculated as follows [1] [2],

$$\begin{aligned} [L] &= \begin{bmatrix} L_U & M_{UV} & M_{UW} \\ M_{VU} & L_V & M_{VW} \\ M_{WU} & M_{WV} & L_W \end{bmatrix} \\ &= \begin{bmatrix} L_U & -\frac{1}{2}L_V & -\frac{1}{2}L_W \\ -\frac{1}{2}L_U & L_V & -\frac{1}{2}L_W \\ -\frac{1}{2}L_U & -\frac{1}{2}L_V & L_W \end{bmatrix} \quad , \end{aligned} \tag{5}$$

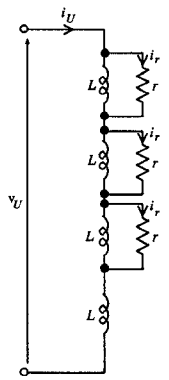

where

$$L = \frac{N^2}{2R_g} \tag{1}$$

N : number of the turns of the U-phase coil

r : resistance of the ring coil

i_r : current which flows in the ring coil .

Fig. 4: Equivalent electric circuit (in case of the rotor position shown in fig.2)

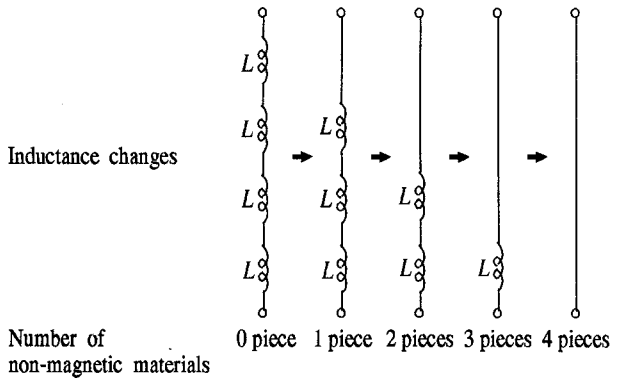

Fig. 5: Equivalent circuit of coil

where

L_V : self-inductance of the V-phase coil

L_W : self-inductance of the W-phase coil .

2.4 Relation between Rotor Position and Opened Phase Voltage

Fig.7 shows a configuration of an inverter. In fig.7, a state that transistors T_U and T_Y are on and other transistors are off is called a $U-Y$ conduction state, and a state that transistors T_V and T_X are on and other transistors are off is called a $V-X$ conduction state. When the $U-Y$ and $V-X$ conduction states are selected, the W-phase of the motor is open. A voltage v_{WG} at this time is called an opened phase voltage. Especially, a voltage v_{WG} in the $U-Y$ conduction state when the $U-Y$ conduction state and the $V-X$ one occur alternately is called an opened phase voltage v_{WGU-Y}.

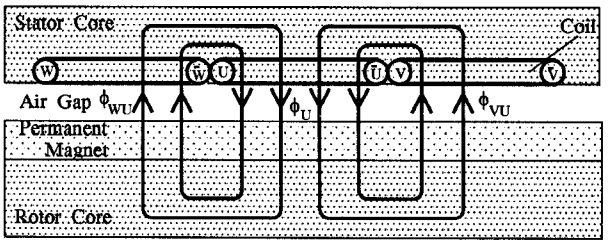

Fig. 6: Flux flow from U-phase to another phase

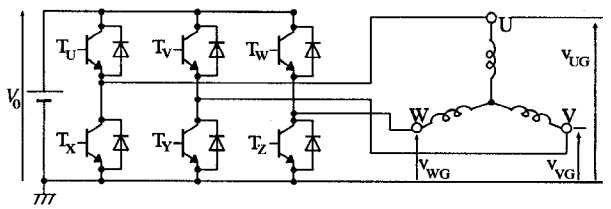

Fig. 7: Configuration of inverter

Now we discuss the opened phase voltage v_{WGU-Y}. Fig.8 shows the motor circuit when the $U-Y$ conduction state is chosen. The winding resistance is neglected. The voltage e_U, e_V, and e_W are an e.m.f. of each phase.

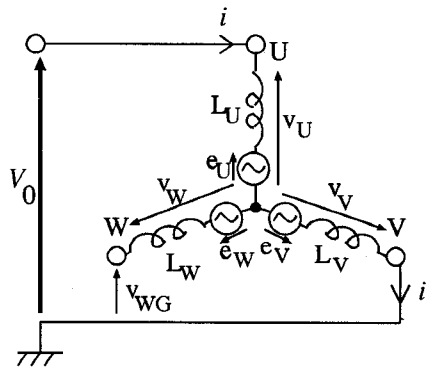

Fig. 8: Motor circuit in which T_U and T_Y are on

The differential pi of the current i is calculated using eq.(5) as follows,

$$\begin{aligned} V_0 &= v_U - v_V \\ &= L_U \cdot pi + M_{UV} \cdot p(-i) + e_U \\ &\quad - \{L_V \cdot p(-i) + M_{VU} \cdot pi + e_V\} \\ &= L_U \cdot pi + \frac{1}{2} L_V \cdot pi + e_U \\ &\quad - \{L_V \cdot p(-i) - \frac{1}{2} L_U \cdot pi + e_V\} \\ &= \frac{3}{2}(L_U + L_V) pi + e_U - e_V \quad . \end{aligned} \tag{6}$$

Therefore,

$$pi = \frac{2}{3} \cdot \frac{V_0 - (e_U - e_V)}{L_U + L_V} \quad , \tag{7}$$

where

p:differential operator.

The opened phase voltage v_{WGU-Y} is calculated using eqs.(5) and (7) as follows,

$$\begin{aligned} v_V &= L_V \cdot p(-i) + M_{VU} \cdot pi + e_V \\ &= -L_V \cdot pi - \frac{1}{2} L_U \cdot pi + e_V \end{aligned} \quad (8)$$

$$\begin{aligned} v_W &= M_{WU} \cdot pi + M_{WV} \cdot p(-i) + e_W \\ &= -\frac{1}{2} L_U \cdot pi + \frac{1}{2} L_V \cdot pi + e_W \ . \end{aligned} \quad (9)$$

Therefore,

$$\begin{aligned} v_{WGU-Y} &= v_W - v_V \\ &= \frac{L_V}{L_U + L_V} V_0 \\ &\quad - \frac{L_V}{L_U + L_V}(e_U - e_V) + e_W - e_V \ . \end{aligned} \quad (10)$$

From eq(10), the opened phase voltage v_{WGU-Y} includes both the position information caused by the inductance change and the e.m.f.. Therefore, we consider eliminating an influence of e.m.f. by using the opened phase voltage v_{WGV-X} in the $V-X$ conduction state.

The voltage v_{WGV-X} in the $V-X$ conduction state is shown by following equation.

$$\begin{aligned} v_{WGV-X} &= \frac{L_U}{L_U + L_V} V_0 \\ &\quad - \frac{L_U}{L_U + L_V}(e_U - e_V) + e_W - e_U \end{aligned} \quad (11)$$

From eqs.(10)(11), an absolute value of a difference v_{WGp-p} between the voltage v_{WGU-Y} and v_{WGV-X} is shown by following equation.

$$\begin{aligned} v_{WGp-p} &= |v_{WGU-Y} - v_{WGV-X}| \\ &= \left| \frac{L_V - L_U}{L_U + L_V} V_0 \right| \end{aligned} \quad (12)$$

Note that the difference v_{WGp-p} between opened phase voltages is not influenced by the e.m.f..

Now we discuss that the difference v_{WGp-p} changes according to the rotor position. For example, the difference v_{WGp-p} in case of the rotor position $\theta_{rm} = 45°$ is calculated as follows. The non-magnetic material is divided into 6 pieces. In this case, 3 pieces of the non-magnetic material are superimposed on the U-phase coil, and 3 pieces of them are superimposed on the V-phase coil. Therefore, from fig.5, the inductances L_U and L_V are shown as follows,

$$L_U = L, \text{and } L_V = L \ . \quad (13)$$

From eqs.(12) and (13), the difference v_{WGp-p} is shown as follows,

$$v_{WGp-p} = 0 \ . \quad (14)$$

The qualitative change of the difference v_{WGp-p} against the rotor position θ_{re} at an electrical angle is shown in fig.9. The relation between the electrical angle θ_{re} and the mechanical one θ_{rm} is $\theta_{re} = 2\theta_{rm}$.

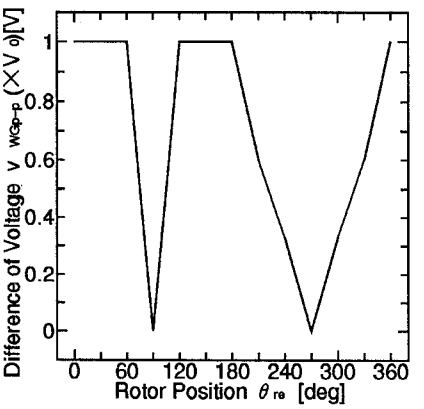

Fig. 9: Difference of voltage of opened phase v_{WGp-p} against rotor position

To use the difference v_{WGp-p} for the low speed drive, it is desirable that the change of the difference v_{WGp-p} is smooth. Therefore, the position where the non-magnetic materials are pasted is adjusted as in the next chapter.

3 Position where Non-magnetic Material is Pasted

In the preceding chapter, we assume that the permeance of a permanent magnet is equal to that of air. However, in case of small motors, there is a small difference between permeance P_d of a d-axis and P_q of a q-axis because the rotor is magnetized in the direction as shown in fig.10. Therefore, when non-magnetic materials are not pasted, an inductance of a coil changes slightly according to a rotor position despite of the cylindrical motor, and an opened phase voltage changes too. On the assumption of $(P_d - P_q)/(P_d + P_q) = -0.1$, the change of the difference v_{WGp-p} against the rotor position θ_{re} is shown in fig.11 when the $U-Y$ conduction state and the $V-X$ one occur alternately. The change of the voltage may be too small to be measured for a rotor position estimation.

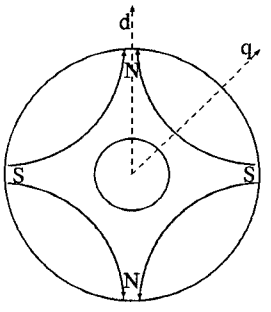

Fig. 10: Rotor which has magnetization in direction of pole

On the proposed rotor, non-magnetic materials are pasted and they also make changes of the voltage. Ac-

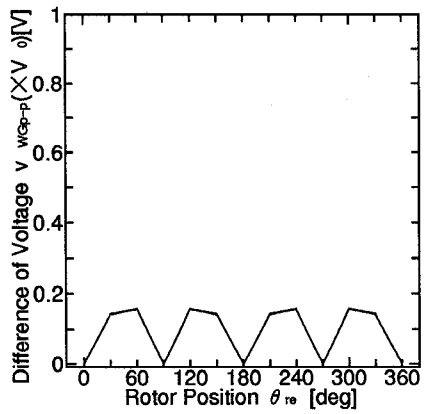

Fig. 11: Difference of voltage of opened phase v_{WGp-p} in which non-magnetic materials are not pasted

cording to the principle of superposition, a measured waveform of the difference v_{WGp-p} is synthesized from the waveform in fig.9 and one in fig.11. Therefore, by adjusting the positions where the non-magnetic materials are pasted, it is possible to make the difference v_{WGp-p} change smoothly. For reasons mentioned, the non-magnetic materials are pasted on the boundary line between N-pole and S-pole as shown in fig.1. The position where non-magnetic material is pasted is the optimal one in the position estimation method without a position sensor at the standstill [1].

4 Measurement of Difference Between Opened Voltages

To verify the principle in chapters 2 and 3, the opened phase voltage v_{WG} is measured when the $U-Y$ conduction state and the $V-X$ one occur alternately at a duty ratio of 50%. The motor is 65W. The aluminum whose thickness is 0.08mm is used for the non-magnetic material. The frequency of the conduction state is high i.e. 20kHz. The voltage V_0 in fig.7 is 33V.

Fig.12 shows the U-phase voltage v_{UG} and the opened phase voltage v_{WG} when the electrical rotor position θ_{re} is 180°. The $U-Y$ conduction state is selected when the U-phase voltage v_{UG} is V_0. The $V-X$ conduction state is selected when the U-phase voltage v_{UG} is 0. The opened phase voltage v_{WG} is not constant because of the winding resistance. We regard the peak value of the opened phase voltage in the $U-Y$ conduction state as the voltage v_{WGU-Y}, and regard the peak value of the opened phase voltage in the $V-X$ conduction state as the voltage v_{WGV-X}.

Fig.13 shows the difference v_{WGp-p} between the opened phase voltages against the rotor position θ_{re}. The change of the difference v_{WGp-p} is synthesized from the waveform in fig.9 and one in fig.11, and changes smoothly according to the rotor position.

5 Principle of Low Speed Drive

5.1 Adopted Conduction Method

A conduction type of the proposed method is 120° conduction type. The conduction state is changed in

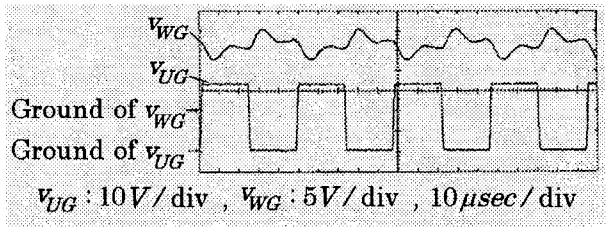

Fig. 12: U-phase voltage and voltage of opened phase

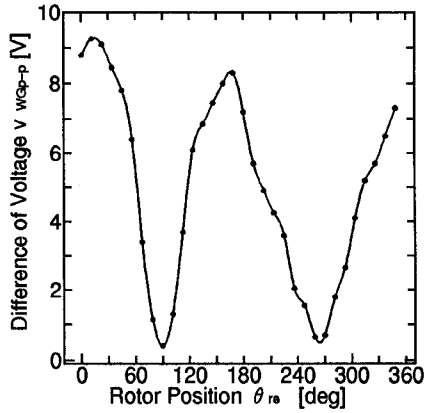

Fig. 13: Difference of voltage of opened phase v_{WGp-p} against rotor position

sequence according to the rotor position as shown in table5.1.

It is possible to control a torque by changing the duty of each conduction state. For example, a $U-V$ conduction state whose duty is 65% is defined as a conduction state that the $U-Y$ conduction state whose time is 65% for one cycle and $V-X$ one whose time is 35% occur alternately. Similarly, a $U-W$ conduction state, a $V-W$ one, a $V-U$ one, a $W-U$ one and a $W-V$ one are defined.

Table.5.1 Relation between position and conduction state

position θ_{re}(electrical angle)	conduction state
330° ~ 360(0)°,0°~30°	V-U
30°~90°	W-U
90°~150°	W-V
150°~210°	U-V
210°~270°	U-W
270°~330°	V-W

5.2 Principle of Low Speed Drive

The difference v_{WGp-p} between the opened phase voltages is shown in fig.13 when the $U-V$ conduction state or the $V-U$ one occur. From table.5.1, the torque is maximum at θ_{re}=180° in the $U-V$ conduction state and θ_{re}=0° in the $V-U$ conduction state. From fig.13, these rotor positions coincide with ones

which give a maximum value of the difference v_{WGp-p}. Therefore, the conduction state is changed into next one when the difference v_{WGp-p} passes the maximum value and decreases to the voltages which corresponds to the rotor position(30° or 210°) for the change of conduction state. Similarly, in case of the other conduction states 120° conduction type is capable of carrying out. In this method, the position sensorless drive becomes possible in low speeds.

6 Experiment for Low Speed Drive

6.1 Experimental Setup

Fig.14 shows an experimental setup. The motor, non-magnetic materials, the frequency of the conduction state and the voltage V_0 is already shown in chapter 4. The maximum torque of the motor is 0.294Nm. A sampling circuit measures the each opened phase voltage, and calculates the difference v_{UGp-p},v_{VGp-p} or v_{WGp-p} and outputs it to a microcomputer.

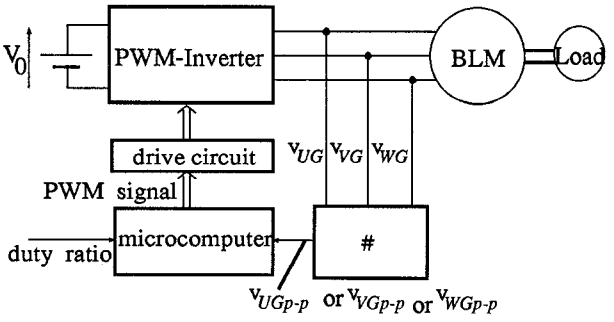

Fig. 14: Structure of experimental equipment

The microcomputer is H8/3048F. The microcomputer changes the conduction state using the difference v_{UGp-p},v_{VGp-p} or v_{WGp-p} and outputs a PWM signal. A load is realized by attaching a weight to disk.

6.2 Starting and Low Speed Drive without Position Sensor at Un-known Load

In fig.14, the microcomputer estimates the rotor position at a standstill using the method [1] and starts to rotate the motor by generating the PWM signal whose duty is 85% in the optimal conduction state. When the motor begins to rotate, the microcomputer changes the conduction state to the optimal one in sequence by the method shown in the chapter 5. When the starting and low speed drive without a position sensor are carried out by the above method, the relation between the load torque T_{load} and the steady state velocity ω_{rms} is shown in fig.15. For a example, the mechanical rotor position θ_{rm} and a signal of conduction state in a case where the load torque is 0.259Nm at a speed of 51rpm is shown in fig.16. The conduction state changes when the signal moves up or down.

Fig.15 and 16 show that the starting and low speed drive of the cylindrical motor without position sensor is realized without a reverse rotation despite the un-known load.

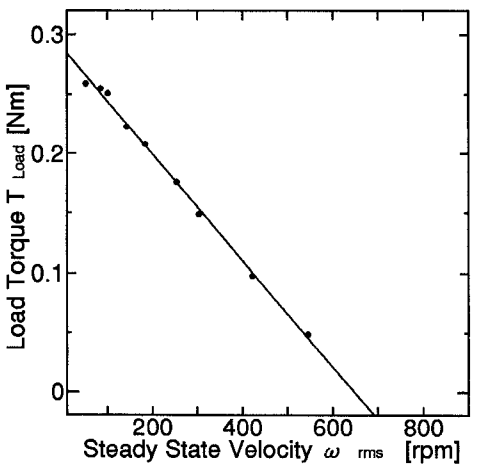

Fig. 15: Relation between load torque and steady state velocity

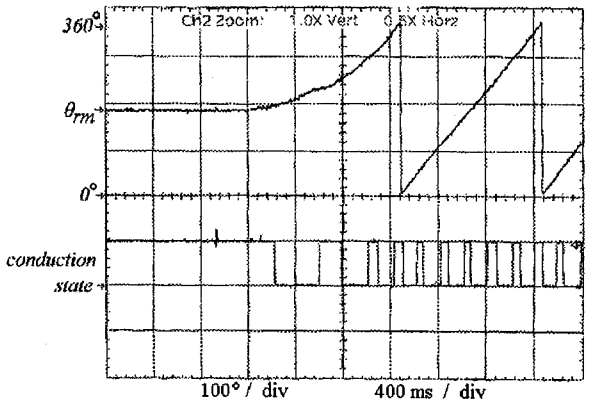

Fig. 16: Starting and low speed drive of motor

7 Conclusion

To realize the starting and low speed drive of the cylindrical brushless dc motor without a position sensor at the un-known load, we proposed to paste the non-magnetic materials on the rotor surface and to measure the opened phase voltage. The experimental results showed that the starting and low speed drive without a position sensor is realized without a reverse rotation at the un-known load.

References

[1] M.Tomita,H.Yamaguchi,S.Doki and S.Okuma. A Sensorless Estimation of Rotor Position of Cylindrical Brushless DC Motors Using Eddy Current . *Proceedings of the 1996 IEEE IECON*, 3 of 3:1723–1728, 1996.

[2] M.Tomita,M.Satoh,H.Yamaguchi,S.Doki and S.Okuma. Sensorless Estimation of Rotor Position of Cylindrical Brushless DC Motors Using Eddy Current . *1996 4th International Workshop on Advanced Motion Control Proceedings*, 1 of 2:24–28, 1996.

[3] T.Maeda et al. Single-Phase Linear Actuator with Semi-Closed Magnetic Circuit. *Trans.IEE Japan D*, 108-8:749–756, 8 1988. (in Japanese).

Initial Rotor Position Estimation of Salient-Pole Brushless DC Motors by Artificial Neural Network

Tomonobu Senjyu, Naomitsu Urasaki, and Katsumi Uezato
Faculty of Engineering, University of the Ryukyus
1 Senbaru Nishihara-cho Nakagami Okinawa 903-01, JAPAN
FAX: +81-98-895-8686, Phone: +81-98-895-8686
E-mail: b985542@tec.u-ryukyu.ac.jp

Abstract **– This paper presents an initial rotor position estimation method for salient-pole brushless dc motors (BLDCMs). An artificial neural network (ANN) is employed as an estimator of BLDCM at standstill. The ANN can express the relationship between voltage and current of BLDCM. The initial rotor position can be estimated by using the only current-signals from the ANN. The proposed method has the advantage of measurement noise immunity as well as no sensitivity to machine parameters. Computer simulation results verify the usefulness of the proposed method.**

I . Introduction

Brushless dc motors (BLDCMs) are receiving wide attention for industrial drives, such as robotics, electric vehicles, etc., because of their high torque/weight ratio, high efficiency and maintenance freedom. Since BLDCM drives require rotor position information to commutate, a position sensor such as absolute encoder or resolver should inevitably be fitted to motor in order to sense the rotor position. However these position sensors increase cost and size of motor and reduce reliability of the system, as a result, restrict industrial drive applications. Accordingly many position sensorless control strategies have been reported to avoid the problem[1-2]. Some researchers have achieved good results partially, however, almost all of them are incapable of estimating rotor position at standstill. Thus it is difficult to start BLDCM from standstill when the initial rotor position estimation error is large.

Recently, some researchers have proposed initial rotor position estimation methods for salient-pole BLDCMs utilizing the feature which their self-inductance sinusoidally varies with rotor position. In one study[3], the initial rotor position can be estimated by observing the stator current variation corresponding to the inductance variation when a certain voltage is applied. However it appear to be difficult to detect current exactly because of measurement noise. In other study[4], the phase difference between the stator current and voltage reference is used to estimate the initial rotor position. This method, however, suffers from inductance variation.

This paper presents a novel initial rotor position estimation method of salient-pole BLDCMs using artificial neural network (ANN). ANNs have attracted the attention of many researches in recent years because they have the advantage of fast parallel computation, noise immunity and fault tolerance. In motion control field, some researchers have reported ANN approach for induction motor drive[5-6]. In this paper an ANN is employed as an estimator of salient-pole BLDCM at standstill and plays an important role in suppressing the affection of measurement noise. The proposed initial rotor position estimation algorithm is composed of three stages. In the first stage, a three phase alternating voltage is applied to BLDCM and some date of voltage-current pairs at that time are sampled. Using the sampled data, the learning procedure of an ANN is implemented so that the ANN can obtain the relationship between voltage and current of BLDCM at standstill. In the second stage, the current-signals generated from the ANN fed a certain sinusoidal voltage-signal are used in the initial rotor position estimation algorithm. The initial rotor position can be estimated by using the only time derivative of the current-signal which has the information of rotor position. Thus the proposed method has the advantage of no sensitivity to machine parameters. Furthermore, the algorithm is seldom affected by measurement noise because this stage is entirely implemented in computerization. Since the initial rotor position cannot be determine uniquely in this stage, the polarity discrimination based on variation of peak exciting current due to magnetic saturation phenomenon is executed in the final stage. The initial rotor position can be estimated uniquely through the whole stages. Computer simulation results verify the usefulness of the proposed method.

II . Artificial Neural Network

In this section, a brief of general artificial neural network is presented. Fig. 1 illustrates a multi-layer feed

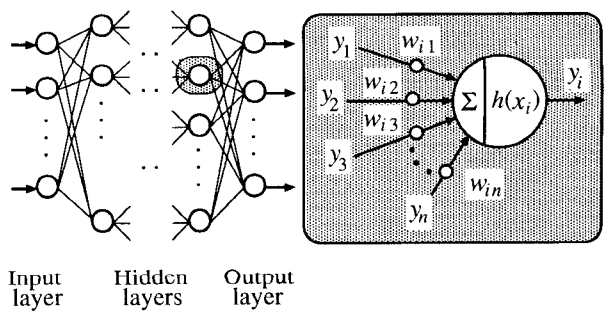

Fig. 1. A multi-layer feed forward ANN.

0-7803-3823-5/97/$10.00© 1997 IEEE

forward ANN. The ANN consists of an input layer, an output layer and some hidden layers. Each layer has some neurons that are connected to the next layer neurons by links. Each link has a different connection weight. The inputs to an i-th neuron are the outputs of previous layer neurons multiplied by the connection weights.

The activation of the i-th neuron is calculated as a sum of the inputs:

$$x_i = \sum_{j=1}^{l} w_{ij} y_j \tag{1}$$

where y_j is the output of previous layer j-th neuron, w_{ij} is the connection weight from j-th neuron to i-th neuron, and l is the number of previous layer neurons.

Then, the activation is transmitted to next layer neurons through a nonlinear transfer function as follows

$$y_i = h(x_i). \tag{2}$$

The nonlinear transfer function used in this paper is the following sigmoidal function:

$$h(x_i) = (1 + e^{-x_i})^{-1} \tag{3}$$

The nonlinear transfer function plays the important role in giving a ANN nonlinear mapping property. ANNs can obtain capability such as pattern recognition and any nonlinear function imitation by adjusting the connection weights appropriately. The process is called the *learning*, and error back propagation algorithm (BP algorithm) is generally used for the learning. BP algorithm is based on gradient descent method, *i.e.*, connection weights are iteratively updated so that the mean squared error E can decrease:

$$w_{ij}[n+1] = w_{ij}[n] + \eta\left(\frac{\partial E}{\partial w_{ij}[n]}\right) + \beta \Delta w_{ij}[n] \tag{4}$$

$$\Delta w_{ij}[n] = w_{ij}[n] - w_{ij}[n-1]$$

where η and β are the learning rate and the momentum coefficient, respectively.

The mean squared error E is calculated as

$$E = \frac{1}{2}\sum_{h=1}^{m}(d_h - y_h)^2 \tag{5}$$

where d_h is the desired output of the h-th neuron in output layer, and y_h is the corresponding actual output, respectively, and m is the number of output layer neurons.

III. Initial Rotor Position Estimation Algorithm

The initial rotor position estimation algorithm is composed of three stages. Details of the each stage is presented in this section.

A. Learning of ANN

In the proposed algorithm, an ANN is employed as an estimator of salient-pole BLDCM at standstill.

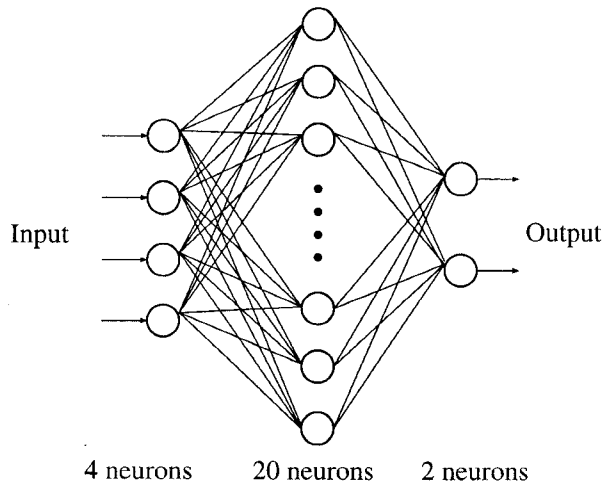

Fig. 2. The three-layer ANN used in the estimation algorithm.

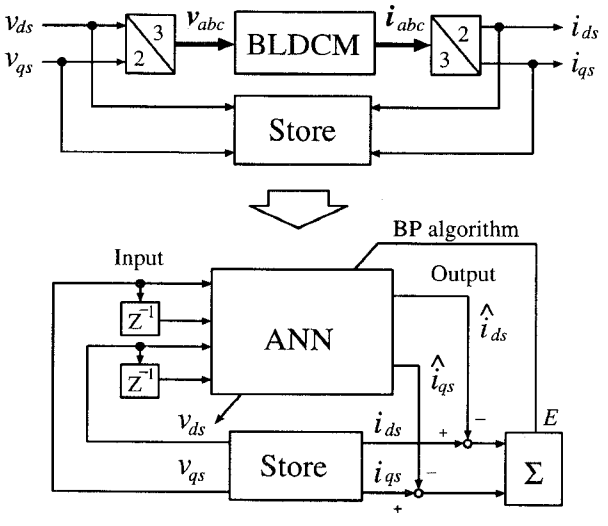

Fig. 3. The learning procedure of the ANN.

The electromagnetic model of salient-pole BLDCM at standstill expressed in stationary frame is given by

$$[\,\boldsymbol{v}\,] = R\,[\,\boldsymbol{i}\,] + p\,[\,\boldsymbol{L}\,][\,\boldsymbol{i}\,] \tag{6}$$

$$[\,\boldsymbol{v}\,]^T = [\,v_{ds}\;\; v_{qs}]$$

$$[\,\boldsymbol{i}\,]^T = [\,i_{ds}\;\; i_{qs}]$$

$$[\,\boldsymbol{L}\,] = \begin{bmatrix} L_1 + L_2\cos 2\theta_r & L_2 \sin 2\theta_r \\ L_2 \sin 2\theta_r & L_1 - L_2 \cos 2\theta_r \end{bmatrix}$$

where $L_1 = (L_d + L_q)/2$, $L_2 = (L_d - L_q)/2$, L_d and L_q are the self-inductance in synchronous reference frame. R is the armature resistance. v, i and θ_r represent the stator voltage, current, and rotor position, respectively. p is the differential operator.

Fig. 2 shows the three-layer ANN to imitate the input-output characteristic of salient-pole BLDCM described in Eq. (6). The ANN has four input-neurons,

twenty hidden-neurons and two output-neurons , respectively. The learning of the ANN is executed so that the ANN can obtain the relationship between voltage and current of BLDCM at standstill. The procedure is illustrated in Fig. 3. First, three phase alternating voltage is applied to BLDCM. Its amplitude is sufficiently small so that BLDCM cannot start. Some data of voltage-current pairs at that time are simultaneously sampled. Next, BP algorithm is implemented using the data. Take notice that the learning of ANN should be executed each time when the initial rotor position must be estimated because the electromagnetic model of salient-pole BLDCM at standstill changes with rotor position.

B. Initial Rotor Position Estimation

The ANN has obtained the relationship between voltage and current of BLDCM at standstill in the first stage. The initial rotor position estimation algorithm utilizing the ANN is developed in this subsection.

Now, ignoring the armature resistance R, Eq. (6) is arranged as follows

$$\left.\begin{aligned} pi_{ds} &= \frac{1}{L_1^2 - L_2^2}\{(L_1 - L_2\cos 2\theta_r)v_{ds} \\ &\qquad -L_2 \sin 2\theta_r v_{qs}\} \\ pi_{qs} &= \frac{1}{L_1^2 - L_2^2}\{(L_1 + L_2\cos 2\theta_r)v_{qs} \\ &\qquad -L_2 \sin 2\theta_r v_{ds}\} \end{aligned}\right\} \quad (7)$$

First, the sinusoidal voltage-signals expressed as Eq. (8) are fed into the ANN as shown in Fig. 4

$$\left.\begin{aligned} v_{ds1} &= \cos(2\pi ft) \\ v_{qs1} &= \sin(2\pi ft) \end{aligned}\right\} \quad (8)$$

where f represents the frequency of the voltage-signals and equals one of the three phase alternating voltage in the first stage. Since the ANN imitates the salient-pole BLDCM at standstill, the time derivative of the current-signals generated from the ANN should fit in Eq. (7).

Hence, the time derivative of current-signals are expressed as follows

$$\left.\begin{aligned} pi_{ds1} &= \frac{1}{L_1^2 - L_2^2}\{(L_1 - L_2\cos 2\theta_r)\cos(2\pi ft) \\ &\qquad -L_2 \sin 2\theta_r \sin(2\pi ft)\} \\ pi_{qs1} &= \frac{1}{L_1^2 - L_2^2}\{(L_1 + L_2\cos 2\theta_r)\sin(2\pi ft) \\ &\qquad -L_2 \sin 2\theta_r \cos(2\pi ft)\} \end{aligned}\right\} \quad (9)$$

Again, the voltage-signals expressed as Eq. (10) are fed into the ANN

$$\left.\begin{aligned} v_{ds2} &= \sin(2\pi ft) \\ v_{qs2} &= -\cos(2\pi ft) \end{aligned}\right\} \quad (10)$$

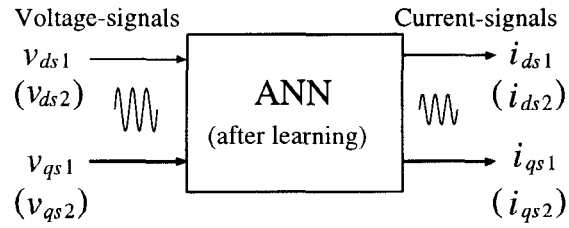

Fig. 4. Input and output of the ANN in the initial rotor position estimation algorithm.

Table 1. Rough estimation of initial rotor position.

Condition	Rotor position
$\sin 2\theta_r \geq 0,\ \cos 2\theta_r > 0$	$0° \leq \widehat{\theta}_r < 45°$ $180° \leq \widehat{\theta}_r < 225°$
$\sin 2\theta_r > 0,\ \cos 2\theta_r \leq 0$	$45° \leq \widehat{\theta}_r < 90°$ $225° \leq \widehat{\theta}_r < 270°$
$\sin 2\theta_r \leq 0,\ \cos 2\theta_r < 0$	$90° \leq \widehat{\theta}_r < 135°$ $270° \leq \widehat{\theta}_r < 315°$
$\sin 2\theta_r < 0,\ \cos 2\theta_r \geq 0$	$135° \leq \widehat{\theta}_r < 180°$ $315° \leq \widehat{\theta}_r < 360°$

From Eq. (7), the time derivative of the current-signals at that time are similarly expressed as follows

$$\left.\begin{aligned} pi_{ds2} &= \frac{1}{L_1^2 - L_2^2}\{(L_1 - L_2\cos 2\theta_r)\sin(2\pi ft) \\ &\qquad +L_2 \sin 2\theta_r \cos(2\pi ft)\} \\ pi_{qs2} &= -\frac{1}{L_1^2 - L_2^2}\{(L_1 + L_2\cos 2\theta_r)\cos(2\pi ft) \\ &\qquad +L_2 \sin 2\theta_r \cos(2\pi ft)\} \end{aligned}\right\} \quad (11)$$

Note that since the output of the ANN are not actual currents and are current-signals generated by the pattern recognition of the ANN in computerization, they are seldom affected by the measurement noise which causes undesirable phenomenon in practical situation. Furthermore, feeding pure sinusoidal voltage-signals into the ANN, the ANN generates pure sinusoidal current-signals. Thus the time derivative of the currents-signals are also pure sinusoidal wave form.

From Eqs. (9) and (11), we can successfully obtain the information of the rotor position θ_r of the form

$$D_4 D_1 - D_2 D_3 = \left(\frac{2}{L_1^2 - L_2^2}\right)^2 L_1 L_2 \sin 2\theta_r, \quad (12)$$

$$D_1 D_2 + D_3 D_4 = \left(\frac{2}{L_1^2 - L_2^2}\right)^2 L_1 L_2 \cos 2\theta_r \quad (13)$$

where $D_1 = -pi_{ds1} - pi_{qs2}$, $D_2 = pi_{ds1} - pi_{qs2}$, $D_3 = pi_{qs1} - pi_{ds2}$, $D_4 = pi_{qs1} + pi_{ds2}$.

Since the signs of $\cos 2\theta_r$ and $\sin 2\theta_r$ are directly distinguished from Eqs. (12) and (13), the rotor position is roughly estimated as shown in table 1. Furthermore the rotor position can be estimated as

$$\hat{\theta}_r' = \frac{1}{2}\tan^{-1}\left(\frac{D_4D_1 - D_2D_3}{D_1D_2 + D_3D_4}\right) \tag{14}$$

However Eq. (14) cannot determine the initial rotor position θ_r uniquely because it is derived from the information of 2 θ_r. Accordingly we must discriminate the polarity, N-pole or S-pole, in other way.

C. Polarity Discrimination

In the last stage, the polarity should be discriminated to determine the initial rotor position uniquely. The polarity is discriminated utilizing the variation of peak exciting current due to magnetic saturation phenomenon. The polarity discrimination is implemented as follows. First, we apply the voltage vector v_{dr1} according to $\hat{\theta}_r'$ estimated by Eq. (14) to BLDCM and measure a peak exciting current I_{peak1} at that time. Next, another peak exciting current I_{peak2} are sequentially measured when the voltage vector v_{dr2} according to the other side, *i.e.*, $\hat{\theta}_r' + 180°$ is applied to BLDCM. In the case $\hat{\theta}_r'$ corresponds to N-pole, I_{peak1} is greater than I_{peak2} due to magnetic saturation phenomenon. In another case, I_{peak1} is less than I_{peak2}. Thus the polarity discrimination can be achieved by distinguishing the sign of the difference of peak currents $I_{dif}(= I_{peak1} - I_{peak2})$ as illustrated in Fig. 5.

According to the sign of I_{dif}, the rotor position can be estimated uniquely as follows

$$\left.\begin{aligned} \hat{\theta}_r &= \hat{\theta}_r' \quad \text{at } I_{dif} > 0 \\ \hat{\theta}_r &= \hat{\theta}_r' + 180° \quad \text{at } I_{dif} < 0 \end{aligned}\right\} \tag{15}$$

The initial rotor position estimation algorithm proposed in this paper is summarized in Fig. 6:

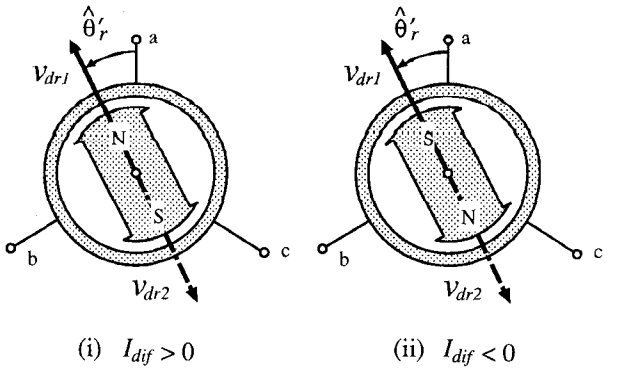

(i) $I_{dif} > 0$ (ii) $I_{dif} < 0$

Fig. 5. The polarity discrimination procedure.

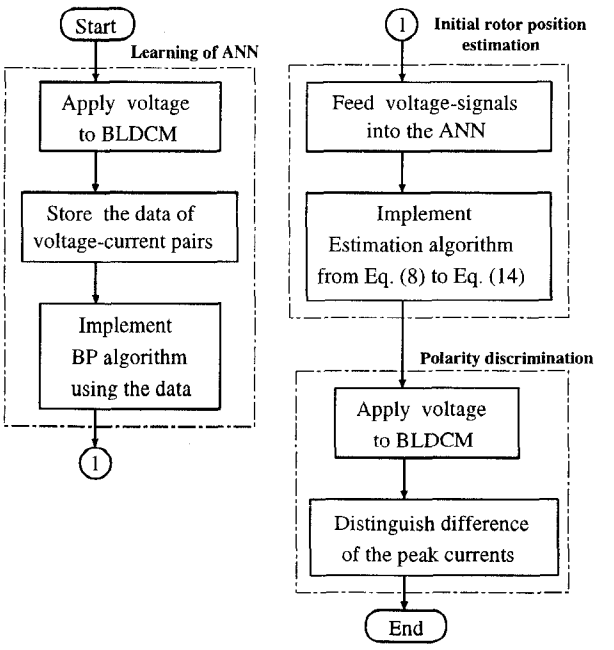

Fig. 6. Summary of the initial rotor position estimation.

- Learning of ANN

  BP algorithm is implemented using the data of voltage-current pairs so that an ANN imitates a salient-pole BLDCM at standstill.

- Initial rotor position estimation

  Initial rotor position is estimated by using the output of the ANN in accordance with the presented algorithm.

- Polarity discrimination

  polarity is discriminated utilizing the variation of peak exciting current due to magnetic saturation phenomenon.

IV . Simulation Results

Computer simulation results are illustrated to confirm the validity of the propose method. Table 2 lists the nominal machine parameters and control condition in this simulation.

In the first stage, three phase alternating voltage is applied to the tested BLDCM. 600 sampled data of voltage-current pairs are stored for the learning of the

Table 2. Nominal machine parameters and control condition.

rated power: 160 (W)	$J_n = 0.0026$ (kg·m^2)
$R_n = 2.48$ (Ω)	$D_n = 0.0005$ (N·m·s/rad)
$L_{dn} = 29.6$ (mH)	$P = 1$
$L_{qn} = 14.5$ (mH)	$f = 100$ (Hz)
$K_{en} = 0.28$ (N·m/A)	$T_s = 0.1$ (msec)

ANN as shown in Fig. 2 at that time. The learning is achieved by implementing BP algorithm as illustrated in Fig. 3. Learning rate η and momentum coefficient β used in the BP algorithm are 0.2 and 0.7, respectively. The learning procedure is repeated about 10,000 time steps so that the mean square error can be sufficiently small.

In the second stage, the initial rotor position estimation algorithm is executed. Fig. 7(a) shows the estimation result by Eq. (14) and the result shown in Table 1. As can be seen from this figure, the estimated rotor position $\widehat{\theta}_r'$ exists over the only range of 0° to 180° even though the actual rotor position exists all over the range of 0° to 360°. The reason is that Eq. (14) has the only information of $2\theta_r$. Thus the initial rotor position cannot be determined uniquely. However the estimation result is expected to result in acceptable accuracy if the polarity can completely be discriminated.

In the last stage, the polarity discrimination is executed to determine the estimated rotor position uniquely. The voltage vector according to $\widehat{\theta}_r'$ and the other side are applied to the BLDCM sequentially. Its amplitude is sufficiently large so that the magnetic saturation phenomenon may appear. Then, peak exciting currents at that time are measured and compared each other. Fig. 7(b) shows the difference of peak currents I_{dif} for actual rotor position. I_{dif} completely distributes with the polarity as illustrated in Fig. 5. Thus the polarity can be discriminated by distinguishing the sign of the difference of peak currents. Note that the polarity discrimination is achieved without strict measurement of current because it merely requires sign of the difference of peak currents.

From the results of Fig 7(a) and (b), the initial rotor position is estimated uniquely as shown in Fig. 7(c). On average, the initial rotor position is estimated within 5.2° error which includes maximum error 6.7°. The estimation error occurs due to ignoring armature resistance in the estimation algorithm as well as incomplete learning of the ANN. But the estimation error appears to be sufficient small so that BLDCM can start from standstill without trouble.

The proposed method is simply applied to different rated motors because it never requires any machine parameters. To confirm generalization of the proposed method, additional computer simulation results in the several situation are illustrated. Fig. 8(a) shows the estimation errors in the case the armature resistance is different from the nominal value listed in Table 2. As can be seen from this figure, the larger armature resistance increases estimation error while the smaller one contrariwise decreases estimation error. The reason is that the proposed method ignores the armature resistance in the estimation algorithm. The estimation error, however, settles within 10° in the worst case. Thus, it appears to hardly lead to fatal results. Fig. 8(b) shows the estimation errors in the case of different direct axis self-inductance. Although the estimation error does not dramatically change in the each case, it trends to decrease for larger direct-axis self-inductance. Thus it is seen that the proposed method for the motor with larger salient results in more accurate estimation. Fig. 8(c) shows the estimation errors in the case the frequency of

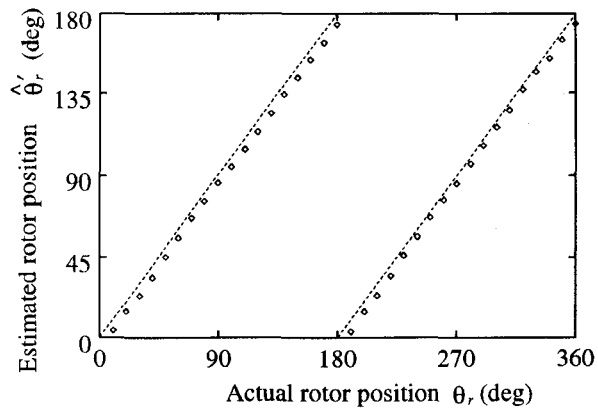

(a) Estimation results before polarity discrimination.

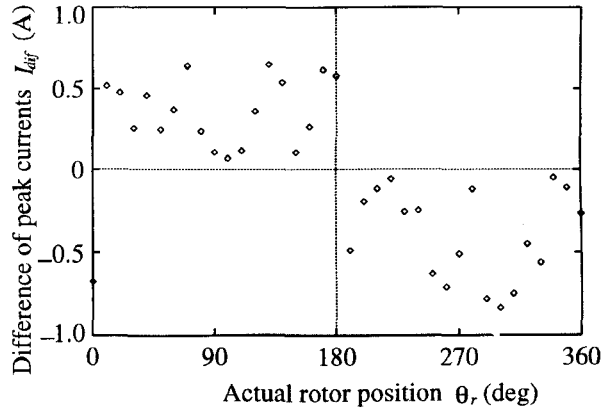

(b) Difference of peak currents for rotor position.

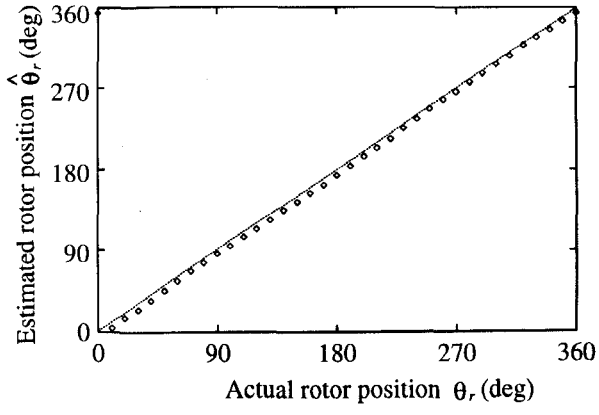

(c) Estimation results after polarity discrimination.

Fig. 7. Initial rotor position Estimation results.

three phase alternating voltage in the first stage is different from the nominal condition. The estimation error decreases when high frequency voltage is applied to BLDCM because the influence of ignoring the armature resistance is comparatively reduced in such a case.

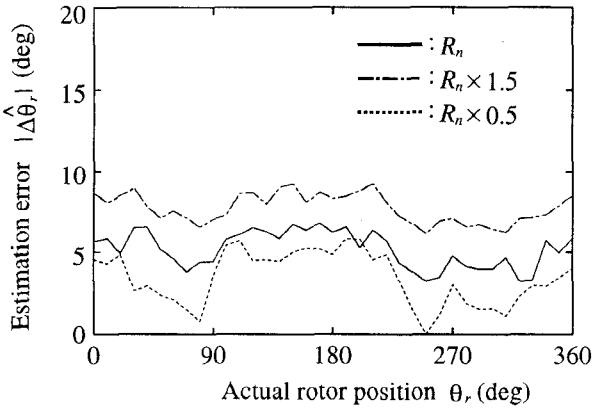

(a) Estimation error for armature resistance values.

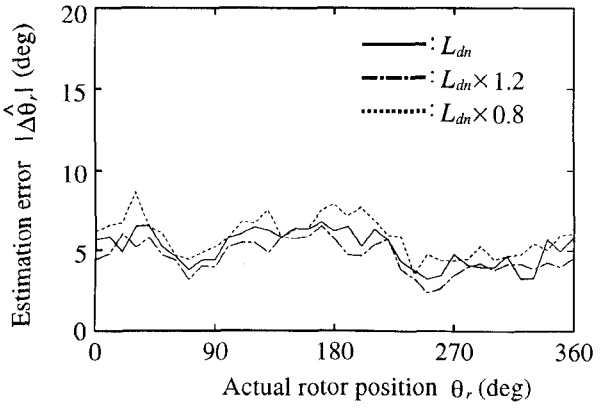

(b) Estimation error for self-inductance values.

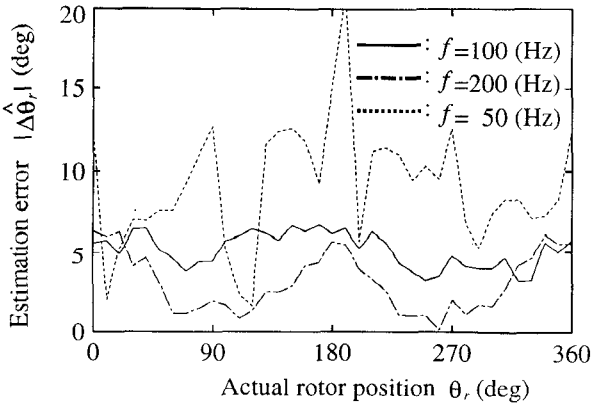

(c) Estimation error for frequency values of applied voltage.

Fig. 8. Initial rotor position estimation performance for several situation.

Table 3. Estimation error in the several situation.

Situation	Mean value	Maximum value
Nominal	5.2°	6.7°
$R_n \times 1.5$	7.7°	9.3°
$R_n \times 0.5$	3.4°	5.8°
$L_{dn} \times 1.2$	4.6°	6.6°
$L_{dn} \times 0.8$	5.9°	8.6°
$f = 200$Hz	3.1°	6.3°
$f = 50$Hz	9.1°	20.9°

However high frequency voltage may not necessarily be selected because the calculation of it requires powerful processor. Thus we should balance the accuracy of estimation with economy. Table 3 also lists the estimation error in the several situation. It can be seen from these results that the proposed method appears to have sufficiently generalization although the estimation performance to some extent changes according to the situation.

V . Conclusions

In this paper, the initial rotor position estimation method for salient-pole BLDCM using ANN is proposed. An ANN is employed as an estimation of BLDCM at standstill. The initial rotor position can be estimated by using the only current-signals generated from the ANN. Polarity discrimination is also executed to determine the initial rotor position uniquely utilizing the variation of peak exciting current due to magnet saturation phenomenon. The proposed method has the advantage of measurement noise immunity as well as no sensitivity to machine parameters. Computer simulation results verify the useful of the proposed method.

References

[1] R. Wu and R. Selman, "A Permanent Magnet Motor Drive Without a Shaft Sensor," *IEEE Transaction on Industry Applications*, Vol. 27, No. 5, pp. 1005-1011, 1991.

[2] N. Ertugral and P. Acarnley, "A New Algorithm for Sensorless operation of Permanent Magnet Motors," *IEEE Transaction on Industry Applications*, Vol. 30, No. 1, pp. 126-133, 1994.

[3] T. Takeshita, M. Ichikawa, N. Matsui, E. Yamada and R. Mizutani, "Initial Rotor Position Estimation of Sensorless Salient-Pole Brushless DC Motor," *Transaction IEE Japan*, 116-D, No. 7, pp. 736-742, 1996 (in Japanese).

[4] T. Noguchi, K. Yamada, S. Kondo and I. Takahashi, "Rotor Position Estimation Method of Sensorless PM Motor at Rest with No Sensitivity to Armature Resistance," IECON '96 proceeding, pp. 1171-1176, 1996

[5] M. T. Wishart, and R. G. Harley, "Identification and Control of Induction Machines Using Artificial Neural Networks," *IEEE Transactions on Industry Applications*, Vol. 31, No. 3, pp. 612-619, 1995.

[6] M. G. Simões, and R. G. Harley, and B. K. Bose, "Neural Network Based Estimation of Feedback Signals for a Vector Controlled Induction Motor Drive," *IEEE Transactions on Industry Applications*, Vol. 31, No. 3, pp. 620-629, 1995.

Dynamic Matrix Control (DMC) for the Step Motion of Synchronous Motor[1]

Sun Hexu, Ge Baoming, Chi Yan, Zang Xiaojie and Li Wenjiang
Department of Electrical Engineering, Liaoning Technology University
123000 Fuxin, Liaoning, P.R.China
Fax: 86-418-2823977 , Phone: 86-418-3350483

Abstract—**In this paper, a novel control method—dynamic matrix control—is developed to apply to drive system of synchronous motor. For synchronous motor, stator flux are discretized to some positioning points by controlling the stator currents accurately, which make it step motion .It breaks traditional control method of drive control and uses predictive models of step-response, rolling optimization strategy and feedback control algorithm to solve the problem of modeling and control for synchronous motor on step motion. The simulation and experiment research had been made on position control of synchronous motor with two kinds of control modes, L_∞ and L_2 performance index. It is shown by those research that DMC can get better dynamic and static characteristics on servo control system of synchronous motor.**

I . INTRODUCTION

In the motion control, synchronous motor gradually becomes important drive motor. In comparison with DC machine and asynchronous machine, synchronous motor has a specific property of positioning, which could control torque and position successfully on condition that controls stator magnetomotive force vector and rotor field vector. For synchronous motor, step motion is different from variable speed control [1]. We should concern on not only rotating speed and torque of the motor, but also position and torque of the motor. The important parameters on step motion are space position of stator flux vector and rotor flux vector, that is, rotating speed, direction and angle between them.

The step motion of a synchronous motor is a new drive technology. For synchronous motor, we can discretize stator flux to discrete positioning point by controlling the stator current accurately. That can make synchronous motor step motion. This is an ideal servo system.

The models of synchronous motor drive system are very complicated, the construction and parameters of models influence the drive characteristics directly. DMC [2] is a computer algorithmic based on predictive control [3]. The multivariable process to be controlled is represented by its step-responses with constitute the internal model. This model is used on-line for prediction, its inputs and outputs are updated according to the actual state of process. The strategy is fixed by means of a reference trajectory which defines the closed-loop behavior. The modeling is very simply,and the control system has a strong robustness. It doesn't take control as a pure mathematics problem, but as a engineering problem by means of information. In this paper,the DMC are proposed for step motion of synchronous motor to solve the problem of optimizing drive control.

[1] The project supported by National Natural Science Foundation of China and Natural Science Foundation of Liaoning Province

II . STEP MOTION OF SYNCHRONOUS MOTOR

For a synchronous motor, stator magnetomotive force $\vec{F}^s$ rotates synchronously with rotor magnetomotive force $\vec{F}^r$, as a result of producing electromagnetic torque.

$$T_e \propto F^s F^r \sin\angle\left(\vec{F}^s,\ \vec{F}^r\right) \tag{1}$$

Assuming the magnetomotive force amplitude of stator and rotor are constant, the stator windings current supplied by static power inverter is discretized to stepping sinusoidal waves by some law as follow , in [4]

$$\left.\begin{aligned} i_a(k) &= I_m \cos\left(\frac{2\pi}{b_H}k\right) \\ i_b(k) &= I_m \cos\left(\frac{2\pi}{b_H}k-\frac{2\pi}{3}\right) \\ i_c(k) &= I_m \cos\left(\frac{2\pi}{b_H}k+\frac{2\pi}{3}\right) \end{aligned}\right\} \tag{2}$$

where b_H is cycle beats, k is number of command pulse.

The step numbers per revolution may be

$$b = pb_H \tag{3}$$

Where p is pole pairs. The basic numbers of subdivision for step control, that is, b_H should be multiple of 6 to realize balanced three phase output currents.

Fig.1 shows the wave of subdivision methods in b_H=24. The position that stator magnetic pole can exist in space is dispersed. The rotor position may move continuously, and torque angle, $\delta = \angle\left(\vec{F}^s, \vec{F}^r\right)$, may equal any value according to different control process.

In step motion, after stator magnetomotive force goes forward one step, rotor rotates fixed angle from steady state.

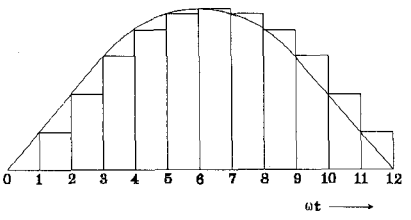

Fig.1. Stepping current wave (b_H=24)

III. Predictive Models of Step Motion

Proceeding from step-responses of controlled object, the dynamic characteristic of object can be described by a series of dynamic coefficient $a_1, a_2, \ldots, a_N$, that is, it can be described by the values of step responses at sampling time $t = T, 2T, \ldots, NT$. The NT is blocking point, N is called "time domain length of model" .

That is information modeling, i.e. predictive models. The models can represent the dynamic characteristic of position control of synchronous motor. On DMC for the step motion of synchronous motor, we may tack the dynamic responses of rotor step motion as predictive model. If the stepping sinusoidal current waves as in (2) are supplied to stator windings, the stator flux will go forward one step by one step and angle error is

$$\delta = \theta_s - \theta_r \tag{4}$$

According to (1), the torque will force the rotor flux vector to follow the stator flux vector, i.e. $\delta \to 0°$. From the step motion of rotor, we can get the dynamic characteristic needed in modeling for DMC.

Using predictive models, we can predict process output by setup input control increment, while input control increment act on system, the output can be predicted by

$$\tilde{\mathbf{y}}_{PM(k)} = \tilde{\mathbf{y}}_{P0(k)} + \mathbf{A}\Delta\mathbf{u}_{M(k)} \tag{5}$$

where

$$\mathbf{A} = \begin{bmatrix} a_1 & 0 & \cdots & 0 \\ a_2 & a_1 & \ddots & \vdots \\ \vdots & \vdots & \ddots & 0 \\ a_M & a_{M-1} & \cdots & a_1 \\ \vdots & \vdots & & \vdots \\ a_P & a_{P-1} & \cdots & a_{P-M+1} \end{bmatrix}$$

$$\tilde{\mathbf{y}}_{P0(k)} = \begin{bmatrix} \tilde{y}_{0(k+1|k)} & \cdots & \tilde{y}_{0(k+N|k)} \end{bmatrix}^{\mathrm{T}}$$

$$\Delta\mathbf{u}_{M(k)} = \begin{bmatrix} \Delta u_{(k)} & \cdots & \Delta u_{(k+M-1)} \end{bmatrix}^{\mathrm{T}}$$

$$\tilde{\mathbf{y}}_{PM(k)} = \begin{bmatrix} \tilde{y}_{M(k+1|k)} & \cdots & \tilde{y}_{M(k+N|k)} \end{bmatrix}^{\mathrm{T}}$$

When we get "step" as unit in step motion, the elements of matrix **A** are

$$\hat{a}_1 = \frac{a_1}{\theta_b}, \quad \ldots, \quad \hat{a}_N = \frac{a_N}{\theta_b} \tag{6}$$

where θ_b is stepping angle.

IV. Optimum Control Strategy

DMC is control algorithm with optimization to determine control strategy. On every instant k, to determine M control increments from this time, let the output predictive value of controlled object acted by these increments on future P instants follow the desired setup value. Where the M is control time domain, the P is optimization domain. For making the control problem significant, the following condition must be needed

$$M \le P \le N$$

Therefore, the optimization problem is

$$\min J = \left\| \mathbf{w}_{P(k)} - \tilde{\mathbf{y}}_{PM(k)} \right\|_{\mathbf{Q}} + \left\| \Delta\mathbf{u}_{M(k)} \right\|_{\mathbf{R}} \tag{7}$$

where

$$\mathbf{w}_{P(k)} = \begin{bmatrix} w_{(k+1)} & \cdots & w_{(k+P)} \end{bmatrix}^{\mathrm{T}}$$

is the desired output value for future P instants at time $t = kT$,

$$\mathbf{Q} = \mathrm{diag}\begin{pmatrix} q_1 & \cdots & q_P \end{pmatrix}$$

is error weighting matrix,

$$\mathbf{R} = \mathrm{diag}\begin{pmatrix} r_1 & \cdots & r_M \end{pmatrix}$$

is control weighting matrix.

However, the optimum control is

$$\Delta\mathbf{u}_{M(k)} = (\mathbf{A}^{\mathrm{T}}\mathbf{Q}\mathbf{A} + \mathbf{R})^{-1}\mathbf{A}^{\mathrm{T}}\mathbf{Q}\left[\mathbf{w}_{P(k)} - \tilde{\mathbf{y}}_{P0(k)}\right] \tag{8}$$

But in DMC, this doesn't be used as complete optimum solution of the control system. We only get the control increment $\Delta u_{(k)}$ in instant k to constitute the reality control

$$u_{(k)} = u_{(k-1)} + \Delta u_{(k)} \tag{9}$$

At next instant the similar optimization problem would be proposed again to get the $\Delta u_{(k+1)}$. This is so called "rolling optimization" strategy.

From (8), control increment is derived as

$$\Delta u_{(k)} = \mathbf{C}^{\mathrm{T}} \Delta \mathbf{u}_{M(k)} = \mathbf{d}^{\mathrm{T}} \left[\mathbf{w}_{p(k)} - \tilde{\mathbf{y}}_{p0(k)} \right] \tag{10}$$

where

$$\mathbf{d}^{\mathrm{T}} = \mathbf{C}^{\mathrm{T}} \left(\mathbf{A}^{\mathrm{T}} \mathbf{Q} \mathbf{A} + \mathbf{R} \right)^{-1} \mathbf{Q} \triangleq \left[d_1 \quad \cdots \quad d_p \right] \tag{11}$$

is called control vector.

$$\mathbf{C}^{\mathrm{T}} = \left[1 \quad 0 \quad \cdots \quad 0 \right]$$

express the operation taking the first element. Once the optimum control strategy is chosen, the $\mathbf{d}^{\mathrm{T}}$ can be calculated off-line.

V. Feedback Control Algorithm

Because the model errors, nonlinear characteristic, interrupt etc., it isn't certainly lead system to follow. The desired value that optimum control strategy was be got by predictive models. It will make great error that open loop control algorithm are repeat after thorough M instants. So the closed loop control algorithm must be proposed.

By (10), only one control increment is adopted to next sampling time, first to detect the real output $y_{(k+1)}$, next to compare with the predictive output $\tilde{y}_{1(k+1/k)}$, to constitute the output error

$$e_{(k+1)} = y_{(k+1)} - \tilde{y}_{1(k+1/k)} \tag{12}$$

The output error in future are predicted by this error to replenish the system distortion based predictive models. The future output predicted at previous instant will be corrected by weighting factor $h_i \left(i = 1, \ 2, \ \ldots, \ N \right)$

$$\tilde{\mathbf{y}}_{cor(k+1)} = \tilde{\mathbf{y}}_{N1(k)} + \mathbf{h} e_{(k+1)} \tag{13}$$

where

$$\tilde{\mathbf{y}}_{cor(k+1)} = \left[\tilde{y}_{cor(k+1|k+1)} \quad \cdots \quad \tilde{y}_{cor(k+N|k+1)} \right]^{\mathrm{T}} \tag{14}$$

$$\mathbf{h} = \left[h_1 \quad \cdots \quad h_N \right]^{\mathrm{T}}$$

Since the basic point of time has changed, the future time point of predictive will be moved to $k+2, \ldots, k+N+1$. The elements of $\tilde{\mathbf{y}}_{cor(k+1)}$ should be shifted to become the initial value of predictive at $k+1$ instant

$$\tilde{\mathbf{y}}_{N0(k+1)} = \mathbf{S} \tilde{\mathbf{y}}_{cor(k+1)} \tag{15}$$

where

$$\mathbf{S} = \begin{bmatrix} 0 & 1 & & 0 \\ 0 & 0 & \ddots & \\ \vdots & \vdots & & 1 \\ 0 & 0 & \cdots & 1 \end{bmatrix}$$

VI. Stepping Control System

The controlled object of predictive control is PM synchronous motor fed by hysteresis band PWM. Fig.2 shows the schematic block diagram of DMC of synchronous motor.The simulation schematic block diagram of DMC for step motion of synchronous motor is showed in Fig.3.

The SIMNON based on personal computer is used to simulate the DMC system. The dynamic and steady characteristic are studied by computer simulation. In Fig.3, C indicates continuous subsystem and D indicates the discrete subsystem.

Subsystem 1: d-q axis equivalent circuit model of PM synchronous motor

Subsystem 2: inverter model of hysteresis band PWM

Subsystem 3: predictive control algorithm

Subsystem 4: power supply of three phases currents.

A. Modeling of subsystem 1

In computer simulation, the models of PM synchronous motor at subsystem block 1 are described as continuous system. The d-q axis equivalent circuit models are written as

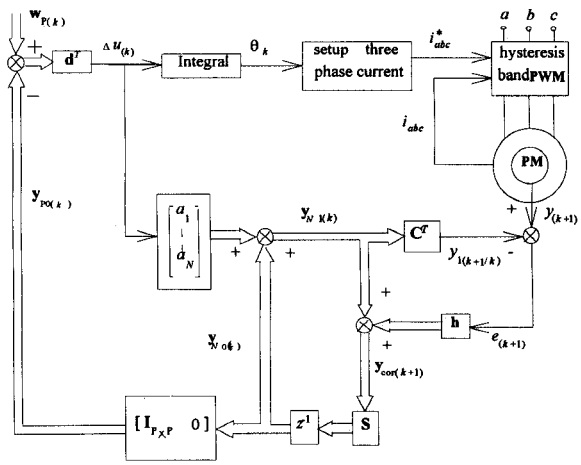

Fig.2. The schematic block diagram of DMC for synchronous motor

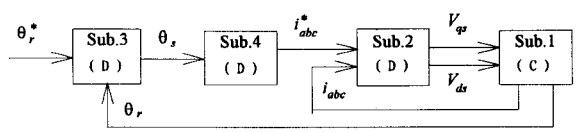

Fig.3. The simulation block diagram of DMC for synchronous motor

$$\frac{di_{qs}}{dt} = \frac{\omega_b}{X_{qs}}\left(V_{qs} - R_s i_{qs} - \frac{\omega_e X_{ds} i_{ds}}{\omega_b} - \frac{\omega_e V_{f0}}{\omega_b}\right) \quad (16)$$

$$\frac{di_{ds}}{dt} = \frac{\omega_b}{X_{ds}}\left(V_{ds} + \frac{\omega_e X_{qs} i_{qs}}{\omega_b} - R_s i_{ds}\right) \quad (17)$$

$$T_e = \frac{3}{\omega_b}\left[\left(i_{ds} X_{ds} + V_{f0}\right) i_{qs} - i_{qs} X_{qs} i_{ds}\right] \quad (18)$$

where V_{f0} is induction voltage of motor in basic speed ω_b, and

$$\frac{d\theta_e}{dt} = \omega \quad (19)$$

The point-to-point control of synchronous motor is a typical motion mode of step motion in incremental motion control, which the motor moves forward one step by one step under the command pules. After the transient process of first step stopped thoroughly, the second step begin to moves, and so on. Because the stepping frequency is very low, the electrical transient process may be negated in contrast with step motion .We could consider that the one stator magnetomotive force go forward one step immediately

The dynamic equation of step motion in point-to-point control is as follow

$$\frac{d^2\alpha}{dt^2} = -\frac{B}{J}\frac{d\alpha}{dt} - \frac{M_{\max}}{J}\sin(p\alpha - k\theta_b) - \frac{M_s}{J}\operatorname{sign}\frac{d\alpha}{dt} \quad (20)$$

where k=0 , 1 , 2,... ;

B is damping torque coefficient;

M_s is friction torque coefficient;

$M_{\max}$ is maximal torque coefficient;

J is rotating inertia;

$\alpha = \frac{\theta}{p}$.

B. Modeling of subsystem 2

In hysteresis band PWM inverter, the current error is produced by comparing setup current i^* with real current i . The switching state is produced by comparing current error with hysteresis band. In computer simulation, this block is described as a discrete system that sampling time is 0.1ms. The inverter switch is expressed with "0" and "1" . That is

$$V_{as} = V_d NA$$

$$V_{bs} = V_d NB$$

$$V_{cs} = V_d NC$$

where V_d is DC voltage, NA、NB、NC is switch state.

C. Modeling of subsystem 3

The control value are calculated by adopting DMC algorithm in subsystem. For accomplishing predictive control, first we should detect step responses of controlled object. Then determine dynamic matrix **A** and control vector $\mathbf{d}^T$ off-line.

The simulation and experiment motor is 70 h.p, by adopting direct control of torque angle, $b_H = 24$, $I_m = 340\text{A}$, $\theta_b = 0.26167\text{rad}$. The rotor position response are gotten by inputting step currents $i_a^* = 330.61\text{A}$, $i_b^* = -266.76\text{A}$, $i_c^* = -177.65\text{A}$.

The sampling time T is 0.1s, N is 20, so

a=[0.089 0.241 0.331 0.334 0.290 0.250 0.235 0.243

0.258 0.267 0.268 0.264 .0.259 0.258 0.259 0.260

0.261 0.261 0.261 0.261]

if getting "step" as unit, then

$\hat{\mathbf{a}}$ =[0.340 0.920 1.265 1.276 1.110 0.954 0.899 0.930

0.987 1.022 1.023 1.077 0.991 0.986 0.989 0.994

0.996 0.997 0.998 0.999]

$$\Delta\theta_s = \theta_b \Delta u_{(k)} \quad (21)$$

D. Modeling of subsystem 4

This block products setup three phase currents supplying to PWM inverter. The angle move of stator magnetomotive force be set up as state θ_s. When having a new increment $\Delta\theta_s$, the new state is

$$N\theta_s = \theta_s + \Delta\theta_s \quad (22)$$

In step motion, the torque angle control is

$$\left.\begin{aligned} i_a^* &= I_m \cos(N\theta_s) \\ i_b^* &= I_m \cos(N\theta_s - \frac{2\pi}{3}) \\ i_c^* &= I_m \cos(N\theta_s + \frac{2\pi}{3}) \end{aligned}\right\} \quad (23)$$

adopted, so the amplitude of stator currents are set up as constant value.

VII. Characteristic Analyses of DMC for the Step Motion

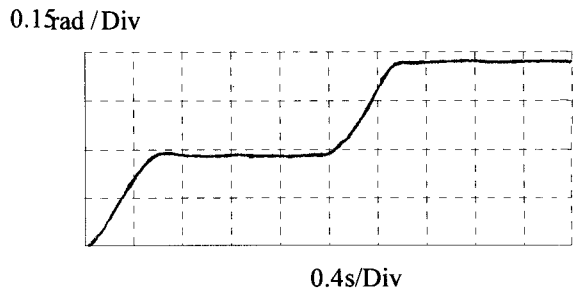

Fig.4 . The oscillogram of the experiment results

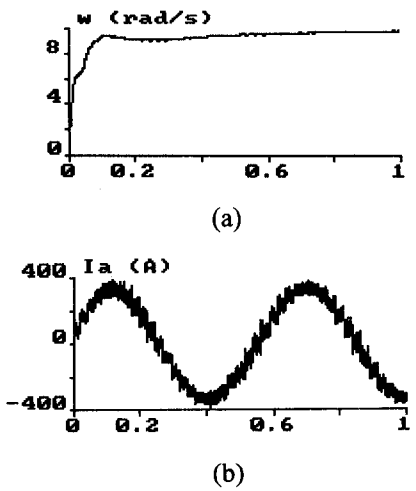

Fig.5. Simulation results of DMC on speed control
(a) simulation result of ω (b) simulation result of i_a

The simulation and experiment research had been made on position control of synchronous motor.

Three kinds of control mode are used, the DMC algorithms with L_∞ and L_2 performance index and vector control. The characteristics of parameter change, load interrupt, stability and robustness. are analyzed in this paper.

The simulation results of DMC are shown in Fig.5 and Fig.6. The predictive control have a same characteristics of steady and dynamic as vector control for position control of synchronous motor .The control property of DMC with L_∞ performance index is better than that of L_2 performance. Even in $r=0$, the system is stable. The predictive control with L_∞ performance index have excellent characteristics, especially reducing the rolling optimization time domain P. The choice of parameters h_i should emphasize the robustness of DMC system. In the simulation, as the h_1 is 1 and h_i equal λ, the system is stable only λ satisfied with

$$0<\lambda<2$$

In the research, bring a interrupt, at the two kind of control mode can restrain interrupt, the L_∞ is fast than L_2 method. For increasing ability of against interrupt, the h_i should be increased as fully as possible under the condition of robustness.

The Fig.4 show the oscillogram of the experiment result of position. The experiment results are very similar with simulation results. The speed control results of DMC are shown in Fig.5. From current curves, the stepping characteristics can be saw clearly.

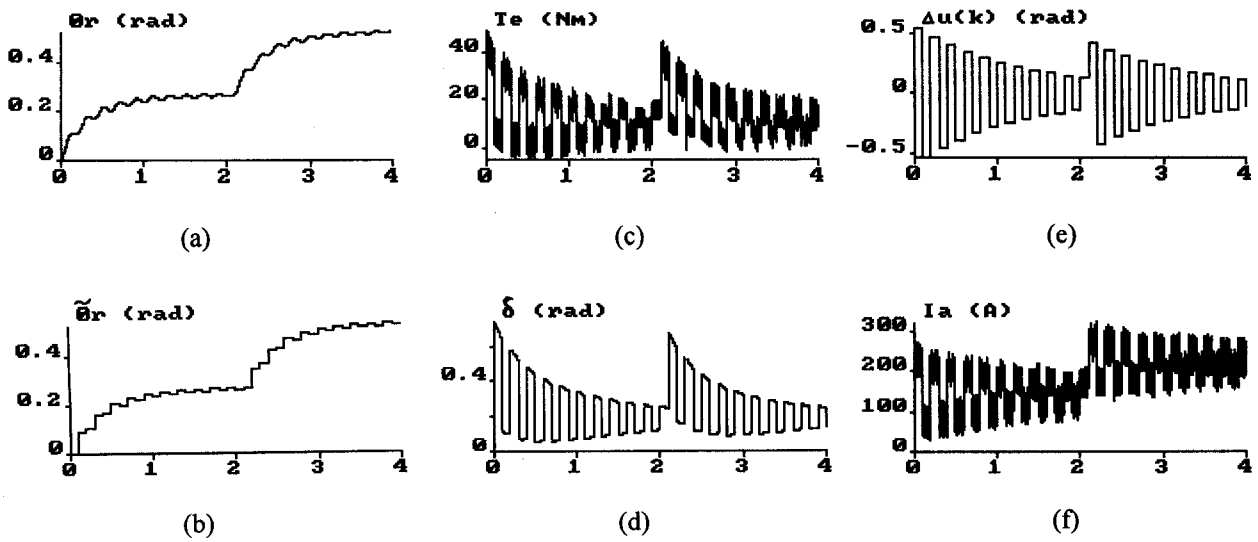

Fig.6. Simulation results of DMC with L_2 performance index for position control on two steps

(a) rotor angle θ_r (b) predictive of $\tilde{\theta}_r$ (c) torque T_e
(d) torque angle δ (e) control increment $\Delta u_{(k)}$ (f) stator current i_a

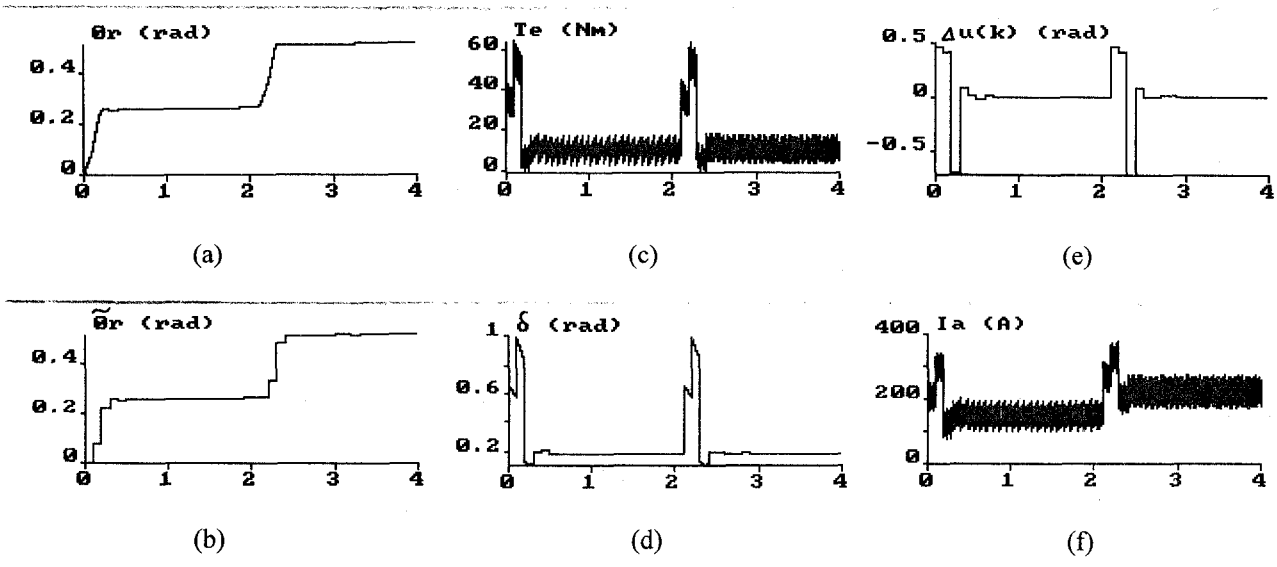

Fig.7. Simulation results of DMC with L_∞ performance index for position control on two steps

(a) rotor angle θ_r (b) predictive of $\tilde{\theta}_r$ (c) torque T_e
(d) torque angle δ (e) control increment $\Delta u_{(k)}$ (f) stator current i_a

VIII. CONCLUSION

This paper presents a DMC algorithm on step motion of synchronous motor. It not only presents a adjusted speed system, but also a position control system. We can take some conclusion as follow:

a) It breaks traditional control method and uses predictive model of step response, avoid the problem of modeling for synchronous motor

b) The predictive control is applied firstly to drive control system. The new research domain has be open up to DMC

c) Comparing with L_2 performance index, L_∞ has the better dynamic and static characteristics.

d) The rolling optimization adapts most step motion control.

ACKNOWLEDGMENT

The author gratefully acknowledges National Natural Science Foundation of China and Natural Science Foundation of Liaoning Province for surported in thisstudy project.

REFERENCES

[1] Sun Hexu, et al, "Torque Vector Control for the Step Motion of Synchronous Motor" , in proceeding of The First International Power Electronics and Motion Control Conference, 1994, Beijing , China, pp. 414-419.

[2] Cutler C R, Ramaker B L, " Dynamic Matrix Control — A computer control Algorithm " ,in Proceedings of the 1980 Joint Automatic Control Conference,1980,San Francisco: American Automatic control Council. Vol. WP5-13.

[3] Richalet J, et al, "Model Predictive Heuristic Control: Applications to industrial Processes" , Automatic, 1978, 14(5): pp. 428-431 .

[4] S. Hexu, et al, "A Novel Cycloconverter Based on Microprocessor Digital Control" , in Proceeding of 5th European Conference on Power electronics and Applications, 1993, UK,Vol.5 :Drives 1, pp. 133-138.

Advantageous use of a dual operation, linear and switching power module in drive control with no deadtime

Kenji Yanagawa Takeshi Tohya Kouki Matsuse
Meiji University
1-1-1, Higashimita, Tama-ku, Kawasaki 214, JAPAN
FAX: +81-44-934-7298, Phone: +81-44-934-7298
E-mail: matsuse@isc.meiji.ac.jp

Abstract —**This paper investigates the difference between linear and PWM driving method for speed sensorless control of permanent magnet synchronous machines (PMSM) using intelligent power module (IPM). Futhermore, using the suspected PWM inverter, which is constructed by the new IPM, this paper compare the PWM operation mode of the IPM with PWM control of this inverter. Furthermore, the usefulness of two operation mode switching control is discussed.**

I. Introduction

In industrial application, PWM techniques using inverter constructed of power devices are widely favored because of their low conduction losses. However, higher carrier frequency for PWM techniques result in an increase in switching losses and noise. In sensorless motor drives, especially at low speed, they are one of the causes that decrease the accuracy of estimated value.

This paper present that the accuracy of estimated speed is improved by using the intelligent power module (IPM) for sensorless control of permanent magnet synchronous motor (PMSM) at low speed. The new IPM used in this experiment is a high-power operational amplifier (OP-AMP) that can also operate PWM mode. Two mode, linear and PWM, are alternative corresponding to its input signal.

In the experiment, using a suspected PWM inverter, which is constructed of IPM, this paper also compares the characteristic for IGBT inverter with the one for IPM inverter and the advantageous of the dual mode is pointed out for sensorless drive.

Furthermore, the switching control of two operation mode which is linear and PWM is examined in this paper.

II. IPM technology

Figure 1 and 2 show the schematic of the IPM and its input vs. output characteristic, respectively.

As is shown in figure 2, IPM is essentially a linear amplifier. The output voltage is in proportion to input voltage. Conventional linear amplifiers have difficulties how to dissipate the higher conduction losses. But, by using PWM operation , this IPM is a lower conduction loss. The switch of two operation mode depend on its input voltage signal level. It is important that output MOSFETs saturate, when the input voltage is higher 3 to 4V or so. As a result, a lower conduction loss suitable for PWM operation can be obtain. Therefor, in the application such as servo system, it is possible that the two operation mode of the IPM is chosen ,as occasion demands, to combing the best feature of each technique.

III. The feature of the IPM inverter

In case of a three phases bridge inverter using IGBTs, when this devices is switching, a certain deadtime is required. Because they have a certain turn-off time. There are higher switching losses caused by it in these devices. Therefor, faster switching is required in decreasing switching losses.

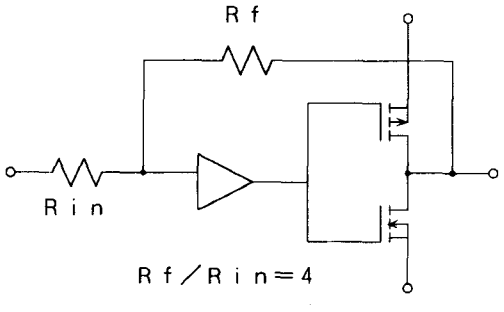

Fig.1. Schematic of the IPM

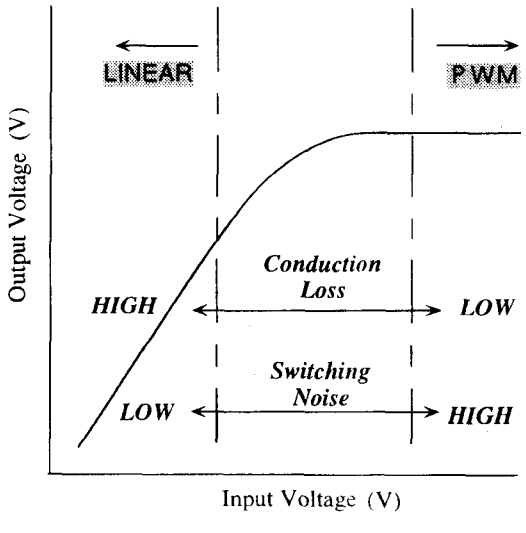

Fig.2. Input voltage vs. output voltage characteristic of the IPM

As is shown in figure 2, the IPM has the complimentary pair that consist of P-channel and N-channel MOSFET. Since the turn-off of P-channel MOSFET is significantly slower than that of N-channel MOSFET, a complimentary pair has the problem, so that a short circuit current flows the devices from positive and negative power supplies. But, to solve this problem, the peculiar gate driver circuit in this IPM is constructed, as is shown in [2]. By using this gate driver circuit, faster switching is possible and switching losses decrease in PWM operation mode. because of turn-off time is nealy equal to zero. Therefor, A ideal switching is possible in the PWM mode of the IPM.

In additional, the IPM has a overcurrent protection circuit , thermal protector and control circuit in this module. According to using this module in servo system, the system is simplifed and miniaturized.

The specification of this IPM is expressed as follows.

1. High output : ± 50V 25A
2. Overcurrent self-limited around 25A
3. Current shutdown by an external signal
4. Built in 10 m Ω current sensing resistor
5. Power supplies to the module are two pairs of positive and negative supplies owing to common drain configuration in output stage
6. High speed OP amp in the input stage enables 10V/ microsecond slew late

IV . Experimental results

In this section, the IPM is applied for open-loop control and sensorless control using adaptive observer of PMSM. This PMSM, with the parameters as listed in Table 1, is driven by three phases the IPM inverter. Two operation modes of this IPM are switched by the program in the microprocessor. To compare characteristic of PWM control using IGBT inverter with one using the IPM, the suspected PWM inverter constructed by the IPM is used in this experiment. This inverter can be realized by given the IPM a reasonable deadtime. This deadtime is about 10 microsecond. The PWM control in this experiment is used the current following control method. Futhermore, all experiments in this section practice under no load condition.

A. Application for open-loop control of PMSM

This section presents experimental results, when the two operation modes of the IPM are applied for open-loop control of PMSM. Figure 3 show the measured current waveform for each of operation modes for linear operation, PWM operation of this IPM, and the suspected PWM inverter . This supply frequency is 50 Hz.

B. Application for sensorless control of PMSM

1) Sensorless control strategy: To compare the performance of two operation mode, which is linear mode and PWM mode, the sensorless control strategy based adaptive observer is used.

Table I

Rating and prameters of the moter

Rating or parameters	Value	Unit
Output	154	[w]
Poles	6	
Current	2.1	[A]
Torque	5.0	[kg-cm]
Motor speed	3000	[rpm]
Resistance	2.85	[Ω]
Indcutance	0.0042	[H]

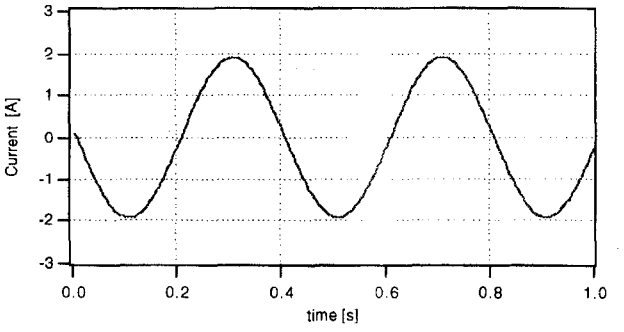

a) Linear operation mode

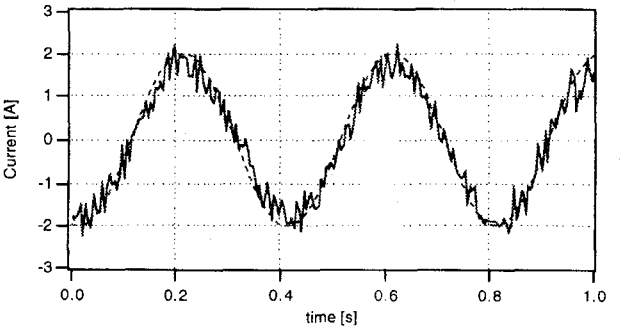

b) PWM operation mode

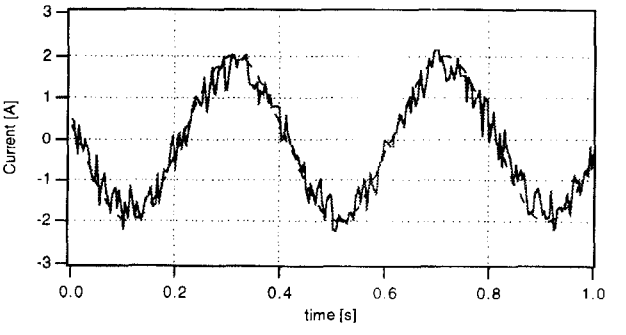

c) Suspected PWM inverter mode

Fig. 3. Measured current waveform for each operation mode

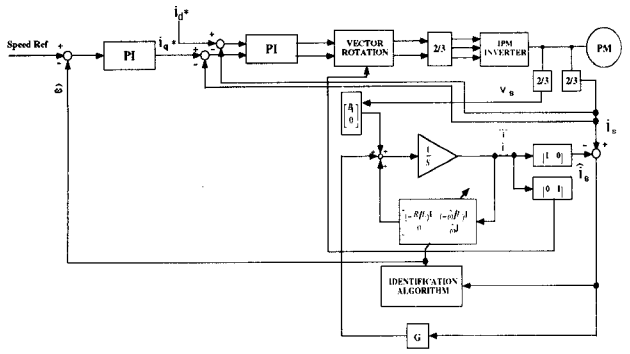

Fig. 4. Overall brock diagram sensorless control system

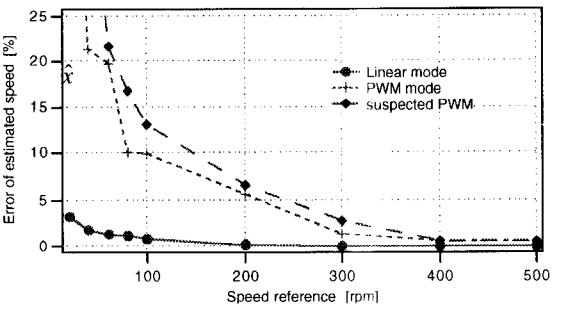

Fig. 5. Average values of estimated speed error

Fig. 4 shows a block diagram of the sensorless control system used in this experiment.

The adaptive observer which estimates the stator currents and the rotor flux for PMSM is described by the following equation [1] in d-q stationary reference frame.

$$P\begin{bmatrix}\hat{i}\\ \hat{\lambda}\end{bmatrix}=\begin{bmatrix}-(R/L)\mathbf{I} & -(\hat{\omega}/L)\mathbf{J}\\ \mathbf{0} & \hat{\omega}\mathbf{J}\end{bmatrix}\begin{bmatrix}\hat{i}\\ \hat{\lambda}\end{bmatrix}+\frac{1}{L}\begin{bmatrix}v\\ \mathbf{0}\end{bmatrix}+\mathbf{G}\begin{bmatrix}i-\hat{i}\\ \lambda-\hat{\lambda}\end{bmatrix}. \quad (1)$$

where,

$$v=\begin{bmatrix}v_d & v_q\end{bmatrix}^T,\quad i=\begin{bmatrix}i_d & i_q\end{bmatrix}^T,\quad \lambda=\begin{bmatrix}\lambda_d & \lambda_q\end{bmatrix}^T,$$

$$\mathbf{I}=\begin{bmatrix}1 & 0\\ 0 & 1\end{bmatrix},\quad \mathbf{J}=\begin{bmatrix}0 & -1\\ 1 & 0\end{bmatrix},\quad \mathbf{G}=\begin{bmatrix}g_1\mathbf{I}+g_2\mathbf{J} & 0\\ g_3\mathbf{I}+g_4\mathbf{J} & 0\end{bmatrix}.$$

The used observer gain matrix is given as

$$\begin{cases} g_1=-(k-1)R/L\\ g_2=(k-1)\hat{\omega}\\ g_3=kR\\ g_4=-kL\hat{\omega}\end{cases} \quad (2)$$

The meanings of the parameters are as follows.

i_d , i_q : d- and q-axis stator currents

v_d , v_q : d- and q-axis stator voltages

λ_d , λ_q :d- and q-axis rotor fluxes

R , L :stator resistance and self-inductance

ω :electrical rotor angular velocity

The identification algorithm is expressed as follows [2]:

$$\hat{\omega}=(K_p+K_i/P)(\varepsilon_{id}\hat{\lambda}_q-\varepsilon_{iq}\hat{\lambda}_d). \quad (3)$$

where, is estimated value of x. K_p and K_i is PI gain of identifier. ε_{id} and ε_{iq} is the error between the estimated current calculated in this observer and the measured current in d-q stationary reference frame.

2) Experiment result : Fig. 5 shows the average values of estimated error at the steady state for linear operation, PWM operation of this IPM, and the suspected PWM inverter.

When motor driving speed range is lower than 200 rpm, the usefulness of the linear operation is obvious. The estimated speed accuracy for linear operation mode is the best in that of the each operation modes. Therefor, it is possible that this motor is more widely at low speed range ,when the IPM is driven in linear operation mode.

C. Switching of the operation mode

This section is described about the two mode switching of the IPM. Experiment results described above section pointed out that linear operation mode of the IPM improves the accuracy of estimated speed at low speed. But, this linear operation wastes a higher conduction losses in switching device. Because output MOSFETs are non-saturated, when the IPM is driven linear operation mode.

1) Comparison of the conduction losses: Fig. 6 shows the conduction losses in this IPM for the two operation mode, which is linear and PWM. This experiment results is obtained by measured output voltage and output current of this inverter under resistance load condition. The resistance used this measurement is 26 ohm. It is noted that the intersection point of two curves points out the saturation point of this device. Therefor, the operation mode is then PWM mode. In each of operation mode, the conduction losses is calculated approximately by the following equations.

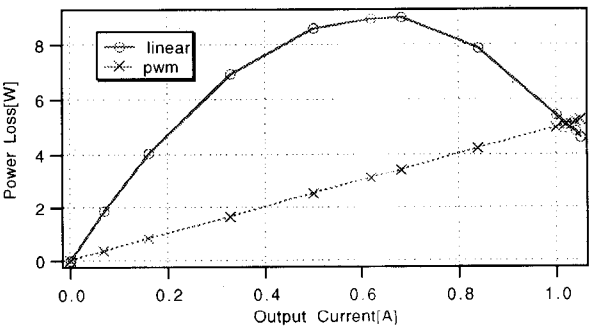

Fig. 6 Characteristic of power loss for linear mode and PWM mode

Linear operation:

$$P_{loss} = (E - v_{out}) * i_{out} \quad (4)$$

PWM operation:

$$P_{loss} = (v_{satu} + \alpha) * i_{out} \quad (5)$$

where, P_{loss} is conduction losses for two mode. E is supply voltage. v_{out} and i_{out} is output voltage and current of this inverter, respectively. v_{satu} is the saturation voltage of output MOSFETs. α is a margin to deny influence of temperature.

2) Switching condition: Switching condition of PWM mode and linear mode depends on its application. For example, in case of the oscillation problem at standstill, if the motor is rotating, PWM mode is used. If the motor is a standstill, linear mode is used. In this experiment, when the motor is driven at low speed or estimated speed error is smaller than a certain value, the two mode is switched.

3) Experiment of switching operation mode: Fig. 7 shows the speed response for sensorless control speed by switching of operation mode, which linear and PWM. The speed reference is a step-up function with value from 200 to 300 rpm. In figure, the solid line shows the estimated speed. The dash line shows the given speed references. The switching of the two operating mode is carried out, when the error between speed reference and estimated speed is 10 rpm. The estimated value has very small overshoot at transient state. The estimated value at the steady state has a good following performance for speed references. The error rate is within about 0.006 percent at the steady state.

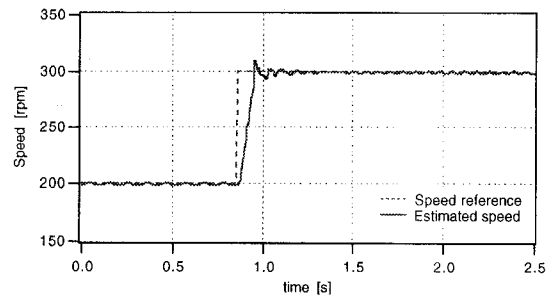

Fig.7. The step response of estimated speed by switching of operation mode

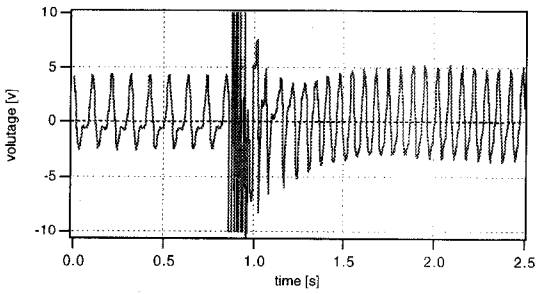

Fig.8. Voltage reference waveform for switching of operation mode

Fig. 8 shows the U-phase voltage reference waveform, when operation mode is switched over. This figure points out that the two modes is switched at the transient state. Note that the largely transient component of this volutage waveform is occured by switching of the two mode. This occuring transient component produces a problem, which is that this motor is afraid to pull out of synchronism. Because the estimated state variable in the observer are indirectly under the influence of this voltage reference. Therefor, the influence of this transient component must be eliminated by using a particular correct algorithm. But, this problem is very important, when this IPM is applied for various application, and must be solved after this.

V. Conclusions

This paper presents advantageous use of the IPM for the motor drive system. This IPM has a dual mode, which is linear and PWM. By using the linear mode of this device, this paper is verified and realized a lower speed drive system for PMSM. Furthermore, by switching this operation mode, it is possible that the system which has a lower conduction losses compared with conventional power OP-amp and a more precise compared with the one using conventional PWM inverter is realized. These features of this device is usefulness for the application such as position and speed control of servo motor.

Acknowledgment

The authors wish to thank Mr. Mitome and Mr. SHinriki of Nihon Inter Electronics Corporation for giving us this IPM samples.

References

[1] G. Yang and T. H. Chin, "Adaptive Speed Identification Scheme for Vector Controlled Speed Sensorless Inverter-Induction Motor Drive," Conf.Rec. IEEE IAS '91. pp. 404-408, 1991

[2] M. Mitome, N. Tokuda, and K.Matsuse, "A New High-Power Linear/ PWM Dual modes IPM," IPEC- YOKOHAMA '95, pp. 1111-1116, 1995

A Control Method of Active Power Filter in Unsymmetrical and Distorted Voltage System

Yasuhiro Komatsu, Takao Kawabata

Ritsumeikan University
1-1-1 Nojihigasi, Kusatsu 525-77, JAPAN
Fax:+81-775-61-2663, Phone:+81-775-61-2671
E-male:komatsu@bkc.ritsumei.ac.jp

Abstract — In this paper, the authors propose a calculation method for the compensating current reference of the active power filter, where a nonlinear load exists in the three-phase three-wire unsymmetrical voltage system. This new method has been named extension pq method. The authors have experimented with the extension pq method and the pq method, using the same current controlled IPM inverter for both methods. The results of the experiments proved that in the unsymmetrical voltage system, the source current was distorted in case of the pq method, but undistorted in case of the extension pq method. Finally, the authors propose the calculation method for the compensating current reference in unsymmetrical and distorted line voltage system. Experimental results show that the active power filter based on this method gives satisfactory operation.

I. Introduction

The pq theory, since its proposal, has been applied in the control of three-phase active power filters[1]. However, power system voltages being often unsymmetrical, the authors have shown that the control in unsymmetrical voltage system using the pq theory does not provide good performance[2]. The authors then proposed the extension pq theory which gives adequate compensating current reference even for the unsymmetrical voltage system[2].

In this paper, we show experimentally the difference between the pq theory and extension pq theory. We use a current-controlled IPM inverter as the power circuit of the active power filter and implement two compensating current reference calculation methods based on the pq theory and extension pq theory respectively.

II. Relation between extension pq theory and pq theory

In this section, we summarize the pq theory and the extension pq theory and their relationship.

A.The Extension pq Theory

In the extension pq theory, p and q are respectively defined as,

$$p = e_a i_a + e_b i_b + e_c i_c \tag{1}$$

$$q = e_a' i_a + e_b' i_b + e_c' i_c \tag{2}$$

where e_a', e_b' and e_c' lag e_a, e_b and e_c respectively by 90°.

Kirchhoff's current law equation for a three-wire system is,

$$i_a + i_b + i_c = 0 \tag{3}$$

From (1)-(3) we may derive (4) and (5).

$$\begin{bmatrix} p \\ q \end{bmatrix} = \begin{bmatrix} e_a - e_c & e_b - e_c \\ e_a' - e_c' & e_b' - e_c' \end{bmatrix} \begin{bmatrix} i_a \\ i_b \end{bmatrix} \tag{4}$$

$$\begin{bmatrix} i_a \\ i_b \end{bmatrix} = \frac{1}{\Delta'} \begin{bmatrix} e_b' - e_c' & e_c - e_b \\ e_c' - e_a' & e_a - e_c \end{bmatrix} \begin{bmatrix} p \\ q \end{bmatrix} \tag{5}$$

where $\Delta' = (e_a - e_c)(e_b' - e_c') - (e_a' - e_c')(e_b - e_c)$

From (2), clearly q is positive when the current is lagging. There are two denotations, q or -q, that are used to represent three-phase reactive power. If we denote the reactive power as q, then reactive power is positive when current is lagging. However, this is the reverse of the IEC recommendation which stipulates that reactive power is positive when current is leading. If we use the IEC convention, we obtain the following equations:

$$q = e_a'' i_a + e_b'' i_b + e_c'' i_c \tag{2}'$$

where e_a'', e_b'' and e_c'' lead e_a, e_b and e_c respectively by 90 degrees.

From (1), (2)' and (3), we may derive the equations:

$$\begin{bmatrix} p \\ q \end{bmatrix} = \begin{bmatrix} e_a - e_c & e_b - e_c \\ e_a'' - e_c'' & e_b'' - e_c'' \end{bmatrix} \begin{bmatrix} i_a \\ i_b \end{bmatrix} \tag{4}'$$

$$\begin{bmatrix} i_a \\ i_b \end{bmatrix} = \frac{1}{\Delta''} \begin{bmatrix} e_b'' - e_c'' & e_c - e_b \\ e_c'' - e_a'' & e_a - e_c \end{bmatrix} \begin{bmatrix} p \\ q \end{bmatrix} \tag{5}'$$

where $\Delta'' = (e_a - e_c)(e_b'' - e_c'') - (e_a'' - e_c'')(e_b - e_c)$

B.The pq Theory

In this theory, e_0, e_α and e_β are defined by the equation:

$$\begin{bmatrix} e_0 \\ e_\alpha \\ e_\beta \end{bmatrix} = F \begin{bmatrix} e_a \\ e_b \\ e_c \end{bmatrix}, \quad \begin{bmatrix} i_0 \\ i_\alpha \\ i_\beta \end{bmatrix} = F \begin{bmatrix} i_a \\ i_b \\ i_c \end{bmatrix} \tag{6}$$

where

$$F = \frac{\sqrt{2}}{\sqrt{3}} \begin{bmatrix} 1/\sqrt{2} & 1/\sqrt{2} & 1/\sqrt{2} \\ 1 & -1/2 & -1/2 \\ 0 & \sqrt{3}/2 & -\sqrt{3}/2 \end{bmatrix}$$

p is defined by (1). From (1) and (6), we obtain,

$$p = e_0 i_0 + e_\alpha i_\alpha + e_\beta i_\beta \tag{7}$$

From (7) and (3) we have that,

$$p = e_\alpha i_\alpha + e_\beta i_\beta \tag{8}$$

and q is defined by[1],

$$q = e_\alpha i_\beta - e_\beta i_\alpha \tag{9}$$

From (8) and (9) we have the following equation,

$$\begin{bmatrix} p \\ q \end{bmatrix} = \begin{bmatrix} e_\alpha & e_\beta \\ -e_\beta & e_\alpha \end{bmatrix} \begin{bmatrix} i_\alpha \\ i_\beta \end{bmatrix} \tag{10}$$

$$\begin{bmatrix} i_\alpha \\ i_\beta \end{bmatrix} = \frac{1}{\Delta} \begin{bmatrix} e_\alpha & -e_\beta \\ e_\beta & e_\alpha \end{bmatrix} \begin{bmatrix} p \\ q \end{bmatrix} \tag{11}$$

where $\Delta = e_\alpha^{\,2} + e_\beta^{\,2}$

C. Relation between the Extension pq Theory and the pq Theory

From (6) we may derive the equation:

$$\begin{bmatrix} i_a \\ i_b \\ i_c \end{bmatrix} = F^{-1} \begin{bmatrix} i_0 \\ i_\alpha \\ i_\beta \end{bmatrix} = \frac{\sqrt{2}}{\sqrt{3}} \begin{bmatrix} 1/\sqrt{2} & 1 & 0 \\ 1/\sqrt{2} & -1/2 & \sqrt{3}/2 \\ 1/\sqrt{2} & -1/2 & -\sqrt{3}/2 \end{bmatrix} \begin{bmatrix} i_0 \\ i_\alpha \\ i_\beta \end{bmatrix} \tag{12}$$

From (12) and (3) we may derive the equation:

$$\begin{bmatrix} i_a \\ i_b \end{bmatrix} = \frac{\sqrt{2}}{\sqrt{3}} \begin{bmatrix} 1 & 0 \\ -1/2 & \sqrt{3}/2 \end{bmatrix} \begin{bmatrix} i_\alpha \\ i_\beta \end{bmatrix} \tag{13}$$

From (11) and (13) we may derive the equation:

$$\begin{bmatrix} i_a \\ i_b \end{bmatrix} = \frac{1}{\Delta} \frac{\sqrt{2}}{\sqrt{3}} \begin{bmatrix} 1 & 0 \\ -1/2 & \sqrt{3}/2 \end{bmatrix} \begin{bmatrix} e_\alpha & -e_\beta \\ e_\beta & e_\alpha \end{bmatrix} \begin{bmatrix} p \\ q \end{bmatrix}$$

$$= \frac{1}{\Delta} \frac{\sqrt{2}}{\sqrt{3}} \begin{bmatrix} e_\alpha & -e_\beta \\ -\frac{1}{2}e_\alpha + \frac{\sqrt{3}}{2}e_\beta & \frac{1}{2}e_\beta + \frac{\sqrt{3}}{2}e_\alpha \end{bmatrix} \begin{bmatrix} p \\ q \end{bmatrix} \tag{14}$$

From (6) we may derive the equation:

$$\begin{bmatrix} e_\alpha \\ e_\beta \end{bmatrix} = \frac{\sqrt{2}}{\sqrt{3}} \begin{bmatrix} e_a - \frac{1}{2}e_b - \frac{1}{2}e_c \\ \frac{\sqrt{3}}{2}e_b - \frac{\sqrt{3}}{2}e_c \end{bmatrix} \tag{15}$$

Substituting (15) into (14) leads to the equation:

$$\begin{bmatrix} i_a \\ i_b \end{bmatrix} = \frac{1}{\Delta} \begin{bmatrix} \frac{1}{3}(2e_a - e_b - e_c) & \frac{1}{\sqrt{3}}(e_c - e_b) \\ \frac{1}{3}(2e_b - e_a - e_c) & \frac{1}{\sqrt{3}}(e_a - e_c) \end{bmatrix} \begin{bmatrix} p \\ q \end{bmatrix} \tag{16}$$

where

$$\Delta = \frac{2}{3}(e_a^{\,2} + e_b^{\,2} + e_c^{\,2} - e_a e_b - e_b e_c - e_a e_c)$$

$$= \frac{1}{\sqrt{3}}\{(e_a - e_c)\left(\frac{e_a - e_c}{\sqrt{3}} - \frac{e_b - e_a}{\sqrt{3}}\right) - \left(\frac{e_c - e_b}{\sqrt{3}} - \frac{e_b - e_a}{\sqrt{3}}\right)(e_b - e_c)\} \tag{17}$$

From (16) and (17) we may derive the equation:

$$\begin{bmatrix} i_a \\ i_b \end{bmatrix} = \frac{1}{\{(e_a - e_c)(\frac{e_a - e_c}{\sqrt{3}} - \frac{e_b - e_a}{\sqrt{3}}) - (\frac{e_c - e_b}{\sqrt{3}} - \frac{e_b - e_a}{\sqrt{3}})(e_b - e_c)\}}$$

$$\times \begin{bmatrix} \frac{e_a - e_c}{\sqrt{3}} - \frac{e_b - e_a}{\sqrt{3}} & e_c - e_b \\ \frac{e_b - e_a}{\sqrt{3}} - \frac{e_c - e_b}{\sqrt{3}} & e_a - e_c \end{bmatrix} \begin{bmatrix} p \\ q \end{bmatrix} \tag{18}$$

Equation(18) is the expression of (11) of the pq theory using phase voltages and currents. If we compare (18) with (5)′ of the extension pq theory, we see that (18) may be derived from (5)′ by the following substitutions:

$$e_a'' = \frac{e_c - e_b}{\sqrt{3}},\quad e_b'' = \frac{e_a - e_c}{\sqrt{3}},\quad e_c'' = \frac{e_b - e_a}{\sqrt{3}} \tag{19}$$

Equation (19) holds only in symmetrical voltage systems. Thus, we see that the pq theory is a particular case of the extension pq theory and the former can be derived from the latter by using the symmetrical voltage condition.

In this paper, we have defined the reactive power to be positive for lagging current. Thus, we may derive the equations of the pq theory from (5) by the following substitution:

$$e_a' = \frac{e_b - e_c}{\sqrt{3}},\quad e_b' = \frac{e_c - e_a}{\sqrt{3}},\quad e_c' = \frac{e_a - e_b}{\sqrt{3}} \tag{20}$$

Ⅲ. CALCULATION OF THE COMPENSATING CURRENT REFERENCE

In the experiments, we set p_c equal to $\bar{p}_L$ and q_c equal to q_L. Hence, we have p_s equal to $\bar{p}_L$ and q_s equal to 0. By using these relations, we may construct a simple compensating current reference calculation scheme. We calculate compensating current reference i_{ca}^* and i_{cb}^* from the following equation.

$$\begin{bmatrix} i_{Ca}^* \\ i_{Cb}^* \end{bmatrix} = \begin{bmatrix} i_{La} \\ i_{Lb} \end{bmatrix} - \begin{bmatrix} i_{Sa}^* \\ i_{Sb}^* \end{bmatrix} \tag{21}$$

where i_{sa}^* and i_{sb}^* are the ideal source currents, and i_{La} and i_{Lb} are the measured values of the load currents.

If we rewrite (5) using subscript S, we have the following,

$$\begin{bmatrix} i_{Sa}^* \\ i_{Sb}^* \end{bmatrix} = \frac{1}{\Delta'}\begin{bmatrix} e_b'-e_c' & -(e_b-e_c) \\ -(e_a'-e_c') & e_a-e_c \end{bmatrix}\begin{bmatrix} p_S \\ q_S \end{bmatrix}$$

$$= \frac{1}{\Delta'}\begin{bmatrix} e_b'-e_c' & -(e_b-e_c) \\ -(e_a'-e_c') & e_a-e_c \end{bmatrix}\begin{bmatrix} \bar{p}_L \\ 0 \end{bmatrix}$$

$$= \frac{\bar{p}_L}{\Delta'}\begin{bmatrix} e_b'-e_c' \\ -(e_a'-e_c') \end{bmatrix} \quad (22)$$

$$\Delta' = (e_a-e_c)(e_b'-e_c') - (e_a'-e_c')(e_b-e_c) \quad (23)$$

For the pq theory, we may derive equations corresponding to (22) and (23) as,

$$\begin{bmatrix} i_{Sa}^* \\ i_{Sb}^* \end{bmatrix} = \frac{\bar{p}_L}{\Delta}\begin{bmatrix} \dfrac{e_c-e_a}{\sqrt{3}} - \dfrac{e_a-e_b}{\sqrt{3}} \\ -\left(\dfrac{e_b-e_c}{\sqrt{3}} - \dfrac{e_a-e_b}{\sqrt{3}}\right) \end{bmatrix} \quad (24)$$

where $$\Delta = \{(e_a-e_c)\left(\frac{e_c-e_a}{\sqrt{3}} - \frac{e_a-e_b}{\sqrt{3}}\right) - \left(\frac{e_b-e_c}{\sqrt{3}} - \frac{e_a-e_b}{\sqrt{3}}\right)(e_b-e_c)\} \quad (25)$$

It is obvious from (22) or (24) that the calculation of q is not necessary to calculate i_{Ca}^* and i_{Cb}^*. Therefore, we can simplify the control structure. Fig.1 is the block diagram for the calculation of the compensating current reference based on the extension pq theory. Fig.1 is realized with analog circuits based on (21), (22) and (23).

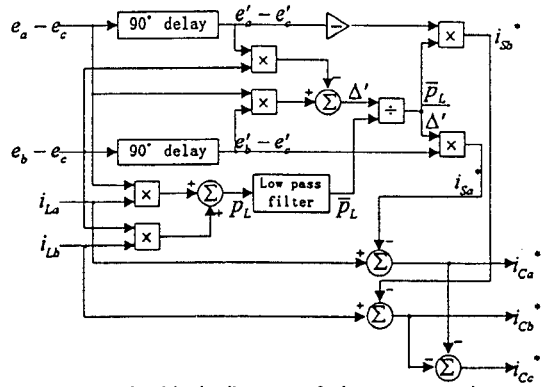

Fig.1. The block diagram of the compensating current reference calculation.

IV. EXPERIMENTAL RESULTS

In this section, we give the results of the experiments based on the theories explained above.

A. Experimental Method

The experimental configuration is shown in Fig.2. A three-phase diode bridge rectifier feeding a series RL load is used as the nonlinear load. The IPM inverter specifications are 600V, 30A. The current controller is a hysteresis-type control.

We step-down the line voltage to 40V. This is a three-phase symmetrical voltage system. By reducing e_a to 60%, we obtain an unsymmetrical voltage system and, by further changing the transformer connections from Δ-Y to Y-Y, we obtain an unsymmetrical distorted phase voltage system. These voltage waveforms are shown in Fig.3 and Fig.4.

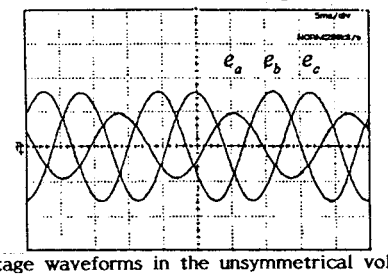

Fig.3. Voltage waveforms in the unsymmetrical voltage system.

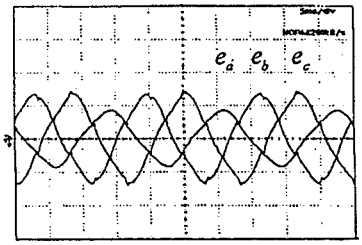

Fig.4. Voltage waveforms in the unsymmetrical and distorted phase voltage system.

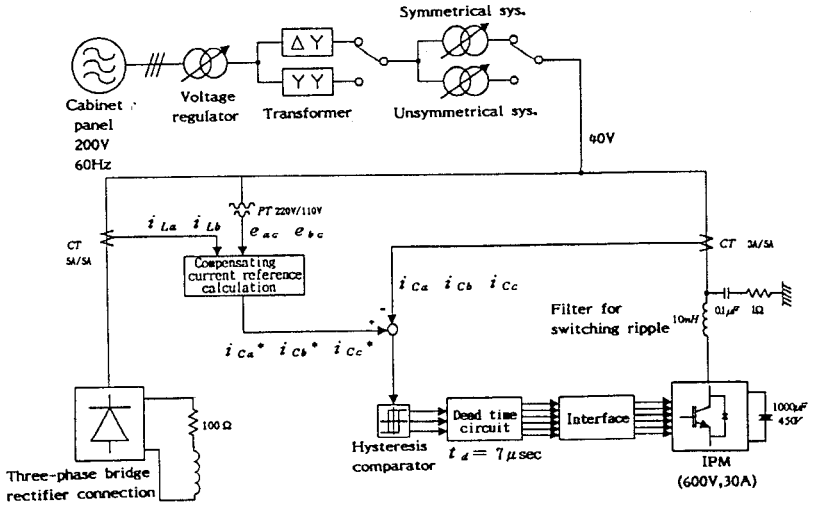

Fig.2. Structure of the experimental equipment.

B.The Characteristics of the Compensating Current Reference Calculation System

The system voltage e_a, the load current i_{La}, the ideal source current i_{Sa}^* and the compensating current reference i_{Ca}^* are shown in Fig.5 to Fig.7. In Fig.9 to Fig.11, Δ, Δ', p_L and p_L are shown. For the unsymmetrical voltage system, Fig.5 shows that i_{Sa}^* according to the pq theory is distorted while Fig.6 and Fig.7 show that i_{Sa}^* according to the extension pq theory is undistorted. Therefore, the performance of the extension pq theory is better than that of pq theory. In Fig.8 and Fig.9 p_L and p_L are in agreement, because in both methods, the same equation is used for the calculation of p_L. In the unsymmetrical voltage system, Δ of the pq theory contains the second-order harmonic. Therefore, the ideal source current i_{Sa}^* is distorted as can be understood from (24). Δ' of the extension pq theory is almost constant as shown in Fig.9 and Fig.10.

In the unsymmetrical distorted phase voltage system (Fig.10), the phase voltages e_a, e_b, and e_c have distortion as shown in Fig.4. However, good results can be obtained by the extension pq theory. The reason for this is considered as follows. If the line voltages e_{ac} and e_{bc} have no distortion and Δ' is constant, we may obtain sinusoidal ideal source currents from (22) of the extension pq theory. In Fig.10, the phase voltages are distorted, but the line voltages have no distortion. The line voltage waveforms shown in Fig.11 are almost sinusoidal.

C.General Characteristics of the Active Power Filte

Fig.12, Fig.13 and Fig.14 show the measured currents, corresponding to Fig.5, Fig.6 and Fig.7 respectively. These figures show that the actual

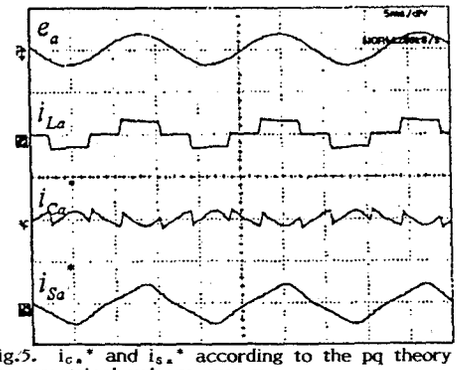

Fig.5. i_{Ca}^* and i_{Sa}^* according to the pq theory in the unsymmetrical voltage system.

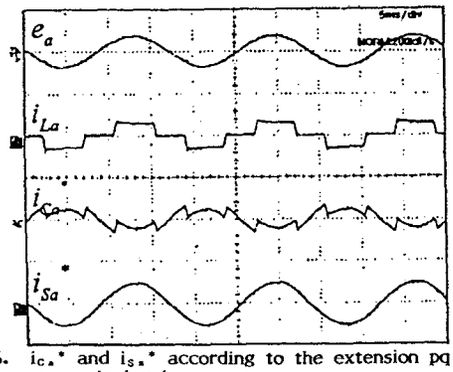

Fig.6. i_{Ca}^* and i_{Sa}^* according to the extension pq theory in the unsymmetrical voltage system.

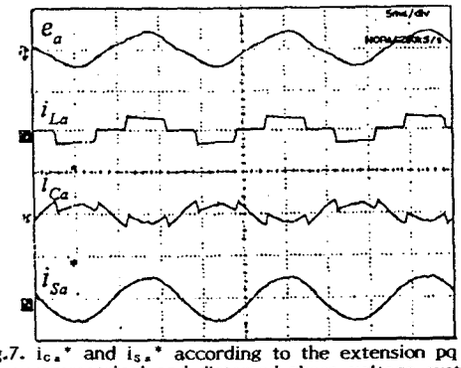

Fig.7. i_{Ca}^* and i_{Sa}^* according to the extension pq theory in the unsymmetrical and distorted phase voltage system.

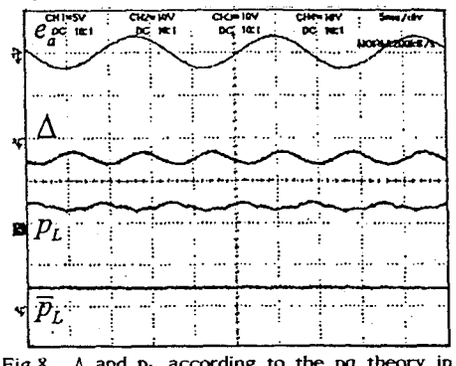

Fig.8. Δ and p_L according to the pq theory in the unsymmetrical voltage system.

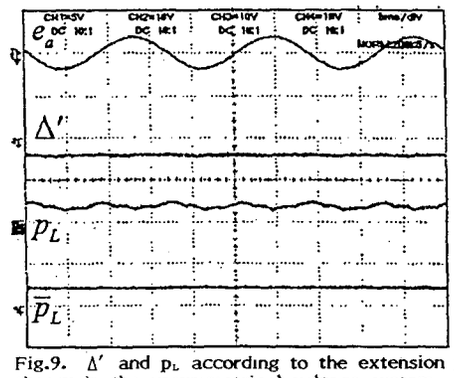

Fig.9. Δ' and p_L according to the extension pq theory in the unsymmetrical voltage system.

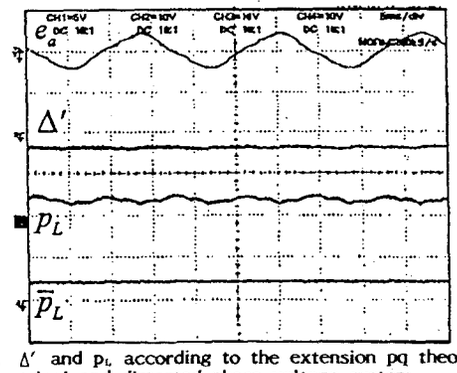

Fig.10. Δ' and p_L according to the extension pq theory in the unsymmetrical and distorted phase voltage system.

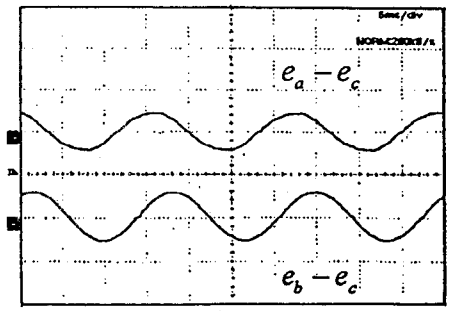

Fig.11. Waveforms of line voltage in the unsymmetrical and distorted phase voltage system.

currents almost agree with the reference currents. Fig.15, Fig.16 and Fig.17 show the frequency spectra of currents i_{La} and i_{Sa} in Fig.12, Fig.13 and Fig.14 respectively. In the unsymmetrical voltage system, the results obtained by the pq theory are not good. However, the extension pq theory gives good results for both the unsymmetrical voltage system and unsymmetrical distorted phase voltage system.

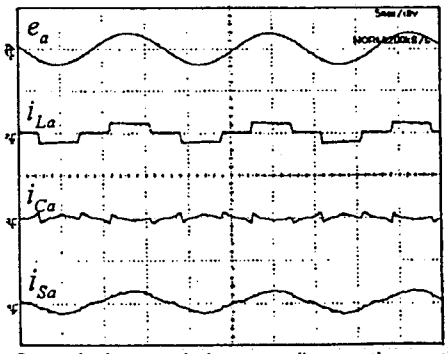

Fig.12. General characteristics according to the pq theory in the unsymmetrical voltage system.

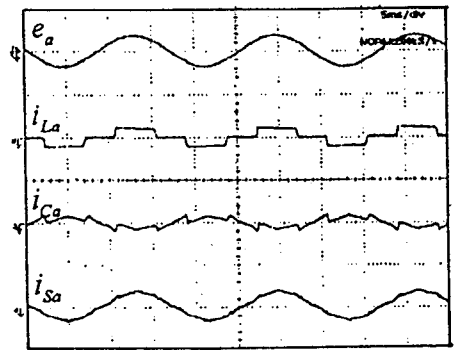

Fig.13. General characteristics according to the extension pq theory in the unsymmetrical voltage system.

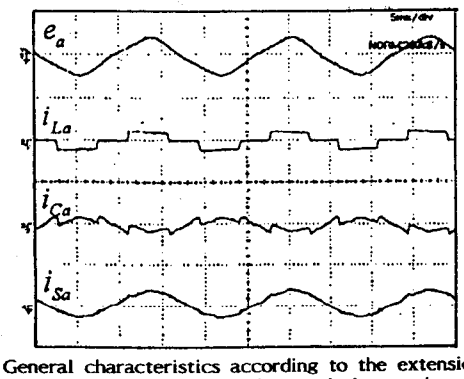

Fig.14. General characteristics according to the extension pq theory in the unsymmetrical and distorted phase voltage system.

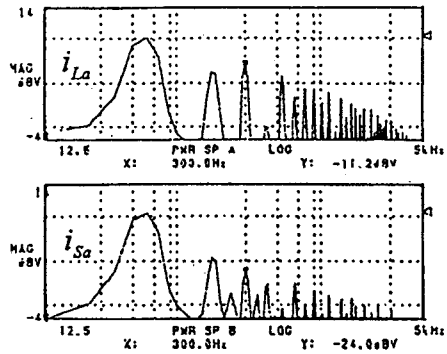

Fig.15. Frequency spectra of i_{La} and i_{Sa} according to the pq theory in the unsymmetrical voltage system.

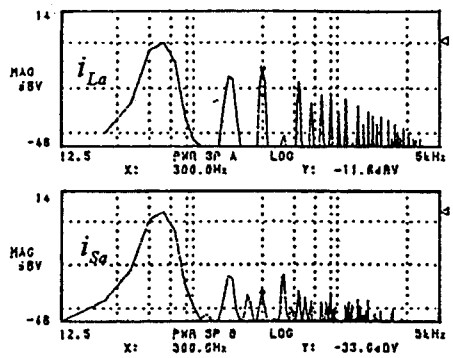

Fig.16. Frequency spectra of i_{La} and i_{Sa} according to the extension pq theory in the unsymmetsical voltage system.

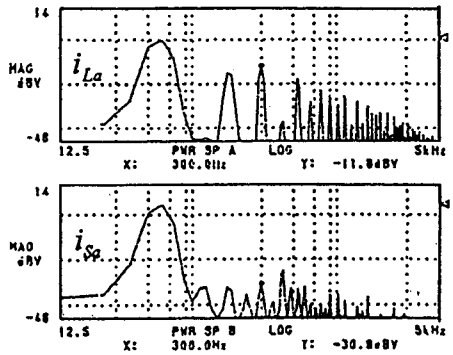

Fig.17. Frequency spectra of i_{La} and i_{Sa} according to the extension pq theory in the unsymmetrical and distorted phase voltage system.

D.Characteristics of Active Power Filter in Distorted Line Voltage System

To distort the line voltage, we connect a three-phase bridge rectifier as system load. The phase and line voltages are shown in Fig.18. Both waveforms contain the 5th, 11th and 7th harmonics mainly. In this case, the characteristics of the active power filter according to the extension pq theory are shown in Fig.19. As shown in Fig.19, i_{Sa}^* and i_{Sa} have distortion. Mainly, i_{Sa} has the 5th and 11th harmonics. As mentioned above, the performance of the active power filter in distorted line voltage system is not good.

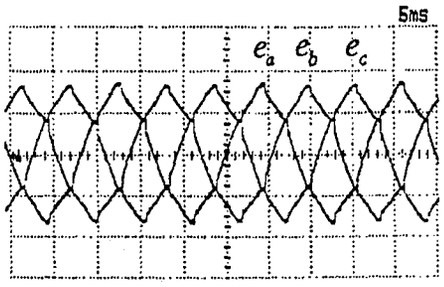

(a) Phase voltages

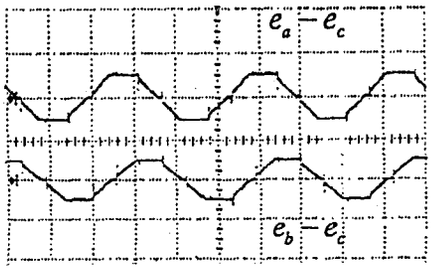

(b) Line voltages

Fig.18. Voltage waveforms in the distorted line voltage system.

V. CONTROL METHOD OF ACTIVE POWER FILTER IN UNSYMMETRICAL AND DISTORTED LINE VOLTAGE SYSTEM

A. The Proposed Method

In this section, we propose a calculation method for the compensating current reference applicable in unsymmetrical and distorted line voltage system and show the experimental results of the active power filter based on it.

We redefine q as

$$q = e_{a1}' i_a + e_{b1}' i_b + e_{c1}' i_c \qquad (26)$$

where e_{a1}', e_{b1}' and e_{c1}' have 90° delay than fundamental components of e_a, e_b and e_c respectively.

p is defined by (1). From (1), (3) and (26), we may derive the equations:

$$\begin{bmatrix} p \\ q \end{bmatrix} = \begin{bmatrix} e_a-e_c & e_b-e_c \\ e_{a1}'-e_{c1}' & e_{b1}'-e_{c1}' \end{bmatrix} \begin{bmatrix} i_a \\ i_b \end{bmatrix} \qquad (27)$$

$$\begin{bmatrix} i_a \\ i_b \end{bmatrix} = \frac{1}{\Delta} \begin{bmatrix} e_{b1}'-e_{c1}' & -(e_b-e_c) \\ -(e_{a1}'-e_{c1}') & e_a-e_c \end{bmatrix} \begin{bmatrix} p \\ q \end{bmatrix} \qquad (28)$$

where $\Delta=(e_a-e_c)(e_{b1}'-e_{c1}')-(e_{a1}'-e_{c1}')(e_b-e_c)$.

Equations (27) and (28) are applicable to every part of system. For instance, we may obtain the equation:

$$\begin{bmatrix} p_S \\ q_S \end{bmatrix} = \begin{bmatrix} e_a-e_c & e_b-e_c \\ e_{a1}'-e_{c1}' & e_{b1}'-e_{c1}' \end{bmatrix} \begin{bmatrix} i_{Sa} \\ i_{Sb} \end{bmatrix}. \qquad (29)$$

From Kirchhoff's current law equation and (3), we may delive the equation:

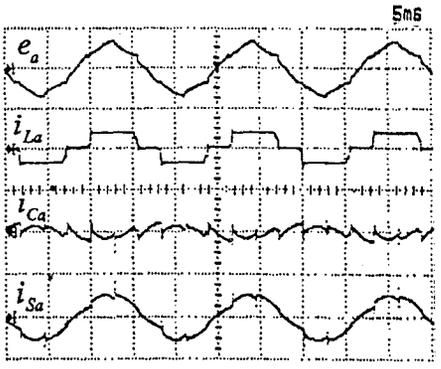

(a) i_{Ca}^* and i_{Sa}^*

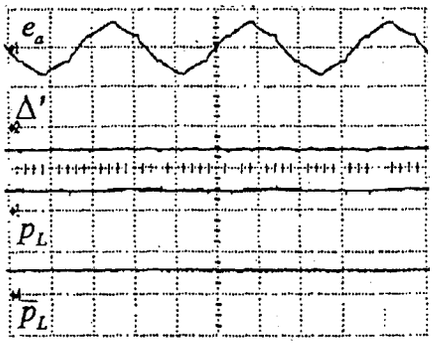

(b) Δ', p_L and $\bar{p}_L$

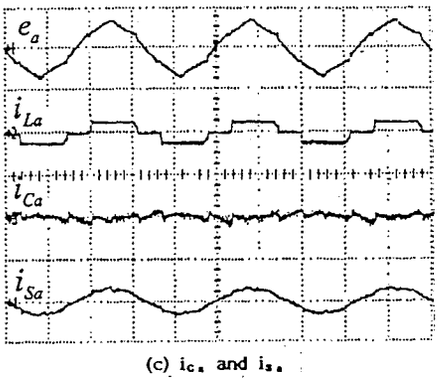

(c) i_{Ca} and i_{Sa}

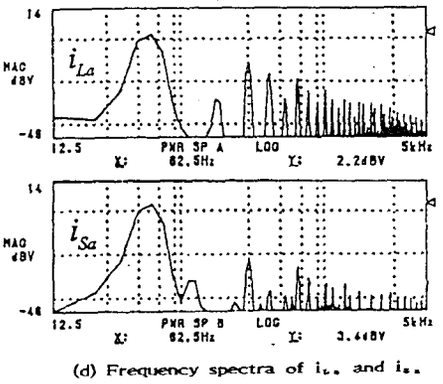

(d) Frequency spectra of i_{La} and i_{Sa}

Fig.19. Characteristics according to the extension pq theory in the distorted line voltage system.

$$\begin{bmatrix} p_S \\ q_S \end{bmatrix} + \begin{bmatrix} p_C \\ q_C \end{bmatrix} = \begin{bmatrix} p_L \\ q_L \end{bmatrix} \qquad (30)$$

It is desirable that source currents are sinusoidal. We determine the ideal source currents i_{Sa}^* and i_{Sb}^* from the equation:

$$\begin{bmatrix} i_{Sa}^* \\ i_{Sb}^* \end{bmatrix} = \frac{1}{\Delta_1}\begin{bmatrix} e_{b1}'-e_{c1}' & -(e_{b1}-e_{c1}) \\ -(e_{a1}'-e_{c1}') & e_{a1}-e_{c1} \end{bmatrix}\begin{bmatrix} p_s' \\ q_s' \end{bmatrix} \quad (31)$$

where $\Delta_1=(e_{a1}-e_{c1})(e_{b1}'-e_{c1}')-(e_{a1}'-e_{c1}')(e_{b1}-e_{c1})$.

We make p_s' and q_s' in (31) constant value. Δ_1 is also constant value. Therefore, i_{Sa}^* and i_{Sb}^* are sinusoidal. From (29) and (31), we may derive the equation:

$$\begin{bmatrix} p_s \\ q_s \end{bmatrix} = \frac{1}{\Delta_1}\begin{bmatrix} \Delta & (e_{a1}-e_{c1})(e_b-e_c)-(e_a-e_c)(e_{b1}-e_{c1}) \\ 0 & \Delta_1 \end{bmatrix}\begin{bmatrix} p_s' \\ q_s' \end{bmatrix}. \quad (32)$$

In (32), the equation related to q_S is

$$q_s = q_s'. \quad (33)$$

and, the equation related to p_S is

$$p_s=\{p_s'\Delta+\{(e_{a1}-e_{c1})(e_b-e_c)-(e_a-e_c)(e_{b1}-e_{c1})\}q_s'\}/\Delta_1. \quad (34)$$

Now, we set p_S' and q_S' as

$$p_s' = \overline{p}_L, \quad q_s' = 0 . \quad (35)$$

Substituting (35) into (34) leads to the equation:

$$p_s = \overline{p}_L\Delta/\Delta_1 . \quad (36)$$

Substituting (35) into (33) leads to the equation:

$$q_s = 0 . \quad (37)$$

From (36) we may derive the equation:

$$\overline{p}_S = \overline{p}_L\overline{\Delta}/\Delta_1$$

$$=\overline{p}_L\{\overline{(e_a-e_c)(e_{b1}'-e_{c1}')}-(e_{a1}'-e_{c1}')(e_b-e_c)\}/\Delta_1$$

$$=\overline{p}_L . \quad (38)$$

From (30) and (38) we may derive the equation:

$$\overline{p}_C = 0 . \quad (39)$$

Equation (39) is necessary for the good operation of the active power filter.

B. Experimental Results

We set p_S' and q_S' as (35), and calculate i_{Sa}^* and i_{Sb}^* using (31). Then we calculate i_{Ca}^* and i_{Cb}^* using (21).

The phase voltages are shown in Fig.20. Each phase currents and their spectra are shown in Fig.21 to Fig.23. It is evident that the active power filter based on the proposed method gives good operation as seen from Fig.21 to Fig.23.

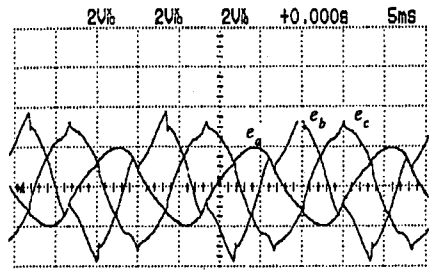

Fig.20. Voltage waveforms in the unsymmetrical and distorted line voltage system.

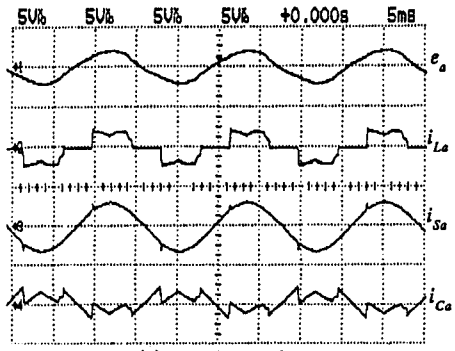

(a) i_{La}, i_{Sa} and i_{Ca}.

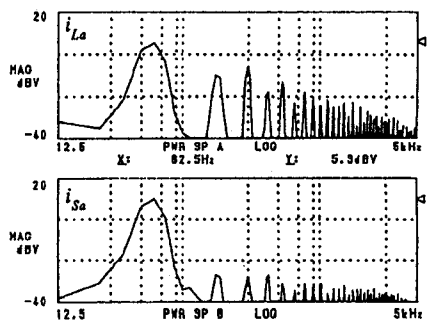

(b) Frequency spectra of currents.

Fig.21. i_{Sa} and i_{La} in the unsymmetrical and distorted line voltage system.

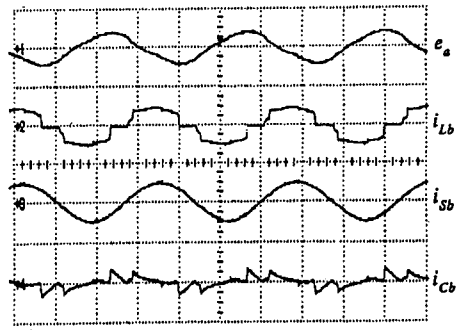

(a) i_{Lb}, i_{Sb} and i_{Cb}.

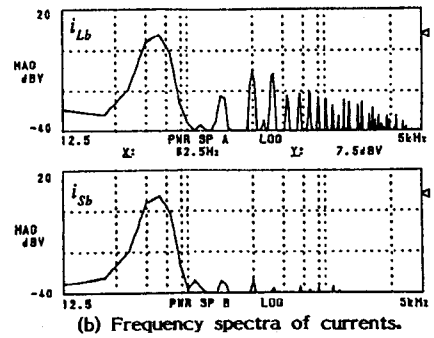

(b) Frequency spectra of currents.

Fig.22. i_{Sb} and i_{Lb} in the unsymmetrical and distorted line voltage system.

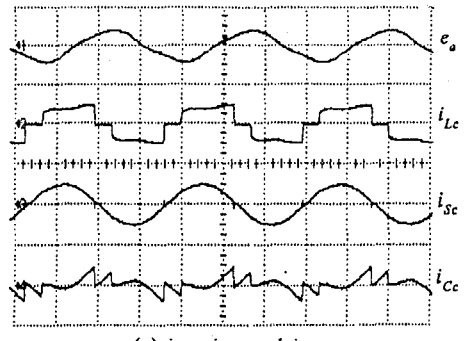

(a) i_{Lc}, i_{Sc} and i_{Cc}.

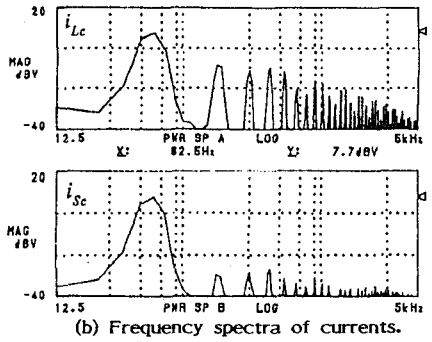

(b) Frequency spectra of currents.

Fig.23. i_{Sc} and i_{Lc} in the unsymmetrical and distorted line voltage system.

VI. CONCLUSIONS

In this paper, we clarified the excellent features of the extension pq theory by experiments. The results that we obtained are as follows.

(1) In unsymmetrical voltage system, the source currents by the pq theory have distortions, while the source currents by the extension pq theory have no distortion.

(2) In unsymmetrical voltage system, Δ' of the extension pq theory is almost constant, while Δ of the pq theory contains the second-order harmonic. Therefore, we may not obtain accurate compensating current reference by use of the pq theory.

(3) Active power filters based on the extension pq theory gives satisfactory operation even when the system phase voltages are unsymmetrical and distorted, because no distortion appears in the line voltages and Δ' is constant.

(4) In distorted line voltage system, the active power filter based on the extension pq theory does not give satisfactory operation.

(5) The active power filter in unsymmetrical and distorted line voltage system according to the proposed method give satisfactory operation.

ACKNOWLEDGEMENT

The authors gratefully acknowledge the contributions of Dr. Emenike C. Ejiogu of Ritsumeikan University.

REFERENCES

[1] H.Akagi,Y.Kanazawa and A.Nabae,"Instantaneous Reactive Power Compensators Comprising Switching Devices Without Energy Storage Components,"*IEEE Trans.Ind.Appl.*, vol.20, pp.625-630,1984

[2] Y.Komatsu and T.Kawabata,"A Control Method of Active Power Filter Where System Voltage Contains Negative-Phase-Sequence Component or Zero-Phase-Sequence Component,"in *Proceedings of PEDS Conference'95*, 1995,pp 583-586/vol.2

A New Control Method for Active Power Filters with Voltage Detection

Yukihiko Sato,* Hidenori Chigira,* and Teruo Kataoka**

* Tokyo Institute of Technology
2-12-1, O-okayama, Meguro-ku,
Tokyo, 152 JAPAN
Fax: +81-3-5734-2898 Phone: +81-3-5734-3562
E-mail: ysato@tk.ee.titech.ac.jp

** Tokyo Denki University
2-2, Kanda-Nishiki-cho, Chiyoda-ku,
Tokyo, 101 JAPAN
Fax: +81-3-5280-3573 Phone: +81-3-5280-3304
E-mail: tkataoka@cck.dendai.ac.jp

Abstract- In this paper, a new control method for active power filters with voltage detection is proposed. The proposed control method is based on the real-time simulation of an LC filter accomplished by a digital signal processor. Thus the proposed active power filter acts equivalently as an LC filter whose circuit parameters, such as the resonant frequency and quality factor, can be adjusted to obtain the most effective compensation characteristics during the operating condition. The effectiveness of the proposed control method is demonstrated by some experimental results and computer simulation.

I. Introduction

In recent years, active power filters have been widely investigated for the compensation of harmonics in electric power systems. [1]–[5] The active power filters are divided into two types: current detection type and voltage detection type. Most of the active power filters which have been put into practice are those with the current detection. In these active power filters, the compensation current is generated according to the detected harmonic components in the load current or supply current. Adequate compensation characteristics can be obtained in the cases where the sources of the harmonic currents are clearly specified. However, the active power filters with current detection may cause some practical problems [6] in the cases where the sources of the harmonic currents can not be specified. In such cases, the active power filter with voltage detection may realize the desirable characteristics in the harmonic compensation. In this paper, a new control method for the active power filter with voltage detection is proposed.

The proposed active power filter is based on the real-time digital simulation of a passive tuned LC filter. The calculation of the simulation is accomplished by a digital signal processor (DSP) using the detected signal of the voltage at the point where the active power filter is connected. The input current or compensating current of the active filter is determined by the detected terminal voltage. Thus, the compensating current is adjusted automatically according to the condition of the ac line. Therefore, the practical problems of the existing active power filters with current detection can be solved. Because the calculation algorithm is based on the real-time simulation of a passive LC filter, the proposed active power filter acts equivalently as a passive LC filter. However, the proposed active power filter is completely different from the conventional passive LC filters in the following points.

- There are no physical restrictions in the selection of the circuit parameters of the filter components, such as inductance, capacitance, and resistance.
- The ideal LC filter, such as loss-less LC filter, can be realized.
- The power dissipated in the simulated LC filter can be returned to the ac line as a fundamental active power component. Thus, an LC filter with a low quality factor can be realized without deteriorating the efficiency.
- The circuit parameters and circuit configuration can be changed even during the operating condition. This allows the on-line adaptation of the circuit parameters of the simulated LC filter.

In this paper, the principle of the proposed control strategy is discussed. A control system implementation using a digital signal processor is shown. To confirm the effectiveness of the proposed control method, some experimental results are shown. Finally, an example of the on-line parameter adaptation is demonstrated by the results of the computer simulation.

II. Control Principle

A. Control Principle

Fig.1 shows a schematic diagram of the main circuit and control system of the proposed active power filter. A real-time simulator of the LC filter using a digital signal processor (DSP) is introduced as a compensating current reference generator. The calculation algorithm is based on the real-time simulation of the LC filter using the state equation. The circuit diagram of the LC

0-7803-3823-5/97/$10.00© 1997 IEEE

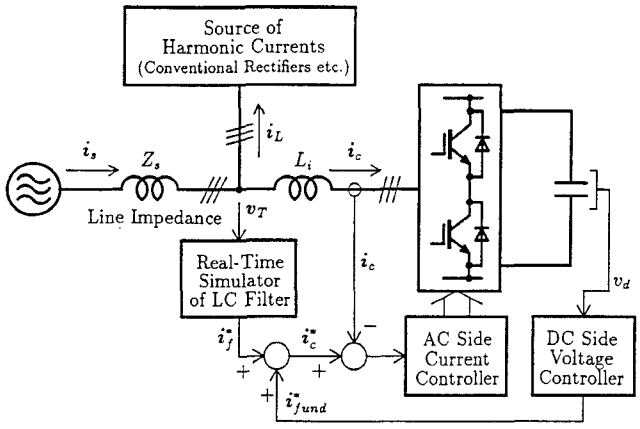

Fig.1. Main circuit and control block diagram

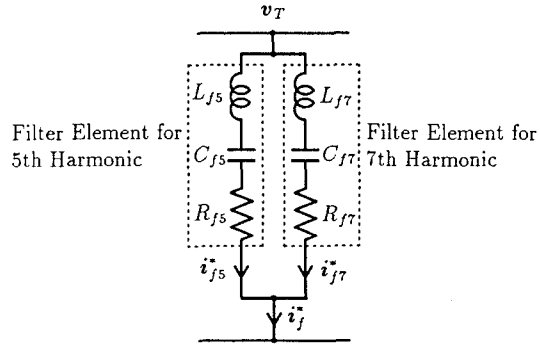

Fig.2. Circuit configuration of simulated LC filter

filter simulated in the DSP is shown in Fig.2. The LC filter consists of two elements of the tuned LC filter whose resonant frequencies are set to the 5th and 7th harmonic frequencies. i_{f5}^* and i_{f7}^* are the calculated values of the currents which flow through the filter elements tuned for the 5th and 7th harmonics, respectively. (Hereafter, variables shown by boldface letters such as i_{f5}^* and i_{f7}^* are three phase quantities.) The values of i_{f5}^* and i_{f7}^* are calculated from the detected signal of the terminal voltage v_T. The sum of these values $i_f^*(= i_{f5}^* + i_{f7}^*)$ is used as the compensating current reference for the proposed active power filter. In the control system shown in Fig.1, i_{fund}^* is a reference signal of the fundamental current component to keep the dc side voltage v_d constant and is added to i_f^* to produce the ac side current reference i_c^*:

$$i_c^* = i_f^* + i_{fund}^* \tag{1}$$

The actual ac side current i_c of the active power filter is compared with i_c^*, and the difference signal $i_c^* - i_c$ is applied to the ac side current controller shown. In this way, the compensating current component i_f of the actual ac side current i_c is controlled so as to coincide with the reference signal i_f^*. Since the control is performed using the detected terminal phase voltage v_T and the state equation of the equivalent LC filter, the relationship between v_T and i_f is exactly the same as that of the LC filter shown in Fig.2. Thus, the proposed active power filter acts as an LC filter shown in Fig.2 when it is viewed from the ac side. In this paper, the LC filter shown in Fig.2 which has only two filter elements for the 5th and 7th harmonics is treated as a simple example. The investigation in this paper can be extended to cases when the number of the filter elements is more than two.

B. On-Line Parameter Adaptation

In the proposed active power filter, the circuit parameters, such as the resonant frequency and quality factor, of the simulated LC filter can be changed even when the system is operating. For example, in the filter element for the 5th harmonic, the current i_{f5}^* decreases when the resistance R_{f5} is increased. This means that the compensation capability for the 5th harmonic components can be controlled by adjusting the value of R_{f5}, or the quality factor Q_{f5} of the filter element for the 5th harmonic. In the same way, the compensation capability for the 7th harmonic can be controlled by adjusting the quality factor Q_{f7} of the filter element for the 7th harmonic. Note that the values of Q_{f5} and Q_{f7} do not affect the compensation capability for the 7th and 5th harmonics, respectively. Thus, the control of the compensation capability for each harmonic component can be done independently.

In the proposed system, the information of the currents i_{f5}^* and i_{f7}^* flowing through the simulated filter elements are stored in the memory of the DSP as digital data. Thus, the values of i_{f5}^* and i_{f7}^* are available without any additional hardware such as current sensors. If the quality factor is adjusted appropriately according to the information of the current flowing through the corresponding filter element, the effective utilization of the harmonic compensation capability can be achieved. As mentioned before, the compensation capability for each harmonic component can be controlled selectively. Thus, the total compensation capability which is determined mainly by the current rating of the main circuit of the active power filter can be distributed concentratively to the harmonic components whose compensations are strongly required.

III. Implementation of Control System

Fig.3 shows a calculation model of a filter element simulated by the DSP. The state equation in the con-

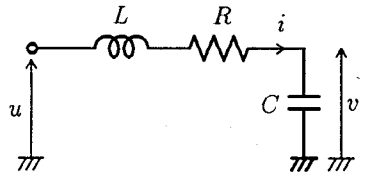

Fig.3. Calculation model of LC filter

tinuous time domain is given by

$$\frac{d}{dt}\begin{bmatrix} v \\ i \end{bmatrix} = \begin{bmatrix} 0 & 1/C \\ -1/L & -R/L \end{bmatrix}\begin{bmatrix} v \\ i \end{bmatrix} + \begin{bmatrix} 0 \\ 1/L \end{bmatrix} u \quad (2)$$

For the convenience in the calculation, the values of L and C are set to the reciprocal $1/\omega_n$ of the resonant frequency ω_n which is equal to the n-th harmonic angular frequency. The transfer function of the LC filter is then given by

$$\frac{i}{u} = \frac{s/\omega_n}{1 + sR/\omega_n + s^2/\omega_n^2} \quad (3)$$

From equation (2), the state equation of the filter element for the n-th harmonic component in the discrete time domain is given by

$$\begin{bmatrix} v(k+1) \\ i(k+1) \end{bmatrix} = \boldsymbol{P}\begin{bmatrix} v(k) \\ i(k) \end{bmatrix} + \boldsymbol{Q}u(k) \quad (4)$$

where,

$$\boldsymbol{P} = \begin{bmatrix} e^{-\alpha T}\{\cos\beta T + (\alpha/\beta)\sin\beta T\} & * \\ (-\omega_n/\beta)e^{-\alpha T}\sin\beta T & * \end{bmatrix}$$

$$\begin{bmatrix} * & (\omega_n/\beta)e^{-\alpha T}\sin\beta T \\ * & e^{-\alpha T}\{\cos\beta T - (\alpha/\beta)\sin\beta T\} \end{bmatrix}$$

$$\boldsymbol{Q} = \begin{bmatrix} \frac{\omega_n^2}{\alpha^2+\beta^2}\{1 - e^{-\alpha T}\{\cos\beta T + (\alpha/\beta)\sin\beta T\}\} \\ (\omega_n/\beta)e^{-\alpha T}\sin\beta T \end{bmatrix}$$

$$\alpha = \omega_n R/2 \qquad \beta = \omega_n\sqrt{1 - R^2/4}$$

In these expressions, T is the calculation interval, $v(k)$, $i(k)$, and $u(k)$ are the k-th sampled values of v, i, and u, respectively. From expression (4), the state variables $v(k+1)$ and $i(k+1)$ of the $(k+1)$-th time step can be calculated consecutively using the state variables $v(k)$, $i(k)$ and input $u(k)$ of the k-th time step. The expressions for $\boldsymbol{P}$ and $\boldsymbol{Q}$ contain trigonometric functions and exponential functions, but these functions are constant for given values of the resonant frequency ω_n and calculation interval T. Thus, the calculation of expression (4) requires just multiplication and addition.

In equation (4), it has been assumed that $L = C = 1/\omega_n$. For any combination of L_{fn} and C_{fn} of the filter element in Fig.2 whose resonant angular frequency is ω_n, the calculation of the LC filter can be done in the following way. By introducing a parameter h, L_{fn} and C_{fn} are expressed as follows.

$$L_{fn} = \frac{L}{h} = \frac{1}{h\omega_n} \quad (5)$$

$$C_{fn} = hC = \frac{h}{\omega_n} \quad (6)$$

The transfer function of the filter element which consists of L_{fn}, C_{fn}, and R_{fn} is given by

$$\frac{i_{fn}}{v_T} = \frac{sC_{fn}}{1 + sC_{fn}R_{fn} + s^2L_{fn}C_{fn}} \quad (7)$$

Substituting expressions (5) and (6) into (7), the transfer function is written as

$$\frac{i_{fn}}{v_T} = \frac{sh/\omega_n}{1 + shR_{fn}/\omega_n + s^2/\omega_n^2} \quad (8)$$

Comparing expressions (3) and (8), we can see that the calculation of the LC filter can be extended to the cases in which $L_{fn} \neq C_{fn} \neq 1/\omega_n$ by multiplying v_T and R_{fn} by the parameter h.

IV. Experimental Investigation

To confirm the effectiveness of the proposed control method, some experiments have been made employing a laboratory test system. The specifications of the laboratory test system and the parameters of the simulated LC filter are listed in Table.1 and Table.2, respectively. The real-time simulator of the LC filter is implemented by a digital signal processor (TI, TMS320C52). The calculation interval is 40[μs].

Fig.4 shows an experimental result of the current waveforms of the test system when a diode bridge rectifier with a smoothing reactor is connected as a source of the harmonic currents shown in Fig.1. The top and second traces show the waveforms of the terminal voltage $v_{T\ell}$ (line-to-line voltage of v_T) and the input current i_L (Load Current) of the diode bridge. The third and bottom traces show the waveforms of the total input current i_s and the ac side current i_c (AF Current) of the proposed active power filter. In this figure, the 5th and 7th harmonic components of the input current of the diode bridge rectifier are effectively compensated by the proposed active filter. From this result, we can see that the proposed active filter acts as an LC filter. Fig.5 shows the experimental results of the frequency contents of the terminal voltage $v_{T\ell}$ of the active power filter. Fig.5 (a) is the result without the harmonic compensation by the proposed active power filter. Fig.5 (b) and (c) are the results with the proposed active power filter when the resistance R_{f5} is 0.2 [Ω] and 0.05 [Ω], respectively. From this result, we can see that the 5th and

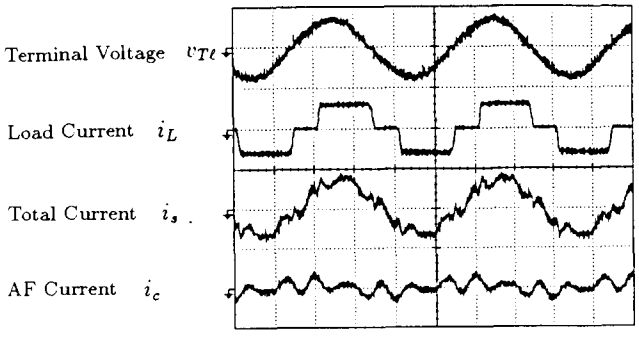

Fig.4. Current waveforms when a diode bridge rectifier with smoothing inductor is connected (5[ms/div], 100[V/div], 10[A/div])

Table.1. Specification of test system

AC Side Line-to-Line Voltage	100[V]
Source Frequency	50[Hz]
AC Side Inductor L_i	5.2[mH]
Resistance of L_i	0.2[Ω]
Average Switching Frequency	4[kHz]
DC Side Voltage v_d	200[V]
Calculation Interval of DSP	40[μs]

Table.2. Parameters of simulated LC filter

5th Harmonic	L_{f5}	10[mH]
	C_{f5}	40.53[μF]
	R_{f5}	0.1[Ω]
7th Harmonic	L_{f7}	10[mH]
	C_{f7}	20.68[μF]
	R_{f7}	0.1[Ω]

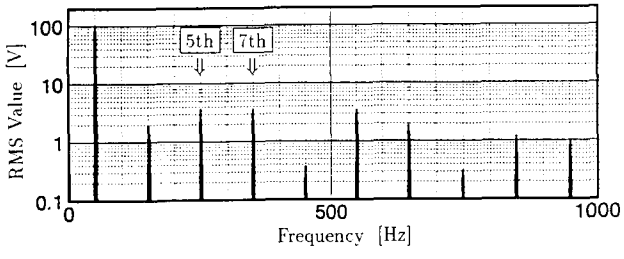

(a) Without proposed active filter

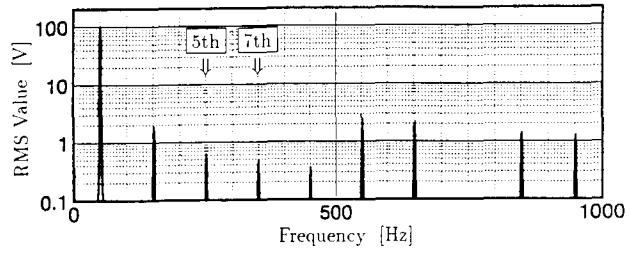

(b) With proposed active filter ($R_{f5} = 0.2$ [Ω])

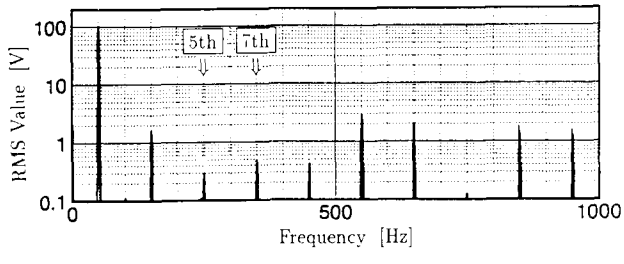

(c) With proposed active filter ($R_{f5} = 0.05$ [Ω])

Fig.5. Frequency contents of terminal voltage $v_{T\ell}$

7th harmonic components are reduced significantly by the harmonic compensation. The quality factor of the 5th filter element used in Fig.5 (c) is larger than that used in Fig.5 (b). As a result, the 5th harmonic component in Fig.5 (c) becomes smaller than that in Fig.5 (b). Furthermore, comparing both figures, we can see that there is no difference between the 7th harmonic components. This is because the value of the resistance R_{f7} of the 7th filter element was not changed. From these results, we can say that the compensating capability for the 5th harmonic component is controlled selectively by adjusting R_{f5}. Therefore, the selective control capability of the harmonics compensation characteristics for each harmonic component has been confirmed experimentally.

V. Control of Compensation Capability

As mentioned in II.*B.*, the proposed active power filter can realize the on-line adaptation of the circuit parameters even when the system is operating. For example, the harmonic compensation capability for the n-th harmonic component can be controlled by adjusting the quality factor Q_{fn} or resistance R_{fn}. If the value of R_{fn} is properly adjusted according to the input current of the filter element for the n-th harmonic component, the compensating capability of the active power filter can be utilized effectively.

Fig.6 shows an example of the control system configuration for the parameter adaptation. In this figure, $I^*_{fn.rms}$ is the nominal rms value of the n-th harmonic component in the filter input current which is determined considering mainly the current control capabil-

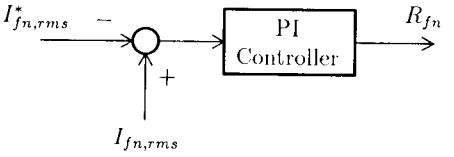

Fig.6. Control system of compensating capability

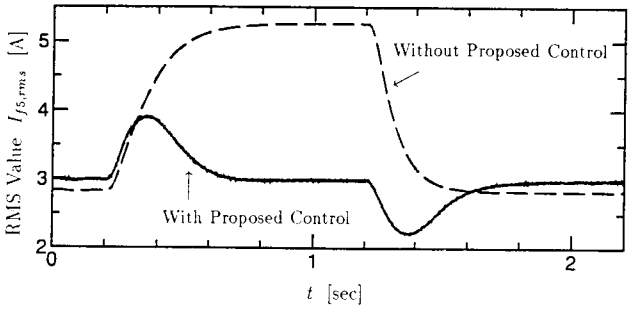

Fig.7. Compensating current $I_{f5,rms}$ when harmonic source changes (computer simulation result)

ity of the main circuit. $I_{fn,rms}$ is the actual rms value of n-th harmonic component of the filter input current. $I_{fn,rms}$ can be calculated from the data of i^*_{fn} (three phase quantity) stored in the DSP memory using the $\alpha\beta$ transformation. The difference ($I_{fn,rms} - I^*_{fn,rms}$) is applied to the PI controller. The output signal of the PI controller is used as the value of R_{fn}. When the actual value $I_{fn,rms}$ is larger than its nominal value $I^*_{fn,rms}$, the value of R_{fn} becomes large. In this way, the value of $I_{fn,rms}$ in the steady state coincides with its nominal value.

To confirm the effectiveness of the control system shown in Fig.6, a result of the computer simulation is shown in Fig.7. In this simulation, a diode bridge rectifier with a dc side smoothing reactor is connected as a source of the harmonic currents. The adaptive control system shown in Fig.6 is introduced in the filter element only for the 5th harmonic components. The solid line and broken line show the result with and without the adaptive control, respectively. At the instant $t = 0.2$ [sec], the dc side current of the diode bridge rectifier is suddenly increased. Then, the dc current is reduced to its initial value at the instant $t = 1.2$ [sec]. In this case, the nominal value $I^*_{f5,rms}$ is set to 3[A]. When the adaptive control system is not used, the 5th harmonic component $I_{f5,rms}$ of the filter input current changes according to the change in the 5th harmonic current caused by the diode bridge rectifier. In contrast

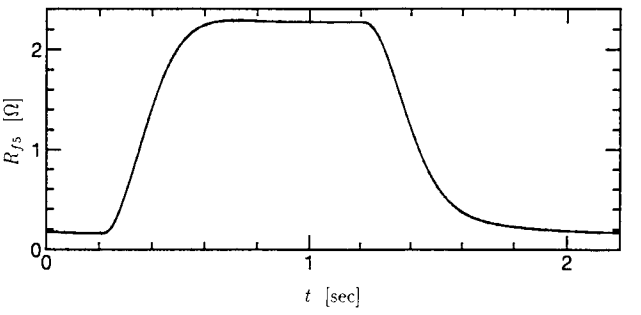

Fig.8. Resisntace R_{f5} when harmonic source changes (computer simulation result)

to this, $I_{f5,rms}$ in the steady state is kept to its nominal value 3[A] when the adaptive control is introduced. Fig.8 shows the change in the resistance R_{f5} of the filter element for the 5th harmonic during the simulation shown in Fig.7. From this figure, R_{f5} changes automatically according to the change in the 5th harmonic current caused by the diode bridge rectifier.

The basic effectiveness of the adaptive control has been demonstrated by the computer simulation. From the view point of the effective utilization of the active power filter, the nominal value of the filter input current for each harmonic component should be determined considering the total current control capability and the requirement of the compensation of each harmonic component.

VI. Conclusion

In this paper, a new control method of the active power filters with voltage detection has been presented. The proposed control method is based on the real-time digital simulation of the passive tuned LC filter. The simulated LC filter is realized by the calculation in the digital signal processor. Thus, the parameter of the simulated LC filter can be selected without considering practical restrictions such as weight, size, cost, and efficiency. This freedom of the selection of the circuit parameters allows the excellent compensation characteristics which can not be realized by the conventional passive LC filters. In addition, the proposed active filter can realize the selective control of the compensating capability for each harmonic component and the on-line adaptation of the circuit parameters. The effectiveness of the proposed active power filter and control strategy has been confirmed by some results of computer simulation and experimental work employing the test system.

The proposed active filter is suitable for the harmonic compensation in the power distribution systems

where the sources of the harmonic currents are not clearly specified. Although, in this paper, the basic effectiveness of the proposed active power filter has been confirmed, the detailed analysis of the behavior of the proposed active filter in the practical power distribution systems operating under various conditions is required. This subject is left for future investigation.

REFERENCES

[1] F. Z. Peng, H. Akagi, and A. Nabae, "A new approach to harmonic compensation in power system — A combined system of shunt passive and series active filters," *IEEE Trans. Ind. Applicat.*, vol. 26, pp983-990, 1990

[2] K. Oku, O, Nakamura, J. Inoue, and M. Kohata, "Suppression effects of active power filter on harmonics of distribution system including capacitors," *Trans. IEEJ* vol. 115-B, pp1023-1028, 1995

[3] S. Fukuda, and T. Endoh, "Control method for a combined active filter system employing a current source converter and a high pass filter," *IEEE Trans. Ind. Applicat.*, vol. 31, pp590-597, 1995

[4] S. Saetieo, R. Devaraj, and David A. Torrey, "The Design and Implementation of a three-phase active power filter based on sliding mode control," *IEEE Trans. Ind. Applicat.*, vol. 31, pp993-1000, 1995

[5] T. Miyata, S. Murakami, and N. Watanabe, "Trends in power electronics applications for the electric power systems. II Static Var compensators and active filters," *Trans. IEEJ* vol. 115-D, pp.365-369, 1995

[6] H. Akagi, "Control strategy and site selection of a shunt active power filter for installation on a power distribution system," *Trans. IEEJ* vol. 116-D, pp.285-293, 1996

[7] H. Chigira, F. Saito, Y. Sato, and T. Kataoka, "New control strategy of a shunt active power filter based on voltage detection", IEEJ SPC-97-32, pp.39-44, 1997

Novel Active Filter System Composed of Inverter Bypass Circuit for Suppression of Harmonic Resonance at the Yamanashi Maglev Test Line

Ikuo Kawaguchi Haruo Ikeda
Railway Technical Research Institute
2-8-38, Hikari-cho, Kokubunji, 185, JAPAN

Jun-ichi Kitano
Central Japan Railway Company
1-6-6, Yaesu, Chuo-ku, Tokyo 103, JAPAN

Yoshiya Ogihara Miyokazu Syogaki Hiroshi Morita
Nissin Electric Co.,Ltd.
47 Umezu-takase-cho, Ukyo-ku, Kyoto 615, JAPAN

Abstract **– We have developed and proposed a novel active filter system composed of inverter bypass circuit for suppression of harmonic resonance condition caused between the inductance behind the load bus and the capacitance of var equipment especially at lower harmonic frequencies.**

We have installed this new scheme of harmonic compensation system in combination with TCR-type SVC and shunt LC filters at Yamanashi Maglev Test Line.

We will describe the outline of the reactive power and harmonic compensation systems, and harmonic resonance test results which show satisfactory performance of the active filter.

1. INTRODUCTION

The authors have proposed an active filter (AF) that consists of high-frequency PWM inverter bypass circuit to suppress the harmonic current magnification phenomenon caused by the resonance generated between the tuned harmonic filter (LC filter) and the short-circuit impedance seen from the load bus. We have shown that the AF can suppress the harmonic current magnification phenomenon generated from the harmonic source both on the power supply system side and on the load side, together with test results obtained by using a small capacity model [1]–[5].

At the Yamanashi Maglev Test Line, we have installed the new type of AF with minimum required capacity as the hybrid harmonic current and reactive power compensation equipment in combination with the Static Var Compensator (SVC) and LC filters.

This paper will first describe the principle of operation of the AF of the present system, and show the configuration of the system we have installed at the Yamanashi Maglev Test Line, providing the design concept of the main circuit and control method of the AF. The calculation result is then compared with the result of the effect test on the AF used in the real line to verify the effectiveness of the system.

2. PRINCIPLE OF AF

When the harmonic-generating load with high reactive power consumption is connected to the power supply system, LC filters are generally installed in parallel with the load as a means to improve the power factor and suppress the harmonic current because of its simple configuration and the low cost per compensation capacity. In this case, the parallel resonance generated between the impedance on the power supply system side and the filter/capacitor circuit causes a lower-order harmonic voltage magnification. This may result in the unstable operation of the thyrister converter (harmonic instability phenomenon), a substantial increase in the amount of the harmonic current flow into the power supply system, and an overload of the LC filter. It will be very difficult to solve all these problems with the LC filter design because of changes in the system impedance.

To suppress the harmonic current magnification phenomenon generated by the system impedance and the LC filter, we have developed and proposed the AF using the PWM inverter bypass circuit system [1]–[5].

Fig.1 shows the concept of construction of the harmonic current suppression system.

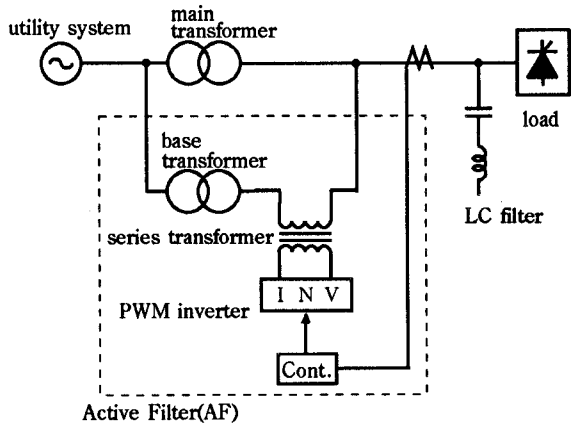

Fig.1 Construction of the harmonic current suppression system

This system consists of a base transformer connected in parallel with the main tranformer, series transformer, PWM inverter, and LC filter.

The LC filter absorbs the large-capacity theoretical harmonic currents generated by the load, while the PWM inverter is controlled so that it operates as a damping resistor to prevent the lower-order non-theoretical harmonic current resonance between the LC filters and the power supply system. The primary side of the base transformer is connected in parallel with the main transformer. The PWM inverter is connected to the secondary side of the series transformer, one side of which is connected to the base tranformer and the other to the secondary side of the main transformer, forming a harmonic bypass circuit to the main transformer. Since the fundamental frequency voltage is offset by the base transformer, the PWM inverter only have to generate the harmonic voltage theoretically, to have a much lower capacity. Consequently, the whole system will be more efficient and available at a lower cost.

Fig.2(a) shows the equivalent circuit of the system, where Ls is the inductance of the power suplly system, L_T is the leakage inductance of the main transformer, and C is the equivalent capacitance of the LC filter. The voltage drop V_T generated in the leakage inductance of the main transformer related to the current I_{Th} is:

$$V_T = sL_T * I_{Th} . \qquad (1)$$

The voltage drop by the harmonic current I_{Sh} flowing out to the power suplly system is determined by the following equation from the equivalent circuit in Fig.2(b), because the AF operates so as to acquire the damping resistor Req:

$$V_T = (Req + sL_T) * I_{Sh} . \qquad (2)$$

Since $I_{Th} = I_{Sh} - I_{AF}$ in Fig.2(a), the AF current I_{AF} is determined by the following equation from (1) and (2):

$$I_{AF} = \frac{Req}{sL_T} I_{Sh} . \qquad (3)$$

Fig.2 shows that the current I_{AF} is controlled to follow the reference signal treated with transfer function G(s) given by (4) to the harmonic current I_{Sh} :

$$G(s) = - \frac{Req}{sL_T} , \qquad (4)$$

so that the characteristics of the power suplly system become equivalent to those of the circuit including the damping resistor Req in series, and the AF can suppress the harmonic current magnification

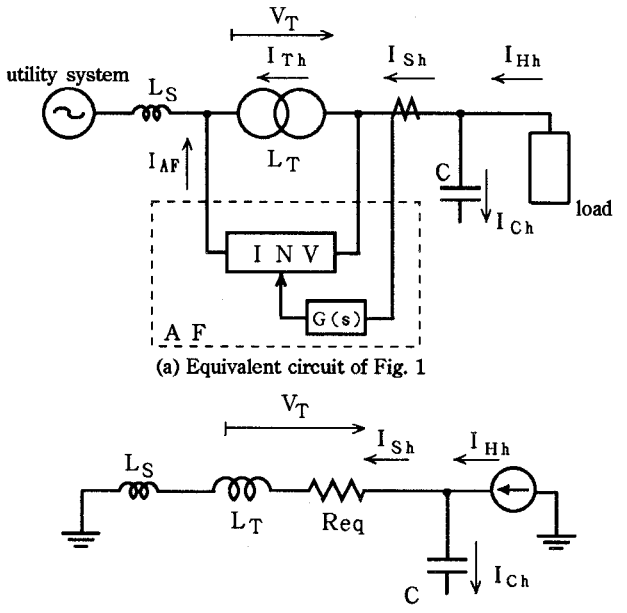

(a) Equivalent circuit of Fig. 1

(b) Equivalent circuit at harmonic compensation

Fig. 2 Equivalent circuit of harmonic current suppression system

phenomenon due to its resonance.

Therefore, the AF with the harmonic inverter bypass circuit system is provided with the function of a harmonic isolator, which separates the harmonic interference between the power supply system side and the load side.

3. Equipment Configuration of The Yamanashi Maglev Test Line

In the magnetic levitation test line that is being developed as the next-generation high-speed mass transport system, the large-capacity variable voltage and variable frequency (VVVF) power supply must be installed on the ground in order to control the speed of the linear motor-driven train. In the Yamanashi Maglev Test Line, the thyristor converter is used on the rectifier side of the VVVF power supply[6].

Fig.3 shows the power supply system at the Yamanashi Maglev Test Line.

Power is supplied by two 154kV lines to the main transformer that will then step down the voltage to 66kV. The 66kV bus is connected to the thyristor converter, which acts as a harmonic current generator and fluctuating reactive power consumer. Because it is necessary to compensate for this reactive power and harmonic current, we have installed hybrid reactive power and harmonic current compensation system together with the SVC, LC filters, and AF.

This system is connected to the 66kV bus. The TCR-type SVC is used to control fluctuations in reactive power at a high speed, and leading reactive power of the LC filters is used to improve the power

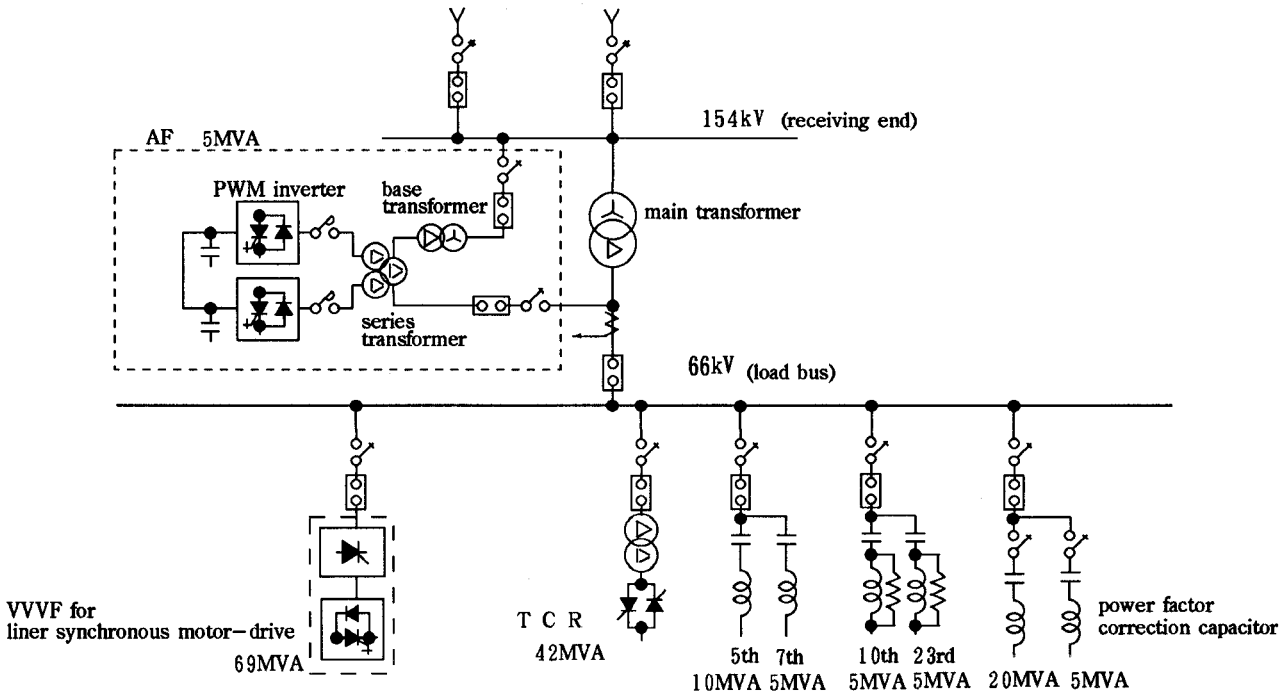

Fig. 3 Power supply system at the Yamanashi Maglev Test Line

factor. LC filters are also used to absorb the theoretical harmonic current, which are generated by the thyristor converter and the TCR. Thus, the theoretical harmonic current is filtered by the 5th- and 7th-order tuned filters, and by the 10th- and 23th-order high-pass filters. The capacity of these filters have be decided so that only LC filters can meet the target value[7] of the outflow current against the amount of theoretical harmonic currents generated by the thyristor converter, and the TCR. Two sets of power facter correction capacitors with series inductor of 6% reactance are installed to adjust the reactive power in accordance with load conditions during the magnetic levitation test.

Therefore, the fundamental rated capacity of the compensation equipment as follows: 42MVA for the TCR part to compensate fluctuations in the reactive power of the thyristor converter, and 50MVA for all the LC filters to supply the reactive power to the thyristor converter.

Judging from the normal short-circuit capacity on the 66kV side of the Yamanashi Maglev Test Line, this system has the largest resonance point at or around the 3rd-order harmonic frequency. However, the resonance point may shift to the 2nd- or 6th-order harmonic frequency for system with different short-circuit capacity.

4. AF Design Concept

In this system, the AF consisting of the harmonic bypass circuit system is provided as the means of magnification suppression of the non-theoretical harmonic current caused by resonance between the system impedance and the filter circuit. Since LC filters are used to treat the theoretical harmonic current generated by the thyristor converter and the TCR, this AF have to only compensate for the harmonic component that is magnified by resonance. That is to say, we could reduce the rated capacity of the AF by eliminating the active compensation of harmonic components except the resonance conditions.

In addition, the AF consists of a base transformer that is connected in parallel with the main transformer as shown in Fig.3 to share the fundamental frequency voltage of the power supply system, the series transformer connected in series between the secondary side of the base transformer and the load bus, and the PWM inverter connected to the secondary side of the series tranformer. Therefore, the inverter hardly need to generate the fundamental frequency voltage at interconnection. It only has to generate the harmonic voltage, which can substantially reduce the capacity of the inverter.

Fig.4 shows the construction of the AF including the block diagram of the inverter control.

The circuit is provided with a rectifier and a DC capacitor to supply DC voltage to the DC side of the inverter. The control part contains a notch filter that removes the fundamental frequency component from the outflow current to the power suplly system and the band pass filter (BPF) to detect the harmonic component to be compensated. The detected signal is

given to the transfer function calculation part indicated in (4), and the output signal is then used as the inverter current command value for output current control.

The calculation using each circuit constant of the power supply system at the present Yamanashi Maglev Test Line indicated that the resonance frequency was in the vicinity of the 3rd-order harmonic frequency. Therefore, we decided the equivalent resistance value Req of the transfer function, so that the ratio of the harmonic current flowing out to the power supply system to the generated amount of the harmonic current would be 1:1 or less at the 3rd-order harmonic frequency. We decided Req = 25 Ω from:

$$\text{Magnification factor} = \frac{3 * 7.33\ \Omega}{\text{Req}} < 1 \qquad (5)$$

because the back reactance seen from the load bus is about 7.33 Ω .

The compensation capacity of the AF is 5MVA. We decided this capacity by taking into account the harmonic current generated by the converter and TCR, and the harmonic current that flows from the power suplly system to the LC filters. Since the inverter only needs to generate the harmonic voltage, it has a capacity of 1.6MVA, and an output voltage and current are 22kV/$\sqrt{3}$, 43A, respectively, on the 66kV side.

Table 1 lists the parameters of the PWM inverter.

Therefore, an economical and effective compensation system of harmonic current and reactive power can be realized by using a small-capacity AF, a large-capacity SVC, and LC filters.

TABLE 1 PARAMETERS OF PWM INVERTER

Item	Parameter
Capacity	1.6 MVA
Configuration	Three single-phase, full-bridge inverters in a parallel connection
Output voltage	635V (phase voltage)
Output current	420A (phase current)
Carrier frequency	800Hz
Switching device	GTO (2500V, 2000A)
DC voltage	1100V

5. FIELD TEST RESULTS

To verify the performance of the AF, we have conducted harmonic resonance suppression test by the AF using the TCR as the harmonic-generating load. In field test all LC filters were switched in.

Figs.5 and 6 indicate the measured waveforms and the frequency spectrum of current I66 (=Ish) flowing out to the power suplly system without and with AF operation, respectively. As described before, the resonance tends to occur at the 3rd-order harmonic frequency between the system impedance and LC filters under present test conditions. The test results show that the AF has suppressed the 3rd-order component that had been dominated in the current I66 before the AF was activated.

Fig.7 shows the waveforms by EMTP simulation conducted before the test. The measured waveforms are in good agreementwith the results of culculation.

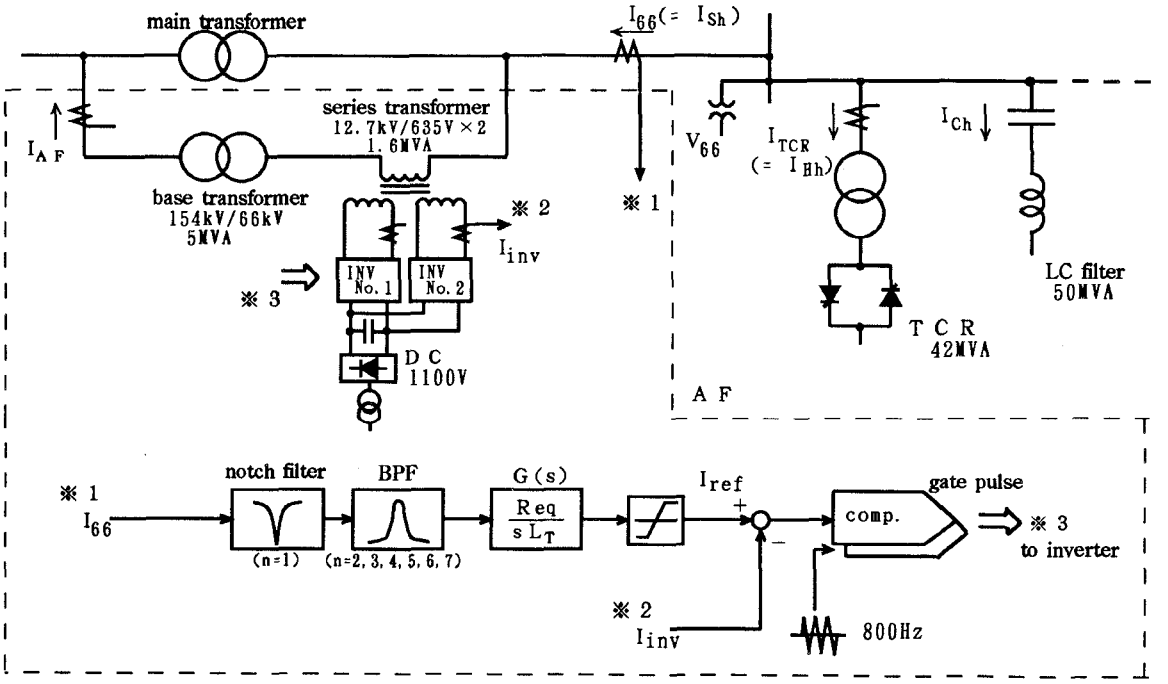

Fig. 4 Construction of the active filter

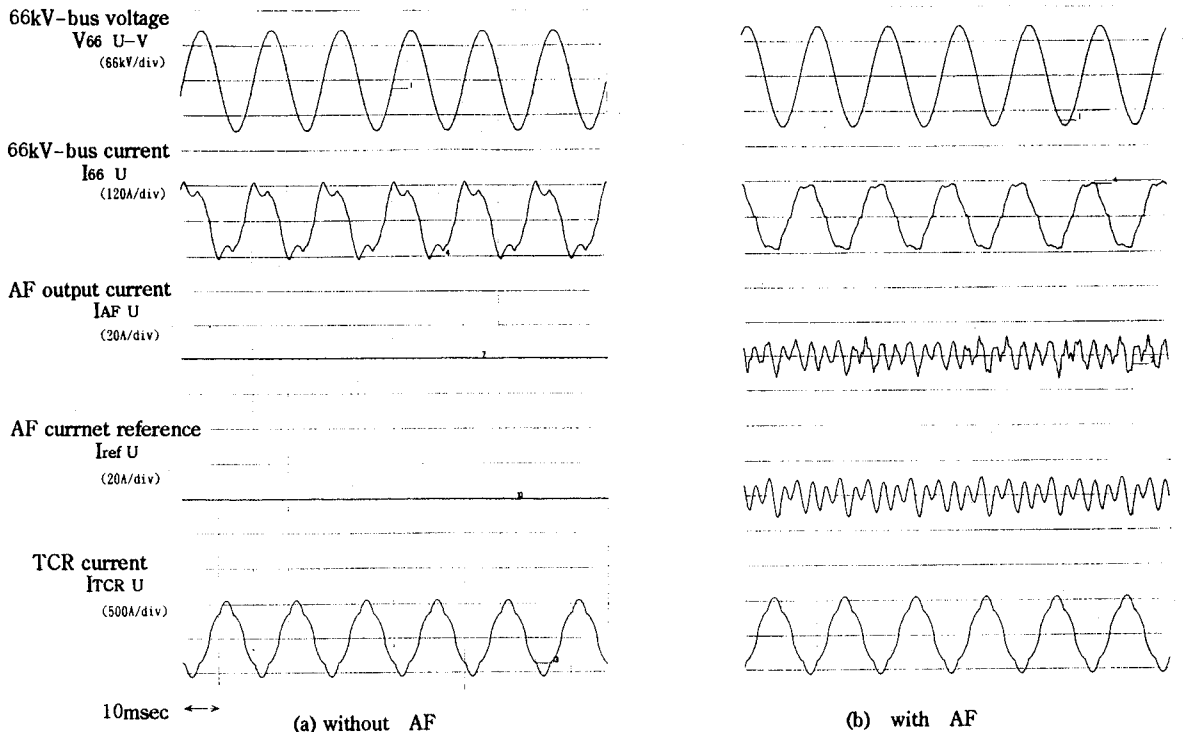

(a) without AF (b) with AF

Fig. 5 Recorded waveforms during the operational test

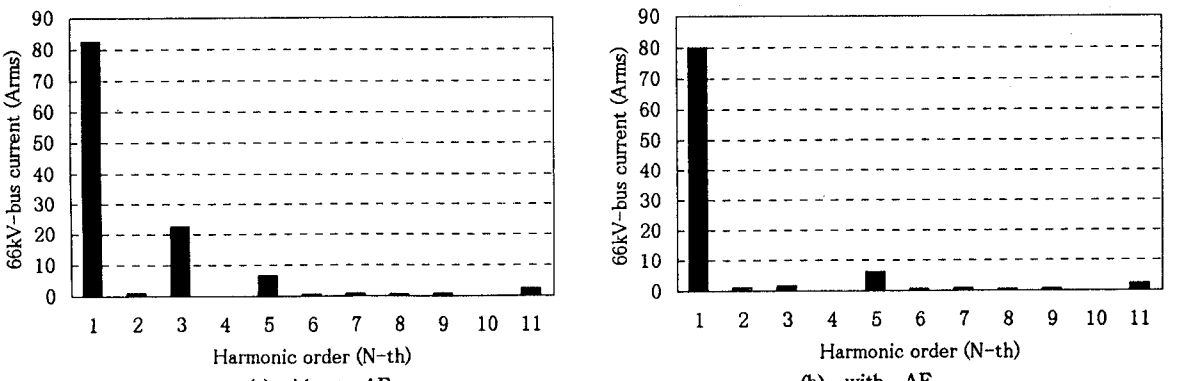

(a) without AF (b) with AF

Fig. 6 Frequency spectrum of 66kV-bus current I66

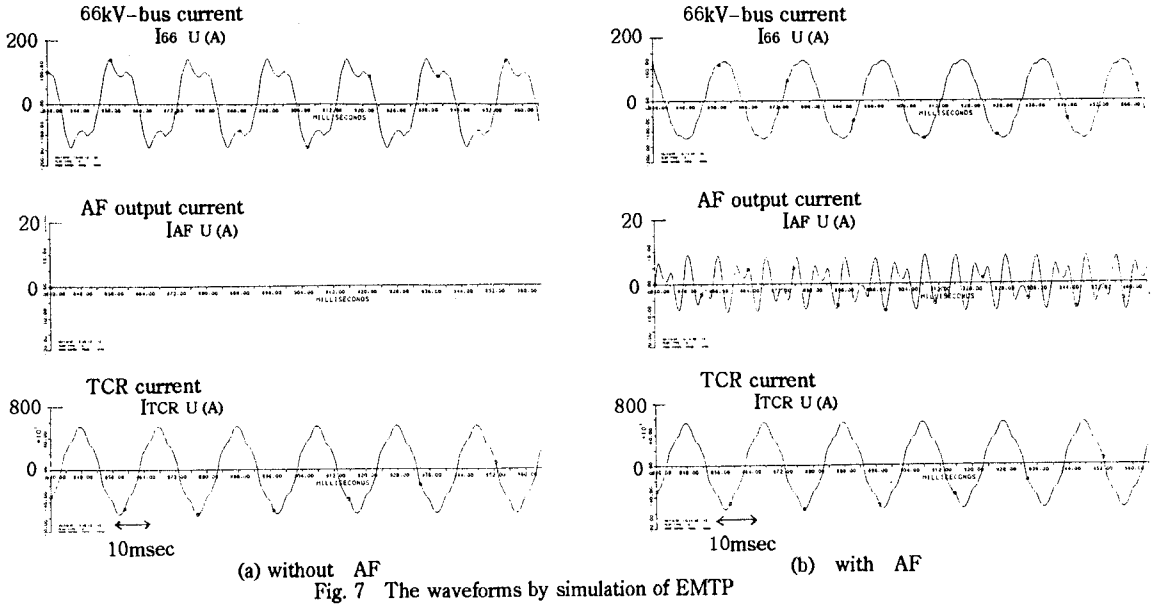

(a) without AF (b) with AF

Fig. 7 The waveforms by simulation of EMTP

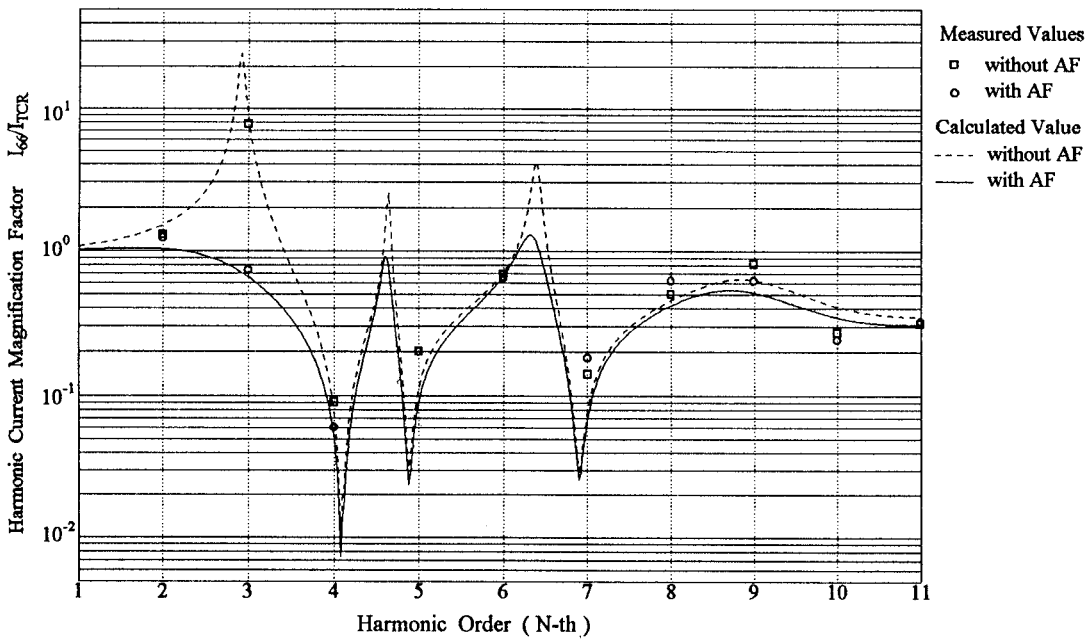

Fig. 8 Frequency characteristics of the harmonic current magnification factor

Fig.8 shows the frequency characteristics of the magnification factor in the ratio of the current I66 flowing out to the power suplly system to the harmonic current ITCR (=IHh) generated by the TCR. The circle (○) and square (□) marks in the figure indicate the measured values. As shown in Fig.8, the ratio that was increased (7.72 times) at the 3rd-order harmonic component before the AF was activated was suppressed to 1:1 or less (0.74 time) when the AF was operated. Results show that the AF has no effect on the theoretical 5th-, 7th-, and 11th-order harmonic currents. The solid and broken lines in the figure indicate the results of calculation conducted before the test. The calculation results are in good agreement with the test results, which also verifies the concept of the AF design.

6. CONCLUSION

We have installed a hybrid compensation system consisting of the SVC, LC filters, and the AF to solve the problems of reactive power fluctuation and harmonic current generation on the Yamanashi Maglev Test Line. We have conducted a harmonic resonance suppression test on the AF by using the TCR as a harmonic generating load, and obtained satisfactory results quite similar to the theoretical values, enabling us to confirm the effectiveness of the hybrid compensation system. This system has the same effect of harmonic resonance suppression effect when the harmonic voltage source is on the power supply system side, just like a harmonic isolater.

We will continue to verify the effects of the AF on harmonic resonance suppression at real-load operation during the magnetic levitation test.

This active filter was manufactured by the financial support from the government.

REFERENCES

[1] Ogihara, Matsukawa, Tada, Ikeda, Shiraishi, and Kawaguchi: "Verification of the Performance of a New Type of Active Filter (Higher Harmonic Isolator)"; I.E.E. Japan National Convention (1990) , p.564 (in Japanese)

[2] I. Kawagudhi, H.Ikeda, S.Kaga, Y.Ogihara, M. Matsukawa, S. Tada: "Suppresion of Harmonics Resonance Using Active Filter in Cycloconverter System", IPEC-Tokyo '90. p.809

[3] Ogihara, Matsukawa, Tada, Ikeda, Kawaguchi, and Shiraishi: "Development of a Reduced Capacity Harmonic Current Suppression System"; The 88th Japan Society for Power Electronics (1990), p.60 (in Japanese)

[4] Ogihara, Matsukawa, Tada, Ikeda, Kawaguchi, and Shiraishi: "Active Filter System Composed of Inverter Bypass Circuit for Suppression of Harmonic Resonance"; I.E.E. Japan D113-3 (1993) (in Japanese)

[5] Ikeda, Kawaguchi, Nakajima, Ogihara, Tada, and Morita: "Suppression of Magnification of Power Harmonic Voltage by an Active Filter using an Inverter Bypass Circuit"; I.E.E. Japan National Convention (1993), p.596 (in Japanese)

[6] Ikeda, Ohtsuki, Kitano, and Yokoyama; "Power Supply System of Yamanashi Linear Test Line"; Japan Society of mechanical Engineers (1994), 1207R (in Japanese)

[7] Japan Electric Association: "Guidelines to The Control of Harmonics by Consumers of High or Special High Voltage Power Supply"

Design of Harmonic Current Detector and Stability Analysis of A Hybrid Parallel Active Filter

Santhiphong Khositkasame, Somboon Sangwongwanich
Dept. of Electrical Eng. Faculty of Engineering Chulalongkorn University
Payatai Bangkok 10330 Thailand
Tel +662-2186533 Fax. +662-2518991

Abstract-- **A promising method to solve harmonic problems in the power system is by using a hybrid parallel active power filter. This filter is composed of both active and passive filters. The active filter will suppress low-order harmonic currents of the system and the remaining high-order harmonic currents in the system will be reduced by a high-pass passive filter. In this hybrid structure one has to consider both the detection method for harmonic current to be compensated by the active filter, and the stability in the presence of the passive filter.**

In this paper, the authors present a new design method for the harmonic current detector which will detect precisely the low-order harmonic currents (5^{th} , 7^{th}) using a band-pass filter built on the rotating frame of the fundamental frequency (50 Hz). In addition, stability analysis of the whole system when the point of detection is located at various positions is investigated. Experimental results shown in the paper indicate the effectiveness and validity of the method proposed.

I. INTRODUCTION

One serious problem of power quality is the harmonic problem which is generated by non-linear loads, such as rectifiers, cycloconverters etc. Two most popular methods to solve the problem are the method using passive filters, and the method using parallel active filters. The disadvantages of the first method are (i) the filtering characteristic depends on source impedance, which is usually not know accurately and varies with the power system configuration, and (ii) a parallel resonance between the passive filter and the source impedance may exist and cause an excessive amplification of harmonic currents. The above disadvantage will not occur when the active filter is applied for harmonic suppression. The active filter will suppress harmonic currents by injecting an appropriate current to cancel out the harmonic currents from the load side. However, solving harmonic problems with an active filter alone to absorb the whole harmonic currents will lead to an expensive system of large capacity [1].Therefore , a hybrid parallel active filter was proposed to reduce the kVA rating of the active parts [2]. In such a case, the active filter will compensate the low-order harmonic currents, while the passive filter will suppress the remained higher-order harmonics.

In applying this hybrid filter, two important issues which need to be considered are :

(1) how to detect and compensate harmonic currents, and

(2) stability of the filter taking into account the existence of the passive filter.

In this paper, the authors present a new design method for the harmonic current detector which will detect precisely the low-order harmonic currents (5^{th} , 7^{th}) using a band-pass filter built on the rotating frame of the fundamental frequency (50 Hz). In addition, stability analysis of the whole system when the point of detection is located at various positions is also studied. Finally, experimental results will be shown to verify the effectiveness and feasibility of the method proposed.

II. SYSTEM CONFIGURATION

Configuration of the hybrid parallel active filter proposed in this paper is shown in Fig.1. It is composed of an active filter connected in parallel with a passive filter which is a high-pass filter. The control of active filter is composed of three main parts 1) the harmonic currents detector, 2) control function for calculation of compensating current, and 3) the current control. In this paper, the hysteresis current control is selected to reduce the computation time of the controller. The harmonic current detector which detects only low-order harmonic currents, and the control function will be described in the sequel.

III. DESIGN OF HARMONIC CURRENT DETECTOR

The block diagram of harmonic current detection is shown in Fig. 2. The main structure of the system is similar to the conventional detecting method. What differs from the conventional detecting method is that we use a band-pass filter instead of a high-pass filter [1],[2]. The

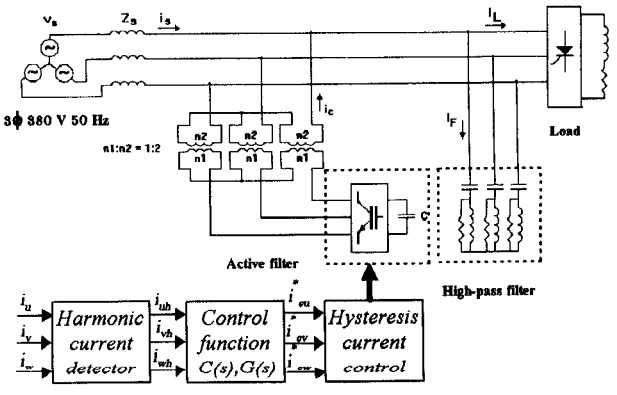

Fig.1 Configuration of of hybrid parallel active filter

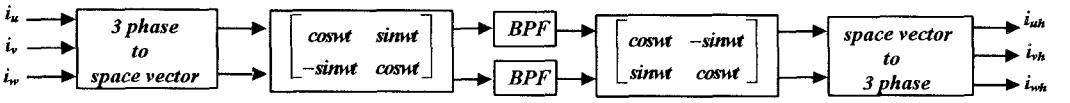

$\omega = 100\pi$ rad/s.
BPF = band-pass filter

Fig. 2 Block diagram of harmonic current detection

high-pass filter in the conventional method will detect all orders of harmonics in the system , and is not applicable for a hybrid parallel active power filter. The reason is that if the active filter injects also the high-order harmonic current, an excessive current may flow into the passive filter due to its low impedance characteristics. On the contrary, the band-pass filter will detect only low-order harmonic currents , and in this paper, the active filter is designed to suppress only 5th and 7th harmonic currents. The transfer function of the band-pass filter is given by eqn.(I)

$$F(s) = \frac{K_F w_h s}{(s + w_h)(s + w_l)} \qquad (1)$$

where

K_F : gain of filter

ω_h : corner frequency at high frequency side (rad/s.)

ω_l : corner frequency at low frequency side (rad/s.)

Normally , the 5th and 7th harmonic currents are of negative and positive sequence , respectively. So , when we transform both harmonic currents to the rotating frame of the fundamental frequency, both harmonic currents will be seen as 6th harmonic currents. Therefore, the band-pass filter built on the rotating frame of the fundamental frequency must be designed for 6th harmonic currents detection following the next guidelines :

(i) selecting ω_h based on high order harmonics ($\geq 11^{th}$) currents sharing between the active and passive filters,

(ii) calculate ω_l from the geometric mean eqn.(2) in order that the phase shift of the filter becomes 0 degree for 6th harmonic currents, and

$$\sqrt{w_l w_h} = 600\pi \qquad (2)$$

(iii) calculate K_F so that the gain of the filter becomes 0 dB for 6th harmonic currents.

As a result, we get the parameters K_F , ω_h , and ω_l in eqn.(1) as 1.25 , 1200π rad/s, and 300π rad/s, respectively. The so-designed harmonic current detector has a good detection characteristic as shown in Fig .3. It is seen that the 5th and 7th harmonic components will be exactly detected, while the fundamental component (50 Hz) is notched out.

IV. CONTROL FUNCTION OF ACTIVE FILTER

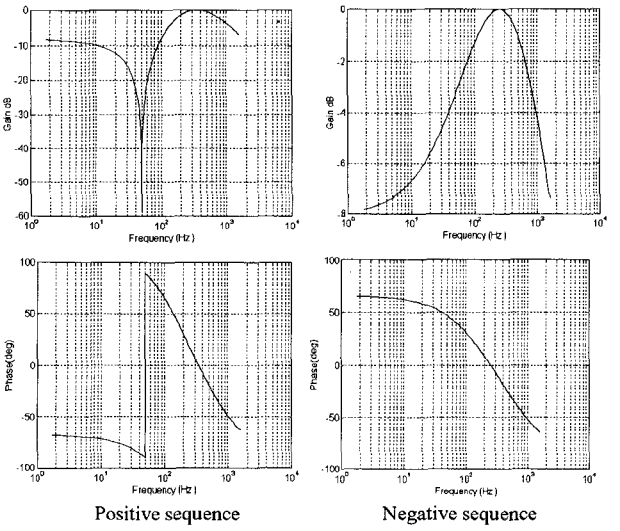

Fig. 3 The detection characteristic of harmonic current detector

The harmonic components which are detected by the harmonic current detector will be multiplied by a control function in order to get the compensating current (i_c). When the active filter detects current from the source side, normally three different types of control function G(s) are used in order that the active filter acts as three different types of virtual impedance such as an inductor, a resistor, and an inductor with resistor in series [2]. In this paper, we use the control function in eqn.(3) to get the active filter behave like an inductor with resistor in series (see Fig. 4). In this case the resonant frequency of the system caused by the source impedance and the passive filter will be shifted to a higher frequency, and the resonant peak will be also damped which is a preferable compensation characteristic. In the same way, the active filter which detects current from load side can also behave like three types of virtual impedance by using three types of control

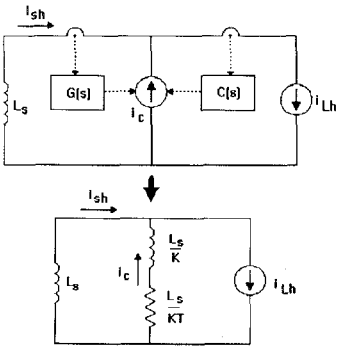

Fig. 4 An equivalent circuit of harmonic frequency of active filter

function C(s) equivalent to G(s) as shown in eqn.(4). So the control function C(s) in eqn.(5) can be used so as to have the active filter behaves like an inductor with resistor in series. In eqn.(5) , when gain K is increased to infinity, control function C(s) will converge to 1 and becomes just a conventional active filter which completely compensates the harmonics.

$$G(s) = \frac{i_c}{i_{sh}} = \frac{KTs}{1+Ts} \tag{3}$$

$$C(s) = \frac{G(s)}{1+G(s)} \tag{4}$$

$$C(s) = \frac{i_c}{i_{Lh}} = \frac{KTs}{1+(K+1)Ts} \tag{5}$$

V. STABILITY ANALYSIS

When we use a hybrid filter, it is necessary to consider stability of the whole system in the existence of the passive filter. Therefore, in this section we will investigate compensation characteristics of the active filter taking into account the following factors which have effects on the stability of the hybrid filter :

(1) detecting point (2) detecting method
(3) control function (4) delay time in control

Hybrid Filter Type A

When we detect harmonic currents at the position (a) in Fig. 5 , the active filter will compensate the harmonics in an open loop fashion as shown in block diagram(Fig.6) because no current from the active filter will flow back to the harmonic source. In this case, conventional concept with C(s) = 1 can be used to achieve good compensation characteristics. Block diagram of this hybrid filter is shown in Fig.6 where in

Z_{hp} : impedance of passive filter
Z_s : source impedance
$F(s-j\omega_r)$: transfer function of harmonic current detector on the stationary frame
e^{-Tds} : transfer function of delay time
ω_r : fundamental frequency = 100π rad/s.

$$Z_{hp} = \frac{L_{hp}C_{hp}R_{hp}s^2 + L_{hp}s + R_{hp}}{L_{hp}C_{hp}s^2 + R_{hp}C_{hp}s} \tag{6}$$

$$Z_S = L_S s \tag{7}$$

$$F(s-jw_r) = \frac{K_F w_h (s-jw_r)}{(s-jw_r+w_h)(s-jw_r+w_l)} \tag{8}$$

This system is simple and always stable , since it is an open loop system and the compensation is good if current control is ideal and has no delay time. However,

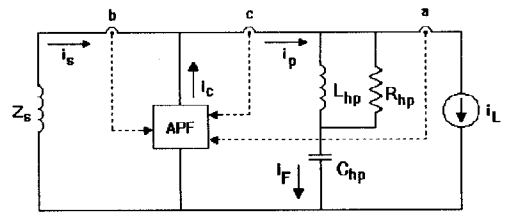

Fig. 5 Equivalent circuit of hybrid parallel active filter

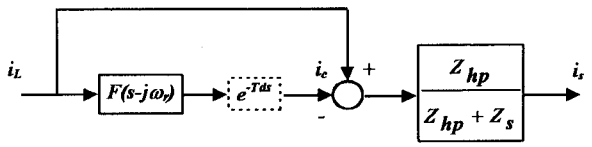

Fig. 6 Block diagram representation of hybrid filter which detects harmonic currents at point (a)

practically as a result of incomplete compensation (caused by the delay time and non-ideal current control) some residual harmonics of low order (5^{th} ,7^{th}) always exist. These residual harmonics cannot be suppressed as there is no feedback loop , and will be amplified by the resonance between the capacitor of passive filter and the source impedance. (see simulation results and experimental results in Fig.12(b) and Fig.13(a) respectively.)

Hybrid Filter Type B

The block diagram of the system which detects harmonic currents at position (b) in Fig.5 is shown in Fig.7. In this case, the active filter will be controlled to behave like a virtual impedance. By using G(s) in eqn.(3) (K=20 , T=0.5 ms) and the parameters in Table I, we can see that the system is stable as shown by the nyquist plot in Fig. 8. But in practical situation when a microcontroller is used for calculation of compensating currents (i_c), the delay time of microcontroller calculation will affect the stability of the system. The system which has a delay time of 62.5 μs will become unstable when the gain K of G(s) is only 18 as shown by nyquist plot in Fig.9. This indicates that the limitation of feedback gain in the system depends mainly on the delay time. The advantages of this hybrid filter are that:

(1) even if current control is not ideal, the compensation characteristic is still good (see simulation results and experimental results in Fig.12(c) and Fig.13(b) respectively.),

(2) this system can damp resonant peak, and shift resonant frequency,

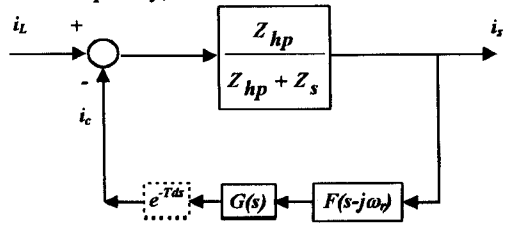

Fig. 7 Block diagram representation of hybrid filter which detects harmonic currents at point (b)

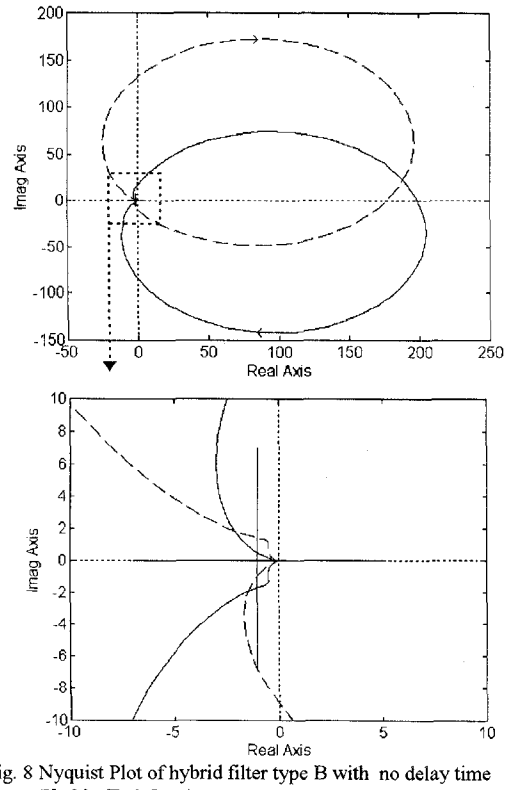

Fig. 8 Nyquist Plot of hybrid filter type B with no delay time (K=20 , T=0.5ms.)

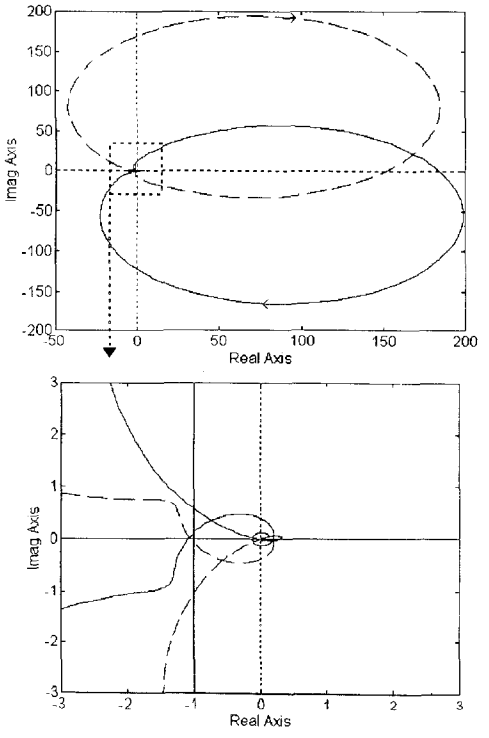

Fig.9 Nyquist Plot of hybrid filter type B with delay time of 62.5μs (K=18 , T=0.5ms.)

(3) the amplification of harmonic currents between the active and passive filters can be avoided, and

(4) delay time in control can be easily handled in the design stage.

Hybrid Filter Type C

The block diagram of the system which detects harmonic currents at position (c) in Fig.5 is shown in Fig.10.

In this case, because of the low impedance characteristic of the passive filter, if the conventional concept (C(s)=1) is used for perfect compensation, it will lead to instability. So the concept of virtual impedance is used instead. By using C(s) in eqn.(5) with the same gains as those of Fig.8 (K=20 , T=0.5 ms) and the parameters in Table I, we can see that the system is unstable as shown by nyquist plot in Fig.11.

It is seen that the hybrid filter type C is not equivalent to the hybrid filter type B, and this hybrid filter type C is unstable eventhough we use the control function C(s) equivalent to G(s) to get the same value of virtual impedance. This is because the transfer function of harmonic current detector ($F(s-j\omega_r)$) is considered in stability analysis but not in the design of control function. Stability can be restored by reduction of gain C(s) but this will deteriorate the compensation characteristics. Another way to get stability is by using C(s) given in eqn.(9), and the two hybrid filters will become equivalent. However, the implementation of the hybrid filter type B which detects currents from the source side is easier.

$$C(s) = \frac{F(s - jw_r)G(s)}{1 + F(s - jw_r)G(s)} \tag{9}$$

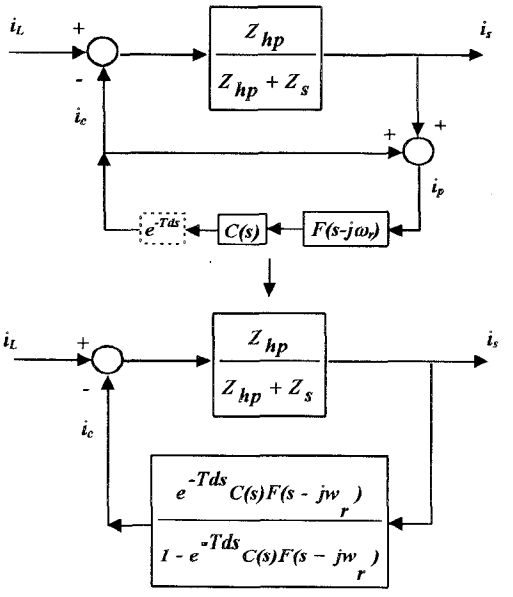

Fig. 10 Block diagram representation of hybrid filter which detects harmonic currents at point (c)

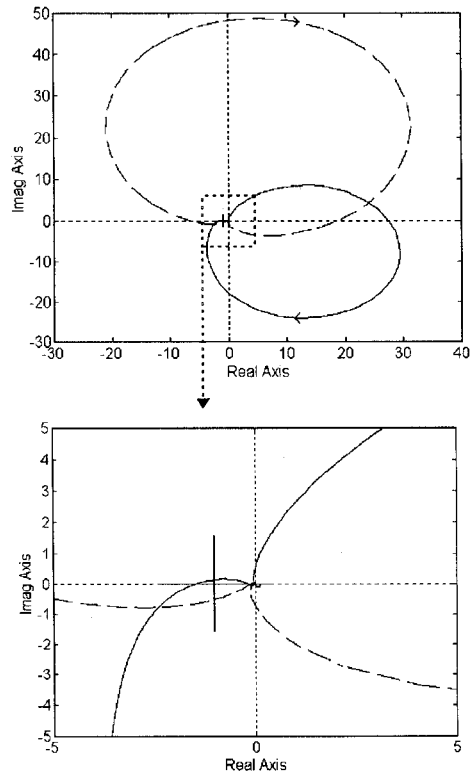

Fig. 11 Nyquist Plot of hybrid filter type C with no delay time (K=20 ,T=0.5 ms.)

VI. SIMULATION RESULTS

The active filter for 3 phase 380 V 50 Hz system will be simulated, with the parameters of passive component shown in Table I. The harmonic source is a 2.5 kVA rectifier with a smoothing dc reactor. The simulation is carried out under 3 different conditions corresponding to:

- *CASE A)* The active filter is of type A which detects the current from load side and current control is ideal.
- *CASE B)* The active filter is of type A but with hysteresis current control (hysteresis band is ±0.5A.)
- *CASE C)* The active filter is of type B which detects the current from source side with K= 15 ,T=0.5ms and hysteresis current control.

Fig.12(a) , (b) and (c) show the simulation results, corresponding to CASE A), B), and C), respectively. The harmonic contents of source current (in percentage) are shown in Table II.

It is seen that when the current control is ideal , the compensation with the hybrid filter type A is good. However, when using hysteresis current control, 5th harmonic still largely remains. The above problem can be solved by using the hybrid filter type B. These simulation results is in good agreement with the description in section V.

VII. EXPERIMENTAL RESULTS

The tested system and parameters for the experiment is similar to the simulated system, and three conditions are tested as well:

- *CASE A)* Hybrid filter type A.

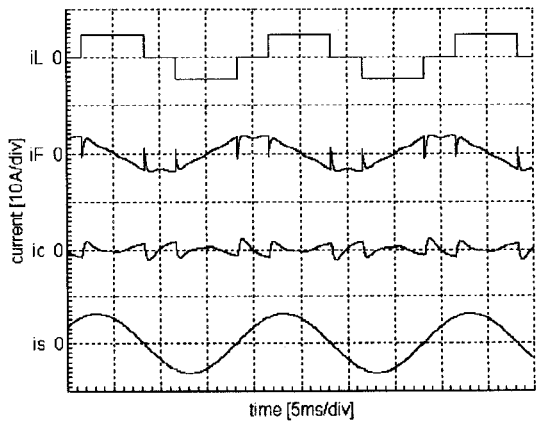

(a) hybrid filter type A with ideal current control

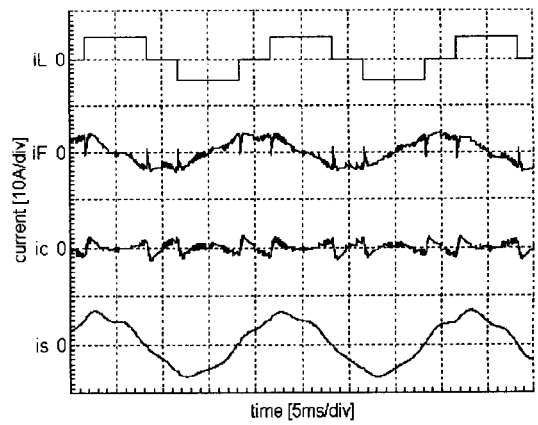

(b) hybrid filter type A with hysteresis current control

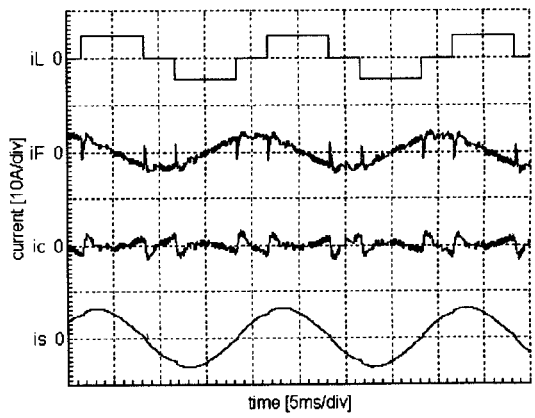

(c) hybrid filter type B (K=15 , T=0.5 ms)

Fig. 12 Simulation results

TABLE I PARAMETERS OF PASSIVE COMPONENTS

type of component	L_s	L_{hp}	C_{hp}	R_{hp}
component value	8.5 mH	1.85 mH	33.85 μF	10.45 Ω

TABLE II HARMONIC CONTENTS OF SOURCE CURRENT IN SIMULATION RESULTS

	5th(%)	7th(%)	11th(%)	THD(%)
no filter	19.94	14.33	8.99	29.95
condition a)	0.00	0.00	0.68	1.16
condition b)	6.59	0.45	0.91	7.18
condition c)	2.04	1.36	1.13	3.00

- *CASE B)* Hybrid filter type B with K=10 , T=0.5 ms.
- *CASE C)* Hybrid filter type B with K=15 , T=0.5 ms.

Fig.13 (a), (b) and (c) show the experimental results, corresponding to three testing conditions, respectively. The percentage of harmonic currents in experimental results are summarized in Table III.

It is seen that with the hybrid filter type A 5^{th} harmonics still largely remains, as is observed in the simulation result. When the hybrid filter type B is used , the above problem can be solved, and 5^{th} harmonics is reduced. When we increase the gain K to 15, harmonic components of source current are reduced, that is the compensation characteristic is better. However, it is seen that the wave form of compensating current i_c oscillates. This oscillation shows that the stability of system may be lost easily, which can be understood from the nyquist plot in Fig.9.

VIII. CONCLUSION

In this paper, a hybrid parallel active filter for harmonics suppression is proposed . The compensation characteristic of the hybrid filter is the best if

(1) a band-pass filter built on synchronous rotating frame of fundamental frequency is used for low-order harmonic currents (5^{th} ,7^{th}) detection, and

(2) active filter detects current from the source side and uses control function G(s) in eqn.(3) in order that the active filter acts as an inductor with resistor in series.

The stability of the proposed system is confirmed by the nyquist plot of open loop system. It is pointed out that the delay time in control effects stability and must be considered in design stage. The experimental and simulation results show in this paper indicate the effectiveness and feasibility of the method proposed.

ACKHOWLEDGMENT

This research was financially supported by the Center of Excellence in Electrical Power Technology (CEEPT) of Thailand.

REFERENCES

[1] H.Akagi and A.Nabae, "Control Strategy of Active Power Filters Using Multiple Voltage-Source PWM Converters", IEEE Tran. Ind. App. Vol. IA-22, No.3 May/June, pp. 460-465, 1986.

[2] M.Takeda, K.Ikeda, and Y.Tominaga, "Harmonic Current Compensation with Active Filter", IEEE/PESC, pp.808-815, 1987.

[3] H.Akagi, Y.Kanazawa, and A.Nabae, "Generalized Theory of the Instantaneous Reactive Power in Three-Phase Circuits", Proc.of IPEC-Tokyo, pp.1375-1386, 1983.

[4] F.Z.Peng, H.Akagi, A.Nabae, "A Study of Active Filters Using Quad-Series Voltage-Source PWM Converters for Harmonic Compensation", IEEE/PESC, pp.204-211, 1987.

[5] K.Ito, M.Aoki, and Y.Tsunehiro, "Improving the Behavior of Active Filter for Power Distribution System", T.IEE Japan, Vol.116-D, No. 10, pp.1079-1080, 1996.

[6] A.Salem nia and S.Saadate, "Digital Control Active Filter Suppressing Particular Harmonics : Numerical Simulation and Experimentation", Proc. of ICHQP-Las Vegas, pp.632-636, 1996.

[7] N.Nanaumi, S.Kuramoti, and M.Yano, "Comparision of Versatile Harmonics Current Compensation and Specific Harmonics Number Current Compensation", Conf. Rec. of Japan IAS, pp.407-410, 1996.

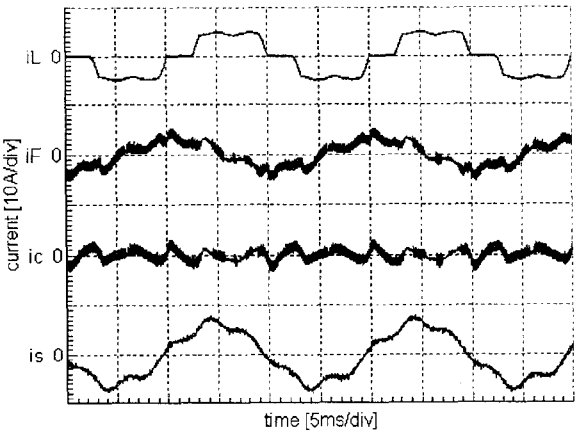

(a) hybrid filter type A

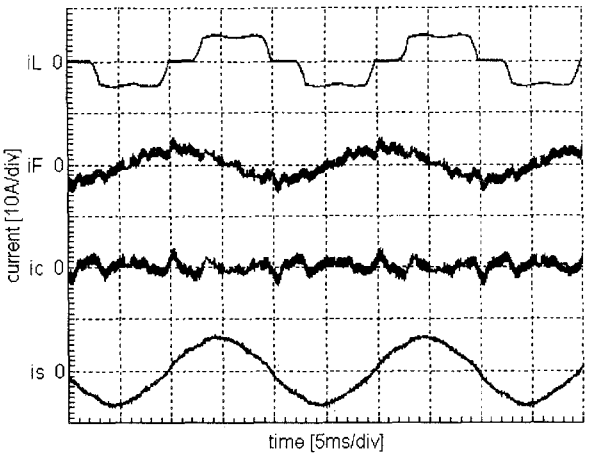

(b) hybrid filter type B with K=10 , T= 0.5 ms

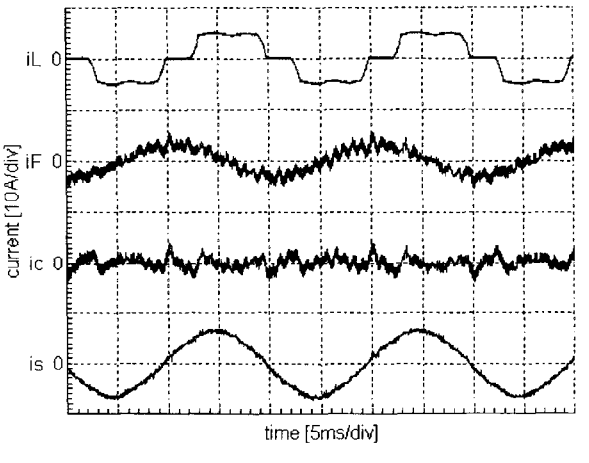

(c) hybrid filter type B with K=15 , T= 0.5 ms

Fig.13 Experimental results

TABLE III HARMONIC CONTENTS OF SOURCE CURRENT IN EXPERIMENTAL RESULTS

	5^{th}(%)	7^{th}(%)	11^{th}(%)	THD(%)
no filter	19.67	8.92	4.17	22.30
testing condition a)	14.99	2.12	0.78	15.46
testing condition b)	3.40	1.88	0.69	4.32
testing condition c)	2.18	1.38	0.62	3.25

Development of Dispersion Type Active Filter

Katsuhiro Shinzen †, Masakatsu Nomura, Masayuki Terashima (Meidensha Co.)
Fumimasa Anan, Kiyomi Yamasaki (Kyushyu Electric Power Co.)

† Product Development Laboratory, Meidensha Corporation.
1-17, Ohsaki 2-chome Shinagawa-ku, Tokyo 141, Japan
Fax: +81-3-5487-1598, Phone: +81-3-5487-1585
E-mail: shinzen@ohsaki.meidensha.co.jp

Abstract **The increase in various types of harmonics has led to the establishment of harmonic suppression guidelines. In response, the active filter has been developed. This paper proposes a dispersion type active filter, which reduces harmonics in the input voltage that appear in the load voltage. The load voltage can be independent from input voltage by using two active filters in series. We also report the experimental results obtained for the dispersion type active filter.**

I. INTRODUCTION

The existence of harmonics in power lines has recently become a problem, leading to the publication of guidelines on harmonics.[1] There is a demand for technical measures to solve such problems. With regard to consumer electric equipment, the active filter has been used to compensate for harmonics and reduce their effect on power lines. The use of the active filters makes it possible to compensate for the harmonics of a particular load current [2], but the following situations may possibly to occur.

- When voltage harmonics exist in the upper power line, such harmonics appear at the connection points of active filters, and there are cases where the current harmonics of the lower power line increase.
- Similarly, if the load works as a filter, there are cases where compensation for the harmonics causes an increase in the total harmonics of the over all power line.
- An active filter may become oscillative and increase harmonics because of the impedance of the power line.

In this paper, we explain the above cases and propose a dispersion type active filter enabling both the current and voltage harmonics to be simultaneously compensated for.

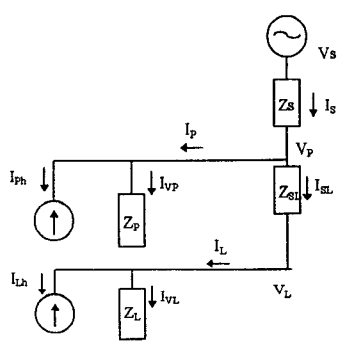

Fig. 1. Model of power line

II. CONVENTIONAL ACTIVE FILTER SYSTEM

Fig. 1 shows a power line model, and Fig. 2 shows the conventional method of installing an active filter in this power line. The equations applicable to Fig. 2 are given in Eq. (1).

In this case, the lower power line's current harmonics I_L is compensated by AF1, and the inflow of the current to the upper power line I_{SL} becomes 0. The equation for the lower power line in relation to voltage and current is given by Eq. (2).

At this time, the upper power lines voltage harmonics V_P becomes equal to the lower power lines voltage harmonics V_L, and the effect of Vp appears in the lower power line.

Fig. 3 shows the equivalent circuit of the conventional active filter system. As indicated in this figure, the upper power lines voltage harmonics V_P appears at the connection point between the upper and lower power lines.

$$
\begin{aligned}
V_S &= Z_S \cdot I_S + V_P \\
V_P &= Z_{SL} \cdot I_{SL} + V_C \\
V_P &= Z_P \cdot I_P \\
V_C &= V_L + V_{AF} \\
I_S &= I_P + I_{SL} \\
I_{SL} &= I_L + I_{AF} \\
I_L &= I_L + I_{HL} \\
V_L &= Z_L \cdot I_L
\end{aligned}
\qquad (1)
$$

$$I_L = V_P/Z_L + I_{LH} \qquad (2)$$

III. DISPERSION TYPE ACTIVE FILTER SYSTEM

Fig. 4 shows the dispersion type active filter system. An impedance Z_C is installed in series with the source and variable current sources AF1 and AF2, as shown in Fig. 4. Variable current source AF1 works in the same manner as a conventional active filter and compensates for the current harmonics. The equations for the equivalent circuit shown in Fig.5 are as follows:

$$
\begin{aligned}
V_S &= Z_S \cdot I_S + V_P \\
V_P &= Z_{SL} \cdot I_{SL} + V_C \\
V_P &= Z_P \cdot I_P \\
V_C &= V_L + V_{AF} \\
I_S &= I_P + I_{SL} \\
I_{SL} &= I_L + I_{AF} \\
I_L &= I_L + I_{HL} \\
V_L &= Z_L \cdot I_L
\end{aligned}
\qquad (3)
$$

The variable current source AF1 and AF2 outputs following current:

$$I_{AP}=I_C \qquad (4)$$

$$I_{AL} = I_{Lh} - \frac{V_{Ch}}{sZ_C} \qquad (5)$$

where I_{AL} output of AF2
I_{Lh} harmonics of load current
V_{Ch} harmonics of load voltage
Z_C impedance

When AF1 and AF2 output the current in (4) and (5), the upper power line's voltage harmonics flow into the lower power line can be formulated as follows:

$$V_{Lh}=V_{Ch}-Z_C(I_{Lh}-I_{AL})=0 \qquad (6)$$

where V_{Lh} harmonics of load side.

Equation (6) shows the case where the upper voltage harmonics flow into the lower power line is 0. Fig. 5 shows the equivalent circuit of the dispersion type active filter system shown in Fig. 4 at this time. This indicates that it is possible to insulate the upper power line and lower power line in terms of voltage and current harmonics by means of dispersion type active filters, and the compensate for the load current harmonics and voltage distortion in the upper power line by a current Ic of the appropriate phase and magnitude. The impedance Zc is installed between the active filters.

IV. COMPARISON OF BOTH SYSTEMS BY SIMULATION

We carried out simulation of harmonics and confirmation of the compensation effect on voltage and current with the system shown in Fig. 6. This system had a 20 MVA power source and the system reactance was set at 0.2 pu . The reactance between AF1 and AF2 was 0.05 pu. The standard load was equivalent to 4 MVA, the power factor was 0.8. The harmonics generating load was a 6-pulse rectifier. Fig. 7 shows the voltage and current compensation effect on the conventional active filters, and Fig. 8 shows that of the dispersion type active filters. Figs. 7 and 8 show that the compensation effect on current harmonics is almost same for two systems.

On the other hand, Fig. 7 shows that the voltage harmonics compensation effect achieved by the

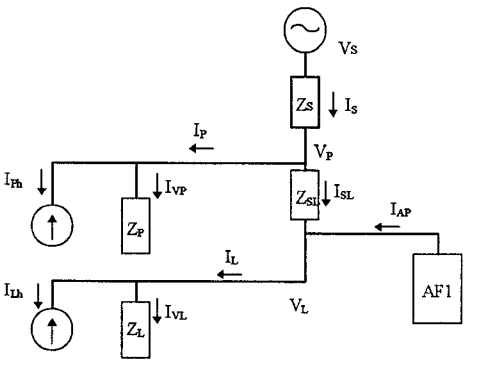

Fig. 2. Conventionally active filter system

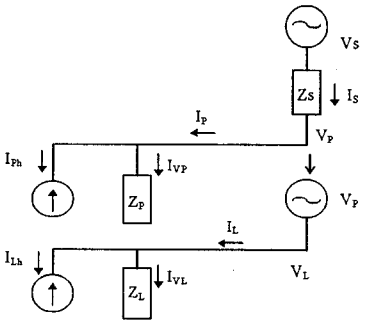

Fig. 3. Equivalence circuit of conventional active filter system shown in Fig 2

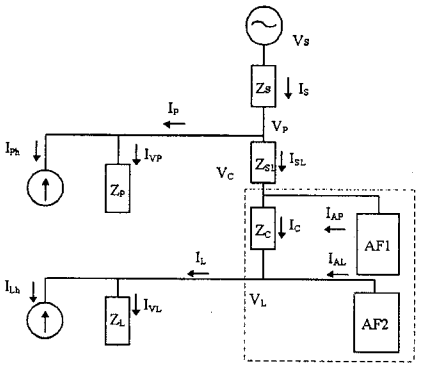

Fig. 4. Dispersion type active filter system

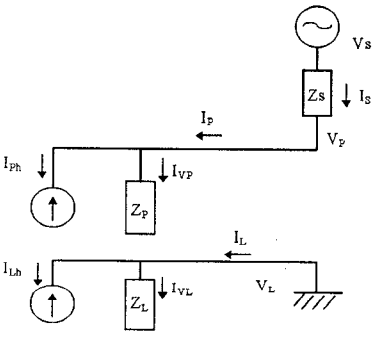

Fig. 5. Equivalent circuit of dispersion type active filter system shown in Fig.4

conventional active filter insufficient, while the dispersion type active filter shown in Fig. 8 compensates for the voltage harmonics, and voltage distortion at the source side does not appear on the load side for the most part.

V. Experimental Results

Fig 9 shows the experimental circuit. A 3-phase, 200 V source was employed, and the capacity of the converter used in the active filters was 10 kVA. At the alternating side, power supply was used that could accumulate optional voltage harmonics. A digital signal processor (TM320C40) was used at AF2 to calculate electric current command value of above-mentioned (5). The load consisted of three-phase rectifiers, and a 5 mH reactor was installed between the two active filters.

Fig. 10 shows the control block of the AF2. The source side voltage distortion detected by PT was passed through an integrator. The voltage signal phase was changed by the integrator, the signal was added to the current signal. The harmonic elements were then detected at the filter, and the signals input as the active filter's current order.

Figs. 11 and 12 show the voltage wave forms. The upper side wave form in each figure is that of the source side voltage, and the lower wave form is that of the load side voltage. As shown in these two figures voltage distortion at the source side was reduced when using the dispersion type active filter. With the conventional active filter, on the other hand, the source side voltage distortion appeared on the load side. Voltage distortion on the source side was reduced by about 80% using the distortion type active filter.

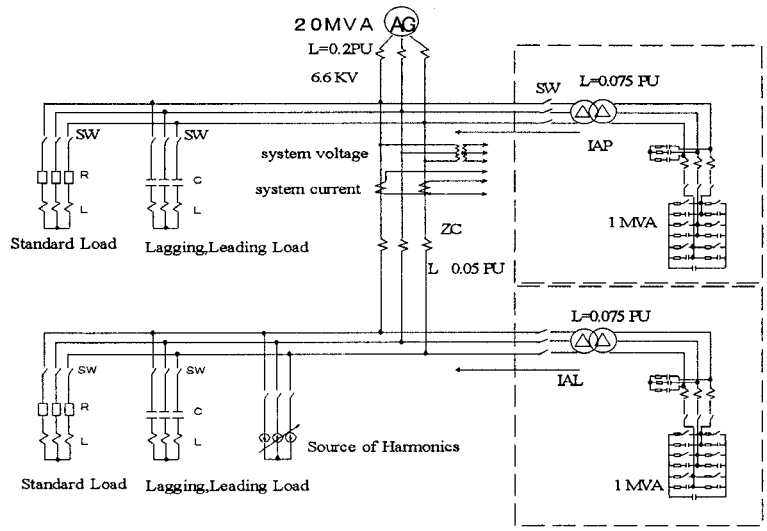

Fig. 6. Simulation system

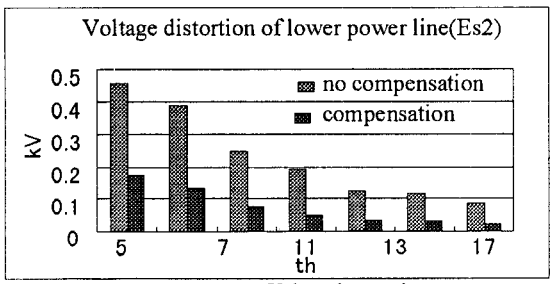

(a) Voltage harmonics

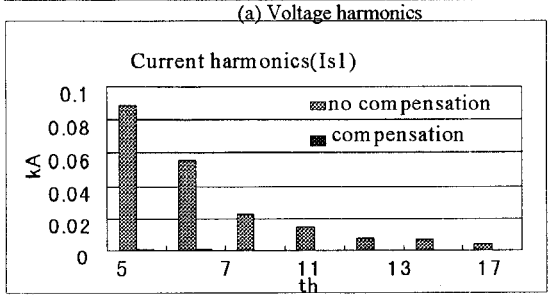

(b) Current harmonics

Fig. 7. Compensation effect of conventional active filter

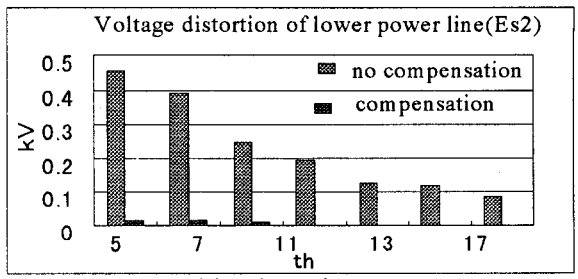

(a) Voltage harmonics

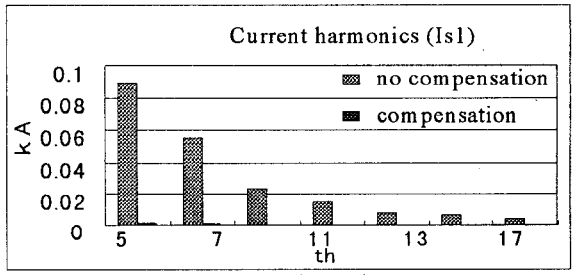

(b) Current harmonics

Fig. 8. Compensation effect of dispersion type active filter

Table 1 shows the compensation ratio when no voltage distortion existed. The compensation ratio is defined as follows:

(Compensated harmonics voltage)

/(Uncompensated harmonics voltage)

Table 2 shows the compensation ratio when the 5th voltage distortion harmonics (30 % of the primary voltage) was added to the source, and Table3 shows the compensation ratio when the 7th voltage distortion harmonics was added to source .

VI. Conclusion

A dispersion type active filter is proposed, which uses two active filters and compensates for not only current harmonics but also voltage harmonics. Verification was carried out by simulation and experiments. As a result, we have demonstrated that the effect of voltage harmonics on the lower power line can be reduced by dispersion type active filter. This dispersion type active filter is able to use either the power line's reactance or the transformer's reactance.

Table 1 No voltage distortion

	No compensation	Compensation	Compensation ratio
Bases	214	214	-
5th	7.8	3.2	59
7th	2.8	2.2	20
11th	3.4	3.2	3

Table 2 5th voltage distortion in source voltage

	No compensation	Compensation	Compensation ratio
Bases	214	214	-
5th	30	3	92
7th	3	6	-86
11th	3	4	-7

Table 3 7th voltage distortion in source voltage

	No compensation	Compensation	Compensation ratio
Bases	214	213	-
5th	7	6	9
7th	23	2	91
11th	6	2	58

References

[1] IEEJ Technical Report: "The technology of active filter for electric power systems ", IEEJ, No.-425, 1993.

[2] Semiconductor Electric Power Transformation System Survey Specialty Committee: " Semiconductor electric power transformation circuit," IEEJ

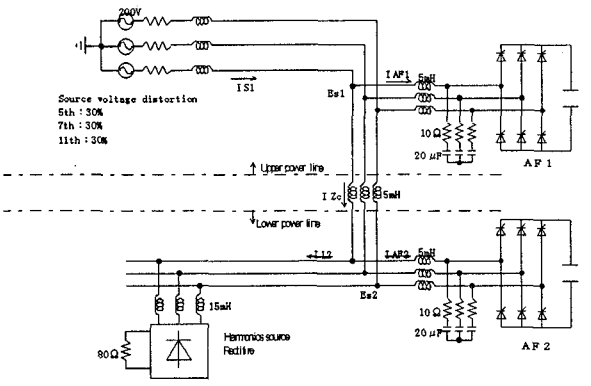

Fig. 9 Experimental circuit

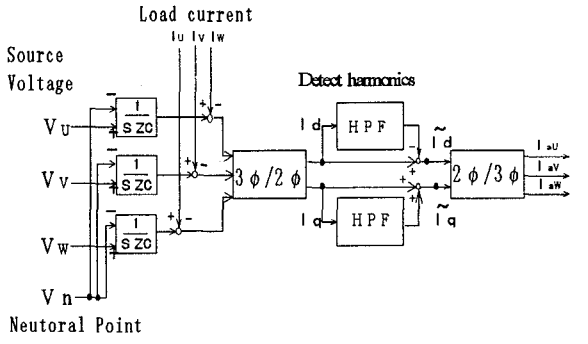

Fig. 10. Control block of AF2

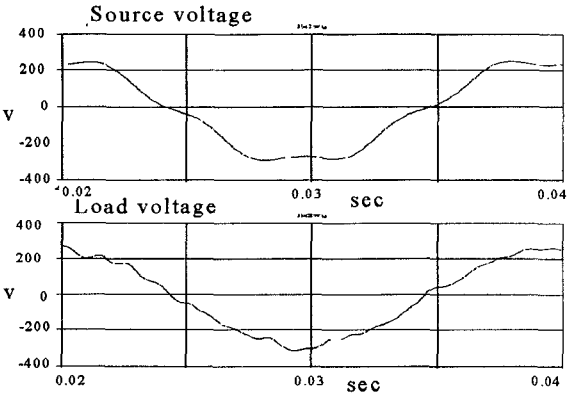

Fig. 11. Voltage wave form of dispersion type

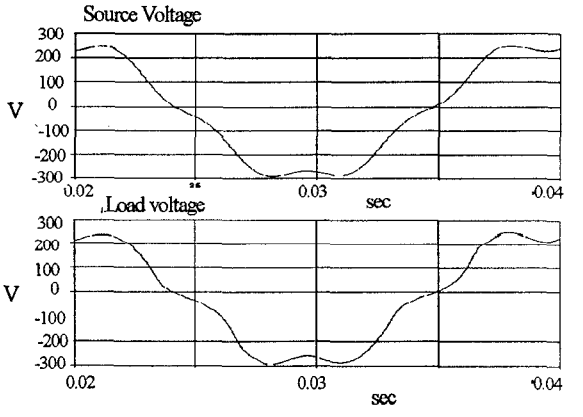

Fig. 12. Voltage wave form of conventional

AN ADAPTIVE NOISE CANCELING THEORY BASED SINGLE-PHASE SHUNT ACTIVE POWER FILTER

Chen Weiji, Chen Wenhong
Faculty of Science and Technology
University of Macau
P.O. Box 3001, Macau
Fax: 853-831694 Phone: 853-3974469

Ma Xiaojun, Chen Jianye , Wang Zhonghong, Han Yingduo
Dept. of Electrical Engineering
Tsinghua University
Beijing 100084, P.R. China
Fax: 8610-62781532 Phone: 8610-62781527

Abstract - The most critical issues associated with Active Power Filter (APF) control is that of finding an algorithm which can obtain an accurate harmonic reference signal for control purpose, particularly in the practical case where the harmonics and the system frequency of a power system are time varying. In this paper an adaptive filtering technology called "Adaptive Noise Canceling (ANC)" based APF is developed, it uses a primary input containing the corrupted signal and a reference input correlated with the fundamental component of the system voltage. The reference input is adaptively filtered and subtracted from the primary input to get the wanted control reference signal. Its validity is assessed by the simulation and experimental results.

Key Word Active power filter, Adaptive noise canceling(ANC)

1 Introduction

With the rapid development of power electronic technology , the various electronic equipment are used widely in industrial application and transmission/ distribution system such as AC/DC static power inverter , adjustable motor drives and switching supply . However , the proliferation of these nonlinear load results in a variety of undesirable phenomena in the operation of power system . The most important among these are harmonic contamination , increased reactive power demand and power system voltage fluctuation . Harmonic contamination has become a major concern for power system specialists due to its effects on sensitive load on the power distribution system . Conventionally , passive LC filter have been used to eliminate line current harmonics and to increase the load power . However , in practical application these passive second order filter based on resonance principle exists many disadvantages. In order to overcome these problems , active power filter(APF) have been researched and developed . In recent years , various active power filter configurations with their respective control strategies have been proposed , and have gradually been recognized as a viable solution to the problems created by nonlinear loads . However, the time-varying characteristic makes the effective harmonics elimination a difficult tasks.

An adaptive noise canceling theory based control strategy for APF power filter is proposed in this paper. The simulation results as well as the test results of a prototype equipment implemented with analogous device demonstrate its effectiveness despite its very simple structure.

2. Principles and Configuration

The topology of the single-phase active power filter presented in this paper is shown in Fig.1 . The APF is connected in parallel with the load . By using a fixed switching frequency , the high-frequency ripple current generated by the proposed APF can be easily removed from the power system .The single-phase APF , based on a force-commutated pulse-width voltage-source inverter with capacitor for energy storage is designed to continuously compensate for the reactive power and harmonics in the load current . An analogue adaptive detecting circuit , based on adaptive interference canceling theory, is used to extract the reactive power and harmonics components of the load current as the control signal of the APF and then a current equal in magnitude but opposite in phase of the detected current is injected into the system by the APF. By using a fixed switching frequency , the high-frequency ripple current generated by the proposed APF can be easily removed from the power system .

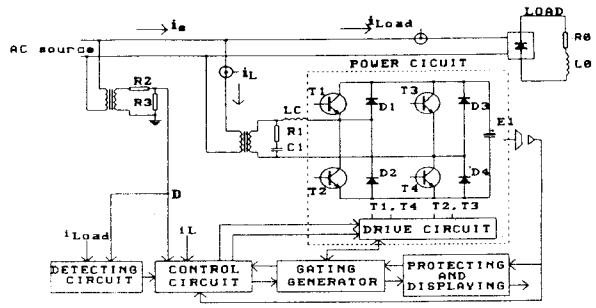

Fig 1 The block scheme of the single-phase APF

The block diagram of the APF control system can be found in Fig.1. In control system , it consists of a current control unit , the dc voltage control unit , the adaptive detecting circuit unit and the gating signals generator . The ac current generated by the inverter is forced to follow the reference current signal obtained from the adaptive detecting circuit . The adaptive detecting circuit is used to retrieve the reactive and harmonic components from load current as reference signal for the active filter control . A constant switching frequency is achieved by comparing the current error signal with a triangular reference waveform and makes the design of high-frequency filter and inductor L easier .The constant voltage across the dc capacitor is maintained to prevented the power inverter from entering the

uncontrollable rectifying range and deteriorating the quality of compensation . By keeping the dc voltage constant , the inverter voltage gain is increased and the amplitude of the high-frequency inverter ripple current component is reduced .In this paper , the voltage-source inverter is adopted due to its simple structure , small size and high efficiency .

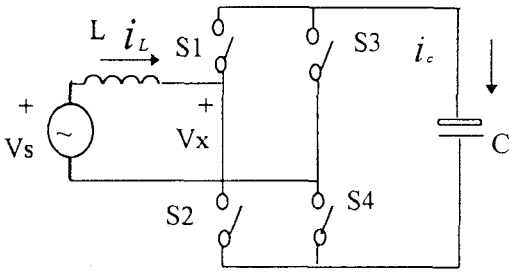

Fig.2 The block diagram of power inverter

In Fig 2 , S1~S4 are four ideal switch . By controlling on-time and off-time of these switch, arbitrary current waveform i_L can be achieved . If the current injected by APF is the same as that of the reactive power and harmonic components of a nonlinear load, the current provided by ac power source will only have fundamental real component as shown in Fig.1 ,

$$i_S = i_{Load} - i_L \qquad (1)$$

where i_s the source line current; i_L the compensating current; i_{Load} the load current The mathematical model of the voltage-source inverter is shown in Fig.2.

$$\dot{i}_L = \frac{1}{L}(V_S - SV_C) \qquad (2)$$

$$\dot{V}_C = \frac{1}{C}i_C = \frac{1}{L}Si_L \qquad (3)$$

$$\begin{cases} S = 1 & \text{S1,S4 turn - on, S2,S3 turn - off} \\ S = -1 & \text{S2,S3 turn - on, S1,S4 turn - off} \end{cases}$$

From above Eq. (2) and (3) , the voltage across the dc capacitor should be greater than the peak value of ac source voltage in order to guarantee the current flow in positive and negative direction , i.e. the current can go up and down in one period time . The ability to track the reference current is affected by the difference (Vs - Vc) and L . Reducing L and increasing (Vs - Vc) will improve this ability and the quality of compensation for reactive and harmonic currents .

The most critical problem of a successful active filtering is to find an algorithm which can obtain an accurate harmonic reference signal for control purpose. In this paper , a detecting method based on adaptive noise canceling theory ,which is used widely in the signal processing in recent years , is adopted to measure the reactive power and harmonic components of nonlinear load current and is implemented with the analogue device . The block diagram of the adopted scheme is shown in Fig 4 . Where i_{load} the load current; i_o the output signal of the adaptive detecting circuit ; D ac source voltage; D' the fundamental reference voltage which is in phase with ac source voltage $D' = E_m \sin\omega t$。 As seen in Fig 3,

$$i_o = i_{load} - (K \cdot D' \cdot \int_0 i_o \cdot D'dt) \qquad (4)$$

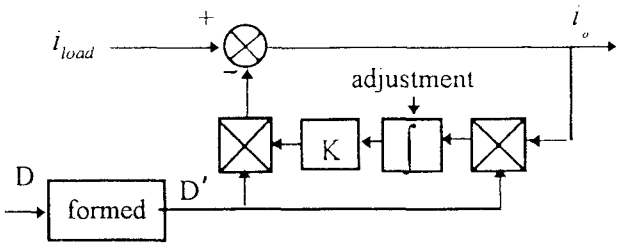

Fig.3 The block diagram of the ANC circuit

From the theory of ANC and Eq.(4), as the input sinusoid reference signal, i.e. the fundamental component of the system voltage, has the same frequency and in phase with the desired fundamental component of load current, the dc component of the output of integrator will tune accordingly until they are equal in magnitude. The corresponding fundamental real component of the current is then extracted from the sampled load current . Under the action of ANC loop, in steady state the output current i_o of detecting circuit does no longer include the fundamental real component , the dc component of the integrator output will keep a constant value, which is in proportional to the magnitude of the fundamental real component of load.

$$i_o = i_{load} - KE_m \sin\omega t(K_0 + \frac{1}{\omega RC}\int_{t_0} i_o E_m \sin\omega t d\omega t)$$
$$= i_{load} - KK_0 E_m \sin\omega t - KK_1 E_m \sin\omega t \qquad (5)$$

where, $K_1 = \frac{1}{\omega RC} \cdot \int_{t_0} i_o \cdot E_m \sin\omega t d\omega t$

and E_m is the peak value of the fundamental reference voltage; K the proportional coefficient; K_0 the dc component of the integrator output.

Due to the large time constant of the integrator and the orthogonality , all the components in K_1 except the fundamental real component which is in phase with the reference input, i.e. the system voltage, will be approximate to zero , and because in steady state the fundamental real component in i_o is also approximated to zero, K_1 will be also approximate to zero. Then the last term in Eq.(5) can be omitted. Assume that the load current can be expressed as

$$i_{load} = i_p + i_q + i_h$$

where i_p is fundamental active component; i_q fundamental reactive component; i_h harmonic components. Then

$$i_o = i_{load} - KK_0 \cdot E_m \sin\omega t$$
$$= i_p + i_q + i_h - KK_0 E_m \sin\omega t$$
$$i_o = i_q + i_h \; ; \qquad (6)$$

$$i_p = K K_0 E_m \sin\omega t \qquad (7)$$

From Eq. (6)and (7) , the output signal of the adaptive detecting circuit is just the reactive power and harmonic components of the nonlinear load currents. The adaption speed and accuracy of the adaptive detecting circuit which determine tracing ability of APF is related to the time constant RC and the proportional coefficient *K*. The simulation analytical results is given in Table I,II. The T_r and THD are used to represent respectively the response time and tracing accuracy of APF in steady-state. The dynamic compensating process of the APF is shown in Fig. (4) . The adaptive detecting circuit of the APF starts operation at t_0.

From Table I,II, it is known that as the time constant RC increases, the compensating accuracy will be improved, but the response time becomes longer with constant proportional coefficient *K*. If the time constant RC is kept constant , as the coefficient *K* increase, the response time gets shorter , and the detecting accuracy varies non-linearly with K value. A trade-off must be considered in the selection of K and RC. In our case, the optimum *K* value is in the range 100 to 200 as the time constant RC is approximately 20ms corresponding to the shorter response time.

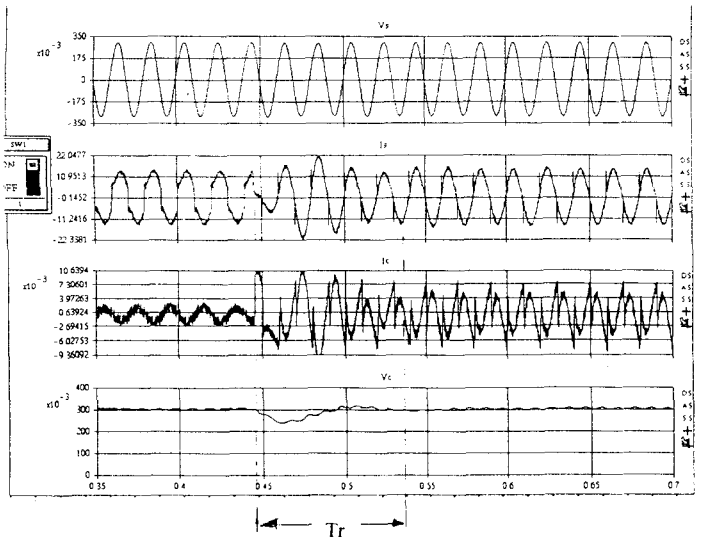

Fig.4 Simulation waveform

where, Vs: ac source voltage; Is: ac source current; Ic: the compensating current; and Vc: the dc voltage across the capacitor.

Table I

	6.7ms	10ms	20ms	50ms
Tr	0.048s	0.13s	0.24s	0.48s
THD	0.1176	0.082	0.065	0.051
K	100			

Table II

	RC=20ms				
K	10	50	100	200	400
Tr	2.2s	0.48s	0.24s	0.12s	0.06s
THD	0.086	0.083	0.065	0.082	0.092

Because the power system voltage is adopted as the reference signal of the ANC detecting circuit, the characteristic of maintaining the null exactly at the reference frequency, during the total adaptive process makes the output signal of ANC circuit automatically tracing the system frequency as well as its voltage phase. Such a ANC circuit based APF not only has high measuring accuracy and wide adaptability to the variation of system frequency and voltage as well as load harmonics, but also is simple in structure and can be easily implemented with hardware. Experimental and simulation results demonstrate that the implemented controller acts effectively over the whole operating conditions despite of its very simple control rules.

3. Parameters Design

A The dc voltage limitation

The acceptable maximum value of the dc voltage is limited by the capacitor and the power device used in power inverter , and the minimum value is also restrained by the power inverter gain . It is assumed that the switching frequency of the switching device is f , the minimum on-time $T_{\min}$ and dead-time T_d. Corresponding to PWM method as see in Fig . 5a , the maximum Vx is

$$V_{x\max} = (1/f - (T_{\min} + T_d)) \cdot Vc \cdot f$$
$$= (1 - f \cdot (T_{\min} + T_d)) \cdot Vc \qquad (8)$$

In normal operation , APF has less power losses . Assumed that the reactive power and harmonic current are not compensated by active filter , the simplified equivalent circuit and phasor diagram of active filter is shown in Fig 5b and 5c. From phasor diagram , we can get

$$V_{x\max} \geq V_{s\max}$$
$$\therefore (1 - f \cdot (T_{\min} + T_d)) \cdot Vc \geq V_{s\max}$$
$$Vc \geq V_{s\max} / (1 - f \cdot (T_{\min} + T_d)) \qquad (9)$$

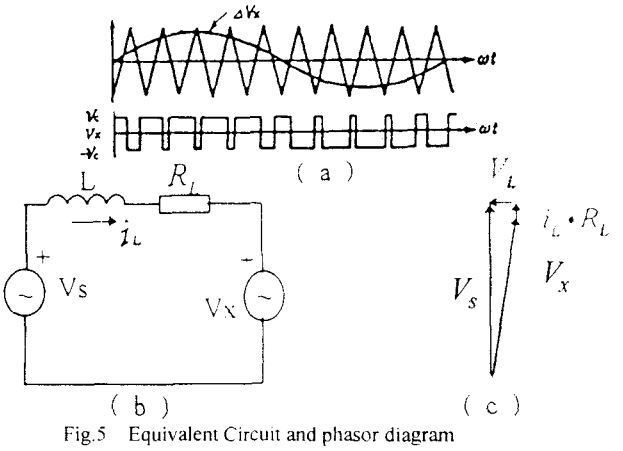

Fig.5 Equivalent Circuit and phasor diagram

As seen in (4), the lower desired voltage can be achieved if the less on-time and dead-time can be satisfied. But the minimum on-time and dead-time are restrained by the used power device and parameters of snubber circuit , the permitting selection range is limited .Therefore , the feasible scheme is that the down-scale transformer is used .

B The selection of the dc capacitor

From (3), we have

$$S = (V_s - L\dot{i}_L)/V_c \qquad (10)$$

Substituting (10) into (3) gives

$$Vc = \frac{\left(Vs - L\cdot \dot{i}_L\right)\cdot i_L}{C\cdot Vc} \quad \text{and}$$

$$\frac{1}{2}C\,(Vc^2 - Vo^2) = \int_0 Vs\cdot i_L\,dt - \frac{1}{2}L i_L^2 \qquad (11),$$

The left-side of Eq (11) represents the storage-energy variation of the dc capacitor .where Vo is initial capacitor voltage .Assumed that an acceptable variation of the dc capacitor voltage is ΔVc and let $\Delta Vc = \varepsilon Vo$ then, with

$$\Delta W = \int_0 Vs\cdot i_L\,dt - \frac{1}{2}L i_L^2 \qquad (12)$$

Eq.(17) can be rewritten as

$$\Delta W = \frac{1}{2}C\,(Vc^2 - Vo^2) \approx C\cdot \Delta Vc\cdot Vo$$

$$C \approx \frac{\Delta W}{\Delta Vc\cdot Vo} = \frac{\Delta W}{\varepsilon\cdot Vo^2} \qquad (13)$$

thus ,the required capacitor value for the acceptable voltage ripple can be determined using above equation .

C The design of the link inductor

The design of the link inductor is performed with the constraints that the minimum slope of the link inductor current is greater than that of reactive and harmonic currents of the load and meantime the maximum slope is smaller than the slope of the triangular waveform that defines the switching frequency .In this way , the interaction between the current error signal and the triangular waveform will always exists and the excellent ability to follow the reference signal is guaranteed . Assume that the slope of the triangular waveform λ ,is decided by

$\lambda = 4V_{tM}f$

where V_{tM} is the amplitude of the triangular waveform , which is equal to the maximum possible output of the error amplifier , and f is the frequency of triangular waveform . As seen in Fig 2 , the maximum slope of the inductor current is equal to

$$\frac{di_L}{dt} = (V_{x\max} + V_{s\max})/L \qquad (14)$$

$$\therefore \quad L \geq (V_{x\max} + V_{s\max})/4V_{tM}f \qquad (15)$$

D System control

The double loop control strategy is adopted in the control system of the single-phase APF proposed in this paper. The control system includes an inner loop of the current-following control and an outer loop of the dc voltage control . The main block diagram is shown in Fig .6 .

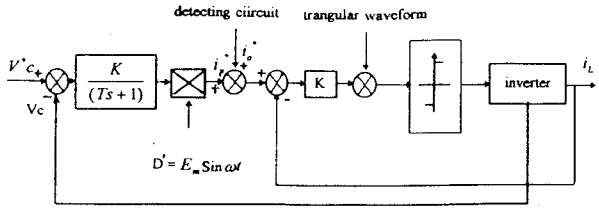

Fig 6 The block diagram of control system

The constant frequency PWM technology is incorporated in current-following control。The differential signal ΔV_r between the synthetic reference current signal $(i_p + i_o)$ and the actual compensating current signal i_L is modulated by the triangular-carrier signal and produces the pulse sequence which width varies with the synthetic current signal, then this pulse sequence is delivered to the pulse distribution and drive units as the gate driving signal by which the power device are controlled, to force the compensating current i_L to following the synthetic reference current signal .

The dc voltage across the capacitor should be maintained higher than the peak value Em of ac source voltage to prevented entering uncontrolled rectified state from the power inverter. In order to keep the dc voltage constant, the active power should be absorbed into the inverter to counteract the switching and other losses. The dc voltage control is performed in the outer loops in control system . where ΔV_c is the differential between the actual dc voltage across the capacitor and the reference value.

4. Simulation and Experiment

Corresponding to above analysis and design of the single-phase APF., the simulation and experiments of active filter are performed with a rated 1-*kVA* APF used for compensating reactive and harmonic components of inductive and capacitive load currents. Under nearly same conditions , the simulation and experimental results agree with each other very well. In the test equipment, the dc voltage of the shunt active filter was 300V , the power devices were four high-speed IGBT, the capacitor was 1000uF / 450 V, the turn rate of the down-scale transformer is 2:1 .

Fig.7 shows the dynamic simulation waveform of the starting process of the APF. At t=0.4s, the detecting circuit is started to trace the harmonic and reactive components of the load current. The transient process is completed with reactive component as well as most harmonics eliminated in ac source current Is at t= 0.5s. Before t=0.4s, the current Ic is the current required for counteracting the active power losses

of the APF and maintaining capacitor voltage constant, and the current Is is approximately equal to load current. (The symbol is the same as that in Fig.4.)

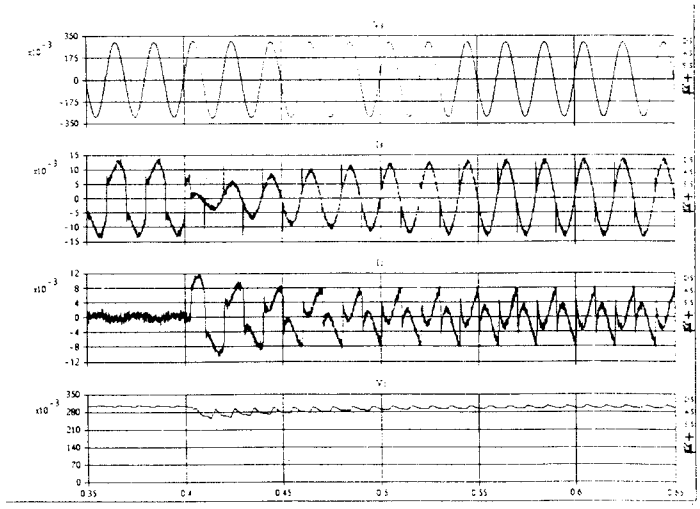

Fig. 7 The compensating operation of the APF

Fig.8 gives the simulation and experimental results for the compensating of a diode-rectifier supplied inductive load respectively. Fig. 8(a) shows the simulation waveform.

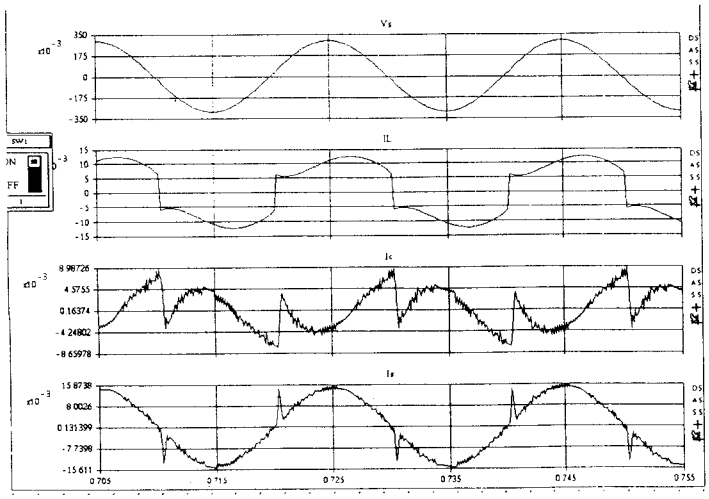

Fig.8(a) Simulation results

Fig.8(b) shows the experimental waveform. The top-upper is the ac source voltage and top-lower the load current without AF, center-upper the compensating current and center-lower the ac source current with APF, bottom-upper and bottom-lower are the ac source current frequency spectrum without and with APF.

From Fig.8 , it may be found the compensated current is in phase with the source voltage and the ac source current is approximate to sinusoidal waveform. The THD of the compensated ac source current is decreased from 24% of that of the uncompensated one to 9% as shown in Fig. 8(b).

And the waveforms in Fig.8 show that the simulation results and the experiment results have a good agreement.

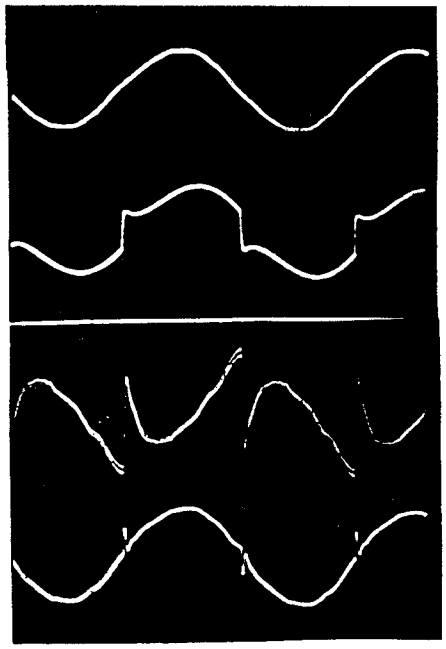

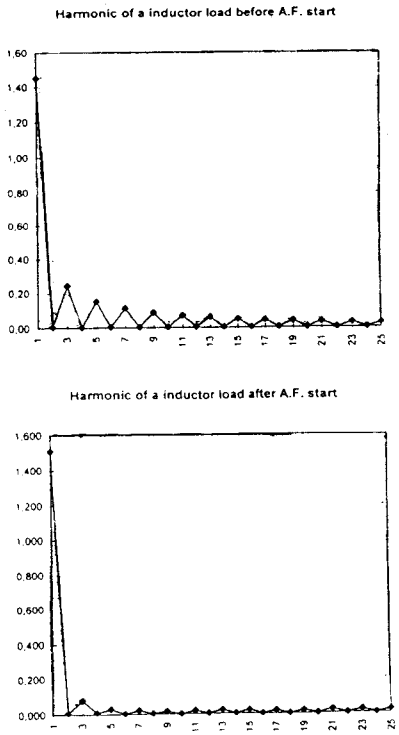

Fig. 8(b) experimental waveforms

Fig.8 The compensation for inductive rectifier load

In Fig.9, the simulation and experimental waveform are shown respectively in Fig. 9(b) and 9(a) for capacitive load, a monitor power source compensation . The sequence of the waveforms in Fig.9(a) are the same as that in Fig.8(b). From Fig.9, it can be seen that the reactive and most of harmonic components are compensated by APF, the THD of ac source current with APF is reduced to 20% from 126% of that without APF . However, it should be pointed out that

some part of harmonic components is still remained in ac source current, it requires much more additional capacity to further improve its performance.

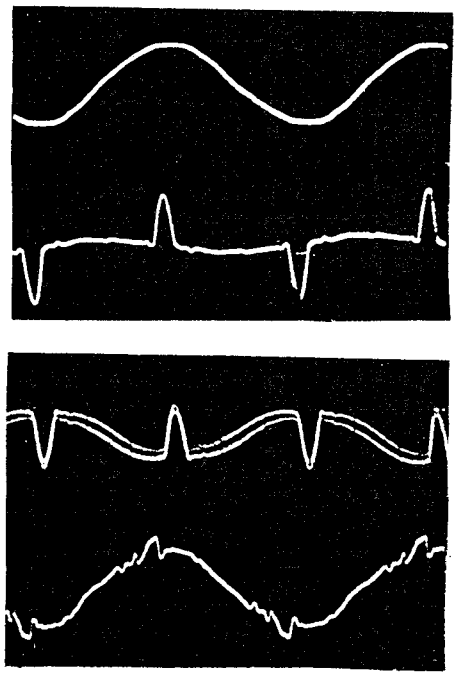

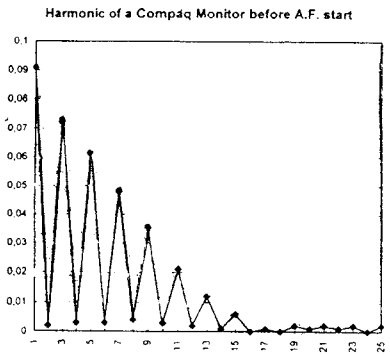

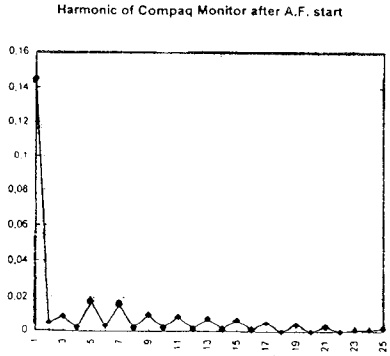

(a) experimental waveform

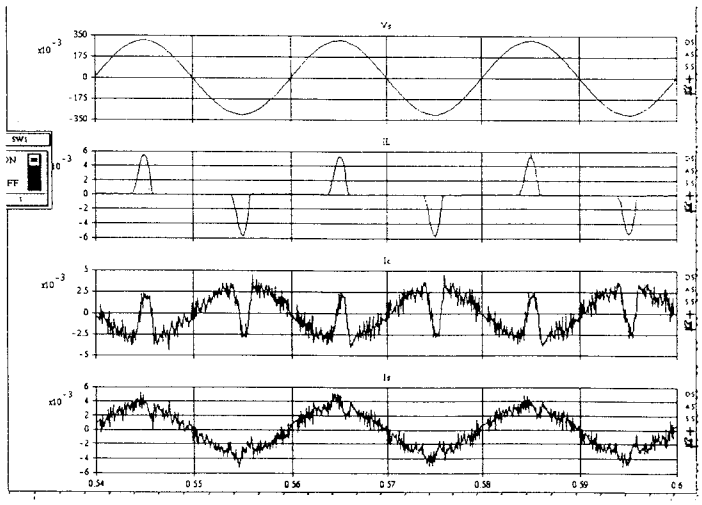

(b) Simulation waveform

Fig. 9 The compensation for capacitive load

5. Conclusion

In this paper, an adaptive noise canceling approach theory based single-phase active power filter has been proposed and the design procedure of APF is discussed in detail . The simulating and experimental results demonstrate the validity of the proposed APF for compensating reactive and harmonic components to improve the system performance. The characteristic of maintaining the null exactly at the reference frequency, in our case the power system frequency, during the total adaptive process makes it generally superior to other kinds of frequency fixed schemes of APF. The requirement of improving the effectiveness of harmonic elimination, which calls for a large time constant of integrator, is in contradiction with that of a fast adaptation speed. However, the high compensating accuracy, the wide adaptability to the frequency variation and the simple structure make it a promising way in developing APF.

Reference

[1] Hirofumi Akagi "Trends in Active Power Line Condition" IEEE Trans on Power Elec,Vol.9, No.3, MAY. 1994.

[2] Product and Applications Handbook 1995-1996 Unitrode.

[3] Zhao Liangbing, Ma Weixin, Chen Jianye "Modern Power Electronics & Its Application In Power System " Power System Technology, Vol.19, No.4, Apr. 1995.

[4] Hirofumi Akagi et al "Instantaneous Reactive Power Compensations Switching Device Without Energy Storage Components" IEEE Trans on Ind Appl, Vol.LA-20, No.3, May. 1984.

[5] S. Luo et al., 'An adaptive Detecting Method For Harmonic And Reactive Currents' IEEC, Trans. 42-46, Aug.1993.

Transformerless Reactive Series Compensators with Voltage Source Inverters

H. Stemmler, A. Beer
The Swiss Federal Institute of Technology (ETH)
Power Electronics and Electrometrology Laboratory
Physikstrasse 3, CH-8092 Zurich, Switzerland
Fax: +41-1-6321212, Phone: +41-1-6326575
E-mail: beer@lem.ee.ethz.ch

Abstract — **This paper proposes a configuration for transformerless connected compensators consisting of voltage source inverters with parallel and series connected capacitors. The behavior of transmission lines and power flow control with reactive series compensators are described. After presentation of the circuits and configurations their mode of operation is shown in more details using an example which is representative for practical applications.**

I. Introduction

In electric power systems large converters using conventional turn-on thyristors are state of the art for more then twenty years. Driven by the semiconductor technology, which allows to build improved turn-off power devices and driven by new market demands caused by the emerging deregulation in power systems, new activities in this field are coming up. With turn-off-thyristors or transistors the characteristics of modern converters can be improved to such an extent that new applications for FACTS (Flexible AC Transmission Systems) will be opened. They allow to control the active and reactive power flow in ac systems in a much more refined way and, therefore, they allow to make much better use of existing generators and power lines.

In this paper a configuration for reactive series compensators consisting of voltage source inverters with parallel and series connected capacitors is proposed and investigated. In chapter II the behavior of transmission lines and in chapter III power flow control with reactive series compensators are described. Chapter IV presents circuits and configurations and in chapter V their mode of operation is shown in more details. Chapter VI gives a summary.

II. Behavior of Transmission Lines

Transmission lines can be described with phasor equations and illustrated with phasor diagrams. Focussing at the receiving end (index 2) it is suitable to use (1) and (2) which are represented in fig.1. For reasons of simplification the losses are neglected in (1), (2), (5) and (6).

$$\underline{U}_1 = \underline{U}_2 \cos\beta l + j\underline{I}_2 Z_0 \sin\beta l \quad (1)$$

$$P = \frac{U_1 \cdot U_2}{Z_0 \sin\beta l} \sin(\varphi_{u1} - \varphi_{u2}) \quad \text{where:} \quad (2)$$

$\underline{U}_{1/2} = U_{1/2} e^{j\varphi_{u1/2}}$	: Input/Output voltage phasor	(3)
$\underline{I}_2 = I_2 e^{j\varphi_{i2}}$	: Output current phasor	(4)
P	: Transfer power	
$Z_0 = \sqrt{L'/C'}$	: wave impedance	(5)
$\beta = \omega\sqrt{L'C'}$	: phase constant	(6)
l	: length of the line	
L', C'	: inductance/km, capacitance/km	

The phasor diagram in fig.1 illustrates the eqs. (1) and (2) for a 500*km* 400*kV* transmission line. The real axis is fixed in the direction of the phasor $\underline{U}_2 = U_2$, the amplitude of which is kept at its rated value $U_2 = 1p.u.$. When the current phasor $\underline{I}_2$ - multiplied with Z_0 - at the receiving end is moving in the $\underline{I}_2 Z_0$-sector, then the voltage phasor $\underline{U}_1$ at the sending end moves correspondingly in the $\underline{U}_1$-sector - which is a linear conformal mapping of the $\underline{I}_2 Z_0$-sector, according to (1).

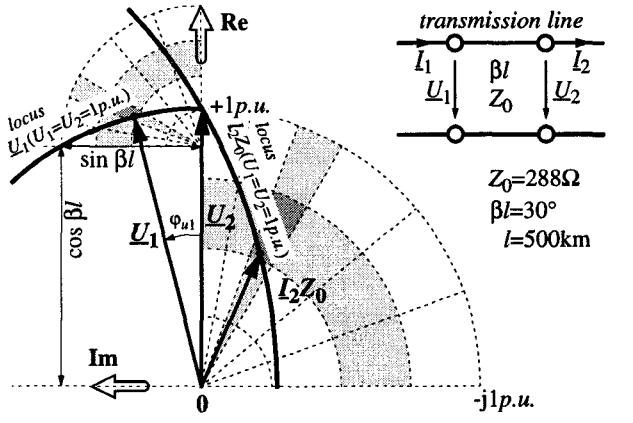

Fig.1. Transmission line, phasor diagram

Fig.1 shows: Increasing the consumption of active current $Re(\underline{I}_2)$ at the receiving end rises the angle $\varphi_{u1} = \angle(\underline{U}_1, \underline{U}_2)$ between the voltage phasors $\underline{U}_1$ and $\underline{U}_2 = U_2$ at the terminals of the line. See also eq. (2).

The amplitude U_1 of the phasor $\underline{U}_1$ can only be kept at its rated value $U_1 = 1p.u.$ if the current phasor $\underline{I}_2$ follows the characteristic $\underline{I}_2 Z_0(U_1 = U_2 = 1p.u.)$ in the $\underline{I}_2 Z_0$-sector. This characteristic is a linear conformal mapping of the phasor $\underline{U}_1$ in the $\underline{U}_1$-sector, following a circle with radius $U_1 = 1p.u.$. That means: In order to keep the voltage at both ends of the line at the rated values $U_1 = U_2 = 1p.u.$ the generators - or reactive power compensators - in the ac system at the receiving end of the line have to compensate the reactive current consumption of the load in such a way that the current $\underline{I}_2$, taken out of the line, follows the above mentioned characteristic $\underline{I}_2 Z_0(U_1 = U_2 = 1p.u.)$.

III. Power Flow Control by Reactive Series Compensators

A. Reactive series compensators

Reactive series compensators are voltage sources through which the line current is flowing. They, however, need no power supply because they only deliver reactive power. Their voltage phasor $\underline{U}_{comp}$, therefore, must be kept in a 90° leading or lagging position relative to the line current phasor $\underline{I}_2$.

$$\underline{U}_{comp} = jU_{comp}e^{j\varphi_{i2}} \quad \text{if} \quad \underline{I}_2 = I_2 e^{j\varphi_{i2}} \qquad (7)$$

U_{comp} pos./neg.: ind./cap. power consumption

In the leading position the compensator behaves like a controllable inductance and in the lagging position like a controllable capacitance. The amplitude U_{comp} of the compensator voltage phasor $\underline{U}_{comp}$ can be freely controlled between a positive and a negative maximum value by means of a PWM inverter. In chapter 4 and 5 circuits, configurations and operation modes of reactive series compensators are shown in more details.

B. Benchmark system

To demonstrate the power flow control with series compensators the configuration in fig.2 is used as a benchmark system: Two ac systems, 1 and 2, each consisting of distributed generators G and loads L are linked together via two transmission lines A and B. Line B is equipped with a series reactive power compensator. This configuration allows bidirectional power transfer. The ac system 2, however, shall be regarded as the system which normally receives energy. Therefore the main focus is on the receiving end of the transmission lines. It is assumed that both lines are coupled to the ac system 2 via transformers which reduce the high transmission voltage to an adequate level. These line transformers are represented in fig.2 by their leakage inductances L_σ. For reasons of simplification the transformers at the sending end are neglected.

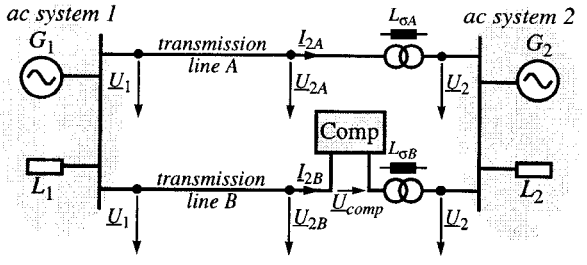

Fig.2. Benchmark system

The assumed energy deficit in the ac system 2 has to be covered by an energy surplus in the ac system 1. The power transfer $P=P_A+P_B$ of both lines compensates for the difference between generated and consumed power $P_{L_2}-P_{G_2}$ in the ac system 2.

$$P = P_A + P_B = P_{L_2} - P_{G_2} \qquad (8)$$

The series compensator fulfils the task to control the shares P_A and P_B of the total transfer power P.

C. Controlled and uncontrolled transmission lines

In the following equations it is assumed that both ac system voltages $\underline{U}_1$ and $\underline{U}_2$ are related to the high transmission voltage level.

a) *The characteristics of controlled transmission lines* - see fig.2 line B - can be derived from the equations of the line (1), the compensator (7) and the voltage (9) of the receiving end of the line.

$$\underline{U}_1 = \underline{U}_{2B}\cos\beta l_B + j\underline{I}_{2B}Z_0\sin\beta l_B \qquad (1)$$

$$\underline{U}_{2B} = \underline{U}_{comp} + j\omega L_{\sigma B}\underline{I}_{2B} + \underline{U}_2 \qquad (9)$$

$$\underline{U}_{comp} = jU_{comp}e^{j\varphi_{i2B}} \qquad (7)$$

Introducing (3) and (4) for the phasors

$$\underline{U}_1 = U_1 e^{j\varphi_{u1}}; \qquad \underline{I}_{2B} = I_{2B}e^{j\varphi_{i2B}} \qquad (3); (4)$$

and eliminating $\underline{U}_{2B}$ leads, after short, purely algebraic calculations, to (10). In equation (10) the real axis is fixed in the direction of the voltage phasor $\underline{U}_2 = U_2$.

$$U_1 e^{j\varphi_{u1}} = U_2\cos\beta l_B + je^{j\varphi_{i2B}}(U_{comp}\cos\beta l_B + I_{2B}X_{L_B}) \qquad (10)$$

where: $\underline{U}_2=U_2$; $\quad X_{L_B}=Z_0\sin\beta l_B+\omega L_{\sigma B}\cos\beta l_B \qquad (11)$

b) *The characteristics of uncontrolled transmission lines* follows from (10) for $U_{comp}=0$:

$$U_1 e^{j\varphi_{u1}} = U_2\cos\beta l_A + je^{j\varphi_{i2A}}I_{2A}X_{L_A} \qquad (12)$$

where: $\underline{U}_2=U_2$; $\quad X_{L_A}=Z_0\sin\beta l_A+\omega L_{\sigma A}\cos\beta l_A \qquad (13)$

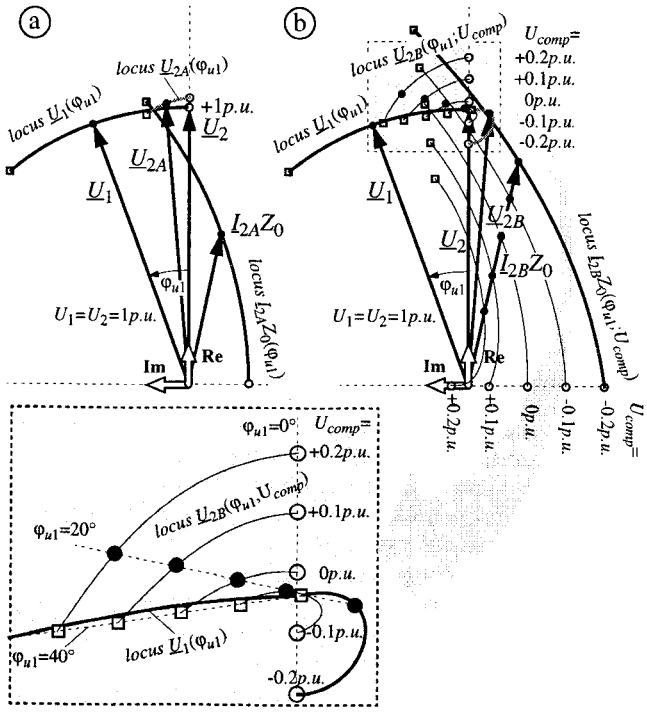

Fig.3. Uncontrolled and controlled transmission lines

The characteristics of controlled and uncontrolled transmission lines - according to fig.2 - are illustrated in fig.3 for 500*km* 400*kV* ($\beta l_{A,B}$=30°) transmission lines with a transformer ($\omega L_{\sigma A,B}/Z_0$=15%) at the receiving end. In both cases the real axis is fixed in the direction of the voltage phasor $\underline{U}_2=U_2$ in the ac system 2. It is assumed that the voltage control of both ac systems keeps the amplitudes U_1 and U_2 at their rated value 1*p.u.*. Fig.3a contains the characteristics for the *uncontrolled* line A. It shows the locus of the phasors $\underline{U}_1(\varphi_{u1})$, $\underline{I}_{2A}Z_0(\varphi_{u1})$ and $\underline{U}_{2A}(\varphi_{u1})$ as a function of the phase angle φ_{u1} between the phasors $\underline{U}_1=U_1\cdot e^{j\varphi_{u1}}$ and $\underline{U}_2=U_2$ of both ac systems.

Fig.3b contains the same phasors $\underline{U}_1(\varphi_{u1};U_{comp})$, $\underline{I}_{2B}Z_0(\varphi_{u1};U_{comp})$ and $\underline{U}_{2B}(\varphi_{u1};U_{comp})$ for the *controlled* line B with the amplitude U_{comp} of the series compensator voltage as a parameter: U_{comp} = -0.1*p.u.*; -0.2*p.u.*; +0.1*p.u.* and +0.2*p.u.*.

In the *uncontrolled* line A the phase angle φ_{u1} between the phasors $\underline{U}_1$ and $\underline{U}_2=U_2$ of both ac systems determines the active current $Re(\underline{I}_{2A})$ and the transfer power $3/2\cdot U_2\cdot Re(\underline{I}_{2A})$.

In the *controlled* line B the transfer power at a given phase angle φ_{u1} can be controlled with the amplitude U_{comp} of the compensator voltage (the phasor $\underline{U}_{comp}$ of which has a 90° phase shift to the current phasor I_{2B} - as explained in chapter III.A (7)). Fig.3b shows how the control works: The amplitude I_{2B} of the current I_{2B} is amplified or reduced when the amplitude U_{comp} of the compensator voltage phasor $\underline{U}_{comp}=jU_{comp}e^{j\varphi_{i2B}}$ is rising in the negative or positive direction. That means: *Reactive series compensators act on the amplitude I_{2B}, not on the phase angle φ_{i2B}, of the current phasor $\underline{I}_{2B}=I_{2B}e^{j\varphi_{i2B}}$ at the receiving end of the line B.*

The control characteristics are represented in fig.4. It shows the current amplitude I_2 at the receiving end of the line and the transmission power $P=3/2\cdot U_2 Re(I_2)$ as a function of the angle φ_{u1} between the voltage phasors $\underline{U}_1$ and $\underline{U}_2=U_2$ of the ac systems 1 and 2, with the amplitude U_{comp} of the compensator voltage phasor $\underline{U}_{comp}=jU_{comp}e^{j\varphi_{i2}}$ as a parameter. In fig.4 currents, voltages and active power are related to their nominal values I_N, U_N and S_N, defined in chapter V.A.

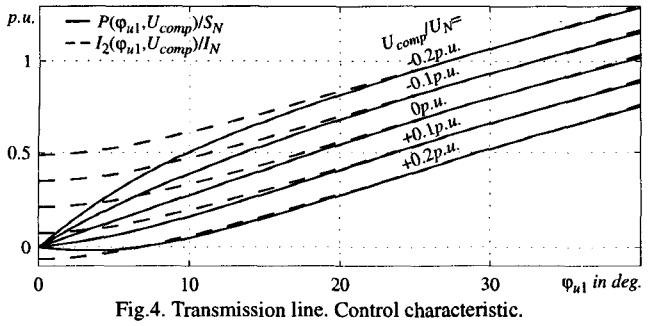

Fig.4. Transmission line. Control characteristic.

Reactive series compensators shorten or lengthen the transmission line electrically: At a given phase angle φ_{u1} between the voltage phasors $\underline{U}_1$ and $\underline{U}_2$ of both ac systems, the compensator increases the power transfer when absorbing capacitive reactive power (U_{comp} neg.). At the same phase angle φ_{u1} the power transfer is reduced when the compensator absorbs inductive reactive power (U_{comp} pos.).

D. Power flow control in networks

Electrical power utilities are under pressure to deregulate, allow access to network by independent power producers and lend their network to big customers for wheeling power from chosen suppliers. This change in operation presents new challenges.

Reactive series compensators are means to control the power flow in highly interconnected electrical power transmission networks with distributed generation and loads. Shortening or lengthening the transmission lines electrically they allow to choose the optimal routes for power transfer.

IV. Circuits and Configurations

In commercial FACTS applications, up to now, only line commutated high voltage converters with series connected turn-on thyristors could be used. GTOs with their high individual differences in turn-off time did not allow series connection on a commercial basis.

Recent developments, however, with hard driven, low inductance ring-gate GTOs shortened and equalized the individual turn-off times to such an extend that series connection becomes a problem that can be solved easily. In addition solutions to supply the gate unit directly out of the power circuit - instead of energy transfer from ground potential - are on the way to be developed [2]. This opens the way for real high voltage high capacity voltage source inverters in fault tolerant N+1 configuration, which are suited for FACTS applications.

A. Basic circuits

Future reactive series compensators basically consist of transformerless connected voltage source inverter bridges in each of the three phases in the transmission line. These bridges consist of two 2- or 3-level halve bridges. They need no dc power supply because they generate only reactive power.

The focus in this paper is on 3-level halve bridges. In fig.5 top each 3-level halve bridge is represented by a change over switch, the output of which can be connected to the positive, negative or zero potential of the dc voltage. Fig.5 left also shows the circuit of a 3-level halve bridge with four reverse conducting GTOs and two clamping diodes.

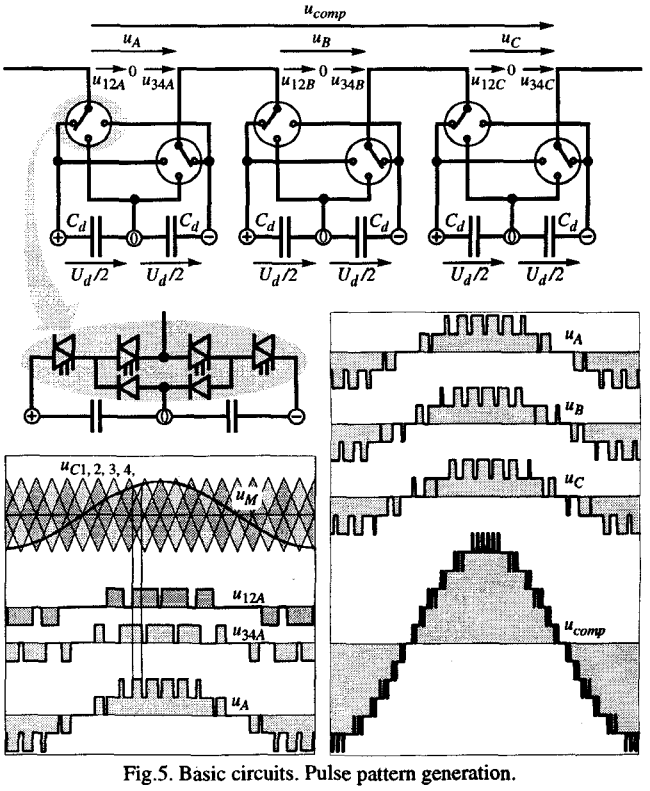

Fig.5. Basic circuits. Pulse pattern generation.

Each 3-level halve bridge can be controlled with *two* independent 2-level pulse patterns. The full bridge, therefore, can generate an output voltage, which is composed of *four* pulse patterns. As illustrated in fig.5 left each of the four pulse patterns is generated by the intersections of the same sinusoidal modulation signal u_M with one of the four triangular carrier signals $u_{C1,2,3,4}$ which are 90° phase shifted against each other.

The sinusoidal modulation signal u_M determines amplitude U_{inv} and frequency f of the fundamental component of the inverter output voltage u_{inv}. The frequency F of the carrier signals $u_{C1,2,3,4}$ determines the switching frequency F per GTO. The 90° phase shift between the carrier signals leads to a staggered switching sequence of the individual GTOs and to a four times higher pulse frequency $4F$ in the

resultant output voltage of the inverter bridge - thus reducing the harmonics drastically.

B. Series connection

Single inverter bridges consisting of 3-level halve bridges without direct series connection of GTOs can be built with today's GTOs for about the following ratings:

rated dc voltage:	U_d	$\approx 5kV$
max. output voltage ampl.:	$U_{comp} \approx U_d$	$\approx 5kV$
rated power per phase:	$S \approx 1/2 \cdot U_d \cdot 2kA$	$\approx 5MVA$

In most cases this are too low ratings for FACTS applications. Therefore series connection is a must. Two kinds of series connection have to be taken into account: series connection of semiconductors and of inverter circuits.

a) *Series connection of N semiconductors* has two main advantages: It allows to build high voltage inverter bridges with higher capacity per single unit and with fault tolerant design using one semiconductor more (N+1) than needed. The above mentioned ratings per single unit increase with the number N of series connected GTOs. With N=4, for example, the ratings are:

rated dc voltage:	U_d	$\approx 20kV$
max. output voltage ampl.:	$U_{comp} \approx U_d$	$\approx 20kV$
rated power per phase:	$S \approx 1/2 \cdot U_d \cdot 2kA$	$\approx 20MVA$

b) *Series connection of inverter bridges* - shown in fig.5 top - has the main advantage, that the resultant pulse frequency increases with the number of series connected bridges. With three series connected bridges the resultant pulse frequency is 4·3=12 times higher than the switching frequency per GTO. This reduces the harmonics drastically while keeping the GTO switching frequency low and the inverter efficiency high. See fig.5 right. With three bridges in series, for example, the ratings are:

rated dc voltage times 3:	$3 \cdot U_d$	$\approx 15kV$
max. resultant voltage ampl.:	$U_{comp} \approx U_d$	$\approx 15kV$
res. rated power per phase:	$S \approx 3/2 \cdot U_d \cdot 2kA$	$\approx 15MVA$

c) The *combination of series connected semiconductors and series connected inverter bridges* combines the advantages of both methods. With N+1=4+1 GTOs in direct series connection and with three inverter bridges in series, for example, the resultant ratings are:

rated dc voltage times 3:	$3 \cdot U_d$	$\approx 60kV$
max. resultant voltage ampl.:	$U_{comp} \approx U_d$	$\approx 60kV$
res. rated power per phase:	$S \approx 3/2 \cdot U_d \cdot 2kA$	$\approx 60MVA$

That means: The resultant voltage amplitude U_{comp}=60kV of the series compensator is U_{comp}/U_N=18.3% of the phase voltage U_N=400$kV \cdot \sqrt{2}/\sqrt{3}$=327$kV$ in a 400kV transmission line. As shown in chapter III fig.3, this is the order of magnitude to control the power flow in a 500km 400kV line.

C. Hybrid configurations

The power flow control range of inverters is basically symmetrical: The power flow can be increased or decreased when the inverter absorbs capacitive (U_{comp} negative) respectively inductive (U_{comp} positive) reactive power. This was shown in chapter III.C, figs. 3 and 4.

Reactive series compensators, however, can also be composed as a combination of inverters with series connected capacitors C_s or reactors as shown in fig.6b. The purpose of these hybrid configurations is to fulfil the control task with reduced inverter capacity. This is, however, only possible with an unsymmetrical control range: Inverters combined with *series connected capacitors* C_s extend the control range for power flow increase (U_{comp} neg.) and reduce the control range for power flow reduction (U_{comp} pos.). Inverters combined with *series connected reactors* do exactly the contrary. In the following the focus is on inverters in combination with series connected capacitors.

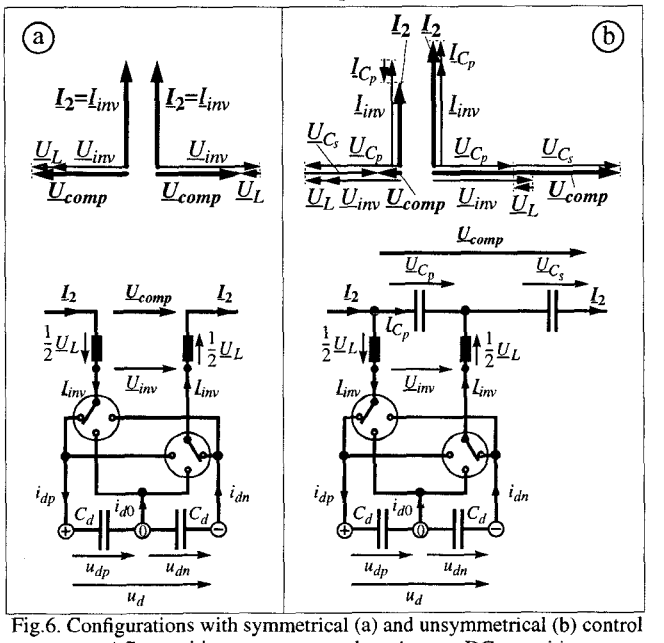

Fig.6. Configurations with symmetrical (a) and unsymmetrical (b) control range. AC quantities are represented as phasors, DC quantities as instantaneous values.

In addition it is useful to install parallel connected capacitors C_p which serve as filters. Dimensioned only for a small fundamental component of the current they, however, are able to absorb the current harmonics of the inverter. Fig.6b shows the hybrid circuit for one phase and the corresponding phasor diagram. Fig.6a shows the inverter alone for comparison. The mode of operation will be illustrated and explained in more details in the following chapter V.

V. Mode of Operation

A. Phasor diagrams and control range

The hybrid configuration in fig.6b with a capacitor C_s in series to the inverter and a filter capacitor C_p in parallel can be described by the following phasor equations and illustrated by the phasor diagram in fig.6b top.

$$\underline{U}_{comp} = \underline{U}_{C_p} + \underline{U}_{C_s}; \qquad \underline{I}_2 = \underline{I}_{C_p} + \underline{I}_{inv} \tag{14}$$

$$j\omega L \underline{I}_{inv} = \underline{U}_{C_p} - \underline{U}_{inv}; \qquad j\omega C_p \underline{U}_{C_p} = \underline{I}_{C_p} \tag{15}$$

$$j\omega C_s \underline{U}_{C_s} = \underline{I}_2 \tag{16}$$

If the inverter works in the capacitive mode (fig.6b top right) the inverter voltage $\underline{U}_{inv}$ (minus $\underline{U}_L$, which is small) and the series capacitor voltage $\underline{U}_{C_s}$ sum up to an increased resultant voltage $\underline{U}_{comp}$ of the compensator. With the inverter working in the inductive mode (fig.6b top left) the inverter voltage $\underline{U}_{inv}$ is in opposite direction to the series capacitor voltage $\underline{U}_{C_s}$ and the resultant compensator voltage $\underline{U}_{comp}$ becomes small. In this way the control range of the

compensator becomes unsymmetrical: an increased range for power flow increase and a reduced range for power flow reduction.

This is shown in fig.7 which contains the compensator voltage amplitude U_{comp} as a function of the inverter voltage amplitude U_{inv} with the line current amplitude I_2 as parameter. (U_{comp} pos./neg. in the ind./cap. mode for power flow reduction/increase). Fig.7 shows: The higher the line current I_2 the more unsymmetrical is the power flow control range.

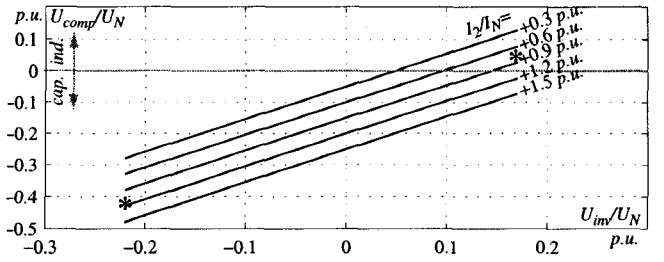

Fig.7. Unsymmetrical control range

The characteristics in fig.7 are valid for $500km$ $400kV$ transmission lines for the following figures, which could be representative in future applications.

Transmission line:

$Z_0 = 288\Omega$; $\beta l = 30°$; $l = 500km$ (17)

$\omega L_{\sigma A,B}/Z_0 = 15\%$ (18)

$U_N = 400kV \cdot \sqrt{2}/\sqrt{3} = 326.60\ kV$ (19)

$I_N = U_N/Z_0 = 1.13\ kA$ (20)

$S_N = 1/2\ U_N I_N = 185.19\ MVA$ (21)

Z_0: Wave impedance; β: phase constant; l: length

$\omega L_{\sigma A,B}$: Transformer leakage reactance

U_N, I_N : Rated phase voltage and current amplitude

S_N: Rated apparent power per phase

Inverter (series connection of three inverters):

$U_d = U_{inv}(m_0=1) = 20\% U_N = 3 \cdot 21.8kV = 65.4\ kV$ (22)

$Q_{inv} = 1/2 U_{inv} I_N = 20\% S_N = 37\ MVA$ (23)

$X_{inv} = U_{inv}(m_0=1)/I_N = 57.6\ \Omega$ (24)

$F = 225\ Hz$ (25)

U_d : Rated dc voltage

U_{inv} : Rated ac voltage amplitude (m_0=1)

m_0 : Modulation degree (m_0=0...1)

Q_{inv} : Rated reactive power per phase

X_{inv} : Rated equivalent reactance

F : Switching frequency per GTO

Capacitances and inductance:

$X_{C_d} = (\omega C_d/2)^{-1} = 50\%\ X_{inv} = 28.8\Omega$ (26)

$X_L = \omega L = 20\%\ X_{inv} = 11.5\Omega$ (27)

$X_{C_p} = (\omega C_p)^{-1} = 500\%\ X_{inv} = 288\ \Omega$ (28)

$X_{C_s} = (\omega C_s)^{-1} = 100\%\ X_{inv} = 57.6\Omega$ (29)

X_{C_d} : Reactance of the inverters dc capacitance $C_d/2$

X_L : Reactance of the decoupling inductance L

X_{C_p} : Reactance of the parallel filter capacitance C_p

X_{C_s} : Reactance of the series capacitance C_s

It is interesting to note that the rated reactive power $3Q_{inv}$=111.1MVA of the inverter is only Q_{inv}/S_N=20% of the rated transmission power $3S_N$=555.5MVA of the line.

B. Line diagrams

The line diagrams in fig.8 illustrate two operation modes - marked with "*" in fig.7 - in more details for the figures given in chapter V.A.

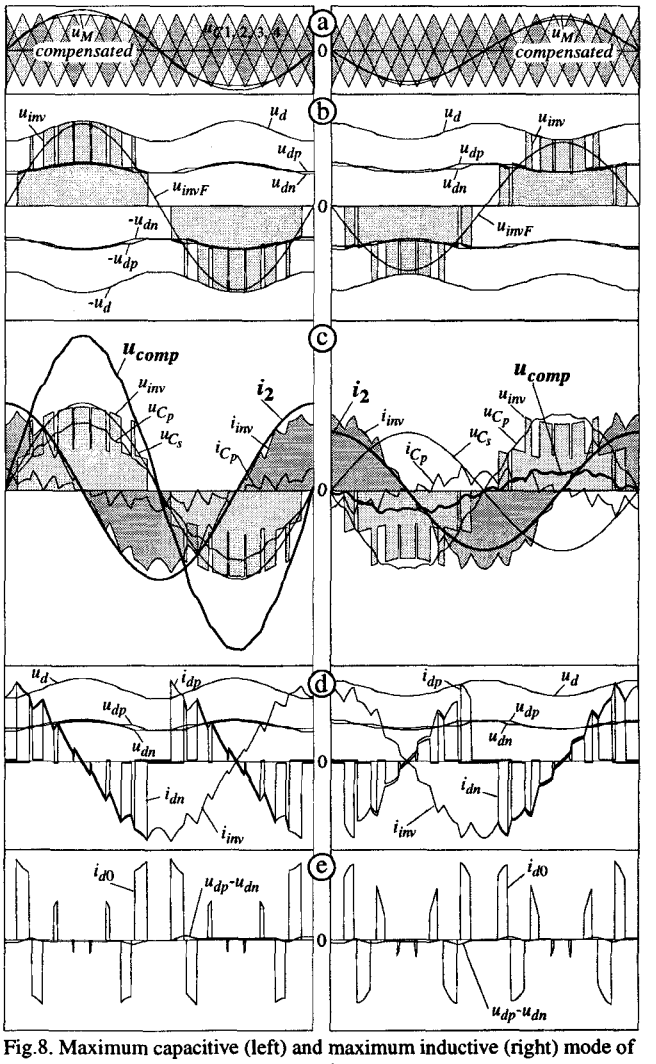

Fig.8. Maximum capacitive (left) and maximum inductive (right) mode of operation.

a) capacitive compensator voltage

The mode with maximum capacitive compensator voltage u_{comp} for power flow increase is shown in fig.8 left for a line current i_2, which is assumed to be 118% of the rated current I_N. The modulation signal u_M and four carrier signals $u_{C1,2,3,4}$ in fig.8a generate the resultant inverter output voltage u_{inv} in fig.8b with a staggered switching sequence of the individual GTOs.

This picture also contains the dc voltages u_d, u_{dp} and u_{dn} of the inverter. They oscillate around the rated values U_d resp. $U_d/2$ for reasons, which are explained below. The modulation signal u_M in fig.8a, therefore, has to be compensated in such a way, that the short term mean value u_{invF} of the inverter output voltage remains purely sinusoidal - despite of the deviations in the dc voltages.

The inverter current i_{inv} in fig.8c generated in the decoupling inductance L by the difference of the inverter voltage u_{inv} and the smoothing capacitor voltage u_{C_p}

$$i_{inv} = \frac{1}{L} \cdot \int (u_{C_p} - u_{inv}) dt \qquad (30)$$

contains harmonics, the pulse frequency of which is four times higher than the GTO switching frequency: $4F$=4·225Hz=900Hz. The lower the switching frequency F per GTO, the better is the efficiency of the inverter - but the higher are the harmonics. F=225Hz is a suitable switching

frequency for todays GTOs.

Fig.8c shows that the harmonics i_{invH} in the inverter current i_{inv} are absorbed by the smoothing capacitor C_p.

$$i_{invH} = -i_{C_pH} \qquad \textit{(index H: Harmonics)} \qquad (31)$$

The capacitor C_p - dimensioned according to (28) - is large enough to keep its voltage u_{C_p} in a good sinusoidal shape and small enough to draw only a small fundamental current component. The resonance frequency f_{res} of the filter is above the fundamental frequency f and below the resultant pulse frequency $4F$.

$$f_{res} = \frac{1}{2\pi\sqrt{LC_p}} = 250Hz \qquad (32)$$

$$f=50Hz \; < \; f_{res}=250Hz \; < \; 4F=900Hz \qquad (33)$$

The harmonics in the line current i_2 are nearly negligibly for reasons explained below. The series capacitor voltage u_{C_s}, therefore, is sinusoidal.

$$u_{C_s} = \frac{1}{C_s}\int i_2 dt \qquad (34)$$

Fig.8c also contains the resultant compensator voltage u_{comp} which is the sum of the capacitor voltages u_{C_p} and u_{C_s}.

$$u_{comp} = u_{C_p} + u_{C_s} \qquad (35)$$

The resultant compensator voltage u_{comp} is about two times higher than the inverter voltage u_{inv} - according to the objective of this hybrid configuration.

Fig.8d shows the reasons for the dc voltage deviations of the inverter: In reactive single phase inverters the short term mean values of the dc currents i_{dp} and i_{dn} follow a $2f$=$100Hz$ sinus-line and cause a $100Hz$ ripple in the dc voltages u_{dp}, u_{dn} and u_d.

$$u_{dp}=\frac{1}{C_d}\int i_{dp}dt\,; \qquad u_{dn}=\frac{1}{C_d}\int i_{dn}dt\,; \qquad u_d=u_{dp}+u_{dn} \qquad (36)$$

The higher the dc capacitance C_d - dimensioned according to (26) - the lower is the $100Hz$ ripple in the dc voltage - but the higher are cost and volume of the inverter. The $100Hz$ ripple in the dc voltage could also be eliminated with a $100Hz$ LC filter at the inverters dc side. This is state of the art in inverter locomotives with single phase ac supply. Inductances, however, are rather bulky components which should be avoided, if possible, in voltage source inverters.

Fig.8e finally shows the zero point current i_{d0}=i_{dp}-i_{dn}. Its mean value must be kept at zero in order to avoid an unbalance of the dc voltages u_{dp} and u_{dn} [3]. See u_{dp}-u_{dn} and i_{d0} in fig.8e.

The harmonic content of the resultant compensator voltage u_{comp}, which is already low, can be further reduced to a negligible level with, for example, three series connected compensators each with a dc voltage of U_d=$21.8kV$ (and N=4 series connected GTOs). In this case the groups of four carrier signals allocated to the modulator of each of these three compensators have to be phase shifted against each other in such a way, that all harmonics up to the resultant pulse frequency $4F$·3, which is 12 times higher than the individual GTO switching frequency F, are eliminated: The harmonics generated in the line current i_2 by the compensator become negligibly low.

$$4F \cdot 3 = 12F = 12 \cdot 225Hz = 2.7kHz \qquad (37)$$

b) Inductive compensator voltage

Figs.8a..e right show - in exactly the same sequence of line diagrams as in fig.8 left - the operation mode with maximum inductive inverter voltage for a line current i_2 which is assumed to be 79% of the rated current.

Since inverter voltage u_{inv} and series capacitor voltage u_{C_s} now are in opposite direction the resultant inductive compensator voltage u_{comp} is very small. See also "*" in fig.7.

Comparing the inverter output voltages u_{inv} in fig.8b left and fig.8b right it is interesting to note that the inverter voltage in fig.8b left is at its maximum, when the dc voltage u_d is also at its maximum. In fig.8b right, however, the inverter voltage maximum is at the dc voltage minimum. That means: the maximum amplitude of the fundamental component u_{invF} in the inverter output voltage has to be kept lower in case of inductive inverter voltage and can be increased in case of capacitive inverter voltage.

VI. Conclusion

Based on improved GTOs with hard driven, low inductance ring-gate and with gate unit power supply out of the main power circuit, high-voltage inverters with series connected GTOs can be built, the ratings of which are sufficiently high for high power FACTS applications. This paper proposes and describes a transformerless connected reactive series compensator consisting of voltage source inverters and parallel and series connected capacitors for power flow control in interconnected electrical power transmission system networks.

Transformerless connection means the elimination of a bulky and expensive system component.

The compensator needs a considerably lower insulation level, when it is shifted to the side of the grounded neutral point of the line transformer.

Power flow control can - of course - also be used to damp low frequency power system oscillations.

It has been shown that power flow can be controlled with inverters, the rated power of which is very small compared to the controlled power flow. By means of staggered switching sequences and filter capacitors the harmonics which the compensator introduces into the ac system can be kept at a negligibly low level - despite of a low GTO switching frequency, which is necessary to keep the inverter efficiency at a high level. Circuits, configurations and mode of operation have been illustrated.

References

[1] Peng F.Z., Lai J.S., McKeever J.W., VanCoevering J., "A Multilevel Voltage-Source Inverter with Separate DC Sources for Static Var Generation", IEEE Transactions on Industry Applications, Vol.32, No.5, pp. 1130-1138, September/October 1996.

[2] Okayama H., Tsuchiya T., Kimata M., 1997, "Novel Gate Power Supply Circuit Using Snubber Capacitor Energy for Series-Connected GTO Valves", will be presented at the EPE-Conference, Trondheim, Norway, September 8-10, 1997.

[3] Scheuer G. and Stemmler H., "Analysis of a 3-Level-VSI Neutral-Point-Control for Fundamental Frequency Modulated SVC-Applications", 6th. AC & DC Power Transmission Conference, IEE Conf. Pub. 423, pp. 303-310, 1996.

Series Power Line Compensator using Self-Commutated Inverter

Hirokazu Tokuda Naoya Eguchi
Fuji Electric Corporate Research and Development, Ltd.
1, Fuji-machi, Hino-shi, Tokyo 191, JAPAN
Fax: +81-425-86-9665 Phone +81-425-86-1102
E-mail: tokuda-hirokazu@fujielectric.co.jp

Satoshi Uemura Ryuichi Shimada
Tokyo Institute of Technology
2-12-1, Ookayama, Meguro-ku, Tokyo 152, JAPAN
Fax: +81-3-5499-7217 Phone: +81-3-5734-3064
E-mail: rshimada@nr.titech.ac.jp

Abstract – **A novel power line compensator is proposed, which has an inverter connected to a power transmission line in series. One of the advantages of this compensator is to compensate even the voltage drop which occurs in the power supply side of the transmission line, which needs a larger capacity for the SVC.**

The operating principle and control systems of this compensator are described in this paper. The protective method of the compensator is also treated. The validity of this compensator and its control system are examined by experimental tests, including static and transient characteristics, harmonic effects and the protective functions.

I. Introduction

Today, electric power requires high quality and high reliability for integrated electronic equipment. As power electronics technology has progressed, it has been applied to a power line compensator. SVCs using TCR (Thyristor Controlled Reactor) are already in practical use, and SVCs employing the self-commutated inverters have also been developed. These can compensate line voltage with higher speed response and lower distortion.[1] We call these compensators "parallel compensator" because they are connected to a power line in parallel.

On the other hand, there is another type of compensator which is connected to a power line in series. We call it a "series compensator". Conventional phase-shifters with a mechanical tap changer and series capacitors have been in use as a series compensator. TCSC (Thyristor Controlled Series Capacitor) which is applied thyristors has been developed as a new series compensator[2]. Another type of a series compensator can also be constructed using the self-commutated inverter. It is a new type compensator which we call high speed phase shifter. It realizes high speed response without power oscillation which often occurs on series capacitors. This is because the compensator can generate and control the output voltage with required phase and amplitude within the capacity of the compensator.

The advantages of this compensator are as follows: Its capacity is smaller than parallel compensators such as SVCs used to improve the load voltage. It is because the capacity of the series compensator needs the same capacity as the percentage of the line impedance of the load, unlike the parallel compensator which needs a full load capacity.[3] The other advantage is that a series compensator has the ability to compensate even the voltage drop which occurs in the power supply side of transmission line. This compensation requires a larger capacity using a SVC. Further, it also works as a phase shifter and it can control the power flow of a loop power system.

II. Configuration and Operating Principles

The Basic configuration and the phasor diagram of voltage and current of the compensator which employs the self-commutated inverter are shown in Fig.1 and Fig.2. This series compensator mainly consists of a self-commutated inverter and a series transformer which is connected to a power line in series. The configuration of this compensator is shown in Fig.1. This compensator is equivalent to a voltage source connected to the power line in series. (Fig.3)

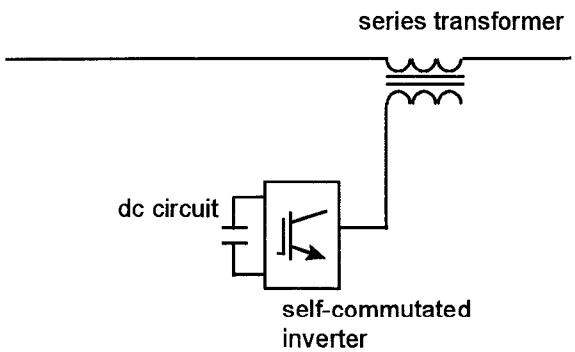

Fig.1. Basic Configuration of the Series compensator

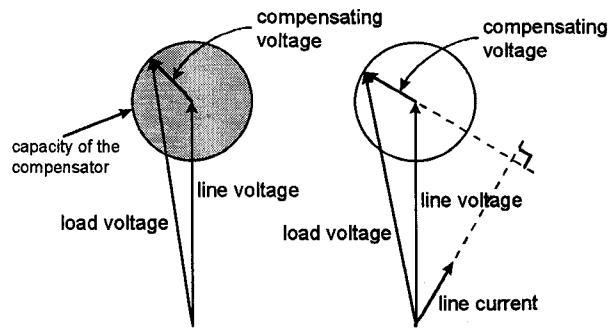

a) general operation b)variable reactor operation

Fig.2. Phasor diagram of voltage and current

The operating principle to compensate the load voltage using the series compensator is that the voltage which is generated by the compensator is added to the line voltage which drops because of the line impedance in the series transformer. The compensator employs a self-commutated inverter which can generate voltage freely within its capacity. This compensator can keep load voltage constant continuously, while the line voltage changes.

Usually, the compensation mentioned above needs sending or receiving active power to/from the power system, and a converter connected to the power line in parallel is used to manage the active power.

On the other hand, in the case of the inductive line impedance, almost all of the voltage drop can be compensated by the reactive voltage which is orthogonal to line current shown in Fig.2b. When the load voltage is compensated only by the reactive voltage, there is only reactive power flow between the power line and the compensator. So, the additional parallel converter is not necessary, theoretically. We call this compensator "variable reactor". Although this compensator works as a series capacitor, the harmful line oscillation problem which often appears on the series capacitors can be avoided with suitable control system.

In the following section, we describe the control methods and the experimental results of the series compensator driven as a variable reactor.

III. Control System of the Compensator

A. Control System of the Variable Reactor

1) For Balanced Load: First, we describe the control system for balanced load. To pursue calculation, a d-q coordinate system is used. The relation between the line current and the voltage orthogonal to it, is shown by the following admittance matrix $\left[Y_{C_{P0}}\right]$.

$$\left[Y_{C_{P0}}\right]=\begin{bmatrix} C\dfrac{d}{dt} & -\omega C \\ \omega C & C\dfrac{d}{dt} \end{bmatrix}$$

This matrix contains the transient term(d/dt). As this term might cause harmful oscillations, we neglect it. Further, to calculate voltage from the line current, the following impedance matrix $[C_P]$ is obtained from the inverse matrix of $\left[Y_{C_{P0}}\right]$.

$$[C_P]=\begin{bmatrix} 0 & 1/\omega C \\ -1/\omega C & 0 \end{bmatrix}$$

The block diagram of the control system using this matrix $[C_P]$ is shown in Fig.4.

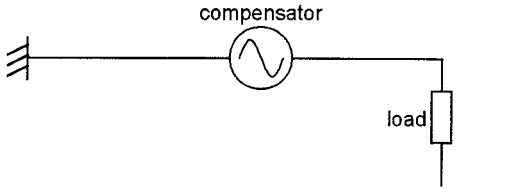

Fig.3. Theoretical model for series compensator

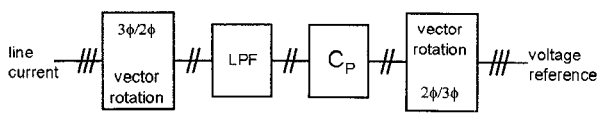

Fig.4. Block diagram of the control system (for balanced load)

2) For Unbalanced Load: When the line current is unbalanced, the current can be divided into two components which are called positive-phase-sequence and negative-phase-sequence. To calculate the compensating voltage, the line current is divided into two components and reactive voltage components are calculated respectively. These voltages are added together to obtain the reference for inverters. To calculate positive-sequence voltage component from positive-sequence current component, the matrix $[C_P]$ is available. For negative-sequence, the following matrix $[C_N]$ should be used which is derived in a similar way to $[C_P]$.

$$[C_N]=\begin{bmatrix} 0 & -1/\omega C \\ 1/\omega C & 0 \end{bmatrix}$$

The block diagram of the control system using these matrices is shown in Fig.5.

3) DC Voltage Regulator: It is expected that there is no active power flow between the power system and compensator, because the variable reactor generates only reactive voltage. But, in actuality, active power management is needed because there are energy losses in the inverter and errors in the control system. To do this, it is effective to add the resistive voltage component which lets the compensator imitate a resistor. When the main control system treats only a balanced load, the phase of the added voltage must be in-phase with the phase of the line current, and the magnitude of it is determined to make the dc voltage of the inverter constant. While the main control system treats an unbalanced load, the power reference to make dc voltage constant must be divided in the ratio of i_P^2:i_N^2. Also, the in-phase voltage component with each positive or negative current component must be added to each main component, respectively. The block diagram

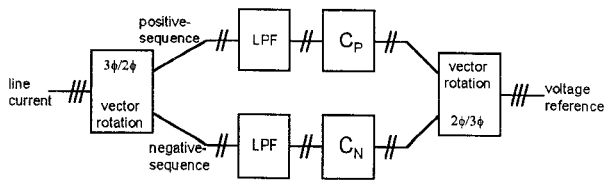

Fig.5. Block diagram of the control system (for unbalanced load)

which has the added dc voltage regulator for unbalance compensation is shown in Fig.6.

B. Simulation Results

To show the validity of the control system for the variable reactor, we pursue digital simulation with EMTDC[4]. In the simulation model the inverter is driven by 15 pulses PWM. The filter rejecting harmonics voltages is used in the output side of the inverter.

The simulation results are shown in Fig.7. They include the cases with compensation and without compensation. Fig.7a and 7b are the cases of the balanced load and Fig.7c and 7d are the cases of the unbalanced load. From these results, the expected operation of the compensators is obtained and the validity of this control method is shown.

IV. The Protective Method

When a line fault occurs, the over current of the power line flows into the series compensator. The compensator which employs a self-commutated inverter may be damaged from it, so the compensator should be protected as fast as possible.

A. Current Limiting Function of the Variable Reactor

When the over current of the power line is rather light, it can be suppressed by making the compensator which usually works as a capacitor change to work as a reactor. To realize this, the sign of the impedance matrix is multiplied by -1 in the control system.

B. Protective Method of the Thyristors

When it is too serious to suppress the over current by the current limiting function, the compensator should be protected from the line fault. Because the series compensator is connected to a power line in series, it cannot be released from the power line like parallel compensators and it must be short-circuited to be protected. Further, as it must be done in a short time, the output of the compensator should be short-circuited by switches like thyristor valves.

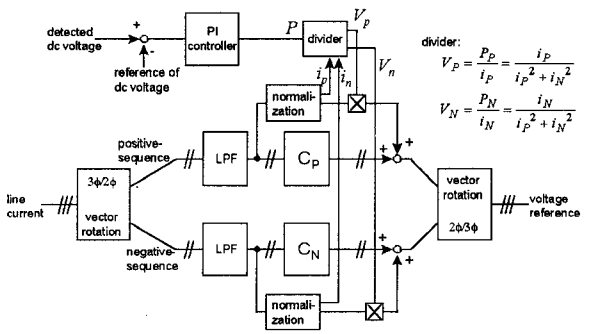

Fig.6. Block diagram of the dc voltage regulator

V. Experimental Equipment and Results

A. Configuration of the Experimental Equipment

To evaluate the performance of the variable reactor, we prepared a 210V/ 16kVA prototype model and tested it. The configuration of the prototype model is shown in Fig.8. The inverter is 2 multiples driven in 27 pulses PWM. The capacity of the model is 4kVA to compensate a 25% line voltage drop. Further, the model has a rectifier for initial

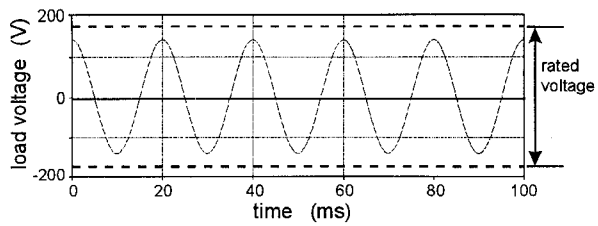

(a) without compensation for balanced load

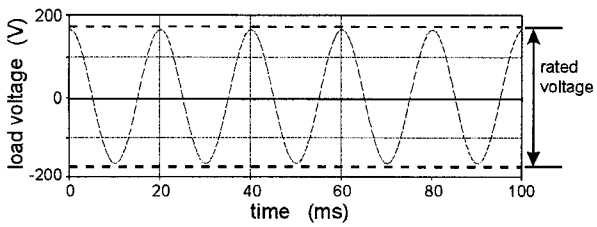

(b) with compensation for balanced load

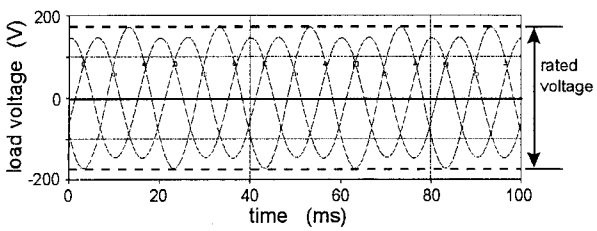

(c)without compensation for unbalanced load

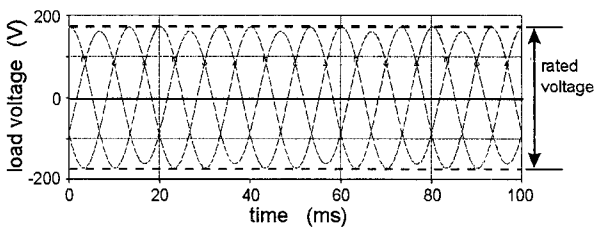

(d)with compensation for unbalanced load

Fig.7 Simulation Results.

charge of dc circuit. All of the controls are by digital control with a multiple CPU system which has 3DSPs and 3CPUs.

B. Experimental Results

1) Static Characteristics: Fig.9a shows the static characteristics of the compensator with the balanced load, and Fig.9b shows the waveform corresponding to the case with 100% load. To show the performance only by the compensator, the dc voltage regulator is not used and the compensator is driven with the initial charging circuit while this experiment is performed. From this result, it is shown that the compensator outputs the voltage which agrees to our theory.

Fig.10a shows the static characteristics with unbalanced load, and Fig.10b shows the wave form corresponding to a 58% unbalanced load. These results show that the unbalance factor of the load voltage is improved effectively.

2) Harmonics: The harmonics of the voltage corresponding to Fig.9b is shown in Fig.11. These results show that harmonic voltage of the line generated by the compensator is very little because the maximum output voltage of the compensator is only 25% for line voltage.

3) Transient Characteristics: The transient waveforms when the balanced and unbalanced load change quickly, are shown in Fig.12 and Fig.13, respectively. The results of both cases show that the transient time is approximately 20ms. This means that this compensator can compensate load voltage quickly without harmful oscillations which are caused by series capacitors.

4) Characteristics of DC Voltage Regulator: Fig.14 shows that the experimental result of the balanced load with the dc voltage regulator, and Fig.15 shows the case of the unbalanced load. These results show that this compensator can continue to operate without a parallel converter, though the performance of the compensator becomes a little lower than the case without the dc voltage regulator.

The fluctuation of the dc voltage with the load change

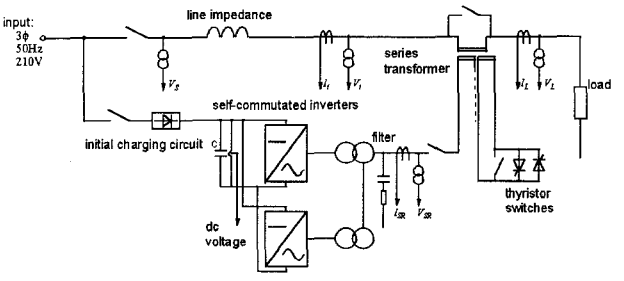

Fig.8. Configuration of the prototype model

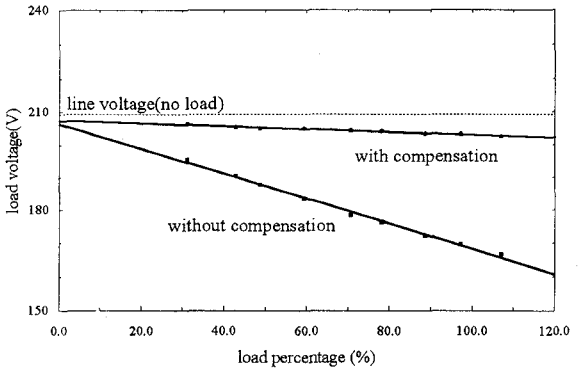

(a)

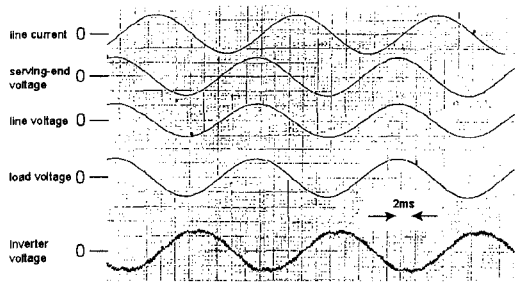

(b)

Fig.9. Static characteristics with balanced load

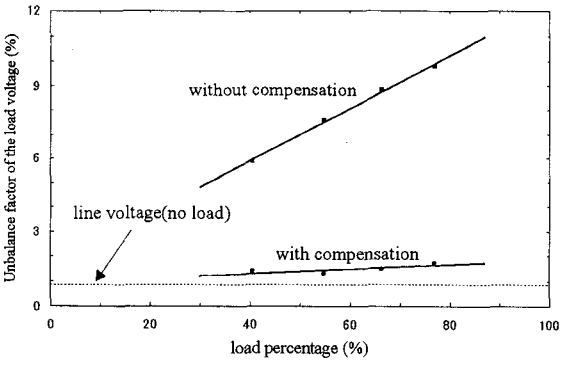

(a)

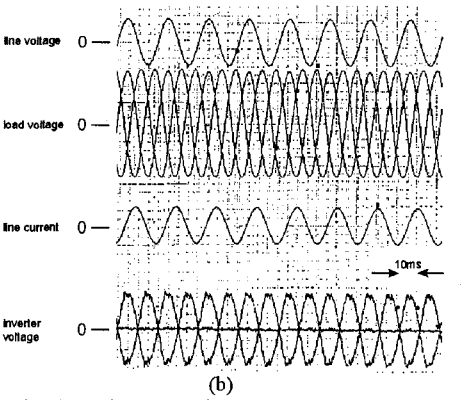

(b)

Fig.10. Static characteristics with unbalanced load

is also shown in Fig.16. It shows that the dc voltage can go back to the rated value in stable response after the load change.

5) Results of the current limiting function: Fig.17 shows that the waveforms of the current limiting function when an over current flows on the power line. Fig.17a shows the result without this function. In this case, the variable reactor keeps the voltage compensation after the line fault. Fig.17b shows the result with current limiting function. These waveforms show that the over current is suppressed by this function of the series compensator.

6) Results of the short-circuited Protection: The waveform in the case that the compensator is urgently short-circuited with thyristor switches to protect the compensator when the over current is detected, is shown in Fig.18. Fig.18a shows the waveforms when the inverter stopped without the thyristor switch and Fig.18b shows the waveforms with the thyristor switch. From the comparison of these two cases, it is shown that the compensator can be stopped without an over voltage by protecting it in a short time using the thyristor switches

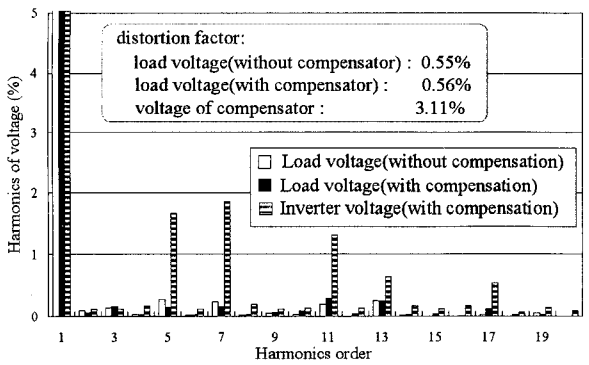

Fig.11. Voltage harmonics

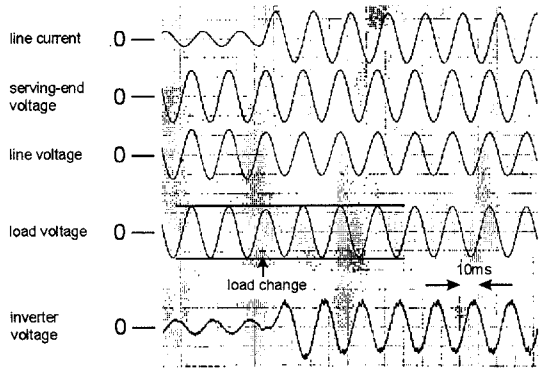

Fig.12. Transient wave form(Balanced load)

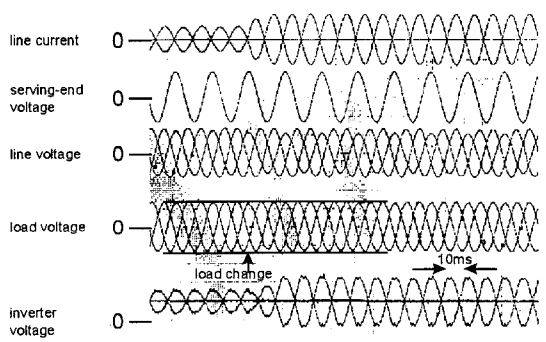

Fig.13. Transient wave form(Unbalanced load)

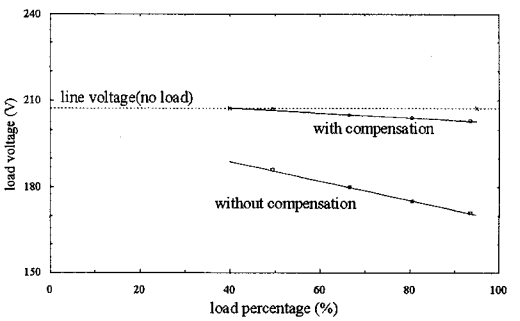

Fig.14. Compensate with dc voltage regulator(Balanced load)

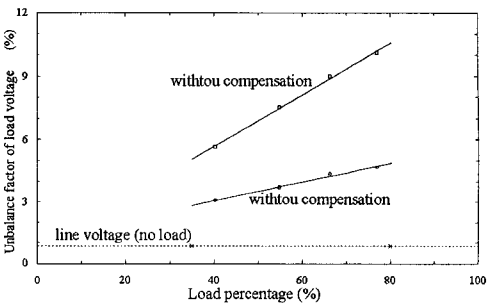

Fig.15. Compensate with dc voltage regulator(Unbalanced load)

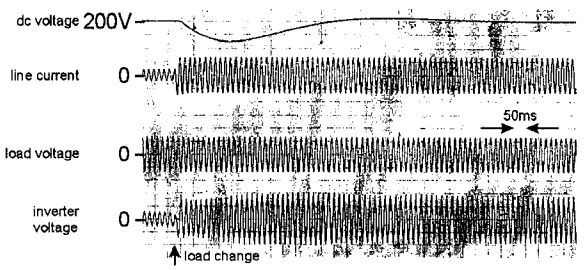

Fig.16. Change of dc voltage with dc voltage regulator

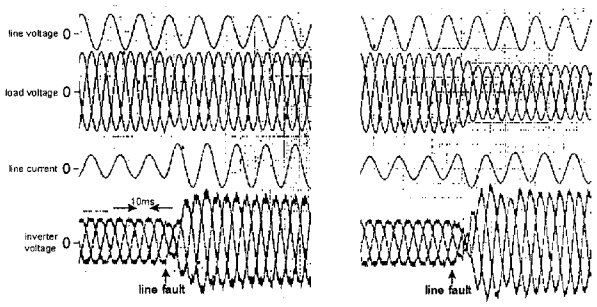

(a) (b)

Fig.17. Waveform of the current limiting function with the line fault. (a) is without current limiting function and (b) is with it.

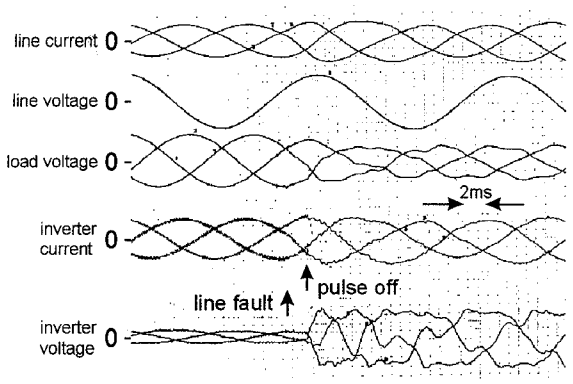

(a)

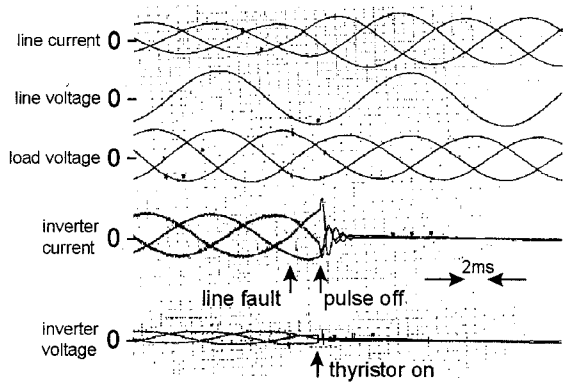

(b)

Fig.18. Wave form of the thyristor switch protection (a) is without the thyristor switch protection and (b) is with it.

VI. Conclusion

In this study, a new line compensator is proposed, which employs self-commutated inverter and is connected in series to the power system. The control method to operate it as a variable reactor is also proposed and its validity is checked by digital simulations. Further, we made the 16kVA prototype model and a performance test was pursued. The results are as follows:

- It is possible to compensate the load voltage, as seen in our theory, in both cases of the balanced load and the unbalanced load.
- The influence of the harmonics on a power line is small.
- It is possible to drive the variable reactor continuously by the dc voltage regulator without additional converters.
- It is possible to suppress a line over current by the current limiting function of the variable reactor when the line over current is rather light.
- It is possible to stop the compensator without over voltages by protecting it with high speed thyristor switches, when a line fault too heavy to suppress by the current limiting function occurs.

The variable reactor described in this paper is under development for early practical use in the actual power system. This compensator will be used widely and become one of the most significant equipment to control power systems flexibly.

References

[1] Ichikawa, "Static Var Compensator using Large Capacity Self-Commutated Converters(Self-Commutated Converter Compensator)", *T.IEE Japan*, Vol.112-B, No.6, 1992.

[2] M. Pereira et al, "Assessing the FACTS at Kayenta", *Modern Power Systems*, December, 1993.

[3] N. Eguchi et al, "Variable reactor using Solid State Phase Shifter (Compensation for voltage fluctuation)", *T.IEE Japan*, Vol.116-B, No.8, 1996.

[4] P. Kuffel et al, "Development and Validation of Detailed Control Models of the Nelson River Bipole 1 HVDC System", *IEEE Trans on Power Delivery*, Vol.8, No.1, January, 1993.

Continuous Operation Control during Electric Power Network Faults in an Adjustable Speed Generation System with a Flywheel Excited by a DC Link Converter

Tohru Nishio*, Kiyoshi Minoguti*, Seinosuke Uno*
Motoo Futami**, Mitsuyuki Hombu**, Masaya Ichinose**, Akihiro Maoka**
* Technical Research Center, The Kansai Electric Power Company, Inc.
11-20 Nakoji 3-chome Amagasaki-shi, Hyogo-ken, 661 Japan.
** Power & Industrial Systems R & D Division, Hitachi, Ltd.
7-2-1 Omika-cho, Hitachi-shi, Ibaraki-ken, 319-12 Japan.
(Phone: +81-294-53-3111 Fax: +81-294-52-7607 E-mail: mfutami@hrl.hitachi.co.jp)

Abstract **- For an adjustable speed generation system with a flywheel, not only quick active power and voltage responses, but also continuous operation during electric power network faults are necessary to stabilize electric power networks. Quick active power response of 40 rad/s and voltage response of 40 rad/s are obtained in a 30-kVA test model. To realize these quick responses, a controller with multi microprocessors is used, in which the minimum sampling time is 185 μ s. Moreover, cooperative power flow control between the rectifier and inverter is added to power, voltage and speed controls of the generator/motor. Chopper control for overvoltage suppression is added to the dc link voltage control. Continuous operation can be realized even during such electric power network faults as 1-line, 2-line and 3-line ground faults due to these controls.**

I. Introduction

Today, adjustable speed pumped-storage power plants are used to keep a constant frequency for electric power networks. Actual plant applications have included systems using a cycloconverter or dc link GTO converter to excite the generator/motor which is an ac excited synchronous machine type. In the field of adjustable-speed drives, these systems are called slip-power recovery control schemes[1],[2]. Besides adjustable speed pumped-storage power plants, adjustable speed generation systems with a flywheel are receiving attention as stabilizers for electric power networks[3]-[6]. In order to improve the electric power network stability, it is very important to realize quick control of active

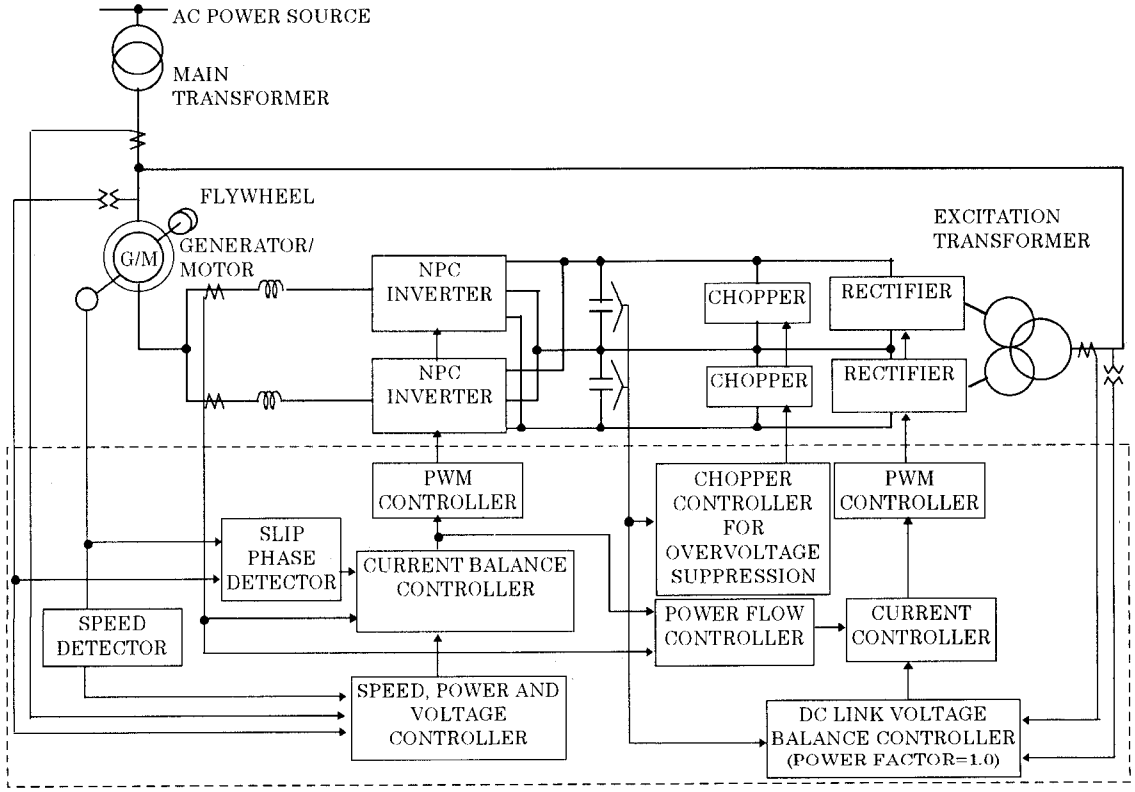

Fig. 1 Adjustable speed generation system with a flywheel using slip-power recovery control of the induction machine.

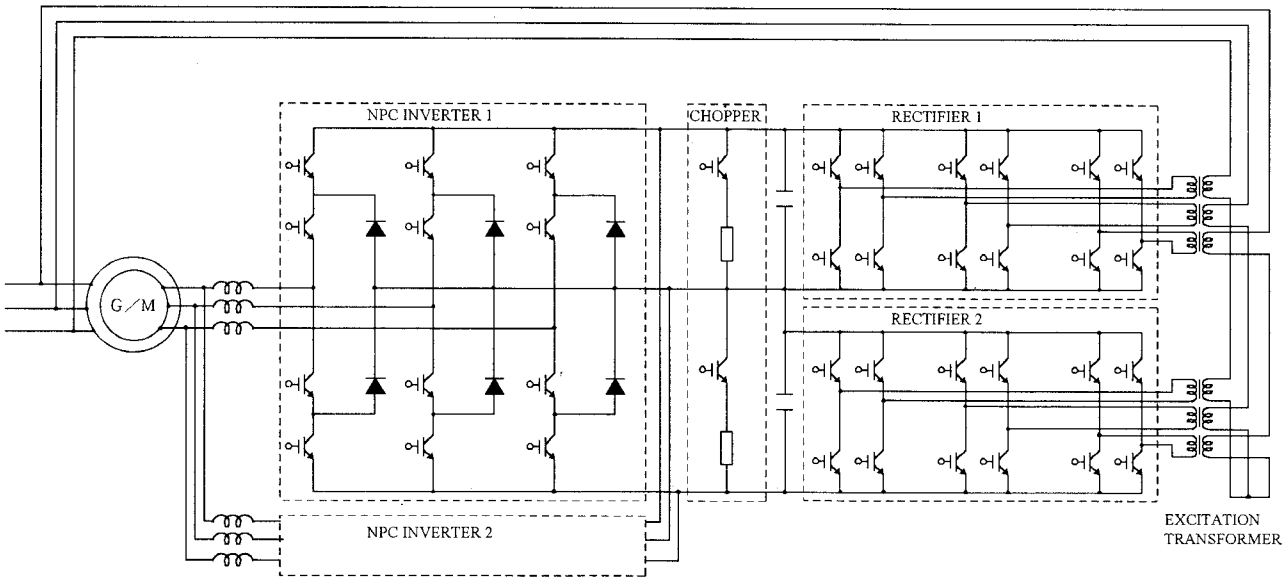

Fig. 2 Detailed main circuit configuration

power and voltage in induction machines and stable continuous operation during electric power network faults.

In this paper, the basic control performance values obtained using a 30-kVA test model are compared with simulated results. The model consists of a generator/motor (wound-rotor induction machine) with a flywheel and dc link IGBT converter for excitation. EMTP (Electro-Magnetic Transient Program) was used for the simulation. It is demonstrated that the system can be operated continuously and stably even during such electric power faults as 1-line, 2-line or 3-line ground faults.

II. SYSTEM CONFIGURATION

Fig.1 shows the configuration of an adjustable speed generation system using a slip-power recovery control scheme of an induction machine. The generator/motor G/M (wound-rotor induction machine) is excited by a dc link converter which consists of a PWM controlled rectifier and inverter. Since the capacity of the dc link converter reaches several tens of MVA in practical applications, parallel and/or multiple connections of several sets of inverters and rectifiers are used and GTOs are employed as the switching devices.

A 30-kVA test model is developed to confirm the basic performance values of the system. Fig.2 shows a detailed main circuit configuration of the model. Two neutral-point clamped (NPC) inverters and two PWM rectifiers with three single full-bridge circuits are used, considering capacity of the converter and harmonics in the electric power network in practical applications. Though IGBTs are employed as switching devices, switching frequency of the IGBTs is limited below 450Hz (9 pulses $\times$ 50Hz), supposing that GTOs are employed in practical applications. Two choppers are connected to the dc link to suppress the overvoltage induced in the secondary windings of the generator/motor during electric power network faults.

Fig.3 shows a detailed control block diagram of the system. In the inverter control section, there is active power and voltage control of the adjustable-speed generation system in the major loop and active/reactive currents control of the secondary currents of the induction machine in the minor loop. To control the active power preferentially, speed control is set outside the active power control. The inverter controls active power and voltage of the system in agreement with commands.

In the rectifier control section, there is dc link voltage control in the major loop and active/reactive currents control in the minor loop. The rectifier keeps the dc link voltage constant, by operating at a power factor of unity in the ac input.

Power flow control between the inverter and the rectifier is employed for continuous operation during faults, in addition to overvoltage suppression control by the choppers. In the former, the power flow from the generator/motor to the inverter is detected by multiplying inverter currents and voltages, and then the current component equivalent to the power flow is added to the active component command of the rectifier currents which is obtained by the link voltage controller. As a result, the dc link voltage can be prevented from changing rapidly and kept nearly constant even during faults. When the power flow is too large, the choppers operate to suppress the dc link overvoltage because only the power flow control cannot sufficiently suppress the rapid change of the dc link voltage.

The control block is composed of multi 32-bits RISC type microprocessors to obtain quick responses. The minimum sampling time is 185 μs in these micro

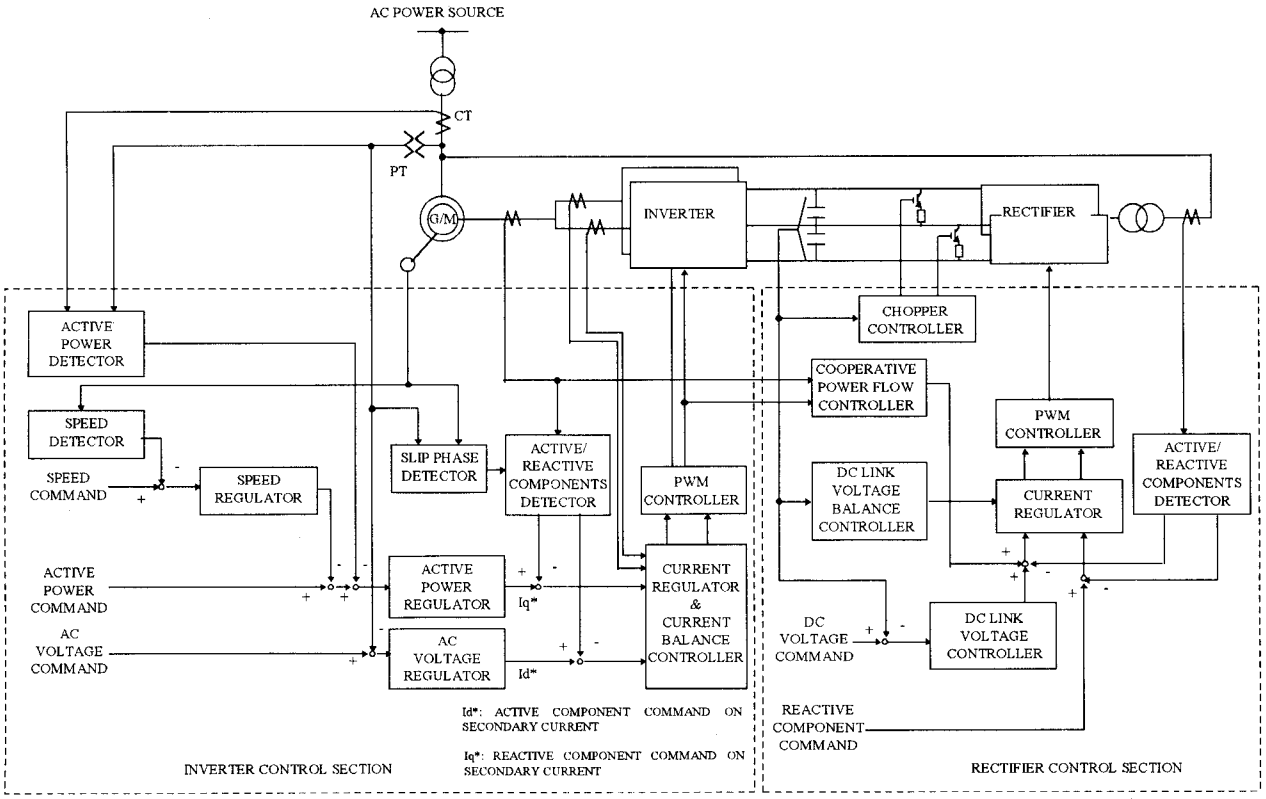

Fig. 3 Detailed control block diagram.

processors.

III. Control Characteristics

In this section, the basic control characteristics of the 30-kVA test model are shown.

A. Active power control

Fig. 4 shows experimental results in the 30-kVA model at the step response of active power on the secondary side of the main transformer, which is the active power supplied or consumed by the adjustable speed generation system. In this case, power flow is from the ac power source (electric power network) to the generator/motor. Therefore, the generator/motor operates as a motor. Very quick response of the active power is obtained. The peak value of the active power is 0.7pu, and the time constant of the response is 25ms, namely the cutoff angular frequency is 40 rad/s. In the figure, the reactive power on the secondary side of the main transformer changes rapidly to keep the primary voltage of the generator/motor constant. This is because the primary voltage changes due to the effect of the impedance in the main transformer and generator/motor, if the current of the power network is changed. For the active power change, the phase of secondary currents of the generator/motor changes rapidly, and the peak value of the secondary currents increases to 0.8pu. Since the generator/motor is accelerated, the frequency also

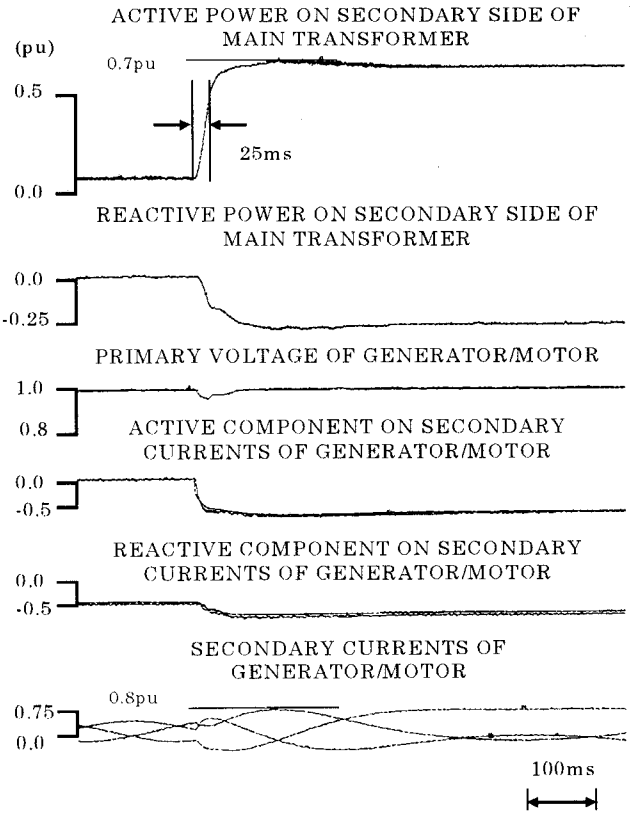

Fig. 4 Step response of active power (Experimental results)

changes.

B. Voltage control

Fig. 5 shows experimental results at the step response of voltage on the secondary side of the main transformer, that is the voltage generated by the adjustable speed generation system. In this case, the ac voltage command changes from 0.8pu to 0.6pu. The time constant of the response is 25ms, namely the cutoff angular frequency is 40rad/s. Active power on the secondary side of the main transformer is kept constant. In this case, the amplitude of secondary currents of the generator/motor increases rapidly, and reactive power on secondary side of the main transformer changes from 0.5pu to 0.7pu.

As shown in figs. 4 and 5, both active power and voltage of the system can be controlled within nearly one cycle of the electric power network frequency which is 50Hz. So, it is confirmed that sufficient control performances for stabilization of the electric power networks can be obtained.

IV. Simulated Results During Electric Power Network Faults

For practical applications of the adjustable speed generation system with a flywheel to the electric power network stabilizer, stable continuous operation during electric power network faults is very important. Behaviors are simulated during electric power network faults.

A. 1-line ground fault

Fig. 6 shows the simulated behavior by EMTP (Electro-Magnetic Transient Program) during a 1-line ground fault. In this case, the electric power network experiences the 1-line ground fault for 90 ms. After that, the line with the ground fault is opened to clear the fault and then the network keeps the condition of one-phase open for about 900ms. In this case, a step change of the active power command on the secondary side of the main transformer is also applied when the line with the ground fault is opened. A large voltage with a frequency of (2-s)f is induced in the secondary windings of the generator/motor during the fault, where s is slip of the generator/motor and f is frequency of the electric power network. However, the secondary current due to the large voltage can be suppressed and the dc link voltage can also be kept almost constant by the power flow control between the inverter and rectifier. Primary voltage of the generator/motor decreases about 0.71pu during the fault. Peak values of secondary currents and the dc link voltages are 1.40pu and 1.06pu, respectively. As a result, there is no need to stop operation of the system. Although the power network is an unbalanced circuit, the active power is rapidly increased and kept

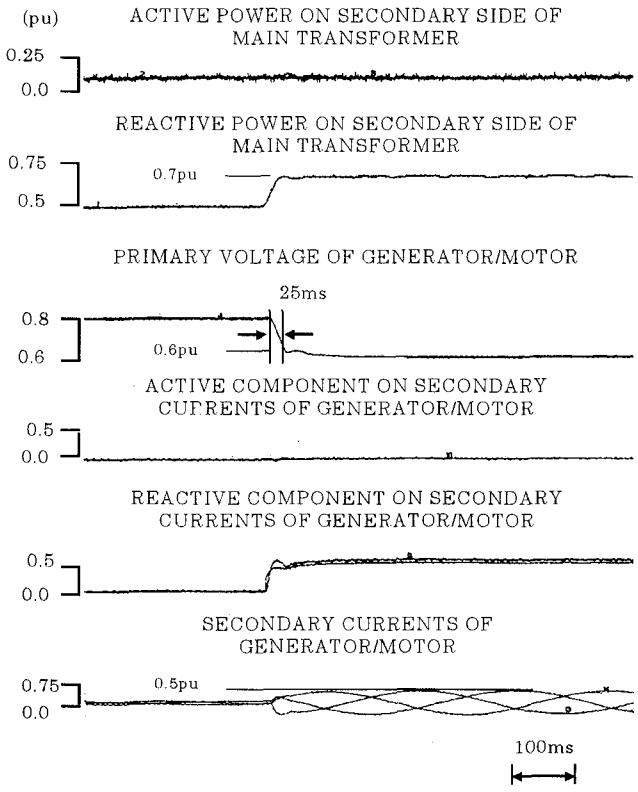

Fig. 5 Step response of primary voltage of generator/motor

(Experimental results)

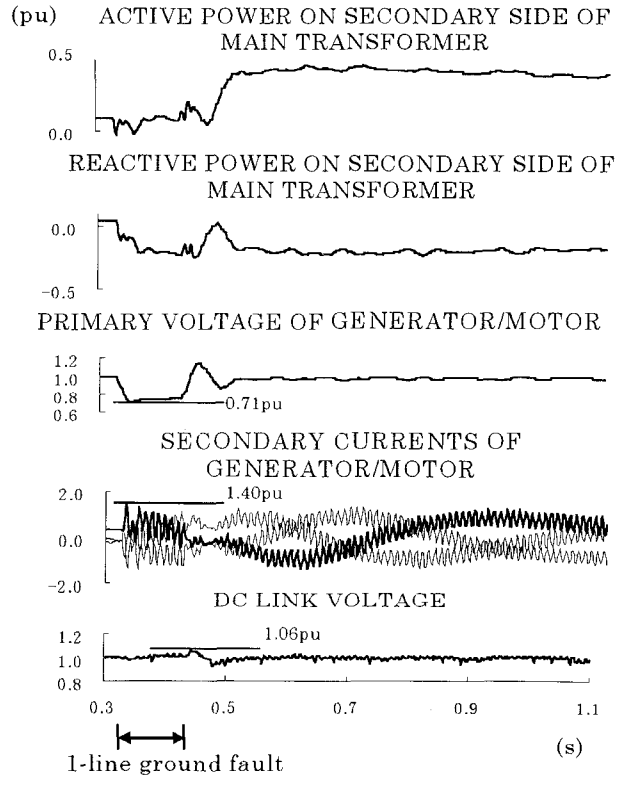

Fig. 6 Behavior during 1-line ground fault in electric power network

(Simulated results)

almost constant, and voltage of the generator/motor is also kept constant.

B. 3-line ground faults

Fig. 7 shows simulated behavior during a 3-line ground fault. In this case, the electric power network experiences a 3-line ground fault for 90 ms, and the lines with the ground fault are opened to clear the fault after that. Since the network has two sets of transmission lines, the network recovers to normal conditions after the lines with the ground fault are opened, though the impedance of the network increases a little. Also in these cases, the active power command changes in step just after the fault is cleared the same as in fig. 6. Overvoltages with a frequency of (1-s)f, or rotating frequency are induced in the secondary windings of the generator/motor, because dc currents flow in the primary windings during the fault. However, the secondary currents due to the overvoltage can be suppressed by cooperative power flow control between the inverter and rectifier, and chopper control. From the figure, it can be seen that the chopper starts to operate to suppress the dc link overvoltage when the dc link voltage reaches 1.2 pu. As a result, the dc link voltage is suppressed below 1.2 pu and is kept nearly constant a little while after the fault is cleared. The primary voltage of the generator/motor, namely the voltage generated by the adjustable speed generation system decreases to nearly zero during the fault, and peak value of the secondary currents of generator/motor is 2.35pu. After the fault, the primary voltage is immediately returned to the value before the fault by the voltage control in the inverter section. Continuous operation and quick active power control during the fault are also possible.

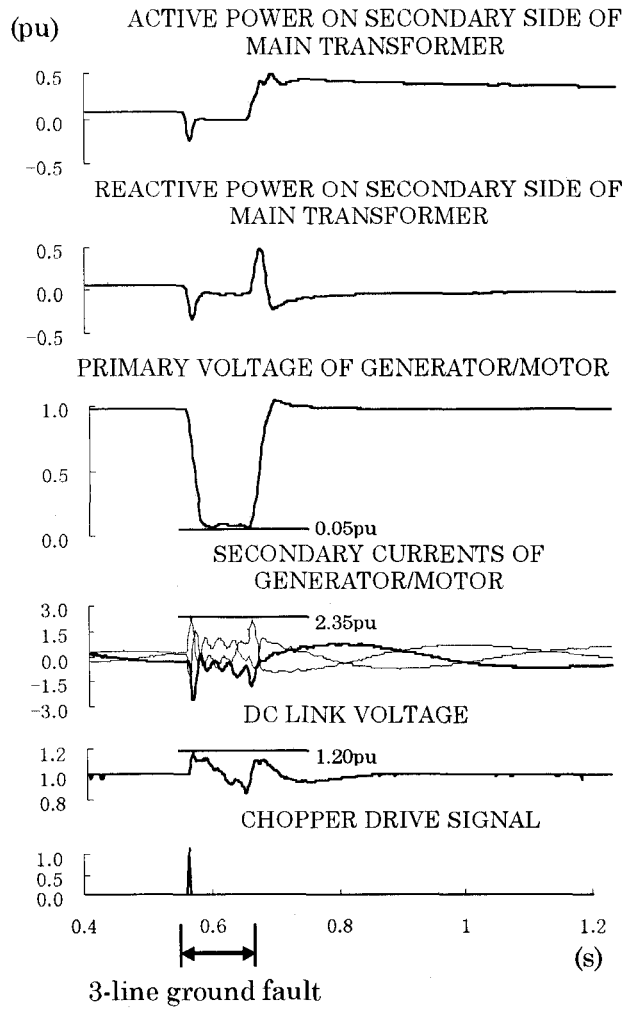

Fig. 7 Behavior during 3-line ground fault in electric power network (Simulated results)

V. Experimental Results During Electric Power Network Faults

A. 1-line ground fault

Fig.8 shows experimental results of the 30-kVA model for the same conditions as the simulated results shown in fig. 6. Primary voltage of the generator/motor decreases 0.77pu during the fault, peak value of secondary currents is 1.40pu, and peak value of dc link voltage is 1.10pu. The experimental results are in good agreement with simulation findings. The secondary currents due to the large voltage induced in the secondary windings of the generator/motor can be suppressed and the dc link voltage can also be kept almost constant by the power flow control between the inverter and rectifier. As a result, there is no need to stop operation of the system. Moreover, the active power can be controlled stably and quickly though it shows a little fluctuation during and after the fault.

B. 3-line ground faults

Fig. 9 shows experimental results for the same conditions as the simulations shown in fig. 7. From figs. 7 and 9, it can be seen that the experimental results agree approximately with the simulated results. Choppers start to suppress the dc link overvoltage when the dc link voltage reaches 1.2 pu. As a result, the dc link voltage is suppressed below 1.2 pu and is kept nearly constant a little while after the fault is cleared. The primary voltage of the generator/motor is decreased to nearly zero, and peak value of secondary currents is 2.40pu during the fault. After the fault, the primary voltage is immediately recovered to the value before the fault by the voltage control in the inverter section.

From figs. 6 to 9, it is seen that continuous operation and quick active power control are also possible without breakdown of the dc link converter during and after 1-line ground fault, or 3-line ground fault. For other faults such as 2-line ground fault, continuous operation and stable active power control can be realized.

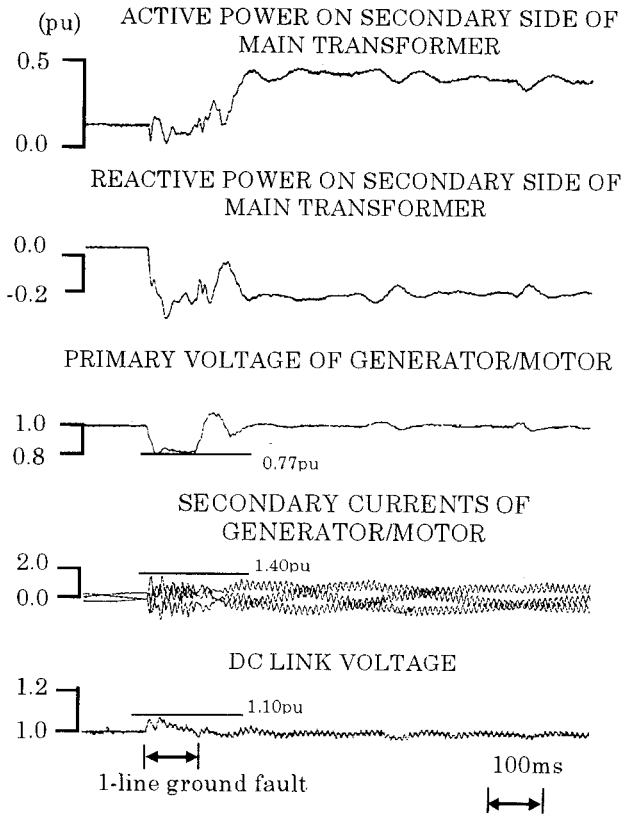

Fig. 8 Behavior during 1-line ground fault in electric power network

(Experimental results)

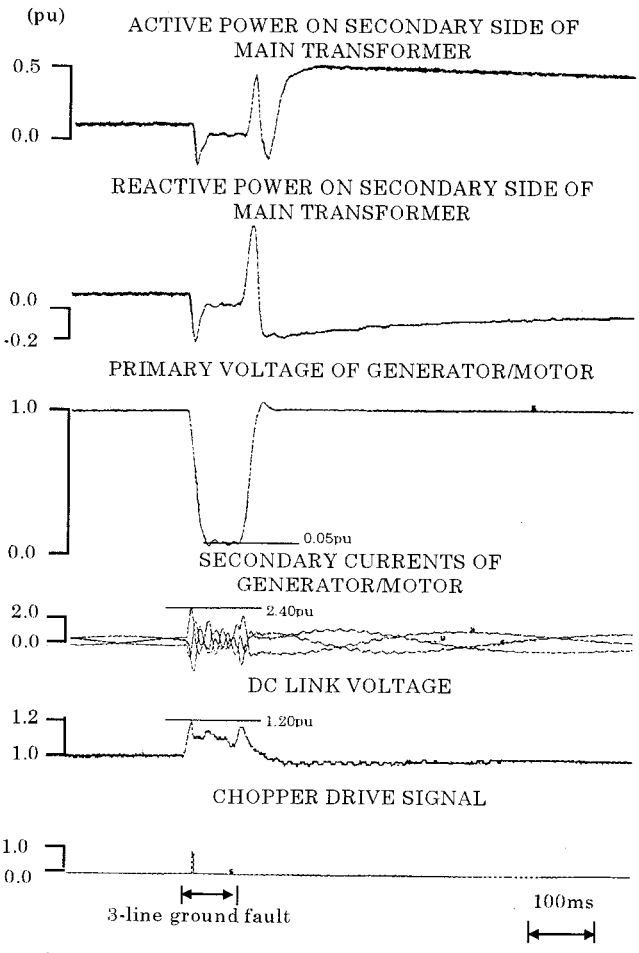

Fig. 9 Behavior during 3-line ground fault in electric power network

(Experimental results)

Although differences between the simulated and experimental results exist, simulations can evaluate the behaviors during electric power network faults including the control characteristics.

VI. Conclusion

To put an adjustable speed generation system with a flywheel into practical application as an electric power network stabilizer, a 30-kVA model was developed to evaluate basic control characteristics and the probability of continuous operation during electric power network faults.

For active power and voltage controls of the system, quick responses of 40 rad/s could be obtained. Continuous operation and stable active power control could be realized even during such faults as 1-line, 2-line and 3-line ground faults. These characteristics were considered sufficient to improve the electric network stability.

From comparison of the experimental and simulated results, it was confirmed that the simulations have high accuracy. Therefore, it is possible to make use of simulated results for designing and manufacturing practical systems with capacities of hundreds of MVA.

The adjustable speed generation system with a flywheel should contribute remarkably to stability and overvoltage suppression of electric power networks.

References

[1] J. Noda, et al., "Speed Control Systems for Wound-Rotor Induction Motors," *Hitachi Review*, 30, 1981, pp263-268

[2] M. Hombu, et al., "Harmonic Analysis on a Slip-Power Recovery System Fed by DC Link GTO Converter," *Conference Record of EPE '95*, 1995, pp3.239-3.244.

[3] T. Nishio, K. Minoguti, M. Endo, Y. Yasaka and M. Goto, "Study of Super Rotary Stabilizing System," in *Proceedings of the Seventh Annual Conference of Power & Energy Society. I.E.E. Japan*, 1996, pp349-350(in Japanese).

[4] T. Nishio, K. Minoguti, M. Higuti, and A. Maoka, "Equipment For Verification Of Super Rotary Stabilizing System," in *Proceedings of the Seventh Annual Conference of Power & Energy Society. I.E.E. Japan*, 1996, pp351-352(in Japanese).

[5] T. Nishio, K. Minoguti, M. Futami, M. Ichinose and Y. Kubota, "Control Response of Super Rotary Stabilizing System," in *Proceedings of the Seventh Annual Conference of Power & Energy Society. I.E.E. Japan*, 1996, pp353-354(in Japanese).

[6] T. Nishio, A. Ryoman, A. Maoka, M. Futami and M. Endo, "Step Response Test of Super Rotary Stabilizing System," in *National Convention Record I.E.E. Japan*, 1997, pp6.524-6.525(in Japanese).

Stabilization of Electric Power System using the Variable Speed Flywheel Generator

Satoshi Uemura, Shinichi Nomura, Ryuichi Shimada
Tokyo Institute of Technology
2-12-1 O-okayama, Meguro-ku, Tokyo 152, JAPAN
Fax:+81-3-5499-7217, Phone:+81-5734-3328
E-mail:suemura@nr.titech.ac.jp

The consumption of electric power will be more enormous and an electric power system must transfer larger active power surely. It is necessary to equip the system to control active power continuously and rapidly. In recent years, a variable speed flywheel generator (VSFG) is used to compensate a flicker caused by an arc furnace [1].

In this paper, authors propose to use the VSFG for stabilizing a power system and show that parallel-type of the VSFG generator stabilizes system power swing and series-type generates reactance voltage to compensate line inductance of power system by experiment.

The experiment using the M-G set simulator with wound type induction motor with flywheel are carried out to demonstrate the stabilizing and controlling ability.

I .INTRODUCTION

The consumption of an electric power will be more enormous and an electric power system must transfer larger active power surely. However, at present, an energy storage component does not exist in the power system. So, it is necessary to equip the system to control active power continuously and rapidly. In recent years, the variable speed generator that is excited by cycloconverter has been developed to sophisticate the pumped storage power station. Moreover the variable speed flywheel generator is used to compensate flicker caused by an arc furnace.[1]

Authors propose to use the VSFG for a power system equipment and show the stabilizing and controlling ability [2,3].

II . VARIABLE SPEED FLYWHEEL GENERATOR

When a flywheel generator charges or discharges the energy, the rotor speed must change according to the variance of stored energy. Therefore, the output frequency of a conventional synchronous generator should change, too. To use the flywheel generator for a power system controller, the output voltage and frequency must be kept constant regardless of variance of the rotor speed.

Now consider a case that the stator is connected to power system that commercial frequency is ω_1, and the rotor speed is ω_r. The rotor has three phase windings. This winding is connected to the power supply that is driven with a slip frequency ω_s. This slip excites a flux that is rotating with ω_1 when the flux is observed from the rotor. So, the generator can be operated as the DC-excited rotor is rotating with ω_r. Therefore, the voltage that is induced on the stator becomes constant regardless of the rotor speed by changing the exciter frequency according to the rotor speed.

A. *Control method for the Variable Speed Generator*

In order to obtain a rated armature current when the variable speed generator is connected to power system, it is necessary to keep the flux direction at $\theta+\pi/2$ rad relative to the voltage vector, where θ is the load angle or the internal phase angle.

The flux reference direction, ds-axis, on the rotor coordinate is determined by the voltage phase detector which are attached to the generator shaft. Then the excitation converter controls magnitude and angle of the flux to keep the rated armature current at this control method, it becomes possible to control the instantaneous power at any shaft speed. Though the current controlled exciter is used to control this generator , we chose the voltage controlled exciter for the following reason.

(1) It is necessary to control the secondary current by the exciter when the secondary voltage is a manipulated variable for the control system. Therefore, the configuration of control system becomes simple.

(2) Secondary sensor is not required, because the exciter can be controlled by the primary voltage and current.

The d-q voltage equation for the variable speed generator can be expressed as follows:

$$\begin{pmatrix} v_{1d} \\ v_{1q} \\ v_{2d} \\ v_{2q} \end{pmatrix} = \begin{pmatrix} r_1+pL_1 & -\omega_1 L_1 & pM & -\omega_1 M \\ \omega_1 L_1 & r_1+pL_1 & \omega_1 M & pM \\ pM & -\omega_s M & r_2+pL_2 & -\omega_s L_2 \\ \omega_s M & pM & \omega_s L_2 & r_2+pL_2 \end{pmatrix} \begin{pmatrix} i_{1d} \\ i_{1q} \\ i_{2d} \\ i_{2q} \end{pmatrix} \quad (1)$$

Where, L_1, L_2 and M are primary self-inductance, secondary self-inductance and mutual inductance, r_1 and r_2 are primary and secondary winding resistance. Suffixes 'd' and 'q' means d-axis and q-axis component, and suffixes

'1' and '2' means primary and secondary values respectively.

P_1 and Q_1 are active and reactive power of the stator, P_2 and Q_2 are active and reactive power of the rotor. These parameters are given by below equations,

$$\left.\begin{aligned} P_1 &= \frac{3}{2}\left(v_{1d}i_{1d} + v_{1q}i_{1q}\right) \quad P_2 = \frac{3}{2}\left(v_{2d}i_{2d} + v_{2q}i_{2q}\right) \\ Q_1 &= \frac{3}{2}\left(v_{1q}i_{1d} - v_{1d}i_{1q}\right) \quad Q_2 = \frac{3}{2}\left(v_{2q}i_{2d} - v_{2d}i_{2q}\right) \end{aligned}\right\} \tag{2}$$

This control method does not require the shaft torque control, but fast control of the stator power is necessary. Therefore, primary interlinkage flux and primary current are used as state variables. Not only the influence of the primary leakage inductance is negated, but also there is an advantage that the flux will be kept constant when the infinite-bus is connected to the stator. The primary interlinkage flux λ_{1d} and λ_{1q} are obtained by following equation,

$$\begin{pmatrix} \lambda_{1d} \\ \lambda_{1q} \end{pmatrix} = L_1 \begin{pmatrix} i_{1d} \\ i_{1q} \end{pmatrix} + M \begin{pmatrix} i_{2d} \\ i_{2q} \end{pmatrix} \tag{3}$$

The voltage equation is obtained from Equation(1) and (3) as follows:

$$\begin{pmatrix} v_{1d} \\ v_{1q} \\ v_{2d} \\ v_{2q} \end{pmatrix} = \begin{pmatrix} r_1 & 0 & p & -\omega_1 \\ 0 & r_1 & \omega_1 & p \\ -\frac{L_1}{M}r_2 - pl_m & \omega_s l_m & \frac{r_2}{M} + p\frac{L_2}{M} & -\omega_s\frac{L_2}{M} \\ -\omega_s l_m & -\frac{L_1}{M}r_2 - pl_m & \omega_s\frac{L_2}{M} & \frac{r_2}{M} + p\frac{L_2}{M} \end{pmatrix} \begin{pmatrix} i_{1d} \\ i_{1q} \\ i_{2d} \\ i_{2q} \end{pmatrix} \tag{4}$$

where, the leakage inductance l_m is defined as $l_m = \left(L_1 L_2 - M\right)/M$. The reference axis, d-axis is set on the direction of primary interlinkage flux, and λ_{1q} is defined zero. When the voltage drop by the primary resistance is enough small, v_{1d} can be treated as zero. When the bus voltage v_{1q} and frequency ω_1 are constant, λ_{1d} also becomes constant. Therefore, $p\lambda_{1d}$ and $p\lambda_{1q}$ are zero. When these approximations are introduced, the generator output and the exciter voltage are expressed by the primary voltage and the primary current as following equations, and the reference value of the exciter voltage is obtained,

$$\left.\begin{aligned} P_1 &= \frac{3}{2}v_{1q}i_{1q} \\ Q_1 &= \frac{3}{2}v_{1q}i_{1d} \end{aligned}\right\} \tag{5}$$

$$\begin{pmatrix} v_{2d} \\ v_{2q} \end{pmatrix} = \begin{pmatrix} \frac{r_2}{\omega_1 M}v_{1q} \\ \frac{\omega_s L_2}{\omega_1 M}v_{1q} \end{pmatrix} + \begin{pmatrix} -\frac{L_1}{M}r_2 & \omega_s l_m \\ -\omega_s l_m & -\frac{L_1}{M}r_2 \end{pmatrix} \begin{pmatrix} i_{1d} \\ i_{1q} \end{pmatrix} \tag{6}$$

The stator current i_{1d} and i_{1q} are obtained from P_1 and Q_2, the exciter voltage is determined, then generator output power is controlled. But the current is expressed by both the primary current and the primary projected secondary current because the controlled object is primary current. Owing to these approximations and control errors, sufficient primary current cannot be gained from only the exciter voltage. Therefore, some feedback control is required[4].

Ⅲ. STABILIZATION OF SYSTEM POWER SWING BY PARALLEL-TYPE VARIABLE SPEED FLYWHEEL GENERATOR

A. *Configuration of the experimental system*

Figure1 shows a model power system which is used in the experiment. The system has synchronous generator that

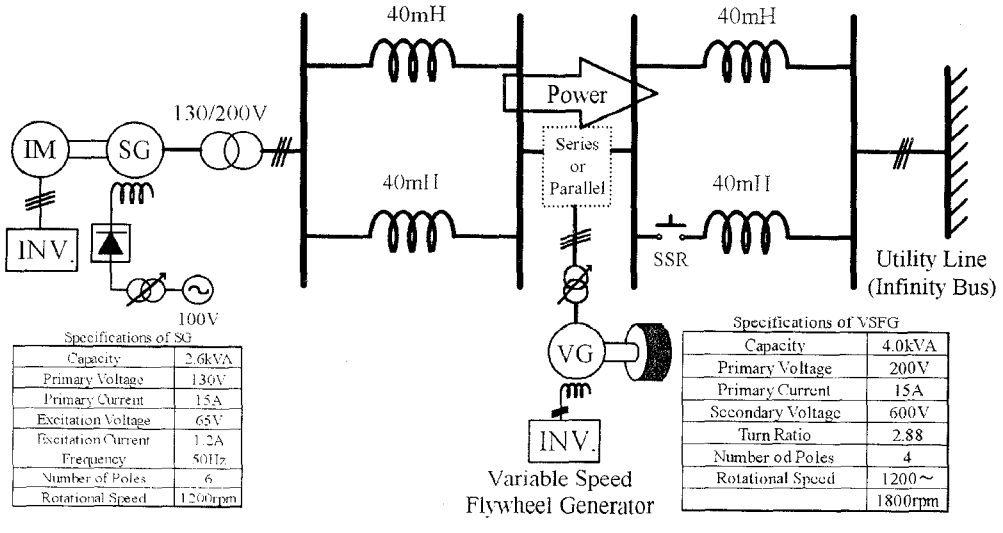

Specifications of SG

Capacity	2.6kVA
Primary Voltage	130V
Primary Current	15A
Excitation Voltage	65V
Excitation Current	1.2A
Frequency	50Hz
Number of Poles	6
Rotational Speed	1200rpm

Specifications of VSFG

Capacity	4.0kVA
Primary Voltage	200V
Primary Current	15A
Secondary Voltage	600V
Turn Ratio	2.88
Number od Poles	4
Rotational Speed	1200~
	1800rpm

Fig.1. Experimental system

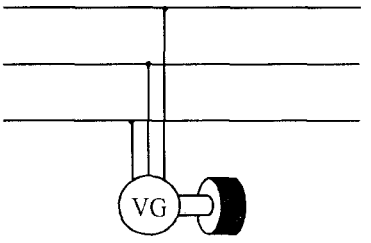

Fig.2. Parallel-type VSFG

is connected with infinite-bus through the reactors being equivalent to line inductance. This reactors is connected in parallel as shown in Fig.1. The parallel-type VSFG is connected in parallel as shown in Fig.2 at the middle point of a synchronous generator and an infinite-bus. The power system swing is caused by opening one line by Solid State Relay and is leveled by the parallel-type VSFG. VSFG is composed of a wound type induction motor with a flywheel and a PWM inverter to excite secondary windings.

B. *Control method for the parallel-type VSFG*

Figure3 shows a control block diagram for the parallel-type VSFG. The control method which described in section Ⅱ is represented with a block diagram as shown in Fig.3. P^* and Q* are desired values of active and reactive power. These values is made according to the block diagram as shown in Fig.4. Active power is leveled by pid control and

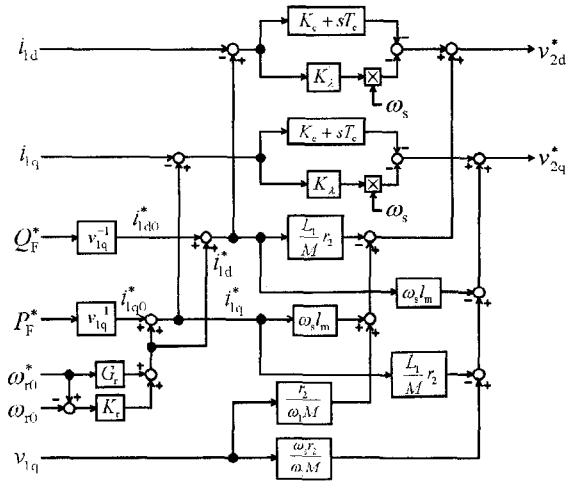

Fig.3. Control block diagram

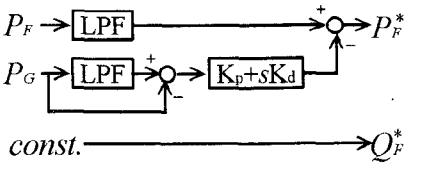

Fig.4 Block diagram for desired values, P_F* and Q_F*

desired value of reactive power is constant.

C. *Experimental Result*

Figure5 shows experimental results of stabilizing the model power system using the parallel-type VSFG.

(a) shows an active power swing when voltage phase difference between an infinite-bus and a synchronous generator is 40 degree. The parallel-type VSFG levels an active power swing rapidly.

(b) shows an active power swing when voltage phase difference between an infinite-bus and a synchronous generator is 75 degree. In the case of non-VSFG system, the synchronous generator steps out. In the case of VSFG system, active power is leveled rapidly.

Ⅳ. COMPENSATION OF LINE INDUCTANCE BY SERIES-TYPE VARIABLE SPEED FLYWHEEL GENERATOR

A. *Configuration of the experimental system*

The model power system is the same as a system which is described in section Ⅲ-A except VSFG. The series-type VSFG is connected in series through the transformer at the

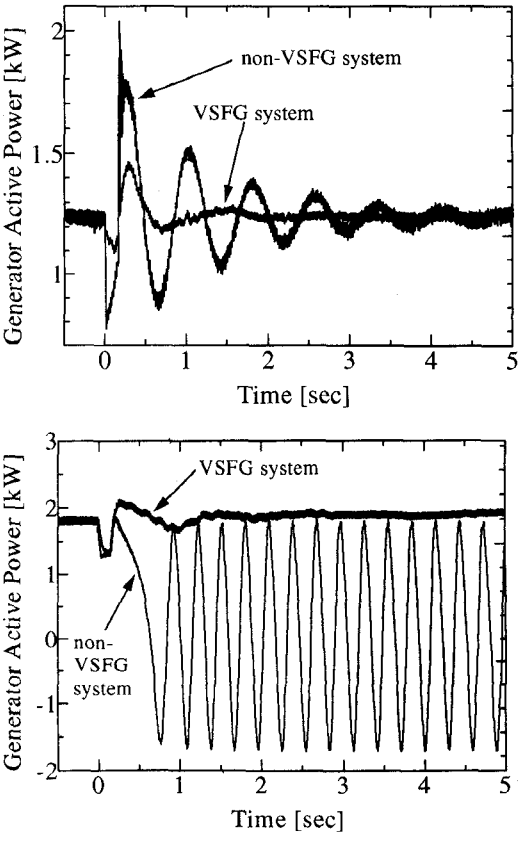

Fig.5. Experimental results of stabilizing power system

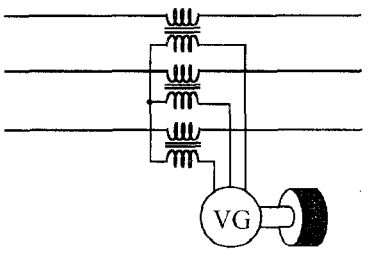

Fig.6. Series-type VSFG

same point as parallel-type as shown in Fig.6.

B. Control Method for the series-type VSFG

Figurer7 shows a control block diagram for a series-type VSFG. The phase angle of primary current i_1 must become quadrature to that of primary voltage in order to generate reactance voltage. Therefore, the desired values i_{1d}^* and i_{1q}^* decided by primary voltage v_{1d} and v_{1q}.

C. Experimental Result

Figure8 shows an experimental result of generating reactance voltage. The horizontal axis shows generating voltage by series-type VSFG and the vertical axis shows reactance value that calculated from the voltage of a transformer (power system side) and the current of the power system. The relation of two values is almost linear. This graph means that series-type VSFG can generate reactance voltage which has desired value.

V. CONCLUSION

This paper describes the results of the test on stabilization by a parallel-type variable speed flywheel generator on a model power system. The effect of the use of

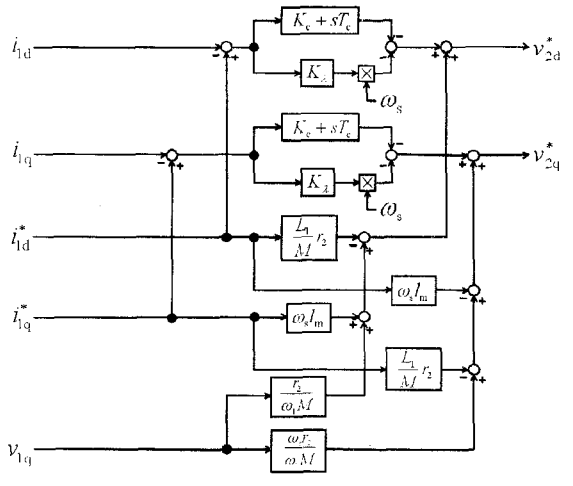

Fig.7. Control block diagram

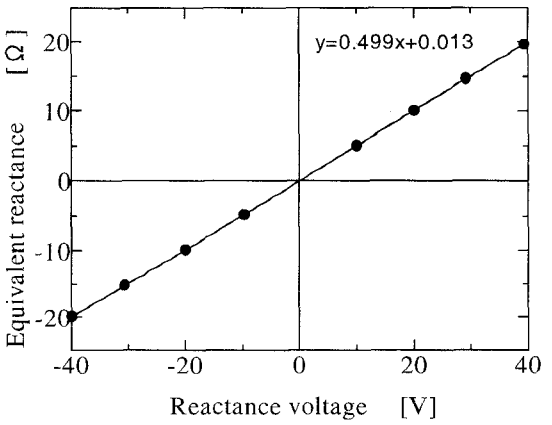

Fig.8. Experimental results of generating reactance voltage

the parallel-type variable speed flywheel generator on stabilizing the power system swing was verified.

Moreover, this paper describes the results of the test on generation by a series-type variable speed flywheel generator on a model power system. The effect of the use of a series-type variable speed flywheel generator on generating the reactance voltage was verified.

Authors expect using this system for a power system equipment because this system has many fine functions.

However, there is a problem of protecting this machine, especially series-type when power system fault occur.

APPENDIX

Table 1. Constants of Variable Speed Flywheel Generator

Constants of VSFG			
Primary Resistance	r_1	0.353	Ω
Secondary Resistance	r_2	4.15	Ω
Primary self-inductance	L_1	136	mH
Secondary self-inductance	L_2	1040	mH
Mutual Inductance	M	352	mH
Equivalent Leakage Inductance	l_m	8.2	mH
Inertial Moment		0.17	kgm^2

REFERENCES

[1] M.Kaneshiro, N.Miyagi, S.Nohara,T.Yamamoto, T.Takanashi, *IEE Japan* PE-92-114 (1992)

[2] M.Tatematsu, A.Yokoyama, "Stabilization of Multi-Machine Power System by Coordinated Excitation Control of Multiple Adjustable-Speed Generator/ Motor", *T.IEE Japan* **116B**, 197(1995).

[3] K.Nojiri, T.Kikuchi, H.Nakagawa, "Improvement of Power System Stability by High Speed Power Control of Adjustable Speed Machine", *T.IEE Japan* **117B**, 203(1997)

[4] H.Chikaraishi, N.Eguchi, H.Hirayama, S.Uemura, R.Shimada,"Fast Response Power Stabilizer using the AC-Excited Flywheel Generator", Proceeding of IPEC-Yokohama, Vol.2, pp1044-1049 (1995).

Design Procedure and Performance Evaluations of Utility-Interactive Bidirectional Resonant DC Link Three Phase ZVS-PWM Power Conditioner

T.Shimizu, M.Kurokawa, Y.Matsumoto, A.Chibani and M.Nakaoka
The Graduate School of Engineering and Science,
Yamaguchi University,
2557 Tokiwadai Ube-City Yamaguchi,755 Japan
Tel:+81-836-35-9946 Fax: +81-836-35-9449
E-mail : shimizu@pe-news1.eee.yamaguchi-u.ac.jp

Abstract - **This paper describes an operating principle and features of a newly-developed parallel resonant DC link circuit with active voltage clamped PWM control scheme. In particular, a new conceptual design procedure of resonant DC Link treated here is illustrated and discussed including a practical design example under a zero voltage and zero current soft switching. In this paper, bidirectional power flow three phase voltage-fed PWM converter using a resonant DC link which is applied for utility-interfaced battery energy storage system is analyzed for load leveling, battery charging, reactive current compensation and active filtering schemes. Finally, the system performances of this converter mode or inverter mode and the effectiveness of this resonant DC link circuit topology and resonant DC link power processor are demonstrated on the basis of system simulation results.**

1. INTRODUCTION

In recent years, a variety of three phase voltage-fed inverter or rectifier systems using MOS gate controlled power devices such as MOSFETs, IGBTs, MCTs and MOS SITh, which make the most of converter with soft switching circuit topologies have attracted special interest in power network systems. Three phase voltage-fed inverters and converters with soft-switching circuit topologies are roughly divided into three; resonant-pole, resonant AC Link and resonant DC Link.

In this paper, a new type of the parallel resonant DC Link circuit with active voltage clamped PWM control scheme is adopted, and its operating principle and feautures is introduced. A new conceptual design procedure of resonant DC link treated here is proposed and illustrated from a simulation point of view. Finally, this resonant DC link circuit is newly adopted as the bidirectional power flow three phase voltage-fed PWM converter for utility-interfaced battery energy storage system. This power professor is analyzed and evaluated on the basis of simulation results.

2. PARALLEL RESONANT DC LINK CIRCUIT

Fig.1 shows a prototype of resonant DC Link[1),(2)] treated here. This circuit is connected to the DC bus line of the three phase voltage-fed hard-switching PWM inverter in order to realize soft-switching PWM operation. In principle, AC-side load of the sinewave PWM inverter can be represented as a variable current source Io.Because filter-side inductor is enormously more higher than a resonant inductor, this current source model is more exact. This resonant DC link circuit consists of three active switches (voltage-clamp switch S_1,quasi resonant sub-switches S_2 and S_3), resonant components L, C_1 and C_2 as well as four anti-parallel diodes(D_1, D_2, D_3, D_4).Quasi resonant mode occurs while the switch S_1 is turned off. The voltage across the capacitor C_2 is clamped to Vd. Fig.2 illustrates gate switching sequence for S_1 and S_2 and S_3, and the operating waveforms of voltage across the capacitors C_1 and C_2,and current across the inductor L. Such a quasi resonant operation i achieved.

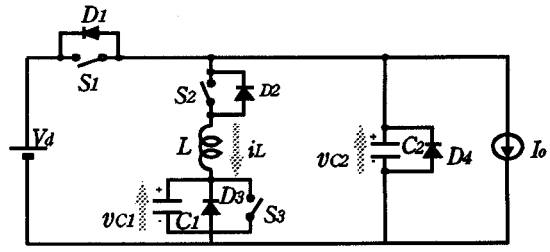

Fig1. Resonant DC link circuit

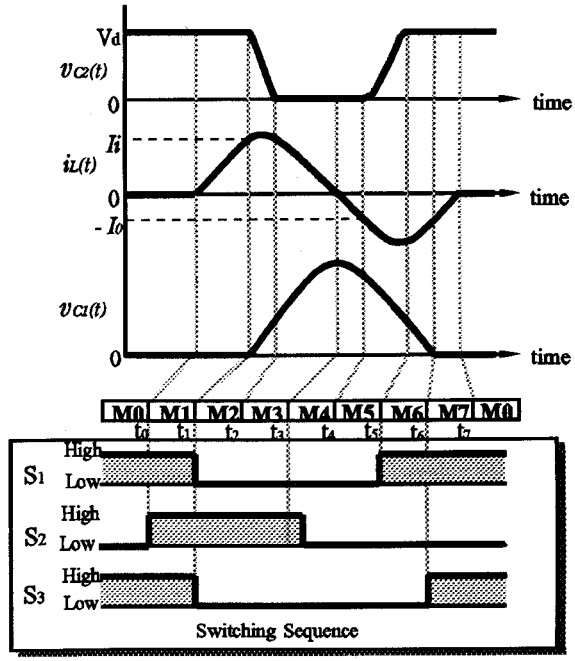

Fig2. Resonant DC Link operating waveform

0-7803-3823-5/97/$10.00© 1997 IEEE

3. EXACT OPERATION OF RESONANT DC LINK CIRCUIT

Fig.3 shows an equivalent circuit of the resonant DC link in the case of energy supply mode for one cycle of operation. The exact operation of this circuit can be divided into eight modes. The operating principle can be explained as follows by using this equivalent circuit .

■ MODE 0 : S_1 and S_3 are ON state, and S_2 is OFF state. PWM operation is achieved by controlling the period of ON-state for S_1. When S_3 is turned ON, the circuit mode changes into the mode 1.

■ MODE 1 : When S_2 is turned OFF with zero current, the resonant inductor current i_L is increasing. When i_L reaches the initial resonant current Ii, S_1 and S_3 are turned off and the circuit mode changes into the mode 2.

■ MODE 2 : When S_1 is turned OFF with zero voltage, quasi-resonant phenomena is begun to start. C_2 is begun to be discharging and C_1 is begun to be charging. When v_{C2} reaches zero, the diode D_4 starts to conduct and the circuit mode changes into the mode 3.

■ MODE 3 : When v_{C2} is equal to zero, D_4 is turned ON under the condition of zero voltage and zero current modes. Thus v_{C2} must not reaches negative value in principle, and v_{C2} holds to zero. Zero voltage soft switching of the converter bridge arm can be achieved by changing converter switching mode while v_{C2} holds to zero. When i_L reaches to negative value, D_2 is turned ON with zero current and the circuit mode changes mode 4. On the other hand, at energy storage mode, when i_L becomes more than Io, D_4 is turned off and the circuit mode changes into mode 4.

■ MODE 4 : At energy supply mode, S_2 can be achieved to be turned OFF with zero voltage while D_2 is conducting. C_1 becomes discharging. when i_L becomes more than Io, D_4 is turned off with zero current and the circuit mode changes into mode 5. On the other hand, at energy storage mode, when i_L becomes more than Io and D4 is turned OFF with zero current, resonant phenomena is begun to start again. When i_L becomes negative value, D_2 is turn ON, the circuit mode changes mode into 5.

■ MODE 5 : When i_L becomes more than Io and D_4 is turned ON with zero current, resonant phenomena is begun to start again at L-C_1-C_2 circuit. At this circuit, S_2 can be turned OFF with zero voltage state. If v_{C2} reaches to V_d, the mode circuit changes into mode 6. If v_{C1} reaches to zero, the mode circuit changes into mode 6'.

■ MODE 6 : In case of mode 6, when v_{C2} reaches to V_d, D_1 is turned ON with zero current and C_1 starts discharging. When v_{C1} reaches to zero, the mode circuit changes mode 7. In case of mode 6', when v_{C1} reaches to zero, D_3 is turned ON with zero voltage and C_2 starts charging. When v_{C2} reaches to V_d, the mode circuit changes mode 7. On the other hand, at energy storage mode, MODE 6' doesn't exist.

■ MODE 7 : When v_{C1} reaches to zero or v_{C2} reaches to V_d, i_L starts decreasing linearly. S_3 can be turned ON with zero voltage while D_3 is ON-state. When i_L reaches to zero, D_2 and D_3 are turned OFF with zero voltage and the circuit mode changes into mode 1.

4. DESIGN CONSIDERATIONS OF RESONANT DC LINK

The design approaches for resonant parameter of DC link are considered as follows. (1) At discharging mode, v_{C2} is exactly decreased to zero from V_d. (2) At charging mode, v_{C2} is exactly increased to V_d from zero.

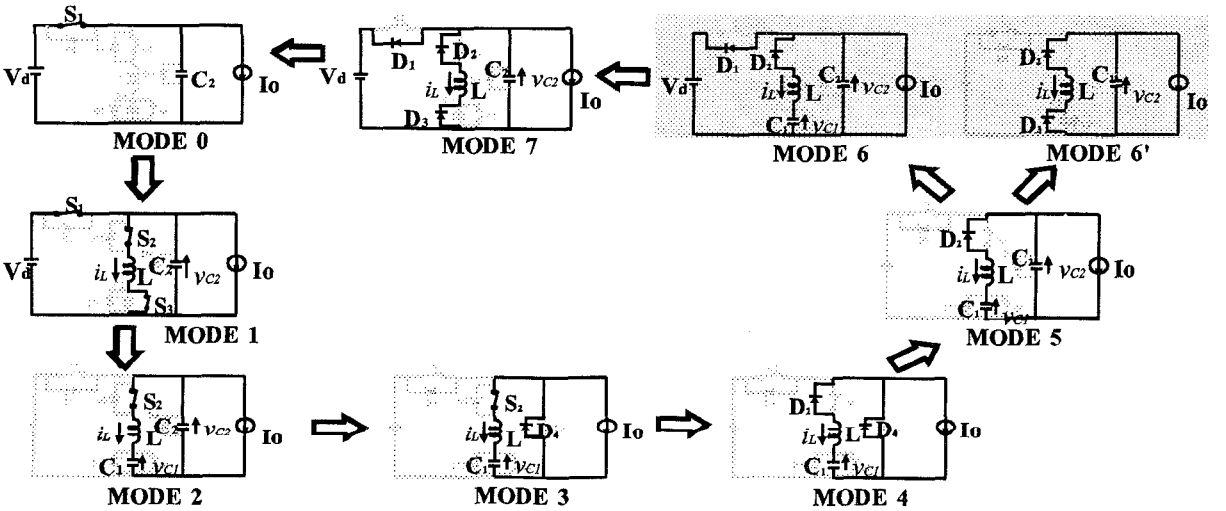

Fig.3 Operating modes equivalent circuit for one cycle
(at energy supply mode)

(3) At resonant mode, maximum value of resonant current is made as small as it can in order to minimize power losses. (4) After resonant phenomena is achieved, the duration times of resonant inductor current flow back to the source are made as short as they can. (5) At a discharge mode, initial resonant current duration times are made short. Initial resonant current is made as small as it can. The new method how to design resonant parameter in the resonant DC link shown in Fig1 is described as follows.

In the first place, the equation (1) is given by using energy balancing law at two initial states of mode2 and mode4. (see Fig. 2 and Fig. 3)

$$\frac{1}{2}L\cdot I_i^2 + \frac{1}{2}C_2\cdot V_d^2 = \frac{1}{2}C_1\cdot v_{C1max}^2 \quad (1)$$

where, resonant circuit parameters; L,C_1,C_2 . Therefore, we must consider the ratio of C_1 and C_2.

In the second place, resonant frequency F_r are defined by

$$F_r=\frac{1}{2\pi\sqrt{LC_1}} \quad (2)$$

if the ratio of resonant capacitor C_1 and C_2 is assumed to be k_1, we can get.

$$k_1=\frac{C_2}{C_1} \quad (3)$$

Thus, C_1 is specified by using ω_r and k_1 .

$$C_1=\frac{I_i}{\sqrt{(v_{C1max}^2 - k_1\cdot V_d^2)\cdot\omega}} \quad (4)$$

If I_i is made minimum, the maximum value of resonant inductor current and inductor current after the resonant phenomena are achieved so as to be minimum value. Therefore, the conditions (3), (4) and (5) for the resonant parameters of this resonant DC link are mentioned, before they are satisfied at the same time. Furthermore, we suppose the ratio of initial resonant inductor current I_i and the maximum value of load current I_{omax} is k_2 ($I_i = k_2 \cdot I_{omax}$) , and the ratio of maximum voltage value across the resonant capacitor C_1 (v_{C1max}) and DC source voltage (V_d) is k_3 ($v_{C1max} = k_3 \cdot V_d$).

Thus, C_1, C_2 and, L are estimated by

$$C_1=\frac{k_2\cdot I_{omax}}{\sqrt{(k_3^2 - k_1)\cdot V_d\cdot\omega_r}} \quad (5)$$

$$C_2=k_1\cdot C_1 \quad (6)$$

$$L=\frac{1}{\omega_r^2\cdot C_1} \quad (7)$$

Therefore, if k_1 and k_2 and k_3 are defined , C_1, C_2 and L can be calculated theoretically.

Design example -

Let, F_r = 150 kHz, V_d = 440V, I_{omax} = 65A .

$k_2=k_3=2$ are obtained, because I_i/I_{omax} and v_{C1max}/V_d are put down less than two times.

The relationships between initial resonant current Ico (Ii =Ico - Io) and k_1 and ZVS area are illustrated while I_o/I_{omax} are changed from -1 to 1 are shown in Fig.4,5,6 and 7.

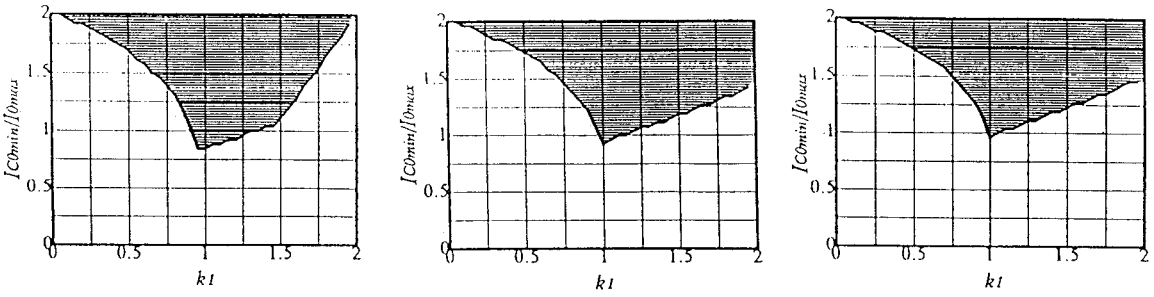

(i) I_o/I_{omax}=0.0 (ii) I_o/I_{omax}=0.6 (iii) I_o/I_{omax}=1.0

Fig4. ZVS Region at the case of changing to Io > 0.0 from Io = 0.0

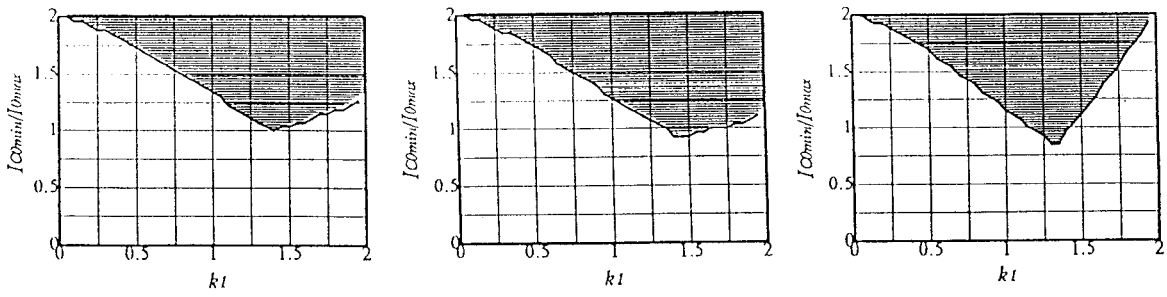

(i) I_o/I_{omax}=1.0 (ii) I_o/I_{omax}=0.6 (iii) I_o/I_{omax}=0.0

Fig5. ZVS Region at the case of changing to Io = 0.0 from Io > 0.0

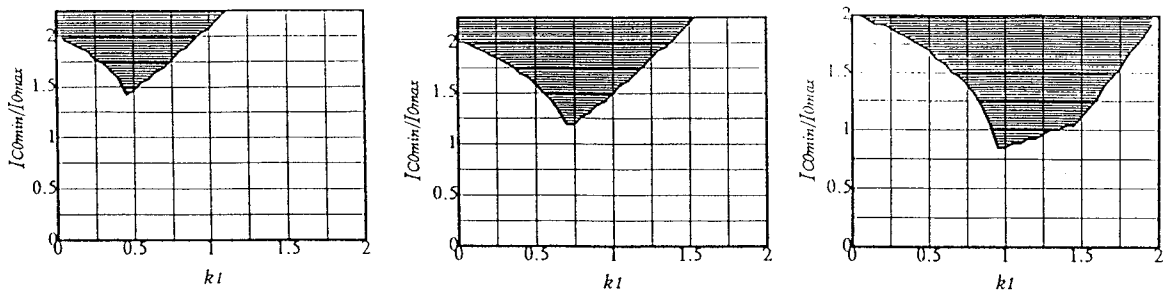

(i) I_o/I_{omax}=-1.0 (ii) I_o/I_{omax}=-0.6 (iii) I_o/I_{omax}=0.0

Fig6. ZVS Region at the case of changing to Io = 0.0 from Io < 0.0

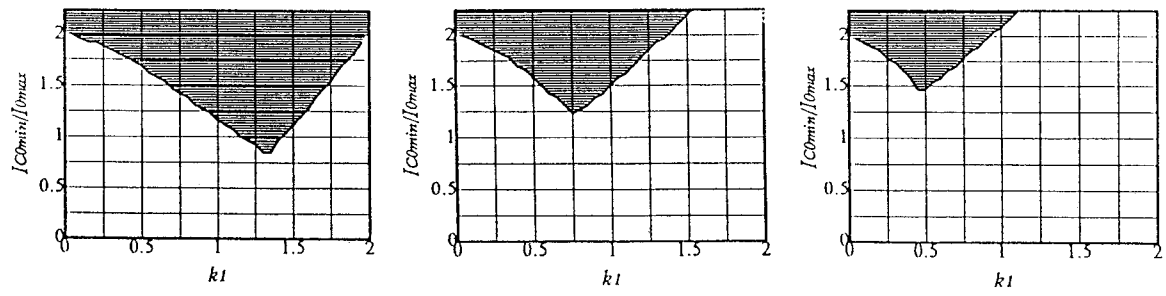

(i) I_o/I_{omax}=0.0 (ii) I_o/I_{omax}=-0.6 (iii) I_o/I_{omax}=-1.0

Fig7. ZVS Region at the case of changing to Io < 0.0 from Io = 0.0

In Fig4, if this power conditioner is operating at energy supply mode, when k_1 equals to 1, ZVS can be achieved at the minimum value of initial resonant current for every load condition. At that time, I_{comin}/I_{omax} nearly equals to 1 at every load condition . That is because it can be specified that k_1 is 1 and I_{co} is 70(A)at inverter operating mode. But if this resonant DC link is used for bidirectional converter, we must consider the converter mode and inverter mode. It is more difficult to specify k_1 and I_{co} for bidirectional application because the characteristics of ZVS region at converter mode is significantly different from ZVS region at inverter mode. (see Fig. 5,6,7)We must work out a compromise. Thus, it si specified that k_1 is 0.6 and I_{co} is 120 (A) which is allowed for a margin. Therefore L=6.62 (μ H), C_1=0.170 (μ F) and C_2=0.102 (μ F), can be estimated by solving the equations (5), (6) and (7).

5.ACTIVE POWER FILTER DIGITAL CONTROL SCHEME

Fig8 shows utility-interactive ZVS-PWM converter with a prototype of resonant DC link. Output voltage v_A and AC reactor current i_c and utilty-grid voltage v_C and load current i_L are defined as follows.

$$v_A=[\,v_{Aa}\ v_{Ab}\ v_{Ac}\,]^T,\quad i_c=[\,i_{Ca}\ i_{Cb}\ i_{Cc}\,]^T$$
$$v_C=[\,v_{Ca}\ v_{Cb}\ v_{Cc}\,]^T,\quad i_L=[\,i_{La}\ i_{Lb}\ i_{Lc}\,]^T$$

v_A, i_c, v_C, i_L is converted into α-β axis plain are defined as follows.

$$\hat{v}_A=[v_{A\alpha}\ v_{A\beta}]^T \quad \hat{i}_C=[i_{C\alpha}\ i_{C\beta}]^T$$
$$\hat{v}_C=[v_{C\alpha}\ v_{C\beta}]^T,\quad \hat{i}_L=[i_{L\alpha}\ i_{L\beta}]^T$$

For batteery Energy Storage System (BESS), the satate equation is

$$L_f\frac{d}{dt}i_c=v_c-v_A-R_{Lf}i_c \quad (8)$$

Converting equation (8) into α-β axis plain are as follows.

$$L_f\frac{d}{dt}\hat{i}_c=\hat{v}_A-\hat{v}_c-R_{Lf}\hat{i}_c \quad (9)$$

If v_A would be constant value for one sampling time Ts, equation (9) can be substituted for

$$\hat{i}_c(i+1)=\frac{1-\exp\left(-\frac{R_{Lf}T_s}{L_f}\right)}{R_{Lf}}\begin{bmatrix}1&0\\0&1\end{bmatrix}(\hat{v}(i)-\hat{v}(i))+\exp\left(-\frac{R_{Lf}T_s}{L_f}\right)\begin{bmatrix}1&0\\0&1\end{bmatrix}\hat{i}(i) \quad (10)$$

Thus, the reference output voltage is given by

$$\hat{v}_A^*(i)=\hat{v}_c(i)+\frac{R_{Lf}}{1-\exp\left(-\frac{R_{Lf}T_s}{L_f}\right)}\begin{bmatrix}1&0\\0&1\end{bmatrix}\left(\hat{i}_c^*(i)-\exp\left(\frac{R_{Lf}T_s}{L_f}\right)\hat{i}_c(i)\right) \quad (11)$$

In a practical system, control equation (11) can not be used, because correction for calculation delay time must be considered.

The pridictive control equation which is considered for calculation delay time is given by

$$\hat{v}_A^*(i+1)=\hat{v}_c'(i+1)+\frac{R_{Lf}}{1-\exp\left(-\frac{R_{Lf}T_s}{L_f}\right)}\begin{bmatrix}1&0\\0&1\end{bmatrix}\left(\hat{i}_c^*(i+1)-\exp\left(-\frac{R_{Lf}T_s}{L_f}\right)\hat{i}_c'(i+1)\right) \quad (12)$$

where,

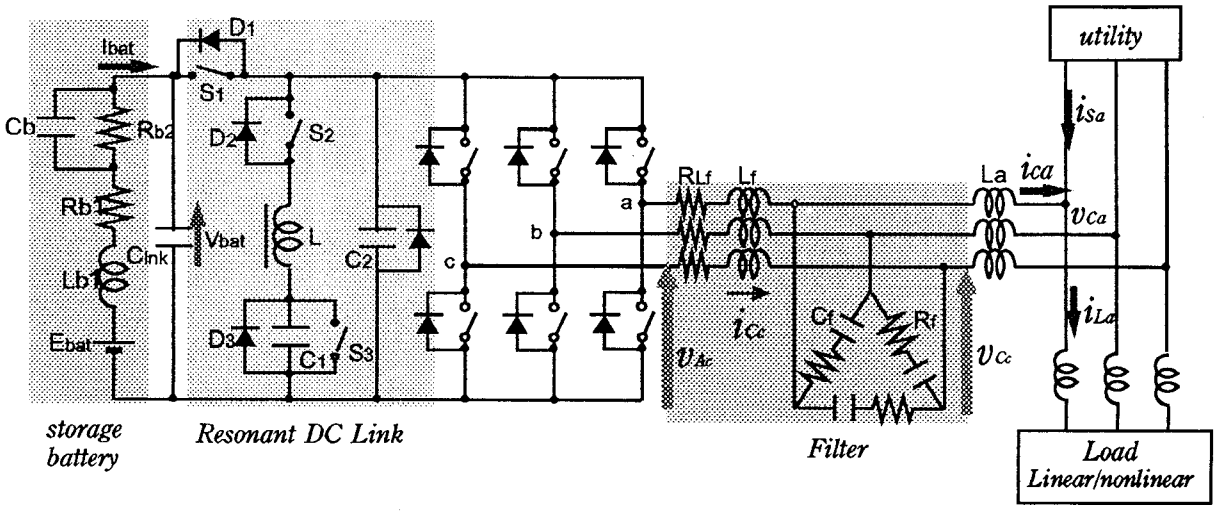

Fig8. Utility-interconnected Soft-Switched Power Conditioners For Battery Energy Storage System (BESS)

$$i_c'(i+1)=\frac{1-exp\left(\frac{R_{Lf}T_S}{L_f}\right)}{R_{Lf}}\begin{bmatrix}1&0\\0&1\end{bmatrix}\left(\dot{v}_A(i)-\dot{v}_c(i)\right)+exp\left(-\frac{R_{Lf}T_S}{L_f}\right)\begin{bmatrix}1&0\\0&1\end{bmatrix}i_c(i) \quad (13)$$

5. SIMURATION RESULTS AND EVALUATIONS

Fig9 shows the waveforms of every phase currents under space voltage vector control strategy at an energy supply mode in this converter system. The relationships of i_{La} , i_{sa} and i_{ca} are the same phase. The storage battery bank supplies the energy without generating higher harmonic currents and instantaneous reactive power. Fig10 shows the current waveforms in every phase under space voltage vector control strategy at energy storage mode in this converter system. The relationships between i_{La} and i_{ca} are at the opposite phase and the relationship between i_{La} and i_{sa} are the same phase. The storage battery is stored the energy without generating higher harmonic currents and instantaneous reactive power. Fig11(a) shows current waveforms in every phase at the three phase reactive load. Fig11(b)shows waveforms of utility grid current and utility-grid voltage at the three phase reactive load. The utility-grid voltage and load current are not same phase. But utility-grid voltage and utility-grid current are same phase. Therefore active power filter digital control strategy in this converter is verified. BESS using hard switching strategy is compared with BESS using soft switching strategy. As a result, BESS using soft switching scheme is equivalent to BESS using hard switching. Therefore, BESS using soft switching is more better than BESS using hard switching from the viewpoints of total power conversion efficiency and EMI/RFI noises.

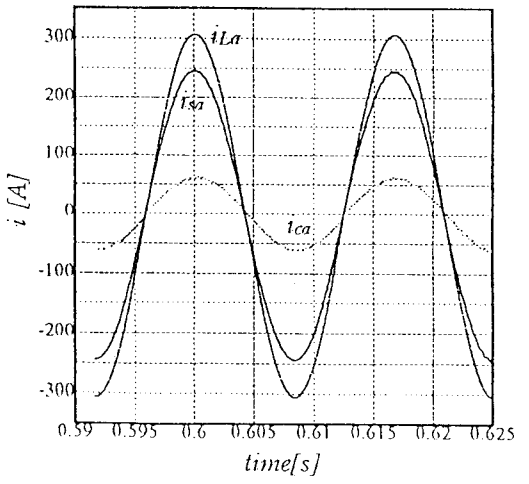

Fig9 a-phase current waveforms (at energy supply mode)

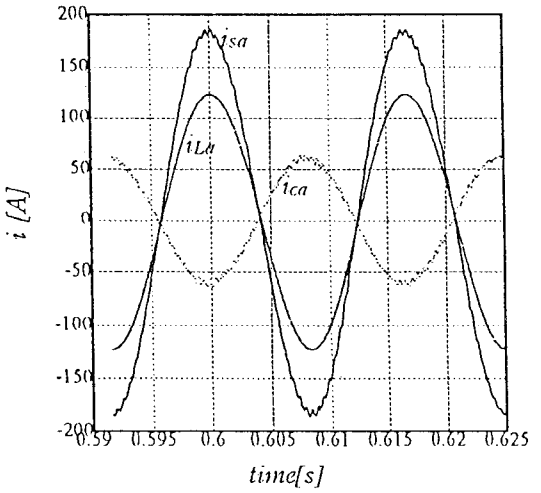

Fig10 a-phase current waveforms (at energy storage mode)

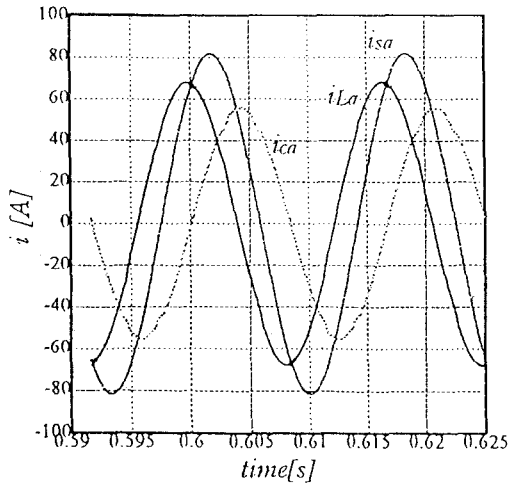

(a) a-phase current waveforms
(at three phase reactive load)

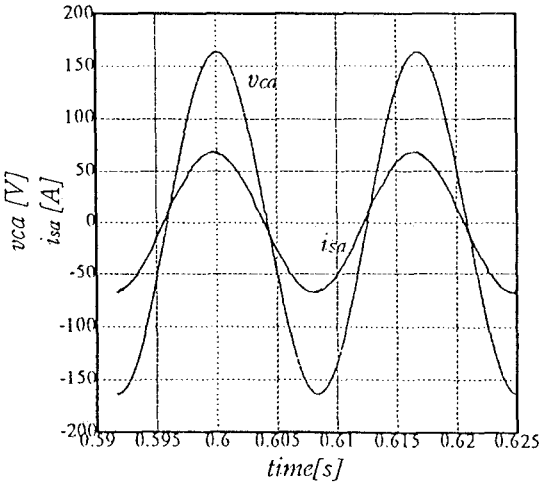

(b) a-pahse utility-grid voltage and utility-grid current waveform

Fig11. every a-pahse current and voltage waveforme

6. CONCLUSIONS

This paper have described an operating principle and features of the new prototype parallel resonant DC link circuit with voltage active clamped PWM control scheme. The new conceptual design procedure of resonant DC link treated here has been clarified and discussed by using the simulation results for various load conditions. In this paper, bidirectional type three phase voltage-fed ZVS-PWM converter using a new resonant DC link prototype was effectively applied for utility-interfaced energy storage battery system and converter system performances were evaluated. Finally, the performances for soft- switched converter mode or soft-switched inverter mode as well as the effectiveness of this resonant DC link converter as BESS for load leveling and battery charging and active filtering were demonstrated on the basis of simulation results.

REFERENCE

[1]T. Aoki, Y.Nozaki, Y.Kuwata, and T.Koyashiki " A Quasi-Resonant DC Link Inverter " IPEC Yokohama *95.pp.1203-1208

[2]T.Aoki, Y.Nozaki, and Y.Kuwata, " Characteristics of a Quasi-Resonant DC Link PWM Inverter " IEEE *95.pp.602-607

[3]J.G.Cho, H.S.Kim and C.H.Cho, " Novel Soft Switching PWM Converter Using A New Parallel Resonant DC-Link " IEEE *91. pp.241-247

[4]Y.C.Jung, H.L.Lin, G.C.Cho and G.H.Cho, " Soft Switching Space Vector PWM Inverter Using A New Quasi-Parallel Resonant DC-Link " IEEE*95. Pp.936-942

[5]C.E.Lin, M.T.Tsai, W.I.Tsai, C.L.Huang, " Development of a General-Purpose Demand-Side Battery Energy Storage System " IEEE *95. Pp1893-1899.

[6]H.Yonemori, K.Hayashi and M.Nakaoka, " A novel space-voltage vector modulated three-phase inverter with high-frequency transformer-coupled resonant DC link",IEEE-PESC Record,June,1994,pp.652-658

[7]H. Yonemori, K.Hayashi and M.Nakaoka, " Next generation space voltage vector ZVT-PWM AC-DC active power converter with auxiliary transformer-assisted resonant DC link ", IEEE Proceeding of 1995 international conference on power electronics and drive systems, Feb.,1995, pp7-12

[8]G.L.Skibinski and D.M.,Divan, " Characterization of Power Transistors under Zero Voltage Switching ", Record of IEEE -IAS Annual ·Meeting, Oct ., 1987,pp.493-503

[9]R.W.DeDonker and J.P.,Lyon, " The Auxiliary Quasi-Resonant DC Link Inverter ", IEEE-PESC Recod,, June,1991,pp.248-253

A State-Space Modeling and A Neutral Point Voltage Control For An NPC Power Converter

Chiharu Osawa, Yasushi Matsumoto, Tetsuya Mizukami, and Satoru Ozaki
Fuji Electric Corporate Research and Development Ltd.
1 Fuji-machi, Hino, Tokyo 191, JAPAN
Fax: +81-425-86-9665, Phone: +81-425-86-1102
E-mail: osawa-chiharu@fujielectric.co.jp

Abstract -- Fluctuations of neutral point voltage in NPC converters cause problems such as excessively high voltage applied to power devices. This paper presents a novel method of controlling the neutral point voltage by adjusting the dead-time that is required to prevent a dc-link short circuit. To analyze the dynamic effects of dead-time, a state-space averaged model for an NPC converter is derived. This control method is applicable to single phase NPC converters, independent of the polarity of power flow, and free from the undesired variation of switching frequency of PWM. Experimental results have revealed satisfactory control performance.

I. Introduction

Multilevel converters have been increasingly used to realize large capacity converters and to reduce undesired harmonics. Especially in the field of rail road traction drives, high-voltage IGBTs accelerate the application of three-level (or neutral point clamped, NPC[1]) converters.

It is widely recognized that the neutral point potential of such three-level converter fluctuates due to various reasons. For instance, when a 3-phase motor is fed by an NPC inverter, the neutral point potential varies at a frequency dependent on the inverter frequency. Imbalance in circuit component characteristics, and/or non-ideal features of switching devices and their operation induce and amplify the voltage imbalance between positive-side and negative-side capacitors. Excessively large imbalance imposes stress to switching devices and other components, therefore, appropriate countermeasures are indispensable.

Various analyses and countermeasures regarding the neural point potential variation have been reported and applied[2-4]. However, most of these methods focus on 3-phase systems, and control methods often require the polarity of the current and/or the direction of the energy flow to achieve the effective control performance.

We have proposed a neutral point voltage control method using the dead-time adjustment and explained its control mechanism rather intuitively[5]. This method is applicable to single-phase converters and independent of the polarity of the energy flow. In this paper, we construct a state-space model for an NPC converter, and evaluate the effectiveness of the proposed control method analytically and experimentally.

This paper is organized as follows. First, investigating the circuit configuration modes determined by the status of switching devices, we derive a state-space averaged model for a single-phase NPC converter. Then we use this model to show how the dead-times affect the dynamic behavior of the converter. After that, the possibility of controlling the neutral point voltage by adjusting the dead-times are explained. Experimental results follow to demonstrate the validity of the proposed control method.

II. A State-Space Averaged Model for an NPC Converter

A. Assumptions

To derive a state-space averaged model of the converter, we make the following five assumptions:

#1 PWM pulses are generated by a dipolar PWM method in which two voltage command wave forms are compared with a single triangular carrier wave form[6]. Fig.1 illustrates an example of gate pulses in one leg of an NPC converter.

#2 The frequency of the carrier is high enough so that the voltage commands in one carrier period can be regarded as constant.

#3 All switching devices are ideal switches with uniform characteristics.

#4 Parasitic elements in circuit components, such as an equivalent series resistance of a capacitor, are negligible.

#5 Snubber circuits added switching devices are omitted for simplicity.

B. Derivation of a State-Space Averaged Model[7]

Following the steps described below, we derive a state-space averaged model of a single-phase converter circuit depicted in Fig. 2.

STEP 1: Obtain a state-space representation for the circuit in each circuit configuration mode determined by the

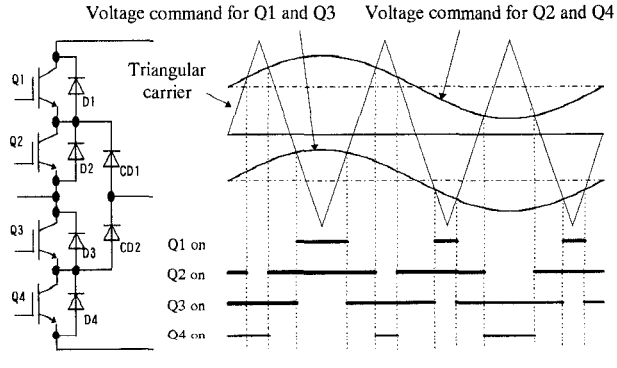

Fig.1 Gate pulse wave forms generated by a dipolar PWM method.

states of the switching devices.

STEP 2: Calculate the total duration that each circuit configuration mode appears in one carrier period. The ratio of this duration to one carrier period is termed a duty ratio.

STEP 3: Using the duty ratios as weighting coefficients, average the state-space representation obtained earlier.

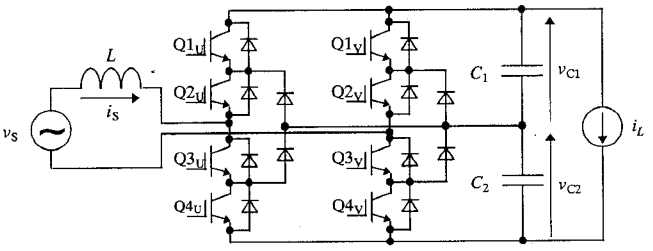

Fig. 2 A circuit configuration of a single-phase NPC converter.

1)State-space representation of the converter circuit

Selecting $\mathbf{x} = [i_S \quad v_{C1} \quad v_{C2}]^T$ as a state variable vector and $\mathbf{u} = [v_S \quad i_L]^T$ as an input vector, we can obtain a state equation of the form

$$\frac{d\mathbf{x}}{dt} = \mathbf{Ax} + \mathbf{Bu} \tag{1}$$

for each circuit configuration. A superscript T denotes matrix transpose.

Fig. 3 shows five switch configuration modes in one leg of an NPC converter. Devices encircled are commanded to turn on. Mode 2 and Mode 4 correspond to dead-times, or on-delay period, to prevent a dc-link short circuit. The length of a dead-time is usually determined by the switching characteristics of the power devices and those of the snubber circuits. The transition among the switch configuration modes in one leg is permitted only between two modes next to each other.

Since a single-phase converter circuit in Fig. 2 consists of Phase U and Phase V, we have at most $5 \times 5 \times 2 = 50$ circuit configuration modes, considering the polarity of the ac current i_S. Let us distinguish these circuit configuration modes using combinations of the switch configuration modes in each leg. For instance, when Phase U and Phase V are in Mode 2 and Mode 3, respectively, we call the circuit configuration mode corresponding to this as Mode 23.

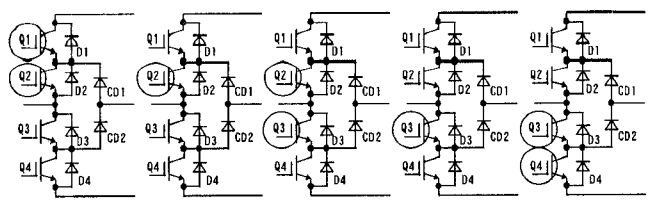

Fig. 3 Five switch configurations in one leg of an NPC converter: (a)Mode 1; Q1 and Q2 on, (b)Mode2; Q2 on, (c)Mode 3; Q2 and Q3 on, (d)Mode 4; Q3 on, and (e)Mode 5; Q3 and Q4 on.

In Mode 23, for example, the current flows along the path shown in Fig. 4(a), if $i_S > 0$. Then, the state variables, i_S, v_{C1}, and v_{C2}, satisfy

$$\begin{aligned} L\, di_S/dt &= -v_{C1} + v_S \\ C_1\, dv_{C1}/dt &= i_S - i_L \\ C_2\, dv_{C2}/dt &= -i_L \quad . \end{aligned} \tag{2}$$

Using matrix representation as in (1), we have

$$\mathbf{A}_{23P} = \begin{bmatrix} 0 & -1/L & 0 \\ 1/C_1 & 0 & 0 \\ 0 & 0 & 0 \end{bmatrix}, \quad \mathbf{B}_{23P} = \begin{bmatrix} 1/L & 0 \\ 0 & -1/C_1 \\ 0 & -1/C_2 \end{bmatrix}. \tag{3}$$

Subscripts 23 and P indicate that these matrices govern the circuit dynamics in Mode 23 with positive i_S. Similarly, when $i_S < 0$, the current path in Fig. 4(b) yields

$$\mathbf{A}_{23N} = \begin{bmatrix} 0 & 0 & 0 \\ 0 & 0 & 0 \\ 0 & 0 & 0 \end{bmatrix}, \quad \mathbf{B}_{23N} = \begin{bmatrix} 1/L & 0 \\ 0 & -1/C_1 \\ 0 & -1/C_2 \end{bmatrix}. \tag{4}$$

Subscript N suggests that i_S is negative.

The state equations corresponding to possible circuit configuration modes involve seven distinctive system matrices, or **A** matrices, as shown in TABLE I. Roman numerals correspond to the system matrices detailed in APPENDIX A.

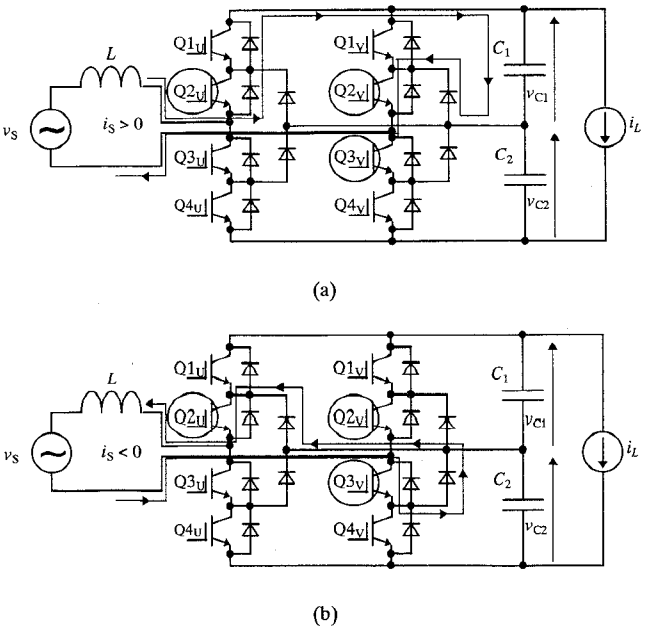

Fig. 4 Examples of current flow paths in circuit configuration mode Mode 23: (a) $i_S > 0$, (b) $i_S < 0$.

TABLE I
SYSTEM MATRICES CORRESPONDING TO
CIRCUIT CONFIGURATION MODES

	$i_S > 0$					$i_S < 0$				
U \ V	1	2	3	4	5	1	2	3	4	5
1	I	II	II	IV	IV	I	I	II	II	IV
2	I	II	II	IV	IV	III	III	I	I	V
3	III	I	I	V	V	III	III	I	I	V
4	III	I	I	V	V	VI	VI	VII	VII	I
5	VI	VII	VII	I	I	VI	VI	VII	VII	I

2)Duty ratios of configuration modes

Fig. 5 details one carrier period of dipolar PWM operation. Horizontal lines v^*_{U1}, v^*_{U2}, and v^*_{V1}, v^*_{V2} are parts of voltage command wave forms, which appear constant in this period due to assumption #2. Dead-times in Q1-Q3 switching, τ_1, and in Q2-Q4 switching, τ_2, correspond to Mode 2 and Mode 4 in Fig. 3, respectively.

Closely investigating Fig. 5, we have time T_{jk} occupied by each circuit configuration mode Mode *jk* as follows.

$$\begin{aligned} T_{11} &= T_1 - \tau_1 & T_{12} &= 2\tau_1 \\ T_{13} &= T_2 - T_1 - 2\tau_1 & T_{23} &= 2\tau_1 \\ T_{33} &= 1 - 2T_2 - \tau_1 - \tau_2 & T_{34} &= 2\tau_2 \\ T_{35} &= T_2 - T_1 - 2\tau_2 & T_{45} &= 2\tau_2 \\ T_{55} &= T_1 - \tau_2 \quad , \end{aligned} \tag{5}$$

where T_1 and T_2 are calculated in the following manner. Owing to the symmetry of the voltage command wave forms, we can write $\left|v^*_{V1}\right| = \left|v^*_{U2}\right| = v_1$ and $\left|v^*_{V1}\right| = \left|v^*_{U1}\right| = v_2$, then we have $T_1 = (1-v_1)/2$ and $T_2 = (1-v_2)/2$. Further simplification using $v_2 = 1 - v_1$ allows us to let $v_1 = v$, and yields

$$T_1 = (1-v)/2 \text{ and } T_2 = v/2. \tag{6}$$

If we choose the amplitude of the triangular carrier as unity and define v as $0 \le v \le 1$, then T_{jk}'s become duty ratios with respect to the carrier period, and their total sum equals unity.

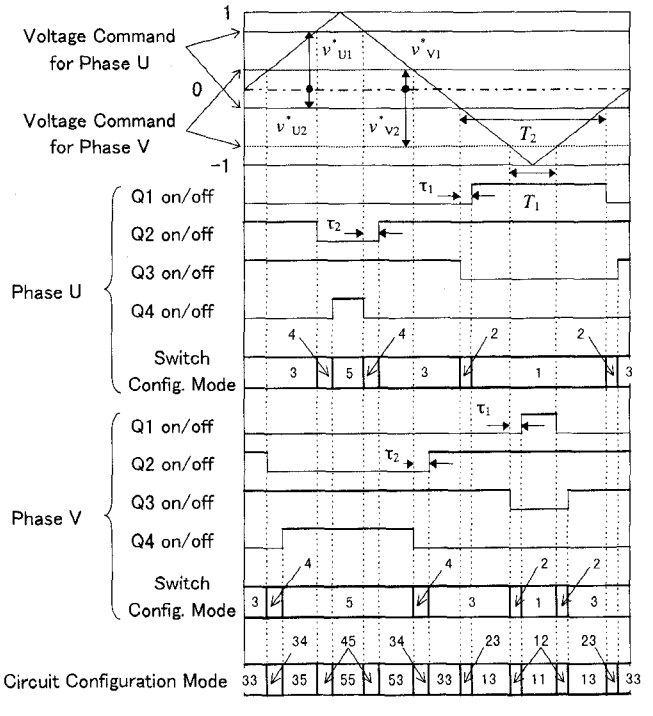

Fig.5 Gate pulse wave forms and the circuit configuration modes generated by a dipolar PWM method.

3)Averaging the state-space equations

Using the duty ratios corresponding to circuit configuration modes, we can "average" the system matrices as follows.

An averaged system matrix for positive i_S is

$$\mathbf{A}_P = \sum_{jk} \mathbf{A}_{jkP} \cdot T_{jk} = \begin{bmatrix} 0 & -t_1/L & -t_2/L \\ t_1/C_1 & 0 & 0 \\ t_2/C_2 & 0 & 0 \end{bmatrix}, \tag{7}$$

where $t_1 = T_{12} + T_{13} + T_{23}$, and $t_2 = T_{34} + T_{35} + T_{45}$. An averaged system matrix for negative i_S is

$$\mathbf{A}_N = \sum_{jk} \mathbf{A}_{jkN} \cdot T_{jk} = \begin{bmatrix} 0 & -T_{13}/L & -T_{35}/L \\ T_{13}/C_1 & 0 & 0 \\ T_{35}/C_2 & 0 & 0 \end{bmatrix}. \tag{8}$$

Substituting (5) and (6) into (7) and (8), we can express the system matrices for $i_S > 0$ and $i_S < 0$ as functions of v, τ_1, and τ_2.

$$\mathbf{A}_P = \begin{bmatrix} 0 & -\dfrac{2v + 4\tau_1 - 1}{2L} & -\dfrac{2v + 4\tau_2 - 1}{2L} \\ \dfrac{2v + 4\tau_1 - 1}{2C_1} & 0 & 0 \\ \dfrac{2v + 4\tau_2 - 1}{2C_2} & 0 & 0 \end{bmatrix} \tag{9}$$

$$\mathbf{A}_N = \begin{bmatrix} 0 & -\dfrac{2v - 4\tau_1 - 1}{2L} & -\dfrac{2v - 4\tau_2 - 1}{2L} \\ \dfrac{2v - 4\tau_1 - 1}{2C_1} & 0 & 0 \\ \dfrac{2v - 4\tau_2 - 1}{2C_2} & 0 & 0 \end{bmatrix} \tag{10}$$

Matrix **B** used in (1) is uniquely determined as

$$\mathbf{B} = \begin{bmatrix} 1/L & 0 \\ 0 & -1/C_1 \\ 0 & -1/C_2 \end{bmatrix}, \tag{11}$$

and is common to all circuit configuration modes.

C. Analysis of the Dead-time Effects

Since the entries of the system matrices (9) and (10) are functions of τ_1 and τ_2, we understand that the dead-times affect the rates of change of i_S, v_{C1}, and v_{C2}.

The difference in the rates of change of two capacitor voltages causes the fluctuations in the neutral point voltage. This difference can be obtained by subtracting the third row of the state equation (1) from its second row. When $i_S > 0$, the difference is written as

$$\frac{dv_{C1}}{dt} - \frac{dv_{C2}}{dt} = \left(\frac{1}{C_1} - \frac{1}{C_2}\right)\left\{\left(v - \frac{1}{2}\right)i_S - i_L\right\} + 2\left(\frac{\tau_1}{C_1} - \frac{\tau_2}{C_2}\right)i_S \tag{12}$$

Equation (12) shows that when the characteristics of two capacitors deviate from their nominal values and there exists some difference between those capacitances, the rates of change of the two capacitor voltages are unequal. Assuming that $C_1 = C_2 = C$ in (12), we can conclude that

$$\frac{dv_{C1}}{dt} - \frac{dv_{C2}}{dt} = \frac{2}{C}(\tau_1 - \tau_2)i_S . \tag{13}$$

Similarly, for $i_S < 0$, we have the following:

$$\frac{dv_{C1}}{dt} - \frac{dv_{C2}}{dt} = \frac{2}{C}(\tau_2 - \tau_1)i_S . \tag{14}$$

Equations (13) and (14) suggest that the difference in the rates of change of two capacitor voltages depends on the product of the difference between τ_1 and τ_2, and i_S, and is independent of the variation of v and i_L. Taking into account that $i_S > 0$ in (13) and $i_S < 0$ in (14), we see that

$$\text{if } \tau_1 \geq \tau_2, \text{ then } \frac{dv_{C1}}{dt} \geq \frac{dv_{C2}}{dt},$$
$$\text{and if } \tau_1 \leq \tau_2, \text{ then } \frac{dv_{C1}}{dt} \leq \frac{dv_{C2}}{dt}. \tag{15}$$

It should be noted that (15) holds independent of the polarity of i_S.

III. Neutral Point Voltage Control by Dead-Time Adjustment

A. Basics of the Proposed Control Method

Assume, for example, that v_{C2} has become greater than v_{C1}. To recover the balanced voltages, we would like to make dv_{C1}/dt greater than dv_{C2}/dt. Equation (15) tells that τ_1 should be larger than τ_2 to meet this end. Our voltage balancing control method is based on this principle.

This control method has several advantages compared with conventional control strategies.

- The operation of control is independent of the polarity of the ac current and the direction of the energy flow.
- The control is free from the undesired increase of the switching operation and that of the switching losses.
- The control performance is not limited by the limitation of the switching frequency.
- The control response can be quantitatively designed by adjusting the difference of two dead-times.

Actually, there exist minimum values of dead-times. In applying this control method, however, the control input is obtained as a difference between two dead-times. Therefore, desired control performance can be attained while the required minimum value of each dead-time is observed.

B. Application to a Single-Phase NPC Converter

The neutral point voltage of an NPC converter can be effectively controlled by incorporating this voltage balancing control. A control block diagram for a single-phase NPC converter in Fig. 6 includes constant dc voltage control, unity power factor control, and voltage command distributor for three-level PWM operation.

The response of this control using a PI controller, whose input is the difference between two capacitor voltages, can be formulated as follows. From equation (13) or (14), the amount of correction in the capacitor voltages in one carrier period is expected as $\Delta v_{bal} = 2 \cdot i_S |\tau_1 - \tau_2| / C$. When the unity power factor control effectively functions, we can assume that i_S is a sinusoid in phase to the ac source voltage v_S. Using I_S for the rms value of i_S, and f_C for the carrier frequency, the amount of correction in one source period v_{bal} becomes

$$\begin{aligned} v_{bal} &= f_C \int_0^{T_{src}} \left|\Delta v_{bal}\right| dt \\ &= \frac{f_C \cdot 2 \cdot \Delta\tau_d}{C} \int_0^{T_{src}} \sqrt{2} I_S \left|\sin \frac{2\pi}{T_{src}} t\right| dt \\ &= \frac{f_C \cdot \Delta\tau_d}{C} \cdot \frac{4\sqrt{2}}{\pi} I_S \cdot T_{src} , \end{aligned} \tag{16}$$

where $\Delta\tau_d = |\tau_1 - \tau_2|$ and T_{src} is one source period. With a proportional gain K_P and a sufficiently large integration time of the PI controller, the response time of this control method, T_{bal}, is approximated by

$$T_{bal} = \frac{1}{K_P} \cdot \frac{\pi}{4\sqrt{2}} \cdot \frac{C}{f_C} \cdot \frac{1}{I_S} . \tag{17}$$

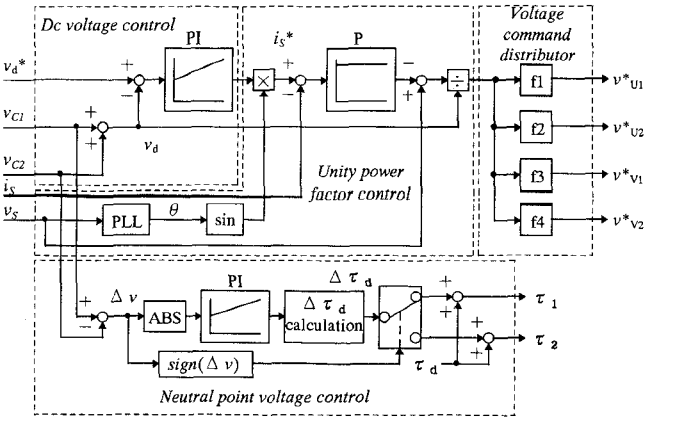

Fig.6 A control block diagram for a single-phase NPC converter.

Although the analysis so far has been concentrated on the dipolar PWM method, it is also applicable to unipolar PWM methods. In unipolar PWM, since each device continues switching only in one half of the ac source period, the number of the balancing operation reduces to one half compared with the dipolar PWM case. Therefore, the amount of the correction and the response time become one half and doubled, respectively.

$$v_{bal}' = \frac{v_{bal}}{2} = \frac{f_C \cdot \Delta T_d}{C} \cdot \frac{2\sqrt{2}}{\pi} I_S \cdot T_{src} \quad (18)$$

$$T_{bal}' = 2T_{bal} = \frac{1}{K_P} \cdot \frac{\pi}{2\sqrt{2}} \cdot \frac{C}{f_C} \cdot \frac{1}{I_S} \quad (19)$$

IV. Experimental Results

A. Experimental Setups

The validity of the proposed control method has been evaluated with a converter-inverter system specified in TABLE II. The induction motors operate at a constant speed of 750min^{-1}, and the load torque is adjusted so that i_S meets desired values. In the following experimental results, the motor current is represented by i_U.

TABLE II
SPECIFICATIONS OF THE EXPERIMENTAL SYSTEM

AC Power Source	140V, 50Hz
AC Current	20A
DC Voltage	260V
Reactor	2.5mH
Capacitors	(i) 9000 μF + 9000 μF (ii) 9000 μF + 8000 μF
Switching Devices	IGBT (1200V / 75A)
Induction Motors	1.5kW ×4, 4Poles, 200V/1500min^{-1}

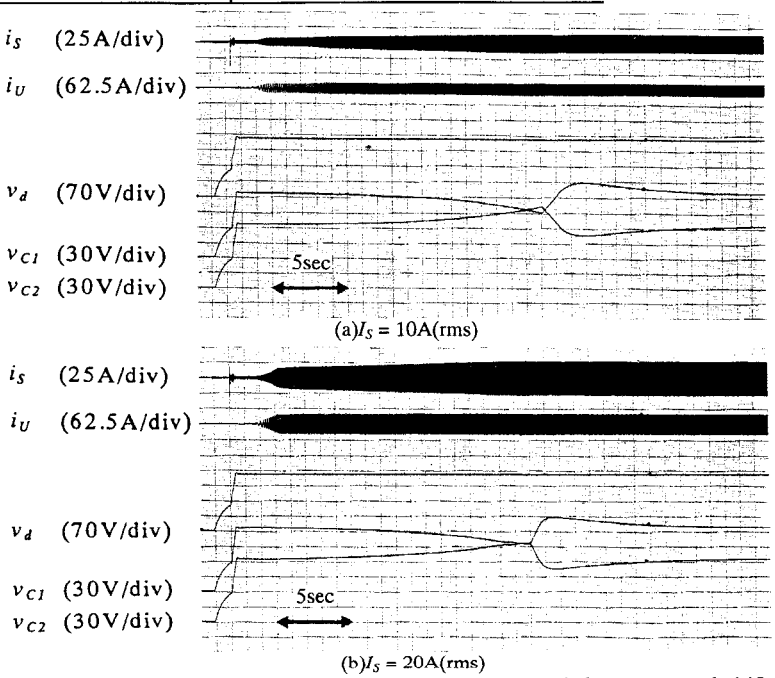

Fig.7 The capacitor voltage imbalance and the effect of the balancing control: (a)I_S = 10A(rms), (b)I_S = 20A(rms). Time; 1sec/div.

B. Evaluation of the Results

1)Fluctuations in capacitor voltages

In Fig. 7, the difference in two capacitor voltages increases according to the increase in i_S , though the nominal capacitances are equal. When the voltage difference reaches 60V, the balancing operation starts and the voltage balance is recovered. During this period, the total dc voltage is kept constant at the desired set point voltage. Fig. 7 also demonstrate the dependence of the control performance to I_S (10A and 20A): When I_S is doubled, the rise time decreases to one half.

Fig. 8 corresponds to the case in which two capacitances differ by a rate of 9:8. After the initial charge operation, there exists a voltage difference of 15V between two capacitor voltages. Without the balancing control, this voltage difference increases until the converters are cut off for protection. In contrast to this, with the balancing control, the voltage difference after the initial charge disappears within 10sec.

2)Ac current harmonics

The ac side voltage and current wave forms under the balancing control are compared in Fig. 9. Unity power factor control keeps the current wave form in phase to the voltage. With unbalanced capacitance, the balancing control is steadily in operation and slightly increases the discontinuous conduction at zero crossing.

Harmonic contents of i_S are shown in Fig. 10. When the balancing control operates steadily, the 3rd and 11th harmonics increase, though the harmonics higher than 15th and those of even orders are nearly unchanged. Each harmonic content is less than 3% and the total harmonic distortion up to 40th order is about 4%, which are independent of the incorporation of the balancing control.

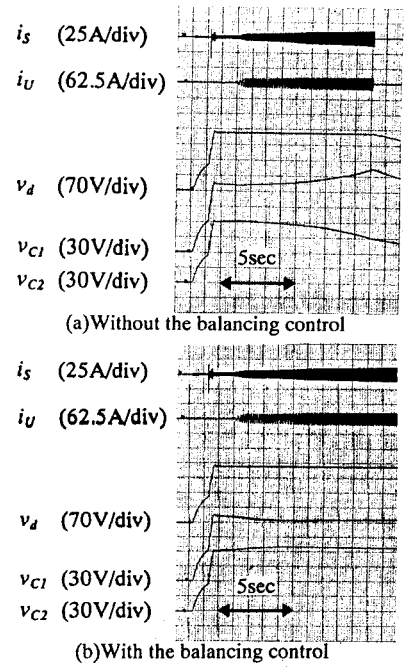

Fig. 8 The capacitor voltage imbalance caused by unequal capacitances: (a)without control, (b)with control. Time; 1sec/div.

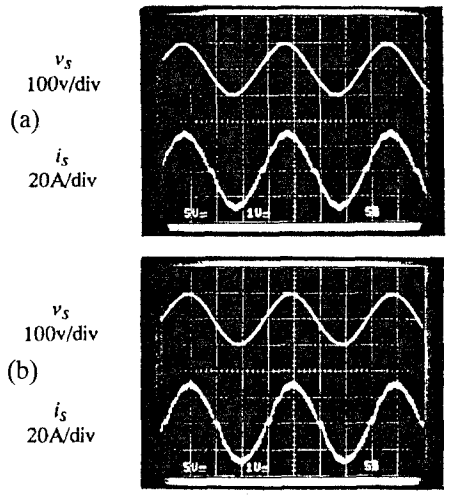

Fig. 9 Ac side voltage and current wave forms: (a)balanced capacitance, (b)unbalanced capacitance. Time; 5ms/div.

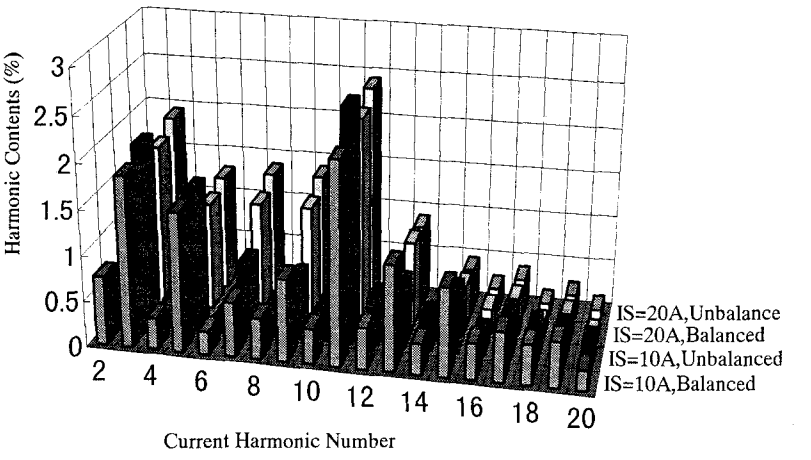

Fig. 10 Harmonic contents of ac side current i_S: From forward to back, 10A(rms) with balanced capacitance, 10A(rms) with unbalanced capacitance, 20A(rms) with balanced capacitance, and 20A(rms) with unbalanced capacitance.

V. Conclusion

A state-space model for a single-phase NPC converter was derived, and the dynamic effects of dead-times were analyzed. A novel method for controlling the neutral point voltage by adjusting dead-times was proposed. This control method is applicable to single phase NPC converters, independent of the polarity of power flow, and free from the undesired increase of the switching in PWM. Experimental results have shown satisfactory control performance.

References

[1] A. Nabae, et. al., "A new neutral-point-clamped PWM inverter," *IEEE Trans. Ind. Applicat.*, vol. IA-17, no.5, pp.518-523, 1981.

[2] S. Ogasawara and H. Akagi, "Analysis of variation of neutral point potential in neutral-point-clamped voltage source inverters," in *Conf. Proc. IEEE IAS Ann. Mtg.*, pp.965-970, 1993.

[3] S. Bertini, *et. al.*, "Ac/dc/ac high voltage traction drives with quasi-zero reactive power demand," *IEEE Trans. Power Electronics*, vol. 8, no. 4, October 1993.

[4] J. Steinke, "Switching frequency optimal PWM control of a three-level inverter," IEEE Trans. Power Electronics, vol.7, no.3, pp.487-496, 1992

[5] Y. Matsumoto, *et. al.*, "A neutral point voltage control method for NPC power converters," (in Japanese) *JIASC '96 Record IEE Japan*, pp. 171-174.

[6] B. Velaerts, *et. al.*, "A novel approach to the generation and optimization of three-level PWM wave forms," *PESC '88 Record*, pp.1255-1262, 1988.

[7] J. Kassakian, M. Schlecht, and G. Verghese, *Principles of Power Electronics*. Reading, MA. Addison-Wesley, 1991.

Appendix A

System matrices corresponding to 50 circuit configuration modes consist of seven distinctive matrices as found in TABLE A.

TABLE A
System Matrices and Circuit Configuration Modes

	System Matrix	$i_S > 0$	$i_S < 0$
I	$\begin{bmatrix} 0 & 0 & 0 \\ 0 & 0 & 0 \\ 0 & 0 & 0 \end{bmatrix}$	A_{11P}, A_{21P} A_{32P}, A_{33P} A_{42P}, A_{43P} A_{54P}, A_{55P}	A_{11N}, A_{12N} A_{23N}, A_{24N} A_{33N}, A_{34N} A_{45N}, A_{55N}
II	$\begin{bmatrix} 0 & -1/L & 0 \\ 1/C_1 & 0 & 0 \\ 0 & 0 & 0 \end{bmatrix}$	A_{12P}, A_{13P} A_{22P}, A_{23P}	A_{13N}, A_{14N}
III	$\begin{bmatrix} 0 & 1/L & 0 \\ -1/C_1 & 0 & 0 \\ 0 & 0 & 0 \end{bmatrix}$	A_{31P}, A_{41P}	A_{21N}, A_{22N} A_{31N}, A_{32N}
IV	$\begin{bmatrix} 0 & -1/L & -1/L \\ 1/C_1 & 0 & 0 \\ 1/C_2 & 0 & 0 \end{bmatrix}$	A_{14P}, A_{15P} A_{24P}, A_{25P}	A_{15N}
V	$\begin{bmatrix} 0 & 0 & -1/L \\ 0 & 0 & 0 \\ 1/C_2 & 0 & 0 \end{bmatrix}$	A_{34P}, A_{35P} A_{44P},A_{45P}	A_{25N}, A_{35N}
VI	$\begin{bmatrix} 0 & 1/L & 1/L \\ -1/C_1 & 0 & 0 \\ -1/C_2 & 0 & 0 \end{bmatrix}$	A_{51P}	A_{41N}, A_{42N} A_{51N}, A_{52N}
VII	$\begin{bmatrix} 0 & 0 & 1/L \\ 0 & 0 & 0 \\ -1/C_2 & 0 & 0 \end{bmatrix}$	A_{52P}, A_{53P}	A_{43N}, A_{44N} A_{53N}, A_{54N}

Neutral Point Potential and Unity Power Factor Control of NPC Boost Converters

Shoji Fukuda and Yasumasa Matsumoto

Systems and Information Engineering,
Hokkaido University
North-13, West-8, Kita-Ku, Sapporo, 060 JAPAN
Fax: +81-11-706-7890, Phone: +81-11-706-6464
E-mail: fukus@e4.hines.hokudai.ac.jp

Abstract- **Neutral-point-clamped boost PWM converters (NPCC) are able to reduce harmonic currents, without requiring the devices to be operated at a high frequency switching, and are suitable for high voltage systems because of their circuit structure. Thus, they are expected to play a greater role in high power applications where device switching is limited below several hundreds hertz. The NPCCs, however, have a problem that the neutral point potential (NPP) varies when the current flows into or out of the neutral point. The variations cause voltage deviations in the input waveforms as well as unbalanced voltage stress on the devices. Accordingly, reducing NPP variations is very important.**

This paper describes a controlling method for NPCCs. It is shown that the system can be modeled by 3-input 3-output 5th-order state equations. The controller is designed based on the optimal regulator theory in order to achieve the control of DC voltage, power factor (PF) and NPP, simultaneously. The validity of the proposed method is demonstrated by experimental results.

1. INTRODUCTION

With the increasing use of high power static converters, the effects of the harmonic and/or reactive currents generated by these converters are becoming a troublesome problem for the utilities. A voltage source PWM converter is promising because it can provide sinusoidal AC currents with unity power factor. Furthermore, it can provide a bilateral power flow.

In this paper a neutral-point-clamped[1] PWM converter (NPCC) is described. NPCC is suitable for high power converters because the device voltage stress is a half of a conventional converter, given the same DC link voltage, and the generated harmonics are less than those generated by a conventional converter, given the same switching frequency. However, it has a problem: its neutral point potential (NPP) deviates, thus resulting in an excess voltage stress to either the upper or lower set of the devices. Thus, NPCC is required an additional control function, namely the NPP control.

In this paper, the modeling of a NPCC is carried out and the state equations, which include the NPP, are obtained. It is shown that a NPCC can be described by a 3-input 3-output system. An optimal regulator referred to as a linear quadratic integral regulator (LQI regulator)[2] is used because the regulator is suitable for a multi-input multi-output system and its stability is insensitive to small parameter variations. The neutral point current, the current flowing into or out of the neutral point, is treated as one of the inputs[3] along with the voltage inputs. Experimental results prove the validity of the proposed modeling and control strategy.

2. MODELING OF AN NPCC

Fig. 1 shows a NPC voltage source converter which is the object of this paper. The DC load consists of R_{dc} and L_{dc}. The voltages and currents on the AC side are transformed into the d-q coordinate reference frames, which are rotating at the source voltage angular frequency ω. The following equations are obtained:

$$\frac{d}{dt}i_d = -\frac{R}{L}i_d + \omega i_q - \frac{1}{L}v_d + \frac{1}{L}E_1 \quad (1)$$

$$\frac{d}{dt}i_q = -\omega i_d - \frac{R}{L}i_q - \frac{1}{L}v_q \quad (2)$$

where the d and q axes are selected to be $e_d = E_1$: the source line-to-line voltage, and $e_q = 0$. As the instantaneous power on the AC side is always equal to that on the DC side, the following equation holds[3]:

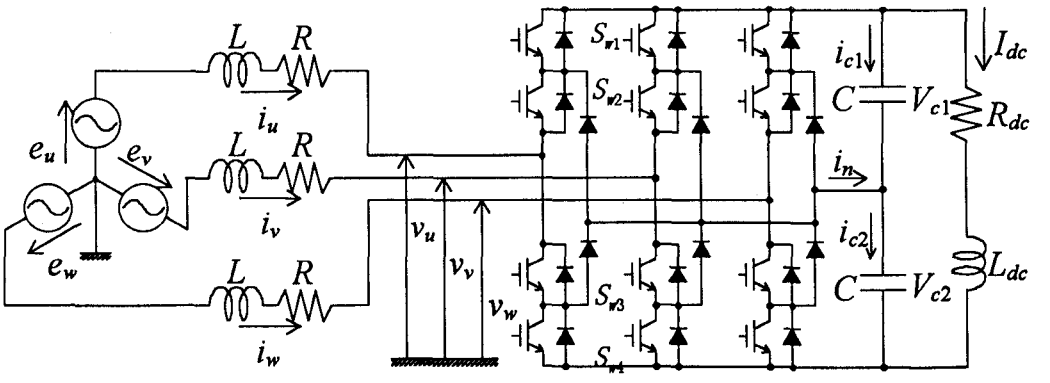

Fig. 1. A neutral-point-clamped voltage source converter.

$$v_d i_d + v_q i_q = V_{c1} i_{c1} + V_{c2} i_{c2} + (V_{c1} + V_{c2}) I_{dc}$$
$$i_{c1} = C\frac{V_{c1}}{dt}, \quad i_{c2} = C\frac{V_{c2}}{dt}, \quad i_{c1} + i_n = i_{c2} \qquad (3)$$

Substituting (1) and (2) into (3), we have

$$\frac{d}{dt}V_{c1} = \frac{v_d i_d + v_d i_d - V_{c2} i_n}{C(V_{c1} + V_{c2})} - \frac{I_{dc}}{C} \qquad (4)$$

$$\frac{d}{dt}V_{c2} = \frac{v_d i_d + v_d i_d + V_{c1} i_n}{C(V_{c1} + V_{c2})} - \frac{I_{dc}}{C} \qquad [5]$$

The equation in the DC link is

$$\frac{d}{dt}I_{dc} = \frac{V_{c1} + V_{c2}}{L_{dc}} - \frac{R_{dc}}{L_{dc}} I_{dc}. \qquad (6)$$

The NPCC is described by (1)-(2) and (4)-(6).

3. CONTROL SYSTEM DESIGN

A. State Equations

There are three control performance criteria for the NPC converter namely; to keep the PF at unity, to keep the DC link voltage constant, and to keep the neutral point potential at zero volts. These conditions are described mathematically as

$$i_q = 0, \quad V_{c1} = V_{c2} = \frac{V_{dc}^*}{2}$$

where V_{dc}^* denotes the reference of the DC link voltage. The number of control inputs is three; the converter input voltages v_d, v_q and the neutral point current i_n. Thus, the system is a 3-input 3-output 5th order system. As (4) and (5) include nonlinear terms they must be linearized at an appropriate operating point. The operating point and linearized equations are given in APPENDIX. After the linearization the equations are transformed into a discrete time system. Modifying the original equations according to the above process, we finally have the state equations:

$$\mathbf{x}(k+1) = \mathbf{A}\mathbf{x}(k) + \mathbf{B}\mathbf{u}(k-1) + \mathbf{E}d(k) \qquad (7)$$

where every variable represents a small deviation from the operating point. $\mathbf{u}(k-1)$ represents the input delay caused by a computational time of one sampling period. This is always the case if a microprocessor-controlled system is employed. The output equation is given by

$$\mathbf{y}(k) = \mathbf{C}\mathbf{x}(k). \qquad [8]$$

In equations (7) and (8)

$$\text{state variable} : \mathbf{x} = [i_d\ i_q\ V_{c1}\ V_{c2}\ I_{dc}]^T, \quad \text{input} : \mathbf{u} = [v_d\ v_q\ i_n]^T,$$
$$\text{output} : \mathbf{y} = [i_q\ V_{c1}\ V_{c2}]^T, \quad \text{disturbance} : d = e_d = E_1.$$

B. An Optimal Regulator

It is known that applications of state feedback control are essential for multi-input and multi-output systems. In this paper, an optimal regulator is selected because it guarantees a stable feedback system and is insensitive to small parameter variations. To remove steady state errors in response to a step reference and/or disturbance change an integral-type optimal regulator, which is called a linear quadratic integral (LQI) regulator[2], is employed.

The object of an LQI regulator is to find an optimal input that quickly reduces the error in the state variables to zero. Therefore, (7) must be expanded using new state space variables so as to meet the LQI regulator requirements. Thus the error system[4] is applied. The new state variables are the error vector between reference, $\mathbf{R}(k)$, and output, $\mathbf{y}(k)$; the first-order difference of state vector, $\Delta\mathbf{x}(k)$; and the first-order difference of delayed input, $\Delta\mathbf{u}(k-1)$. These definitions are:

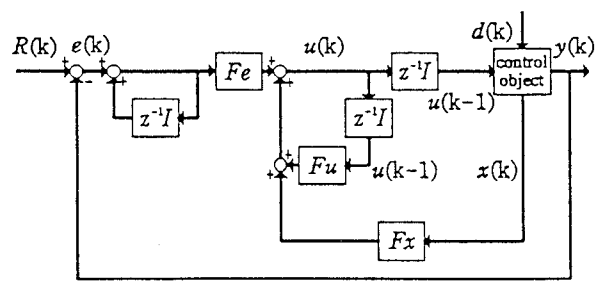

Fig. 2. Structure of the control system.

$$\mathbf{e}(k) = \mathbf{R}(k) - \mathbf{y}(k)$$
$$\Delta\mathbf{x}(k) = \mathbf{x}(k) - \mathbf{x}(k-1)$$
$$\Delta\mathbf{u}(k-1) = \mathbf{u}(k-1) - \mathbf{u}(k-2)$$

where $\mathbf{R}[i_q^*\ V_{c1}^*\ V_{c2}^*]$ is a reference vector, and $\Delta\mathbf{u}(k-1)$ is introduced as one of the state variables to take into account the output of the delay time of one sampling interval needed for computation. Thus, the augmented state equations in the expanded system is

$$\begin{bmatrix}\mathbf{x}_0(k+1)\\ \Delta\mathbf{u}(k)\end{bmatrix} = \begin{bmatrix}\Phi & \mathbf{G}\\ \mathbf{0} & \mathbf{0}\end{bmatrix}\begin{bmatrix}\mathbf{x}_0(k)\\ \Delta\mathbf{u}(k-1)\end{bmatrix} + \begin{bmatrix}\mathbf{0}\\ \mathbf{I}_r\end{bmatrix}\Delta\mathbf{u}(k) + \begin{bmatrix}\mathbf{G}_R\\ \mathbf{0}\end{bmatrix}\Delta\mathbf{R}(k+1) + \begin{bmatrix}\mathbf{G}_d\\ \mathbf{0}\end{bmatrix}\Delta d(k)$$
$$\mathbf{x}_0(k) = \begin{bmatrix}\mathbf{e}(k)\\ \Delta\mathbf{x}(k)\end{bmatrix}, \quad \Phi = \begin{bmatrix}\mathbf{I}_m & -\mathbf{CA}\\ \mathbf{0} & \mathbf{A}\end{bmatrix}, \qquad (9)$$
$$\mathbf{G}_R = \begin{bmatrix}\mathbf{I}_m\\ \mathbf{0}\end{bmatrix}, \quad \mathbf{G} = \begin{bmatrix}-\mathbf{CB}\\ \mathbf{B}\end{bmatrix}, \quad \mathbf{G}_d = \begin{bmatrix}-\mathbf{CE}\\ \mathbf{E}\end{bmatrix}.$$

Equation (9) indicates that $\mathbf{x}_o(k)$ and $\Delta\mathbf{u}(k-1)$ approach zero at steady state if the variations in the reference and/or disturbance are stepwise, then the LQI regulator requirements are satisfied. This is the reason for introducing the augmented state variables. Equation (9) also indicates that the effects of the input time delay can be taken into account.

An LQI regulator minimizes the following cost function:

$$J = \sum_{k=1}^{\infty}\left\{\begin{bmatrix}\mathbf{x}_0^T(k) & \Delta\mathbf{u}^T(k-1)\end{bmatrix}\begin{bmatrix}\mathbf{Q} & \mathbf{0}\\ \mathbf{0} & \mathbf{0}\end{bmatrix}\begin{bmatrix}\mathbf{x}_0(k)\\ \Delta\mathbf{u}(k-1)\end{bmatrix}\right\} + \Delta\mathbf{u}^T(k)\mathbf{H}\Delta\mathbf{u}(k) \qquad (10)$$

where the diagonal matrices $\mathbf{Q}$ and $\mathbf{H}$ denote the weight for the output and input, respectively. Responses are adjustable by changing the weight values; i.e., larger weights correspond to smaller responses. For example, if a larger value of Q_{iq} is chosen, the transient variation in i_q becomes smaller, and vice versa. The weight values are decided by simulation-based examinations of the transient responses.

The control input that minimizes the cost function will be given in a feedback form as:

$$\mathbf{u}(k) = \mathbf{F}_e\sum_{i=1}^{k}\mathbf{e}(i) + \mathbf{F}_x\mathbf{x}(k) + \mathbf{F}_u\mathbf{u}(k-1) \qquad (11)$$

$$[\mathbf{F}_e\ \mathbf{F}_x\ \mathbf{F}_u] = -[\mathbf{H} + \mathbf{G}^T\mathbf{P}\mathbf{G}]^{-1}\mathbf{G}^T\mathbf{P}\Phi(\Phi\mathbf{G}) \qquad (12)$$

where $\mathbf{P}$ is the semi-definite matrix which satisfies the following *Riccati* equation:

$$\mathbf{P} = \mathbf{Q} + \Phi^T\mathbf{P}\Phi - \Phi^T\mathbf{P}\mathbf{G}[\mathbf{H} + \mathbf{G}^T\mathbf{P}\mathbf{G}]^{-1}\mathbf{G}^T\mathbf{P}\Phi. \qquad (13)$$

Equation (11) clearly indicates that a servo system of 1-type with integral compensation can be constructed as shown in Fig. 2.

Table 1. Switching states and corresponding switching function S_i and input voltage V_i (i=u, v, w).

S_{w1}	S_{w2}	S_{w3}	S_{w4}	S_i	V_i
ON	ON	OFF	OFF	1	V_{c1}
OFF	ON	ON	OFF	0	0
OFF	OFF	ON	ON	-1	V_{c2}

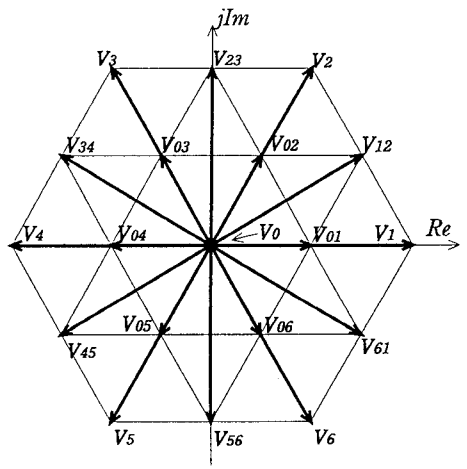

Fig. 3. Space vectors generated by NPCC.

4. PWM PATTERN CREATION PRINCIPLE

Here a PWM pulse pattern creation method which can realize an arbitrary control input given by the LQI regulator is presented.

A. Instantaneous space vector

The switching function, S_i (i= u, v, w), is defined in Table 1. The definition of the instantaneous space vector V_k is given by

$$\mathbf{V}_k = v_u + v_v\, e^{j\frac{2\pi}{3}} + v_w\, e^{j\frac{4\pi}{3}}. \tag{14}$$

The input potential of the converter, v_u, v_v, v_w, takes on three values, V_{c1}, 0 and $-V_{c2}$. Thus, there are 27 switching modes corresponding to each of the three phase switching states (S_u, S_v, S_w).

If the NPP is maintained at zero which means V_{c1}=V_{c2} then there are 19 space vectors. They are shown by the apexes of the small triangles in Fig. 3. The largest ones, V_1 - V_6 are called LL-vectors; the second largest ones, V_{12} - V_{61} are called L-vectors; the ones reduced by a factor of 2, V_{01} - V_{06} are called half (HF) vectors; and the zero vector is V_0. There are two kinds of HF-vectors, e.g., V_{01} of (1,0,0) and of (0,-1,-1). Both vectors produce the same line voltages as far as V_{1c}=V_{c2} but produce different phase voltages. The former is called a positive HF vector and is specified as V_{01p}, because it provides positive zero-sequence voltage, and the latter is called a negative HF vector, and is specified as V_{01n}, because it provides negative zero-sequence voltage. The HF-vectors are very important in controlling the NPP because if the output of V_{01p} results in a decrease in the NPP for one sampling interval, the output of V_{01n} results in an increase in the NPP for the same sampling interval, and vice versa.

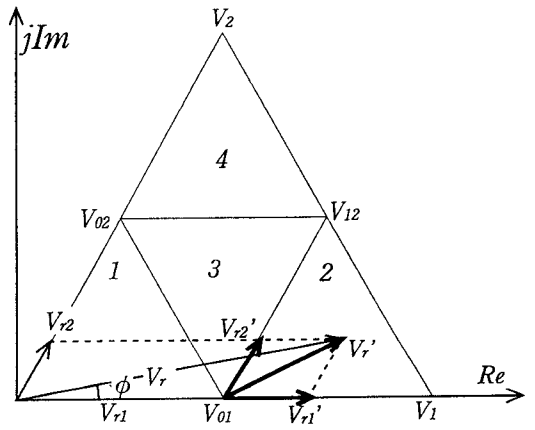

Fig. 4. Reference vector V_r' in space vector notation for $0 \le \phi \le \pi/3$.

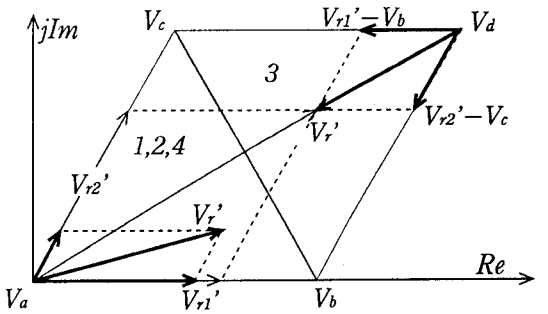

Fig. 5. Decomposition of reference vector V_r' into three space vectors to calculate pulse width.

There are three kinds of zero vectors, V_0 (1,1,1), (0,0,0) and (-1,-1,-1).

The reference input voltages should be represented in the space vector form. When input voltages, v_d and v_q, are given by (11) they are transformed into the d and q components of the modulation index[4][5]:

$$M_d = \frac{\sqrt{2}v_d}{V_{c1}+V_{c2}}, \quad M_q = \frac{\sqrt{2}v_q}{V_{c1}+V_{c2}}. \tag{15}$$

Then, the modulation index, M, and the phase angle, ϕ, are given by

$$M = \sqrt{M_d^2 + M_q^2}, \quad 0 \le M \le 1 \tag{16}$$

$$\phi = \omega t + \delta, \quad \delta = \tan^{-1}\left(\frac{M_q}{M_d}\right). \tag{17}$$

B. Pulse Width Calculation

Let the input reference voltage represented by the space vector be:

$$V_r = \frac{\sqrt{3}}{2} V_{dc}\, M e^{j\phi}, \quad V_{dc} = V_{c1} + V_{c2}. \tag{18}$$

Consider the case where V_r exists in the range $0 \le \phi \le \pi/3$, where ϕ hereafter is measured from the real axis. The range $0 \le \phi \le \pi/3$ is divided into four small triangular regions, 1, 2, 3 and 4 as shown in Fig. 4. The principle of PWM control is that the reference vector V_r is approximated by using three adjacent vectors represented by the three apexes of one of the four

triangles, the vectors V_{01}, V_1 and V_{12} are used if V_r is located in region 2 as is the case in Fig. 4. Decomposing V_r into the two directions, V_1 and V_2 in Fig. 4, we have

$$\left.\begin{aligned} \mathbf{V}_r &= \mathbf{V}_{r1} + \mathbf{V}_{r2} \\ \mathbf{V}_{r1} &= \frac{V_{dc}}{2} M(\sqrt{3}\cos\phi - \sin\phi) \\ \mathbf{V}_{r2} &= V_{dc} M \sin\phi. \end{aligned}\right\} \quad (19)$$

The region where V_r exists can be identified if V_{r1} and V_{r2} are compared to the side length, V, of the small triangle. The apexes of the triangle can be rewritten as a function of V_a, V_b, and V_c. Also the new reference vector V_r' is defined on the basis of the new origin V_a as shown in Fig. 5. Decompose V_r' into V_{r1}' and V_{r2}', and define the normalized voltages:

$$x = \frac{2V_{r1}'}{V_{dc}}, \quad y = \frac{2V_{r2}'}{V_{dc}}.$$

The normalized output times for each of the three vectors, V_b, V_c and V_a are:

$$\alpha_b = x, \quad \alpha_c = y, \quad \alpha_a = 1 - \alpha_b - \alpha_c \quad (20)$$

respectively. If $x+y>1$, V_r will exist in the region 3. In this special case V_d is selected as the new origin instead of V_a as is shown in Fig. 5. Thus, the normalized output time for V_b, V_c and V_d are in this case:

$$\alpha_b = 1 - x, \quad \alpha_c = 1 - y, \quad \alpha_d = 1 - \alpha_b - \alpha_c \quad (21)$$

respectively. The actual time width for the output vectors is the product α's and the sampling interval T.

C. Output Sequence of Voltage Vectors

In order to decide the output sequence of voltage vectors the following conditions must be considered:

1) the sequence for which one of the input variables, i_n, is controllable.
2) the sequence under which a single switching enables us to change one vector to the following vector.
3) the sequence for which the pulse width is larger than the minimum requested pulse width for the devices.

Suppose that a reference V_r is located in region 2 as shown in Fig. 4. The vectors V_{01}, V_{12} and V_1 are used in this case because they satisfy the condition 2). The time width during which each vector is used is given by (20), e.g., α_a provides the normalized time for the HF-vector, V_{01}. Each HF-vector has two kinds: V_{01p} as well as V_{01n} can be output for an arbitrary time duration as far as the sum of the each output time equals to α_a. If the output of V_{01p} results in a decrease in the NPP for one sampling interval, the output of V_{01n} results in an increase in the NPP for the same sampling interval. Thus, the ratio of the output time of V_{01p} to V_{01n} varies NPP. This is the control principle of the NPP.

Taking account of the condition 3), the output sequence of voltage vectors is summarized as shown in Table 2 and depend on the areas in which V_r exists[6] as shown in Fig. 6. Notice that three different vectors (four kind vectors) are used for one sampling interval. The same HF vector is used as the first and last vectors, but if the first one is a positive HF vector then the last one must be a negative HF-vector, and vice versa. For the next sampling interval, the reverse sequence of output vectors is used to assure symmetrical operation.

D. NPP Control Method

Define the switching function related to the NPP for phase-u as:

$S_{nu} = 1$ when $S_u = 0$,
$= 0$ when $S_u = 1$ or -1.

Table 2. Output sequence of space vectors in each area for $0 \le \phi \le \pi/3$.

Area	Space vector sequence
①	$V_{01p} - V_0 - V_{02n} - V_{01n}$
②	$V_{02p} - V_{01p} - V_0 - V_{02n}$
③	$V_{01p} - V_{12} - V_1 - V_{01n}$
④	$V_{01p} - V_{12} - V_{02n} - V_{01n}$
⑤	$V_{02p} - V_{01p} - V_{12} - V_{02n}$
⑥	$V_{02p} - V_2 - V_{12} - V_{02n}$

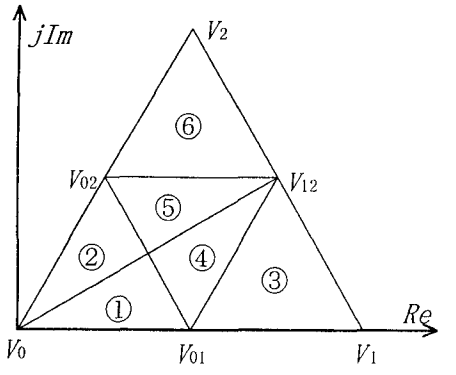

Fig. 6. Six areas used to determine the output voltage vector sequence for $0 \le \phi \le \pi/3$.

Then, the current flowing into the neutral point at the j-th subinterval, i_{nj}, is given by

$$i_{nj} = S_{nuj} i_u + S_{nvj} i_v + S_{nwj} i_w, \quad j = 1, 2, 3, 4 \quad (22)$$

If currents are assumed to be constant during a sampling interval, which is the case in our discrete-time system, the average neutral point current for one sampling interval, i_n, will be given by

$$i_n = \alpha_1 i_{n1} + \alpha_2 i_{n2} + \alpha_3 i_{n3} + \alpha_4 i_{n4} \quad (23)$$

where α_1 - α_4 represent the normalized times during which each of the four kinds of input vectors are used for one sampling interval, and i_{n1} - i_{n4} are the neutral point currents provided by each of the four vectors. Equations (22) and (23) indicate that the value of i_n depends on the magnitude of three phase currents, i_u, i_v or i_w, and the time widths, $\alpha_1+\alpha_4$, α_2, and α_3. Therefore, an arbitrarily large amount of i_n can not be provided during one sampling period. If an excessive amount of i_n is required by the regulator, it must be provided over several sampling intervals.

According to the output vector sequence shown in Table 2, the first and last vectors are the same HF-vector but one is positive and the other is negative. Considering the fact that $i_u+i_v+i_w=0$, we have

$$i_{n1} + i_{n4} = 0 \quad (24)$$

Establish the normalized time during which a positive and negative HF-vector are used as

$$\alpha_p = \frac{\alpha}{2}(1+r), \quad \alpha_n = \frac{\alpha}{2}(1-r) \quad (25)$$

respectively, where $\alpha(= \alpha_1 + \alpha_4)$ is the total time width for the HF-vector. The variable r takes the value $-1 \le r \le 1$. Substituting (25) into (23), we have

$$r = \frac{i_n^* - \alpha_2 i_{n2} - \alpha_3 i_{n3}}{\alpha i_{n1}}. \quad (26)$$

Substitution of the required control input i_n^* into (26) gives us the time ratio, r, which will produce i_n. However, it should be noted that the required amount of neutral point current, i_n, may not be provided because r is limited. Slower NPP responses will result in this situation.

5. EXPERIMENTAL RESULTS

The Experiments were carried out under the following conditions: the AC source voltage: E_1=100V, AC reactor: L=5mH, R=1.0Ω, DC capacitor: C=500μF, and DC load: L_{dc}=5mH, R_{dc} = 52Ω or 32Ω. The references are V_{c1}^*= V_{c2}^*= 80V and i_q^*=0A. The sampling frequency was 1800Hz, which means that the average switching frequency of the devices was below 500Hz.

Voltage and current waveforms at steady state are shown in Fig. 7. We can observe that the AC current is sinusoidal with unity power factor.

Responses to the parameter variations are shown in Fig. 8, where the load resistance R_{dc} is changed in a stepwise fashion from R_{dc}=52Ω to 32Ω in 150 steps, and then back to 52Ω in 350 steps where 10 sampling steps = 5.55ms. We have confirmed that the system is stable when subjected to load variations, which suggests that a robust control system has been obtained, and the control purposes have been achieved.

Fig. 9 shows the effects of the NPP control. The NPP reference was initially set at NPP=20V (V_{c1}=100V, V_{c2}=60V). The NPP reference was then changed to NPP=0V at 100 steps. We can observe that the NPP approaches zero in a stable fashion which indicates that if there is a deviation in the NPP by some reason, it will eventually be forced to zero. As the maximum value for the current flowing in the neutral point for one sampling period, i_n, is limited, the response time for the NPP control is relatively slow. The required i_n is provided over several sampling periods in this situation.

Static var generator (SVG) operation was carried out, where the load in the dc link, R_{dc} and L_{dc}, in Fig. 1 was removed. The responses when a reactive current reference, i_q^*,was changed from i_q^*=-10A to 10A at 150 steps, and then back to -10A at 350 steps are shown in Fig. 10.
We can confirm that there is no problem in very low power factor operation.

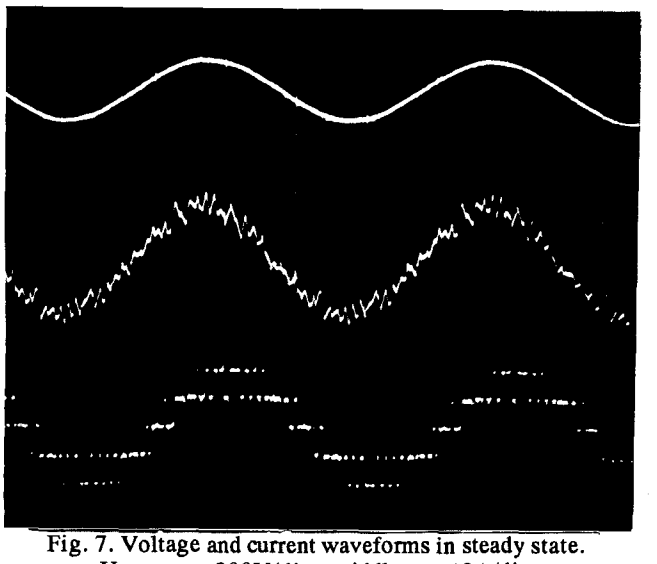

Fig. 7. Voltage and current waveforms in steady state.
Upper: e_u, 200V/div., middle: i_u, 10A/div
and lower: v_u, 200V/div. 5ms/div.

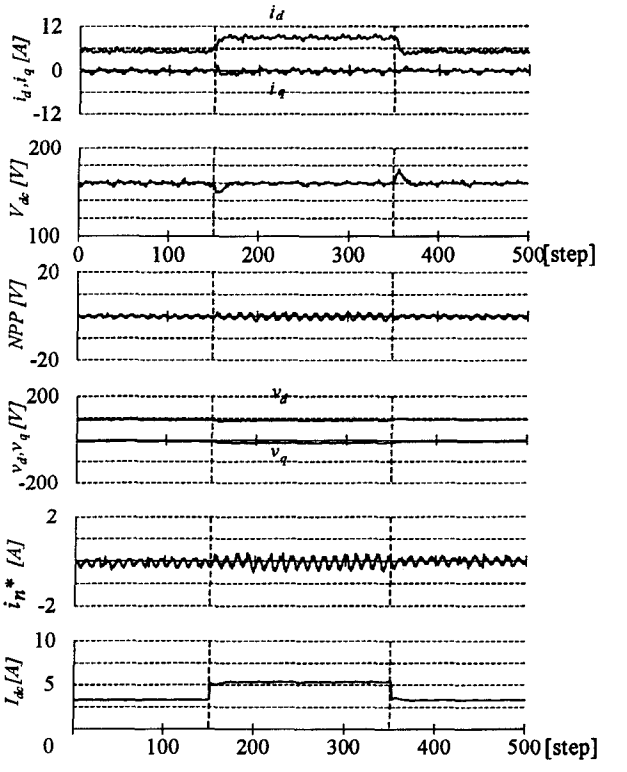

Fig. 8. Responses to step changes in a load resistance R_{dc}=52Ω → 32Ω → 52Ω. 5.55ms(10 samples)/div.

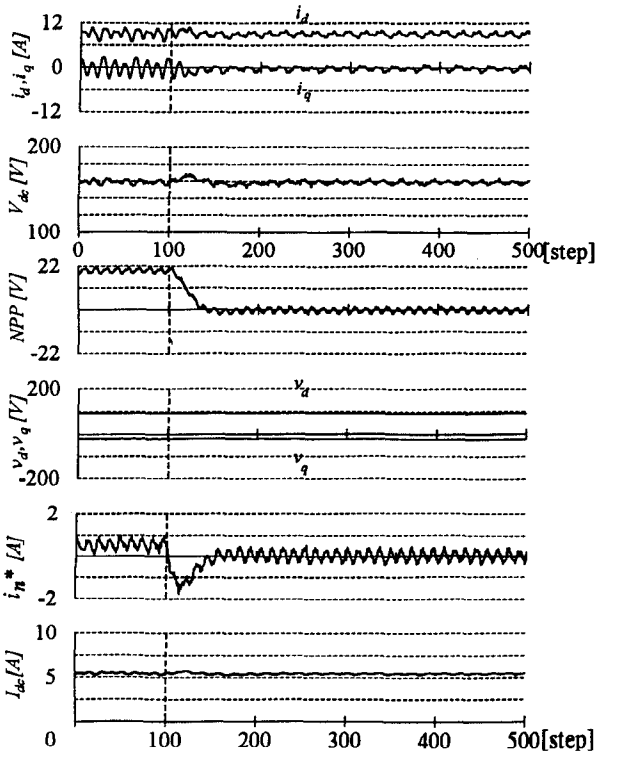

Fig. 9. Responses to step changes in an NPP reference.
NPP=20V → 0V. 5.55ms/div.

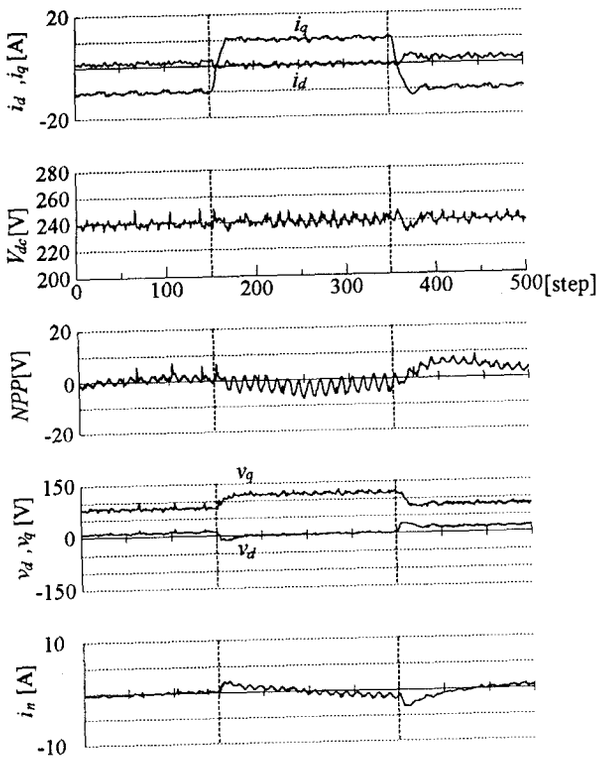

Fig. 10. Responses to step changes in a reactive current reference in SVG operation. i_q^* = -10A → 10A. 5.55ms/div.

The average switching frequency of the devices is below 500Hz for Figs. 7 to 10, thus indicating that high power GTOs may be applicable.

6. CONCLUSION

In this paper, the modeling and control of a neutral point clamped three phase voltage source boost converter have been carried out. The linear state equations obtained from the analysis are useful for designing a state feedback control system.

The relation between the neutral point current and the half vectors used are clarified. The method of controlling the neutral point potential (NPP) by adjusting the output time ratio of a positive half vector to a negative half vector is proposed. An integral-type optimal regulator is used for the converter control. The regulator enables us not only to accomplish three control purposes, PF control, NPP control and DC link voltage control, simultaneously but to realize a stable system in the event of load variations. The validity of the modeling and the control strategy are confirmed by experimental results.

ACKNOWLEDGMENT

The authors express their sincere thanks to A. Sagawa of Hitachi Co. Ltd. for his initial efforts toward this project, and A. Nii of Hokkaido University for his assistance to building the experimental setup.

REFERENCES

[1] A. Nabae, I. Takahashi and H. Akagi, "A neutral -point-clamped PWM inverter," IEEE Trans. on IA-17, no.5, pp.518-523, 1981.

[2] Y. Takahashi, "Systems and control," Iwanami, 1978.

[3] S. Fukuda and A. Sagawa, "Modeling and control of a neutral-point-clamped voltage source converter," Conf. Rec. of IPEC-Yokohama, pp.470-475, 1995.

[4] Y. Iwaji and S. Fukuda, "A parameter designing method of PWM voltage source rectifier," IEEJ Trans. vol.112-D, no.7, pp.639-647, 1992.

[5] A. Sagawa, S. Fukuda and H. Ohgose, "A PWM control method of three level inverters for suppressing the neutral point potential variations," Conf. Rec. of IAS-Japan, pp.351-356, 1993.

[6] K. Koyama et al., "PWM of NPC inverter considering minimum pulse width and neutral voltage balance," Conf. Rec. of IAS-Japan, pp.368-373, 1992.

APPENDIX

The operating points identified by the subscript "o" are:

$$i_{q0} = 0, \quad v_{d0} = E_1, \quad i_{n0} = 0,$$

$$I_{dc0} = \frac{V_{c10} + V_{c20}}{R_{dc}},$$

$$i_{d0} = \frac{E_1 - \sqrt{E_1^2 - 4R(V_{c10} + V_{c20})I_{dc0}}}{2R},$$

$$v_{d0} = E_1 - Ri_{d0},$$

$$v_{q0} = -\omega L i_{d0}$$

Linearizing (1)-(2) and (4)-(6) around the operating point, a state equation of the following form is obtained:

$$\frac{d}{dt}\mathbf{x} = \mathbf{A}_c\mathbf{x} + \mathbf{B}_c\mathbf{u} + \mathbf{E}_c\mathbf{d}, \quad \mathbf{y} = \mathbf{C}\mathbf{x}$$

where

$$\mathbf{A}_c = \begin{bmatrix} -\frac{R}{L} & \omega & 0 & 0 & 0 \\ -\omega & -\frac{R}{L} & 0 & 0 & 0 \\ \frac{v_{d0}}{C(V_{c10}+V_{c20})} & \frac{v_{q0}}{C(V_{c10}+V_{c20})} & -\frac{1}{CR_{dc}} & -\frac{1}{CR_{dc}} & -\frac{1}{C} \\ \frac{v_{d0}}{C(V_{c10}+V_{c20})} & \frac{v_{q0}}{C(V_{c10}+V_{c20})} & -\frac{1}{CR_{dc}} & -\frac{1}{CR_{dc}} & -\frac{1}{C} \\ 0 & 0 & \frac{1}{L_{dc}} & \frac{1}{L_{dc}} & -\frac{R_{dc}}{L_{dc}} \end{bmatrix},$$

$$\mathbf{B}_c = \begin{bmatrix} -\frac{1}{L} & 0 & 0 \\ 0 & -\frac{1}{L} & 0 \\ \frac{i_{d0}}{C(V_{c10}+V_{c20})} & \frac{i_{q0}}{C(V_{c10}+V_{c20})} & -\frac{1}{2C} \\ \frac{i_{d0}}{C(V_{c10}+V_{c20})} & \frac{i_{q0}}{C(V_{c10}+V_{c20})} & \frac{1}{2C} \\ 0 & 0 & 0 \end{bmatrix},$$

$$\mathbf{C} = \begin{bmatrix} 0 & 1 & 0 & 0 & 0 \\ 0 & 0 & 1 & 0 & 0 \\ 0 & 0 & 0 & 1 & 0 \end{bmatrix}, \quad \text{and} \quad \mathbf{E}_c = \begin{bmatrix} \frac{1}{L} & 0 & 0 & 0 & 0 \end{bmatrix}^T$$

DC Ripple Current Reduction Method on A Single Phase PWM Voltage Source Converter

Toshihisa Shimizu, Yasuhiro Fujioka, Gunji Kimura
Tokyo Metropolitan University
1-1, Minami-Ohsawa, Hachioji-shi, Tokyo 192-03, JAPAN
Fax: +81-426-77-2737, Phone: +81-426-77-2743
E-mail: shimizu@eei.metro-u.ac.jp

Abstract - **The present paper introduces a novel topology for a single phase PWM voltage source converter and related control method that can produce not only a sinusoidal input current but also zero-ripple output current. The main circuit of this converter is composed of a conventional single phase PWM voltage source converter and a ripple reduction circuit. The ripple reduction circuit is composed of a additional switching leg, an inductor, and a switching leg that is shared with the PWM converter.**

Input current control is achieved by the conventional high-frequency PWM current control technique. On the other hand, DC ripple reduction control is associated with some difficulties because one of the switching legs in the ripple reducing portion is shared with the PWM converter portion. In order to reduce the DC ripple current, the inductor current at the ripple reducing portion must be maintained to the adequate value which is deeply influenced by the modulation factor on the PWM converter. The relationship between the modulation factor and the inductor current was analysed, and the inductor current necessary for DC ripple current reduction was studied. The effectiveness of this circuit was confirmed experimentally and by simulation. The converter is useful for UPS's and DC power supplies, particulary in the case in which batteries are connected to the DC line.

I . Introduction

The generation of harmonics and their subsequent propagation into utility lines is a topic of increasing concern for power supply authorities. To reduce harmonics in power lines, unity power factor PWM converters are used. However, single-phase PWM converters have serious defects including low frequency ripple current which appears on the DC output increases in proportion to the input current into the PWM converter, resulting in low frequency ripple voltage in the DC output.

Therefore, a very large capacitor or a passive L-C filter circuit is generally connected to the DC line in order to reduce low frequency ripple voltage. Furthermore, when batteries are connected to the DC output, most of the DC ripple current generated by the PWM converter flows into the battery because the impedance of the battery is comaratively much lower than that of the prior-art circuit. Battery ripple current, particularly at low frequencies, results in battery heating and a corresponding rise in temperature. It is well known that battery life time decreases as temperature increases.

The present paper introduces a new topology for a single phase PWM voltage source converter which produces not only sinusoidal input current but also zero-ripple output current. This new toplogy is accomplished by adding only a pair of switching devices and a reactor to a conventional single-phase PWM converter circuit. Using a simple control technique, the ripple energy in the DC line is converted by the action of the additional switches into energy which is stored in the additional inductor. The effect of this converter is confirmed experimentally using a bread board set-up as well as by simulation.

II . Main Circuit Configuration

Fig.1 shows the configuration of the main circuit of the proposed PWM converter. Table 1 shows the circuit parameters of the main circuit. The rectifier portion of the single-phase PWM converter consists of U-phase switches (S_1, S_2), V-phase switches (S_3, S_4), a DC capacitor (C_D), and an input AC filter circuit (L_{AC}, C_{AC}). The ripple reducing portion consists of additional switches (S_5, S_6) which we call W-phase switches, V-phase switches which are shared with the rectifier portion, and an additional inductor (L_W) that is connected between the junction of the V-phase switches and the junction of the W-phase switches.

III . Operation Principle

A. Rectifier Portion

For PWM modulation in the rectifier portion and ripple reducing portion, a triangular signal with a frequency of 20kHz is used in common. The switching frequency of switches S_1 - S_6 is then comparatively higher than the AC input frequency. Fig.2 shows the waveforms of the carrier signals v_{tri} and control signals v_U and v_V. Fig.3 shows the detailed waveforms of v_{tri}, v_U, and v_V during one switching period. S_1 and S_2 are controlled based on a comparison of v_U and v_{tri}, and S_3 and S_4 are controlled based on a comparison of v_V and v_{tri}. Hence, the "ON duty factor" D_U of S_1 and

0-7803-3823-5/97/$10.00© 1997 IEEE

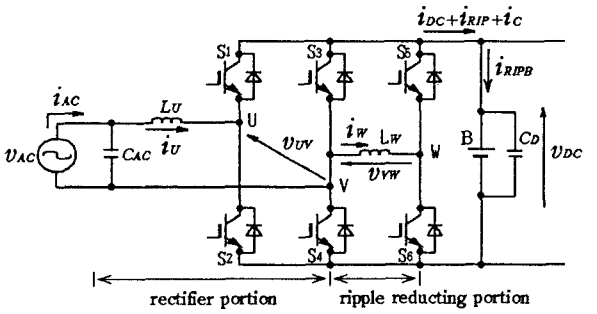

Fig.1. Main circuit.

Table 1. Circuit parameters.

AC Filter Inductor : L_U	1.16mH
AC Filter Capacitor : C_U	5.0μF
IGBT Switch : S_1–S_6	2MBI75–060(Fuji)
DC Filter Capacitor : C_D	1000μF
AC Inductor : L_U	20mH
Battery : B	12V–6AH ×9

the "ON duty factor" D_V of $S3$ are defined as shown in Fig.3. Depending on the combination of D_U and D_V, switching stages, stage 1a – stage 3a, of the main circuit of the rectifier portion are defined and the switching sequence during one switching period is determined. Fig.4(a) – (c) show the equivalent circuits that correspond to each stage. AC input current i_U flows into the DC output in stage2a, but circulates in the switching devices in stages 1a and 1c.

If v_U and v_V are sinusoidal waveforms as shown in Fig.2, D_U,D_V, and λ are defined as,

$$D_U = (1+\lambda)/2 \quad (1)$$

$$D_V = (1-\lambda)/2 \quad (2)$$

$$D_U + D_V = 1 \quad (3)$$

$$\lambda = \lambda m \sin(\theta-\varphi)\ . \quad (4)$$

where λ is the modulation factor, and λm is the maximum value of the modulation factor.

Therefore, the averaged DC output current i_{out} during one switching period is,

$$i_{out} = (D_U - D_V)\, i_U \quad (5)$$

If the parameters of the input AC filter circuit are selected to provide fast response time, input current i_U follows as a sinusoidal current according to the following formula,

$$i_U = I_U \sin(\theta-\varphi-\delta). \quad (6)$$

Substituting (1),(2), and (6) into (5), the DC output current is given as,

$$i_{out} = 1/2\ \lambda m I_U \cos\delta - 1/2\ \lambda m I_U \cos 2(\theta-\varphi-\delta/2)$$
$$= i_{DC} + i_{RIP}\ . \quad (7)$$

Where i_{DC} is the pure DC current component, and i_{RIP} is the AC ripple current component that has twice the frequency of the input AC current.

B. Ripple Reducing Portion

In order to reduce the DC ripple current, both V–phase and W–Phase switches are used. Similar to

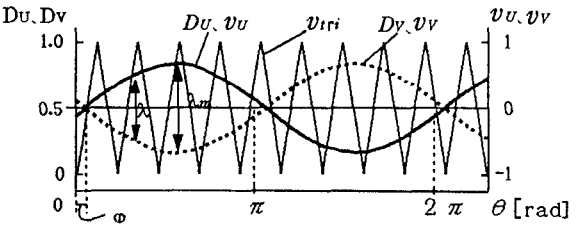

Fig.2. Modularion principle.

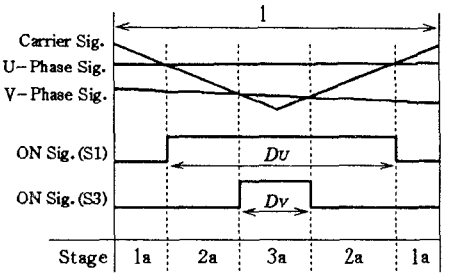

Fig.3. Switching stages of the rectifier portion.

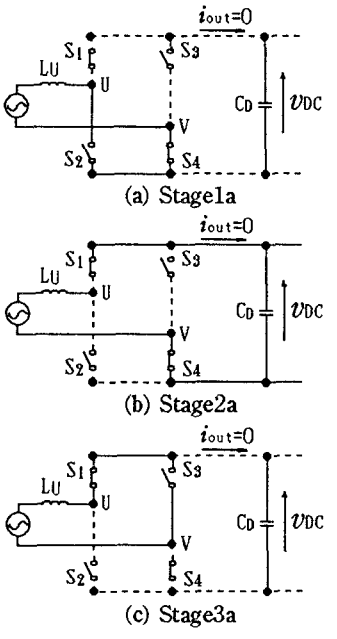

Fig.4. Equivalent circuits of the rectifier portion.

the rectifier portion, the "ON duty factor" D_W of $S5$ is defined and switching stages, stage1b – stage4b, of the ripple reducing circuit are defined as shown in Fig. 5(a) and (b). The equivalent circuits that correspond to each stage are shown in Fig. 6(a)–(d). Assuming that the current i_W flowing into the inductor L_W is a DC current as shown in Fig. 6, i_W flows in the same direction as compensating current i_C in stage4b and in the opposite direction in stage2. In stage1b and 4b, i_W circulates in the switching devices and i_C=0. Therefore, the energy stored in the inductor L_W is discharged when the switching sequence in Fig.5(a) is selected, and is charged when the switching sequence in Fig.5(b) is selected. We call the former sequence, "discharge sequence" and the latter sequence, "charge

sequence". Depending on the charge and discharge sequence, compensating current ic which flows from the ripple reducing portion into the DC output is given by,

$$ic=iw\,(Dv-Dw). \qquad (8)$$

where, discharge seq. : $Dv-Dw>0$,

charge seq. : $Dv-Dw<0$.

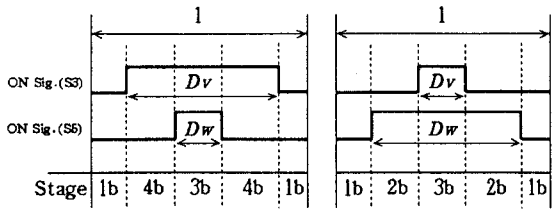

Fig.5. Switching stages of the ripple reducing portion.

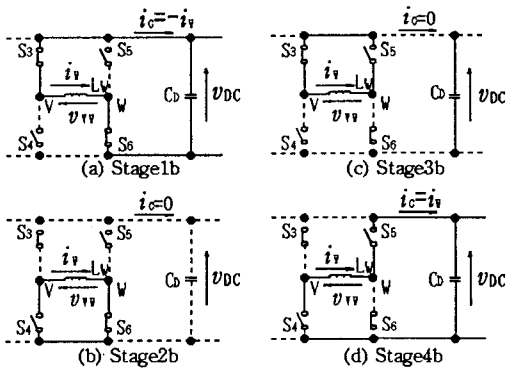

Fig.6. Equivalent circuits of the ripple reducing portion.

C. DC Ripple Current Reduction

If ic is controlled in order to eliminate ripple current i_{RIP}, the current that appears in the DC output will be pure DC current. A sufficient current iw is essential to realize this operation because ic control is restricted by Dv which is decided in preference to input current control.

In the discharge condition, the maximum discharging duration is obtained when Dw=0. Therefore, the minimum current $iwmin$ necessary for ripple reduction is given by,

$$iwmin=iRIP\,/\,ic$$
$$=\lambda m IU\cos 2(\theta-\varphi-\delta/2)\,/\,\{1+\lambda m\sin(\theta-\varphi)\}. \qquad (9)$$

In the charge condition, the maximum charging duration is obtained when Dw=1. Therefore, the minimum current $iwmin$ necessary for ripple reduction is given by,

$$iwmin=iRIP\,/\,ic$$
$$=\lambda m IU\cos 2(\theta-\varphi-\delta/2)\;/\;\{1-\lambda m\sin(\theta-\varphi)\}. \qquad (10)$$

The calculated absolute value of $iwmin$ is shown in Fig.7. The current $iwmin$ varies according to the instantaneous phase angle, such that that the larger the modulation signal λm, the larger the minimum current $iwmin$.

The energy stored in the Lw varies according to the discharging or charging operation. As Lw is connected to the constant DC output voltage source during these operations, iw varies in proportion to the stored energy. "The give and receive energy" between Lw and the rectifier portion should be studied in order to estimate iw.

The ripple energy generated by the rectifier portion is given as,

$$QB=\int iRIP\,vDC\,dt$$
$$=QB0-(1/4\omega)\lambda m\,IU\,vDC\,\sin 2(\theta-\varphi-\delta/2)\ . \qquad (11)$$

The stored energy QL in the Lw is given as,

$$QL=(1/2)\;Lw\;iw^{2} \qquad (12)$$

In case which QB is converted to QL,

$$QB=QL\ , \qquad (13)$$

iw is obtained by substituting (11) and (12) into (13) such that,

$$iw=\sqrt{(2/Lw)\{QB0-(1/4\omega)\lambda m\,IU\,vDC\,\sin(\theta-\varphi-\delta/2)\}}. \qquad (14)$$

where $QB0$ is the energy stored in Lw at "the instantaneous phase angle"=0.

In order to perform ripple reduction, iw must be larger than $|iwmin|$ in all the instantaneous phases,

$$iw \geq |iwmin|\ . \qquad (15)$$

The boundary condition of iw in each λm is obtained by calculating $QB0$ which satisfies $iw=|iwmin|$. The waveforms of iw at the boundary conditions are shown in Fig.7. Current iw contains both DC and AC components. The amplitude of the AC component becomes larger as the inductance Lw becomes smaller. Thus, the minimum inductance Lw should be selected so as not to cross the $|iwmin|$ waveform and iw waveform.

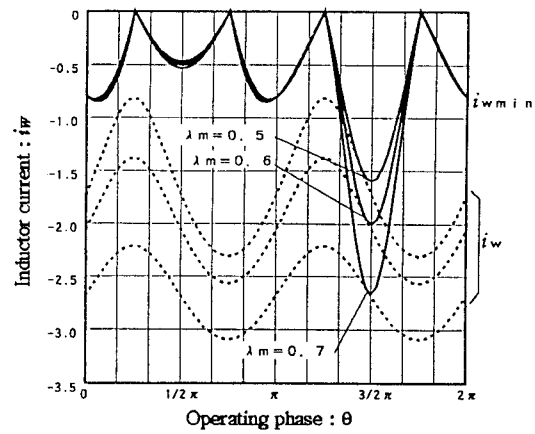

Fig.7. Minimum condition of iw_{min} and operating current of iw.

IV . Control Circuit

Based on the above discussion, the very simple control circuit shown in Fig.8 can be constructed. In the control block diagram shown in Fig.7, sig.1 ~ sig.6 represent the trigger signals of the main switches, S1 ~ S6, respectively. In Fig.8, the upper portion represents the PWM rectifier circuit and the lower portion represents the ripple reduction circuit. For input current control, the current reference iU^{*} is obtained by multiplying the input voltage waveform

signal, v_{AC}, and the output of the DC voltage regulator. The input AC current, i_U, is obtained from the current detector. Since one of the inputs to the error amplifier, Kp1, is i_U and the other is i_U^* the output of the error amplifier is the control signal e_U. The control signal e_V is obtained by multiplying e_U by -1. Control signals e_U and e_V are modulated at the comparators by the triangular waveform, v_{tri}. The output of the comparators are the triggering signals sig1 ~ sig4. For ripple reducing control, the ripple current, i_{RIP}, is the input to the error amplifier, Kp2. In order to maintain the inductor current, the inductor current i_W and the reference signal i_W^* are the inputs to the error amplifier Kp3. The sum of the outputs of Kp2, Kp3, and $-e_V$ is the control signal, e_Z. The control signal, e_Z, is modulated by e_{tri}, as described previously.

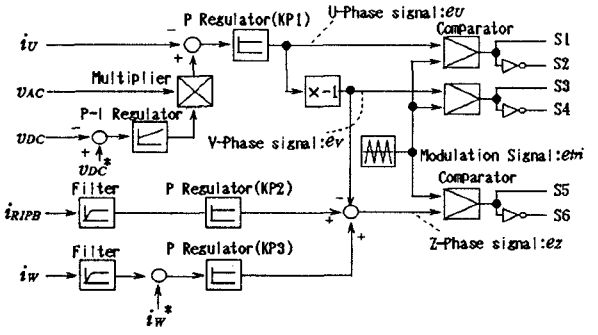

Fig.8. Block diagram of the control circuit.

V . Experimental Results

Fig.10 and 11 show the results of applying and not applying the proposed method, respectively. The effective value of the ripple current in Fig.10 is reduced to approximately 1/20 of that in Fig.11. These results clearly demonstrate that the DC ripple current is effectively reduced when the proposed method is applied. According to the charging and discharging action on the inductor L_W, ripple current occurs in the inductor current i_W. The input AC current i_U in Fig.10 has a sinusoidal waveform that is the same waveform as that shown in Fig.11. This result demonstrates that both sinusoidal input current control and ripple reduction control are accomplished by the proposed method.

VI . Conclusions

The present paper introduced a novel circuit topology for a PWM rectifier. The proposed PWM converter is designed to produce both a unity power factor with a sinusoidal input current, and reduce the DC ripple current that flows into an output-side battery. Presentation of the operating principle and the control scheme, a theoretical analysis, and experimental examination of the proposed rectifier were performed. The present results suggest that the ripple current that flows into a battery can be significantly reduced through the use of W-phase switche control.

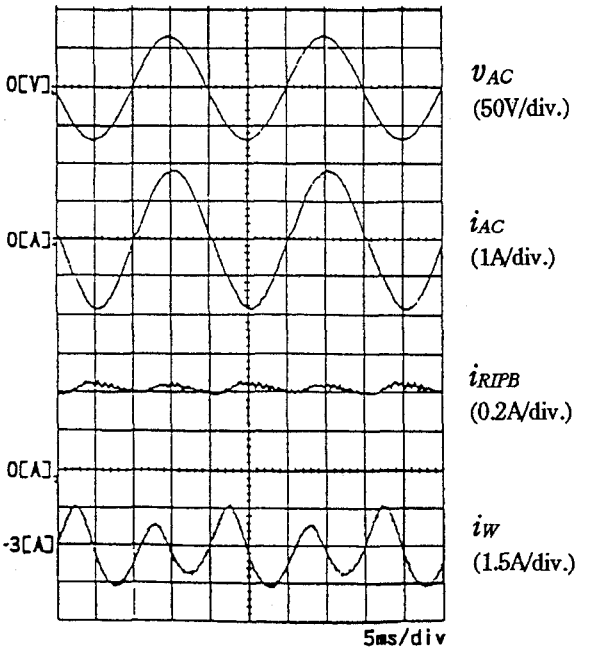

Fig.10. Experimental waveforms(with repple reduction control).

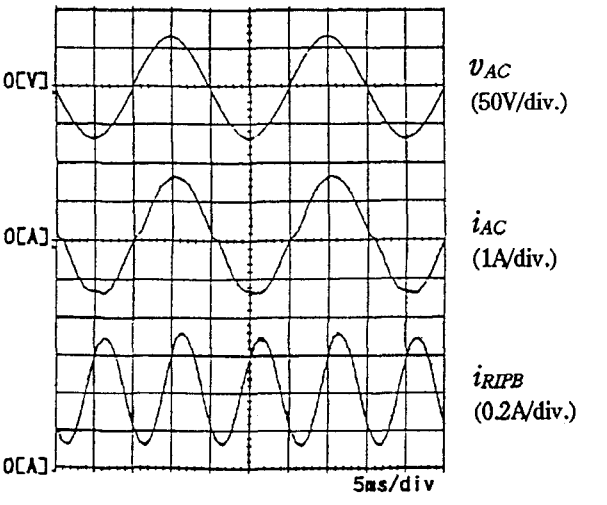

Fig.11. Experimental waveforms(without repple reduction control).

References

[1] T.Shimizu, T.Fujita, G.Kimura, J.Hirose, "Unity power factor PWM converter with DC ripple compensation." Trans. on IEE of Japan, D-117, Vol.4, pp.434-442, 1997.(in Japanese)

[2] T.Shimizu, T.Fujita, G.Kimura, J.Hirose, "Unity power factor PWM converter with DC ripple compensation." Proc. of IECON'94 Vol.1, pp.657-662, 1994

[3] T.Kitano, M.Matsui, "A single phase PWM converter which has an active filter function on both the input and the output." National convention records, IEE of Japan, No.720, pp.77, 1995.(in Japanese)

A Simple Sensorless Method for Sinusoidal PWM Converters

Itaru Ando, *member, IEEE*, Isao Takahashi, *fellow, IEEE*
Nagaoka University of Technology
1603-1 Kamitomioka Nagaoka 940-21, JAPAN
FAX:+81-258-47-9500, phone:+81-258-47-9515
E-mail : andoh@vos.nagaokaut.ac.jp

Kouji Utsunomiya, *member, IEEJ*
Takaoka Electric MFG. Co., Ltd.
1 Kikyoudaira Ohhira Miyagi, 981-36, JAPAN
FAX:+81-22-345-5836, phone:+81-22-345-1811
E-mail : k.utsu@sen.takaoka.co.jp

Abstract—**This paper describes about a simple sensorless method of PWM converters which can remove the line voltage sensors. It has following characteristics.**

(1) The voltage sensorless method is realized only by adding two operation amplifiers to the conventional PWM control circuit. Therefore, it makes low cost and small size.

(2) The line current waveform can be improved by compensating voltage drops of input filter reactor and dead-time of IGBTs.

(3) Quick response is also obtained on the high speed fluctuation of voltage and frequency or transient states.

(4) It can get characteristics than the conventional complexity sensorless control methods.

As a result, the input power factor and the total input current distortion are achieved more than 99.5% and less than 2.3%, respectively on 3kW system.

It is not only obtain excellent performance but also realized the small size, simple control construction and low cost converter.

I . INTRODUCTION

Increasing of power electronic loads with a diode rectifier, many bad influences on power systems are being arising such as low input power factor and harmonic distortions. A countermeasure is providing a PWM converter which has unity input power factor and sinusoidal line current waveforms. It is necessary three sensors, a dc link voltage sensor, a line current sensor and a line voltage sensor. It is requested to remove these sensors for improving reliability and manufacturing cost of the converter. But, the sensors of the dc link voltage and the line current can not remove by reason of the dc link over voltage and the line over current protection.

This paper describes about a simple line voltage sensorless method of PWM converters. It has following characteristics.

(1) The voltage sensorless method is realized only by adding two operation amplifiers to the conventional PWM control circuit. Therefore, this method makes low cost and small size.

(2) The line current waveform can be improved by input filter reactor voltage drops and IGBTs dead-time compensations. And it is achieved by using a band pass filter even if using bad line voltage waveforms.

(3) By using the high speed PI circuit, high speed response is also obtained on the high speed fluctuation of voltage and frequency or transient states.

(4) It is almost same characteristics as the conventional complexity sensorless methods. [1][2][3][4]

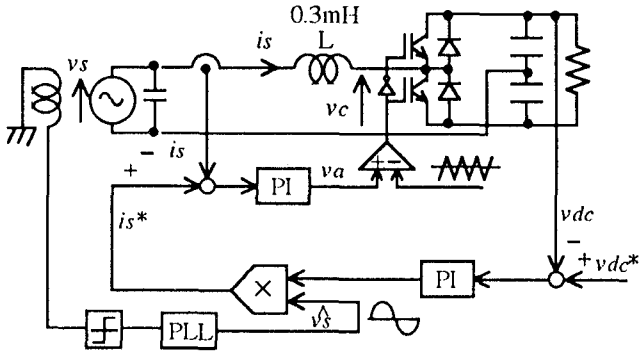

Fig.1. Conventional single phase sinusoidal PWM converter.

II . PRINCIPLE AND CIRCUIT OF THE SIMPLE LINE VOLTAGE SENSORLESS METHOD

Fig.1 shows the configuration of a sinusoidal PWM converter of the half bridge type. Current control of the converter is achieved by the amplitude modulation of a follow up method using PI compensator. In this case, line voltage v_s is given as follows;

$$v_s(t)=L\frac{d\,i_s(t)}{d\,t}+v_c(t) \qquad (1)$$

where v_c and i_s are converter output voltage and line current, respectively.

The line voltage v_s is nearly equal to the reference signal v_a of converter output voltage v_c when input filter reactor drop v_L (=L d $i_s(t)$/dt) is small and the switching harmonics and the dead-time voltage drop are omitted. The converter model and its vector diagram are shown in Fig.2. The basic idea of the line voltage estimation is based on using the estimated line voltage value v_a from the power line voltage instead of the real ones. [5]

Fig.3 shows the configuration of the half bridge type converter main and control circuits presented in this papers. In this figure, details of the control blocks (a) and (b) are

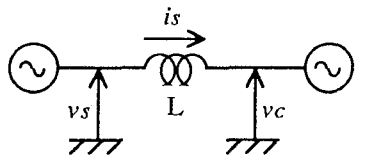

(a) Converter model.

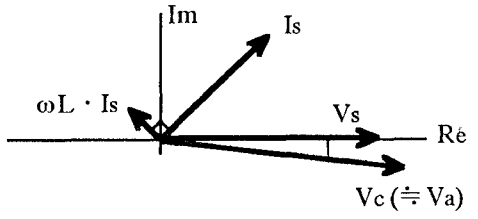

(b) Vector diagram of the converter.

Fig.2. Converter model and its vector diagram.

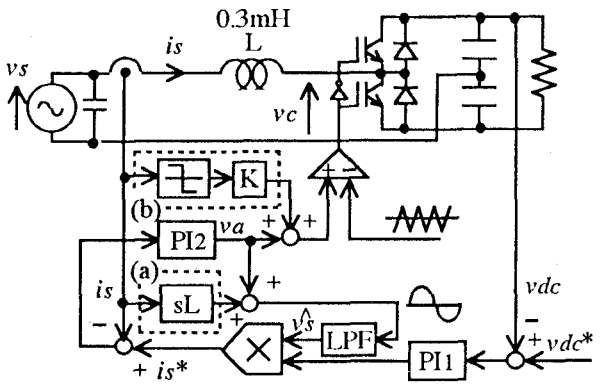

Fig.3. Half bridge PWM converter with the simple line voltage sensorless method.

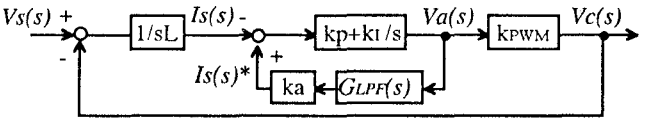

kPWM : gain from control circuit to main circuit.
kp, kI : proportional and integral gain of PI2 compensator.
ka : output value of PI1 compensator.
$G_{LPF}(s)$: transformer function of low pass filter

Fig.4. Line current control block diagram of the sensorless PWM converter.

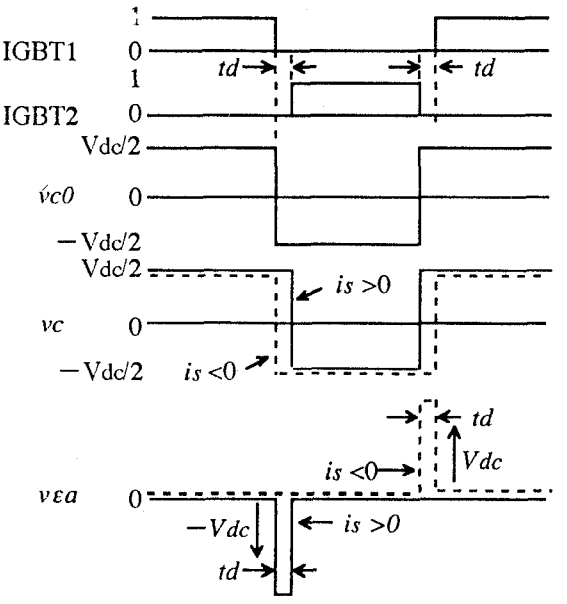

Fig.5. Error voltage v_{ea} during the dead time *td*.

presented later.

When the dc link capacity is enough, the time constant of the dc link voltage control is long enough than that of the line current. Therefore, it is note that the dc link voltage control can be achieved if the line current is stable.

Fig.4 shows the line current control block diagram of the sensorless PWM converter. In this case, the converter is assumed to the ideal sinusoidal output source. Therefore, equation (2) is given by Fig.4. And equation (3) is obtained at the high compensation PI gain, the low pass filter of unity gain, and the small input filter reactance.

$$\frac{I_s(s)}{V_s(s)} = \frac{s - k_a G_{LPF}(s)(sk_p + k_I)}{sL\{s - k_a G_{LPF}(s)(sk_p + k_I)\} - k_{PWM}(sk_p + k_I)} \quad (2)$$

$$\doteqdot \frac{k_a}{k_{PWM}} \quad (3)$$

Therefore, It is clear that the line current i_s is equaled waveform to the line voltage v_s and the phase of i_s is agreed with that of v_s.

But, the line current i_s would be included many harmonic distortion if above principle is applied to the practical converter.

Voltage drop compensation of the input filter reactor and the dead-time

The reference signal v_a is included harmonic distortion by influence of the input filter reactor voltage drop v_L and the dead-time *td* of IGBTs. It would be clear from equation (1).

The control block (a) of Fig.3 works the reactor voltage drop compensation. The harmonic distortion of the estimated line voltage v_a that is caused by the voltage drop v_L (=sL i_s) is compensated by adding it to v_a.

The dead-time *td* makes error between the averaging output voltage v_c of the converter and the estimated value v_a of line voltage. This error is most distortion factor on estimation of the line voltage.

Fig.5 shows the error voltage v_{ea} during the dead-time *td*. During the dead-time, the converter output voltage v_c is decided on following equation by the polarity of the line current i_s.

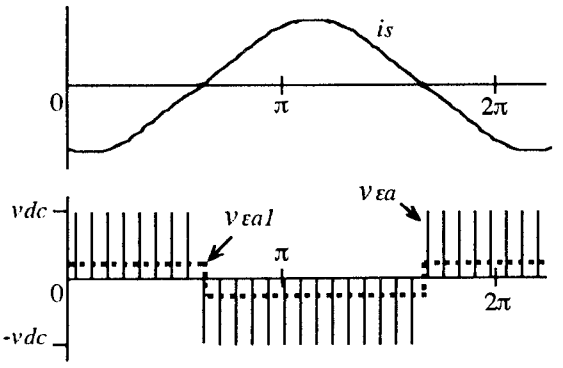

Fig.6. Averaging waveform v_{ea1} of the error pulse v_{ea}.

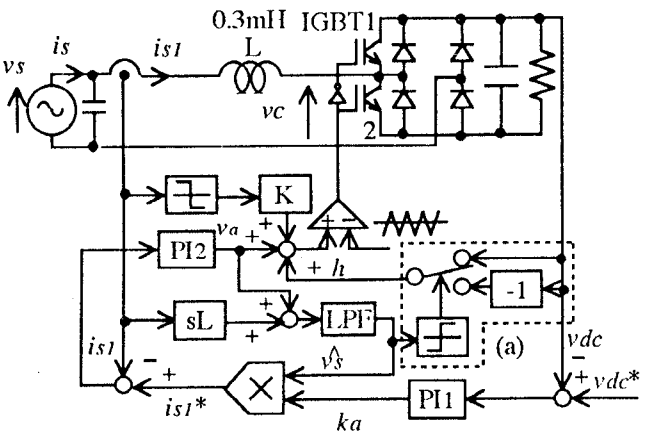

Fig.7. Main and control circuits of the hybrid bridge single phase PWM converter with the simple voltage sensorless method.

$$v_c = v_{dc}/2 \text{ .....in the case of } i_s > 0$$
$$v_c = -v_{dc}/2 \text{ .....in the case of } i_s < 0 \quad (4)$$

The error voltage v_{ea} to the ideal converter output voltage v_{c0} is obtained by adding such pulses as shown in Fig.5. The average waveform of the pulse arisen each cycle at switching times is equaled to square waveform v_{ea1}. The phase of its fundamental harmonic is coincided with the phase of i_s as shown in Fig.6. The crest value of v_{ea1} is given by following equation (5).

$$V\varepsilon = td \cdot Vdc \cdot fc \quad (5)$$

Where fc is the carrier frequency.

Therefore, The dead-time compensation is achieved by adding the square waveform v_{ea1} whose phase is controlled by the line current i_s to the estimated line voltage v_a. [6]

Ⅲ. APPLICATION TO THE HYBRID BRIDGE SINGLE PHASE PWM CONVERTER

Fig.7 shows the main and control circuits of a hybrid bridge single phase PWM converter with the simple voltage sensorless method. The hybrid converter output voltage

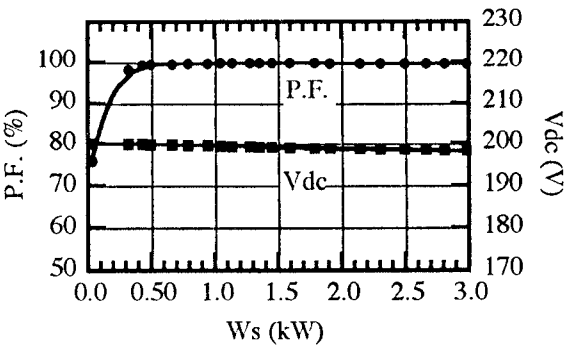

Fig.8. Steady state basic characteristics.

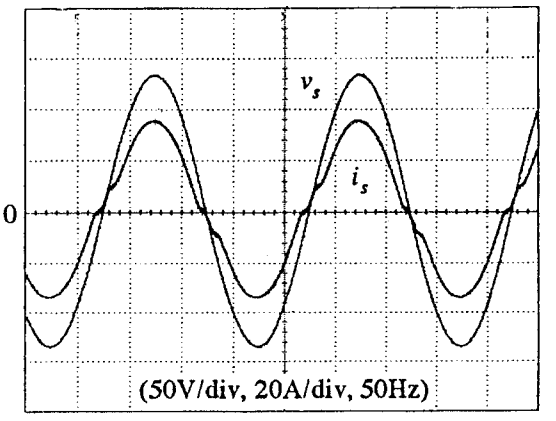

Fig.9. Line voltage v_s and the current i_s waveforms without the reactor and the dead-time compensations.

reference v_a must be contolled to positive or negative value with same value to the dc link voltage by the line voltage polarities when the line current is controlled to the sinusoidal waveform and unity power factor. The control block (a) in Fig.7 is supplementary circuit for reasons of PI2 should not compensate above control. Because the developed sensorless method is based on the line voltage estimation from v_a. Therefore, the control block (a) is not need on the full and half bridge converter.

Experimental results of the hybrid bridge converter

The experiment is carried the condition under v_s 100V, v_{dc}* 200V and the carrier frequency of 16kHz.

Fig.8 shows basic characteristics on steady-state. It is noted that the input power factor P.F. over 99% is achieved over an input power W_s of 0.35kW, the dc link voltage V_{dc} is kept almost constant and its regulation is also within 1%.

Fig.9 shows the line voltage v_s and the current i_s waveforms without the reactor and the dead-time compensations when the input power W_s is 2.5kW. The current waveform is contained some harmonic distortion because of no reactor and dead-time compensations.

Fig.10 shows the line voltage v_s and current i_s waveforms and the frequency spectrum of that current i_s with

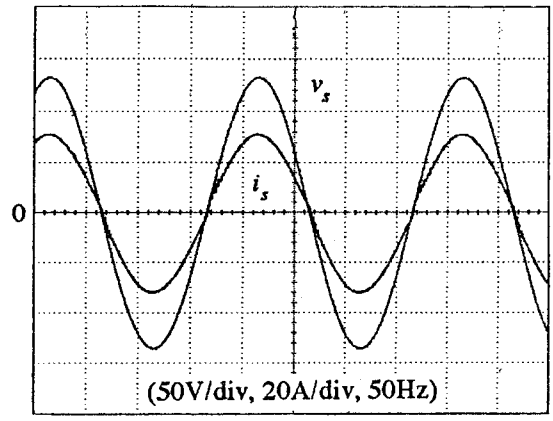

(a) Line voltage v_s and current i_s waveforms.

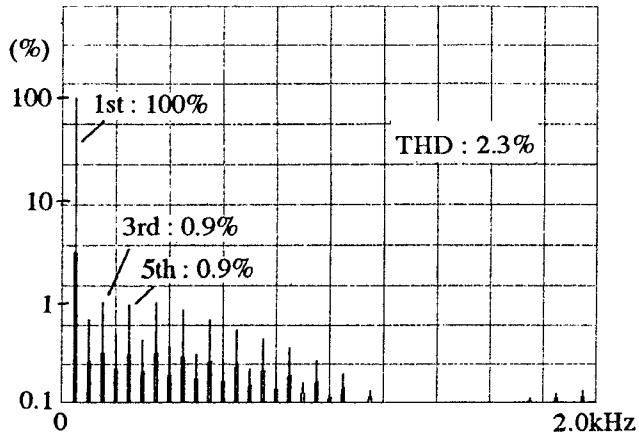

(b) Current frequency spectrum.

Fig.10. Line voltage v_s and current i_s waveforms and the frequency spectrum of i_s with the reactor and the dead-time compensations.

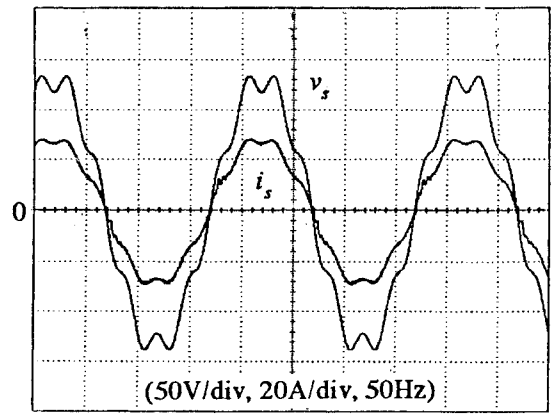

Fig.11. Line voltage v_s and current i_s waveforms when the line voltage is contained harmonics component (7th, 10%).

the reactor and the dead-time compensations at the input power W_s = 2.0kW. It is clear that the excellent results are realized such as a total current harmonic distortion THD is 2.3% and unity input power factor.

Fig.11 shows the line voltage v_s having harmonic component (7th, 10%) and current i_s waveforms. It is noted that the line current i_s is almost similar to the waveform of

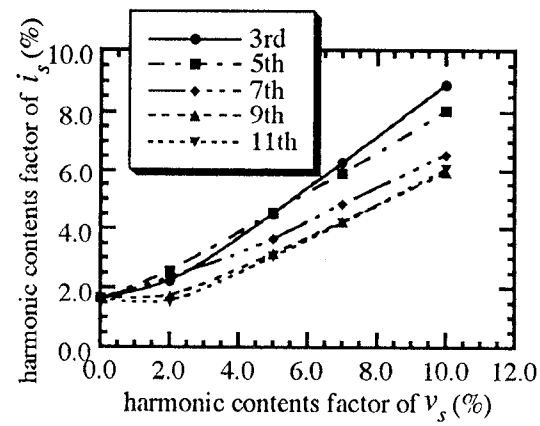

Fig.12. Contents factor of the harmonic current against the line voltage harmonic one.

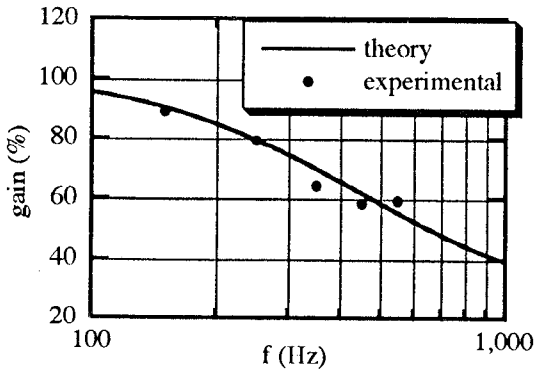

Fig.13. Gain chracteristic of the transfer function $I_s(s)/V_s(s)$

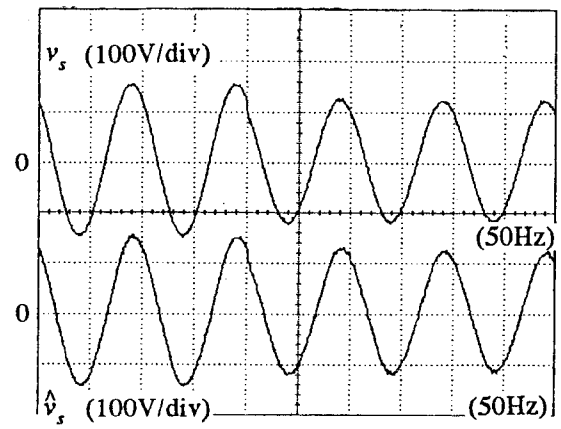

Fig.14. Estimation characteristic of the line voltage.

the line voltage v_s. The contents factor of the harmonic current against the every line voltage harmonic one is shown in Fig.12. The harmonic current is decreased in accordance with high frequency because of the low pass filter in Fig.7.

Fig.13 shows the gain characteristics of the transfer function $I_s(s)/V_s(s)$ which is given by Fig.4. Its characteristics is normalized the gain on 50Hz to 100%. The experimental results is almost same as the theory of this converter. Therefore, It is noted that the same results are obtained as principle of simple sensorless method in consideration of

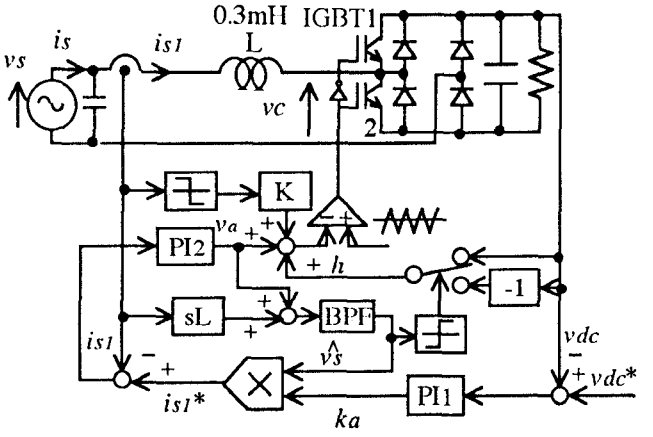

(a) Main and control circuits.

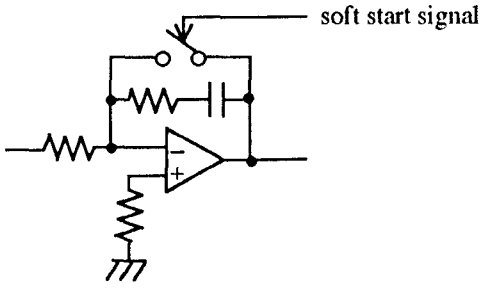

(b) PI1 and PI2 circuits.

Fig.15. Main and control circuits with the line voltage harmonic compensation.

the low pass filter characteristics.

Fig.14 shows the estimation characteristic of the line voltage under the state of the sudden changing of the line voltage. It is notes that the estimated line voltage $\hat{v}_s$ is estimated to the line voltage v_s in very high speed on this state.

Compensation of the line voltage harmonics

Usually, the line current i_s is desired to control the ideal sinusoidal waveform even if the line voltage v_s contains harmonic components. Developed sensorless method is estimated to the line voltage in very high speed response as above results. But, the low pass filter which is shown in Fig.7 has large influence to the estimated line voltage $\hat{v}_s$ and the line current i_s as Fig.13.

Fig.15 shows the main and control circuits with the line voltage harmonics compensation. The band pass filter which is adopted instead of the low pass filter which has the characteristics such as 50Hz cut-off frequency, about 1.0 quality factor and 1.0 gain.

Fig.16 shows the waveforms of the line voltage v_s and the line current i_s with the line voltage harmonic compensation. And, the frequency spectrum of the line current i_s is shown in Fig.17. The line current i_s is controlled to the states of the sinusoidal waveform even if the harmonic component (3rd, 10%) is contained to the line voltage. The 3rd harmonic component of the current is large decreased to 3.7% by this

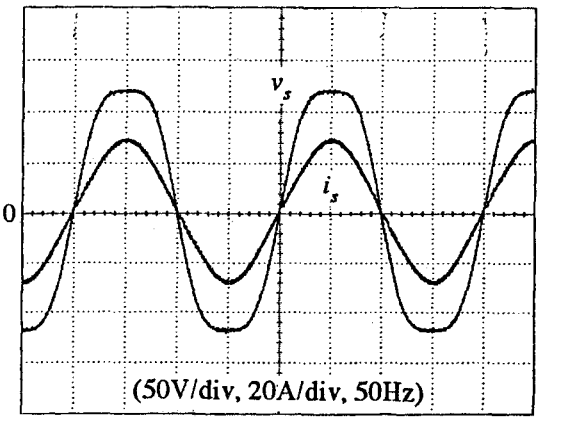

Fig.16. Waveforms of the line voltage v_s and the line current i_s with the line voltage harmonic compensation

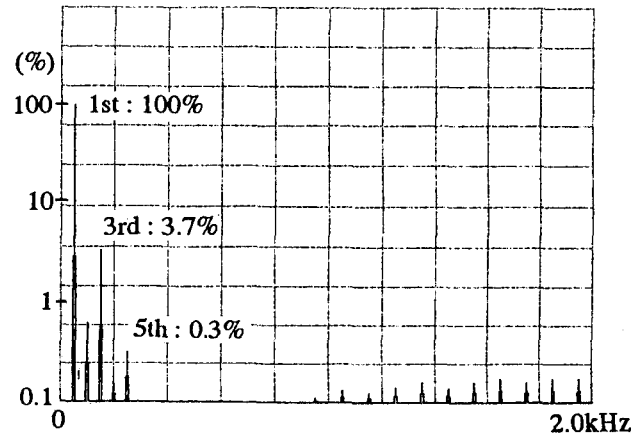

Fig.17. Frequency spectrum of the line current i_s.

simple method using the band pass filter. Its 3rd harmonic component is almost the input filter capacitor current by the distorted line voltage. Therefore, the input filter capacity is design as small as possibile. But, It is so difficult to design of the high quality band pass filter on analog circuits. Consequently, it is desirable to design digital filter on microcomputer software.

It has possibility to have over current on the start up state. Because, the estimated line voltage $\hat{v}_s$ can not be estimated before the converter is actived. Therefore, the converter should be operated with soft start up method.

The soft start is achieved by the following;

(1) Before the converter is actived, the output voltage of PI1 and PI2 are zero and the dc link capacitor is charged to the diode rectifier voltage at turn off states of the every IGBTs. (Fig.15.)

(2) The dc link voltage reference v_{dc}* is built up to the its final reference from the charged dc link voltage with slow curve after start up operation.

(3) The time constant of the current control is set up speedily than the current build up time constant decided input reactor.

Fig.18 shows the start up transient phenomena on the

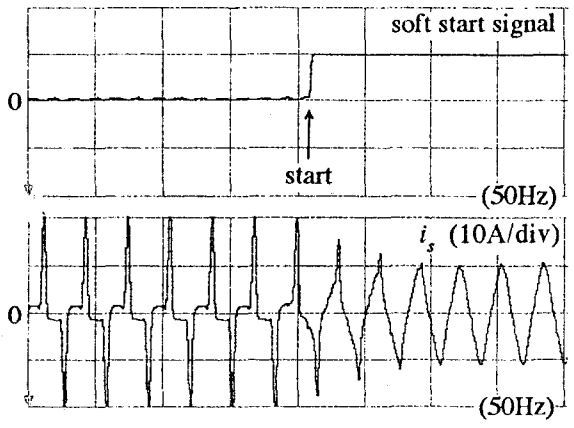

Fig.18. Start up transient phenomena on the soft start control.

soft start control. It may be noted that the dc link voltage v_{dc} is built up with slow curve, the line current phase is immediately agreed with the line voltage one and the transient phenomena of the line current i_s can be controlled under permissible range.

Ⅳ. Conclusion

In this paper, the development of the simple sensorless method of PWM converter which can remove line voltage sensor is described.

As a result, the input power factor and the total input current distortion are achieved more than 99.5% and less than 2.3%, respectively. And the every experimental results can be achieved as well as the conventional complexity sensorless control method.

It is not only obtain excellent performance but also realized the small size, simple control construction and low cost converter.

Acknowledgment

The authors would like to express their appreciation to Power Electronics Laboratory members of Nagaoka University of Technology.

References

[1] T.Takeshita and N. Matsui, "Single Phase High Power Factor PWM Converter without Line Phase Angle and Voltage Detectors" *IEEJ Trans. on IAS*, Japan, vol 113-D, No-10, pp.1211-pp.1219, 1993

[2] T.Takeshita, T.Kobayashi and N.Matsui, "A Scheme of Power Line Voltage Sensorless Three-Phase PWM AC/DC Converter" *IEEJ Trans. on IAS*, Japan, vol 114-D, No-12, pp.1211-pp.1219, 1994

[3] T.Noguchi, H.Tomiki, S.Kondo and I.Takahashi, "Instantaneous Active and Reactive Power Control of PWM Converter by Using Switching Table" *IEEJ Trans. on IAS*, Japan, vol 116-D, No-2, 222-pp.223, 1996

[4] Y.Ito and Y.Kanno, "Line Coltage Sensor-less Digital Control Using Observer for PWM Converter" *IEEJ Trans. on IAS*, Japan, vol 117-D, No-3, pp.314-pp.320, 1997

[5] I.Ando, I.Takahashi and K.Utsunomiya, "A Simple Line Voltage Sensorless Method for Sinusoidal PWM Converter" *IEEJ National Convention Record*, Japan, No.825, 1997

[6] Y.Murai, I.Hosono and Y.Tsunehiro, "On System Stability of PWM Inverter Fed Induction Motor" *IEEJ Trans.-B*, Japan, vol 105-B, No-5, pp.49-pp.56, 1985

Line Voltage Sensorless Three Phase PWM Converter by Tracking Control of Operating Frequency

Tokuo Ohnishi and Kentarou Fujii
The University of Tokushima
2-1, Minami-josanjima, Tokushima,770, JAPAN
FAX:0886-56-7319, Phone:0886-56-7456
e-mail:ohnishi@ee.tokushima-u.ac.jp

Abstract —**Many researches about power line voltage sensorless PWM converter have been presented from the view points of the simplicity and the reliability of the control system. Most schemes need some calculations to estimate the power line voltage using circuit parameters.**

In this paper, we propose a novel control strategy of the three phase PWM converter by tracking control of the operating frequency based on the power balance of the converter. The system is composed of the direct PWM control loop of the instantaneous active and reactive current. The features of the proposed PWM control system are simplicity without sensing the line voltage, high reliability with poor dependence of the circuit parameters, high efficiency and fast response and so on.

I. INTRODUCTION

Three phase PWM converter has been widely used for many applications because it has inherent some good properties such as the bidirectional power flow function and the sinusoidal AC line current waveform resulting in the ripple free DC voltage. The conventional PWM control signals are obtained from the three comparators between the three phase sinusoidal reference waveforms and the triangular carrier signal. And the synchronized reference signal with the AC line voltage by sensing the phase angle of that is usually used.

The conventional sinusoidal PWM technique has some problems to be improved such as the complicate construction and the PWM switching losses. We proposed a new simple PWM switching technique based on the active and reactive power component of the three phase current[1].

Many investigation of power line voltage sensorless PWM converter have bee presented [2][3] from the view points of the simplicity and the reliability of the control system. Most schemes however need some calculations to estimate the power line voltage using circuit parameters.

In this paper, we propose a novel control strategy of the three phase PWM converter by tracking control of the operating frequency based on the power balance between the AC power source and the DC load [4][5][6]. The system is combined with the instantaneous active and reactive current control loops described above [1].

The features of the proposed PWM control system are simplicity without sensing the line voltage, high reliability with poor dependence of the circuit parameters, high efficiency by selecting an appropriate voltage vector, fast response and so on.

In the paper, we mainly describe the sensorless control technique and we show its characteristics by some simulation and experimental results.

II. PRINCIPLE OF SENSORLESS CONTROL

Figure 1 shows the schematic diagram of the sensorless three phase PWM converter by removing the detection loop of the AC line voltage for PWM control. The system is composed of the AC line current and DC voltage control

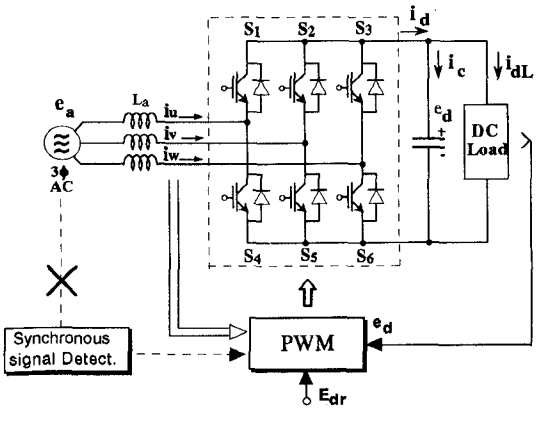

Fig.1 Sensor Less Three Phase PWM Converter

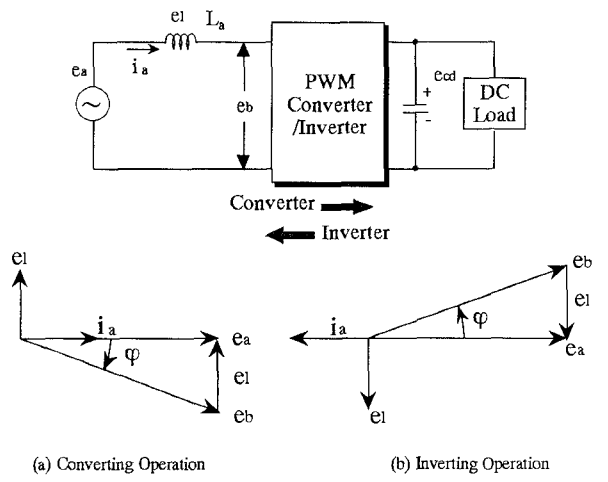

Fig.2 Power flow by phase difference

loops which are not able to remove in order to their control. But, the information of the AC line voltage can be obtained or estimated from line currents and the PWM voltages.

Most schemes of the sensor less PWM converter need some calculations using DSPs or microprocessors to estimate the power line voltage using circuit parameters. So, the control system is somewhat complicate and the control characteristics may be hardly affected by the parameter variations.

Figure 2 show the schematic circuit of the PWM converter and the relations of the phase angle and the power directions. When the phase of the AC side voltage e_b of the PWM converter lags (a), the power flow from AC side to DC side as a converter operation then the DC voltage become high and vice versa (b). So, the line voltage phase information for synchronization of the PWM control can be obtained from the DC voltage variation.

III. INSTANTANEOUS SPACE VECTOR AND CURRENT CONTROL METHOD

From the relation between the line voltage ea and the AC side voltage e_b of the PWM converter shown in Fig.2 ,the voltage equation is obtained as next.

$$e_a = L\frac{di}{dt} + e_b \qquad \text{----------(1)}$$

The two axis components of three phase quantities can be obtained as next by using the following transformation matrix

$$C(\theta) = \sqrt{\frac{2}{3}}\begin{bmatrix} \sin\theta & \sin(\theta - 2\pi/3) & \sin(\theta + 2\pi/3) \\ \cos\theta & \cos(\theta - 2\pi/3) & \cos(\theta + 2\pi/3) \end{bmatrix} \quad (2)$$

Where, $\theta(=\omega t)$ is the rotational angular frequency.

$$e_{ap} = L\frac{di_p}{dt} - \omega L i_q + e_{bp} \qquad \text{----------(3)}$$

$$e_{aq} = L\frac{di_q}{dt} + \omega L i_p + e_{bq} \qquad \text{----------(4)}$$

Where the subscript p,q represent the p-q two axis components of voltage and current respectively. The notations e_p, e_q and i_p,i_q are the instantaneous voltage and current vectors for two axis components. From (2),(3),

$$L\frac{di_p}{dt} = e_{ap} + \omega L i_q - e_{bp} \qquad \text{----------(5)}$$

$$L\frac{di_q}{dt} = e_{aq} - \omega L i_p - e_{bq} \qquad \text{----------(6)}$$

The instantaneous current i_p,i_q can be controlled by the instantaneous voltage vector e_{bp},e_{bq}. When the instantaneous quantities become ripple free, three phase sinusoidal waveform can be obtained [1]. And, the derivative become zero as next

$$L\frac{di_p}{dt} = 0 \quad \text{and} \quad L\frac{di_q}{dt} = 0 \qquad \text{----------(7)}$$

In this case, we can get the next

$$e_{ap} = -\omega L i_q + e_{bp} \qquad \text{----------(8)}$$

$$e_{aq} = +\omega L i_p + e_{bq} \qquad \text{----------(9)}$$

If the q-axis component of e_b is fixed to zero (e_{bq}=0), and the q-axis component of i_a is controlled as a appropriate value, the current vector i is in phase with the voltage vector e and the system is operated under the unity power factor.

Figure 3(a) illustrate the vector relation at this operating

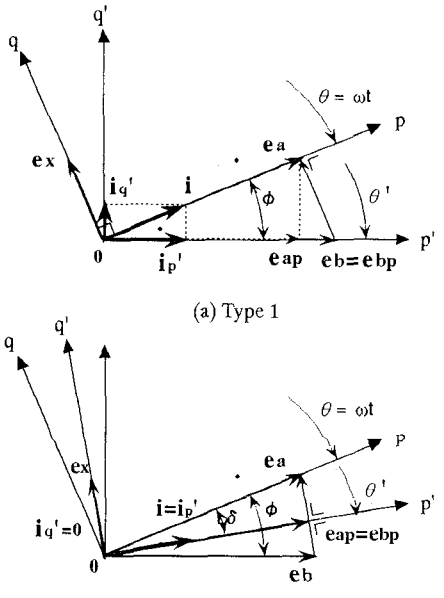

Fig3 Relations among the instantaneous voltage and current vectors.

condition (Type 1). Where, we assume that he p'-q' axis is the estimated rotating coordinate axis and the p-q axis is the actual axis of the AC line voltage. From the figure, the reference value (I_{pr}) of i_p components is obtained as follows;

$$I_{qr} = I_p \tan(\phi) = I_p \frac{\omega L I_p}{E_{ap}} \fallingdotseq \frac{\omega L I_p^2}{E_{bp}} \qquad \text{----------(10)}$$

If the q' axis component of i is controlled to zero ($i_q'=0$), the current vector is aligned with the p' axis.

Figure 3(b) shows their vector relations for this case (Type 2). As can be seen, the P axis component e_{ap} become the same as e_{bp}. Although the current vector i is somewhat out of phase, the phase difference is less than the phase angle φ and small.

The phase angle φ between the line voltage e_a and the AC side fundamental voltage e_b of the PWM converter is proportional to the power flow quantities P_d. The relations is given by

$$P_d = \frac{E_a E_b}{\omega L} \sin \varphi \qquad \text{----------(11)}$$

The phase angle φ is generally small because we can use the small inductance L so that the switching frequency of the PWM converter is high. So, the estimated p'-q' axis is closed to the actual p-q axis by controlling the instantaneous q' axis component. (i_q'). The magnitude of the instantaneous p' axis component (i_p') is depended on the power P_d. Therefore, basically the ripple component of i_p' must be controlled to zero ($\tilde{i}_{p'} = 0$) in order to obtain the sinusoidal current.

IV. OPERATING AXIS AND VOLTAGE VECTOR SELECTION

As mentioned above, the instantaneous current vector is controlled by the voltage vector $\mathbf{e}_b$ which is obtained by the average value of the switched vector among the eight vectors of the three phase bridge converter circuit.

Figure 4 shows relations between the voltage vector e_a,e_b together with the selectable voltage vector V_n(n=0-7) .

When the voltage vector $\mathbf{e}_b$ is in the same region as the vector $\mathbf{e}_a$ (see Fig.4(a)),the instantaneous current vector i can be controlled from (5),(6) by switching the neighbor two vectors and the zero vector [1].

When the voltage vector $\mathbf{e}_b$,however, is located in different region from the vector $\mathbf{e}_a$ (see Fig.4(b)), the current vector i can not be controlled so that the same vector selecting method is used even if the operating p'- q' axis too depart from the actual p-q axis.

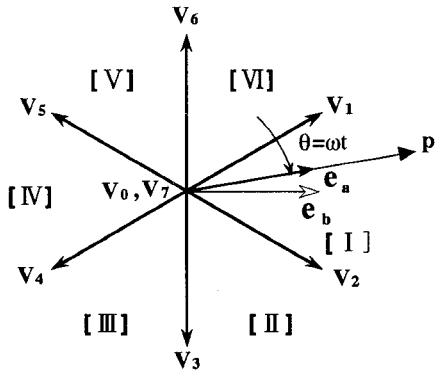

(a) Synchronized state (vector $\mathbf{e}_a$ and $\mathbf{e}_b$ are in the same area)

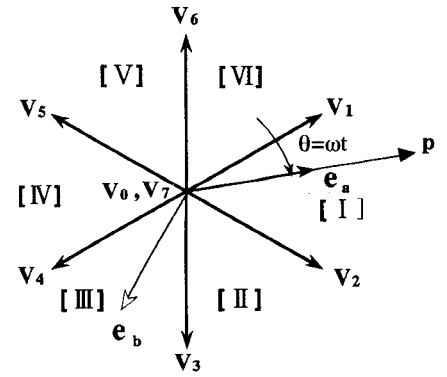

(b) Asynchronized state (vector $\mathbf{e}_a$ and $\mathbf{e}_b$ are in the different area)

Fig.4 Relation among the voltage vector $\mathbf{e}_a$,$\mathbf{e}_b$ and $\mathbf{V}_n$.

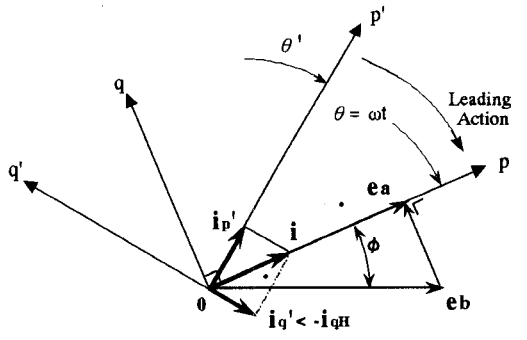

(a) Phase Retard Condition

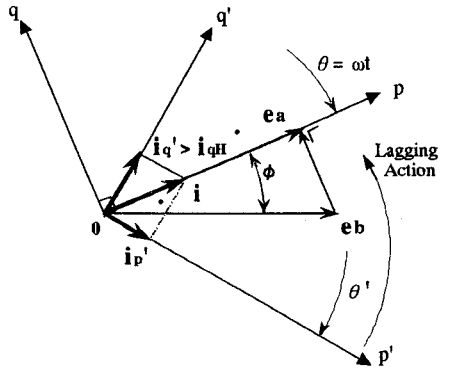

(b) Phase Advanced Condition

Fig.5 Phase Tracking of the Operating Axis to the Actual Axis.

V. DETECTION AND TRACKING THE P-Q AXIS

Now, we assumed that the three phase currents are in phase with the three phase voltages given as next;

$$\begin{bmatrix} i_u \\ i_v \\ i_w \end{bmatrix} = \sqrt{2}I \begin{bmatrix} \sin\theta \\ \sin(\theta - 2\pi/3) \\ \sin(\theta + 2\pi/3) \end{bmatrix} \quad \text{----------(12)}$$

The two axis components (i_p, i_q) of the current vector **i** for the estimated p'-q' axis (θ') are given by

$$\begin{bmatrix} i_{p'} \\ i_{q'} \end{bmatrix} = C(\theta') \begin{bmatrix} i_u \\ i_v \\ i_w \end{bmatrix} = \sqrt{3}I \begin{bmatrix} \cos(\theta - \theta') \\ \sin(\theta - \theta') \end{bmatrix} \quad \text{----------(13)}$$

As can be seen, q' axis component of the current is given by the sin function of the axis phase difference $\Delta\theta = (\theta - \theta')$ between them. So, we can know the information of the phase difference from the sign and magnitude of i_q'.

Figure 5 illustrates the observable current vector under the phase difference between the operating axis and the actual axis for the two case of the phase retard and the phase advanced condition. It may be possible to compensate the phase difference by leading or lagging the operating phase due to the i_q' detected signal.

VI. CONTROL SYSTEM

Figure 6 shows the proposed line voltage sensorless three phase PWM converter control system. The system is composed of three control blocks(①–③) enclosed by dotted line. The voltage control loop is used to deliver the phase angle as mentioned above (II).

The PWM switching pulse can be obtained by the instantaneous active and reactive current control block. As mentioned earlier, pure sinusoidal currents can be obtained by the ripple free control of them.

In this control block, the reactive reference current I_{qr} given by (10) is used for giving the unity power factor operation as the Type 1 control scheme. But the phase difference between the voltage and current is small. So, this control block is removed for the Type 2 control scheme and the system become more simple. In this case, the system can be constructed not by using any circuit parameters. The input signals σ_p, σ_q to the comparator for PWM switching are given as next;

$$\sigma_p = -\tilde{i}_p + k_p\varepsilon \quad \text{----------(14)}$$

$$\sigma_q = i_q - I_{qr} \quad \text{----------(15)}$$

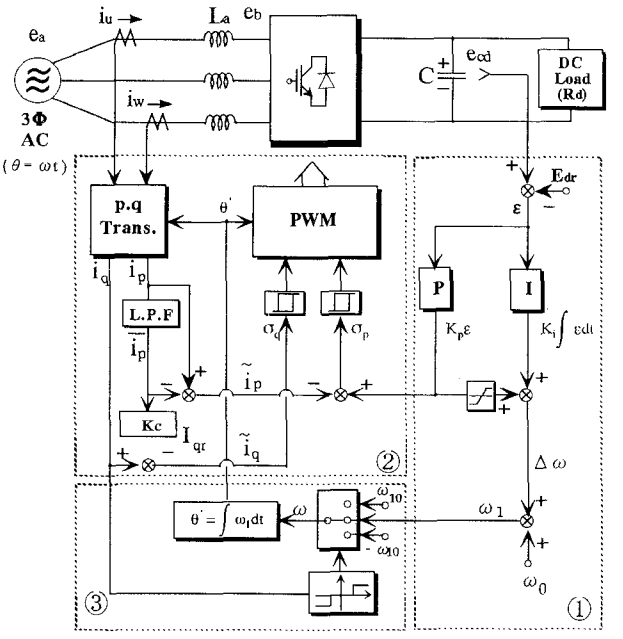

Fig.6 Control System.

Where, the control signal to the i_p control variables from the voltage control loop is used for giving fast response of the instantaneous active current for the cases such as the change of the DC voltage, load change. If this loop is not appended, the system can not change operating conditions because of the ripple free control of the active current.

Next, the phase angle θ' of the control system can be obtained by the integration of the angular frequency ω_1 as ;

$$\theta' = \int \omega_1 dt \quad \text{----------(16)}$$

The operating angular frequency $\varpi 1$ is given as;

$$\omega_1 = \omega_0 + \Delta\omega \quad \text{----------(17)}$$

Where, $\Delta\omega$ is the nominal value of the angular frequency of the AC power line. ω_0 is obtained by the output of the PI controller for the DC voltage control loop. The power flow of the PWM converter is a function of the phase difference φ between the line voltage e_a and the AC side voltage e_b of the PWM converter as shown in (11). So,$\Delta\omega$ is used for tracking the operating frequency and the operating phase of the PWM converter. If the phase difference between the actual p axis and the estimated p' axis is small, the system may be successfully operated because of the frequency tracking loop for the DC voltage control.

But, when the difference become large, the system may not be operated. The third control block is used for this case. The large phase difference $\Delta\theta$ can be observed from the reactive current component i_q' as given by (10). In this case,

the phase difference can be quickly compensated by giving large angular frequency ω_{10} for the too large lagging reactive current i_q' or by giving large negative angular frequency $-\omega_{10}$ for the too large leading reactive current i_q'. The compensation signal can be easily obtained by the reactive current i_q' which is used for the current control loop.

As can be seen, the proposed control system shown in Fig.6 is very simple and the system can be easily constructed without using any circuit parameters for the Type 2 control.

VII. SIMULATION AND EXPERIMENTAL RESULTS

Table 1 shows the system parameters and operating conditions. The current control scheme showed is Type1 but the results of the Type 2 are almost the same.

Figure 7 shows the basic waveform of the PWM converter controlled by the selection of the appropriate voltage vector based on the instantaneous active and reactive currents (i_p,i_q). The sinusoidal PWM control can be attained only by the ripple free control of them. The waveform of e_{bp},e_{bq} are the transformed quantities of the PWM controlled three phase voltages. The PWM switching frequency is adjustable by the value of the line inductance or the hysteresis width for the current control.

Figure 8 shows the more precisely controlled waveform than the basic waveform. The hysteresis width for the instantaneous current control is decided by the requirement of the control accuracy. As can be seen from the operating phase angle θ' is almost the same as the actual phase angle θ of the line voltage.

Figure 9 represents the transient response for the step change of the operating phase by 90 degree without the phase compensation loop using i_q'. Although the system can be successfully operated for the small phase difference less than 30 degree, the system is no longer operated for more phase difference.

Figure 10 shows the transient response of the system for various step change of the operating phase angle. The proposed control system, however, can be successfully operated by the compensation loop mentioned above

Table 1 Syetem parameters and Operating Conditions.

Source Voltage	Ea	: 200[V]
Source Frequency	f	: 60[Hz]
Inductance	La	: 1[mH]
DC Capacitance	C	: 1000[μF]
DC Resistance	Rd	: 20[Ω]

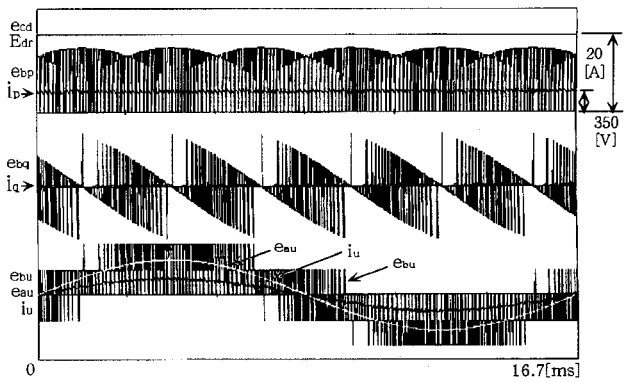

Fig.7 PWM Waveforms by the Instantaneous Current Vector Control.

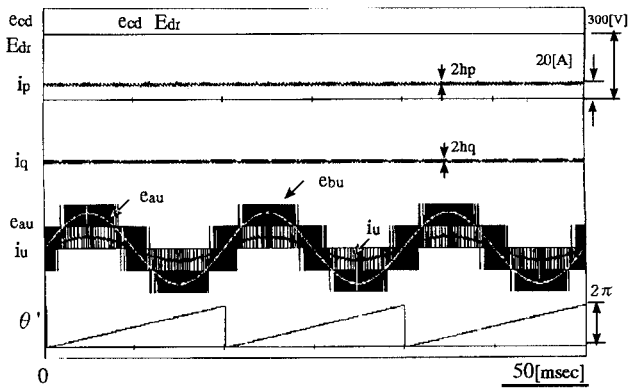

Fig.8 Operating Waveforms of the Control System.

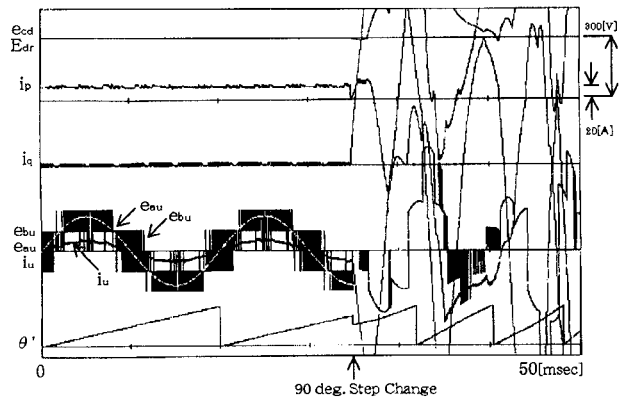

Fig.9 Operating Waveforms for Step Change of the Phase by 90 degree Removing the Phase Compensation Loop.

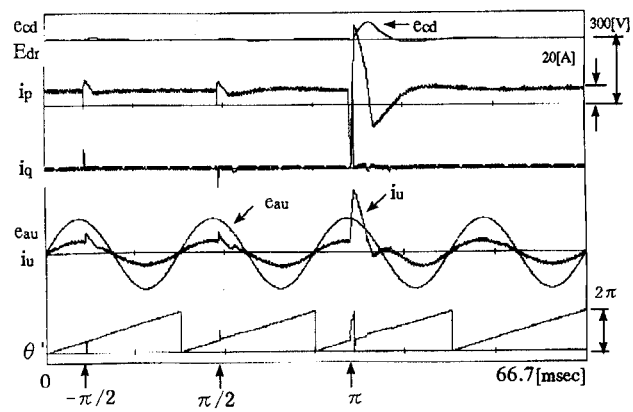

Fig.10 Operating Waveforms for Step Change of the Phase by ±90 and 180 degree with Phase Compensation Loop.

independent of the phase difference. In this case, the detection level of the i_q' is set by about 3 times of the hysteresis control width. The information of the phase difference with the actual phase can be clearly observed from the i_q' for ± 90 degree differences. But, it seems to be impossible to detect the phase difference for the 180 degree difference as expressed in (13). However, the operating frequency is decided not only by the compensation loop but also the DC voltage control loop. So, the phase difference varies and then the phase difference information appear and then the system quickly recovers to the normal operating modes as shown in Fig.10.

Figure 11 shows the starting waveforms of the control system from the uncontrolled full bridge converter under the 90 degree difference. It can be seen that the system is easily operated by giving the control signal to the PWM converter without any troublesome.

Figure 12 ,13 shows the transient response for the reference voltage variations and the load variations respectively. The fast response of the DC voltage may be attained by the voltage control loop to the active current shown in (14). The similar fast response can be observed for the load variations too.

The last figure 14 shows the experimental waveform of the prototype control system. The feasibility of the control system can be confirmed.

VIII. CONCLUSION

The excellent features of the proposed sensor less PWM converter control system needs not any calculations to estimate the actual phase and then the system has expected some good characteristics as mentioned.

REFERENCES

[1] T.Ohnishi "Three phase PWM converter/inverter by means of instantaneous active and reactive Power Control" Proc. of IEEE/IECON, pp.819-824, 1991.

[2]T.Takeshita et al "A scheme of power source voltage sensorless three-phase PWM AC/DC converter", Trans. Of IEEJ, Vol.114D, No.2, 1994.

[3]H.Tomiki et al "Instantaneous Active and reactive Power Control of PWM converter without Voltage Sensors" No.736, National Convent.Record of JIEE, 1996 .

[4] K.Fujii,T.Ohnishi "Line Voltage Sensor Less Three Phase PWM Converter " No. T-14, National Convent. Record of JIEE,-Ind. Appl. Society-,1996.

[5] K.Fujii,T.Ohnishi "Improvement of Phase Tracking Characteristics of Line Voltage Sensor Less Three Phase PWM Converter" No.736, National Convention Record of JIEE, 1996

[6] K.Fujii,T.Ohnishi "by Phase Tracking Control System" National Convention Record of JIEE,-Ind. Appl. Society-1997.

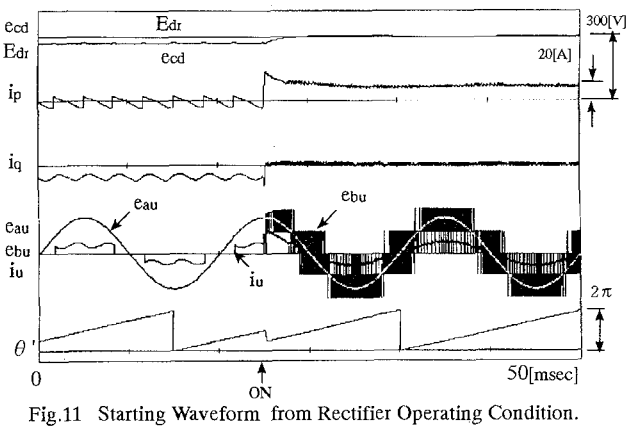

Fig.11 Starting Waveform from Rectifier Operating Condition.

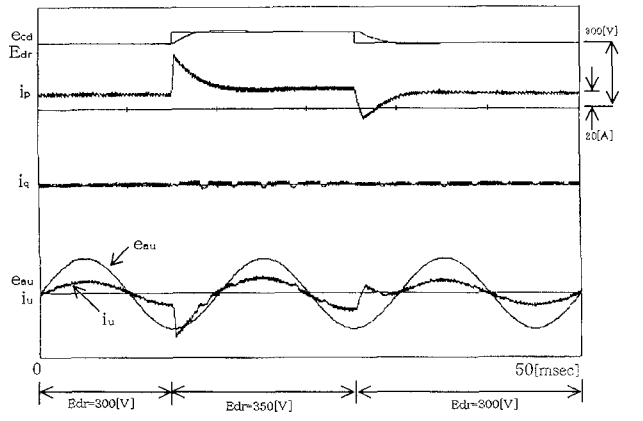

Fig.12 Transient Response for Step Variation of DC Reference Voltage.

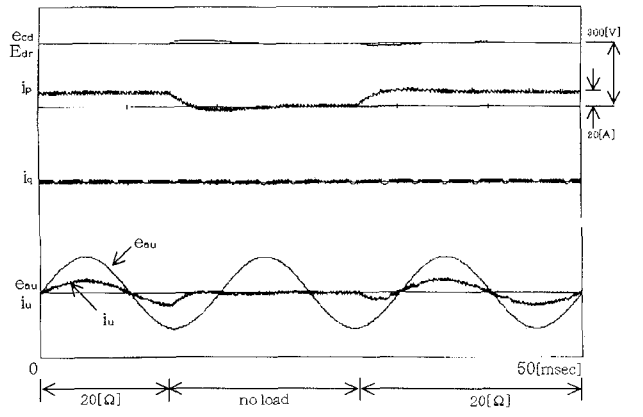

Fig.13 Transient Response for Step Variation of Load..

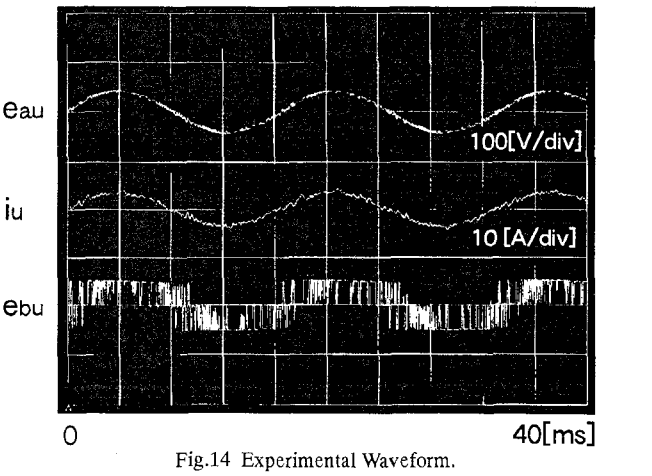

Fig.14 Experimental Waveform.

Transient Oscillation Suppression of Input Filter Voltage and Current for Current-Source Three-Phase PWM AC/DC Converter

Koji Toyama, Takaharu Takeshita, Nobuyuki Matsui

Department of Electrical and Computer Engineering
Nagoya Institute of Technology
Gokiso, Showa, Nagoya 466, JAPAN
Fax: +81-052-735-5442, Phone: +81-052-735-5420
E-mail: toyama@active.elcom.nitech.ac.jp

Abstract—In contrast to the voltage-source converter, the current-source PWM ac/dc converter has the LC filter between the source and the converter, which may cause an LC resonance both in steady and transient states. Many reports have been published to improve the current distortion in steady state and to suppress the current oscillation in transient state of the current-source PWM converter.

In this paper, the authors propose the two suppression schemes of transient oscillation for the current-source three-phase PWM ac/dc converter. One suppression method is based on the feedback control of the fluctuation component of the capacitor voltage. Another one is based on the open-loop control with the rate limiter of the input current reference. The design of the suppression control system and the LC filter is described. The effectiveness of the proposed approach has been verified by experiments.

I. Introduction

PWM ac/dc converters have been proposed to achieve the unity input power factor and the sinusoidal ac input current. These ac/dc power converters are classified into the voltage-source type and the current-source type and the voltage-source PWM ac/dc converters are widely used. On the other hand, the current-source PWM ac/dc converter, which is used in SMES for instance, has a feature that the input current control can be realized without the current and voltage detectors at the ac side. However, the LC filter must be connected between the source and the converter to reduce the current harmonics due to the PWM control operation. The LC filter may cause an LC resonance both in the steady and the transient states. To overcome this problem, many reports have been published [1],[2].

In this paper, authors propose two suppression schemes of the transient oscillation of the filter capacitor voltage for the current-source three-phase PWM ac/dc converter. One suppression method is based on the feedback control of the fluctuation component of the capacitor voltage. Another one is based on the open-loop control of the input current reference whose waveform is ramp-wise. With these suppression methods, the transient oscillation suppression can be achieved without additional detector. For the design of the suppression control, the relations between the oscillation amplitude and the control parameters are examined. Furthermore, a design rule of the LC filter is shown from the viewpoint of the high voltage suppression. The effectiveness of the proposed approach has been verified by experiments.

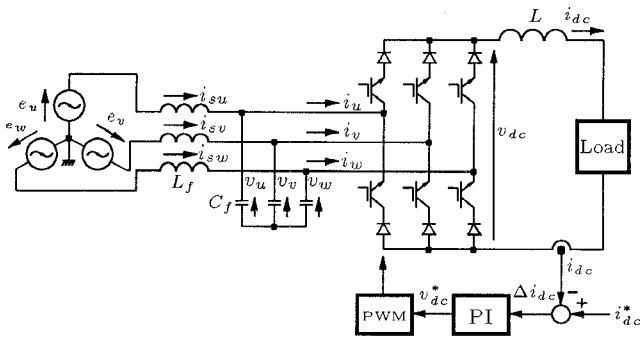

Fig. 1. Current-source three-phase PWM ac/dc converter.

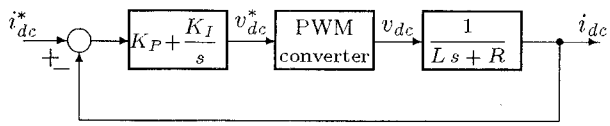

Fig. 2. DC current control block diagram.

TABLE I
System specifications.

source voltage	E	200V
source angular frequency	ω	$2\pi \cdot$ 60rad/sec
DC reactor	L	85mH
load resistance	R	25Ω
filter reactor	L_f	4mH
filter capacitor	C_f	19.8μF
rated output power		1.2kW
rated output current		7A

II. Main Circuit Configuration and DC Current Control Method

A. Main Circuit Configuration

Fig.1 shows a current-source three-phase PWM ac/dc converter which has the smoothing reactor L at the dc side and the LC filter at the ac side to reduce the input current harmonics due to the PWM control. TABLE I shows the specifications of the current-source ac/dc converter.

Fig.2 shows a dc current control block diagram of the ac/dc converter assuming that the load is a pure resistor

R. The current difference Δi_{dc} between the reference i_{dc}^* and the detected current i_{dc} is given in (1).

$$\Delta i_{dc} = i_{dc}^* - i_{dc} \tag{1}$$

Using Δi_{dc}, a PI controller calculates the dc voltage reference v_{dc}^* as follows;

$$v_{dc}^* = K_P \Delta i_{dc} + K_I \int \Delta i_{dc}\, dt \tag{2}$$

where K_P and K_I are proportional and integral gains, respectively. The gains are determined as in (3) by using the time constant τ so that the system should behave as the first-order system.

$$K_P = \frac{L}{\tau}, \quad K_I = \frac{R}{\tau} \tag{3}$$

Under the p-q coordinate system rotating with the source angular frequency ω, the active and reactive source voltages E_p, E_q are represented in (4) by using the source voltages e_u, e_v, e_w and the active and reactive converter input currents I_p, I_q are represented in (5) by using the converter input currents i_u, i_v and i_w.

$$\begin{bmatrix} E_p \\ E_q \end{bmatrix} = \boldsymbol{C} \begin{bmatrix} e_u \\ e_v \\ e_w \end{bmatrix} \tag{4}$$

$$\begin{bmatrix} I_p \\ I_q \end{bmatrix} = \boldsymbol{C} \begin{bmatrix} i_u \\ i_v \\ i_w \end{bmatrix} \tag{5}$$

$$\boldsymbol{C} = \sqrt{\frac{2}{3}} \begin{bmatrix} \cos\theta & \cos(\theta - \frac{2}{3}\pi) & \cos(\theta + \frac{2}{3}\pi) \\ -\sin\theta & -\sin(\theta - \frac{2}{3}\pi) & -\sin(\theta + \frac{2}{3}\pi) \end{bmatrix} \tag{6}$$

$$\theta = \omega t + \phi \tag{7}$$

If the source voltage is the balanced three-phase voltage, the p-axis component E_p is equal to the line to line voltage E and the q-axis component E_q is zero.

Assuming that the capacitor voltage is equal to the source voltage, the instantaneous effective input power $E \cdot I_p$ is equal to the dc power $v_{dc} \cdot i_{dc}$. Therefore, the active current reference I_p^* is given in (8) using the dc voltage reference v_{dc}^* in (2).

$$I_p^* = \frac{i_{dc}}{E} \cdot v_{dc}^* \tag{8}$$

The reactive current reference I_q^* is controlled to be zero, and the unity input power factor control is achieved.

B. Transient Oscillation in Input LC Filter.

The voltage equations of the input LC filter shown in Fig.1 are given in (9), (10).

$$\begin{bmatrix} e_u \\ e_v \\ e_w \end{bmatrix} = L_f \frac{d}{dt} \begin{bmatrix} i_{su} \\ i_{sv} \\ i_{sw} \end{bmatrix} + \begin{bmatrix} v_u \\ v_v \\ v_w \end{bmatrix} \tag{9}$$

$$C_f \frac{d}{dt} \begin{bmatrix} v_u \\ v_v \\ v_w \end{bmatrix} = \begin{bmatrix} i_{su} - i_u \\ i_{sv} - i_v \\ i_{sw} - i_w \end{bmatrix} \tag{10}$$

Transforming these voltage equations into the p-q coordinate system by using the transformation matrix $\boldsymbol{C}$ in (6), the following equations are obtained.

$$\boldsymbol{e} = L_f (P + \boldsymbol{J}\omega) \boldsymbol{i}_s + \boldsymbol{v} \tag{11}$$

$$C_f (P + \boldsymbol{J}\omega) \boldsymbol{v} = \boldsymbol{i}_s - \boldsymbol{i} \tag{12}$$

where the vectors and P are defined as follows;

$$\left.\begin{aligned} \boldsymbol{e} &= [E_p\ E_q]^T = [E\ 0]^T = \boldsymbol{C}[e_u\ e_v\ e_w]^T \\ \boldsymbol{v} &= [V_p\ V_q]^T = \boldsymbol{C}[v_u\ v_v\ v_w]^T \\ \boldsymbol{i}_s &= [I_{sp}\ I_{sq}]^T = \boldsymbol{C}[i_{su}\ i_{sv}\ i_{sw}]^T \\ \boldsymbol{i} &= [I_p\ I_q]^T = \boldsymbol{C}[i_u\ i_v\ i_w]^T \\ \boldsymbol{J} &= \begin{bmatrix} 0 & -1 \\ 1 & 0 \end{bmatrix}, \quad P = \frac{d}{dt} \end{aligned}\right\} \tag{13}$$

Fig.3 shows the ac side block diagram of the current-source three-phase PWM ac/dc converter according to (11), (12). When the active current reference I_p^* has a step-wise change, the transient oscillation in the input LC filter is generally followed. The coupling terms between the p-axis with the q-axis behave as the disturbances given in (14), (15).

$$I_{dis} = \omega C_f V_p \tag{14}$$

$$V_{dis} = \omega L_f I_{sp} \tag{15}$$

However, the coupling terms between the q-axis with the p-axis can be neglected because the source frequency is low enough compared with the resonant frequency of the LC filter. Then, the block diagram shown in Fig.3 can be rewritten in Fig.4. The transfer functions from I_p^* to V_p, and from I_{dis} and V_{dis} to V_q are given in (16), (17).

$$V_p = -\frac{sL_f}{L_f C_f s^2 + 1} I_p^* \tag{16}$$

$$V_q = -\frac{1}{L_f C_f s^2 + 1} V_{dis} - \frac{sL_f}{L_f C_f s^2 + 1} I_{dis} \tag{17}$$

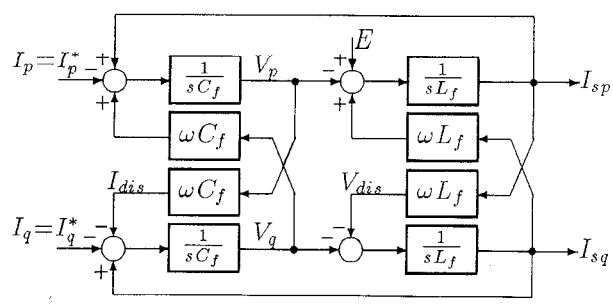

Fig. 3. Block diagram of the input LC filter.

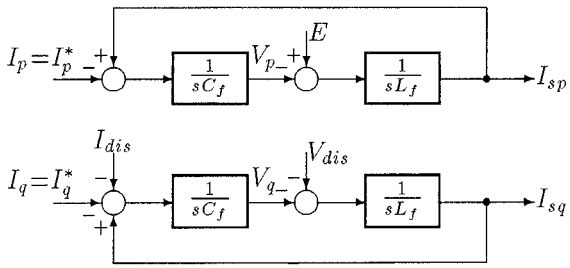

Fig. 4. Block diagram of the input LC filter.

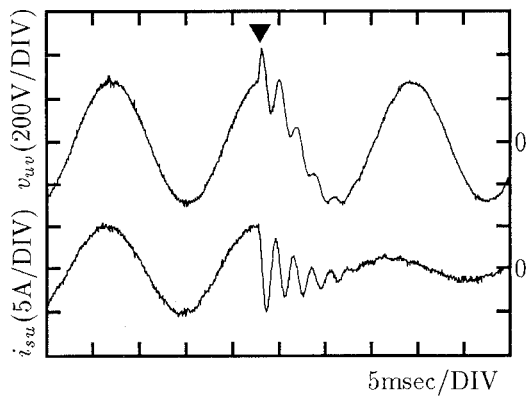

Fig. 5. Experimental result.

Since the solutions of the characteristic equation in (16), (17) are the pure imaginary numbers, the responses of V_p and V_q for the step-wise input I_p^* are oscillatory.

Fig.5 shows the experimental waveforms of the capacitor voltage $v_{uv}(=v_u-v_v)$ and the source current i_{su} when the active current reference I_p^* is changed from 7.2A to 1.2A at the instant denoted by a symbol ▼. In this figure, the transient oscillation having the resonant frequency of the LC filter is generated. The voltage amplitude of the transient oscillation is almost 120V and the capacitor voltage v_{uv} reaches to as high as 400V. The transient oscillation must be suppressed to protect the switching devices from the over voltage.

III. Suppression Method of Transient Oscillation

A. Feedback Control Method

Fig.6 shows the block diagram for the transient oscillation suppression based on the feedback control. The fluctuation components of the filter capacitor voltage are fed back to the current references I_p^* and I_q^* through the gain K_f. The transfer functions corresponding to (16) and (17) are given in (18) and (19), respectively. The proper selection of the feedback gain K_f realizes the transient oscillation suppression of the capacitor voltages V_p and V_q.

$$V_p = -\frac{sL_f}{L_fC_fs^2+K_fL_fs+1}I_p^* \tag{18}$$

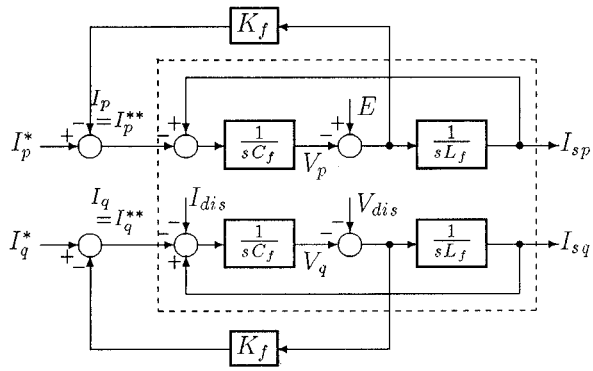

Fig. 6. Block diagram for suppression control based on feedback control.

$$V_q = -\frac{1}{L_fC_fs^2+K_fL_fs+1}V_{dis} - \frac{sL_f}{L_fC_fs^2+K_fL_fs+1}I_{dis} \tag{19}$$

However, the proposed suppression control requires the voltage detectors of the filter capacitor. The additional detectors are disadvantage from the standpoints of cost and space.

To realize the suppression control without the voltage detectors, the authors propose the capacitor voltage estimation algorithm in (20). The estimation voltages $\widehat{V}_p$ and $\widehat{V}_q$ are calculated by using the detected source currents I_{sp}, I_{sq} and the current reference I_p^{**}, I_q^{**}.

$$\left.\begin{aligned}\widehat{V}_p &= \frac{1}{C_f}\int(I_{sp}-I_p^{**})dt \\ \widehat{V}_q &= \frac{1}{C_f}\int(I_{sq}-I_q^{**})dt\end{aligned}\right\} \tag{20}$$

B. Open Loop Control Method

The authors propose a simpler suppression control based on the open loop control of the input current reference which dose not require any voltage and current detectors at the ac side. In the proposed suppression control, the change of the input current reference is not step-wise, but ramp-wise as shown in Fig.7 .

Since the ramp time T_0 is much shorter than the time constant of the dc current response, the dc current i_{dc}

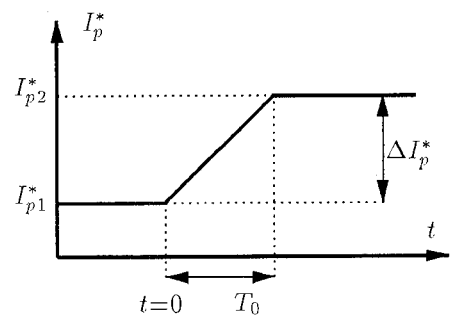

Fig. 7. The input current reference for the suppression control.

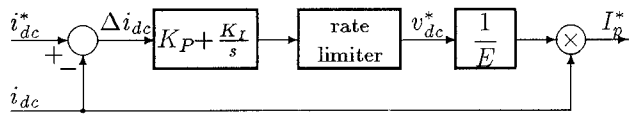

Fig. 8. DC current control scheme of proposed transient oscillation.

is constant during the ramp time of T_0. Under this assumption, the current reference I_p^* is in proportion to the voltage reference v_{dc}^* in (8). Therefore, the rate limiter of the voltage reference v_{dc}^* makes the current reference I_p^* ramp-wise. Fig.8 shows the dc current control scheme of the proposed open loop transient oscillation suppression.

The rate limiter of the v_{dc}^* is given in (21) since the amplitude of change Δv_{dc} of the dc voltage reference can be approximated by the proportional term in (2).

$$\left(\frac{\Delta v_{dc}}{\Delta t}\right)_{lim} = \frac{1}{T_0} K_P \left|\Delta i_{dc}^*\right| \tag{21}$$

where Δi_{dc}^* is the amplitude of change in the dc current reference.

IV. Design of Transient Oscillation Suppression

A. Analyses of Transient Oscillation Suppression

To design the control system of the transient oscillation suppression, the relation between the oscillation amplitude of the capacitor voltage and the control parameters in each suppression control should be examined.

1) Feedback Control: To design the feedback gain K_f in (18), the oscillation amplitude of the capacitor voltage V_p is calculated for the step-wise current reference I_p^*. The reduction ratio η is given in (22) as the ratio of the capacitor voltage under no suppression control to the capacitor voltage under suppression control.

$$\eta = \begin{cases} 1 & ;\zeta_f = 0 \\ \exp(-\frac{\alpha}{\beta}\tan^{-1}\frac{\beta}{\alpha}) & ;0 < \zeta_f < 1 \\ \exp(-1) & ;\zeta_f = 1 \\ \exp(-\frac{\alpha}{\gamma}\tanh^{-1}\frac{\gamma}{\alpha}) & ;\zeta_f > 1 \end{cases} \tag{22}$$

$$\alpha = \frac{K_f}{2C_f}, \quad \omega_f = \frac{1}{\sqrt{L_f C_f}}$$

$$\beta = \sqrt{\omega_f^2 - \alpha^2}, \quad \gamma = \sqrt{\alpha^2 - \omega_f^2}$$

where $\zeta_f = \frac{1}{2}\sqrt{\frac{L_f}{C_f}}\,K_f$ is the damping coefficient.

Fig.9 shows the relation between η and ζ_f. From this figure, the voltage amplitude of the transient oscillation at $\zeta_f = 1$ can be reduced nearly as half as that at $\zeta_f = 0 (K_f = 0)$.

2) Open Loop Control: Fig.10 shows a single phase equivalent circuit for the ac side of the current-source PWM ac/dc converter. R_f is a winding resistance of the filter reactor and the converter is expressed as a controlled current source. By using Fig.10 , the relation between the ramp time T_0 and the oscillation voltage amplitude is examined.

The amplitude of change in the u, v phase currents are given by using the amplitude of change ΔI_p^* of the active current reference as follows;

$$\left.\begin{aligned} \Delta I_u^* &= \sqrt{\tfrac{2}{3}}\,\Delta I_p^* \cos\theta_0 \\ \Delta I_v^* &= \sqrt{\tfrac{2}{3}}\,\Delta I_p^* \cos(\theta_0 - \tfrac{2}{3}\pi) \end{aligned}\right\} \tag{23}$$

where, θ_0 is the phase angle of the source voltage when the reference changes.

Since the ramp time of T_0 is short enough compared with the one cycle of the source, the change Δi_u of the converter input current i_u is obtained in (24) by using ΔI_u^* in (23).

$$\Delta i_u(t) = \frac{\Delta I_u^*}{T_0}\Big\{ t \cdot u(t) - (t - T_0)\cdot u(t - T_0)\Big\} \tag{24}$$

$u(t)$: unit step function

When the converter input current i_u changes by $\Delta i_u(t)$ in the equivalent circuit shown in Fig.10 , the oscillation

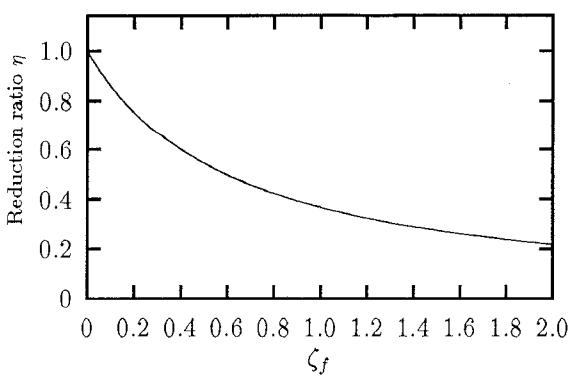

Fig. 9. The relation between η and ζ_f.

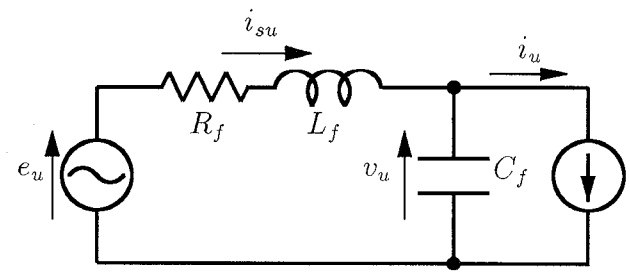

Fig. 10. Single phase equivalent circuit for the ac side of the current-source PWM ac/dc converter.

component $i_{tu}(t)$ of the source current i_{su} is given in (25).

$$i_{tu}(t) = \frac{\Delta I_u^*}{T_0}\Big\{ f(t)\cdot u(t) - f(t-T_0)\cdot u(t-T_0)\Big\} \quad (25)$$

$$\begin{aligned} f(t) &= t + \frac{\alpha^2-\beta^2}{\omega_f^2}\frac{1}{\beta}e^{-\alpha t}\sin\beta t \\ &\quad + \frac{2\alpha}{\omega_f^2}e^{-\alpha t}\cos\beta t - \frac{2\alpha}{\omega_f^2} \\ &\simeq t - \frac{1}{\omega_f}e^{-\alpha t}\sin\omega_f t \end{aligned} \quad (26)$$

It is obvious from (25) and (26) that the longer ramp time of T_0 makes the amplitude of the transient oscillation smaller.

The oscillation voltage component v_{tu} which is caused by the current oscillation i_{tu} in (25) is given as follows;

$$\begin{aligned} v_{tu}(t) &= -L_f\frac{d}{dt}i_{tu}(t) \\ &= -L_f\frac{L_f\Delta I_u^*}{T_0}\Big\{f'(t)\cdot u(t) \\ &\qquad -f'(t-T_0)\cdot u(t-T_0)\Big\} \end{aligned} \quad (27)$$

$$\begin{aligned} f'(t) &= \frac{d}{dt}f(t) \\ &= 1 + \frac{\alpha}{\omega_f}e^{-\alpha t}\sin\omega_f t - e^{-\alpha t}\cos\omega_f t \\ &\simeq 1 - e^{-\alpha t}\cos\omega_f t \end{aligned} \quad (28)$$

From (25) and (27), the oscillation component v_{tuv} of the line to line voltage is given in the following equation.

$$\begin{aligned} v_{tuv}(t) &= v_{tu}(t) - v_{tv}(t) \\ &= -\frac{\sqrt{2}L_f\Delta I_p^*}{T_0}\cos(\theta_0 - \frac{\pi}{6}) * \\ &\quad *\Big\{ f'(t)\cdot u(t) - f'(t-T_0)\cdot u(t-T_0)\Big\} \end{aligned} \quad (29)$$

Eq. (29) indicates that a small inductance L_f and long T_0 make the oscillation voltage amplitude small.

In the case of T_0=0, the oscillation voltage component v_{tuv} is given in (30) under the condition of $\alpha\simeq 0$ and $T_0\rightarrow 0$ in (29).

$$v_{tuv}\Big|_{T_0=0} = -\sqrt{2}\,\omega_f L_f \Delta I_p^*\cos(\theta_0 + \pi/6)\sin\omega_f t \quad (30)$$

From (29), (30), the reduction ration η is obtained in (31) under the approximation of $\alpha\simeq 0$.

$$\eta = \begin{cases} \dfrac{1}{\pi}\dfrac{T_f}{T_0}\sin(\dfrac{T_0}{T_f}\pi) & ;0 \le \frac{T_0}{T_f} < \frac{1}{2} \\ \dfrac{1}{\pi}\dfrac{T_f}{T_0} & ;\frac{1}{2} \le \frac{T_0}{T_f} \end{cases} \quad (31)$$

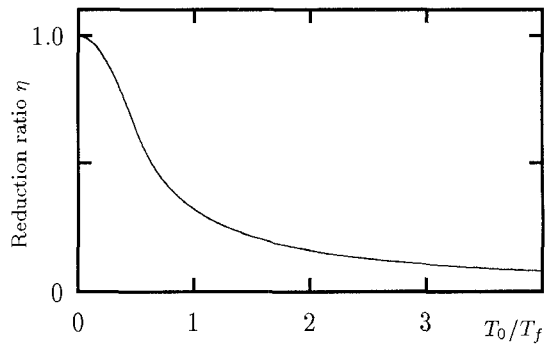

Fig. 11. The relation between η and T_0/T_f.

The reduction ratio η is decided by T_0/T_f and Fig.11 shows the relation between η and T_0/T_f. If the ramp time T_0 is selected to be equal to the resonant period $T_f(=2\pi/\omega_f)$, the oscillation voltage component v_{tuv} is not only reduced to $1/\pi$ times compared with that of T_0=0, but also canceled after $t>T_0$ because of $f'(t)u(t)\simeq f'(t-T_0)u(t-T_0)$ in (29).

B. Design of LC Filter.

Since the amplitude of the oscillation voltage is in proportion to ΔI_p^* from (16) or (30), the maximum value of ΔI_p^* generates the maximum amplitude of the oscillation voltage. From (8), when the dc current reference changes step-wise, the amplitude of change ΔI_p^* under the large i_{dc} is larger than that under the small i_{dc}. Therefore, the maximum amplitude of change ΔI_{pMAX} is given in (32) when the dc current is reduced from the rated dc current I_{DC} by the maximum amplitude of change ΔI_{DC}^* of the dc current reference.

$$\Delta I_{pMAX} = \frac{I_{DC}}{E}\cdot K_P\Delta I_{DC}^* \quad (32)$$

By replacing ΔI_p^* in (30) with ΔI_{pMAX} in (32), the maximum oscillation voltage amplitude of $\sqrt{2}\omega_f L_f \Delta I_{pMAX}$ is obtained. To protect the switching devices from the over voltage, the filter inductance L_f must be selected so that (33) should be satisfied.

$$\sqrt{2}\,\eta\omega_f L_f\Delta I_{pMAX} + \sqrt{2}\,E < V_{AC} - \Delta \quad (33)$$

where, V_{AC} is the maximum forward voltage of the switching devices and Δ is the margin for the over voltage. Then the filter capacitance C_f can be selected by using the resonant angular frequency ω_f as follows;

$$C_f = \frac{1}{\omega_f^2}\frac{1}{L_f} \quad (34)$$

V. Experimental Results

Fig.12 shows the system configuration for experiments. The control circuit uses the DSP(TMS320C25). The sampling period is 100μsec and the switching frequency of the converter is 5.0kHz. The resonant angular frequency of the input LC filter is $2\pi\times 566$rad/s,

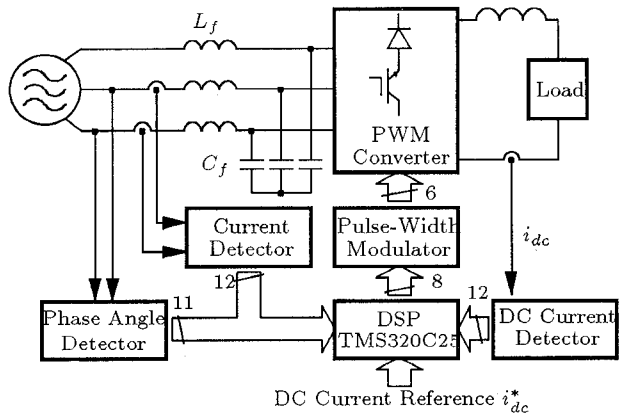

Fig. 12. System configuration for experiments.

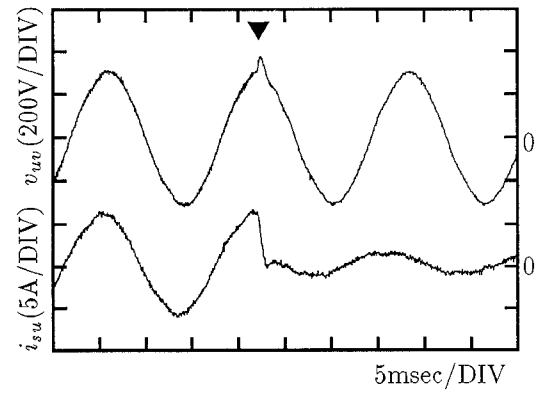

Fig. 13. Experimental result under the feedback suppression control.

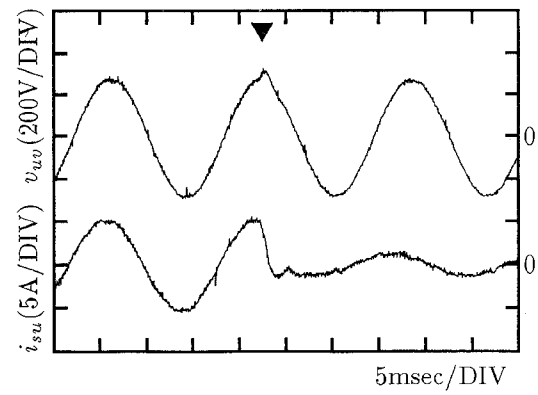

Fig. 14. Experimental result under the open loop suppression control.

which is selected nine times the source angular frequency $2\pi\times60$rad/s to reduce the source current distortion at the steady state. According to this resonant frequency, the filter inductance and capacitance are selected as L_f=4mH, C_f=19.8μF to satisfy (33) and (34) under the conditions that V_A=600V, Δ=250V, ΔI^*_p=7A and η=0.5.

Fig.13 shows the experimental waveforms of the filter capacitor voltage $v_{uv}(=v_u-v_v)$ and the source current i_{su} under the feedback control with the feedback gain of K_f=0.14A/V(ζ_f=1.0). It is observed that the transient oscillation of the capacitor voltage v_{uv} and the source current i_{su} are well suppressed. Compared with that in Fig.5, the maximum amplitude of the voltage oscillation is as half as that without the feedback control in Fig.5, which corresponds to that calculated by the theoretical design for η=1/2.

Fig.14 shows the experimental waveforms of the filter capacitor voltage v_{uv} and the source current i_{su} under the open loop suppression control with the ramp time T_0=1.8msec and the time constant τ=2msec. The transient oscillation of the capacitor voltage v_{uv} and the source current i_{su} is suppressed. The maximum amplitude of the voltage oscillation is about 40V and smaller than that in the case of the feedback control in Fig.13.

VI. Conclusion

In this paper, the authors propose the two suppression schemes of transient oscillation for the current-source three-phase PWM ac/dc converter. One suppression method is based on the feedback control of the fluctuation component of the capacitor voltage. Another one is based on the open-loop control with the rate limiter of the input current reference. The simple suppression method of the open-loop control has an advantage of having no current and voltage detector in the ac side. The design of the transient oscillation suppression control to protect the switching devices from the over voltage is examined. The effectiveness of the proposed suppression control is verified by experiments.

The authors would like to express the gratitude for the financial supports of Research Fellowships of the Japan Society for the Promotion of Science for Young Scientists.

References

[1] Y. Sato, T. Kataoka, "State Feedback Control of Current-Type PWM AC-to-DC Converters", *IEEE Trans. on Ind. Appl.*, vol. 29, pp. 1090-1097, 1993.

[2] Y. Sato, T. Kataoka, "A Current Type PWM Rectifier with Active Damping Function", *IEEE IAS Annual Meeting*, Orlando, Florida, USA, 1995, pp. 2333-2340.

[3] K. Toyama, O. Mizuno, T, Takeshita, N. Matsui, "Suppression for Transient Oscillation of Input Voltage and Current in Current-Source Three-Phase PWM AC/DC Converter", *Trans. on IEE of Japan*, Vol.117-D, No.4, April, 1997

[4] K. Toyama, T, Takeshita, N. Matsui, "Input Current Rate Limiter-Based Transient Oscillation Suppression of Input Filter Voltage and Current for Current-Source Three-Phase PWM AC/DC Converter", *Trans. on IEE of Japan*, Vol.117-D, No.8, August, 1997(in printing)

HARMONIC EVALUATION OF CARRIER-BASED PWM METHODS USING HARMONIC DISTORTION DETERMINING FACTOR

Shoji Fukuda and Kunio Suzuki

Systems and Information Engineering, Hokkaido University
North 13 West 8 Sapporo, 060 JAPAN
Fax: +81-11-706-7890, Phone: +81-11-706-6464
E-mail: fukus@e4.hines.hokudai.ac.jp

Abstract **This paper describes harmonic evaluation of three phase carrier-based two-level and three-level PWM methods. The harmonic distortion determining factor, which represents the intrinsic spectral property of individual PWM methods, is used as the common basis. Almost all the carrier-based PWM schemes that have been proposed so far are considered. It is concluded that in ac drives the third harmonic injected sine PWM scheme is suitable for two-level inverters, and the double carrier unipolar PWM scheme is suitable for three-level inverters.**

1. INTRODUCTION

Many real time PWM schemes for three phase inverter control have been proposed[1]-[5]. To compare and evaluate the harmonic characteristics of these PWM schemes, a common quality index which is independent of the inverter operating conditions such as the switching frequency and load parameters is desirable. In our previous paper[6], the harmonic distortion determining factor (HDDF) has been introduced as one of the common quality indices, and three carrier-based PWM schemes and four space vector PWM schemes have been evaluated based on their HDDF values.

The HDDF is also useful for predicting the current harmonics or torque ripples in ac drives. When selecting inverter system parameters, such as switching frequency, filter inductance, and dc source voltage, analysis of harmonic components of the inverter current is necessary. As the harmonic characteristics of the inverter current are usually obtained by a time domain simulation and Fourier transformation, it is not easy to select them. However, if HDDF values for individual PWM schemes are known, approximate current harmonics are easily calculated by using the HDDF values[7].

In this paper, three phase carrier-based PWM schemes for 2-level and 3-level inverters are examined. Nine 2-level and six 3-level schemes, which include almost all the carrier-based PWM schemes that have been proposed so far, are compared and evaluated based on their HDDF values. It is concluded that in terms of RMS values of the current harmonics and torque ripples of driven motors, the third harmonic injected sine PWM and space vector PWM of typt-C schemes would be best suitable for 2-level inverters; and the combination of of the double carrier unipolar and dipolar for 3-level inverters.

2. HDDF FOR THREE PHASE PWM INVERTERS

Consider a single phase PWM inverter with an inductive load. If the carrier angular frequency, ω_S, is high enough, the RMS values of the harmonic component of the load current, I_h, is proportional to the dc source voltage, V_{dc}; and inversely proportional to the load inductance, L, and ω_S :

$$I_h = \frac{V_{dc}}{\omega_s L} P(M) \tag{1}$$

The constant, P, is called HDDF. P is basically only a function of the modulation index, M, and the functional relationship between P and M depends on the PWM methods.

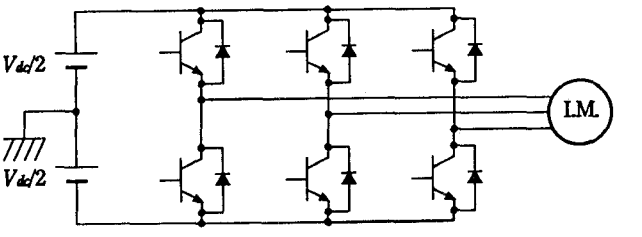

Fig. 1. A three phase PWM inverter with an inductive load.

A Definition of HDDF for three phase inverters

Fig. 1 shows a three phase PWM inverter. The switching function for phase-u, S_u, of this inverter is defined as

S_u=1 when the output potential is $V_{dc}/2$,

S_u=-1 when the output potential is $-V_{dc}/2$.

The switching functions for the other phases, S_v and S_w, are defined similarly. S_u, S_v, S_w are, then, transformed into S_d and S_q in the d-q coordinate reference frames which is rotating at an angular frequency of an inverter output, ω. The fundamental component of the inverter output will then be represented by a dc component. The d axis is selected to make its dc component equal to zero. Let S_{dh} and S_{qh} be the ac components of S_d and S_q, respectively. S_{dh} and S_{qh} correspond to the harmonic voltages of the inverter output.

As the carrier angular frequency, ω_S, is high enough, the harmonic component of the output voltage at frequency ω_S is applied almost completely across the load inductance, L. Thus, the harmonic component of q-axis load current, i_{qh}, will be determined as follows[6]:

$$i_{qh} = \frac{V_{dc}}{\omega_s L}\varepsilon_q, \quad \varepsilon_q = \omega_s \int_0^{\omega t} \frac{S_{qh}}{2} dt \tag{2}$$

The deviation component, ε_q, is normalized by ω_S in (2). Now the q-axis HDDF value of the inverter is defined as

$$P_q = \sqrt{\frac{1}{T}\int_0^T \varepsilon_q^{\,2} dt} \tag{3}$$

where T denotes the interval of the fundamental component. Similarly. the d-axis HDDF value, P_d, is defined. The total HDDF is then defined as

$$P = \sqrt{P_d^2 + P_q^2} \tag{4}$$

Performing the integral operation in (3), the following expression for the HDDF of a conventional sine-triangular PWM inverter is obtaied[6]:

$$P = \frac{\pi}{4\sqrt{2}} M \sqrt{\frac{3}{4}M^2 - \frac{8\sqrt{3}}{3\pi}M + 1} \quad (5)$$

It is to be noted that HDDF is a only function of the modulation index, M. Neither P_d nor P_q depends on the frequency ratio, ω_S/ω, if $\omega_S/\omega > 30$[6]. See APPENDIX for analytical expression of HDDF for other PWM schmes.

B. Relation between HDDF and inverter performance

1) Induction Motor Drives: The harmonic characteristics of PWM inverters are easily predicted by using HDDF. The RMS values of the harmonic current, I_h, and the torque ripples, T_h, are approximately obtained by [6]

$$I_h = \sqrt{\frac{2}{3}} \frac{V_{dc}}{\omega_s L_\sigma} P \quad (6)$$

$$T_h = \frac{3}{2} p_n \frac{M V_{dc}^2}{\sqrt{2}\omega\omega_s L_\sigma} P_q \quad (7)$$

where L_σ denotes the leakage inductance of the motor per phase and p_n is the number of pole pairs. T_h in (7) corresponds to the generated ripples, the ripples of the torque component current, caused by PWM inverters. To evaluate the motor torque ripples exactly, it is necessary to consider the mechanical resonant characteristics of the motor and load driven by PWM inverters.

2) Line-Side Converters and Static Var Generators: In this situation, we have shown[8] that RMS values of the ac input harmonic current, I_h, and RMS values of the dc output harmonic voltage, V_{dch}, are given approximately by

$$I_h = \sqrt{\frac{2}{3}} \frac{V_{dc}}{\omega_s L} P, \qquad V_{dch} = \frac{\sqrt{3} I}{\omega_s C} \sqrt{(P_q \cos\phi)^2 + (P_d \sin\phi)^2} \quad (8)$$

where I and ϕ denote the fundamental component of the ac current and the displacement power factor angle, respectively; and L denotes the inductance of the ac reactor. In the case of a static var generator (SVG), as I_q=0, the harmonic voltage in the dc link, V_{dch}, will be given by

$$I_h = \sqrt{\frac{2}{3}} \frac{V_{dc}}{\omega_s L} P, \quad V_{dch} = \frac{I_d}{\omega_s C} P_d \quad (9)$$

3. TWO LEVEL PWM METHODS

Here, the HDDF values of following three-phase 2-level carrier-based PWM schemes and their equivalents are compared and evaluated based on their HDDF values. They are:
- sine-triangular PWM scheme (SIN),
- third harmonic injected sine-triangular PWM scheme (THI)[1]
- sine-sawtooth PWM scheme (SAW),
- two-phase modulation PWM scheme (TPM1, TPM2)[2],
- modified sine PWM scheme (MS)[3],
- regular sampling PWM scheme (RSM)[4],
- space vector PWM scheme of type C (SVC)[5],
- space vector PWM scheme of type D (SVD)[5].

The above schemes include almost every carrier-based PWM scheme and its equivalents that have been proposed so far.

A. PWM Schemes under Consideration

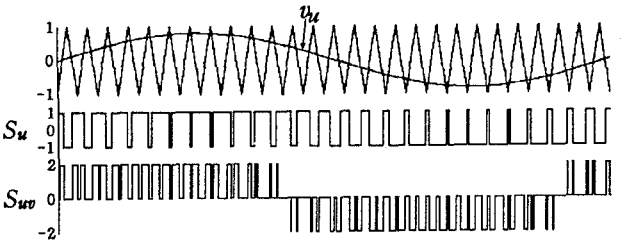

Fig. 2. Sine-triangular PWM scheme (SIN).

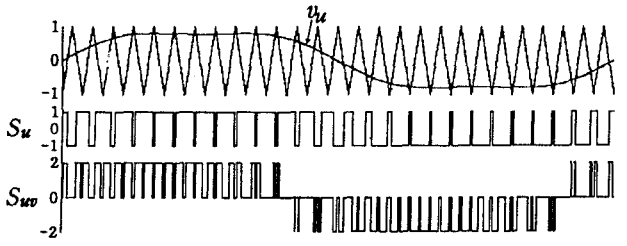

Fig. 3. Third harmonic injection sine PWM scheme (THI).

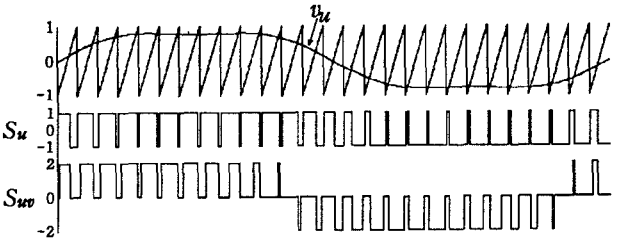

Fig. 4. Sine-sawtooth PWM scheme (SAW).

1) SIN, THI and SAW schemes: The SIN and THI schemes use a triangular carrier wave, while the SAW scheme uses a sawtooth carrier wave. For the THI and SAW schemes, the 16.6% third-harmonic component is added to the original three phase sine reference waveforms to increase the maximum fundamental output up to the DC source voltage, V_{dc}. See Figs. 2, 3 and 4. Thus, the reference voltage for phase-u is defined as

$$v_{ref} = \frac{2}{\sqrt{3}} M \sin\omega t + \frac{1}{3\sqrt{3}} M \sin 3\omega t. \quad (10)$$

2) TPM scheme: The TPM scheme uses distorted three phase reference waves while keeping the line-to-line reference waves being sinusoidal. With the TPM1, one of the reference waves is always fixed to the negative peak value of the carrier waves during a one-third of the output period as shown in Fig. 5. With the TPM2, one of the reference waves is always fixed to the positive peak value and then negative peak value of the carrier waves alternately during a one-sixth period as shown in Fig. 7. For both schemes, switching does not occur in the phase whose reference wave is fixed to the peak value.

3) MS scheme: The MS scheme defines the output on a line-to-line basis. Only the first and last 60° intervals (per half cycle) of the ac voltage waveform are directly defined through intersections of respect sine and triangular waves.

4) RSM scheme: The reference wave is held at a constant sampled value for the carrier interval. If the carrier frequency is very high compared to the output frequency, sampling does not

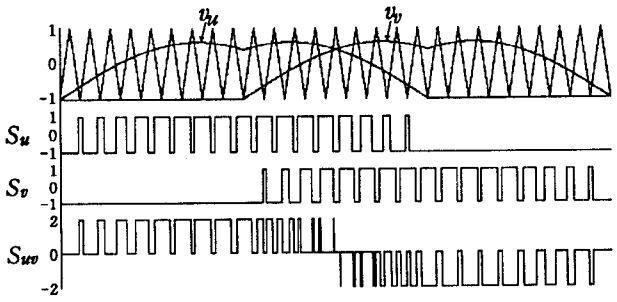

Fig. 5. Two-phase modulation PWM scheme-1 (TPM1).

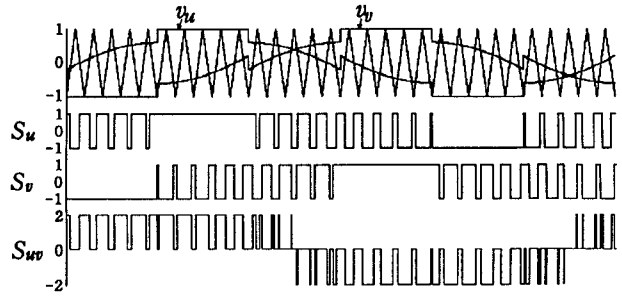

Fig. 6. Two-phase modulation PWM scheme-2 (TPM2).

affect HDDF values. For example, if the frequency ratio, f_S/f, is 15, the difference in P values between the RSM and THI schemes is below 4.5%. Thus substantially, the RSM scheme provides the same HDDF values of the THI scheme under the same M values.

5) Space vector PWM schemes, SVC and SVD: The SVC and SVD schemes (see ref.[5] and [6] in detail) use the flux vector U, which is obtained by integrating voltage vectors in terms of time, as the basis. PWM patterns are determined so that U may follow its reference U^* locus as closely as possible. With the SVC, U follows U^* from the inside at one sampling, and then from the outside at the next sampling, alternating. With the SVD, U follows U^* from the inside, and then from the outside alternately at every sampling. Microprocessor based control is essentially suitable for the SVC and SVD schemes.

B. Evaluation of 2-level PWM Schemes

HDDF curves[8] under variable voltage conditions are shown in Figs. 7 and 8, where the frequency ratio of the carrier to the inverter output, f_S/f, is forty-five, To compare PWM schemes under the same switching loss condition, the carrier frequencies are normalized. The HDDF caurves in Figs. 7 and 8 are obtained by halving the original HDDF values of the SVC scheme, and by multiplying those of the TPM and SVD schemes by the coefficient 2/3. V_{nrm} denotes the output line-to-line voltage normalized by V_{dc} and it has identical values of M. From these figures, the following observations can be made.

As for P curves or harmonic currents:

- SIN scheme is the basis of PWM schemes but its harmonic characteristics are inferior to THI scheme.
- THI and SVC schemes show similar P-curves, while TPM and SVD schemes show similar P-curves. Let's call the former and the latter the group-1 and the group-2, respectively. The group-1 generate the fewest harmonic currents for a low to medium voltage region, while the group-2 generate the fewest for a high voltage region.
- TPM1 scheme generates fewer harmonic currents than TPM-2 scheme.
- SAW and MS schemes generate more harmonic currents than the other schemes almost over the whole voltage region.
- The minimum harmonic current operation will be achieved if the group-1 are used for the voltage region, $0<V_{nrm}<0.7$, and the group-2 are used for $0.7<V_{nrm}<1$. For a simpler switch-over between the group-1 and the group-2, it is preferable to choose SVC scheme for the group-1, and SVD scheme for the group-2 because the switch-over can be done by software.

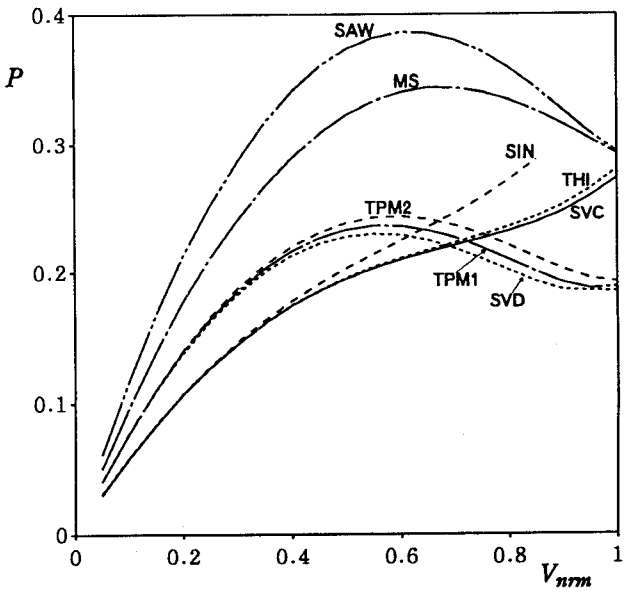

Fig. 7. Comparison of total HDDF values, P.

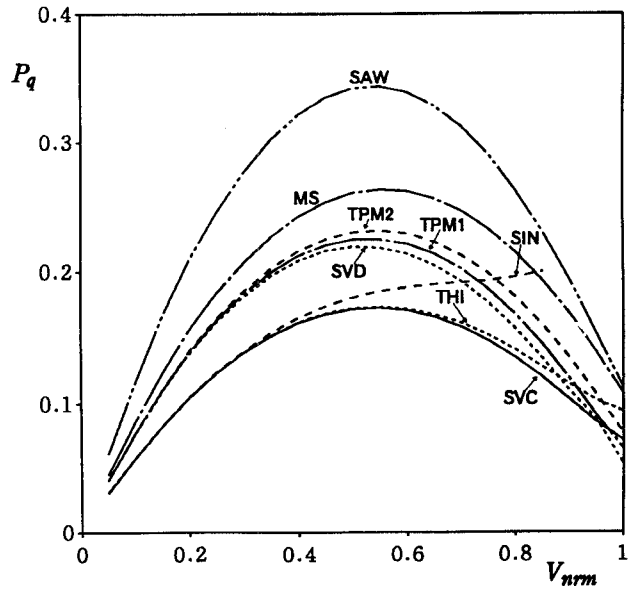

Fig. 8. Comparison of q-axis HDDF, P_q.

As for P_q curves or torque ripples, the following observations can be made:

– SIN scheme is inferior to THI scheme.
– The group-1 show similar P_q-curves, and the group-2 show similar P_q-curves. The group-1 generate fewer torque ripples than the others almost over the whole voltage region, while the group-2 generates fewest torque ripples only for the very high voltage region, $0.95<V_{nrm}<1$.
– TPM1 scheme generates fewer torque ripples than TPM2 scheme.
– SAW and MS schemes generate more torque ripples than the other schemes over the whole voltage region.

As a whole, SVC scheme is the space vector based alternative of carrier based THI scheme, and SVD scheme is the space-vector based alternative of carrier based TPM1 scheme. In ac drives, suppression of torque ripples over the whole voltage region is important because of noise and vibration problems. Also suppression of RMS value of the harmonic current is important to minimize copper losses in the driven motors. From this point of view, SVC and THI schemes have an advantage over the others in the low to medium speed region, while SVD and TPM1 schemes have an advantage over the others in the high speed region. Thus, the combination of two schemes provides the best harmonic performance.

In line-side converter and UPS applications, suppression of RMS value of the harmonic current for a high voltage region, say V_{nrm} = 0.8 to 0.9, is important. SVD and TPM1 schemes have an advantage over the others because they exhibit lower dc voltage ripples in line-side converter applications and lower copper losses in filter inductors in line-side converter and UPS applications

4. THREE LEVEL PWM METHODS

A. PWM Schemes under Consideration

Fig. 9 shows a 3-level inverter[9]. The switching function for phase-u is defined as:

$S_u = 1$ when the output potential is $V_{dc}/2$,
$S_u = 0$ when the output potential is 0,
$S_u = -1$ when the output potential is $-V_{dc}/2$.

Here, the HDDF values of following 3-level carrier-based PWM schemes are compared and evaluated.

- original unipolar PWM scheme (UNI1)[10],
- double carrier unipolar PWM scheme (UNI2)[7],
- Δe-biased PWM scheme (ΔeB)[11].
- original dipolar PWM scheme (DI1)[10],
- double carrier dipolar PWM scheme (DI2)[7],
- square wave biased PWM scheme (SQA)[12]

Power semiconductor devices require a minimum ON-time during which the snubber is allowed to discharge its stored energy. The minimum ON-time restriction imposes a lower bound on the attainable output voltage or modulation index for 3-level inverters. The DI1, DI2, ΔeB, and SQA schemes have been proposed to circumvent the minimum voltage restriction. In these modulation schemes, positive zero and negative output voltages are generated in sequence.

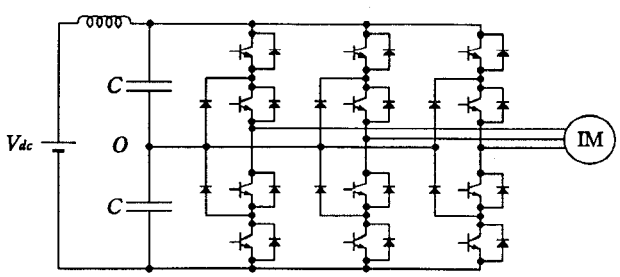

Fig. 9. A three phase 3-level PWM inverter.

1) UNI1 schemes: The UNI1 scheme uses a single triangular carrier wave and two reference waves. The amplitude of the carrier wave and the dc bias is 0.5. Positive and negative half reference waves, v_r+ and v_r-, respectively are used. The output state transition are directly defined by the instances at which intersections of respective reference and triangular waves as shown in Fig. 10 occur. The modulation scheme creates a unipolar pulse train within a half period of the reference wave.

2) DI1 schemes: The DI1 scheme is considered as an outgrowth of the bipolar modulation scheme. A single carrier wave with an amplitude of 1.0 and two sinusoidal reference waves are generated. The dc biases $+\Delta h$ and $-\Delta h$ are added to an original reference wave, forming an upper reference wave v_r+ and a lower reference wave v_r-, respectively as shown in Fig. 11. An optimal bias value is Δh=0.5. The carrier frequency is half of the value employed in a UNI scheme so as to maintain a constant switching frequency. This scheme can be employed for a modulation index range $0<M<0.5$.

3) UNI2 and DI2 schemes: UNI2 and DI2 schemes use double carrier waves. In a UNI2 scheme, the amplitude of the carrier waves is 0.5 and the dc biases are 0.5 and -0.5 respectively as shown in Fig. 12. In the DI2 scheme, the amplitude of the carrier waves is increased to 1.0, and the frequency is decreased to half of the value employed in the UNI2 scheme as shown in Fig. 13. This scheme can be employed for a modulation index range $0<M<0.5$. The UNI2 and DI2 schemes use one reference wave.

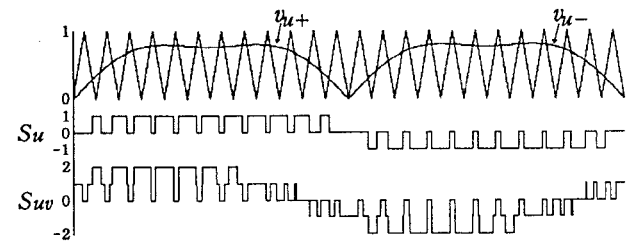

Fig. 10. Original unipolar PWM scheme (UNI1).

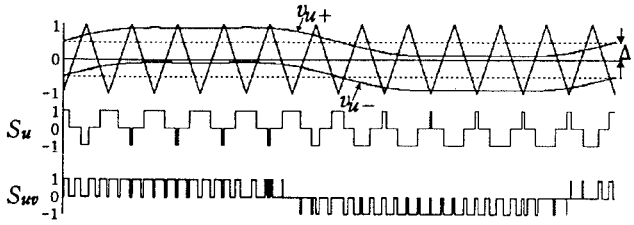

Fig. 11. Original dipolar PWM scheme (DI1).

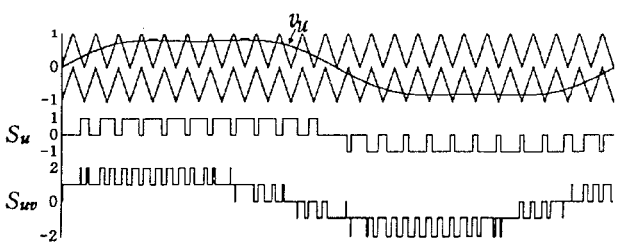

Fig. 12. Double carrier unipolar PWM scheme (UNI2).

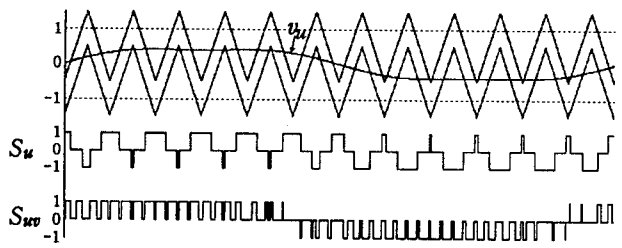

Fig. 13. Double carrier dipolar PWM scheme (DI2).

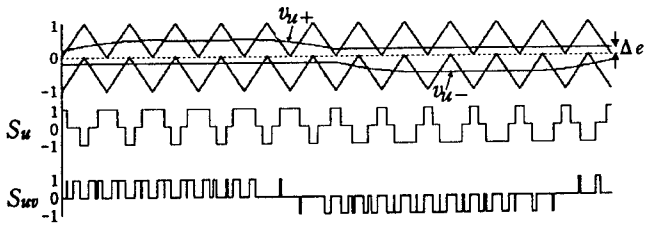

Fig. 14. Δe-biased PWM scheme (ΔeB).

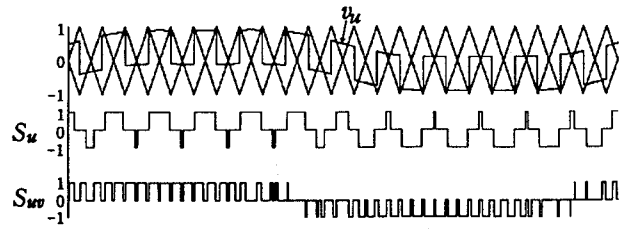

Fig. 15. Square wave biased PWM scheme (SQA).

4) ΔeB schemes: The ΔeB scheme uses double carrier waves and double reference waves. The carrier waves are identical to those of the UNI2 scheme. The dc biases $+\Delta e$ and $-\Delta e$ are added to positive and negative half reference waves respectively, forming an upper reference wave v_r+ and a lower reference wave v_r-, respectively as shown in Fig. 14. A typical bias value is Δe=0.1. This scheme can be employed for a modulation index range $0<M\leq 0.9$.

5) SQA schemes: In the SQA scheme, a square wave with an amplitude of 0.5 is added to each of the original sinusoidal reference waves. Then, the new reference waves are compared to the triangular carrier waves as shown in Fig. 15 to create PWM patterns. It is noted that the two carrier waves are in opposite disposition with each other.

B. Evaluation of 3-level PWM Schemes

HDDF-curves under variable voltage conditions are shown in Figs. 16 and 17, where the frequency ratio of the carrier to the inverter output, f_s/f, is forty-five. For every PWM scheme, a 16.6 percent third harmonic component is added to the original sine reference waveform to increase the maximum fundamental output voltage. To compare PWM schemes under the same switching loss condition, the carrier frequencies are normalized. The HDDF curves in Figs. 16 and 17 are obtained by doubling the original HDDF values for the dipolar PWM schemes, DI1, DI2 and ΔeB, taking UNI2 as the basis.

From these figures, the following observations can be made:

– UNI2 has the best harmonic characteristics for a medium to high voltage region, while UNI1 has the poorest and is even worse than the conventional 2-level PWM scheme. As each phase has one switch-transition at every carrier period, the output line-to-line voltage pattern generated by UNI1 always starts with 0[V] and ends with 0[V] for every carrier period. This is the main reason that HDDF exhibits high values. In contrast to UNI1, UNI2 has two carrier waves, and the positive and negative references require switch-transitions at different carrier periods. Thus, the apparent carrier frequency will be doubled. This is the reason that HDDF shows low values.

– UNI2 generates 2-level output for $0<M<0.5$, while 3-level output for $0.5<M<1.0$. As UNI2 outputs the maximum 2-level voltage pulses at M=0.5, the P and P_q curves have a local minimum around V_{nrm}=0.5.

Because of the minimum-ON time restriction, dipolar PWM schemes must be employed in a low voltage region.

– ΔeB satisfies the minimum-ON time restriction when the amplitude of the voltage is very low as well as when the voltage crosses zero volts. However, ΔeB is required to acquire half its carrier frequency so as to maintain the same switching frequency employed in UNI2, and is furthermore, the width of the shorter voltage pulses having opposite polarity of the reference is kept at a constant value regardless of the instantaneous values of the reference. Thus, harmonic characteristics in a high voltage region could be very poor.

– DI2 and UNI2 show almost the same harmonic characteristics in a low voltage region, though DI2 requires to halve its carrier frequency so as to keep the same switching frequency employed in UNI2. Therefore, DI2 exhibits the best harmonic characteristics in a low voltage region.

– The optimal biased DI1, DI2 and SQA create the identical pulse patterns. The HDDF curves of the three schemes are also identical.

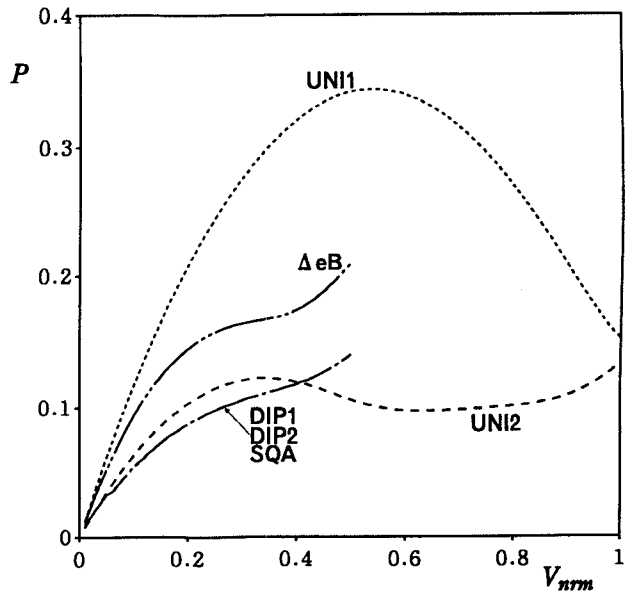

Fig. 16. Comparison of total HDDF curves, P.

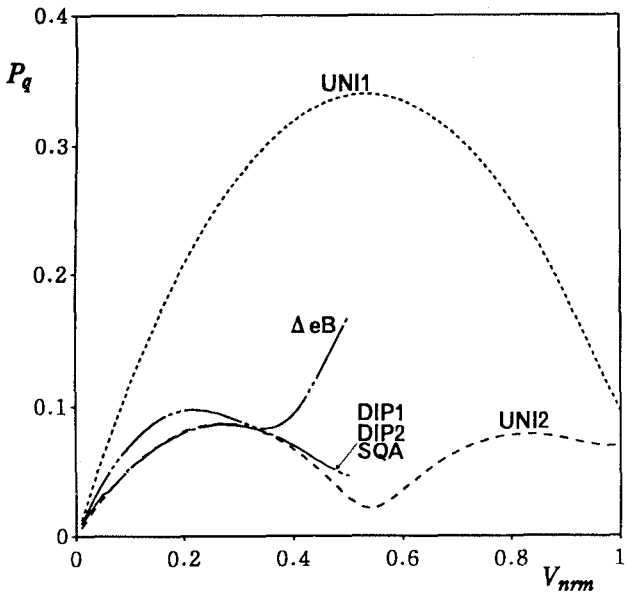

Fig. 17. Comparison of q-axis HDDF curves, P_q.

In ac drives, the UNI2 has an advantage over the others in the medium to high speed region, while the DI2 has an advantage over the others in the low speed region. Thus, the combination of two schemes, the UNI2 and DI2, provides the best harmonic performance. The UNI2 is also better for line-side converters because it exhibits fewer current harmonics and lower dc voltage ripples than the others.

If 3-level PWM schemes are compared to 2-level schemes in terms of harmonic performance, the following observation can be obtained: As for the unipolar PWM schemes for 3-level inverters, each device ceases switch-transition during a half of the output interval. Thus, the P and P_q curves in Figs. 16 and 17 may be halved in order to compare them under the same average switching frequency condition. It is noted that the UNI2 scheme greatly reduces the harmonic component of the inverter load current compared to the THI scheme.

6. CONCLUSION

The harmonic evaluation of three phase two-level and three-level carrier-based PWM schemes is carried out based on their HDDF values. Almost all the PWM schemes proposed so far are compared and evaluated under the same device switching frequency condition. It is concluded that in terms of RMS values of the current harmonics and torque ripples of driven motors, the third harmonic injected sine PWM and space vector PWM of type-C schemes would be best suitable for 2-level inverters; and the combination of the double carrier unipolar and dipolar PWM schemes for 3-level inverters. For line-side converters, the two phase modulation-1 and space vector PWM of type-D schemes would be best suitable for 2 level inverters; and the double carrier unipolar PWM scheme for 3-level inverters.

Harmonic evaluation of PWM schemes when the carrier to output frequency ratio is very low is one of the research projects which should be investigated in the future.

REFERENCES

[1] J. Houldsworth and D. Grant, "The use of harmonic distortion to increase the output of a three phase PWM inverter," IEEE Trans. Ind. Appl. vol.IA-20, no.5, pp.1224-1228, 1984.

[2] K. Taniguchi and H. Irie, "A modulating signal for three-phase sinusoidal PWM inverter," Trans. of IEE J, vol.105-B, no.10, pp.880-886, 1985.

[3] T. Ohnishi and H. Okitsu, "A novel PWM technique for three phase inverter/converter," IPEC-Tokyo, pp.384-395, 1983.

[4] J. Richardson and O. Kukrer, "Implementation of a PWM regular sampling strategy for a.c. drives," IEEE PESC, pp.649-656, 1989.

[5] S. Fukuda, Y. Iwaji and H. Hasegawa, "PWM technique for inverter with sinusoidal output current," IEEE Trans. Power Elect., vol.5, no.1, pp.54-61, 1990.

[6] S. Fukuda and Y. Iwaji, "Introduction of the harmonic distortion determining factor and its application to evaluating real time PWM methods," Trans. of IEE J, vol.115-D, no.10., pp.1237-1244, 1995.

[7] Y. waji, T. Okuyama, T. Ikimi and S. Fukuda, " Using harmonic distortion determining factor for harmonic evaluation of a neutral point clamped inverter," IPEC-Yokohama'95, pp.476-681, 1995.

[8] K. Suzuki and S. Fukuda, "Harmonic evaluation of two-level PWM schemes employing the Harmonic Distortion Determining Factor," IAS-Japan, vol.3., pp.395-398, 1996.

[9] A. Nabae, I. Takahashi and H. Akagi, " A new neutral-point-clamped PWM inverter," IEEE Trans. Ind. Applicat, vol.IA-17, no.5, pp.518-523, 1981.

[10] B. Velaerts, P. Mathys, E. Tatakis and G. Bingen, " A novel approach to the generation and optimization of three-level PWM wave forms," IEEE PESC, pp.1255-1262, 1988.

[11] S. Tanaka, K. Miura, S. Tadakuma and K. Satou, " Consideration on PWM control for neutral point clamped inverters," IAS-Japan , pp.356-361, 1992.

[12] Y. Nakazawa and H. Naitoh, "A new PWM scheme for NPC inverters reducing waveform distortion caused by pulse width limitation and a new neutral point voltage control," IAS-Japan, vol.3., pp.191-190, 1995.

APPENDIX

Analytical Expression of HDDF for PWM Schemes

For several PWM schemes, the analytical expression of their HDDF values has been obtained. The reference voltage, which includes a third harmonic component, is given by:

$$v_{ref} = aM \sin \omega t + bM \sin 3\omega t$$

Then the HDDF expression is as follows:

THI scheme :

$$P=\frac{\pi}{4\sqrt{2}} M\sqrt{1+\frac{3}{4}(Ma)^2-\frac{8\sqrt{3}}{3\pi}Ma-\frac{3}{4}M^2ab+\frac{3}{2}(Mb)^2}$$

SAW scheme:

$$P=\frac{\pi}{2\sqrt{2}} Ma\sqrt{1+\frac{9}{16}(Ma)^2-\frac{8\sqrt{3}}{3\pi}Ma}$$

SVC scheme:

$$P=\frac{\pi}{2\sqrt{6}} M\sqrt{1+(\frac{3}{2}-\frac{9\sqrt{3}}{8\pi})M^2-\frac{16}{3\pi}M}$$

SVD scheme:

$$P=\frac{2\pi}{3\sqrt{6}} M\sqrt{1+(\frac{3}{4}+\frac{3\sqrt{3}}{8\pi})M^2-(\frac{31}{3\pi}-\frac{5\sqrt{3}}{2\pi})M}$$

Unified PWM Technique for Real Time Power Conversion

Dae-Woong Chung, Seung-Ki Sul
Dept. of Electrical Engineering
Seoul National University, Seoul, Korea
Phone: +82-2-880-7251-ext.108 Fax: +82-2-878-1452
E-Mail: cdw@plaza.snu.ac.kr
Web: http://eepel.snu.ac.kr

Joohn-Sheok Kim
Dept. of Electrical Engineering
Inchon City University, Inchon, Korea
Phone: +82-32-760-8435 FAX: +82-32-765-8118
E-Mail: jskim@lion.inchon.ac.kr
Web: http://eepel.snu.ac.kr

Abstract - **In this paper, a new voltage modulation technique named 'unified PWM(Pulse Width Modulation)' is described for high performance voltage generation in 3-phase voltage-fed inverter. By considering the operation of the inverter, a simple but useful concept named 'effective time' could be established. And, fully employing this concept, a new voltage modulation technique is presented with detailed explanation and actual test results. The results shows that (1) the implementation burden of PWM is conspicuously reduced, (2) change from one modulation scheme to another is also obtained easily and seamlessly and (3) widely used overmodulation schemes are easily implemented.**

I. INTRODUCTION

Due to the improvement of fast-switching power semiconductor devices and machine control algorithms, more precise PWM method finds particularly a growing interest. A large variety of methods for PWM exist on which a survey was recently given[1].

There are some requirements of PWM method. Among them, full utilization of the dc bus voltage is extremely important (a) to achieve the maximum output torque under all operating conditions for ac machine drive application and (b) to obtain the control voltage margin even under increased source voltage for 3-phase PWM rectifier applications. Another important point is the minimization of the current ripple and/or the total losses of the power converter system. And, needless to say, the whole modulation task should have the simplest form to easily applied in the actual applications. To answer simultaneously the different requirements mentioned above, a synthetic modulation method should be established in the viewpoint of the global inverter operation.

Considering the voltage generation fashion of the voltage-fed inverter that comprises 6 power devices in parallel with freewheeling diode, it can be found that the output voltage of the inverter is just determined by the different voltage between each inverter arms and the time duration in which the different voltage is maintained. Especially, an interest should be focused on the time duration when the voltage difference is not zero because an effective power flow is made in this duration. In this paper, this time interval will be named as 'effective time'. Actually, the idea for the effective time was already introduced in the space voltage vector PWM(SVPWM) method[2]. In that literature, the applying time for certain available voltage vector was evaluated on the basis of the average voltage concept. Practically, this PWM scheme is superior to any other schemes in the point of dc link voltage utilization and current harmonics. However, the implementation of this scheme is formidable to be applied in the actual field because the applying time is calculated by trigonometric function and recombination process for actual gating times should be performed[3]. Moreover, since this scheme was evaluated on the foundation of the switching states, the relationship among PWM schemes failed to be noticed.

In this paper, a novel voltage modulation technique named as 'unified PWM' introduced in [4] at first is described with detail. When the effective time concept is properly utilized, the voltage modulation task can be greatly simplified since the inverter output voltage is directly synthesized by the effective time. In the proposed PWM method, the actual gating times for each inverter arm are immediately deduced simply using the 'effective time' relocation algorithm. Furthermore, by employing the one degree of freedom that the effective time can be relocated anywhere within the sampling interval, various carrier-based PWM strategies can be easily implemented without hardware modification. Therefore, in no time, the operating fashion of the proposed scheme can be changed to any carrier-based PWM strategies such as sinusoidal PWM, SVPWM and discontinuous modulation schemes. As well as giving a detail explanation of the new PWM algorithm, this paper presents the experimental results in various operating modes.

II. UNIFIED VOLTAGE MODULATION

In Fig.1(a), a typical power stage of the 3-phase inverter and equivalent circuit of load are presented. And, in Fig.1(b), the available eight different switching vectors of the inverter are depicted with space vector concept[2,3]. The switching state '1' means the firing for upper device of one arm and the pole voltage(V_{an}, V_{bn}, V_{cn}) will have the half of dc link voltage value. And, the modulation index is defined as the ratio of phase voltage amplitude to $V_{dc}/2$.

Note that the switching states of each arm should be combined with each other to compose a required 3-phase output voltage. Because each pole voltage has only two levels according to the related switching state, the time duration in which the different voltage is maintained is

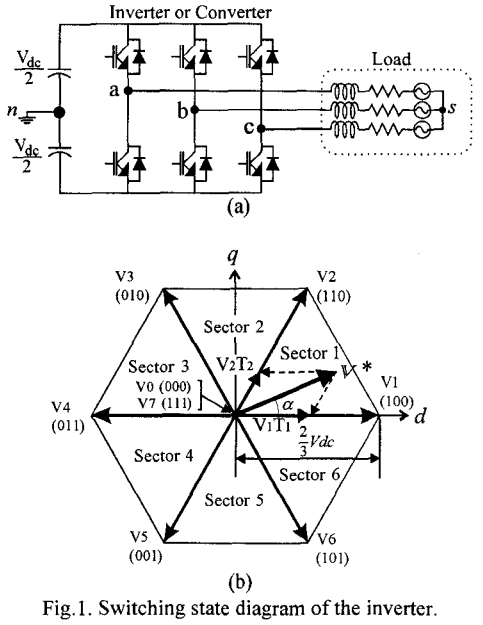

Fig.1. Switching state diagram of the inverter.
(a) Three-phase inverter system.
(b) Space vector diagram of the available switching vectors.

definitely concerned to the voltage modulation task. Therefore, the modulation task can be greatly simplified by considering the relation between the time duration and the output voltage.

In this moment, a focus is addressed on the effective voltage that makes an actual power flow between inverter and load. As shown in Fig.2(a), when the switching states of each phase become 0 from 1 at different time during one sampling interval, an effective voltage is applied to the load side. T_s denotes the sampling time and T_{eff} denotes the time duration in which the different voltage is maintained. T_{eff} is called the 'effective time' in this paper. For the purpose of explanation, an fictitious time value could be introduced. This value is directly related to the phase voltage and one proportional formation can be defined as follows:

$$\begin{aligned} V_{as}^* : V_{dc} = T_{as} : T_s \;\Rightarrow\; \therefore\; T_{as} \equiv \frac{T_s}{V_{dc}} \cdot V_{as}^* \\ V_{bs}^* : V_{dc} = T_{bs} : T_s \;\Rightarrow\; \therefore\; T_{bs} \equiv \frac{T_s}{V_{dc}} \cdot V_{bs}^* \\ V_{cs}^* : V_{dc} = T_{cs} : T_s \;\Rightarrow\; \therefore\; T_{cs} \equiv \frac{T_s}{V_{dc}} \cdot V_{cs}^* . \end{aligned} \tag{1}$$

V_{as}^*, V_{bs}^*, V_{cs}^* mean A-phase, B-phase, C-phase reference voltage respectively. This switching time could be negative in the case that negative phase voltage is commanded. So, this time is called 'fictitious switching time' in this study. Now, the effective time can be defined as the time duration between the smallest and the largest one among three fictitious times as given by

$$\begin{aligned} T_{eff} &= T_{max} - T_{min} \\ where\ T_{min} &= \min(T_{as},\ T_{bs},\ T_{cs}), \\ T_{max} &= \max(T_{as},\ T_{bs},\ T_{cs}). \end{aligned} \tag{2}$$

When the actual gating signals for power devices are generated in the PWM algorithm, there is one degree of freedom that the effective time can be relocated anywhere

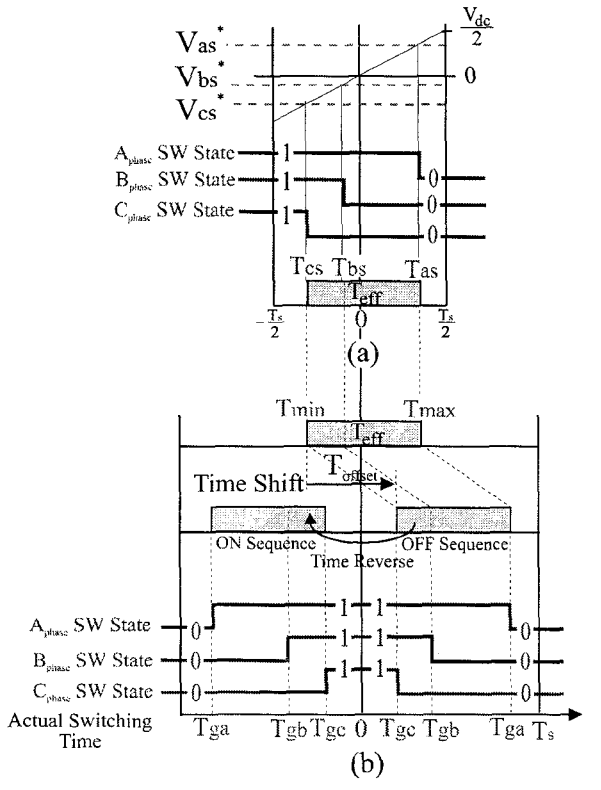

Fig.2. Implementation of unified PWM. (at OFF sequence)
(a) Relationship between the effective time and the output voltage.
(b) Actual gating time generation.

within the sampling interval. Therefore, a time shifting operation will be applied to the fictitious switching times to generate the actual gating time for each inverter arm, T_{ga}, T_{gb}, T_{gc} as shown in Fig.2(b). This task is just accomplished by adding a same value to the fictitious times as follows:

$$\begin{aligned} T_{ga} &= T_{as} + T_{offset} \\ T_{gb} &= T_{bs} + T_{offset} \\ T_{gc} &= T_{cs} + T_{offset} . \end{aligned} \tag{3}$$

This gating time determination task is just performed for the sampling interval in which all of the switching state of each arm go to 0 from 1. This interval is called 'OFF sequence' in this paper. In the other sequence, called 'ON sequence', in order to generate symmetrical switching pulse pattern within two sampling interval, the actual switching time will be replaced by the subtraction value with sampling time as follows:

$$T_{ga,gb,gc} = T_s - T_{ga,gb,gc} . \tag{4}$$

To guarantee the full utilization of dc link voltage, the actual gating times should be restricted to a value from 0 to T_s as below.

$$\begin{aligned} 0 &\le T_{min} + T_{offset} \\ T_{max} + T_{offset} &\le T_s . \end{aligned} \tag{5}$$

From the above, the range of the available offset time can be calculated as follows:

$$\begin{aligned} &T_{offset.min} \le T_{offset} \le T_{offset.max} \\ &where\ T_{offset.min} = -T_{min},\ T_{offset.max} = T_s - T_{max} . \end{aligned} \tag{6}$$

$T_{offset.min}$ and $T_{offset.max}$ mean the available maximum and minimum value of T_{offset} respectively. For example, Fig.3(a) shows the range of the available offset time and corresponding phase voltage when modulation index M is 0.9. Fig.3(b) represents the $T_{offset.min}$ and $T_{offset.max}$ with a variation of modulation index. As shown in this figure, the lines of $T_{offset.min}$ and $T_{offset.max}$ intersect when modulation index reaches the value of $2/\sqrt{3}$. This value is the maximum modulation index of the proposed PWM scheme.

In the next section, it will be shown that various carrier-based PWM schemes can be obtained by changing the T_{offset} arbitrarily between $T_{offset.min}$ and $T_{offset.max}$ for wide applicability in various fields.

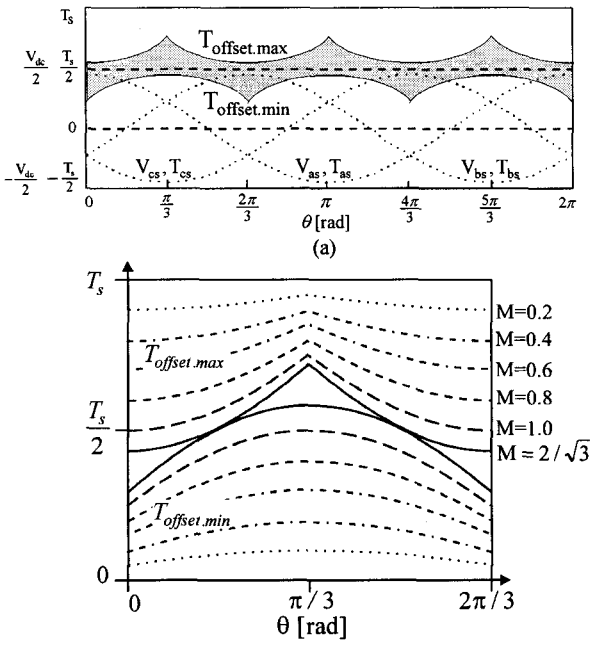

Fig.3. Graphical representation of offset time
(a) Range of available offset time (modulation index : 0.9)
(b) Maximum and minimum value of offset time
with a variation of modulation index

III. VARIOUS CARRIER-BASED PWMS BY UNIFIED PWM STRATEGY

A. Sinusoidal PWM

The sinusoidal PWM scheme is a classical and widely used method. In this case, there is no difference between phase voltage(V_{as}) and pole voltage(V_{an}). Therefore, the duty ratio of A-phase inverter output pulse becomes

$$\frac{T_{ga}}{T_s} = \frac{1}{2} + \frac{V_{an}^*}{V_{dc}} = \frac{1}{2} + \frac{V_{as}^*}{V_{dc}} \tag{7}$$

and T_{ga} can be rearranged as

$$T_{ga} = \frac{T_s}{2} + \frac{T_s}{V_{dc}} V_{as}^* = \frac{T_s}{2} + T_{as} . \tag{8}$$

Therefore, to implement the conventional sinusoidal PWM, the offset value is defined as follows:

$$T_{offset} = \frac{1}{2} T_s . \tag{9}$$

As widely known, this PWM method has decisive disadvantage that the linear range of controllable voltage is limited to the modulation index 1. This disadvantage is basically caused by the improper location of the effective time. Regardless of operating condition, the location of the effective time is always fixed as shown in (9). Fig.4 shows the offset time and phase, pole voltage of sinusoidal PWM scheme. For the monitoring purpose, the pole voltage of this figure is synthesized using the calculated gating time by following equation.

$$V_{an} = \left(\frac{T_{ga}}{T_s / 2} - 1 \right) \cdot \frac{V_{dc}}{2} . \tag{10}$$

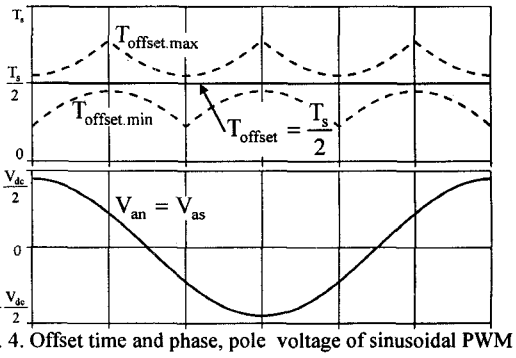

Fig. 4. Offset time and phase, pole voltage of sinusoidal PWM
(modulation index : 0.9)

B. Space Voltage Vector PWM (SVPWM)

The Space voltage vector PWM method was evaluated on the basis of the average voltage concept during one sampling period[2]. If a constant reference voltage vector V* is given in the hexagon area as shown in Fig.1(b), this vector can be represented by the nearest two active vectors as follows:

$$V^* = (T_1 \cdot V_n + T_2 \cdot V_{n+1})/T_s . \tag{11}$$

And, the applying times T_1, T_2 are deduced using the stationary reference frame voltage $V_d^s{}^*, V_q^s{}^*$ [5].

$$\begin{aligned} T_1 &= \frac{\sqrt{3} \cdot T_s}{V_{dc}} \left[\sin\left(\frac{\pi}{3} m\right) \cdot V_d^s{}^* - \cos\left(\frac{\pi}{3} m\right) \cdot V_q^s{}^* \right] \\ T_2 &= \frac{\sqrt{3} \cdot T_s}{V_{dc}} \left[-\sin\left(\frac{\pi}{3}(m-1)\right) \cdot V_d^s{}^* + \cos\left(\frac{\pi}{3}(m-1)\right) \cdot V_q^s{}^* \right] \\ T_0 &= T_s - T_1 - T_2 \end{aligned} \tag{12}$$

$$\text{where } V_d^s{}^* = |V^*| \cdot \cos(\theta),\ V_q^s{}^* = |V^*| \cdot \sin(\theta),$$

$$\theta = \alpha + \frac{\pi}{3}(m-1),\ m = \text{sector number } (1, 2, \ldots, 6).$$

Note that the applying times mean the duration in which active voltages are applied, but don't imply the actual gating times. Therefore, to calculate the actual gating times, the applying times should be recombined with the zero voltage applying time T_0 according to the reference vector location. In this PWM method, the zero voltage applying time is distributed symmetrically at the start and end of the sampling interval to generate actual gating signal in the symmetric manner. Therefore, to employ this PWM method for inverter operation, more complicate task should be performed to identify the sector number and recombine applying times. Owing to this approaching manner of the

conventional technique, the overall process would be complex.

However it is possible to reconstruct the actual gating time without complicated tasks by introducing the effective time concept. If the zero voltage time is symmetrically distributed in one sampling period, the whole modulation task for SVPWM is easily accomplished by the proposed algorithm. More detailed explanation is presented in [3]. To relocate the effective time at the center of the sampling interval, the time shifting value T_{offset} is

$$T_{offset} = \frac{1}{2} T_0 - T_{min} \quad \text{where } T_0 = T_s - T_{eff}. \tag{13}$$

Fig.5 shows the offset time and phase, pole voltage of SVPWM scheme. It is noticed that the offset time is the middle of $T_{offset.min}$ and $T_{offset.max}$.

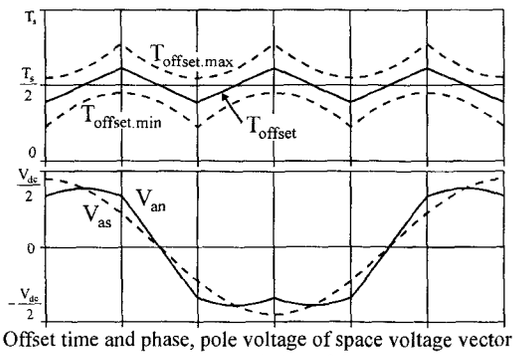

Fig. 5. Offset time and phase, pole voltage of space voltage vector PWM (modulation index : 0.9)

C. Discontinuous Modulation Scheme

This PWM scheme which also leads to the maximum modulation range as SVPWM uses a discontinuous switching operation. In this case each output of the inverter legs is alternately left on the positive or negative rail of the link voltage for 120^0 intervals of the electrical fundamental period. Although this PWM scheme in general leads to higher current harmonics compared with the SVPWM, it is of special interest because it reduces the average switching frequency to 67% and thus leads to less switching loss.

Among various discontinuous modulation PWMs, that of Fig 6(a) is of special interest for line converter to minimize switching loss. The principle of this PWM scheme can be depicted in terms of effective time as follows. If A-phase voltage reference is positive(or negative) and has maximum magnitude, A-phase switch should be fixed to ON(or OFF) state. That is to say,

$$\begin{aligned} &if\ T_{min} + T_{max} \geq 0 \Rightarrow T_{max} + T_{offset} = T_s \\ &if\ T_{min} + T_{max} < 0 \Rightarrow T_{min} + T_{offset} = 0 \end{aligned} \tag{14}$$

Therefore, the time shifting value T_{offset} is

$$\begin{aligned} &if\ T_{min} + T_{max} \geq 0 \Rightarrow T_{offset} = T_s - T_{max} \\ &if\ T_{min} + T_{max} < 0 \Rightarrow T_{offset} = -T_{min} \end{aligned} \tag{15}$$

In some application fields, with the viewpoint of current harmonics minimization, it is required to change the inverter switching sequence from SVPWM to this scheme or back[6,7]. In the proposed unified PWM method, this transition can be accomplished seamlessly by changing only the offset time from (13) to (15), or back.

The shift of ON duration by $\pm 30^0$ is possible without any restriction of the modulation range. In [8], the ON duration for each inverter arm is shifted $+30^0$ to minimize the switching loss according to the power factor of a motor. This PWM scheme is also implemented easily by modifying the offset time in the proposed scheme as shown in Fig.6(b),(c).

The 30^0 discontinuous PWM scheme is reported in [9]. In this scheme, switching loss is not dependent on the phase angle since the ON region is distributed evenly over the fundamental period[6], and the current harmonics is smallest among the discontinuous PWMs[9]. The switching pattern of this scheme is opposite to that of the 60^0 discontinuous PWM mentioned above. Therefore, the offset time is given by

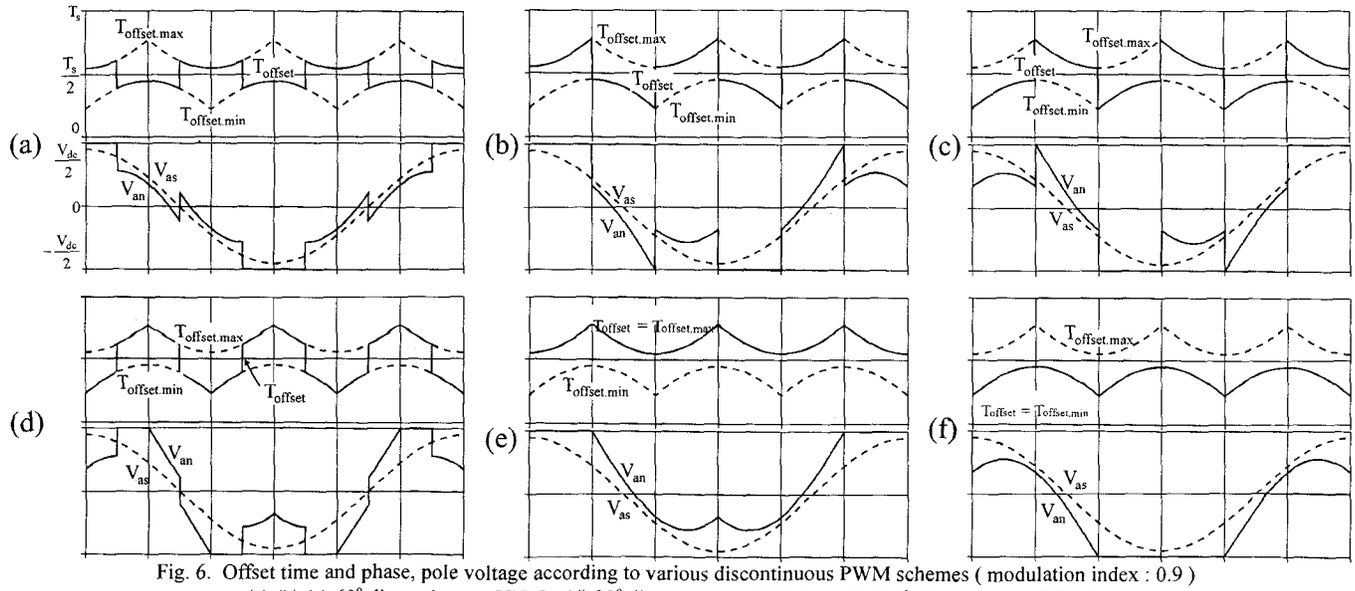

Fig. 6. Offset time and phase, pole voltage according to various discontinuous PWM schemes (modulation index : 0.9)
(a),(b),(c) 60^0 discontinuous PWMs. (d) 30^0 discontinuous PWM. (e),(f) 120^0 discontinuous PWMs.

$$\text{if } T_{min} + T_{max} \geq 0 \Rightarrow T_{offset} = -T_{min}$$
$$\text{if } T_{min} + T_{max} < 0 \Rightarrow T_{offset} = T_s - T_{max}. \quad (16)$$

The 120^0 discontinuous PWM scheme is also reported in [9]. The pole voltage of this scheme is not half-wave symmetric and it contains the dc component. In the viewpoint of the offset time, following equations can be written. For the PWM scheme of Fig. 6(e),

$$T_{offset} = T_s - T_{max} \quad (17)$$

and for the PWM scheme of Fig. 6(f),

$$T_{offset} = -T_{min}. \quad (18)$$

Fig.6 shows the offset time and phase, pole voltage according to the various discontinuous PWM schemes.

IV. OVERMODULATION

The effective time T_{eff} becomes larger than the sampling time T_s in the case that the reference voltage vector exceeds the hexagon area as shown in Fig. 7. In this case, a proper overmodulation technique should be implemented because it determines the transient dynamics of system. By the proposed PWM scheme, commonly used simple overmodulation strategies can be easily implemented in which the available voltage vector on the point 'b' is selected for an actual output vector instead of original vector on the point 'a' as shown in Fig.7.

In the overmodulation scheme proposed in [10], the voltage vector at the point 'b' is selected as an approximate vector which has the same angle as the original reference as shown in Fig. 7(a). In this case, the offset time and the actual gating times are calculated from the scaled-down effective time as below steps.

$$\text{step 1: } T'_{as,bs,cs} = T_{as,bs,cs} \cdot \frac{T_s}{T_{eff}} \ (Scale\ Down)$$
$$\text{step 2: } T_{offset} = -T_{min} \cdot \frac{T_s}{T_{eff}} \quad (19)$$
$$\text{step 3: } T_{ag,bg,cg} = T'_{as,bs,cs} + T_{offset}$$

In the overmodulation scheme proposed in [11,12], the voltage vector at the point 'b' is selected as the closest vector to the original reference as shown in Fig. 7(b). In this case, the offset time and the actual gating times are calculated from the effective time which is cut off at the both ends equally as below steps.

$$\text{step 1: } T'_{as,bs,cs} = T_{as,bs,cs} - \frac{T_{eff} - T_s}{2} \ (Centering)$$
$$\text{if } T'_{as,bs,cs} > \frac{T_s}{2},\ T'_{as,bs,cs} = \frac{T_s}{2} \ (Cut\ Off)$$
$$\text{if } T'_{as,bs,cs} < -\frac{T_s}{2},\ T'_{as,bs,cs} = -\frac{T_s}{2} \quad (20)$$
$$\text{step 2: } T_{offset} = \frac{T_s}{2}$$
$$\text{step 3: } T_{ag,bg,cg} = T'_{as,bs,cs} + T_{offset}$$

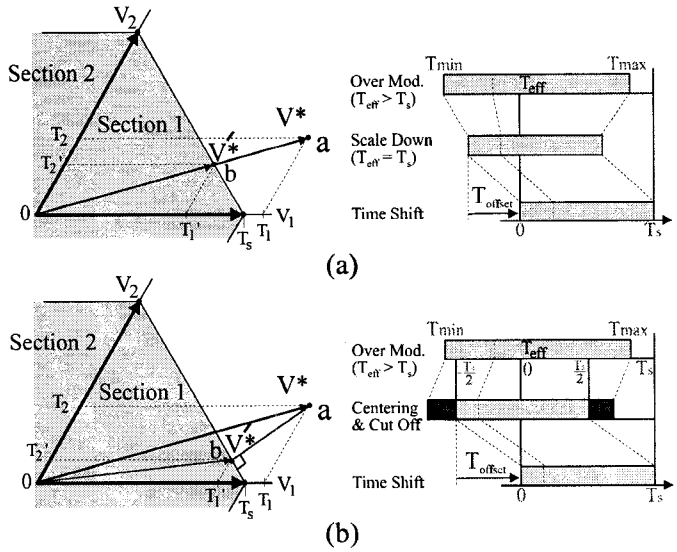

Fig.7. Common Overmodulation schemes
(a) Scheme of [10]. (b) Scheme of [11,12]

IV. IMPLEMENTATION RESULTS

Experiments are conducted to evaluate the performance of the proposed unified PWM algorithm. Though the proposed algorithm can be implemented by analog circuit, a digital circuit is more recommendable to change the offset time arbitrarily for various PWM schemes. A typical block diagram of the gating circuit is depicted in Fig.8. By loading the pre-calculated gating times(T_{ga}, T_{gb}, T_{gc}) to each counter at every sampling time, the gating sequence automatically runs for proper inverter action. In the experiment, this gating circuit is implemented on EPLD(Erasable Programmable Logic Device).

The various modulation features of the unified PWM method are illustrated in Fig.9. In this figure, the sampling time is 150[μsec] and the frequency of reference voltage is 100[Hz]. By the effective time shifting operation, relative gating patterns are generated according to the various modulation schemes. For monitoring purpose, the pole voltage(V_{an}) and offset voltage(V_{sn}) of each figure are synthesized using the calculated gating times by (10).

In Fig.10, the PWM modulation strategy is changed in real time by the proposed unified PWM method. The current of an inductive load is regulated to 20[A]. Fig.10(a) shows the A-phase current and Fig.10(b) shows the A-phase reference voltage given to the PWM algorithm. Pole voltage is synthesized as shown in Fig.10(c). In Fig.10(d), upper gating signal is generated according to each modulation scheme. From these results, it can be seen that the real-time transition of PWM method also can be accomplished easily and seamlessly by changing the offset time.

V. CONCLUSION

In this paper, a novel voltage modulation technique for the high performance voltage modulation has been described. Since the actual gating times are directly deduced by using only the phase reference voltages, the calculation effort of

the proposed scheme is greatly reduced compared with any other PWM schemes. Therefore proposed PWM scheme can be implemented by low-performance microprocessor without any tables and trigonometric functions and can be easily applied in the actual application fields. Moreover, the real time change of modulation scheme is implemented easily and seamlessly by changing only the offset time without any extra hardware. Widely used overmodulation schemes are also easily implemented by the proposed method. The performance of the proposed PWM method has been proved by laboratory tests.

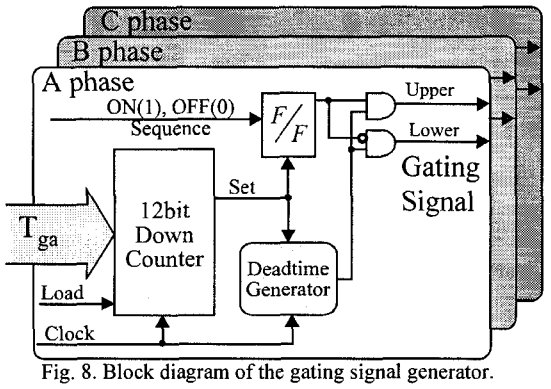

Fig. 8. Block diagram of the gating signal generator.

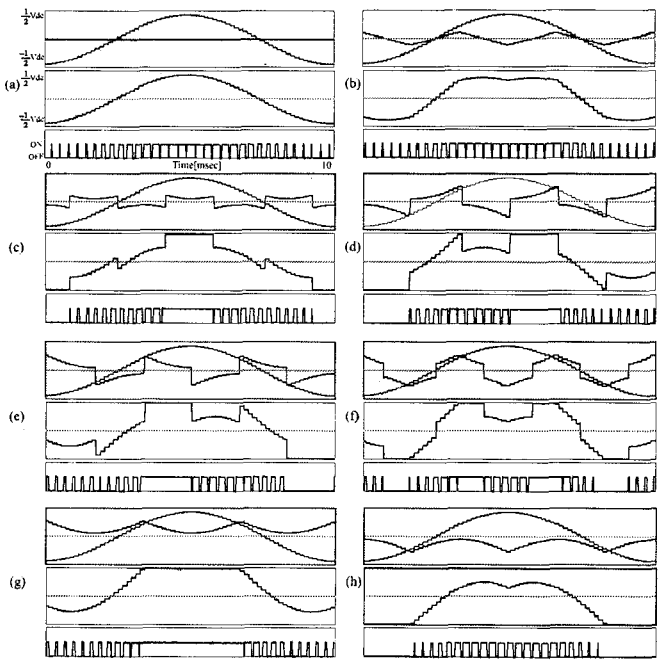

Fig.9. Voltage modulation features of the proposed 'unified PWM method' (modulation index: 0.9)
(a) Sinusoidal PWM. (b) SVPWM.
(c) 60° discontinuous modulation.
(d) 60° discontinuous modulation shifted by 30° [Elec. Angle].
(e) 60° discontinuous modulation shifted by -30°.
(f) 30° discontinuous modulation.
(g) 120° discontinuous modulation-I.
(h) 120° discontinuous modulation-II.
(In each figure, top trace: phase voltage reference and synthetic offset voltage, middle trace: synthetic pole voltage, bottom trace: A-phase upper gating signal)

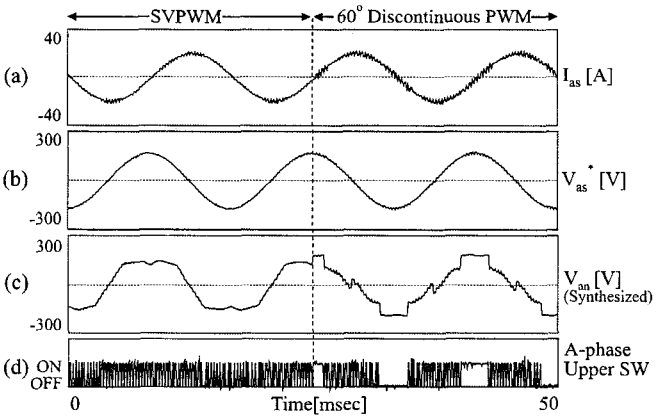

Fig.10. Real-time change of voltage modulation method by proposed unified PWM method (modulation index: 0.9).
(a) A-Phase current. (b) A-Phase reference voltage.
(c) Synthesized A-Pole voltage. (d) A-Phase upper gating signal.

REFERENCES

[1] J. Holtz, "Pulsewidth Modulation - A survey," *IEEE Trans. on Ind. Elec. vol.39, no.5, pp.410-420, 1992.*

[2] H.W. Van der Broeck and H.C. Skudelny, "Analysis and Realization of a Pulse Width Modulator Based on Voltage Space Vectors," *IEEE Trans. on Ind. Appl. vol.24, no.1, pp.142-150, 1988.*

[3] J.S. Kim and S.K. Sul, "A Novel Voltage Modulation Technique of the Space Vector PWM," in Conf. Rec. of Yokohama IPEC'95, pp.742-747, 1995.

[4] D.W. Chung, J.S. Kim and S.K. Sul, "Unified Voltage Modulation Technique for Real Time Three-Phase Power Conversion," in Conf. Rec. of IAS'96, vol.2, 1996, pp.921~926

[5] J.F. Moynihan, et alii ,"Indirect Phase Current Detection for Field Oriented Control of a Permanent Magnet Synchronous Motor Drive," in Conf. Rec. of EPE'91, no.3, pp.641-646, 1991.

[6] J.W. Kolar, H. Ertl and F.C. Zach, "Influence of the Modulation Method on the Conduction and Switching Losses of a PWM Converter System," *IEEE Trans. on Ind. Appl., vol.27, no.6, pp.1063-1075, 1991.*

[7] S. Ogasawara, H. Akagi and A.Nabae,"A Novel PWM Scheme of Voltage Source Inverters Based on Space Vector Theory," in Conf. Rec. of EPE'89, pp.1197-1202, 1989.

[8] A.M. Trzynadlowski and S. Legowski, "Minimum-Loss Vector PWM Strategy for Three-Phase Inverters," *IEEE Trans. on Power Electron., vol.9, no.1, pp.26-34, 1994.*

[9] H.W. Van der Broeck, "Analysis of the Harmonics in Voltage Fed Inverter Drives Caused by PWM Schemes with Discontinuous Switching Operation," in Conf. Rec. of EPE'91, vol.3, pp.261-266, 1991.

[10] T.G. Habetler, F. Profumo, M. Pastorelli, and L.M. Tolbert, "Direct Torque Control of Induction Machines Using Space Vector Modulation," *IEEE Trans. on Ind. Appl., vol.28, no.5, pp.1045-1053, 1991*

[11] H. Mochikawa, T. Hirose and T. Umemoto, "Overmodulation of Voltage Source PWM Inverter," JIEEE Ind. Soc. Ann. Conf. Rec., 1991, pp.466-471.(In Japanese)

[12] D. R. Seidl, D. A. Kaiser and R. D. Lorentz, "One-Step Optimal Space Vector PWM Current Regulation Using a Neural Network", in Conf. Rec. of IAS'92, pp.570-577, 1992

Walsh Function Based Synthesis Method of PWM Pattern for Full-Bridge Inverter

Seiji Kondo and Krit Choeisai
Nagaoka University of Technology
1603-1, Kamitomioka-cho, Nagaoka 940-21, JAPAN
Fax: +81-258-47-9500, Phone: +81-258-47-9507
E-mail: kondo@voscc.nagaokaut.ac.jp

Abstract—**This paper applies the Walsh function to simplify the on-off pattern synthesis of a single phase full-bridge PWM inverter with low harmonics. Owing to the digital nature of the Walsh function, the synthesis process becomes straightforward. It is the remarkable feature of the proposed method over a conventional method using Fourier series. Several examples are shown in the paper, which verifies the validity of the proposed synthesis method.**

I. INTRODUCTION

The Fourier series expansion is conventionally used to derive optimal PWM pattern with low harmonics [1]. The trigonometric function used in the Fourier series causes a problem. It is that an equation including trigonometric function requires a numerical iteration process to find its solution. The iteration loop shown in Fig. 1 is necessary for searching optimal PWM pattern with low harmonics and it takes long calculation time.

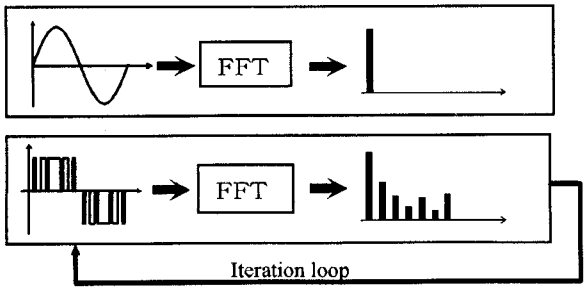

Fig.1 Outline for searching optimal PWM pattern

The Walsh function has only two level signal of ± 1 and is suitable for the application to switching process [2]. As it will be described in section III, the equation relating the on-off switching timing with the Walsh spectrum results in a liner algebraic equation which can be solved directly without any iteration process. Hence, the PWM pattern synthesis using the Walsh function becomes straight-forward and its computation is simpler and faster than that using trigonometric function.

II. FUNDAMENTALS OF WALSH FUNCTION

A. Definition of Walsh Function

The Walsh function forms an ordered set of rectangular waveforms taking only two amplitude values, +1 and -1, over one normalized frequency period [0, 1] as illustrated in Fig.2. The Walsh function, wal(n,t), has Walsh's original order, where n is the number of zero axis crossing for one cycle. There are many way to create wal(n,t). In this paper, the Walsh function wal(n,t) is indirectly generated by the recurrence relation of H(·):

$$\mathrm{H}(0,t) = \begin{cases} 1 & -\frac{1}{2} \le t \le \frac{1}{2} \\ 0 & \text{otherwise.} \end{cases} \tag{1}$$

$$\left.\begin{aligned} \mathrm{H}(2n+p,t) \;=\; & (-1)^{[n/2]+p}\{\mathrm{H}(n,2(t+\tfrac{1}{4}))\} + \\ & (-1)^{n+p}\{\mathrm{H}(n,2(t-\tfrac{1}{4}))\}, \end{aligned}\right\} \tag{2}$$

n=0,1,2,3,...,
p=([n/2]%2)=0 or 1,

where, [n/2] is maximum integer that is smaller than n/2, and (m%2) is the reminder of m divided by 2. Then the function H(·) gives the Walsh function wal(·) as:

$$\mathrm{wal}(n,t) = \mathrm{H}(2n+p,t). \tag{3}$$

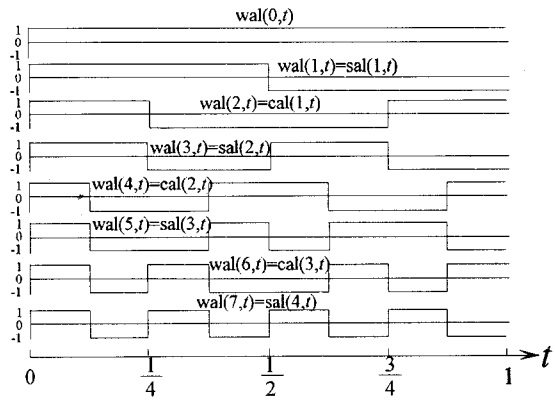

Fig.2 Walsh Function

Similar to the trigonometric function, the Walsh function can be classified into odd-function and even-function:

$$\begin{aligned} &\mathrm{sal}(m,t) = \mathrm{wal}(2m-1,t) \quad \text{[odd-function]}, \\ &\mathrm{cal}(m,t) = \mathrm{wal}(2m,t) \quad \text{[even-function]}. \end{aligned} \tag{4}$$

The sal() and cal() are corresponding to sine-Walsh and cosine-Walsh, respectively. Unlike the sine and cosine functions in the Fourier series, the sal() and cal() have rectangular waveforms. This kind of binary nature of the Walsh function makes the calculation of the series expansion simpler than that of the Fourier series expansion.

B. Walsh Series Expansion

An appropriately continuous function $x(t)$ can be expressed by the Walsh series in the similar way as the Fourier series expansion:

$$x(t) = A_0 \mathrm{wal}(0,t) + \sum_{i=1}^{\infty} \{A_i \mathrm{cal}(i,t) + B_i \mathrm{sal}(i,t)\}, \quad (5)$$

where,

$$\left.\begin{aligned} A_0 &= \int_0^1 x(t)\mathrm{d}t \\ A_i &= \int_0^1 x(t)\mathrm{cal}(i,t)\mathrm{d}t \\ B_i &= \int_0^1 x(t)\mathrm{sal}(i,t)\mathrm{d}t \end{aligned}\right\} \quad (6)$$

C. Comparison between Fourier and Walsh Expansions of PWM pattern

In order to compare calculation time between Fourier and Walsh expansions, it is assumed that the *f(t)*is a PWM switching pattern of which first quarter cycle is shown in Fig. 3(b) and whole one cycle is shown in Fig. 3(a). The Fourier and Walsh series-expansions can be derived as follows.

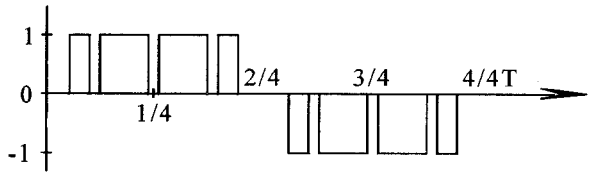

(a). One cycle of Full-bridge PWM inverter

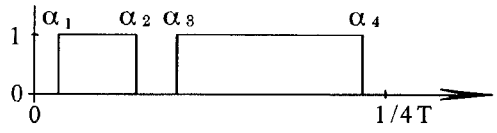

(b). First quarter cycle

Fig.3 Example of PWM pattern

Fourier series expansion:

$$f(t) = \sum_{i=1,3,5,\ldots}^{\infty} C_i \sin(i\omega t)$$

$$C_i = 4\int_0^{1/4} f(t)\sin(i\omega t)\mathrm{d}t$$

$$\frac{C_i}{4} = \int_{\alpha_1}^{\alpha_2} f(t)\sin(i\omega t)\mathrm{d}t + \int_{\alpha_3}^{\alpha_4} f(t)\sin(i\omega t)\mathrm{d}t$$

for i=1,

$$\frac{C_1}{4} = \frac{1}{\omega}\{ -(\cos(\omega\alpha_2) - \cos(\omega\alpha_1)) - (\cos(\omega\alpha_4) - \cos(\omega\alpha_3)) \} \quad (7)$$

Walsh series expansion:

$$f(t) = \sum_{i=1,3,5,\ldots}^{\infty} B_i \mathrm{sal}(i,t)$$

$$B_i = 4\int_0^{1/4} f(t)\mathrm{sal}(i,t)\mathrm{d}t$$

$$\frac{B_i}{4} = \int_{\alpha_1}^{\alpha_2} f(t)\,\mathrm{sal}(i,t)\mathrm{d}t + \int_{\alpha_3}^{\alpha_4} f(t)\,\mathrm{sal}(i,t)\mathrm{d}t$$

for i=1,

$$\frac{B_1}{4} = (\alpha_2 - \alpha_1) + (\alpha_4 - \alpha_3). \quad (8)$$

For the Fourier expansion, the computation of C_1 in (7) requires the calculation of cos(), which takes relatively long time. On the other hand, for the Walsh expansion, the computation of B_1 in (8) requires only plus/minus operations. This benefit of the Walsh function can make the calculation faster. By the computer simulation result, it was found that the computation time ratio of (8)/(7) was 0.029.

III. Proposed Synthesis Method of PWM Pattern

A. Outline of Proposed Method

Fig. 4 illustrates the outline of the PWM pattern synthesis process proposed in this chapter. The goal of the synthesis is to make the PWM pattern close to the commanded output waveform which is illustrated as a sine-wave in Fig. 4. In the following, it is assumed that the commanded output waveform is a sine-wave to make the explanation simple.

At the first step, the values of B_i, which are the Walsh series coefficients of the commanded waveform, are calculated. This will be described in the section-B of this chapter.

Secondary, the equation which relates the PWM on-off timing to the Walsh coefficients B_i' is derived. This will be given in the section-C.

Here at this point, if $B_i' = B_i$ for i = 1,3,5,...,∞, the PWM wave should coincide with the commanded wave. This is true in theoretical sense. But this kind of coefficients matching can not be achieved actually, because the switching frequency of the PWM inverter can not be infinity. Therefore, we limit the maximum value of i for the coefficient matching taking account of the switching speed of the power device.

At the last step, the switching timing α of the PWM pattern can be determined directly from the Walsh series coefficients B_i of the commanded waveform, which is based on a equation derived in the section-D of this chapter.

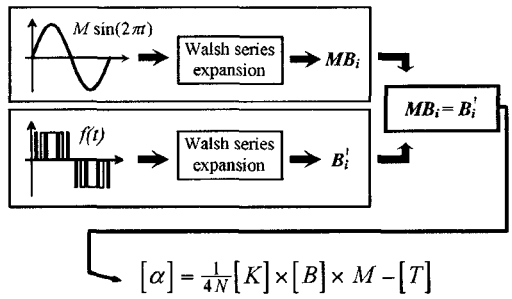

Fig.4 Outline of propose PWM pattern synthesis method

B. Walsh Series Expansion of Commanded Waveform

In order to make the synthesis simple, it is assumed that the commanded waveform of the PWM inverter output has the property of quarter-wave symmetry. As an example, the case when the output command equals to $M\sin(2\pi t)$, where M is modulation ratio, will be explained in what follows. The Walsh series expansion is given as:

$$M\sin(2\pi t) = \sum_{i=1}^{\infty} \{MB_{2i-1}\mathrm{sal}(2i-1,t)\}, \tag{9}$$

$$B_{2i-1} = 4\int_0^{1/4} \sin(2\pi t)\mathrm{sal}(2i-1,t)\mathrm{d}t \qquad i = 1,2,3,4,... \tag{10}$$

Since the output command is assumed to be the sine-wave, in the right hand side of (9), the coefficient B_{2i-1} remains but the coefficients A_0 and A_i and B_{2i} appeared in (5) and (6) become zero. The calculated values of B_{2i-1} for M=1 are shown in Fig. 5.

B_i	Amplitude	B_i	Amplitude
B_1	6.3479163e-01	B_{17}	-4.5329788e-03
B_3	-2.6175649e-01	B_{19}	2.8312203e-03
B_5	-5.4188331e-02	B_{21}	-1.2723538e-03
B_7	-1.2470090e-01	B_{23}	2.2541680e-03
B_9	-1.4214565e-02	B_{25}	-7.8280793e-03
B_{11}	6.8687577e-03	B_{27}	4.1339117e-03
B_{13}	-2.7644381e-02	B_{29}	-1.4509166e-02
B_{15}	-6.0704612e-02	B_{31}	-2.9590249e-02

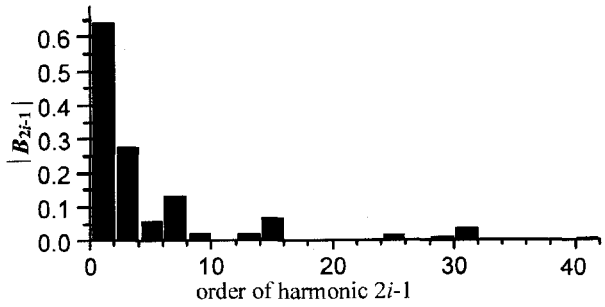

Fig. 5. Calculated values of coefficients B_1 to B_{31} (M=1)

C. Walsh series expansion of PWM pattern

Fig. 3 shows an example of whole one cycle of Full-bridge PWM inverter waveform which has 3-level. By using the symmetrical property of the PWM pattern, it is enough to calculate only the first quarter cycle. The PWM pattern is setting to be $f(t)$ which is the function of α.

$$f(t) = \begin{cases} 1 & t = [\alpha_1,\alpha_2],[\alpha_3,\alpha_4],... \\ 0 & \text{otherwise} \end{cases} \tag{11}$$

where

$0 \le t \le 1/4$.

The Walsh series expansion of $f(t)$ is given as:

$$f(t) = \sum_{i=1}^{\infty} \{B'_{2i-1}\mathrm{sal}(2i-1,t)\}, \tag{12}$$

$$B'_{2i-1} = 4\int_0^{1/4} f(t)\mathrm{sal}(2i-1,t)\mathrm{d}t \qquad i = 1,2,3,4,... \tag{13}$$

D. Proposed Synthesis Method of PWM pattern

In order to derive the synthesis method of the on-off switching function of the PWM inverter, the first quarter cycle of the output command is divided into N subintervals, where N should be chosen to be an integer of power of two. The sample quarter cycle of the PWM switching function $f(t)$ for N=4 is shown in Fig.6.

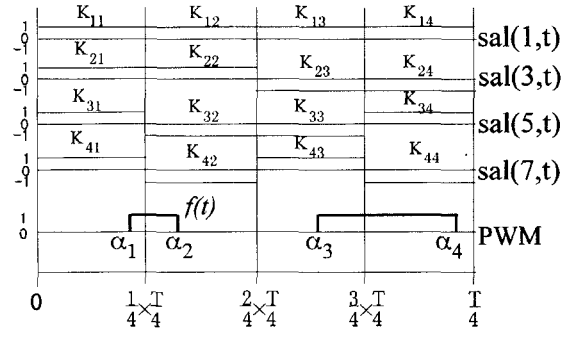

Fig.6 PWM design (N=4)

To make the switching function $f(t)$ close to the output command $M\sin(2\pi t)$, the B'_{2i-1} in (12) should be set equal to the MB_{2i-1} in (9), that is,

$$MB_{2i-1} = B'_{2i-1}. \tag{14}$$

As shown in Fig.6, the value of sal function is +1 or -1 for N subintervals, which makes the calculation simple. Letting the value of the sal function for each subinterval be K_{ij}:

$$K_{ij} = \mathrm{sal}(2i-1, \frac{j-1}{4N}). \quad (15)$$

According to the property of sal(), the following relations hold:

$$K_{ij} = K_{ji}, \quad (16)$$

$$\sum_{i=1,2,3,\ldots}^{N} (K_{ij})^2 = N. \quad (17)$$

From (13) and (14), the following equation holds:

$$\begin{aligned} \frac{M}{4} B_{2i-1} &= \int_0^{1/4} f(t)\mathrm{sal}(i,t)\mathrm{d}t \\ &= K_{i1}\int_0^{1/4N} f(t)\mathrm{d}t + K_{i2}\int_{1/4N}^{2/4N} f(t)\mathrm{d}t + \ldots \\ &+ K_{i(N-1)}\int_{\frac{N-2}{4N}}^{\frac{N-1}{4N}} f(t)\mathrm{d}t + K_{iN}\int_{\frac{N-1}{4N}}^{1/4} f(t)\mathrm{d}t. \end{aligned} \quad (18)$$

Substituting (11) into (18), the following equation can be obtained:

$$\begin{aligned} \frac{M}{4} B_{2i-1} &= K_{i1}(T_1 - \alpha_1) + K_{i2}(\alpha_2 - T_1) + \ldots + \\ &\quad K_{i(N-1)}(T_{N-1} - \alpha_{N-1}) + K_{iN}(\alpha_N - T_{N-1}) \\ &= K_{i1}(-\alpha_1) + K_{i2}(\alpha_2) + \ldots + \\ &\quad K_{i(N-1)}(-\alpha_{N-1}) + K_{iN}(\alpha_N) + \\ &\quad K_{i1}T_1 + K_{i2}(-T_1) + \ldots + \\ &\quad K_{i(N-1)}(T_{N-1}) + K_{iN}(-T_{N-1}) \end{aligned} \quad (19)$$

where,

$$T_{2i-1} = \frac{2i-1}{N} \times \frac{1}{4} \qquad i=1,2,3,\ldots,N/2. \quad (20)$$

Rewriting (19) in matrix form,

$$\begin{aligned} \frac{M}{4}\begin{bmatrix} B_1 \\ B_3 \\ \cdots \\ B_{2N-1} \end{bmatrix} &= \begin{bmatrix} K_{11} & K_{12} & \cdots & K_{1N} \\ K_{21} & K_{22} & \cdots & K_{2N} \\ \cdots & & & \\ K_{N1} & K_{N2} & \cdots & K_{NN} \end{bmatrix} \times \begin{bmatrix} -\alpha_1 \\ \alpha_2 \\ \cdots \\ \alpha_N \end{bmatrix} + \\ &\quad \begin{bmatrix} K_{11} & K_{12} & \cdots & K_{1N} \\ K_{21} & K_{22} & \cdots & K_{2N} \\ \cdots & & & \\ K_{N1} & K_{N2} & \cdots & K_{NN} \end{bmatrix} \times \begin{bmatrix} T_1 \\ -T_1 \\ \cdots \\ -T_{N-1} \end{bmatrix}. \end{aligned} \quad (21)$$

The simple form of the above equation is given as:

$$\frac{M}{4}[B] = [K]\times[\alpha] + [K]\times[T]. \quad (22)$$

By the property of the Walsh function, the [K] matrix is a complete orthogonal matrix, and the relations (16) and (17) hold. Taking these properties into account, the inverse matrix of [K] can be simply calculated as:

$$[K]^{-1} = \frac{1}{N}[K]. \quad (23)$$

Solving (22) with respect to the $[\alpha]$ and using (23), the switching timing vector $[\alpha]$ can be calculated as:

$$[\alpha] = \frac{1}{4N}[K]\times[B]\times M - [T]. \quad (24)$$

The proposed synthesis method is summarized as follows:

step-1. calculate B_{2i-1} matrix by (10), or use data listed in Fig. 5 if N less than 16.

step-2. calculate T_{2i-1} by (20),

step-3. calculate $[K]$ by (15),

step-4. then, determine the $[\alpha]$ by (24).

IV. Simulation Results

The harmonics of the proposed method and the conventional triangular wave modulation method will be compared in the condition when the switching frequencies of both methods are kept the same.

A. The Case for Pure Sine-Wave Output

In the first quarter of one cycle the number of switching angle of both methods is set to N. For N=4 the calculation of the Walsh's calculation method and the conventional triangular wave modulation method are shown in Fig.7 and Fig.8 respectively. For N=16 the calculation of the Walsh's calculation method and the conventional triangular wave modulation method are shown in Fig.9 and Fig.10.

As shown in Fig.7(c) and Fig.9(c), the relation between modulation ratio and switching angle of the Walsh's calculation method are linear. Comparing Fig.7(b) and Fig.9(b), the calculation with larger N results in less harmonics shifted to higher frequency range. Comparing Fig.7(b) and Fig.8(b), the Walsh's calculation method can decrease the harmonics (3^{rd},5^{th},7^{th}) more than the conventional triangular wave modulation method. For the calculation by N=16, the harmonics of both method are almost the same as shown in Fig.9(b) and Fig.10(b).

B. The case for the third harmonic including

In this case, the fundamental wave including the third harmonic is a command waveform for a sample simulation. The amplitude of the third harmonic is setting to 1/6 on the fundamental component, then the command waveform is $\sin(2\pi t)+1/6\sin(6\pi t)$. Both calculation methods are compared in the same condition when N=16. The Walsh's calculation method is shown in Fig. 11 and the conventional triangular wave modulation method in Fig. 12. The harmonics of both calculations method are shown in Table I.

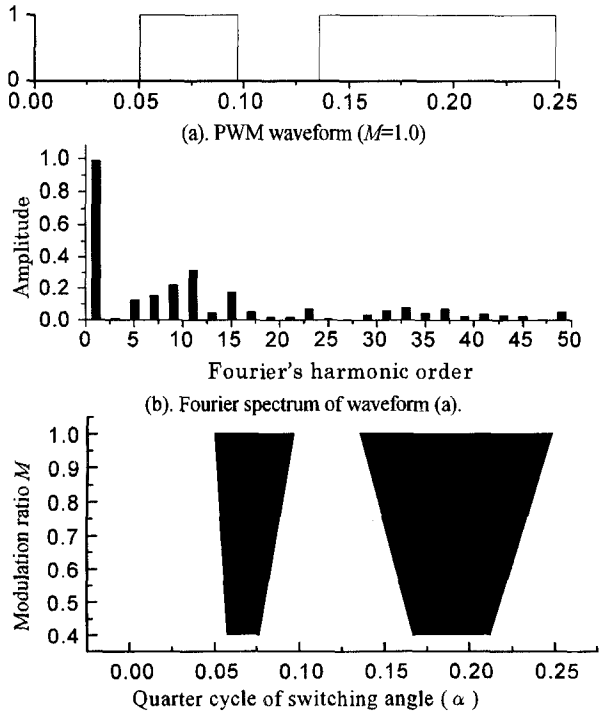

(a). PWM waveform (M=1.0)

(b). Fourier spectrum of waveform (a).

(c). Relation between modulation ratio M and α relation

Fig. 7 Walsh's calculation waveform when N=4

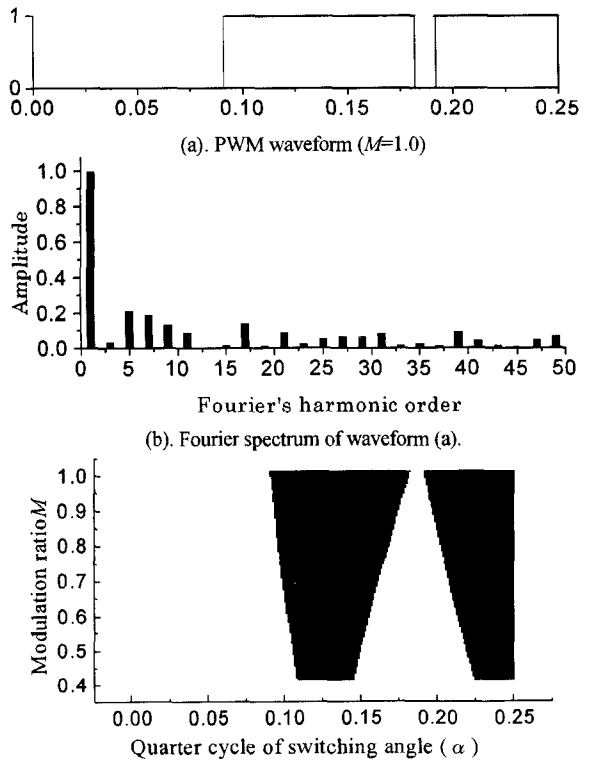

(a). PWM waveform (M=1.0)

(b). Fourier spectrum of waveform (a).

(c). Relation between modulation ratio M and α relation

Fig. 8 Triangular 's modulation waveform when switching angle=4

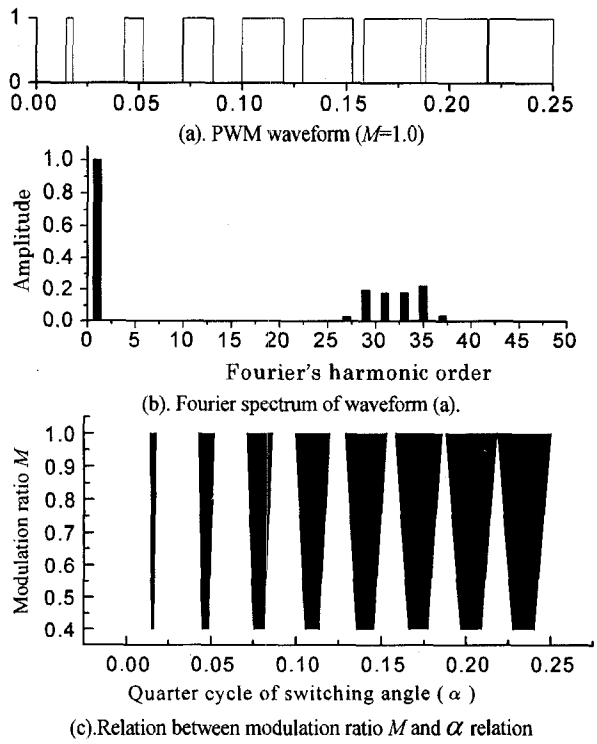

(a). PWM waveform (M=1.0)

(b). Fourier spectrum of waveform (a).

(c).Relation between modulation ratio M and α relation

Fig. 9 Walsh's calculation waveform when N=16

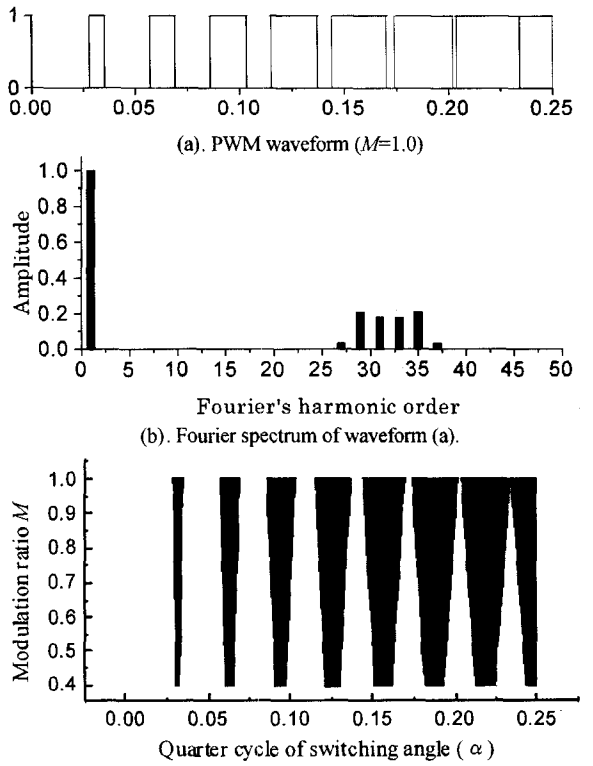

(a). PWM waveform (M=1.0)

(b). Fourier spectrum of waveform (a).

(c). Relation between modulation ratio M and α relation.

Fig. 10 Triangular 's modulation waveform when switching angle=16

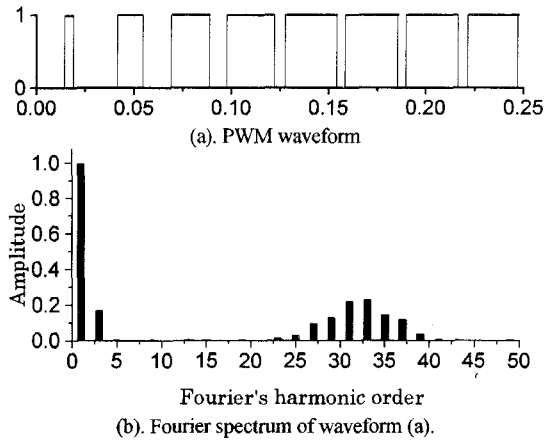

(a). PWM waveform

(b). Fourier spectrum of waveform (a).

Fig. 11 The Walsh 's calculation for 3rd harmonic including when N=16

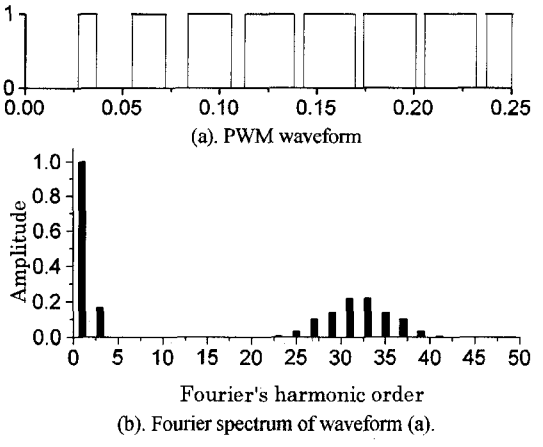

(a). PWM waveform

(b). Fourier spectrum of waveform (a).

Fig. 12 Triangular waveform modulation for 3rd harmonic including when N=16

From Table I , by the calculation of the triangular wave modulation method we can verify that the amplitude of fundamental and third harmonic matches to the command waveform. The amplitude of harmonics in switching length are symmetry, when the 31st and 33rd harmonics are suppose to be a center of switching.

By the calculation of the propose method, we found the amplitude of fundamental and third harmonic does not match to the command waveform. That is because we limit the number N of Walsh series coefficients (B_i) to designed the PWM pattern. For matching the amplitude of fundamental and/or the third harmonic, we should adjust infinitely large number of Walsh series coefficients. Also, the amplitude of harmonics in switching length are not symmetry as the amplitude of harmonics calculated by the triangular wave modulation method. The amplitude of harmonics in lower length of the center (25th to 31st) are smaller but the amplitude of harmonics in the higher length of the center (33rd to 43rd) are larger than the amplitude of harmonics calculated by triangular wave modulation method.

TABLE I
Fourier spectrum

Harmonics (th)	Walsh's calculation	Triangular's modulation
1	0.996	1.000
3	0.169	0.167
5	0.003	0.000
7	0.002	0.000
9	0.004	0.000
11	0.002	0.000
13	0.003	0.000
15	0.003	0.000
17	0.002	0.000
19	0.004	0.000
21	0.000	0.002
23	0.011	0.009
25	0.026	0.033
27	0.094	0.103
29	0.129	0.140
31	0.221	0.222
33	0.228	0.222
35	0.144	0.140
37	0.115	0.103
39	0.035	0.033
41	0.010	0.009
43	0.003	0.002
45	0.000	0.000
47	0.002	0.001
49	0.004	0.003

V. CONCLUSION

This paper proposes the algorithm to design full-bridge PWM pattern with low harmonics by using the Walsh function. The proposed algorithm process becomes straightforward, in opposition to the algorithm process of the conventional method using Fourier series, which requires an iteration process for searching the PWM pattern. The Walsh function, which has only two level signals of +1 and -1, is suitable to design an algorithm process simpler and faster than that using trigonometric function.

REFERENCES

[1] I. Takahashi, H. Mochikawa: "A New Control of PWM Inverter Waveform for Minimum Loss Operation of an Induction Motor Drive", IEEE Trans. on IA, Vol. IA-21, No. 4, p. 580 (1985)

[2] T.J. Liang and R.G. Hoft "Walsh Function Method of Harmonic Elimination", pp.847-853, APEC conf., March 1993 proceedings.

Indirect Current Control Scheme in PWM Voltage-Sourced Converter

Jae-Ho Choi, Hyong-Cheol Kim, Joo-Sik Kwak
School of Electrical and Electronics Engineering
Chungbuk National University
48 Gaesindong, Cheongju, Chungbuk, South Korea 361-763
Phone: +82-431-61-2425, FAX: +82-431-276-7217
E-mail: choi@choijae.chungbuk.ac.kr

Abstract- **An indirect current control scheme for PWM voltage source converter is proposed in this paper. The main advantages of this proposed system are that the sinusoidal line current waveforms with nearly unity power factor and the ripple-free DC output voltage waveform are achieved without any current sensors. The mathematical model based on space vector is derived and the principle of the indirect current control is described. From the comparison of the simulation and experimental results between the direct current control scheme and the indirect current control scheme, the validity of this proposed indirect current control is verified.**

I. INTRODUCTION

Up to now, AC to DC converters have been dominated by diode bridge rectifiers or line- commutated phase-controlled rectifiers in many industry applications including battery charger because the system structure and control strategy is very simple.

Those rectifiers, however, have some disadvantages of poor power factor and high content of harmonics in the line currents, which may have a harmful effect on the other loads connected with the same utility line, so that require large inductors and capacitors to reduce the harmonic contents.

To overcome these advantages, PWM voltage-sourced converter(VSC) have been studied for many years. These converters have the following characteristics basically:

- Sinusoidal input current with unity power factor
- Ripple-free DC output voltage
- Bilateral power flow

Many research reports about the control strategies of PWM-VSC have been presented. Although the phase and amplitude control technique of the input line current is simple, it's dynamic response is slow and the offset in transient states is not eliminated.[1][2] The hysteresis current control method is capable of delivering nearly sinusoidal current waveform with unity power factor and regulating the DC output voltage constant with fast dynamic response, but the switching frequency varies with the variation of the DC load current. A simple control system, which the PI-type DC-voltage controller and the phase locked loop are lumped together and the feedforward controller of the load current combined to improve the dynamic response are also reported.[3][4]

Such control schemes usually employ two or three current sensors to implement the instantaneous current control and to limit the line currents for the protection of switching devices. But these current sensors bring some additional hardwares such as A/D converters in case of digital implementation in its train and cause the system complexity, cost-up and reduction of system reliability.[5][6]

In this paper, the indirect current control scheme for PWM voltage source converter is proposed. The main advantages of this proposed system are that the sinusoidal line current waveforms with nearly unity power factor and ripple-free DC output voltage waveform are achieved without any current sensors. The mathematical model based on space vector is derived and the principle of the indirect current control is derived. From the comparative results of the simulation and experiments between the direct current control scheme and the indirect current control scheme, the validity of this proposed indirect current control is verified.

II. PROPOSED INDIRECT CURRENT CONTROL STRATEGY

A. Mathematical model of voltage-sourced converter

The main power circuit of PWM voltage-sourced converter is shown in Fig. 1. It consists of six IGBTs with six antiparallel freewheeling diodes, a three phase AC input inductor, and a DC output capacitor. The voltage equations in the converter input sides are derived as following.

0-7803-3823-5/97/$10.00© 1997 IEEE

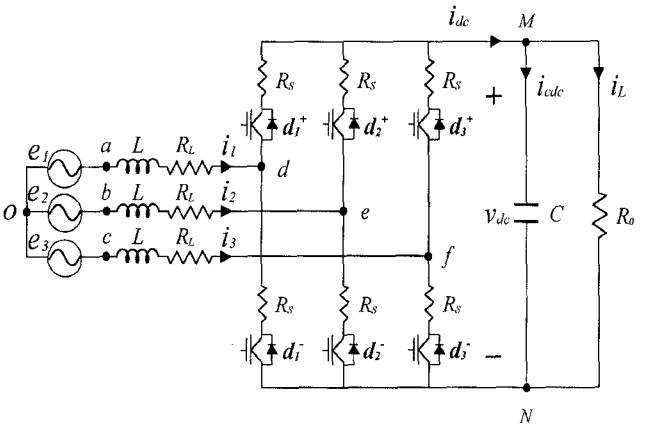

Fig.1. Configuration of PWM voltage-sourced converter.

$$e_i = L\frac{di_i}{dt} + Ri_i + (V_{dc}d_i^+ + V_{N0}) \quad i=1, 2, or\ 3 \tag{1}$$

where e_i is the utility source voltage, $L\frac{di_i}{dt}$ and Ri_i are voltage drops in the line inductor and the total series resistance through one phase, $(V_{dc}d_i^+ + V_{N0})$ is the fundamental value of the modulated voltage acquired from DC voltage as converter input voltage, and d_i is the switching functions corresponding to each of the switches.

From Fig. 1, the capacitor current is described by the subtraction of load current from converter DC output current as following.

$$C\frac{dV_{dc}}{dt} = (i_1 d_1^+ + i_2 d_2^+ + i_3 d_3^+) - \frac{V_{dc}}{R_0}. \tag{2}$$

Using (1) and (2), the differentiation equation of complete matrix-form for PWM voltage-sourced converter in a stationary frame can be derived as followings.

$$Z\dot{\boldsymbol{x}} = A\boldsymbol{x} + B\boldsymbol{e} \tag{3}$$

where $$\dot{\boldsymbol{x}} = [\ \dot{i}_1\ \ \dot{i}_2\ \ \dot{i}_3\ \ \dot{v}_{dc}\ ]^T \tag{4}$$

$$\boldsymbol{x} = [\ i_1\ \ i_2\ \ i_3\ \ v_{dc}\ ]^T \tag{5}$$

$$A = \begin{bmatrix} -R & 0 & 0 & -(d_1^+ - \frac{1}{3}\sum_{i=1}^{3} d_i^+) \\ 0 & -R & 0 & -(d_2^+ - \frac{1}{3}\sum_{i=1}^{3} d_i^+) \\ 0 & 0 & -R & -(d_3^+ - \frac{1}{3}\sum_{i=1}^{3} d_i^+) \\ d_1^+ & d_2^+ & d_3^+ & -\frac{1}{R_0} \end{bmatrix} \tag{6}$$

$$Z = \begin{bmatrix} L & 0 & 0 & 0 \\ 0 & L & 0 & 0 \\ 0 & 0 & L & 0 \\ 0 & 0 & 0 & C \end{bmatrix} \tag{7}$$

$$B = \begin{bmatrix} 1 & 0 & 0 & 0 \\ 0 & 1 & 0 & 0 \\ 0 & 0 & 1 & 0 \\ 0 & 0 & 0 & -1 \end{bmatrix} \tag{8}$$

$$\boldsymbol{e} = [\ e_1\ \ e_2\ \ e_3\ \ 0\ ]^T. \tag{9}$$

The matrix A is time-varient so that the dq-axis transformation with the synchronously rotating reference frame to the utility source angular frequency ω can be applied. The following time-invarient state space equation in the synchronously rotating reference frame is obtained by using the transformation matrix T and its inverse matrix T^{-1}.

$$Z_{dqo}\,\dot{\boldsymbol{x}}_{dqo} = A_{dqo}\,\boldsymbol{x}_{dqo} + B_{dqo}\,\boldsymbol{e}_{dqo} \tag{10}$$

where

$$\begin{aligned} \dot{\boldsymbol{x}}_{dqo} &= T\,\dot{\boldsymbol{x}} \\ A_{dqo} &= TAT^{-1} - TZ\dot{T}^{-1} \\ \boldsymbol{x}_{dqo} &= T\boldsymbol{x} \\ B_{dqo} &= TB \end{aligned} \tag{11}$$

$$T = \frac{2}{3}\begin{bmatrix} \cos\omega t & \cos(\omega t-\gamma) & \cos(\omega t+\gamma) & 0 \\ \sin\omega t & \sin(\omega t-\gamma) & \sin(\omega t+\gamma) & 0 \\ 1/2 & 1/2 & 1/2 & 0 \\ 0 & 0 & 0 & 3/2 \end{bmatrix} \tag{12}$$

$$T^{-1} = \begin{bmatrix} \cos\omega t & \sin(\omega t) & 1 & 0 \\ \cos(\omega t-\gamma) & \sin(\omega t-\gamma) & 1 & 0 \\ \cos(\omega t+\gamma) & \sin(\omega t+\gamma) & 1 & 0 \\ 0 & 0 & 0 & 1 \end{bmatrix} \tag{13}$$

$$\gamma = \frac{2\pi}{3}. \tag{14}$$

Finally, the steady-state equations are to be simplified as following.

$$\begin{bmatrix} \dot{i}_{qe} \\ \dot{i}_{de} \\ \dot{v}_{dc} \end{bmatrix} = \begin{bmatrix} -\frac{R}{L} & -\omega & -\frac{d_{de}}{L} \\ \omega & -\frac{R}{L} & -\frac{d_{qe}}{L} \\ \frac{3d_{de}}{2C} & \frac{3d_{qe}}{2C} & -\frac{1}{R_0 C} \end{bmatrix} \begin{bmatrix} i_{qe} \\ i_{de} \\ v_{dc} \end{bmatrix} + \begin{bmatrix} \frac{E}{L} \\ 0 \\ 0 \end{bmatrix} \quad (15)$$

where, E is the phase peak voltage of power source. In (15), the direction of the q-axis coincides with that of the AC power source, so that e_{qe} and e_{de} become E and zero, respectively.

B. DC output voltage regulation

To regulate the DC output voltage, the desired value of q-axis reference current is determined from the power valance condition.[4] This is accomplished by an outer PI feedback control loop, which compares V_{dc} with a set voltage reference V_{dc}^* and uses the error as a reference value of q-axis current.

$$i_{qe}^* = K_v \left[\Delta V_{dc} + \frac{1}{\tau} \int \Delta V_{dc} dt \right] \quad (16)$$

where, ΔV_{dc} is the difference of V_{dc} from V_{dc}^* and K_v is gain of voltage controller.

C. AC input current regulation

1) PI-type current controller: PI current controller is used to make the real current track the reference current value determined from (16). A line inductor voltage drop is accomplished by an inner PI feedback control loop, which compares the real current i_{qe} with the reference current i_{qe}^* and uses the error as an input. Equation (16) can be rewritten including converter input voltage vectors as (17).

$$\begin{bmatrix} \dot{i}_{qe} \\ \dot{i}_{de} \end{bmatrix} = \begin{bmatrix} -R/L & -\omega \\ \omega & -R/L \end{bmatrix} \begin{bmatrix} i_{qe} \\ i_{de} \end{bmatrix} - \begin{bmatrix} v_{de}/L \\ v_{qe}/L \end{bmatrix} + \begin{bmatrix} E/L \\ 0 \end{bmatrix} \quad (17)$$

where, v_{de} is $d_{de}V_{dc}$ and v_{qe} is $d_{qe}V_{dc}$.

If i_{de} is controlled to be zero, namely, converter input voltage vector v_{de} is controlled to be $\omega L i_{qe}$, AC input power factor is kept equal to 1.0. Consequently, if converter input voltage vectors is controlled by the following relationship,

$$\begin{aligned} v_{de} &= K_i(i_{de}^* - i_{de}) + \omega L i_{qe} \\ v_{qe} &= K_i(i_{qe}^* - i_{qe}) - \omega L i_{de} + E \end{aligned} \quad (18)$$

then the interacting term ωL can be removed and the coupled d-q components of input currents can be controlled with decoupling control technique. The output value of PI-type current controller is correspond to the voltage in line inductor.

2) Indirect current control: If the inductance value L and resistance value R of line inductor are clearly defined, then the inductor voltage can be calculated and the desired value of dq components of the converter voltage is described as (19).

$$\begin{aligned} v_{qe}^* &= E - \left(R + L\frac{d}{dt} \right) i_{qe}^* \\ v_{de}^* &= \omega L i_{qe}^* \end{aligned} \quad (19)$$

The line current will be regulated to follow the reference value in case that the voltage can be controlled exactly to track the reference value as (19).

3) Practical consideration of indirect current control: In transient states, the DC voltage error causes the converter voltage to differ slightly from the modulation reference. values. This problem can be avoided by dividing the modulation reference value with the measured output voltage. If analog modulators are used, then the same results can be achieved by multiplying the triangular carrier by the actual value of the DC voltage. This method used in this paper is basically exact and is based on the linearization technique at the operating points. Because the error is dependent on the q-component of the converter voltage, DC voltage error is subtracted only from the d-component and is acquired as (20).

$$\begin{aligned} v_{qe}^*(t) &= \frac{v_{dco} v_{qe}^*(t)}{v_{dco} + \Delta v_{dc}(t)} \\ &\fallingdotseq v_{qe}(t) - \frac{v_{qeo}}{v_{dco}} \Delta v_{dc}(t) \fallingdotseq v_{qe}(t) - \frac{e_{qeN}}{v_{dcN}} \end{aligned} \quad (20)$$

where subscripts 'o' and 'N' denote the operating point and the nominal value.

$$v_{qe}^* = E - \left(R + L\frac{d}{dt} \right) i_{qe}^* - \frac{E}{V_{dc}^*} \Delta V_{dc} \quad (21)$$

4) Space vector modulation:: It is well known that space vector modulation techniques have advantages in voltage utility, output harmonic contents, and so on, compared with the sinusoidal PWM or hysteresis PWM.

Therefore, the space vector modulation techniques are used in this paper to generate the PWM pulse

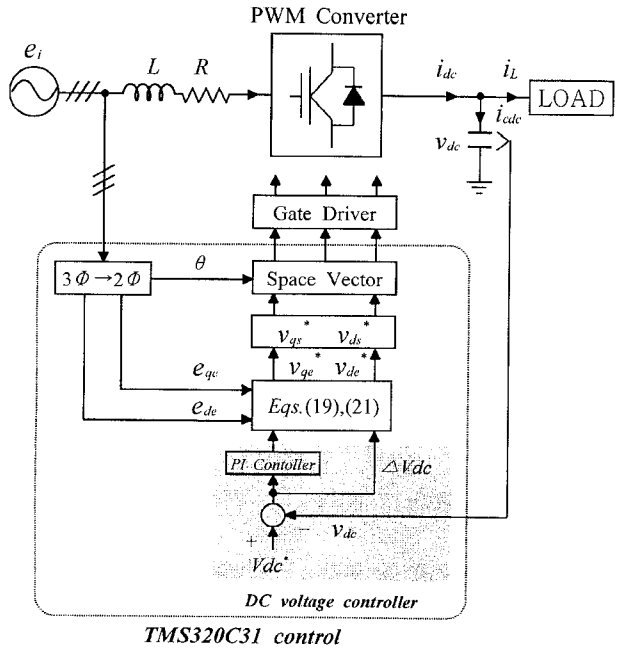

Fig. 2. System configuration of indirect current controller.

pattern to follow the reference voltage vector.

Fig. 2 shows the overall system configuration of the indirect current controller.

III. SIMULATION

Fig. 3 and Fig. 4 show the simulation results of direct and indirect current controlled PWM voltage sourced converter, respectively. In case of indirect current controlled PWM, the AC line current is controlled nearly sinusoidal with unity power factor and the DC output voltage is regulated constant almost same as the direct current controlled PWM, although this indirect current control scheme is based on the calculation technique without any current sensors. In case of the step load change, the line source current and the DC output voltage is illustrated in Fig. 3 and 4. From the simulation, the validity of the proposed algorithm is verified. Table 1 shows the constants used for simulation and experiment. It is obvious, that further improvement can be obtained using load feedforward techniques as using in [3] and [4]. This requires, however, an expensive current sensor.

While a feedback current controller has the complete information about the input current in indirect current controller, the magnitude of input current may vary with the variation of system parameter such as inductance value L and resistance value R of line inductor and switching devices. Therefore, it is respecting to verify the validity of indirect current control techniques according to the parameter variation.

Fig. 5 shows the AC input voltage and current, and

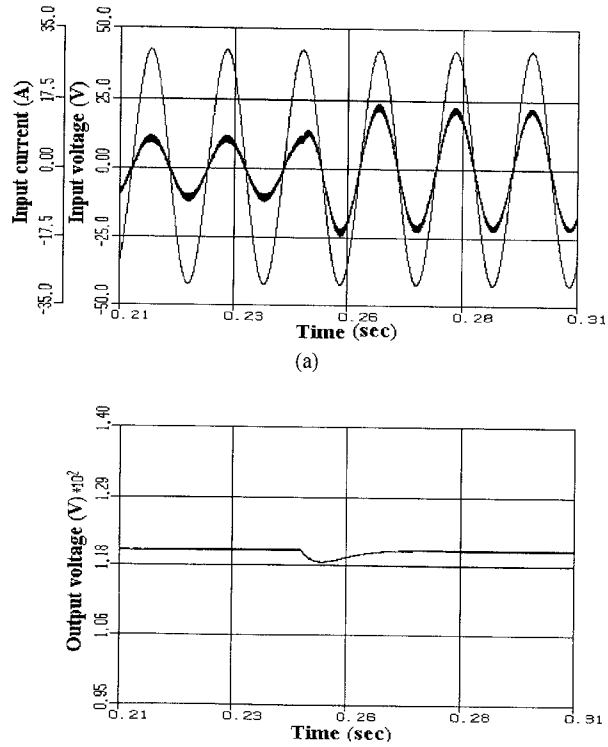

Fig. 3. Simulation results in case of step load change(direct current control); (a) AC input voltage and current waveforms for phase A (b) DC output voltage waveform.

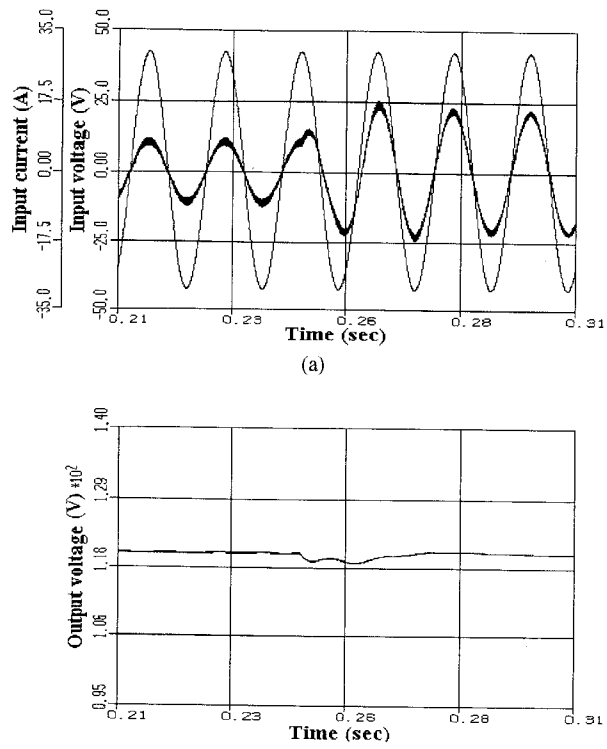

Fig. 4. Simulation results in case of step load change(indirect current control); (a) AC input voltage and current waveforms for phase A (b) DC output voltage waveform.

Table 1. System parameters for simulation and experiment.

Inductor (Ls)	0.5	mH
Input phase voltage rms	30	V
DC voltage reference	120	V
Sample period	100	us
DC capacitor	4200	uF
DC resistor	30	Ω
Switching frequency	10	kHz

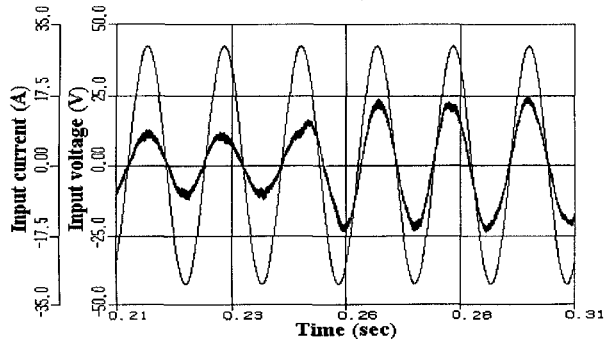

(a)

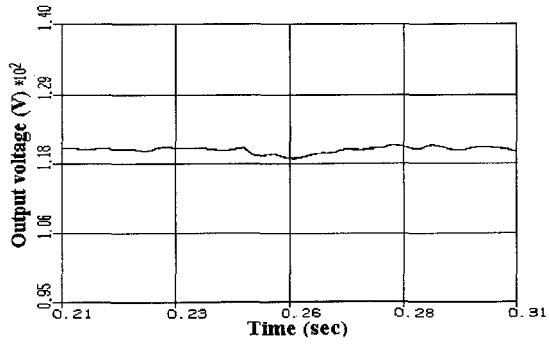

(b)

Fig. 5. Simulation results in case of system parameter change from 4[mH] to 6[mH] randomly(indirect current control); (a) AC input voltage and current waveforms for phase A (b) DC output voltage waveform.

the DC output voltage waveforms according to the parameter variation. The line inductor L changes from 0.4[mH] to 0.6[mH] randomly. From the simulation, it is shown that AC input current and output DC voltage are nearly regulated even though the parameter variation. However, to improve the system performance of indirect current controller, some modern control techniques such as parameter estimation methods should be considered.

Ⅳ. SYSTEM CONFIGURATION AND EXPERIMENT

A. Hardware configuration

The overall control system is configurated using

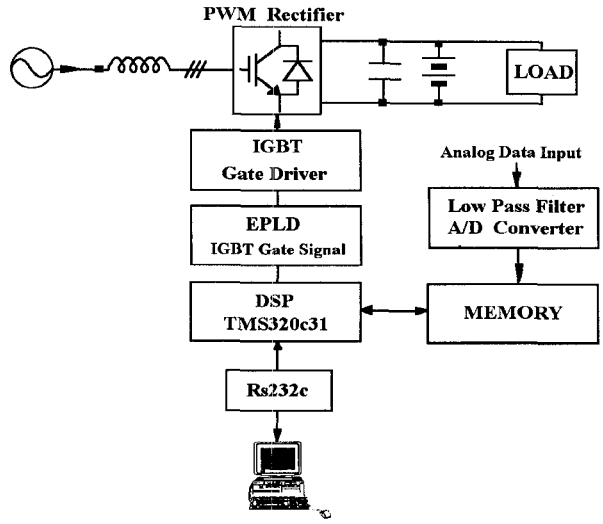

Fig. 6. Hardware configuration of control system.

TMS320c31 DSP and EPLD, and the addresses of peripheral devices such as A/D and D/A converter, Mux etc. are assigned by EPLD. Analog input and output voltages are scaled to 5V range and filtered by active filter composed of Op-Amps. Analog values are transformed into digital values by A/D converter and used for control algorithm and monitoring. Finally, internal counter of EPLD receives duty-ratio from CPU and triggers IGBTs gate pulse. Fig. 6 is shown the hardware configuration of control system.

B. Experimental results

Fig. 7 and Fig. 8 show the experimental results of direct and indirect current controlled PWM voltage-sourced converter, respectively. From these results, it is verified again that the AC input current and DC output voltage waveforms can be controlled to follow each of the reference values by using the indirect current control schemes based on the calculation technique without any current sensors.

Ⅴ. CONCLUSION

To save the cost and improve the system reliability, the indirect current control scheme of PWM voltage-sourced converter is proposed. The fully digital control technology based on TMS320c31 DSP is used to implement the proposed control algorithm for the application of a battery charger and its validity is verified from the digital simulation and experimental results.

In this paper, actually inductor resistor component is only measured and defined as R so that error can be occurred by neglecting the equivalent resistance of switching devices.

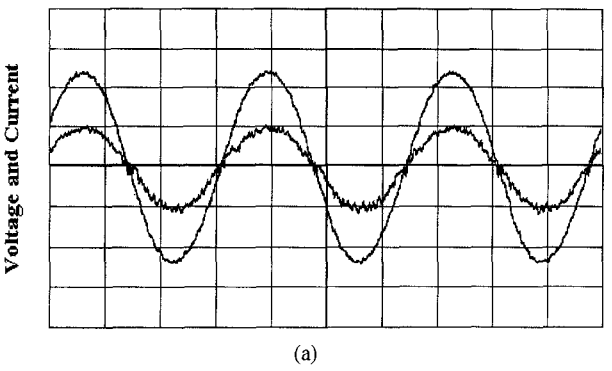

(a)

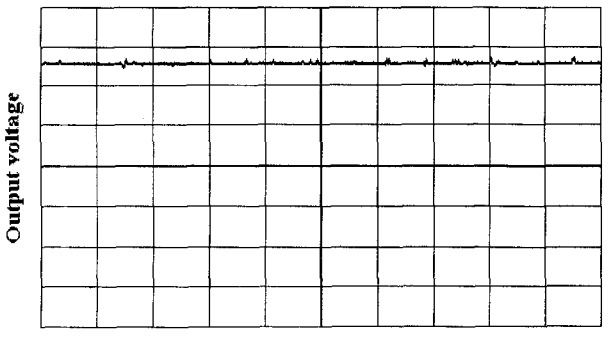

(b)

Fig. 7. Experimental results(direct control); (a) AC input voltage and current waveforms for phase A (b) DC output voltage waveform.

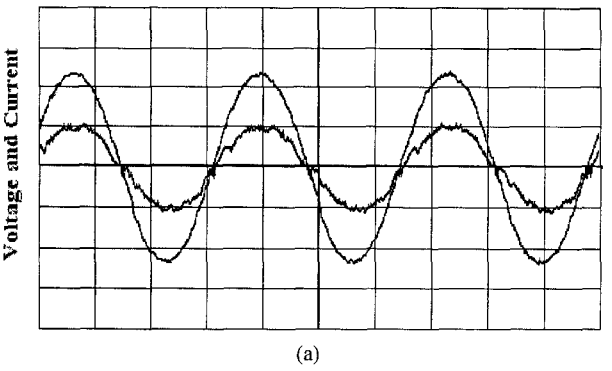

(a)

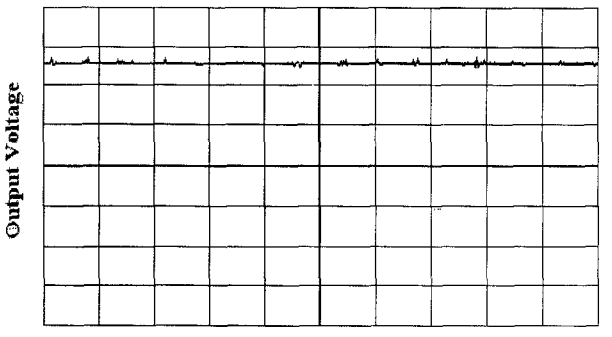

(b)

Fig. 8. Experimental results(indirect control); (a) AC input voltage and current waveforms for phase A (b) DC output voltage waveform.

Therefore, if the equivalent resistor of switching device influenced by temperature, switching time and so on is considered as the value of R, it is possible to expect the futher improved system performance.

REFERENCES

[1] R. Wu, S. B. Dewan, and G. R. Slemon, "A PWM ac-to-dc converter with fixed switching frequency," *IEEE Trans. Ind. Appl.*, vol. 26, no. 5, pp. 880-885, Sept./Oct., 1990.

[2] R. Wu, S. B. Dewan. and G. R. Slemon, "Analysis of an ac-to-dc voltage source converter using PWM with phase and amplitude control," *IEEE Trans. on Ind. Appl.*, vol. 27, no. 2, pp. 355-364, March/April, 1991.

[3] H. Sugimoto, S. Morimoto, and M. Yano, "A High Performance control method of a voltage-type PWM converter," *in Conf. Rec. IEEE PESC'88*, pp.. 360-368, 1988.

[4] T. G. Habetler, "A space vector-based rectifier regulator for AC/DC/AC converter," *IEEE Trans. on Power Electron.*, vol. 8, no. 1, pp.. 30-36, Jan., 1993.

[5] J. Ollila, "A PWM-rectifier without current measurement," *EPE Journal*, vol. 4, no. 2, June, 1994.

[6] C. T. Pan, "Modelling and analysis of a three phase PWM AC-DC convertor without current sensor," *IEE Proceedings*, vol. 40, no. 3, May, 1993.

Jae-Ho Choi Chungbuk National University, School of Electrical and Electronics Engineering, Cheongju, Chungbuk, 361-763, Korea
Tel: 82-431-61-2425, Fax: 82-431-276-7217
E-mail: choi@choijae.chungbuk.ac.kr

Hyong-Cheol Kim Woojin Industrial Systems Co. Ltd., Research & Development, Koesangun, Chungbuk, Korea
Tel: 82-445-820-4111, Fax: 82-445-36-7405

Joo-Sik Kwak Korea Electric Power Research Institute, Yusongku, Taejon, 305-380, Korea
Tel: 82-42-865-5425, Fax: 82-42-865-5404
E-mail: kwakjs@kepri.re.kr

Development of Multiple Space Vector Control for Direct Connected Parallel Current Source Power Converters

Ryuichi Abe Yoshiaki Nagai Kazuhiko Tsuyuki
Electric Power Development Co., Ltd., Japan
6-15-1, Ginza, Chuoku, Tokyo 104, Japan
Fax: +81-3-3546-1685, Phone: +81-3-3546-2211

Hiroyuki Nishikawa* Takeo Shimamura Akira Kawaguchi Kazuhiko Shimada
TOSHIBA Corporation, Japan
1, Toshiba-cho, Fuchu-city, Tokyo 183, Japan
Fax: +81-423-40-8078, Phone: +81-423-33-2566
E-mail: hiroyuki1.nishikawa@toshiba.co.jp

Abstract --- **The Current source self-commutated converter has been developed for use in motor drive systems. It however has technical problems such as L-C series resonance, the requirement of transformers for multiple converter connections and DC current unbalance in the converters. This paper presents a new control method to solve these problems for converters connected directly in parallel. The control method consists of a multiple space vector control including resonance suppression control. Results of a mini-model experiment confirming the control method will also be presented.**

I . Introduction

The application of power electronics technology to power systems such as HVDC (High Voltage Direct Current transmission) and SVC (Static Var Compensator) was conventionally accomplished by using externally-commutated converters. The progress of semiconductor devices such as self-commutated elements and their application technology have however increased the capacity of the self-commutated converter, and made possible its use in HVDC, SVC, as well as variable-speed pumping storage system. On the other hand, due to the lack of space, power plants are increasingly located in remote areas and the number of transmission lines is reduced to the minimum possible. As a result, the stability of the system is degraded. The concept of FACTS (Flexible AC Transmission System) aims at using power electronics technology to make power transmission system work up to the limit of the heat capacity of the power-transmission line.

Recent research has shown that, SMES (Superconducting Magnetic Energy Storage) which can store electric power, is capable of adjusting the power fluctuations level by controlling active power at high speed and is also capable of adjusting the voltage fluctuations level by controlling reactive power. SMES, which consists of a superconductive coil and an AC/DC converter, converts AC power to DC power. It then stores the converted energy into a superconductive coil as electromagnetic energy. Since a superconductive coil acts as a current source, the use of a current source converter will simplify the system configuration. A current source converter however requires an AC filter capacitor between the input transformer and the converter. The presence of this capacitor causes resonance in the transmission line. Various approaches were proposed to overcome this problem[1]~[6] and examples of application for low power motor drive were reported in[7]~[9]. However, these methods spoil the merits of using the self-commutated current source converter. Furthermore, the proposed methods did not treat the large capacity application case (high voltage - large current).

The authors proposed a new current source converter (a snubber loss free converter) which can theoretically realize power conversion without snubber loss. Unlike the conventional method, the regeneration of snubber energy is carried out by the main circuit's operation. The proposed configuration consists of multiple converters connected in parallel and uses a phase-shifting transformer. This current source converter configuration is illustrated in Fig.1 and allows the handling of large current[10]~[12].

In this paper, direct connected parallel converters without the use of phase-shifting transformers as shown in Fig.2 is proposed. This configuration is more economical, efficient and requires less installation space than the previous one (Fig.1). A new control method, including multiple space vector control, balancing control of DC-current and resonance suppression control, is also proposed. This control reduces the line current harmonics as well as the cross current between converters. The principle of operation, modeling, theoretical analysis as well as simulation and experimental results are described in this paper.

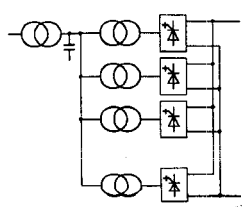

Fig.1 A unit converter through the phase-shifter transformers

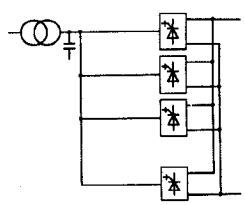

Fig.2 A direct connected parallel converters

II. Multiple space vector control

A. Current vector

Fig.3 shows the configuration of a three phase bridge current source converter. Current source converter operation involves the firing of one of the switches in the upper-half arms (U,V,W) and also one of the switches in the lower-half arms (X,Y,Z). Therefore, the converter is able to output six possible current vectors (①~⑥) and "zero" vector (short circuit of upper and lower arm) as shown in Fig.4.

Fig.5 shows the seven possible current vectors, gate signals and output currents of the converter.

The left side of Fig.5 shows the 120 degree duty cycle operation where the maximum output current can be produced. The right side of Fig.5 shows the zero vector which is selected occasionally to control the output current amplitude.

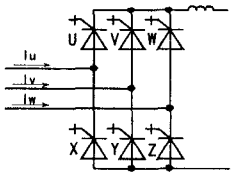

Fig.3 A three phase converter

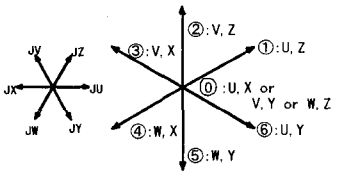

Fig.4 Output current vectors

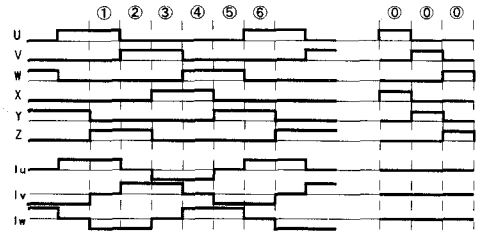

Fig.5 Gate signal and output currents of the converter

B. Selection and division into the output vectors

Fig.6 shows the configuration of a quadruple converter, with the AC/DC converters connected directly in parallel.

This paper explains the multiple space vector control for four parallel converters. The control method can however be used for any number of parallel converters.

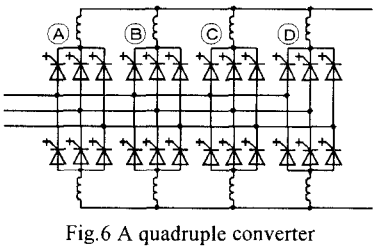

Fig.6 A quadruple converter

The quadruple converter is able to output 61 possible current vectors through combinations of the A,B,C,D-converters' output vectors. Fig.7 shows the current vectors within a 60° area.

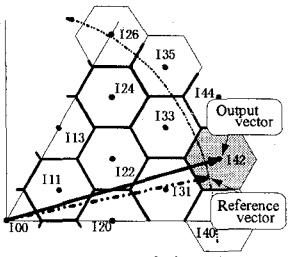

Fig.7 Output current vectors, Select the output vectors

The multiple space vector control selects instantaneously the output vector nearest a current reference vector, and outputs the vector to the converters immediately.

When a current reference vector is in a position as shown in Fig.7, it chooses the nearest output vector I42 (the hexagon shape serves as the boundary line of an output vector). When a current reference vector varies with time, it selects similarly the output vectors I40, I42, I33, I35, and I26 one by one as shown in the figure.

Supposing I42 is selected, as shown in Fig.8, it can be expressed as a combination of the unit vector of each converter. In this case, three converters output the ①(U, Z) vector and one converter output the ⑥(U, Y) vector. In other words, when the four U-phase switches, one Y-phase switch and three Z-phase switches are turned on, vector I42 can be output.

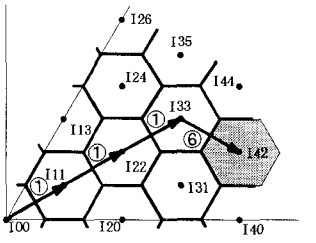

Fig.8 Divide into the output vector

C. DC-current Balance Control

Selecting the output vector does not determine which switch is turned on in each converter. Random allocation of the switches to be turned on could result in unbalance among the voltages across DC reactors as shown in Fig.9, and that could in turn cause unbalance among the currents of the converters.

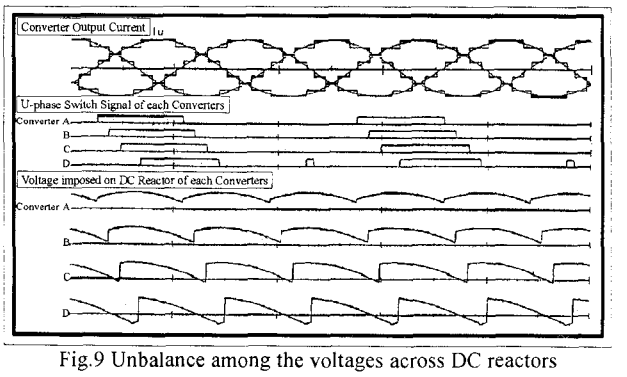

Fig.9 Unbalance among the voltages across DC reactors

This problem can be solved by detecting the DC currents in the DC reactors of each converter and the AC voltage, and selecting appropriate switches so that current balance is maintained.

Suppose I42 is selected as an output current vector, in the upper-half arms, four U-phase switches are turned on, and equal voltages are applied to all the upper-half DC reactors. DC currents in the DC reactors are, as a result balanced.

In the lower-half arms, one Y-phase switch and three Z-phase switches are turned on, and the division of the DC currents to enable current balancing has to be considered. Since the AC phase voltage is imposed on to DC reactors as negative value in the case of the lower-half arms, it increases the current of reactors connected to smaller AC voltage, and the current of reactor connected to larger AC voltage on the other hand decreases.

Suppose current which flows through the lower-half arms presupposes that IdBN<IdAN<IdCN<IdDN and AC phase voltage are Vr<Vt<Vs as shown in Fig.10.

In this case, as shown in the top diagram of the figure, the lower-arms of converters with the smaller DC currents are connected to the lower AC voltage. Consequently, the B, A, and C-converters fires Z-phase switches, and D-converter fires Y-phase switch.

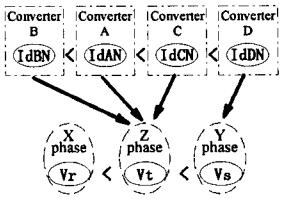

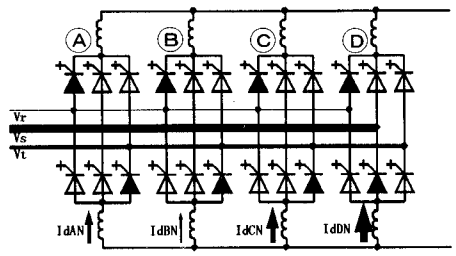

Fig.10 DC currents, AC voltage and turned on switches

By replacing the switch state of each converter with consideration of the value of DC current, the average value of the voltage imposed on the DC reactor of each converter becomes equal as shown in Fig.11, and DC current of each converter is balanced.

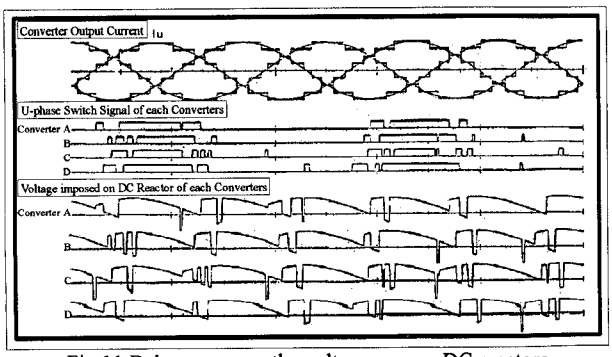

Fig.11 Balance among the voltages across DC reactors

Ⅲ. Resonance suppression control

The current source converter requires AC filter capacitors for removing harmonics as shown in Fig.13.

These capacitors with the reactance of the AC line and the transformer create a series resonant circuit. Therefore, when there are harmonics in the AC line at frequencies close to the resonant frequency of this series circuit, large series resonant current could flow. Capacitor voltages could also fluctuate in the case of fast current control or AC line faults. This could disable system operation.

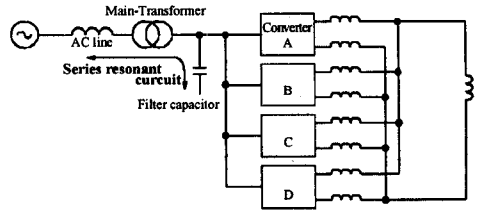

Fig.13 Configuration of the current source converter system

A. Modeling the equivalent circuit and dq frame of a current source converter

Although the output current waveform of a real current source converter is stairs-like waveform by PWM, in order to examine the stability of a control system and its response, the resonance suppression control approximates the output current as a current source in which continuous control is possible, and expresses the power-transmission line as a LR and a voltage source.

An equivalent circuit is shown in Fig.14. Where i_{su},i_{sv},i_{sw} denote current source converter output currents, v_u,v_v,v_w denote voltages of filter capacitors, i_u,i_v,i_w denote currents in power-transmission line, e_u,e_v,e_w denote the voltage source.

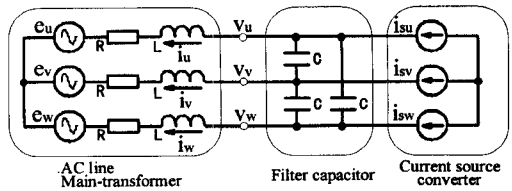

Fig.14 Equivalence circuit of the current source converter

The circuit equation of this equivalent circuit is as follows,

$$Cs\begin{bmatrix}2 & -1 & -1\\ -1 & 2 & -1\\ -1 & -1 & 2\end{bmatrix}\begin{bmatrix}v_u\\ v_v\\ v_w\end{bmatrix}+\begin{bmatrix}i_u\\ i_v\\ i_w\end{bmatrix}=\begin{bmatrix}i_{su}\\ i_{sv}\\ i_{sw}\end{bmatrix} \quad \cdots\cdots(1)$$

$$\begin{bmatrix}R+Ls & 0 & 0\\ 0 & R+Ls & 0\\ 0 & 0 & R+Ls\end{bmatrix}\begin{bmatrix}i_u\\ i_v\\ i_w\end{bmatrix}=\begin{bmatrix}v_u\\ v_v\\ v_w\end{bmatrix}-\begin{bmatrix}e_u\\ e_v\\ e_w\end{bmatrix} \quad \cdots\cdots(2)$$

If dq transformation to equation (1)·(2) are performed using equation (3),

$$\begin{bmatrix}u\\ v\\ w\end{bmatrix}=\begin{bmatrix}1 & 0\\ -1/2 & \sqrt{3}/2\\ -1/2 & -\sqrt{3}/2\end{bmatrix}\begin{bmatrix}-\cos\omega t & \sin\omega t\\ -\sin\omega t & -\cos\omega t\end{bmatrix}\begin{bmatrix}d\\ q\end{bmatrix} \quad \cdots\cdots(3)$$

The resulting model in the dq frame will be as shown in

equation (4) and (5).

$$\begin{bmatrix} 3Cs & -3\omega C \\ 3\omega C & 3Cs \end{bmatrix}\begin{bmatrix} v_d \\ v_q \end{bmatrix}+\begin{bmatrix} i_d \\ i_q \end{bmatrix}=\begin{bmatrix} i_{sd} \\ i_{sq} \end{bmatrix} \quad \cdots\cdots\cdots\cdots(4)$$

$$\begin{bmatrix} R+Ls & -\omega L \\ \omega L & R+Ls \end{bmatrix}\begin{bmatrix} i_d \\ i_q \end{bmatrix}=\begin{bmatrix} v_d \\ v_q \end{bmatrix}-\begin{bmatrix} e_d \\ e_q \end{bmatrix} \quad \cdots\cdots\cdots\cdots(5)$$

B. Resonance suppression by AC current feedback

The control diagram used in the resonance suppression control is shown in Fig.15 below with a current feedback loop used for resonance suppression. The interference clauses of equations (4) and (5) can be omitted by using the control block in the shaded area of the figure.

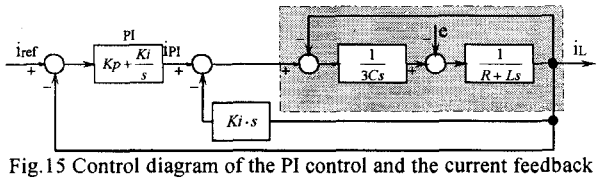

Fig.15 Control diagram of the PI control and the current feedback

Since value of R is relatively small it can usually be disregarded. The transfer function from the output of the PI controller, i_{PI}, to output i_L is given by equation (6) below, and it becomes a second order oscillation system.

$$i_L = \frac{1}{1+k_i s+3CLs^2} i_{PI} \quad \cdots\cdots\cdots\cdots\cdots\cdots(6)$$

Standard second order system parameters are therefore given as:

$$k_i = 3LC\alpha\,, \quad \alpha = 2\zeta\omega_n\,, \quad \omega_n = 1/\sqrt{3LC} \quad \cdots\cdots\cdots(7)$$

Damping can be increased by selecting damping factor ζ to be greater than 1.0 in order to control oscillation. Fig.16 shows the simulation results.

During time period t = 5ms - 10ms the gain ki is increased and the resonance is then suppressed.

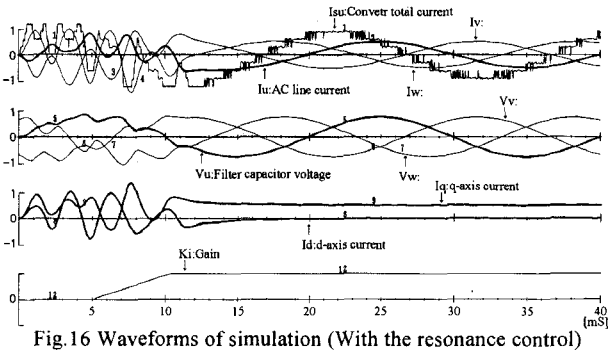

Fig.16 Waveforms of simulation (With the resonance control)

IV. Configuration of mini-model

A. Main circuit configuration

Fig.17 shows the configuration of the test circuit. The explanation of the control method was presented above with only one switch on in the upper and lower arms. However, the converter arm of the test circuit consisted of the snubber-loss-free arm as shown in the Figure. The mini-model includes four snubber-loss-free converters connected directly in parallel and the capacity is 10kVA(DC-current:100A,DC-Voltage:100V). A thyristor rectifier was used to simulate a superconducting coil.

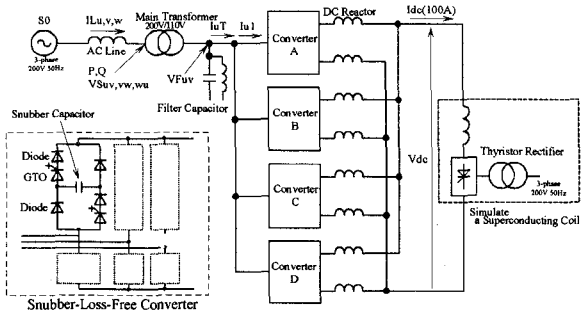

Fig.17 Configuration of the main circuit

B. Control block diagram

Fig.18 shows the control block diagram of the test circuit. It consists of power control, resonance suppression control, and multiple space vector control blocks.

The power control block detects electric power of the power system, takes the difference with the reference value, and calculates the current reference value Id* and Iq* by PI control. The resonance suppression control block detects the AC currents of the power system, calculates its rate of change (di/dt) on d-q axis coordinates, and, thereby, rectifies current reference value (Id*, Iq*). Multiple space vector control and DC control balancing selects the output vector nearest the current reference vector, distributes a vector to each converter, and outputs a gate signal so that the DC currents may be balanced.

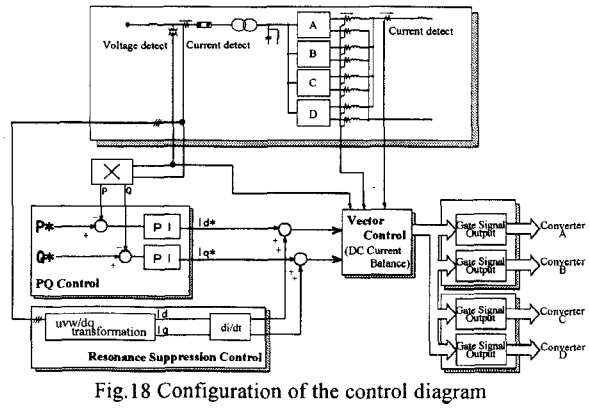

Fig.18 Configuration of the control diagram

V. Simulation analysis and experimented results

A. Steady state operation
(effect of resonance suppression control)

The harmonic resonance was generated by the series resonance of the filter capacitor and the inductance in the AC power system. The converter system was then operated

to verify the effect of the control against this resonance. Figs.19 and 20 show the simulation results. Fig.19 shows the waveforms during steady state without the resonance suppression control. Series resonance was present in the currents of the AC line. Fig.20 shows the waveforms during steady state with the proposed control performed. As can be noted, the AC line currents were effectively controlled.

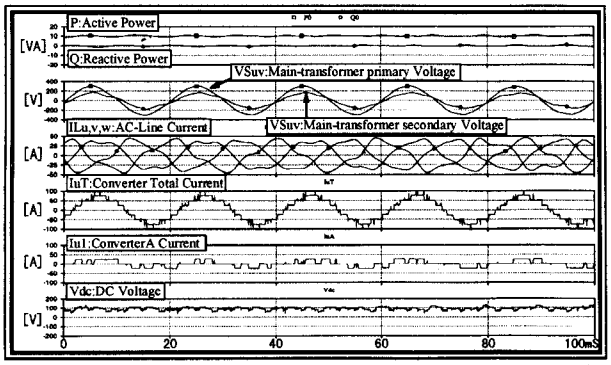

Fig.19 Waveforms of steady state (Without the resonance control) [Results of simulation]

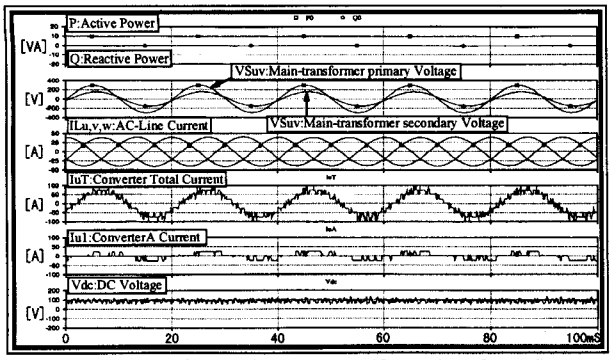

Fig.20 Waveforms of steady state (Control performed) [Results of simulation]

Figs.21 and 22 show the experimental results. Fig.21 shows the waveforms during steady state without the resonance suppression control. Series resonance as in the simulation result was present in the currents of the AC line. Fig.22 shows the waveforms during steady state with the proposed control performed. As can be noted, the AC line currents were effectively controlled.

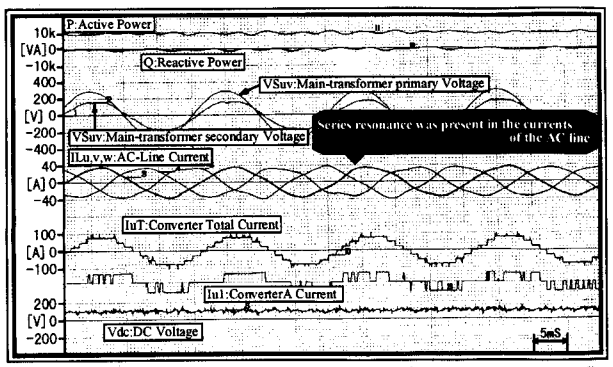

Fig.21 Waveforms of steady state (Without the resonance control) [Results of experiment]

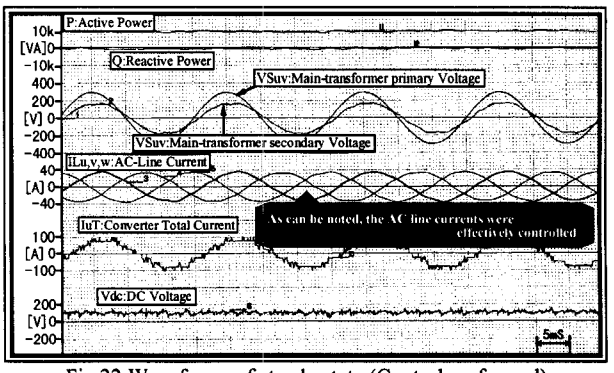

Fig.22 Waveforms of steady state (Control performed) [Results of experiment]

The results of the FFT (Fast Fourier Transformation) analysis are shown in Fig.23. In the case without the resonance suppression control present, the amplitude of the harmonics due to the series resonance was about -32dB (2.8%). The harmonic can be reduced to about -41dB (0.89%) using the proposed control scheme.

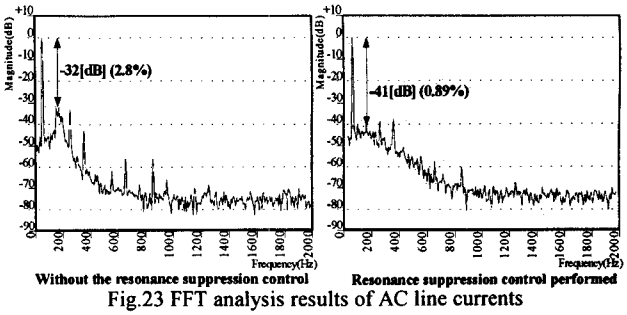

Fig.23 FFT analysis results of AC line currents

B. Power control operation characteristic

The fast power control response was verified by changing the power reference. Fig.24 and 25 show waveforms by simulation analysis and experiment for a response during an active power reference change from -10kW to +10kW in 20msec. It was confirmed that active power smoothly follows the reference, due to the use of the resonance suppression control.

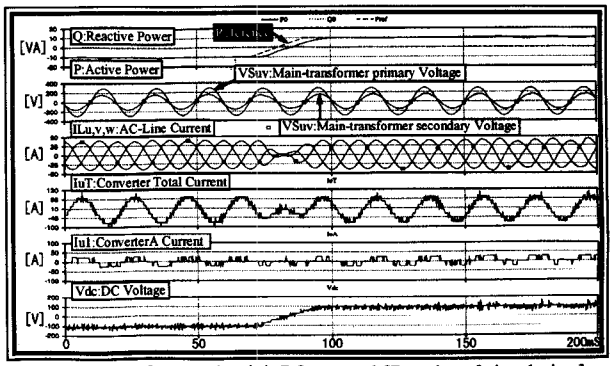

Fig.24 Waveforms of quick PQ control [Results of simulation]

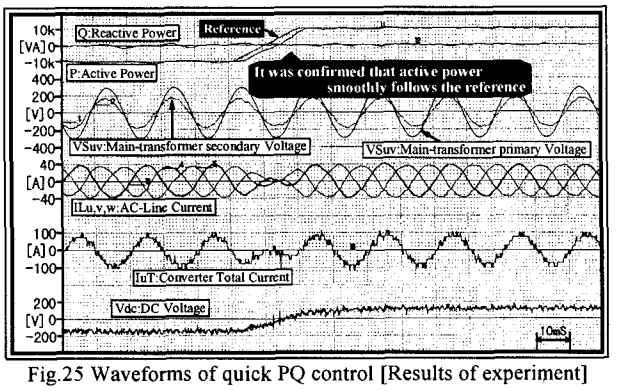

Fig.25 Waveforms of quick PQ control [Results of experiment]

C. Operation characteristic at the time of the power-transmission line fault

The mini-model was connected to an imitation power-transmission line, and experiments were carried out to test the circuit operation during a ground fault near the converter.

Figs.26 and 27 are the results of the simulation and experiment where the fault (1LG) happens in one circuit of a 2 circuit power-transmission line. After 70mS, the grounded power-transmission track is opened (1LO).

The converter continues to operate stably also during the time of the fault, and no resonance (oscillation) is noted. After fault recovery the supply of electric-power is quickly restored.

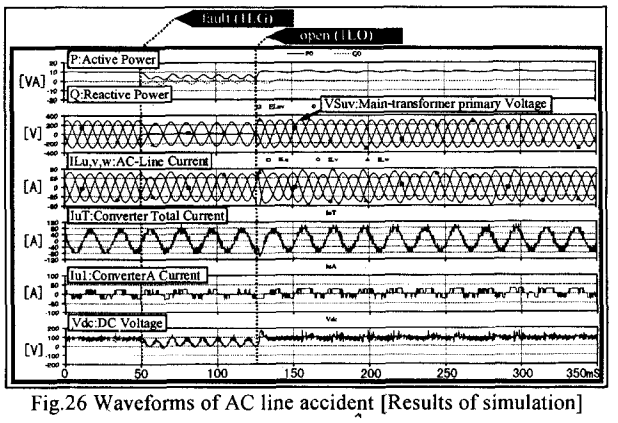

Fig.26 Waveforms of AC line accident [Results of simulation]

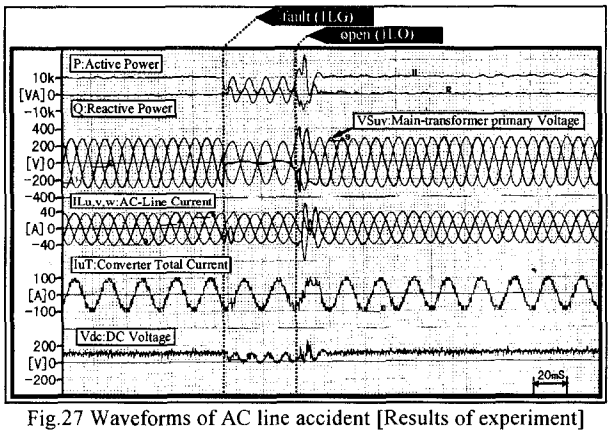

Fig.27 Waveforms of AC line accident [Results of experiment]

VI. Conclusion

The main circuits system for direct connected parallel converters without the use of phase-shifting transformers was described and a new control method was proposed. Results of the simulation analysis and the mini-model experiment confirming the correct operation of the system were presented.

The multiple space vector control selects an output vector instantaneously based on the reference value and the converters output the vector immediately. The system exhibits quick response, and the number of switchings are few. The resonance suppression control enables the reduction of the harmonics and therefore a highly efficient converter. It suppresses effectively the series resonance phenomenon formed at the AC system side. A system with high reliability which can carry out operation continuation in the case of the AC system ground fault can therefore be built.

By conducting experiments using a mini-model the following was confirmed ① The effectiveness of the resonance suppression control which suppresses the series resonant harmonics. ② Power was controllable at high speed and stably (effect of multiple space vector control and resonance suppression control). ③ The system supplied output current stably during the time of the power-transmission line fault, and after fault recovery the supply of power was quickly and stably restored.

The application of the direct connected parallel converters using space vector control and resonance suppression control to Superconducting Magnetic Energy Storage (SMES) therefore looks promising.

References

[1] S.Nonaka, Y.Neba: "New GTO Current Source Inverter with Pulse width Modulation Control Technique," IEEE IAS Annual Meeting, p.442 (1985)
[2] D.Hintze, D.Schroder: "Four Quadrant AC-Motor Driven with a GTO Current Source Inverter with Low Harmonics and on Line Optimized Pulse Pattern," IPEC-Tokyo, p.405 (1990)
[3] S.Ueda, M.Hombu, K.Honda et al.: "A Multiple Current Source GTO Inverter with Sinusoidal Outputs" The Transactions of IEE-Japan Vol.111-D, No.8, 645 (1991)
[4] Y.Sato, H.Miyazawa, T.Kataoka: "A Control Method for Improving AC Input Current Waveform of Current Type PWM Rectifiers" The Transactions of IEE-Japan Vol.112, No.8, 703 (1992)
[5] T.ohnishi, Y.Minamoto: "Three Phase Current Fed Type PWM Converter by Control of Instantaneous Current Vector" The Transactions of IEE-Japan Vol.115-D, No.8, 984 (1995)
[6] K.Toyama, O.Mizuno, T.Takeshita et al.: "Suppression for Transient Oscillation of Input Voltage and Current in Current-Source Three-Phase PWM AC/DC Converter" JIASC'96, 1-29 (1996)
[7] H.Inaba et al., "Development of a High Speed Elevator Controlled by Current Source Inverter System with Sinusoidal Input and Output" IEEE IAS Annual Meeting, pp.442 (1985)
[8] M.Hombu et al.: "PWM Control Method on Current Source GTO Inverter with Sinusoidal Outputs" Transactions of IEE Japan Vol.106-B, No.579 (1986)
[9] M.Hombu et al.: "A Multiple Current Source GTO Inverter with Sinusoidal Outputs," Transactions of IEE-Japan, Vol.111-D, No.654, (1991)
[10] H.Uchino et al., "GTO Converters with Regeneration of Snubber Energy" IEE Japan Ann. Mtg. Mar. 25-27, 1992, No.478, pp.5.23-5.24 (1992)
[11] H.Naitoh et al.: "A Snubber Loss Free Current Source Converter For High Power Use" CIGRE 1995 Symposium, Tokyo, 57 (1995)
[12] H.Hibana et al.: "Development of Snubber-Loss-Free Current Source Converter" International Colloquium Sept. 1995, in Quebec & Montreal in Canada (1995)

A Novel Control Strategy on Single-Phase PWM Current Source Inverter Incorporating Pulse Area Modulation

Katsuya Hirachi and Yasuharu Tomokuni
Yuasa Corporation
2-3-21 Kosobe-cho Takatsuki-City Osaka, 569, Japan
Fax: +81-726-83-3351, Phone: +81-726-85-0451
E-mail: nbe03144@niftyserve.or.jp

Abstract — **Single-phase PWM current source inverter has many advantages for utility-interactive system. It is suitable especially for the non-insulated type utility-interactive topology which is widely used for residential photovoltaic generating system. But this type of inverter has a significant disadvantage, that is to say, output current of inverter has large harmonic components when its smoothing reactor is not large enough to eliminate the ripple component of its current. This paper presents a new control strategy to reduce the harmonic component of the single-phase PWM current source inverter sufficiently even when the ripple current in the smoothing reactor is large. Principles of the proposed control strategy and simulation results are described.**

INTRODUCTION

PWM current source inverters provide high AC voltages, can be used advantageously with high-impedance DC power supplies, and have considerable resistance to output shorts. These features are behind the research on their many applications. In recent years there is also a good deal of research on their applications as interactive inverters that supply the power of photovoltaic cells, storage batteries, and other sources to commercial grids. Over the past few years the use of photovoltaic generating systems has increased sharply in response to heightened social interest in clean energy. These systems almost exclusively use PWM voltage source inverters, while PWM current source inverters are chosen on only rare occasions. However, this paper will show that the use of PWM current source inverters offers prospects for simplifying system configuration, improving efficiency, and lowering costs.

It is necessary for utility-interactive systems to reduce the harmonics components in the output current to a small revel. For example, Japanese guideline for utility-interactive inverter restrain the THD (Total Harmonic Distortion) of output current to the level under 5%[7]. For this reason, special implementation to reduce the harmonic current is required for the utility-interactive current source inverter. In this paper, we propose a new control strategy to reduce the harmonic component of the single-phase PWM current source inverter sufficiently without feedback control.

CIRCUIT TOPOLOGY OF INTERACTIVE INVERTER FOR PV SYSTEM

In recent years the number of Japanese homes using PV generating systems has increased rapidly, and there is a great deal of research and development for interactive inverters suitable for these systems. Conventional interactive inverters have been of the low-frequency link type that insulates PV cells from the grid using commercial transformers, but since this type of transformers have large weight and volume, high-frequency link types are now used in order to employ smaller transformers. In recent years systems have been employing the non-insulated type of inverter, which does not include a transformer, in order to further lighten systems and improve economy.

Fig.1 shows the circuit configuration of the non-insulated interactive inverter now in use. Commercial power supplies are generally 100V single-phase three-wire systems, inverters are interconnected through the U- and V-phases at 200V. The interactive inverter is a PWM voltage source inverter which need a DC voltage that is higher than the peak value of the AC output voltage, but raising the output voltage of PV cells involves problems with safety. For this reason a step-up chopper is added to the forestage of the inverter. This chopper raises to about 400V the output of PV cells whose rated voltage is about 200 V, and supplies this voltage to the inverter.

Fig.2 indicates how a residential PV generating system is configured when employing a PWM current source inverter as its interactive inverter. Because PWM current source inverters can step up voltage,

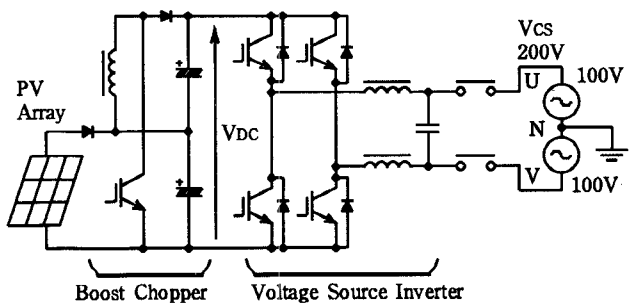

Fig.1 Conventional Non-Insulated Interactive Inverter

they allow the use of low-voltage PV cells, and, as shown in Fig.2, PV cell output can be supplied directly to the inverter, which simplifies system configuration. This makes the use of PWM current source inverters an advantageous choice in non-insulated interactive systems.

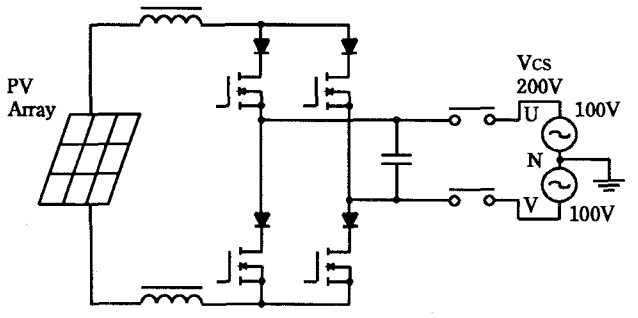

Fig.2 Non-Insulated Interactive Inverter with Current Source Topology

VARIOUS CONTROL STRATEGIES FOR CURRENT SOURCE INVERTER

Fig.3 shows the circuit configuration of current source PWM inverter. T1-T4 construct the full bridge inverter. DCL reduce the ripple component of the input current to the inverter. Cf and Lf eliminate the high frequency components in the output current of the inverter.

In order to make the output current waveform to a sine wave, current-mode control PWM inverter adopts a method that compare a reference sine wave with a high frequency sawtooth waveform (carrier wave) to determine the PWM pattern of switching elements. In this method, when the inductance of smoothing reactor DCL is sufficiently large, and then the ripple component of DCL current iDCL can be ignored, it is possible to obtain an output current with a distortion-free sine wave. But because inverter must be made smaller and more economical, inductance of DCL must be reduced to the small value, and having done so, it is necessary to develop the method of keeping the output current distortion of inverter to a small value even when the ripple component of DCL current is large.

As this discussion shows, to reduce the output current distortion when the ripple current in the smooth reactor is large, is a major theme that must be accomplished in order to practicalize single-phase current source utility-interactive inverter. For this purpose, the following methods have been proposed.

(1) Impose the third harmonic on a reference sine wave. [1]
(2) To heighten effectiveness, the magnitude of that third harmonic is controlled through feedback. [2]
(3) Impose the second harmonic on a reference sine wave. [5]
(4) Provide a parallel resonance circuit for the second harmonic in series with DCL. [4]
(5) Put a DC-DC converter in the forestage of inverter. [6]

However, those conventional methods are not perfect because they have problems such as inadequate effectiveness for reducing harmonic current, more complicated circuits, or higher costs. The strategy proposed here, for the control of current source inverter, realize the suppression of harmonics by adopting a control method known as pulse area modulation which is proposed for the advanced control strategy on high-power-factor converters [8, 9]. With this method, perfect harmonic suppression is possible incorporating simple control circuits.

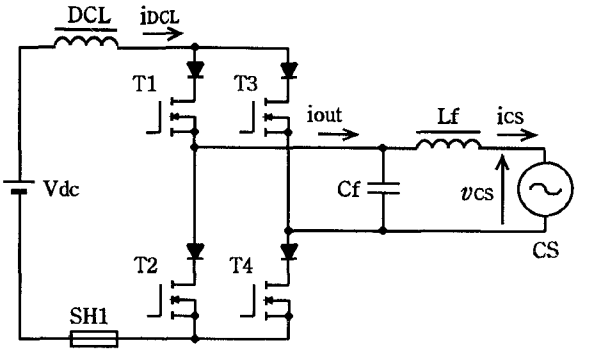

Fig.3 Circuit Configuration of Current Source PWM Inverter

CONVENTIONAL CONTROL STRATEGY

A. When Reactor Ripple Current Can Be Ignored

Fig.4 illustrates the conventional control strategy for current source PWM inverter. T1 and T3 turn on and off at each half cycle of the commercial frequency. T2 and T4 turn on and off according to the comparison between the high-frequency sawtooth waveform carrier signal and the commercial frequency sine wave. A carrier signal of 800 Hz is specified in Fig.4, but high frequencies of several tens of kHz are used in practical inverters. Fig.5 shows the control circuit configuration for the control strategy of T2 and T4 described in Fig.4.

Incorporating the control strategy of Fig.4 and Fig.5, the output current will be formed into a perfect sine wave when the smoothing reactor DCL is large enough and the ripple component of its current IDCL can be ignored. Fig.6 shows simulation of waveforms when IDCL does not have any ripple component. Fig.7 describes the spectrum analysis obtained for iout shown in Fig.6(b), which indicates that there appear low-order harmonics very slight level.

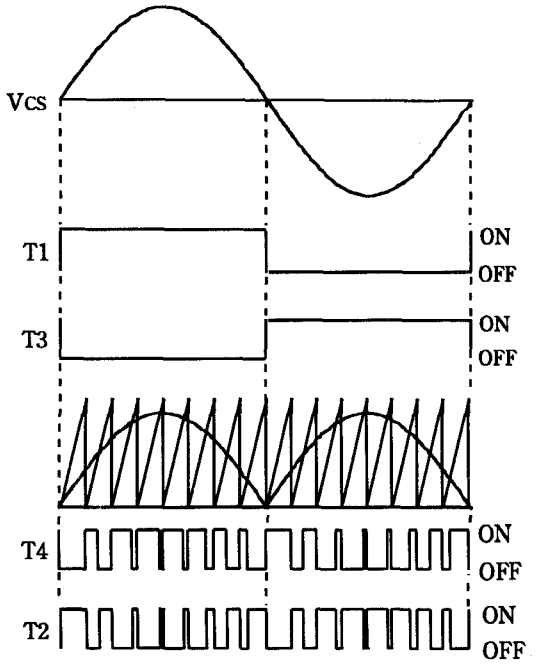

Fig.4 Conventional PWM Control Strategy

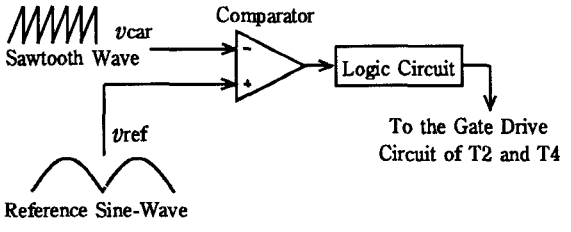

Fig.5 Conventional Control Circuit

To make the circuit operation easy to see, the carrier frequency was set at 2 kHz in this simulation. In practical inverters the frequency is set at several tens of kHz. The simulations described in this paper were all performed at 2 kHz.

B. When Reactor Ripple Current Cannot Be Ignored

As seen above, even conventional control strategy is to eliminate the harmonic current component sufficiently when the smoothing reactor is large enough and the ripple current component can be ignored. But for making the inverter smaller and more economical, the size and inductance of smoothing reactor must be reduced to smaller value.

Fig.8 illustrates the simulated waveforms obtained when the inductance of reactor DCL is small and its ripple current cannot be ignored. Simulation conditions are describes in Table 1. Reactor current iDCL includes a 19Ap-p ripple component, which brings the large fluctuations to the peak values of each pulse of the output current iout. Fig.9 indicates the spectrum analysis of iout. As much as 15% of the third harmonics is appear comparing to the amount of fundamental wave, which means that this control strategy is not satisfy the specification required for the utility-interactive inverter.

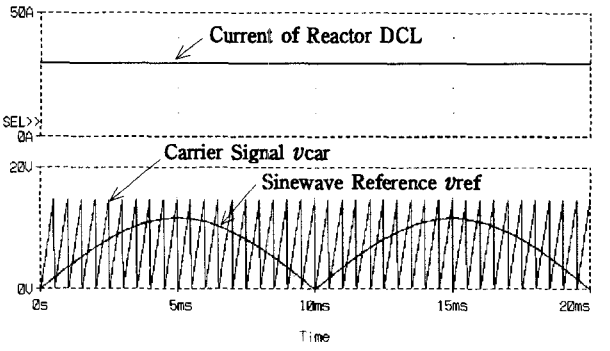

(a) Waveforms of Reactor and Control Circuit

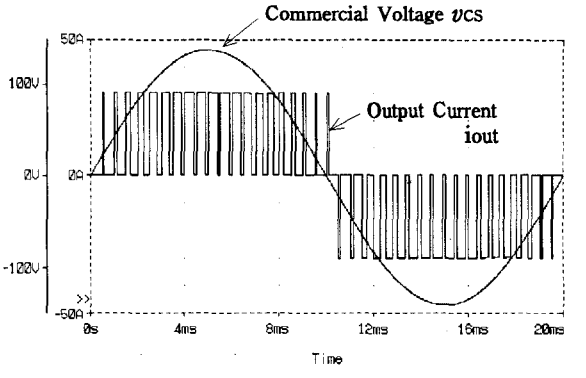

(b) Output Voltage and Current Waveforms of Inverter

Fig.6 Waveforms When Ripple Current of Smoothing Reactor DCL can be Ignored

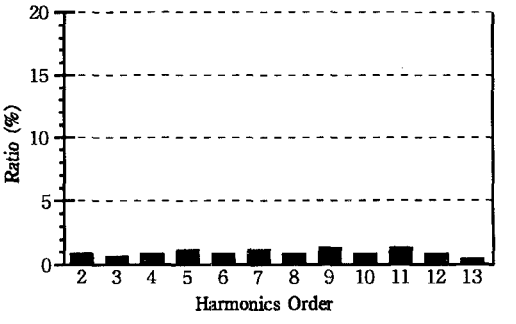

Fig.7 Spectrum Analysis of Output Current iout with no Ripple Current at Smoothing Reactor

PROPOSED CONTROL STRATEGY

A. Operating Principle

Fig.10 shows the proposed control circuit configuration with pulse area modulation. Reactor current iDCL is detected at shunt SH1, whose voltage vSH1 is amplified and fed into the integrating circuit.

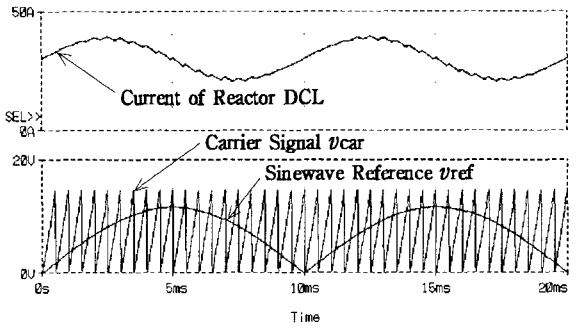

(a) Waveforms of Reactor and Control Circuit

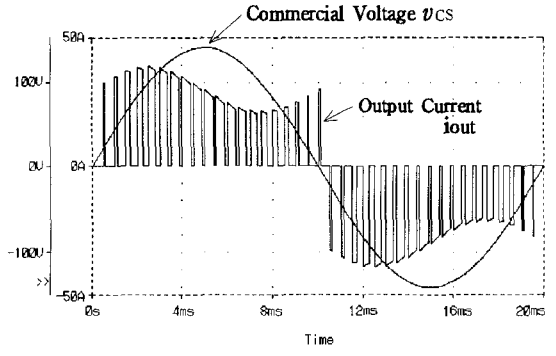

(b) Output Voltage and Current Waveforms of Inverter

Fig.8 Waveforms When Ripple Current of Smoothing Reactor DCL can not be Ignored

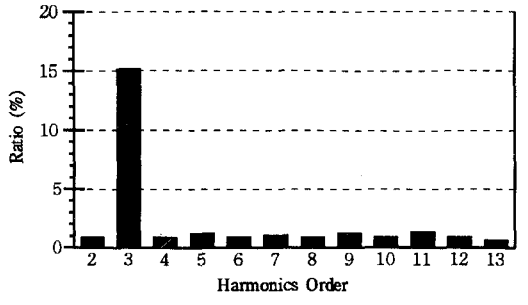

Fig.9 Spectrum Analysis of Output Current iout with Large Ripple Current at Smoothing Reactor

Table 1 Simuration Specification

Input Voltage Vdc	60V
Smoothing Reactor DCL	10mH
Commercial Voltage vcs	100Vrms

This integrating circuit is reset at a constant interval, and its output voltage becomes the sawtooth wave vcar, which has peak voltage that is proportional to the value of iDCL. This sawtooth wave is compared to the reference sine-wave vref, which is specified by the full-wave rectified commercial voltage vCS, thereby obtaining the PWM wave that drives the switching device T2 and T4.

Fig.11 illustrates the principle of pulse area modulation which is employed in this control circuit. Because the sawtooth wave vcar used in the modulation is created by integrating the reactor current iDCL, its peak voltage varies proportionally to iDCL. When reactor current gradually increases, the current becomes a sawtooth wave whose peak voltage increases gradually as shown in Fig.11. Assuming that the reference wave vref has a constant voltage as shown in Fig.11, the duty ratio of T4 gradually decreases. So, the output current waveform iout becomes square wave in which peak value gradually increases and the pulse width gradually decreases as illustrated in Fig.11.

The pulse shown with hatched lines has twice the peak value as the pulse shown with dotted area, but it has one-half of pulse width with equal area. If the reference waveform is constant, the areas of these pulses will not change, but if the reference waveform increases or decreases, the pulse areas increase or decrease proportionally. And pulse area is equal to the instantaneous value of the output current iout. Thus, if

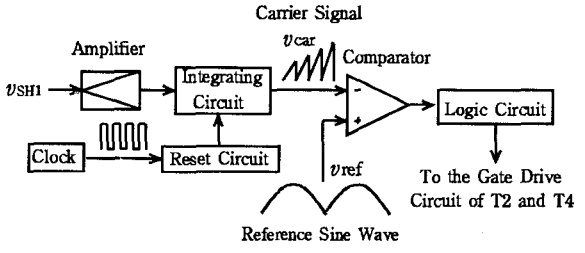

Fig.10 Proposed Control Circuit Configuration

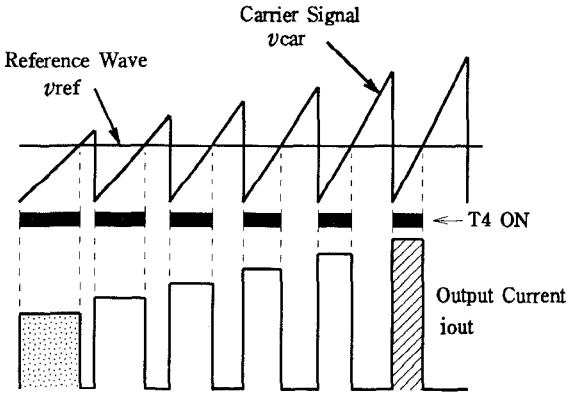

Fig.11 Principle of Pulse Area Modulation

the reference waveform is changed into a sinewave as shown in Fig.10, the output current will change into a sinewave.

B. Simulation Results

Fig.12 shows the simulated waveforms obtained for the current source inverter with the proposed control circuit shown in Fig.10. Reactor current iDCL has large ripple of 18Ap-p. The peak value of carrier signal vcar changes in proportion to the reactor current. The output current iout has a pulse width that, in the low-peak region, is larger than that in Fig.8(b), which shows that this control method is operating properly. Pspice was used to perform this simulation, and the circuit file is described in the appendix.

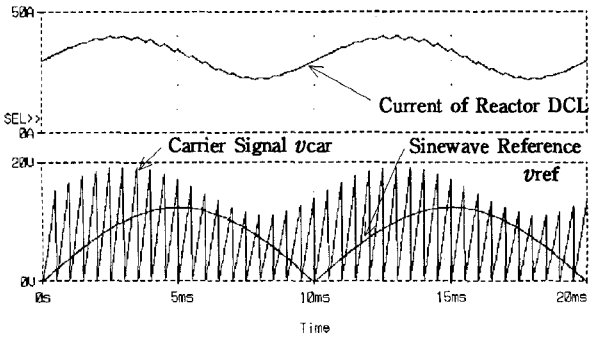

(a) Waveforms of Reactor and Control Circuit

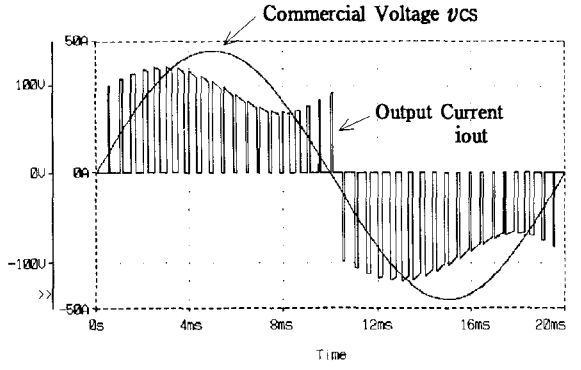

(b) Output Voltage and Current Waveforms of Inverter

Fig.12 Waveforms with Proposed Control Strategy

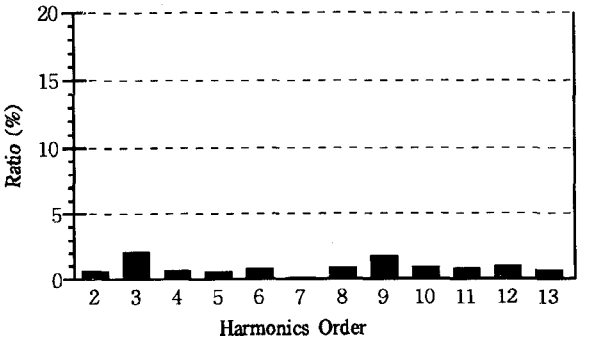

Fig.13 Spectrum Analysis of Output Current iout with Proposed Control Strategy

Fig.13 shows the spectrum analysis for the output current iout illustrated in Fig.12(b). The third harmonic is much smaller than in Fig.9, which clearly demonstrates the effectiveness of this control strategy.

CONCLUSION

We discussed the application of the control strategy known as pulse area modulation which is proposed for the control strategy on high-power-factor converter, to current source PWM inverter. Simulation results indicates that the harmonics in the output current of the inverter is able to almost completely eliminated by the proposed control strategy. The circuits needed for this control method comprise only a current detection device such as a shunt, an integrating circuit, and other simple control circuits. As demonstrated above, this control strategy is effective for improving the characteristics of single-phase current source PWM inverter, and is suitable for practical applications. In the future, this control strategy must be investigated and evaluated experimentally.

REFERENCES

[1] S.Nonaka and Y.Neba, "An Investigation of Input Current Harmonics in Single-Phase Converter", National Convention Record of IAS IEE Japan, pp.271-274, 1990

[2] S.Nonaka, K.Kesamaru, K.Yamasaki, G.Zhao and H.Uchiyama, "Decreasing the Harmonics of the Input Current from Interactive Photovoltaic Generation System to the Distribution Line", National Convention Record of IAS IEE Japan, pp.518-523. 1991

[3] S.Nonaka, K.Kesamaru and K.Yamasaki, "Utility Interactive Photovoltaic System with PWM Current Source Inverter", Trans. IEE of Japan, vol.112-B, No.5, pp.439-447, May 1992

[4] S.Nonaka, "A Suitable Single-Phase PWM Current Source Inverter for Utility Interactive Photovoltaic Generation System", National Convention Record of IAS IEE Japan, pp.518-523, 1991

[5] Y.Monden, S.Masukawa and S.Iida, presented at the Meeting on Semiconductor Power Conversion of IEE in Japan, SPC-95-110, pp.111-120, 1995

[6] Y.Monden, S.Masukawa and S.Iida, "A Utility Interactive Photovoltaic Power System with a Current Source Inverter and a DC-DC Converter", Tran. of IEE Japan, pp.718-719, 1996

[7] JEAG9701-1993

[8] Y.Nishida, A.Maeda, H.Tomita, "A New Instantaneous-Current Control for Three-Phase Buck-Boost and Buck Converters with PFC Operation", Proc. IEEE APEC'95, pp.875-883, 1995

[9] K.Hirachi, T.Iwade, K.Shibayama, "A Specific Control Implementation on Buck-Type Active Power Filtering Converters", Proc. IEEE INTELEC'95, pp.444-449, 1995

[10] K.Hirachi, "An Overview of PWM Inverters in Industry Applications", National Convention Record of IAS IEE Japan, S.11 -6, 1996

APPENDIX

<Circuit File for the Simulation Shown in Fig.12>

```
PV-4ES : PWM INVERTER : HIRACHI
******PV-4ES.CIR***HIRACHI******
.TRAN 20US 20mS 0mS 20US UIC
.FOUR 50Hz 13 I(ROUT)
******MAIN CIRCUIT******
VPV 1   0   DC 60V
L1   1   2A 10mH IC=30A
RSH 2A 2   1m
S1   2   3A 11 10 SMOD1
S2   3   3B 12 10 SMOD1
S3   2   4A 13 10 SMOD1
S4   4   4B 14 10 SMOD1
.MODEL SMOD1 VSWITCH(Ron=0.05 Roff=10000
+ Von=1V Voff=0V)
D1   3A 3 DMOD
D2   3B 0 DMOD
D3   4A 4 DMOD
D4   4B 0 DMOD
RD1 3A 3 1MEG
RD2 3B 0 1MEG
RD3 4A 4 1MEG
RD4 4B 0 1MEG
ROUT 3 5 1m
RL    5 4 1MEG
VCS   5 4 SIN(0 141 50 0 0 0)
******SINEWAVE REFERENCE******
E101   102 104 5 4 1
RE101 101 103 1MEG
D101   102 103 DMOD
D102     0 102 DMOD
D103   104 103 DMOD
D104     0 104 DMOD
.MODEL DMOD D()
RD101 102 103 1MEG
RD102    0 102 1MEG
RD103 104 103 1MEG
RD104    0 104 1MEG
R101   103 101 10k
R102   101    0 962.4515
******PULSE AREA MODURATION******
G101   100    0 2 2A 1
RG101 100    0 1MEG
Ct      100    0 1UF
R103   100 112 2
S101   112    0 113 0 SMOD2
.MODEL SMOD2 VSWITCH(Von=0.1)
Vp      113    0 PULSE(-1 10 0 1U 1U 15U 500U)
RVp    113    0 1MEG
******LOGIC CIRCUIT******
S11   9   15     5    4 SMOD2
S31   9   35     4    5 SMOD2
S21   9   25A 100 101 SMOD2
S22 25A 25     5    4 SMOD2
S23   9   25B 101 100 SMOD2
S24 25B 25     4    5 SMOD2
S41   9   45A 101 100 SMOD2
S42 45A 45     5    4 SMOD2
S43   9   45B 100 101 SMOD2
S44 45B 45     4    5 SMOD2
Vcc   9    0   DC 15V
RVcc 9    0   1MEG
Vr   10    0   DC   5V
RVr 10    0   1MEG
R11 15   11    10
R21 25   12     1
R31 35   13    10
R41 45   14     1
R12 11    0 1000
R22 12    0   100
R32 13    0 1000
R42 14    0   100
C11 11    0 0.1UF IC=15V
C21 12    0 0.1UF IC=15V
C31 13    0 0.1UF IC=0V
C41 14    0 0.1UF IC=0V
.PROBE V(1) V(2) V(2A) V(3) V(4) V(5) V(10) V(11) V(12)
+ V(13) V(14) V(101) V(102) V(104) V(100) V(112) V(113)
+ V(15) V(25) V(35) V(45) I(L1) I(S1) I(S2) I(S3) I(S4)
+ I(ROUT) V(3A) V(3B) V(4A) V(4B)
.END
```

Design and Analysis of a Novel Soft-Switched Push-Pull Boost Converter

Yu-Ming Chang*, Jia-You Lee* and Kuan-Hui Fang**,
Control System Laboratory, Department of Electrical Engineering,
National Cheng Kung University, Tainan, Taiwan
**Delta Electronics Incoporation

May 11, 1997

Abstract-A novel soft-switched push-pull boost converter is proposed for using as the front end converter of the uninterruptible power supply. The proposed soft-switched topologies and technologies have advantages of unity power factor, low current and low voltage stresses, small size, light weight and high efficiency. A stabilized power P_S is introduced for stabilizing the output voltage. Experimental results of the proposed soft-switched push-pull boost converter are presented for verifying the proposed topologies and the analytical methods.

I Introduction

In recent years, computer systems have increasing requirement for uninterruptible power supplies of small size and light weight, meanwhile featuring input current with low total harmonic distortion (THD) and unity displacement power factor (DPF). A number of topologies have been developed to achieve this goal. They can be summarized in two major ways. One is to develop new topologies which have much less numbers of power processing stage and main path components [1-3]. This kind of UPSs are referred to as hard-switched double-conversion UPSs, whose block diagram is shown in Fig. 1(a). The hard-switched double-conversion UPSs are composed of an isolated power-factor-correction converter and a DC to AC inverter. The other one, shown in Fig. 1(b), uses the soft-switched technologies in the PFC converter, DC to DC converter and DC to AC inverter [4-5]. This kind of UPSs are referred to as soft-switched triple-conversion UPSs. However, the size and weight cannot be much reduced due to the three power processing stages for the soft-switched triple-conversion UPSs and hard-switching for the hard-switched double-conversion UPSs. The best way to greatly reduce the size and weight is to use the soft-switched technologies in the double-conversion UPSs, which are referred to as soft-switched double-conversion UPSs.

In this paper, a new topology is proposed for the front stage of the soft-switched double-conversion UPSs. The topology as shown in Fig. 2 is composed of a boost choke, push-pull transformer, switch S_1 and S_2, output diode, output capacitor C_O and three terminal soft-switched cell. This topology has the following advantages: (i) small size and light weight as the soft switching make possible the high frequency operation of the boost choke and push-pull transformer. (ii) unity power factor and low THD of input current can be easily obtained by using commercial PFC IC with some logic IC. (iii) low noise due to soft switching makes the EMC achieve much easier (iv) low battery numbers as battery is located in the front of the soft-switched push-pull boost converter.

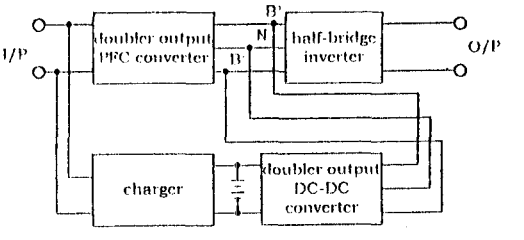

Fig .1(a)

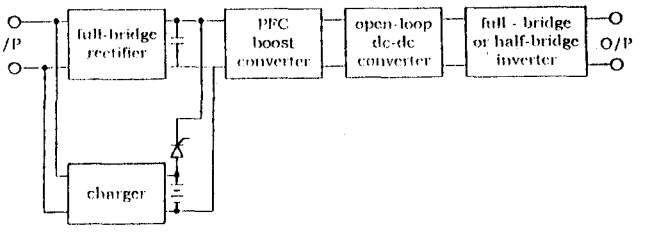

Fig .1(b)

Fig.1 Block diagrams of the conventional UPS

An unstable phenomenon that happened in light load and high line condition of the proposed push-pull boost converter is analyzed in this paper. For solving the unstable phenomenon, a stabilized power P_S is derived to make sure the design of the proposed converter is operating in stable condition. Based on the analysis, the effect of the minimum duty d_{min} and turn ratio a to the stabilized power P_S is discussed. Furthermore, a design procedure of the proposed converter is submitted to properly design the transformer turn ratio a and the required minimum stabilized power P_S. Finally, a proposed soft-switched push-pull boost converter is built to verify the proposed topologies and analysis.

II Operational Principle and Analysis

The input source whose voltage is devoted by V_i of the proposed converter can be drawn from the rectified AC source or battery. The AC source whose voltage is denoted by V_u may be the commercial AC line or an AC generator's output. For simplifying the analysis, the operation modes in the two different input are the same, based on the following assumptions.

Assumptions:

1. The boost choke inductor L is large enough so that the choke current I_L can be regarded as a constant current source over a resonant period.
2. The resonant inductance $(N_p/N_s)^2 L_r$ is much smaller than the choke inductance L.
3. All switching devices and resonant components are ideal and the resonant capacitor C_{r1} is the same as the resonant capacitor C_{r2}.
4. The transformer leakage inductance and magnetizing inductance are respectively small and large enough so that they can be neglected.

Fig. (3) and Fig. (4) show the operations of the proposed push-pull boost converters and the key waveforms respectively. The explanations of these operation modes are given as follows.

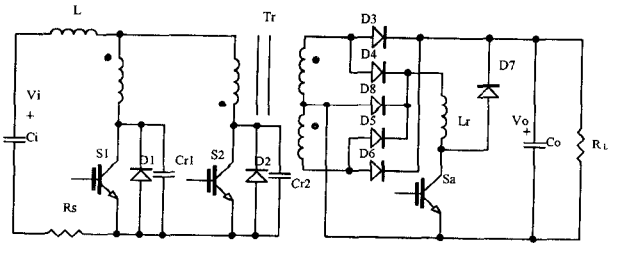

Fig. 2. Configuration of the proposed soft-switched push-pull boost converter

Mode 1 ($T_0 \leq t \leq T_1$) : In this mode, switch S_1 is turned on and the operation is the same as traditional current-fed push-pull converters in discharging mode. The resonant inductor current i_{Lr} and the resonant capacitor voltage v_{Cr1} and v_{Cr2} in Mode 1 are given by

$$i_{Lr}(t) = 0 \quad (1)$$

$$v_{Cr1}(t) = 0 \quad (2)$$

$$v_{Cr2}(t) = 2V_O(N_p/N_s). \quad (3)$$

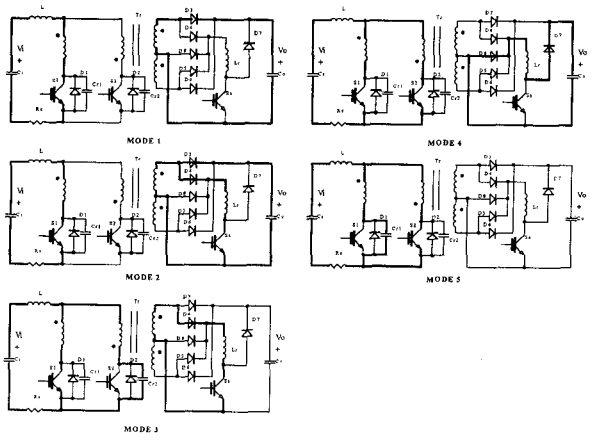

Fig. 3. Operation modes of the proposed soft-switched push-pull boost converter

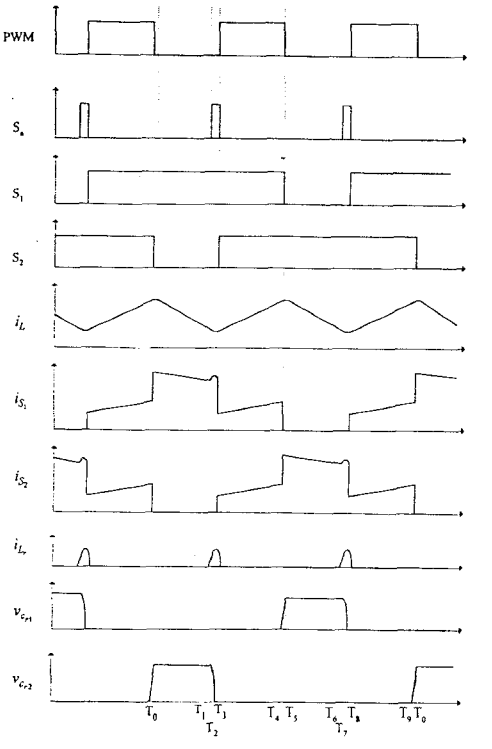

Fig. 4. Key waveforms of the proposed converter

Mode 2 ($T_1 \leq t \leq T_2$) : S_a is turned on at T_1 under zero current condition and the resonant inductor

current i_{Lr} increases linearly with a slope V_O/L_r. Therefore the resonant equations can be written as

$$i_{Lr}(t) = (t - T_1)V_O/L_r \quad (4)$$
$$v_{Cr1}(t) = 0 \quad (5)$$
$$v_{Cr2}(t) = 2V_O(N_p/N_s). \quad (6)$$

This mode is ended when i_{Lr} rises to $i_{Lr}(T_2) = I_L(N_p/N_s)$, then the duration time can be written as

$$T_2 - T_1 = L_r I_L(T_2)(N_p/N_s)/V_O. \quad (7)$$

Mode 3 ($T_2 \le t \le T_3$) : The initial conditions of i_{Lr} and v_{Cr1} for Mode 3 are

$$i_{Lr}(T_2) = I_L(T_2)N_p/N_s \quad (8)$$
$$v_{Cr1}(T_2) = 0 \quad (9)$$
$$v_{Cr2}(T_2) = 2V_O(N_p/N_s). \quad (10)$$

The resonant capacitor voltage v_{Cr1} resonates from the initial value $2V_O(N_p/N_s)$ to 0, while the resonant inductor current i_{Lr} resonates from the initial value $i_{Lr}(T_2)$ to peak value $I_{Lr,pk}$. Thus, the equations of the resonant inductor current i_{Lr} and the resonant capacitor voltage v_{Cr1} are given by

$$i_{Lr}(t) = V_O(2N_p/N_s)\sin w_r(t - T_2)/Z_r + I_L(T_2)N_p/N_s \quad (11)$$
$$v_{Cr1}(t) = 0 \quad (12)$$
$$v_{Cr2}(t) = V_{Cr1}(T_2)\cos w_r(t - T_2) \quad (13)$$
$$where \quad w_r = 1/(a\sqrt{L_r C_r}) \quad (14)$$
$$Z_r = \sqrt{L_r/C_r}/a. \quad (15)$$
$$a = N_p/N_s \quad (16)$$

By setting $v_{Cr}(T_3) = 0$, we obtain the duration time

$$T_3 - T_2 = a\pi\sqrt{L_r C_r}/2 = \pi/2w_r. \quad (17)$$

The peak resonant inductor current $I_{Lr,pk}$ is given by

$$i_{Lr}(T_3) = I_L(T_2)N_p/N_s + V_O(2N_p/N_s)/Z_r. \quad (18)$$

Mode 4 ($T_3 \le t \le T_4$) : As v_{Cr2} reaching zero and S_2 is turned on under zero voltage condition. In the duration time, the switch S_1 and S_2 are turned on and the net flux in the transformer is zero, the operation is the same as traditional current-fed push-pull converters in charging mode. The resonant inductor current i_{Lr} and the resonant capacitor voltage v_{Cr1} and v_{Cr2} in this Mode are given by

$$i_{Lr}(t) = I_{Lr,pk} - \frac{V_O}{L_r}(t - T_3) \quad (19)$$
$$v_{Cr1}(t) = 0 \quad (20)$$
$$v_{Cr2}(t) = 0. \quad (21)$$

The auxiliary switch S_a is turned off at T_3 and the energy stored in the resonant inductor L_r is discharged to the output capacitorC_O.

Mode 5 ($T_4 \le t \le T_5$) : The switch S_1 is turned off at T_4 and $v_{C_{r1}}(t)$ will be linearly increased with a slope of $I_L/2C_r$. The resonant state equations can be written as

$$i_{Lr}(T_4) = 0 \quad (22)$$
$$v_{C_{r1}}(t) = I_L(t - T_4)/2C_r \quad (23)$$
$$v_{C_{r2}}(t) = 0. \quad (24)$$

At T_5, $V_{C_{r1}}$ is charged to $2N_pV_O/N_s$, the output rectifier will turn on and the energy stored in the choke begins discharging to the output capacitor C_O. The following operations are similar to the above-mentioned, which can be obtained by changing the operating position of the switch S_1 and S_2.

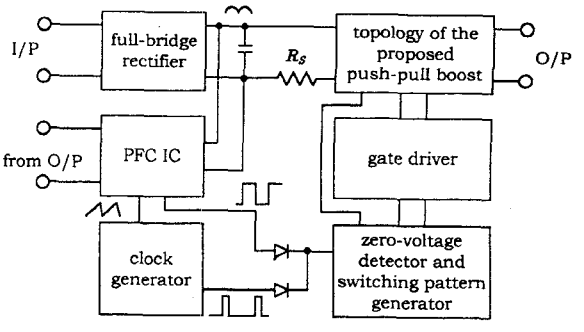

Fig. 5 Control block diagram of the proposed converter

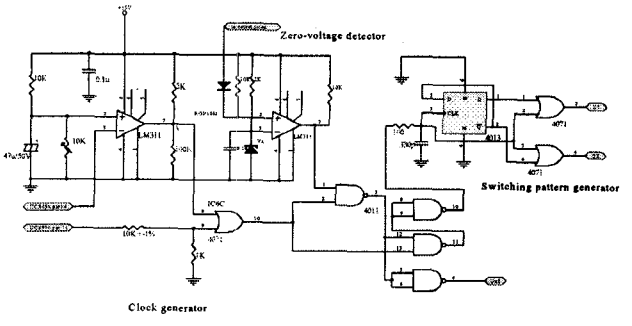

Fig. 6. Circuit of the clock generator, zero-voltage detector and pattern generator

III Practical Design Considerations

Fig. 5 shows the control block diagram of the proposed push-pull boost converter. The PFC IC can be used by the commercial IC and the clock generator is produced a clock signal to give

the push-pull transformer worked in a fix frequency. The zero voltage detector and switching pattern generator is to obtain the soft switching of the main switch S_1 and S_2.

A. Stabilized power P_S The right block of the Fig. 6 shows the circuit of the clock generator. The comparator LM311 is used to generate a minimum duty or with PFC IC output drive signal to make sure the following counter can work at a fix frequency, so the volt-seconds of the push-pull transformer can be balanced in light load. The value of the minimum duty is decided by the resonant components, output voltage and load. Unfortunately, the minimum duty d_{min} is not in the feedback control loop, so the noncontrolled input energy will be transferred to the output through the push-pull transformer. It is apparent that the output is required to have enough dummy load to dissipate the energy, otherwise the output voltage will raise up until the output power can balance the noncontrolled power. The noncontrolled power is from two sources: one is from line; the other is from the choke. In this paper, this noncontrolled power is referred to as stabilized power P_s. The following derivation is intended to find the stabilized power P_s and is based on the assumptions :

(a) The input voltage V_i can be regarded as constant over a switching period.

(b) The converter is operated in discontinuous conduction mode (DCM).

(c) The output voltage V_o is larger than $V_i/a(1-d_{min})$.

The stabilized power P_S can be written by

$$P_s = \frac{1}{T_L}\int_0^{T_L} i_{L_d}(t)v_i(t)dt \quad (25)$$

$$= \frac{f_L}{f_s}\sum_{k=0}^{f_s/f_L} avg\{i_{L_d}(kT_S)\} \; avg\{v_i(kT_S)\}, \quad (26)$$

where $f_L = 1/T_L$ denotes the input line frequency and i_{L_d} denotes the choke current when the converter operated in minimum duty condition. The averaged choke current $avg\{i_{L_d}(kT_S)\}_{T_S}$ can be obtained by the following equations

$$avg\{i_{L_d}(kT_S)\}_{T_S} = \frac{1}{T_S}\int_0^{T_S} i_{L_d}(t)dt \quad (27)$$

$$= \frac{d_{min}V_i(kT_S)T_S}{2L}(d_{min}+d_d) \quad (28)$$

$$= \frac{d_{min}^2 T_S V_i(kT_S)}{2L} (1+\frac{aV_o}{aV_o - V_i(kT_s)}) \quad (29)$$

, where d_d denotes the required duty when the choke current i_{L_d} discharges the energy to zero. By substituting the above equations, the stabilized power P_s is given by

$$P_s = \frac{f_L}{f_s}\sum_{k=0}^{f_s/f_L}\frac{d_{min}^2 T_S V_i^2(kT_S)}{2L}(1+\frac{aV_o}{aV_o - V_i(kT_s)} \quad (30)$$

In case of battery input, the stabilized power P_s can be written by

$$P_s = \frac{1}{2}d_{min}^2\frac{V_B^2 T_S}{L}(1+\frac{aV_o}{aV_o - V_B}). \quad (31)$$

From (30) and (31), we can see that the smaller the minimum duty d_{min} is designed, the less stabilized power P_s is required. By selecting the parameter of $a = 1$, $L = 250\mu H$, $f_s = 70kHz$, $f_L = 60Hz$ and $V_o = 200v$, we can obtain the fig. 7 and fig.8. Fig. 7 shows the curves of the battery voltage V_B against the stabilized power P_s in different minimum duty d_{min}. Fig. 8 shows the curves of the time against the instant stabilized power p_s in the condition of $V_i = 180sin2\pi f_L t$ and different turn ratio a. It is apparent that the stabilized power P_s is decreased as minimum duty d_{min} decreasing or turn ratio a increasing.

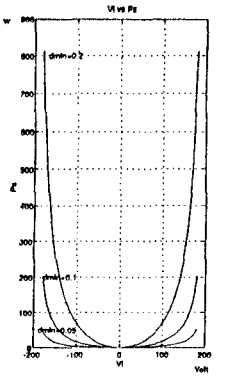

Fig. 7. Curves of the minimum duty d_{min} against the stabilized power P_S

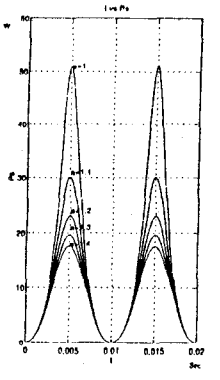

Fig. 8. Curves of the time against the stabilized power P_S

B. Design procedure

1. Define the specification as follows:

. input line voltage range ($V_{u(min)}$, $V_{u(max)}$)(rms value)

. output voltage V_O

. maximum output power $P_{O(max)}$

. minimum efficiency η_{min} for maximum output power $P_{O(max)}$

. switching frequency f_s

2. Calculate the maximum choke current $I_{L(max)}$ by the equation

$$I_{L(max)} = \frac{V_{u(min)}(aV_O - V_{u(min)})}{2Lf_s aV_O} + \frac{\sqrt{2}P_{O(max)}}{\eta_{min}V_{u(min)}}. \quad (32)$$

3. Select the current $V_O(2N_p/N_s)/Z_r$ in the range $0.05I_{L(max)}$-$0.15I_{L(max)}$, so that the current stress of the auxilliary switch is not too much.

4. Select the resonant frequency $w_r/2\pi$ in the range $5f_s$-$20f_s$ with consideration given to the effect caused by the dv/dt, di/dt and duty loss.

5. Calculate the maximum values of L_r and C_r by the following equations.

$$L_r = Z_r/w_r \quad (33)$$

$$C_r = 1/(Z_r w_r) \quad (34)$$

6. Calculate the minimum duty d_{min} by the following equation

$$d_{min} \geq f_s\left(\frac{aLI_{L(max)}}{V_O} + \frac{a\pi\sqrt{L_rC_r}}{2}\right). \quad (35)$$

The selection of the minimum duty d_{min} to be larger than $f_s(\frac{aLI_{L(max)}}{V_O} + \frac{a\pi\sqrt{L_rC_r}}{2})$ is to prevent the main switches from destroying in the condition of full load changing to no load.

7. Calculate the transformer turn ratio a by the equation

$$a \geq \frac{V_{u(max)}}{(1-d_{min})V_O}. \quad (36)$$

We know that the larger the turn ratio a the less the stabilized power P_S is required. But, the selection of the turn ratio a cannot just consider the required stabilized power P_S, also have to consider the design of push-pull transformer. It is well-known that the larger the turn ratio a the larger the rms current of push-pull transformer flows into, it may increase the size of the push-pull transformer. That is to say, the value of the turn ratio a is the tradeoff of the stabilized power P_S and the push-pull transformer size.

8. Select the battery operating voltage $V_{B(min)}$ and $V_{B(max)}$. In order to regulate the output voltage to meet the total harmonic distortion of UPS specification. The selection of the minimum battery voltage is given as the following

$$V_{B(min)} \geq aV_O(1 - D_{max} + d_{min}) \quad (37)$$

, where D_{max} denotes the maximum duty of the PFC IC output. The selection of the maximum battery voltage $V_{B(max)}$ is to be less than $a(1-d_{min})V_O$, i.e.

$$V_{B(max)} \leq a(1 - d_{min})V_O. \quad (38)$$

9. Use (30) and (31) to calculate the stabilized power P_S when the input is in the maximum line voltage $V_{u(max)}$ or maximum battery voltage $V_{B(max)}$ conditions and choose the maximum one as the required.

10. Check if $V_{B(min)}$ less than $V_{u(min)}$, then reselect the $V_{B(min)}$=$V_{u(min)}$.

IV Experimental result

In order to demonstrate the features and theoretical analysis, a prototype of the isolated push-pull boost converter is built and shown in Fig. 9. The specifications of this converter are given as follows. The input line voltage range is from 85 to 132 volts, the nominal voltage is 110 volts and the output voltage is 200 volts. The rated output power is 900W. The switching frequency is 70 kHz. The semiconductor components of the experimental power stage are shown in Fig. 9 and the boost choke L, the resonant inductor L_r, the resonant capacitor C_r and the push-pull transformer are chosen as following.

L : 250 μH inductor winding on an iron powder core of T-184-33

T_r : ferrite core of EE 55-55-21 with turn ratio $a = 1$

L_r : 20 μH winding on a gapped ferrite core of ETD-39

C_{r1}, C_{r2}: each one of MPP 1000 pF 630v capacitor

Fig. 10 shows the waveforms of the switch voltage and the switch current, it is apparent that the switch turns on under zero voltage condition. Fig. 11 and Fig. 12 show the waveforms of the output diode voltage and the transformer secondary current in the conventional hard-switched topology and the proposed soft-switched topology respectively. Comparing the above two figures, the waveforms in hard-switched topology have ringing in the switching transition which is caused by the reverse recovery time of the output diode. Fig. 13 shows the waveform of the unfiltered line current which is sinusoidal and in phase with the line voltage, the input power factor is larger than 0.995. So, the above experimental results agree with the proposed methods and analysis.

V Conclusion

The proposed soft-switched push-pull boost converter is a very attractive solution for UPS

application. It provides not only the power factor correction but also the galvanic isolation function. Furthermore, the battery can be put inside the proposed topology and use the same power stages for back up , therefore requires two power stage only and makes the proposed UPS very cost effective. Having the isolation function, the proposed converter can be connected in front of the full bridge SPWM inverter. It is well-known that the full bridge inverter has an advantage over the half bridge inverter that it can easily handle the asymmetric load, like the half-wave rectified load. That is to say, the potential disadvantages of the double-conversion UPS which adopts the half-bridge inverter can be eliminated by the proposed soft-switched double-conversion UPS. Utilization of the zero voltage-transition PWM on the push-pull boost converter gives the advantages of light weight, small size, low EMI and high efficiency. A stabilized power is introduced and derived to solve the unstable phenomenon that happened in high line and light load. The curve of the stabilized power P_S against the minimum duty d_{min} presented that the smaller the minimum duty d_{min}, the less the stabilized power P_S is required. A design procedure has been submitted to avoid the proposed converter being operated in unstable condition and to obtain a proper stabilized power P_S'. Finally, the proposed topology and analysis have been verified on a soft-switched push-pull boost converter, which is very suitable for the application in the medium capacity UPSs.

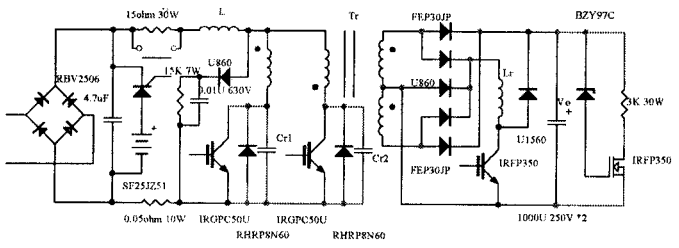

Fig. 9. Power stage of the experimental push-pull boost converter

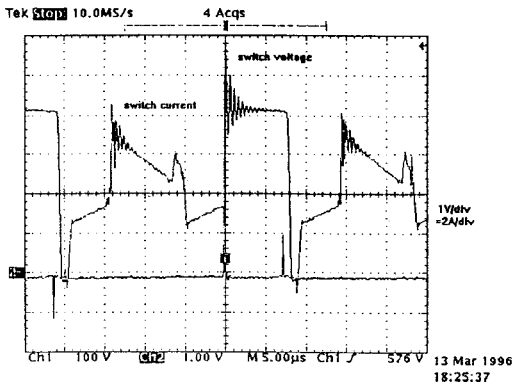

Fig. 10. Waveforms of the switch voltage and the switch current

REFERENCES

[1] K. Hirachi, H. Yamamoto, M. Sakane, Y. Tomokuni and Y. Nagai, " A Novel 3KVA UPS Using a Switch Mode Rectifier", IEEE INTELEC Conference Record, 1990, pp. 392-399.

[2] A. Chibani and M. Nakaoko, "A New Control Topology of Single- Stage HF Link Switch-Mode-Rectifier with Sinusoidal line current", IEEE, 1990, pp. 1157-1162.

[3] Ryuji Yamda, Kazuo kuroki, Jun'ichi Shinohara and Takami Kagotani, " High-Frequency isolation UPS with Novel SMR", IEEE Power Electronic Specialist Conference Record, 1993, pp. 1258-1263.

[4] Robert Streit and Daniel Tollik, "High efficiency telecom rectifier using a novel soft-switched boost-based input current shaper", IEEE INTELEC Conference Record, 1991, pp. 720-726.

[5] Guichao Hua, Eric X. Yang, Yimin Jiang and Fred C. Lee, "Novel zero-current-transition PWM converters", in IEEE Power Electronic Specialist Conference Record, 1993, pp. 538-544.

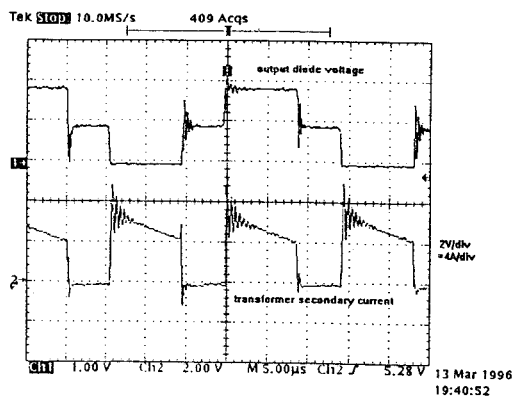

Fig. 11 Waveforms of the output diode voltage and the transformer secondary current in the conventional hard-switched converter

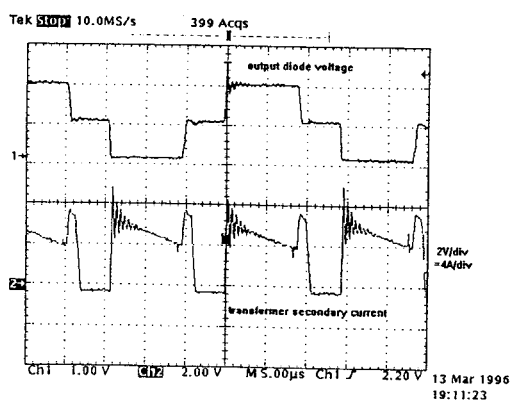

Fig. 12 Waveforms of the output diode voltage and the transformer secondary current in the proposed soft-switched converter

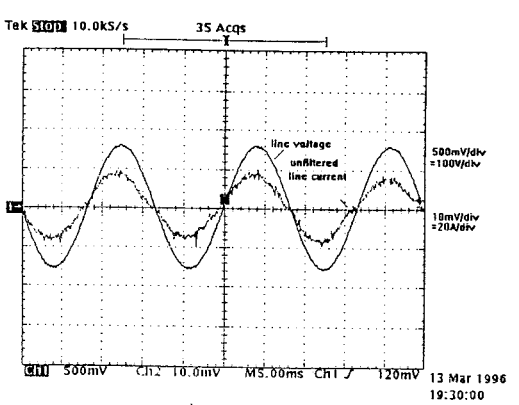

Fig. 13. Waveforms of the line unfiltered current and the line voltage

Performance of Series-Resonant AC Link Inverter

Masahito Hayashi, Kouki Matsuse
Meiji University
1-1-1,Higashimita,Tama-ku,Kawasaki 214,JAPAN
Phone / Fax: +81 - 44 - 934 - 7293
E-mail: ce66029@isc.meiji.ac.jp
matsuse@isc.meiji.ac.jp

***Abstract*—This paper presents performance of series-resonant AC link inverter. The topology consists of inverter, LC resonant circuit and cycloconverter sections. We have proposed the method to apply a Pulse Amplitude Modulation (PAM) and a Pulse Density Modulation (PDM) controls for improving output current [1][2]. By using this method, harmonic components of output current can be eliminated. In this paper, experimental results are presented. It is shown that the method of improving output current by PDM and PAM controls is available.**

I. Introduction

Recently, various Soft-Switched DC-AC Converters using either Zero Current Switching (ZCS) or Zero Voltage switching (ZVS) have been investigated [3].

A high frequency series-resonant converter has been developed in response to demand for improving output voltage or current waveforms , light weight, high efficiency and so on. Switching losses at high frequency also has been improved by ZVS or ZCS utilizing high speed power device.

We proposed a Pulse Amplitude Modulation (PAM) control of resonant current for improving output current in addition to a Pulse Density Modulation (PDM) control and ZCS at turn-off of switching devices.

In this paper, we present experimental results, and explain that output current can be improved by the proposed method.

II. Basic topology and Principle of operation

A. Main Circuit Configuration

Fig.1 shows the main circuit configuration of series-resonant AC link inverter. The topology consists of inverter, LC resonant circuit, cycloconverter and filterload sections.

The inverter section on the left side is composed of four IGBTs (Insulated Gate Bipolar Transistors) as switching devices with antiparallel diodes. In LC resonant circuit, a resonant current i_r oscillates with resonant frequency, which is determined by the inductance L_r and the capacitance C_r. PAM is performed by controlling the eight switches (IGBTs and diodes) in the inverter section.

The cycloconverter section on the right side is composed of eight IGBTs. Diodes in series with each IGBT are necessary to prevent reverse-current from conducting in eight IGBTs. Cycloconverter output current waveform is controlled by switching timing of eight IGBTs in the cycloconverter section as shown in Fig.2. Here, we call sign i_{rL} cycloconverter output current in Fig.1.

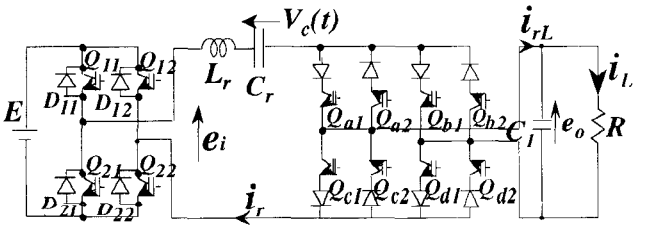

Fig.1. Main circuit configuration of series-resonant AC link inverter

B. Principle of operation

Fig.3 shows resonant current and capacitor voltage waveforms. We assume that resonant capacitor voltage $V_C(0)=-V_{C0}$ as an initial condition. In the idealized series-resonant circuit, by means of firing IGBT switches in the inverter section, a square-wave voltage is generated across the resonant circuit. In addition, resonant current waveform is composed of successional period of two different sinusoidal functions.

We divide the topology into three different modes.

In the first period (from 0 to t_1), resonant current flows from resonant circuit to voltage source E via D_{12} and D21 [mode1]. Therefore, we call resonant current in mode 1 Diode

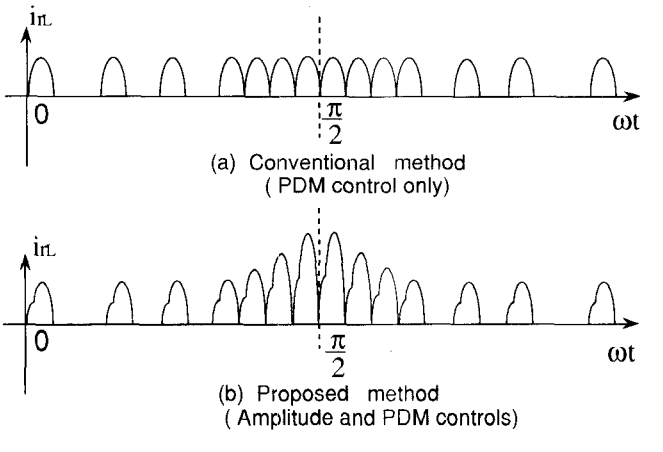

Fig.2 The difference of output current waveform between conventional and proposed methods

current.

In the second period (from t_1 to t_2), resonant current flows from voltage source E to resonant circuit via Q_{11} and Q22 [mode2], which results in a increase of the amplitude of resonant capacitor voltage. Therefore, we call resonant current in mode2 IGBT current. That is, energy has flowed between resonant circuit and voltage source E in mode1 and mode2 and the amplitude of resonant current is controlled by varying the value of angle. We call sign α delay angle in Fig.3.

The interval (from t_2 to t_3) between current pulses is required to PDM.

The equivalent circuit for mode1 and mode2 is shown in Fig.4 as e_i and e_o are input and output voltages of resonant circuit, respectively.

The following differential equation is obtained from Fig.4.

$$L_r di_r/dt+(1/C_r)\int i_r dt=U_e. \quad (1)$$

where $U_e=e_i-e_o$

Solving (1) with Laplace transforms, current i_r is given as

$$i_r(t)=i_r(0)COS\omega_r t-(1/Z_r)\{V_C(0)-U_e\}\sin\omega_r t. \quad (2)$$

where $Z_r=\sqrt{L_r/C_r}$, $\omega_r=1/\sqrt{L_rC_r}$

Here, we should notice that there is a difference of direction of connected voltage source E between mode1 and mode2. We assume that output voltage is constant V_0. Thus diode current for $0<t<t_1$ and IGBT current for $0<t'<t_2-t_1$ expressed by (2) are sinusoidal function of mode1 and mode2 in Fig.3, respectively.

In addition, the relationship between resonant current and capacitor voltage are satisfied with the following expression, which can be obtained by transforming (1).

$$(Z_r i_r)^2+(V_C-U_e)^2=const. \quad (3)$$

The form of (3) is a circle equation about $Z_r i_r$ and V_C.

Figuring (3) for each mode, we can describe Fig. 5 which is named the state diagram. Besides, It is determined by a boundary condition that which locus is chosen. For example, setting $(Z_r i_r, V_C)=(0, V_{Cref})$ as a boundary condition for mode2, the following expression [4] can be given by means of using (3).

$$(Z_r i_r)^2+(V_C-U_{e2})^2=(V_{Cref}-U_{e2})^2. \quad (4)$$

Therefore, the locus of mode2 in this case become the bold line as shown in Fig.5. This figure essentially represent the relationship between resonant current i_r and capacitor voltage VC, because impedance Z_r is constant.

III. Control system

Fig.6 shows a block diagram of control system of this main

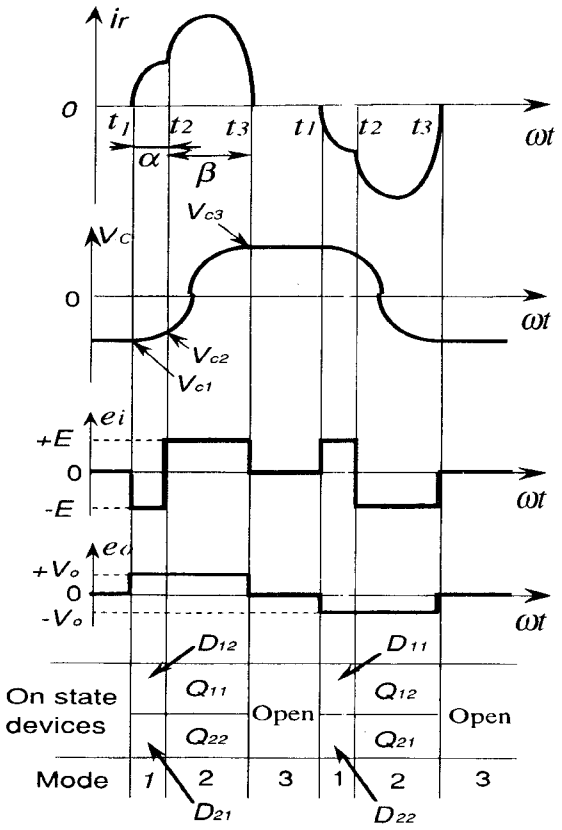

Fig.3 Resonant current and capacitor voltage waveforms for each mode

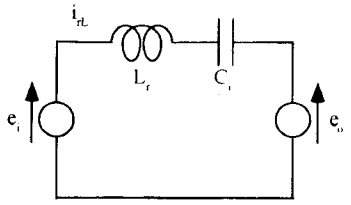

Fig.4 Equivalent circuit for each mode

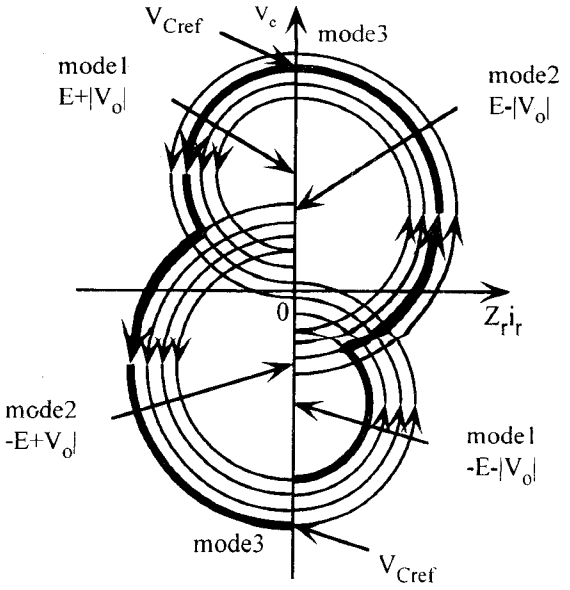

Fig.5 The state diagram

circuit. In order to control the value of turnover time t_2, operating circuit as shown in Fig.7 is composed of the right term of the next equation.

$$f(t)\equiv\{V_C(t)-U_{e2}\}^2-(V_{Cref}-U_{e2})^2+\{Z_r i_r(t)\}^2 . \quad (5)$$

X square represents multiplication in Fig. 7. (5) is derived from (4). Voltage source E and output voltage e_o, which correspond either +E or –E and either + e_o or $-e_o$, respectively, resonant capacitor voltage V_C and resonant current i_r are obtained from actual measurement. V_{Cref}, which is relevant to the amplitude of resonant current, is a reference value of resonant capacitor peak voltage.

These measured values and V_{Cref} are transmitted to the operating circuit in Fig. 6. When (5) is equal to zero, i.e. (3) is satisfied, the turnover time t_2 is obtained and the operating circuit generate the output signal CLK to control IGBTs of the inverter section via control circuit. Then the state of the main circuit become mode2. Resonant capacitor voltage V_C move into V_{Cref} along the locus which satisfy (3).

Thus, the amplitude of resonant current can change with the locus by varying V_{Cref}.

IV. Experimental Results

The main circuit parameters are presented in Table I. The value of output filter capacitor C_1 is determined larger than that of resonant capacitor C_r not to influence resonant phenomenon.

Fig.8 shows waveform of resonant current i_r and capacitor voltage V_C. This figure is similar to that shown in Fig.3 in section II.B. In addition, ZCS at turn-off of switching devices is realized.

Fig.9 and Fig.10 shows waveforms of cycloconverter output current i_{rL}, output current i_L and output voltage e_o at output frequency 50[Hz] by PDM control and by both PDM and PAM control, respectively. Fig.9(b) indicates that PAM control is available to make sinusoidal current waveform. And the maximum value of output current and voltage by both PDM and PAM is much larger than that by PDM only as shown in Fig.10.

Fig.11 shows FFT analysis of waveform of cycloconverter output current i_{rL}. This figure indicates that the lower order harmonic components by the proposed method become those by PDM only.

V. Conclusion

In this paper, we has presented a method of improving output current waveform of series-resonant AC link inverter. It is confirmed by experimental results that output current waveform was approximate to sinusoidal waveform and harmonic components of cycloconverter output waveform was eliminated. Furthermore, it was clear that larger maximum value of output current using PAM control is obtained.

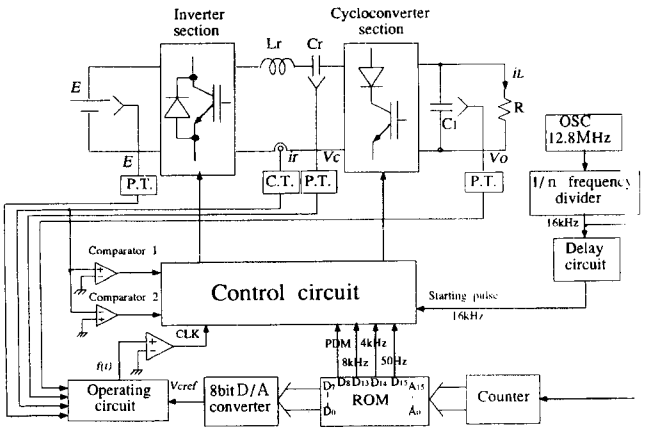

Fig.6 Block diagramof control system

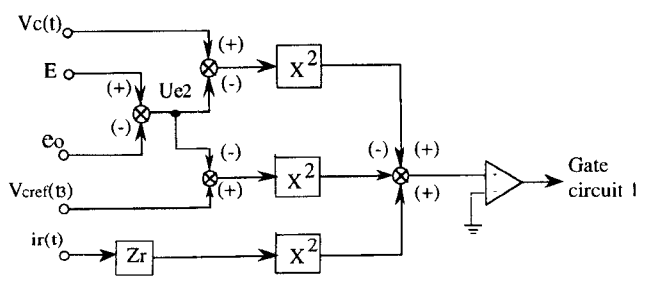

Fig.7 Operating circuit of turnover time t2

TABLE I
PARAMETERS OF EXPERIMENTAL CIRCUIT

E=25[V]	L_r=52.4[μF]
C_r=[μF]	C_1=1600[μF]
R=2.5[Ω]	
Resonant frequency f_r=8[kHz]	

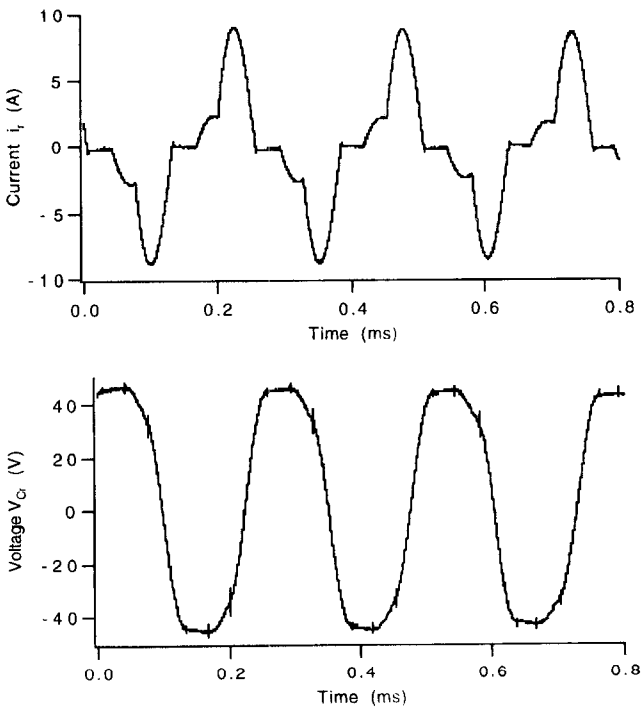

Fig.8 Resonant current and Capacitor voltage waveforms

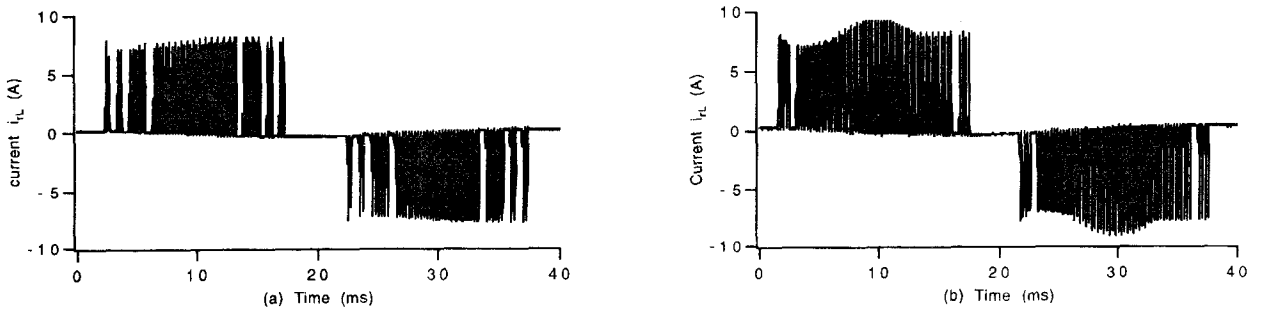

Fig.9 Cycloconverter output current waveform
((a) PDM control only, (b) PDM and PAM control)

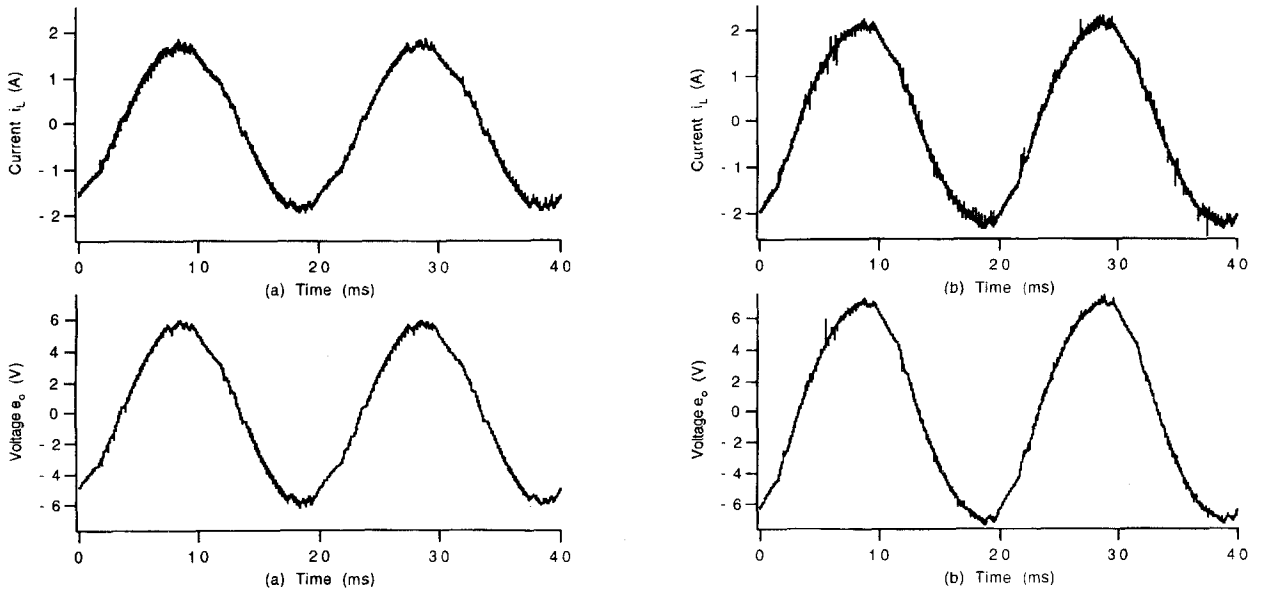

Fig.10 Output current and vo waveforms
((a) PDM control only, (b) PDM and PAM control)

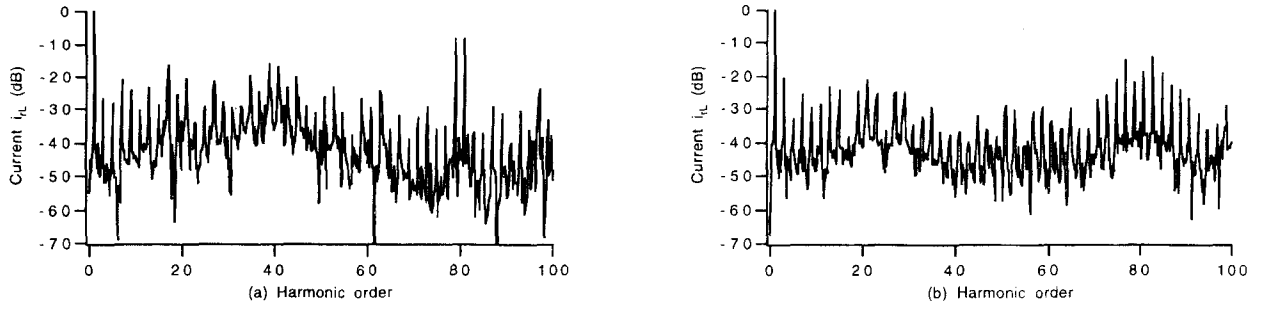

Fig.11 FFT analysis of cycloconverter output current i_{rL}
((a) PDM control only, (b) PDM and PAM control)

VI. Acknowledgment

The authors would like to express our appreciation to Dr. S.Yamamoto of Polytechnic university and Mr.Miyazaki of Nippon Thermonics for discussion.

VII. References

[1] H.Hayasaka, S.Yamamoto and K.Matsuse, "A method for improving output current of series-resonant AC link cycloconverter," in Proceedings of IECON'93,pp.1292-1296.

[2] S.Yamamoto, H.Hayasaka and K.Matsuse, "Analysis of Series-Resonant AC Link Inverter for Improving Output Current," in Proceedings of the IEEE PESC'94,pp.965-969.

[3] T.S.Wu, M.D.Bellar, A.Tchamdjou, J.Mahdavi and M.Ehsani, "A Review of Soft-Switched DC-AC Converters," in Proceedings of the IEEE IAS Annual Meeting, pp.1133-1144,1996

[4] S.W.H.de Haan and J.D.Lodder, "A formalistic approach to series-resonant power conversion," EPE,pp.231-238,1987.

A Basic Study on a Parallel Resonant Link Converter for a High Frequency Link System

Mikihiko Matsui, Toshio Akiyama
Tokyo Institute of Polytechnics
1583, Iiyama, Atsugi-shi, Kanagawa 243-02 JAPAN
Fax: +81-462-42-9563, Phone: +81-462-42-9563
E-mail: matsui@ee.t-kougei.ac.jp

Abstract **— The parallel resonant link high frequency power distribution system can be an attractive system as a supplementary local distribution line linked with existing ac commercial system line in a building or a plant, if some new energy sources and energy storage systems are combined and connected with the link. This paper deals with some basic issues of a unit converter for such system from both microscopic (stable switching operation) and macroscopic (energy flow) points of view. A PDM (pulse density modulation) gate control circuit for stable operation and self start-up from stand still is tested. Effect of PDM sampling period on steady state waveforms is compared on three cases. Bad effect of parasitic capacitance of switching arm is shown, and its countermeasure is given. Based on probabilistic switching function technique, a dc equivalent circuit model suited for simulating macroscopic energy flow is proposed.**

I. INTRODUCTION

In general, filters and transformers for distribution system can be reduced both in size and weight if the frequency becomes higher. For this reason, 400Hz system has been adopted in airplanes, and 20kHz or higher frequency system has been considered for power system in space stations[1]-[4]. The major advantage of the high frequency link system include following points.

1. Compact size and light weight of filters and transformers.
2. Easy isolation and easy voltage transform by using transformers.
3. Flexible use of energy becomes possible if some new energy sources as solar cells and adequate energy storage systems, e.g. battery, flywheel etc., are connected together at the link bus.
4. Moreover, ZVS (zero voltage switching) operation advantageous for reducing switching losses and EMI problems becomes available if a PDM scheme is adopted.

These merits can be expected also on the ground. In such cases, the type of converter and its operating frequency etc. are selected depending on the needs and their kVAs. For instance, 500Hz power distribution systems using thyristor converters for buildings or plants have been proposed expecting the merits 1 to 3 shown above[5][6]. Whose typical kVA is around 10MVA and the distribution length is more than several kilo meters.

On the contrary, the objective system here is a supplementary local high frequency distribution system whose frequency range is around 20 kHz, whose kVA is as much as 100kVA at most and its distribution length is several hundred meters at the longest. Assuming a sinusoidal line voltage, a parallel resonant link using LC tank circuit may be the most possible candidate. Fig.1 shows such system having new energy sources and energy storage systems. The HF bus is linked with the existing ac commercial system line via a cycloconverter whose operating current waveform and power factor on the commercial line side are both excellent. The power conversion is done by using inverters and cycloconverters operating in PDM mode.

In this paper, keeping the system in Fig.1 in mind, some basic issues on a unit power converter, i.e. a current source PDM inverter, will be studied from two different points of view. One is a macroscopic point of view, i.e. concerning to every switching operations.

- In order to keep stable ZVS PDM operation, a gate control circuit using PLL (phase locked loop) and some interlock circuits to cut effect of noise and enabling self start-up ability from stand still condition has been proposed and tested as a proto-type.
- Bad effect of parasitic capacitance in diode connected in series with main switch on soft switching characteristics is pointed out. A countermeasure to realize true ZVS operation is shown.
- Effect of sampling period for PDM on the steady state waveforms have been compared on three cases, half-

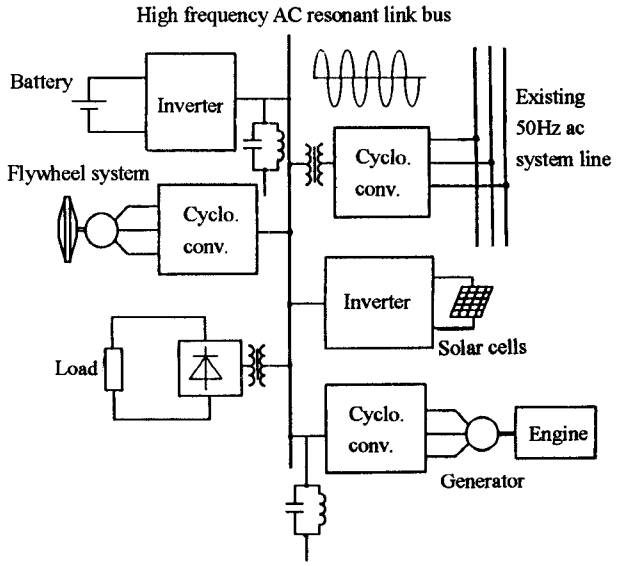

Fig.1 High frequency link power system having new energy sources and energy storage systems applied for a local distribution line linked with existing ac commercial system line.

0-7803-3823-5/97/$10.00© 1997 IEEE

cycle period, full-cycle period and their hybrid cases. The features of each method have been clarified.

The other point of view is a macroscopic one, i.e. the energy flow which is not affected by the switching ripples. For the design of tank circuit or control circuit for stabilizing the link voltage, such viewpoint is essential.

- Based on probabilistic switching function technique, a dc equivalent circuit of HF link is proposed. A transient response has been simulated to prove its usefulness.

II. PDM CONTROL OF AN UNIT INVERTER

A. Operation of an unit inverter

Fig.2 shows a current source parallel resonant inverter which is the most essential power converter unit for HF link system. It has a current smoothing reactor L1 on DC side and a parallel resonant LC tank on HF side whose resonant frequency is tuned to be 20kHz. Only a pure resistor is connected as a load. One switching arm is composed of a series connection of a main switching power device, MOS-FET (Fuji 2MI50F-050), and a fast switching type diode (Fuji ERG24).

The switching patterns of the proto-type inverter transfer along with arrows shown in Fig.3, where the shaded switch numbers correspond to the on state devices. Plus(+) mode or minus(-) mode is selected according to the output link voltage polarity. Selection of the cross-mode or short (circuit) - mode depends on the dc side current control error polarity. For instance, if the actual current is smaller than its command, the short-mode would be taken in the next coming sampling period to increase the amplitude by shortening the dc bus. Every switching timing is chosen to be coincide with the zero crossing point of HF link voltage. Mode 0 is called as overlap mode of 1 μsec period during which all of the four switching arm gates are forced to be turned-on. This mode guarantee the continuity of dc side current, and prevents a voltage serge occurrence due to open circuit of both dc side smoothing reactor and ac side leakage inductor.

B. PDM control circuit

Fig.4 shows the block diagram of a PDM control circuit, and its control timing chart is shown in Fig.5. In order to realize ZVS operation, precise voltage detection of the resonant tank circuit is necessary. However, there may occur some voltage notches during the commutation overlap period which disturbs the precise zero voltage detection. Moreover, the delay time of control circuit and main power device is not negligible to affect the true ZVS timings. In the test circuit, PLL(phase locked loop), noise filters, delay time compensation blocks, Interlock blocks are adopted to make a stable detection.

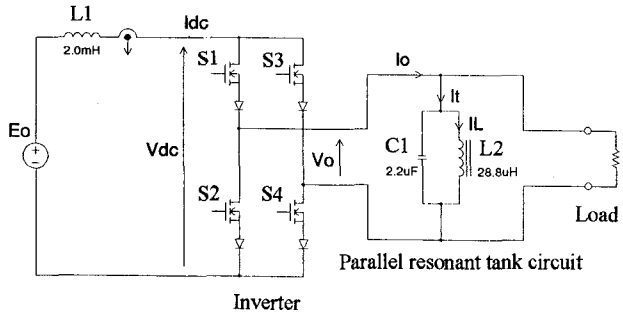

Fig.2 Main circuit configuration of a high frequency inverter.

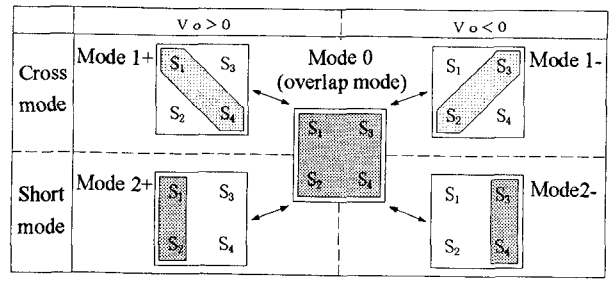

Fig.3 Switching mode of an inverter.

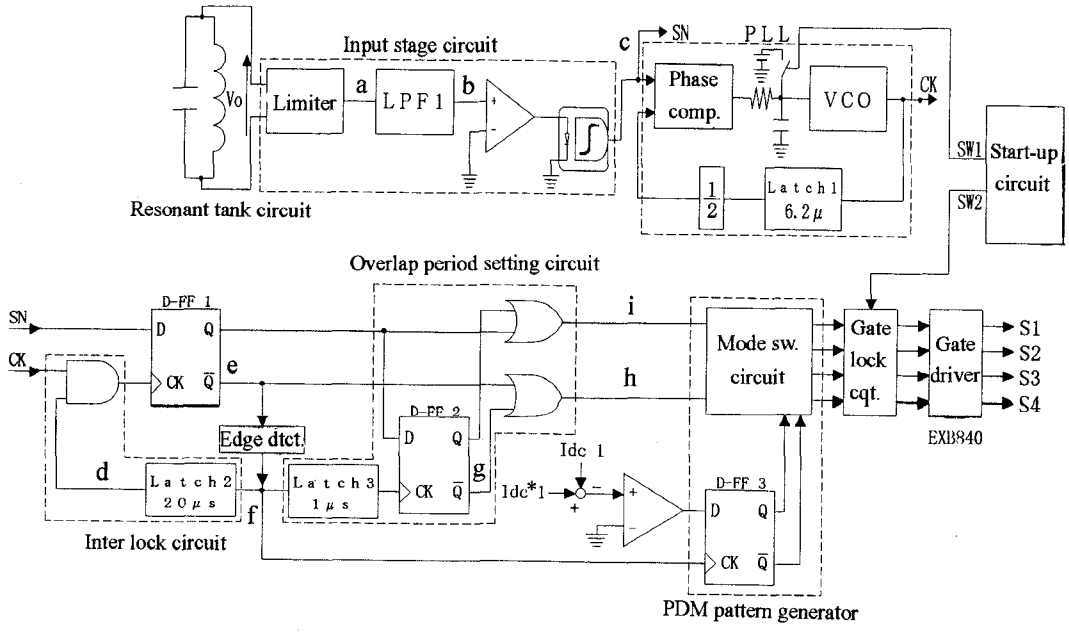

Fig.4 Block diagram of a pulse dencity modulation control circuit having starting-up ability from a stand still condition.

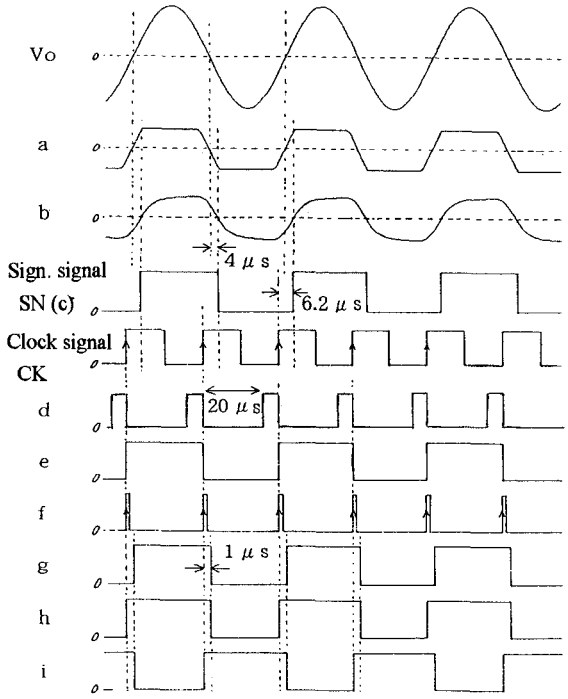

Fig.5 Timing chart of the control circuit shown in Fig.4.

1) Input stage circuit: The detected link voltage is shaped by a limiter(see waveform (a) in Fig.5), and filtered by a LPF(low pass filter) (b). Then, reshaped signal is isolated by a photo-coupler (c), and forwarded as signature signal SN to the next PLL stage and D-FF1.

2) PLL stage circuit: In the PLL, precise gate timing pulse to realize true ZVS is generated. By delaying the feedback signal by Latch-1, totally 6.2 μsec delay time is compensated in this loop, where 6.2 μsec is the sum of 4.0 μsec delay at LPF-1 and 2.2 μ sec at gate driver and power device etc..

3) Interlock circuit: Based on the polarity information signal SN and the timing information signal CK, D Flip-flop D-FF1 generates pulse train for next stage . In this part, the clock input is inhibited by the signal (d) from Latch-2 for 20 μsec (which corresponds to 80% of the half cycle) after the last change of state has occurred in (e).

4) Overlap period setting circuit: Latch-3 and D-FF2 are for setting 1 μ sec overlap period , Mode 0 in Fig.3.

5) PDM pattern generator: Based on the error signal of the dc current control loop, cross-mode ($Idc \geqq Idc^*$) or short-mode ($Idc < Idc^*$) is selected in the mode switching circuit.

C. Start-up circuit

Once the HF link voltage is established, stable synchronization of the gate drive pulse to the link voltage is maintained regardless of the switching noise or deviation of link voltage amplitude due to the load condition changes. However, to start-up from the stand still condition, there need some special starting sequence. The start-up circuit shown in Fig.4 is for controlling the initial starting sequence by operating two logic signals SW1 and SW2. A typical experimental waveform at starting-up from stand still is shown in Fig.6. At the

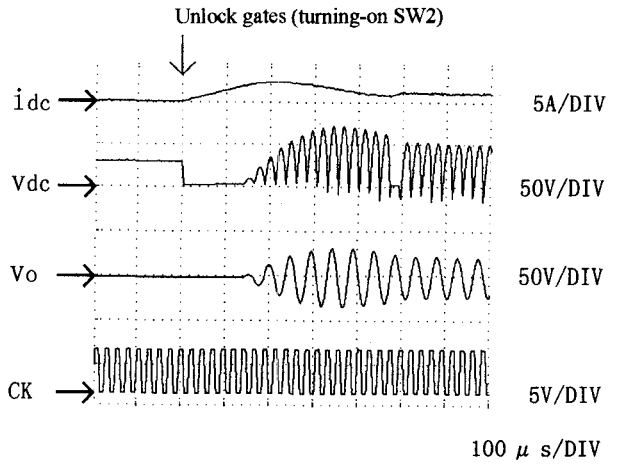

Fig.6 Experimental waveforms at starting-up from stand still.

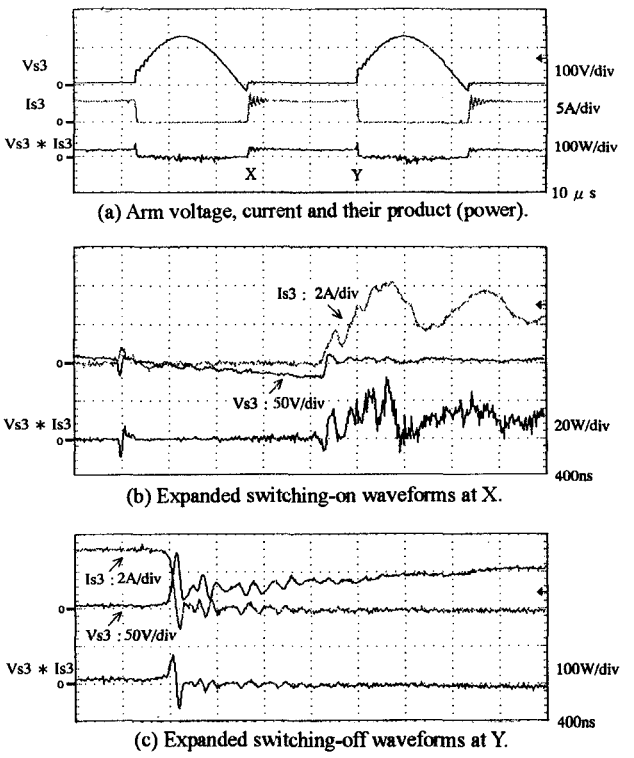

Fig.7 Experimental waveforms at steady state condition.

initial condition, all the gate signals are locked by turning-off SW2, and SW1 is closed, i.e. in on state, to force the VCO (voltage controlled oscillator) to oscillate at constant steady state frequency of 40kHz, which is twice as high as the link voltage frequency. No sooner has SW2 been unlocked, the dc side current starts to flow. Before the dc side current amplitude reaches its command, the switching mode is fixed to short-mode. When the dc side current amplitude reaches its command, the cross-mode starts to appear, and as a result, the HF link voltage starts to be established. After the initial transient is over, which is about ten cycles later in this example, the other switch SW1 is turned-off. Then the PLL is pulled into a locked-in condition.

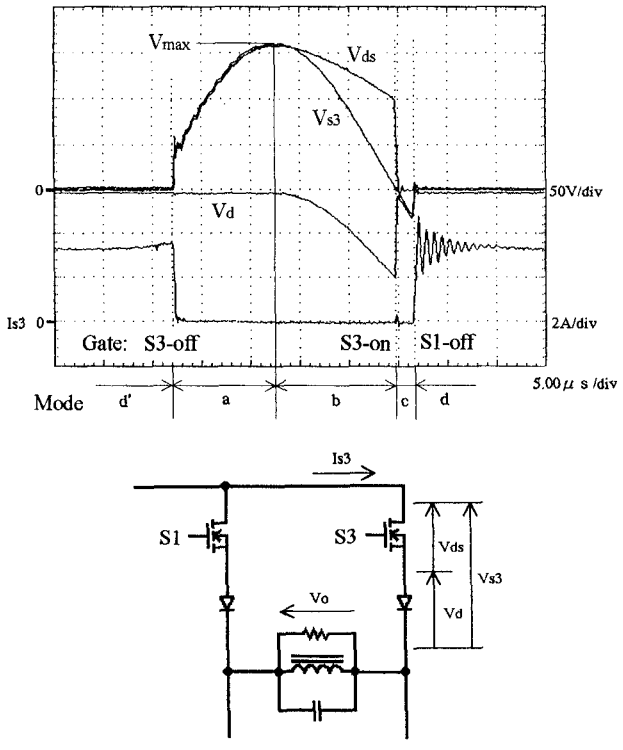

Fig.8 Voltage and current waveforms in one inverter arm.

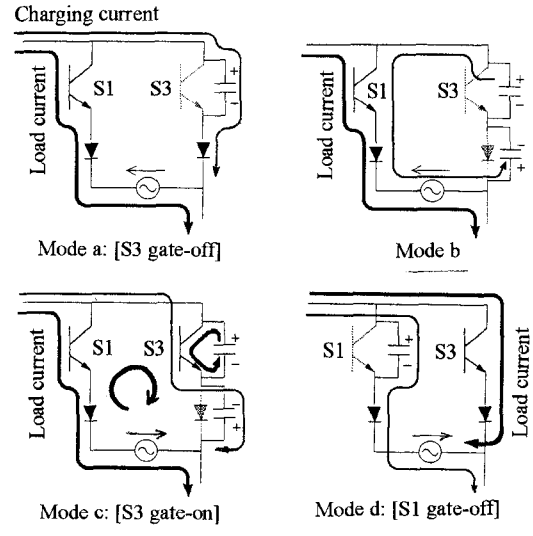

Fig.9 Charging and discharging current paths for each modes 'mode a' to 'd ' shown in Fig.9.

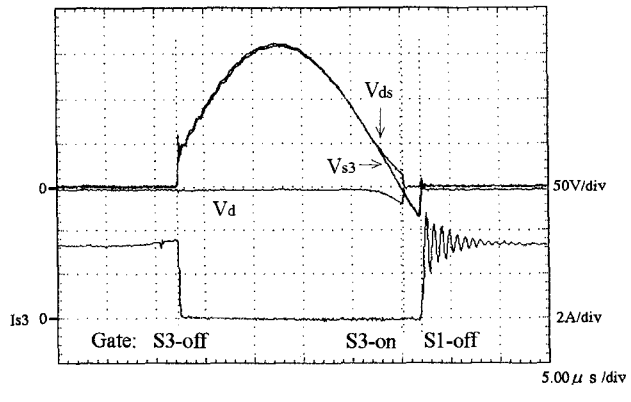

Fig.10 Improved waveforms by means of parallel discharging resistors.

D. ZVS operation of switching arm

Fig.7 shows experimental waveforms of arm voltage and current at steady state condition. The product of voltage and current, i.e. the instantaneous power dissipated in an arm, is also shown. By glancing at these waveforms, it seems that ZVS operation of switching arm is done. However, one switching arm is composed of a main switching device and a diode for reverse voltage blocking. Fig.8 shows the waveforms for each devices, which shows that the inner voltages v_{ds} and v_d of an arm contains abrupt voltage changes. An operating cycle is divided into four modes, mode-a to -d, whose current paths are shown in Fig.9, respectively. Note that the main device is symbolized with a transistor for simplicity here. In the beginning of Mode C, the discharging current spikes of the parasitic capacitors seem to be generating a serious amount of EMI noise. One simple solution is to connect a discharging resistor of 10 k Ω in parallel with every diodes. The improved waveforms are shown in Fig.10. The additional losses dissipated in these resistors is very small so long as the overlap period is short enough as 1 micro second.

E. Effect of sampling period

As previously mentioned, either the cross-mode or the short-mode is selected every sampling period of PDM control. Fig.11 shows the comparison of operating waveforms and current spectrum on HF side for three types of sampling period, i.e. half-cycle, full-cycle and their hybrid cases. Dc side current ripple and ac side voltage amplitude deviation are both minimum in the case of (a) half-cycle sampling. However, this method has a drawback of flowing dc current component into the LC resonant tank circuit as shown in the spectrum. This dc component becomes larger than the fundamental 20 kHz component in the worst case as shown in (a), causing a problem of reactor saturation due to the dc magnetization of iron core. For this reason, the effect of dc magnetization of iron core should be taken into account for the design of reactor for LC tank. On the contrary, in the case of (b) full-cycle sampling, dc current component cannot be observed on HF side at all. In stead, the deviation in amplitude of dc current and link voltage is fairly larger than (a). In the case of (c) hybrid-cycle sampling, in which the short-mode is arranged to be taken every half cycle, these deviation are somewhat improved with remaining no dc current generation on HF side.

From the point of view of minimizing the control error of the dc side current, shorter sampling period is the better. In that sense, half-cycle sampling period is the best choice. But it should be noted that the dc magnetization effect on iron core is not negligible. The hybrid-cycle sampling method may be another choice in the case of no dc magnetization of core is permitted.

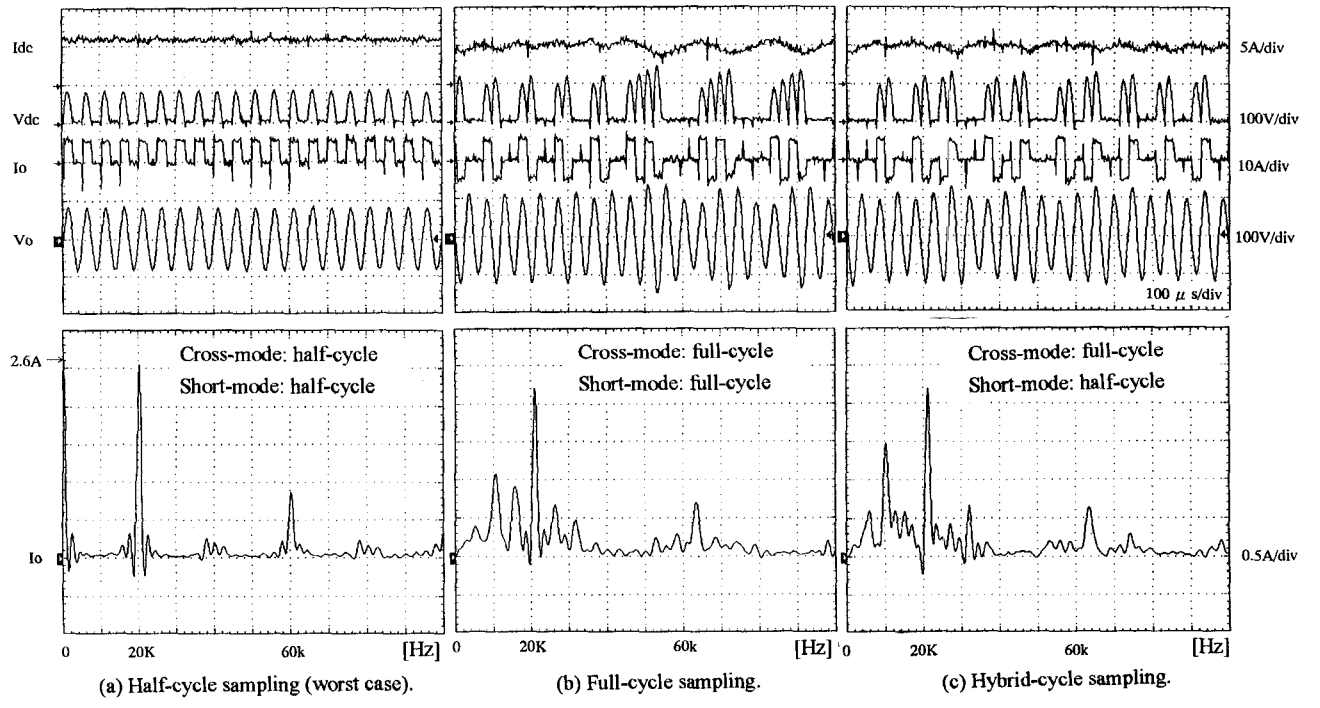

Fig.11 Operating waveforms and current spectram on output ac side.

III. EQUIVALENT MACROSCOPIC MODELING

In analyzing and designing the resonant link power converters, the design of LC tanks and the control parameters to maintain stable oscillation of the tanks during the transient response are the most significant points. However, the instantaneous power flow contains high frequency twice as high as the link frequency component, and it makes the total order of the differential equations of the system higher. It is impossible to apply d-q transformation technique because the resonant link is single-phase circuit. These factors make it difficult to analyze the macroscopic transient power flow of the system. For this reason, a simple mathematical modeling method to know the macroscopic power flow is strongly required for the purpose of optimum control and design. in order to simplify the analysis and control methods in transient operations, a novel probability switching function analysis method suited for resonant type converters is introduced in the following.

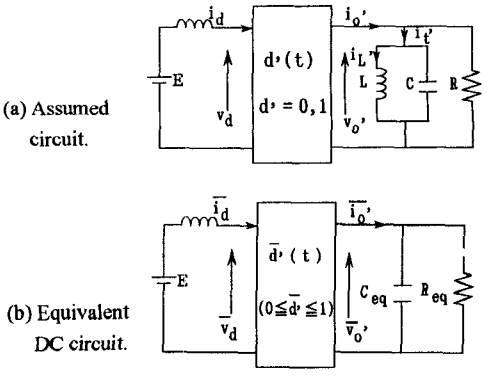

Fig.12 A macroscopic modeling of high frequency link circuit based on probabilistic switching function method.

Fig.12 shows the idea of macroscopic modeling of HF link circuit. In modeling the switching operation of PDM inverter, the converter is described as ON/OFF switching function d(t). For instance, in Fig.3, the cross-mode 1+ and 1- correspond to d=1 and d=-1 , respectively. The short-mode 2+ and 2- are both represented by d=0. The overlap mode is neglected in an ideal condition. Thus, d(t) is a three state function, i.e. d=0, +1,-1. Before deducing the final equivalent circuit, the actual circuit is converted into an assumed circuit whose switching function d'(t) is given by multiplying the original switching function d(t) with sign(vo), where sign(vo) takes 1 or -1 corresponding to the link voltage polarity. Then the link frequency is considered to be high enough, permitting every variables can be treated as "instantaneous average value". Under such assumptions, the switching function is defined as probability whose value is not digital but analog between 1 and 0. Thus, the LC tank circuit and Load resistor can be replaced with equivalent capacitance $C_{eq}=(\pi^2/4)C$ and equivalent load resistance $R_{eq}=(8/\pi^2)R$, respectively.

Fig.13 shows simulation results of transient response by using two methods, ON/OFF switching function method and proposed probabilistic switching function method. The macroscopic behavior simulated with the later method agrees well with the former's one, although the switching ripple is completely neglected. The deduced dc equivalent model is quite useful for modeling and analysis of macroscopic behavior of such resonant converters.

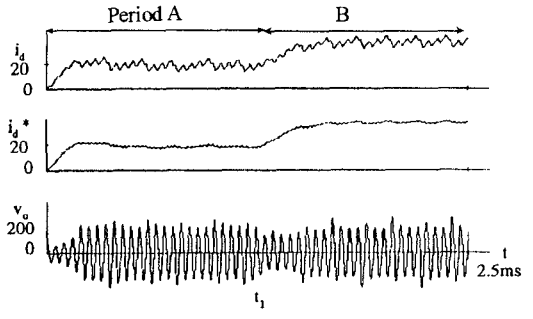

(a) On-off switching function method.

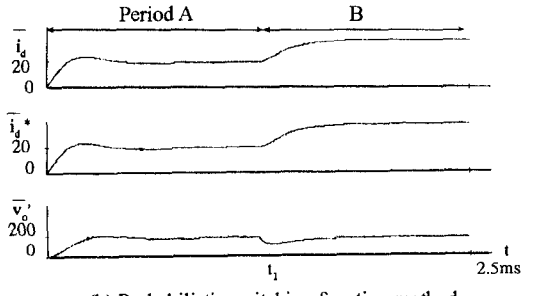

(b) Probabilistic switching function method.

Fig.13 Comparison of a transient response simulated with two methods.

IV. CONCLUSION

This paper discussed on some basic problems in control, analysis and design of a parallel resonant high frequency link system.

1. From a microscopic point of view, following points have been clarified.

- A gate control circuit for stable ZVS PDM operation has been given. It also enables self start-up from stand still.
- Based on experimental results, the parasitic capacitance of diode in switching arm was proved to affect its ZVS characteristics. Practically, a discharging resistor connected in parallel with the diode is effective enough as a countermeasure.
- The half-cycle sampling is excellent in the sense of controllability. However, it should be noted that the dc magnetizing effect of iron core should be taken into account in designing a tank reactor. On the other hand, the dc current component flowing into HF side can be cut completely by using the hybrid-cycle sampling method, though the controllability is worse than half-cycle sampling case .

2. From a macroscopic point of view, an idea of equivalent circuit analysis based on probabilistic switching function has been explained. The simulation results show its validity and usefulness. Application of such a macroscopic model in a closed-loop link voltage control will be treated in the next paper to be presented [7].

ACKNOWLEDGMENT

The authors would like to thank members of the System Engineering Laboratory of Tokyo Institute of Polytechnics, Mr.S.Ishikawa, S.Uemura, M.Hirabuki and M.Inaba for their cooperation in experiment, and Ms.Y.X.Yang for her help in analysis and simulation.

REFERENCES

[1] I.G.Hansen, "Description of a 20 kilo hertz distribution system", 21st IECEC, San Diego (1986)
[2] P.K.Sood et al., "Power conversion distribution system using a high frequency ac link", IEEE Trans. on IA, Vol.IA-24, No.2, pp.288-299 (1988)
[3] P.K.Sood et al., "A versatile power converter for high-frequency link system", IEEE Trans. on PE, Vol.PE-3, No.4, pp.383-390 (1988)
[4] R.L.Hockney et al., "Flywheel energy strage for electro-mechanical actuation system", 26th IECEC Conf. Rec., pp.233-237 (1991)
[5] T.Fukao et al., "Operation limit of HF distribution use cycloconverter and its characteristics on commercial line side ", IEE/Japan Trans. Vol.106-B, No.7, pp.571-578 (1986)
[6] I.Takahashi et al., "A 500Hz power system", IEEE-IAS-1989 Annual Meeting Conf. Rec., p.988 (1989)
[7] M.Matsui et al., "Macroscopic modeling of a parallel resonant link PDM converter and closed-loop control of link voltage", To be presented in IEEE-IAS-1997 Annual Meeting in New Orleans (1997)

NEW DEVELOPMENTS IN RESONANT DC LINK INVERTERS

Deepak Divan Ian Wallace

Soft Switching Technologies Corporation
2224 Evergreen Road #6
Middleton, WI 53562
Tel: 608-836-6552; Fax: 608-836-6553
email: divan@softswitch.com

Abstract - **Soft switching inverters differ significantly from hard switching PWM inverters in the areas of device behavior, modulation methods, design trade-offs, output spectra, and load performance. This paper will outline and discuss the foundations of these differences as well as present substantial new data to show the current status of resonant dc link inverters. This data will cover performance issues such as efficiency, conducted EMI, output THD, suitability for operation with long motor cables, as well as device utilization and rating.**

I. Introduction

Resonant dc link inverters were the first soft switching inverter reported in the literature, and represent the beginning of significant research activity world-wide in this field. In spite of the attention that soft switching inverters have received there have been no commercially available units until recently. This is because, unlike many previous developments in power conversion which tended to be incremental in nature, soft switching inverters represent a major paradigm shift, requiring the development of new design guidelines, new components and new engineering intuition before a cost effective design can be built.

Some of the more significant differences when compared with state of the art 'hard switched' inverters include issues of device rating, device characterization under soft switching conditions, reactive component design, use of discrete pulse versus pulse width modulators, metrics of spectral performance for PWM versus DPM systems, and overall cost of the inverter. This paper attempts to revisit the design concepts embedded in the resonant dc link, and other soft switching inverters.

II. Soft Switching Inverter Classification

Soft switching of power devices can be achieved by either zero voltage or zero current switching. It is typically effected by the use of snubber components to divert switching loss from the device to a reactive component. In hard switched inverter snubbers, the trapped energy is normally dissipated or handled by a separate regenerative converter. Alternatively, the snubbers in a soft switching converter are reset in a lossless manner by intrinsic operation of the converter circuit itself. Soft switching inverters are generally classified into two distinct categories: resonant link and resonant pole inverters. Resonant link inverters tend to use one set of resonant components per inverter, and achieve low loss switching of all its power semiconductors using a common zero voltage (or current) crossing point. Known configurations include the passively clamped and actively clamped resonant dc link inverters (shown in Fig. 1a), and various forms of quasi-resonant dc link inverters [1-3]. Resonant pole inverters, on the other hand, tend to use one set of reactive L-C components per inverter phase. Known forms include the basic resonant pole inverter, the auxiliary resonant commutated pole inverter (shown in Fig. 1b) and various forms of resonant snubber circuits [4,5]. While soft switching circuits can be of both the zero voltage or zero current switching types, and often include both types, this paper will focus on configurations which realize a voltage source inverter function and primarily use zero voltage switching of the main devices.

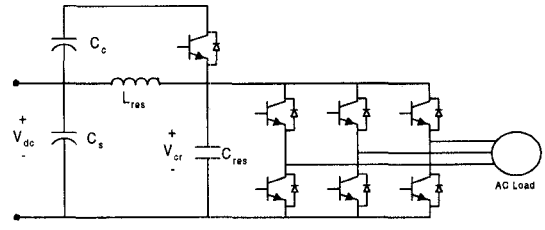

Fig. 1a. Actively clamped resonant dc link inverter.

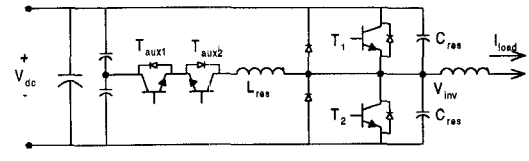

Fig. 1b. One phase of an auxiliary resonant commutated pole inverter.

III. Device Behavior Under Zero Voltage Switching

The behavior of IGBTs under zero voltage switching differs significantly from that under hard switching conditions. This difference needs to be understood and accounted for as one moves to an actual inverter design. In the case of IGBT's, certain anomalous behaviors have been reported including; significant tail current bump due to trapped charge in the device drift region, high temperature

sensitivity of switching loss, a di/dt dependent conduction voltage drop attributed to a conductivity modulation lag effect, parasitic current oscillations with snubber capacitors, and impact of internal device package inductance on device rating [6-8]. The suitability of epitaxial versus non punch through devices for zero voltage switching has also received considerable attention [8,9]. It has also been proposed that new devices which are optimized for soft switching will allow significant improvement in device performance while lowering the cost of the device.

Until such new devices become available, one has to design converters based on commercially available devices. Design trade-offs for hard switching inverters primarily revolve around the issue of conduction versus switching loss. Lower switching frequencies tend to improve device utilization, suggesting that an inverter operating frequency be the lowest that would be suitable for a given application. The choice is considerably more complex in a soft switching inverter. In a zero voltage switching environment, the turn-on losses for a device can be assumed to be very low. Conduction losses include the normal conduction voltage drop, as well as a di/dt dependent component. The turn off loss is rather low at low currents, but is designed to normally be the dominant switching loss component at rated current conditions.

A. IGBT Loss Mechanisms under Soft Switching

The dominant loss mechanisms under soft switching are:

a. Turn off loss due to extended tail current
b. Turn on loss due to dynamic saturation
c. Conduction loss related to device di/dt
d. Conduction loss (Vce *Ic)

While these loss mechanisms have been reported on in the literature, practically, it is the turn off and conduction loss which dominate typical designs [6,7].

The waveforms depicting a hard switched turn off are shown in Fig. 2. Notice that significant switching loss is incurred by the simultaneous presence of current and voltage on the device. Fig. 3 shows the soft switching turn off wave forms with a capactior of 300ηF across the device and has two distinct stages. Initially, the current falls rapidly due to the turn off of the internal MOSFET, while the voltage is still low. Then, due to the trapped charge in the n- drift region, a tail current persists. The tail bump, especially at elevated temperatures, can contribute significant switching losses since it is present while the voltage is non-zero.

The relationship between hard and soft switching losses at a junction temperature of 125°C is presented in Fig. 4. As expected under soft switching, lower losses are achieved with a larger capactior and lower dv/dt across the device. With the right choice of capacitance, significant improvements over hard switching can be achieved.

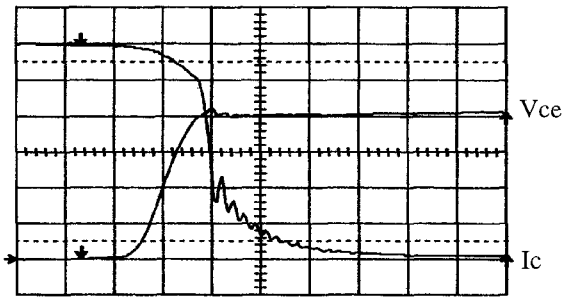

Fig. 2. Hard switching turn off waveforms.
Vce = 200 V/div, Ic = 50 A/div, 0.2 μsec/div, 125°C

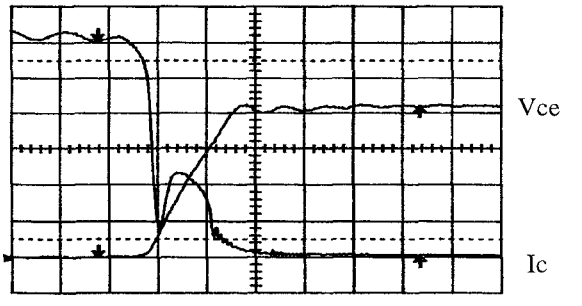

Fig. 3. Soft switching turn off waveforms.
Vce = 200 V/div, Ic = 50 A/div, 0.5 μsec/div, 125°C, Cs = 300nF

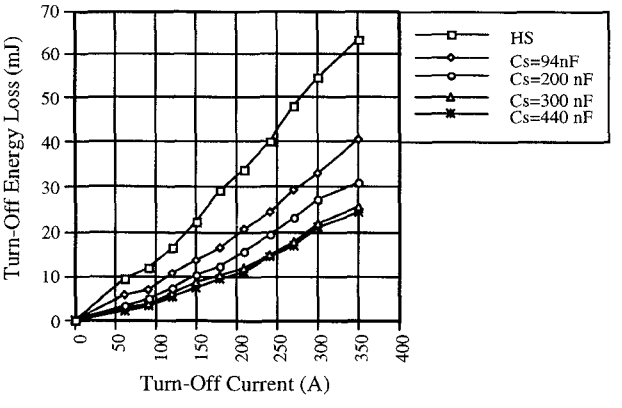

Fig. 4. Zero voltage turn off losses as a function of capacitance and current @ 125°C.

It should be noted that available IGBT models (in simulators such as SABER) are quite good at predicting device behavior under hard switching conditions, but have difficulty predicting behavior of the devices under soft switching conditions. As such, the most accurate loss model for soft switching devices uses measured loss data. In-circuit device losses are then calculated by superimposing the operating characteristics of the inverter obtained via simulation with the measured device losses under appropriate soft switching conditions. Approximate methods for computing device losses in a resonant dc link inverter have been previously discussed and provide adequate accuracy for basic design [10].

B. Device Utilization Comparison

The benefits, achievable under soft switching, can be shown in a simple example. Since the turn off energy dissipated in a device is less under soft switching, it can be operated at higher switching frequencies and be subjected to the same losses as a hard switched device. Alternatively, the devices utilization may be increased by reducing the switching frequency and increasing the forward current while maintaining the same total loss. These two scenarios, of trading off switching an conduction losses, are outlined in this example, for which it is assumed that a single IGBT is turning on and off 200 amps with a 50% duty cycle at 125°C.

A 400A, 1200V device (Powerex CM400HA-24H) under such conditions has conduction losses of 170 watts. The hard switched turn on and turn off energy totals 60mJ, resulting in an overall loss of 470 watts when switched at 5kHz. Under zero voltage switching, the turn on loss is eliminated, while the turn off loss is reduced to 12mJ per cycle (using Fig. 4). If the conduction loss remains unchanged, then the device can switch at 25 kHz before it reaches the same total loss of 470 watts. Maximizing the effective switching frequency also results in smallest size of reactive components and best spectral and dynamic performance. Alternatively, the switching frequency can be constrained to a lower value, say 10 kHz, using the remaining thermal margin to increase the current handled by the device to 300 amps, and thus its effective power rating. There is little to be gained in this case by choosing a switching frequency which limits device losses to insignificant values if the thermal margin is not fully utilized.

C. Converter Design Trade-offs

The design of a complete soft switching converter introduces even more trade-offs. Examining the actively clamped resonant dc link inverter as a case in point, where the trade-offs between reactive component selection and device losses has been extensively reported [10-12]. The choice of the resonant capacitor is typically governed by the worst case dv/dt targeted, with its associated peak device switching loss. Choice of the resonant inductor value is then based on an iterative process of trading off the switching frequency with the total device loss. Other parameters that govern the choice of the link resonant frequency includes the peak load current, the voltage at which the active clamp operates and the di/dt conduction losses of the clamp device. With these design trade-offs made correctly, the 50-200 kW soft switching inverter can have a significant efficiency advantage over the hard switched inverter.

A typical design of a 480 volt input, 165 kW resonant dc link inverter operates with a link resonant frequency of approximately 65 kHz, and allows 200 Amperes rms continuous on the output with 200 Ampere 1200 volt dual IGBT modules for the main devices. This is 30 to 50% above the limit attainable with conventional hard switching inverters operating at reasonable switching frequencies of 8 to 16 kHz. Under these operating conditions, the inverter device losses are predominantly conduction losses, as can be seen from a measured efficiency for the inverter section plus an output LC filter, in a grid connected application, of 98% at 100 kW. At a 10% load point, the measured efficiency was still 93%, as shown in Fig. 5.

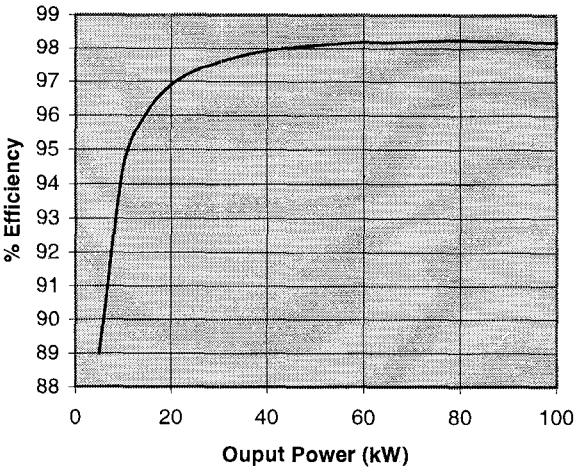

Fig. 5. Measured efficiency of an actively clamped resonant dc link inverter with LC filter.

IV. Modulation and Control

A significant level of misunderstanding in the literature concerns the performance of resonant link type systems against PWM type systems. PWM strategies used with hard switching inverters are based on averaging concepts, wherein the average of a PWM waveform over a carrier cycle equals the value of the reference signal. Most implementations, ranging from sine-triangle modulation to sophisticated space vector modulation schemes are all based on the above principle. As pulse widths can, at least in principle, be specified with infinite precision, it is possible to visualize inverter output waveforms in which the spectral content is precisely specified. On the other hand, soft switching inverters may use schemes such as sigma-delta modulation or quasi-pwm, depending on their ability to the control the pulse widths. These methods produce different type of voltage spectra than a PWM algorithm and need to be analyzed in a different manner. The performance of these different modulation methods are discussed in this section.

A. Modulation Techniques

There are two distinct types of modulation strategies possible with soft switching inverters. Resonant link inverters, which need to synchronize device switching with zero crossing instances, are controlled by sigma-delta modulation. On the other hand, resonant pole and quasi-

resonant inverters may use quasi-pwm. Here, the pulse width is controlled to provide the required volt-seconds and zero voltage switching (via a resonant transition) is still achieved.

1) Sigma-Delta Modulation

A sigma-delta modulator operates as a closed loop system and actively matches the volt-seconds on the inverter output to the reference. Figure 6 shows a block diagram of the modulator for one phase of a three phase resonant dc link inverter. The error between the voltage command and feedback is integrated and then quantized. The gate drive signals are updated with the new switch states only at the zero crossing instances of V_{cr}.

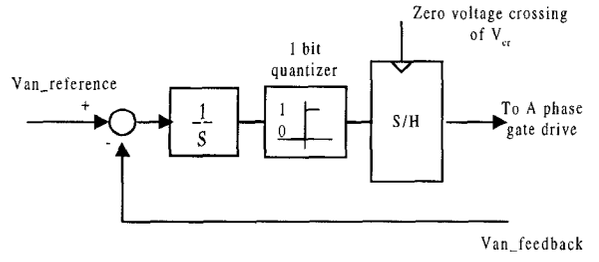

Fig. 6. A sigma delta modulator.

Sigma-delta modulator principles are well known in communication literature and have been adapted for use in the power electronics systems [13]. Advanced, higher order modulators have shown further improvement in inverter spectral performance. Experimental results indicate that, based on the performance metric used to compare PWM and discrete pulse strategies, a ratio of sampling frequency to a carrier frequency of 5-7 gives systems with comparable performance.

2) Quasi-PWM

Resonant pole type inverters, which allow control of the pulse width on individual phases, seem to offer the best of all worlds; control of inverter output pulse widths, low switching loss and high switching frequency. However, this can only be achieve with a reduction in dc bus utilization.

Device losses are reduced by the snubber capacitors that provide a zero voltage switching environment. The capacitors are chosen, as discussed in the previous section, to provide a switching loss reduction so that the frequency can be raised. However, the reset of the capacitor is accomplished by a resonant pulse. The width of the resonant pulse, as well as the slope of a turn-off transition is dependent on the load current, and on the overall control strategy. Figure 7 shows the inverter output waveform for a typical auxiliary resonant commutated pole inverter (ARCP). The minimum dwell time imposed by the reset cycle and slope variability on the output, limit the precision with which the inverter output spectral content can be specified. For instance, if the resonant pulse duration is 10μs for an inverter switching frequency of 20 kHz, then a duty cycle greater than 0.8 or lower than 0.2 cannot be obtained without resorting to pulse dropping or losing spectral purity. This represents a significant constraint on the dc bus utilization, if spectral purity is important.

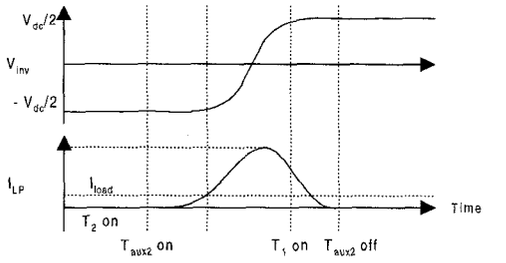

Fig. 7. Inverter output voltage (Vinv).

Quasi-resonant dc link inverters represent a hybrid between pure resonant dc link inverters and PWM inverters [3,14]. In such inverters, an example of which is shown in Fig. 8, the pulse width of Vcr is made variable above a minimum value. For this inverter, conduction through D1 and S2 will extend the pulse width of Vcr [14]. The idea is to use the control available over the pulse width to obtain the desired spectral purity. These converters have less degrees of freedom than their resonant pole counterparts and are thus more constrained in obtaining a specified spectrum.

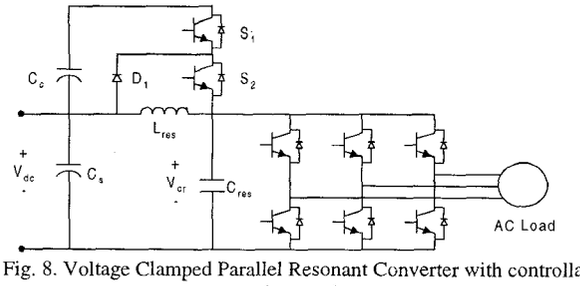

Fig. 8. Voltage Clamped Parallel Resonant Converter with controllable duty cycle.

If only one pulse width is variable, then it is difficult to control a three phase three wire output completely. If two pulse widths are independently controllable, it is possible, at least in principle, to control the output space vector to a desired value However, if the frequency is to be maintained constant, then three pulse widths need to be controlled independently.

It is seen as an advantage that the quasi resonant inverter can be used in conjunction with space vector-PWM, as the expected benefits include both the high efficiency of zero-voltage switching, and a familiar spectral performance. However, full bus utilization and superior spectral performance (high switching frequencies) are not attainable simultaneously. Given a minumum pulse width of 15usec, and assuming that three voltage vectors (two active and one zero state) make up one 16kHz PWM cycle, Fig. 9a shows the voltage vectors which are achievable. Notice that the full bus utilization is not attainable because of the minimum zero state vector (as with the resonant pole

inverter). Also, as you transition from one state to another, there is a region of unattainable vectors. Thus, the spectral performance of this modulation scheme will be degraded from a pure PWM spectrum. Figure 9b shows the voltage vectors achievable with a lower switching frequency of 4kHz. While more voltage vectors are attainable, is not necessary to invoke soft switching of the devices for this switching frequency.

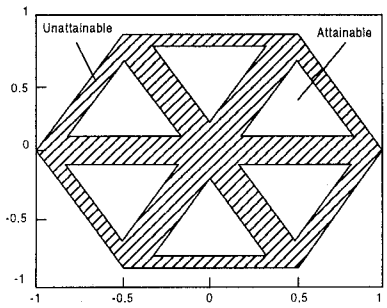

Fig. 9a. Voltage vectors with a space vector modulator. Tmin = 15μsec, fs = 16kHz

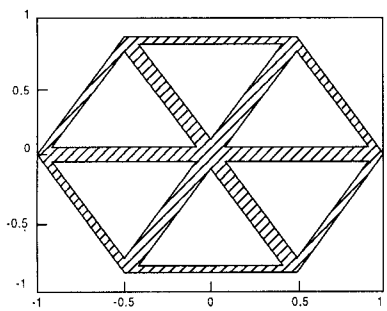

Fig. 9b. Voltage vectors with a space vector modulator.Tmin = 15μsec, fs = 4kHz

Further, with the same devices and resonant components, it would be possible to switch a resonant link inverter at approximately 65 kHz, at which operating point its spectral performance would be much better than that of the 'PWM inverter' switching at 4 kHz. This simplified analysis demonstrates that quasi-resonant dc link inverters typically cannot match the performance of the more basic resonant dc link inverters. Further, the simplicity and lower parts count of the basic resonant dc link circuit also makes that a more cost effective solution.

C. Spectral Evaluation

Finally, it is also important to consider the metrics of spectral measurement that are used in power electronics and drives. Historically, power conversion waveforms for line commutated converters were stationary in nature, as all switching was synchronized to the line frequency. Such waveforms featured stationary line spectra at harmonics of the line frequency. In the area of PWM inverters, early inverters used synchronous techniques, wherein the carrier frequency was a multiple of the fundamental frequency. This still yielded stationary line spectra at harmonics of the fundamental frequency. Under such conditions, the total spectral energy contained in the waveform could be obtained by an rms summation of individual harmonic components. Given that the non-fundamental energy was primarily concentrated in harmonics of the fundamental frequency, it also made sense to consider that total harmonic distortion was an important parameter. As the industry moved to higher frequency asynchronous techniques, the use of a Bessel function approximation allowed us to continue using a line spectra based concept to analyze PWM waveforms. Non-stationary regulators and modulators such as hysteritic current regulators were considered an oddity, and were not seriously examined in terms of spectral performance.

It is important to understand what aspect of spectral performance is important in a particular application. For instance in motor drives, motor loss is governed by the rms current in the machine, if spectral dependence of the winding resistance is ignored. In the case of a stationary waveform, the rms summation of line spectral components gives us the correct value of the loss producing spectral current. In the case of a non-stationary waveform such as that produced by a resonant link inverter, a line spectrum as produced by a DFT analyzer has no meaning because it assumes that the waveform repeats itself, i.e. is stationary. A much more meaningful property is the spectral power density of the current over the frequency range of interest, which is obtained by averaging the spectrum produced by the DFT analyzer. Similarly, other parameters of interest include a signal to noise ratio (S/N) as opposed to a THD based on harmonic levels. Similar attributes have been used to judge the fidelity of modulation processes in communications literature, and seem to be more appropriate for many problems in the field of power conversion as well [13]. Figure 10 shows the spectral power density of the output current for a 165 kW resonant dc link inverter with a link frequency of approximately 65 kHz, and shows that the S/N ratio is >40 dB for a frequency range of up to 10 kHz. Under these operating conditions, an inverter control bandwidth of >2 kHz has been experimentally measured. Higher order modulators can improve the spectral performance substantially.

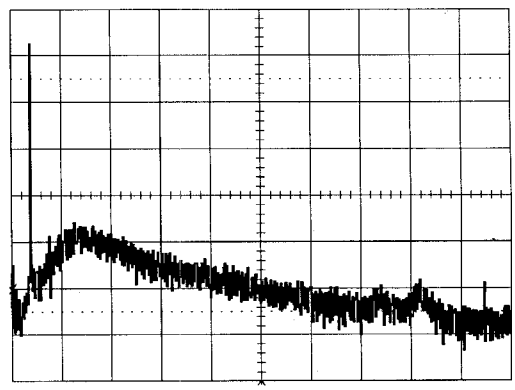

Fig. 10. Output current of a resonant dc link inverter. 80 Amps@ 2kHz with 150μH load inductance. 10 dB/div, 5 kHz/div

V. Load and Line Side Behavior of Resonant DC Link Inverters

A. Motor Insulation Issues

One of the important benefits that accrue from the use of zero voltage switching inverter circuits is the low dv/dt that a capacitive snubber yields. The dv/dt for hard switched IGBT inverters approaches 5-10,000 volts/μs, and causes substantial problems in motor drives and other inverter applications. In particular for motor drives, the high dv/dt causes motor winding insulation failure due to high inter-turn voltages [15]. When a long cable is used to connect the inverter to the motor, reflections cause even higher voltages at the motor end. The seriousness of the problem is illustrated by the fact that major motor manufacturers in the US have moved to use a higher insulation grade inverter spike resistant (ISR) wire in all motors manufactured by them. Further, many drive manufacturers now offer motor termination networks to absorb energy due to voltage reflections.

The use of soft switching inverters can reduce the dv/dt to less than 500 volts/μs, a level specified for general purpose motors. The resonant dc link inverter, for instance, has dv/dt levels of 200-400 volts/us.

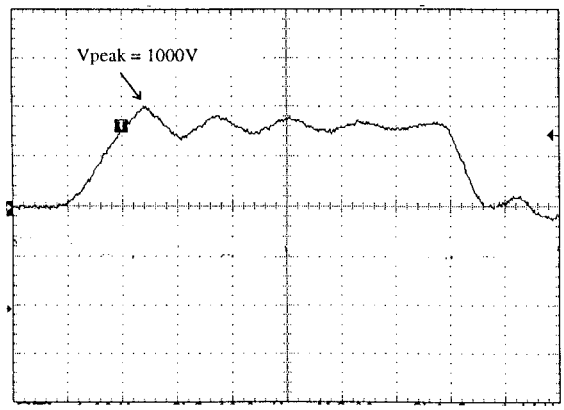

Fig. 11a. Motor terminal voltage with 100 meters cable and rdcl inverter (Vcr = 840V). $V_{line\text{-}line}$: 500V/div, 2.0 μsecs/div

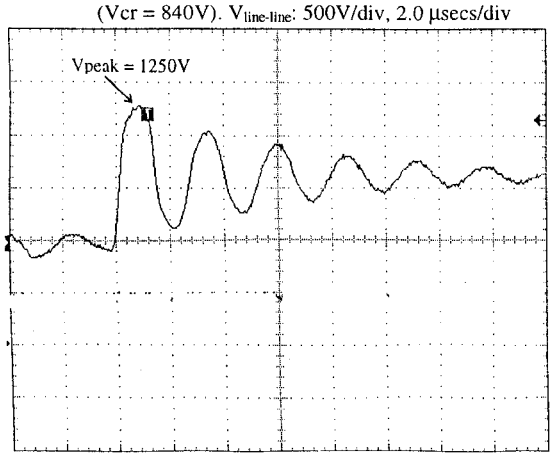

Fig. 11b. Motor terminal voltage with 100 meters cable and a hard switched inverter (Vdc = 650V). $V_{line\text{-}line}$: 500V/div, 2.0 μsecs/div

This restricts the voltage overshoot to less than 19% with 100 meters of cable between inverter and motor, as can be seen from Fig 11a. This may be contrasted to a comparably rated hard switched inverter tested under identical conditions, where the peak overshoot measured was 91% above the supply voltage (see Fig. 11b). The percent overshoot is an important parameter because it contains the higher frequencies that get unevenly divided across the machine coils. Based on a distributed high frequency model of the induction machine, the higher frequency content in the motor terminal waveform is unevenly distributed across the first few turns of the machine phase winding [17]. A special induction machine, instrumented with search coils in the first 26 coils of one phase, was used to compare the distribution of inter-turn voltages for a hard switching and a resonant dc link inverter. Figure 12a. depicts the spread of voltages for a hard switching inverter, while Fig. 12b shows the voltages for the resonant dc link circuit. The peak voltage across turns was measured to be 412 volts for the hard switching case, and 98 volts for the soft switching case, a substantial improvement [18].

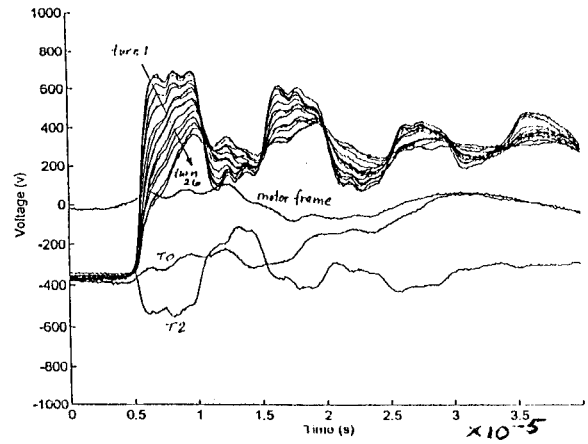

Fig. 12a. Coil voltage for 100 meters cable and hard switched inverter.

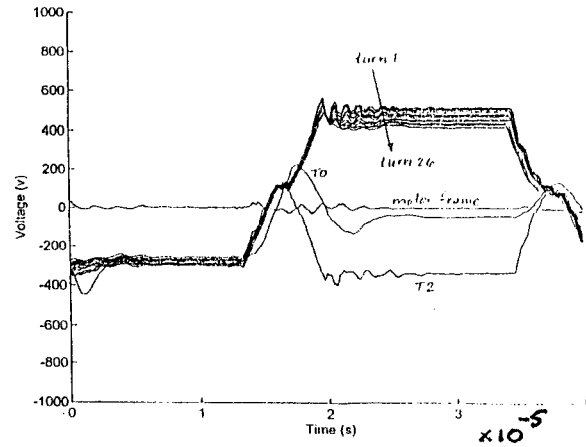

Fig. 12b. Coil voltage for 100 meters cable and rdcl inverter.

Another important insulation factor concerns the peak voltage from coil to motor stator iron (ground) for the two inverters. In a separate test, the peak voltage for the hard switched inverter was measured to be 900 volts for the

hard switching inverter, versus 560 volts for the soft switching inverter, when operated with 100 meters of cable. All tests comparing hard and soft switching inverters were run in cooperation with major motor and drive manufacturers. The voltage stress and voltage distribution tests indicate that soft switching inverters such as the resonant dc link inverters do not require to operate with inverter grade motors, and can in fact operate with general purpose motors. In addition to other traditional drive applications, this feature also makes them uniquely suitable for use in retrofit applications where existing fixed speed motors are converted for adjustable speed use.

B. EMI Issues

The other aspect of soft switching inverters that has received much attention is the possibility of realizing low conducted EMI levels, as compared with their hard switching counterparts. While it has been suggested that soft switching inverters inherently generate lower levels of EMI, there has not been sufficient proof of this reported in the literature. In fact, it has been suggested that PWM inverters switching at 10 kHz have lower levels of conducted EMI in the 150 kHz to 30 MHz frequency band specified by EN 1000, than resonant dc link inverters switching at 70 kHz. It is our contention that it is easier to design resonant dc link inverters to meet EMI norms because there is not much noise generated in the 1 to 30 MHz frequency range, where preventing multi-path signal propagation is difficult. Figures 13 and 14 depict a commercial hard switching and a commercial soft switching resonant dc link inverter tested for conducted EMI at the UL Laboratory in Chicago. The hard switching inverter is shown under identical test conditions as the soft switching inverter. The hard switching inverter was operated both with and without a Schaffner EMI filter, and could not meet the EMI specification without the input filter. It is seen that the resonant dc link circuit shows significantly lower EMI and offers the promise of being able to meet European EMI norms without requiring an input EMI filter.

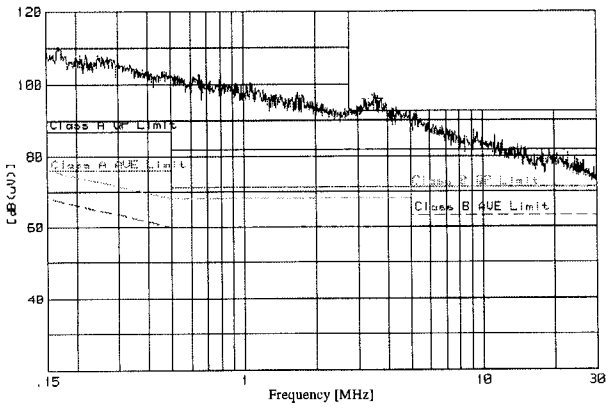

Fig. 13a Conducted EMI results for hard switched inverter.

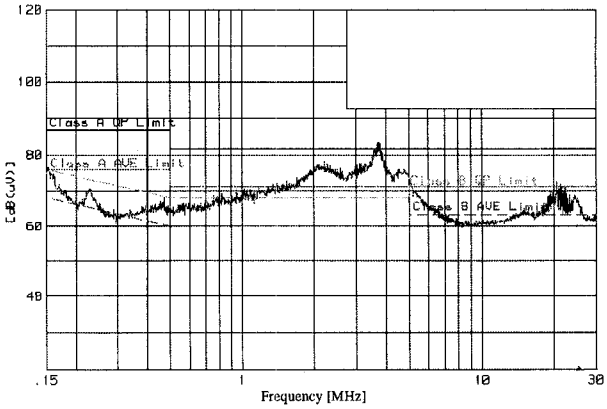

Fig. 13b Conducted EMI results for hard switched inverter with Schaffner EMI filter.

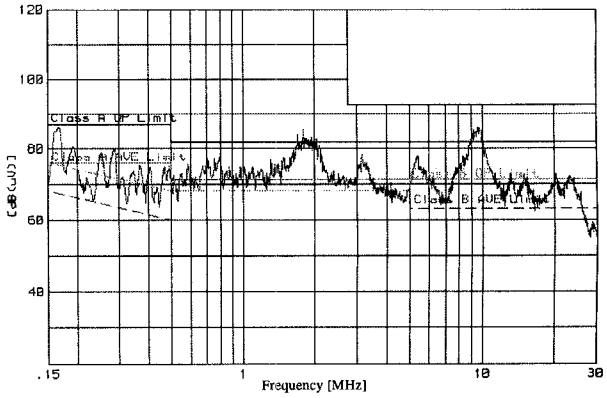

Fig. 14. Conducted EMI results for an resonant dc link inverter.

VI. Conclusions

This paper has presented substantial new data to show the current status of soft switching inverters, in particular resonant dc link inverters. Such inverters are now commercially available at ratings of up to 200 kVA at 480 volts. These inverters feature unprecedented device current rating utilization, giving for instance 200 Amperes rms continuous load current with 200 A/1200 V dual IGBTs. At the same time, the 65 kHz link frequency results in current THD levels of 1-2% in the load, control bandwidth of approximately 2 kHz, and gives very low acoustic noise. Inverter efficiency has been measured at 98% from full load to approximately half load, decreasing to 93% at 10% load. The low dv/dt of 200-300 volts/us minimizes voltage overshoot on cables of up to 100 meters, and also allows the use of general purpose motors by removing the danger of motor winding insulation failure. The inverter has also been tested and shown to have low EMI levels compared to similarly rated hard switched inverters.

Soft switching inverters still represent a nascent and emerging technology. It seems likely that soft switching inverters will ultimately displace hard switching inverters, initiating the next power electronics revolution. Propelling

this revolution will be a new generation of power devices optimized for zero voltage switching conditions. Such devices promise lower conduction loss, lower switching loss and faster switching, as a result of needing lower safe operating area. The rate at which soft switching inverter technology will appear in the market is determined by several key factors including competitive forces, problems faced presently in the field, and difficulty of designing competitive products based on this technology. It is felt that this product will take hold during the next 2-4 years in the global market.

VII. References

[1] Y. Murai and T. A. Lipo, "High Frequency Series Resonant DC Link Power Conversion, " IEEE-IAS Conference Record, 1988, pp., 772-779.

[2] D. M. Divan, "The Resonant DC Link Inverter - A New Concept in Static Power Conversion," IEEE-IAS Conference Record, 1986, pp., 648-656.

[3] S. Chen, T. A. Lipo, "A Passively Clamped Quasi Resonant DC Link Inverter," IEEE-IAS Conference Record, 1994, pp., 841-848.

[4] J. S. Lai et. Al, "A Novel Resonant Snubber Based Inverter," IEEE Applied Power Electronics Conference, Mar. 1995, pp. 797-803.

[5] R. W. De Doncker and J. P. Lyons, "The Auxiliary Resonant Commutated Pole Inverter," IEEE-IAS Conference Record, 1990, pp., 1228-1235.

[6] A. Kurnia, O. Stielau, G. Venkataramanan, D. M. Divan, "Loss Mechanisms in IGBT's Under Zero Voltage Switching", IEEE-PESC Conference Record, 1992, pp. 1011-1018.

[7] H. H. Li, H. Wiegman, N. Kutkut, A. Kurnia, D. M. Divan, K. Shenai, "High Temperature Characteristics of IGBTs in Soft and Hard-Switching Converters," IEEE-APEC Conference Record, 1995, pp. 733-735.

[8] M. Trivedi, K. Shenai, "Modeling the Turn-Off of IGBTs in Hard and Soft-Switching Applications," IEEE-APEC Conference Record, 1997, pp.156-160.

[9] A. El-Asser, M. J. Schutten, V. Vlatkovic and D. A. Torrey, "Switching losses of IGBTs under zero-voltage and zero-current switching," IEEE Power Electronics Specialists Conference 1996.

[10] A. Kurnia, H. Cherradi, D. M. Divan, "Impact of IGBT Behavior on Design Optimization of Soft Switching Inverter Topologies," IEEE-IAS Conference Record 1993, pp. 807-813.

[11] R. W. De Doncker, G. Venkataramanan, D. Divan, "Design Methodologies for Soft Switching Inverters," IEEE-IAS Conference Record 1987, pp.152-160.

[12] A. Mertens, D.M. Divan, "A High Frequency Resonant DC Link Inverter Using IGBTs," IPEC-Tokyo 1990, pp.152-160.

[13] G. Luckjiff, I. Dobson, D. Divan, "Interpolative Sigma Delta Modulators for High Frequency Power Electronic Applications," IEEE-PESC Conference Record 1995, pp.444-449.

[14] H. K. Lauw, R. S. Zedwick, "Voltage Clamped Parallel Resonant Converter with Controllable Duty Cycle," United States Patent Number 5,559,685, September 24, 1996.

[15] E. Person, "Transient Effects in Application of PWM Inverters to Induction Motors," IEEE Transactions on Industry Applications, VOL. 28, NO. 5, Sept/Oct 1992, P1095.

[16] R. Kerkman, D. Leggate, G. Skibinski, "Interaction of Drive Modulation and Cable Parameters an AC Motor Transients," IEEE-IAS Conference Record, 1996, pp.143-152.

[17] D. Hyypio, "Simulation of Cable and Winding Response to Steep Fronted Voltage Waves", IEEE-IAS Conf. Rec. 1995. pp800-806.

[18] Coil voltage measurement data supplied by Maraton Electric.

Improvement of Performance of a Series Resonant DC Link PWM Inverter

Hiroki Ishikawa, Yoshihiro Murai
Gifu University
1 - 1, Yanagido, Gifu 501-11, Japan
Fax: +81-58-230-1894, Phone: +81-58-293-2708
E-mail: ishikawa@cc.gifu-u.ac.jp

Abstract **- This paper proposes a series resonant dc link PWM inverter which is improved for better performance. The prototype inverter had the advantage of a small dc inductance and output capacitors. At smaller dc inductance, it is important that the energy at dc inductance is controlled to be constant for better output control. Therefore, in this paper, the inverter is improved for better output performance and efficiency. As the result, the losses becomes smaller. This paper presents the design of improved inverter, the experimental results and the characteristics of the losses.**

I. INTRODUCTION

The resonant conversion system can be operated at higher switching frequency with high efficiency because of no switching losses theoretically. And EMI (electro-magnetic interference) problems are solved easily by using smooth voltage (or current) pulses. [1]

The voltage resonant conversion system is often studied and analyzed in detail because of easy circuit configuration and design for the small-sized system. However, the electrolytic capacitor at dc link has relatively shorter life-time, requires the high frequency quality, and the size is large. [2][3]

The current resonant conversion system is characterized by no dead-time distortion, the small high frequency components at the output, and so on. The system without the electrolytic capacitor has no problem about the life-time. However, the system is more heavy and on-state loss in dc inductance is larger because of large dc inductance. [4]

In the past, the output of resonant conversion system was controlled by PDM (pulse density modulation). In this way, the current or voltage stresses of the switching devices were higher because the pulse peak was higher. Recently, the pulse peak is controlled low by the clamped circuit or PWM (pulse width modulation) using quasi resonance. [5][6]

We presented a series resonant dc link PWM inverter. [7] This inverter has a small-sized dc inductance and the output capacitors at fixed pulse frequency. Though it is more important that the energy in dc inductance is kept to be constant, the weight of the system becomes light. The peak of the current pulse becomes lower because of the flat-topped current pulse using quasi resonance. However, the voltage of the resonant capacitor must be inverted for stable circuit operation, and the turn-off time of the switching devices limited the pulse frequency. We improved the series resonant dc link PWM inverter to solve the problems. As the result, the improved inverter can make the efficiency higher. This paper presents the design, the experimental result, and the loss characteristics of the improved inverter.

II. SERIES RESONANT DC LINK PWM INVERTER SYSTEM

The prototype inverter is shown in Fig. 1, and the improved inverter is shown in Fig. 2. E is dc source, and L_d is dc inductance which is tightly coupled with the inductance L_f. The inductance L_0, the thyristor Th_0 and L_f control the energy W_{LD} in L_d and L_f. If W_{LD} becomes larger, the feed-back current i_f flows to E through the diode D_f to reduce W_{LD}. If W_{LD} becomes smaller, Th_0 turns on and the loop current i_{d0} flows to keep W_{LD} constant. The capacitor C_0 and the inductance L_1 make up a series resonant circuit to make the main current pulse i_s off. The output thyristors Th_L distributes i_s to three phases. The output capacitors C_L filter the high frequency components in i_s. When C_0 is charged, the thyristors Th_1, Th_2, Th_3 and Th_4 are selected automatically by the polarity of the voltage of C_0. Therefore, the voltage v_{C0} of C_0 need not to invert, the control of the resonant circuit becomes easier, and the pulse frequency is not limited by the turn-off time of the switching devices.

III. THE OPERATION OF INVERTER

The black thyristors Th_a^+ and Th_c^- are initially on, i_s is flowing, and C_0 is charged as in Fig. 2. The switching time charts are shown in Fig. 3, and the waveforms of i_d, i_s, v_{C0} and i_f are shown in Fig. 4.

Mode 1: In order to stop i_s, Th_1, Th_2, Th_3 and Th_4 are fired. Th_2 and Th_3 are off because the voltages across Th_2 and Th_3 are reverse-biased. Therefore, Th_1 and Th_4 turn on. The resonant current by C_0 and L_1 starts flowing in a direction opposite to i_s, i_s is reduced. When i_s becomes zero, Th_a^+ and Th_c^- are off.

Mode 2: C_0 is charged to left side plus until v_{C0} becomes a

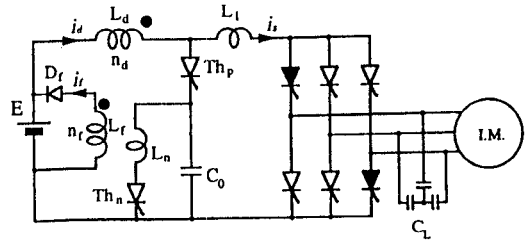

Fig. 1 Prototype inverter.

certain level. When v_{C0} reaches to the level, D_f turns on, and the feed-back current i_f starts flowing. The details about the level will be described later.

Mode 3: When i_f starts flowing, the current i_d in L_d dissipate rapidly. At last, i_d becomes zero, and Th_1 and Th_4 turn off.

Mode 4: i_f feeds back the surplus W_{LD} to E. When i_f is reduced to a certain level, Th_0 turns on and the current i_{d0} in L_0 flows. W_{LD} is kept to be constant.

Mode 5: The black thyristors turn on again, and i_{d0} is reduced. When i_{d0} becomes zero, Th_0 turns off.

The improved inverter operate repetitively from Mode 1 to Mode 5. Though v_{C0} becomes the opposite polarity as in Fig. 2, it is no problem because Th_1 and Th_4 become off, and Th_2 and Th_3 turn on at Mode 1 of the next cycle. At starting mode, either Th_1 and Th_4, or Th_2 and Th_3 turn on and C_0 is charged.

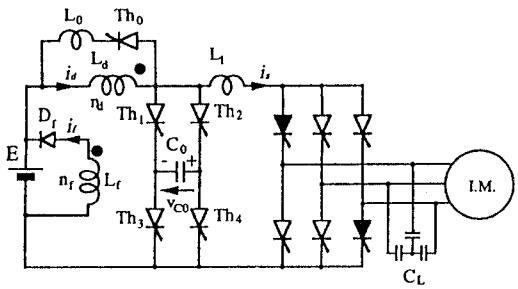

Fig. 2 Series resonant dc link PWM inverter.

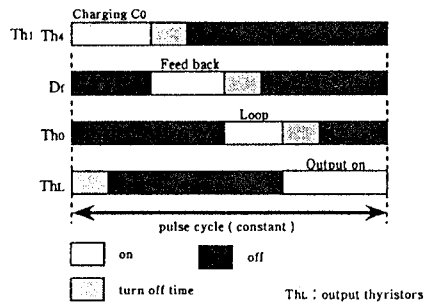

Fig. 3 Swiching time charts.

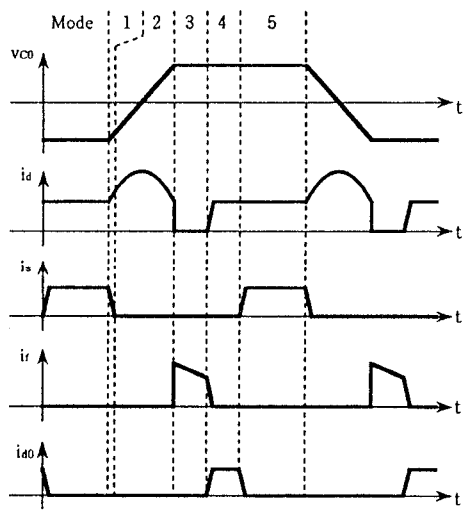

Fig. 4 Waveforms of current and voltage.

IV. Design of the Inverter

For the stable operation of the improved inverter, it is the point that the switching devices damage by v_{C0}, which becomes the highest voltage of the system, are avoided, and i_s turns off. In this section, the inverter design to operate stably and safely is described.

1) The Selection of the Switching Devices by v_{C0}: The equivalent circuit at Mode 2 is shown in Fig. 5. The voltage equations are expressed as follows:

$$E = L_d \frac{di_d}{dt} - M\frac{di_f}{dt} + \frac{1}{C_0}\int i_d dt \tag{1}$$

$$E = L_f \frac{di_f}{dt} - M\frac{di_d}{dt} \tag{2}$$

$$M = k\sqrt{L_d L_f} \tag{3}$$

where M is the mutual inductance of L_d and L_f, and k is the coefficient of coupling of them. When i_f starts flowing, v_{C0} can be changed from (1), (2) and (3) as follows:

$$\begin{aligned} v_{C0} &= \frac{1}{C_0}\int i_d dt \\ &= E - L_d\frac{di_d}{dt} + M\frac{di_f}{dt} \\ &= E\left(1+\frac{M}{L_f}\right) + \left(\frac{M^2}{L_f} - L_d\right)\frac{di_d}{dt} \\ &= E\left(1+k\sqrt{\frac{L_d}{L_f}}\right) + L_d\left(k^2-1\right)\frac{di_d}{dt}. \end{aligned} \tag{4}$$

If k = 1, (4) can be changed from (3) as follows:

$$\begin{aligned} v_{C0} &= E\left(1+\sqrt{\frac{L_d}{L_f}}\right) \\ &= E\left(1+\frac{n_d}{n_f}\right) \end{aligned} \tag{5}$$

where n_d is turns of L_d, n_f is turns of L_f. When (5) satisfies as follows:

$$E = 200\ [V] \tag{6}$$

$$\text{the turns ratio of } L_d \text{ to } L_f \quad n_d : n_f = 1 : 1, \tag{7}$$

v_{C0} equals to 400 [V] from (5).

The reverse voltages V_r of Th_2 and Th_3 become the maximum at Mode 1. If Th_1 and Th_4 turn on, the equivalent circuit at Mode 1 including off-thyristors is shown in Fig. 6. For easier design of the resonant circuit, the output is converted into the single phase circuit. The output voltage is converted into equivalent dc supply because C_L is much larger than C_0, and Mode 1 is very short time. Therefore, $V_r = v_{c0} =$ 400 [V] at Mode 1 from (5).

However, v_{C0} becomes a little higher than 400 [V] from (4) because k<1 at real system. Therefore, the reverse voltages become a little higher (about 10-30 volts).

2) L_1 and C_0 in the Resonant Circuit Part: The equivalent circuit at Mode 1 is shown in Fig. 7. The output voltage is

converted into equivalent dc supply. The voltage equations at Mode 1 are expressed as follows:

$$E = L_d \frac{di_d}{dt} + L_1 \frac{di_s}{dt} + V_{CL} \tag{8}$$

$$E = L_d \frac{di_d}{dt} + \frac{1}{C_0}\int (i_d - i_s)dt. \tag{9}$$

From (8) and (9), i_s is given by

$$i_s = \left(\frac{V_{C0}(0)(L_d + L_1) - L_d V_{CL} - L_1 E}{L_1(L_d + L_1)}\right)\sqrt{\frac{C_0 L_d L_1}{L_d + L_1}} \times \sin\sqrt{\frac{L_d + L_1}{C_0 L_d L_1}}t + \frac{E - V_{CL}}{L_d + L_1}t + i_s(0) \tag{10}$$

where $i_s(0)$ is i_s and $V_{C0}(0)$ is v_{C0} just before Mode 1. In order to cut i_s off, i_s must become less than zero at the following time from (10),

$$t = \frac{\pi}{2}\sqrt{\frac{C_0 L_d L_1}{L_d + L_1}}. \tag{11}$$

The following must be satisfied from (10) and (11).

$$0 \geq \left(\frac{V_{C0}(0)(L_d + L_1) - L_d V_{CL} - L_1 E}{L_1(L_d + L_1)}\right)\sqrt{\frac{C_0 L_d L_1}{L_d + L_1}} + \frac{E - V_{CL}}{L_d + L_1}\frac{\pi}{2}\sqrt{\frac{C_0 L_d L_1}{L_d + L_1}} + i_s(0). \tag{12}$$

(12) can be changed approximately as follows:

$$0 \geq \left(\frac{V_{C0}(0) - V_{CL}}{L_1}\right)\sqrt{C_0 L_1} + i_s(0) \tag{13}$$

because L_d is much larger than L_1. If $i_s(0)=20$ [A], $V_{C0}(0)$ is given by $V_{C0}(0)= -400$ [V]. Therefore,

$$\frac{20}{V_{CL} + 400} \leq \sqrt{\frac{C_0}{L_1}}. \tag{14}$$

If V_{CL} becomes the minimum, the left term of (14) is the maximum. Though V_{CL} is decided by the switching pattern of Th_L, the minimum of V_{CL} becomes -200 [V] from (6) and Fig. 7. Therefore, (14) can be changed as follows:

$$0.1 \leq \sqrt{\frac{C_0}{L_1}}. \tag{15}$$

C_0 and L_1 must be selected like (15) is satisfied

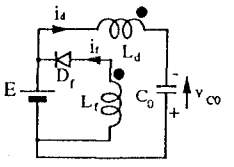

Fig. 5 Equivalent circuit at Mode 2.

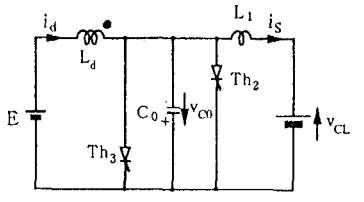

Fig. 6 Equivalent circuit including off-thyristor at Mode 1.

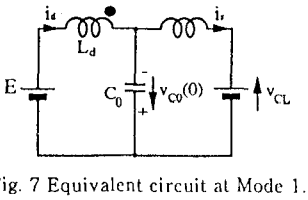

Fig. 7 Equivalent circuit at Mode 1.

V. Experimental System and Results

The experimental system is shown in Fig. 8. The gate signals of Th_1, Th_2, Th_3 and Th_4 are synchronized with the output PWM signals. For easy output current control, the output currents of two phases, for example, the output current i_a of phase a and the output current i_b of phase b are sensed. They are substituted into as follows:

$$\varepsilon_a = k_p(i_a^* - i_a) + k_i\int(i_a^* - i_a)dt + k_d\frac{d(i_a^* - i_a)}{dt} \tag{16}$$

$$\varepsilon_b = k_p(i_b^* - i_b) + k_i\int(i_b^* - i_b)dt + k_d\frac{d(i_b^* - i_b)}{dt} \tag{17}$$

where k_p, k_i and k_d are constants. i_a^* is the referent current of i_a, and i_b^* is the referent current of i_b.

The generation of switching pattern at Th_L is shown in Fig. 9. The width of i_s is decided as follows:

$$T_a = \alpha \mid i_a^* + \varepsilon_a \mid \tag{18}$$

$$T_b = \alpha \mid i_b^* + \varepsilon_b \mid \tag{19}$$

where T_a and T_b are the width of i_s at phase a and phase b. α is constant. The on-thyristors are selected by the sign of $i_a^*+\varepsilon_a$ and $i_b^*+\varepsilon_b$. For example, when $i_a^*+\varepsilon_a$ is positive and $i_b^*+\varepsilon_b$ is negative, Th_a^+, Th_c^- and Th_c^+, Th_b^- are selected. These two selections are used by turns every other pulse.

When i_f is less than the reference i_f^* of i_f at Mode 3, Th_0 turns on and W_{LD} is kept to be constant.

The experimental parameters are shown in Table. 1, and the waveforms of i_a and i_s are shown in Fig. 10. W_{LD} is controlled to be constant, and the peaks i_{sp} of i_s become constant. Therefore, i_a is the perfect sinusoidal current. The waveforms of i_a and the line-to-line voltage v_{ab} of phase a and b are shown in Fig. 11. Though v_{ab} includes the component of the pulse frequency, it becomes the sinusoidal voltage better.

VI. Characteristics of the System

The characteristics of losses by on-state voltages in the switching devices are shown in Fig. 12. The losses are the mean values for a cycle of output. In order to analyze the losses in the system, Th_1, Th_2, Th_3, Th_4 and Th_L are replaced with the high speed thyristors, and Th_0 is replaced with an IGBT and a series diode because of the pulse frequency and

turn-off time of the devices.

The parameters are shown in Table. 2, and the switching device types are shown in Table. 3.

1) Characteristics of On-State voltages in the Devices: The characteristics of on-state voltages in the switching devices are shown in Fig. 12(a). The gray curves are quoted from the data sheets. For easier analysis, they approximate the straight lines as the blacks.

2) Characteristics of Losses in the System: The characteristics of the losses versus output frequency f_{out} are shown in (b), and the details of losses are shown in (c). Assuming the electric vehicle drive, the torque of the induction motor (I.M.) is constant at $f_{out} \leq 90$ [Hz]. The output of the I.M. is constant at $f_{out} > 90$[Hz]. As in (c), the losses in Th_L are in proportion to the value of the output current. And the losses in Th_1, Th_2, Th_3 and Th_4 are constant regardless of the output current and f_{out}.

At constant torque area, much influence of the loss in D_f appears as in (b) and (c). In this area, the output impedance becomes smaller. W_{LD} becomes larger, and i_{sp} becomes higher. Therefore, Mode 3 becomes longer time and the loss in D_f becomes larger, because the width of i_s is narrower.

At constant output area, much influence of the loss in Th_0 appears as in (b) and (c). In this area, the output impedance becomes larger, W_{LD} becomes smaller, and i_{sp} becomes smaller. Therefore, Mode 4 becomes longer time, and the loss in Th_0 becomes larger.

The characteristics of the losses versus output current are shown in (d), and the details of the losses are shown in (e). f_{out} is set to 60[Hz].

At larger output current, much influence of the loss in Th_L appears. At smaller output current, much influence of the loss in Th_0 appears as in (e). The width of i_s becomes narrower at smaller output current. Therefore, Mode 4 becomes longer time, and the loss in Th_0 becomes larger.

However, the loss in Th_0 can be reduced in half if Th_0 can be replaced with the high speed thyristor. Therefore, the loss in Th_0 is not very serious, and the effect described at next section is more important.

Table.1 Parameters of the inverter.
(experimental)

E	100 [V]	L_1	5 [μH]
L_d	470 [μH]	L_0	3 [μH]
n_d/n_f	1	C_L	25 [μF]
C_0	1.2 [μF]	pulse frequency	10 [kHz]
I.M.	0.75 [kW]	output frequency	15 [Hz]

Table.2 Parameters of the inverter.

E	200 [V]	L_1	10 [μH]
L_d	200 [μH]	L_0	5 [μH]
n_d/n_f	1	C_L	5 [μF]
C_0	0.5 [μF]	pulse frequency	20 [kHz]

Table.3 Switching devices.

Devices	Model
IGBT	CM75DY-24E (Mitsubishi Electric Corp.)
high speed thyristor	SH50L13A (Toshiba)
diode	30JG11 (Toshiba)

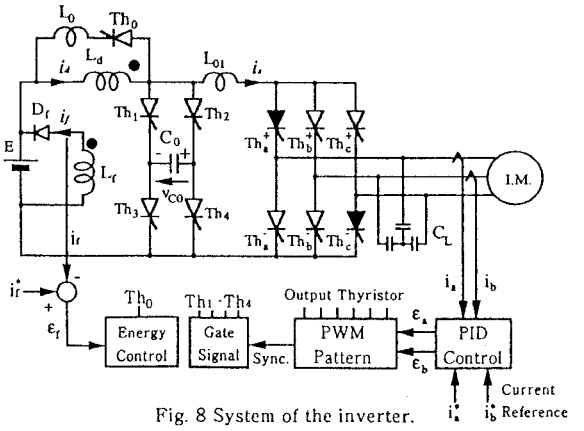

Fig. 8 System of the inverter.

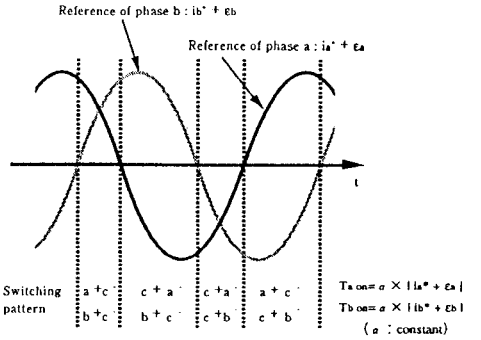

Fig. 9 Generation of PWM pattern.

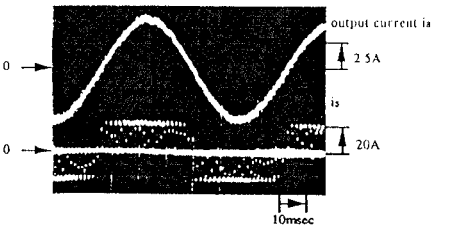

Fig. 10 Output current and i_s.

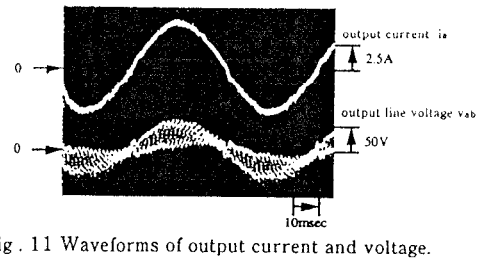

Fig. 11 Waveforms of output current and voltage.

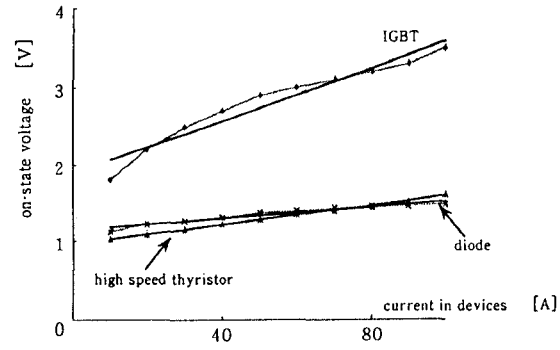

(a) Characteristics of on-state voltage.

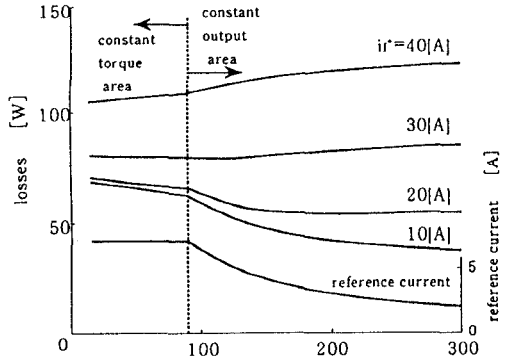

(b) Characteristics of losses versus f_{out}.

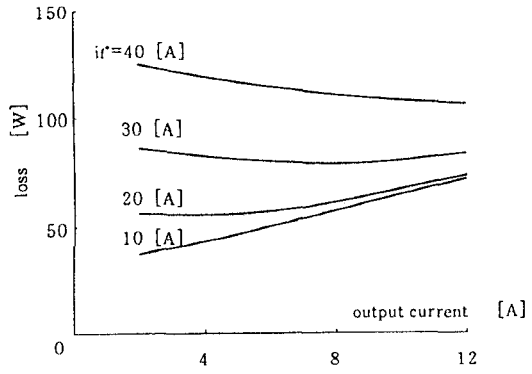

(c) Characteristics of losses versus output current.

VII Effect of Improvement for the Output Current by Mode 4

The effects of the improvement for the output current at Mode 4 are shown in Fig. 13. The switching time charts with W_{LD} control and without it are shown in (a). Mode 2 is constant time because the time is decided by only resonant frequency of L_d and C_0. The time at Mode 5 is decided by the output current. The pulse frequency set to 20 [kHz]. Therefore, it is considered that the width of i_s is controlled at Mode 3 or Mode 4. If W_{LD} should not be controlled, the width of i_s is controlled at Mode 3. If W_{LD} should be controlled, Mode 3 is constant time, and the width of i_s is controlled at Mode 4. When W_{LD} is not controlled all the time, the output current is clamped around zero as in (b), because i_{sp} becomes lower and the width becomes narrower. For the improvement of the output current, i_{sp} must be controlled to be constant. The conventional current type PWM inverter used larger L_d. The characteristics of the irregularities of i_{sp} versus L_d in the improved inverter are shown in (c). The irregularities i_{ir} of i_{sp} are defined as follows:

$$i_{ir} = \frac{1}{n}\sum_{k=1}^{n}\left|i_{ave} - i_s(k)\right| \qquad (20)$$

where n is the number of i_s, $i_s(k)$ is the peak of k-th i_s, and i_{ave} is the average of $i_s(k)$ for a output cycle. The smaller i_{ir} become, the more regular i_{sp} becomes. If L_d equals to about 30 [mH], i_{sp} becomes the most regular. However, the system becomes heavy, and the on-state loss in L_d becomes larger.

The characteristics of i_{sp} versus i_f^* and L_0 by proposed control are shown in (d). When i_f^* equals to about 40 [A], i_{sp} is the most regular. However, i_{sp} becomes more irregular again at i_f^*>40 [A], because the energy, which is stored in L_0 while Mode 4, is not released completely at Mode 5. It is advisable for i_f^* to be set to the minimal value at each curve in (d). Compared with (c), it is concurred to get the same effect as L_d=10 [mH], if i_f^*=40 [A], L_0=10 [μH] and L_d=200 [μH].

VIII. Conclusion

This paper describes the improvement of the performance for the series resonant dc link PWM inverter about output characteristics, especially the switching devices losses by on-state voltages, using simulation and experimental results. And the design for the inverter are shown in order to operate the inverter safely and stably.

The inverter connected Th_0 and L_0 in parallel with L_d. This part gets the same effect as larger L_d, even if L_d is much smaller. The experimental results show that the output current becomes perfectly sinusoidal wave. The losses in the switching devices are larger, if i_f^* is larger or the output current becomes smaller. In order to avoid this, Th_0 should be replaced with a high speed thyristor because it has much smaller on-state voltage than IGBT and a series diode.

Further experiment will be made in the future. Especially, the performance at light-load for induction motor drives, and the examination of the total efficiency for the system including the loss of the inductances will be studied.

References

[1] D. M. Divan, "The Resonant DC Link Converter -- A New Concept in Static Power Conversion" *IEEE IAS Trans.*, vol. 25, No. 2, 1989.

[2] P. K. Dahono, Y. Sato, T. Kataoka, "Analysis and Minimization of Ripple Components of Input Current and Voltage of PWM Inverters", *IEEE IAS Trans.*, vol. 32, No. 4, pp. 945-950; 1996.

[3] V. Agarwal, A. K. S. Bhat, "Small Signal Analysis of the LCC-Type Parallel Resonant Converter Using Discrete Time Domain Modeling", , *IEEE Transaction on Industrial Electronics*, vol. 42, No. 6, pp. 604-614, 1995.

[4] Y. Murai, T. A. Lipo, "High Frequency Series Resonant DC - Link Power Conversion", *IEEE IAS Trans.*, vol. 1A-28, No. 6, pp. 1277-1285, 1992.

[5] V. V. Deshpande, S. R. Doradla, "A New Topology for Parallel Resonant DC Link with Reduced Peak Voltage" , *IEEE IAS Trans.*, vol. 32, No. 2, pp. 301-307, 1996.

[6] L. Malesani, P. Tenti, P. Tomasin, V. Toigo, "High Efficiency

Quasi-Resonant DC Link Three-Phase Power Inverter for Full-Range PWM", *IEEE IAS Trans.*, vol. 31, No. 1, pp. 141-147, 1995.

[7] Y. Murai, H. Ishikawa and T. A. Lipo, "New Series Resonant DC Link Inverter for Electric Vehicle Drives", *IEEE IAS Conference Record*, vol. 1, pp. 443 - 447, 1994.

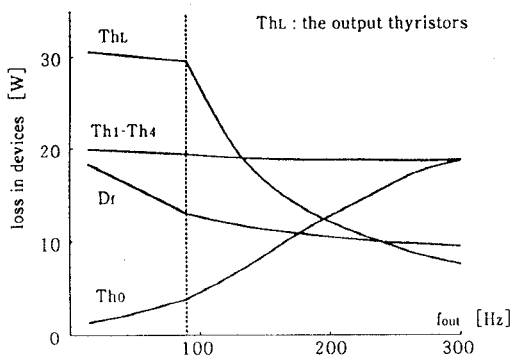

(d) Characteristics of each switch loss versus f_{out} at $i_f^* = 20$ [A].

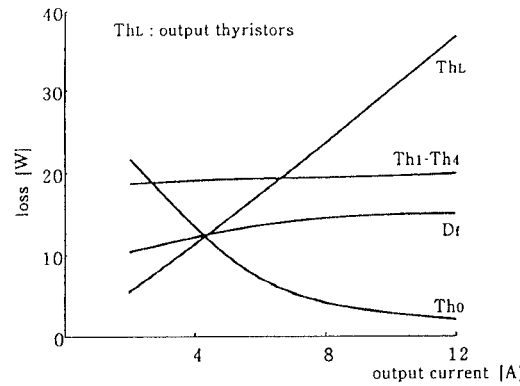

(e) Characteristics of each switch loss versus output current at $i_f^* = 20$ [A].

Fig. 12 Characteristics of the devices losses.

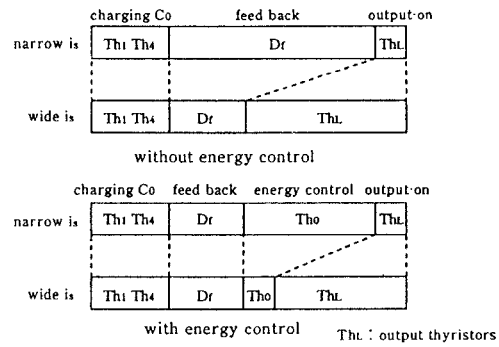

(a) Switching time charts.

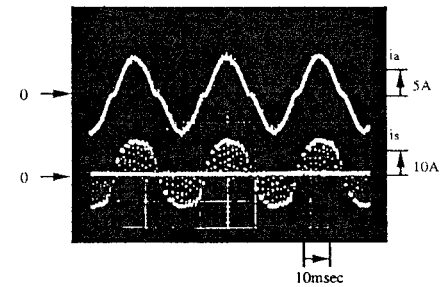

(b) Waveforms of i_a and i_s without energy control.

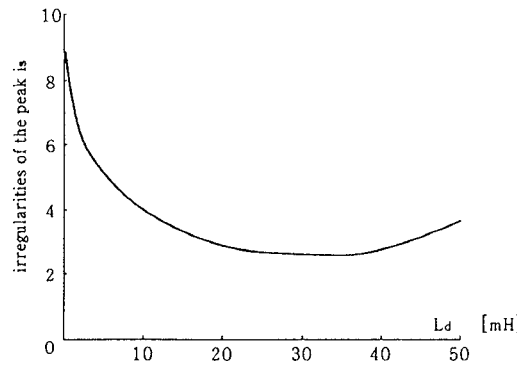

(c) Characteristics of irregularities of peak of i_s versus L_d.

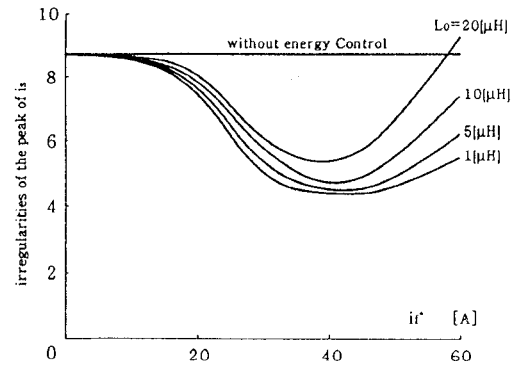

(d) Characteristics of irregularities of peak of i_s versus i_f^*.

Fig. 13 Characteristics of peak i_s.

A Novel Resonant DC Link Circuit with Two Level PWM Control Scheme and Its Application to Three-Phase Voltage-Fed Converter Operating at New Pulse Vector Modulation

Arihi Kambe, Manabu Kurokawa, Ali Chibani, and Mutsuo Nakaoka
The Graduate School of Engineering and Science, Yamaguchi University 2557,Tokiwadai,Ube,Yamaguchi,755
Fax: 0836-35-9449 Phone: 0836-35-9946
E-mail: kanbe@pe-news1.eee.yamaguchi-u.ac.jp

Abstract; This paper presents a novel prototype of resonant DC link with two level PWM control scheme and a three-phase voltage-fed PWM inverter with this resonant DC link. This resonant DC link circuit capable of controlling two level PWM modes; a clamped supply voltage PWM and zero voltage PWM modes in DC bus line can operate under the principle of zero voltage and zero current soft-switching. The operating analysis is carried out and design procedure of this resonant DC link is described on the basis of simulation results. Three-phase voltage-fed inverter and converter using this unique resonant DC link are analyzed which operate at a new pulse vector moduration scheme and their performances for utility-interactive power processor for Battery Energy Storage System (BESS) are evaluated and discussed including reactive current compensator and active power filter using this resonant DC link.

I. Introduction

In recent year, the difference of power use between day and night tends to become larger and larger. Therefore, the necessity of load leveling and energy storage systems becomes more important. In such a social back ground, the development of a high performance power conversion system which has multi-functional operation such as reactive power compensation, and harmonic current reduction has been required. In order to realize multi-functional operation high performance power conversion system and its much higher performance, high-frequency switching is indispensable. However, the conventional hard-switched power conversion system, high-frequency switching produces a large amount of switching losses in addition to EMI and RFI noises. Thus, resonant DC link circuit is introduced into the DC bus line of bidirectional three-phase converter as one of the soft-switching schemes. By using soft-switching technologies, all the switching devices in the converter can be pulsed with the zero voltage and dv/dt and di/dt stresses are basically reduced. Hence, the feasible problem discussed above can be solved effectively. However, the conduction losses at additional soft-switching circuit could be increased. This is a significant problem in power conversion efficiency.

Newly-proposed resonant DC link circuit discussed here has a special effectiveness that zero voltage interval of DC bus line for soft-switching can be controlled by its unique circuit topology. The switching number of the resonant DC link circuit can be reduced by using its interesting feature in order to decrease the conduction losses of this auxiliary circuit.

In this paper, a newly-proposed resonant DC link circuit is proposed and incorporated as inverter and converter utility-interactive energy storage system which has multi-functional operations such as reactive power compensation, active power filter, battery charging mode and peak-cut mode. DSP based digital control method on the basis of instantaneous space voltage vector principle are presented. The total system operation of this converter is evaluated by means of the computer simulation.

II. Resonant DC Link Circuit

Figure 1 illustrates the newly proposed resonant DC link circuit. This circuit consists of three active switching power

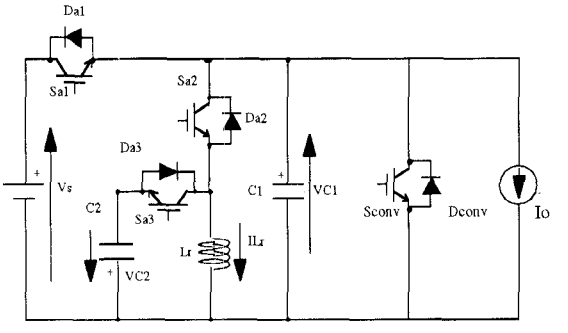

Fig.1 Basic Resonant DC Link Circuit Configuration

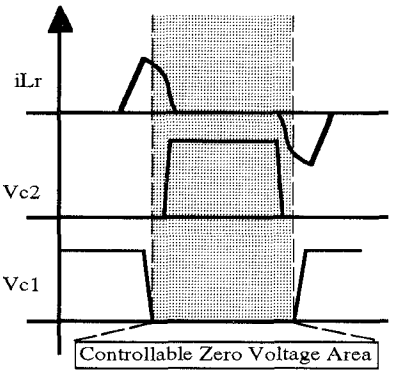

Fig.2 Resonant DC Link Operation Waveforms

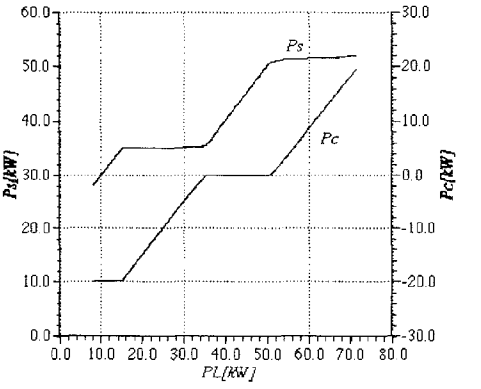

Fig.4 Control Characteristic of BESS

devices, (voltage clump switch Sa1, starting switch Sa2, and zero-voltage interval control switch Sa3) inductor Lr , and two capacitor (main capacitor Cr1 and energy storage capacitor Cr2), load current DC source Io, converter arm switching device and its anti-parallel diode. Making use of this resonant DC link circuit, soft-switching can be achieved for all switching devices. When converter switching pattern is changed, this additional circuit can step down the DC bus line voltage to the zero. ZVS can be realized by switching the converter arm devices within the zero-voltage interval. Moreover, remarkable point of this new DC link circuit is that zero voltage interval can be controlled with no resonant current in Figure 2. This new advantage provides the operation number of this resonant DC link circuit in addition to less conduction losses reduction because zero voltage vector generating interval can be replaced by zero voltage hold interval of this new circuit. This new advantage is based on a new PWM pulse pattern.

III. Resonant DC Link Multi-Functional Converter Control Strategy

Figure 3 shows bidirectional converter using new resonant DC link circuit for BESS configuration which can realize multi-functional operation such as load leveling, battery charging, reactive power compensate, and active power filter. In this system, there are two control modes, which include normal inverter mode and converter mode. As shown in Figure 4, these two control methods are appropriately selected by loaded power of utility-grid (PL). In this figure, Ps: utility power, Pc: BESS treated power. In case of load power under 35kW, this system is operated at energy storage mode. On the contrary, in case of load power over 50kW, this system is operated at peak cut mode, so load leveling operation is completely achieved. This bidirectional converter output is connected with a utility-grid AC line through the LC low pass filter. The control strategy as total system is presented. Its reference voltage is estimated by mathematically procedure and realized by means of instantaneous space voltage vector-based PWM scheme.

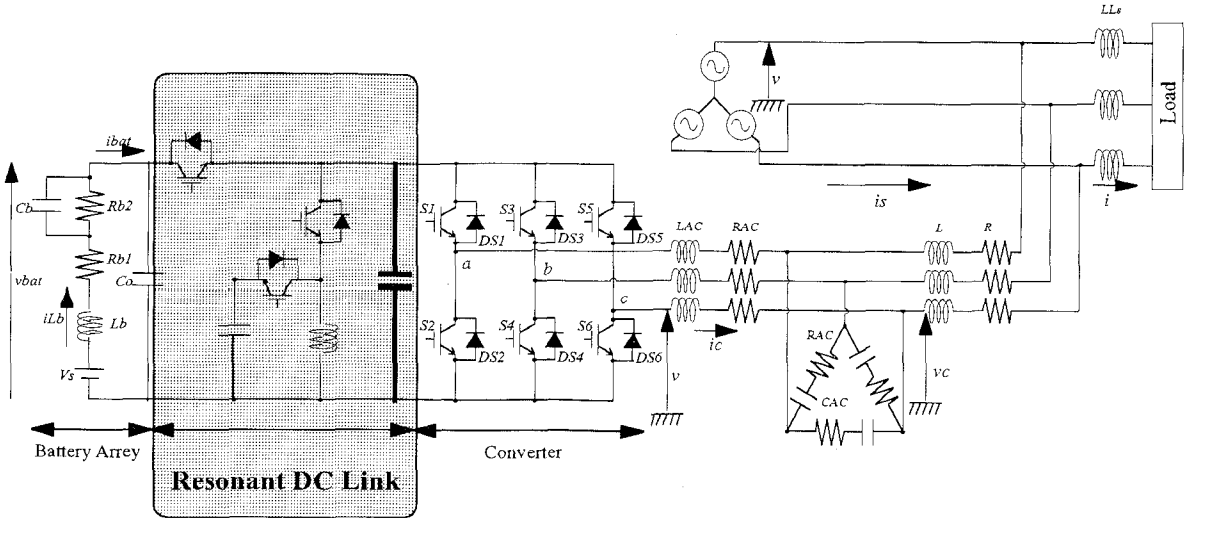

Fig. 3 Resonant DC Link ZVS-PWM Converter for Battery Energy Straage System

The state equation as BESS is written as follows by defining the output voltage of the converter $v_A(t)$, AC reactor current $i_c(t)$, utility grid voltage $v_C(t)$ and, load current $i_L(t)$.

$$L_{AC}\frac{d}{dt}i_C(t) = v_A(t) - v_C(t) - R_{AC}i_C(t) \quad (1)$$

This equation is transferred to the rotating axis plane and discreated, while the current is taken as constant since sampling time is much smaller than the period in this system. Thus, the reference voltage of bidirectional converter is given,

$$\hat{v}_A^*(i+1) = \hat{v}_C(i) + \frac{1}{T_s}L_f i_c^*(i) + \begin{bmatrix} R_{AC} - L_f/T_s & -\omega_e L_f \\ \omega_e L_f & R_{AC} - L_f/T_s \end{bmatrix}\hat{i}_c(i) \quad (2)$$

Here, the reference currents for energy supply and storage mode are estimated as follows, respectively.

$$\hat{i}_{pw} = \begin{bmatrix} I_{pw} \\ 0 \end{bmatrix} = \frac{P_L - P_{L\max}}{E}\begin{bmatrix} 1 \\ 0 \end{bmatrix} \quad \text{for energy supply} \quad (3)$$

$$\hat{i}_{pw} = \begin{bmatrix} I_{pw} \\ 0 \end{bmatrix} = \frac{P_L - P_{L\min}}{E}\begin{bmatrix} 1 \\ 0 \end{bmatrix} \quad \text{for energy storage} \quad (4)$$

where, $P_{L\max}$: maximum load power for load leveling

$P_{L\min}$: minimum load power for load leveling

P_L : average load power

This converter works as also active filter. In this paper, this converter compensate the harmonic current and reactive current.

According to the p-q theory, a power is divided into active power "p" and reactive power "q". And each component is divided into $\bar{p}$ and $\bar{q}$, and harmonic component $\tilde{p}, \tilde{q}$. That is, $P = \bar{p} + \tilde{p} + \bar{q} + \tilde{q}$.

In this case, taking the output power of converter P_c as $[p_c, q_c] = [\tilde{p}_L, q_L]$, three phase currents become sinusoidal wave with unity power factor.

The reference voltage which can realize active filter should be estimated.

Transforming into d-q axis plane and discreating, the state equation (2) becomes,

$$\tilde{i}_C(i+1) = \frac{1-e^{-\frac{R_{Lf}}{Lf}}}{R_{Lf}}\begin{bmatrix} 1 & 0 \\ 0 & 1 \end{bmatrix}(\tilde{v}_A(i) - \tilde{v}_C(i)) + e^{-\frac{R_{Lf}}{Lf}T_s}\begin{bmatrix} 1 & 0 \\ 0 & 1 \end{bmatrix}\tilde{i}_C(i) \quad (5).$$

Solve the this equation for $\tilde{v}_A$. However, in the actual system, preceding value has to be predicted in consideration of delay by calcuration. For preceding time, we are get

$$\tilde{v}_A^*(i+1) = \tilde{v}_C(i+1) + \frac{R_{Lf}}{1-e^{-\frac{R_{Lf}}{Lf}}}\begin{bmatrix} 1 & 0 \\ 0 & 1 \end{bmatrix}\left(\tilde{i}_C^*(i+1) - e^{-\frac{R_{Lf}}{Lf}T_s}\tilde{i}_C(i+1)\right) \quad (6).$$

Using the utility grid voltages $\tilde{v}_C(i)$, $\tilde{v}_C(i-1)$, $\tilde{v}_C(i-2)$ and load currents $\tilde{i}_L(i), \tilde{i}_L(i-1), \tilde{i}_L(i-2)$, the preceding value $\tilde{v}_A(i+1)$ and $\tilde{i}_L(i+1)$ can be estimated. Then, from p-q theory, preceding reference current is obtained. As considering $\tilde{v}_A$ in eq.(5) as $\tilde{v}_A^*$ of present time, $\tilde{v}_A^*(i+1)$ is given.

Therefore, the preceding reference voltage can be calculated by equation (6).

IV. NEW PWM PULSE PATTERN

In the instantaneous space voltage vector control method for resonant DC link three-phase inverter, its phase voltages are represented as six discrete voltage vectors and two zero voltage vectors specified in Fig 5. The output voltage vector is allocated by three voltage vectors including zero voltage

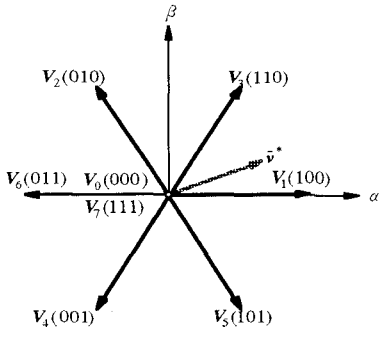

Fig.5 Instantanious Voltage Vector

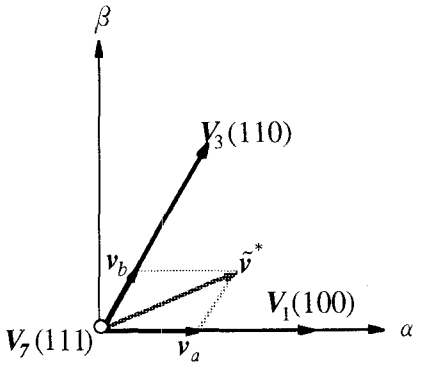

Fig.6 Refference Voltage Vector Composition

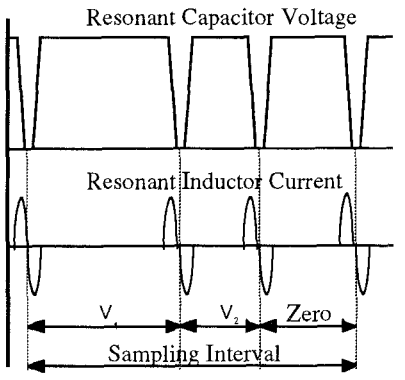

Conventional Pulse Pattern

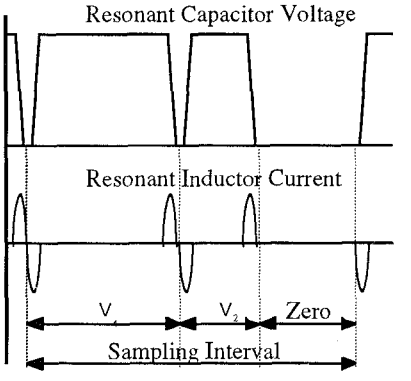

New Pulse Pattern (a)

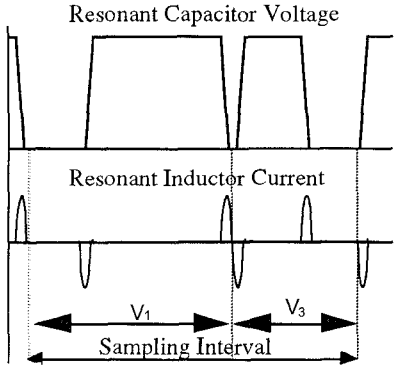

New Pulse Pattern (b)

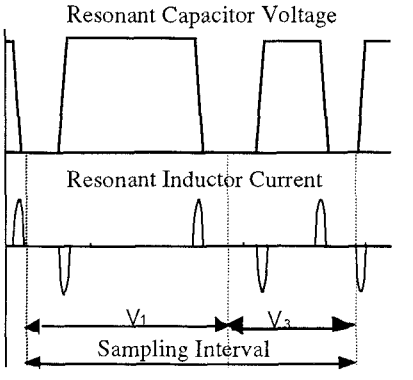

New Pulse Pattern (c)

Fig. 7 Conventional and Novel type of PWM pulse patterns

vector shown in Figure 6. In order to generate three vectors, the resonant DC link circuit has to operate at resonant mode three times per one sampling interval shown in Figure7-(a). However, this converter needs not operate resonant circuit when zero vector generates, as can be seen in Figure 7-(b), because this two level PWM resonant DC link circuit can control zero voltage interval in DC bus line. The operation time of the resonant DC link circuit can be reduced up to twice resonant operation. As a result, conduction losses of this new converter become lowered value. Furthermore, if V1 or V3 vector is generated in place of zero vector, PWM can be realized by only two switching vector pattern under the conditions of twice resonant operation as shown in Figures 7-(b) and (c).

However, in order to select the (b) or (c) type pattern, the load current vector location is required to meet the condition as follows.

(1) When V1 vector is generated, the load current vector must be in both quadrant area of V1.

(2) When V3 vector is generated, the load current vector must be in both quadrant area of V3. These conditions are

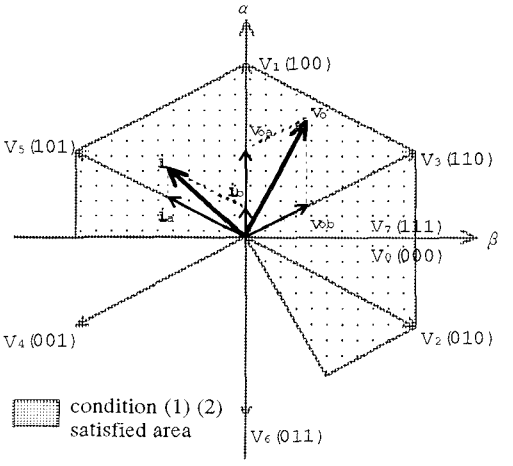

Fig.8 Pattern (b)(c) Possible Area

summarized as Figure 8. If the current vector can not be satisfied these conditions, the load current flows into the main capacitor at the DC link circuit. The zero voltage vector can not be realized by this unique technique because DC bus voltage is boosted. In such a case, the type (a) pattern in Figure 7 should be selected. Thus, the converter switching and the operation number of resonant DC link circuit can be reduced in all over the load to decrease the switching losses and conduction losses.

V. Simulation Results and Evaluations

In order to verify this operating principle, the resonant DC link three-phase ZVS-PWM converter system is simulated. Figure 9 shows the simulated resonant DC link voltage and current waveforms. It can be observed that the ZVS operation are achieved completely, indicating the peak voltage across the power switching devices are exactly clamped at the DC output voltage level.

Figure 10 illustrates a-phase current at energy supply mode in this converter system for reactive load (a) and (b), and rectifier load (c) and (d). As can be seen in these figures, the relationships of i_{La}, i_{Sa} and, i_{Ca} are in phase. Therefore, utility-grid AC side line current has low harmonic component and this converter delivers the energy without instantaneous reactive power for both load types. Figure 11 shows a-phase current and voltage at energy storage mode. The system storages the energy to the battery with unity power factor.

From these simulation results, it is evident that resonant DC link soft-switching method is more suitable for the proposed BESS, This system has excellent performances to realize load leveling including reactive power compensation and power active filter. Introducing soft-switching technique to the BESS, EMI/RFI noise could be substantially reduced.

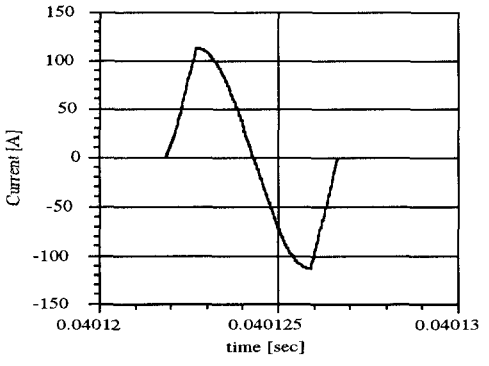

(a) Inductor Lr Current

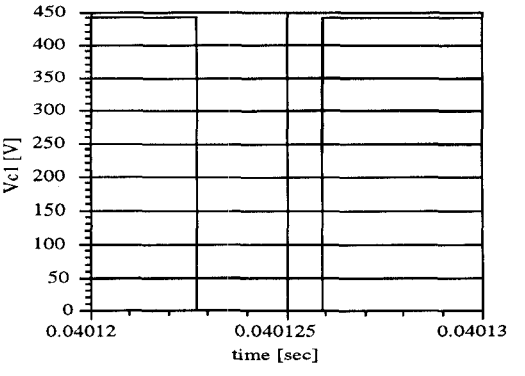

(b) Main Capacitor C1 Voltage

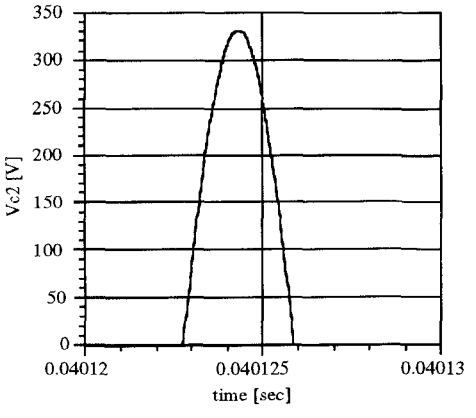

(c) Sub Capacitor C2 voltage

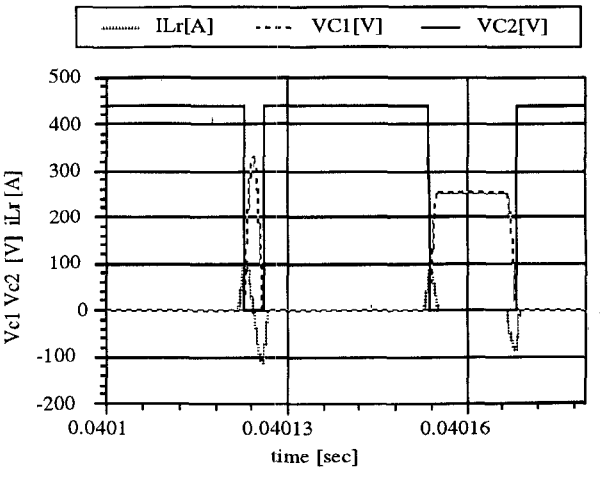

(d) Resonant DC Link Operation waveform with (b) type pulse pattern

Fig.9 Resonant DC Link Simulation Waveforms

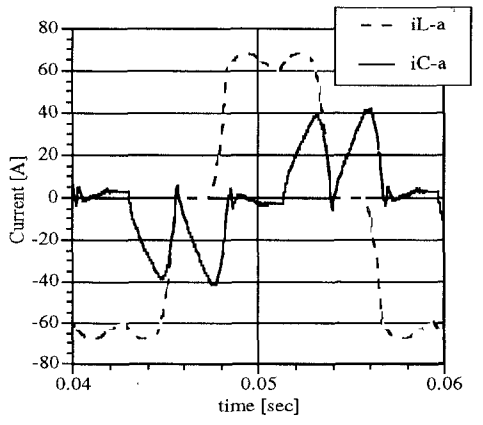

(a) Converter Output Current and Load Current for Rectifire Load

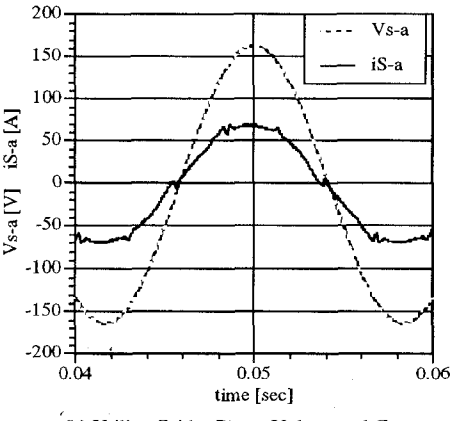

(b) Utility-Grid a-Phase Volage and Current for Rectifire Load

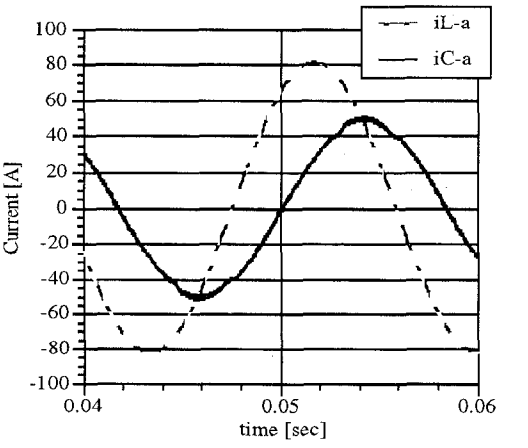

(c) Converter Output Current and Load Current for Leactive Load

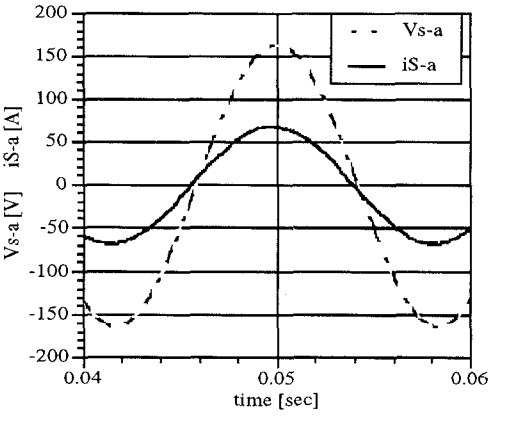

(d) Utility-Grid a-Phase Volage and Current for Leactive Load

Fig.10 Simulation Waveforms fot Energy Supply Mode

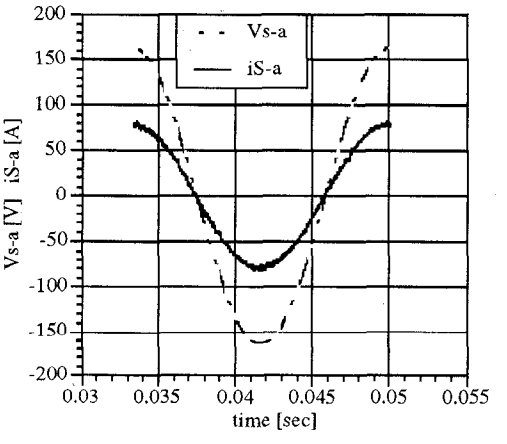

Fig. 11 Simulation Waveform for Energy Strage Mode

VI. Conclusions

In this paper, the principle of newly-proposed DC link circuit topology and bidirectional ZVS-PWM converter using this resonant DC link circuit for BESS has been introduced which operates under a digital control scheme.

New voltage vector pulse pattern has been proposed using advantage of this resonant DC link circuit topology.

It was proved that the BESS has a remarkable capability in addition to its controllability and environmental adaptability from computer aided simulation analysis.

In the future, this introduced converter system and its related control strategy should be experimentally investigated and evaluated.

REFERENCES

[1] Y.C.Jung and G.H.Cho, "Low-loss Quasi-Parallel Resonant DC Link Inverter with Advanced PWM Capability"; IntJ.Electronics,1996,Vol.81,NO. 2, pp. 219-234.

[2]H.Yonemori,H.Ishii, M.Yoshida and M.Nakaoka,"Three-Phase ZVS-PWM Inverter Systemwith Transformer-Assisted Quasi-Resonant DC Link and its Feasible Comparative Evaluations"; IEEE-PESC,1996,Vol.1,pp. 171-176

Active EMI Filter for Switching Noise of High Frequency Inverters

Isao Takahashi, *fellow, IEEE*, Akihiro Ogata, *IEEJ*
Nagaoka University of Technology
1603-1 Kamitomioka, Nagaoka 940-21, JAPAN
FAX: +81-258-47-9500, Phone: +81-258-47-9515
taki@ voscc.nagaokaut.ac.jp, aogata@voscc.nagaokaut.ac.jp

Hidetoshi Kanazawa, *IEEJ*, Atsuyuki Hiruma, *IEEJ*
Toshiba Co., Ltd.
336 Tadewara, Fuji 416, JAPAN
FAX: +81-545-64-1473, Phone: +81-545-62-5614

Abstract — **In high frequency inverter fed ac motor systems, high frequency leakage current generated by high dv/dt at switching times flows to the ground wire through the stray capacitor between motor windings and core. This paper proposes an active EMI filter to compensate common mode current using high frequency transistors as active elements and a high frequency common mode CT.**

It works just as a power active filter in the harmonic compensation in the power system. The leakage current is actively suppressed to under 1/50 of the uncompensated circuit. The proposed method is also effective to decrease the EMI more than 40 dBμV.

I. INTRODUCTION

High speed switching inverters using IGBTs and high carrier frequency makes several problems as follows;

- misbehavior of earth leakage current breakers, control circuits of factory automation machines
- winding insulation deterioration
- electric shock by the leakage current
- EMI

Common and normal mode passive LC filters are applied to solve these problems[1]. Fig.1 shows conventional common mode LC filter method of type I. Fig.2 shows conventional method of type II which uses a large LC filter to prevent switching noise.

They can suppress rapid variation of voltage and current (high dv/dt, di/dt) of switching devices which cause the noise. In the case of type I, the filter is fairly expensive and has large size. Also resonance phenomenon happens with load stray capacitors and system impedance, owing to the passive filter resonance frequency. In the case of type II, some resistance is necessary to damp high frequency vibration. Also the LC filter becomes large and heavy.

This paper proposes an current injection type active EMI filter to compensate the common mode high frequency leakage current using two complementary transistors as active elements and a common mode current transformer (CT)[2]~[4]. The leakage current is actively suppressed by the proposed method in high frequency PWM inverter fed ac motor systems.

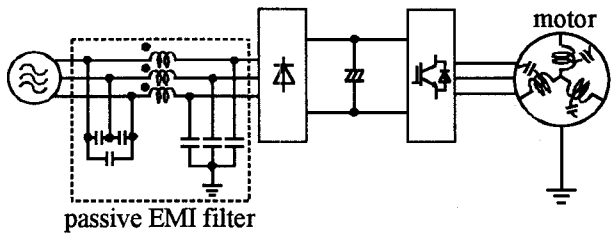

Fig.1. Conventional method of type I

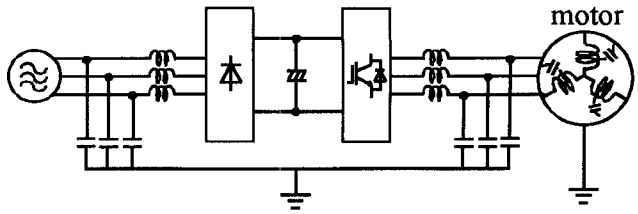

Fig.2. Conventional method of type II

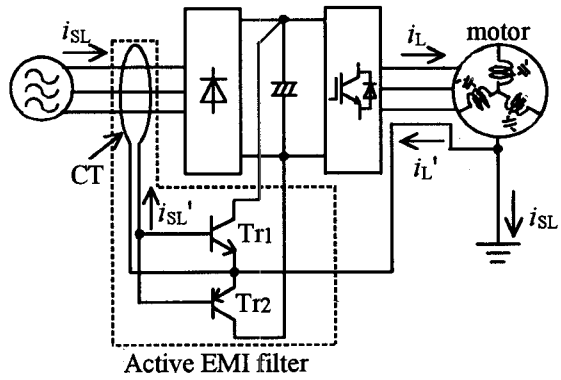

Fig.3. Principle of active EMI filter

II. ACTIVE EMI COMMON MODE FILTER

Fig.3 shows the principle of the active EMI filter, applies in an ac motor fed by a three phase voltage source PWM inverter system. As shown in the figure, the active EMI filter is consisted of a small common mode current transformer and complementary high frequency transistors Tr_1, Tr_2. They are directly connected to the dc link capacitor and the motor frame. Every switching, high frequency leakage

current is flowed to the earth through the stray capacitor between motor windings and frame.

If this filter is not connected ($i_L'=0$), the leakage current i_L almost equals to the common mode current i_{SL} which flows to the source side.

The common mode current can be detected by the common mode CT. The secondary current of CT i_{SL}' is decided by turn ratio ($N = N_1/N_2$).

$$i_{SL}' = i_{SL} \cdot N \quad (1)$$

The compensation current i_L' is represented using the gain h_{FE} of transistor where h_{FE} is in B class operation.

$$i_L' = h_{FE} \cdot i_{SL}' \quad (2)$$

where, $$i_{SL} = i_L - i_L' \quad (3)$$

From Equations (1),(2) and (3), the common mode current i_{SL} flowing to the source side is represented as

$$i_{SL} = i_L/(1 + h_{FE} \cdot N) \quad (4)$$

Note that this current becomes almost zero for large $h_{FE} \cdot N$. As shown in Fig.3, if the leakage current flows in positive direction, the compensation current flows because Tr2 becomes active. In the same way, if the leakage current flows in negative direction, Tr1 becomes active.

The common mode current flowing to the source side can be actively suppressed by the compensation current i_L' which cancels the leakage current i_L.

III. Design of the Active EMI Filter

Actually, to practice the active EMI filter for ac motor fed PWM inverter system decide the condition as follows.

A. Transistors

A push-pull amplifier is composed of the complementary transistors which must have high speed operation and high gain (h_{FE}) to output the compensation current i_L'. In this case, this current can trace the high frequency leakage current i_L. Therefore it would be satisfied the rated value as follows.

- Withstand voltage $V_{CE}>1.5E_{d0}$
- Transition frequency $f_T>10f_L$ (frequency of i_L)
- Gain $h_{FE}>10\sim50$
- Collector current $I_C>0.3i_{Lm}$ (maximum of i_L)

Table I shows the rated values of transistors used in the active EMI filter. The loss of each transistor is 12.4[mW] by calorimetric measurement

B. Common mode CT

A small ferrite toroidal core is used in the common mode CT for detecting the high frequency and small leakage current. So it should satisfy the rated value as follows.

- N=1~10

Table I. Rated values of transistors

	2SA1772	2SC4615
V_{CEO}[V]	400	400
i_{Cp}[A]	2	2
$h_{FE(min)}$	40	40
f_T[MHz]	50	70
P_C[W]	1	1

Table II. Specifications of toroidal core

material and size[mm]	HS72 T20×10×12
cross section S[mm^2]	39.1
length ℓ[mm]	48.1
A_L-value[nH/N^2]	7600±25%
flux density B_S[mT]	410

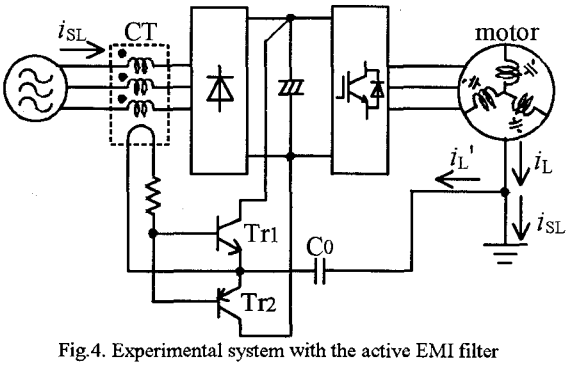

Fig.4. Experimental system with the active EMI filter

Table III. Specification of PWM inverter and induction motor

Inverter	source voltage	3ϕ200V 50Hz
	rated power	3.7kW
	rated current	17A
	carrier frequency	10kHz
	switching device	IGBT
IM	source voltage	3ϕ200V 50Hz
	rated power	1.5kW
	capacitance between motor windings and frame	3nF

Table II shows the specifications of toroidal core used in the common mode CT. Turn ratio of N=10 is decided.

C. Capacitor

The dc cut capacitor C0 needs high withstand voltage to protect the proposed filter when inverter circuit is submitted to withstand voltage test.

IV. Application of the Active EMI Common Mode Filter

Fig.4 shows an actual circuit of the experimental system which consists of an induction motor fed by a three phase voltage source PWM inverter and an active EMI common mode filter. Table III shows the specification of the PWM inverter and the induction

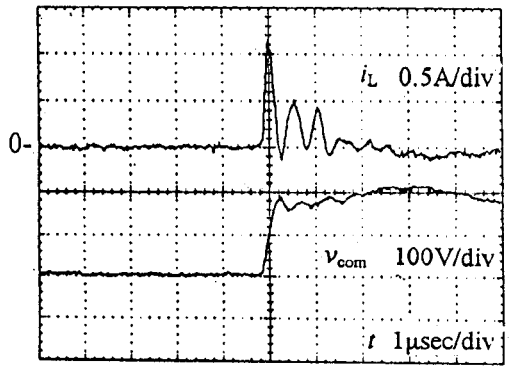

Fig.5. Waveform of the high frequency leakage current and the common mode voltage

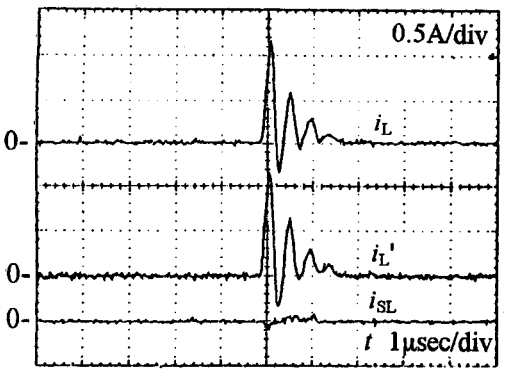

Fig.6. Waveform of the common mode currents with the active EMI filter

motor used in this experiment. The Common mode voltage v_{com} is changed by 280/3 every one phase switching of the inverter, the high frequency leakage current flows to the ground wire through the stray capacitor between motor windings and frame. In Fig.5, note that two phase are switched. The leakage current has the peak value of 1.2[A] and oscillation frequency of about 2[MHz]. Attention should be paid that the noise and switching current are relatively large for the rated current of the system.

Fig.6 shows the waveform of the common mode currents using the proposed filter. It is shown that the leakage current i_L is canceled by the compensation current i_L' and then the common mode current is prevented flowing to the source side. Note that the leakage current is actively suppressed under 1/50 of uncompensated circuit.

V. APPLIFICATION TO THE ROOM AIR CONDITIONER

Recently inverter driven systems are used for room air conditioners. Generally home electric products as ones must be connected to the earth. In case measures against EMI aren't practiced, high frequency leakage current flows to the grounding wire and radiates electromagnetic noise. So the active EMI filter is applied to suppress this current and EMI noise of the room air conditioner.

Fig.7 shows the room air conditioner with a passive EMI filter at ac side and a common mode choke at dc

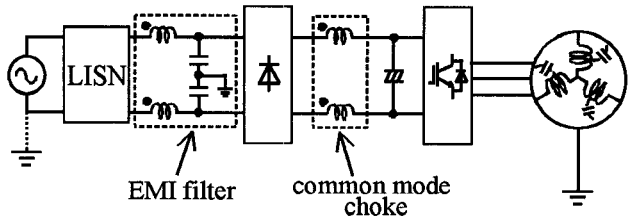

Fig.7. Room air conditioner with the passive EMI filter

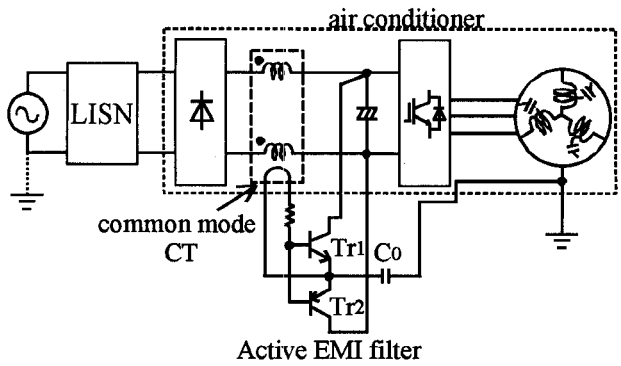

Fig.8. Room air conditioner with the active EMI filter

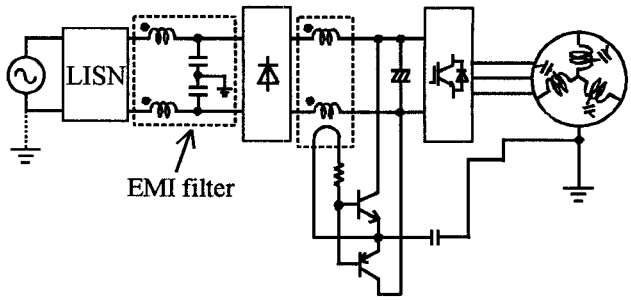

Fig.9. Room air conditioner with the active EMI filter and the passive EMI filter

side. In case rated power increases, both the filter and choke coil becomes large and heavy. Fig.8 shows the room air conditioner with the active EMI filter. The common mode CT is small enough to detect the high frequency common mode current. Fig.9 shows the room air conditioner with both the active and passive EMI filters. Because the passive filter is used only for high frequency range, the filter size can be small.

In these cases, normal mode noise is decreased by the normal mode filter.

The mains terminal interface voltage was measured according to CISPR pub.14 with the Line Impedance Stabilization Network (LISN) at the Anechoic Chamber[5][6].

As shown in Fig.10, when no compensation is applied note that the mains terminal interface voltage is larger than the limit value. In this case, the misbehavior of the earth leakage breakers, factory automation machines and control circuits can be caused by the common mode current and EMI noise.

Fig.11 shows that the mains terminal interface voltage is almost decreased by the passive filter under the limit value shown in Fig.7.

The common mode noise at frequency range under 500kHz is difficult to decrease and the filter size becomes large shown in Fig.12. The common mode noise is suppressed more than 40dBμV from 150kHz to 3MHz by the proposed filter. Note that the active EMI filter has advantage at low frequency range.

Fig.13 shows that the common mode noise is suppressed at all frequency range by combining both the active and passive EMI filter as shown in Fig.9. Because the common mode noise at low frequency is decreased by the active one, only a small conventional passive one is needed.

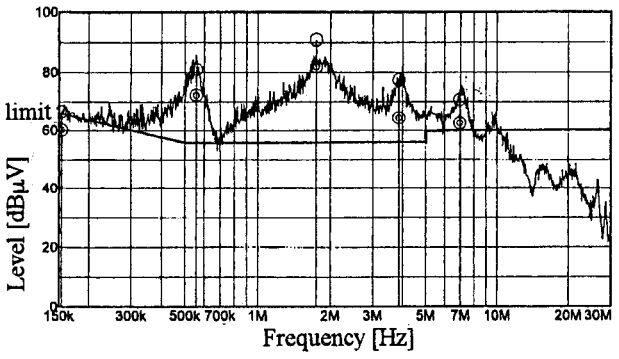

Fig.10. Experimental result with no compensation

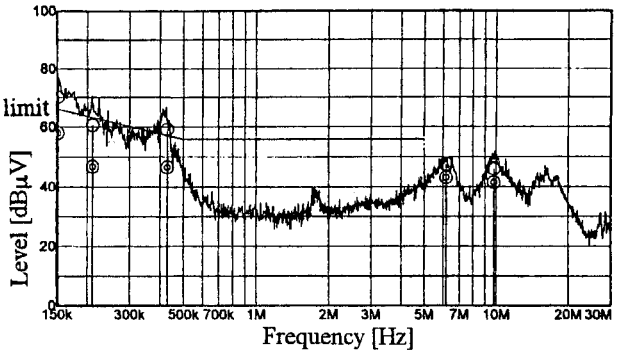

Fig.11. Experimental result with the passive filters

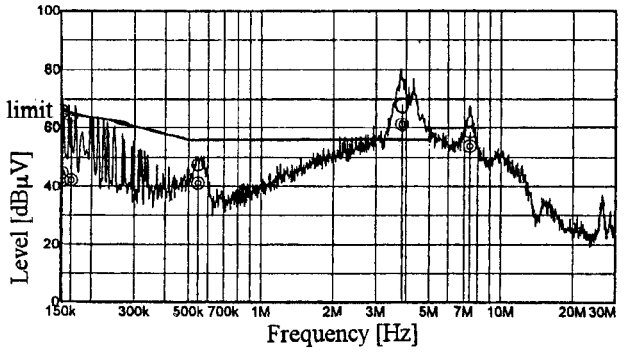

Fig.12. Experimental result with the active EMI filter

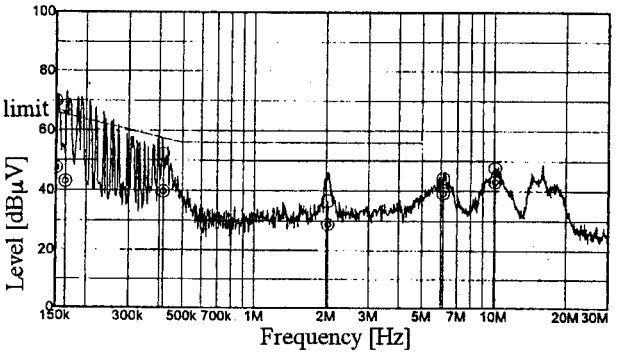

Fig.13. Experimental result with the active EMI filter and the passive EMI filter

VI. Conclusion

The paper proposes the current injection type active EMI filter to prevent the high frequency common mode current. As result the advantages are clear as follows.

- The high frequency leakage current flowing to the source side under 3MHz is actively suppressed by the compensation current generated by the proposed method in the PWM inverter fed induction motor.
- As the active EMI filter is consisted of the common mode CT, complementary transistors and a capacitor, resonance phenomenon wouldn't happen with load and system impedance.
- The proposed method is also available to apply to the room air conditioner.
- The measurement of the mains terminal interface voltage, proved that the active EMI filter is effective to decrease the common mode noise.

References

[1] A. Von Jouanne, D. Rendusara, P. Enjeti, W. Gray, "Filtering Technique to Minimize the Effect of Long Motor Leads on PWM Inverter Drives," *IEEE/IAS Annual Meeting*, pp. 37-44, 1995.

[2] I. Takahashi, A. Ogata, "Active Compensation Circuit of Leakage Current in Inverter Drived Load," in Proceedings of the joint Conf. of *Hokuriku Chapters*, IEEJ, 1995, pp. 46

[3] I. Takahashi, "Noise suppress device of power conversion device," applied patent 1995, 99254

[4] I. Takahashi, A. Ogata, "Active Compensation Circuit of Leakage Current in PWM Inverter Fed AC Motor Drive System," in Proceedings of the joint Conf. of *Hokuriku Chapters, IEEJ*, 1996, pp. 41

[5] S. Ogasawara, H. Akagi, "Measurement and Reduction of EMI Radiated by a PWM Inverter-Fed AC Motor Drive System," *IEEE/IAS Annual Meeting*, pp. 1072-1079,1996

[6] E. Zhong, S. Chen, and T. A. Lipo, "Improvement in EMI performance of inverter-fed motor drives," in *APEC 94 Conf. Rec.*, pp. 608-614, vol. 2, 1994.

Low Cost Power Factor Correction(PFC) Converter Using Delay Control

K. C. Lee [*,**] **and B. H. Cho** [*]

[*] Dept. of Electrical Engineering
Seoul National University, Seoul, Korea
Phone: +82-2-880-7260
Fax: +82-2-878-1452
E-Mail:lkc@plaza.snu.ac.kr

[**] Hyosung Industries Co., Ltd.
Seoul, Korea
Phone: +82-2-630-8780
Fax: +82-2-679-0077

[1] *Abstract* - **A low cost universal input voltage (90~264V) Power Factor Correction (PFC) converter for 200W power supply in a personal computer (PC) is proposed. It consists of the PFC part followed by a dc-dc converter as in a conventional two-stage scheme. However a single PWM controller is used as in a single-stage, single-switch PFC scheme. The switch in the PFC part is synchronized with the switch in the dc-dc converter and it has a fixed frequency. Employing a simple delay scheme using the pulse and feedback signal of the dc-dc converter, the PFC switch is controlled to limit the capacitor voltage within a range for the optimum efficiency and cost. A tradeoff study shows that it indeed offers better efficiency and cost reduction compared to single switch approaches for this power level. The design procedure and experimented results are presented.**

I. INTRODUCTION

Recently the suppression on the line current harmonics and the power factor requirements were being imposed to lower power level applications. In particular 200~300W power supplies in PC belong to the IEC-1000-3-2 class D. For the last several years a great deal of effort has been made to develop efficient and cost effective power factor correction (PFC) schemes. A number of single-stage schemes were proposed [1][2] in order to improve efficiency and to reduce cost from conventional two stage schemes which PFC pre-regulator followed by a dc-dc converter.

This type of converters operate in discontinuous conduction mode (DCM) , which offer inherent power factor correction capability. The single switch is controlled by a conventional PWM control scheme hence an additional control circuitry for PFC can be eliminated. However, one of the major problems in this type of converters is that they have high capacitor voltage, which forces to use high voltage rating switching devices. To reduce the capacitor voltage, frequency modulation technique can be employed[3]. In this scheme, the operating frequency varies over a wide range, and converter efficiency is deteriorated. This is particularly true for the power supply in a PC which has a wide range of input voltage (90~264V) and load current specification. Also, the switch of the single-stage converter has a large current stress because it carries both the boost current operating in DCM and dc-dc converter current. This may result in using two or more switches in order to limit the current stress on the device in above 100W applications. In fact, a trade off study shows that a single stage, single-switch scheme is not a good candidate for 200W power supply in the PC in terms of efficiency and cost. In order to overcome above mentioned problems in single switch circuits, a two switch scheme with a single PWM controller is proposed. It resembles conventional two stage schemes, however, a single PWM controller with a simple delay scheme drives the switches for the PFC part and the dc-dc converter part differently to make the capacitor voltage within the optimal range. Also it operates with a fixed frequency.

In Section 2, the proposed scheme is described and its operating principle is explained. A design procedure and delay control scheme are summarized in Section 3. In Section 4, the loss analysis of the proposed converter is described for an optimal efficiency, cost and device selection while meeting the PF specification. In Section 5 and 6 selected simulation results and experimental verifications are presented.

II. OPERATING PRINCIPLES

The circuit diagram of the proposed PFC converter employing the delay control is shown in Fig 1.

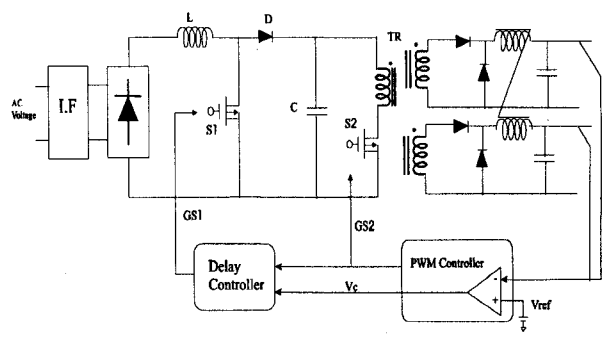

Fig 1. Circuit diagram of the proposed PFC converter

The converter has a PFC switch S1 that is

1 This research work was supported by SAMSUNG ELECTRO-MECHANICS CO.,LTD., Kyungki Do, Korea

synchronized with a cascaded dc-dc converter switch S2. The switch S2 is controlled to regulate the dc output voltage, and the switch S1 is controlled for reduction of the capacitor voltage and DCM operation at the same time without frequency modulation. A proposed delay scheme using only the gate drive signal for S2(GS2) and the output of the feedback control voltage, controls the capacitor voltage within a designed range depending on the operating condition. Also when dc-dc converter is protected by alarm signals such as over current, over voltage, the switch S1 is protected automatically. Same operation happens at no load condition and soft start-up condition. Therefore the PFC part of proposed converter need not have an additional protection scheme and soft start-up circuit and that can reduce the cost and complexity.

For an inherent PFC capability, the boost PFC part operates in DCM, and the power factor is a function of the capacitor voltage for given input voltage[4]. The maximum capacitor voltage can be selected considering the device voltage rating and the transformer design. Since this condition occurs at the high input voltage with minimum load, the delay scheme for S1 can be designed to limit the capacitor voltage while meeting the power factor specification. The inputs of the delay controller are the gate drive signal for S2(GS2) and the output of the feedback control voltage, V_c. As the capacitor voltage increases, V_c decreases. The amount of turn-on delay for S1, D_{delay} is thus inversely proportioned to V_c. This is shown in Fig 2-(a) where D_{pfc} and D_F are the duty ratio of S1 and S2 respectively.

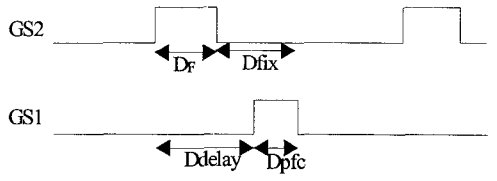

(a) at high input voltage with light load

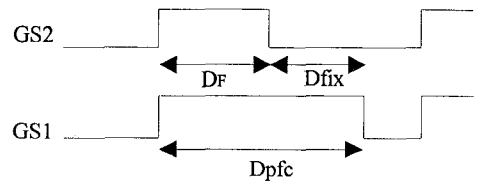

(b) at low input voltage with full load

Fig 2. Gate signals of the switch S1,S2

For the low input voltage, selection of the capacitor voltage influences the DCM condition and efficiency. In order to reduce the switching loss, the capacitor voltage should be lower than the maximum value selected for the above case. This can be achieved by continuously introducing a delay for S1. However, as the capacitor voltage decreases, the conduction loss in S1 increases, and thus there exists a minimum capacitor voltage for the optimum efficiency at this operating condition. In order to limit the capacitor voltage within a desired range for all operating conditions., a variable delay can be implemented. Moreover, at this operating condition, DCM operation must be ensured. Thus, at this extreme condition, it is necessary to introduce the turn-off delay D_{fix}, to make D_{pfc} larger than D_F as shown in Fig2-(b) for the capacitor voltage to be higher than the minimum set value.

III. DELAY CONTROL

Using the energy balance for the capacitor, the capacitor voltage can be expressed :

$$V_{dc} = \frac{2\sqrt{2}}{\pi} V_s + \eta \frac{V_s^2 D_{pfc}^2 V_{dc}}{2Lf I_o V_o} \quad (1)$$

where, V_s : input voltage in rms
D_{pfc} : duty ratio of the PFC switch S1
I_o : load current
V_o : output voltage
L : inductance
f : switching frequency
η : estimated efficiency

Using delay control scheme as shown in Fig. 2, D_{pfc} is given by

$$D_{pfc} = D_F + D_{fix} - D_{delay} \quad (2)$$

where D_{delay} is the variable delay duty ratio by delay controller and D_{fix} is the fixed duty ratio for the optimal efficiency at minimum input voltage with full load. In order to ensure the DCM operation for all conditions, it needs to be designed at the minimum input voltage with full load case, and DCM condition must be satisfied at the peak of the input voltage. The condition for ensuring DCM operation is satisfied if

$$\frac{V_{dcmin}}{V_{dcmin} - \sqrt{2} V_{smin}} \le \frac{1}{D_{pfcmax}} \quad (3)$$

where D_{pfcmax} is given by

$$D_{pfcmax} = D_{Fmax} + D_{fix} \quad (4)$$

Once the value of the product Lf is selected, the desired minimum V_{dc} can be calculated for DCM condition at the minimum input voltage with full load using equation (5).

$$aV_{dc}^2 + bV_{dc} + 2V_s^2 = 0$$

$$a = 1 - \frac{\eta V_s^2}{2LfI_oV_o} \qquad (5)$$

$$b = -2\sqrt{2}\,V_s + \eta\frac{V_s^2}{2LfI_oV_o}\frac{2\sqrt{2}}{\pi}V_s$$

Using the loss analysis in section 4, the optimum Lf and V_{dcmin} can be determined and the maximum value of D_{pfc} and corresponding D_F can be calculated. Thus the D_{fix} can be determined by equation (4). For the maximum V_{dc} at the high input voltage and minimum load, the minimum D_{pfc} and the maximum D_{delay} can be calculated using equation (1) and (2). D_{delay} can be realized by delay controller using D_F as follows

$$D_{delay} = AD_F + B \qquad (6)$$

where A is the gain of the delay controller and B is the offset.. Using equation (6), D_{pfc} can be implemented by equation (7).

$$D_{pfc} = (1-A)D_F + D_{fix} - B \qquad (7)$$

A simplified algorithm for D_{pfc} is illustrated in Fig 3. It is found that a constant delay for D_{fix} is sufficient and the slope of D_{delay} can be determined by the two extreme points A and B.

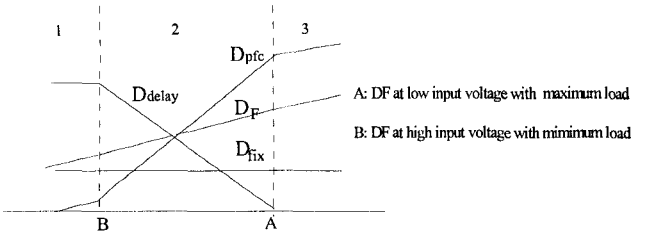

Fig 3. the proposed delay scheme characteristics

As shown in Fig. 3, the proposed delay controller has three different operating modes according to the dc-dc converter duty ratio D_F. In the first mode, variable delay duty ratio D_{delay} is limited by its maximum value and D_{pfc} is only proportional to D_F. At high input voltage with very light load, this mode is performed until the D_{pfc} is zero. When the D_{pfc} is zero, the converter can not perform the PFC action and it becomes the diode rectifier converter. Therefore the capacitor voltage is not higher than the peak input voltage. In the second mode, D_{pfc} is proportional to D_F with gain (1-A) for the reduction of capacitor voltage. At all conditions within specification, the converter is operated in this mode. In third mode, as same as in the first mode, D_{pfc} is proportional to D_F. At low input voltage with very heavy load, the converter is operated in this mode. This condition may occur when the inputs are beyond the specified limits and the proposed converter operates in continuous current mode(CCM).

The delay control is implemented using one CMOS IC4011, one transistor and one op amp as shown in Fig 4.

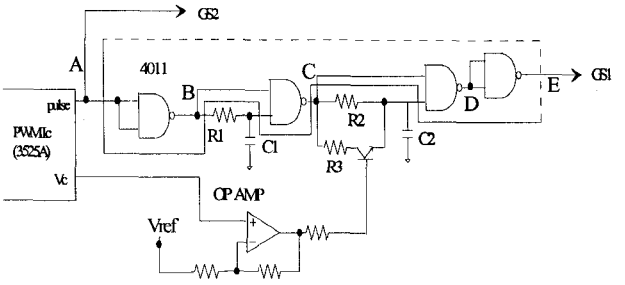

Fig 4. The circuit implementation of proposed delay scheme

The inputs of the delay controller are the gate drive signal for S2(GS2) and the output of the feedback control voltage, V_c. As the capacitor voltage increases, V_c decreases and D_F increases. The amount of D_{delay} is thus inversely proportioned to V_c. The resistor R1 and capacitor C1 sets the fixed delay T_{fix}. The resistor R2 and capacitor C2 sets the maximum delay. The transistor and R3 acts as the voltage-controlled current source which makes the variable delay T_d. The op amp and V_{ref} sets the gain of the T_{onF} and T_d. The wave forms in this circuit are shown in Fig 5.

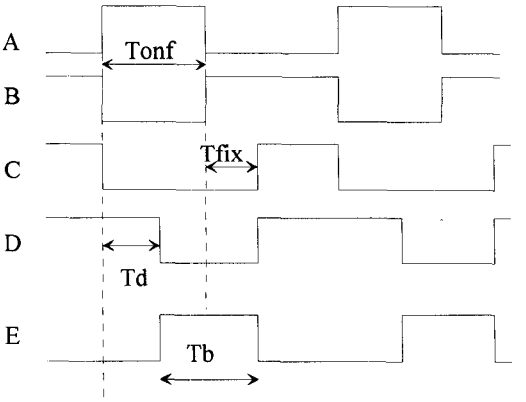

Fig 5. The wave forms in the proposed delay circuit

IV. LOSS ANALYSIS

In order to design the proposed converter for optimal efficiency, the loss analysis is performed. according to the design specifications as shown in Table 1. As discussed earlier, the values of L and f affects V_{dc}, the peak current in S1 and efficiency. Fig 6-(a) shows the efficiency at 90V input with 200W

load as a function of the Lf. Fig 6-(b) shows the capacitor voltage and PFC switch S1 peak current.

Table 1. specification of power supply in PC

Input voltage	90 V ~ 264 V
Maximum Output Power	+5V, 30A +12V, 4.5A
Minimum Output Power	+5V, 3A +12V, 0.3A
Efficiency	70% over at maximum load 55% over at minimum load
Ripple and Noise	50mV at +5V
Hold-up time	20ms at 115V with max. load

From the results of loss analysis in Fig 6, the switching frequency is chosen at 62kHz, and the inductance is 105uH for the optimal efficiency at 90V input with full load.

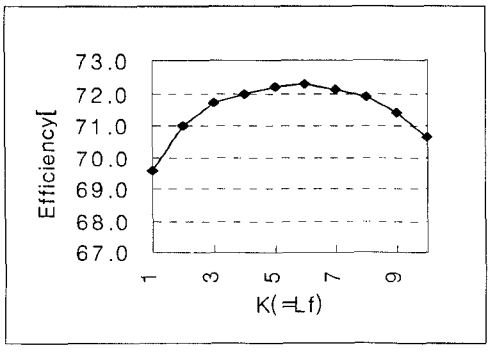

(a) Efficiency at 90V input with 200W load

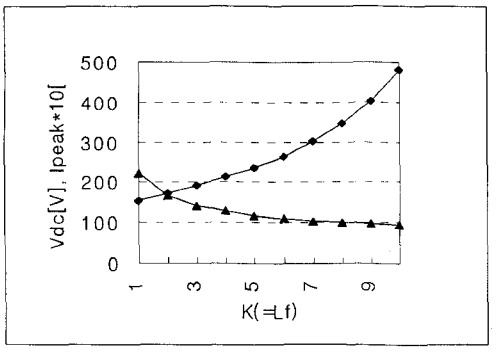

(b) capacitor voltage Vdc and S1 current

Fig 6. Simulated efficiencies, Vdc and S1 peak current

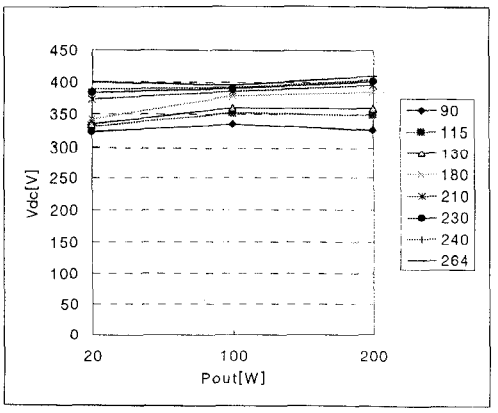

Fig 7. Simulated capacitor voltages

The resulting capacitor voltage at different loads can be analyzed as shown in Fig 7. The capacitor voltage is between 320V and 410V. The transformer turns ratio is selected by 17.5:1 and the delay gain and offset are A=-5.17 and B=1.767 and fixed duty ratio D_{fix}=0.26.

V. Simulation Results

In order to verify the effects of the proposed delay control, computer simulations using PSPICE are performed to predict the wave forms of the input current and capacitor voltage under various operating conditions. The block diagram of the circuit to be simulated is shown in Fig. 8.

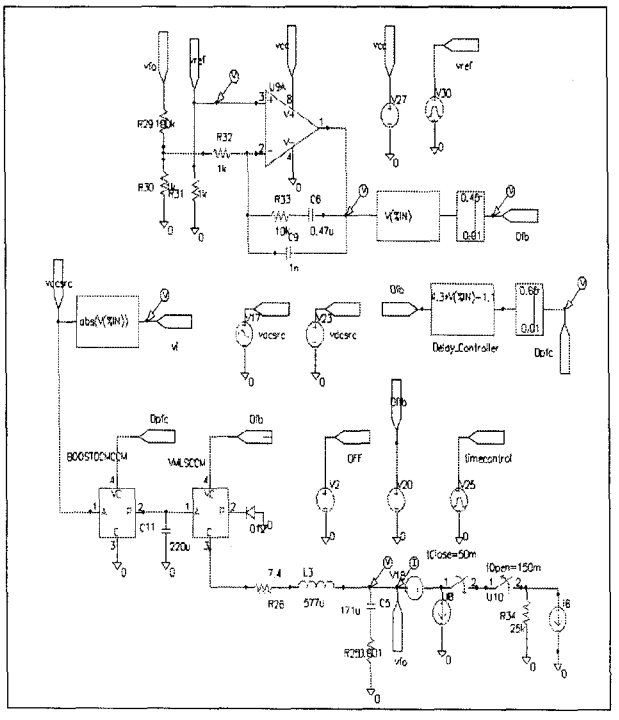

Fig. 8 The block diagram of the proposed converter

The PFC part model is based on low frequency behavioral model[5] as shown in Fig.9 and the dc-dc converter is simulated using PWM switch model. Using the behavioral model, the simulation time can be short, thus long time simulations such as load transient responses and start-up characteristics can be performed.

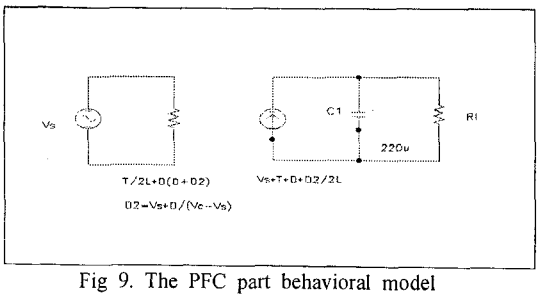

Fig 9. The PFC part behavioral model

Fig. 10 shows the simulated the capacitor voltage, rectified input voltage and current wave forms of the converter under 90V and 264V with a 200W load.

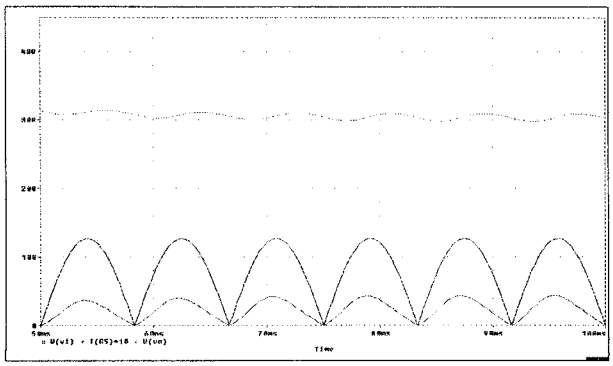

(a) 90V, 200W

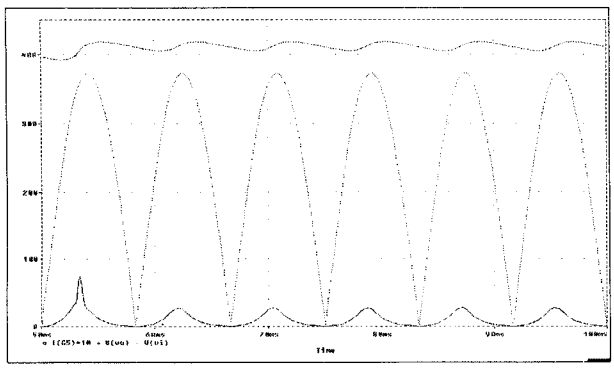

(b) 264V, 200W

Fig 10. The capacitor voltage, rectified input voltage and input current wave form

As shown in Fig.10, the capacitor voltage is limited between 320V~410V. Fig. 11 shows the capacitor voltage and input current wave forms of the converter when the load current is stepped from 20A to 40A. The capacitor voltage is regulated between 320V~410V by the proposed delay controller.

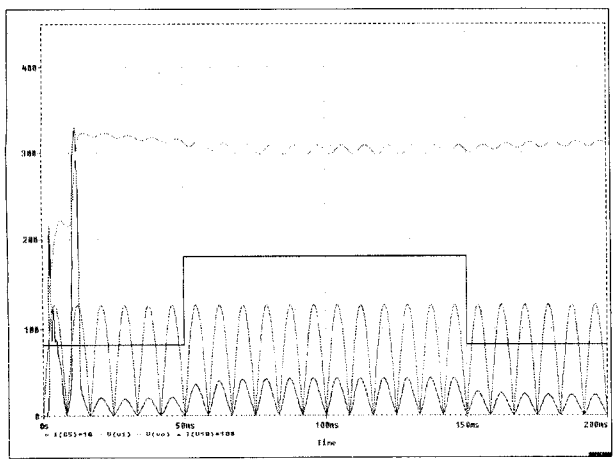

Fig 11. The load transient responses of the proposed converter

VI. EXPERIMENTAL VERIFICATIONS

A prototype hardware is built for the 200W power supply in PC which is implemented with the following major components: S1 - IRFP450 , S2 - 2SK1217, D - MUR860, C - 450V 220uF , L - 105uH (PQ3220), and TR (EER35 primary 70turns, +5V secondary 4turns, +12V secondary 9turns).

Fig 12 shows the measured capacitor voltage as a function of the output power and input voltage. As compared to simulation results, experimental results are approximately same. Fig. 13 shows the measured efficiency and power factor. Above 100W, the power factor is up to 0.95 and efficiency is within the given specifications of a PC.

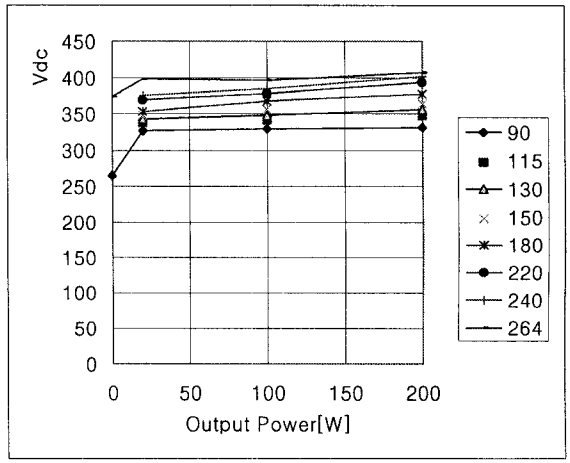

Fig 12. Measured capacitor voltages

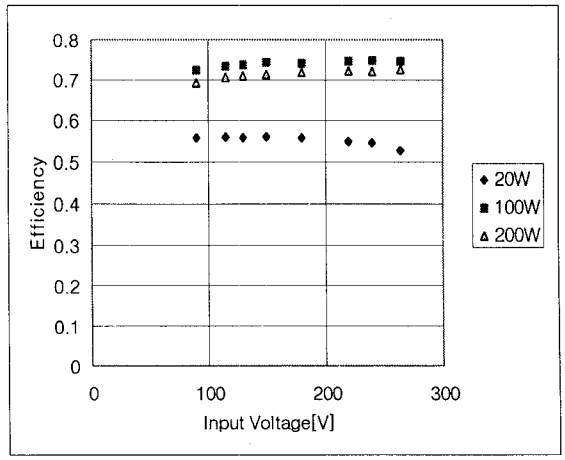

Fig 13. Measured efficiency of the proposed converter

Fig. 14 shows line current wave forms and output voltage ripple and noise at 90V input voltage and 264V input voltage with 200W load. The line current distortions for both conditions are within the limit of the IEC 1000-3-2 specification, and output ripple and noise are within the limit of the 50mV specification.

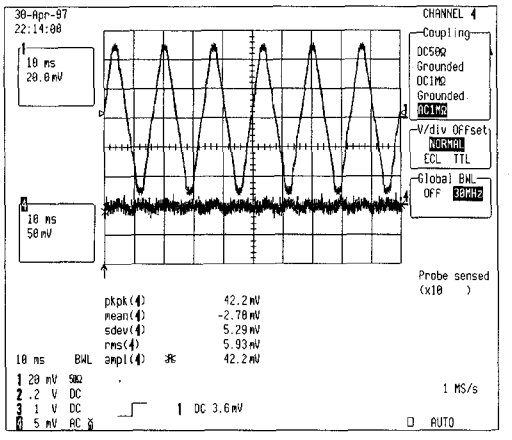

(a) 90V, 200W

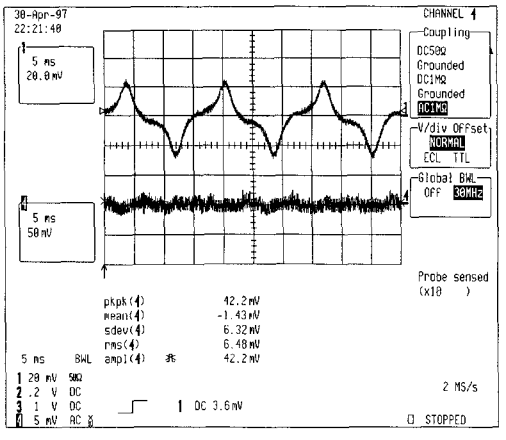

(b) 264V, 200W

Fig 14. The input current and output voltage (+5V) ripple and noises

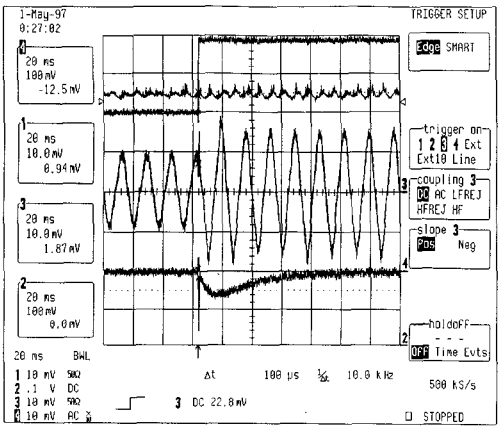

Fig 15. The load transient responses

Fig 15. shows the transient responses of the converter when +12V is loaded at 2A and +5V is stepped from 10A to 20A. The capacitor voltage is not changed and output voltage variations are within 100mV.

VII. CONCLUSION

Due to the high current and voltage stresses, a single stage, single switch PFC converter is not suitable for the efficiency and the cost requirements to a 200W power supply in a PC. In the proposed converter, the PFC switch and dc-dc converter switch are separated for optimum device selection and the simple delay control scheme limits the capacitor voltage within the optimum range. It is shown in this paper that the proposed converter can reduce the cost compared to conventional two-stage scheme while meeting all the specifications including the IEC 1000-3-2.

REFERENCES

[1] I.Takahasi and R.Y.Igarashi, "A switching power supply of 99% power factor by the dither rectifier," *INTELEC '91 Proceedings*, pp.714-719

[2] M.Madigan, et al, "Integrated high quality rectifier-regulators," *PESC'92 record*, pp. 1043-1051

[3] M.M.Jovanovic, et al, "Reduction of voltage stress in integrated high -quality rectifier-regulators by vailable-frequency control, "Proceedings of *APEC'94*, pp. 569-575

[4] K.H. Liu, Y.L. Lin, "Current waveform distortion in power factor correction circuits employing discontinuous-mode boost converter," *IEEE Power Electronics Specialists Conf. (PESC) Record*, pp. 825-829, June 1989

[5] Y.S.Lee and K.W.Siu, "Single-Switch Fast-Response Switching Regulators with Unity power Factor," *APEC'96*, pp. 791-796, March 1996

High-Efficiency Power Supply for Resistive Loads with Sinusoidal Input Current

L. Rossetto*, L. Malesani*, G. Spiazzi**
J. A. Pomilio***, M. Monacchi****

*Department of Electrical Engineering, **Department of Electronics and Informatics
University of Padova, Via Gradenigo 6/a, 35131 Padova - ITALY
Phone: +39-49-828.7500 Fax: +39-49-828.7599/7699
***Dept. de Sistemas e Controle de Energia
UNICAMP, c.p. 6101, 13.081 Campinas - BRASIL
****Whirlpool Europe
Viale G. Borghi, 27, 21025 Comerio (Varese) - ITALY

Abstract. **A high-quality rectifier for supplying resistive loads is presented. It features high power factor, low input current ripple and high efficiency. Device stresses are the same as for a buck converter, and input current is continuous.**

A suitable auxiliary network provides zero voltage switching for both power switch and diode.

The ripple steering technique was applied in order to reduce the input current ripple.

The converter, suitable for heating and lighting applications, was analyzed and experimentally tested on a 1kW prototype.

I. Introduction

The market for household appliances is becoming an important application area for power electronics. In fact, as compared to electromechanical devices, electronic power supplies offer superior performances at a similar cost. One of the main application area regards supplies for resistive loads in lighting and heating applications where futures like continuous power regulation, accuracy irrespective of line voltage variations, protection against short-circuits and open-circuits, power limitation etc. are becoming mandatory requirements.

On the other hand, electronic power supplies must be considered carefully as regards efficiency, reliability and harmonic distortion. From these points of view, topologies which provide low input current ripple are preferred, in order to reduce the size of the input filter. EMI problems are also crucial, calling for soft-switching techniques. Other common requirements for resistive loads are: direct supply from the utility line; high power factor; output power regulation from a few percent to 100% of rated power; high power density; limited power loss.

The care reserved to the utility line interface comes from the attempt to meet standard regulations and recommendations (like IEC 1000-3-2) while the severe environmental conditions, in terms of available space and ambient temperature, in which these power supplies can work call for high power density and efficiency.

In the following a simple high-quality rectifier for supplying resistive loads is presented and briefly analyzed in its several operating modes. The circuit features: high power factor, zero-voltage switching, obtained by using a suitable auxiliary network and low input current ripple, achieved by exploiting the ripple steering phenomenon.

Experimental results of a prototype are reported, showing actual converter performances.

II. Basic Converter Scheme

The proposed converter scheme, shown in Fig. 1, is a step-down topology derived from the Cuk cell by a cyclic rotation of the components[1-3]. Due to the presence of the input inductor L_1, it draws a current with a much lower frequency content as compared to a standard buck converter. Moreover, this topology is suitable for the application of the ripple steering concept which further reduces the input current high-frequency ripple.

Due to the presence of two inductors and the diode bridge rectifier, more operation modes are possible. As reported in [3], besides the usual Continuous Conduction Mode (CCM) and Discontinuous Conduction Mode (DCM), the converter can work in Discontinuous Input Current Mode (DICM) in which only the input diodes stop conducting during the switch off-interval, and in Discontinuous Input and Output Current Mode (DIOCM), characterized by discontinuous currents in both inductors. Both these latter operation modes lead to different fundamental relations as compared to the buck converter; however, as suggested in [3], they are not recommended since produce a higher input current ripple and, above all,

a higher switch voltage stress at light load, which limits the load range the converter can work with.

In the next section we will briefly review the converter behavior only for CCM and DCM operation modes; for a more comprehensive treatment the reader is suggested to consult [3].

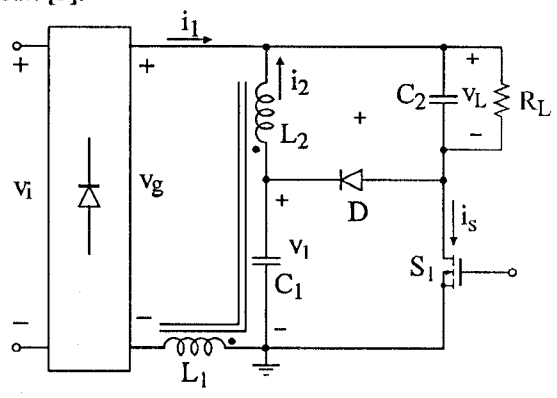

Fig.1 - Basic converter scheme

III. Review of Operation Modes: CCM and DCM

In the following analysis we will consider two separate inductors L_1 and L_2; the effects of the coupling will be taken into account later. For the application we are dealing with, the instantaneous output voltage, as well as the output power, is allowed to vary during the line cycle, since the goal is to control the average power supplied to the load. Thus, the circuit does not include large energy storage devices.

Assuming a switching frequency much higher than the line frequency, we can write:

$$v_g(\theta) = V_i \cdot |\sin(\theta)| \tag{1}$$

$$v_L(\theta) = V_L \cdot |\sin(\theta)|, \qquad \theta = \omega_i t$$

where ω_i is the line angular frequency. Since all reactive elements of the converter are designed to handle energy at the switching frequency, from the power balance in a switching cycle, assuming unity converter efficiency, we can write:

$$v_g(\theta)\cdot \bar{i}_1(\theta) = \frac{v_L^2(\theta)}{R_L} \quad \Rightarrow \quad \bar{i}_1(\theta) = \frac{M^2}{R_L} V_i |\sin(\theta)| \tag{2}$$

where the overbar means averaged quantities in a switching period and $M = \frac{v_L(\theta)}{v_g(\theta)} = \frac{V_L}{V_i}$ is the voltage conversion ratio. This relation reveals that a high power factor is achieved for constant duty-cycle and switching frequency.

The relations and converter waveforms given hereafter are valid provided that the high-frequency voltage ripple across capacitors C_1 and C_2 is neglected.

1) CCM operation. Looking at Fig. 2a which reports the main converter waveforms during a switching period for the case of CCM operation, both inductor currents are continuous and the converter equations are the same of the buck topology. Both switch and freewheeling diode carry the sum of the two inductor currents during the on- and off-intervals respectively.

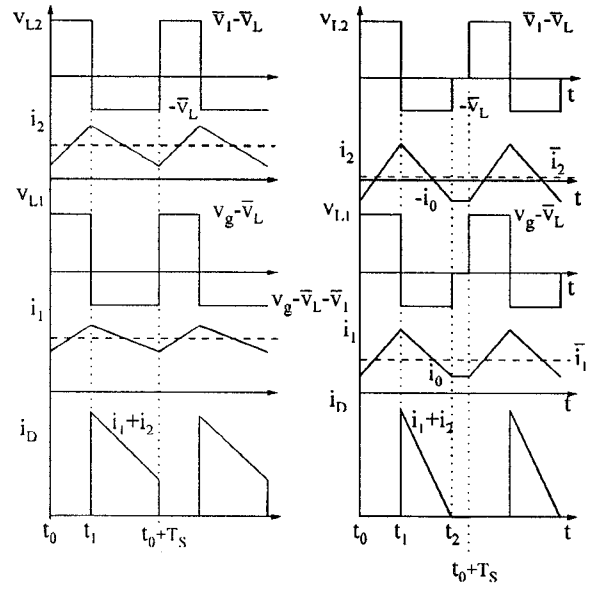

Fig.2 - Main converter waveforms in a switching period. a) CCM operation, b) DCM operation

The volt-second balance applied to inductors L_1 and L_2 gives:

$$v_1(\theta) = v_g(\theta)$$

$$M = \frac{v_L(\theta)}{v_g(\theta)} = \frac{V_L}{V_i} = d \tag{3}$$

where d is the duty-cycle ($dT_S = t_0 \div t_1$). It is important to note that, due to the presence of the input diode bridge rectifier, current i_1 must always be greater than zero, leading to the following constraint on inductor L_1:

$$L_1 > \frac{R_L}{2 f_S} \cdot \left(\frac{1-M}{M}\right) \tag{4}$$

where f_S is the switching frequency.

From Fig. 2a it is also possible to calculate the peak current in both switch and freewheeling diode:

$$i_{S,peak} = i_{D,peak} = \frac{V_i}{R_L} \cdot M \cdot \left(1 + \frac{1-M}{k}\right)$$

$$k = \frac{2 L_e f_S}{R_L}, \qquad L_e = \frac{L_1 \cdot L_2}{L_1 + L_2} \tag{5}$$

1) DCM operation. With this operation mode the freewheeling diode current is discontinuous, leading to the typical waveforms of Fig. 2b. The main difference respect to the buck converter is that the input current remains continuous in spite of the zeroing of the diode current which, in fact, is the sum of the two's.

From the analysis of the waveforms of Fig. 2b we find that the first of (3) is still valid while the voltage conversion ratio results:

$$M = \frac{2}{1+\sqrt{1+\frac{4k}{d^2}}} \tag{6}$$

which is the same relation of a buck converter having an inductance equal to L_e.

Note that for the application we are dealing with, parameter k is constant because the load is assigned, while M must vary from zero to one in order to regulate the power delivered to the load. Thus, the value M_1 corresponding to the boundary between DCM and CCM operation is:

$$M_1 = 1-k \tag{7}$$

The condition which ensures a current i_1 greater than zero is given by the inequality:

$$\frac{L_1}{L_2} > \frac{1-M}{M} \tag{8}$$

The switch and diode current stress is given by:

$$i_{S,peak} = i_{D,peak} = \frac{2V_i}{R_L}\cdot M \cdot \sqrt{\frac{1-M}{k}} \tag{9}$$

IV. Power Stage Design Criteria

As explained before it is convenient to design the converter for CCM and DCM operation modes only, in order to limit current and voltage stresses. While CCM operation, compared to DCM, ensures the lowest current ripples and thus the minimum current stresses and minimum conduction losses, it has the drawback of having higher turn on losses as well as EMI due to hard recovery of the freewheeling diode. Moreover, it requires high inductance values.

Taking into account the above considerations, it seems reasonable to design the converter in such a way that its operation mode changes from CCM to DCM when the voltage conversion ratio decreases from one to zero.

1) Converter Specification:

Peak Input voltage:..... V_i
Load Resistance:..... R_L
Switching Frequency:..... f_S

2) Switch and Diode Current Stress. As stated above, at maximum output voltage (M = 1) the converter operates in CCM. Calling M_1 the value of the voltage conversion ratio in correspondence of which the converter enters the DCM region, the maximum normalized switch and diode current stress results (from (5) and (9)):

$$i_{SN,peak} = \frac{i_{S,peak}\cdot R_L}{V_i} = \begin{cases} \frac{4}{3\sqrt{3}}\frac{1}{\sqrt{k}} & \text{if } k < \frac{1}{3} \\ \frac{(1+k)^2}{4k} & \text{if } k > \frac{1}{3} \end{cases} \tag{10}$$

in which the relation $k = 1-M_1$ was used (see (7)).

Fig. 3 reports the variation of the normalized current stress as a function of parameter k. This plot can be useful to chose the value of k (and thus of M_1) making a trade off between the maximum allowed current stress, which calls for a high k value, and the inductor size, as it will result from the following analysis (in fact, high k means a wider range of CCM operation).

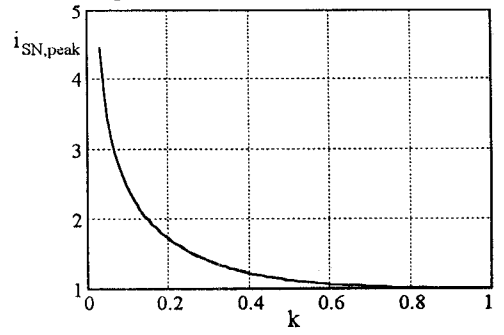

Fig. 3 - Normalized switch and diode current stress as a function of parameter k

3) Inductances L_1 and L_2. From (7) the value of parameter k is found as $k = 1-M_1$ and from its definition the value of equivalent inductance L_e is obtained as:

$$L_e = \frac{L_1 L_2}{L_1+L_2} = \frac{R_L}{2f_S}\cdot(1-M_1) \tag{11}$$

A second constraint on the two inductors is given by inequality (8):

$$\frac{L_1}{L_2} > \frac{1-M_2}{M_2} \tag{12}$$

where M_2 is the value of the conversion ratio in correspondence of which current i_1 zeroes every switching cycle. This value must be chosen suitably lower than M_1, in order to reduce the input current ripple, thus reducing input filter requirements. From (11) and (12), the values of inductances L_1 and L_2 are derived as follows:

$$L_1 = \frac{R_L}{2f_S}\cdot\left(\frac{1-M_1}{M_2}\right) \tag{13.a}$$

$$L_2 = \frac{R_L}{2f_S}\cdot\left(\frac{1-M_1}{1-M_2}\right) \tag{13.b}$$

Note that the value of L_1 obtained from (13.a) automatically satisfies constraint (4) which, as demonstrated in [3], ensures a transfer from CCM to DCM operation without entering the DICM region.

4) Capacitance C_1 and C_2. The values of the two capacitances is chosen on the basis of the desired voltage ripples. For a detailed derivation of these ripples see reference [3].

V. Ripple Steering Concept

The ripple-steering phenomenon was originally investigated in Cuk converters [5], but it can effectively be

applied to all converter topologies in which two or more inductors are fed by similar (scaled) voltage waveforms. And this is exactly the case for the proposed step-down topology (see Fig. 2a and 2b), since the first of (3) remains valid both for CCM and DCM operations. Thus we can draw the equivalent circuit model shown in Fig. 4.

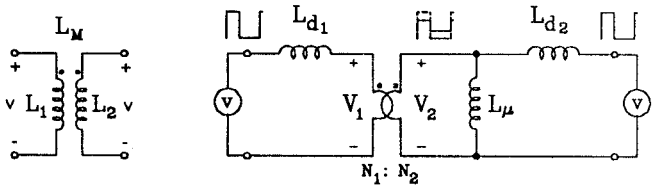

$$L_M = \frac{N_1}{N_2}\cdot L_\mu, \quad L_1 = L_{d1} + \left(\frac{N_1}{N_2}\right)^2 \cdot L_\mu, \quad L_2 = L_{d2} + L_\mu$$

Fig. 4 - Coupled-inductor equivalent circuit

As stated above, due to converter operation, the same voltage v is applied to both windings. Accordingly, zero ripple condition of primary current is easily derived by observing that secondary leakage inductance L_{d2} and magnetizing inductance L_μ form an inductive divider which scales the voltage applied to the secondary winding without altering its shape (voltage V_2 in Fig. 4). If turn ratio N_1/N_2 is chosen to step-up the voltage V_2 to the original value v, zero current ripple on the primary side is obtained. Thus, the zero ripple condition is [6]:

$$\frac{N_2}{N_1} = \frac{L_\mu}{L_\mu + L_{d2}} = k_r \tag{14}$$

where k_r is defined as secondary coupling coefficient. The input current ripple does not simply disappear, but it is "steered" into the other winding.

We can obtain the same result starting from the mutual inductor equations: assuming the same voltage applied on both windings, we can derive the rate of change of the currents in the two windings:

$$\frac{di_1}{dt} = \frac{v}{L_{1eq}}, \qquad \frac{di_2}{dt} = \frac{v}{L_{2eq}} \tag{15}$$

where,

$$L_{1eq} = L_1 \cdot \frac{1 - \frac{L_M^2}{L_1 L_2}}{1 - \frac{L_M}{L_2}}, \qquad L_{2eq} = L_2 \cdot \frac{1 - \frac{L_M^2}{L_1 L_2}}{1 - \frac{L_M}{L_1}} \tag{16}$$

From these expressions, it is seen that, to obtain zero ripple current in the input winding, the equivalent input inductance L_{1eq} must be infinity, which is accomplished by selecting $L_2 = L_M$. With this choice, we obtain also $L_{2eq} = L_2$. Using the relations reported in Fig. 4, it is easily verified that this zero ripple condition is equivalent to the previous one (14).

It is important to observe that the actual coupled inductor behavior deviates from the ideal one mainly for the following two reasons: the zero ripple condition (14) cannot be achieved due to integer number of turns and difficulty to set the gap thickness to the exact value required, and a real converter does not apply the same voltage to both inductor windings due to a non-zero voltage ripple on capacitors, DC voltage drop on inductors, switching noise and so on. As a consequence, the actual input current ripple depends also on the leakage inductance L_{d1} on the primary side.

As far as the design of the coupled inductors is concerned, there are three constraints that must be satisfied:

1) zero current ripple condition (14);
2) inductance L_2 must have the desired value imposed by the power stage design; in fact the equivalent inductance L_e as defined in (11), coincides with $L_{2eq} = L_2$ since L_{1eq} tends to infinity (see (16));
3) core saturation must be avoided.

For a detailed design procedure see [6].

VI. Auxiliary Circuit for Soft-Switching

In order to reduce the electromagnetic noise generated during commutations a suitable auxiliary circuit was used, which allows soft transitions for all switches and diodes. The auxiliary circuit, composed by components S_r, D_{r1}, D_{r2}, C_r and L_r, is shown in the equivalent scheme of Fig. 5 in which I_0 corresponds to the sum of the two inductor currents i_1+i_2 and V_{in} represents the voltage across capacitor C_1 given by the first of (3). As described in [4], switch S_r is activated prior the main switch turn-on in order to discharge the parasitic capacitance of the main devices. In this way, the main switch turns on at zero voltage and, above all, a soft turn-off of the freewheeling diode is achieved, so avoiding the losses due to its recovery time.

Its behavior can be better understood by looking at the main converter waveforms reported in Fig. 6. Let us consider, initially, I_0 and V_{in} constants. Before instant t_0, diode D is conducting the current I_0. At t_0 the auxiliary switch is turned on under zero current condition and the resonant current I_{Lr} rises linearly until it reaches the value I_0. Then, diode D is turned off in soft manner and L_r can resonate with parasitic capacitances C_d and C_s. At time t_2, the body diode of the main switch starts to conduct allowing the zero voltage turn on of S_1. When S_r is turned off (instant t_3), L_r resonates with C_r charging it to V_{in} through D_{r1}. Note that the auxiliary switch is turned off at zero voltage due to the presence of C_r. At instant t_4, D_{r2} starts conducting and I_{Lr} decreases linearly to zero flowing through S_1 and D_{r2}.

When S_1 is turned off its voltage increases linearly due to the charge of C_s and discharge of C_d and C_r until, at instant t_7 the diode D starts conducting initiating the usual freewheeling period. Note that all devices commutations are soft, both at turn on and turn off.

This is only one of the two possible operation modes in which we have assumed that, at instant t_3, the energy stored in L_r is able to completely charge C_r to V_{in}, i.e.:

$$\frac{1}{2}L_r\left(I_o + V_{in}\sqrt{\frac{C_{eq}}{L_r}}\right)^2 > \frac{1}{2}C_r V_{in}^2 \tag{17}$$

The other operation mode will be not considered here because it turns out to be less convenient then the first one. For more information see [4].

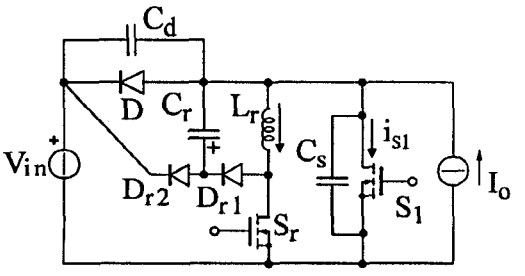

Fig 5 - Simplified schematics for analysis of the auxiliary circuit

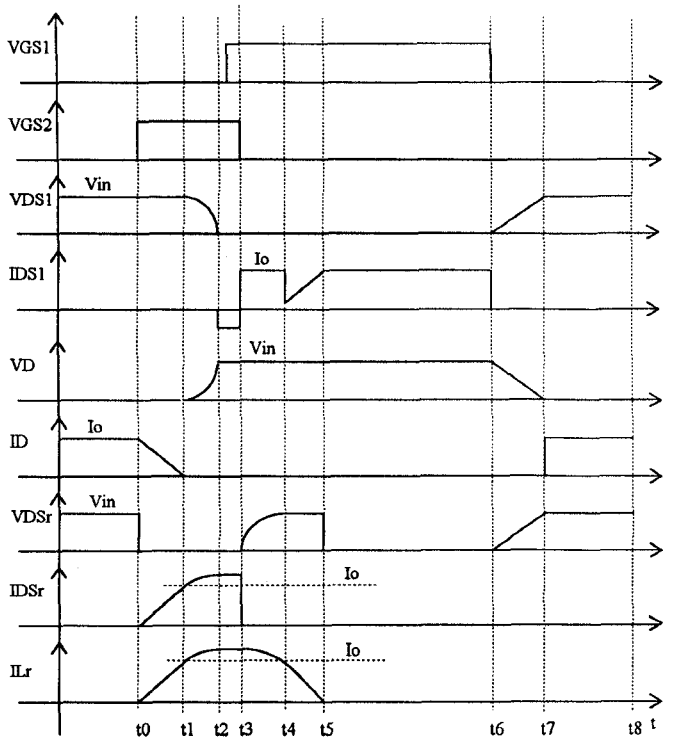

Fig. 6 - Main waveforms of the simplified circuit of Fig. 5b in a switching period

VII. Auxiliary Circuit Design

The presence of the auxiliary circuit limits the available duty-cycle. In order to estimate these limits we define an effective off time as [4]:

$$t_{offe} = \frac{1}{V_{in}}\int_0^{T_s} v_{DS1}dt \tag{18}$$

Of course, such definition gives the usual off time in the case of hard switching converters in which v_{DS} is a square wave. According to (18), the equivalent duty-cycle is then given by:

$$\delta_e = \frac{t_{one}}{T_s} = \frac{T_s - t_{offe}}{T_s} \tag{19}$$

From the analysis of the waveforms of Fig. 6 the minimum value of the equivalent off time, which limits the maximum duty-cycle achievable, is:

$$t_{offemin} = \frac{I_o L_r}{V_{in}} + \sqrt{L_r C_{eq}} + \frac{V_{in}}{2I_o}\left(C_{eq} + C_r\right) \tag{20}$$

where $C_{eq} = C_d + C_s$. In the same manner the minimum switch on time can be derived as:

$$t_{onemin} = \left(\frac{\pi}{2} - 1\right)\sqrt{L_r C_{eq}} + \frac{\pi}{2}\sqrt{L_r C_r} + \frac{V_{in}}{2I_o}\left(C_{eq} + C_r\right) \tag{21}$$

Now, we have to take into account that quantities I_o and V_{in} in the implementation of Fig. 1 are not constant. In particular, neglecting the high frequency voltage ripple across C_1, voltage V_{in} is equal to $v_g(\theta)$ while, I_o is equal to the load current $i_L(\theta)$ (the low frequency current in C_2 is negligible) given by:

$$i_L(\theta) = \frac{v_L(\theta)}{R_L} \tag{22}$$

Thus, since in (20) and (21) always compares the ratio between the two quantities we can write:

$$\frac{V_{in}}{I_o} = \frac{v_g(\theta)}{i_L(\theta)} = \frac{R_L}{M(\delta_e)} \tag{23}$$

Thus specifying the maximum and minimum duty-cycles from (3,17,19-22) the values of the auxiliary circuit parameters L_r, C_r and C_{eq} can be derived, and the current and voltage stresses of these components can be calculated [4]. It is worthy to note instead that current and voltage stresses of the main devices remain the same as the hard-switching solution.

Note that, in this application, the limitation on the maximum duty-cycle achievable does not cause particular problems. In fact, the maximum power transfer can be anyway achieved by keeping the main switch always closed and thus avoiding the commutation losses at maximum power.

VII. Experimental Results

A prototype was designed and built with the following specifications: $V_i = 220\ V_{RMS}$; $P_L = 1$ kW; $f_s = 25$ kHz.

The converter parameter values are listed in Table I in which the value of L_1 refers to the converter without magnetic coupling.

Fig. 10 shows the measured input current with and without magnetic coupling. The measurement was taken at a conversion ratio value which maximizes the current ripple: by comparison the magnetic coupling reduces the current ripple by a factor of six.

Table I - Converter parameters

$L_1 = 400\ \mu H$	$L_2 = 160\ \mu H$	$C_1 = 2\ \mu F$	$C_2 = 1\ \mu F$
$C_r = 15$ nF	$L_r = 31\ \mu H$	$C_{eq} = 7.5$ nF	$R_L = 48\ \Omega$

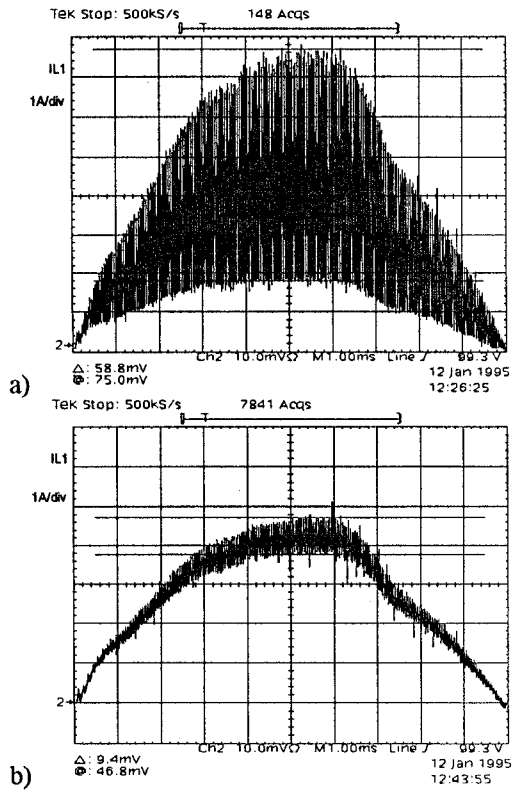

Fig. 10 - Input current waveform at $V_i = 220V_{RMS}$ and $I_i = 3A_{RMS}$
a) without magnetic coupling; b) with magnetic coupling

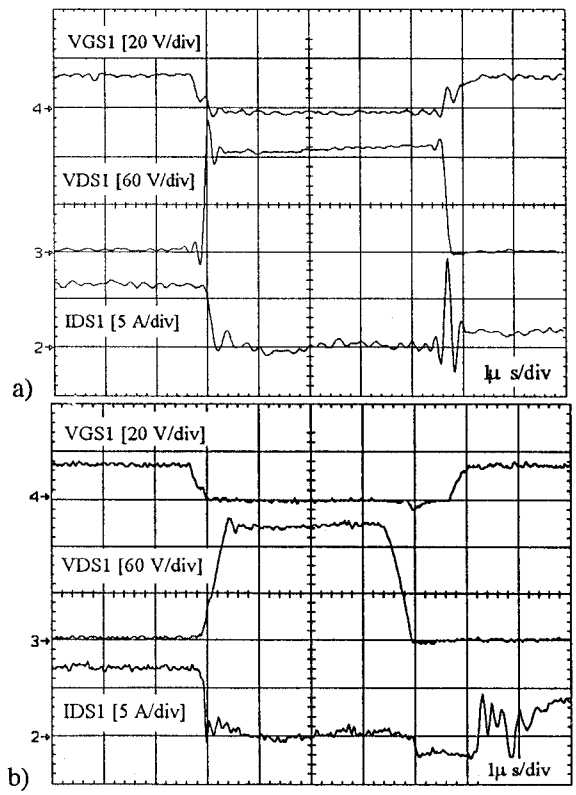

Fig. 11 - S_1 waveforms in a switching period.
a) without auxiliary circuit; b) with auxiliary circuit

The current total harmonic distortion is 5.8% while the line voltage distortion is 2.8%. The measured power factor is 0.998.

As far as the operation of the auxiliary circuit is concerned, Fig. 11 reports the comparison between the high frequency voltage and current waveforms of the main switch S_1 for the hard-switched and the soft-switched converter. The effects of the soft commutations are easily recognizable from Fig. 11b: at turn off the switch voltage stress is considerably reduced and, at turn on, no overlap between voltage and current occurs. Moreover, the big current spike due to the reverse recovery of diode D is eliminated.

The converter efficiency at the rated power remains approximately the same (about 95%) with and without the zero-voltage transition network. However the main advantage of the soft transitions is the reduced EMI.

VIII. Conclusions

A high-quality rectifier for supplying resistive loads, featuring continuous power regulation, high power factor, low input current distortion and high efficiency is presented. It has continuous input current and same device stresses of a standard buck converter.

A suitable auxiliary circuit was used which allows soft commutations for all devices .

Converter design criteria were given and experimental tests done on a 1kW prototype showed good agreement with the theoretical forecasts.

Acknowledgments

The authors would like to thank Dr. M. Miolo, whose dedicated work made possible experimental tests.

Thanks are also due to Mr. R. Sartorello, who supervised experimental activities.

References

[1] J. L. White, W. J. Muldoon, "Two-Inductor Boost and Buck Converters," IEEE Power Electronics Specialists' Conf. Rec., 1987, pp. 387-392.

[2] Z. Zhang, S. Cuk, "A High Efficiency 1.8 kW Battery Equalizer," IEEE Applied Power Electronic Conf. Proc., 1993, pp. 221-227.

[3] L. Rossetto, L. Malesani, G. Spiazzi, P. Tenti, J. A. Pomilio, C. Bocchiola, " High-Quality Rectifier for resistive Loads," Int. Conf. on Power Electronics, Drives and Energy Systems for Industrial Growth (PEDES), New dehli (India), January 1996, pp. 190-196.

[4] S. B. Yaakov, G. Ivensky, O. Levitin and A. Treiner, "Optimization of the Auxiliary Switch Components in a Flying Capacitor ZVS PWM Converters," Applied Power Electronics Conf. Proc., 1995, pp.503509.

[5] R.D.Middlebrook and S.Cuk, *Advances in Switched-Mode Power Conversion*, vols. I and II, TESLAco, Pasadena, California, 1983.

[6] S.Cuk and Z.Zhang ,"Coupled-Inductor Analysis and Design", PESC Conf. Proc., 1986, pp. 655-665.

Distortion-Free Regulated AC Power Supply using Variable Capacitance Device

Akihiko KATSUKI, Hidetatsu IWATA, and Takeshi MATSUI
Department of Computer Science and Electronics
Faculty of Computer Science and Systems Engineering
Kyushu Institute of Technology
680-4 Kawazu, Iizuka-shi, Fukuoka 820, JAPAN
Fax: +81-948-29-7651, Phone: +81-948-29-7677
E-mail: katsuki@cse.kyutech.ac.jp

Abstract — **An entirely new type of ac voltage regulator is proposed by the use of our original Variable Capacitance Device. This circuit theoretically makes no distortion of output voltage waveform, because only linear reactance devices are utilized in power stage. Here, the Variable Capacitance Device was employed as linear capacitor to control output voltage. A boost-type dc-to-dc converter was used for a high-speed driver of this device.**

1. INTRODUCTION

As ac constant-voltage power supply, ferroresonant circuits[1] and so on are well known. Ferroresonant circuits have the advantages of current limitation against short circuit and absorption of noise flowing from ac line. However, waveform of output voltage is distorted because the output voltage is controlled by nonlinear elements, e.g., saturable core or magnetic-saturation simulation circuit[2]. Therefore, to obtain sinusoidal output, additional filter is needed for suppression of higher-harmonic voltage[3].

In this paper, we propose an entirely new type of ac voltage regulator. This circuit theoretically makes no distortion in waveform of output voltage, since only linear reactance devices are utilized in power stage. Moreover, distortion in input-voltage waveform can be reduced because they constuct a low-pass filter. It is needed for output voltage to be controlled that inductance and/or capacitance can be varied. The inductance should be fixed so that the maximum load current may be limited at overloading. Here, our original Variable Capacitance Device[4][5] is employed as a linear capacitor. An ac voltage regulator is presented by using a boost-type dc-to-dc converter as feedback- and feedforward-control circuit. We investigated basic characteristics of the proposed circuit.

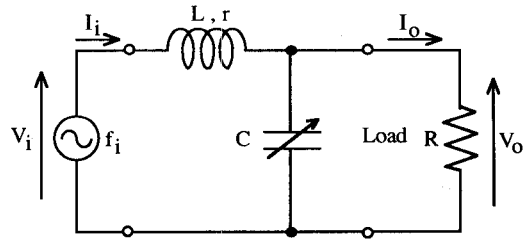

Fig.1. Power stage of the distortion-free ac power supply using Variable Capacitance Device.

2. POWER STAGE

Fig.1 shows a basic circuit of power stage in the proposed distortion-free ac power supply. It is important that the capacitor is linear though its capacitance C is controllable. When the resonant frequency f_r of this circuit equals the frequency f_i of the input voltage V_i and reactance components are lossless, it is known that this circuit is called "Boucherot circuit"[6] and the output current I_o is constant regardless of the load resistance R. Here, f_r is given by

$$f_r = \frac{1}{2\pi\sqrt{LC}} \qquad (1)$$

where L represents the inductance of linear inductor. When the abovementioned conditions are unsatisfied because of variation in L and/or C, I_o depends on the output voltage V_o. Even if the load is short-circuited, the inductor limits I_o and the input current I_i. When waveform of V_i is distorted, that of V_o becomes almost sinusoidal because this circuit operates as a low-pass filter against higher-harmonic components of V_i.

From Fig.1, the following equations

$$V_o = \frac{\sqrt{\left\{\left(1-\omega_i{}^2 LC\right)^2+\left(\omega_i Cr\right)^2\right\}\left\{V_i{}^2-\left(\omega_i{}^2L^2+r^2\right)I_o{}^2\right\}+r^2I_0{}^2}-rI_o}{\left(1-\omega_i{}^2LC\right)^2+\left(\omega_i Cr\right)^2} \quad , \tag{2}$$

$$\cos\theta = \frac{1+r\left(\frac{I_o}{V_o}+\omega_i{}^2C^2\frac{V_o}{I_o}\right)}{\sqrt{\left\{1+r\left(\frac{I_o}{V_o}+\omega_i{}^2C^2\frac{V_o}{I_o}\right)\right\}^2+\omega_i{}^2\left\{\left(1-\omega_i{}^2LC\right)C\frac{V_o}{I_o}-L\frac{I_o}{V_o}\right\}^2}} \tag{3}$$

can be obtained, where $\cos\theta$, r, and ω_i ($=2\pi f_i$) represent input power factor, loss in the inductor, and angular frequency respectively. Output characteristics and input-output characteristics can be calculated from (2). Combining (2) with (3), we can obtain input power-factor characteristics.

Fig.2(a) and Fig.2(b) show examples of output characteristics and input power-factor characteristics in this power stage. On the other hand, Fig.3(a) and Fig.3(b) present input-output characteristics and input power-factor characteristics. These graphs were computed with respect to the lossless (r=0) circuit. In Fig.2(a) and Fig.3(a), f_r is higher than f_i because $C \leqq C_r$, where

$$C_r = \frac{1}{4\pi^2 f_i{}^2 L} \quad . \tag{4}$$

In contrast with this, f_r is lower than f_i because $C \geqq C_r$ in Fig.2(b) and Fig.3(b). From these figures, we can see that input power-factor characteristics with $C \leqq C_r$ is far superior to those with $C \geqq C_r$. Therefore, the case of $C \leqq C_r$ is considered in the following discussions.

Next, experimental results are shown in Fig.4 and Fig.5. The former is output characteristics while the latter input-output characteristics. In these figures, calculated values are depicted by curves. It is seen that these characteristics change according to C. If C can be controlled by control signal, V_o becomes controllable. It is obvious from physical consideration or (2) that V_o equals V_i when C=0 and I_o=0 (no-load). Therefore, a boost-type constant-voltage power supply can be constructed by the use of proposed circuit.

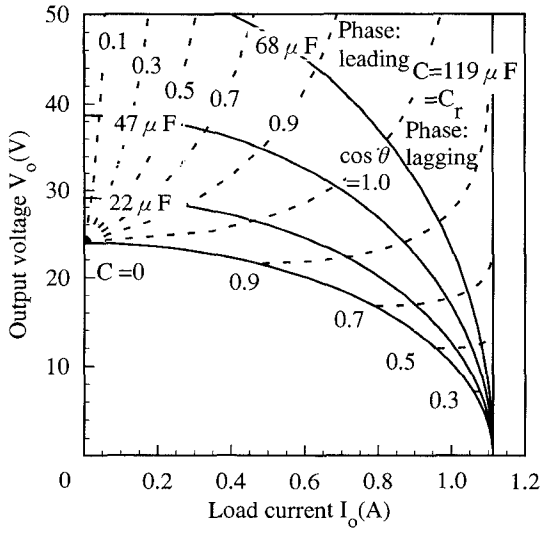

(a) $C \leqq C_r$

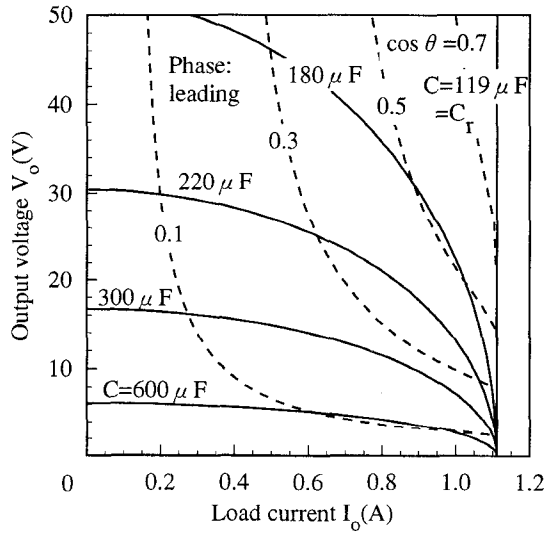

(b) $C \geqq C_r$

Fig.2. Output characteristics and input power-factor characteristics of the power stage (L=59mH, r=0, V_i=24V, f_i=60Hz).

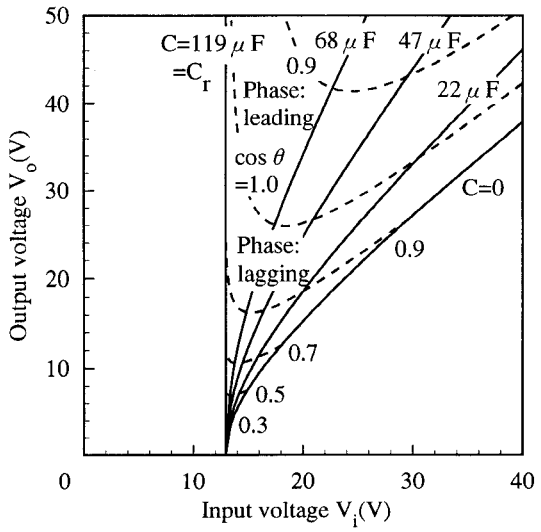

(a) $C \leqq C_r$

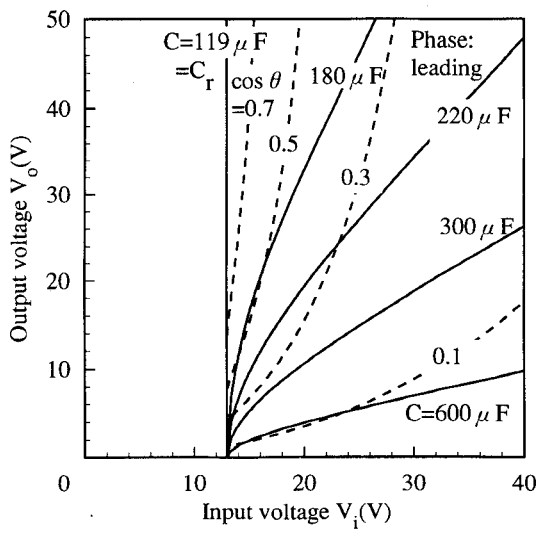

(b) $C \geqq C_r$

Fig.3. Input-output characteristics and input power-factor characteristics of the power stage (L=59mH, r=0, I_o=0.6A, f_i=60Hz).

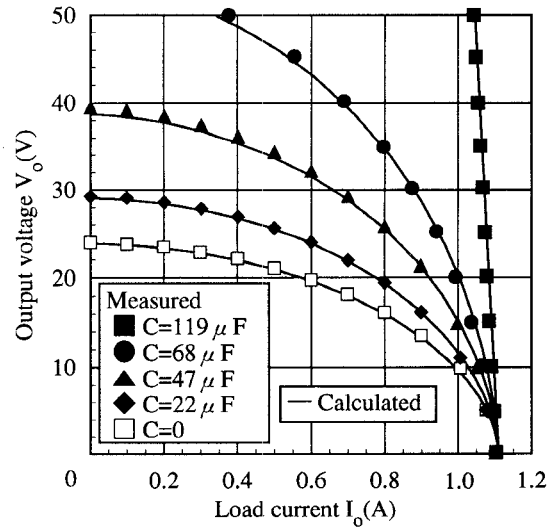

Fig.4. Output characteristics of the power stage (L=59mH, r=0.6Ω, V_i=24V, f_i=60Hz).

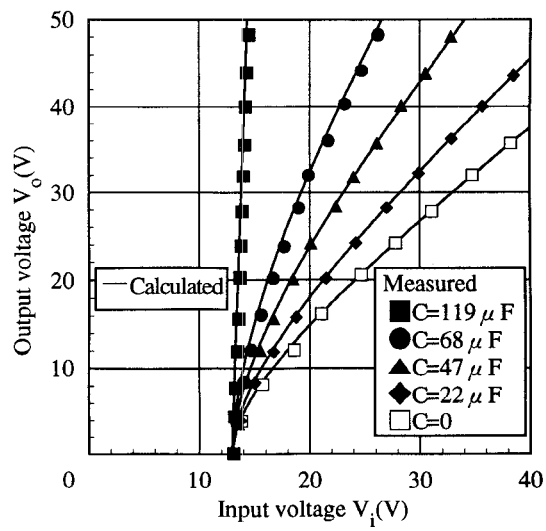

Fig.5. Input-output characteristics of the power stage (L=59mH, r=0.6Ω, I_o=0.6A, f_i=60Hz).

3. VARIABLE CAPACITANCE DEVICE

If we can obtain a device of variable capacitance for use in power electronics, many applications to electronic circuits will be possible. For example, resonant converters can be controlled with the switching frequency fixed[4][5][7]. Because output voltage of a resonant converter is expressed by a function of the ratio of resonant frequency to switching frequency, output control can be performed by adjusting the resonant capacitance. In this case, employment of these devices contributes to miniaturing the output filter components.

By the way, variable capacitance diodes are well known as variable capacitance device. However, operating current is up to about 10μ A, because this device of a p-n junction diode is reverse-biased. In addition, a variable capacitance circuit composed of some capacitors and auxiliary switching devices[7] needs a complicated drive circuit and a large number of electronic parts.

So, we proposed the Variable Capacitance Device for the purpose of dealing with a certain degree of power. This device has the third terminal (control-voltage terminal) for controlling

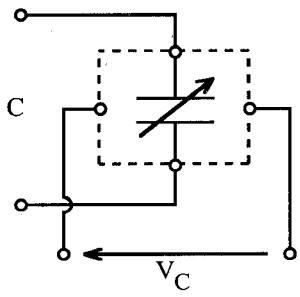

Fig.6. Circuit symbol of Variable Capacitance Device.

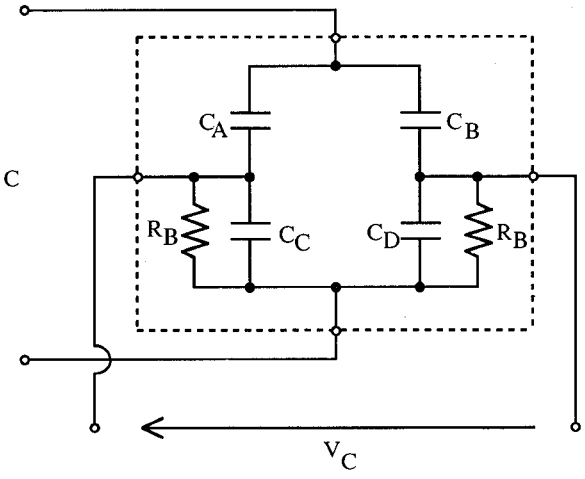

Fig.7. Structure of Variable Capacitance Device.

its capacitance[4]. A multilayered ceramic capacitors made of ferroelectric varies its capacitance with dc-bias voltage. The Variable Capacitance Device can be realized by utilizing this characteristics.

Fig.6 and Fig.7 show the circuit symbol and the structure of the four-terminal Variable Capacitance Device[5] used in the proposed power supply. Since four well-balanced capacitors C_A, C_B, C_C, and C_D are bridge-connected, ac leakage current which flows from the control voltage terminals is extremely small and employment of low-output-impedance driver makes high-speed operation possible. Two resistances R_B's are used to yield the same dc voltage on C_C and C_D. Fig.8 presents control characteristics (relations between the capacitance C and the dc control voltage V_C) of this device.

Measured results on output characteristics and input-output characteristics of the power stage using Variable Capacitance Device are given in Fig.9 and Fig.10, respectively. We can see that V_o can be controlled by V_C.

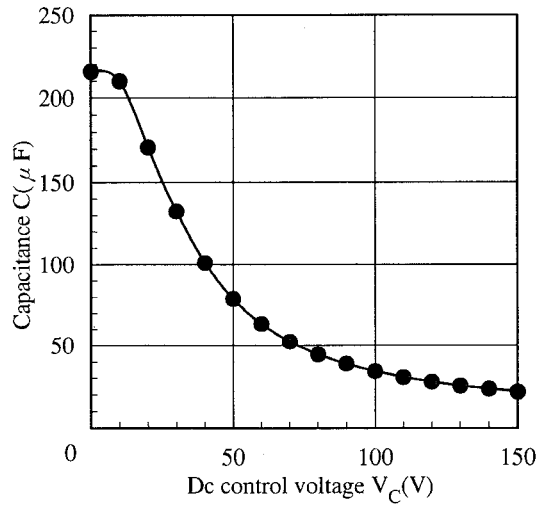

Fig.8. Control characteristics of Variable Capacitance Device.

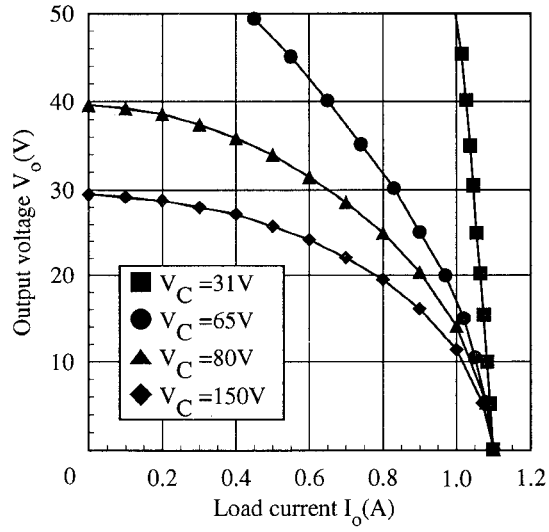

Fig.9. Output characteristics of the power stage using Variable Capacitance Device (L=59mH, r=0.6Ω, V_i=24V, f_i=60Hz).

4. CONTROL CIRCUIT

Fig.11 shows the proposed distortion-free regulated ac power supply using Variable Capacitance Device. This circuit is constructed by the power stage and the control circuit.

In the control circuit, both feedback control and feedforward control are performed. A boost-type dc-to-dc converter is used as a high-speed driver of the Variable Capacitance Device, because the switching frequency is extremely high

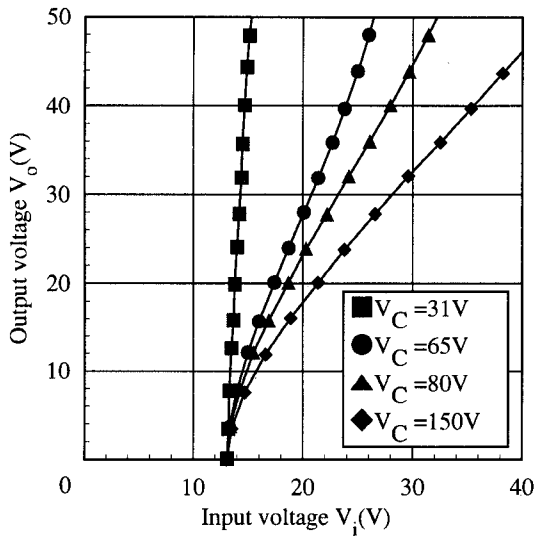

Fig.10. Input-output characteristics of the power stage using Variable Capacitance Device (L=59mH, r=0.6Ω, Io=0.6A, f_i=60Hz).

in comparison with f_i and the output impedance seen by this device is sufficiently low. The load of this converter is almost capacitive. Therefore, its output power is a negligible amount in the steady-state. The capacitance seen by the converter can be utilized as a part of the output capacitor in the converter. This converter plays an important role in expanding a dynamic range of the dc control voltage.

A. Feedback control

To adjust the output voltage V_o, its amplitude is detected by the use of a rectifier and a low-pass filter. Error-amplified signal is transduced to a duty ratio by PWM (Pulse Width Modulation) circuit. Because the output voltage of the converter (that is, the dc control voltage V_C of the Variable Capacitance Device) increases hyperbolically with the duty

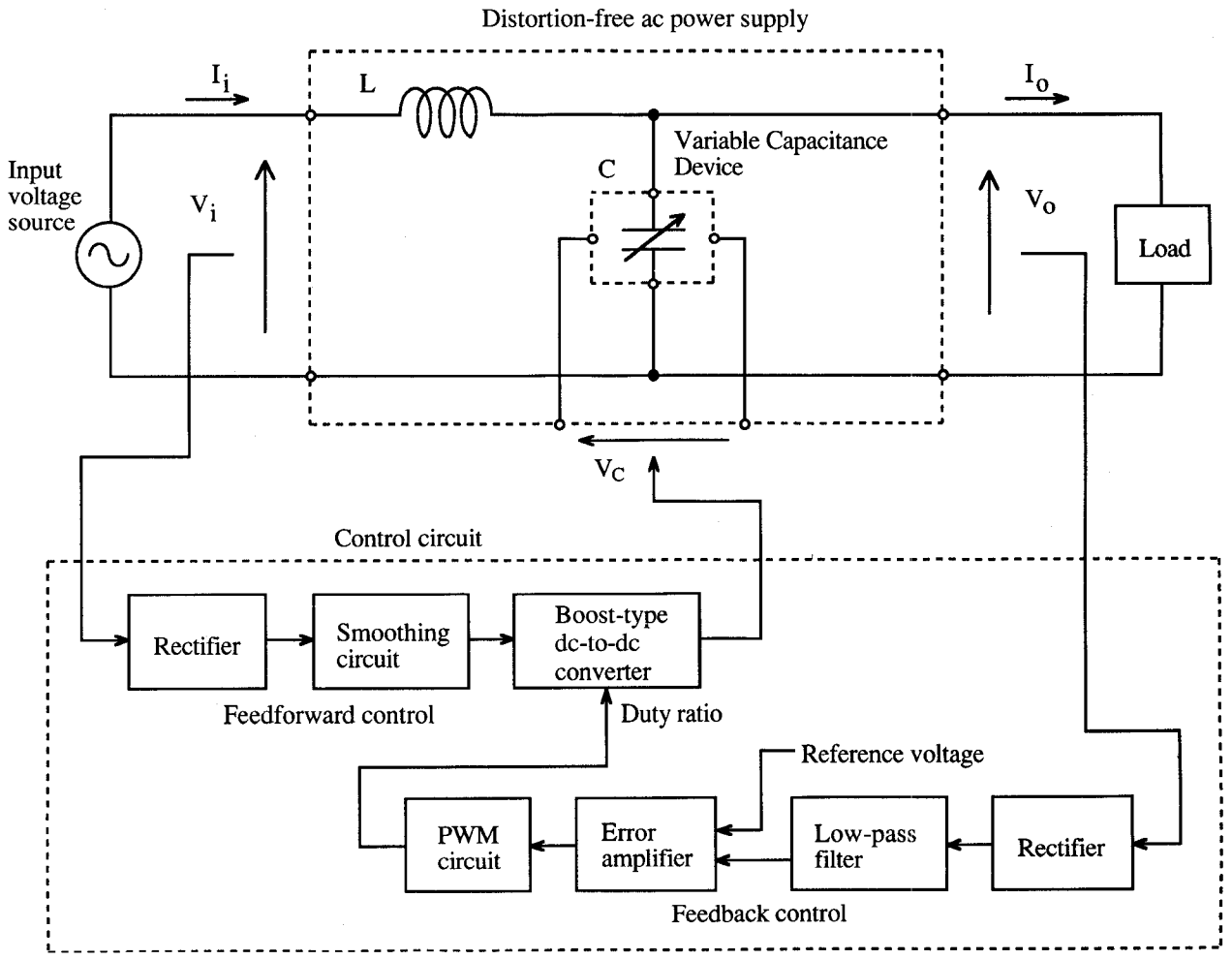

Fig.11. Distortion-free regulated ac power supply using Variable Capacitance Device.

ratio, the control range of output characteristics in the regulated ac power supply can be made wide-spreading.

B. Feedforward control

When the input voltage V_i becomes high, the capacitance C must be reduced by a gain in V_C in order that V_o may decrease. So, the input voltage of the dc-to-dc converter is made to be proportional to V_i. This makes the control range of input-output voltage characteristics wide. Since the input power of this converter reaches up to several watts when occasion demands, the dc-component detecter was constructed by not a low-pass filter but a smoothing circuit.

5. Experimental Results

Measured data on the proposed regulated ac power supply are presented. Fig.12 shows the relations between V_o and I_o (output characteristics). We can see from Fig.12 that the output voltage is well stabilized and the overload protection is possible. The efficiency η and the input power factor $\cos\theta$ are depicted in Fig.13. Fig.13 tells us that η of about 95 percent can be observed in the load current more than about 20 percent of the full-load current. Similarly, $\cos\theta$ of 90 percent or more can be observed in a range of about 45-95 percent of the full-load current.

Next, Fig.14(a), Fig.14(b), and Fig.14(c) show the relations between V_o and V_i (input-output characteristics). In these figures, the data with feedback- and feedforward-control are marked by " ● " and those with only feedback-control marked by " □ ". By the employment of feedforward-control, V_o can be kept almost constant against a wide variation in V_i. It is seen that the effect of feedforward-control becomes more remarkable as the load current increases.

Finally, Fig.15 and Fig.16 present examples of waveforms of V_i and V_o. Fig.15 was observed in the case where amplified oscillator-output was used as V_i. On the other hand, the photographs on commercial-ac voltage in our labolatory are shown in Fig.16. We can see that the generation of distortion in output-voltage waveform is small and the distortion in input-voltage waveform can be effectively removed.

6. Conclusion

A distortion-free regulated ac power supply was proposed by using our original Variable Capacitance Device and its operations were confirmed by experiments. In this circuit, a boost-type dc-to-dc converter is used as a high-speed driver of the Variable Capacitance Device. Efficiency of the proposed power supply is very high (about 95%), because this converter delivers no power in the steady-state.

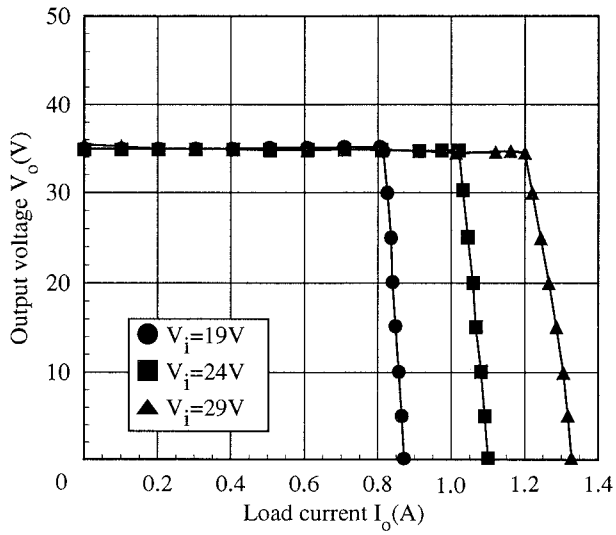

Fig.12. Output characteristics of the regulated power supply using Variable Capacitance Device (L=59mH, r=0.6Ω, f_i=60Hz).

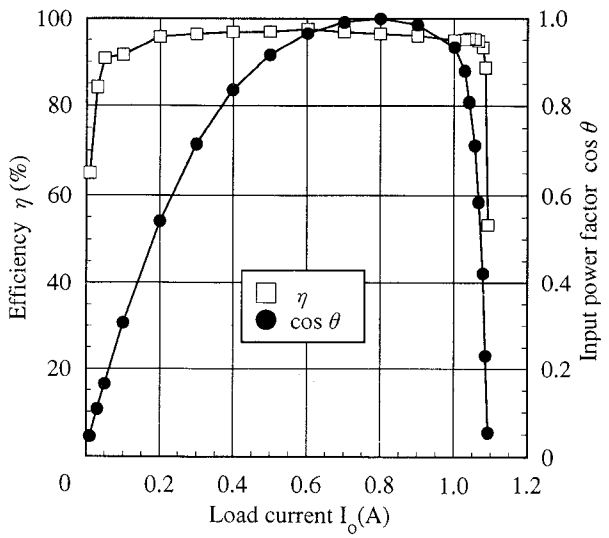

Fig.13. Efficiency and input power factor of the regulated power supply using Variable Capacitance Device (L=59mH, r=0.6Ω, V_i=24V, f_i=60Hz).

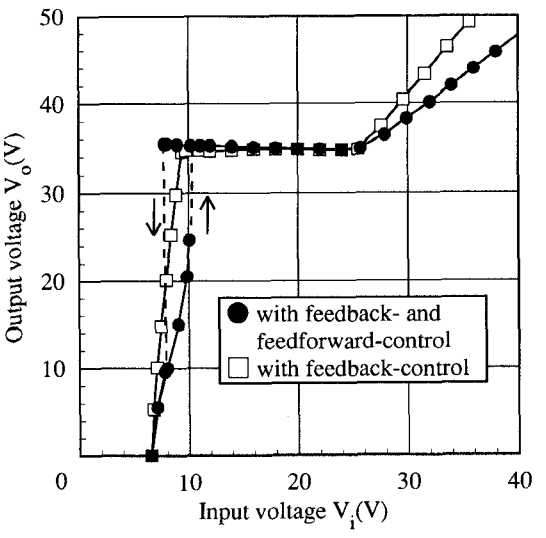

(a) I_o=0.3A

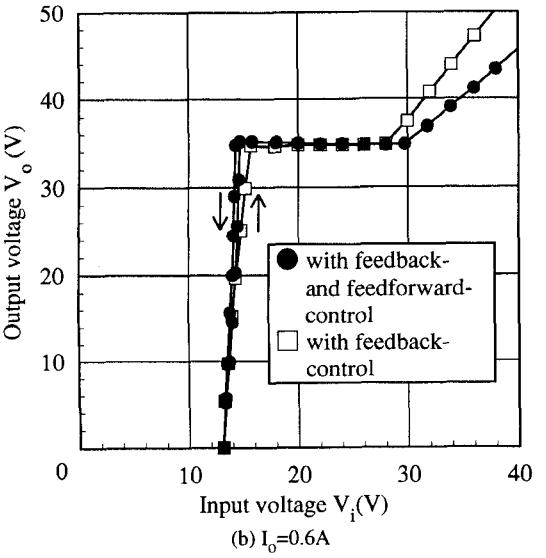

(b) I_o=0.6A

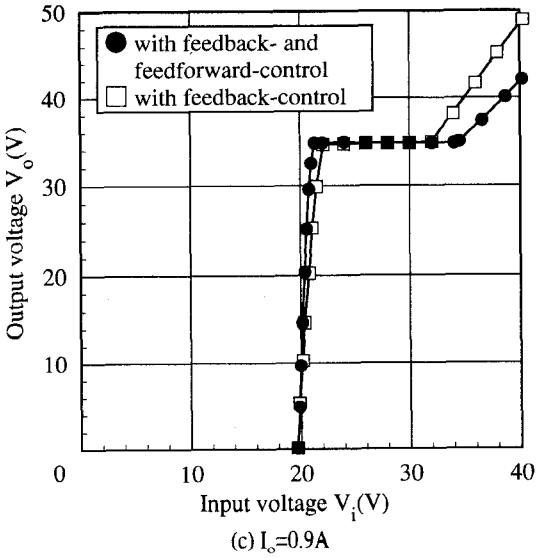

(c) I_o=0.9A

Fig.14. Input-output characteristics of the regulated power supply using Variable Capacitance Device (L=59mH, r=0.6Ω, f_i=60Hz).

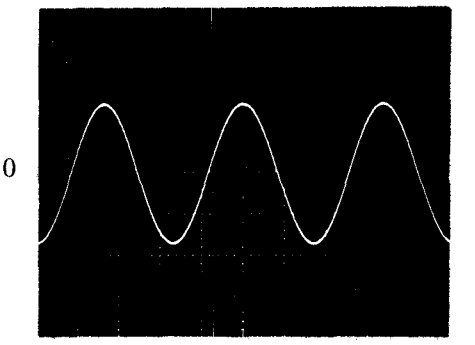

(a) Input voltage (THD=0.10%)

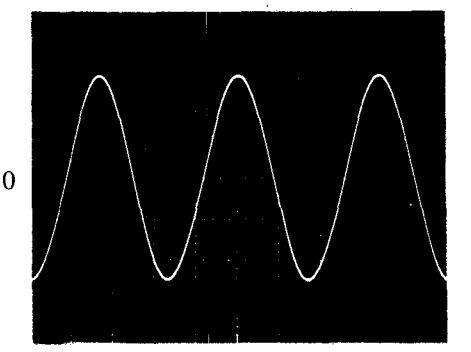

(b) Output voltage (THD=1.2%)

Fig.15. Waveforms of the input (amplified oscillator-output) voltage and the output voltage (L=59mH, r=0.6Ω, V_i=24V, V_o=35V, I_o=0.6A, f_i=60Hz; vertical: 20V/div, horizontal: 5ms/div).

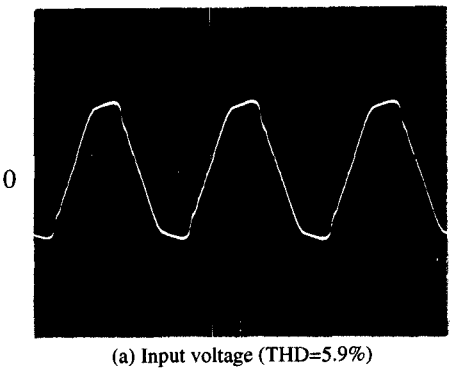

(a) Input voltage (THD=5.9%)

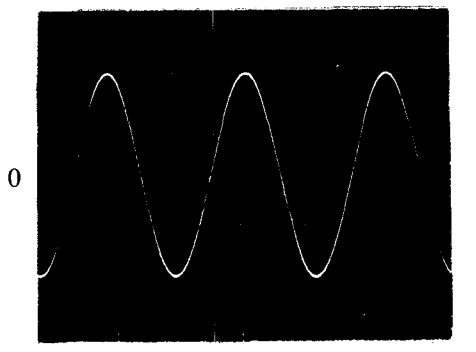

(b) Output voltage (THD=0.67%)

Fig.16. Waveforms of the input (commercial-ac) voltage and the output voltage (L=59mH, r=0.6Ω, V_i=24V, V_o=35V, I_o=0.6A, f_i=60Hz; vertical: 20V/div, horizontal: 5ms/div).

REFERENCES

[1] T.Hasumi, Applications of ferroresonance. Tokyo: OHM-SHA, Ltd., 1952, p.96. (in Japanese)

[2] R.J.Kakalec, "A feedback-controlled ferroresonant voltage regulator," IEEE Trans. Magnetics, vol.6, pp.4-8, March 1970.

[3] R.Rando, "Ac Triport - a new uninterruptible ac power supply," in Proceedings of IEEE INTELEC'78, October 1978, pp.50-58.

[4] K.Harada, A.Katsuki, M.Fujiwara, H.Nakajima, and H.Matsushita, "Resonant converter controlled by Variable Capacitance Devices," IEEE Trans. Power Electronics, vol.8, pp.404-410, October 1993.

[5] A.Katsuki, K.Shirouzu, K.Harada, and M.Fujiwara, "Improved Variable Capacitance Device and its applications to resonant converters," in Proceedings of IEEE INTELEC'93, September 1993, pp.242-246(vol.2).

[6] Edited by Y.Sakaki, Y.Oono, and H.Ozaki, Electric circuit (1) (2nd ed.). Tokyo: OHM-SHA, Ltd., 1980, ch.7, pp.134 and pp.251. (in Japanese)

[7] K.Harada, W.J.Gu, and K.Murata, "Controlled resonant converter with switching frequency fixed," in IEEE PESC'87 Record, June 1987, pp.431-438.

Improvement of Reactance Compensator using Variable Active-Passive Reactance with Output Filter

Hirohito Funato*[1], Atsuo Kawamura†, Takao Watanabe* and Kenzo Kamiyama*[2]

* Dept. of Electrical and Electronic Eng.
Utsunomiya University
2753 Ishii-cho, Utsunomiya-city
Tochigi 321 JAPAN
Phone +81-28-689-6089, Fax +81-28-689-6009
E-mail: *1 funato@cc.utsunomiya-u.ac.jp
*2 kamiyama@cc.utsunomiya-u.ac.jp

†Dept. of Elec. and Comp. Eng.
Yokohama National University
79–5 Tokiwadai, Hodogaya-ku
Yokohama 240 JAPAN
Phone +81-45-339-4129, Fax +81-45-338-1157
E-mail: kawamura@kawalab.dnj.ynu.ac.jp

Abstract— **A reactance circuit affects the operation in a power circuit. For example, the transmission power of the ac power line depends on the interconnecting line impedance between the two places.**

A new compensating method of inductance using Variable Active-Passive Reactance (VAPAR) has been proposed to control the existing reactance of a power circuit.

In this paper, first, the authors propose an improved control method of the VAPAR to suppress resonances of the output voltage and current caused by the output filter using a state feedback method.

The produced virtual impedance becomes the desired virtual inductance up to the limited frequency. Then, the frequency characteristics of the virtual inductance generated by the VAPAR is analyzed to clarify the relationship between the frequency characteristics of the virtual inductance and transient response through simulations. From these considerations, the design method of the required characteristics are discussed.

I. Introduction

A reactance affects the operation in a power circuit. For example, the transmission power of the ac power line depends on the interconnecting line impedance between the two places.

A new inductance compensation method using Variable Active-Passive Reactance (VAPAR) has been proposed to control a reactance of power circuits. It can be applied to many application fields, for example, the stabilization of a power system [3].

VAPAR needs an output filter to reduce the harmonics if it is connected to the power system. The output filter may cause resonance in current and/or voltage. Although a resonance suppression method has been proposed in [3], a large derivative gain is required in the proposed method.

In this paper, the novel control strategy of VAPAR with an output filter is proposed to suppress the resonance caused by the output filter using a state feedback method. At first, a design procedure is described to assign the poles and zeros on the left-half plane to stabilize the terminal impedance function of the VAPAR.

Using the proposed state feedback method, the produced virtual inductance has frequency characteristics. In other words, the produced impedance becomes the desired virtual inductance up to a certain frequency. Then, the the frequency characteristics of the virtual inductance generated by the VAPAR is clarified to discuss the relationship between the frequency characteristics of the virtual inductance and its transient response through simulations. From these considerations, the design method of the required characteristics are discussed.

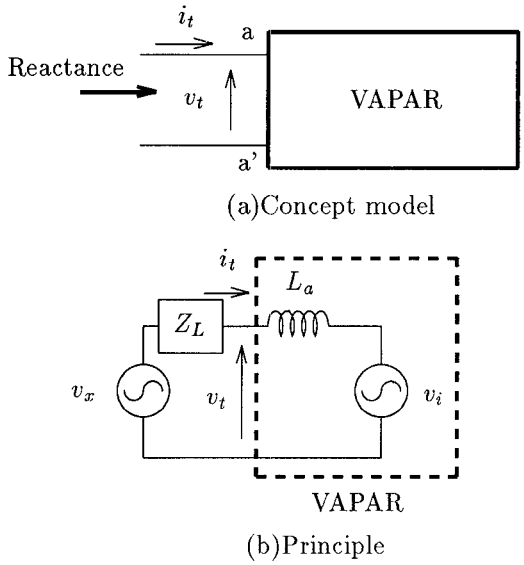

Fig. 1. Concept and principle of VAPAR.

In the chapter 2, the principle and realization of the VAPAR are introduced. The chapter 3 shows the novel control method of the VAPAR. In the chapter 4, the frequency characteristics of virtual inductance produced by the VAPAR are analyzed and the required characteristics are discussed. The chapter 5 concludes this paper.

II. Principle and Realization of Inductance Compensator

A. Principle and Realization of VAPAR

If the terminal voltage v_t and current i_t in Fig.1(a) are determined by the following equation,

$$v_t = L\frac{di_t}{dt} \tag{1}$$

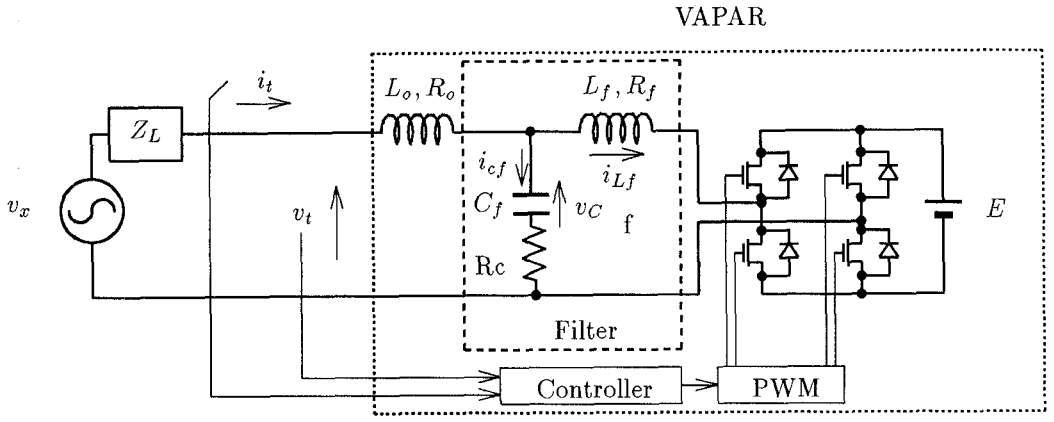

Fig. 3. VAPAR with output filter.

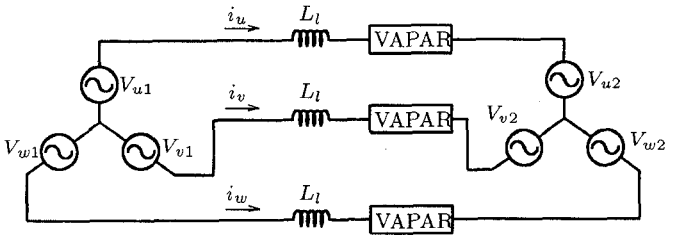

Fig. 2. Example of application of VAPAR.

the two-terminal element VAPAR behaves as an inductance L, including in steady and transient states.

The Variable Active-Passive Reactance (VAPAR) consists of an interconnecting inductor and a controlled voltage source as shown in Fig.1(b). The detailed control scheme and properties have been described in [1] – [3].

VAPAR can generate a negative inductance to set the inductance command as a negative value.[2] A negative inductance is different from a capacitance, while both have the same function in steady state. One of the obvious difference is the frequency characteristics. The magnitude of impedance of a capacitance is in inverse proportion to frequency, while that of a negative inductance is in proportion to frequency.

VAPAR has many applications, for example, the impedance of a transmission line as shown in Fig.2 can be regulated by VAPAR and the transmission power can be controlled. In the following sections, the external circuit of VAPAR is assumed as shown in Fig.1(a) in which Z_L is limited to an $R-L$ series-equivalent circuit for simplification.

III. State feedback control of VAPAR with output filter

A. Output filter

When VAPAR is applied to a power system, the ripple of the output current and/or voltage may be obstacle. To remove this ripple, an output filter should be inserted at the output. The filter is composed of $L-C-R$, which is selected to satisfy the following conditions.

$$\text{at } f = f_{com}, Z_{cf} \gg Z_{Lf} \quad \text{at } f = f_{sw},\ Z_{cf} \ll Z_{Lf},\ Z_{cf} \ll Z_{Lo} \tag{2}$$

where

f_{com} : the frequency of the voltage command of the inverter.

f_{sw} : the switching frequency of the inverter.

In the previous study [3], a derivative element is added to the current controller to suppress oscillations of resonance, however it needs a large derivative gain which may be difficult to implement. In this paper, a novel control strategy is employed to suppress the resonance of output using the state feedback method. In this method, VAPAR is composed of an inverter and a control circuit as shown in Fig.3

Because Variable Active–Passive Reactance (VAPAR) is a two terminal element, a general stability criterion of a feedback control system cannot be applied. In this case, "stable VAPAR" is defined as follows,

" Voltage and/or current of VAPAR is not divergent when only passive elements are connected to VAPAR."

When the controller in Fig.4 is a PI controller, the terminal impedance function Z_v can be expressed as follows where L_v is desired virtual inductance and Z_r is the residual term which is desired to be $|Z_r| = 1$ and $\angle Z_r = 0$.

$$\begin{aligned} Z_v(s) &= sL_v Z_r(s) \\ &= sL_v \frac{K(s-z_1)(s-z_2)(s-z_3)(s-z_4)}{(s-p_1)(s-p_2)(s-p_3)(s-p_4)} \end{aligned} \tag{3}$$

In order to satisfy the above-mentioned stable condition, all real part of poles and zeros have to be negative. When VAPAR works as a negative inductance, the stability has to be considered with the external series inductance L_x which satisfies $L_v + L_x > 0$, because a negative inductance is essentially unstable by itself [3].

In order to accomplish the stable VAPAR, state feedback is employed as shown in Fig.4. The control and feedback gains are decided as the following procedure.

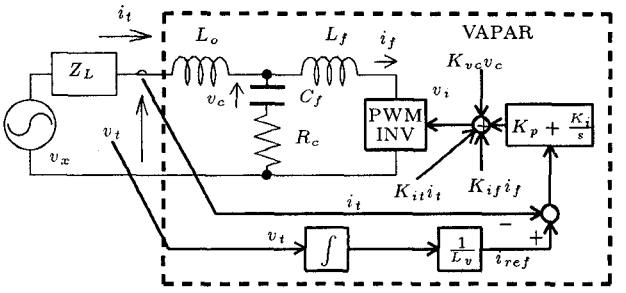

Fig. 4. VAPAR with output filter using state feedback control

TABLE I
USED PARAMETERS.

$L_f = L_o = 2mH$, $R_f = R_o = 0.1\Omega$, $C_f = 50\mu F$
$R_f = 0.5\Omega$, $Z_L = 10mH + 3\Omega$, $L_v = \pm 5mH$
$K_p = 3.875 \times 10^2$,$K_i = 5.0 \times 10^5 (L_v = +5mH)$
$K_p = -3.875 \times 10^2$,$K_i = -5.0 \times 10^5 (L_v = -5mH)$
$K_{if} = -3.94 \times 10^1$,$K_{vc} = 1.27891 \times 10^1$
$K_{it} = 2.0 \times 10^2$

1. Decide K_p,K_i,K_{if},K_{vc} so that all the poles may become desired values.
2. Then, decide K_{it} to stabilize all the zeros.

The gains obtained by the proposed procedure are calculated and shown in Table I, where the circuit parameters are also shown in the same table. Figs. 5 and 6 are the frequency responses of the produced virtual impedance L_v , where L_v = 5mH and L_v = −5mH respectively.

Figs. 7 and 8 show the simulation results of the response to the sinusoidal external voltage v_x, where the VAPAR is operated with an output filter using proposed control. From these figures, VAPAR with proposed method can produce virtual inductance including in transient state without voltage ripples.

It should be noted that a negative inductance has the same characteristics as a capacitance, in other words, the terminal current i_t leads the terminal voltage v_t of VAPAR as shown in Fig.8. However, in transient state, i_t and v_t do not follow the terminal voltage–current relationship for a capacitor. They follow the terminal voltage–current relationship for an inductor.

IV. FREQUENCY CHARACTERISTICS OF INDUCTANCE COMPENSATION

A. *Frequency characteristics of virtual negative inductance*

The virtual inductance produced by the VAPAR has frequency characteristics due to the control. In this section the following conditions are assumed to simplify the theoretical analysis.

1. The VAPAR are composed as shown in Fig.9 with ideal controlled voltage source.
2. The VAPAR has not an output filter.
3. The current controller has a proportional gain K_p and an integral gain K_i.

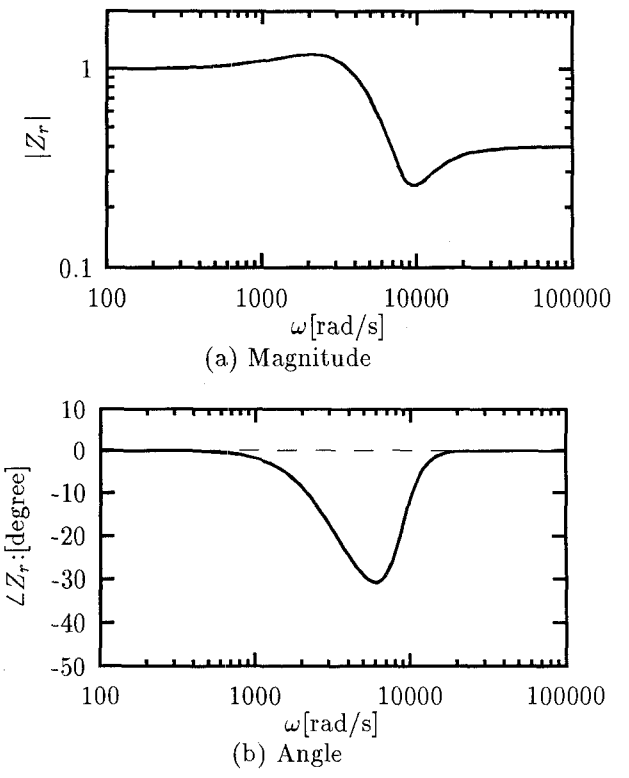

Fig. 5. Bode plots of the residual term Z_r of virtual positive inductance L_v = 5mH produced by VAPAR

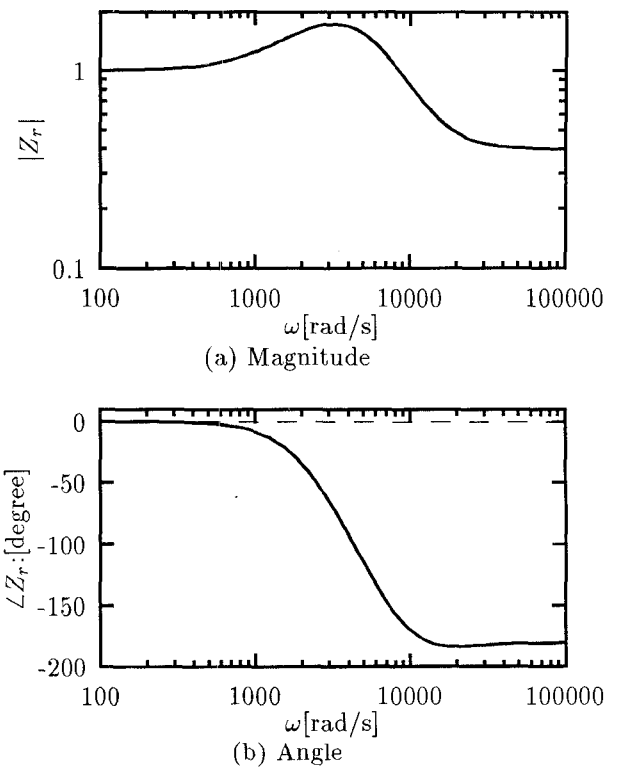

Fig. 6. Bode plots of the residual term Z_r of virtual negative inductance L_v = −5mH produced by VAPAR

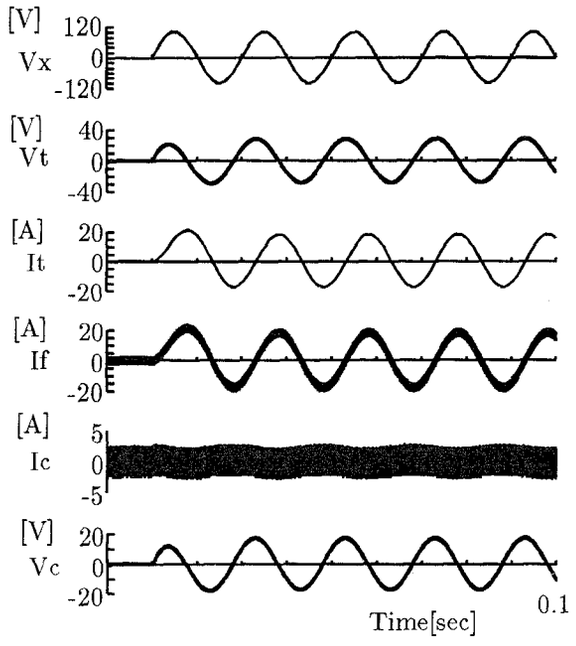

Fig. 7. Positive inductance response

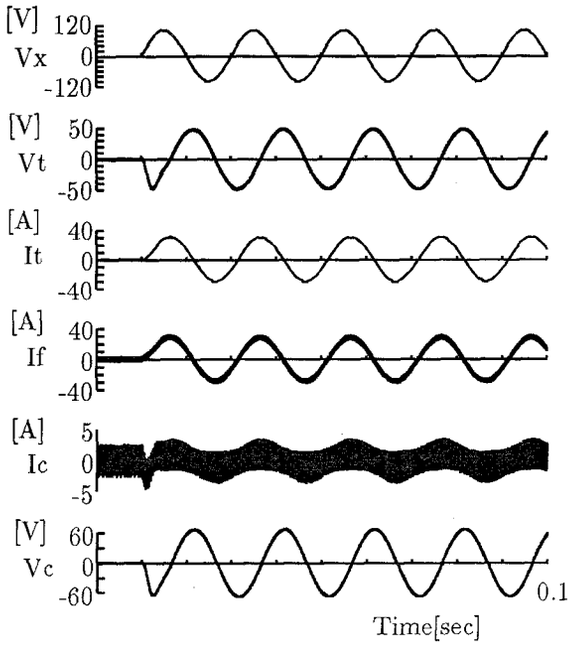

Fig. 8. Negative inductance response

Under these assumptions, the driving point impedance function of an ideal inductance L_v is sL_v, so the driving point impedance of the VAPAR Z_t can be modified as the following equation where $Z_r(s)$ is the residual term due to the control.

$$Z_t(s) = Z_r(s)sL_v \quad (4)$$

$$Z_r(s) = \frac{s^2L_o + s(K_p + R_o) + K_i}{s^2L_v + K_ps + K_i} \quad (5)$$

The VAPAR can be considered to be a virtual inductance if both $|Z_r(\omega)| \cong 1$ and $\angle Z_r(\omega) \cong 0$ are satisfied.

In this section, the proportional gain K_p and the integral gain K_i are decided as the following procedure.

1. Decide K_i.
2. Find K_{pn} which makes the numerator of Z_r be a critical damped case.
3. Find K_{pd} which makes the denominator of Z_r be a critical damped case.
4. Select the larger value of K_{pn} and K_{pd} as K_{p0}. Then, K_p is defined as twice as large as K_{p0} for stabilization of the produced virtual impedance.
5. If $L_v < 0$, Z_r has inherently unstable zeros. Therefore the gains should be decided including the external inductance L_x which satisfies $L_v + L_x > 0$.

Figs. 10 and 11 show the bode plot of the produced virtual inductance using the gains obtained by the above-mentioned procedure. The circuit parameters are shown in Table II. These parameters are selected to emphasize the difference of the responses for the different gains. From these figures, the upper limit frequency of VAPAR can be determined.

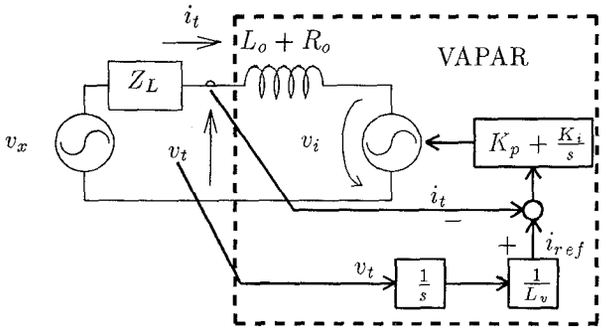

Fig. 9. Simplified model of VAPAR for analysis of inductance control.

TABLE II
USED PARAMETERS IN FIGS. 12 AND 13.

Fig 12 :	L_o = 1mH, R_o = 0.1Ω, Z_L = 1mH+3Ω, L_v = +9mH
Fig 13 :	L_o = 1mH, R_o = 0.1Ω, Z_L = 9mH+3Ω, L_v = −8mH

B. Inductance compensation

The relationship between frequency characteristics of the virtual inductance and the inductance compensation response is analysed in this section.

Figs. 12 and 13 are step voltage responses of the $R-L$ series circuit as shown in Fig.9. In Fig. 12 (b)-(d), the VAPAR generates +5mH. Because L_x is 10mH, the total inductance becomes 15mH if the VAPAR works as a complete inductance +5mH. Fig. 12(a) is an ideal $R-L$ circuit response for a step voltage as a reference. From

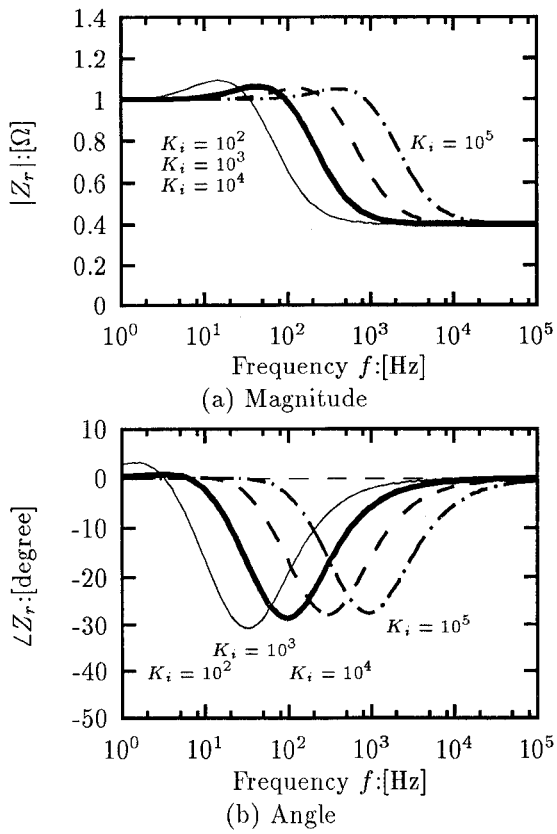

Fig. 10. Bode plots of the residual term Z_r of virtual positive inductance $L_v = +5$mH produced by simplified VAPAR. (The corresponding K_p for each K_i is shown in Fig.12.)

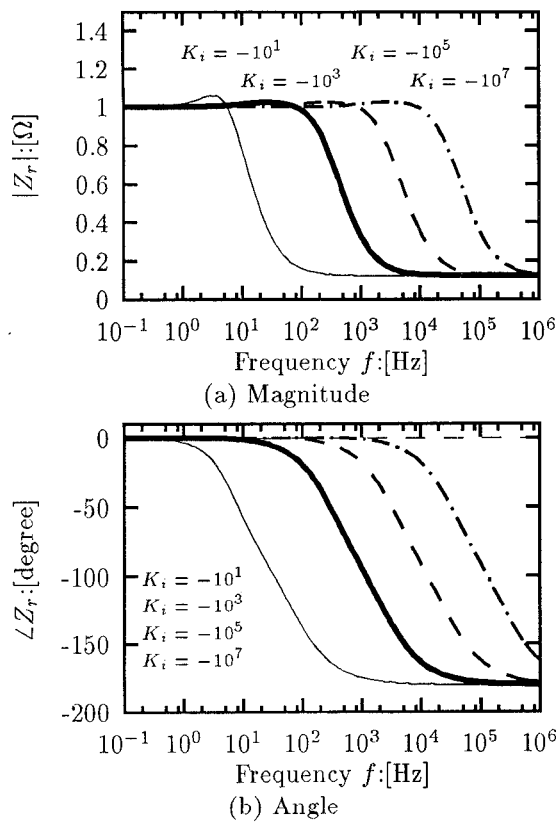

Fig. 11. Bode plots of the residual term Z_r of virtual negative inductance $L_v = -5$mH produced by simplified VAPAR. (The corresponding K_p for each K_i is shown in Fig.13.)

these figures, the enough response is achieved when the upper limit frequency of the VAPAR f_u is larger than the reciprocal of the time constant of the controlled $R-L$ series circuit. In this case, the time constant of (3Ω+ 15mH) is 5ms, therefore f_u should be larger than 200Hz. From Fig. 10, the produced impedance with $K_i = 10^5$ can satisfy this condition.

The responses of i_t and v_t in Fig. 12 (a) and (b) are very slow, which indicate that VAPAR no longer works as the desired inductance. These results verify analysis of this section to be correct.

In the case of Fig.11 where VAPAR are commanded to generate a negative inductance, the same discussions can be applied.

V. Conclusion

In this paper, first, the inductance compensation method achieved by the virtual inductance generated by the Variable Active-Passive Reactance (VAPAR) was introduced. Using this method, an undesired inductance can be controlled, for example, a power flow control. The VAPAR needs an output filter to remove the switching ripple of a PWM inverter. Because the output filter may cause resonance, a novel control method of the VAPAR with an output filter using the state feedback was proposed. Using the proposed method , the excellent result of a virtual inductance simulation was obtained. These results make it possible for VAPAR to be applicable to power systems.

Second, the frequency characteristics of the virtual inductance were analyzed, then the relationship between the frequency characteristics of the virtual inductance and the compensation characteristics was considered. From these considerations, the improved design method to decide the optimal frequency characteristics was proposed.

VI. Acknowledgements

The authors would like to thank TEPCO Research Foundation for the financial support.

References

[1] H.Funato and A.Kawamura, "Proposal of Variable Active–Passive Reactance", *IECON '92* ,PE-10 vol.1 pp381–388, Nov. 1992, in San Diego, U.S.A..

[2] H.Funato, A.Kawamura and K.Kamiyama, "Realization of Negative Inductance Using Variable Active–Passive Reactance (VAPAR)" *IEEE Trans. on Power Electronics*,To be published, July 1997.

[3] H.Funato and A.Kawamura, " Power Transmission System Stabilization using Adjustable Negative Inductance Produced by Variable Active-Passive Reactance (VAPAR)",*IEEJ IPEC-Yokohama, pp632-637, Apr 1995, in Yokohama*

[4] D.M.Divan, "Nondissipative Switched Networks for High-power Applications" *Electronics Letters*,Vol.20, No.7, pp277–279, Mar. 1984.

[5] T.Tanaka, K.Wada and H.Akagi, "Voltage Oscillation on AC Side of Series Active Filters and Its Suppression" *IEEJ Trans. on IA*,Vol.117-D, No.6, pp680–687, 1997.(in Japanese)

[6] T.Ise and Y Murakami, "Series Connected Type Active and Reactive Power Controller Using PWM Inverters" *IPEC-Yokohama*,pp137–142, Apr. 1995.

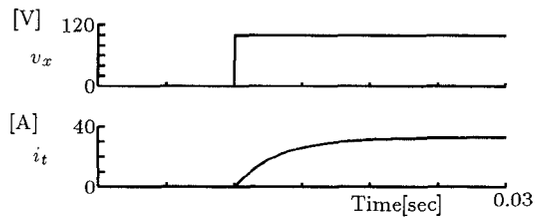

(a) Reference

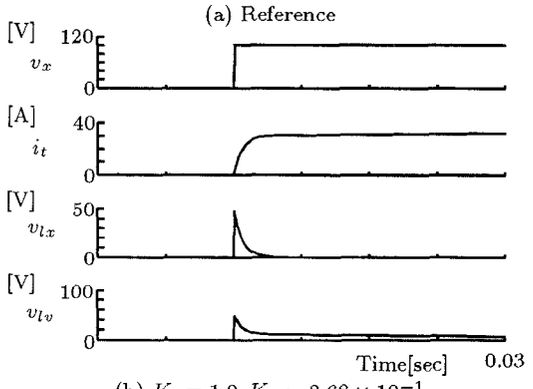

(b) $K_i = 1.0, K_p = 2.68 \times 10^{-1}$

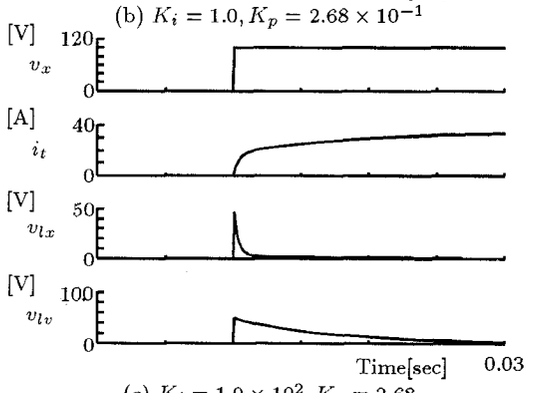

(c) $K_i = 1.0 \times 10^2, K_p = 2.68$

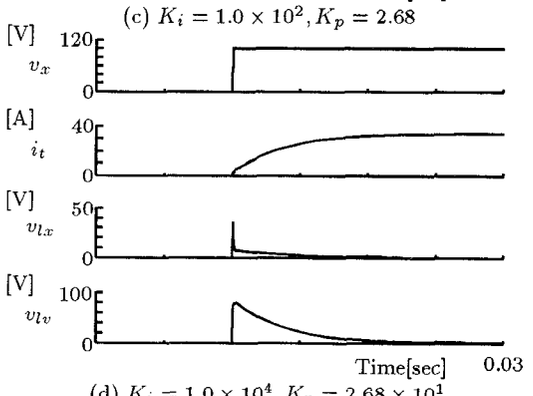

(d) $K_i = 1.0 \times 10^4, K_p = 2.68 \times 10^1$

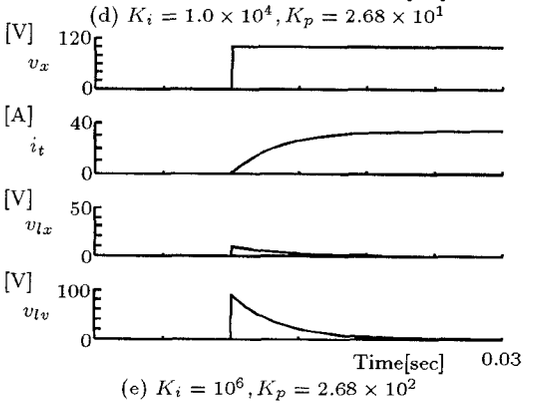

(e) $K_i = 10^6, K_p = 2.68 \times 10^2$

Fig. 12. Step response of virtual positive inductance $L_v = +5$mH produced by simplified VAPAR

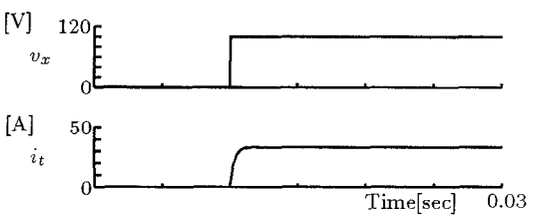

(a) Reference

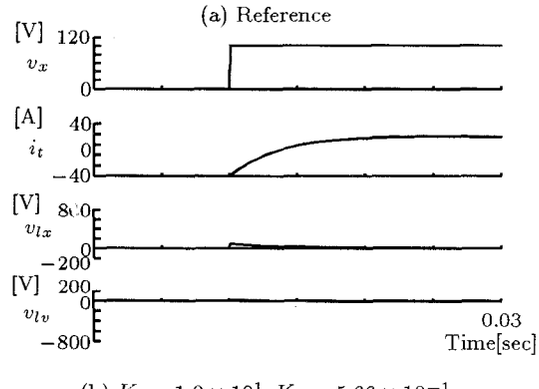

(b) $K_i = 1.0 \times 10^1, K_p = 5.66 \times 10^{-1}$

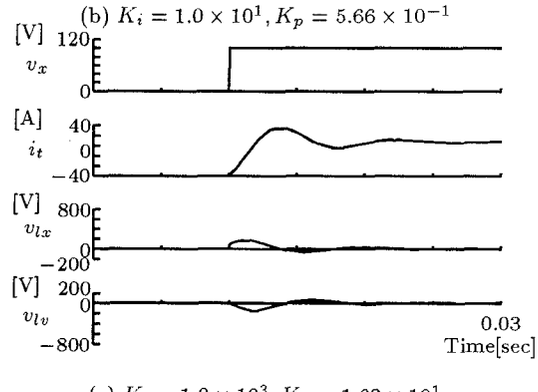

(c) $K_i = 1.0 \times 10^3, K_p = 1.63 \times 10^1$

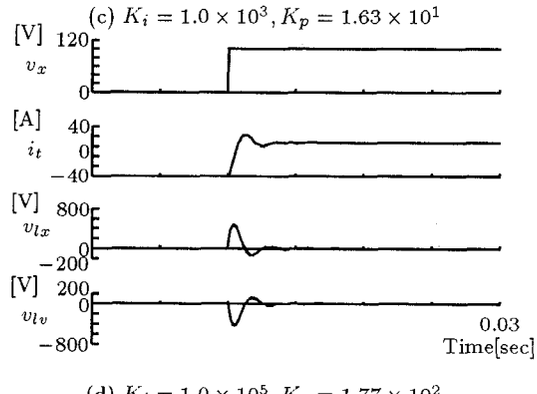

(d) $K_i = 1.0 \times 10^5, K_p = 1.77 \times 10^2$

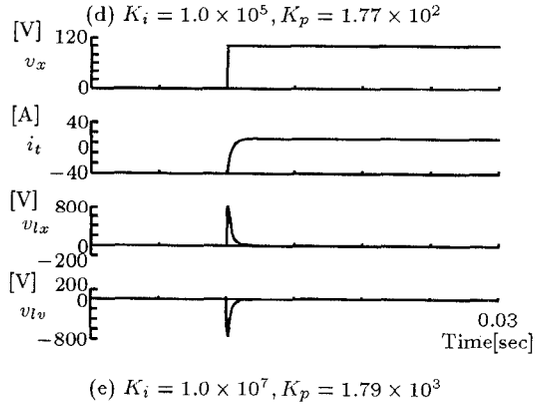

(e) $K_i = 1.0 \times 10^7, K_p = 1.79 \times 10^3$

Fig. 13. Step response of virtual negative inductance $L_v = -5$mH produced by simplified VAPAR

The Instantaneous Power Theory Based on Mapping Matrices in Three-Phase Four-Wire Systems

Hyosung KIM °
Dept. of Control & Measurement Eng.
Cheonan Technical College, KOREA
Tel) 82-417-550-0286
Fax) 82-417-63-3689
Email) hyoskim@dragon.cntc.ac.kr

Hirofumi AKAGI *
Dept. of Electrical & Electronics Eng.
Okayama University, JAPAN
Tel) 81-86-251-8117
Fax) 81-86-256-1959
Email) akagi@power.elec.okayama-u.ac.jp

Abstract - Characteristics of the instantaneous active/reactive powers and zero-sequence current/voltages are analyzed in three-phase four-wire systems. Control strategy for an active filter without energy storage components is proposed on the basis of mapping matrices. It can compensate for the zero-sequence current, irrespectively of whether or not a zero-sequence voltage exists in three-phase four-wire systems.

I. INTRODUCTION

Traditionally, active power, defined as the average value of the product of voltage and current, has been recognized to cause real electric energy flow between two subsystems. Conversely, reactive power, defined as a conservative and orthogonal term against active power, has been considered not to cause real energy flow but to increase an unuseful amount of current in steady state under sinusoidal systems. This traditional definition which is explicit and confirmative in single-phase systems becomes ambiguous and ineffective in multi-phase, distorted, unbalanced, and unsymmetrical systems [1]. Under these undesirable system conditions, many discussions have been made on the definition without succeeding in unifying it [2].

Instantaneous real and imaginary powers have been first defined in a time-domain, and their concept has been successfully applied to harmonic/reactive current compensation in three-phase three-wire systems [3]. In the so called 'p-q theory', three-phase voltages and currents in a three-phase three-wire system are transformed into two-phase current/voltage components on orthogonal α-β coordinates, and then the instantaneous real and imaginary powers can be calculated without any time delay from the two-phase components. The theory provides a theoretical proof that the instantaneous real and imaginary powers are uniquely related with active and reactive currents in three-phase three-wire systems. No reactive current flows after compensating for the instantaneous imaginary power without using energy storage elements.

Introduction of the Park's vector has redescribed the instantaneous real and imaginary powers as instantaneous active and reactive powers which has shown similarity in phasorial formalism between single-phase systems and three-phase systems [4]. The powers have been defined, and then the currents have been decomposed orthogonally in both time and frequency domains. The concept of the instantaneous real and imaginary powers has been expanded from three-phase to multi-phase systems [5]. It has been pointed out that zero-sequence current/voltage components affect not only the instantaneous active power but also the instantaneous reactive power, but without providing any compensation algorithm for the zero-sequence current.

In three-phase four-wire systems, the instantaneous zero-sequence power has been additionally defined as the multiplication of the zero-sequence voltage and the zero-sequence current, separately from the instantaneous real and imaginary powers [3]. Since the zero-sequence power looks like an active power, it would be impossible to compensate for the zero-sequence current without affecting the real power. That means that an energy storage element is necessary to eliminate the zero-sequence current in three-phase four-wire systems [6], [7], [8], [9], [12].

A space vector of the instantaneous reactive power has been defined as the vector product of the voltage space vector and the current space vector in three-phase four-wire systems [10], [11]. The instantaneous reactive current vector has been calculated from the vector product of the instantaneous reactive power space vector and the voltage space vector. Compensation for the instantaneous reactive power would enable to draw no zero-sequence current from the utility if no zero-sequence voltage exists in a three-phase four-wire system.

This paper expands the 'p-q theory' to three-phase four-wire systems, yielding a lucid concept of mapping between instantaneous active/reactive powers and instantaneous current/voltages. The relation between the instantaneous powers and the zero-sequence current/voltage is analyzed in three-phase systems. Control strategy for an active filter without energy storage components is presented in either case where a zero-sequence voltage exists or not. As a results of the analysis, the idea of pseudo-mapping matrices is proposed to provide flexibility in compensating for the zero-sequence current in three-phase four-wire systems including the zero-sequence voltage.

II. DEFINITION OF MAPPING FUNCTIONS

A. Instantaneous Active/reactive Powers

In three-phase systems, three-phase voltages can be transformed to 0-α-β coordinates as follows:

0-7803-3823-5/97/$10.00© 1997 IEEE

$$\begin{bmatrix} e_0 \\ e_\alpha \\ e_\beta \end{bmatrix} = \sqrt{\frac{2}{3}} \begin{bmatrix} \frac{1}{\sqrt{2}} & \frac{1}{\sqrt{2}} & \frac{1}{\sqrt{2}} \\ 1 & -\frac{1}{2} & -\frac{1}{2} \\ 0 & \frac{\sqrt{3}}{2} & -\frac{\sqrt{3}}{2} \end{bmatrix} \begin{bmatrix} e_a \\ e_b \\ e_c \end{bmatrix} \quad (1)$$

Since an amount of zero-sequence current may flow in a three-phase four-wire system, the three-phase currents can be also transformed to 0-α-β coordinates.

$$\begin{bmatrix} i_0 \\ i_\alpha \\ i_\beta \end{bmatrix} = \sqrt{\frac{2}{3}} \begin{bmatrix} \frac{1}{\sqrt{2}} & \frac{1}{\sqrt{2}} & \frac{1}{\sqrt{2}} \\ 1 & -\frac{1}{2} & -\frac{1}{2} \\ 0 & \frac{\sqrt{3}}{2} & -\frac{\sqrt{3}}{2} \end{bmatrix} \begin{bmatrix} i_a \\ i_b \\ i_c \end{bmatrix} \quad (2)$$

An instantaneous active power and a space vector of instantaneous reactive power can be defined as scalar and vector products of the voltage and current space vectors, respectively [4], [10], [11].

$$p \triangleq \vec{e}_{0\alpha\beta} \cdot \vec{i}_{0\alpha\beta} = e_0 \cdot i_0 + e_\alpha \cdot i_\alpha + e_\beta \cdot i_\beta \quad (3)$$

$$\vec{q}_{0\alpha\beta} \triangleq \vec{e}_{0\alpha\beta} \times \vec{i}_{0\alpha\beta} = \text{Det} \begin{bmatrix} \hat{0} & \hat{\alpha} & \hat{\beta} \\ e_0 & e_\alpha & e_\beta \\ i_0 & i_\alpha & i_\beta \end{bmatrix} \quad (4)$$

where,

$\hat{0}$, $\hat{\alpha}$, $\hat{\beta}$: unit vectors for 0, α and β axises.

Each component of the instantaneous reactive power space vector can be expressed as follows:

$$\begin{bmatrix} q_0 \\ q_\alpha \\ q_\beta \end{bmatrix} = \begin{bmatrix} 0 & -e_\beta & e_\alpha \\ e_\beta & 0 & -e_0 \\ -e_\alpha & e_0 & 0 \end{bmatrix} \cdot \begin{bmatrix} i_0 \\ i_\alpha \\ i_\beta \end{bmatrix} \quad (5)$$

Since the mapping matrix of (5) has the rank of 2, one of the three rows is linearly dependant on the other two rows. This means that equation (5) can be expressed as two linearly independent chain equations. If we multiply e_0 to q_0, e_α to q_α, and e_β to q_β, then equation (5) is changed into (6).

$$\begin{bmatrix} e_0 \cdot q_0 \\ e_\alpha \cdot q_\alpha \\ e_\beta \cdot q_\beta \end{bmatrix} = \begin{bmatrix} 0 & -e_0 \cdot e_\beta & e_0 \cdot e_\alpha \\ e_\alpha \cdot e_\beta & 0 & -e_0 \cdot e_\alpha \\ -e_\alpha \cdot e_\beta & e_0 \cdot e_\beta & 0 \end{bmatrix} \begin{bmatrix} i_0 \\ i_\alpha \\ i_\beta \end{bmatrix} \quad (6)$$

Thus, the following relation exists among the three reactive powers:

$$0 = e_0 \cdot q_0 + e_\alpha \cdot q_\alpha + e_\beta \cdot q_\beta \quad (7)$$

If one of e_0, e_α and e_β is not zero, it's corresponding instantaneous reactive power can be expressed with the linear combination of the other ones. For example, if e_β is not zero, q_β can be calculated from q_0 and q_α. In this case, the current components can be inversely calculated from p, q_0, q_α as follows:

$$\begin{bmatrix} i_0 \\ i_\alpha \\ i_\beta \end{bmatrix} = \frac{1}{e_\beta e^2_{0\alpha\beta}} \begin{bmatrix} e_0 e_\beta & e_0 e_\alpha & e_\alpha^2 + e_\beta^2 \\ e_\alpha e_\beta & -(e_0^2 + e_\beta^2) & -e_0 e_\alpha \\ e_\beta^2 & e_\alpha e_\beta & -e_0 e_\beta \end{bmatrix} \begin{bmatrix} p \\ q_0 \\ q_\alpha \end{bmatrix} \quad (8)$$

where, $e^2_{0\alpha\beta} = e_0^2 + e_\alpha^2 + e_\beta^2$.

As the same way, if e_α is not zero, the current components can be inversely calculated from p, q_0 and q_β as follows;

$$\begin{bmatrix} i_0 \\ i_\alpha \\ i_\beta \end{bmatrix} = \frac{1}{e_\alpha e^2_{0\alpha\beta}} \begin{bmatrix} e_0 e_\alpha & -e_0 e_\beta & -(e_\alpha^2 + e_\beta^2) \\ e_\alpha^2 & -e_\alpha e_\beta & e_0 e_\alpha \\ e_\alpha e_\beta & (e_0^2 + e_\alpha^2) & e_0 e_\beta \end{bmatrix} \begin{bmatrix} p \\ q_0 \\ q_\beta \end{bmatrix} \quad (9)$$

As mentioned earlier, equation (8) cannot be used when $e_\beta = 0$. Conversely, equation (9) cannot be used when $e_\alpha = 0$. One way to overcome this problem is to linearly combine (8) and (9) with the coefficients of $e_\beta^2 / (e_\alpha^2 + e_\beta^2)$ and $e_\alpha^2 / (e_\alpha^2 + e_\beta^2)$, respectively.

$$\begin{bmatrix} i_0 \\ i_\alpha \\ i_\beta \end{bmatrix} = \frac{1}{e^2_{\alpha\beta} e^2_{0\alpha\beta}} \times \begin{bmatrix} e_0 e^2_{\alpha\beta} & 0 & e_\beta e^2_{\alpha\beta} & -e_\alpha e^2_{\alpha\beta} \\ e_\alpha e^2_{\alpha\beta} & -e_\beta e^2_{0\alpha\beta} & -e_0 e_\alpha e_\beta & e_0 e_\alpha^2 \\ e_\beta e^2_{\alpha\beta} & e_\alpha e^2_{0\alpha\beta} & -e_0 e_\beta^2 & e_0 e_\alpha e_\beta \end{bmatrix} \begin{bmatrix} p \\ q_0 \\ q_\alpha \\ q_\beta \end{bmatrix} \quad (10)$$

where, $e^2_{\alpha\beta} = e_\alpha^2 + e_\beta^2$.

Applying (7) can simplify equation (10) as follows:

$$\begin{bmatrix} i_0 \\ i_\alpha \\ i_\beta \end{bmatrix} = \frac{1}{e^2_{0\alpha\beta}} \begin{bmatrix} e_0 & 0 & e_\beta & -e_\alpha \\ e_\alpha & -e_\beta & 0 & e_0 \\ e_\beta & e_\alpha & -e_0 & 0 \end{bmatrix} \begin{bmatrix} p \\ q_0 \\ q_\alpha \\ q_\beta \end{bmatrix} \quad (11)$$

Equation (11) is valid whenever $e_0^2 + e_\alpha^2 + e_\beta^2 \neq 0$. If the instantaneous reactive power space vector $\vec{q}_{0\alpha\beta}$ is compensated to be zero, the following results can be obtained.

$$e_0 : e_\alpha : e_\beta = i_0 : i_\alpha : i_\beta \quad (12)$$

Equation (12) means that the current space vector becomes in phase with the voltage space vector. Furthermore, the zero-sequence current i_0 becomes proportional to the zero-sequence voltage e_0 as expressed in (13).

$$i_0 = \frac{i_\alpha}{e_\alpha} \cdot e_0 = \frac{i_\beta}{e_\beta} \cdot e_0 \quad (13)$$

If no zero-sequence voltage exists, no zero-sequence current flows.

B. Instantaneous Active/reactive Currents

From (11), each component of the instantaneous current space vector can be calculated as follows.

$$
\begin{aligned}
i_0 &= \frac{1}{e^2_{0\alpha\beta}} e_0 p + \frac{1}{e^2_{0\alpha\beta}} (e_\beta q_\alpha - e_\alpha q_\beta) \\
i_\alpha &= \frac{1}{e^2_{0\alpha\beta}} e_\alpha p + \frac{1}{e^2_{0\alpha\beta}} (e_0 q_\beta - e_\beta q_0) \\
i_\beta &= \frac{1}{e^2_{0\alpha\beta}} e_\beta p + \frac{1}{e^2_{0\alpha\beta}} (e_\alpha q_0 - e_0 q_\alpha)
\end{aligned} \tag{14}
$$

Equation (14) shows that each current can be separated into two parts related with the instantaneous active or reactive powers. Here, instantaneous active/reactive current space vectors are defined as follows.

1) Instantaneous active current space vector:

Instantaneous active current space vector is defined as the vector sum of the current components which are related with the active power.

$$
\vec{i}_{0\alpha\beta p} \triangleq \vec{i}_{0p} + \vec{i}_{\alpha p} + \vec{i}_{\beta p} \tag{15}
$$

where,

$$
\begin{aligned}
\vec{i}_{0p} &= \frac{e_0 p}{e^2_{0\alpha\beta}} \hat{0} \\
\vec{i}_{\alpha p} &= \frac{e_\alpha p}{e^2_{0\alpha\beta}} \hat{\alpha} \\
\vec{i}_{\beta p} &= \frac{e_\beta p}{e^2_{0\alpha\beta}} \hat{\beta} .
\end{aligned}
$$

2) Instantaneous reactive current space vector:

Instantaneous reactive current space vector is defined as the vector sum of the current components related with the reactive powers.

$$
\vec{i}_{0\alpha\beta q} \triangleq \vec{i}_{0q} + \vec{i}_{\alpha q} + \vec{i}_{\beta q} \tag{16}
$$

where,

$$
\begin{aligned}
\vec{i}_{0q} &= \frac{e_\beta q_\alpha - e_\alpha q_\beta}{e^2_{0\alpha\beta}} \hat{0} \\
\vec{i}_{\alpha q} &= \frac{e_0 q_\beta - e_\beta q_0}{e^2_{0\alpha\beta}} \hat{\alpha} \\
\vec{i}_{\beta q} &= \frac{e_\alpha q_0 - e_0 q_\alpha}{e^2_{0\alpha\beta}} \hat{\beta} .
\end{aligned}
$$

3) Instantaneous current space vector:

The instantaneous current space vector can be defined as the vector sum of the instantaneous active/reactive current space vectors.

$$
\vec{i}_{0\alpha\beta} \triangleq \vec{i}_{0\alpha\beta p} + \vec{i}_{0\alpha\beta q} \tag{17}
$$

The instantaneous active/reactive currents are orthogonal each other since the scalar product $\vec{i}_{0\alpha\beta p} \cdot \vec{i}_{0\alpha\beta q} = 0$.

C. Power Compensation

The instantaneous active power can be expressed as an arithmetic sum of three-axises active power components as follows.

$$
p = p_0 + p_\alpha + p_\beta \tag{18}
$$

where,

$$
\begin{aligned}
\begin{bmatrix} p_0 \\ p_\alpha \\ p_\beta \end{bmatrix} &= \begin{bmatrix} \vec{e}_0 \cdot \vec{i}_0 \\ \vec{e}_\alpha \cdot \vec{i}_\alpha \\ \vec{e}_\beta \cdot \vec{i}_\beta \end{bmatrix} \\
&= \begin{bmatrix} \vec{e}_0 \cdot \vec{i}_{0p} \\ \vec{e}_\alpha \cdot \vec{i}_{\alpha p} \\ \vec{e}_\beta \cdot \vec{i}_{\beta p} \end{bmatrix} + \begin{bmatrix} \vec{e}_0 \cdot \vec{i}_{0q} \\ \vec{e}_\alpha \cdot \vec{i}_{\alpha q} \\ \vec{e}_\beta \cdot \vec{i}_{\beta q} \end{bmatrix} .
\end{aligned} \tag{19}
$$

If (15) and (16) are applied into (18) and (19), the following results are obtained.

$$
\begin{aligned}
p &= p_0 + p_\alpha + p_\beta \\
&= e_0 i_{0p} + e_\alpha i_{\alpha p} + e_\beta i_{\beta p}
\end{aligned} \tag{20}
$$

$$
0 = e_0 i_{0q} + e_\alpha i_{\alpha q} + e_\beta i_{\beta q} \tag{21}
$$

When the instantaneous reactive powers are compensated, only the instantaneous reactive currents are changed as (16). In this case, no instantaneous active power flows by the power compensator as shown in (20) and (21), so that no energy storagement is necessary for the compensator.

III. Control Strategies

A. Without Zero-sequence Voltage($e_0 = 0$)

When any zero-sequence voltage does not exist($e_0 = 0$), the mapping matrix in (11) is modified, resulting in the following compensation strategy.

$$
\begin{bmatrix} i_{C0} \\ i_{C\alpha} \\ i_{C\beta} \end{bmatrix} = \frac{1}{e^2_{0\alpha\beta}} \begin{bmatrix} 0 & 0 & e_\beta & -e_\alpha \\ e_\alpha & -e_\beta & 0 & 0 \\ e_\beta & e_\alpha & 0 & 0 \end{bmatrix} \begin{bmatrix} p^*_C \\ q^*_{C0} \\ q^*_{C\alpha} \\ q^*_{C\beta} \end{bmatrix} \tag{22}
$$

Many combinations are possible for the reference compensating powers [11]. In the following, they are determined as $p^*_C = 0$, $q^*_{C0} = q_{L0}$, $q^*_{C\alpha} = q_{L\alpha}$, $q^*_{C\beta} = q_{L\beta}$.

B. With Zero-sequence Voltage($e_0 \neq 0$)

When a zero-sequence voltage exists($e_0 \neq 0$), the mapping matrix in (11) can be applied as the following compensation strategy.

$$
\begin{bmatrix} i_{C0} \\ i_{C\alpha} \\ i_{C\beta} \end{bmatrix} = \frac{1}{e^2_{0\alpha\beta}} \begin{bmatrix} e_0 & 0 & e_\beta & -e_\alpha \\ e_\alpha & -e_\beta & 0 & e_0 \\ e_\beta & e_\alpha & -e_0 & 0 \end{bmatrix} \begin{bmatrix} p^*_C \\ q^*_{C0} \\ q^*_{C\alpha} \\ q^*_{C\beta} \end{bmatrix} \tag{23}
$$

Although the rms value of the supply current can be minimized without affect the active power when the reactive powers are compensated to be zero, zero-sequence current component still exists, which is proportional to the zero-sequence voltage. Moreover, unless the supply is three-phase balanced sinusoidal voltages, the source currents would not be three-phase balanced sinusoidal waveforms.

C. Pseudo-mapping Matrix

When we introduce pseudo-mapping matrices which are constructed by artificial voltage components instead of the real voltage components, various compensation characteristics can be obtained.

As an example, let's consider a pseudo-mapping matrix in which the zero-sequence voltage component is artificially excluded even though a zero-sequence voltage exists in the system. In other words, instead of (5), equation (24) is intentionally applied to calculate the pseudo-reactive powers as,

$$\begin{bmatrix} q_{L0} \\ q_{fL\alpha} \\ q_{fL\beta} \end{bmatrix} = \begin{bmatrix} 0 & -e_\beta & e_\alpha \\ e_\beta & 0 & 0 \\ -e_\alpha & 0 & 0 \end{bmatrix} \cdot \begin{bmatrix} i_{L0} \\ i_{L\alpha} \\ i_{L\beta} \end{bmatrix}, \tag{24}$$

and the compensation currents are determined as follows:

$$\begin{bmatrix} i_{C0} \\ i_{C\alpha} \\ i_{C\beta} \end{bmatrix} = \begin{bmatrix} \frac{e_0}{e^2_{0\alpha\beta}} & 0 & \frac{e_\beta}{e^2_{\alpha\beta}} & \frac{-e_\alpha}{e^2_{\alpha\beta}} \\ \frac{e_\alpha}{e^2_{0\alpha\beta}} & \frac{-e_\beta}{e^2_{\alpha\beta}} & 0 & \frac{e_0}{e^2_{\alpha\beta}} \\ \frac{e_\beta}{e^2_{0\alpha\beta}} & \frac{e_\alpha}{e^2_{\alpha\beta}} & \frac{-e_0}{e^2_{\alpha\beta}} & 0 \end{bmatrix} \begin{bmatrix} p^*_C \\ q^*_{C0} \\ q^*_{C\alpha} \\ q^*_{C\beta} \end{bmatrix} \tag{25}$$

where, $p^*_C = 0$, $q^*_{C0} = q_{L0}$, $q^*_{C\alpha} = q_{fL\alpha}$, $q^*_{C\beta} = q_{fL\beta}$.

Here, the pseudo-reactive power vector $\vec{q}_{fL0\alpha\beta} = [q_{L0} \; q_{fL\alpha} \; q_{fL\beta}]^t$ becomes different from the original reactive power vector $\vec{q}_{L0\alpha\beta}$, because a new pseudo-mapping matrix is used. Strictly speaking, q_{L0} is the same but $q_{fL\alpha}$ and $q_{fL\beta}$ are changed. Their difference, $\triangle q_{L\alpha}$ and $\triangle q_{L\beta}$, can be described as follows:

$$\begin{bmatrix} \triangle q_{L\alpha} \\ \triangle q_{L\beta} \end{bmatrix} = \begin{bmatrix} q_{L\alpha} - q_{fL\alpha} \\ q_{L\beta} - q_{fL\beta} \end{bmatrix} = \begin{bmatrix} 0 & -e_0 \\ e_0 & 0 \end{bmatrix} \cdot \begin{bmatrix} i_{L\alpha} \\ i_{L\beta} \end{bmatrix} \tag{26}$$

In this case, the zero-sequence compensation current becomes same as the zero-sequence load current as (27).

$$i_{C0} = \frac{1}{e^2_{\alpha\beta}} (e_\beta q_{L0} - e_\alpha q_{fL\beta}) = i_{L0} \tag{27}$$

Even though a zero-sequence voltage exists in the supply, the zero-sequence current component can be controlled to be zero by only compensating for the pseudo-reactive powers without energy storage elements. In this case, although the zero-sequence current is excluded, the current rms value is not minimal, because instantaneous reactive powers still remain as $\triangle q_\alpha$ and $\triangle q_\beta$ as shown in (26).

IV. Simulation

A. Simulation Model

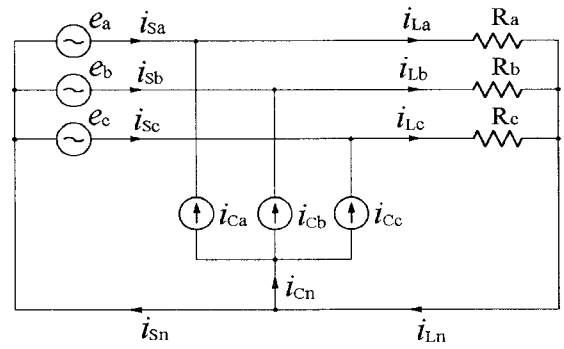

Fig.1 Proposed simulation model.

TABLE I
SIMULATION CONDITIONS.

Items		Case-1	Case-2	Case-3
Source Voltages	e_a[V]	127	127	127
	e_b[V]	127	127	127
	e_c[V]	127	102	102
Load Resistances	R_{La}[Ω]	3.87	3.87	3.87
	R_{Lb}[Ω]	4.84	4.84	4.84
	R_{Lc}[Ω]	4.84	4.84	4.84
Control Strategy		Real Mapping Matrix		Pseudo Mapping Matrix

Fig.1 shows a simulation model, in which the three-phase four-wire system has ideally sinusoidal balanced or unbalanced voltage sources. The load consists of three unsymmetrical resistances. The output power is rated at 10kVA and the line voltage is rated at $220V_{rms}$. Thus the rated load resistance per phase is 4.84Ω.

Three simulation conditions, Cases 1, 2 and 3 were considered; Case-1 is in balanced source voltages and unsymmetrical loads, Case-2 is in unbalanced source voltages and unsymmetrical loads, and Case-3 is in unbalanced source voltages, unsymmetrical loads with a pseudo-mapping matrix. Table I describes the detailed simulation conditions. The a-phase load resistance is set to 80% of the rated resistance. Under the unbalanced voltage conditions in Cases 2 and 3, the c-phase voltage is reduced to 80% of the rated phase voltage.

B. Simulation results

Simulation was performed by PSpice Design Center V6.0. Table II summarizes the simulation results. Each value is measured on the peak point. The load currents in Case-1 are unbalanced due to unsymmetrical load resistances; i_{La} is 1.25 times as large as the other phase load currents. The load currents in Cases 2 and 3 are unbalanced due to both the unsymmetrical load resistances and unbalanced source voltages; i_{La} is 1.25 times as large as i_{Lb} but i_{Lc} is 0.8 times as small as i_{Lb}. The ratios of the power rating of the active filter to that of the source are calculated based on the peak values.

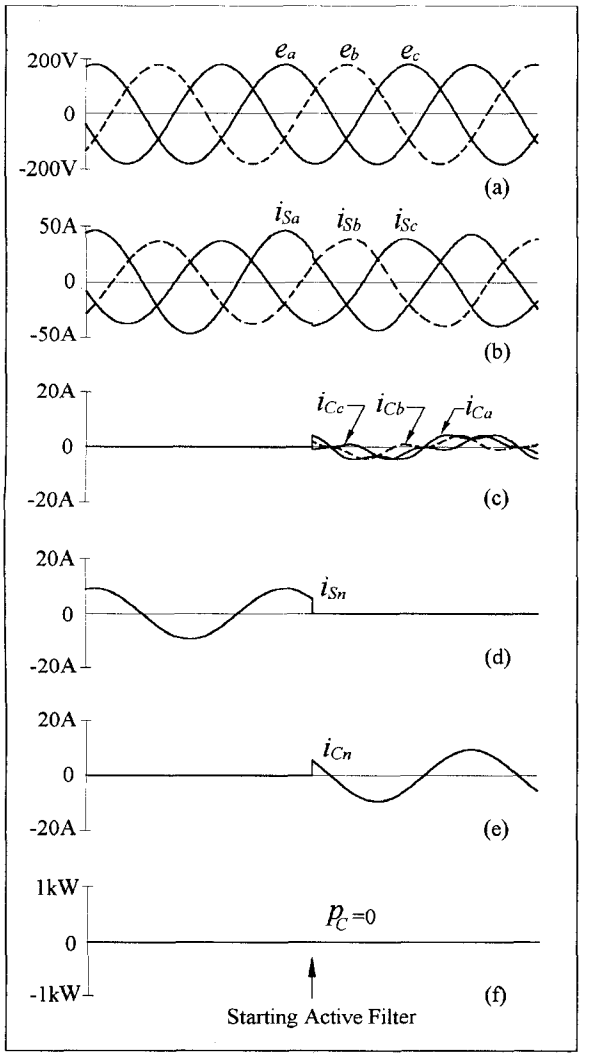

Fig.2 Simulation results in Case-1; (a) balanced source voltages, (b) source currents, (c) compensating currents, (d) neutral current on the source side, (e) neutral current of the active filter, (f) instantaneous active power generated by the active filter.

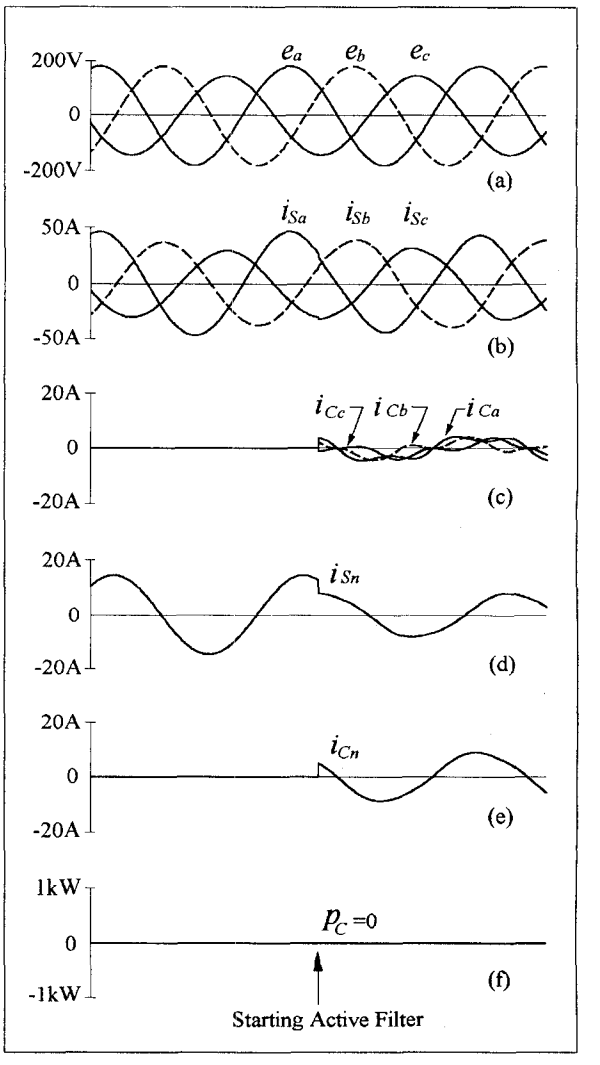

Fig.3 Simulation results in Case-2; (a) unbalanced source voltages, (b) source currents, (c) compensating currents, (d) neutral current on the source side, (e) neutral current of the active filter, (f) instantaneous active power generated by the active filter.

TABLE II
SIMULATION RESULTS.

		Case-1	Case-2	Case-3
Source [A]	I_{Sa}	43.4	43.8	42.2
	I_{Sb}	39.2	39.2	38.4
	I_{Sc}	39.2	31.9	34.3
Load [A]	I_{La}	46.4	46.4	46.4
	I_{Lb}	37.1	37.1	37.1
	I_{Lc}	37.1	29.7	29.7
AF [A]	I_{Ca}	4.4	4.4	6.7
	I_{Cb}	4.2	4.2	4.9
	I_{Cc}	4.2	4.0	6.2
Neutral [A]	I_{Sn}	0.0	8.0	0.0
	I_{Ln}	9.3	14.5	14.5
	I_{Cn}	9.3	8.7	14.5
VA_{AF}/VA_{SRC}		0.1	0.1	0.16

In Case-1, the zero-sequence current is completely controlled to be zero by compensating for the reactive powers. The simulation waveforms are shown in Fig.2. To distinguish them more clearly, all the waveforms in b-phase are noted with dashed lines. Fig.2(d) shows the waveform of the source side neutral current, which is perfectly controlled to be zero after starting the active filter. Fig.2(e) shows the neutral current of the active filter which is equal to the sum of the three-phase currents on the active filter. In Fig.2(f), p_C is calculated as:

$$p_C = e_a i_{Ca} + e_b i_{Cb} + e_c i_{Cc} \tag{27}$$

In Case-2, both the zero-sequence and negative-sequence currents cannot be controlled to be zero by compensating the reactive powers. The simulation waveforms are shown in Fig.3. Note that the neutral current on the source side is not zero even after starting the active filter.

Simulation waveforms in Case-3 are shown in Fig.4. The source voltages shown in Fig.4(a) are the same as those of Case-2. The source currents shown in Fig.4(b) are similar to those of Case-2. But the source side neutral

current shown in Fig.4(d) are perfectly controlled to be zero by compensating the pseudo-reactive powers. Note that no instantaneous active power flows in the active filter in these simulations so that no energy storage is necessary.

V. Conclusion

This paper expanded the 'p-q theory' to three-phase four-wire systems. Mapping matrices between instantaneous active/reactive powers and instantaneous currents were presented by instantaneous voltages. Instantaneous current vector was orthogonally decomposed into instantaneous active and reactive current vectors related with the active/reactive powers respectively.

It was proved that compensating for instantaneous reactive powers has no effect on instantaneous active currents without energy storage in three-phase systems. pseudo-mapping matrices introduced in this paper have the capability of providing flexibility without energy storages, which are effective in compensating for a neutral current on the source side in three-phase four-wire systems including a zero-sequence voltage. Simulation was performed to verify the theory, which showed good agreement between the theory and simulation results.

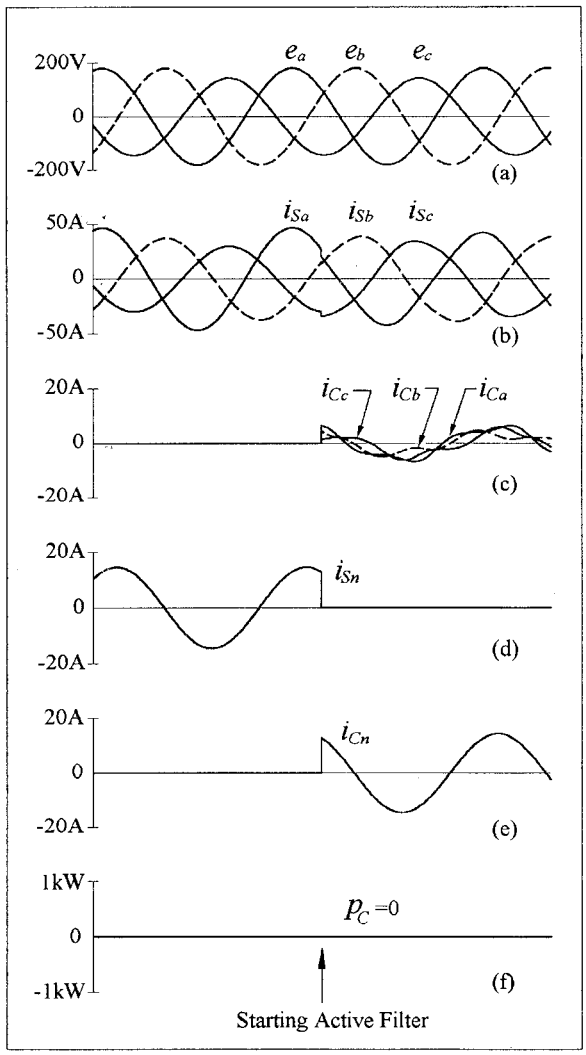

Fig.4 Simulation results in Case-3; (a) unbalanced source voltages, (b) source currents, (c) compensating currents, (d) neutral current on the source side, (e) neutral current of the active filter, (f) instantaneous active power generated by the active filter.

Acknowlegment

This paper was supported(in part) by NON DIRECTED RESEARCH FUND, Korea Research Foundation, 1996. The authors also deeply thank Mr. Eiji Miyake for his contribution to simulation.

References

[1] Leszek S.Czarnecki, "On some deficiencies of Fryze's approach to describing power properties of systems under nonsinusoidal condition," *Proc. of IEEE ICHPS VI, Bologna*, Sept. 21-23, 1994, pp.360-364.

[2] P.S.Filipski, "Apparent Power - A Misleading Quantity in the Nonsinusoidal Power Theory. Are All Nonsinusoidal Power Theories Doomed to Fail?," *International Workshop on Power Definitions & Measurement*, 1991, pp.39-47.

[3] Hirofumi Akagi, Yoshihira Kanazawa, Akira Nabae, "Instantaneous Reactive Power Compensators Comprising Switching Devices without Energy Storage Components," *IEEE Trans. on IA-20, No.3*, May/June 1984, pp.625-630.

[4] Alessandro Ferrero, and Gabrio Superti-Furga, "A New Approach to the Definition of Power Components in Three-Phase Systems Under Nonsinusoidal Conditions," *IEEE Trans. on IM-40, No.3*, June 1991, pp. 568-577.

[5] Jacques L. Willems, "A New Interpretation of the Akagi-Nabae Power Components for Nonsinusoidal Three-Phase Situations," *IEEE Trans. on IM-41, No.4*, Aug. 1992, pp.523-527.

[6] Mauricio Aredes and Edson H. Watanabe, "New Control Algorithms for Series and Shunt Three-Phase Four-Wire Active Power Filters," *IEEE PES Winter Meeting*, 95 WM 240-2 PWRD, 1995.

[7] P. Enjeti, W. Shireen, P. Packebush, I. Pitel, "Analysis and Design of A New Active Power Filter to Cancel Neutral Current Harmonics in Three Phase Four Wire Electric Distribution Systems," *in Conf. Rec. of IEEE IAS*, pp.939-946, 1993.

[8] Girish Kamath and Ned Mohan, "A Novel, Reduced Rating Active Filter for 3-Phase, 4-Wire Loads," *in Conf. Rec. of IEEE IAS*, pp.936-940, 1994.

[9] Thierry Thomas, Kevork Haddad, Geza Joos, Alain Jaafari, "Performance Evaluation of Three Phase Three and Four Wire Active Filters," *in Conf. Rec. of IEEE IAS*, pp.1016-1023, 1996.

[10] Feng Zheng Peng, Jih-Sheng Lai, "Generalized Instantaneous Reactive Power Theory for Three-Phase Power Systems," *IEEE Trans. on IM-45, No.1*, Feb. 1996, pp.293-297.

[11] Feng Zheng Peng, Jih-Sheng Lai, "Reactive Power and Harmonic Compensation Based on the Generalized Instantaneous Reactive Power Theory for Three-Phase Power Systems," *Proceedings on 7th International Conference on Harmonics and Quality of Power*, Oct. 1996, pp.83-89.

[12] A.Nabae, L.Cao, T.Tanaka, "A Universal Theory of Instantaneous Active-Reactive Current and Power Including Zero-Sequence Component," *Proceedings on 7th International Conference on Harmonics and Quality of Power*, Oct. 1996, pp.90-95.

Periodic Steady-State Analysis by a Modified Shooting Method for a Power Electronic Circuit

Toshiji Kato and Wataru Tachibana
Doshisha University
Kyotanabe, Kyoto, 610-03, JAPAN
Fax; +81-774-65-6322, Phone +81-774-65-6812
E-mail; kato@kairo1.doshisha.ac.jp

Abstract – An efficient periodic steady-state analysis method of power electronic circuits is proposed. The method finds initial values which satisfy a steady-state boundary condition by solving a sensitivity matrix equation. For this matrix computation process, consideration of switch timing variations is essential especially for closed-loop controlled circuits to improve stability of the algorithm. Furthermore, it is possible to reduce computation time by separating initial value variables into dominant and dependent groups from their interactive relations. This paper derives a precise and general computation algorithm of the method, which is validated through application examples of converters.

1. INTRODUCTION

Power electronic (PE) circuits are often analyzed for their operation behaviors in circuit design and parameter determination. It is often necessary to analyze steady-state operations after initial transients in PE circuits which are switched on and off periodically according to clock signals. It is efficient to find periodic steady-states directly instead of analyzing full transients.

Periodic steady-state (PSS) analysis methods have been developed in the circuit theory field[1]–[3],[7],[9] and also in the power electronics field[4]–[6],[8] in these two decades. The shooting method is one of them and it is mostly used because of its simplicity and efficiency. It directly solves a PSS boundary value condition that the initial values are equal to the final values after an one-period transient. This paper proposes two improvements for the shooting method.

As the first improvement, this paper shows necessity of taking into account of switch timing variations or switch timing sensitivities(STS) in sensitivity matrix computation between the two boundary values and proposes a general computation algorithm. For this improvement in STS computation, first a state-variable technique has been proposed[5]. According to the method, sensitivity matrix is expressed with the chain rule of state-transition matrices with STS. However, it is not correct and yet its computation process is unclear. In this paper a general computation method with correct STS is described[8].

As the second improvement, this paper proposes to separate initial value variables into two groups and to make the computation process of the sensitivity matrix in two steps. First large sensitivity variables are computed and then small sensitivity variables are computed dependently from the former. It is possible to reduce CPU time in sensitivity matrix computation. This principle has already proposed in [9]. However it is still a problem how to separate them into the groups. This paper proposes a criterion which estimates effects between them. The proposed improvements are applied to PSS analysis of converters.

2. PERIODIC STEADY-STATE(PSS) ANALYSIS BY THE SHOOTING METHOD

This paper deals piecewise-linear switch circuits which are separated into linear circuit topological modes between switching timings. A circuit equation for them is expressed with the following ordinary differential equation with notations of a circuit state variable vector $\boldsymbol{x}(t)$ for inductor currents and capacitor voltages and its time-differential vector $\dot{\boldsymbol{x}}(t)$.

$$\dot{\boldsymbol{x}}(t) = \boldsymbol{f}(\boldsymbol{x}(t), t) \tag{1}$$

When an initial value vector $\boldsymbol{x}(0)$ is given, the solution $\boldsymbol{x}(t)$ is caluculated by integrating it. The PSS analysis is a problem to find such $\boldsymbol{x}(0)$ which satisfies the PSS condition.

The PSS analysis principle of the shooting method is derived as follows. When $\boldsymbol{x}(0)$ is an initial value vector which satisfies the PSS condition, it equals to the final value $\boldsymbol{x}(T) = \boldsymbol{F}(\boldsymbol{x}(0))$ where $\boldsymbol{F}()$ is one-period integration.

$$\begin{aligned} \boldsymbol{x}(0) &= \boldsymbol{F}(\boldsymbol{x}(0)) \\ &= \boldsymbol{x}(0) + \int_0^T \boldsymbol{f}(\boldsymbol{x}(t), t)dt \end{aligned} \tag{2}$$

This PSS condition becomes nonlinear when a switch timing is dependent on $\boldsymbol{x}(0)$. In this case, the solution

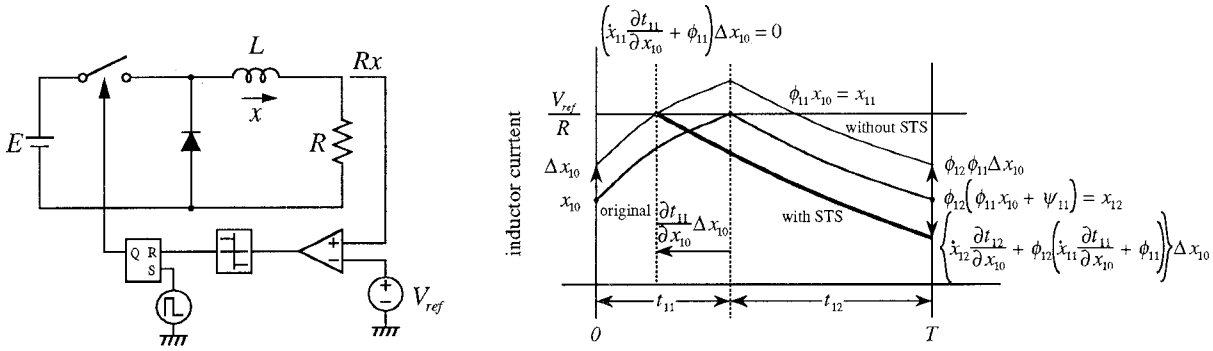

(a) Circuit configuration

(b) Switch timing

Fig.1. Simplified converter example I.

$\boldsymbol{x}(0)$ should be computed by numerical iterations. A condition that the two boundary values for one period from $t = 0$ to $t = T$ coincide with a variation $\Delta\boldsymbol{x}(0)$, gives the following equations with an identity matrix $\boldsymbol{I}$.

$$\Delta\boldsymbol{x}(0)^{(i+1)} = -\left(\boldsymbol{I} - \frac{\partial\boldsymbol{x}(T)}{\partial\boldsymbol{x}(0)}\right)^{-1}\left(\boldsymbol{x}(0)^{(i)} - \boldsymbol{F}(\boldsymbol{x}(0)^{(i)})\right) \tag{3}$$

$$\boldsymbol{x}(0)^{(i+1)} = \boldsymbol{x}(0)^{(i)} + \Delta\boldsymbol{x}(0)^{(i+1)} \tag{4}$$

where $^{(i)}$ denotes iteration times and this iteration is repeated until the correction vector $\Delta\boldsymbol{x}(0)^{(i+1)}$ becomes small enough. Especially for a linear circuit, it converges in one time iteration. Furthermore $\frac{\partial\boldsymbol{x}(T)}{\partial\boldsymbol{x}(0)}$ shows sensitivity of $\boldsymbol{x}(T)^{(i)}$ with respect to $\boldsymbol{x}(T)^{(0)}$. In the following expressions, this superscript $^{(i)}$ is omitted because all cases express the i-th iteration process.

3. STEADY-STATE ANALYSIS METHOD WITH SWITCH TIMING SENSITIVITIES BY THE SHOOTING METHOD

3.1 Importance of switch timing sensitivities(STS)

It is necessary to compute the sensitivity matrix between the two boundary values $\frac{\partial\boldsymbol{x}(T)}{\partial\boldsymbol{x}(0)}$, and in this process variations of switch timings or STS should be taken into account. A basic concept of this sensitivity calculation problem in the PSS analysis of converters is introduced through a simplified first order converter example with a closed-loop control in Fig.1(a). The converter switch is turned on according to a clock pulse with a fixed interval T and it is turned off when the load voltage v reaches to a reference voltage level V_{ref} in Fig.1(b). Assuming that the inductor current is continuous, the circuit has two topological modes. One is that the switch is on and the diode is off and the other is that the switch is off and the diode is on. These time intervals of the modes are denoted as t_{11} and t_{12} respectively. The same subscripts are used for the inductor currents x, state transition matrices ϕ, source related terms ψ. An initial current value is denoted as x_{10}. A typical inductor current of the state-variable is illustrated in Fig.1(b). The final current value x_{12} is:

$$x_{12} = \phi_{12}x_{11} = \phi_{12}(\phi_{11}x_{10} + \psi_{11}) \tag{5}$$

From (3), the initial value correction term Δx_{10} is given by the following.

$$\Delta x_{10} = \left(1 - \frac{\partial x_{12}}{\partial x_{10}}\right)^{-1}(x_{10} - x_{12}) \tag{6}$$

For evaluation of the above equation, it is necessary to get the sensitivity $\frac{\partial x_{12}}{\partial x_{10}}$ between the two boundary values. The state-transition factors ϕ_{11}, ϕ_{12} are dependent on x_{10} and the sensitivity should include these interval variations. If this effect is not taken into account, a variated x value does not satisfy the switch condition even when x becomes larger than V_{ref}/R. On the contrary when this effect is taken into account, first an initial value variation generates an variation of the length of the first circuit mode $\partial t_{11}/\partial x_{10}$. Then the variation affect the second interval length under the constraint that sum of the two intervals is T. The sensitivity value is:

$$\begin{aligned}\frac{\partial x_{12}}{\partial x_{10}} &= \dot{x}_{12}\frac{\partial t_{12}}{\partial x_{10}} + \phi_{12}\left(\dot{x}_{11}\frac{\partial t_{11}}{\partial x_{10}} + \phi_{11}\right)\\ &= \phi_{12}\phi_{11} + (\phi_{12}\dot{x}_{11} - \dot{x}_{12})\frac{\partial t_{11}}{\partial x_{10}}\end{aligned} \tag{7}$$

The second is the proposed correction term. However according to the reference [5], the sensitivity is expressed with the following chain rule and it does not coincide with the proposed one.

$$\left(\dot{x}_{12}\frac{\partial t_{12}}{\partial x_{11}} + \phi_{12}\right)\left(\dot{x}_{11}\frac{\partial t_{11}}{\partial x_{10}} + \phi_{11}\right) \neq \frac{\partial x_{12}}{\partial x_{10}} \tag{8}$$

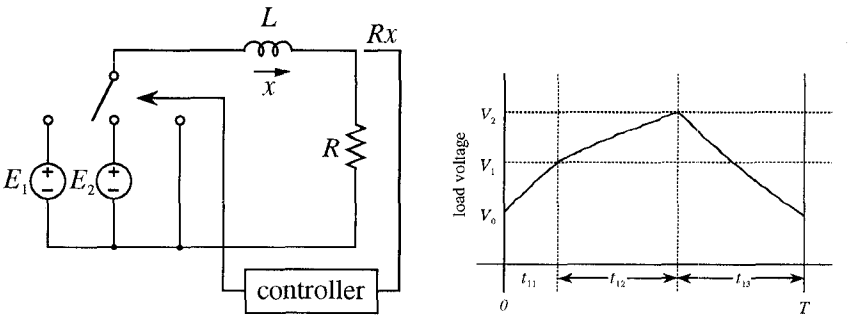

(a) Circuit configuration (b) Switch timing

Fig.2. Simplified converter example II.

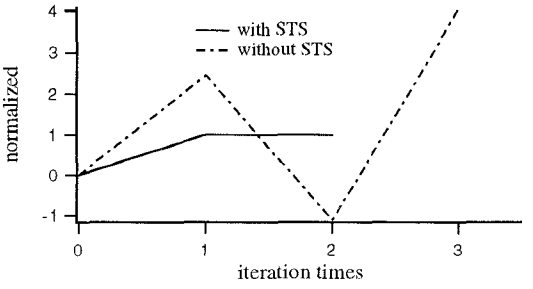

Fig.3. Comparison of convergent behavior.

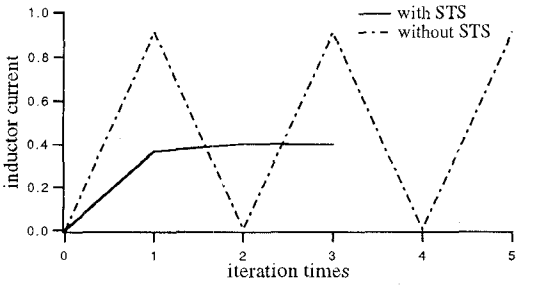

Fig.4. Comparison of convergent behavior.

There are three contradictory points of this chain rule; the first is that the last term $\dot{x}_{11}\dfrac{\partial t_{11}}{\partial x_{10}} + \phi_{11}$ becomes zero because of the switch condition, the second is that the term $\dfrac{\partial t_{12}}{\partial x_{11}}$ can not be defined because x_{11} is a constant, and the third is that there is no description how to compute $\dfrac{\partial t_{12}}{\partial x_{11}}$ in the reference. The reference neglects the fact that the effect of the switch timing variations is expressed not with the chain rule itself but with a constant sum rule of all variations. The reference [5] is not discussed any more because it is erroneous. The reference [7] expresses the above equation with the following equation which coincide with (7) in this case.

$$\phi_{12}\left(\dot{x}_{11}\frac{\partial t_{11}}{\partial x_{10}} + \phi_{11}\right) - \dot{x}_{12}\frac{\partial t_{11}}{\partial x_{10}} \equiv \frac{\partial x_{12}}{\partial t_{11}}\frac{\partial t_{11}}{\partial x_{10}} = \frac{\partial x_{12}}{\partial x_{10}} \tag{9}$$

Furthermore another converter example in Fig.2(a) is investigated. The switch is turned on E_1 side according to a start clock pulse with a fixed interval T, then it is turned on E_2 side when the load voltage v reaches to a level V_1, finally it is short-circuited when the voltage reaches to another level V_2. The sensitivity $\dfrac{\partial x_{13}}{\partial x_{10}}$ between two boundary values is the following.

$$\begin{aligned}\frac{\partial x_{13}}{\partial x_{10}} &= \dot{x}_{13}\frac{\partial t_{13}}{\partial x_{10}} \\ &+ \phi_{13}\left(\dot{x}_{12}\frac{\partial t_{12}}{\partial x_{11}} + \phi_{12}\right)\left(\dot{x}_{11}\frac{\partial t_{11}}{\partial x_{10}} + \phi_{11}\right)\end{aligned} \tag{10}$$

However the reference [7] can deal only one switch timing variation in a fixed time interval and it can not deal this second example.

Actually PSS initial value of the converter in Fig.1 is computed from the zero initial value and compared between two cases without the STS and with the STS by the proposed method. The computed initial values during iterations are normalized and shown in Fig.3. In the former case, the process diverged because of its fatal disadvantage that solution correction directions are quite opposite. On the contrary, in the latter case the process converged in two time iterations.

The second example is also analyzed and compared between without the STS and with the STS by the proposed method. The computed initial values during iterations are shown in Fig.4. In the former case, the process oscillated and did not converge. On the contrary, in the latter case the process converged in three time iterations. This example can be analyzed only by the proposed method. It is necessary to take account of STS in such a general form.

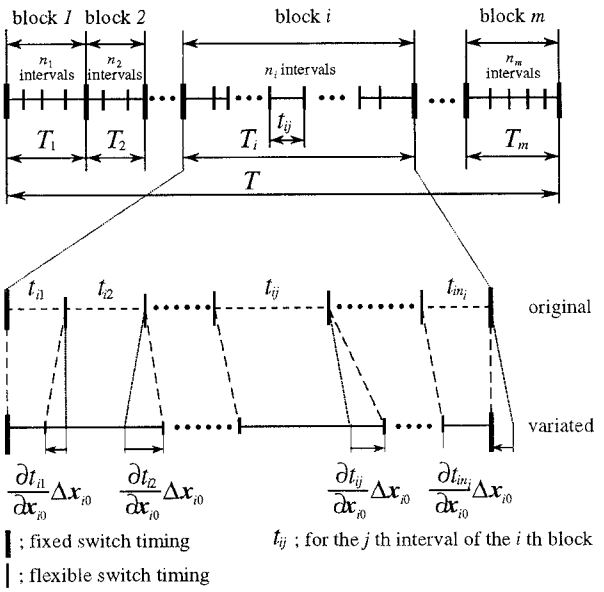

Fig.5: Generalized switch timings and their variations due to an initial value variation.

3.2 General algorithm for switch timing sensitivity computation

There are two types of switch timings. One is fixed and the other is flexible. Fixed switch timings are generated by gate signals of open-loop controls and flexible ones are by those of closed-loop controls and by diodes. These two types of timings are generated independently and they are mixed in a time chart. A general switch timing chart is shown in Fig.5. Beyond fixed switch timings, a state-variable variation in an interval affects other state-variable variations but does not affect switch timing variations. A fixed timing is considered to give a boundary of a block. It is assumed that one cycle T is divided into m blocks by m fixed switch timings and further that the i-th block of T_i is divided into n_i intervals t_{ij} by $(n_i - 1)$ flexible switch timings in the figure.

Basically an initial value variation is delivered to the final value by using a sort of a chain rule for each switch timing. However this chain rule terms are different between the fixed and the flexible timings. Flexible switch timing variations are accumulated in one block between two fixed timings and the total variation is cancelled at the right side fixed timing of the block. An initial value variation is delivered after one flexible switch timing interval t_{i1} by the following chain term.

$$\frac{\partial \boldsymbol{x}_{i1}}{\partial \boldsymbol{x}_{i0}} = \dot{\boldsymbol{x}}_{i1}\frac{\partial t_{i1}}{\partial \boldsymbol{x}_{i0}} + \boldsymbol{\phi}_{i1} \tag{11}$$

where $\boldsymbol{\phi}_{i1}$ denotes the state-transition matrix for the interval t_{i1} and $\dot{\boldsymbol{x}}_{i1}$ denotes the left-side differential at the first switch timing of the i-th block, the variation at the $(n_i - 1)$-th switch timing of the block is:

$$\begin{aligned}\frac{\partial \boldsymbol{x}_{in_i-1}}{\partial \boldsymbol{x}_{i0}} &= \frac{\partial \boldsymbol{x}_{in_i-1}}{\partial \boldsymbol{x}_{in_i-2}}\frac{\partial \boldsymbol{x}_{in_i-2}}{\partial \boldsymbol{x}_{in_i-3}}\cdots\frac{\partial \boldsymbol{x}_{i1}}{\partial \boldsymbol{x}_{i0}} \\ &= \prod_{j=1}^{n_i-1}\frac{\partial \boldsymbol{x}_{ij}}{\partial \boldsymbol{x}_{ij-1}} \\ &= \prod_{j=1}^{n_i-1}\left(\dot{\boldsymbol{x}}_{ij}\frac{\partial t_{ij}}{\partial \boldsymbol{x}_{ij-1}} + \boldsymbol{\phi}_{ij}\right)\end{aligned} \tag{12}$$

At the end of the block of the fixed switch timing, there is a constraint for the total time of the intervals. The total variation for the i-th block is derived using the following constraint

$$\sum_{j=1}^{n_i} t_{ij} = T_i \rightarrow \sum_{j=1}^{n_i}\frac{\partial t_{ij}}{\partial \boldsymbol{x}_{i0}} = 0 \tag{13}$$

$$\frac{\partial \boldsymbol{x}_{in_i}}{\partial \boldsymbol{x}_{i0}} = \dot{\boldsymbol{x}}_{in_i}\frac{\partial t_{in_i}}{\partial \boldsymbol{x}_{i0}} + \boldsymbol{\phi}_{in_i}\frac{\partial \boldsymbol{x}_{in_i-1}}{\partial \boldsymbol{x}_{i0}} \tag{14}$$

The total sensitivity for one cycle, or for m blocks, is derived from the following chain rule of the above process.

$$\frac{\partial \boldsymbol{x}_{mn_m}}{\partial \boldsymbol{x}_{10}} = \prod_{i=1}^{m}\frac{\partial \boldsymbol{x}_{in_i}}{\partial \boldsymbol{x}_{i0}} = \prod_{i=1}^{m}\left(\dot{\boldsymbol{x}}_{in_i}\frac{\partial t_{in_i}}{\partial \boldsymbol{x}_{i0}} + \boldsymbol{\phi}_{in_i}\frac{\partial \boldsymbol{x}_{in_i-1}}{\partial \boldsymbol{x}_{i0}}\right) \tag{15}$$

4. REDUCTION OF CPU TIME BY SEPARATION OF INITIAL VALUE VARIABLES

4.1 Relations between initial value variables and their sensitivities

Initial value variables are divided into two groups by sensitivity matrix for one period. One group is those of which sensitivities to the other variables are large. The other group is those of which sensitivities to the other variables are small. The initial variables are divided into the former set $\boldsymbol{p}$ and the latter set $\boldsymbol{q}$. The iteration process of the shooting method becomes the following.

$$\begin{aligned}\left[\begin{array}{c}\boldsymbol{p}^{(i+1)}\\ \hline \boldsymbol{q}^{(i+1)}\end{array}\right] &= \left[\begin{array}{c}\boldsymbol{p}^{(i)}\\ \hline \boldsymbol{q}^{(i)}\end{array}\right] \\ &- \left(\left[\begin{array}{c|c}\boldsymbol{I}_{pp} & \boldsymbol{0}\\ \hline \boldsymbol{0} & \boldsymbol{I}_{qq}\end{array}\right] - \left[\begin{array}{c|c}\boldsymbol{J}_{pp}^{(i)} & \boldsymbol{J}_{pq}^{(i)}\\ \hline \boldsymbol{J}_{qp}^{(i)} & \boldsymbol{J}_{qq}^{(i)}\end{array}\right]\right)^{-1} \\ &\times \left(\left[\begin{array}{c}\boldsymbol{p}^{(i)}\\ \hline \boldsymbol{q}^{(i)}\end{array}\right] - \left[\begin{array}{c}\boldsymbol{F}_p\left(\boldsymbol{x}(0)^{(i)}\right)\\ \hline \boldsymbol{F}_q\left(\boldsymbol{x}(0)^{(i)}\right)\end{array}\right]\right)\end{aligned} \tag{16}$$

This equation is approximated to the following two equations by neglecting the minor elements of $\boldsymbol{J}_{pp}$, $\boldsymbol{J}_{qq}$ in the sensitivity matrix.

$$\boldsymbol{p}^{(i+1)} = \boldsymbol{p}^{(i)} - \left(\boldsymbol{I}_{pp} - \boldsymbol{J}_{pp}^{(i)}\right)^{-1}\left(\boldsymbol{p}^{(i)} - \boldsymbol{F}_p\left(\boldsymbol{x}(0)^{(i)}\right)\right) \tag{17}$$

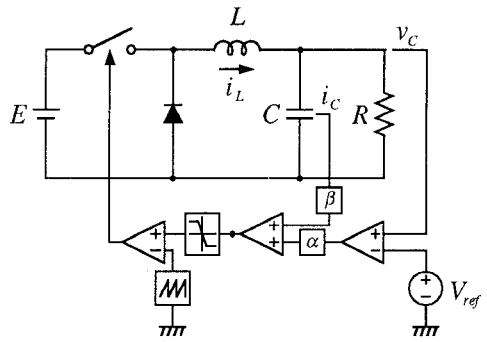

Fig.6: Buck DC-DC converter with sliding-mode control.

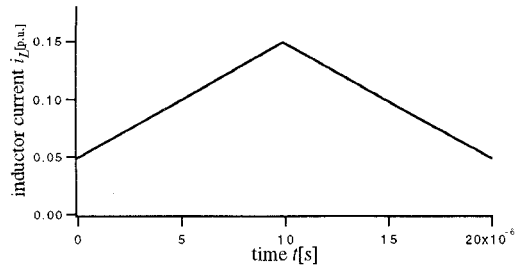

Fig.7. Periodic steady-state solution.

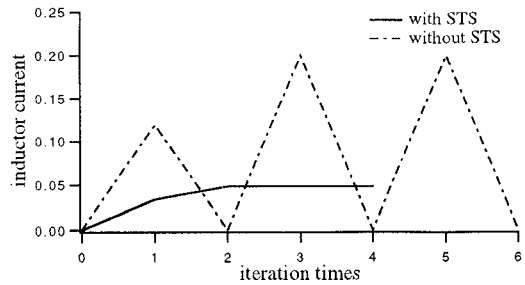

Fig.8. Convergent processes.

$$\boldsymbol{q}^{(i+1)} = \boldsymbol{F}_p\left(\boldsymbol{x}(0)^{(i)}\right) + \boldsymbol{J}_{qp}^{(i)}\left(\boldsymbol{p}^{(i+1)} - \boldsymbol{p}^{(i)}\right) \quad (18)$$

This process consists of the above two steps. First, only the initial value vector $\boldsymbol{p}$ of which sensitivities are large is computed, and then the other initial value vector $\boldsymbol{q}$ is computed dependently from $\boldsymbol{p}$. By this process, computation of sensitivities with respect $\boldsymbol{q}$ is ommited.

4.2 Criterion using sensitivities for separation of initial value variables

It is necessary to give a criterion which shows how to separate initial value variables into two groups of which effects are large or small. The following value is used to judge the groups by averaging n sensitivities with a variable x_i for $N_s(1 \leq N_s \leq N)$ steps and by comparing with a constant ϵ.

$$\frac{1}{N_s}\sum_{j=1}^{n}\sum_{k=1}^{N_s}\left|\frac{\partial x_j(t_k)}{\partial x_i(0)}\right| \leq \epsilon \quad (19)$$

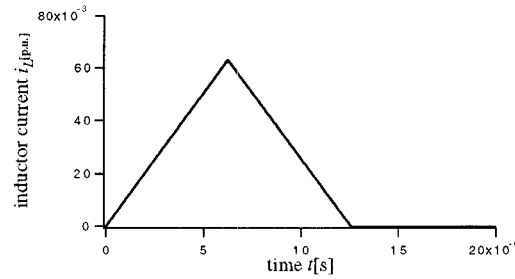

Fig.9. Periodic steady-state solution.

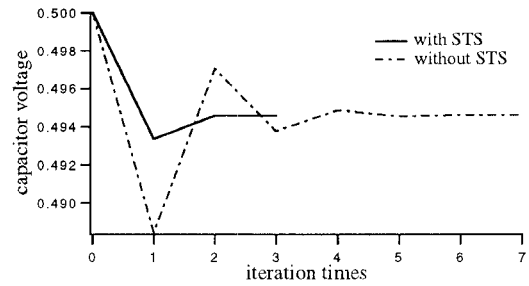

Fig.10. Convergent processes.

One is enough for N_s for most cases. Even if N_s is N for the longest case, this criterion is used only in the first iteration of the shooting method and still reduction of computation time is effective.

5. APPLICATION EXAMPLES

5.1 DC-DC converter with Sliding Mode control

As the first application example of the proposed shooting method with STS, a DC-DC converter with a sliding mode control in Fig.6 is analyzed for its PSS. Its circuit parameters are selected to be $E = 1.0[p.u.], L = 50[\mu H], C = 50[\mu F], R = 5[\Omega], V_{ref} = 0.5[p.u.], \alpha = 10, \beta = 1$. The computed PSS waveform for the inductor current i_L is shown in Fig.7. Its convergent behavior in the iteration process is shown in Fig.8 and the current initial value converged in five time iterations by the proposed method. On the contrary, without taking into account of STS, the value oscillated and did not converge.

When the load resistance value is changed to 25Ω, the inductor current becomes discontinuous in Fig.9. In this case, the method of the reference[7] cannot be applied because there are two flexible timings in one fixed block. The convergent process by the proposed method with STS is faster than the conventional method without STS in Fig.10.

5.2 Clamped-Mode series resonant DC-DC converter

As the second application example of the proposed shooting method with separation of initial value variables, a clamped-mode series resonant DC-DC converter

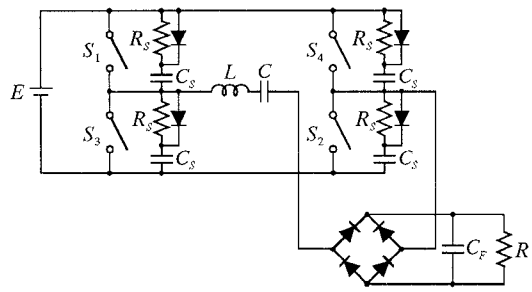

Fig.11: Clamped-mode series-resonant DC-DC converter.

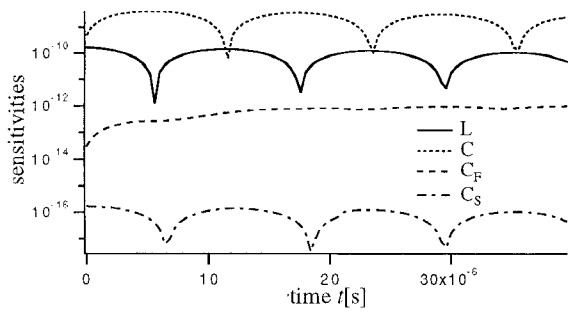

Fig.12. Sensitivities of initial values for C_s.

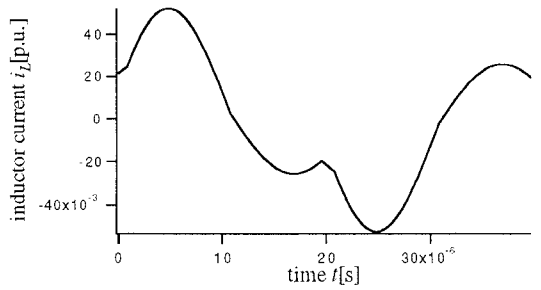

Fig.13. Periodic steady-state waveform of i_L.

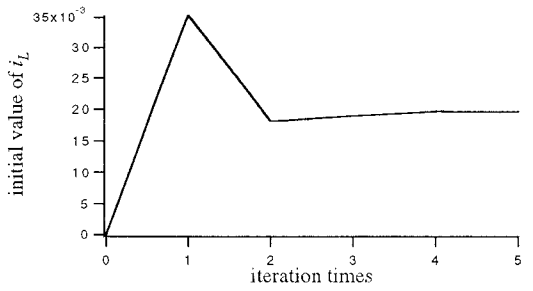

Fig.14. Convergent process.

in Fig.11 is analyzed for its PSS. Its circuit parameters are selected to be $E = 1.0[p.u.], L = 105.2[\mu H], C = 136.3[nF], C_F = 2200[\mu F], R = 10[\Omega], R_S = 56[\Omega], C_S = 18[nF]$. Absolute values of column elements for each initial value in the sensitivity matrix are computed and those for C_s is shown in Fig.12. The initial value effects of C_s can be neglected because the sensitivity vector is small enough. The other initial values in L, C, C_f are computed and then initial values in the snubber capacitors are computed. Computed waveforms and its convergent behavior are shown in Fig.13 and Fig.14 respectively. There is no need to check the separation criterion from the second iteration, computation time for this sensitivity evaluation process is reduced.

6. CONCLUSIONS

The shooting method is useful to find periodic steady-state waveforms of a power electronic circuit. This paper proposed two modifications for the method. As the first proposal, it is necessary to take account of switch timing variations in the sensitivity matrix computation process and a general algorithm was shown. Actual improvement of convergent behaviors in converter example circuits were verified. As the second proposal separation of the initial value variables was investigated. Initial values, which do not affect the other variables like snubber capacitor voltages, can be omitted and the modified sensitivity matrix computation process were verified to be efficient.

REFERENCES

[1] T.J. Aprille, T.N. Trick : "Steady-state analysis of nonlinear circuits with periodic inputs," *Proc. of IEEE*, Vol.60, pp.108-114, 1972.

[2] S. Skelboe : "Computation of the periodic steady-state response of nonlinear networks by extrapolation methods," *IEEE Trans. Circuits and Systems*, Vol.27, pp.161-175, 1980.

[3] K.S. Kundert, J.K. White, A. Sangiovanni-Vincentelli: *Steady-state methods for simulating analog and microwave circuits*, Kluwer Academic Publishers, 1990.

[4] Y. Kuroe, H. Haneda, T. Maruhashi: "A general steady-state analysis program ANASP for thyristor circuits based on adjoint network approach," *IEEE PESC'80 Record*, pp.180-189.

[5] R.C. Wong : "Accelerated convergence to the steady-state solution of closed-loop regulated switching-mode systems as obtained through simulation," *IEEE PESC'87 Record*, pp.682-692.

[6] Y. Kuroe, T. Maruhashi, N. Kanayama : "Computation of sensitivities with respect to conduction time of power semiconductors and quick determination of steady state for closed-loop power electronic systems," *PESC'88 Record*, pp.756-764, 1988.

[7] D.G. Bedrosian, J. Vlach : "An accelerated steady-state method for networks with internally controlled switches," *IEEE Trans. Circuits and Systems I*, Vol.39, No.7, pp.520-530, 1992.

[8] T. Kato : "Efficient steady-state analysis method with sensitivities of switch timings by the shooting method," *PCC-Yokohama*, pp.550-556, 1993.

[9] M. Kakizaki, T. Sugawara : "A Modified Newton Method for the Steady-State Analysis," *IEEE Trans. Computer-Aided Design*, Vol. CAD-4, No.4, pp.662-667, 1985.

Simulation Method for Phase-Shift Controlled AC-AC Converters Based on Switching Vector

Jorma Kyyrä, Sami Väliviita
Helsinki University of Technology
Institute of Intelligent Power Electronics
Otakaari 5A, FIN-02150 Espoo, Finland
Tel.: +358-9-451 2436, Fax: +358-9-460 224
E-mail: Jorma.Kyyra@hut.fi, Sami.Valiviita@hut.fi

Abstract — **An efficient method to simulate voltage and current waveforms of phase-shift controlled ac-ac converters is presented. The method is based on switching vector, which is space-vector of switching functions, and on the complex Fourier-series of it. The only constraints of our method are that the output frequency and modulation method of the converter are predefined. However, it is not necessary to describe the modulation process of the individual thyristors, because switching vector contains the necessary information of the operation of the converter. Waveforms of sinusoidally modulated ac-ac converters and naturally commutated cycloconverters are presented, when the load is a single-phase resistive and inductive network. Output voltage calculation is based on the switching vector and output current is calculated numerically from the known voltage and load. Possible discontinuity of the output current is taken into account.**

I. Introduction

Direct ac-ac converters connect the input phases directly to the output without any intermediate dc voltage or current circuit. Therefore, output voltage consists of pieces of input voltages. Similarly, input currents consist of samples of output currents [1], [2], [3]. Due to this, the converter can act in four quadrants, which is a great advantage in motor drives where regenerative operation is needed in both directions of rotation.

In this paper, simulation of two types of ac-ac converters are discussed. At first, simulation of phase-shift controlled ac-ac converters with sinusoidal modulating functions are discussed. In this case the switches required are bidirectional current-carrying and bidirectional voltage-blocking devices. At the moment, these kind of switches are not available on a single component, but anti-parallel connection of two power components with gate turn-off capabilities are needed. In the second example, the converter is constructed with ideal thyristors. In this case natural commutation is used and it is achieved with anti-parallel connection of two thyristor bridges.

In both cases converters are described with their switching vectors. Switching vector is a space-vector of switching functions, which describe the states of the switches with zeros and ones. Switching vector combines all the phases of the converter into one space-vector. With this vector it is possible to analyze the behavior of polyphase converters in closed form very efficiently as shown in [4]. However, in those cases the output current of the converters were assumed to be ideally sinusoidal. Furthermore, natural commutation with ac-ac converters was not discussed.

The simulation presented in this paper is based on the calculation of the switching vector. Only the time domain behavior of the control angle of the converter must be known in advance. This could be defined as steady state simulation. It is not necessary, however, that the output frequency of the converter remains constant during the simulated period. Similarly, it is possible that the modulation depth, i.e. the amplitude of the output voltage changes. However, these changes must be known in advance. Output voltage is calculated with the switching vector and space-vector of input voltage and output current is simulated when the load is a R-L-circuit.

In Section II the basic ideas behind switching vector theory are shortly reviewed. The principle of phase-shift modulation is explained and the Fourier-series of switching vector is given in Section III. In the beginning of the paper, a general polyphase system is used, however, the waveforms presented are for the most common three-phase system. The nonlinear modulating functions, discussed in Section IV, produce ac outputs but self-commutated power components are still needed. In addition to a nonlinear modulation scheme, natural commutation, where two anti-parallel connected thyristor bridges are required, is discussed in Section V. To select the conducting bridge, the fundamental component of output current is used, because output current can be discontinuous. Final conclusions are given in Section VI.

II. Switching Vector of a Bridge Converter

Basically, an ac-ac converter could be a midpoint converter, where the neutral of the input system is used as a return path for the load current. In most practical applications, however, bridge converters are used because they increase the pulse number of the converter, which increases the quality of the output voltage and input current accordingly [4]. A schematic diagram of a polyphase bridge converter is shown in Fig. 1 (a). The input of the converter is assumed to be an ideal polyphase voltage source and the converter consists of two partial converters, called changeover switches. Both of them connect one end of the load into one of the input phases. Exactly one of the switches within a changeover switch must be closed at the time. Otherwise two input voltage sources are short-circuited or the current source, i.e. inductive load, is opened. These principles are called voltage and current axioms in [5] and [6].

0-7803-3823-5/97/$10.00© 1997 IEEE

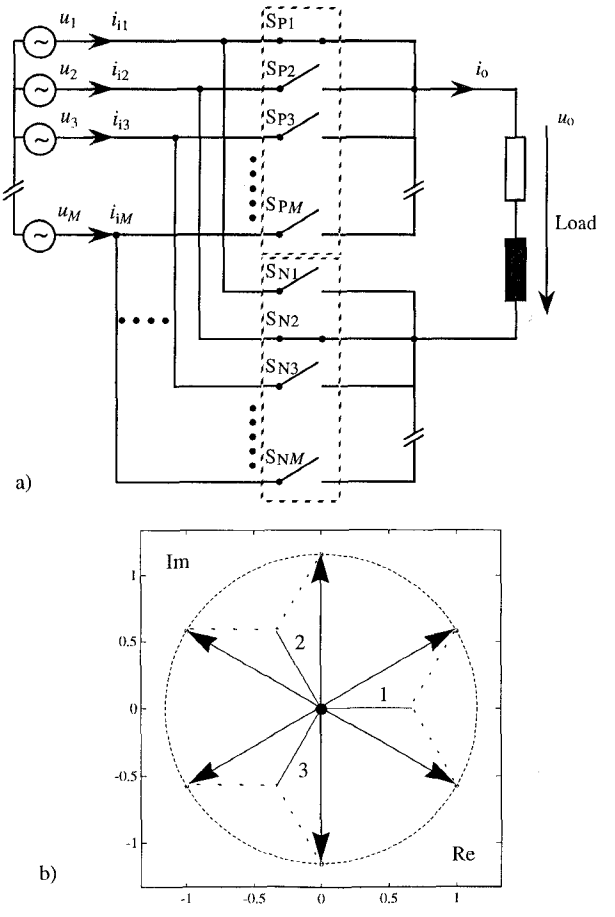

Fig. 1. (a) Two changeover switches connected as an M-phase bridge converter. Ideal switches are grouped into positive and negative changeover switches. (b) The switching vectors of a three-phase bridge converter are highlighted with arrows and the vectors of the midpoint converter are drawn with solid lines and numbered from 1 to 3. There are also three zero-vectors in the bridge converter, when positive and negative switch of the same phase are closed simultaneously.

The switching vector of the bridge converter is calculated by subtracting the switching vector of the positive and negative changeover switches. The switching functions h of the positive changeover switch are subscripted with $_P$ and those of the negative switch with $_N$. The space-vector of an M-phase system is defined as an extension of the space-vector of a three-phase system introduced in [7]. Thus, the switching vector is

$$\vec{h} = \frac{2}{M}\left[(h_{P1} - h_{N1}) + (h_{P2} - h_{N2})\vec{a}_M + \ldots + (h_{PM} - h_{NM})\vec{a}_M^{(M-1)}\right] = \frac{2}{M}\sum_{p=1}^{M}(h_{Pp} - h_{Np})\,\vec{a}_M^{(p-1)} \qquad (1)$$

where $\vec{a}_M = e^{j2\pi/M}$ is the spatial displacement of consecutive phases. Exactly one of the poles in the changeover switch has to be closed at the time. Here we have two changeover switches, which results in $M \cdot M$ different combinations.

In a three-phase bridge converter there are nine combinations for the switches. Three of the resulting switching vectors are zero, when the positive and negative switch of the same phase are closed simultaneously. Thus, there are six non-zero vectors, whose length is $2/\sqrt{3}$ and they are $\pi/3$ radians displaced form each other. These vectors are drawn with arrows in Fig. 1 (b). The vectors of the midpoint converter are drawn with solid lines and numbered from 1 to 3.

Traditionally output and input quantities of changeover switches have been analyzed with the aid of switching functions. The greatest advantage of switching vector, compared to the analysis based on switching functions or traditional circuit theory approach, is obtained when input-output relations are derived by using the switching vector in time domain or the complex Fourier series of it. The output current of a converter can be calculated as follows:

$$i_o = \frac{u_o}{\vec{Z}(\omega)} \qquad \vec{Z}(\omega) = Z\,e^{j\varphi_z} \qquad (2)$$

where $\vec{Z}(\omega)$ is from the angular frequency ω dependent impedance of the load, which is connected to the output voltage u_o. The input current vector of the converter is

$$\vec{i}_i = \vec{h}\,i_o \qquad (3)$$

where i_o is expressed with its Fourier series. Harmonics of the output current are often small compared to the fundamental component and in analytical studies they are often neglected [1], [2], [4]. In a rectifier only the dc component of the output current, and in a converter with an ac output only the fundamental component of the output current can be considered.

In an ideal converter there are no losses and no energy storage elements in the switching matrix and the instantaneous powers in the output and input are equal. When the input power is calculated with space-vectors of input voltage $\vec{u}_i$ and current $\vec{i}_i$ and (3) is used, an equation for the output voltage is derived as follows:

$$p_v = u_{ov} i_o = \frac{M}{2}\,\mathrm{Re}\left\{\vec{u}_i \vec{i}_i^{\,*}\right\} \Rightarrow u_{ov} = \frac{M}{2}\,\mathrm{Re}\left\{\vec{h}^{\,*}\vec{u}_i\right\}. \qquad (4)$$

It has been shown in [4] and [8] that in the M-phase space-vector of any balanced electric quantity only the harmonics $1 + kM$, $k = 0, \pm1, \pm2, \ldots$, remain. All other components produce a zero amplitude vector. This harmonic cancellation may be a serious drawback of space-vectors in the polyphase systems and care must be taken in conflicting situations. However, the power equality $p_v = u_{ov} i_o = u_o i_o$ is true as long as $\vec{u}_i$ is ideal and there is no zero-sequence voltage or current in the supply side, which cancel out in the space-vector representation. Then it is not necessary to use the subscript v, which is used as an identification for quantities calculated with space-vectors. A further prerequisite for (4) is that output current is continuous. When output current becomes discontinuous, output voltage does not follow (4). This is discussed in detailed in Section IV.

III. Phase-Shift Modulation

In the so called naturally commutated converters only a phase delay is possible because line voltages are used to switch off the conducting thyristors. In more advanced converters, self-commutated switches are also used and a phase advance can be applied to the control. The symbol α is used for the phase shift. Negative value of α corresponds to natural commutation with a phase delay and positive value to self-commutation with phase advance. This definition of α is adapted from [3]. In most other textbooks on power electronics only natural commutation with phase-shift controlled ac-dc converters is considered and the standard procedure is to use only positive values for α. However, in this paper general phase-shift controlled ac-ac converters are studied and in that context both signs for control angle are needed.

In a ac-dc converter the control angle α is constant in steady state operation. The switching vectors of a bridge converter are used symmetrically so that the next vector used is the previous one rotated an angle of $2\pi/g$ counterclockwise, $g = M$ when M is even and $g = 2M$ when M is odd. Therefore, the converter can be described with the Fourier-series of the switching vector derived in [4] and [8]. The behavior of the order number n is deduced from the symmetry of the converter and phase number M. The complex Fourier series of the switching vector of a bridge converter is

$$\vec{h} = \sum_{k=-\infty}^{\infty} \frac{4}{n\pi} \sin\left(\frac{n\pi}{M}\right) e^{jn(x_i + \alpha)}, \; n = 1 + kg \tag{5}$$

where and $x_i = \omega_i t = 2\pi f_i t$, f_i is input frequency.

When only the fundamental component of the input voltage is considered, the space-vector of input voltage is $\vec{u}_i = \hat{u}_v e^{jx_i}$, where $\hat{u}_v$ is the peak value of voltage. According to (4) the output voltage of the converter is

$$u_o = \frac{M}{2} \mathrm{Re}\left\{\vec{h}^* \vec{u}_i\right\} = \frac{2M\hat{u}_v}{\pi}\left\{\sin\left(\frac{\pi}{M}\right)\cos\alpha + \sum_{k=1}^{\infty} \frac{1}{n} \sin\left(\frac{n\pi}{M}\right)\cos\left[(1-n)x_i - n\alpha\right]\right\} \tag{6}$$

where $n = 1 \pm kg$. Output voltage contains a dc component, which can be controlled by changing the control angle α. The output voltage and input line-to-line voltages of a three-phase bridge converter are shown in Fig. 2 when $\alpha = -\pi/3$ rad. In a phase-shift controlled bridge converter, output voltage is the difference between the most positive and negative input line-to-neutral voltages.

In phase-shift controlled ac-ac converters the control angle α in (5) is changed into a time-varying modulating function $m(t) = f(r, f_o, t)$, where modulation depth r is used to control the amplitude of the output voltage and f_o is output frequency. Now the Fourier-series of switching vector is

$$\vec{h} = \sum_{k=-\infty}^{\infty} \frac{4}{n\pi} \sin\left(\frac{n\pi}{M}\right) e^{jn(x_i + m(t))}, \; n = 1 + kg \tag{7}$$

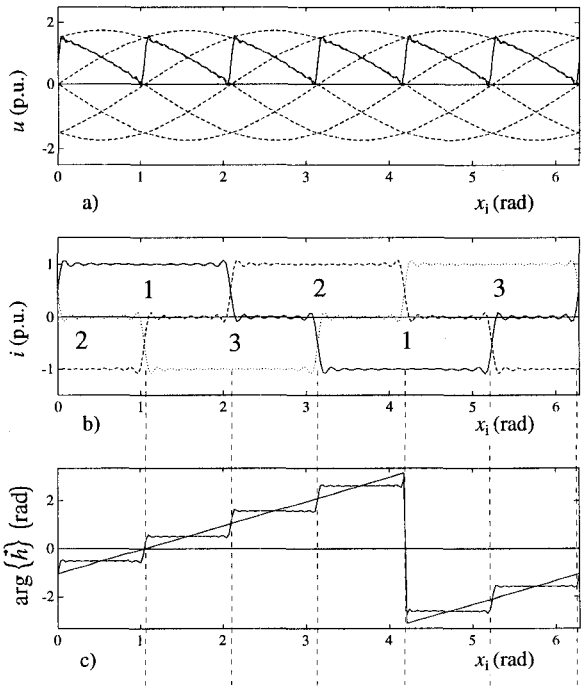

Fig. 2. (a) Output voltage of a three-phase current-sourced bridge converter from (6) when $\alpha = -\pi/3$ rad. Input line-to-line voltages are drawn dashed. (b) Input line currents. (c) Arguments of the switching vector and its fundamental component from (5).

and in analytic studies the question that arises is, how the term containing the modulating function can be expressed with simple functions. As $m(t)$ must be periodic in order to receive a periodic output voltage cos $(m(t))$, it is obvious that $e^{jnm(t)}$ is periodic and it can be expressed with a Fourier series. In some cases the necessary definite integrals can be calculated in closed form but more often it has to be expressed with numerical results under defined operating conditions as discussed in [4], [10]. In this paper this switching vector is used as such for the calculation of the output voltage of the converter with two types of modulating functions.

IV. Nonlinear Modulating Function

If a modulating function

$$m(t) = \arccos\left[r \cos\left(x_o + \psi\right)\right] \tag{8}$$

is used, the output voltage of an ac-ac converter will contain the term $\cos(m) = r\cos(x_o + \psi)$, $x_o = \omega_o t = 2\pi f_o t$. Amplitude of the output can be controlled by changing the modulation depth r, $0 \le r \le 1$. The displacement angle ψ allows the creation of polyphase outputs using multiple converters. Also a modulating function

$$m(t) = -\arccos\left[r \cos\left(x_o + \psi\right)\right] \tag{9}$$

where the control angle of the converter will always be negative can be realized.

Fig. 3 shows the calculated waveforms for both types of modulating functions when $f_o = 5$ Hz, $r = 0.9$. The Fourier-series is first calculated from (7) when $k = 0, \pm 1, \pm 2, \pm 3$ with

modulating functions (8) and (9). Naturally there will be scattering around the ideal switching vectors due to the truncation of the summation. This scattering can be reduced by increasing the number of harmonics. However, this would increase computation time considerably. Therefore, it is more efficient to compare the calculated Fourier-series of switching vector with those of Fig. 1 (b). When the absolute value of the difference between the instantaneous vector and ideal one is smallest, the calculated vector is replaced with the corresponding ideal one. With this procedure there will be no error, caused by the Fourier-series approach used, in the final results.

In Fig. 3 (a) the angle of the switching vector is shown. It has six discrete values and they correspond to the angles of vectors in Fig. 1 (b). Also the modulating function (9) is depicted. The output voltage in Fig. 3 (b) is calculated from (4) and the changes of the switching vectors are clearly reflected in the voltage, which naturally follows one of the input phase-to-phase voltages. In this case, however, the Fourier-series of switching vector is used and this introduces oscillations in the angle and deviation of the output voltage from the ideal one. On the contrary, in Figs. 3 (c) and (d) the corresponding curves with the modulating function (8) are shown, when the switching vectors are replaced with the ideal ones. It can be observed that the angle of the switching vector has exactly the correct values and that output voltage is exactly equal to one of the input voltages. Therefore, in the rest of the figures in the paper, this replacement of the switching vectors with the ideal ones is adopted.

Theoretically the main difference between Figs. 3 (a) and (c) is that the control angle of the converter in Fig. 3 (c) is always positive and this is reflected in the output voltage where the instantaneous changes are always to a more negative or smaller value. These kind of voltage waveforms have been named in [2] as a negative type and this is also adopted here. With the modulating function (8), the changes in the output voltage waveform are opposite and voltage is called a positive type.

V. Natural Commutation

In naturally commutated converters the input phase voltages are used as the driving forces to turn-off the switches and therefore thyristors can be used. In the previous converters natural commutation is achieved when the converter is equipped with two anti-parallel connected thyristor bridges as shown in Fig. 4. A thyristor can conduct current only in one direction. Bridge I is used when output current is positive and during the negative period bridge II is used. Here the selection of the converter bank is based both on the fundamental component of the output current and the simulated waveform of the current. This information is needed because the current can be discontinuous especially in the vicinity of the zero crossing points, i.e. the output current is zero although it should differ from zero. The change of the converter bank in these cases is prevented as long as the known fundamental component reverses its direction.

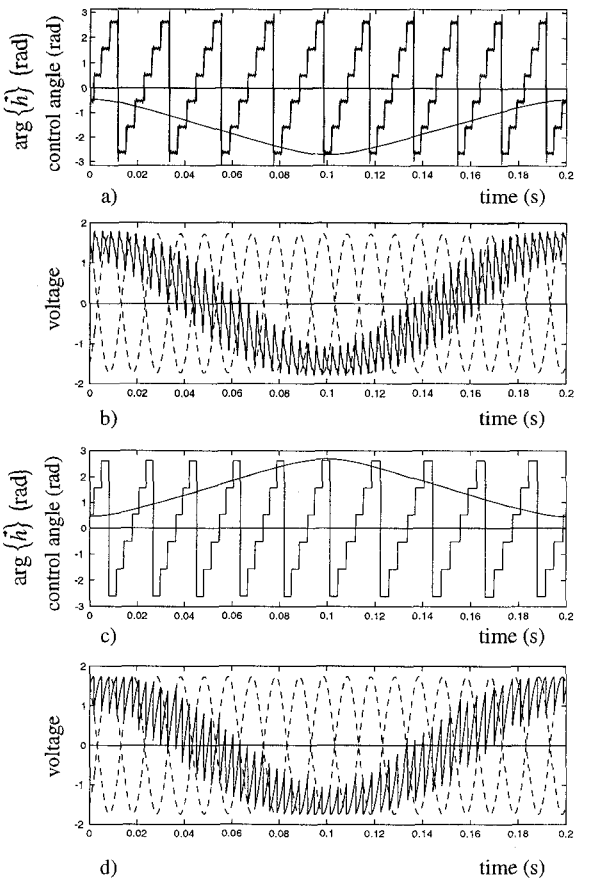

Fig. 3. (a) Modulating function $m(t)$ and angle of switching vector of positive type ac-ac converter when $f_0 = 5$ Hz and $r = 0.9$. (b) Corresponding output voltage and two of the input phase-to-phase voltages. (c), (d) The same waveforms for a negative type converter. In the Fourier-series switching vectors are replaced with the ideal ones.

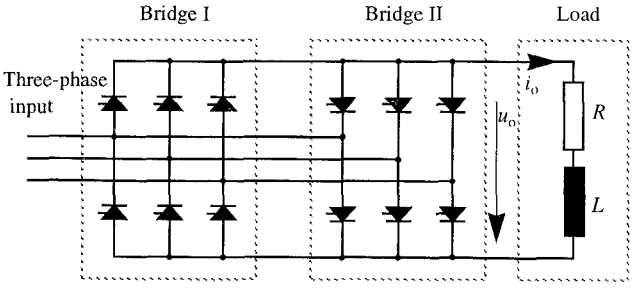

Fig. 4. Diagram of a single-phase naturally commutated ac-ac converter, which is often called a cycloconverter.

A. Steady State Operation

Our simulation is based on calculation of the Fourier-series of the switching vector. In order to do this, the time domain behavior of the control angle of the converter must be known. This can be defined as steady state simulation. However, it is not necessary that the output frequency of the converter remains constant during the simulated period. Similarly, it is possible to change the modulation depth r. These changes must be known in advance.

When the output frequency and modulation depth r are known, the positive and negative voltage waveforms are calculated as already shown in Fig. 3. At first it is assumed that

the output current is sinusoidal or at least continuous. However, self-commutation is needed during some periods of output cycles. The output voltage of the naturally commutated converter consists of the positive and negative type voltage waveforms in such a way that natural commutation is achieved [2]. From this it follows that the voltage type is positive when the output current is positive and negative during the negative half cycle of the output current. Therefore, the selection of the modulating function, (8) or (9), and bridge I or II is based on the polarity of the current. One possibility for this bank selection is to use the simulated waveform of the current, but close to the zero crossings of the current, the instantaneous value can be zero although we are still in the positive half cycle. This is why the fundamental component of the current is needed. It is calculated from

$$i_{o1} = \frac{\hat{u}_o}{\sqrt{R^2 + \omega_o^2 L^2}} \cos\left(x_o - \varphi_o\right), \varphi_o = \arctan\left(\frac{\omega_o L}{R}\right) \quad (10)$$

where the fundamental component of output voltage $\hat{u}_o = r\left(6\,\hat{u}_v/\pi\right)\sin\left(\pi/3\right)$ is obtained when the mean value of (6) is multiplied by r. Here $\hat{u}_v$ is the peak value of the input line-to-neutral voltage and it is assumed that $\hat{u}_v = 1$.

If the simulated current has negative values, even if the fundamental component is positive, the simulated value is set to zero. A similar resetting is done during the negative period of the fundamental current. Simultaneously the output voltage is set to zero because the load is an R-L circuit. If the load would be e.g. a synchronous motor, the output voltage at zero current would be equal to the induced electromotive force.

When the output current is discontinuous, fundamental component of current is somewhat lower than (10) gives, because the fundamental component of voltage is smaller than with continuous current. However, this does not affect simulation results because the critical points, the zero-crossings of the fundamental component of the current, are at correct places.

Simulated current and voltage waveforms of natural commutation corresponding to the voltages of Fig. 3 are shown in Fig. 5. The load is a resistive and inductive network where $R = 2$ and $L = 0.001$ p.u. The angle of the used switching vector and control angle of the converter are illustrated in Fig. 5 (a). The modulating function changes from positive type to negative type when the current polarity changes. This change is also reflected in the voltage waveform of Fig. 5 (b). Current is discontinuous in the vicinity of zero crossings and this can be observed more clearly from Fig. 5 (c), which is an enlarged segment of Fig. 5 (b). It can also be observed that the dashed voltage is zero when current is zero.

Space-vector of the input current is calculated from (3) and the real part of it is shown in Fig. 5 (d). It is equal to the current in input phase one and the instantaneous value follows the waveform of output current, which is drawn dashed. Also the input current resulting only from the fundamental component of output current is drawn.

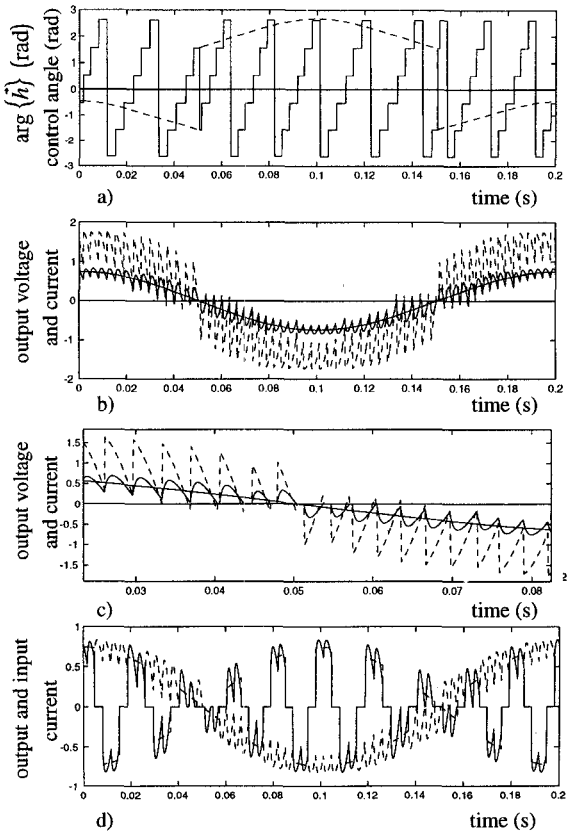

Fig. 5. Simulated waveforms of a naturally commutated cycloconverter when $f_o = 5$ Hz, $r = 0.9$ with load $R = 2$, $L = 0.001$ (a) Modulating function and angle of the switching vector. (b) Simulated output current and its fundamental component (solid lines) and output voltage (dashed). (c) An enlarged part of figure b). (d) Input current in phase one.

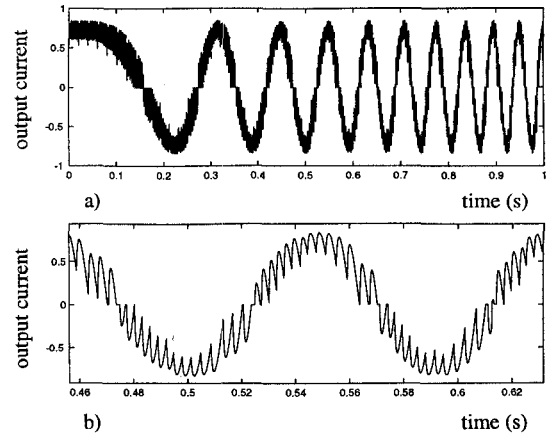

Fig. 6. a) Simulated output current of a cycloconverter when output frequency f_o sweeps in one second, $f_o = 0 \ldots 10$ Hz, $r = 0.9$ and load $R = 2$, $L = 0.001$. b) A zoomed part of current.

B. Frequency Sweep

In the previous cases it was assumed that the output frequency of the converter remains constant. This is not necessary and actually output frequency or more generally output angle x_o can change as desired. In Fig. 6, frequency sweeps linearly from $f_{omin} = 0$ Hz to $f_{omax} = 10$ Hz in one second. In motor drive applications the aim is to keep, for example, the air gap flux of the motor constant. This can be approximated

by keeping the relation u_0/ω_0 constant, which requires that the modulation depth r of the converter is changed together with the output frequency. However, in our simulations r is kept constant as this causes only a very small decrease in the current because load inductance 0.001 is very small compared to the resistive part of 2. The required r can be calculated from (10) in order to keep the peak value of current constant.

Calculation of the waveforms in Fig. 5 took 3.6 seconds with a PowerMacintosh® 7600/132 computer, which is equipped with a 132 MHz PowerPc processor. The calculations were done with MATLAB® 4.2c.1 software. Fig. 5 contains 2000 points with a time step of 0.1 ms, which makes 0.2 seconds and corresponds to one cycle with $f_0 = 5$ Hz. In Fig. 6, there are 10 000 points and the duration of calculations was 17.8 seconds. From these facts it can be estimated that this kind of simulation with the used computer and software takes about 18-times longer than the corresponding real time operation.

In [11], a method to detect the zero-crossings of the output phase current without harmful delay is introduced. That method uses our simulations to produce the current waveform.

VI. Summary

In this paper an efficient simulation method for phase-shift controlled converters was presented. It can be used easily in the production of output voltage and input current waveforms of the converter and no rigorous modeling of the control is required. Natural commutation is achieved when the conducting thyristor bridge is changed based on the polarity of the fundamental component of the output current. The method can be used as an efficient tool in the analysis of network effects of converters and in the analysis of the motor behavior in steady state.

References

[1] B. Pelly, *Thyristor Phase-controlled Converters and Cycloconverters.* New York: John Wiley&Sons Inc., 1971.

[2] L. Gyugyi, B.R. Pelly, *Static Power Frequency Changers*, New York: John Wiley & Sons, 1976.

[3] P. Wood, *Switching Power Converters,* New York: Van Nostrand Reinhold Company, 1981.

[4] J. Kyyrä, *Switching Vector Theory — Unification of Switching and Space-Vector Theory in Polyphase Converter Applications*, Helsinki: Acta Polytechnica Scandinavica, El 83, 1995.

[5] M. Mård, *Electric Drives And Power Electronics,* Espoo: Otakustantamo 889, in Finnish, 1993.

[6] M. Mård, "The Theory of Safe Switching Power Conversion," *Proceedings of PEMC'94*, Poland, Warsaw, vol. 2, September 1994, pp. 1126-1131.

[7] K.P. Kovács, I. Rácz, *Transiente Vorgänge in Wechselstrommaschinen Band 1 & 2,* Budapest: Verlag der Ung. Akademie, 1959.

[8] J. Kyyrä, "Space-vector in the Analysis of Polyphase Systems," in *Proceedings of Speedam'96*, Capri, Italy, June 5-7, 1996, pp. B6-9-14.

[9] J. Kyyrä, "Analysis of Polyphase Phase-shift Controlled ac-dc Converters Based on Switching Vector Theory," *EPE Journal*, vol. 6, no. 1, May 1996, pp. 22-30.

[10] J. Kyyrä, "Analysis of Phase-Shift Controlled ac-ac Converters Based on Switching Vector Theory," will be presented at European Power Electronics Conference, EPE'97, Trondheim, Norway, September 8-10, 1997.

[11] S. Väliviita, J. Kyyrä, S. Ovaska, "Adaptive Signal Processing System for Accurate Zero-Crossing Detection of Cycloconverter Phase Currents," will be presented at Power Conversion Conference, PCC'97, Nagaoka, Japan, August 3-6, 1997.

A Novel Simulation Scheme of Power Electronics System with the Parallel Inference Machine (PIM)

E.Masada J.Baba H.Wakamiya M.Tamura
The University of Tokyo
3-1 Hongo 7, Bunkyo-ku, Tokyo, Japan, 113
Fax: +81-3-5684-3972, Phone: +81-3-3812-2111 ext. 7492
E-mail: baba@masada.t.u-tokyo.ac.jp

Abstract- **For the dynamic simulation of the control system with power converters, it is proposed a novel scheme with the parallel inference machine, which emulates a parallel-computing machine with several hundreds of processors. Utilizing its para-cell soft-ware, the simulation can be realized with a multi-layered structure, which is convenient to separately describe controllers, converters and plants. The authors examine PIM simulator for two cases: the one is HVDC system and the other is SMES system. Simulation results were compared with analog simulator and other simulating methods. It was concluded that power electronics control system simulation can be made on PIM without much knowledge on the numerical technique. The multilayered cell sturucture provides easy access to the model for modification and parameter adjustment. Improvement of PIM itself will make this approach more powerful and possible for the real-time control purpose.**

I. INTRODUCTION

With the progress of power devices and their switching capability, applications of power electronics have been more and more shifted towards control-oriented fields. The performance of the over-all system is affected by the interaction between subsystems such as controllers, converters and controlled processes. It is difficult to analyze them theoretically due to their increased complexity and wide spread of dynamic characteristics in the time domain. The simulation has become an important tool in the design and evaluation of such systems [1], [2].

Because of the complexity of the problem, these simulations have been realized with the direct-analog simulator, the problem-oriented digital software or their hybrid combination. The former one has disadvantages of difficult maintenance, upgrading of hardware, rather low accuracy of results and large spaces of equipment. The latter has problems such as difficulty of making software on the basis of system structure and lack of flexibility for modification in system construction and control schemes. If it is incorporated into a hybrid simulator, difficulties related to the real time digital simulation are introduced.

The recent development of super-parallel computers is expected to solve these problems and to realize full-digital real-time simulator, too. A model has been utilized as a part of the power system simulator including power electronics equipment. However, it is a large scale simulator and very expensive [3].

The parallel inference machine (PIM) is an emulator of the parallel computer system implementing on a microcomputer and microprocessors under development. It has a reasonable scale for the use in laboratories and the user-friendly object-oriented software structure. The authors consider the suitability of PIM to this kind of simulation problems in power electronics.

Its para-cell software, with which the multi-layered program can be easily classified and manipulated independently, can provide convenience to make and adjust the simulation program with adequate correspondence with the hardware structure.

In cooperation with its developer, the authors apply PIM to the simulation of power electronics control systems. In order to evaluate differences in control schemes and converter types, a HVDC system and a SMES system are simulated. The results show that the PIM-based simulation can provide various features compared with existing means related to power electronics simulation. The needed scale of PIM and the requirements for its arithmetic capability for the general use in the field of power electronics, are clarified on the basis of these studies. The feasibility of PIM as a real-time controller for the control in power electronics is also discussed.

II. PARALLEL INFERENCE MACHINE (PIM)

The parallel inference machine (PIM) is an emulator of the super-parallel computer and provides the parallel calculation environment by the time-sharing use of a general purpose micro-processor (MC68040/33MHz) under the host computer of Power Macintosh 8115/110 . It is aimed to simulate or regulate a complicated system with its simultaneous calculation ability of many processes and a use-friendly software structure[4]. It has been applied for a simulator of the automatic train control system of Shinkansen. The machine itself is under development and operates only with the fix point arithmetic processing unit at present. PIM consists of a Macintosh host computer, dealing with programming and debugging of the whole computation, and a PIM-board with a general purpose micro-processor executing parallel processing and the global memory as well as I/O units, connected by Nu-Bus slots of the host computer. Fig.1 shows its configuration.

PIM realizes parallel computation with a single pro-

0-7803-3823-5/97/$10.00© 1997 IEEE

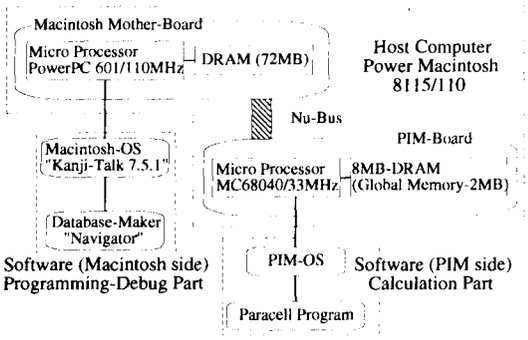

Fig. 1 System configuration of PIM machine

cessor on the basis of principle shown in Fig.2 . It has the virtual processor called "cell" up to 250 in a microprocessor in the PIM board. All cells utilize the global memory in common. Importing and exporting of data to all cells in one computing cycle are done simultaneously. The processing of each cell is executed in the microprocessor serially but it looks as a parallel processing in a cycle. PIM fixes its one computing cycle to 1/60 sec. and creates virtual multi-processor states by time-sharing of a microprocessor as described above.

Fig.3 gives its operation in more details. PIM handles each program sequentially, but it doesn't use the results (x1(n+1), x2(n+1) from Fig.2) until the next calculation period. This characteristic is suitable for dynamic system simulation, because we need not to make routine to store n-th values. Basically, in each program cell, PIM should not calculate sequentially, in order to assure isotropy. But, using local variables, effective in only one program cell, PIM can do sequential calculation. Its para-cell software, with which the multi-layered program can be easily classified and manipulated independently, can provide convenience to make and adjust the simulation program with adequate correspondence with the hardware structure.

The computing cycle in PIM board is fixed to 1/60 second and the processor creates virtual multi-processor states by time-sharing operation in each cycle as shown in Fig.2. If j parallel processors are emulated, one computing cycle is separated into j segments, each one of which correspond to a processor and is called as a cell (program cell). The global memory gives all input data to each cell simultaneously at the beginning of each computing cycle. The data are stored in the local memory of a cell. After the calculation of all cells, the global memory receives all output data from the local memory of each cell at the end of the cycle.

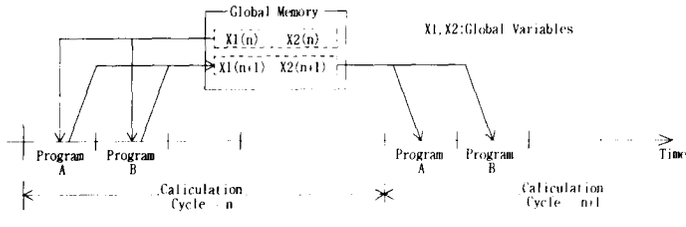

Fig. 2 Calculation cycle in PIM

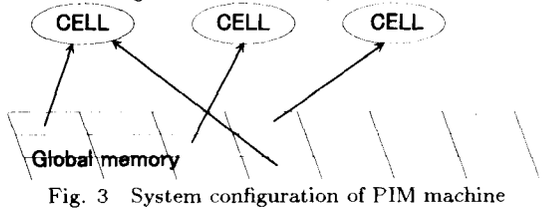

Fig. 3 System configuration of PIM machine

The para-cell software implements each program unit into a cell and connects each other with a multi-layered structure as shown in Fig.4. The calculated data are transferred between cells as specified within the para-cell software. The program in each cell can be easily classified and manipulated independently in the software. This can provide convenience to make and adjust the simulation program with adequate correspondence with the simulated system structure.

Comparing with the general purpose software for the simulation of power electronics systems such as P-SPICE or MATLAB-SIMULINK, where the Graphical User Interface assists to program easily, PIM gives only operating system to program a multi-layered system structure simply as shown in Fig.??. Its programming is done with the host Macintosh utilizing the special language Navigator. This drawback is compensated with the easiness in the system modeling through the multi-layered software structure.

In this study, the feasibility and evaluation of the application of PIM is carried out for the simulation related to the control problems in power electronics systems.

III. APPLICATION OF PIM TO THE SIMULATION OF POWER ELECTRIC CONTROL SYSTEM

As stated above, PIM is a machine under development, so far the application to the simulation of the control problems in power electronics systems, two items should be considered furthermore.

The first point is that the machine is designed to be the real-time controller and simulator of the railway traffic control system [4].It means that it is aimed to process the sequence of events mainly and to simulate the operation of trains with a simple model. In order to utilize it for the more complicated dynamic system simulation of power electronics systems, a new program structure should be introduced in relation with the cell and the global memory. The second point is that the machine is based on the fixed point arithmetic unit. The appropriate algorithm should be implemented to keep the total simulation error less than the specified value within the allowable complexity of calculation allocated for each cell.

The single phase power conditioner is studied as an example to solve these problem and to obtain insight to simulate more complicated cases of power electronics control systems. To cope with the large number of state variables in the system within the rather limited function of a cell, the Euler scheme is utilized successfully to

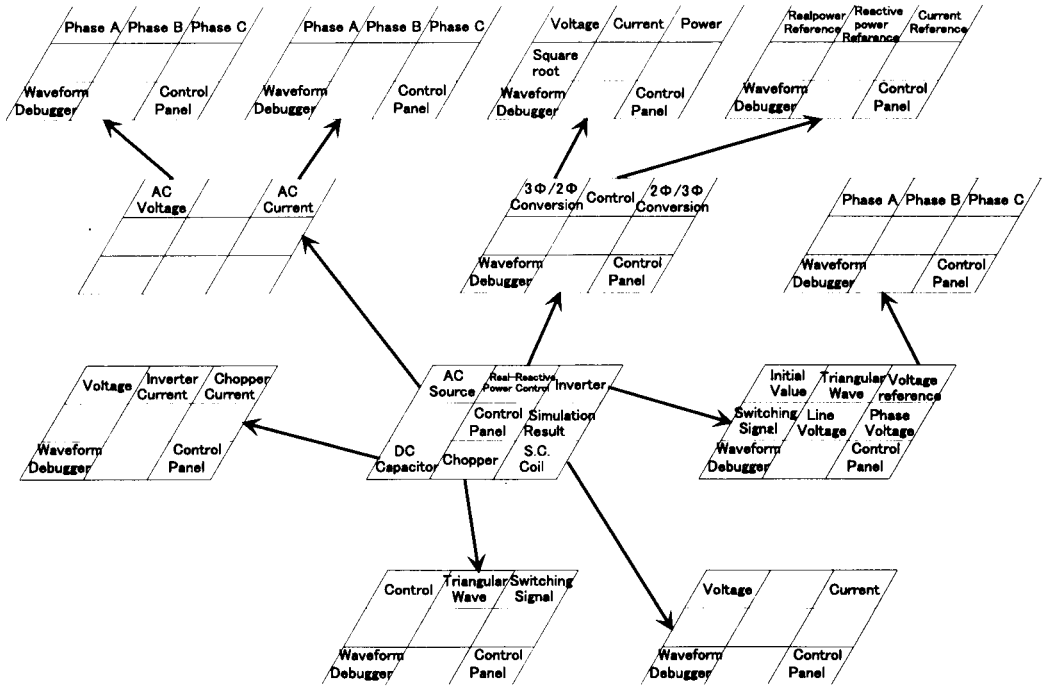

Fig. 4 An example of program configuration of a database

solve the state equation of the system, but the time step for the numerical integration should be kept as short as 10 s. It makes the time ratio between the simulated time and the real time as 1:10000. The results agreed good with those obtained with P-SPICE[5].

As the next step, problems in the more complicate power electric control system are studied to evaluate PIM as a simulation tool. Two typical power electric control systems: HVDC system and the SMES system are simulated. Through these two systems, the modeling of power systems, power converters and their control systems are investigated in order to examine the applicability and ability of PIM in the simulation. In following sections, the simulation results and comparison with experimental results or results from other simulation methods are shown. The characte-ristics of PIM is considered in relation with simulation results.

A. HVDC system simulation

Fig.5 shows the point to point HVDC transmission system configuration. AC-system is assumed to consist of the 3-phase voltage source and a transformer, being expressed with an equivalent resistance and leakage inductance. The frequency of AC voltage sources is 50Hz in both side of the system. The power converters are presumed to be the single 3-phase line-commutated bridge converters because of the limit of the number of available cells. The DC-system is stated with the serial impedance of the line and DC-reactor. The rectifying terminal regulates the DC current of the system and the inverter terminal controls the DC voltage at the terminal. The detailed control scheme follows to the conventional ones utilized in the practical systems.

It is a very important and unique problem of using PIM for the simulation of the converter circuit, that we can't take back a time step and calculate again on the different data for the state variables, since unilateral progress of time steps is allowed to simplify the data transfer between cells and the global memory. This problem especially affects selecting the adequate time step value simulating the operation of valves in the line-commutated converters. The switching valve turns off when the its valve current becomes zero. To simulate this exactly, the switching state of the converter must be changed at the zero-crossing of the current, but the detection of the instant is delayed one time step at least in the operation of PIM. Usually to reduce calculation error caused by such delay, after zero-crossing detection, a short adjusting period is introduced to represent the change of variables after switching. For this purpose the calculation cycle should be repeated with different time step. But PIM can not use this method. And furthermore, the para-cell capacity in this version of PIM is not enough to carry out the numerical integration with Runge-Kutta method. These two accumulate the calculation error for each step and each switching. To cope with these problems, an appropriate time step should be chosen as short as 2μsecond. It means that it takes 1/60 sec of PIM to simulate 2μ second event in the converter circuits.

After these considerations, the operations of the point-to-point HVDC system are simulated. As an example of them, the power reversal, meaning that the converter located at one side changes inverter operation mode and the other one changes respectively keeping DC current constant, is shown in Fig.6. This operation shows the

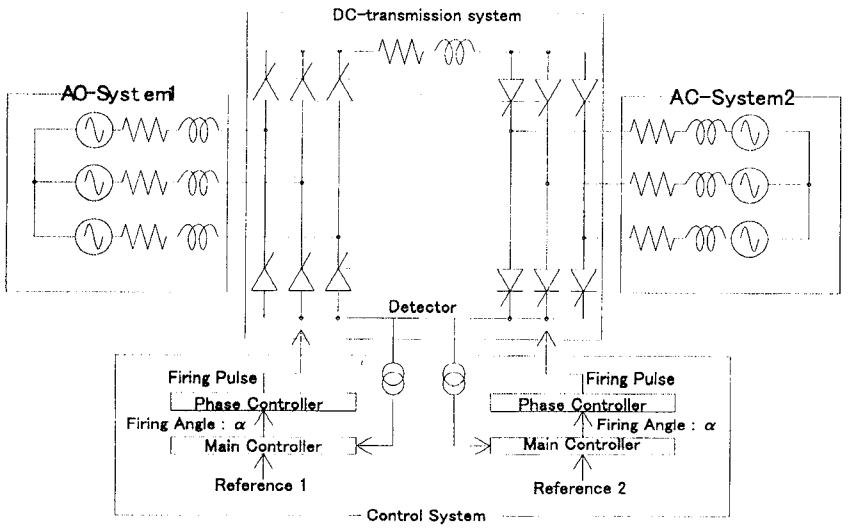

Fig. 5 Configuration of point to point HVDC-transmission system

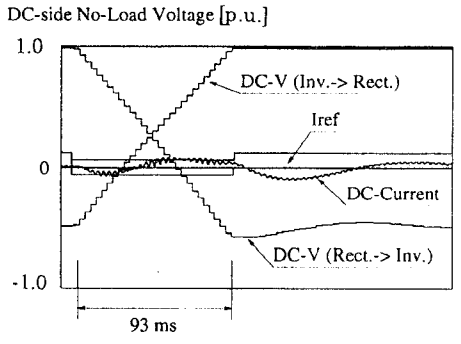

Fig. 6 Power converters operation mode power reversal: PIM simulation result

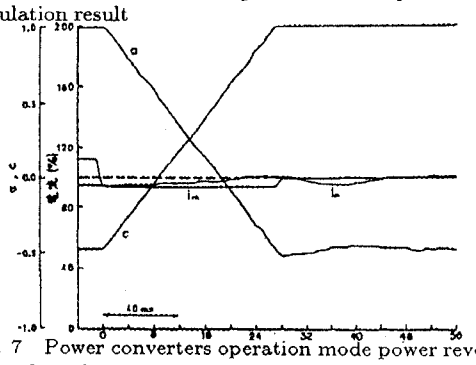

Fig. 7 Power converters operation mode power reversal: Experimental result

PIM's proper performance, which can change the reference values or mode of control at anytime during running programs.

Fig.7 shows the experimental results obtained with an analog simulator [6]. Comparing with the results of PIM simulation differences are observed in DC current and DC voltage in transient-state. This is due to the negligence of the DC filter in the PIM case and the accumulation of calculation error in DC variables. But, considering the firing angle of converters for steady-state behavior and the behavior of DC-terminal voltage and DC-current (small overshoot) in the case of changing the operation mode from rectifier to inverter, we can conclude that PIM carries out a reliable and relatively precise simulation tool.

B. SMES system simulation

Fig.8 shows the circuit configuration of which we have simulated SMES (Superconducting Magnetic Energy Storage System). The superconducting coil is connected to AC line through multiple-connected six DC/DC-converters, which is given by one equivalent unit operated with higher switching frequency in the figure, and a DC/AC voltage source converter. The DC/DC converters and the converter are controlled in cooperation with which it enables to control real and reactive power flow from the AC system independently. For this purpose the utilization of self-commutated converter is presumed. Fig. 9 shows the control block diagram of this simulation. This block indicates that real power is mainly controlled by the DC-choppers which regulate DC voltage, and reactive power is mainly controlled by the converter. Compared with HVDC system, the control method is complex and requires much more para-cells.

The frequency of converter's and chopper's modulation wave are 500Hz. The switching frequency of this case is more than that of HVDC case, but the circuit simulation program becomes simple because we assumed that switching devices are self-commutated and they behave ideally. On the other hand, we determined 1μ second as the simulation time step, which is as half as that of HVDC case, in order to keep necessary precision for results.

Fig.10-13 show the simulation results using PIM, and simulation results using a digital simulation based on the C-language with Runge-Kutta method. Inspecting AC side values(Fig.11,), we can not distinguish between the result of PIM and C-language. We can conclude there are not remarkable difference between results of two method. But seeing DC side (Fig.12,), the difference of these two value become bigger as the simulation time step number increases. The reason is that this version of PIM can not calculate with floating point arithmetic. In this simulation, we use PI control. In AC side

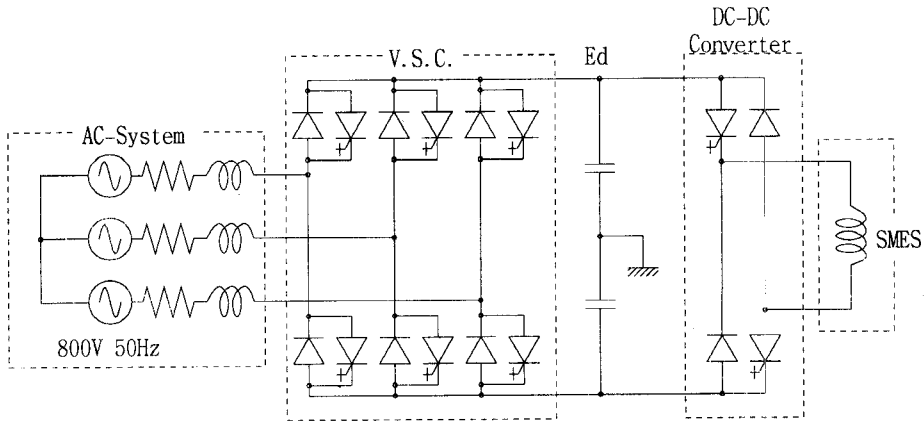

Fig. 8 Configuration of SMES and power system

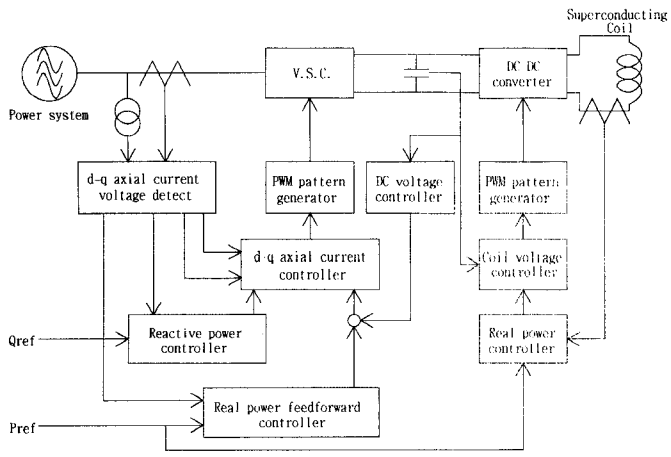

Fig. 9 Control block diagram

calculation, precision is higher than DC side because it is not so important to take into consideration overflow due to the cyclical value change. But in DC side, to avoid overflowing, precision of PI control have to be lower, and error of DC voltage is accumulated owing to DC capacitor. In simulation, DC capacitor voltage is calculated from AC current integration. At the same time, this calculation integrate AC current error and as a result the error of DC voltage is bigger than that of the AC side one. In this case, PIM can simulate 300-400 m sec. behavior owing to accumulation DC error, if we require the result to be as precise as that of analog simulator with 1

This problem is caused by the fixed point arithmetic and lack of para-cell's capacity to study such complicated systems. PIM's essential characteristics, parallel algorithm or multi-layered structure, didn't cause these errors. When PIM machine is upgraded to floating point machine, these problem will be resolved.

IV. EVALUATION AS A SIMULATION TOOL

Examples described in the former section are programmed by undergraduate students who have had only basic knowledge in power electronics. The time required to complete it, is very less than utilizing the general language as C or FORTRAN (around one 10th), and less than the time needed to apply P-SPICE to such complicated systems (around one third). If the subprogram describing the power electronics components or controllers in cells, the efforts to simulate a system would be reduced further.

The PIM machine used in this study can emulate only 250 cells in it. This scale is roughly the limit of the problem size raised in the examples. In the case where a more complicated system should be studied, the PIM-Board should be increased to install 2-3 microprocessors.

In relation with the numerical integration of the dynamic system, it is not so efficient that all cells operate with the same calculation cycle synchronously. It should be pursued to improve this with the modification of the program structure. One possibility is to separate cells into two virtual groups operating in a different program using the parity of the calculation cycle.

The arithmetic unit of PIM at this stage of development can process only fixed point data as numeral. It limits the accuracy of the simulation as well as the simplicity of the model. The new version of PIM machine will be introduced in several month which equips floating point processing units.

The real time operation of the machine is also limited by the number of microprocessors in the PIM-board. For the application for the controller of power electronics system, further studies are needed to optimize its structure.

V. CONCLUSION

A novel simulation scheme utilizing the parallel inference machine is introduced for the simulation of the complicated power electronics control system, verified to reduce the efforts required for the programming very much and shown to be useful to design the control system with exact correspondence with the hardware structure of the system.

There are some difficulties to apply this version PIM to power electronics control system simulation because PIM can deal only with fixed point arithmetic. But PIM's essential characteristics don't increase the difficulties. When PIM machine is upgraded to floating

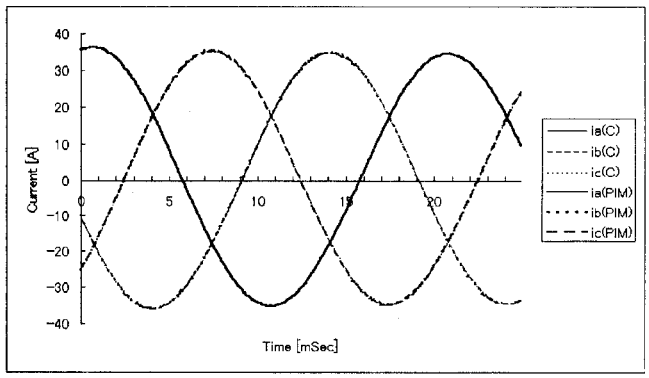

Fig. 10 AC side currents

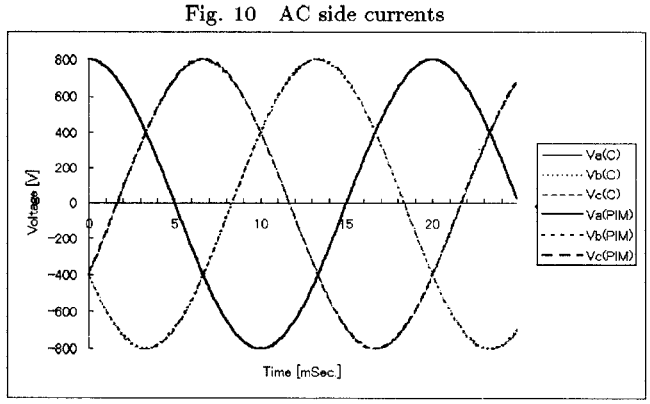

Fig. 11 AC side voltages

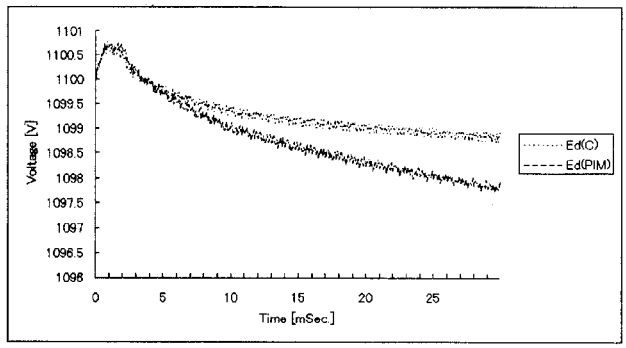

Fig. 12 DC side voltage

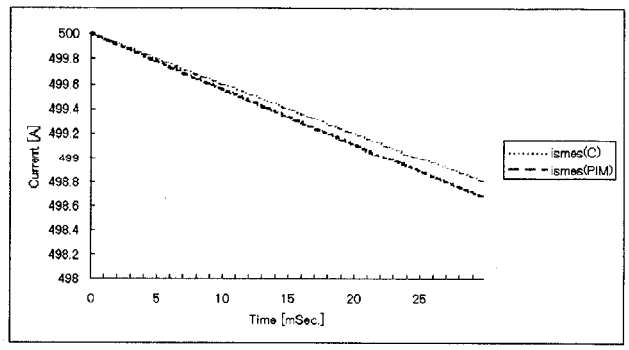

Fig. 13 Current of superconducting coil

point arithmetic machine, more complex and precise simulator will be enable for PIM, and not only circuit simulation but also combination other dynamical system could be simulated.

ACKNOWLEDGMENT

The authors gratefully acknowledges valuable contribution of Mr. H.Kaneda for PIM simulation and Mr.S.Yasukawa for advice about PIM.

REFERENCES

[1] Masada, Fukao, Shimada and Kawamura, *Power Electronics*. Tokyo: OHM-Sha, 1995

[2] "Simulation technologies for electric power systems and equipments" *Electric Corporate Research* Vol.51, No.4, 1996

[3] Sato et al, "Development of digital real-time power system simulator," *Tr. IEEJ* Vol.113-B, No.8, 1993

[4] S.Yasukawa, "Parallel programming paradigm for real-world simulation", Industrial Automation Conference, 1995.3

[5] H.Kaneda, H.Ohsaki, and E.Masada, "Application of parallel inference machine to dynamic simulation of electric power converter." in *proceedings of the ELECTRIMACS '96*, 1996,pp847-852

[6] S.Koseki, *Control of DC-transmission system.*, The University of Tokyo, Doctor-Thesis, 1974

State Vector Equation based Computer Simulation Approach of Digitally Controlled Power Conversion Circuits and Systems

Syed Mobin Ulhaq

Mutsuo Nakaoka,

Department of Electrical and Electronic Engineering
The Graduate School of Engineering and Science,
Yamaguchi University,
2557, Tokiwadai, Ube 755, Yamaguchi, Japan

Phone: 0836-35-9946 Fax: 0836-35-9449

Hiroshi Takano,

Research and Development Department
Hitachi Medical Co, Ltd , Chiba-277 , Japan

Abstract - An efficient simulation approach is presented in order to analyze digitally-controlled switching mode power converter circuits and systems with feedback and feedforward control loops. The general computer-aided simulation procedure is based on a circuit and system equation modeled by time-varying resistors which substitute active power switches and the passive diodes of the converter circuits in addition to a sate equation for the inductors and the capacitors, an algebraic computation method to transform the matrices of the circuit equation into the matrices of the state equation. In this approach, the numerical integration is achieved with rather less numerical calculation steps because of the small matrice size of the state equation. The effectiveness of this approach are proved by introducing our newly-developed PWM DC-DC high-power converter operating at high-voltage transformer parasitic circuit parameters under a digital control scheme.

1. INTRODUCTION

Several general simulation formulations have been developed on the basis of time domain or frequency domain mathematical formulations .

In time domain, the tableau method is described with its nonlinear derivative and the algebraic equations to specify the circuit elements and their connections, and repetitive numerical computation [1][2]. In this method, many calculation steps for simulation are required for power conversion circuits and systems.

For circuit simulation, the envelope-following method [5] and the state-space averaging method [6] in time domain, and the other methodologies in the frequency domain[7] are used in order to reduce the number of calculation steps and the computation time. In these computer-aided simulation techniques, however, it is difficult to simulate complete transient operating waveforms if the circuit has nonlinear characteristics, resonant and quasi-resonant discontinuous current operations.

In this paper, a newly-developed generic power electronic circuit simulation technique is presented in which digital control algorithm can be easily embedded and the operating characteristics are to be obtained on various workstations or personal computers in laboratories. In this approach, steps of numerical calculations required are rather less than the tableau method because the numerical integrations are to be repeated for only one state equation. The mode transition changes are described with simple descriptions for each switching condition. Moreover, this technique can also be applied for various types of switching-mode power converters with digital control scheme.

2. SIMULATION THEORY OF POWER CONVERTERS

2-1 Circuit Model Description

Fig. 1 illustrates an example of the power conversion circuit to be analyzed. This is a series and parallel resonant high-frequency AC linked DC-DC power converter with high-voltage transformer parasitic LC components

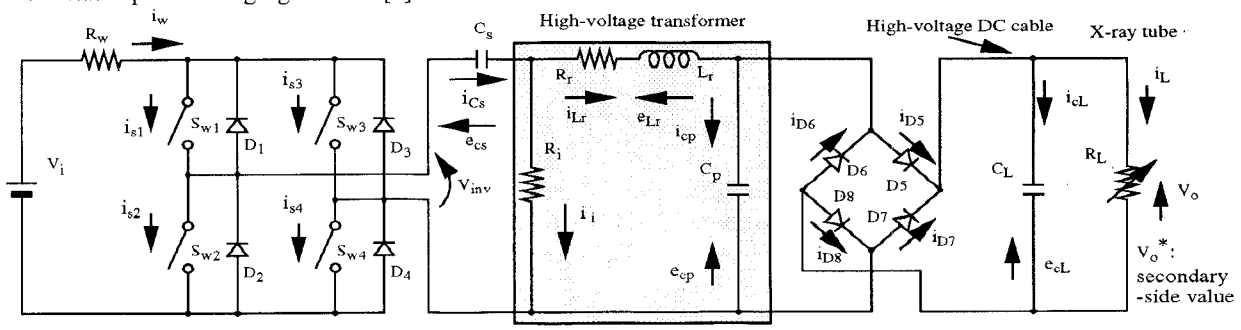

R_w : Wired resistance	10 mΩ	Ri : Iron loss of high-voltage transformer (p)	280 Ω
V_i : DC power source	60 to 450 V	Rr : copper loss of high-voltage transformer (p)	180 mΩ
C_s : Series resonant capacitor	15 μF	Lr :Leakage inductance of high-voltage transformer (p)	15 μH
C_L : Equivalent capacitance of high-voltage cable(p)	310 μF	Cp : Stray capacitance of secondary windings (p)	5 μF
R_L : Load resistance modeled X-ray tube (p)	0.1 to 1 kΩ		

(p) indicates reduced values into the primary-side of the high-voltage transformer.

Fig. 1 Total circuit model of inverter-fed type X-ray high-voltage power generator.

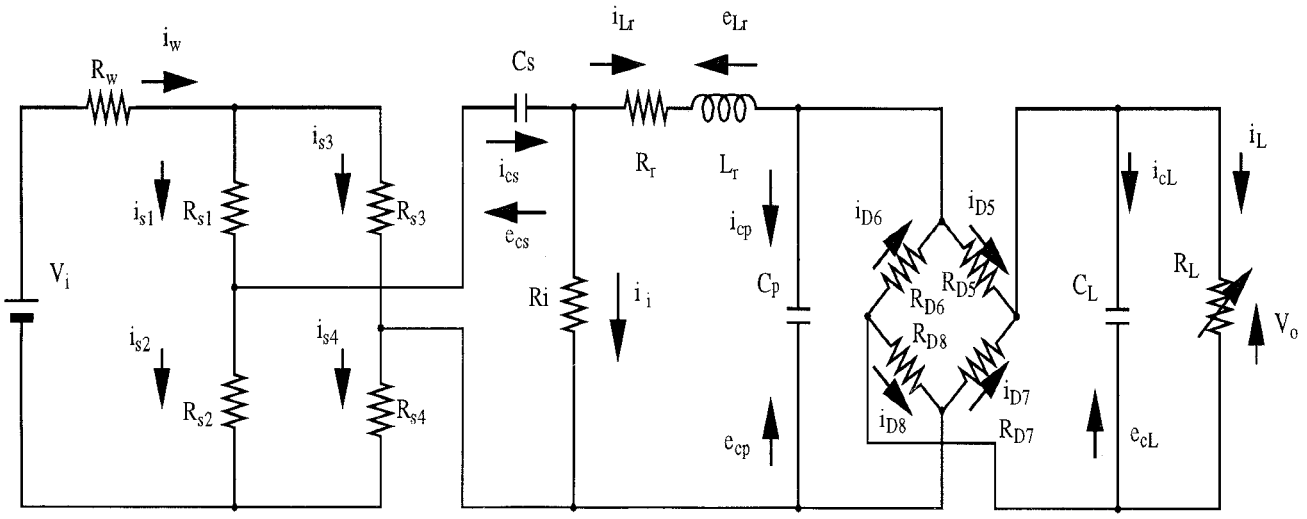

Fig. 2 Circuit model by time-varying resistors taking the place of active switches and diodes.

and loss resistances. The parasitic circuit parameters are represented in Fig. 1. The circuit parameter values in the secondary of the high-voltage transformer are refered to its primary side . The output voltage is regulated under a condition of constant frequency phase-shifted PWM control . The DC output voltage of this converter is regulated from zero to maximum voltage in terms of phase shifted angle ϕ between the left side bridge arms; S_{w1} and S_{w2}, and the right side bridge arms; S_{w3} and S_{w4}.

R_L is a current-dependent load resistance modeled as the X-ray tube. If the load resistance R_L is large, the output voltage waveform has nonlinear characteristics in the transient state because of discontinuous current operation of the high-voltage rectifier (diode D_5 to D_8) connected to the secondary side. In practical applications X-ray high-voltage generator has extremely wide variation ranges of the load resistance R_L, in other words, there are a large number of specified output voltage and current combinations. The output voltage of this power converter is digitally controlled so as to obtain a specific flat voltage waveform with rapid transient rising and falling characteristics.

2-2 Formulation of Circuit Equation

Fig. 2 illustrates the first stage of this analytic approach, the circuit network configuration of power converter circuit model using the periodic time-varying resistances R_{s1} to R_{s4} which represent the power switches SW1 to SW4 (IGBTs) with their antiparallel diodes shown in Fig. 1. their on-state and off-sate are simply considered as an ideal switching condition .

Applying the Kirchhoff's law to the circuit network, the canonical form of the circuit equation is obtained by (1), which arranges the state variables; the current of the reactor i_{Lr}, the voltages of the capacitors e_{cs}, e_{cp}, e_{cL}, and input variable V_i in the right-hand side.

$$\mathbf{R\,I = E} \tag{1}$$

$$\mathbf{R} = \begin{bmatrix}
1 & & & & & & & & & & -1 & -1 & & & \\
 & -1 & & & & & & & & & 1 & -1 & & & \\
-1 & & & & & & & & & & & 1 & & 1 & \\
 & -1 & 1 & & & & & & & & & & & & \\
 & & & -1 & & -1 & 1 & & & & & & & & \\
 & -1 & & & -1 & 1 & & 1 & & & & & & & \\
 & 1 & & & 1 & & -1 & & -1 & & & & & & \\
R_w & & & & & & & & & & R_{s1} & R_{s2} & & & \\
 & -R_i & & & & & & & & & & R_{s2} & & -R_{s4} & \\
 & -1 & R_i & & & & & & & & & & & & \\
 & -1 & & & & -R_{D5} & & R_{D7} & & & -R_{s1} & & R_{s3} & & \\
 & & & & & -R_{D5} & -R_{D6} & & & & & & & & \\
R_L & & & & & & & & & & & & & & \\
R_L & & & & & & & R_{D7} & R_{D8} & & & & & & \\
 & & & & & & -R_{D6} & & R_{D8} & & & & & &
\end{bmatrix}, \tag{2}$$

$$\mathbf{I} = [\, i_w\ i_L\ e_{Lr}\ i_i\ i_{cs}\ i_{cp}\ i_{cL}\ i_{D5}\ i_{D6}\ i_{D7}\ i_{D8}\ i_{s1}\ i_{s2}\ i_{s3}\ i_{s4}\,]^t \tag{3}$$

$$\mathbf{E} = [\, 0\ 0\ 0\ i_r\ -i_r\ 0\ 0\ V_i\ e_{cs}\ e_{cp}+R_r\, i_{Lr}\ e_{cs}+R_r\, i_{Lr}\ e_{cL}\ e_{cL}\ 0\ e_{cp}\,]^t \tag{4}$$

R is called resistance matrix defined by the resistances in the circuit model. **E** is called voltage vector here because it is mainly specified by the voltages across the circuit elements, **I** is called current vector.

$$\mathbf{I} = \mathbf{R}^{-1}\,\mathbf{E}. \tag{5}$$

Each element of the inverse matrix $\mathbf{R}^{-1}$ is generally expressed as

$$\mathbf{R}^{-1} = \begin{bmatrix} Ri_{1,1} & Ri_{1,2} & \cdots & Ri_{1,15} \\ Ri_{2,1} & \cdots & \cdots & \cdots \\ \cdots & \cdots & \cdots & \cdots \\ Ri_{15,1} & \cdots & \cdots & Ri_{15,15} \end{bmatrix} \tag{6}$$

2-3 Formulation of state equation

The canonical form of the state equation is presented as

$$\frac{d}{dt}\mathbf{x}(t) = \mathbf{A}\,\mathbf{x}(t) + \mathbf{B}\,\mathbf{u}(t) \tag{7}$$

where $\mathbf{x}(t)$: the state vector, **A** and **B** : system matrices, $\mathbf{u}(t)$: the input vector. The sate vector **x** is defined as

$$\mathbf{x} = [\, i_{Lr}\ e_{cs}\ e_{cp}\ e_{cL}\,]^t. \tag{8}$$

The voltage vector **E** may be divided into two terms relating the sate vector and the input V_i as

$$\mathbf{E} = \mathbf{K}_x\,\mathbf{x} + \mathbf{K}_u\,\mathbf{u}. \tag{9}$$

$\mathbf{K}_x$ and $\mathbf{K}_u$ are respectively obtained as

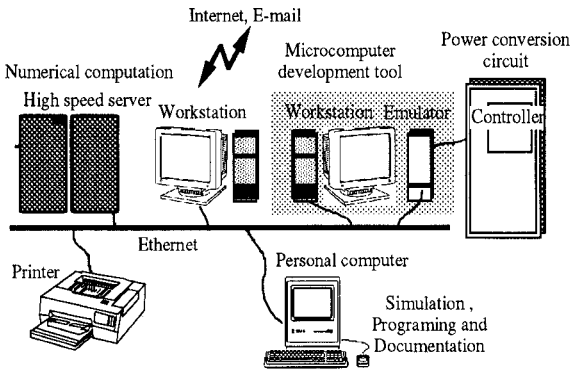

Fig. 4 Example of computer and network system to develop digitally controlled switch mode power converters.

$$\mathbf{K}_x = \begin{bmatrix} 0\ 0\ 0\ 1\ -1\ 0\ 0\ 0\ 0\ R_r\ R_r\ 0\ 0\ 0\ 0 \\ 0\ 0\ 0\ 0\ 0\ 0\ 0\ 0\ 1\ 0\ 1\ 0\ 0\ 0\ 0 \\ 0\ 0\ 0\ 0\ 0\ 0\ 0\ 0\ 0\ 1\ 0\ 0\ 0\ 0\ 1 \\ 0\ 0\ 0\ 0\ 0\ 0\ 0\ 0\ 0\ 0\ 0\ 1\ 1\ 0\ 0 \end{bmatrix}^t, \quad (10)$$

$$\mathbf{K}_u = [\,0\ 0\ 0\ 0\ 0\ 0\ 0\ 1\ 0\ 0\ 0\ 0\ 0\ 0\ 0\,]^t. \quad (11)$$

following relations between the elements of the current vector, e_{Lr}, i_{cs}, i_{cL}, and the state variables are obtained,

$$\frac{d}{dt} i_{Lr} = \frac{1}{L_r} e_{Lr} \quad (12)$$

$$\frac{d}{dt} e_{cs} = \frac{1}{C_s} i_{cs} \quad (13)$$

$$\frac{d}{dt} e_{cp} = \frac{1}{C_p} i_{cp} \quad (14)$$

$$\frac{d}{dt} e_{cL} = \frac{1}{C_L} i_{cL} \quad (15)$$

The left-hand sides of (12) to (15) are identical with the left-hand side of the state equation (7). The right-hand sides of (12) to (15) are calculated by the current vector **I** in (5) and the circuit parameters L_r, C_s, C_p and C_L. Hence, the state equation will be obtained from (5) and the circuit component parameters. next it is necessary to transform the matrices of the circuit equation to the matrices of the state equation.

The current vector **I** can be written as (9) substituting for right-hand side of (5).

$$\mathbf{I} = \mathbf{R}^{-1}(\mathbf{K}_x \mathbf{x} + \mathbf{K}_u \mathbf{u}) = (\mathbf{R}^{-1}\mathbf{K}_x)\mathbf{x} + (\mathbf{R}^{-1}\mathbf{K}_u)\mathbf{u}. \quad (16)$$

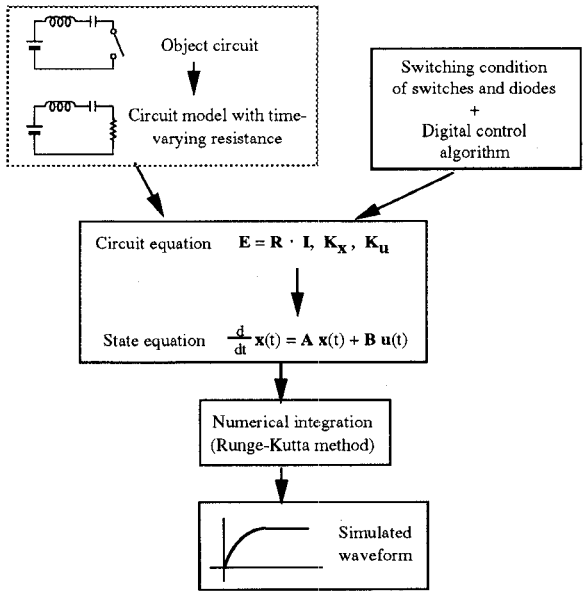

Fig. 5 Strategy of circuit simulation.

The right-hand side of (6) is quite similar to the right hand side of the sate equation (7). Additionally, the right sides of (12) to (15) are calculated with the four elements, e_{Lr}, i_{cs}, i_{cp} and i_{cL} of the current vector **I** of (5) divided by inductance L_r, capacitance C_s, C_p and C_L.

Matrix $\mathbf{R}^*$ is defined as (17) derived 4 rows which relates to L_r, C_s, C_p and C_L in the current vector **I** from the inverse matrix $\mathbf{R}^{-1}$.

$$\mathbf{R}^* = \begin{bmatrix} Ri_{3,1} & Ri_{3,2} & \cdots & Ri_{3,15} \\ Ri_{5,1} & Ri_{5,2} & \cdots & Ri_{5,15} \\ Ri_{6,1} & Ri_{6,2} & \cdots & Ri_{6,15} \\ Ri_{7,1} & Ri_{7,2} & \cdots & Ri_{7,15} \end{bmatrix} \quad 17)$$

the inductance L_r, the capacitances C_s, C_p and C_L are defined by (18).

$$\mathbf{L}^* = [\ L_r\ C_s\ C_p\ C_L\ ]^t. \quad (18)$$

$\mathbf{A}^*$ is picked out some rows related to e_{Lr}, i_{cs}, i_{cp} and i_{cL} in the first term $\mathbf{R}^{-1}\mathbf{K}_x$ of the right-hand side of (16). So, $\mathbf{A}^*$ is 4 x 4-dimension.

$$\mathbf{A}^* = \mathbf{R}^* \mathbf{K}_x. \quad (19)$$

From (17), (18) and (19), **A** is given as

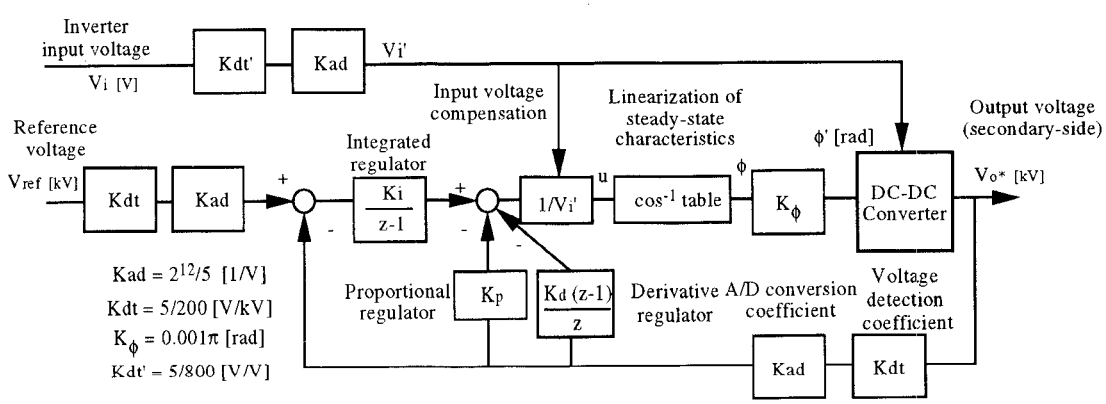

Fig. 3 Control block diagram including power conversion circuit.
(I-PD feedback control, input voltage compensation and linearization for steady-state characteristics.)

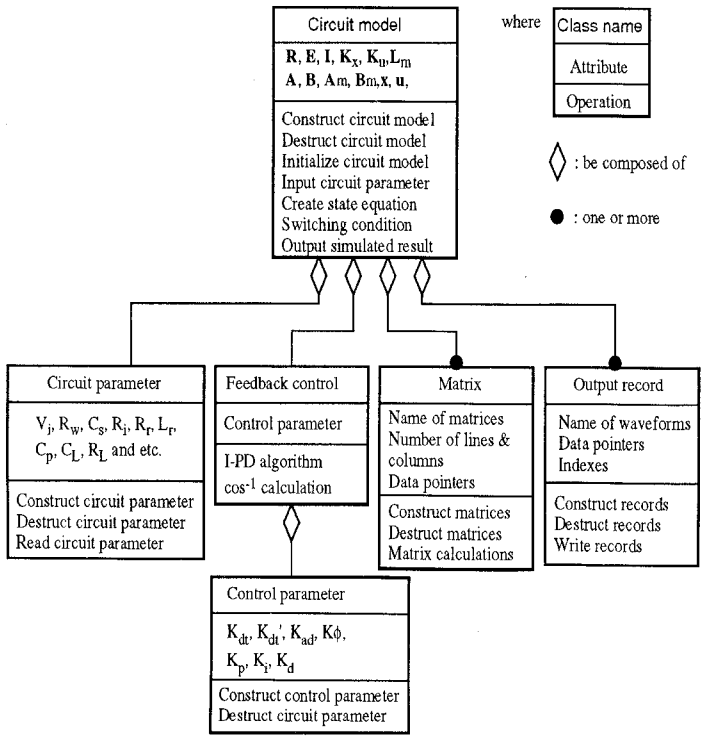

Fig. 6 Object model of the simulation program.

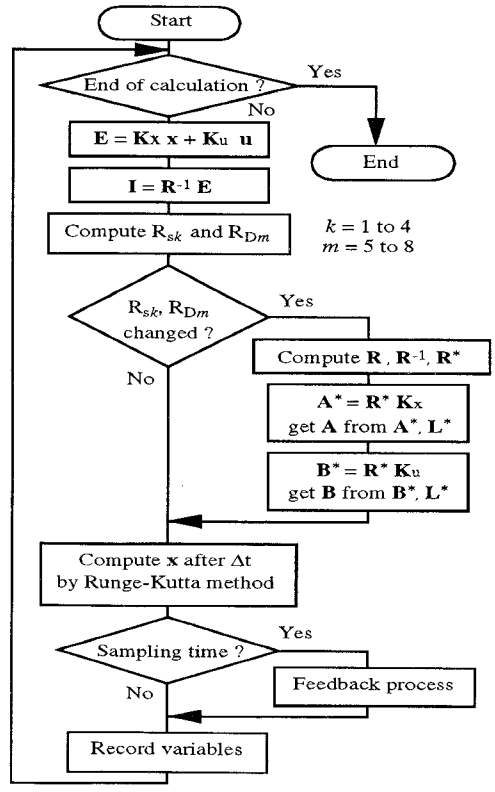

Fig. 7 Flowchart of circuit simulation program.

$$\mathbf{A} = \begin{bmatrix} \frac{A^*_{1,1}}{L^*_1} & \frac{A^*_{1,2}}{L^*_1} & \cdots & \frac{A^*_{1,4}}{L^*_1} \\ \frac{A^*_{2,1}}{L^*_2} & \cdots & \cdots & \cdots \\ \cdots & \cdots & \cdots & \cdots \\ \frac{A^*_{4,1}}{L^*_4} & \cdots & \cdots & \frac{A^*_{4,4}}{L^*_4} \end{bmatrix} \tag{20}$$

where, $A^*_{j,k}$, is an element of $\mathbf{A}^*$; L^*_j is an element of $\mathbf{L}^*$.

In the same way, 4 rows are picked out from $\mathbf{R}^{-1}\,\mathbf{K}_u$, the second term of the right-hand side (16) related to e_{Lr}, i_{cs}, i_{cp}, i_{cL}. As a result, $\mathbf{B}^*$ is 4 x 1-dimension vector andgiven as follows

$$\mathbf{B}^* = \mathbf{R}^*\,\mathbf{K}_u. \tag{21}$$

B is given as

$$\mathbf{B} = \begin{bmatrix} \frac{B^*_1}{L^*_1} & \frac{B^*_2}{L^*_2} & \cdots & \frac{B^*_4}{L^*_4} \end{bmatrix}^t \tag{22}$$

where B^*_j : an element of $\mathbf{B}^*$.

By process described above, all elements of the matrices **A** and **B** of the state equation are obtained from the circuit equation. The simulation program software can be applied to the other circuits with redefined **R**, $\mathbf{K}_x$, $\mathbf{K}_u$, $\mathbf{R}^*$, $\mathbf{L}^*$ and switching sequence. All informations of the circuit operation can be given by **E**, **I**, **R**, and **x**.

2-4 Switching sequence description

If the switch S_{w1} is on state during the time is t_1 to t_2, then in C-language statements

```
if (((t1<=t) &&(t<t2))||(is1<0.0)) Rs1=Ron;
   else Rs1=Roff;
```

where, R_{on} : on-state resistance ; R_{off} :off-state resistance; R_{s1} : the resistance of the switch with the antiparallel diode; i_{s1} : the current through the resistance R_{s1}. In our case, R_{on} = 10 mW; R_{off} = 100 kW high power IGBT (1200V/400A) modules are specified.

The resistance model of the diode is determined as

```
if(iD5 > 0) RD5 = Ron;
   else  RD5 = Roff;
```

where, R_{D5} : the resistance model of the diode D_5; i_{D5} : the current of the diode D_5.

Thus, switching conditions of the active power switches; IGBTs and the passive power switches; diodes can be easily implemented with "if ...then ..." style statements in the simulation program.

In actual program run, in one calculation step, the upper and the lower side switches incorporated into the inverter bridge arms may turn on at the same time resulting in large current flow through switches. The switches may also turn off simultaneously and cause surge voltage. For these cases, special programming techniques are used to depict the switching state.

2-5 Digital control implementation in simulation program

The main merit of the digital control scheme is that the control algorithms like the state feedback control or the adaptive control which are difficult to realize with analog controller can be easily developed by software.

Fig. 3 shows a digital control block diagram of the output voltage for the inverter-fed high-voltage power generator presented in the Fig. 1 [8]. The control algorithms are programmed with C-language in the simulation pro-

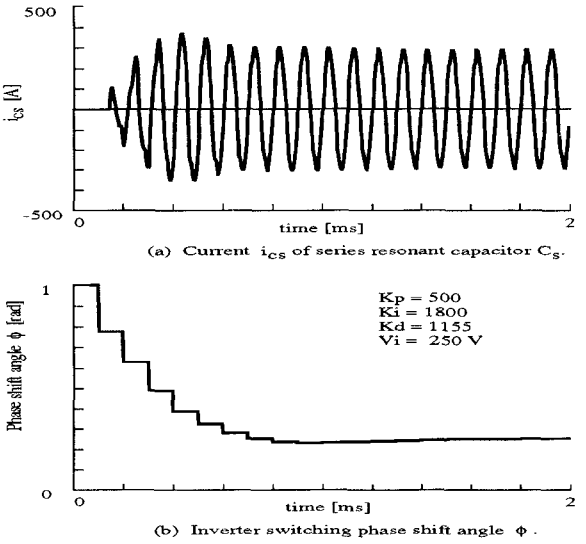

Fig. 8 Simulated close loop transient response waveforms.

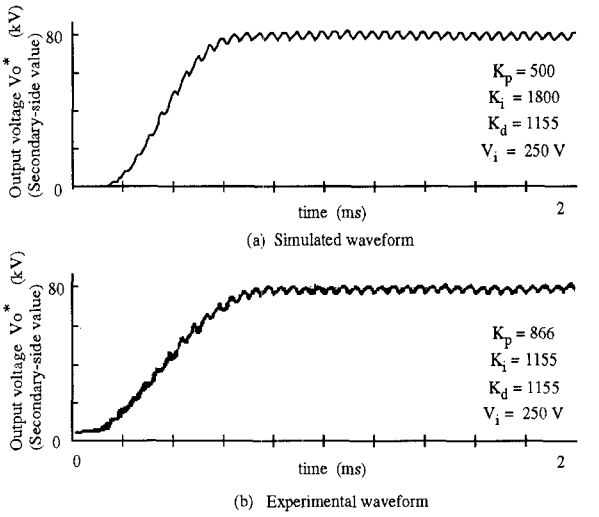

Fig. 11 Simulated and experimental output voltage waveforms with the closed loop shown in the Fig. 5. (R_L=1.04, Vo*=80kV, 25kW)

gram and transfered to the memory of target equipment . This DC-DC converter in the Fig. 1 has nonlinear steady-state characteristics between the output voltage and the phase shift angle ϕ as a control variable. Therefore, the steady-state characteristics is linearized by introducing the arc-cosine function compensation scheme.

The input DC voltage V_i cannot be practically regarded as a constant voltage source because it consists of diode or thyristors. The input voltage has voltage ripple caused by AC input line frequency and the voltage fluctuation due to abrupt changes and periodic disturbances. A feedforward compensation using the inverter input voltage is introduced in Fig. 3 so that the fluctuation of the input voltage may not effect the output high-voltage .

3. COMPUTER & NETWORK SYSTEM AND DESIGN OF SIMULATION PROGRAM

3-1 Computer and Network System

Fig. 4 displays computer and network system to develop digitally-controlled switch mode power converters. A high-speed server is dedicated to numerical computation, various workstations, several distributed personal computers, microcomputer development tools and printers are interconnected with Ethernet. Documentation, programing and debugging for both the circuit simulation program and transfer for control algorithm of the simulation program to target equipment are performed on the computer network system.

3-2 Design of simulation program

Fig. 5 illustrates the main concept of the circuit simulation. The procedure consists of a preprocessor, a solver and a post-processor. **R**, **E**, **I**, $\mathbf{K_x}$, $\mathbf{K_u}$ of the circuit equation are manually defined according to the time-varying resistance model of the active and passive switches. Then the control algorithm and the switching conditions for the switches and the diodes are represented in C-language source code.

Fig. 6 shows an object model of the circuit simulation program. The object-oriented modeling technique is introduced into the programing design in order to easily modify and apply the simulation program for the other power conversion circuits. The transform algorithm of the sate equation, the solver based on Runge-Kutta

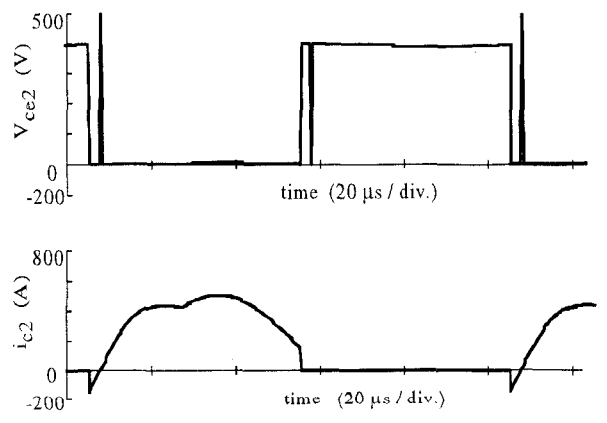

(a) Simulated waveforms

Fig. 9 Simulated waveforms. (Voltage and current waveforms of switch S_{w2}, V_i=400V, R_L=0.78W, output power is 80kW)

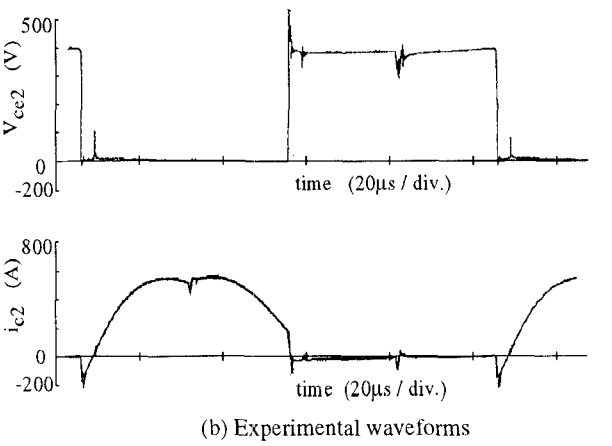

(b) Experimental waveforms

Fig. 10 Experimental waveforms. (Voltage and current waveforms of switch S_{w2}, V_i=400V, R_L=0.78W, output power is 80kW)

method and the post-processor can be generally applied for various power electronic circuits. In the Fig. 6, Type of the object is presented by a box which has three regions. from top to bottom: class name, list of attributes (data structure), and list of operations (behavior.)

Fig. 7 indicates the flowchart of the circuit simulation program . In the first place, the voltage vector **E** is calculated from $\mathbf{K_x}$, $\mathbf{K_u}$, **x**(t) and **u**(t). In the second place, the current vector **I** is estimated from **E** and $\mathbf{R}^{-1}$. The switch and diode model resistances R_{sk} and R_{Dm} (where k=1 to 4, m=5 to 8) are decided from **I** and time *t* with "if.. then..." style switching program. If any one of R_{sk} or R_{Dm} is/are changed, **R**, $\mathbf{R}^{-1}$ and **R*** are computed. Moreover, **A** from $\mathbf{K_x}$ and **L***, and **B** from $\mathbf{K_u}$ and **L*** are estimated. The state variable $\mathbf{x}(t+\Delta t)$ is caluculated by numerical integration, Runge-Kutta method.

For effective numerical computation, $\mathbf{R}^{-1}$, **A** and **B** may be calculated beforehand for all the operating modes in order to avoid wasteful repeat. 2^n sets of $\mathbf{R}^{-1}$, **A** and **B** ought to be prepared for the *nth* time-varying resistance models. In case that all the operating modes may not be realized in the circuit operation, the calculations for non-existent modes can be neglect.

4. SIMULATED RESULTS AND EXPERIMENTAL VERIFICATION

4-1 Simulated and Experimental Waveforms

The simulation waveforms obtained by the proposed simulation technique are basically the same as waveforms obtained from SPICE .

Fig. 8 presents the simulated current waveform i_{cs} of the series resonant capacitor C_s and the phase shift angle ϕ of the inverter-fed power generator operating under the control scheme shown in Fig.3. The sampling frequency of the digital feedback control using DSP is 10kHz which is inverter switching frequency. The control parameters are indicated in the Fig. 8.

Fig. 9 shows the simulated voltage waveform V_{ce2} and the current waveform i_{s2} of the switch S_{w2}. The output voltage is 100kV; the output current is 800mA and the output power is 80kW.

Fig. 10 illustrates the experimentally measured V_{ce2} and i_{s2} waveforms. Comparing simulated results with experimental we find that the simulated V_{ce2} rises rapidly when the antiparallel diode turns off because snubbers of the switches are not used in the simulation.

Fig. 11 shows the rising output high-voltage waveform. The experimental voltage waveform rises slightly slower than the simulated one. If the integral gain is large than the value shown in Fig. 10, rapid transient response is obtained, however, the tube voltage overshoot occurs because of approximation of the voltage versus the current characteristics of the load are represented as a linear resistance [11].

4-2 Application to the other circuits

39 functions out of 58 C-Language functions (67%), can be applied to other circuits without any modification. Only Switching conditions, control algorithm and input/output procedure are programmed for each circuit. About half of the functions which need some modifications consist of simple statements instead of complex logic descriptions.

Simulation algorithm is programed with conventional modular programing technique in practice, for example, a matrix size is defined as a global variable or specified as an argument (input parameter) for all functions of matrix calculations. In both cases, the parameter having matrix size influences upon operations of whole program.

5 CONCLUSIONS

A a simulation technique of the power electronic conversion circuits and systems has been presented, in which the control algorithm described and tested in a simulation computer program can be embedded easily. This technique is based on a circuit equation modeled by time-varying resistance models depicting active switches and the diodes, a sate equation for the inductors and the capacitors, and an algebraic method to transform the matrices of the circuit equation into the matrices of the state equation. In this technique,less number of numerical calculations are performed because calculation is repeated for only one state equation. Moreover, computer and network system has been discussed from a viewpoint to combine simulation and development of digitally-controlled switch-mode power converters together has been presented that . Finally, the experimental results for application to the power generator using high-frequency resonant inverter with high-voltage transformer link have been presented in order to verify the simulation results.

REFERENCES

[1] G. D. Hachtel, R. K. Brayton, F. G. Gustavson : "The sparse tableau approach to network analysis and design," IEEE Transactions on Circuit Theory Vol.ct-18, No.1, pp.101-13, Jan. 1971.

[2] Y. Kuroe, H, Haneda and T. Maruhashi :"An efficient digital simulation program NETCAP-IM for power-electronic induction motor drive systems by means of decomposed tableau approach," Proc. of IEEE International Symposium on Circuits and Systems Part II, pp.704-707, Apr. 1980.

[3] J. Burdio and A. Martinez : "A unified discrete-time state-space model for switching converters," IEEE Trans. on Power Electronics, Vol. 10, No. 6, pp.694-707, Nov. 1995.

[4] K. Kundert, J. White and A. Songinovanni-Vincentelli : "An envelop-following method for the efficient transient simulation on switching power and filter circuit," Proc. IEEE-Int. Conf. on Computer-Aided Design, pp.446-449, Nov. 1988.

[5] H. Takano, H. Uemura, M. Nakaoka : "Advanced constant-frequency PWM resonant DC-DC converter with real time digital control for X-ray power generator," Proceedings of EPE, Vol.1, pp.544-549, Sep. 1991.

[6] H. Takano, T. Hatakeyama, T. Shimizu, J. M. Sun and M. Nakaoka : "32-bit RISC Processor based digital control of high power resonant DC-DC converter for medical-use X-ray high-voltage applications," Proceedings of PEMC, Vol.1, pp.310-316, Sep. 1996.

A study on power factor and efficiency correction of AC-DC boost converter by partial resonant type using a L^2SC

Hyun-Woo Lee, Ki-Young Suh, Young-Chul Kim, Jung-Ham Chun
Kyung-Nam University
449, Wolyung-Dong, Masan, 631-701, KOREA
Fax: +82-551-48-2228, E-mail: lhwoo@hanma.kyungnam.ac.kr

Katsunori Taniguchi
Osaka Institute of Technology
5-16-1 Omiya, Asahi-ku, Osaka, 535, JAPAN
Fax: +81-6-957-2133

Abstract - **In this paper, the authors propose a new AC-DC converter of high power factor and high efficiency by partial resonant method. The input current waveform in proposed circuit is got to be a discontinuous sinusoidal form in proportion to magnitude of ac input voltage under the constant duty cycle switching. Thereupon, the input power factor is nearly unity and the control circuit is simple. Also the switching devices in a proposed circuit are operated with soft switching by the partial resonant method. The result is that the switching loss is very low and the efficiency of system is high. The partial resonant circuit makes use of a inductor using step up and L^2SC (Loss-Less Snubber Condenser). The switching control technique of the converter is simplified for switches to drive in constant duty cycle.**

Some simulative results on computer and experimental results are included to confirm the validity of the analytical results.

I .INTRODUCTION

The efficiency correction of AC-DC converters for high power applications has undergone great development during recent years.

It is serious that an input current drawn by the phase controller or diode rectifiers creates a number of problems for the power distribution network and for other electrical systems. To improve input current waveform and to control the power factor of it unity at the same time, it is proposed to use an active converter, which includes step-up chopper or up-down chopper for the rectifier ciruit.

There are two control modes for the chopper of this usage. One is contin- uous current mode and another is discontinuous it.

In continuous conduction mode (CCM), input ac voltage and current are detected and input current is formed to be sinusoidal waveform by using pulse width modulation (PWM). The control circuit for this mode is complic- ated one.

In discontinuous conduction mode (DCM), the input ac current is nearly sinusodal waveform with the constant duty cycle switching. The control circuit for the discontinuous mode is simple. A discontinuous mode converter is constructed by a single-phase diode rectifier, a boost switch, one inductor and a single-phase line filter as shown in Fig.1.

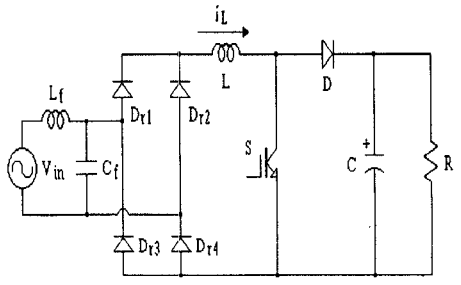

Fig. 1 AC-DC boost converter of high power factor

The boost switch, S, is turned on at constant frequency. The duty cycle of S is varied for

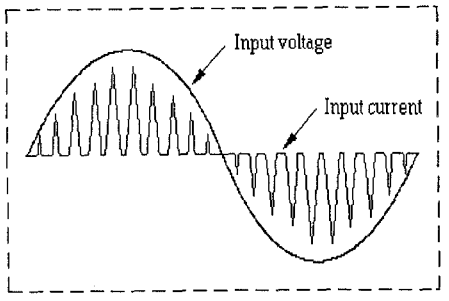

Fig. 2 Waveform of input ac current with DCM

load variation only and it is such that the input current is always discontinuous. During the "on" period of of the boost switch, the input ac phase becomes shorted through the inductor and the conducted diodes. The input current is linearly increasd until the switch is turned off. Also, if the boost switch is turned off at any point of time, the input current is decreased to zero. Consequently, the input current has a sinusoidal pulse row in propo- rtion to magnitude of the instantaneous value of the input single-phase voltage source.

Since the current pulse always begins at zero, it means that the average value also varies sinusoidally. The input voltage and line current waveforms without filtering are shown in Fig. 2.

It results in improving input ac current waveform distortion and input power factor. The discontinuous mode converter eliminates the complicated circuit control requirement, reduces the number of components, and reduces the filter reactive components size.

On the other hand, in this discontinuous mode converter, turn-on of the switching device is a zero current switching. But the device must be switched off at a maximum inductor current and a certain level of voltage in one cycle of the carrier frequency, that is, hard switching operation.

It causes the large current stress of the switching device and electromagn- etic interference (EMI). Being increased switching frequency, the discontinuous mode converter has the disadvantage of increasing the switching power losses and the switching stresses of the switching devices in comparison with the conventional continuous mode converter.

Generally, the power conversion system must be increased switching frequency in order to achieve a small size, a light weight and a low noise.

However the switches of converter are subjected to high switching power losses and switching stresses.

As a result of those, the power system bring on a low efficiency. To improved these, a large number of soft switching topologies, that is, zero current switching(ZCS) and zero voltage switching(ZVS) included a resonant circuit have been proposed. But these circuits increase the number of switch in circuit, complicate sequence of switching operation and increase stresses of components in the resonant circuit.

Therefore authors propose that a new AC-DC converter of high power factor and high efficiency by a partial resonant type using a L^2SC.

II. CIRCUIT CONFIGURATION

Figure 3 shows a new AC-DC converter of high power factor and high efficiency by partial resonant type using a loss-less snubber condenser.

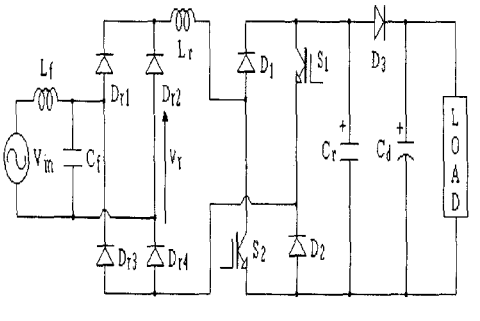

Fig. 3 AC-DC boost converter of high power factor and high efficiency by partial resonant type using a loss-less snubber condenser

The proposed circuit adds the controlling devices and a loss-less snubber condenser in the

conventional boost converter shown in Fig. 1.

The partial resonant circuit makes use of a inductor using step up and a condenser of loss-less snubber. The partial resonant operation makes zero voltage switching for turn-off of the control switches with the discontinuous mode. The current flowing through the inductor L_r is controlled to be discontinuous, and then turn-on operation of swiching device S_1 and S_2 becomes to be ZCS.

It results in not only decreasing switching power losses in the devices drastically, but also improving input ac current waveform distortion and power factor. Also the circuit has a merit which is taken to increase of efficiency and to improve of harmonics distortion factor, as it makes to a regeneration at input source of accumulated energy in snubber condenser without loss of snubber circuit.

Ⅲ. OPERATING PRINCIPLES

If the inductor of the output side is bigger than the inductor using resonant, the load side can consider with a constant current source during one cycle of the carrier frequency. Fig. 4 shows equivalent circuits for operation of switc- hing modes in one cycle.

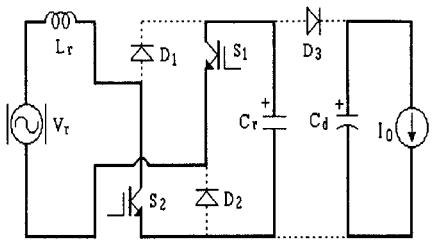

Fig. 4 (a) Mode 1

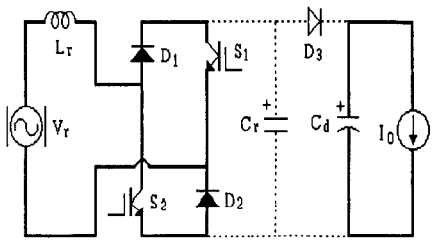

Fig. 4 (b) Mode 2

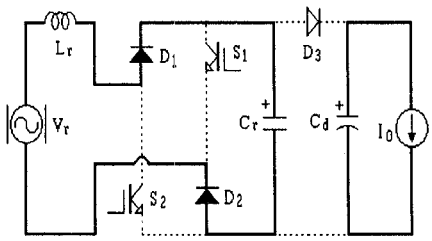

Fig. 4 (c) Mode 3

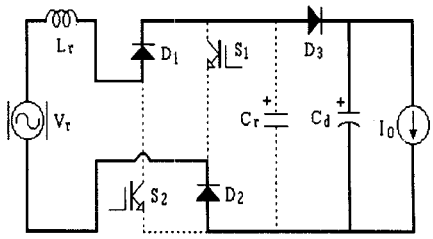

Fig. 4 (d) Mode 4

Fig. 4 Equivalent circuits of switching modes in one cycle

At initial condition, the current flowing through the inductor L_r is zero.

Switch S_1 and S_2 are off-state and condenser C_r is charged at the same voltage of dc output voltage V_{cd}. Also the AC input voltage v_{in} and output voltage of full bridge rectifier v_r is expressed as like eq. (1) and eq. (2).

$$v_{in} = V_m \sin \omega_s t \qquad (1)$$

$$v_r = | v_{in} | = | V_m \sin \omega_s t | \qquad (2)$$

MODE 1 : T_1, $t_0 \leq t < t_1$

Mode 1 begins by turning on both S_1 and S_2 at the same time. The output voltage of rectifier v_r and the voltage of condenser V_{cr} are added and applied to the inductor L_r. Then this mode takes form of a series LC resonance circuit. The condenser C_r discharges its electric charge through the inductor L_r. Turn-on of the switching device occurs in zero current state. Hence this is ZCS.

The condenser voltage v_{cr} is expressed in eq.

(3) and the current flowing inductor i_{Lr} increases as like eq. (4).

$$v_{cr} = (v_r + V_{cd}) \cos \omega_r t - v_r \quad (3)$$

$$i_{Lr} = \frac{v_r + V_{cd}}{X} \sin \omega_r t \quad (4)$$

here, $\omega_r = \frac{1}{\sqrt{L_r C_r}}$, $X = \sqrt{\frac{L_r}{C_r}}$

This mode ends when v_{cr}=0. Time duration of this mode T_1 is evaluated as follows

$$T_1 = \sqrt{L_r C_r} \cos^{-1}\left(\frac{v_r}{v_r + V_{cd}}\right) \quad (5)$$

and the inductor current I_1 at the end of the mode is given by

$$I_1 = \frac{1}{X}\sqrt{v_{cr}^2 + 2 v_r V_{cd}} \quad (6)$$

MODE 2 : T_2, $t_1 \leq t < t_2$

Mode 2 begins when the voltage of across C_r achieves zero. Then diodes D_1 and D_2 start conduction. The inductor current is divided into two paths of S_1-D_2 and S_2-D_1. The inductor current is linearly increased while the switches are turned off as follows

$$i_{Lr} = \frac{v_r}{L_r} t + I_1 \quad (7)$$

This mode ends when both switch S_1 and S_2 are turned off. Using the time duration of on-state of S_1 and S_2, T_{on}, time duration of this mode T_2 can be obtain as follows

$$T_2 = T_{on} - T_1 \quad (8)$$

and the inductor current I_2 at the end of the mode is given by

$$I_2 = \frac{v_r}{L_r} T_2 + I_1 \quad (9)$$

In Mode 1 and Mode 2, ac input current increase and inductor L_r stores the energy.

MODE 3 : T_3, $t_2 \leq t < t_3$

Mode 3 begins by turning off both S_1 and S_2 at the same time. The ac current flowing through L_r takes a route of D_1-C_r-D_2 and charges C_r.

Then this mode takes form of a series LC resonance circuit. Turn-off of S_1 and S_2 occurs in ZVS, because the voltage of C_r is zero voltage.

In this mode, the voltage of C_r and the current of L_r are evaluated as follows

$$v_{cr} = v_r + \sqrt{\frac{L_r}{C_r}} I_a \sin(\omega_r t + \theta) \quad (10)$$

$$i_{Lr} = I_a \cos(\omega_r t + \theta) \quad (11)$$

here,

$$I_a = \sqrt{\frac{C_r}{L_r} v_r^2 + I_2^2}$$

$$\theta = \sin^{-1}\left(-\frac{v_r}{\sqrt{v_r^2 + \frac{L_r}{C_r} I_2^2}}\right)$$

v_{cr}=V_{cd} is achieved and the diode D_3 begins to conduct, then this mode ends. Time duration of this mode T_3 is expressed as follows

$$T_3 = \sqrt{L_r C_r}\left\{\sin^{-1}\left(\frac{V_{cd} - v_r}{\sqrt{v_r^2 + \frac{L_r}{C_r} I_2^2}} - \theta\right)\right\} \quad (12)$$

and the inductor current I_3 at the end of the mode is given by

$$I_3 = I_2 \cos \omega_r T_3 + \sqrt{\frac{C_r}{L_r}} v_r \sin \omega_r T_3 \quad (13)$$

MODE 4 : T_4, $t_3 \leq t < t_4$

Mode 4 begins when the voltage of across C_r achieves output voltage V_{cd}.

The inductor current flowing through L_r flows into the load. Since output dc voltage is higher than input dc voltage, the inductor current is decreased and achieves to zero at the end of mode 4. When the diode D_3 begins to conduct, the inductor current is decreased linearly as

following to the next equation.

$$i_{Lr} = \frac{v_r - V_{cd}}{L_r} t + I_3 \qquad (14)$$

This mode ends when i_{Lr}=0. Time duration of this mode T_4 is expressed as follows

$$T_4 = \frac{L_r}{V_{cd} - v_r} I_3 \qquad (15)$$

Ⅳ. SIMULATION OF PROPOSED CIRCUIT

The simulated waveforms on computer for the proposed converter are shown in Fig. 5. The diodes are ideal and the switches are replaced by the equivalent circuits consisting of a variable resistance and an ideal diode.

voltages and the load current in the simulated circuit. At Fig. 5, the inductor current i_{Lr} has a sinusoidal pulse row in proportion to magnitude of the instantaneous value of the input single-phase voltage source with half period of input source.

Fig. 6 shows waveforms of each part in one cycle switching in order to certify partial resonant operation and soft switching operation of control devices.

In Fig. 6, the controlled switches are turned on at t_0 and C_r begins to discharge. v_{cr} achieves to zero at t_1. At t_2, the controlled switches are turned off and C_r is charged with i_{Lr} and achieves to V_{cd} at t_3. At t_4, i_{Lr} achieves to zero

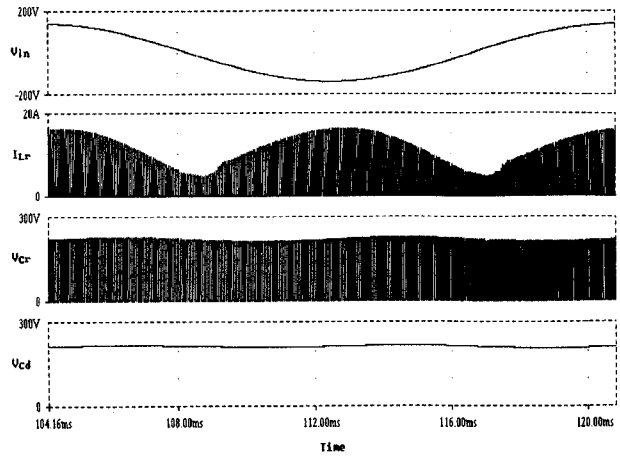

Fig. 5 Simulation waveforms of each part

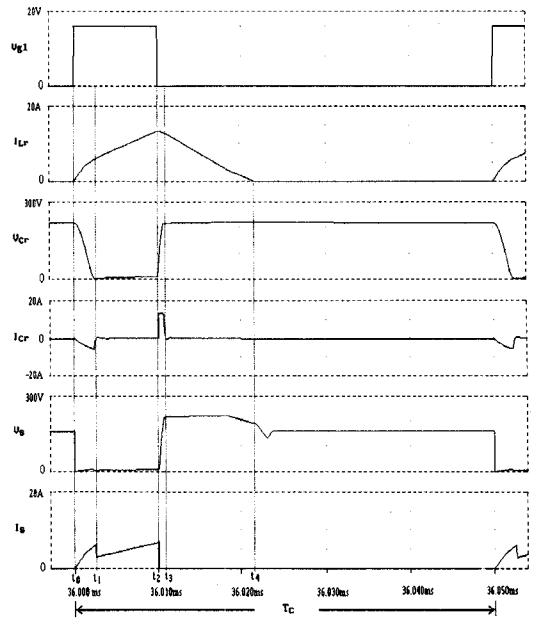

Fig. 6 Simulated waveforms of each part in one cycle switching

and the controlled switches are kept off till the next cycle. T_s is one period of one cycle of switching operation and it is required that (t_4-t_0) is smaller than T_s to keep discontinuous mode of the current. As the current flowing switches is zero at t_0, the controlled switches are turned on with ZCS. Also, as the voltage being across switches is zero at t_2, the switches are turned off with ZVS.

The simulated results are confirmed the validity of the analytical results for each mode as previously stated.

Voltage-current locus (V-I locus) of the controlled switching devices in the conventional hard switching circuit is shown in Fig. 7(a). V-I locus of the proposed soft switching circuit is shown in Fig. 7(b). For the hard switching circuit, V-I characteristic of the controlled switching devices has a large area.

The area surrounded by the switching loci is proportional to switching loss of the device. For the proposed soft switching circuit, V-I characteristics of these have only a small area. It shows that ZCS and ZVS are achieved at switching of the devices, and drastic reduction of the switching loss of the devices are also achieved.

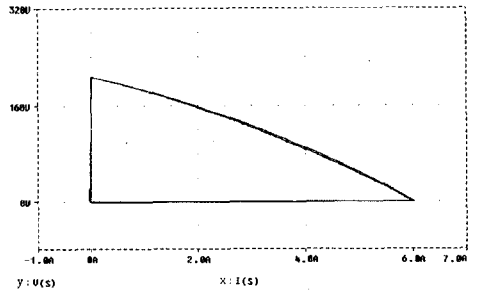

(a) Switching locus of of hard-switching

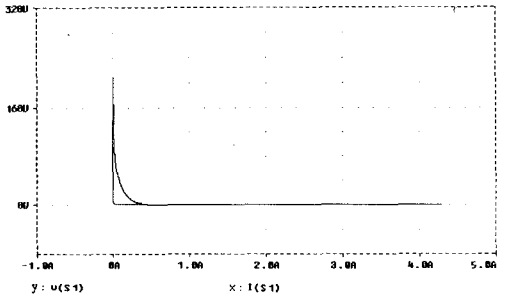

(b) Switching locus of soft-switching

Fig. 7 Switching locus of control device

Fig. 8 show waveform and frequency spectrum of input current and voltage for conventional boost converter shown in Fig. 1.

Fig. 9 show waveform and frequency spectrum of input current and voltage for proposed boost converter shown in Fig. 3.

The waveform of the current of conventional boost converter is smaller than it of proposed boost converter around the zero cross point. Hence the current has quite a little of the third harmonic componant.

It is electrical charge of the snubber condenser C_r to work to increment the amplitude of the current around the zero cross point. The outcome is that the current is more similar to a sinusoidal waveform.

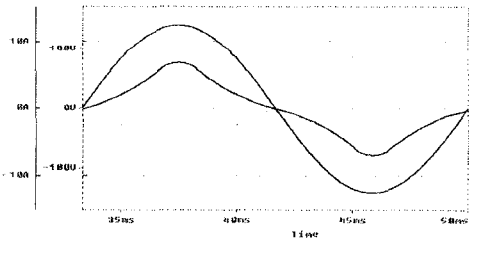

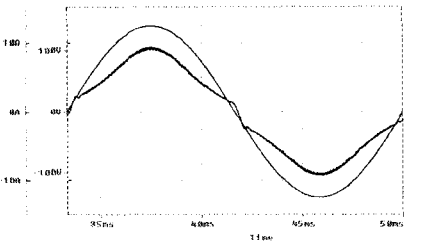

(a) Waveforms of input voltage and current

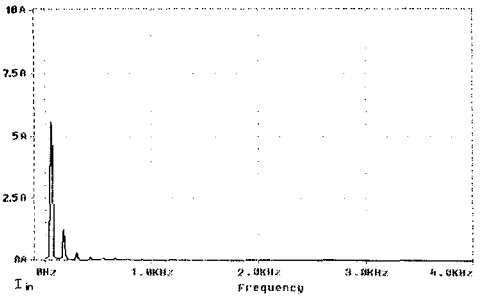

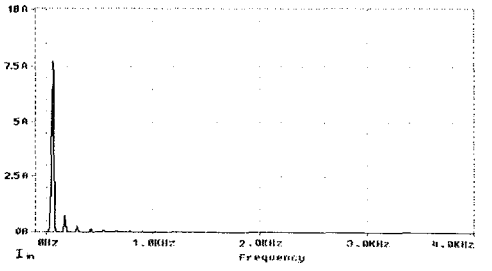

(b) Frequency spectrum of input current

Fig.8 Waveforms and frequency spectrum in Fig.1
Fig.9 Waveforms and frequency spectrum in Fig.3

V. EXPERIMENTAL RESULTS

In order to confirm the feasibility, the propoposed converter of Fig. 3 is experimented with power capacitor of 0.5kW. The experimental circuit is regulated at 200V output with AC 100V input.

In order to analyze the input current, Fig. 11 show waveform and frequency spectrum of input voltage, current through input low pass filter with duty cycle 20[%]. Waveform and frequency spectrum of input voltage, current with duty cycle 20[%], 30[%] is shown in Fig. 12, Fig. 13 respectively.The fundamental component of input current is on the increase following increment of

duty cycle.

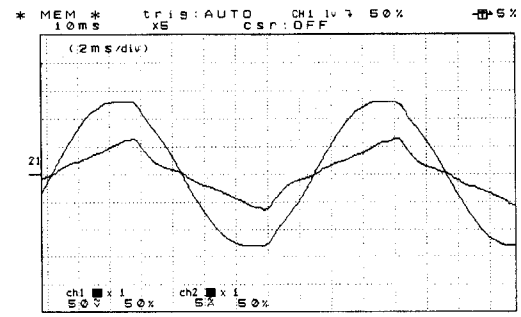

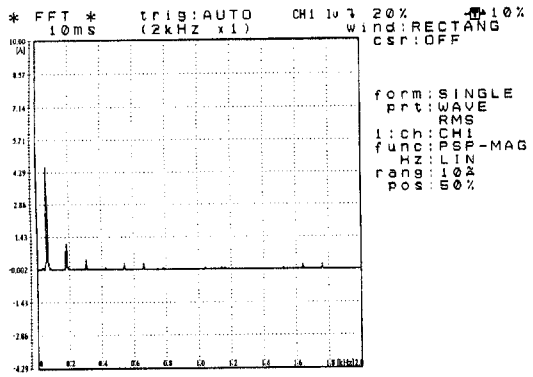

(a) Waveforms of input voltage and current
(b) Frequency spectrum of input current

Fig.10 Input voltage, current andfrequency spectrum (D_c=20[%])

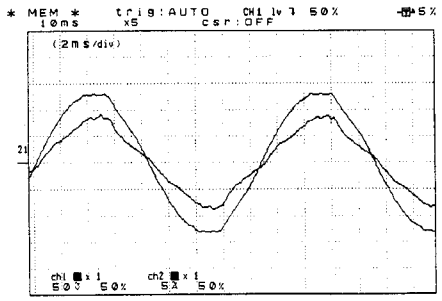

(a) Waveforms of input voltage and current

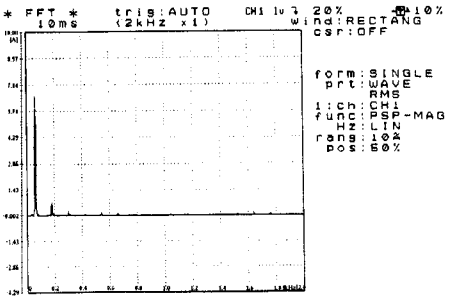

(b)Frequency spectrum of input current

Fig. 11 Input voltage, current and frequency spectrum (D_c=30[%])

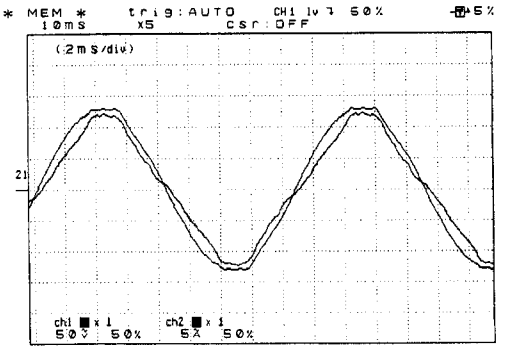

(a) Waveforms of input voltage and current

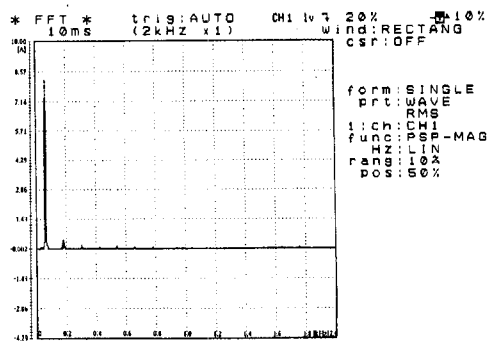

(b) Frequency spectrum of input current

Fig.12 Input voltage, current and frequency spectrum (D_c=40[%])

Fig. 13 shows the relation between power factor PF and duty cycle D_c.

The proposed soft-switched converter maintains high power factor in wide operational range.

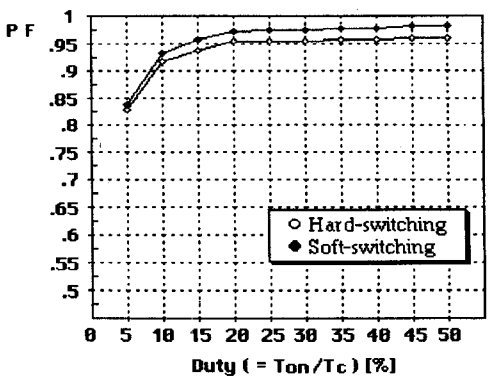

Fig. 13 Relationship between input power factor and duty cycle

Fig. 14 shows the relation between the efficiency and output power.

The efficiency of the soft-switching is increased more than that of the conventional hard

switching.

Here, to make the same power, the duty cycle of soft switching operation is smaller than that of hard switching operation, because it makes to a regeneration at input source of accumulated energy in snubber condenser.

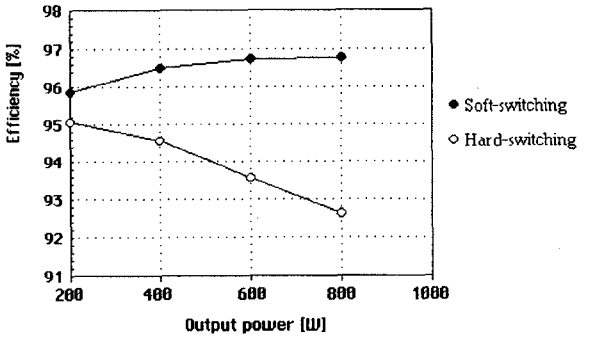

Fig.14 Efficiency comparison of proposed softswitching converter and conventional hard switching converter

VI. CONCLUSIONS

A novel soft switching AC-DC converter of high power factor and high efficiency has been presented in this paper.

To achieve ZVS and ZCS, the proposed circuit is applied a partial resonant technique which is used a inductor of step up and a condenser of loss-less snubber. The result is that switching loss is very low and efficiency of system is high. The switching control technique of the converter is simplified for switches to drive in constant duty cycle.

Also its input current is got to be discontinuous sinusoidal form in proportion to magnitude of ac input voltage under the constant duty cycle switching. Thereupon, the input power factor is nearly unity.

The circuit have a merit which is taken to increase of efficiency and to reduce of the harmonics of input current, as it makes to a regeneration at input source of accumulated energy in snubber condenser without loss of snubber in conventional circuit.

Acknowledgments : The authors would like to appreciate the Korea Electric Power Corporation which supported fund for this project No.96-03.

REFERENCES

[1] B.K. Bose, J.S. Lai, "An Improved Resonant DC Link Inverter for Induction Motor Drives", Conf. Rec. of IEEE/IAS Annu Meeting, pp. 742-748, 1988

[2] R.Keller, G.Baker, "Unity power factor off line switching power supplies", in IEEE INTELEC Record, pp. 332-339, 1984

[3] D.K. Kwak, H.W. Lee, "Single-Phase converter with partial resonant circuit", KIEE Autumn Conf. Rec, pp.129-131, 1993

[4] D.K.Kwak, K.Y.Suh, S.K.Kwon, H.W.Lee, "Novel soft-switching DC-DC converter of high efficiency", International Conference on Power Electronics, '95Proceeding, pp.730-735, 1995

[5] K.Nishiyama, T.Yoshikawa, K.Taniguchi, "A Soft-Switching PWM Converter with High Power Factor ", The 1993 Kansai-section IEE in Japan 93-40, 1993

[6] D.K. Kwak, H.W. Lee, "Partial resonant PWM converter using snubber condenser ", KIEE Spring the West & Kyungnam Local. Conf. Rec, pp. 58-61, 1994

[7] D.K. Kwak, H.W. Lee, etal, "A high Efficiency DC-DC Boost Converter by Partial Resonant Switching Mode", KIEE, Vol. 45, No. 9, pp. 1272-1278, 1996

Analysis and Improvement of Input Current waveforms for Discontinuous-Mode Boost Converter with Unity Power Factor

Katsunori **Taniguchi**, Member, Yukio **Nakaya**, Student Member

OSAKA INSTITUTE OF TECHNOLOGY
DEPARTMENT OF ELECTRICAL ENGINEERING
5-16-1 OMIYA, ASAHI-KU
OSAKA 535 **JAPAN**
FAX 81-6-957-213
TEL 81-6-954-4231
E-mail:taniguchi@ee.oit.ac.jp

Abstract— A boost converter is widely used for power factor correction (PFC). The discontinuous mode (DCM) converter eliminates the complicated circuit control requirement, reduces the number of components, and reduces the filter reactive components size. Analysis of an input current waveform of the DCM boost converter is described in this paper. The components included in the input current waveform are fundamental plus third harmonics and another components can be neglected. Improving method of input current waveform is also proposed.

I. INTRODUCTION

A PWM power factor correction (PFC) techniques have received great attention in recent years. In most cases, PWM PFC converters are constructed by a diode rectifier and an active power circuit such as a boost or a buck-boost chopper[1-3].

A continuous conduction mode (CCM) PWM rectifier achieves an unity power factor rectification and its continuous input current. However, the system requires complicated structure and its circuit control. A discontinuous conduction mode (DCM) converter eliminates the complicated circuit control requirement, reduces the number of components, and reduces the filter reactive components size. Boost type converters with discontinuous current are especially suitable for medium power levels.

Fig. 1 shows a conventional boost PWM converter for power factor correction. The rectifier input voltage and current waveforms for DCM operation are shown in Fig. 2. The boost switch, T_r is turned on at constant frequency. The duty cycle of T_r is varied for load variation only and it is such that the input current is always discontinuous. During the "on" period of the boost switch, the input ac source is shorted through

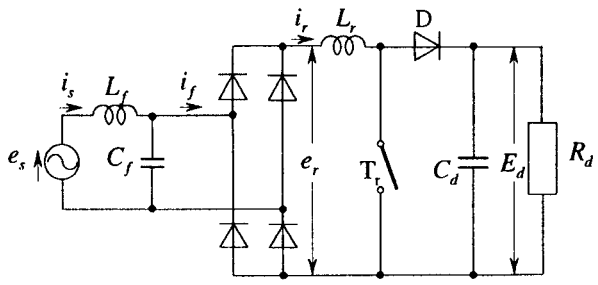

Fig. 1 Single phase boost DCM converter with unity power factor.

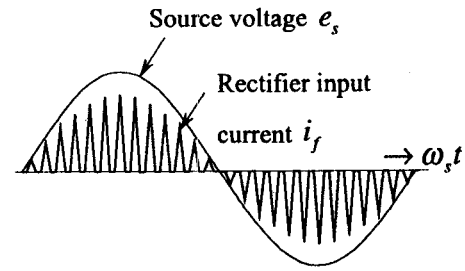

Fig. 2 Rectifier input voltage and current waveforms.

the inductor, the bridge diodes, and the boost switch. Consequently, the input current begin simultaneously to increase at a rate proportional to the instantaneous value of the ac input voltage. Since the current pulses always begin at zero, it means that the average value also vary sinusoidally. However, in the constant-switching-frequency control, the decay time of the inductor current varies the magnitude of the input voltage. The variation of the decay time with the input voltage results in a certain distortion in the input current. The distortion in the input current increases with the low ratio of output voltage to input voltage. On the other hand, the high ratio of output voltage to input voltage occurs the cost up of the converter due to require the high voltage devices. To suppress low order harmonics included in the input current waveform, constant-switching-frequency ac-dc converter using second-harmonic-Injected PWM is reported in [4].

In this paper, conventional constant-switching-frequency DCM converter is analyzed by using the double Fourier series expansion. From the theoretical analysis, the paper proposes a theoretical and fundamental method removing the distortion of the input current waveform even if the ratio of output voltage to input voltage is very low.

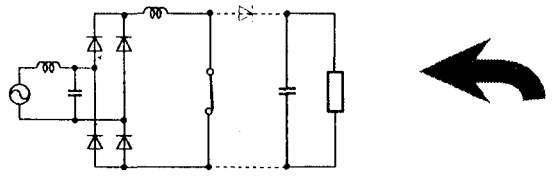

Mode 1 ($t_0 \le t \le t_1$):T_r on ~T_r off

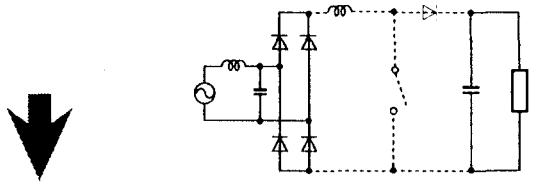

Mode 3 ($t_2 \le t \le t_0$):D off ~ T_r on

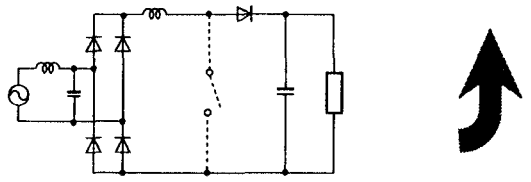

Mode 2 ($t_1 \le t \le t_2$):T_r off, Don ~ D off

Fig.3 Operational modes in conventional boost DCM converte.

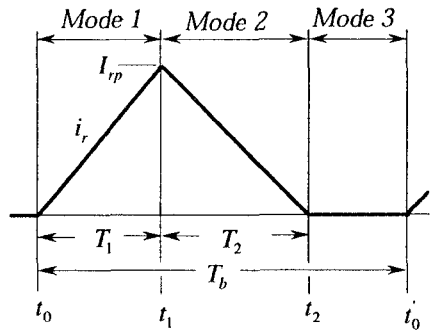

Fig. 4 Inductor current waveforms.

II. OPERATIONAL MODE OF BOOST DCM CONVERTER

The operational modes in the conventional boost DCM converter are illustrated in Fig. 3. As shown in Fig. 3, three operational modes exist within one switching cycle of the converter. Fig. 4 shows an inductor current waveform for one switching cycle. The commutating operation starts at time t_0 when the switch, T_r, is turned on .

Mode 1 ($t_0 \le t \le t_1$):T_r on ~T_r off

After the switch, T_r, is turned on at the time t_0, an inductor L_r is applied the rectified input voltage directly and the inductor current i_r is obtained as

$$i_r = \frac{e_r}{\omega_b L_r}\omega_b t \tag{1}$$

where $\omega_b = 2\pi f_b$, $f_b = 1/T_b$;Switching frequency

The duration of this mode can be controlled by the drive circuit of T_r. T_r is turned off at the end of this mode. The interval of this mode, T_1, is the on-state of the system. A current I_{rp} of T_r at the end of this mode is given by

$$I_{rp} = \frac{e_r}{\omega_b L_r}\omega_b T_2 \tag{2}$$

A duty factor d_F of T_r is

$$d_F = \frac{T_1}{T_b} \tag{3}$$

Mode 2 ($t_1 \le t \le t_2$):T_r off, Don ~ D off

When the T_r is turned off, a diode D starts the conducting. The current i_r through diode D flows into a load. The current i_r decreases linearly as follows;

$$i_r = I_{rp} - \frac{E_d - e_r}{\omega_b L_r}\omega_b t \tag{4}$$

where E_d is the dc output voltage.

The current i_r becomes zero at the time t_2. The duration of the mode, T_2, is obtained from the condition of $i_r(T_2) = 0$;

$$T_2 = \frac{e_r}{E_d - e_r} T_1 \tag{5}$$

Mode 3 ($t_2 \le t \le t_0$):D off ~ T_r on

The T_r, D and L_r are zero current. When main switch, T_r, is turned on at zero current condition, another switching cycle starts.

III. ANALYSIS OF INPUT CURRENT WAVEFORMS

The boost converter shown in Fig. 1 achieves high power factor easily under the condition of constant duty factor and DCM operation. When ac input source voltage e_s is expressed by

$$e_s = E_s \sin \omega_s t \tag{6}$$

Since the ratio of an ac input source frequency and a switching frequency of the converter is generally incommensurable, the PWM input current waveform becomes a nonperiodic function. The harmonic analysis of such a waveform can be carried out by using the double Fourier series[5,6]. The rectifier input current waveform i_f is given by

$$i_f = \sum_{m=0}^{\pm\infty}\sum_{n=0}^{\pm\infty} K_{mn} e^{j(mx+ny)} \tag{7}$$

$$K_{mn} = \frac{1}{(2\pi)^2}\int_0^{2\pi}\int_0^{2\pi} i_r(x,y) e^{-j(mx+ny)} dxdy \tag{8}$$

where $i_r(x,y)$ is an inductor current , ω_b is a switching angular frequency, $x = \omega_b t$, $y = \omega_s t$, m= 0,1,2,..., and n= 0,1,2,...

As a result, the frequency components included in the PWM output waveform are a fundamental component higher-order harmonics, and the sidebands of a carrier frequency. If the frequency ratio becomes large, the sidebands move into the high-frequency region apart from the fundamental frequency. Therefore the sidebands can be removed by the input filter easily. The input current waveform without sidebands is given by

$$i_s = \sum_{n=0}^{\pm\infty} K_{0n} e^{jny} \tag{9}$$

$$K_{0n} = \frac{1}{2\pi}\int_0^{2\pi}\left\{\frac{1}{2\pi}\int_0^{2\pi} i_r(x,y)dx\right\}e^{-jny}dy \tag{10}$$

$$= \frac{1}{2\pi}\int_0^{2\pi}\left\{\bar{I}_r(y)\right\}e^{-jny}dy \tag{11}$$

where $\bar{I}_r(y) = \frac{1}{2\pi}\int_0^{2\pi} i_r(x,y)dx$ (12)

where $\bar{I}_r$ is the mean value of the inductor current i_r. Eq. (11) indicates that the fundamental component and higher-order harmonics included in the input current waveform are obtained by the Fourier series expansion of the mean value of the inductor current i_r.

To obtain the mean value of the inductor current i_r, the area of the triangular waveform shown in Fig. 4 can be easily obtained as

$$\bar{I}_r(\omega_s t) = \frac{1}{T_b} \times \frac{I_{rp}(T_1 + T_2)}{2} \tag{13}$$

$$= A \times \frac{e_r}{E_d - e_r} \tag{14}$$

$$= A \times \frac{\sin \omega_s t}{\alpha - \sin \omega_s t} \tag{15}$$

where $A = \frac{\pi \alpha E_s d_F^2}{\omega_b L_r}$ (16)

$$\alpha = E_d / E_s \tag{17}$$

A fairly good approximation of (15) is given by

$$\bar{I}_r(\omega_s t) \approx A \times \frac{\alpha \sin \omega_s t - \sin^3 \omega_s t}{\alpha^2 - 1} \qquad (18)$$

Calculating $\bar{I}_r$ of (18) by Fourier expansion, a fundamental component and higher order harmonics are obtained as

$$i_s(\omega_s t) = \frac{2\alpha^2}{R_d} E_s \sin \omega_s t - \frac{2\alpha^2}{(4\alpha+3)R_d} E_s \sin 3\omega_s t \qquad (19)$$

Therefore, the components included in the input current waveform are fundamental plus third harmonics and another components can be neglected.

From (19), a total harmonic distortion (*THD*) of the input current waveform is

$$THD = \frac{100}{4\alpha+3} \ [\%] \qquad (20)$$

From a condition of ac input power equal to dc output power, a duty factor d_F is obtained as

$$d_F = \sqrt{\frac{8\omega_b L_r}{\pi R_d} \times \frac{\alpha(\alpha^2-1)}{4\alpha+3}} \qquad (21)$$

IV. CALCULATING RESULTS

The circuit operation was analyzed by PSpice. Principal circuit parameters are listed in Table 1.

Fig. 5 shows an example of simulated input voltage and input current waveforms after filtering for the boost PFC converter. The filter parameters are $L_f = 3\text{mH}$, $C_f = 3\mu\text{F}$, cutoff frequency=1.7kHz and $\alpha \approx 2$. The input current waveform includes large third harmonics.

Table 1 Principal circuit parameters.

Source Voltage (Max)	E_s	$100\sqrt{2}$[V]
Source Frequency	f_s	60[Hz]
Switching Frequency	f_b	20[kHz]
Load Resistor	R_d	200[Ω]
Smoothing Capacitor	C_d	2000[μF]
Reactor	L_r	64[μH]

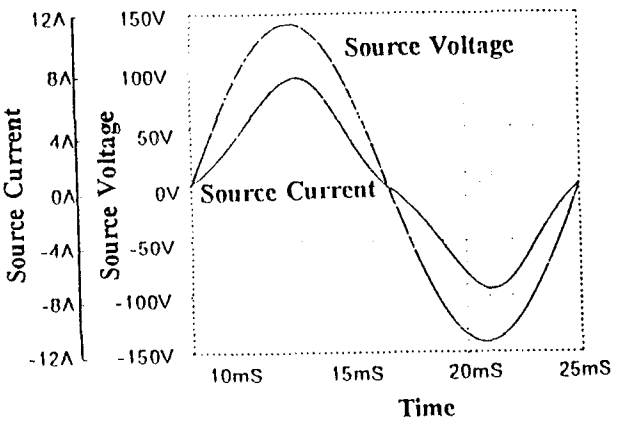

Fig. 5 Example of simulated input voltage and input current waveforms.

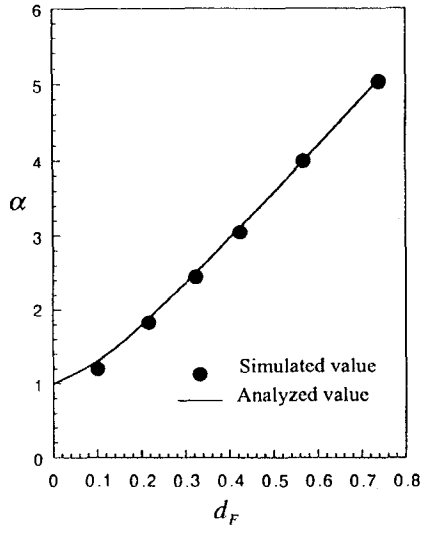

Fig. 6 Relation between α ($= E_d / E_s$) and d_F.

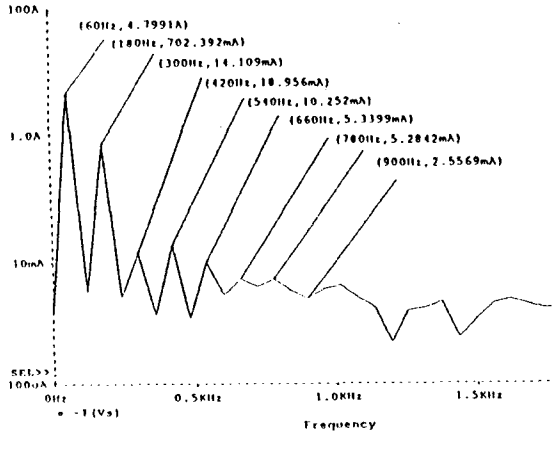

Fig. 7 Frequency spectrum for constant d_F control method ($\alpha = 1.8$).

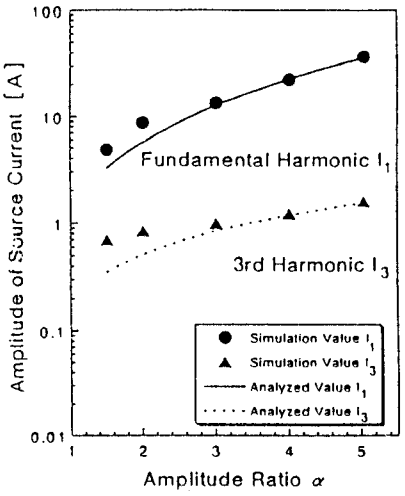

Fig. 8 Amplitudes of fundamental and third harmonic components for verious α.

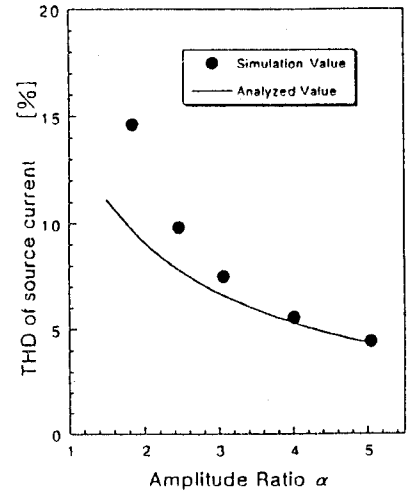

Fig. 9 *THD* of input current waveform.

Fig. 6 shows a relation between α ($= E_d / E_s$) and d_F. As shown in Fig. 6, analyzed values from (21) are agree well with simulated values.

Fig. 7 shows the frequency spectrum for $\alpha = 1.8$. Third harmonic component appears one seventh amplitude of the fundamental component. Higher order harmonics included in the input current waveform without fundamental and third harmonic components can be neglected as shown in Fig. 7 and as expressed by (19). Fig. 8 shows the amplitudes of fundamental and third harmonic components for various α.

The analyzed values and simulated values of the *THD* for input current are shown in Fig. 9. If $\alpha > 2$ in Fig. 9, analyzed values of *THD* are agree well with simulated values.

V. IMPROVEMENT OF INPUT CURRENT WAVEFORM

The improvement of the input current waveform can be derived by applying the theoretical results that the fundamental component and higher-order harmonics included in the input current waveform are obtained by the Fourier series expansion of the mean value of the inductor current. Namely, it is imply that the input current becomes pure sinusoidal waveform when the mean value of the inductor current is proportional to the input voltage waveform completely. Combining $\bar{I}_r$ of (14) and Be_r yields

$$\frac{Ae_r}{E_d - e_r} = Be_r \tag{22}$$

where B is constant.

From (22), a duty factor d_F is obtained as

$$d_F = D_F\sqrt{1 - \frac{1}{\alpha}\sin\omega_s t} \tag{23}$$

$$\text{where } 0 \le \left(D_F = \sqrt{\omega_b L_r B / \pi}\right) \le 1 \tag{24}$$

$$0 \le \omega_s t \le \pi \tag{25}$$

Fig. 10 shows a waveform of d_F from (23). By controlling the duty factor according as (23), the input current waveform does not include lower-order harmonics theoretically.

Comparison of the *THD* between the conventional constant d_F control and the proposed d_F control is shown in Fig. 11. In wide variation of α, the proposed method establishes a great improvement of THD in spite of an open loop system. All harmonics included in the input current waveform can be neglected as shown in Fig. 11.

In Fig. 4, the range of discontinuous mode operation is

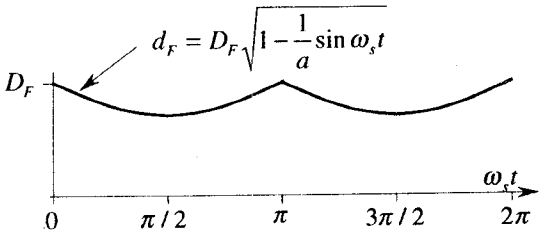

Fig.10 Waveform for proposed d_F control method.

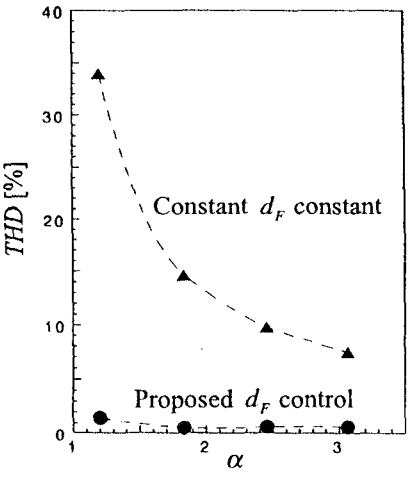

Fig. 11 Comparison of *THD* between conventional constant d_F control and proposed d_F control.

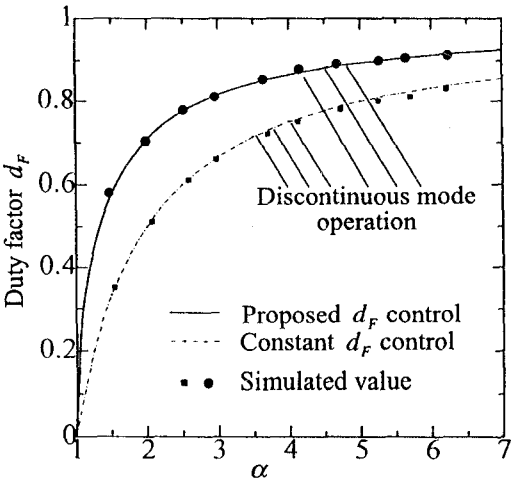

Fig.12 Limitation of the DCM operation ramge.

$$T_1 + T_2 \le T_b \qquad (26)$$

From (3), (5) and (26), a duty factor at DCM operation for the conventional system is given by

$$d_F = 1 - \frac{\sin \omega_s t}{\alpha} \qquad (27)$$

Maximum duty factor occurs when $\omega_s t = \pi / 2$. Therefore, the maximum duty factor for the constant d_F control method is

$$d_{F\max} = 1 - \frac{1}{\alpha} \qquad (28)$$

and , from (23), the maximum duty factor for proposed new d_F control method is given by

$$d_{F\max} = \sqrt{1 - \frac{1}{\alpha}} \qquad (29)$$

Fig.12 shows the limitation of the DCM operation range. Proposed d_F control method has wider operation range than that of the conventional constant d_F control method.

VI. CONCLUSIONS

A conventional constant-switching-frequency discontinuous mode converter has been analyzed by applying the double Fourier series expansion. It is found that the fundamental component and higher-order harmonics included in the input current waveform are obtained by the Fourier series expansion of the mean value of the inductor current. As the result of analysis, components included in the input current waveform are fundamental plus third harmonics and another components can be neglected.

From the theoretical analysis, a theoretical and fundamental method removing the distortion of the input current waveform has been also proposed. In spite of an open loop system, the proposed method establishes a great improvement of THD even if the ratio of output voltage to input voltage is very low.

REFERENCES

[1] A.R.Prasad, P.D.Ziogas, and S.Manias,"An Active Power Fact or Correction Technique For Three-Phase Diode Rectifiers," IEEE PESC'89,1989, pp.58-66.

[2]J.W.Kolar,H.Ertl,F.C.Zach"A Novel Three-Phase Single-Switch Discontinuous-Mode AC-DC Buck-Boost Converter with High-Quality Input Current Waveforms and Isolated Output", IEEE Trans. Power Electron., vol. IE-9, No.2, pp160-172,March(1994)

[3]Taniguchi, Kimura, Morizane, Takeda, Morimoto, Sanada," Novel PAM Inverter system for Induction Motor Drive" International Journal of Electronics, Special issue, ,vol.80, No.2, pp.113/153, (1996-2)

[4]DaFeng and S.Yuvarajan:" Constant-Switching-Frequency AC-DC Converter Using Second-Harmonic-Injection PWM", IEEE Trans. on Power Electronics, Vol.11, No.1, January pp115-121 (1996)

[5]Taniguchi,Tomiyama,Iwatani,Irie"Acoustic Noise Reduced PWM Converter and Inverter using BJTs and IGBTs",EPE'91 Proceed ings Vol.3,pp252/255(1991)

[6]Taniguchi,Inoue,Takeda,Morimoto,"A PWM Strategy for Reduci ng Torque-Ripple in Inverter-Fed Induction Motor", IEEE-Trans actions on Industry Applications, Vol.IA-30,No.1,Jan./Feb., pp71/ 77 (1994-1)

Interleaved Boost Power Factor Corrector Operating in Discontinuous-Inductor-Currrent Mode

C.H. Chan M.H. Pong
Department of Electrical and Electronic Engineering
The University of Hong Kong
Pokfulam Road, Hong Kong

Abstract - This paper presents the basic operation of the Discontinuous-Inductor-Current-Mode (DICM) boost PFC and the improvement achieved by interleaving technique. The PFC is constructed by at least two boost cells, each cell is kept running in DICM. Input current of the PFC is analyzed by numerical method and the optimum power factor is calculated in different modes of operation. The calculated result is verified by experiment and presented in graphical form with detailed discussion. The result shows that interleaving technique can alleviate the ripple current and improve the power factor. The improvement is obvious for the number of boost cells equal to 2 or 3 and the ripple alleviation is better when the PFC is operated in fixed frequency mode. The optimum power factor is improved up to 0.99 even without an input filter.

I. INTRODUCTION

As IEC1000-3-2 become compulsory requirement for the electronic equipment in Europe, Power Factor Corrector (PFC) is always used to reduce input harmonic currents and increase the power factor of power converters. Boost power factor corrector operated in Discontinuous-Inductor-Current Mode (DICM) is popular in low to moderate power level. The input current of this converter naturally follows the sinusoidal line voltage, therefore, the current control loop can be removed and the whole control loop is simplified. Moreover, Zero Current Switching (ZCS) is another advantage for DICM boost PFC, it reduces power losses in the power switches and the snubber circuit which suppresses reverse recovery current of the output rectifier is not required. Although DICM boost PFC has many advantages [4], it is seldom adopted in high power application. The main reason is the pulsating input current which makes the design of input filter difficult. The problem can be solved by interleaving technique [3][5] which effectively alleviates the ripple current.

A DICM boost PFC can be controlled at fixed frequency or variable frequency [4]. For the fixed frequency operation, the duty cycle (or the on-time) of the power switch is fixed within a half line cycle and there is distortion [1] in the input current waveform due to the dead time between current pulses. For the variable frequency operation, the power switch is always turned on immediately after the inductor current has reached zero and the on-time is fixed within a half line cycle.

The equations of rms value and harmonic components of the input currents are the necessary information for calculating the power factor of the boost PFC in different modes of operation. Some of these equations are already derived in [1]&[2] and the power factor of a boost converter with fixed frequency operation is derived in [1]. However, experimental result shows that the actual power factor is much lower than the calculated value provided in [1] because it is assumed that the ripple current is completely removed by an ideal input filter. Therefore, the input current is averaged within a switching period in the calculation and the high frequency (around the switching frequency) harmonic current is ignored. To evaluate the actual performance of the DICM boost PFC (without input filter), harmonic currents over a reasonable range of frequencies should be considered. Since the input current waveform is sophisticated, special numerical method should be adopted in the analysis.

This paper presents the basic operation of the DICM boost PFC and the improvement achieved by interleaving technique. Input current of the PFC is analyzed by numerical method and the optimum power factor is calculated in different modes of operation. The calculated result is verified by experiment and presented in graphical form with detailed discussion.

II. OPERATION OF DICM PFC AND THE INTERLEAVING TECHNIQUE

The interleaved PFC is shown in fig.1. The PFC is constructed by at least two boost cells, all boost cells are kept running in DICM.

A. Fixed Frequency Operation

In this mode of operation, the power switches are operated in fixed switching frequency and duty cycle within a half line cycle. The inductor current in one of the boost cells is shown in fig.2, it is a series of triangular pulses with the envelop follows the input voltage.

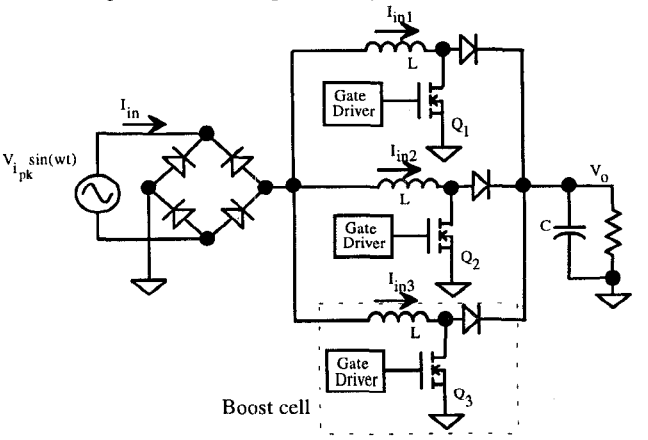

Fig. 1. Interleaved power factor corrector.

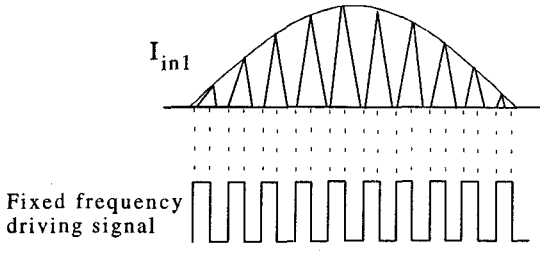

Fig. 2. Fixed frequency operation.

As the duty cycle is fixed, there is dead time in between the pulses which causes low frequency harmonic distortion [1] and the distortion is more obvious when the high frequency ripple current is filtered. To minimize the dead time, the duty cycle (D) should be set as large as possible with the condition that the converter is kept in discontinuous mode throughout the line cycle. The criterion is

$D \leqslant 1-\alpha$ where α is the ratio of peak input voltage to output voltage ($\alpha = \frac{V_{in_{pk}}}{V_o}$)

Therefore, the optimum value of duty cycle is 1-α. The solid lines in fig. 3 shows the power factor of a DICM boost cell with different values of α and duty cycle (the bottom x-axis). The data is obtained by applying numerical analysis to the pulsating input current, the method of analysis will be described in section III. The broken line shows the optimum power factor that can be achieved with different values of α (the top x-axis).

Take a PFC with 200Vac input and 400V output as an example, the peak input voltage is $200 \times \sqrt{2} \simeq 280$V and α is equal to 0.7. According to fig. 3, the optimum power factor is 0.77 when the duty cycle is set equal to 0.3(= 1-α). If the duty cycle is set higher than 0.3, the boost converter will go into continuous mode. In opposite, decreasing the duty cycle will significantly decrease the power factor.

B. Variable Frequency Operation

In this mode of operation, the power switches are always turned on immediately after the inductor current has reached zero. The dead time between current pulses is then eliminated and the input current is free of low frequency distortion that occurred in fixed frequency operation. Some articles designate this control method to "Borderline control" since the PFC always works in the borderline of continuous and discontinuous mode. The input current of the boost cells is shown in fig. 5.

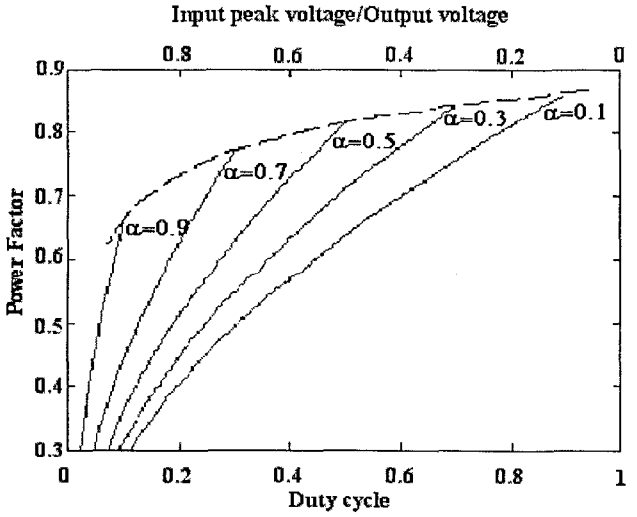

Fig. 3. Power factor of a DICM boost cell with fixed frequency operation.

C. The Interleaving Technique

The interleaved PFC is constructed by a number of parallel connected boost cells with the same components and controlled by the same switching strategy. The driving signal of one cell is shifted in time by an appropriate amount to other cells as shown in fig.4. As the input current of the whole PFC is the sum of the inductor current of all boost cells, the resultant ripple current is reduced.

For the variable frequency operation, there are two methods to apply the interleaving technique. Method 1 uses individual controllers to control the boost cells separately and the boost cells are kept running in borderline mode by their own controllers. To effectively cancel the ripple current, the driving signals from the controllers are synchronized by setting the driving signals to zero at the zero cross of the input voltage and then the signals are restarted with different delay as shown in fig. 5.

However, this method is difficult to implement because the controllers do not have exactly same characteristic, that

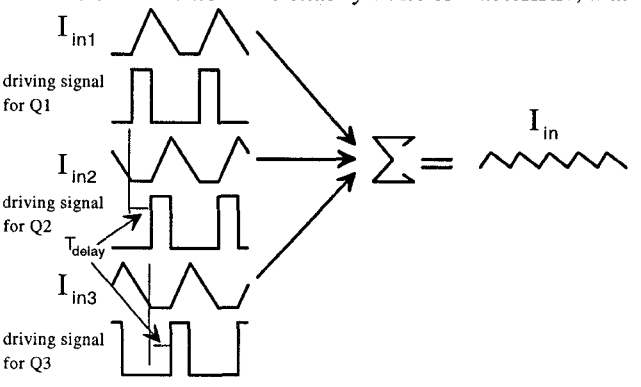

Fig. 4. Interleaving technique

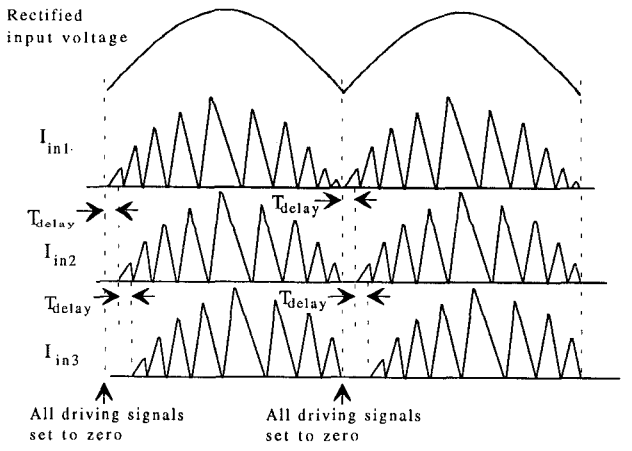

Fig. 5. Interleaving technique for variable frequency operation.

means different drift of current pulses can happen in different cells. The drift of the current waveform will greatly affect the ripple cancellation and deviate the result.

Method 2 is a more practical method which use only one controller to control the first PFC cell. The other PFC cells are controlled by the same driving signal from the controller with time delay. Although the PFC cells are not exactly kept in borderline mode except the first cell, the derivation is so little that all PFC cells are apparently running in borderline mode.

III. The Method of Analysis

The input current waveform is analyzed by dividing it into triangular pulses as shown in fig. 6. By summation of the triangular pulses, the input current waveform can be reconstructed. To simplify the analysis, the following assumptions are made: 1) The input voltage is constant over one switching period. 2) The switching frequency is much higher than the line frequency. 3) The output ripple voltage is negligible and the output voltage is constant. 4) The on-time of the power switch (T_{on}) is constant within a half line cycle. 5) The inductance of the inductors L in all boost cells are equal.

For the fixed frequency operation, the total number of pulses within a line cycle is equal to $K = \frac{T}{T_s}$. To make the equations of the input current clearer, we let $T_1(k)$ be the starting time of the k-th pulse, $T_2(k)$ be the time for the k-th pulse to reach its peak value and $T_3(k)$ be the time for the k-th pulse to fall to zero.

$$T_1(k) = kT_s, \qquad T_2(k) = kT_s + T_{on}\ , \text{and}$$

$$T_3(k) = kT_s + T_{on} + T_d(k) \quad \text{for} \quad k = 0,1,2.....,K\text{-}1 \tag{1}$$

where $T_d(k)$ is the conduction time of the output rectifier.

The equation of the triangular pulse is

$$i_k(t) = \frac{V_{ipk}\sin wT_1(k)}{L}(t - T_1(k)) \quad \text{for} \quad T_1(k) < t \leqslant T_2(k) \tag{2a}$$

$$i_k(t) = \frac{V_{ipk}\sin wT_1(k)}{L}T_{on} + \frac{|V_{ipk}\sin wT_1(k)| - V_o}{L}(t - T_2(k))$$

$$\text{for} \quad T_2(k) < t \leqslant T_3(k) \tag{2b}$$

$$i_k(t) = 0 \qquad \text{for} \quad T_3(k) < t \leqslant T_1(k+1) \tag{2c}$$

The input current is equal to the sum of the triangular pulses.

$$\text{i.e. } i_{in}(t) = \sum_{k=0}^{K-1} i_k(t) \tag{3}$$

for fixed frequency operation.

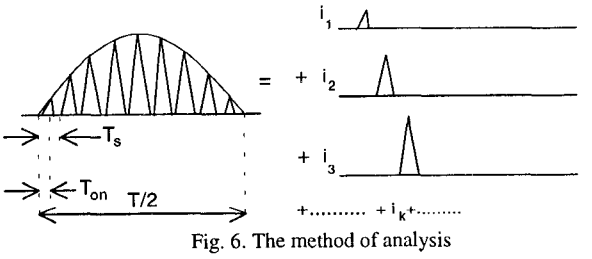

Fig. 6. The method of analysis

For variable frequency operation, the dead time between the triangular pulses is eliminated. The equations of the triangular pulses are basically same as that of fixed frequency operation, however the variables $T_1(k)$ to $T_3(k)$ should be redefined and (2c) is rejected.

$$T_1(k) = T_1(k-1) + T_{on} + T_d(k-1),\ T_2(k) = T_1(k) + T_{on},\ \text{and}$$

$$T_3(k) = T_2(k) + T_d(k) = T_1(k+1) \quad \text{for} \quad k = 0,1,2..... \tag{4}$$

Although the total number of pulses within a line cycle is unknown in this case, we can use the condition ($t \geq T$) to indicate the end of summation in the equation of input current. Therefore,

$$i_{in}(t) = \sum_{k=0}^{t \geq T} i_k(t) \tag{5}$$

for variable frequency operation.

Applying the interleaving technique, the triangular pulses for the second boost cell start with a delay T_{delay} and the triangular pulses for the third boost cell start with a delay $2 \times T_{delay}$ and so on, then the currents flow into the inductors of the boost cells are defined as

$$i_{in1}(t) = \sum_{k=0}^{K-1} i_k(t)\ , \tag{6a}$$

$$i_{in2}(t) = \sum_{k=0}^{K-1} i_k(t - T_{delay}), \quad \text{and} \tag{6b}$$

$$i_{in3}(t) = \sum_{k=0}^{K-1} i_k(t - 2 \times T_{delay}) \quad .....\text{etc} \tag{6c}$$

And the resultant input current will be

$$i_{in}(t) = i_{in1}(t) + i_{in2}(t) + i_{in3}(t) + ... \tag{7}$$

Using (7), we analyzed the input current by Fourier analysis and calculated the power factor of the PFC.

IV. Analysis And Result

A. Fixed Frequency Operation

It is intuitively known that the most effective way to minimize the ripple current is setting $T_{delay} = \frac{T_s}{N}$ (where N = no. of boost cells) because the current pulses of all boost cells can be evenly distributed within a switching period.

With the above information, the input current waveform of the PFC with different number of cells is analyzed by Fourier analysis under the following conditions: 1) The duty cycle is set equal to 1-α, then the power factor is optimum for the corresponding value of α. 2) T_{delay} is set equal to $\frac{T_s}{N}$ with the aforementioned reason.

The result is presented in fig. 7. and the lowest curve is same as the broken line in fig.3 which shows the power factor of the non-interleaved PFC. The result shows that: 1) For N=1, power factor is low and continuously decrease as α increase. 2) For N=2 or above, power factor is much improved and the improvement is obvious when N change from 1 to 2 but it is not obvious when N is further increased. 3) The power factor of the interleaved PFC is not continuously decreased as α increase, this is different from the case of the non-interleaved one. The optimum points for different values of N are shown in Table I. It shows that an

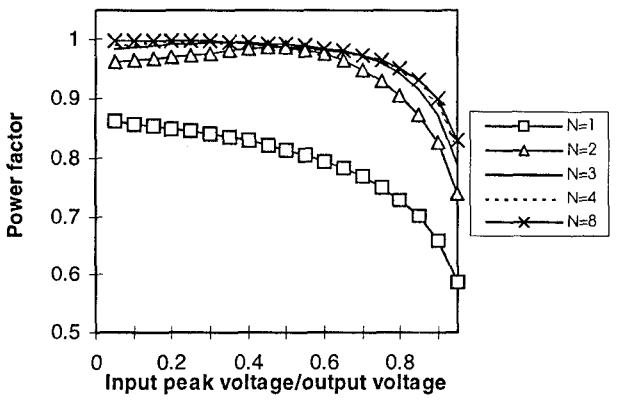

Fig. 7. Optimum power factor of the interleaved PFC

TABLE I
MAXIMUM VALUE OF POWER FACTOR OF INTERLEAVED PFC (FIXED FREQUENCY OPERATION)

N	Value of α when PF is maximum	Maximum PF
1	near zero	0.864
2	0.5	0.987
3	0.33	0.997
4	0.25	0.998
8	0.125	0.999

interleaved PFC with N boost cells can give a maximum power factor when α equal to 1/N.

To verify the above result, three boost cells was built and tested under different input voltages. The test result is compared with the calculated result in fig. 8 which shows that the calculation agrees with the experimental result. The input currents of the PFC with different number of cells are shown in fig. 9 for comparison. Obviously, the ripple current is much reduced using the interleaving technique.

To evaluate the actual contribution of interleaving technique in ripple alleviation, the analysis should focus on the high frequency ripple alone. Therefore, the dead time distortion is extracted and eliminated in the analysis by the following procedure.

The actual input current I_{in} is composed by the high frequency and low frequency harmonic currents, the former is due to the ripple current and the latter is due to the dead time distortion. The distortion factor of I_{in} is defined as

$$\mu_{in} = \frac{I_1}{I_{in,rms}} = \frac{I_1}{\sqrt{I_1^2+I_{low}+I_{high}}} \tag{8}$$

where I_1 = the rms value of fundamental current

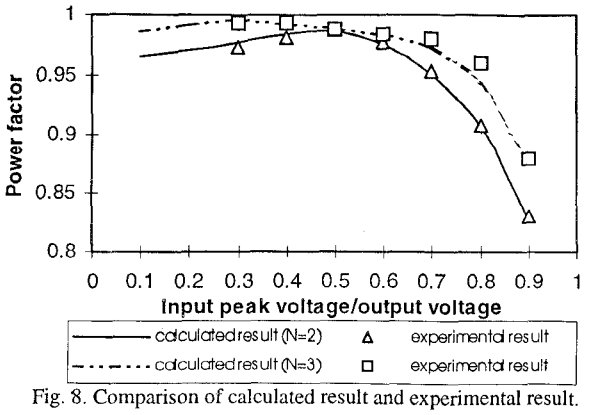

Fig. 8. Comparison of calculated result and experimental result.

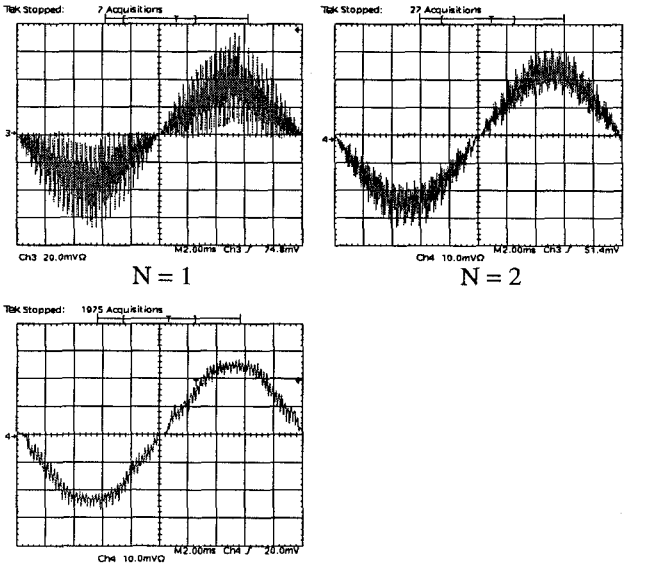

Fig. 9. Input current of interleaved boost PFC.

$I_{in,\,rms}$ = the rms value of the input current

I_{low} = the sum of square of the harmonics due to dead time distortion = $I_2^2 + I_3^2 + I_4^2 + ...$

I_{high} = the sum of square of the harmonics due to the high frequency ripple

Note that

Power Factor = Distortion Factor × Displacement Factor

and Displacement Factor is nearly equal to one, therefore, the Power Factor is equal to the Distortion Factor in this case. (That means fig. 7 can also used to present the value of μ_{in})

The input current and power factor of a single cell PFC are defined in [1] as follow.

$$I_{in}(t) = \frac{V_{pk}D^2T_s}{2L}\frac{\sin wt}{1-\alpha\sin wt} \quad \text{and} \tag{9}$$

$$PF = \frac{\sqrt{2}}{\sqrt{\pi}} \cdot \frac{y}{\sqrt{z}} \tag{10}$$

where $y = \int_0^{\pi} \frac{\sin^2\theta}{1-\alpha\sin\theta}d\theta$ and $z = \int_0^{\pi}\left[\frac{\sin\theta}{1-\alpha\sin\theta}\right]^2 d\theta$

Since the high frequency ripple is ignored in (9) and (10), the current contains only the low frequency harmonics due to the dead time distortion. The distortion factor for the low frequency harmonics is defined as

$$\mu_{low} = \frac{I_1}{\sqrt{I_1^2+I_{low}}} \tag{11}$$

As power factor is equal to distortion factor, μ_{low} can be directly calculated by (10) because the equation refers to the low frequency harmonics only.

Combine (8) and (11),

$$\frac{\mu_{low}}{\mu_{in}} = \frac{\sqrt{I_1^2+I_{low}+I_{high}}}{\sqrt{I_1^2+I_{low}}}$$

$$\frac{\sqrt{I_{high}}}{I_1} = \sqrt{\frac{1}{\mu_{in}^2} - \frac{1}{\mu_{low}^2}} \tag{12}$$

The left hand side of (12) is the ratio of high frequency harmonics to the fundamental current (ripple ratio) and this ratio is suitable for indicating the percentage of ripple current in the input current.

$$\text{Ripple ratio (R)} = \frac{\sqrt{I_{high}}}{I_1} = \sqrt{\frac{1}{\mu_{in}^2} - \frac{1}{\mu_{low}^2}} \quad (13)$$

where μ_{in} is obtained in the Fourier analysis of the input current and μ_{low} can be calculated by (10).

To clearly observe the improvement due to interleaving, the ripple ratios of the PFC with different number of cells are compared with the non-interleaved PFC (i.e. N=1). The ripple attenuation (RA) is then defined as

$$RA_N = \frac{R_N}{R_1} \quad (14)$$

Fig. 10 shows the ripple attenuation of the interleaved PFC with different number of cells and different values of α and the optimum ripple attenuation are shown in Table II.

B. Variable Frequency Operation

For the variable frequency operation, similar numerical analysis has been carried out. Different values of T_{on} are tried in the analysis of non-interleaved PFC. The result shows that the power factor is equal to 0.866 as T_{on} trends to zero and it is nearly constant over a wide range of T_{on}. However, the power factor is deviated from 0.866 if T_{on} is longer than $\frac{\text{line period}}{25}$. It is because the first two assumptions (the input voltage is constant over one switching period and the switching frequency is much higher than the line frequency) are not held as T_{on} has a comparative length to the line period. On the other hand, the value of α has no significant effect on the power factor and the distortion is only due to the high frequency ripple current because the dead time distortion is eliminated in this case.

When the interleaving technique is applied to the PFC using method 1, it is found that the power factor is depended on the delay between the driving signals but not α. The result is shown in fig. 11. Obviously, the power factor is maximum for $T_{delay} = \frac{T_{on}}{N}$. The optimum points for different values of N are shown in Table III.

Same as the case of fixed frequency operation, the power factor is equal to the distortion factor. In this case, the distortion factor of I_{in} is defined as

$$\mu_{in} = \frac{I_1}{I_{in,rms}} = \frac{I_1}{\sqrt{I_1^2 + I_{high}}} \quad (15)$$

and the ripple ratio is then equal to

$$R = \frac{\sqrt{I_{high}}}{I_1} = \sqrt{\frac{1}{\mu_{in}^2} - 1} \quad (16)$$

Again, the ripple attenuation is calculated by (14) and the optimum values are shown in Table IV.

TABLE II
OPTIMUM RIPPLE ATTENUATION
(FIXED FREQUENCY OPERATION)

N	Optimum Ripple Attenuation
2	14.7%
3	8.5%
4	4%
8	1%

TABLE III
MAXIMUM VALUE OF POWER FACTOR OF INTERLEAVED PFC
(VARIABLE FREQUENCY OPERATION - METHOD 1)

N	Value of T_{delay}/T_{on} when PF is maximum	Maximum PF
1	-	0.866
2	0.5	0.986
3	0.33	0.998
4	0.25	0.999
8	0.125	0.999

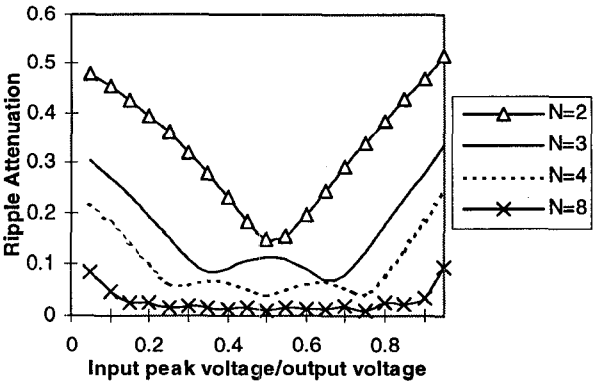

Fig. 10. Ripple Attenuation (fixed frequency operation)

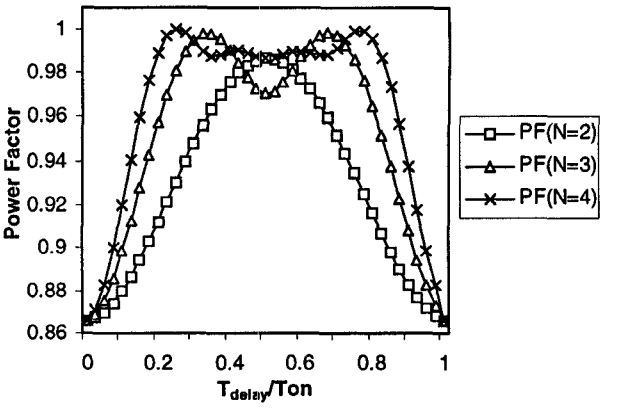

Fig. 11. Power factor of interleaved PFC with variable frequency operation - Method 1.

A completely different result is obtained using method 2. It is found that the power factor is depended on both α and the ratio $\frac{T_{delay}}{T_{on}}$. Fig. 12 and fig. 13 show the power factor of the interleaved PFC with N=2 and N=3 respectively. The optimum values of ripple attenuation are shown in Table V.

V. DISCUSSION

Using the above result, engineers can optimize the number of boost cells in designing PFC for different application. Although the interleaving technique increases the component count, the actual increase of cost may be not significant. It is because using more boost cells can share the current flow in the inductors and power switches so the lower current rating devices (lower price) can be adopted. Actually, some high power PFC use more than one power switches and output rectifiers because the high current rating device is not available in the market.

TABLE IV
OPTIMUM RIPPLE ATTENUATION
(VARIABLE FREQUENCY OPERATION - METHOD 1)

N	Ripple Attenuation
2	29.2%
3	11%
4	7.8%
8	7.8%

TABLE V
OPTIMUM RIPPLE ATTENUATION
(VARIABLE FREQUENCY OPERATION - METHOD 2)

N	α	Value of T_{delay}/T_{on} when PF is maximum	Maximum PF	Ripple Attenuation
2	0.1	0.5	0.966	46.4%
	0.3	0.7	0.981	34.2%
	0.5	0.9	0.99	24.7%
	0.7	1	0.968	44.9%
	0.9	1	0.923	72.2%
3	0.1	0.4	0.988	27.1%
	0.3	0.5	0.997	13.4%
	0.5	0.6	0.994	19.1%
	0.7	0.9	0.993	20.6%
	0.9	1	0.952	55.7%

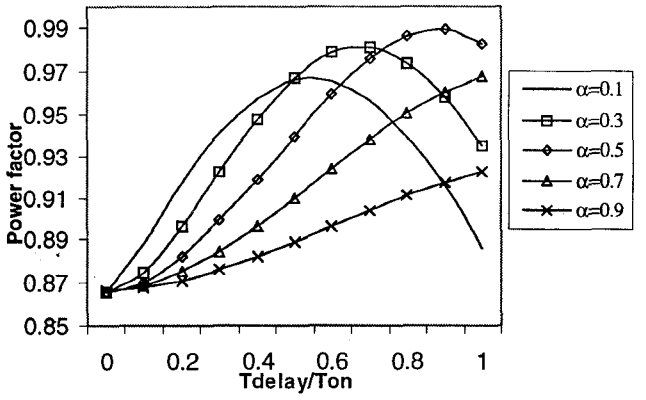

Fig. 12. Power factor of interleaved PFC (N=2) with variable frequency operation - Method 2.

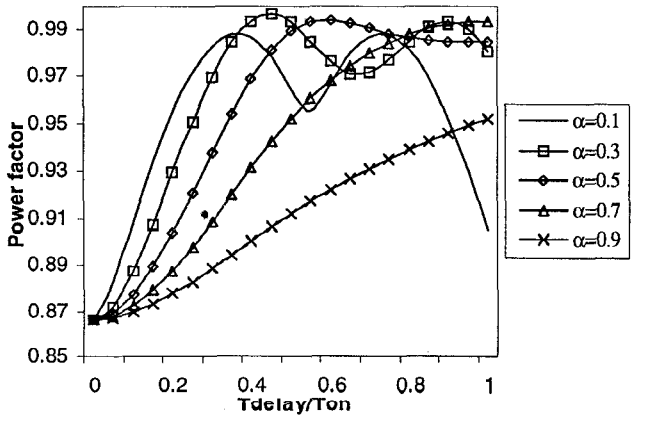

Fig. 13. Power factor of interleaved PFC (N=3) with variable frequency operation - Method 2

However, the effect of interleaving technique is obvious only for N equal to 2 or 3. Thus it is a pitfall for one who think "more cells get better result". In fact, the high frequency ripple current can be effectively reduced using 2 or 3 boost cells.

TABLE VI
COMPARISON OF RIPPLE ATTENUATION

	Fixed frequency operation	Variable frequency operation	
		Method 1	Method 2
Range of Ripple Attenuation (N=2)	14.7% - 50%	29.2%	24.7% - 72%
Range of Ripple Attenuation (N=3)	8.5% - 30%	11%	13.4% - 55.7%

Comparing the result (table VI), the interleaved PFC with fixed frequency operation gives the best ripple attenuation but the attenuation is varied with the value of α, Also, the power factor is lowered by the dead time distortion which is a shortcoming of fixed frequency operation.

For variable frequency operation, the ripple attenuation is constant for the interleaved PFC using method 1. That means the PFC can keep the power factor stable in different input line voltage and output loading. However, the controller is very difficult to implement because of the reason stated in section II(C). Method 2 is a more practical scheme to control the interleaved PFC with variable frequency operation, but the advantage of method 1 is lost. In general, the controller for variable frequency operation is more complicated because it requires sensing the current through the inductor (or output rectifier). Therefore, fixed frequency operation is recommended unless the dead time distortion is intolerable.

VI. CONCLUSION

An accurate input current waveform analysis is carried out to investigate the power factor of the interleaved DICM PFC. The waveform is analyzed by numerical method in both fixed frequency and variable frequency operation. The optimum power factor is calculated and the result shows that interleaving technique can alleviate the ripple current and improve the power factor. The improvement is obvious for the number of boost cells equal to 2 or 3 and the power factor can be improved up to 0.99 even without an input filter. Considering the ripple attenuation and complexity of the controllers, fixed frequency operation is recommended to adopted in the interleaved PFC.

ACKNOWLEDGMENT

Special thanks to ASTEC Custom Power (H.K.) for the help and advice on the research.

REFERENCES

[1] Kwang-Hwa Liu and Yung-Lin Lin, "Current waveform distortion in power factor correction circuits employing discontinuous-mode boost converters", Proceedings of PESC '89, pp. 825-829.

[2] Richard Redl and Laszlo Balogh, " Rms, dc, peak, and harmonic currents in high-frequency power-factor correctors with capacitive energy storage", Proceedings of APEC '92, pp. 533-540.

[3] Laszlo Balogh and Richard Redl, "Power-factor correction with interleaved boost converters in continuous-inductor-current mode", Proceedings of APEC '93, pp. 168-174.

[4] Bill Andreycak, "Controlled On-time, Zero Current Switched Power Factor Correction Technique" Proceedings of HFPC June 1991, pp. 46-60.

[5] Brett A. Miwa, David M. Otten and Martin F. Schlecht, "High efficiency power factor correction using interleaving techniques", Proceedings of APEC '92, pp. 557-568.

Computer-Aided Simulation Technique of Digitally Controlled Switched-Mode Power Conversion Circuits and Systems using State Variable Matrices

H. Takano (Member IEEE)

Research and Development Center
Hitachi Medical Corporation
2-1, Shintoyofuta, Kashiwa, Chiba, 277, Japan
E-mail: takano@rd.hitachi-medical.co.jp

S. Mobin Ulhaq and M. Nakaoka
(Members IEEE)

Department of Electrical and Electronics Engineering,
The Graduate School of Engineering & Science,
Yamaguchi University, 2557, Tokiwadai, Ube, 755, Japan

Abstract - A new generic simulation approach is presented in order to analyze digitally-controlled switching mode power converters. The computer-aided simulation procedure proposed here is based on a circuit equation modeled by time varying resistors taking place of the active switches and diodes, a state equation for the inductors and the capacitors, and an algebraic computation method to transform the matrices of the circuit equation into the matrices of the state equation. The feasible estimation method of the calculation time step in the numerical integration to solve the state equation is also discussed with its eigen-values.

I. INTRODUCTION

A variety of general simulation approaches have been developed as time domain [1]-[3] or as frequency domain [4] mathematical formulations.

Widely available and generic circuit simulation tool such as SPICE (Simulation Program with Integrated Circuit Emphasis) with PSPICE are well known together. Nevertheless, these circuit simulation tools are not always satisfactory to obtain the operating characteristics with digital and software-based control scheme and to evaluate the transient-state performances of the switching-mode power converters. Moreover, the authors have many experiences that the numerical solution could not be acquired due to convergence problems around rapid switching transitions.

In this paper, a newly-developed generic power electronic circuit simulation technique is presented in addition to a feasible estimation method for desirable calculation time step for the numerical integration based on eigen-values of the state equation.

These techniques are suitable to obtain transient operating waveforms of switching mode power electronic circuits including their nonlinear characteristics with digital control algorithms written by computer programming languages [5]. The transient operating waveforms are to be obtained on various workstations or personal computers in laboratories. In this approach, steps of numerical calculations required are rather less than the tableau method [1] because the numerical integration is to be repeated for only one state equation for the inductors and the capacitors instead of the whole circuit elements and their connections. The mode transition changes are decided with simple descriptions for each switching condition.

The methodology described in this paper can also be applied for various types of switching-mode power converters which have the nonlinear characteristics with the resonant operation and the discontinuous current operation.

II. MAIN CONCEPT OF CIRCUIT SIMULATION

Fig. 1 illustrates the strategic concept of the proposed power electronic conversion circuit with active switches.

In the first place, the target circuit is modeled by time-varying resistors taking place of the active switches and diodes. In addition to this, time-varying resistor circuit model, the switching conditions for the active switches and the diodes, and the control algorithm are represented with C language source code. In the second place, the circuit equation which represents the circuit network including all circuit components is manually estimated. The circuit equation is transformed to the state equation for energy storage elements like reactors and capacitors in the target circuit. The numerical integration based on Runge-Kutta method and the waveform visualization program are also utilized. The calcula-

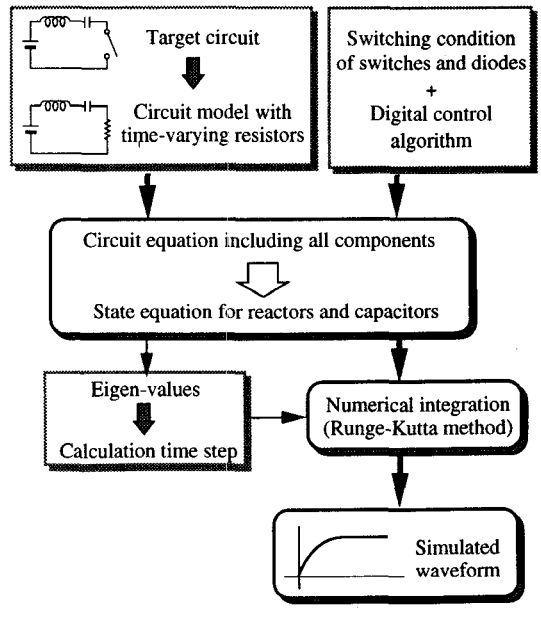

Fig. 1 Procedure of circuit simulation

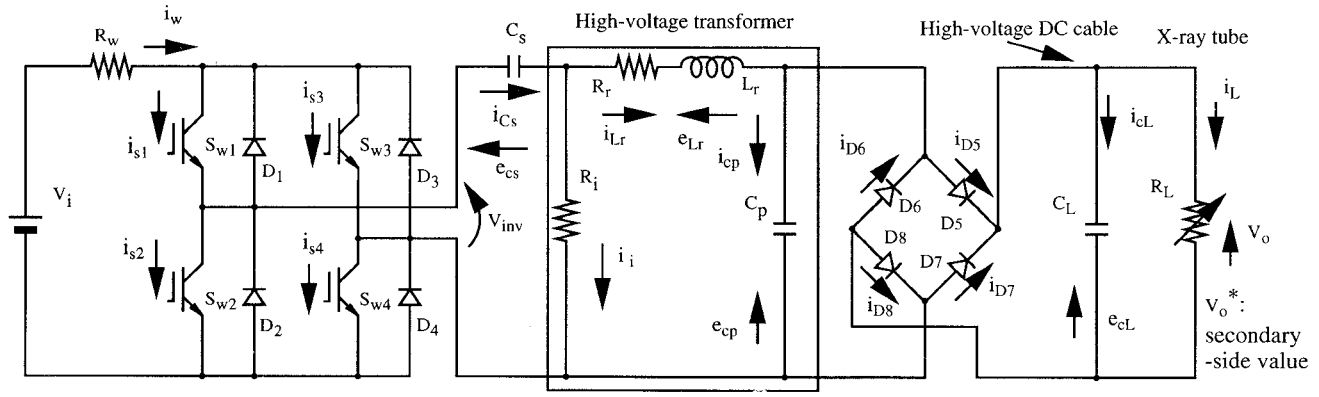

Fig. 2 Total circuit model of inverter-fed type X-ray high-voltage power generator

tion time step in the numerical integration is estimated with the eigen-values of the state equation.

III. Simulation Theory of Switched Mode Power Converters

A. Circuit model description

Fig. 2 illustrates an example of the target power conversion circuit to be analyzed. This is a series and parallel resonant high-frequency AC linked DC-DC power converter with high-voltage transformer parasitic components. This DC-DC power converter is developed by the authors for a digitally-controlled inverter-fed type X-ray power generator for medical use. The circuit parameters including parasitic circuit elements are represented in TABLE I. The circuit parameter values in the secondary of the high-voltage transformer are referred to its primary side under consideration of its turn ratio. The DC output voltage is regulated under a condition of constant frequency phase-shifted PWM control scheme. The DC output voltage of this converter is regulated from zero to maximum voltage in terms of phase-shifted angle ϕ between the left side bridge arms; S_{w1} and S_{w2}, and the right side bridge arms; S_{w3} and S_{w4}.

R_L is a heater current dependent load resistance modeled as the X-ray tube. If the load resistance R_L is large, the output voltage waveform has nonlinear characteristics in the transient state because of discontinuous current operation of the high-voltage rectifier (diodes D_5 to D_8) connected to the secondary side of the high-voltage transformer. In practical applications, X-ray high-voltage generator has extremely wide variations in the range of the load resistance R_L, in other words, there are a large number of specified output voltage and current combinations. The output voltage of this power converter is digitally controlled so as to obtain a specific stabilized flat high-voltage waveform with rapid transient rising and falling characteristics.

Table 1: Circuit parameters of the target circuit ((p) indicates reduced values into the primary-side of the high-voltage transformer)

Symbol	Description	Value
R_w	Wired resistance	10 mΩ
V_i	DC power source	60 to 450 V
C_s	Series resonant capacitor	15 μF
C_L	Equivalent capacitance of high-voltage cable(p)	310 μF
R_L	Load resistance modeled X-ray tube(p)	0.1 to 1 kΩ
Ri	Iron loss of high-voltage transformer(p)	280 Ω
Rr	Copper loss of high-voltage transformer(p)	180 mΩ
Lr	Leakage inductance of high-voltage transformer(p)	15 μH
Cp	Stray capacitance of secondary windings(p)	5 μF

B. Formulation of circuit equation

Fig. 3 illustrates the circuit network configuration of power converter circuit model using the periodic time-vary-

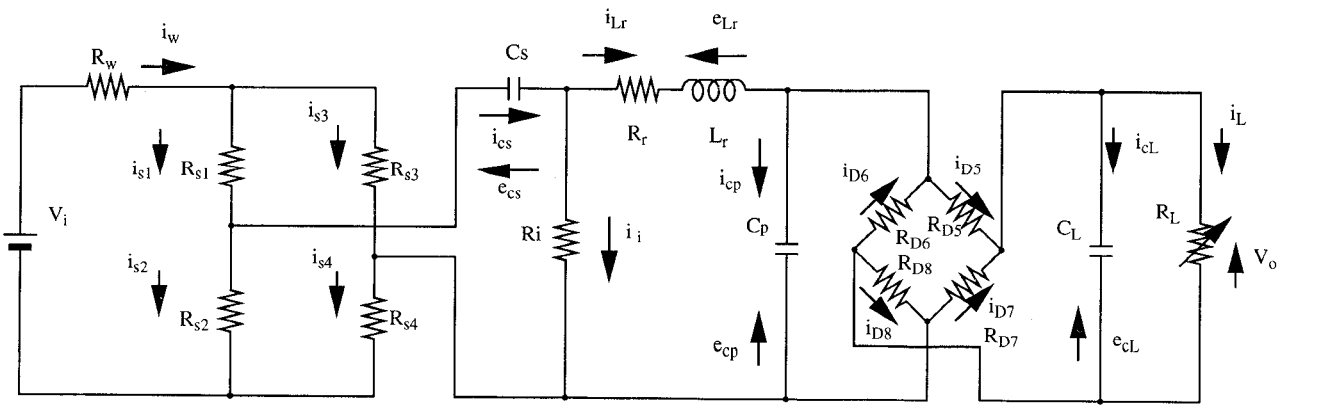

Fig. 3 Circuit model by time-varying resistors taking place of active switches and diodes

ing resistances R_{s1} to R_{s4} which represent the power switches S_{w1} to S_{w4} (IGBTs) with their antiparallel diodes shown in Fig. 2. Although detail circuit models of the power semiconductors can be introduced into the proposed circuit analysis procedure, however, their on-state and off-state are simply considered in this paper as an ideal switching condition.

Applying the Kirchhoff's law to the circuit network, the canonical form of the circuit equation is given by (1), which arranged the state variables; the current of the reactor i_{Lr}, the voltages of the capacitors e_{cs}, e_{cp}, e_{cL}, and input variable V_i in the right-hand side.

$$\mathbf{R\,I = E} \quad \cdots\cdots (1)$$

where,

$$\mathbf{R} = \begin{bmatrix}
1 & & & & & & & & & & -1 & & -1 & & \\
 & & -1 & & & & & & & & 1 & -1 & & & \\
-1 & & & & & & & & & & & 1 & & 1 & \\
 & & -1 & 1 & & & & & & & & & & & \\
 & & & & -1 & & -1 & 1 & & & & & & & \\
 & -1 & & & & -1 & 1 & & 1 & & & & & & \\
 & 1 & & & & 1 & & -1 & & -1 & & & & & \\
R_w & & & & & & & & & & R_{s1} & R_{s2} & & & \\
 & & -R_i & & & & & & & & & R_{s2} & & -R_{s4} & \\
 & & -1 & R_i & & & & & & & & & & & \\
 & & -1 & & & -R_{D5} & & R_{D7} & & & -R_{s1} & & R_{s3} & & \\
 & & & & & -R_{D5} & -R_{D6} & & & & & & & & \\
 & R_L & & & & & & & & & & & & & \\
 & R_L & & & & & & R_{D7} & R_{D8} & & & & & & \\
 & & & & & & -R_{D6} & & R_{D8} & & & & & &
\end{bmatrix},$$

$\cdots\cdots (2)$

$$\mathbf{I} = [\, i_w\ i_L\ e_{Lr}\ i_i\ i_{cs}\ i_{cp}\ i_{cL}\ i_{D5}\ i_{D6}\ i_{D7}\ i_{D8}\ i_{s1}\ i_{s2}\ i_{s3}\ i_{s4}\,]^t, \quad \cdots\cdots (3)$$

$$\mathbf{E} = [\, 0,0,0,i_{Lr},-i_{Lr},0,0,V_i,e_{cs},e_{cp}+R_r i_{Lr},e_{cs}+R_r,e_{cL},e_{cL},0,e_{cp}\,]^t. \quad \cdots\cdots (4)$$

R is called resistance matrix defined by the resistances in the circuit model. **E** is called voltage vector here because it is mainly specified by the voltages across the circuit elements, **I** is called current vector.

If the resistance matrix **R** and the voltage vector **E** are given, the current vector **I** can be estimated by (5).

$$\mathbf{I = R^{-1}\,E}. \quad \cdots\cdots (5)$$

Each element of the inverse matrix $\mathbf{R^{-1}}$ is generally expressed as

$$\mathbf{R^{-1}} = \begin{bmatrix} R^{-1}_{1,1} & R^{-1}_{1,2} & \cdots & R^{-1}_{1,15} \\ R^{-1}_{2,1} & \cdots & \cdots & \cdots \\ \cdots & \cdots & \cdots & \cdots \\ R^{-1}_{15,1} & \cdots & \cdots & R^{-1}_{15,15} \end{bmatrix} \quad \cdots\cdots (6)$$

C. Formulation of state equation

The canonical form of the state equation is presented as

$$\frac{d}{dt}\mathbf{x}(t) = \mathbf{A}\,\mathbf{x}(t) + \mathbf{B}\,\mathbf{u}(t) \quad \cdots\cdots (7)$$

where $\mathbf{x}(t)$: the state vector, **A** and **B** : matrices, $\mathbf{u}(t)$: the input vector. In the case of Fig. 3, $\mathbf{u}(t)$ represents only one element; scaler variable namely the input voltage V_i.

The state vector $\mathbf{x}(t)$, containing four state variables for the inductance and capacitances is defined as

$$\mathbf{x}(t) = [\, i_{Lr}\ e_{cs}\ e_{cp}\ e_{cL}\,]^t. \quad \cdots\cdots (8)$$

The voltage vector **E** may be divided into two terms relating the state vector and the input $\mathbf{u}(t)$ as

$$\mathbf{E = K_X\,x}(t) + \mathbf{K_u\,u}(t). \quad \cdots\cdots (9)$$

$\mathbf{K_X}$ and $\mathbf{K_u}$ are respectively obtained as

$$\mathbf{K_X} = \begin{bmatrix} 0&0&0&1&-1&0&0&0&0&R_r&R_r&0&0&0&0 \\ 0&0&0&0&0&0&0&0&1&0&1&0&0&0&0 \\ 0&0&0&0&0&0&0&0&0&1&0&0&0&0&1 \\ 0&0&0&0&0&0&0&0&0&0&0&1&1&0&0 \end{bmatrix}^t, \quad \cdots\cdots (10)$$

$$\mathbf{K_u} = [\,0\,0\,0\,0\,0\,0\,0\,1\,0\,0\,0\,0\,0\,0\,0\,]^t. \quad \cdots\cdots (11)$$

Matrix $\mathbf{R^*}$ is defined in (12) deriving four rows which relate to L_r, C_s, C_p and C_L in the current vector **I** from the inverse matrix $\mathbf{R^{-1}}$. $\mathbf{R^*}$ is 4 x 4 in dimension.

$$\mathbf{R^*} = \begin{bmatrix} R^{-1}_{3,1} & R^{-1}_{3,2} & \cdots & R^{-1}_{3,15} \\ R^{-1}_{5,1} & R^{-1}_{5,2} & \cdots & R^{-1}_{5,15} \\ R^{-1}_{6,1} & R^{-1}_{6,2} & \cdots & R^{-1}_{6,15} \\ R^{-1}_{7,1} & R^{-1}_{7,2} & \cdots & R^{-1}_{7,15} \end{bmatrix} \quad \cdots\cdots (12)$$

Moreover, the inductance of L_r, the capacitances C_s, C_p and C_L are defined by (13).

$$\mathbf{L^*} = [\, L_r\ C_s\ C_p\ C_L\,]^t. \quad \cdots\cdots (13)$$

A can be estimated as (14) using $\mathbf{A^*}$ defined by (15) and $\mathbf{L^*}$.

$$\mathbf{A} = \begin{bmatrix} \frac{A^*_{1,1}}{L^*_1} & \frac{A^*_{1,2}}{L^*_1} & \cdots & \frac{A^*_{1,4}}{L^*_1} \\ \frac{A^*_{2,1}}{L^*_2} & \cdots & \cdots & \cdots \\ \cdots & \cdots & \cdots & \cdots \\ \frac{A^*_{4,1}}{L^*_4} & \cdots & \cdots & \frac{A^*_{4,4}}{L^*_4} \end{bmatrix} \quad \cdots\cdots (14)$$

$$\mathbf{A^* = R^*\,K_X}. \quad \cdots\cdots (15)$$

where, $A^*_{j,k}$, is an element of $\mathbf{A^*}$; L^*_j is an element of $\mathbf{L^*}$.

In the same way, **B** can be given as (16) using $\mathbf{B^*}$ defined by (17) and $\mathbf{L^*}$.

$$\mathbf{B} = \begin{bmatrix} \frac{B^*_1}{L^*_1} & \frac{B^*_2}{L^*_2} & \cdots & \frac{B^*_4}{L^*_4} \end{bmatrix}^t \quad \cdots\cdots (16)$$

$$\mathbf{B^* = R^*\,K_u}. \quad \cdots\cdots (17)$$

where B^*_j : an element of $\mathbf{B^*}$.

$\mathbf{B^*}$ is 4 x 1-dimension vector.

By process presented above, all elements of the matrices **A** and **B** of the state equation are obtained from the matrices and the vectors of the circuit equation for various types of target circuits. Most of the program source codes can be applied to the other circuits with modification to **R**, $\mathbf{K_X}$, $\mathbf{K_u}$, $\mathbf{R^*}$, $\mathbf{L^*}$ and switching conditions. All information of the circuit operation can be given by **E**, **I**, **R**, $\mathbf{x}(t)$ and $\mathbf{u}(t)$ although the output equation is not defined here.

D. Switching sequence description

The switching conditions of the active power switches; IGBTs and the passive power switches; diodes can be easily implemented with "if ...then ..." style statements in the simulation program. If the switch S_{w1} is on-state during the time t_1 to t_2, then in C-language statement

```
if (((t1 <= t) && (t < t2))||(is1 < 0.)) Rs1 = Ron;
   else Rs1 = Roff;
```

where, R_{on} : on-state resistance ; R_{off} : off-state resistance; R_{s1} : the resistance of the switch S_{w1} with the antiparallel diode D_1; i_{s1} : the current thorough the resistance R_{s1}. In our case, R_{on} = 10 mΩ; R_{off} = 100 kΩ for high power IGBT (1200V/400A) modules are specified.

The resistance model of the diode is determined as

```
if(iD5 > 0) RD5 = Ron;
   else  RD5 = Roff;
```

where, R_{D5} : the resistance model of the diode D_5; i_{D5} : the current of the diode D_5.

IV. Flowchart of Simulation Program

Fig. 4 indicates the flowchart of the circuit simulation program proposed here. First, the voltage vector **E** is calculated from $\mathbf{K}_x$, $\mathbf{K}_u$, **x**(t) and **u**(t). Second, the current vector **I** is estimated from **E** and $\mathbf{R}^{-1}$. The switch and diode model resistances R_{sk} and R_{Dm} (where k=1 to 4, m=5 to 8) are decided from **I** and time *t* with "if.. then..." style switching program. If any one of R_{sk} or R_{Dm} is/are changed, **R**, $\mathbf{R}^{-1}$ and **R*** are computed again. Moreover, **A** from $\mathbf{K}_x$ and **L***, and **B** from $\mathbf{K}_u$ and **L*** are estimated. The state variable **x**(t+Δt) is calculated by numerical integration of Runge-Kutta method.

For effective numerical computation, $\mathbf{R}^{-1}$, **A** and **B** may be calculated beforehand for all the operating modes in order to avoid wasteful repeat. 2^n sets of $\mathbf{R}^{-1}$, **A** and **B** ought to be prepared for the *n* time-varying resistors model. In case that all operating modes may not be realized in the circuit operation, the calculations for nonexistent modes can be neglected.

V. Discussion on Calculation Time Step

Several techniques to estimate the adequate calculation time step Δt in the numerical integrations have been developed for efficient and accurate computation results. In some cases, Δt is treated as a constant during the numerical integration, and in other cases, Δt is dynamically changed. In both cases, for example, large Δt_0 is tested as Δt for the numerical integration in the first place. And $\Delta t_0 / 2$, $\Delta t_0 / 4$ and so on are tested until these time steps don't influence the precisions of the numerical solutions. The largest Δt which can obtain the appropriate accuracy may be selected among these tested calculation time steps.

If possible the calculation time step ought be obtained

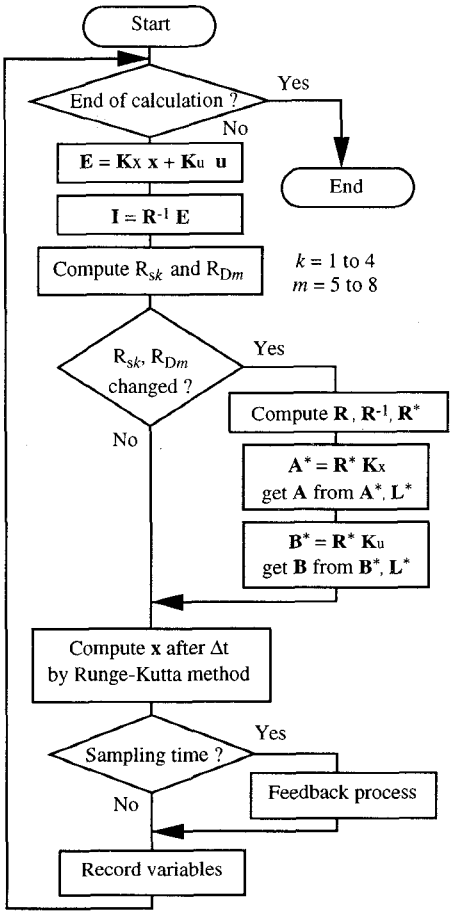

Fig. 4 Flowchart of circuit simulation program

beforehand. The authors would like to describe here the necessary conditions of Δt for the switching mode power converters without repeated trials which increase CPU time.

The considerable points to decide Δt are as follows.

(1) Δt should be enough small against the switching period of the power converter. As Δt from 1 / 1000 to 1 / 100 of the switching period may be assigned except special cases.

(2) Too small Δt spends a lot of CPU time and enlarge round off errors. This point is not so serious because double precision floating point processing is mainly used for the numerical integrations.

(3) In digital control systems, Δt might be determined as the clock pulse period for the power device switching in order to simulate exactly switching operations of the target circuit.

(4) The numerical solution must converge with settled Δt.

The last point is the most important for the simulation of the switching mode power converters to accurately obtain numerical solutions and therefore it is particularly mentioned bellow in detail.

The state equation (7) is a linear differential equation for each circuit operating mode. In general, a linear differential equation is presented with (18) and its general solution is given by (19).

$$a_n \frac{d^n x(t)}{dt^n} + a_{n-1} \frac{d^{n-1} x(t)}{dt^{n-1}} + \cdots\cdots + a_0 x(t) = 0, \quad \text{..... (18)}$$

$$x = c_1 e^{\lambda_1 t} + c_2 e^{\lambda_2 t} + \cdots\cdots + c_n e^{\lambda_n t}, \quad \text{..... (19)}$$

where a_0, a_1, .. a_n, c_1, c_2 .. and c_n : constants, $\lambda 1$, $\lambda 2$ .. and λn ; eigen-values.

All terms of (19) must converge in the numerical integration. The term which has the fastest convergent characteristic is considered here.

Fig. 5 illustrates relations between calculation time step Δt and their numerical solutions for a first order system which has exact solution $x(t) = e^{-\lambda t}$ where λ is the eigen-value of this system. It is obvious that $\Delta t < 2 / \lambda$ is the necessary condition and $\Delta t = 1 / \lambda$ is feasible guideline in order to obtain appropriate numerical solutions for the first order system.

TABLE II presents the eigen-values of each operating mode for the target circuit shown in Fig. 2. These eigen-values are calculated from matrix **A** of the state equation (7). The eigen-values for mode 1 to 8 are under the condition of R_{on} = 10 mΩ and R_{off} = 100 kΩ. The eigen-values for mode 2' are in case of R_{on} = 20 mΩ and R_{off} = 100 kΩ. Eigen-value λ_1 and λ_2 for the mode 2 are complex conjugates and the imaginary part 6.762 x 10^4 indicates the angular frequency and the real part of λ_1 and λ_2 indicates the damping characteristic.

The term with eigen-value λ_3 has the fastest convergent characteristic so the calculation time step Δt ought be estimated as $1 / |\lambda_3|$ that is the appropriate condition to obtain the numerical solution of the state equation (7).

Fig. 6 presents the circuit operating modes corresponding with each eigen-value shown in TABLE II. The eigen-values can be easily estimated from the circuit mode diagram of the target circuit. In Fig. 6, $1 / |\lambda_3|$ indicates discharge time constant for C_p through on-state D_5 and D_8 under the condition that C_L is enough large and regarded as a voltage source. The discharge time constant is calculated with two resistance

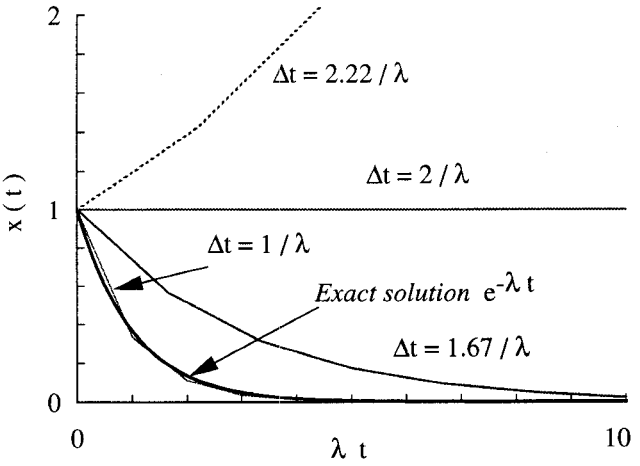

Fig. 5. Effect of calculation time step for first order system by third order Runge-Kutta method (Initial value x(0) = 0).

10 mΩ x 2 and capacitance C_p = 5μF as (10 x 10^{-3} Ω x 2) (5 x 10^{-6} F) = 100 x 10^{-9} s. This value almost corresponds to $1 / |\lambda_3|$ = 98.4 x 10^{-9} s.

VI. Results

A. Calculation time step and eigen-value

Fig. 7 presents effects of the on-state resistance R_{on} to the calculation time step Δt. Fig. 7(a) shows simulated current waveforms i_{cp} in case of Δt = 100 ns and Δt = 250 ns with on-state resistance R_{on} = 10 mΩ and $1 / |\lambda_3|$ = 98.4 ns. Appropriate waveform is obtained with Δt = 100 ns, however, the numerical solution doesn't converge with Δt = 250 ns which is larger than the necessary condition for the all operating mode in TABLE II i.e. $2 / |\lambda_3|$ = 196.8 ns. Fig. 7(b) represents simulated current waveform i_{cp} with the on-state resistance R_{on} = 20 mΩ, in case of Δt = 350 ns which is less than

TABLE II
EIGEN-VALUES FOR EACH OPERATING MODE

Mode	Sw1, D1	Sw2, D2	Sw3, D3	Sw4, D4	D5	D6	D7	D8	λ1, λ2		λ3	λ4
									Real	Imaginary	Real	Real
1	-	on	-	on	on	-	-	on	-7.495×10^3	$\pm 6.768 \times 10^4$	-1.016×10^7	-2.922×10^3
2	on	-	-	on	on	-	-	on	-7.830×10^3	$\pm 6.762 \times 10^4$	-1.016×10^7	-2.922×10^3
3	on	-	on	-	on	-	-	on	-7.495×10^3	$\pm 6.768 \times 10^4$	-1.016×10^7	-2.922×10^3
4	-	on	-	on	-	on	on	-	-7.495×10^3	$\pm 6.768 \times 10^4$	-1.016×10^7	-2.922×10^3
5	-	on	on	-	-	on	on	-	-7.830×10^3	$\pm 6.762 \times 10^4$	-1.016×10^7	-2.922×10^3
6	on	-	on	-	-	on	on	-	-7.495×10^3	$\pm 6.768 \times 10^4$	-1.016×10^7	-2.922×10^3
7	-	on	-	on	-	-	-	-	-6.696×10^3	$\pm 1.332 \times 10^5$	-1.791×10^2	-3.102×10^3
8	on	-	on	-	-	-	-	-	-6.696×10^3	$\pm 1.332 \times 10^5$	-1.791×10^2	-3.102×10^3
2'	on	-	-	on	on	-	-	on	-9.144×10^3	$\pm 6.767 \times 10^4$	-5.078×10^6	-2.922×10^3

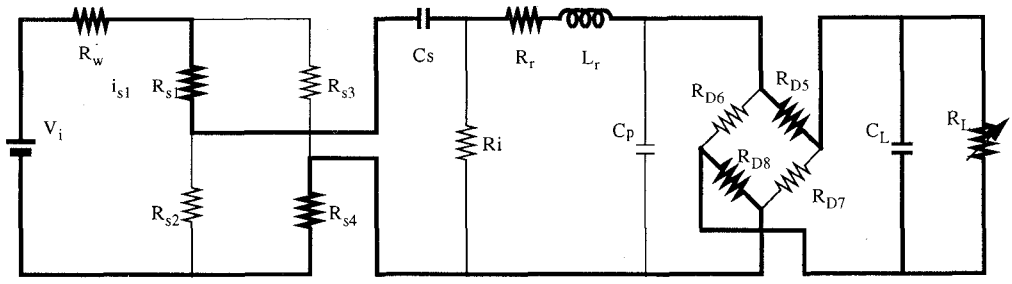

(a) Operating mode for eigen-values λ_1 and λ_2

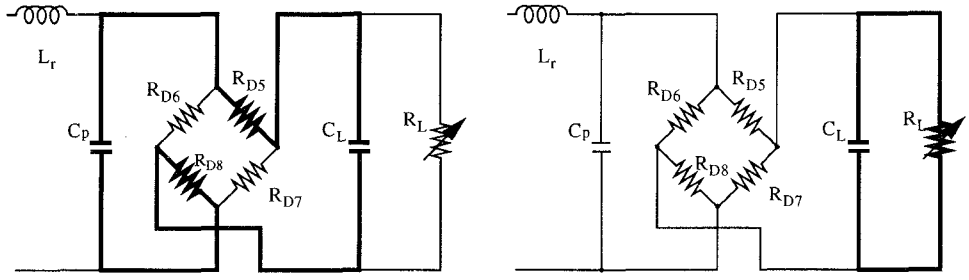

(b) Operating mode for eigen-value λ_3 (c) Operating mode for eigen-value λ_4

Fig. 6. Circuit operating mode for each eigen-value.

the other necessary condition $2 / |\lambda_3| = 393.9$ ns. As shown in Fig. 8(b), the CPU time for the numerical integration can be reduced by larger on-state resistance R_{on} and larger calculation time step Δt.

B. Simulated and experimental waveforms

The simulated waveforms obtained by the proposed simulation technique are basically the same waveforms obtained by SPICE with resistors model for the active switches and the diodes.

Fig. 8 shows the simulated voltage waveform V_{ce4} and the current waveform i_{s4} of the switch S_{w4}. The output voltage is 100 kV; the output current is 1000 mA and the output power is 100 kW.

Fig. 9 illustrates the experimentally measured V_{ce4} and i_{s4} waveforms. Comparing simulated results we find that the reverse recovery current of the diode connected in parallel to S_{w3} and the serge voltage when S_{w4} turns off. Moreover, the simulated current waveform is rather small than the experimental waveforms. The reason of this difference might be that the magnetizing inductance of the high-voltage transformer and the stray capacitances of the high voltage rectifier diodes are not considered in the circuit model shown Fig. 2.

Fig. 10 shows the rising output high-voltage waveforms. The sampling frequency of the digital feedback control using DSP is 10kHz which is identical with the inverter switching frequency. The tendency of the simulated waveforms meet well with the measurements. The experimental voltage waveform rises slightly slower than the simulated one. If the

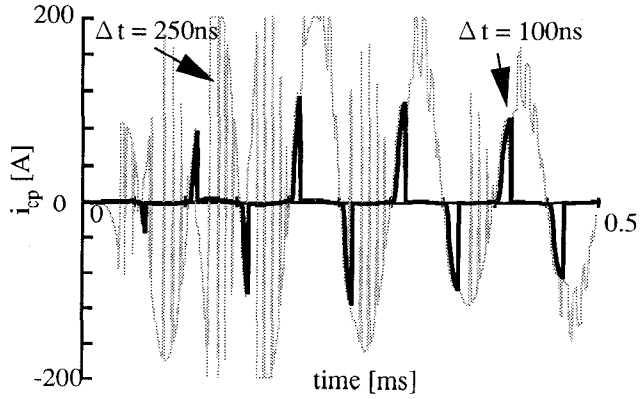

(a) $R_{on} = 10\ m\Omega$, $\Delta t = 100$ ns, 250 ns

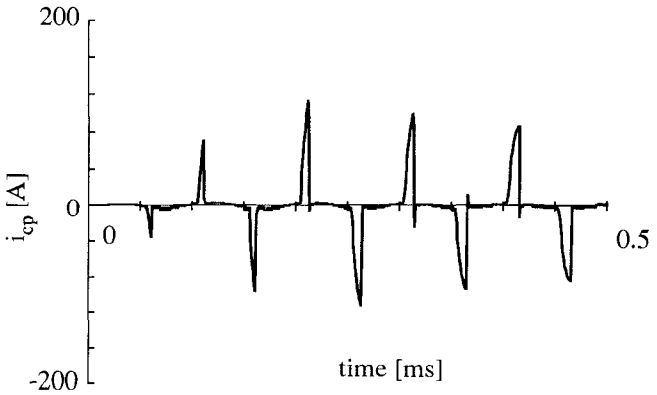

(b) $R_{on} = 20\ m\Omega$, $\Delta t = 350$ ns

Fig. 7. Effects of on-state resistance R_{on} to calculation time step Δt (i_{cp} : current of parallel capacitor C_p).

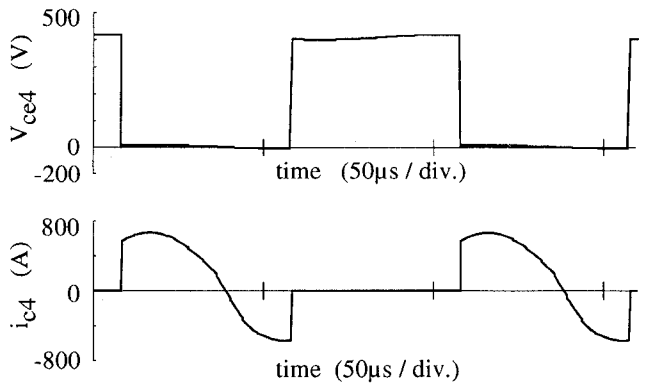

(b) Experimental waveforms

Fig. 8 Simulated waveforms (Voltage and current waveforms of switch S_{w4}, V_i = 420 V, R_L = 0.625 Ω, output power = 100 kW).

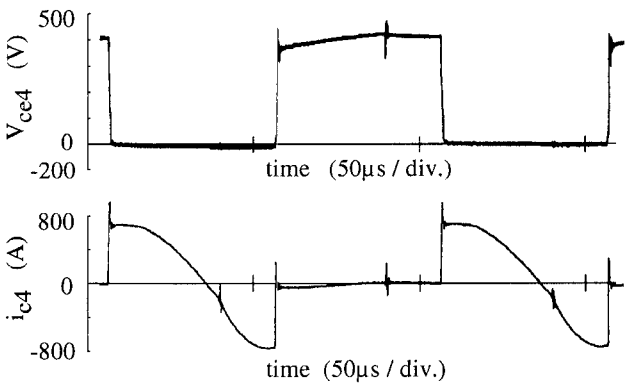

(b) Experimental waveforms

Fig. 9 Experimental waveforms (Voltage and current waveforms of switch S_{w4}, V_i = 420 V, R_L = 0.625 Ω, output power = 100 kW).

integral gain is enlarge than the value then rapid transient response shown in Fig. 10 (b) is obtained . However, the tube voltage overshoot occurs because of approximation of the voltage versus the current characteristics of the X-ray tube load, one of diode vacuum tubes, as a linear resistance [6]. The ripple of the tube voltage is well calculated in the steady-state. Thus, this simulation technique is widely available to study the power electronic converters with feedback control schemes.

C. *Application to the other circuits*

This is the most typical feature of this generic computer-aided simulation approach which consists of the time-varying resistors circuit model, the algebraic computation method to transform the circuit equation into the state equation, and the well standardized numerical integration and the simulated waveform visualization program modules.

The proposed simulation technique has been applied to a single phase thyristor voltage doubler, a three-phase voltage-fed high-power-factor converter and a switching mode current amplifier [7]. In practice, reasonable simulation results have been obtained in all cases.

VII. Conclusions

A simulation technique of the power electronic conversion circuits and systems has been presented, in which the control algorithm described and tested in a simulation computer program can be embedded easily in the target equipment. This technique is based on a circuit equation modeled by time-varying resistance models depicting the active switches and the diodes, a state equation for the inductors and the capacitors, and an algebraic method to transform the matrices of the circuit equation into the matrices of the state equation. A feasible methodology to estimate the desirable calculation time step for the numerical integration was also

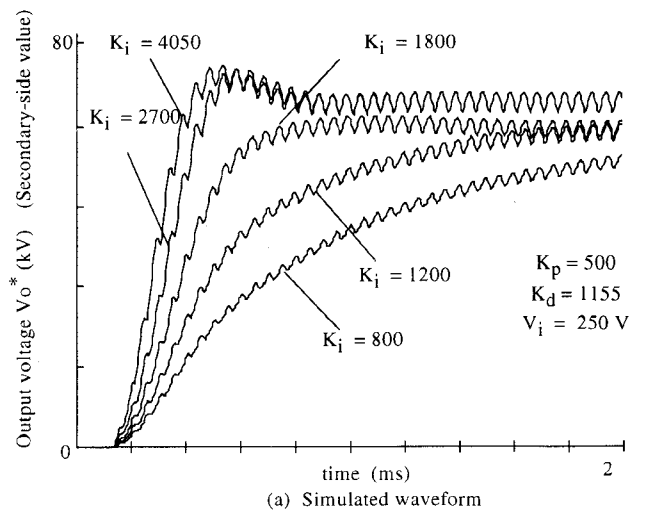

(a) Simulated waveform

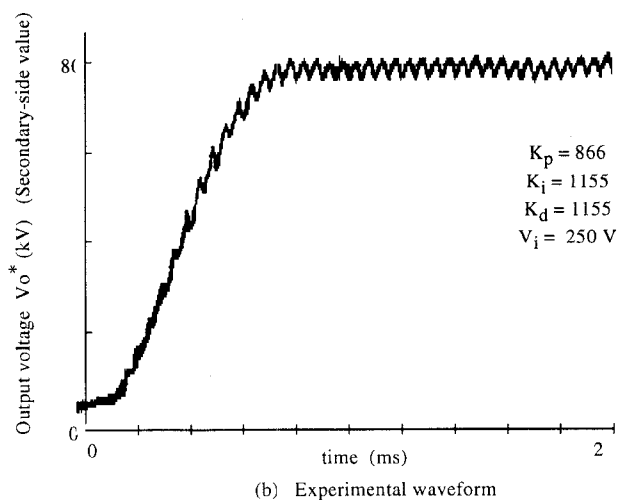

(b) Experimental waveform

Fig. 10 Simulated and experimental output voltage waveforms with the closed loop (R_L=1.04 Ω, V_o^*=80 kV, output power = 25 kW, K_i : integrated gain, K_p : proportional gain, K_d : derivative gain, V_i : inverter input voltage).

discussed based on the eigen-value which has the fastest convergence characteristic in the state equation. In this technique, less number of numerical calculations are performed because calculation is repeated for only one state equation. Moreover, this generic simulation approach is able to be applied for various switching mode power conversion circuits with the definition of the circuit equation, the switching transition and the control algorithm in the simulation program. Finally, the experimental results for application to the X-ray power generator using high-frequency resonant inverter with high-voltage transformer link have been presented in order to verify the simulation results.

In the near future, influences of complex conjugate type eigen-values to the appropriate calculation time step should be considered and investigated in practice.

REFERENCES

[1] G. D. Hachtel, R. K. Brayton, F. G. Gustavson, "The sparse tableau approach to network analysis and design," IEEE Transactions on Circuit Theory Vol.ct-18, No.1, pp.101-13, Jan. 1971.

[2] J. Burdio and A. Martinez, "A unified discrete-time state-space model for switching converters," IEEE Trans. on Power Electronics," Vol. 10, No. 6, pp.694-707, Nov. 1995.

[3] F. Witulski and R. Erickson, "Extension of state-space averaging to resonant switches and beyond," IEEE Trans. on Power Electronics, Vol. PE-5, No. 1, pp. 98-109, Jan. 1990.

[4] A. K. S. Bhat, "A generalized steady-state analysis of resonant converters using two-port model and Fourier-series approach," Proc. of IEEE-APEC, Vol. 1, pp. 920-926, Mar. 1995.

[5] H. Takano, T. Hatakeyama, J. M. Sun, E. Hiraki and M. Nakaoka, "Digital controlled resonant PWM DC-DC converter based on 32-bit RISC processor," Proc. of JIASC, Vol. E, pp. 44-49, Aug. 1996.

[6] H. Takano, T. Domoto, T. Hatakeyama, and M. Nakaoka, "A generic computer-aided simulation approach for digitally controlled switching mode power converter circuits and systems," Proc. of IEE-PEVD, pp. 483-489, Sep. 1996.

[7] H. Fukuda, H. Takano, T. Hatakeyama and M. Nakaoka, "Parallel operation of 4-switch full-bridge circuits and its an unique digital control scheme for advanced magnetic resonance imaging," Proc. of IEE-PEVD, pp. 366-371, Sep. 1996.

General Approach to a Novel Average-Current-Mode Control of the Constant Frequency Power Converters

Marko Janković, Predrag Ninković
Department of Automatic Control
EE Institute NIKOLA TESLA
Koste Glavinića 8a, 11000 BELGRADE, YUGOSLAVIA
Fax: +381-11-2351-823, Phone: +381-11-2351-412
E-mail: jankov00690p@buef31.etf.bg.ac.yu

Abstract - This paper presents stability analysis of a recently proposed average-current-mode control of the constant frequency power converters. In order to asses system stability considerations, small signal model of the proposed control circuit is developed. The model is valid for converters operating in the continuous conduction mode and it is accurate up to half of the switching frequency. Three methods for eliminating subharmonic oscillations are presented. The proposed control circuit is suitable for all applications where the average inductor current needs to be controlled - power factor correction circuits, battery charger/dischargers. Model predictions are well confirmed through the simulation results.

I. Introduction

Current-mode control [1] of switching power converters has significant advantages [4] over the more conventional voltage-mode control. Constant frequency converters are unstable for half of the range of the duty cycle ratio. Use of compensation ramp voltage can increase range of stability, but reduces benefits of current mode operation [4]. There have been reported several possibilities to overcome the above mentioned drawbacks associated with the current mode control. One of them is based on appropriate filtering of the current signal [5]. The filtered current signal is then compared to the sawtooth waveform in order to get switching instants. But proposed method has some drawbakcs. The main drawback of the implementation described is the need to reduce the pass band of the current loop gain in order to get well damped harmonics, as it can clearly be seen .

The novel average-current control method [2,3] is based on the inductor current integration between two turn-off instants. The initial value of the integrator is zero. Two methods for subharmonics oscillations elimination will be presented First method is based on using information about capacitor current, and second one is based on using information about inductor voltage.

Discrete time small signal analysis is presented. The buck converter with embedded control circuit (Fig. 1) has been investigated. It is shown that stability region can be extended well over the one half of the duty cycle range, without any deteriorating influence on the current loop pass band. Simulation results for the buck-boost and boost converters will also be presented.

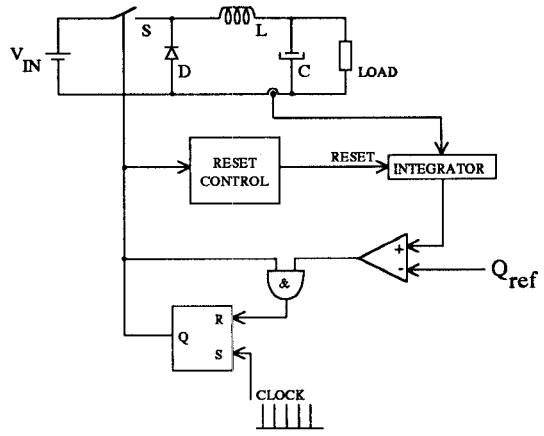

Fig. 1. Buck converter with embedded control circuit

II. Small Signal Discrete Time Analysis of the True Average Current Control

As previously pointed out, this method is based on inductor current integration over period starting from the switch off instant up to reaching the threshold level by the integrator output. Appropriate waveform of the inductor current is shown in Fig. 2. A buck converter is used as an example to show effectiveness of the proposed control method.

The goal of the following analysis is to obtain the poles of a small signal transfer function $i(z)/q_{ref}(z)$, where $i(k)$ and $q_{ref}(k)$ are small signal perturbations of the average inductor current $I_{sr}(kT)$ and the reference signal $Q_{ref}(kT)$ respectively, around their steady-state dc operating values I_{sr} and Q_{ref}. Only a converter operating in a continuous-conduction mode has been considered. Also, in order to simplify our analysis, the perturbation of input voltage V_{in} is assumed to be zero. For the same reason, the active and passive elements are assumed to be ideal.

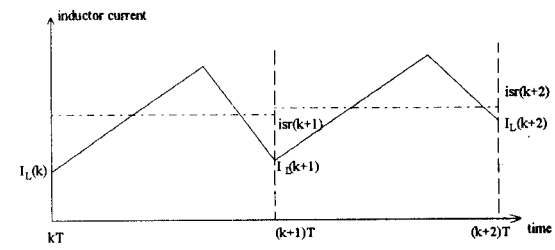

Fig. 2. Inductor current in two successive intervals

According to Fig. 2, the discrete-time equation which describes the large-signal inductor current is:

$$I_L(k+1) = I_L(k) + \frac{V_{in} - V_C(k+1)}{L} D(k+1)T - \frac{V_C(k+1)}{L}(1 - D(k+1))T \quad , \tag{1}$$

where $V_C(k+1)$ and $D(k+1)$ are the average capacitor voltage and duty cycle value over the switching interval k, respectively. This unusual connotation is due to the fact that average value over the switching interval k is available only at the end of the interval (which coincides with (k+1)T instant). Small signal perturbation derived from (1) is:

$$i_L(k+1) = i_L(k) + \frac{V_{in}}{L} d(k+1)T - \frac{v(k+1)}{L} T, \tag{2}$$

where $v(k+1)$ and $d(k+1)$ are the small signal perturbations of the average capcitor voltage and duty cycle over the interval k, respectively; $i_L(k)$ and $i_L(k+1)$ are the small signal perturbations of the inductor current at the instants kT and (k+1)T, respectively.

The discrete-time equation describing the large signal average inductor current (average value over past switching interval) is:

$$I_{sr}(k) = (I_L(k-1) + \frac{V_{in} - V_C(k)}{2L} D(k)T) D(k)T + (I_L(k) - \frac{V_C(k)}{2L}(1 - D(k))T)(1 - D(k))T \quad , \tag{3}$$

Small signal average inductor current perturbations, derived from (3), are described by:

$$i(k) = i_L(k-1)D + i_L(k)(1-D) + \frac{v(k)}{2L}(1-2D)T \tag{4}$$

Constraint equation is:

$$Q_{ref}(k+1) = I_{sr}(k)(1 - D(k))T + I_{sr}(k+1)D(k+1)T, \tag{5}$$

where $Q_{ref}(k+1)$ is average reference value over k-th interval. Small signal perturbations of duty cycle are described by:

$$d(k+1) = -\frac{(1-D)T}{Q_{ref}} i(k) - \frac{DT}{Q_{ref}} i(k+1) + d(k) + \frac{q_{ref}(k+1)}{Q_{ref}} \quad , \tag{6}$$

Small signal perturbations of the average capacitor voltage value can be expresed as:

$$v(k+1) = \frac{1}{1 + \frac{T}{RC}} v(k) + \frac{T}{C} \cdot \frac{1}{1 + \frac{T}{RC}} i(k+1), \tag{7}$$

Using equations (1)-(7) the following set of equations, is derived:

$$\begin{aligned} i(k+1) &= a_1 i(k) + a_2 v(k) + a_3 d(k) + a_4 v(k+1) + a_5 d(k+1) + a_6 q_{ref}(k+1) \\ v(k+1) &= b_1 i(k) + b_2 v(k) + b_3 d(k) + b_4 i(k+1) + b_5 d(k+1) + b_6 q_{ref}(k+1) \\ d(k+1) &= c_1 i(k) + c_2 v(k) + c_3 d(k) + c_4 i(k+1) + c_5 v(k+1) + c_6 q_{ref}(k+1) \quad , \end{aligned} \tag{8}$$

or, after some mathematical transformations:

$$\begin{aligned} i(k+1) &= x_1 i(k) + x_2 v(k) + x_3 d(k) + x_4 q_{ref}(k+1) \\ v(k+1) &= y_1 i(k) + y_2 v(k) + y_3 d(k) + y_4 q_{ref}(k+1) \\ d(k+1) &= z_1 i(k) + z_2 v(k) + z_3 d(k) + z_4 q_{ref}(k+1) \quad , \end{aligned} \tag{9}$$

which represents sampled-data averaged state-space model for small signals. Values of a_1, a_2, ..., c_5, c_6 can simply be evaluted from equations (1)-(6). As well, values of x_1, x_2, ..., z_3, z_4 can simply be evalueted from (8).

For all other converter configurations (boost, buck-boost and Ćuk) such set of equations can be derived in a similar manner.

III. Stability Analysis

From the previous analysis, it's obvious that the system matrix of the averaged state-space model is of the 3rd order. Since the characteristic polynomial is of the 3rd order too, symbolic analysis is difficult to perform. For that reason parametric analysis have been performed.

It is known that asymptotic stability is achieved if the roots of characteristic polynomial lie strictly inside the unit circle in the complex plane. According to this fact, position of the system poles have been considered. The power stage parameters of the buck converter were:

$$\text{Vin} = 20 \text{ V}, \text{ C} = 400 \ \mu\text{F}, \text{ L} = 37.5 \ \mu\text{H}$$

Parameters of this analysis were load resistance (R) and steady-state duty-ratio (D). Over the whole range of load resistance and D, two of the system poles were complex conjugate and the third one was real.

The module of the complex conjugate poles of the system versus load resistance is shown in Fig. 3, with the steady-state duty-ratio as a running parameter. The real pole of the system versus load resistance is shown in Fig. 4, with the steady-state duty-ratio (D) as a running parameter.

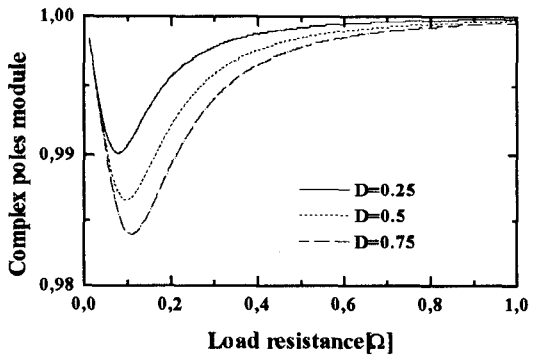

Fig. 3. The module of the complex poles of the system versus load resistance with the D as a running parameter

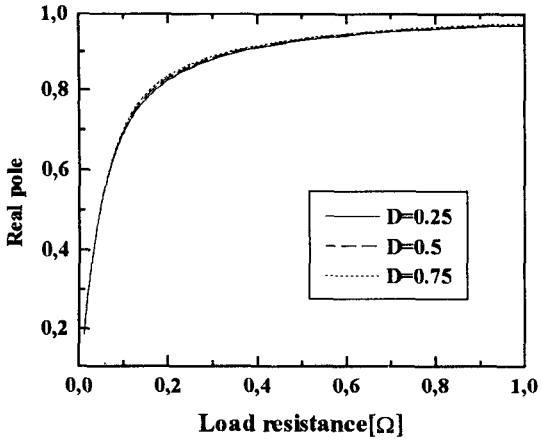

Fig. 4. The module of the real pole of the system versus load resistance with the D as a running parameter

Fig 3. and Fig. 4. show that the system is stable in the considered range. It is obvious, from Fig. 4, that value of the real pole has a weak dependence on value of D. Similar parametric analysis could be performed for other parameters of interest.

Fig 5. show current loop gain characteristic (R=0.1Ω, D=0.75). Subharmonic oscillations are not unexpected if we have in mind presence of the resonant peak.

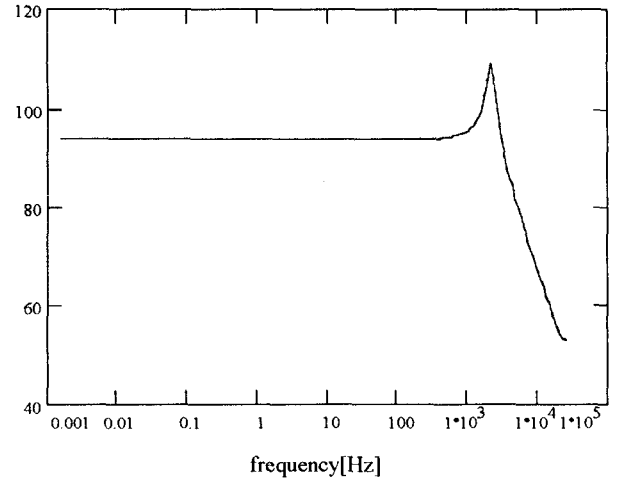

Fig. 5. Current loop gain

IV. Subharmonics Elimination Including Information About Capacitor Current

In this case integrator input is rather sum of inductor current and scaled capacitor current, than the inductor current only. Since the integral of the steady state capacitor current over integration period is zero, it does not introduce stedy-state error. Now, the constraint equation is:

$$\begin{aligned} Q_{ref}(k+1) &= I_{sr}(k)(1-D(k))T \\ &+ I_{sr}(k+1)D(k+1)T \\ &+ p(I_{sr}(k)-\frac{V_c(k)}{R})(1-D(k))T \\ &+ p(I_{sr}(k+1)-\frac{V_c(k+1)}{R})D(k+1)T, \end{aligned} \tag{5'}$$

and small signal perturbations are described by:

$$\begin{aligned} d(k+1) &= -\frac{(p+1)(1-D)T}{Q_{ref}}i(k) \\ &+ \frac{p(1-D)T}{Q_{ref}R}v(k) \\ &+ d(k)-\frac{(p+1)DT}{Q_{ref}}i(k+1) \\ &+ \frac{pDT}{Q_{ref}R}v(k+1)+\frac{q_{ref}(k+1)}{Q_{ref}}, \end{aligned} \tag{6'}$$

Now, in the same manner systems of equations (8) and (9), can be derived .

Fig. 6 shows current loop gain characteristic with p as a running parameter (R=0.1Ω, D=0.75). Benefits of the compensation signal are obvious.

In a similar way, equation (6') can be derived for the other types of converters.

V. Subharmonics Elimination Including Information About Inductor Voltage

In this case integrator input is rather sum of inductor current and scaled inductor voltage than inductor current only.

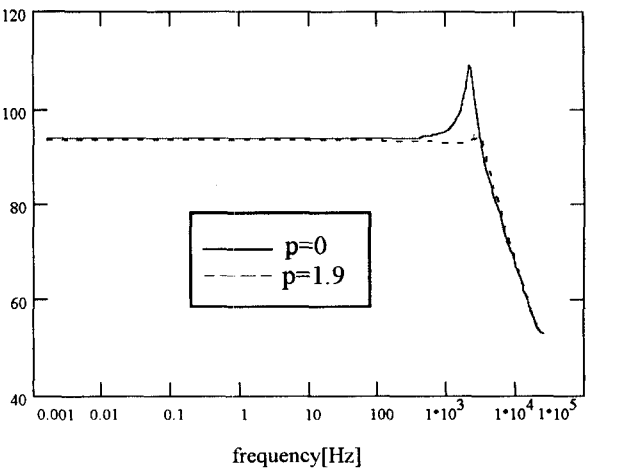

Fig. 6. Current loop gain with p∈{0,1.9} as a running parameter

Since the integral of the steady state inductor voltage over integration period is zero, it does not introduce stedy-state error. Now, the constraint equation is:

$$\begin{aligned} Q_{ref}(k+1) &= I_{sr}(k)(1-D(k))T \\ &+ I_{sr}(k+1)D(k+1)T \\ &+ l\cdot(V_c(k)-V_{in})(1-D(k))T \\ &+ l\cdot V_{in}\cdot D(k+1)T \end{aligned} \quad , \qquad (5")$$

and small signal perturbations are described by:

$$\begin{aligned} d(k+1) &= -\frac{(1-D)T}{Q_{ref}+lV_{in}T}i(k)+\frac{l(1-D)T}{Q_{ref}+lV_{in}T}v(k) \\ &+\frac{Q_{ref}-lV_{in}T\dfrac{D}{1-D}}{Q_{ref}+lV_{in}T}d(k) \\ &-\frac{DT}{Q_{ref}+lV_{in}T}i(k+1)+\frac{q_{ref}(k+1)}{Q_{ref}+lV_{in}T} \end{aligned} \quad , \qquad (6")$$

Fig. 7 shows current loop gain characteristic with l as a running parameter (R=0.1Ω, D=0.75). Benefits of the compensation signal are obvious.

It is interesting that for all types of the converters, equation (6") is the same.

VI. Unified Technique for Subharmonics Elimination

It is possible to unify two foremetioned techniques and create a general technique for subharmonics elimination. In this case integrator input is rather sum of scaled capacitor current, scaled inductor voltage and inductor current than inductor current only. Now, the constraint equation is:

$$\begin{aligned} Q_{ref}(k+1) &= I_{sr}(k)(1-D(k))T \\ &+ I_{sr}(k+1)D(k+1)T \\ &+ p\cdot(I_{sr}(k)-\frac{V_c(k)}{R})(1-D(k))T \\ &+ p\cdot(I_{sr}(k+1)-\frac{V_c(k+1)}{R})D(k+1)T \\ &+ l\cdot(V_c(k)-V_{in})(1-D(k))T \\ &+ l\cdot V_{in}\cdot D(k+1)T \end{aligned} \quad , \qquad (5''')$$

and small signal perturbations are described by:

$$\begin{aligned} d(k+1) &= -\frac{(1+p)(1-D)T}{Q_{ref}+lV_{in}T}i(k)+\frac{(l+\frac{k}{R})(1-D)T}{Q_{ref}+lV_{in}T}v(k) \\ &+\frac{Q_{ref}-lV_{in}T\dfrac{D}{1-D}}{Q_{ref}+lV_{in}T}d(k)-\frac{(1+p)DT}{Q_{ref}+lV_{in}T}i(k+1) \\ &+p\cdot\frac{DT}{R}\cdot\frac{v(k+1)}{Q_{ref}+lV_{in}T}+\frac{q_{ref}(k+1)}{Q_{ref}+lV_{in}T} \end{aligned} \qquad (6''')$$

Effects of the proposed techniques are investigated on the buck topology. Simulations were performed for different circuit parameters and different values of the compensation coefficients (l,p). It was concluded (based on simulation results) that two aforementioned techniques show lack of effectiveness in the light load area. In other words, subharmonics elimination could not be achieved without reducing the gain pass-band. Applying the unified technique subharmonics can be removed without any deteriorating influence on the pass-band. Of course, proper values of compensation coefficients must be chosen.

As an illustration fig. 8 shows effects of the unified compensation technique (dash-dotted line), in the case of the light load, compared to single-signal compensation techniques (scaled capacitor current - dashed line, scaled inductor voltage - dotted line). Solid line curve represents current loop gain characteristics without any compensation.

VII. Simulation Results

Proposed control method is applied to buck topology. Power stage parameters are chosen to fulfill stability conditions. Simulation was based on ideal switches and ideal passive components.

Simulation of the converter response to 10% step change of the reference value Q_{ref} was shown on Fig. 9. Characteristic parameters were:

L= 37.5 μH, C=400μF,
V_{in}= 20 V, R = 0.1Ω,
T = 20 μs,
Q_{ref}= 3000+300μC (corresponds to D=0.75+.075).

Fig. 10 shows response of the converter to 10% step change of reference value Q_{ref}. Figure shows that subharmonic oscillations were present (oscillations are not well damped. Fig. 11 shows response of the same converter to same reference step, but with additional compensation network (addition of capacitor current to

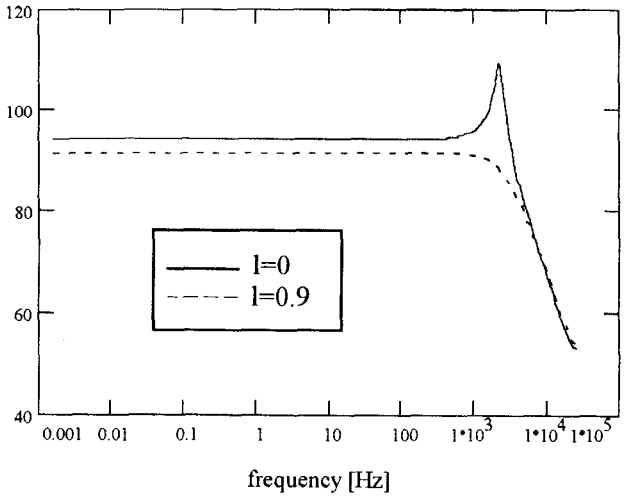

Fig. 7. Current loop gain with l∈{0,0.9} as a running parameter

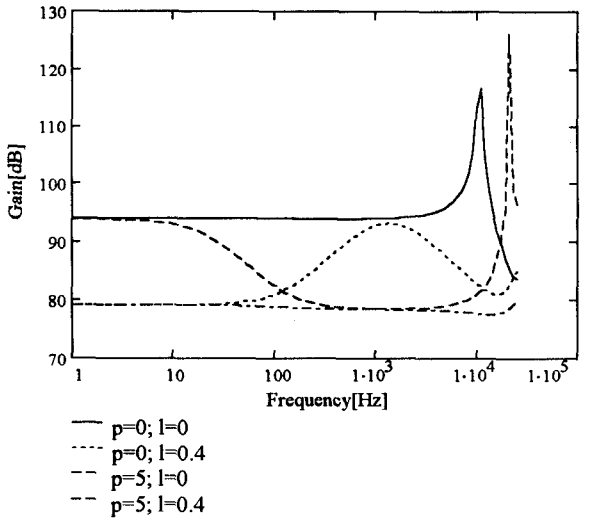

Fig. 8. Current loop gain for different values of compensation factors p and l (R=3Ω, D=0.75)

integrator input) in the current loop. By choosing big enough multiplicand (p) of the capacitor current, subharmonic oscillations can be removed. Characteristic parameters were: L= 37.5 μH, C= 400 μF, V_{in}= 20 V, R= 0.01Ω, T= 20 μs, Q_{ref}= 10000 + 1000 μC (corresponds to D = 0.25 + 0.025).

Similar results can be obtained if inductor voltage is used as a compensation signal.

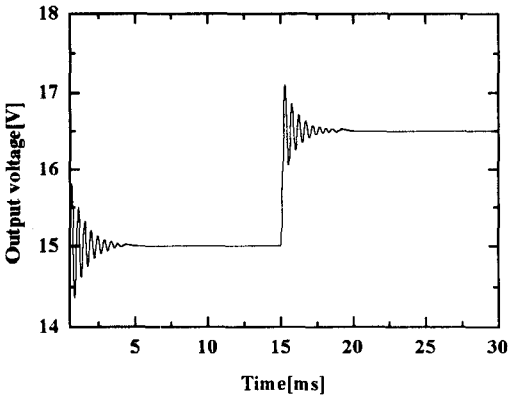

Fig. 9. Converter response to 10% step of reference value

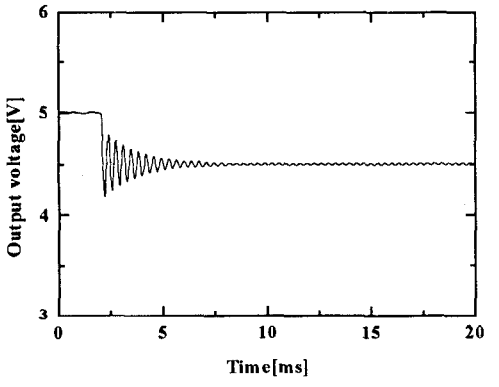

Fig. 10 Simulation of converter response to 10% step change of reference (p=0)

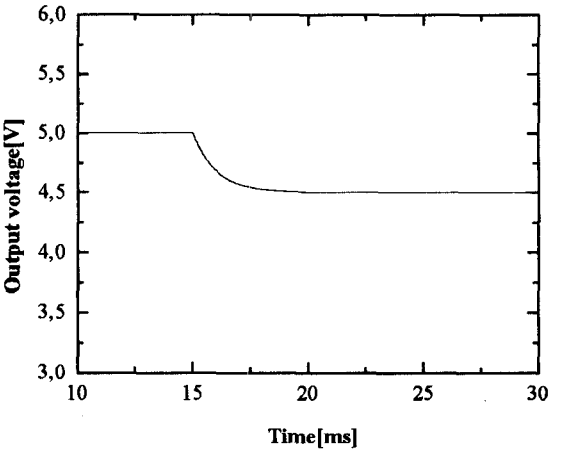

Fig. 11 Simulation of converter response to 10% step change of reference (p=100)

Fig. 12 shows response of the buck-boost converter from zero to steady-state and response to 10 % step change of the reference value in three cases: without compensation (p=0, l=0), including information about capacitor current (p=-0.5, l=0) and including information about inductor voltage (p=0, l=3). Characteristic parameters were:

L=37.5 μH, C=400 μF,
V_{in}= 20 V, R= 0.4Ω,
T=20 μs,
Q_{ref}=3000+300μC.

One of the most interesting aplications of the boost converter is in the PFC circuits. Fig. 13 shows results of the applications of the proposed control algorithm in such circuit. During the first half-period of line voltage, basic algorithm is applied (without compensation). In the second half-period compensation techniques are applied, also. The output voltage of boost converter has already reached steady-state value.

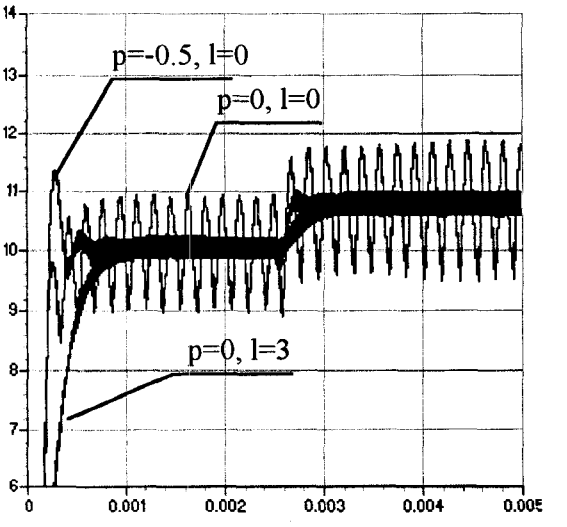

Fig. 12. Influence of the compensation techniques to the buck-boost converter stability

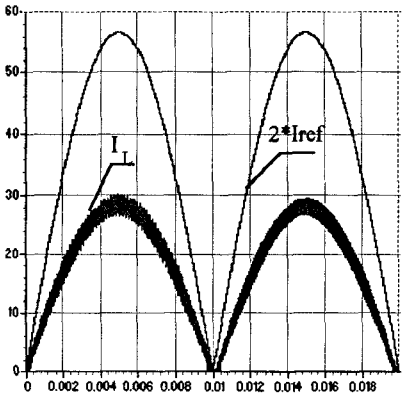

Fig. 13. Boost converter in PFC circuit (first half- period is without compensation, second is with compensation techniques)

VIII. Conclusion

The new control concept for DC/DC converters control with fast inner loop has been presented. The proposed control can be adjusted so that full range of duty cycle is available for stable operation (without subharmonic oscillations). Also, two methods for subharmonic oscillations elimination are analyzed. It was shown that both methods are efficient in improving system stability. An algorithm for choosing the optimal compensanting parameters is under investigation. Also, it was shown that in the light load cases, unified compensation technique is superior in comparison to single-signal compensation techniques.

References

[1] C. Deish, "Simple switch control method changespower converter into a current source," in *Proceedings of the 1978 IEEE PESC,* pp. 300-306.

[2] M. Janković, P. Ninković and Ž. Janda, "A Novel Approach to Current-Mode Control of the Constant Frequency Power Converters," in *Proceedings of the 1996 IEEE International Symposium on Industrial Electronics*, Vol. 1, pp. 488-492.

[3] P. Ninković, Ž. Janda and M. Janković, "Stability Analysis of the Quasi-Charge and Novel Average Current-Mode Control Of The DC/DC Converters," in *Proceedings of the 1996. Power Electronics and Motion Control Conference*, Vol. 1, pp. 263-267.

[4] R. Redl and N.O. Sokal, "Current-mode control, five different types, used with three basic classes of converters," in *Proceedings of the 1985 IEEE PESC* Rec., pp. 771-785.

[5] W. Tang, F.C. Lee and R.B. Ridley, "Small-Signal Modeling of Average Current-Mode Control," *IEEE Trans. Power Electronics*, Vol.8, no. 2, Apr. 1993, pp. 112-119.

The Characteristics Analysis of PWM Inverter-Fed 3-Phase Induction Motor from View Point of Saturation

Katsumi Kamimoto
Dept. of Electric Eng. , Daido Institute of Technology
21-2, Daido-cho, Minami-ku, Nagoya 457, JAPAN
Phone: 052-611-0513 Ext. 243, Fax: 052-612-5653, E-mail: kamimoto@daido-it.ac.jp

Naoyuki Andoh Yoshihiro Murai
Dept. of Electric Eng. , Gifu University
1-1, Yanagido, Gifu 501-11, JAPAN
Phone: 058-293-2703, Fax: 058-230-1894, E-mail: ando@cc.gifu-u.ac.jp, murai@cc.gifu-u.ac.jp

Abstract – **This paper describes how to analyze the characteristics of PWM inverter-fed 3-phase induction motor in consideration of saturation by different means from conventional ones. Starting and steady state characteristics of inverter drive are presented. In steady state, torque characteristics are presented under irregular on-off time of PWM inverter drive. Flux loci, currents and torques are presented with the lapse of time. Above all, flux locus is most interesting and important to know how flux is formed and reaches saturation. Saturation helps a machine come to steady state far quicker and reduce vibrating torque. This paper shows how the saturation exerts the influence upon the starting and steady state characteristics.**

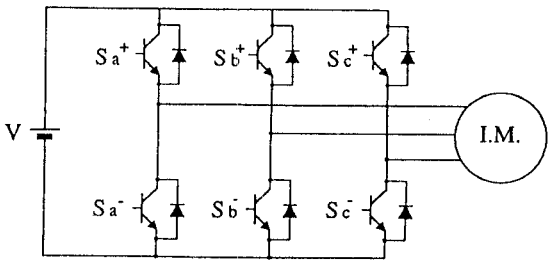

Fig.1. PWM inverter and 3-phase induction motor.

I . INTRODUCTION

The advent of inverter enables us to control a motor freely by variable voltage and frequency. PWM inverter has come into popular use to drive an induction motor. Recent industry requires slight saturation to take into the manufacture of induction motor to reduce size and cost. The transient current and excessive heat from saturation are the urgent affairs and prediction of the saturation characteristics has come to important problems. Although many papers have been published about the characteristics of PWM inverter-fed 3-phase induction motor, few of them discuss the characteristics in consideration of saturation. To author's best knowledge, few papers published so far have discussed the stability alone with PWM inverter and saturation combined, while they have not dealt with individual characteristics at all. [1]~[4] This paper shows how to analyze the starting and steady state characteristics of an induction motor fed by PWM inverter shown in Fig.1 from view point of saturation. In this paper, saturation is expressed by the variable self and mutual inductance with flux. Most part depends on experimental curve based on voltage or flux. But in excessive high voltage, inductance is expressed by Frölich's law.

II .DEFINITION OF NOTATIONS

Followings are main notations used in this paper.
V : effective value of line voltage
R_1 : stator resistance
R_2' : rotor resistance referred to stator resistance
i_γ: γ–component of stator current
i_δ : δ–component of stator current
$i_{2\gamma}$: γ–component of rotor current
$i_{2\delta}$: δ–component of rotor current
Φ_γ: γ-component of stator flux
Φ_δ : δ-component of stator flux
$\Phi_{2\gamma}$: γ-component of rotor flux
$\Phi_{2\delta}$: δ-component of rotor flux
T : instantaneous torque
Φ_m : main saturated flux
$L_1(\Phi m)$: stator self-inductance as the function of Φ_m
$L_2'(\Phi m)$: rotor self-inductance referred to stator self-inductance as the function of Φ_m
$M(\Phi m)$: mutual inductance between stator and rotor as the function of Φ_m
ω : inverter angular frequency
ω_m : motor angular speed

0-7803-3823-5/97/$10.00© 1997 IEEE

s : slip
p : d / dt
ρ : saturation factor of Frölich's formula
ϕ : unsaturated flux
P : the number of pair of poles
fc : carrier frequency

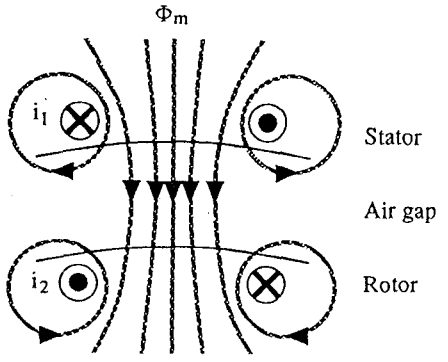

Fig.2. Model of main flux and currents.

III. FUNDAMENTAL EQUATIONS

Followings are motor equations expressed by γ-δ axes which rotate with inverter angular frequency.

$$V = R_1 i_\gamma + p \Phi_\gamma - \omega \Phi_\delta \quad (1)$$

$$0 = R_1 i_\delta + p \Phi_\delta + \omega \Phi_\gamma \quad (2)$$

$$0 = R'_2 i_{2\gamma} + p \Phi_{2\gamma} - s \omega \Phi_{2\delta} \quad (3)$$

$$0 = R'_2 i_{2\delta} + p \Phi_{2\delta} + s \omega \Phi_{2\gamma} \quad (4)$$

Φ_γ, Φ_δ, $\Phi_{2\gamma}$ and $\Phi_{2\delta}$ are generally saturated. The relation between flux and current are expressed by (5)~(8).

$$\Phi_\gamma = L_1 (\Phi_m) i_\gamma + M (\Phi_m) i_{2\gamma} \quad (5)$$

$$\Phi_\delta = L_1 (\Phi_m) i_\delta + M (\Phi_m) i_{2\delta} \quad (6)$$

$$\Phi_{2\gamma} = M (\Phi_m) i_\gamma + L_2' (\Phi_m) i_{2\gamma} \quad (7)$$

$$\Phi_{2\delta} = M (\Phi_m) i_\delta + L_2' (\Phi_m) i_{2\delta} \quad (8)$$

Torque is expressed by (9).

$$T = P M (\Phi_m) \left(i_\delta i_{2\gamma} - i_\gamma i_{2\delta} \right) \quad (9)$$

When M(Φm) is constant, (9) is held in linear form and usually used.

(1)~(4) multiplied by i_γ, i_δ, $i_{2\gamma}$ and $i_{2\delta}$ in this order and then the sum of last each term come to mechanical output (10).

$$P_m = \omega \left\{ \Phi_\gamma i_\delta - \Phi_\delta i_\gamma + s \left(\Phi_{2\gamma} i_{2\delta} - \Phi_{2\delta} i_{2\gamma} \right) \right\} \quad (10)$$

There is another expression of torque.

$$T = P_m / \omega_m \quad (11)$$

(9) and (11) come to the same result in each slip except "s = 1". ω_m is zero at starting "s = 1". Because denominator comes to zero, (11) can not be used. Instead of it, P_m is zero with "s = 1" and "s = 0". This fact can be used to discriminate if the computer software is theoretically right.

IV. THE EXPRESSION OF SATURATION

When circuit contains inductance, it changes with saturation, in broad sense. Here, the new way how to express the self and mutual inductance are described in regard to saturation. Fig.3 shows T-type equivalent circuit of one-phase for 3-phase induction motor under normal load.

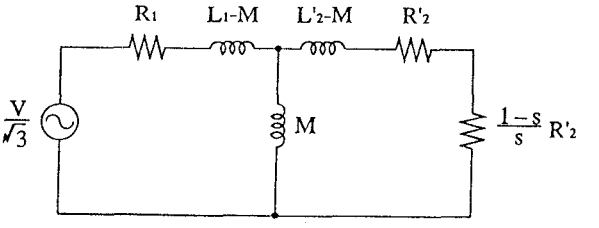

Fig.3. T-type equivalent circuit of induction motor.

L_1 is determined by no-load test. However, it is difficult to make complete no-load in lower voltage. Because the torque is so small that no-load can not be made on account of friction and fan loss. For this reason, tested motor is driven by another motor with synchronous speed. In this way, complete no-load is made. Fig.4 shows no-load equivalent circuit.

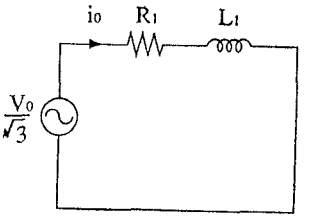

Fig.4. No-load equivalent circuit. (s=0)

Variable line voltages V_0 and their currents i_0 are measured

from zero to over rated voltage. Φ_m is calculated by (12).

$$\Phi_m = \frac{\sqrt{3}\left(V_0/\sqrt{3} - R_1 i_0\right)}{\omega} \tag{12}$$

Foremost $\sqrt{3}$ is the coefficient produced by the conversion from 3-phase to $\gamma-\delta$ axes. Next equation is available in no-load equivalent circuit on condition "s = 0".

$$i_0 \sqrt{R_1{}^2 + \omega^2 L_1{}^2} = V_0/\sqrt{3} \tag{13}$$

L_1 is determined by variable line voltages V_0 and their currents i_0 with (13). Therefore, the relation between L_1 and Φ_m is determined by (12) and (13). L_1 is the function of Φ_m.

On the other hand, M is determined by lock test. Fig.5 shows the lock test equivalent circuit on conditions "s=1" and $L_1=L'_2$.

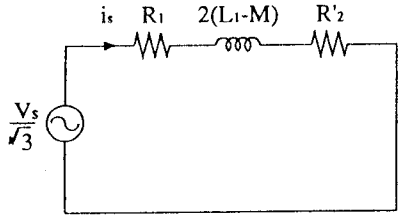

Fig.5. Lock test equivalent circuit. ($s = 1, L_1 = L'_2$)

Next equation is held in lock test.

$$i_S \sqrt{\left(R_1 + R'_2\right)^2 + 4\omega^2\left(L_1 - M\right)^2} = V_S/\sqrt{3} \tag{14}$$

With variable short currents i_s and their line voltages V_s, M is determined by (14) with known L_1. As a result, M is a little smaller than L_1. M is the function of Φ_m, too. As the difference between L_1 and M does not change with Φ_m, leakage inductance is constant in regard to saturation. The experimental result L_1-Φ_m is approximated by the arc of a circle for simple manipulation. The upper part of circle equation is expressed by (15) and shown by part ① in Fig.6.

$$L_1\left(\Phi_m\right) = -\frac{k}{2} + \sqrt{\frac{h^2+k^2}{4} + c - \left(\Phi_m - \frac{h}{2}\right)^2} \tag{15}$$

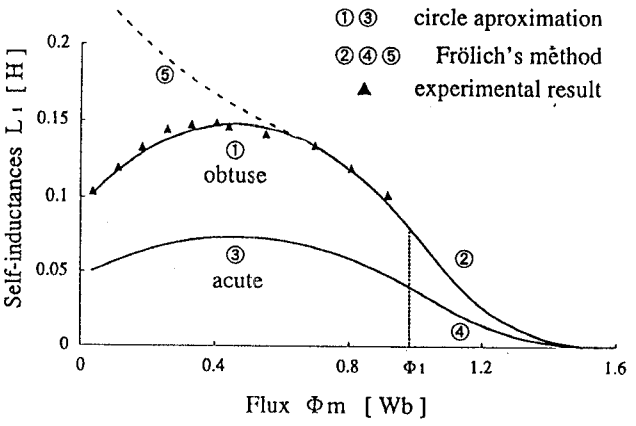

Fig.6. Relation between self-inductances and flux.

Apart from new expression of saturation, discussion comes to conventional way. Frölich's formula has often been used, because it shows the saturation comparatively well. Frölich's formula and its main flux are expressed by (16) and (17), respectively.

$$\Phi_m = \frac{\phi}{1 + \rho\,\phi} \qquad \text{(Frölich's formula)} \tag{16}$$

$$\Phi_m = \sqrt{\Phi_\gamma{}^2 + \Phi_\delta{}^2} \tag{17}$$

Fig.7 shows the outline of Frölich's formula (16) for different ρ.

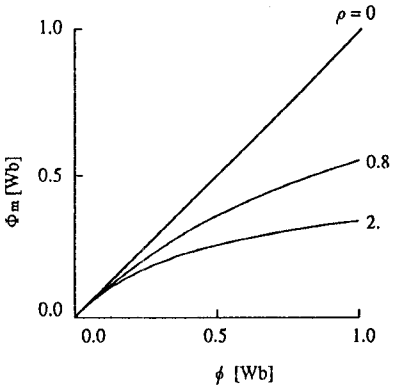

Fig.7. Saturation curves of Frölich's method.

When flux is not saturated, Φ_m is linear in terms of ϕ ($\rho = 0$). Φ_m- ϕ curve changes with ρ. Φ_γ and Φ_δ are usually saturated and determined by (1)~(8). Self-inductance L_1 is determined by next form.

$$L_1 = \partial\,\Phi_m/\partial\,\phi = \left(1 + \rho\,\phi\right)^{-2} \tag{18}$$

L_1 can be expressed by the function of Φ_m from (16) and (18).

$$L_l(\Phi_m) = \left\{ 1 + \rho\Phi_m / (1 - \rho\Phi_m) \right\}^{-2} \qquad (19)$$

(19) is self inductance expressed by Frölich's method and corresponds to part ② and ⑤ in Fig.6.[5] This curve shows monotonous and acute descent. In higher voltage which can not be measured (Φ_l, over 250 [V]), Frölich's method is employed. Because L_l reaches zero acutely in circle approximation but gradually in Frölich's method. The new expression of saturation is the combination of the circle approximation ① and Frölich's method ②. Part ③ and part ④ are 50 [%] of part ① and ②, respectively. Lower curve is much acuter than upper curve in saturation. The degree of saturation is determined by material and shape of iron core. The acute saturation is realized by the iron core with short length and thin air gap. In the voltage usually used, L_l is higher than the experimental result in Frölich's method. In excessive lower voltage, L_l decreases in experimental way, while L_l increases in Frölich's method. The difference becomes larger toward lower voltage. For this reason, Frölich's method can not express the saturation with accuracy, especially in lower voltage. Therefore, the new expression of saturation is much better than that of Frölich's method.

V. THE CHARACTERISTICS

A. Starting characteristics

In starting, lower frequency and voltage are applied to avoid the saturation. So, 30 [V] and 6 [Hz] are applied to get the all starting characteristics. Fig.8(a) and (b) show flux loci in stationary axes which correspond to saturation curve ①, ② and ③,④ in Fig.6, respectively. d-q axes are stationary. Vertical axis is d-axis. Horizontal axis is q axis. On the other hand, $\gamma-\delta$ axes are rotating with inverter angular frequency. Φ_γ and Φ_δ are determined by simultaneous equation (1)~(8) with the lapse of time. Conversion from $\gamma-\delta$ axes to d-q axes using (20) and elimination of time come to these figures.

$$\begin{bmatrix} \Phi_d \\ \Phi_q \end{bmatrix} = \begin{bmatrix} \cos\omega t & -\sin\omega t \\ \sin\omega t & \cos\omega t \end{bmatrix} \begin{bmatrix} \Phi_\gamma \\ \Phi_\delta \end{bmatrix} \qquad (20)$$

The direction of radius is that of resultant flux Φ_d and Φ_q. The locus moves clockwise with the lapse of time and approaches the fixed circle. These figures show us how fluxes are formed and reach saturation. (b) is much acuter than (a) in saturation. In acuter saturation, diameter of flux locus is smaller and flux come to steady state far quicker. Steady state means that flux approaches the fixed circle whose center is situated in the origin. Fig.9 (a) and (b) show A-phase currents and torques which correspond to ①, ② and ③, ④ in Fig.6, respectively. In the first place, fluxes of $\gamma-\delta$ axes are determined by the simultaneous equation (1)~(8). Then, the currents are determined by (5)~(8). Conversion from 2 phases to 3 phases using (21) comes to 3-phase currents.

$$\begin{bmatrix} i_a \\ i_b \\ i_c \end{bmatrix} = \begin{bmatrix} \cos\omega t & -\sin\omega t \\ \cos(\omega t - 2\pi/3) & -\sin(\omega t - 2\pi/3) \\ \cos(\omega t + 2\pi/3) & -\sin(\omega t + 2\pi/3) \end{bmatrix} \begin{bmatrix} i_\gamma \\ i_\delta \end{bmatrix} \qquad (21)$$

On the other hand, torque is obtained by (9). Torque comes to steady state far quicker in an acute saturation. There is a little difference between currents in the degree of saturation. From this fact, special care against heat need not be taken into the consideration.

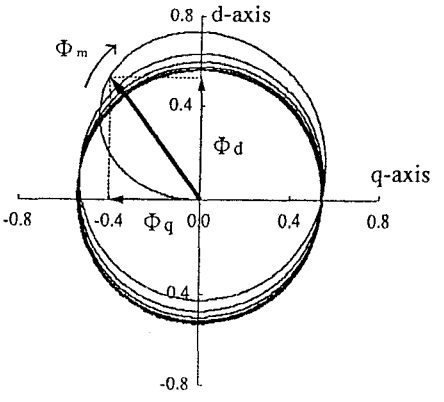

(a) Obtuse saturation.

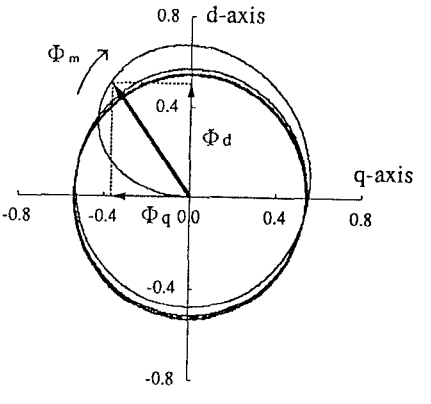

(b) Acute saturation.

Fig.8. Flux loci.

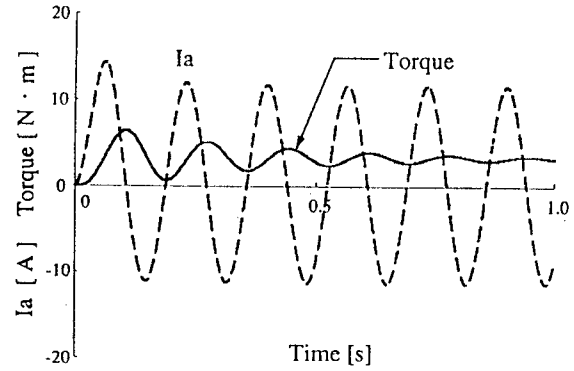

(a) Obtuse saturation.

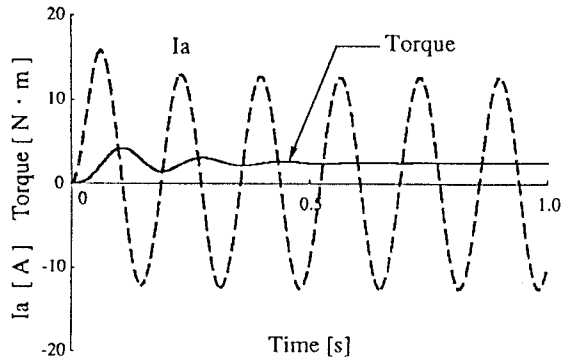

(b) Acute saturation.

Fig.9. A-phase currents and torques.

B. Imbalance switching characteristics in steady state

In the practical use of PWM inverter, it often happens that on-off switching operation is irregular on account of the digital error of controller. The error is about 0.5 [usec] or so. The deviation from the regular PWM operation is remarkable in higher carrier frequency and lower output voltage. On-time happens to be longer or shorter than the regular PWM operation. Here, the on-time of "Sa" in Fig.1 alone is assumed to be longer than the regular PWM operation. The sum of on and off-time does not change. Off-time is shorter than the usual PWM operation. So, the off-time is delayed by certain period. This period is supposed to say "delayed time". B and C-phase on-off time obey PWM rule. Fig.10 shows relation between vibrating torque and delayed time on conditions s=0.04, (rated load), inverter frequency 60 [Hz], carrier frequency 5 [kHz]. Vertical axis is the amplitude of vibrating torque [N · m]. Horizontal axis is imbalance ratio [%]. Characteristics (a) and (b) correspond to ①, ② and ③, ④ in Fig.6, respectively. 3 cases of delayed time 1,3 and 5 [u sec] are tried. Fig.11 shows irregular on-off operation of PWM inverter.

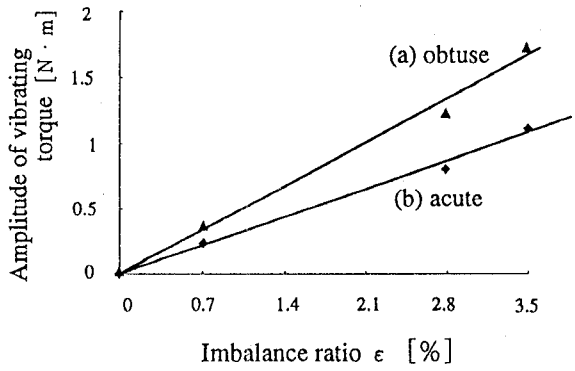

Fig.10. Imbalance ratio and amplitude of vibrating torque. (s = 0.04, f = 60[Hz], fc = 5[kHz])

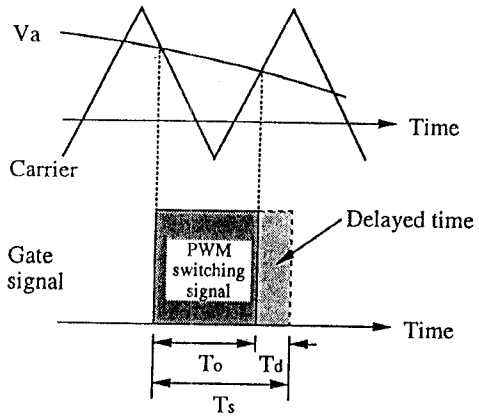

Fig.11 Irregular on-time of PWM inverter.

"To" is regular on-time. "Td" is delayed time. Whole on-time "Ts" is sum of "To" and "Td". "STs" is the whole sum of "Ts" during half period with delayed time. "STo" is the whole sum of "To" during half period without delayed time. Imbalance ratio ε is defined by (22).

$$\varepsilon = \frac{STs - STo}{STo} \times 100 \ [\%] \qquad (22)$$

The amplitude of vibrating torque is greater with greater imbalance ratio and obtuse saturation. Saturation helps vibrating torque decrease in irregular switching operation.

Fig.12 shows the simulation of vibrating torque in regard to the degree of saturation. (a) and (b) correspond to ①, ② and ③, ④ in Fig.6, respectively. Vibrating torque is greater in longer delayed time and obtuse saturation.

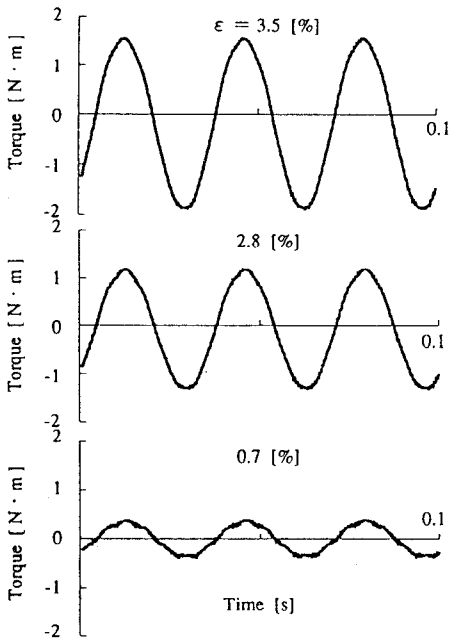

(a) Obtuse saturation.

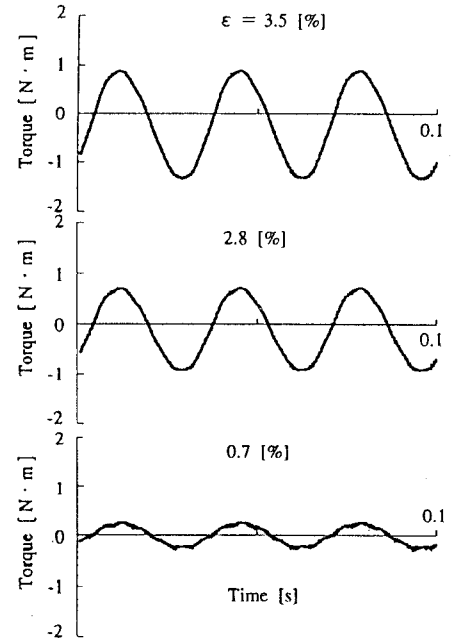

(b) Acute saturation.

Fig.12. Simulation of vibrating torque.
(s = 0.04, f = 60[Hz], fc = 5[kHz])

Table-1 motor and other constants

3-phase induction motor
2.2kw 2 poles
R_1=0.834[Ω] , R_2'=0.435 [Ω]
L_1=L_2'=133 [mH] , M=127 [mH] (rated)
h=-0.905 , k=3.99 , c=-0.409

VI. CONCLUSIONS

The characteristics of PWM Inverter-fed 3-phase induction motor drive have been made clear in starting and steady state. Emphasis is placed on torque. Flux locus is very useful to see how flux is formed and reaches saturation. This paper shows how self and mutual inductance change in Frölich's formula and other unique method. Special care against heat is not needed, because saturation does not make current increase so much. Therefore, saturation is useful for ON-OFF drive of PWM inverter-fed 3-phase induction motor. But effective power has not been discussed yet. This paper rounds off with next conclusions.

(1) Self and mutual inductance change with saturated flux.
(2) Saturation makes torque come to steady state faster in starting.
(3) Saturation decreases vibrating torque in irregular switching operation of steady state.
(4) Saturation does not make current increase so much.

REFERENCES

[1] Takeshi Kishimoto, Kenji Matsumoto, Takayuki Kamakura, Masakatsu Daijo,"Satability Analysis of a Voltage souce PWM Inverter-Fed Induction Motor Drive", The Transaction of the Institute of Electrical Engineer of Japan Vol. 106-B No. 9 Sept.pp.1~8, 1986

[2] Muneaki Isida, Minoru Ueda, "Stability Analysis for Current Source Type Induction Motor Drive Take into Considaration the Iron Loss and the Saturation of the Air-gap Flux" ,The Transaction of IEEE, Vol.100-B, No.9,Aug.,pp.25~32,198

[3] Yi-kang H.E and T.A.Lipo,"Saturation Effects in Stability Analysis of a VSI Induction Motor Drive", IPEC-Tokyo'83,pp.181~192, 1983

[4] J.E.Brown,K.P.Kovacs, P.Vas "A method of including the effects of main flux path saturation in the generalized equation of A.C.machines", IEEE Transactions on Power Apparatus and Systems, Vol.PAS-102,No.1,January pp.96~103,1983

[5] Katsumi Kamimoto, Naoyuki Andoh, Yoshihiro Murai,"Starting characteristics of 3-phase induction motor in considaration of saturation", 1997 National Convention Record I.E.E.Japan Vol.7 1101,pp.5-38~5-39

The IGBT - An Optimized Device for System Integration

by

L. Lorenz

Siemens AG
Semiconductor Group
Balanstr. 73
81541 Munich

Summary:

Recent innovations have clearly shown that the IGBT concept has considerable scope for further development in terms of improving saturation voltage in the on-state as well as dynamic losses whilst maintaining ruggedness and the excellent limit load tolerances. Both the horizontal optimization of the cell structure and the vertical optimization of the Si material have led a to dramatic improvement in $V_{CE\,sat}$ values. This new NPT concept is now applied in the voltage range between 600 V and 3.5 kV. By means of additional charge carrier lifetime adjustment, the turn-off behavior has been improved in terms of lower tail losses. This means the IGBT can now be used in applications which to date have been the preserve of power MOSFETs. The Econopack has extended package families to allow the implementation of new, more economical, flexible and reliable construction techniques for DC/AC converters for drive systems. The Econopack is a solderable package with exceptionally low parasitic inductance and simple parallel connection.

Introduction:

Power components are the driving force behind further innovation in power-electronics systems engineering, especially in terms of energy saving, higher dynamic characteristics, and a reduction in noise, volume and weight. Power semiconductors control the energy flow between the energy source and the load and are thus key components in control systems. Increasing automation and the need to use energy rationally call for modern power components with high switching speeds, low switching losses and a drive drawing minimum power. To improve system efficiency, power switches with high clock frequencies in the range $4\ kHz \le f_T \le 20\ kHz$ for DC/AC converters for motor drives and $40\ kHz \le f_T \le 70\ kHz$ for SMPSs (switch mode power supplies) must exhibit low overall losses, i.e. both low dynamic and static loss ratios. To reduce the system overheads - volume and weight - a uniform switching concept is required over as wide a performance band as possible ($1\ A \le I_L \le 2500\ A$; $50\ V \le U_{BR} \le 3.5\ kV$). The switch clock frequency ($f_T \ge 20\ kHz$) is also crucial in terms of reducing volume and weight for many power-electronics systems, such as UPS systems, switched power supplies etc. With regard to noise generation and the con-

0-7803-3823-5/97/$10.00

trol response for AC motor drives, significant progress has already been made with clock frequencies in the range 4 kHz $\leq f_T \leq$ 10 kHz /6/7/. For noiseless operation, switches must reach clock frequencies of fT $\geq$ 16 kHz, whilst also exhibiting low losses. Great demands are also being placed on ruggedness as well as the control concept of power switches. Components resistant to short circuits, avalanche and latch-up, and power semiconductor switches with parasitic semiconductor structures that are not used in practical applications, are essential. To be able to implement optimized pulse control systems without heavy electronic overhead, power switches must track the pulse plot without delay, i.e. without storage and delay times /5/. In addition, both drive effort and drive power must be as low as possible and switching times adjustable in a selective and reproducible form. Increased use of microelectronics in power control means complex control concepts and optimized pulse control techniques can be implemented whilst, however, placing greater demands on the semiconductor components used. Fig. 1 shows the development of power semiconductor components up to the end of the decade. Following the years of uncertainty between 1985 and 1988 as to which basic semiconductor switching concept would prevail for low and medium-performance power components, today the way forward is clear: power MOSFETs or IGBTs are being designed into all new system developments. Important development goals over the next few years, especially for IGBTs, are: increasing the current range 1 A $\leq I_L \leq$ 2500 A, the voltage range 600 V $\leq U_{BR} \leq$ 3500 V, the switching frequency 2 kHz $\leq f_T \leq$ 100 kHz, improving the pulse compliance, reducing the drive and protection overhead and the V_{CEsat} values, along with manufacturing costs and increase ruggedness.

Semiconductor concepts

In principle there are currently two different solutions for implementing user-specific IGBTs: The "epitaxial structure", also referred to as the PT IGBT and the "homogenous structure", also referred to as the NPT IGBT. The epitaxial structure is characterized by the fact that the charge carrier lifetime is reduced by radiation. The homogenous structure however only includes a specially designed p^+n junction on the reverse and does not require epitaxy. In principle this structure can be used for any voltage provided edge passivation permits. Major recent development goals have been to reduce the saturation voltage V_{CEsat}, increase clock frequency whilst retaining IGBT ruggedness. In the following we illustrate two steps in which power dissipation in the IGBT was drastically reduced /1/.
Step 1 concerns horizontal optimization of the cell structure, step 2 the vertical optimization of the Si material.

Step 1:
For a reduction of IGBT losses, an on-state voltage improvement is necessary. The principal, well-known contributions to IGBT on-state voltage result from the MOS channel resistance, the junction FET resistance between the MOS cells, and the drift resistance in the n^--layer. Therefore, a shrinkage of the MOS transistor cell structure (Fig. 2) by both a significant reduction of the p-well depth "d" (= reduction of junction-FET) and of the channel length "l" (= lower channel resistance and greater forward transconductance), leads to a lower on-state voltage. Unfortunately these two measures result in a drastic worsening of the device ruggedness (latch up, short circuit, avalanche) and thus a restriction of the safe operating area (SOA) of the devices. Consequently, the ob-

jective is to compensate for these degradations through additional technology and design innovations.
First the main influences on the latch up current will be discussed: It is well known that the latch up of the parasitic vertical thyristor structure of the IGBT depends on the emitter efficiency of the parasitic n^+-emitter and on the voltage drop in the p-well under the n^+-emitter region. It is therefore essential to realize a rather high p^+-concentration below the n^+-emitter. A second aspect is to make the n+-emitter doping not too high and the third is to realize a short lateral extension of the n^+-emitter. Of course the new concept is also suitable for a 600 V-IGBT and results in impressive on-state voltage values and ruggedness also for this device. For this 600 V-IGBT in punch-through technology there is an interesting, quite different behavior concerning the cell optimum for lowest on-state values. Here it is better to choose (for the same p-well width "a") a shorter p-well distance "b". This difference results from the larger hole current in contrast to the non-punch-through IGBT. The level of the short-circuit current is another topic to be discussed. Due to the shorter channel, the forward transconductance and hence the value of the short-circuit current increases. To be able to handle the short-circuit condition in such cases of reduced channel length, the short-circuit current must be limited, for example through external measures or by reducing the channel width with the insertion of high gate threshold voltage regions inside the active chip area. The new process being introduced, offers a simple alternative to reduce the current level. By the special method of p^+ and n implants, the emitter sheet resistance is adjusted in such a manner that under normal on-state conditions the voltage drop inside the emitter area is still negligible, but in the case of higher current values (e.g. short circuit) there is already a voltage drop large enough to reduce the effective gate voltage. This negative feedback effect can be used to lower of the short-circuit current level. In addition to these ruggedness aspects, of course, the on-state voltage improvement is of great interest as regards the total losses. With the shorter channel and the reduced p-well depth, the on-state voltage is decreased by 0.8 V. Another improvement of 0.2 V results from optimizing the cell design to the new process parameters: The influence of the p-well width "a" and the p-well distance "b" (as indicated in Fig. 2) can be seen from Fig. 3. The experimentally proven behavior is also shown in Fig 3.

Step 2:
To date, 1200 V - 60-ohm cm blocking IGBTs have been produced using 220 µm silicon material /2/. This material thickness was not required to reach the dielectric strength of the transistor but to be able to handle the wafers during processing without yield loss. Most recent results have shown that for 1200 V blocking IGBTs, a Si thickness of 175 µm is sufficient. This reduction in wafer thickness has meant - as Fig. 4 illustrates - that saturation voltage can be reduced by 15 %. Wafer handling and wafer transport methods, as well as the passivation of the wafer topside and stress-free metallization on the wafer backside have been improved so that no loss of yield occurs. A further advantage of thinner Si material is the fact that in the on-state fewer charge carriers are stored in the IGBT and, as such, the tail charge is less during turn-off which in turn leads to lower turn-off losses. This results in a new optimization criterion for adjusting turn-off losses and the saturation voltage.
In principle, enhancing the backside emitter efficiency reduces on-state voltage and increases turn-off losses. But this can be done in such a moderate way, that the increase in turn-off

losses can almost be compensated by the decrease due to the thinner chips. The trade-off between turn-off energies and on-state voltages for different chip thicknesses and backside emitters is shown in Fig. 5.
Future developments will mean even thinner wafers so that even 600 V IGBT families can be implemented using NPT technology. With 600 V NPT technology, wafers can be ground down to 100 µm. By optimizing this technology, as Fig. 6 shows, turn-off losses can be dramatically reduced - i.e. by a factor of 2. It is also important to realize that with NPT technology the tail current curve is temperature-dependent. This means that the losses and turn-off behavior exhibit the same characteristics across the whole temperature range. Moreover, NPT technology can also be used to produce very robust components with positive temperature coefficients in V_{CEsat}.

Optimum switching performance

Switching performance is a determining factor for dynamic losses, diode behavior, setting the gate series resistance of the parallel connection, and pulse compliance. As already stated above, with NPT IGBTs there are no limitations imposed by the underlying principles in the gate series resistance, so that resistance with reference to the dynamic losses can be minimized. In terms of the turn-off process however, turn-off overvoltages - especially if the short-circuit is turned off - must be taken into account. The freewheeling diode has been developed along these lines- especially for the module and Duopack - using special technologies so that it is ideal at low forward voltage values and low return recovery charge yet exhibits "soft behavior" for fast switching cycles. It has been found that it also exhibits "soft behavior" over the entire current and temperature range for high commutation cycles of $di/dt \geq 1000$ A/µs. The forward characteristics and switching characteristics (tail current, E_{on}, E_{off}) of these IGBTs have been optimized for clock frequencies up to 20 kHz for motor drives and 40 ... 60 kHz for SMPs. The tail current is very low and, because of the semiconductor concept used, is independent of temperature. Switching times, delay times and threshold voltages for IGBTs exhibit extremely low parasitic bandwidths resulting from a very good reproducible manufacturing process so that parallel connection can also be implemented in dynamic operation without problems. Switching performance including dynamic losses and delay times is clearly linked to the driving circuit. With all MOS-driven transistors, a basic distinction is drawn between resistance control and voltage control. With regard to the optimization of the entire turn-on and turn-off process (dynamic losses, delay times) voltage control offers more advantages.

Package concept

Today users have a wide variety of packages in the IGBT range from $5\ A \leq I \leq 2500\ A$ ($600\ V \leq U \leq 3500\ V$) at their disposal. Lower currents are covered both by transistors in the TO 220 (TO 220 SMD) and TO 218 packages and by flow-solderable six-packs. This product range has been extended by the new product known as "Duopack". It is a dual-chip solution IGBT with anti-parallel freewheeling diode - in TO 218 and TO 220 packages. Today even with the existing range of $5\ A \leq I \leq 40\ A$ (600 V) and $8\ A \leq I \leq 35\ A$ (1200 V), converters up to 7.5 kVA are being produced. The current range above this is covered by the new flow-solderable Econopacks.

Using the Econopack 2 and the Econopack 3 in their basic variants 50 A/75 A/100 A, together with the "Tri-Pack" 150 A/200 A, a current range up to 600 A can be covered. Econopacks have been designed in such a way that the entire current range can be covered with only 2 module variants using appropriate connections. Parallel connection can also be implemented easily without any additional effort.

Parallel connection using Econopacks

Siemens introduced a package that can be soldered directly on a printed circuit board (PCB) /1/.
The new Econopack 3 IGBT modules comply with the requirements coming up with the development of smaller and more compact converters. Compared to conventional electrical connections with copper rails, more compact solutions are possible with improved electrical data and higher reliability. Owing to the ease with which the process can be automated, the costs for the assembly of the converter can be considerably reduced. Experience gained with smaller currents now allows an increase in the rated currents by up to 200 A per switch. The terminals of the package show a layout that is optimized in respect of paralleling IGBT modules /2/.
Fig. 7 shows the symmetric internal structure and the layout of the single switches in an Econopack 3 module. The internal rails for the connectors of the DC link and the terminals on the opposite sides of the module provide a very low parasitic inductance.

Electrical considerations of the experimental set-up

Particularly with parallel IGBT modules, care must be taken to achieve symmetric parasitic inductance and resistance. An advantageous design will inhibit or essentially reduce oscillations during switching. The assembly on a PCB facilitates the use of smaller paralleled capacitors. Compared to few capacitors with the same capacity, which are common in conventional railing, the parasitic inductances and resistances are considerably reduced /3/. By exploiting the smaller size of these capacitors they can be allocated closer to the DC link terminals of the module. In addition, small metallic foil capacitors that are suitable for high frequency applications in standard packages instead of expensive special application devices can be soldered adjacent to the module. The two parallel metalled layers of the PCB represent the connection principle with the lowest inductivity possible.
To avoid oscillations of the currents through the single devices during switching, generally the coupling of the gate circuits of the paralleled IGBTs and FWDs respectively has to be reduced. The Siemens IGBTs under investigation support this demand by an integrated gate resistor on each IGBT chip. The external gate resistors should be used for each single transistor and should be connected directly to the gate driving circuit.
For the performed tests, two modules in Econopack 3 packages were mounted on a special PCB. The layout was optimized to achieve a low inductance connection of the Econopack 3 modules to the low inductance capacitors of the DC link. Thus the electrical data of a well-designed industrial converter can be approached. The connections of the negative power rails of the two IGBT packages were separated. It was thus possible to monitor the current of each of the lower IGBTs separately. Fig. 8 shows the schematics and the measured currents and voltages for the experimental set-up

used. As the load, inductances of some 100 µH were used which were connected between the positive rail of the power supply and the two paralleled halfbridges.
All measurements were made with paralleled IGBTs and diodes in separate packages. This forms the worst case because there are greater differences in the current paths compared to the paralleling of the devices in the same package. Measurements were performed using Siemens 1200 V IGBT modules BSM75GD120DN2 (rated current 75 A) and BSM100GD120DN2 (rated current 100 A). Both types consist of three halfbridges which can be configured according to the demands of the user by means of the PCB layout.
The two modules BSM75GD120DN2 were selected to meet equal output characteristics of the IGBTs and the diodes. In this way defined conditions for the parallel operation were secured. Later asymmetric conditions were imitated with external components. However, the geometrical layout of the two halfbridges (see Fig. 7) with one halfbridge at the left side of the module and the other at the right, leads to differences. IGBT 1 (the second chip from the right in Fig. 7) has longer electrical paths to the DC link and the load than IGBT 2 (the left-most chip in Fig. 7). Therefore the inductance and resistance of the wiring of IGBT 1 are higher than that of IGBT 2. With the diodes the layout is reversed, with diode 1 as the right-most diode chip in Fig. 7.
The two modules BSM100GD120DN2 were selected for typical deviations of the forward characteristics of IGBTs and diodes.

Simulation and measurement results

Simulations of the dynamic behavior have been performed using the software SABER with a sophisticated model of the IGBTs as well as simple estimations for the static current distributions. In the latter case the IGBTs and diodes were approximated with a differential resistance describing the conduction resistance of the diode and an offset voltage depicting its exponential forward characteristic. The internal parasitic resistances of the module (mounting on direct copper bond - DCB - and wire bonds) are included in the differential resistance. In both values the typical measured temperature dependencies are taken into consideration. The set of equations was evaluated using Maple V software. Thus a comparison between the SABER simulation, the first order approximation and the measurements can be drawn.
The measurement is performed using multiple (at least 2) positive pulses of the gate driving unit. When turning on the lower paralleled IGBTs for the first time, the load current increases. Then the IGBTs turn-off and the load current commutates into the upper free wheeling diodes. Thus the turn-off behavior of the IGBTs can be monitored. During the subsequent turn-on of the lower IGBTs the load current again commutates into the IGBTs and their turn-on characteristic is measured. Fig. 9 and 10 show the simulated current distribution of the turn-off and turn-on of paralleled modules (Siemens BSM100GD120DN2).

An optimized IGBT for high clock frequencies

With appropriate development, IGBTs can be produced with low switching losses. This opens up new fields of application such as SMPSs and Pre-Converters for power factor correction. With fast 2nd-generation IGBTs, a selective charge carrier lifetime setting is now also being implemented for NPT-type IGBTs. This is the result of using heavy metal diffusion, a technique which has been successfully

applied for years by Siemens for 600 V-PT type IGBTs and for fast diodes (FRED). In this way fast IGBTs with low forward voltages and optimized tail currents can be produced. When using heavy metal diffusion, electrical parameters do not change over time which cannot be ruled out when setting the lifetime using electron radiation. Once again we must stress that for NPT-type IGBTs for drive systems with frequencies of up to 20 kHz, no charge carrier lifetime setting occurs. This is aimed at optimizing IGBTs in high frequencies $f_T \geq 40$ kHz - as required for switched mode power supplies (SMPS). Second-generation IGBTs including the BUP 401 (600 V) and BUP 314 (1200 V) representing standard IGBTs are optimized for low forward voltages. With these IGBTs - as with all NPT-IGBTs without charge carrier lifetime setting - the temperature coefficient of the saturation voltage V_{CEsat} is positive. This has many benefits especially with regards to paralleling and temperature stability. With fast IGBTs however, the temperature coefficient of the saturation voltage is negative. With fast IGBTs, the focus is on optimizing the turn-off characteristics with a fast decaying tail current.

This new development allows fast IGBTs to be used in applications such as SMPSs and UPSs which to date have been covered by power MOSFETs.

	IGBT		Diode	
	I_{C1}	I_{C2}	I_{D1}	I_{D2}
Estimation isothermal 125°C	55 A	56 A	48 A	64 A
Static approximation	55.0 A	55.9 A	48.5 A	63.6 A
Measurement	54.6 A	56.2 A	51.1 A	61.0 A
Relative deviation	0.7 %	0.5 %	5 %	4 %

Table 1: Calculated and measured forward currents for the IGBTs and free wheeling diodes at a junction temperature of 125°C (BSM100GD120DN2).

Literature:

/1/ T. Laska et al.: A Low Loss/Highly Rugged IGBT-Generation - Based on a Self Aligned Process with Double Implanted n/n$^+$-Emitter, Proceedings ISPSD 94

/2/ T. Laska et al.: Optimizing the Vertical IGBT Structure - The NPT Concept as the most economic and Electrically Ideal Solution for a 1200 V-IGBT, Proceedings ISPSD 96

/3/ M. Herfurth et al.: Testing of High-Speed IGBT's in an application-specific circuit and comparison with Standard IGBTs and MOSFETs, Proceedings PCIM 96

/4/ L. Lorenz et al.: Intelligent Power Modules for Driving Systems, Proceedings ISPSD 94

/5/ L. Lorenz et. al.: A New Generation of IGBT's and Concepts for their Protection, Proceedings PCIM 94

/6/ L. Lorenz et al.: The IGBT - A Semiconductor Switch for Driving Systems, EPE-Record 91

/7/ L. Lorenz: MOS-controlled Power Semiconductor Components for Voltages from 50 V to 2000 V, EPE-Journal/Vol. 2, No. 2-92

/8/ A. Mauder et al.: Investigation of the static and dynamic current distribution in paralleled IGBT modules, Proceedings PCIM 97

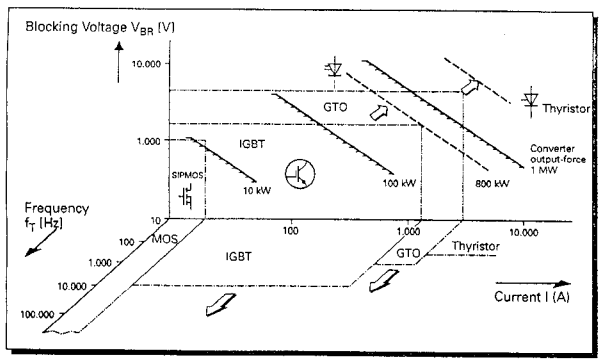

Fig.1: Development targets of Power Semiconductors in this decade

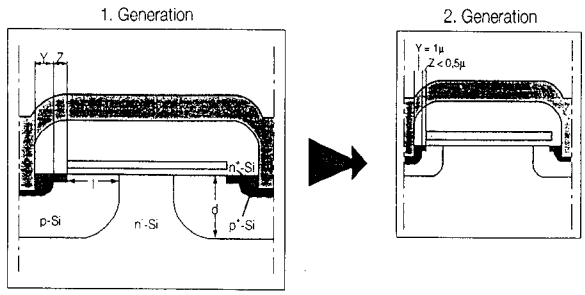

Fig.2: a) Cell structure with deep p-well/long channel
b) Cell structure with reduced p- well depth/channel length

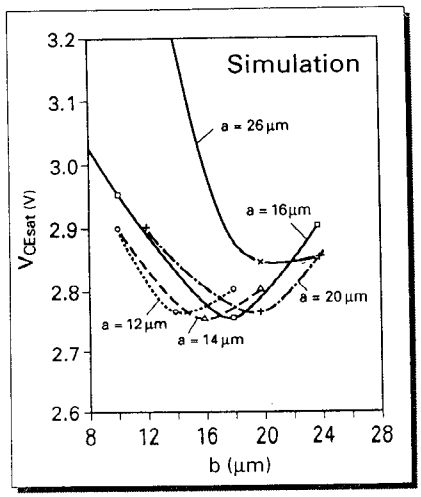

Fig.3: On-state voltage as a function of cell design (1200 V NPT-IGBT)

Modified Charge-Control Equation for More Realistic Simulation of Power Diode Characteristics

K.J. Tseng and S. Pan

School of Electrical and Electronic Engineering, Nanyang Technological University
Blk S2, Nanyang Avenue, Singapore 639798, Republic of Singapore

Fax: +65 791 2687 Email: ekjtseng@ntu.edu.sg

Abstract **- The mathematical diode model currently used in most circuit simulations is not able to fully account for the forward and reverse recovery characteristics. This is due to the quasi-static diffusion charge equation and the fixed internal resistance used in the model. A proposed modification to the charge equation is presented in this paper. This important modification together with a proposed charge-dependent internal resistance equation have been test-implemented in PSpice using the Analog Behavioral Modeling technique. It has been experimentally verified that the new model is able to describe the power diode forward and reverse recovery behaviour more realistically without degrading the convergence properties of the simulators.**

I. INTRODUCTION

If the standard SPICE diode model is used to simulate a high-voltage high-current diode, the forward and reverse recovery characteristics are not satisfactorily predicted [1]. Fig 1 shows a typical experimental trace of the current through a high-power when it is being turned off. The SPICE simulated response is also shown. The soft recovery of the power diode cannot be simulated by the SPICE diode model, leading to erroneous predictions of switching power dissipation.

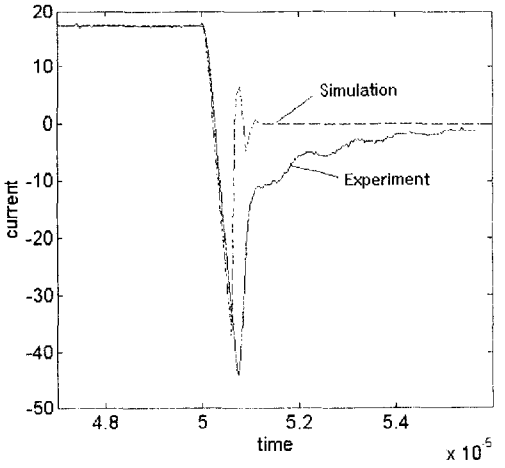

Fig 1: Inability of standard diode model to simulate soft reverse recovery in power diode current

Another drawback of the standard diode model is its inability to simulate the forward recovery, as illustrated in Fig 2. When a diode turns on abruptly under the influence of the external circuit, a sharp voltage overshoot occurs across the diode. This due to a number of factors, the chief of which is the finite time taken by the conductivity modulation process in the bulk of the diode. The fixed internal resistance used in the standard model is inadequate for predicting such characteristics.

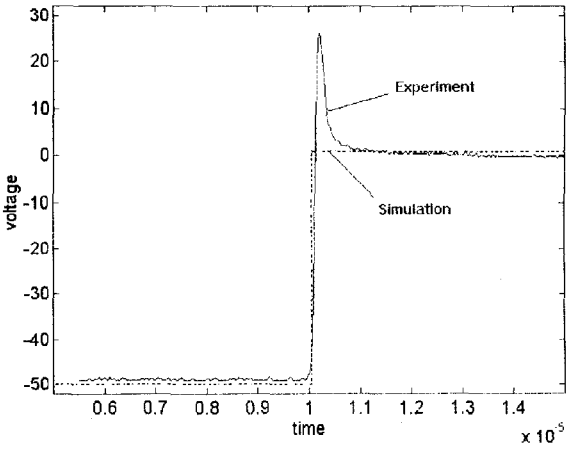

Fig 2: Inability of standard diode model to simulate forward recovery in power diode voltage

In recent years, new models for the diode have been proposed. Some of these are based on simplified finite difference algorithms in which the continuity equation is continuously solved to obtained the dynamic excess carrier distribution profile [2-3]. Another employs the Linvill's lumped-charge model in which the excess carrier distribution profile is discretized into several critical regions, each containing a lumped charge node to represent dynamic charge variation [4]. The complexities of these models rendered them incompatible with circuit simulators such as SPICE. Other models require auxiliary sub-circuits to reproduce the soft recovery behaviour [5-6]. Convergence difficulties, long simulation times and extreme difficulty in parameter extraction are some of their drawbacks [7].

In this paper an alternative model is presented which is based on a simple modification of the charge-control equation currently employed in most diode models used in circuit simulators. The conventional SPICE diode model is briefly re-visited. The proposed modifications are

described in detail followed by a discussion on the experimental verification of the model.

II. Conventional Charge Equation

The inability of the conventional diode model to describe the soft recovery is due to the quasi-static nature of the charge-control equation used in the model. With forward bias applied to the *pn* junction of the diode, there is an excess minority-carrier concentration in the neutral regions near the depletion region. For a practical p^+n type of diode, the *p* region is usually much more heavily doped than the *n* region. Thus it is sufficient to consider the excess hole charge Q_p in the neutral *n*-base region, which is

$$Q_p = qA_j \int_{x_n}^{W_n} p'(x)dx \tag{1}$$

where A_j is the cross-sectional area of the junction, x_n is the edge of the depletion layer and W_n is the width of the *n* region. The excess hole concentration $p'(x)$ can be obtained by solving the semiconductor continuity equation. For a long *n*-base diode at steady-state, this is

$$p'(x) = p_{n0}(e^{qV_j/kT} - 1)e^{-(x-x_n)/L_p} \tag{2}$$

where L_p is the diffusion length. From Eqs (1) and (2), the steady-state excess hole charge is related to the junction voltage V_j by

$$Q_p = qA_j L_p p_{n0}(e^{qV_j/kT} - 1) \tag{3}$$

The diode current supplies holes to the *n*-base region at the same rate as they are being lost by recombination. If the excess minority carrier has a lifetime τ_p, the diode current is then given by

$$I_D = \frac{Q_p}{\tau_p} = \frac{q}{\tau_p} A_j L_p p_{n0}(e^{qV_j/kT} - 1)$$

$$= I_{ss}(e^{qV_j/kT} - 1) \tag{4}$$

where I_{ss} is termed the diode reverse saturation current. Eq 4 is the familiar Shockley's equation which relates, on a static basis, the diode current to the voltage across its *pn* junction. The excess hole charge, also known as stored charge or diffusion charge can be re-written as

$$Q_p = \tau_p I_{ss}(e^{qV_j/kT} - 1) \tag{5}$$

To obtain a dynamic relation, the time rate of change of the excess charge must be included. The diode current is thus given by

$$I_D(t) = \frac{Q_p}{\tau_p} + \frac{dQ_p}{dt} \tag{6}$$

where Q_p is given by Eq 5. This is the fundamental charge control equation for *pn* junction diode which states that the diode current supplies holes to the neutral *n* region at the rate at which the stored charge increases plus the rate at which holes are being lost by recombination. However the stored charge given by Eq 5 is still based on static relationship. Thus this model is sometimes termed as the quasi-static model, and together with secondary equations describing reverse breakdown, depletion capacitance, etc, it has been widely adopted by most standard circuit simulators, e.g. SPICE, Saber, etc.

III. Modified Charge Equation

Our finite element analysis has shown that the excess carrier distribution profile in the neighbourhood of a *pn* junction being turned-off is dependent on the rate of change of the stored charge [8-9]. If dQ_p/dt is low, the typical pattern in which the distribution profile changes with respect to time is shown in Fig 3(a). When $p'(x_n)$ at the depletion layer has decreased to zero, the stored charge Q_p is also approximately zero. The quasi-static charge equation is adequate for such cases. If dQ_p/dt is high, substantial stored charge Q_p remains even when $p'(x_n)$ has dipped to zero, as shown in Fig 3(b). Hence a more general dynamic charge equation is necessary.

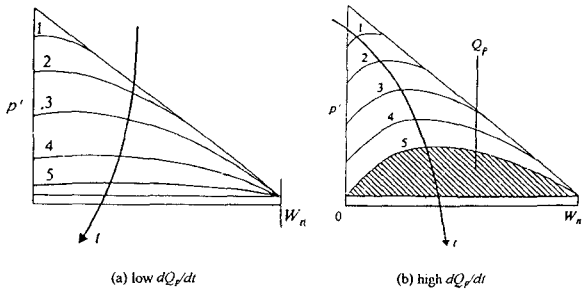

Fig 3: Changes in excess carrier distribution profiles wrt time

To describe the dynamic behaviour of the charge, we proposed to modify the static charge equation as shown below [10]

$$Q_p = \tau_p [I_{ss}(e^{qV_j/kT} - 1) - v_p \frac{dQ_p}{dt}] \tag{7}$$

The charge is now a function of its rate of change. The new parameter v_p is termed as the viscosity of the minority carrier charge. This is analogous to the damping factor which is used to characterize behaviour in mechanical systems. Generally, v_p has a value greater than zero. It is related to the geometrical width of the *n*-base region and the spatial variation of minority carrier lifetime introduced by lifetime killing processes. The more significant the value of v_p, the greater the amount of Q_p which has to be extracted from the base region after the *pn* junction has gone into reverse bias. This implies a softer recovery.

Besides the p^+n structure which has been used in our discussion so far, other structures such as the n^+p and the *p-i-n* have also been used for diodes. The latter is used in most high power diodes. Thus the base region stored charge can be composed of holes, or electrons, or both holes and electrons in cases of high injection levels. A

more general form of Eq. 7 for diode simulation can be written as

$$Q_s = \tau_a[I_{ss}(e^{qV_j/kT} - 1) - v_a \frac{dQ_s}{dt}] \quad (8)$$

where Q_s is the total excess stored charge, τ_a is the average transit time of carriers and v_a is the average viscosity of the ambipolar carriers in the base region. As there is only one additional parameter in Eq. 8 compared with Eq. 5, implementation in existing circuit simulators can be done easily.

IV. Charge-Dependent Internal Resistance

In the standard diode model, a fixed internal series resistance R_s is frequently inserted between the anode terminal and the rest of the model describing the behaviour of the *pn* junction. The purpose is to account for the contact resistance of the diode. This works fine for small signal diodes, and even power diodes during steady on-state. When a power diode is in the process of turning on, it has large bulk resistance because its base region is relatively long and has low initial conductivity. As the forward current increases, this bulk resistance eventually drops due to the effect of conductivity modulation. Hence the voltage across the diode manifests a momentary overshoot termed as the forward recovery, which could not be modelled by the fixed resistance R_s.

In the off-state, the conductance of the base region may be estimated as

$$y_{base} = \frac{q(\mu_n n_0 + \mu_p p_0)A_j}{W_d} \quad (9)$$

where μ_n and μ_p are the mobilities of electrons and holes respectively, and n_0 and p_0 are the respective thermal equilibrium electrons and holes concentrations in the base. As all the terms in Eq. 9 are based on the geometrical dimensions and the thermal equilibrium carrier densities, they can be lumped as the unmodulated conductance Y_0.

$$y_{base} = Y_0 \quad (10)$$

In the steady on-state, the base region in the high-level injection condition, and the modulated conductance can be approximately written as

$$y_{base} = \frac{q(\mu_n + \mu_p)n_a A_j}{W_d} \quad (11)$$

where n_a is the ambipolar carrier concentration level. As the stored charge Q_s in the base region during high-level injection is approximately proportional to n_a, Eq. 11 can be re-written as

$$y_{base} = \alpha Q_s \quad (12)$$

where α is a parameter dependent on the diode geometry and the fabrication processes the diode was subjected to. The stored charge Q_s is related to the junction voltage V_j as given by the proposed modified charge equation of Eq.8. Therefore it is proposed here that the fixed internal resistance R_s in the standard diode model be replaced by a charge dependent resistance of the form

$$r_s = \frac{1}{Y_0 + \alpha Q} \quad (13)$$

Before the diode turns on, charge Q_s is negligible and $r_s \cong 1/Y_0$. This is similar to the usage of a fixed resistance R_s in the conventional model. During steady on-state, $\alpha Q_s >> Y_0$ and therefore $r_s \cong 1/\alpha Q_s$. During the transient turning-on or turning-off, r_s will have a value between the two extremes. As r_s is now a function of Q_s, it is also dependent on dQ_s/dt as evidenced from Eq.8.

V. Model Implementation

The model has been test-implemented in PSpice and Saber, two of the most widely used circuit simulators in the industry. Negative effects of the new model on run-time overheads and convergence properties are insignificant [10]. The PSpice implementation was carried out using the Analog Behavioral Modelling (ABM) technique and is described in detail here. This implementation relies on user-defined controlled E-type voltage sources and G-type current sources which allow transfer functions for non-linear devices to be specified by mathematical expressions, look-up tables, Laplace transforms, or frequency response tables.

Fig 4 shows the PSpice implementation of the schematic of the modified diode model. The standard SPICE diode model has been retained as the core of the new model. This is depicted by the diode symbol $D_{pn\_junction}$. Its function is to simulate the basic *pn* junction behaviour, namely:

(1) the steady-state forward bias and reverse bias junction current (Shockley's model),

(2) the depletion layer capacitance, and

(3) the reverse breakdown characteristics.

This basic diode behaviour is characterized by the familiar parameters such as I_{ss}, C_{J0}, BV_{rev}, etc, which can be specified using the **.MODEL** statement [11].

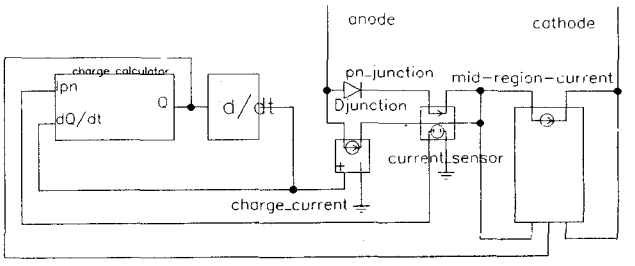

Fig 4: Schematic of PSpice ABM implementation of proposed power diode model

An ABM block *charge-calculator* calculates the stored charge Q_s given by Eq. 8, which is then differentiated to provide the charge current dQ_s/dt in parallel with $D_{pn\_junction}$. The base region current through its charge-

dependent resistance of Eq.13 is calculated by the ABM block *base-region-current*. The netlist of this sub-circuit is given in Appendix A. It requires seven nodes including the anode and cathode terminals of the diode.

There are four new parameters: τ_a, ν_a, Y_0 and α. The original carrier lifetime τ_p and fixed resistance R_s in the standard SPICE diode model are no longer required and should therefore be set to zero in the **.MODEL** statement. As the functions of τ_p and R_s are superseded by the new parameters τ_a and Y_0, there are in fact essentially only two extra parameters: ν_a and α. Parameter extraction procedure currently used to estimate parameters such as I_{ss}, τ_p, C_{jo}, etc are also applicable to obtain the values of these new parameters for each different type of diode.

Fig. 5 shows the effects of τ_a and ν_a on the simulated reverse recovery characterisitics. The transit time affects the amount of reverse recovery charge while increasing ν_a 'soften' the recovery profile. Fig. 6 shows the simulated forward recovery voltages for different values of Y_0 and α. The peak forward voltage is mainly determined by Y_0 while the rate of decay of the recovery voltage and the steady-state voltage drop is dependent on the value of α.

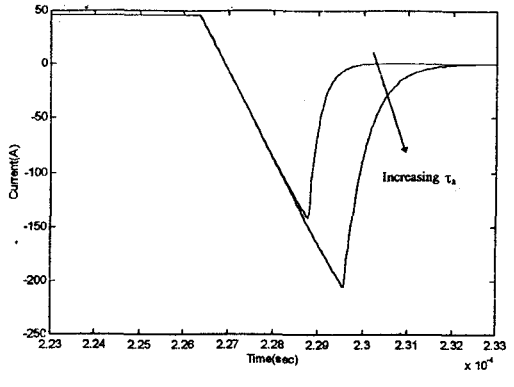

(a) effect of parameter τ_a

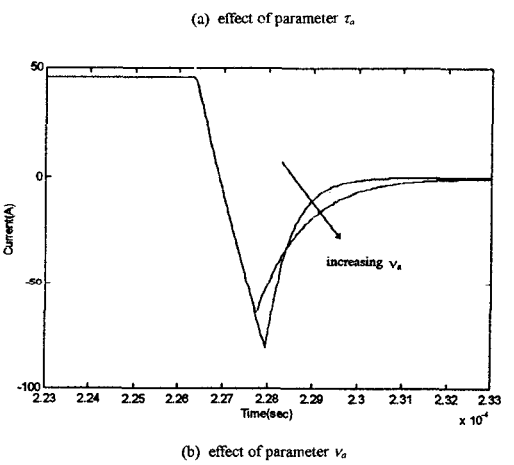

(b) effect of parameter ν_a

Fig. 5: Effect of parameters τ_a and ν_a on simulation of power diode reverse recovery current

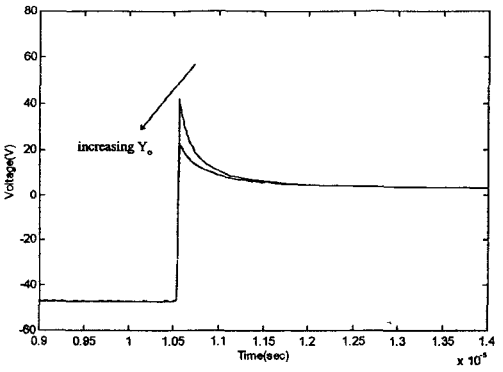

(a) effect of parameter Y_0

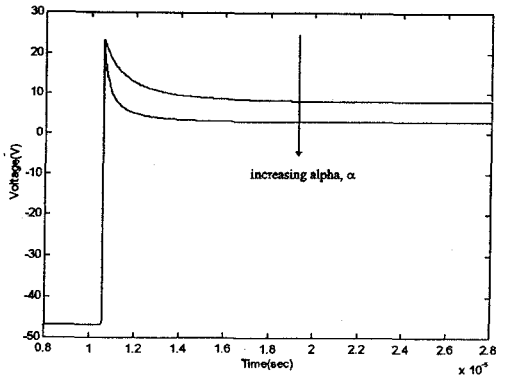

(b) effect of parameter α

Fig. 6: Effect of parameters Y_0 and α on forward recovery simulation

VI. Experimental Verification

To verify the validity of the model, experimental tests and simulations have been conducted using a low-side chopper test circuit as shown in Fig.7(a). The DC voltage source V_s provides the reverse bias voltage across the diode under test (DUT) whenever the IGBT turns on. The IGBT gate pulse waveform is shown in Fig. 7(b). During period t_1, the IGBT is on and a bias current builds up in the large inductor L_{bias}, determined by the duration of t_1. When the IGBT is off during t_2, the bias current flows through the DUT as the forward current I_F. The forward recovery is observed at this moment. The duration of t_2 should be long enough for I_F to stabilise. When the IGBT turns on again during t_3, the current I_F in the DUT decreases at the rate dI_r/dt determined by the small adjustable inductor L_v. The reverse recovery is observed at the beginning of t_3.

A high degree of correlation between the experimental and simulated results has been observed for a wide range of operating conditions. The operating conditions investigated are varying levels of diode forward current prior to turn-off, and varying rates of rise of reverse diode current dI_r/dt. Fig 8 shows the comparison of experimental and simulated diode current waveforms for different values of forward current I_F. The parameters for this particular diode have been chosen for a good prediction of the reverse recovery

current at I_F=20A, the rated operating current of this device. At I_F=3A, the simulated current waveform is still remarkably similar to the experimental trace. At I_F=45A, the predictions of peak reverse current is also well within 10% error.

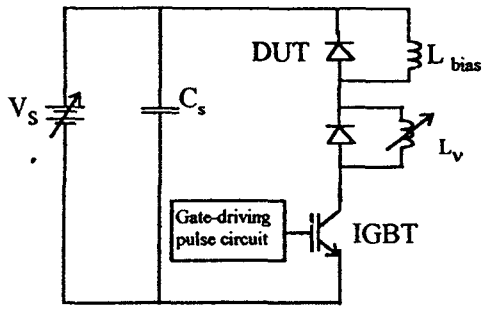

(a) test circuit

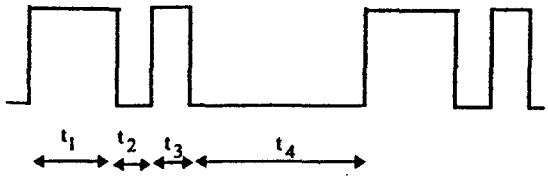

(b) gate drive pulse waveform

Fig. 7: Test circuit for verification of modified diode model

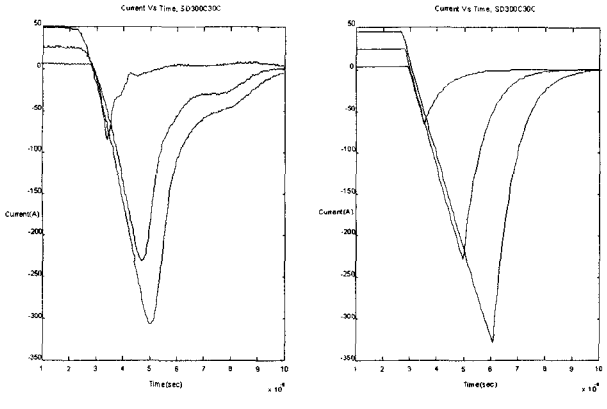

Fig. 8: Experimental and simulated reverse recovery current waveforms, with τ_a = 1.7e-5, ν_a = 0.04, Y_0 = 1.12 and α = 2e5.

Using this same set of parameters, the experimental and simulated diode voltage waveforms for different values of I_F (= 3A, 20A, and 45A) during turn-on is shown in Fig. 9. A good degree of correspondence over the range of I_F is evidenced.

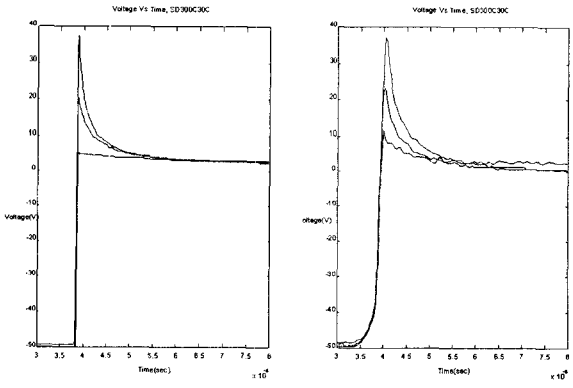

Fig. 9: Experimental and simulated forward recovery voltage waveforms, with τ_a = 1.7e-5, ν_a = 0.04, Y_0 = 1.12 and α = 2e5.

VIII. Conclusions

The charge-control equation in the standard diode model has been modified to allow more realistic simulation of diode reverse recovery characteristics. When further enhanced with a charge-dependent resistance equation, this modified diode model can also simulate forward recovery characterisitics. As only two extra parameters are required, increased complexity in parameter extraction procedure is minimal. The modified model has been successfully test-implemented in PSpice, without noticeable degradation in run-time overheads and convergence properties. Strong correlation between experimental and simulated results has so far been observed.

References

[1] Lauritzen P.O., "Power semiconductor device models for use in circuit simulators," Proc of Conf on Industry Applications, Seattle, USA, Oct 7-12, 1990, pp.1559-1563.

[2] Goebel H.,"A unified method for modeling semiconductor power devices," IEEE Trans. on Power Electronics, Vol.9, No.5, Sep 1994, pp.497-505.

[3] Metzner D., Vogler T., and Schroder D.,"A modular concept for the circuit simulation of bipolar power semiconductors," IEEE Trans. on Power Electronics, Vol.9, No.5, Sep 1994, pp.506-513.

[4] Ma C.L., Lauritzen P.O., Lin P.Y. and Budihardjo I.,"A systematic approach to modeling of power semiconductor devices based on charge control principles," IEEE Power Electronics Specialists

Conference, Taipei, China, Jun 20-25, 1994, pp.31-37.

[5] Xu C.H., and Schroder D.,"Modelling and simulation of power MOSFETs and power diodes," ," IEEE Power Electronics Specialists Conference, Apr, 1988, pp.76-83.

[6] Kraus R., Hoffmann K., and Mattausch H.J., "A precise model for the transient characteristics of power diodes," ," IEEE Power Electronics Specialists Conference, 1992.

[7] Tseng K.J., Foo C.F., and Palmer P.R., "Implementing power diode models in SPICE and Saber," IEEE Power Electronics Specialists Conference, Taipei, China, Jun 20-25, 1994, pp.59-63.

[8] Tseng K.J., and Palmer P.R., "Mathematical model of gate-turn-off thyristor for use in circuit simulations," IEE Proc.-Electr. Power Appl., Vol.141, No.6, Nov 1994, pp.284-292.

[9] Tseng K.J., and Palmer P.R., "Modelling of power semiconductor devices for use in circuit simulations," IEEE Power Electronics Specialists Conference, Taipei, China, Jun 20-25, 1994, pp.38-43.

[10] Tseng K.J. and Pan S., "Modified charge control equation for simulation of diode reverse recovery," IEE Electronics Letters, Vol.32, No.4, Feb 1996, pp.404-406.

[11] Design Center PSpice Reference Manual, MicroSim Corporation, 1995.

Appendix A - Netlist For Diode Model Sub-Circuit

```
* Schematics Netlist *

D_pn_junction          anode              $N_0001
Djunction
C_differentiator       $N_0002
$$U_differentiator     1
V_differentiator       $$U_differentiator 0
0v
E_differentiator       $N_0003            0
VALUE {1.0 * I(V_differentiator)}
H_current_sensor       $N_0005            0
VH_current_sensor 1
VH_current_sensor      $N_0001            $N_0004
0V
G_charge_current       anode              $N_0004
$N_0003        0          1
E_charge_calculator    $N_0002            0   VALUE {
Tau_t*(V($N_0005)-v_p*V($N_0003))   }
G_base-region-current  $N_0004            cathode
VALUE {
                                          + (V($N_0004)-
V(cathode))*(Y0+alpha*V($N_0002))   }
```

Combined Optimality and Robustness Assessments for Interconnected Power Converters - Theoretical and Experimental Results

Catalin Burlacu Hiroyuki Ohsaki Eisuke Masada
The University of Tokyo - Department of Electrical Engineering
7-3-1 Hongo, Bunkyo-ku, Tokyo 113, JAPAN
Fax: +81-3-3812-2111/ ext 7492, Tel:+81-3-3818-5706
Email: burlacu@masada.t.u-tokyo.ac.jp

Abstract - **More reliable and a respective better power quality are the main requirements for any power supply system operating for a distributed power network, an industrial plant or, more particular case, for a train drive. A new algorithm to decide, compute and analyze a compensation method that improves the power system performance is proposed, based on a complex bilinear model of two parallel connected voltage-type power converters. Analysis is performed for normal and faulted operation, with emphasis on the combined purposes - input currents' quality and system's reliability. A specially computed term is used for the feedback compensation, and an optimum parameter identification is explained providing a strong basis for a unified theory of analysis for hybrid bilinear (biconnected) systems. It is proved that the method acts automatically for any of the analyzed operation conditions, and an experimental approach proves the theoretical analysis.**

I. POWER CONVERTER SYSTEMS - GENERAL INTRODUCTION

The main requirements for a utility's customer is to provide power that flows smoothly enough not to trip up electronic equipment, by a secure and reliable supply system. Present situation is characterized by an increased level of interconnections between utilities but also between loads, long distribution lines in addition to heavy loads giving and increased level of instability to the overall system [1], and a respective lower quality for the supplied power.

If components are continuously increasing their switching capability, limitations like high switching frequency (harmonics and EMC bounds) and stability performance are still under the required level. Considering more interconnections between converters together with their respective control method, new approaches can be defined.

Converters can be associated in series or parallel, with or without interconnecting transformers. Despite providing high quality AC current wave forms, all the connections produce high ripple in internal variables [6], that must be adequately bounded. In the case considered by the present study, the parallel transformerless one, they are the individual converter currents which will require oversized inductors and power devices. Problems like very low individual inductance (transformerless connection), variation of the line induction or faulted operation make very difficult any dynamic analysis. For high speed traction drives (Shinkansen- Japan)[1] or superconducting magnetic energy storage (SMES)[2], relative high level of energy can be exchanged by the interconnected subsystems, and to create a system robust to this kind of interference and to understand its behavior, are main goals for our study.

II. SYSTEM MODELING

A. *Model of the parallel connected voltage-type power converters*

For the linear model of the converters in which the operating features are approximated in different ways, the interconnection are more or less "observable" and obvious, the system is modeled with lower accuracy. Therefore, we show a new model for the parallel connected power converters, considering a more precise nonlinear approach - the bilinear model [3].

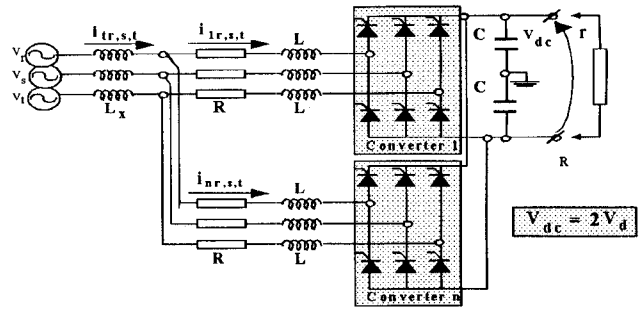

Figure1: Transformerless parallel connection for converters

Figure1. presents the configuration of the transformerless parallel connection of VSC converters, as usually mounted as common converter supplying the internal DC bus line for an industrial plant. The DC sides of the converters are also connected in parallel. Its corresponding bilinear state space model is described by equations (1), (2) and (3) [5].

$$\frac{d\mathbf{i}}{dt} = \frac{1}{L(a_l+1)}(-\mathbf{Ai} - \mathbf{Bm}v_d + \mathbf{F}'\mathbf{v}) \quad (1)$$

$$\frac{dv_d}{dt} = \frac{\mathbf{i}'\mathbf{m}}{2C} - \frac{v_d}{2Cr} \quad (2) \qquad \mathbf{i}_t = \mathbf{Fi} \quad (3)$$

$\mathbf{i}_t = [i_{tr}\ i_{ts}\ i_{tt}]^t$ (4) $\mathbf{i} = [i_{1r} i_{1s} i_{1t} \ldots i_{kr} i_{ks} i_{kt}]^t = [\mathbf{i}_1\, \mathbf{i}_2\, \ldots\ldots \mathbf{i}_k]^t$ (5)

$\mathbf{m} = [m_{1r} m_{1s} m_{1t} \ldots m_{kr} m_{ks} m_{kt}]^t = [\mathbf{m}_1\, \mathbf{m}_2 \ldots . \mathbf{m}_k]^t$ (6)

$a_l = \frac{kL_x}{L}$, k=2 (7)

where we consider $\mathbf{v} = [v_R, v_S, v_R]^T$, $\mathbf{F} = [\mathbf{I}_3\ \mathbf{I}_3\ \mathbf{I}_3]^T$
The state variables are the individual currents **i** and the DC voltage v_d. Vector **m** is the modulation function, considered as the parametrical input (multiplicative control) while **v** is the input voltage (additive control) or system perturbation.
Matrix **B** gives the coupling between the phase currents. The non diagonal components increase with the factor a_l. defined by relation (7). The DC voltage ripple will depend on the difference between the AC and DC instantaneous power, according to equation (2) [6].

B. *Biconnected considerations regarding the proposed model*

Additive linear control can be used to new equilibrium states, while multiplicative linear control can be used to vary the structure and, therefore, the range of attainable states. After some calculations the model can be rewritten as the following structure:

$$\dot{\bar{\mathbf{x}}} = \mathbf{A} \times \bar{\mathbf{x}} + \sum_{i=1}^{6} \mathbf{B}_k \times \bar{\mathbf{x}} * u_k + \mathbf{F} \times \bar{\mathbf{v}} \qquad (8)$$

where the new state vector is $(i_1, \ldots, i_6, v_d)$. The new form is characterized by the interconnection between the two bilinear variables - the current vector $i_1, \ldots, i_6$ and the DC voltage v_d [9], where one's value influences the variation of the other one:

$$\dot{x}_1 = f(\mathbf{m} v_d) \quad and \quad \dot{v}_d = f(\mathbf{mi}) \qquad (9)$$

It is generally recognized that the variable structure of the bilinear systems allows them to be more controllable than the linear systems, just as it frequently provides a more accurate model. In control system design, it may be convenient or even necessary to introduce adaptive or variable structure control to steer the plant throughout the required region of state space [4]. The model of converters, and implicit the more complex one for parallel connected power converters, is already enhanced with this term if no linear approximation is done ($v_{DC} = 0$). The main problem is caused by any nonlinear input (as usually occurs for the DC voltage feedback), but the system keeps its biconnected structure (as we define it for our studies), as the one shown in equation 9.
In the present study we use all previous achievements [10] in order to compensate a current vector control strategy for a faulted operation of two parallel connected power converters, so aims like input currents quality and system reliability are accomplished by using an unified algorithm. The model considered is the one presented in equations (1) and (2). The control set is M, where its elements |m|=1, and the problem is to drive the system from an initial state x(t0) = x0 to the final state (origin of the error plane), so that to minimize the cost function [4]:

$$J = \int_{t_0}^{t_f} (const * (u_1 + u_2 + \ldots + u_7)) d\tau \qquad (10)$$

where we consider a fuel-optimal problem to be solved. The vector **u** is the control corresponding to the modulation vector **m** and the state variables are $i_1, \ldots, i_6$ the individual currents and v_d the DC voltage on one arm of the condenser.
We have to determine the vectors **m** that minimizes H the Hamiltonian of the system. Steepest descent or gradient methods are characterized by iterative algoritms for improving estimates of the control parameters [8], so as to come closer to satisfying the condition $\partial H / \partial u = 0$. In order to do this we calculate the $\partial H / \partial u$ and we obtain condition for iterations as shown in the following equation:

$$\Delta u_j = -K * (const - a * P_j * x_7 + b * p_7 * x_j) \qquad (11)$$

where P_j is a combination of the costate variables and $a_1 = (3a_l + 1) - 3k(a_l + 1)$, $a_2 = 3a_l + 1$, as shown for the case j=1 in the following equation:

$$P_1 = a_1 * p_1 + p_2 + p_3 + a_2 * p_4 + p_5 + p_6 \qquad (12)$$

From the gradient vector we can observe that the bilinearity is between the DV voltage as state variable and each of the individual currents $\mathbf{x}_j = \mathbf{i}_j$ (j=1,...,6).The weighting constants a and b are strictly related to the model characteristics, and a normal linear approach will ignore their influence;

$$a = \frac{1}{6} \frac{1}{L(a_l + 1)} \quad and \quad b = \frac{1}{2C} \qquad (13)$$

Considering the const parameter equal to a, and the second term of the feedback term as the difference between the two converters' currents of the same phase, the feedback compensation term can be rewritten as:

$$\Delta u = K[k_1(1 - v_d) + k_2(i_1 - i_4)] \qquad (14)$$

and this will be the form used for the following analysis.
A problem very sensitive for linear theory too, is the control parameter identification. Trade off between low values (for a reduced noise) and special computed ones

(stability requirements) is done for the bilinear structure through the K, k1 and k2 constants. It can be easily shown that the connection between the two set of state variables (input current vector and the DC voltage), is felt on the system behavior as relation between the input current's quality (harmonic content) and the DC voltage error. Therefore, our aim of improving the quality of the input AC currents is coincident to keeping the DC voltage stiff at the reference value, this being useful as well, for any inverter-type loading. Our statements are proved in figure2, for system parameters as following: line resistance 0.2p.u., relative inductance L=4.0p.u.,DC side capacitor C=1.0, PI feedback parameters Kp=100.0 and Ki=1.0, and a variation for L from 0.2p.u. to 0.5p.u.:

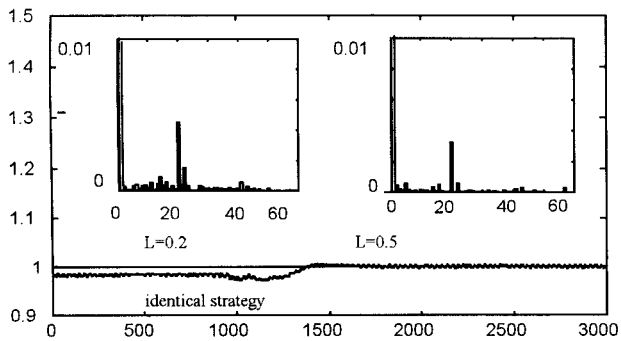

Figure 2: DC voltage waveform and the harmonics content for al varying from 0.2p.u. to 0.5p.u.

Based on the previous explanations, it can be shown that best behavior for our problem is for k2=0.7 as the values that keep the proportion between the calculated parameters (from equation12), and simulations have proved this (for K=1.0, k1=1.0 results k2=0.702):

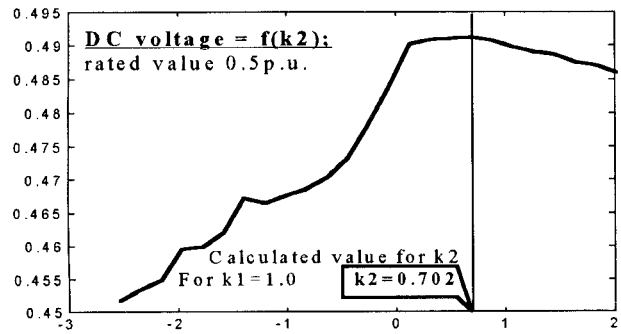

Figure3: DC voltage as function of the k_2 parameter.

Any perturbance will be felt by the DC side by over- or under-voltages, corresponding to DC off-set currents flowing in the AC side, and this will be partially explained by the variation of the system parameters from the values considered for an optimized behavior (as computed above). As a generalization for the defined rule we show the same variation of the DC voltage for a set of values for compensation parameters k1 and k2. Varying the individual inductance from 0.01p.u. to 0.15p.u, the optimal operation should be the one for the highest DC voltage (closest to the reference value). From figure4.a) we see that the "top of the hill" is oriented along the k2=0.5 line, which has been obtained from special calculated values for k1, so as to maintain the same proportion between k1 and k2. The contour graphic 4.c)certifies the domain of best behavior along the k2=0.5 line.

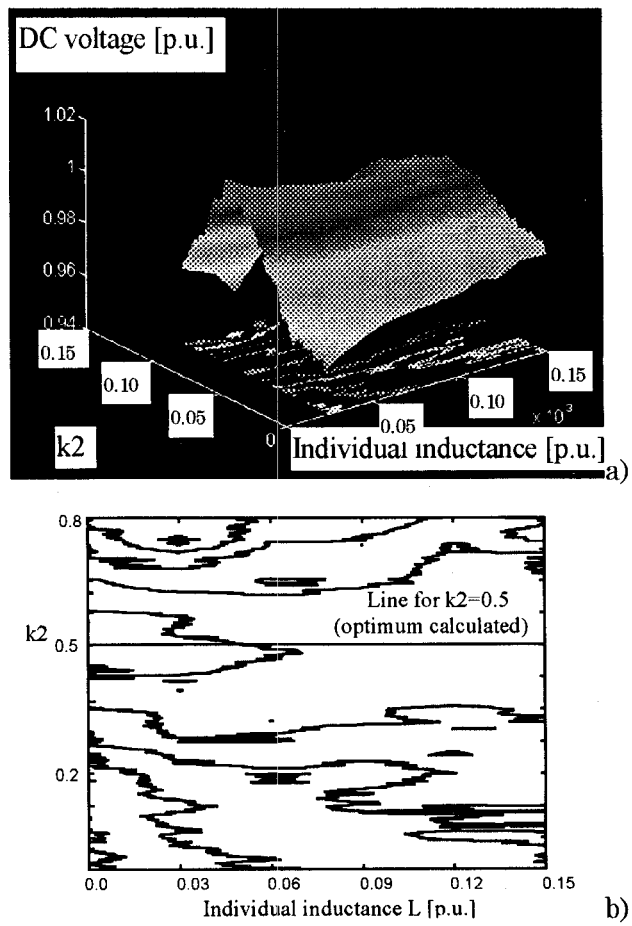

Figure4: a) Plot of DC voltage as function of k2 and individual inductance; b) contour-typr representation

III. CONTROL STRATEGY AND OPTIMALITY ASSESSMENTS

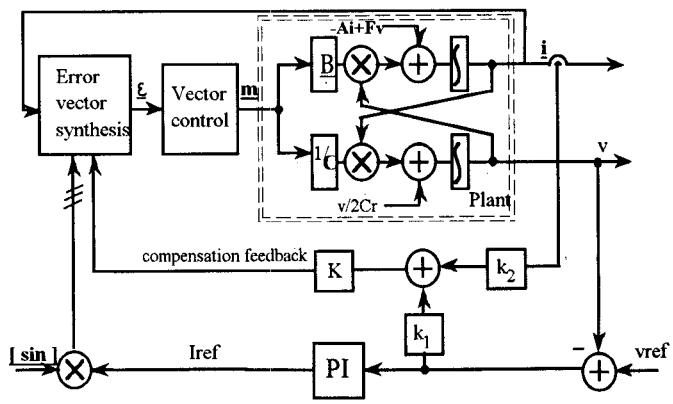

Figure 4: General structure of the system - with emphasis on the plant bilinear model and the compensation feedback.

The control strategy used is current vector based [7],

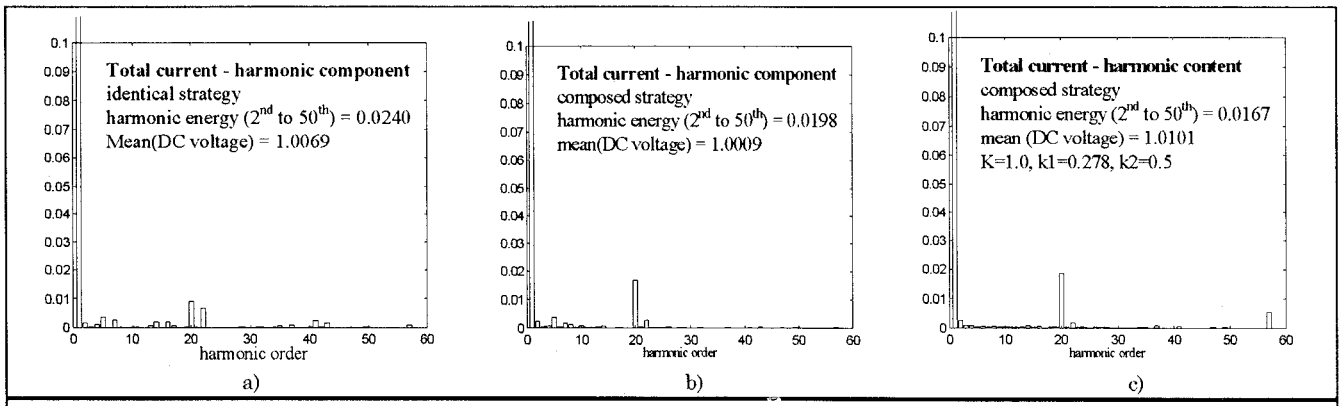

Figure5: Harmonic content for the a)identical strategy, b) the composed one and c) the compensated composed strategy

combining the switching states for the two converters (mentioned as Plant in figure4). As already discussed, a compensation loop is added to the system, and a compensation term characterised by K, k1 and k2 parameters is found by means of theoretical analysis.

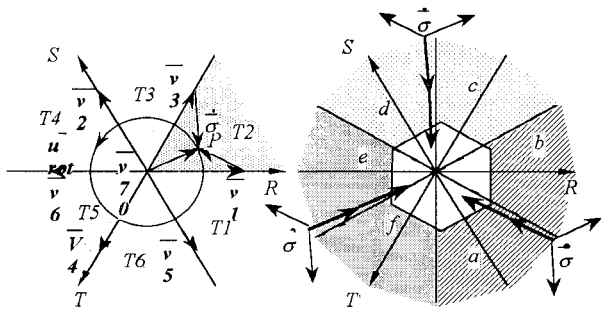

Figure6: Identical current vector control strategy

The control strategy has been discussed in previous items, and eventually an identical strategy and a composed strategy are chosen for the coming developments. The main characteristics are that the identical strategy figure 6 (which drains its name from providing identical individual currents for the same phase of the two converters) is more stable than the composed one (which respectively provides different individual currents, by combining the other two vectors as from the identical case). The composed strategy will be the chosen one since the input currents' harmonic content is improved, and the compensation method improves it further more, assuring the system robustness as well.

In what regards the input currents harmonic content, figure5 shows a comparison between the identical strategy, composed strategy and the compensated composed strategy for system parameters L=0.2p.u., C=1.0p.u., a=2.0, and control parameters Kp=100.0 and Ki=1.0.

IV. SIMULATION ANALYSIS FOR FAULTED OPERATION CONDITIONS

As a faulted condition, one important case is the instantaneous decay of the individual inductance for one converter. The unbalanced operation was implemented for the case of two parallel connected converters, for the two current vector strategies.

For the next simulations, the individual inductance of one converter is considered to decay from 0.1p.u. to a quarter of it (0.025p.u.) a value that reaches the stability limit for an uncompensated system on the composed strategy. System parameters are al=2.0, C=1.0p.u. and control parameters Kp=100.0 and Ki=1.0, for a strategy providing 20 pulses per cycle.

Identical strategy is less illustrative for the present study, but its behavior analysis can be found in [10]. For the composed strategy, the feedback term will have to compensate the increased instability of the system, too. Results show also that for relative small weighting coefficients (K=1.0, k1=1.0, k2=0.6), the stability of the system is assured and the steady state behavior keeps to be at good levels.

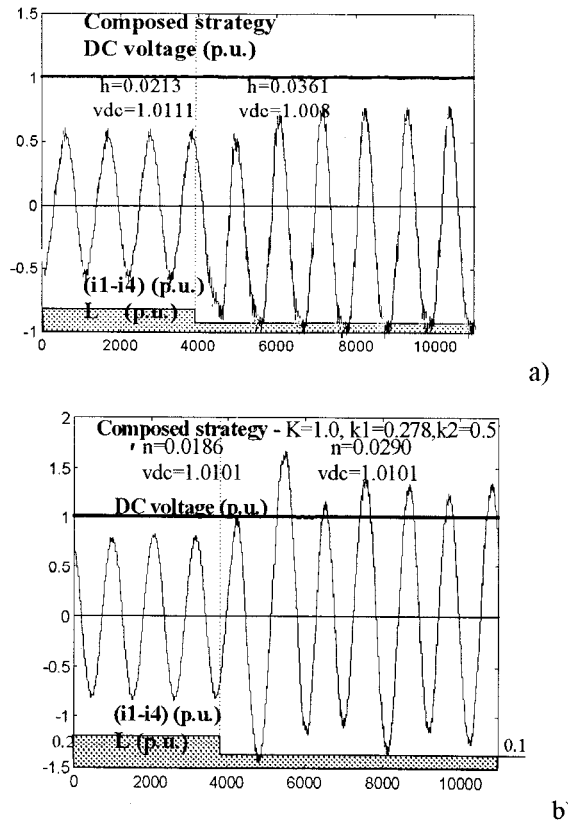

Figure 7 a): State variables wave form for the composed strategy a) uncompensated and b) compensated case.

There is an important observation to be done, regarding the relation between the two indices the mean value of the DC voltage and the harmonics energy calculated for the first 50 harmonics, and which we considered to be in a strict dependency. For the uncompensated case it can be seen that the harmonics energy index is worse after the fault occurs, even though the mean value of the DC voltage is slightly closer to the reference value. Explanation comes from figure8, where the phase currents and the total current error were transformed for a bidimensional representation:

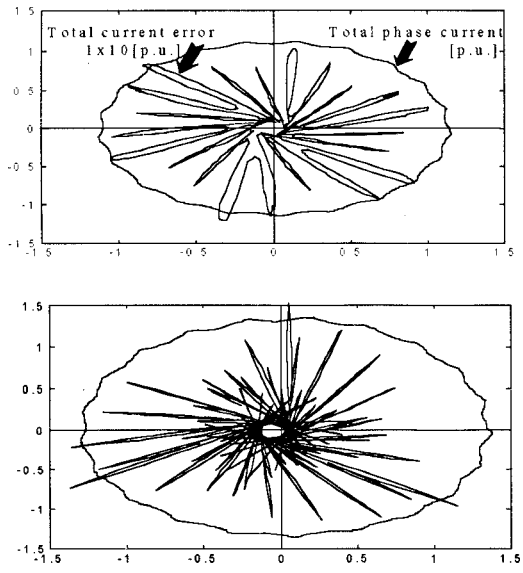

Figure8: Bidimensional representation for the three phase currents and the respective total errors, for the uncompensated case a)before and b) after fault occurs.

It can be seen that for the faulted condition (figure 8.b)) the error shape is displaced in an opposite direction the phase currents are displaced. This is the DC offset current that occurs during the transients, and the method we propose is totally compensating it. For not balanced parameters, the DC offset current continues to flow in the AC side or an opposite one is injected in the system. Related to that, if an energy-problem is considered to be solved for the optimal realization, the switching strategy obtained will be applied direct to the converter input in addition to the strategy provided by the respective control method, and this will be like a zero-sequence injection method

V. EXPERIMENTAL APPROACH

For the real-time validation of the proposed method we consider a transputer based approach, on which a parallel programming language is implemented - OCCAM. The general structure of the system is:

- computer with T805 transputer board incorporated
- transputer block with variable architecture (AD inputs, computational unit, digital output)
- multiconverter unit -four MOSFET converter boards (IRFP350) (2Ax350V)
- interface board:
- line inductance L=0.076H, resistive load (R=1.0Kohm)

and has the structure presented in the next figure:

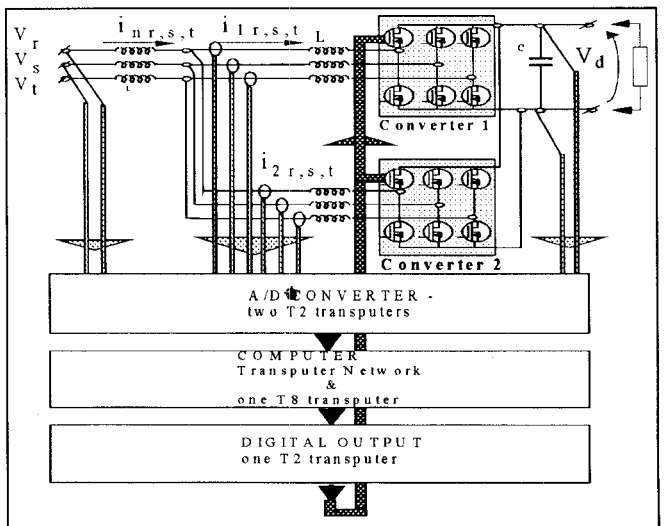

Figure 9: Experimental approach - general structure

Experiments were carried out in order to proved the improved robustness for the system. First remarkable result it was obtained for the faulted operation of the two parallel connected converters, when one inductance failed in value for 50% (the control parameters are Kp=89.0, Ki=74.0). The system proves several points of loosing stability, but compensated with K=1.0, k1=2.12 and k2=1.15 (as resulted from the computation rules stated in the theoretical items), has a normal operation. Results are for the supposed most unstable control method - the composed strategy.

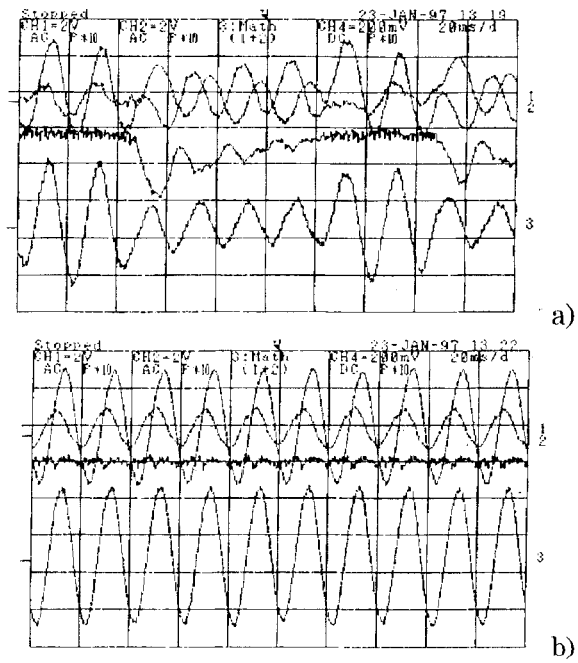

Figure 10: Composed strategy for the faulted operation (L=0.038H) in the a) uncompensated and b) compensated case.

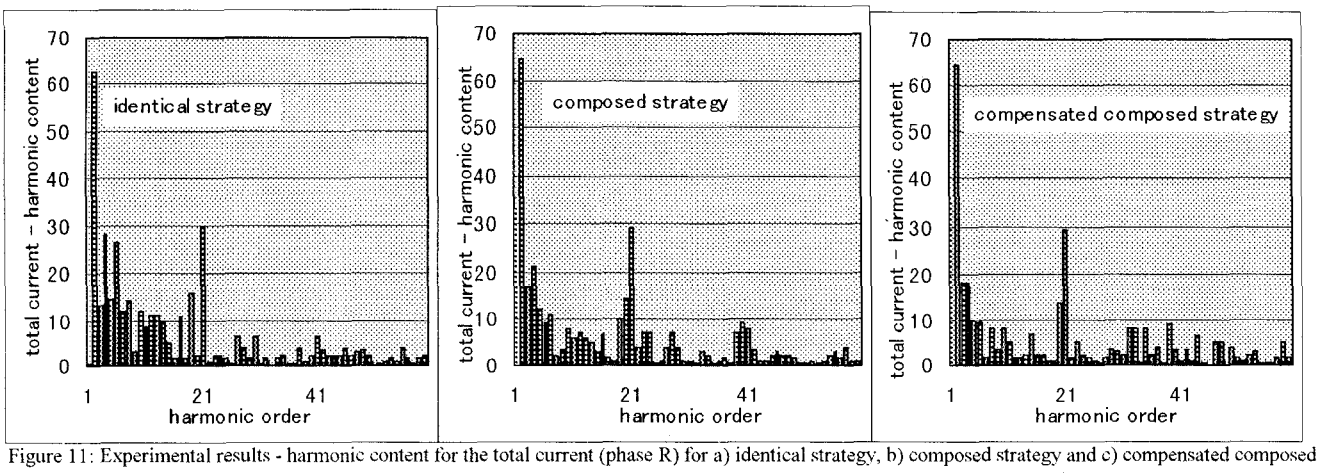

Figure 11: Experimental results - harmonic content for the total current (phase R) for a) identical strategy, b) composed strategy and c) compensated composed strategy.

An important accomplishment is the improvement in the harmonic content for the input currents, and this was proven experimentally as well. We show in figure11 the total current's harmonic content, for normal operating conditions and the improvement obtained for the composed method, and eventually for the compensated case:

VI. CONCLUSIONS

There have been discussed steady state and transient operation conditions, with the emphasis on the bilinear type of the power converters' model, the basis for a compensation method for faulted conditions that produce unbalanced operation between the two converters. If a welknown proportional feedback for high values of its parameter, besides its improvements introduces noise in the system, the compensation feedback we are proposing is positively influencing not only the system reliability but its internal variables (AC input currents) quality.

Based on the mathematical model, the feedback term was deduced, and it has been proved that it produces an automatic compensation for any perturbed operation. An important achievement is the relation between the parameters of the feedback term (DC voltage error and difference of the currents for the same phase), which can be considered related to the DC voltage variation as result of the DC offset currents that tend to flow during any transient period. The proper solution of the trade off between high values of feedback parameters that provide good stability, and low values for a special calculated ratio on steady state conditions, are giving the success of the proposed algorithm. It is obvious that, for normal operating conditions or ,at least, the derated ones, special calculated parameters should be taken into account. If the system reliability is considered more important, a special attention should be given to an increased K parameter, upper limited in value only by the perspective of a high DC component flowing in the AC side.

The new model and method proposed here can be very useful for creating an entire theory for bilinear or hybrid bilinear systems, to cover the lack of an already synthesized theory as in the linear case. Dealing with multivariable structures will complicate the problem, but many equivalent tools for analysis can be found.

VII. REFERENCES

[1] Masada E. - "Power Devices Application's Handbook" IEEJ edited, Chapter 7, Corona-sha, 1995

[2] Juengst K.P., Komarek P., Maurer W. - "Use Of Supreconductivity In Energystorage", World Scientific,1995

[3] Burlacu C, Masada E. - "Bilinear Approach For Parallel Connected Multiconverters And The Respective Control" PEMC '96, Vol.1, pp 243-248

[4] A. E. Bryson, Y.C. Ho "Applied Optimal Control" Hemisphere Publishing Corporation, 1975

[5] L. Matakas Jr. E, Masada "Multiconverter Implementation by Parallel Association of k Voltage Source Converters Control Method " EPE '94 , Brighton , UK , pp.35-40 , Vol.4 , 1994/sept .

[6] Black - Modulation Theory , Van Nostrand , 1953

[7] P.Korondi, S. H. Yang, H. Hashimoto, F. Harashima "Sliding Mode Controller for Parallel Resonant Dual Converters" Journal of Circuits, Systems and Computers,World Scientific Publishing Company, 1996

[8] Hsu.J.C., Meyer A.V." Modern Control Principles and Applications", McGraw-Hill, New York, 1968.

[9] Mohler R.R. "Bilinear Control Processes", Academic Press, New York, 1973.

[10] Burlacu C., Ohsaki H., Masada E. "Control Strategy for Parallel Connected Voltage Type Converters, using Hybrid Bilinear Principles", proposed for Proceedings of IEE Japan, January 1997.

Dual Slope Integrator Type Delta Modulator for High Performance Voltage Source Inverters

K. M. Rahman, M. A. Choudhury , M. Rezwan Khan
Department of Electrical and Electronic Engineering, BUET, Bangladesh
and
M. A. Rahman, Memorial university of Newfoundland, Canada

Abstract – **The integrator of the modulator in a delta modulated (DM) inverter control greatly affects the voltage waveform patterns, fundamental voltage and spectral components. The performance of DM with different types of filters suffers from low fundamental voltage. The previous schemes can not provide fundamental voltage equal to the supply voltage and pulse dropping phenomena occurs as the modulating frequency is increased. To overcome these problems a dual slope integrating (DSI) filter is proposed in this paper. Introduction of DSI filter in the DM loop gives a fundamental voltage equal to the supply voltage at 100% modulation index. The number of pulses per fundamental period can be maintained constant in the modified DSI-DM scheme. The performance of this modulator is better than other DM schemes so far reported. Simulations and experimental results are presented to justify the claims of the paper.**

I. Introduction

In recent years delta modulators have gained popularity for application in Voltage Source Inverters. The delta modulation (DM) offers the opportunity of on-line harmonic minimization [1] of pulse width modulated inverters without conventional optimization processes. The advantages of DM for on-line control of various inverter waveforms are their simple implementation and versatile performances. In single or double integrator DMs [1] the fundamental voltage magnitude is low. Also, when the modulating frequency is increased, pulse dropping phenomena occurs. Hence it is not suitable for wide range of variable frequency applications. Using a tuned filter with frequency dependent slope, pulse dropping phenomena can be minimized [2] with reduction of the fundamental voltage. Variable band DM improves the magnitude of the fundamental voltage [3] by feeding a portion of the input reference modulating signal to the hysteresis quantizer. But still the fundamental magnitude is well below the supply voltage at 100% modulation index.

A.C. motor drives having field oriented hysteresis current control provide high dynamic performances [4,5]. In this method hysteresis comparators are used to impose a fixed dead band or hysteresis around the reference current. The load current waveform of the hysteresis control scheme is confined within a band. Hence its harmonic distortion is very low at small band gap. The output of such a scheme shows good spectral behavior and the fundamental voltage is a direct function of the modulation index. Moreover, the fundamental magnitude is 100% of supply voltage at unity modulation index. This advantage of hysteresis current controlled PWM is used in the proposed dual integrator DM scheme.

In the proposed scheme the integrator of the DM is chosen to give characteristics such that its output follows the waveform of the current in hysteresis current controllers with a PWM waveform applied to it. This is achieved by mapping the load current by an R-C circuit. The current flow through an R-L load from a voltage source is emulated by the capacitor voltage of an R-C load.

This paper also presents a generalized indirect field oriented controller which can be used for any type of VSIs irrespective of applications.

II. Proposed Dual Slope Delta Modulator

The load current of an R-L load circuit is given by,

$$i = i(0)\,e^{-\frac{R}{L}t} + \frac{V_s}{R}\left(1 - e^{-\frac{R}{L}t}\right) \tag{1}$$

where, i(0) = initial value of current and V_s is the supply voltage. Current through a series R-L load is analogous to the voltage across the capacitor of a series R-C load. In an R-C circuit the following relationships hold,

$$V_s = Ri + V_c \;;\quad i = C\frac{dV_c}{dt}$$

$$V_s = RC\frac{dV_c}{dt} + V_c \tag{2}$$

Taking Laplace transformation and Inverse Laplace transform of (2), the following expression can be obtained,

$$V_c(t) = V_s(1 - e^{-\frac{t}{RC}}) + V_c(0)\,e^{-\frac{t}{RC}} \tag{3}$$

Equations (1) and (3) are analogous. Implementation of RC circuit with OPAMPs can easily be done. Taking voltage as reference in the controller and taking feedback from the capacitor voltage will give a true analogous circuit of the hysteresis current controller. Differentiating (3) one obtains,

$$\frac{dV_c(t)}{dt} = m = RC(V_s - V_c(0))\,e^{-\frac{t}{RC}} \tag{4}$$

0-7803-3823-5/97/$10.00© 1997 IEEE

From (4) it is clear that the slope of the capacitor voltage is an exponentially decaying function having two different types of coefficients.

1) Case A : For positive V_s , slope m_1 is positive and its magnitude is given by,

$$m_1 = RC(V_s - V_c(0))e^{-\frac{t}{RC}} \quad (5)$$

2) Case B : For negative V_s , slope m_2 is negative and its magnitude is given by,

$$m_2 = RC(V_s + V_c(0))e^{-\frac{t}{RC}} \quad (6)$$

Thus implementation of the series R-C load to the controller gives rise to dual slope integration.

III. Switching Point Calculations and Spectral Analysis

The DSI-DM can be implemented with an error amplifier, hysteresis comparator and dual slope integrator as shown in Figs. 1 and 2. The dual slope integrator has a transfer function representing (3). For microcomputer simulation and implementation, the switching points for the PWM pattern are calculated based on sampling strategy [6] using the flowchart of Fig. 3. In the flow chart the symbols used are,

N Number of samples per cycle of the modulating signal

V_{ci} Estimated output voltage at i-th sampling instant

X_i DSI-DM PWM output at i-th sampling instant

β Hysteresis band $= \dfrac{R_d}{R_f + R_d}$

δ Step change in voltage per sample

The arrays t_l, t_r and X contain the positive switching points, negative switching points and the entire switching pattern for all samples respectively. The calculations involve only exponential term which is a built in function of the 486 DX4 processors. Time required for calculations is much less and hence it is suitable for real time microcomputer implementation.

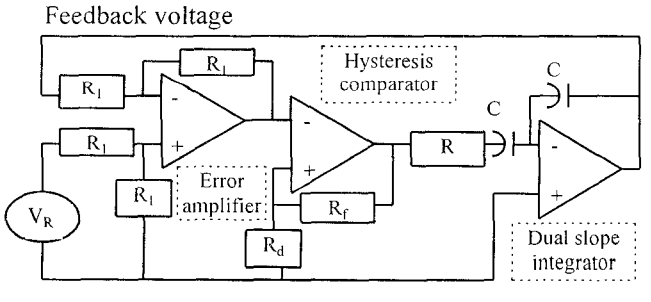

Fig. 1 Fixed band dual slope integrating type delta modulator.

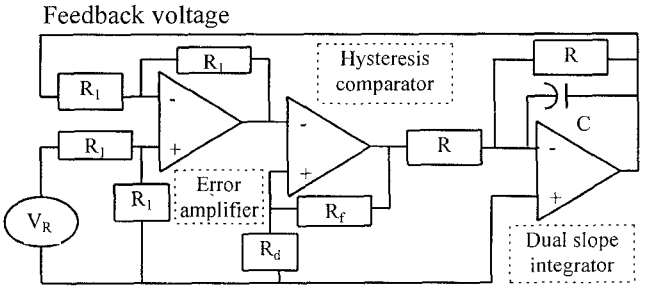

Fig. 2 Alternate circuit scheme for fixed band dual slope integrating type delta modulator.

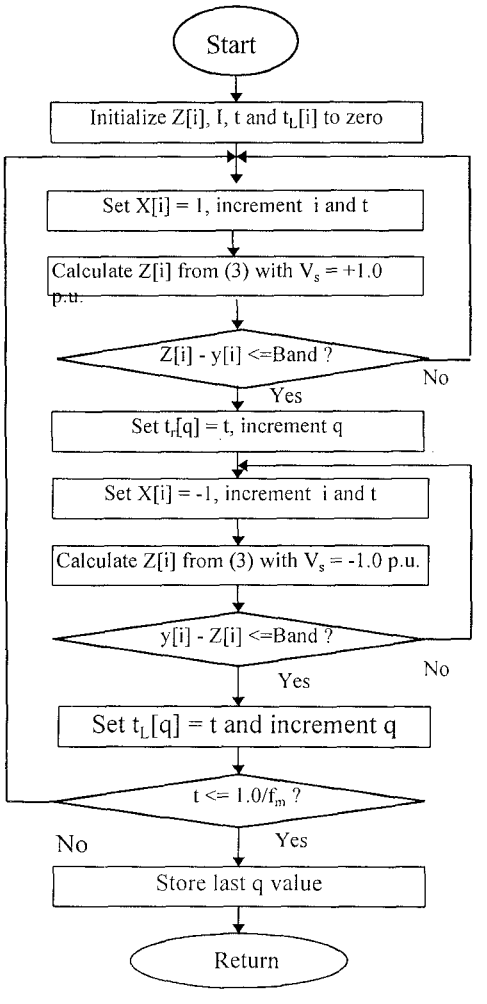

Fig. 3 Flowchart for calculation of switching points and array of PWM pattern of DSI-DM.

The simulated waveform obtained from the switching array of the subroutine for 25 Hz and 100 Hz are shown in Figs. 4, 5 respectively. The corresponding spectra are shown in Fig. 6 and Fig. 7 respectively. The simulated waveforms show that as the frequency is increased from 25 Hz to 100 Hz keeping the other parameters constant, the number of pulses per cycle reduces from 62 to 12. The spectra show that at 100 percent modulation index the fundamental magnitude is around 1.05.

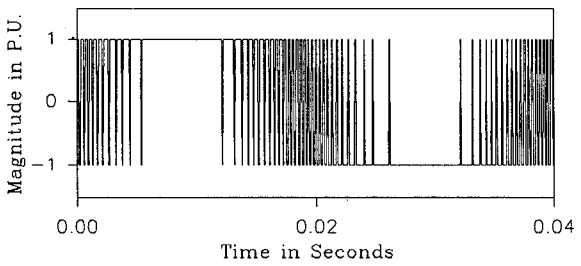

Fig. 4 DSI-DM PWM waveform for f_m =25 Hz, β = 0.05, R = 1.0K, C = 1.25 μF and M = 1.0.

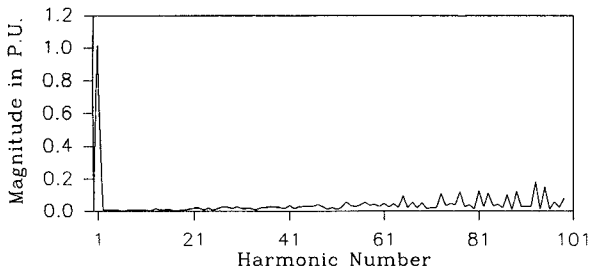

Fig. 5 Spectra of DSI-DM PWM waveform for f_m =25 Hz, β = 0.05, R = 1.0K, C = 1.25 μF and M = 1.0.

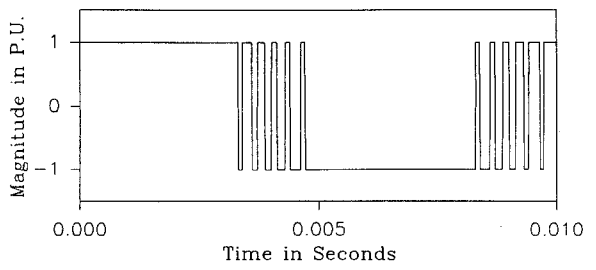

Fig. 6 DSI-DM PWM waveform for f_m =100 Hz, β = 0.05, R = 1.0K, C = 1.25 μF and M = 1.0.

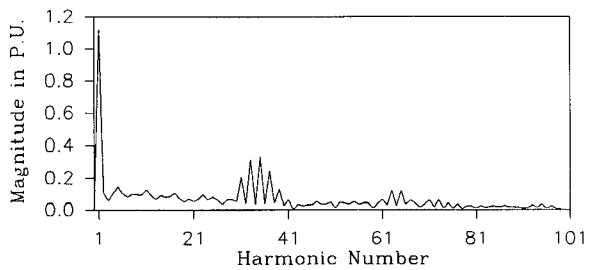

Fig. 7 Spectra of DSI-DM PWM waveform for f_m = 100 Hz, β = 0.05, R = 1.0K, C = 1.25 μF and M = 1.0.

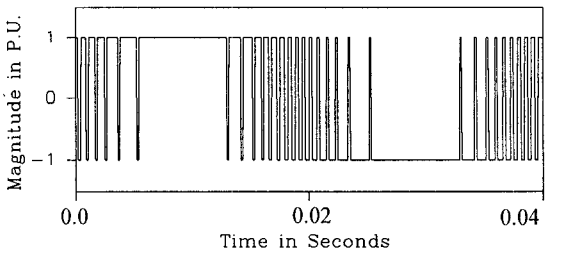

Fig. 8 Modified DSI-DM PWM waveform for f_m = 25 Hz, β = 0.1, δ = 0.03 and M = 1.0.

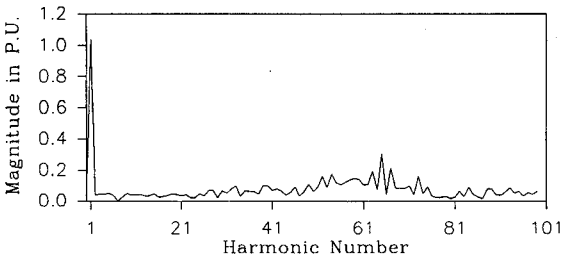

Fig. 9 Spectra of modified DSI-DM PWM waveform for f_m = 25 Hz, β = 0.1, δ = 0.03 and M = 1.0.

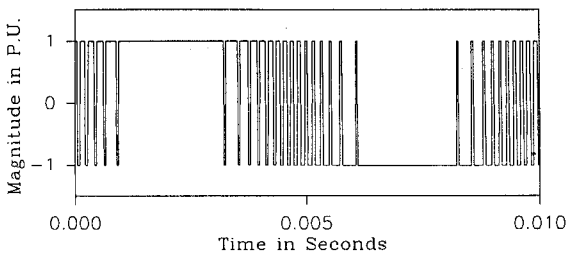

Fig. 10 Modified DSI-DM PWM waveform for f_m = 100 Hz, β = 0.1, δ = 0.03 and M = 1.0.

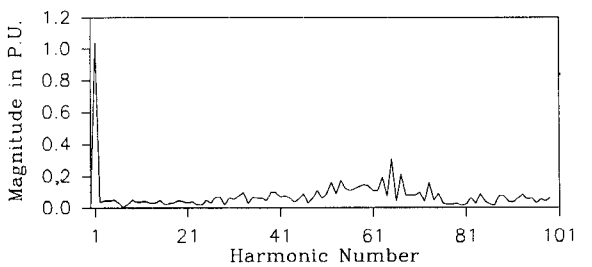

Fig. 11 Spectra of modified DSI-DM PWM waveform for f_m = 100-Hz, β = 0.1, δ = 0.03 and M = 1.0.

Keeping the fundamental magnitude same, pulse dropping phenomena is removed by modifying (3). The exponential terms of (3) are expanded upto the second term. Thus (3) can be simplified as,

$$V_c(t) = V_s\left(\frac{t}{RC}\right) + V_c(0)\left(1 - \frac{t}{RC}\right) \qquad (7)$$

With the identity $\frac{t}{RC} = \delta$, rearranging (7) one gets,

$$V_c(t) = V_c(0) + d[V_s - V_c(0)] \qquad (8)$$

Equation (8) is used to simulate the PWM waveform in modified DSI-DM. The PWM waveform and corresponding spectra are shown in Figs. 8 - 11. The characteristics of DSI-DM and modified DSI-DM are shown in Table I. Implementation of the modified DSI-DM with integrated circuits is shown in Fig. 12.

IV. Microcomputer Implementation and Results

The circuits in Fig. 1 and Fig. 2 are simulated with PSPICE. The PSPICE simulated waveforms substantiate the results discussed in section 3. For microcomputer implementation the number of samples per cycle are maintained constant independent of modulating frequency.

TABLE I
MODULATOR CHARACTERISTICS

f_m	M	DSI - DM			Modified DSI-DM		
		β	τ =RC	q	β	δ	q
10	1.0	.05	0.00125	121	0.1	.03	31
25	1.0	.05	0.00125	62	0.1	.03	31
50	1.0	.05	0.00125	32	0.1	.03	31
100	1.0	.05	0.00125	12	0.1	.03	31
10	0.5	0.1	0.0015	110	.15	.02	28
25	0.5	0.1	0.0015	52	.15	.02	28
50	0.5	0.1	0.0015	27	.15	.02	28
100	0.5	0.1	0.0015	13	.15	.02	28
10	0.2	.03	0.0025	209	0.2	.05	58
25	0.2	.03	0.0025	103	0.2	.05	58
50	0.2	.03	0.0025	58	0.2	.05	58
100	0.2	.03	0.0025	30	0.2	.05	58

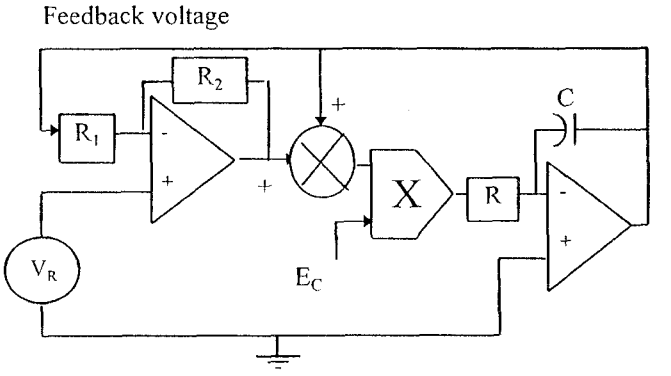

Fig. 12 Circuit implementation of the modified DSI-DM.

Sampling time thus becomes frequency dependent and fixed amount of memory is required for all frequencies.
With constant sampling time the required number of samples per cycle is large at low modulating frequency requiring huge memory. The voltage slope δ is maintained constant. The software designed in the Borland Turbo C/C++ environment gives the switching pattern, graphical output of the waveform and spectra at the computer monitor screen and real time PWM waveform in the hardware parallel port. The oscillogram records of the real time PWM waveforms obtained from microcomputer parallel port are shown in Fig. 13 and Fig. 14 for DSI-DM and modified DSI-DM, respectively.

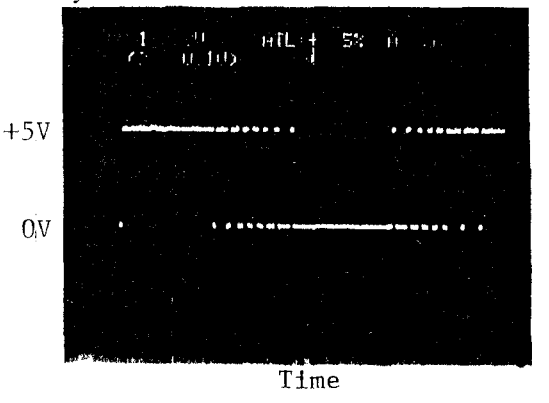

Fig. 13 DSI-DM PWM waveform for f_m = 52 Hz, β = 0.1 , τ = 0.00125 and M = 1.0.

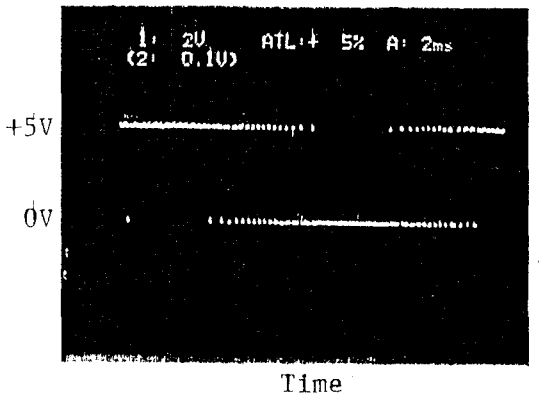

Fig. 14 Modified DSI-DM PWM waveform for f_m = 52 Hz, β = 0.1 ,δ = 0.03 and M = 1.0.

V. CONCLUSION

This paper presents contributions in the application of delta modulators in the operation of voltage source inverters. The problem of low fundamental voltage in DM is improved by using a dual slope integrating (DSI) type low pass filter. The DSI-DM suffers from pulse dropping phenomena. In the modified DSI-DM pulse dropping phenomena at high modulating frequency is reduced by tuning the DSI filter with the modulating frequency. The modified DSI-DM when implemented with a microcomputer is capable of maintaining constant number of pulses per cycle of the modulating signal at any frequency. Thus it is suitable for wide range of variable frequency inverter operation. Simplified circuits are proposed for implementation of DSI-DM and modified DSI-DM. This paper also reports a simplified microcomputer implementation strategy for DM for inverter control.

REFERENCES

[1] M. A. Rahman, J. E. Quaicoe and M. A. Choudhury, "An optimum delta modulation strategy for inverter operation", *IEEE PESC Conf. Record*, Vancouver, B. C., 1986, pp. 410-416.

[2] M. A. Rahman, J. E. Quaicoe and M. A. Choudhury, "Harmonic minimization in Delta modulated inverters using tuned filters", *IEEE PESC Conf. Record*, Tokyo, Japan, 1988, pp. 462-468.

[3] A.H. Choudhury, M. A. Choudhury and M. A. Rahman, "On-line improved inverter waveform by variable step delta modulation", *IEEE PESC Conf. Record*, Tokyo, Japan, 1994.

[4] D. M. Brod and D. W. Novonty, "Current control of VSI-PWM inverters," *IEEE/IAS 1984 Annu. Meeting*, 1984. pp. 418-425.

[5] P. Enjeti, P.D. Ziogas, L.F. Lindsay, and M.H. Rashid,"A novel current controlled PWM inverter for variable speed ac drives," *IEEE/IAS 1986 Annu. Meeting*, 1986. pp. 235-243.

[6] S. R. Bowes and P. R. Clark, "Simple microprocessor implementation of new regular sampled harmonic elimination PWM techniques," *IEEE Trans. Ind. Applicat.*, vol. 28, no. 1, pp. 89-95, 1992.

Development of a General Tokamak Circuit Simulation Program and Some Application Results to the JT-60 Power Supply System

Makoto Matsukawa, Tetsuo Aoyagi, Yushi Miura
Japan Atomic Energy Research Institute
Mukoyama, Naka-machi, Naka-gun, Ibaraki, 311-01, Japan
Tel.:81-29-270-7429, Fax.:811-29-270-7459, E.Mail:matsukaw@naka.jaeri.go.jp

Abstract — **This paper describes the General Tokamak Circuit Simulation Program (GTCSP) developed for designing the power supply system in a large nuclear fusion device JT-60. GTCSP can deal with synchronous generators, phase delayed transformers connected to thyristor converters, inductively coupled passive coils and their combination. Since the GTCSP code is designed for the limited purposes, it has the advantages of smaller number of input parameters and shorter computation time. A time step of the simulation is automatically adjusted according to the change of converter switching mode, and this function suppressed switching noises. Program overview and some application results are presented.**

I. Introduction

In the field of nuclear fusion energy research, the plasma performance has been dramatically improved with increasing the scale of experimental devices. JT-60 is one of the largest tokamak-type magnetic fusion devices in the world and recently achieved the equivalent break-even condition successfully with deuterium discharges [1]. Principally tokamak device is operated with a pulse operation, because the plasma current is driven as a secondary coil current by change of the primary coil current like a transformer. Since a large capacity is required but the necessary energy is small, the combination of a motor-generator and thyristor converters are commonly used in most of tokamaks. For example, a total power supply capacity of about 1GVA is required but the necessary energy is less than 1GJ in JT-60 [2].

The most important issue in the design of power supply system is how to confirm the coil current controllability and the internal behavior of the converters, because the power supply consists of a lot of unit converters connected in series and/or in parallel. Furthermore, the response time of a few milli-seconds is desired from the view point of plasma control so that the control system must be carefully checked by simulation in advanced to the fabrication.

A lot of electric circuit analysis programs, e.g., ATP-EMTP, SPICE and etc., are available today. However, they are too much conventional and complicated, and this means that they involve a certain amount of redundancy to apply a limited purpose and causes a longer computation time. Hence, we decided to develop an own electric circuit analysis program named GTCSP, which is dedicated for designing our power supply system.

GTCSP has following features. (a) A circuit is constructed from the model of synchronous generators, phase delayed transformers connected to thyristor converters, inductively coupled passive coils. (b) Users can create the current control routine and thyristor gate control routine including phase angle detector with Fortran or C language. (c) The computation time is usually shorter than other programs. (d) A time step of the simulation is automatically adjusted when the converter switching mode changed. This function enables to adopt a relatively long time step width of the numerical integration.

In this paper, an overview of the program is described in Section 2, and some results of its application to JT-60 are presented in Section 3. In section 4 evaluation of the program performance is discussed, and a final section is a conclusion.

II. Program Overview of GTCSP

A. Solving method

The basic idea of the circuit conversion comes from the law of Ho-Thévenin which enables to represent a much complicated circuit by a simple impedance and voltage source. Therefore the tokamak power supplies can be converted to the equivalent R-L circuits and the voltage sources as shown in Fig.1, because any condenser banks are usually not used in the coil power supplies. GTCSP creates the circuit equations automatically from the equivalent circuit by its circuit analysis routine [3]. We do not mention here so much about the circuit topology, but it must be noted that it is obtained from the closed loop voltage equations called to cut-set equations [4]. Then GTCSP can be roughly divided into two parts: (a) supervising program which creates a whole circuit equation and controls the process of simulation, (b) component model program which interfaces a complicated circuit of model with a simplified equivalent circuit to be used in the supervising

0-7803-3823-5/97/$10.00© 1997 IEEE

program.

Newton-Cotes integral method was adopted for solving differential equations of electric circuits in GTCSP. However, the calculation steps was shared to the supervising program and the model programs. The procedure is as follows.

Step-1: The supervising program derives time derivatives of the current $d\vec{i}/dt$ at the time t using the equation (1).

$$\vec{e} = L \cdot d\vec{i}/dt + R\vec{i} \quad (1)$$

Here, $\vec{e}$ is a voltage vector of the equivalent circuit, and $\vec{i}$ for current. The L and R are inductance and resistance matrixes.

Step-2: The each model program derives current $\vec{i}'_{new}$ at the time $t + \Delta t$ using the equation (2).

$$\vec{i}'_{new} = \vec{i} + d\vec{i}/dt \cdot \Delta t \quad (2)$$

Step-3: The supervising program derives again time derivatives of the current $d\vec{i}'_{new}/dt$ at the time $t + \Delta t$ using the equation (3).

$$\vec{e} = L \cdot d\vec{i}'_{new}/dt + R\vec{i}'_{new} \quad (3)$$

Step-4, Finally the each model program derives the current $\vec{i}_{new}$ at the time $t + \Delta t$ using the equation (4).

$$\vec{i}_{new} = \vec{i} + \left\{ d\vec{i}/dt + d\vec{i}'_{new}/dt \right\} \cdot \Delta t/2 \quad (4)$$

Step-5, Step-1 described above is repeated by substituting $\vec{i} = \vec{i}_{new}$.

When the switching mode is changed in the thyristor converter model, the return flag informed it to the supervising program. Promptly, the supervising program demands all model program to interpolate on the mode changed time to improve simulation accuracy. The switching mode will be checked again after the interpolation for confirmation. Figure 2 shows the flow-chart of processing of the GTCSP program.

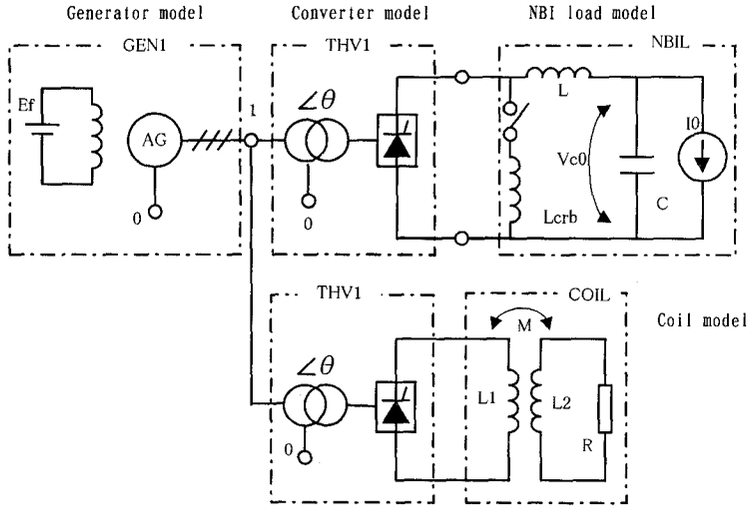

(a) An example of the power supply system.

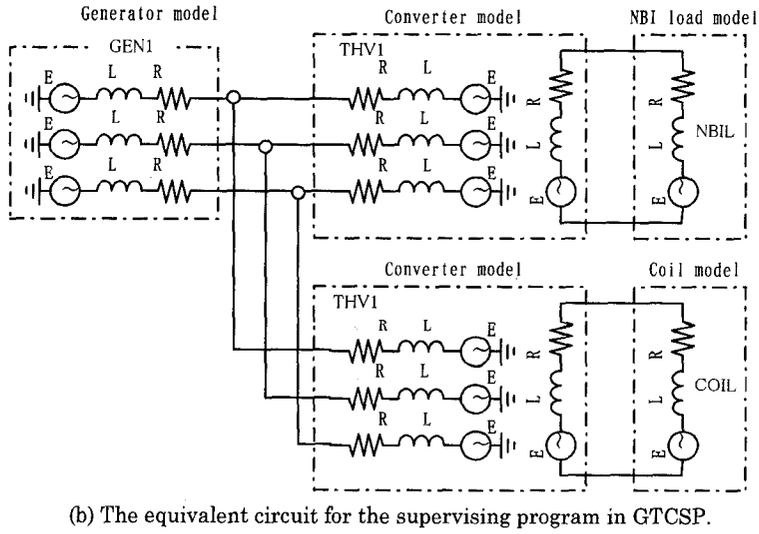

(b) The equivalent circuit for the supervising program in GTCSP.

Fig.1. An example of the power supply system to be analyzed and the equivalent circuit.

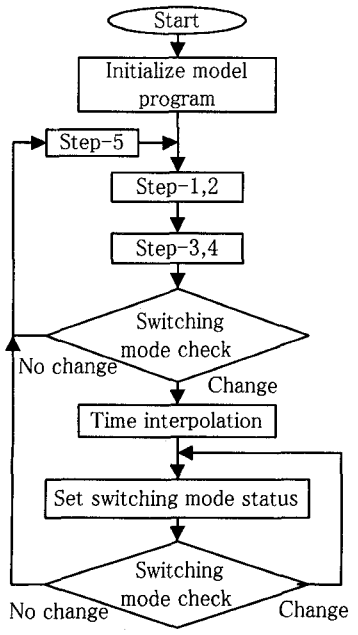

Fig.2. Flow-chart of simulation in the program.

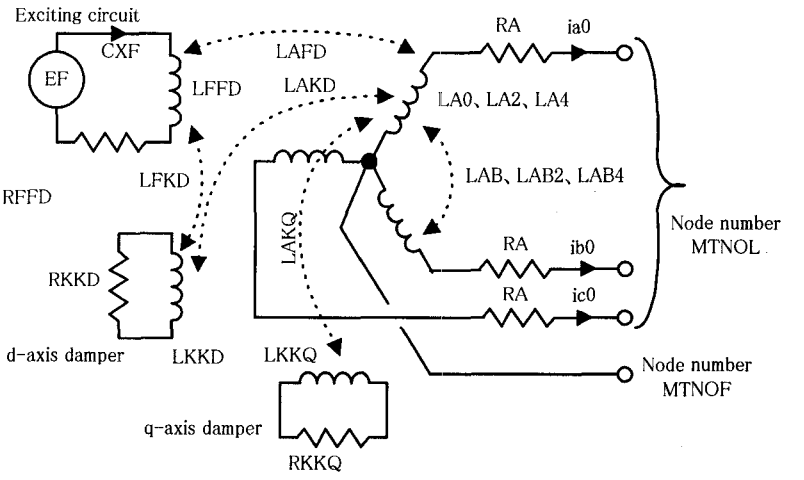

Fig.3. Equivalent circuit of the generator model.

B. Circuit model of each component

(a) Generator model: The synchronous generator model adopted in the program is entirely same with the Park-Model, where the rotor has two damper windings but the iron saturation is not taken into account. Since the equation is solved directly without any coordinate-transformation for the stator winding, the R-L parameters of each windings and the rotating speed must be provided. In other words, we adopted the phase-domain model for generator to connect the converters. In the present model of generator, the motion equation can not be taken into account, but the inductance change as a quadratic function of the rotor position can be provided for the salient machines. The exciting circuit is included into the generator model, then user can only provide the exciter power supply voltage as shown in Fig.3. Recently a very similar model was introduced to ATP-EMTP by Xianglin [5].

(b) Converter model: Figure 4 shows the circuit of phase delayed transformer and the thyristor converter model. Here, the transformer means a numerical phase transformation with a matrix calculation. Therefore the iron saturation and an asymmetrical transformer can not be realized. The number of converter switching mode is 64 in total, and one of them is rigidly determined according to the anode-cathode voltage, current and the provided gate signal for all thyristors. When all gate signals are set active at any time, the behavior of thyristor converter is identical with a diode converter.

(c) Coil model and others: The inductively coupled coil model consists of open and closed coils is available in GTCSP. Each coil can connect to a DC voltage source in series as an option. Moreover, change of its resistance can be given as a function of time. A simplified tokamak plasma model will be developed from this coil model for designing the next generation devices.

The three phase voltage source is also available as a simple model of the generator. Furthermore, a NBI load model is prepared as illustrated in Fig.1. That is a sort of user defined current source, and it can be given as a time function.

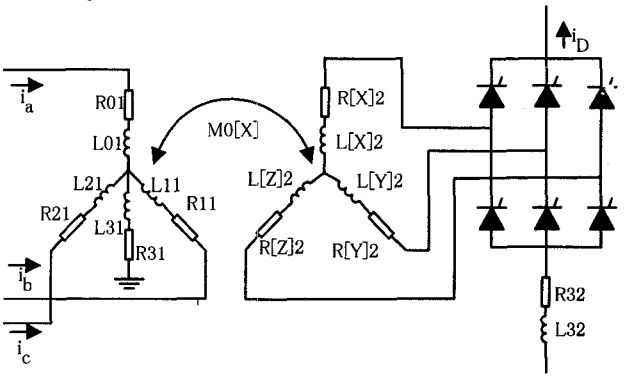

Fig.4. Model circuit of thyristor converter.

III. Application to the JT-60 power supply system

A. Design of the control system

In the tokamak operation, the control objective of the power supply may change from a current reference to a voltage one, or vice versa, corresponding to the time phase of the plasma discharge. Usually a voltage control is applied only to plasma initiation, and after the initiation the control mode is switched to a current control. Since the time constant of passive structure is a

few milli-seconds in JT-60, the same order of response time is required to ensure the plasma control stability. Furthermore, the circulating current among the converters connected with anti-parallel should be controlled when the output current is small in four quadrant operation.

Figure 5 shows a scheme of the JT-60 horizontal filed coil power supply, which is the smallest one among the five coil power supplies, and the circulating current control sequence as a function of the coil current. Concerning the details of dead beat and non-interaction control for the coil and circulating currents, see reference [6]. Here we describe the simulation results briefly.

A step response of the coil current is shown in Fig.6. Here, the circulating current reference was kept constantly to 2.2kA. The coil current follows as expected to the reference within a few milli-seconds under the non-saturation region with a control period of 500μs.

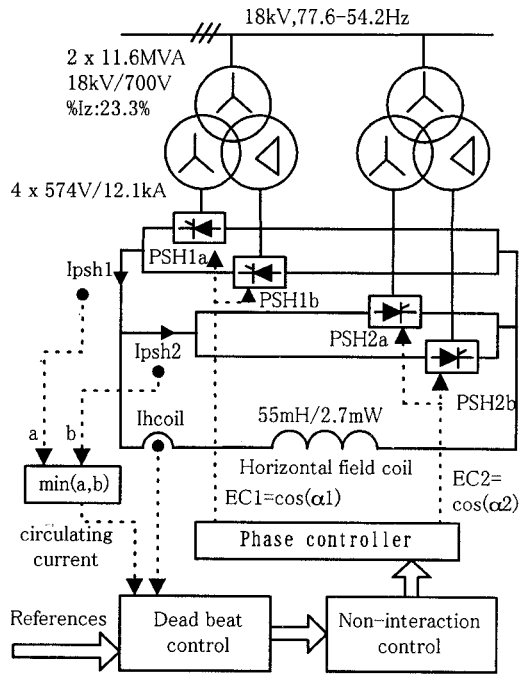

(a) Scheme of the horizontal filed coil power supply

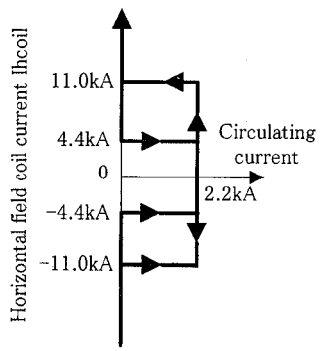

(b) A control mode transition as a function of the coil current.

Fig.5. Scheme of the horizontal field coil power supply and its current control mode.

Another simulation result about the effect of current control mode transition is shown in Fig.7. Here, the circulating current is suppressed forcefully from time of 50 to 75 ms. There is no serious effect on plasma control by the current control mode transition. Here, the user's routine modeled whole of the phase detector, thyristor gate controller and the current feedback controller, because they are strongly depend on a problem. The CPU time required for executing the simulation in a period of 0.1 s with a step of 20 μs is about 6 s using SUN Work Station-10.

B. Oscillation effect of the control angle

In the JT-60 experiments, a lot of disrupted discharges are observed and some of them are caused by an interaction of a MHD instability of plasma itself and a behavior of power supply. The mechanism is as follows. First, a high frequency fluctuation appears in the magnetic sensor signals due to the MHD, then they are transferred to the feedback control system. Second, the converter control angle begins to oscillate by the obtained plasma position and shape from the magnetic

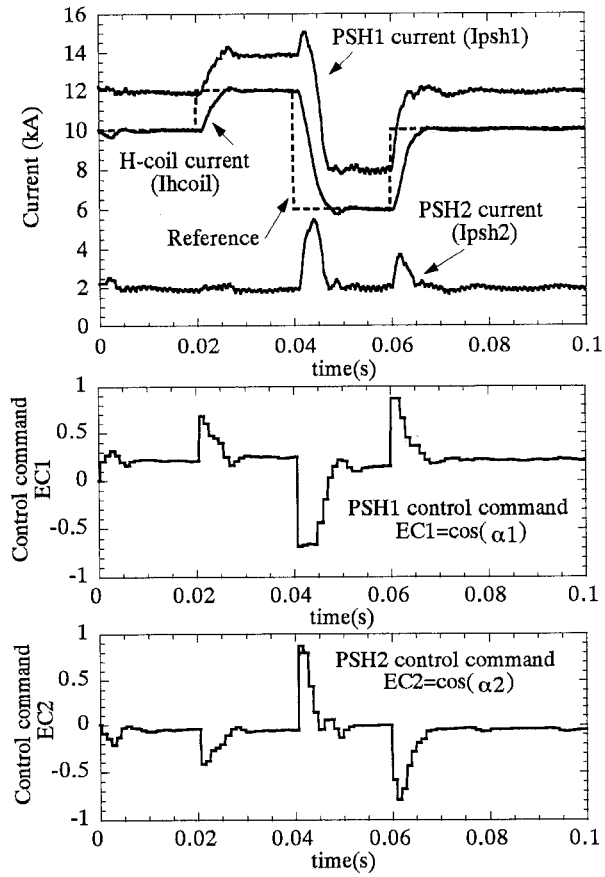

Fig.6. A step response of the horizontal field coil current.

signals. Since the thyristor converter is connected with anti-parallel for four quadrant operation, the circulating current increases to the over current level. The power supply makes switch to close the coil terminal for protection and the control is completely lost. Finally, the plasma column touches onto the first wall and disrupts immediately due to the excessive amount of impurities. Figure 8 shows a typical shot of disruption.

To verify this phenomena, we tested the converter current response with similar condition. Both results of GTCSP simulation and the dummy load test are shown in Fig.9 and 10, respectively. In these case, the current reference changes from 7kA to 13kA with a cycle time of 1ms. Both results of simulation and dummy load test have good coincidence with each other, and this is thought to be one of the evidences of GTCSP validity. In addition, we decided to introduce a limiter for control angle derivative to overcome this difficulty. The limiter may decrease the current control response, but it is expected to continue to discharge even in the MHD period.

IV. Discussion

It is worth to compare GTCSP with other electrical analysis program for evaluation the program performance. For this purpose we converted GTCSP from Sun Work Station to Windows-95 platform, because ATP-EMTP is available only on that in our site. The analyzed circuit is as shown in Fig.11, and it was performed with a period of 0.1s and time step of 10μs. The computation time was 12 s for GTCSP and 31 s for ATP as an average. The used machine for this test is IBM DOS/V compatible with Pentium 166MHz CPU, 96MB memory and FACOM Fortran 90 compiler. It must be noted that the both model are not exactly same but GTCSP has an advantage for the calculation speed at least.

The fault analysis such as ground fault and short fault can not be taken into account in GTCSP, because there is no access way to the internal circuit of the each component model. Such kind of analysis should be role of other programs.

The GTCSP code is written by Fortran-77 and consists of about 3700 statements. The variable dimension is fully adopted so that the executable module size could be optimized for the each

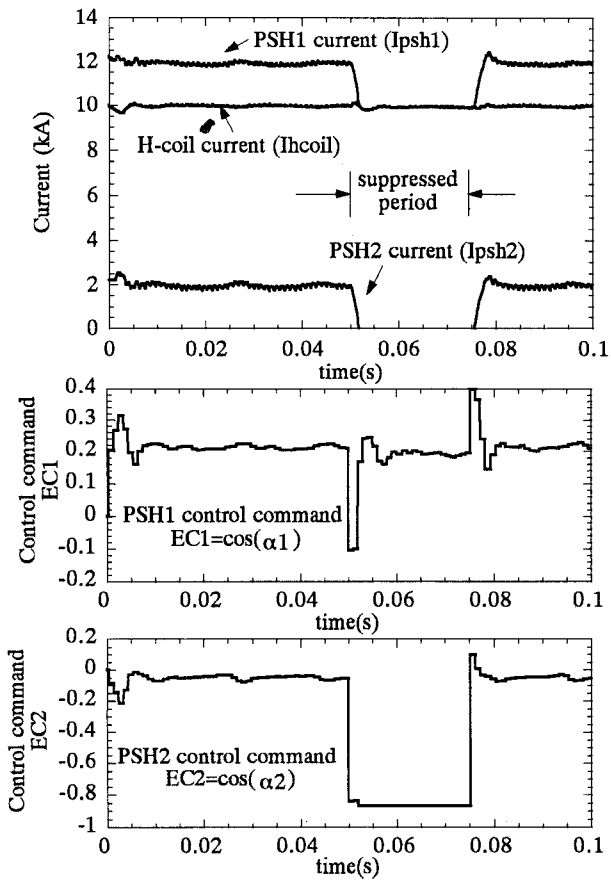

Fig7. Test of circulating current control mode transition.

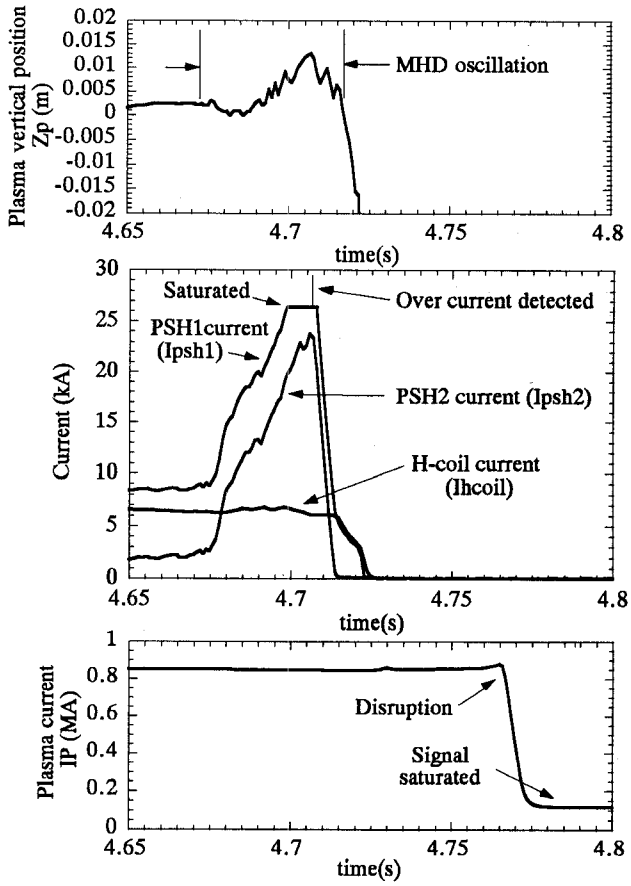

Fig.8. A typical disrupted shot due to MHD in JT-60.

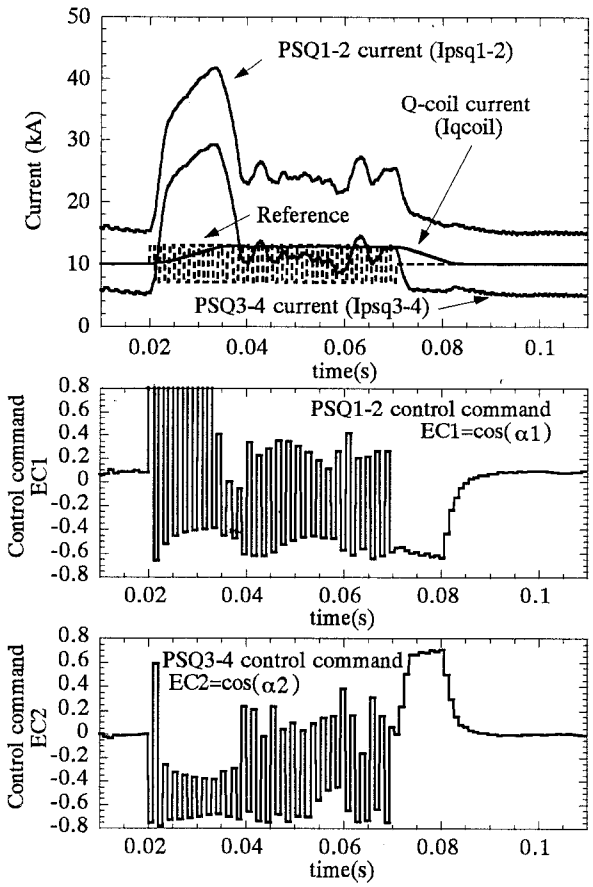

Fig.9. Simulation result with GTCSP for MHD phenomena.

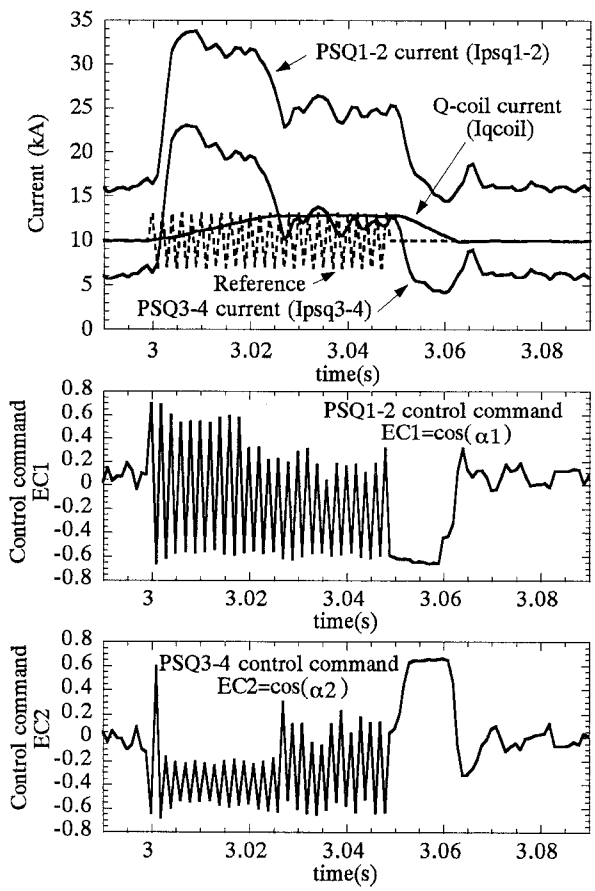

Fig.10. Experimental results using dummy load for MHD phenomena.

subject.

V. Conclusion

In the JT-60 power supply, it was very useful not only for the design but also for the analysis of various phenomena. As a future plan, we are considering to utilize GTCSP for the development of real time control program without the real simulator. Also, the development of several new component models, e.g. a simplified plasma model, GTO converter, SVC and an improved generator model including the motion equation, is under consideration.

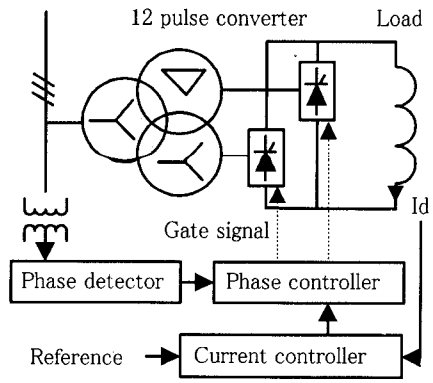

Fig.11. A benchmark model for the code evaluation.

Acknowledgment

The authors would like to thank Mr. T.Terakado, H.Nobusaka, J.Okano for their excellent assist on the field test.

References

[1] K.Ushigusa and JT-60 Team :"Steady-State Operation Research in JT-60U", 16th IAEA Fusion Energy Conference, Montréal, Canada, October 1996.

[2] R.Shimada et al., :"JT-60 Power Supplies", Fusion Engineering and Design, 5,47-68(1987)

[3] M.Matsukawa et al., :"General Tokamak Circuit Simulation Program-GTCSP", JAERI-Data/Code, 97-017, 1997.

[4] Ronald A. Rother :"Circuit theory: An introduction to the state variable approach",

[5] Xianglin Cao et al., :"Improvement of Numerical Stability of Electro-Magnetic Transient Simulation by Use of Phase-Domain Synchronous Machine Model", (in Japanese), Trans. of IEE Japan, Vol.117-B, No.4, 1997.

[6] T.Yamagishi, et al., :"Design and fabrication of DDC system for thryristor converter control ", (in Japanese), JIEE, HV-82-39, 1982.

Genetic Algorithm Based Control for Power Converters

J.Baba E.Masada
The University of Tokyo
3-1, Hongo 7, Bunkyo-ku, Tokyo 113, Japan
Fax: +81-3-5684-3972, Phone: +81-3-3812-2111 ext. 7492
E-mail: baba@masada.t.u-tokyo.ac.jp

Abstract- **In the present study we propose a new adaptive control for power converters, based on a novel genetic algorithms (GA) method. Using a simple circuit structure which contains an AC sinusoidal voltage source and two converters, the control scheme and gene structure have been considered. The optimum GA parameters have been determined from some simulations. Various converters' loads cases have been tested by simulations. As a result, it is found that the GA controller can adapt to changing environment when one controller controls two converters. It can be concluded that the GA controller is able to work in an adaptive way.**

I. INTRODUCTION

With the continuous progress of power devices, the number of power converters operating on connected to power systems has been increased. The disturbances injected on power systems and the increased interactions between converters made their neglection a too rough approximation. To introduce high power converter for applications such as super conducting magnetic energy storage system (SMES) ,flexible AC transmission system (FACTS) and so on, a solution to the above mentioned problems should be established.

Interaction is used to reduce disturbance like harmonics in multi-connnected converter system[1], but in almost other case, it has been neglected because of the difficulty in analysis and the computational power it requires. And it gives more difficulties at their effective use since unpredictable fluctuation of environment affects them very much.

Adaptive control system is one of the most suitable solutions able to cope with these difficulties. Genetic algorithms (GA) are able to realize adaptive control, because GA is suitable for finding maximum value of a function which has many local extremes by changing "gene" s.

In the near future, parallel computing technique must be applied to controlling method. GA is suitable for parallel computing because "gene" s are evaluated independently in each process. Parallel computer is expensive and not popular now, but parallel computing environment can be made on personal computer by using parallel inference machine (PIM), and it is considered possible to make GA system simulator on PIM.

Using a the simple circuit case, the possibility of GA for applying converter control has been studied. Gene's structure and optimum GA parameter for converter control has been studied too, and this study emphasizes the capability of the GA based control.

II. GENETIC ALGORYTHMS

Genetic Algorithms is one of the calculating method which imitates evolutionary process[2],[3]. In this method ,we use "gene" which is only a row of bits but has information of real system. We set many "gene" s, and like for living bodies, "gene" s are subjected to randomly change by mutation and crossover, and eventually select by cost-function. Finally, the optimum "gene" will be found. The main merit of genetic algorithms is that the founded optimum value is seldom in local minimum because of mutations. It is said that genetic algorithms are suitable for searching maximum value of the function which has many local extremes.

In the practical use, GA has following problems.

- Determination of gene's structure
- Determination of probability of mutation and crossover

These determination are usually done using some test searching because it is difficult to determine these things analytically.

III. APPLYING GENETIC ALGORYTHMS FOR CONVERTER CONTROL

A. *Simulated system*

We have considered a simple circuit as the one shown in Fig.1 . In this circuit, there is a AC sinusoidal voltage source and two converters with variable DC voltage on the load side. A converter is a single bridge self commutated converter(Fig.2). To simplify the problem, DC voltage source is used as DC load and to control reactive power and active power independently, DC voltage can be changed arbitrarily.

Usually, adaptive controller should be placed dispersively and detect environmental fluctuation by measuring local value. In this study, GA controller controls two converter at the same time, and only detects load fluctuation so as to adapt them.

The control system structure is shown in Fig.3. This figure shows only one converter side. In real simulation, GA controller controls two converters. As shown in Fig.3, GA controller indicates reactive power and PWM pattern to improve disturbance.

The purpose of this controller is determined as following:

- To reduce harmonics

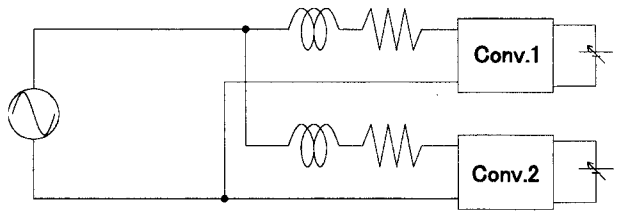

Fig. 1 Simulated circuit

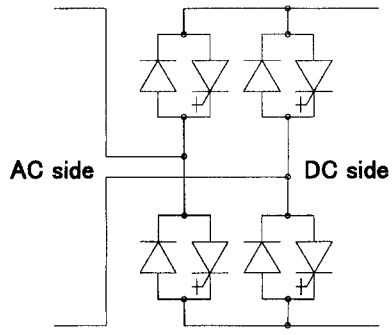

Fig. 2 Converter structure of simulated circuit

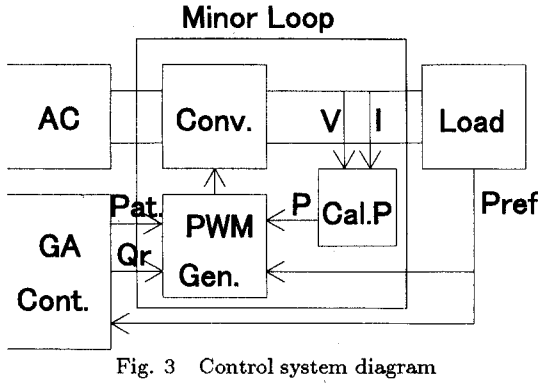

Fig. 3 Control system diagram

- To reduce total reactive power
- To reduce switching losses
- To reduce individual reactive power

To fulfill the above requirements, an adequate gene's structure and cost function should be found.

B. Gene's structure

For converter control, the parameters determined independently are the active power, the reactive power and the PWM pattern for the considered system. Active power is determined by DC load requirement. Reactive power and PWM pattern can be subject of initial setting. To search optimum reactive power and PWM pattern, we employ the gene's structure shown in Fig.4. One gene has information of two converter's PWM pattern and reactive power. Two bits are used to select PWM pattern and four PWM patterns are prepared to select. To reduce harmonics effectively, PWM patterns are calculated using lower harmonics elimination technique proposed by H.S.Patel and R.G.Hoft[4]. Three of four patterns are 5-7th, 5-7-11-13th and 5-7-11-13-17th harmonics eliminated pattern, and last one is pulse without modulation. Fig.5 shows these PWM pattern.

Eight bits are used to search optimum reactive power, but top bit means leading or lagging. Using seven bits, the value 0 to 127 can be represent, and this value is converted to active and reactive power by multiplying with 20. For instance, binary 0001000 code is converted decimal 8 and it means 160 Var at this rule.

C. Cost function

In the previous section, four requirements for control has been shown. We apply (1) as a cost function.

$$
\begin{aligned}
Cost &= K_1\frac{SF}{n} + K_2\frac{SN^2}{n} + K_3\left(\frac{SQ}{SP}\right)^2 \\
&\quad + K_4\frac{SK}{n} + K_5 SQ2 \qquad (1)\\
SF &= \sum_{i=1}^{n}\frac{P_i}{SP}(Switching\ freq.)\\
SN &= \sum_{i=1}^{n}\{(MaximumEquivalentfreq.)\\
&\quad -(Switching\ freq.)\} + \sum_{i=1}^{n}(Nearby\ penalty)\\
(Nearby\ Penalty) &= 1.0 - \frac{x^\circ}{0.01}(|x| < 0.01rad)\\
SK &= \sum_{i=1}^{n} k_i \quad SQ2 = \sum_{i=1}^{n}\frac{Q_i^2}{P_i^2}\\
SP &= \sum_{i=1}^{n} P_i \quad SQ = \sum_{i=1}^{n} Q_i
\end{aligned}
$$

P_i : *Real Power of Converter i*

Q_i : *Reactive Power of Converter i*

k_i : *Ratio DC Voltage to AC Voltage*

$(MaximumEquivalentfreq.) =$
$n \times (Highest\ switching\ frequency)$

The term SF is used to reduce switching loss. Switching losses are considered to be proportional to the square of switching frequency and converter's power.

The term SN is used to reduce harmonics. If all switching phases are different, total switching pulse may be seen as a sum of each converters pulse number from the AC side. But if two or more pulses injected the same

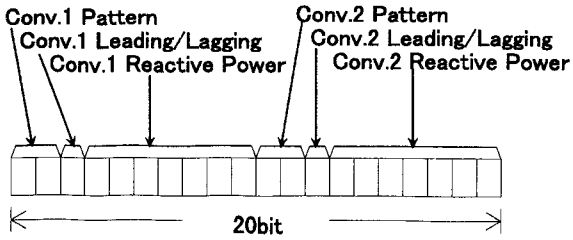

Fig. 4 Gene's structure

TABLE I Multiple constants

K_1	K_2	K_3	K_4	K_5
0.5	0.1	3.0	0.1	10.0

timing or very near, the contribution to increase equivalent frequency is weaken. Then the nearby penalty is employed.

The term SQ and SQ2 is used to reduce total and individual reactive power. The term SK is used in order not to get a very high value for DC voltage.

In this study, multiple constants shown in table I are used. These values are respectively computed in order to get the proper results.

D. GA parameter

1) The number of gene: First, the number of gene must be determined. To do this, we have tested some cases. The condition for all tests is that one converter converts 1kW and the other one converts 800W. We examined 8,16,24,32 gene number case. The number of elite are a fourth of total gene number. Fig.6 shows the results. Horizontal axis means generation of searching. Vertical axis represents the searched minimum value of the cost function by the generation sequence.

Comparing the results, 16 genes case is the best of all, and in the following section, we use the 16 genes for searching.

2) The number of elite: The elite strategy is popular in GA searching because mutation and crossover destroy good genes too. But too much elite prohibit the searching because gene can hardly change. To protect good gene from this harmful action and find optimum point rapidly, optimum elite number must be found. We have tested 6 cases: the number of elite are 2,4,6,8,10,12. Fig.7 shows the result. Seeing the result, 4 elite case is the best, and we employ the 4 elite for searching.

3) Probability of mutations and crossovers: Like other parameter, we have tested some case and determined optimum value of probability of mutations and probability of crossovers. As a result, we employ Pm=0.1 and Pc=0.8 . Fig.8,9 shows the results.

E. Example of changing load

Using the parameters discussed in the above section, we have tested various load cases. Searching has exerted until 100 generation. TableII shows the results. Pattern means : No.0 is single pulse pattern, No.1,2,3 are 5-7,5-7-11-13, 5-7-11-13-17th harmonics eliminated pattern.

When both converters are heavy loaded, low switching frequency pattern was selected and loading and lagging reactive power was injected to reduce harmonics. When the one converter load is light, the higher switching frequency than that of the other converter was selected. Selected switching frequency is inclined to be inversely proportional to the active power.

TABLE II Searching result

Load[W]	Pattern	Reactive Power[Var]	Found Generation	Cost
Conv.1:1000	0	-200	86	73.9
Conv.2:1000	1	200		
Conv.1:800	1	160	46	71.8
Conv.2:1000	0	-160		
Conv.1:500	2	80	52	64.1
Conv.2:1000	0	-60		
Conv.1:200	3	0	89	44.0
Conv.2:1000	0	0		

For comparison, optimum pattern and reactive power have been searched for one converter case. For all searching studies, the conclusion can be that pattern no.0 and no reactive power injection is the best. For this case if GA controllers are placed independently on each converter, all of them will operate at the same PWM pattern and no reactive power injection. It is obvious that this type of controller can not operate adaptively to the environment since it can not detect the other converters' state.

IV. Conclusion

In this study, we have tried to apply genetic algorithms for converter control. Using simple circuit which contains AC sinusoidal voltage source and two converters, we have tested the possibility of GA controller. First, we determined the gene's structure and cost function, and then, several tests have been done to determine optimum paremeter. We have simulated the GA controller for various loads cases considering the respective parameters. When a controller regulates two converters, the selected value changes according to two converter's loads, but in a case one converter controlled, the selected value is constant.

From this result, GA is considered to have ability to realize adaptive control, and more complex system controller can be build up using GA.

ACKNOWLEDGMENT

The authors gratefully acknowledges the contribution of Mr. C.R.Burlacu for proofing this paper.

REFERENCES

[1] C.Burlacu and E.Masada, "Bilinear Model for Parallel Connected Power Converters and Respective Control Synthesis," in *proceedings of the SPEEDAM'96,* 1996, pp.A5-23-28.

[2] H.Iba, *Fundamental of GA.* Tokyo:OHM-sha,1994.

[3] J.R.Koza, *GENETIC PROGRAMMING* , Massachusetts : MIT Press,1992.

[4] H.S.Patel and R.G.Hoft, "Generalized Techniques of Harmonic Elimination and Voltage Control in Thyristor Inverters: Part I-Harmonic Elimination," *IEEE Trans. IA*, Vol.IA-9,No.3,pp.310-317.

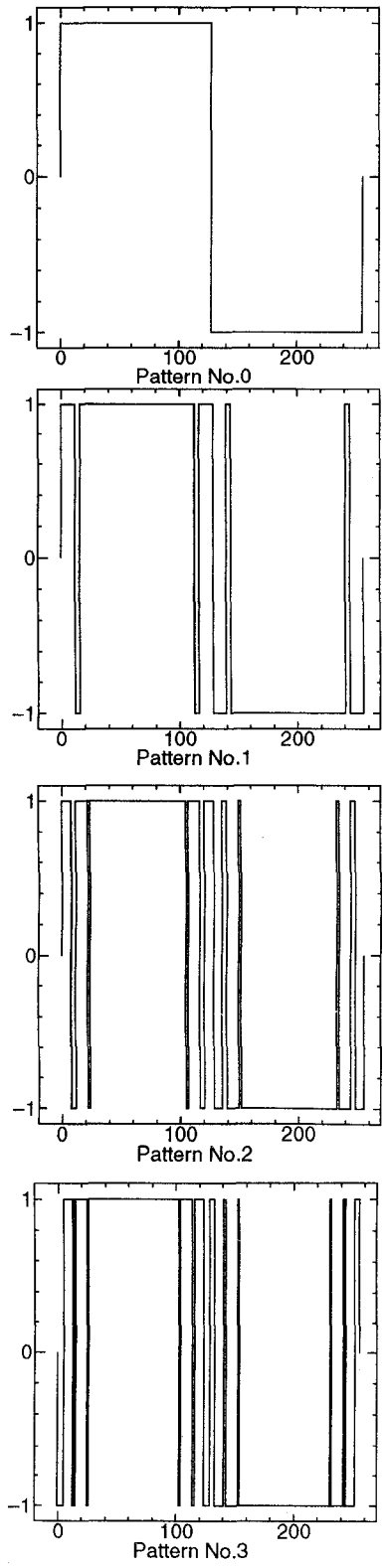

Fig. 5 PWM pattern

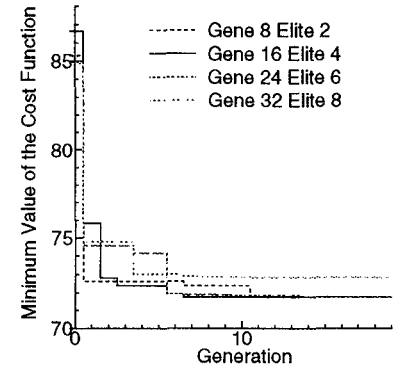

Fig. 6 Minimum value found at the generation: Results of changing the number of gene

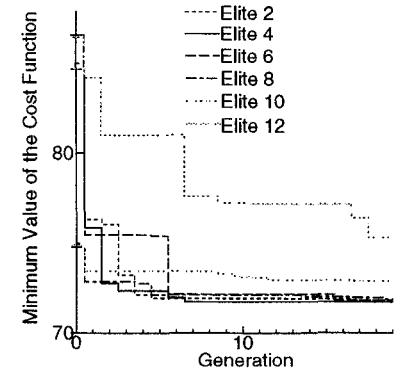

Fig. 7 Minimum value found at the generation: Result of changing the number of elite

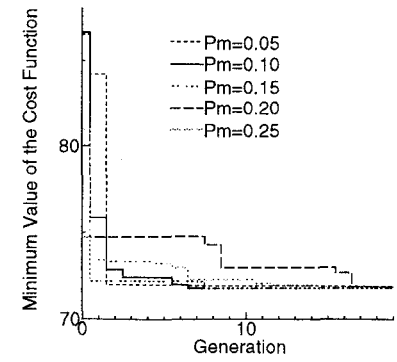

Fig. 8 Minimum value found at the generation: Result of changing the probability of mutation

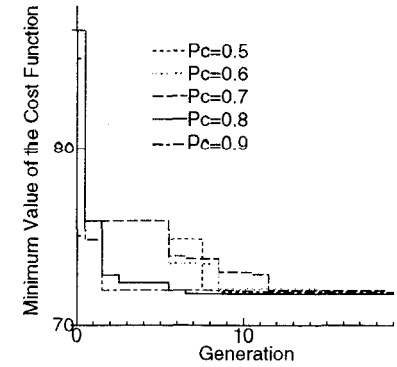

Fig. 9 Minimum value found at the generation: Result of changing the probability of crossover

Adaptive Signal Processing System for Accurate Zero-Crossing Detection of Cycloconverter Phase Currents

Sami Väliviita, Seppo J. Ovaska, and Jorma Kyyrä
Helsinki University of Technology
Institute of Intelligent Power Electronics
Otakaari 5 A, FIN-02150 Espoo, Finland
Tel.: +358-9-451 2433, Fax: +358-9-460 224
E-mail: Sami.Valiviita@hut.fi

Abstract — **We introduce a multistage adaptive digital filtering system for processing of cycloconverter phase current signals. In cycloconverter drives, the zero current periods, related to changing of thyristor bridges, cause torque distortion, which impairs the performance of speed control. The proposed filtering system is used for accurate zero-crossing detection in order to shorten the mandatory zero current periods. Our filtering system combines a low-pass prefilter and an adaptive predictive filter making it possible to extract the sinusoidal primary signal from noise and disturbances *without harmfully phase shifting* the fundamental component even when the frequency or amplitude alters rapidly. The predictive filtering is performed at time-varying sampling rate, so that the relative frequency of the fundamental component remains almost constant.**

I. Introduction

Accurate detection of true zero-crossings is important in many fields of power electronics. In cycloconverter drives, for instance, reliable zero-crossing information of output phase currents is required for switching the current from one converter to another at the exactly correct instants. The main objective of the cycloconverter drive control is speed control by means of torque control. The high quality of the speed control is achieved with rated stator flux and stator current, of which the shape is as pure a sinusoid as possible. The zero current periods cause torque distortion, which heats the motor and impairs the performance of the speed control. Therefore, shorter zero current periods would naturally improve the performance of cycloconverter drives.

In practice, the waveform of the cycloconverter phase current may have several zero current periods during one half-cycle, because the current can be discontinuous in the vicinity of true zero-crossings. With discontinuous current, the zero-crossings of the measured current waveform cannot be used directly for switching the firing pulses from one converter to another. Traditionally, the firing pulses have been switched when the first zero-crossing occurs at the end of the output half cycle. Premature switching has been prevented by ignoring the zero-crossings of the measured phase current until the phase current reference has changed its sign [1]. It is not possible, though, to change bridges instantly when the phase current reverses its direction because of the finite recovery time of the thyristors. A usual practice is to change the bridges when the phase current reference has changed its sign and the measured phase current has been zero for a time greater than the security delay of the thyristors [2]. Typical values for the recovery time and security delay are 400 μs and 700 μs, respectively. In addition to switching the firing pulses from one converter to another, the zero-crossing information can be used in other synchronization and measurement purposes as well. For instance, the rotor position of synchronous reluctance motor was determined by applying extrapolation between the zero-crossings in [3].

The correct zero-crossing instants should be determined without any delay because these instants are used for time-critical synchronization. Our objective is to remove disturbances from the sinusoidal signal without harmfully phase shifting the primary sinusoid. Therefore, zero-crossings can be detected in real-time simply from sign changes of the filtered output. Different zero-crossing detection methods for line-frequency signals were proposed in [4-7]. Filtering schemes introduced in those papers cause no harmful phase shift of the primary sinusoid while they efficiently attenuate superimposed harmonics, commutation notches, noise, and other disturbances. Those filtering systems, designed for zero-crossing detection of the line-frequency signals, have a limited capability of adaptation for wide and rapid frequency alterations. Therefore, they cannot be used in this cycloconverter application. We have, however, successfully extended the basic idea of Vainio and Ovaska [7] for signals with truly altering frequency.

In our multistage and multirate filter structure, a low-pass prefilter is used to remove the undesired frequency components, and an adaptive predictive filter restores the sinusoidal shape of the signal, and compensates for the delay caused by other filtering stages. Finally, the detection resolution is enhanced by interpolation. In Section II, we describe the structure and design principles of our efficient zero-crossing detection method. The method is carefully evaluated, and practical design parameters for construction of a zero-crossing detector for cycloconverter phase currents are provided in Section III. Section IV concludes this paper.

0-7803-3823-5/97/$10.00© 1997 IEEE

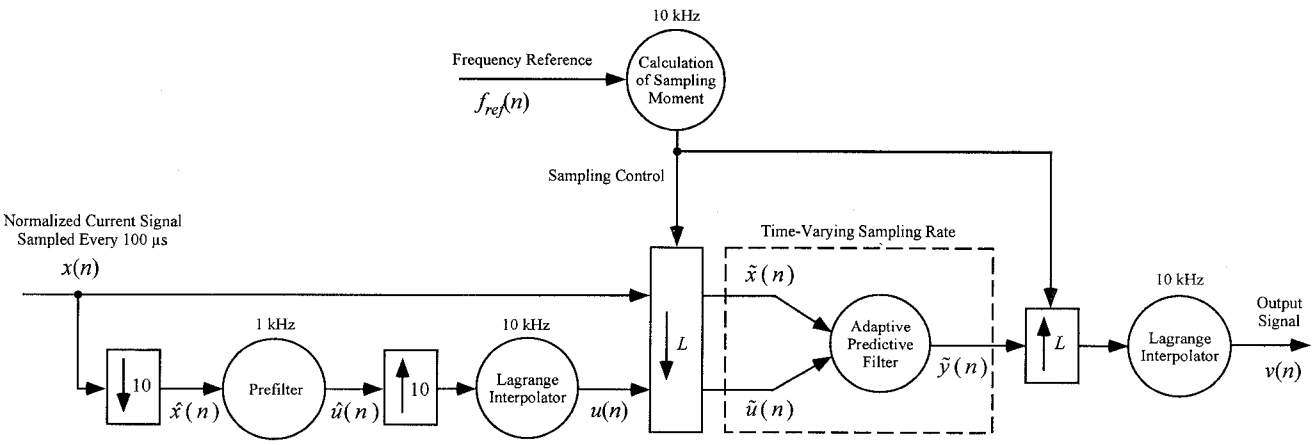

Fig. 1. Data flow diagram of the proposed multistage and multirate filter structure for zero-crossing detection. The sampling rate of the adaptive predictive filter is time-varying, the sampling rate of the prefilter is 1 kHz, and the sampling rate of the interpolator is 10 kHz.

II. Structure and Design Principles of the Zero-Crossing Detector

A data flow diagram of the proposed multistage filter structure is illustrated in Fig. 1. At first, the incoming current signal, $\hat{x}(n)$, is filtered with a low-pass prefilter in order to remove the undesired frequency components at the sampling rate of 1 kHz. This sampling rate was selected in order to facilitate the filtering task, although the normalized current signal, $x(n)$, is sampled at the sampling rate of 10 kHz. The successive filtering stage is performed at time-varying rate because we want to keep the relative frequency of the primary sinusoid a constant. The sampling rate of the adaptive predictive filter is proportional to the frequency reference of the cycloconverter, and the time-varying sampling period is calculated as follows:

$$T\left[f_{ref}(n)\right] = \text{round}_{0.0001}\left(\frac{f_N}{f_{ref}(n)} T_N\right) \tag{1}$$

where $f_{ref}(n)$ is the instantaneous frequency reference of the cycloconverter, f_N is the base frequency of the adaptive predictive filter, and T_N is the corresponding sampling period when $f_{ref}(n) = f_N$. Here, the instantaneous sampling period is rounded to the nearest number divisible evenly by 0.0001 because the execution rate of the sampling period calculation and interpolation is 10 kHz (= 1 / 0.0001 Hz). As the instantaneous sampling rate is proportional to the frequency reference of the cycloconverter, the relative frequency of the primary sinusoid remains almost constant. The relative frequency of a discrete-time signal is as follows:

$$\omega_0 = \frac{2\pi \cdot f}{f_S} \tag{2}$$

where f is the continuous-time frequency, and f_s is the sampling frequency. Additionally, the peak amplitude of the input signal is normalized such that it is always unity. This is realized by dividing the system input by the corresponding current reference. After the interpolation, the system output can be denormalized accordingly. These scalings are done because greatly varying frequency and amplitude are difficult for any adaptive filter.

Alteration of the relative frequency of the primary sinusoid cannot be completely removed due to the stepwise alteration of the sampling period. Because the sampling period calculation is executed only at every 100 μs, all sampling periods must be of length $K \cdot 100$ μs, where K is an integer number. The relative frequency of the primary sinusoid as a function of frequency reference is illustrated in Fig. 2 (a) when $f_N = 20$ Hz and $T_N = 1$ ms. The difference in relative frequency caused by this stepwise behavior is smaller than 5.3 % for signals of which frequency is lower than 20 Hz. As the frequency decreases, the effect of the stepwise alteration is clearly smaller. On the other hand, the actual frequency does not follow $f_{ref}(n)$ exactly. The actual frequency can be delayed from the frequency reference. The effect of the delay is depicted in Fig. 2 (b).

The low-pass prefilter was used to attenuate the undesired frequency components, which would otherwise cause aliasing problems in the time-varying sampling of the input signal. The prefilter can be designed to efficiently attenuate the harmonic components and other disturbances of the input signal, but its drawback is that it causes a delay which is not equal at different signal frequencies. This problem, as well as the problems caused by the time-varying sampling rate (the stepwise alteration of the sampling period, and inaccuracy and delay of the actual frequency), are compensated by the *adaptive* predictive filter.

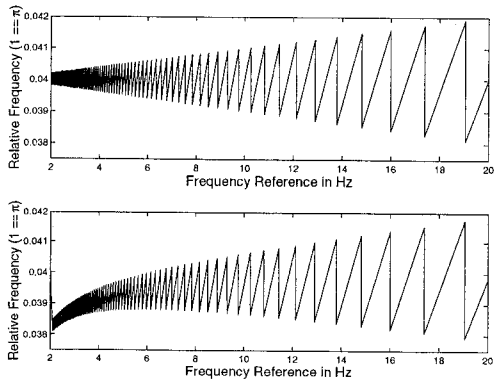

Fig. 2. (a) Relative frequency of the primary sinusoid as a function of frequency reference ($f_N = 20$ Hz, $T_N = 1$ ms). (b) Relative frequency when the actual frequency is delayed 5 ms from the frequency reference.

The adaptive predictive filter predicts one step ahead to allow interpolation in the final processing stage. The predictive filter is based on an adaptive FIR (Finite Impulse Response) filter. An FIR filter adapts to a one-step-ahead predictor when connected in cascade with one unit delay, as shown in Fig. 3. The structure of the FIR filter is illustrated in Fig. 4. The filter automatically settles to predict the desired dominating sinusoid even if the frequency alters. The prefilter has already efficiently attenuated distortion. The adaptation of the FIR filter is realized by using the Widrow-Hoff LMS (Least Mean Square) algorithm [8] for filter coefficient adaptation as in [7]. The LMS-algorithm used is as follows:

$$\mathbf{H}(n+1) = \mathbf{H}(n) + 2\mu\tilde{e}(n)\tilde{\mathbf{U}}(n-1) \tag{3}$$

where

$$\tilde{e}(n) = \tilde{x}(n) - \mathbf{H}^{\mathrm{T}}(n)\tilde{\mathbf{U}}(n-1), \tag{4}$$

$\mathbf{H}(n) = [h(0),...,h(N-1)]^{\mathrm{T}}$ is the filter coefficient vector, $\tilde{\mathbf{U}}(n-1) = [\tilde{u}(n-1),...,\tilde{u}(n-N)]^{\mathrm{T}}$ is the data vector in the filter window, and N is the length of the FIR filter. The adaptation parameter, μ, is fixed small enough to guarantee the stability of the LMS-algorithm. The choice of μ is a trade-off between the adaptation rate and overall stability of the system.

Interpolation is performed at the rate of 10 kHz. Because the sampling rate of the FIR filter is not time-invariant and, at the same time, the sampling rate of the interpolator is fixed, the number of interpolation steps must vary accordingly. Since the objective of our interpolator is to support variable frequencies, a general-purpose adaptive approach is used. The Lagrange interpolator [9] supports curved signal shapes and unevenly spaced samples, and the distortion of resulting sinusoid is negligible. The interpolated values are calculated as follows:

$$v(n) = \sum_{k=0}^{p} \frac{l_k(t)}{l_k(t_k)}\,\tilde{y}(n-k) \tag{5}$$

In our system, we have used a second-order Lagrange interpolator, i.e., $p = 2$, where

$$\begin{aligned} l_0(t) &= (t-t_1)(t-t_2), \\ l_1(t) &= (t-t_0)(t-t_2), \\ l_2(t) &= (t-t_0)(t-t_1), \end{aligned} \tag{6}$$

t_0, t_1 and t_2 are three latest arbitrarily spaced instants, when the sample is brought into the system, $\tilde{y}(n)$, $\tilde{y}(n-1)$, and $\tilde{y}(n-2)$ are the corresponding signal values at those instants, coming from the FIR filter. New samples are interpolated between $\tilde{y}(n-1)$ and $\tilde{y}(n)$, which causes a one-sample delay.

Obviously, at the low signal frequencies a great number of interpolated values are calculated between each pair of sampled true values. Given $f_N = 20$ Hz and $T_N = 1$ ms, and the output resolution of 100 µs, this means that between each filtered sample, 10 to 100 interpolated samples are needed when the signal frequency varies from 20 Hz to 2 Hz. The great number of interpolated samples has only a small effect on the final relative resolution because the angular difference between consecutive true samples is almost a constant. Unfortunately, the absolute accuracy suffers because, e.g., the relative error of 1 % at the signal frequency of 20 Hz causes absolute error of 250 µs (at 20 Hz, true zero-crossings occur every 25 ms) while the same relative error causes absolute error of 2.5 ms when the signal frequency is 2 Hz.

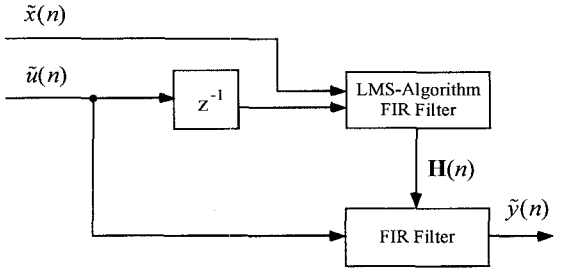

Fig. 3. FIR filter-based adaptive predictor.

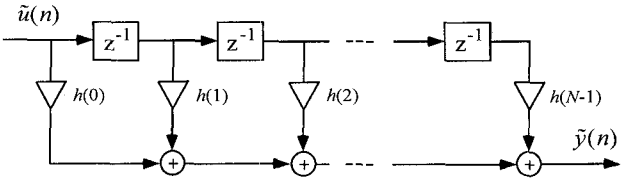

Fig. 4. Structure of the FIR filter.

III. Design Example

For practical evaluation of our method, we constructed a cycloconverter phase current signal based on [10]. In Fig. 5, the frequency reference of the test signal is illustrated. A segment of the phase current signal is shown in Fig. 8. Our test signal models a single-phase output of a three-phase cycloconverter with six-pulse bridge. As a load, we used resistive and inductive network with L/R-ratio 0.01. Because a thyristor bridge can commutate six times in one input period, the average duration of the time between two successive commutations is 3.33 ms (= 20 ms / 6) in 50 Hz power delivery system. Therefore, our test signal is heavily contaminated by the sixth harmonic of the line-frequency (300 Hz). It can also be observed from the test signal, that there are several zero current periods during each half-cycle. The test signal, as well as the simulations, were realized by using the MATLAB® [11] software.

A. Example System

At first, the input signal, $\hat{x}(n)$, was filtered by the low-pass prefilter at the sampling rate of 1 kHz. Because we want to remove the sixth harmonic (300 Hz), we designed the prefilter such that it efficiently attenuates this frequency component. In cycloconverter drives, harmonic components, however, do not have a constant frequency because the control angle is time-varying. Therefore, 300 Hz is only a center frequency of the sixth harmonic with considerable side bands. As a prefilter, we used fifth-order Cheby-

shev type II IIR (Infinite Impulse Response) filter [12] with cutoff frequency 0.385 and stopband ripple 12 decibels. The frequency response of the IIR filter is illustrated in Fig. 6. We can observe that this filter attenuates harmonic component 0.6π efficiently (from (2):
$\omega_0 = 2\pi \cdot 300\text{Hz} / 1\text{ kHz} = 0.6\pi$).

At the time-varying sampling rate, the availability of new samples is required at the resolution of 100 μs although the prefiltering is performed only every 1 ms. Therefore, we need to interpolate the required samples. Here we adopt the Lagrange interpolator introduced in the previous section. Compared to that general interpolator, this one has fixed coefficients, because the instants when new samples are brought into the system are not arbitrary. Such an interpolator can be implemented with a polyphase structure [13] for interpolation by a factor of ten, as illustrated in Fig. 7. The structure consists of ten polyphase filters, operating on three latest samples. The coefficients of the polyphase interpolating filters are the following:

$$
\begin{aligned}
p_0(n) &= [0,\ 1,\ 0] & p_1(n) &= \left[\frac{11}{200}, \frac{99}{100}, -\frac{9}{200}\right] \\
p_2(n) &= \left[\frac{3}{25}, \frac{24}{25}, -\frac{2}{25}\right] & p_3(n) &= \left[\frac{39}{200}, \frac{91}{100}, -\frac{21}{200}\right] \\
p_4(n) &= \left[\frac{7}{25}, \frac{21}{25}, -\frac{3}{25}\right] & p_5(n) &= \left[\frac{3}{8}, \frac{3}{4}, -\frac{1}{8}\right] \\
p_6(n) &= \left[\frac{12}{25}, \frac{16}{25}, -\frac{3}{25}\right] & p_7(n) &= \left[\frac{119}{200}, \frac{51}{100}, -\frac{21}{200}\right] \\
p_8(n) &= \left[\frac{18}{25}, \frac{9}{25}, -\frac{2}{25}\right] & p_9(n) &= \left[\frac{171}{200}, \frac{19}{100}, -\frac{9}{200}\right]
\end{aligned}
\qquad (7)
$$

When the prefiltered signal, $u(n)$, was sampled at the time-varying sampling rate, we obtained the signal shown in Fig. 9. The sixth harmonic has already substantially attenuated in this processing stage, but the signal is clearly delayed. The final output after adaptive predictive filtering and interpolation, $v(n)$, is illustrated in Fig. 10, from which the efficiency of our method can easily be observed. The obtained signal follows accurately the fundamental component of the test signal. The delay caused by prefiltering and interpolation has been compensated by the adaptive predictor. We used an FIR filter with 32 coefficients, and the adaptation parameter was $\mu = 0.002$.

The time-varying sampling rate converted the signal with varying frequency into the signal with approximately constant (relative) frequency. The power spectral density of the converted test signal, $\tilde{x}(n)$, is illustrated in Fig. 11. It can be observed that the greatest frequency component is 0.04π corresponding to the primary component of the test signal, but there are considerable amount of other frequencies as well. These (relative) frequency components are originated from the sixth harmonic of the line-frequency. The power spectral density of the test signal after prefiltering, $\tilde{u}(n)$, is depicted in Fig. 12, in which the signal still contains some distortion caused by the sixth harmonic. In Fig. 13, the power spectral density of the test signal after adaptive predictive filtering, $\tilde{y}(n)$, is illustrated. The harmonic components have been efficiently attenuated in this filtering stage.

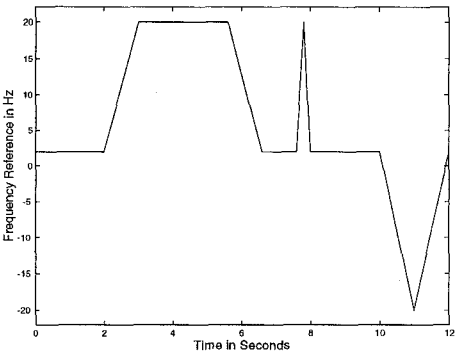

Fig. 5. Frequency reference of the test signal.

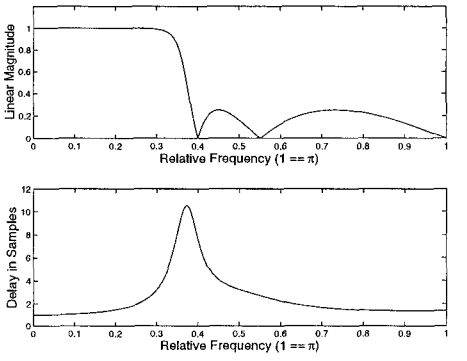

Fig. 6. Frequency response of the fifth-order IIR filter used as a prefilter.

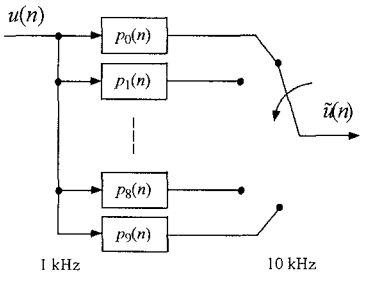

Fig. 7. Commutator model for one-to-ten interpolator.

As the frequency of the sixth harmonic of the line-frequency remains constant regardless of the signal frequency, the relative frequency of this harmonic component varies inversely proportionally to the sampling frequency. The relative frequency of the sixth harmonic can be represented as a function of sampling frequency as in (2). When the frequency reference varies from 20 Hz to 2 Hz, the sampling rate varies from 1 kHz to 100 Hz, and the relative frequency of the sixth harmonic varies accordingly from 0.6π to 6π. This causes an aliasing problem because frequencies greater than one half of the sampling frequency are mapped into the relative frequency domain from 0 to π. This problem is worst when the undesired frequency component is mapped into the same relative frequency as the primary sinusoid, because then they cannot be separated by filtering. If the undesired frequency component is mapped into some higher frequency than the primary sinusoid, it can, however, easily be removed. In Fig. 14, the relative frequency of the 300 Hz frequency component is illustrated as a function of the frequency reference.

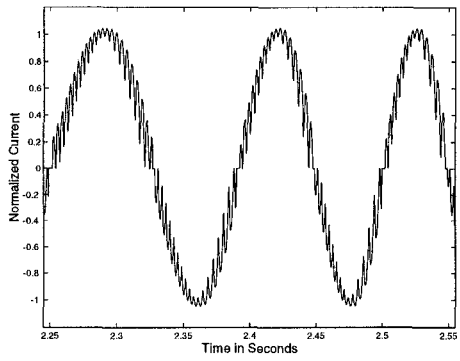

Fig. 8. A segment of the test signal.

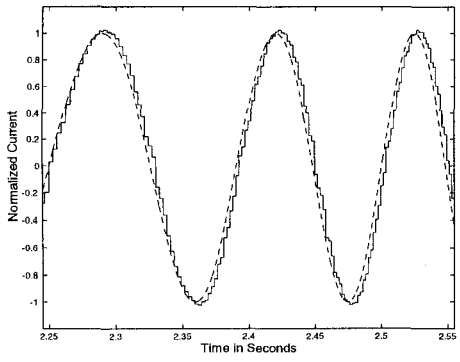

Fig. 9. Test signal after prefiltering.

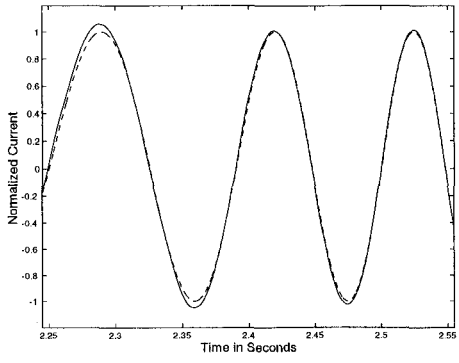

Fig. 10. System output after interpolation. Solid line: system output, dashed line: ideal fundamental sinusoid.

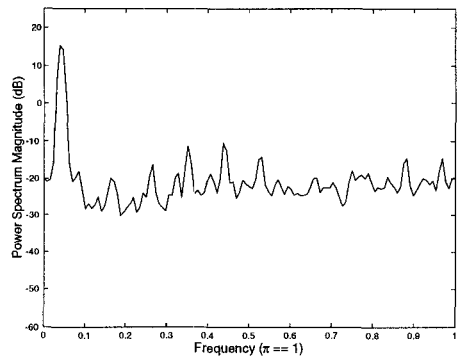

Fig. 11. The power spectral density of the test signal after sampling at the time-varying sampling rate.

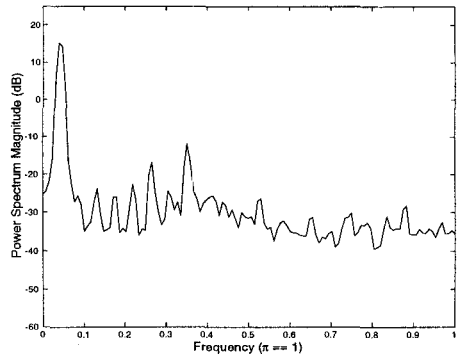

Fig. 12. The power spectral density of the test signal after prefiltering, and sampling at the time-varying sampling rate.

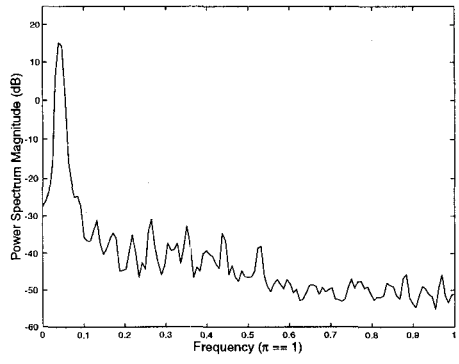

Fig. 13. The power spectral density of the system output before interpolation.

B. Evaluation

The objective of our signal processing system was to detect the true zero-crossing instants of the cycloconverter output phase current. In Fig. 15, the misplacements of the zero-crossings are shown when the signal frequency is between 8 Hz and 20 Hz. We can observe that 86 % of the filtered zero-crossings are placed within 300 μs from the true zero-crossing instants. When the frequency of the primary component decreases, the error increases. This is due to the fact that as the performance of the adaptive predictive filter is same for all the signal frequencies, the possible relative error causes absolute error which is inversely proportional to the signal frequency. On the other hand, with the system parameters used in our application, the relative frequency of the sixth harmonic of the line-frequency is zero when the signal frequency is 2 Hz. Thus, it is seen as a DC-component. This frequency component cannot be completely removed, especially because the frequency of this harmonic component is not exactly 300 Hz, but varies in time such that it is very difficult to predict. Furthermore, as the frequency of the primary sinusoid varies, the results are not as accurate as in steady-state. Thus, the largest errors in Fig. 15 occurred during acceleration or deceleration.

The proposed filter structure shows good convergence properties for signal frequencies from 8 Hz to 20 Hz, reduces significantly the distortion of the primary sinusoid, and adapts to fast frequency alterations. Therefore, the proposed method can be used to synchronize the changing of thyristor bridges at this frequency band. At smaller signal frequencies, traditional methods provide more accurate results, and thus they should be used in parallel with this new method. This is not, however, a considerable drawback for the proposed method, because the torque distortion

problem becomes greater at higher signal frequencies. This is due to the fact that the ratio of a constant zero current period and signal period is greater at higher signal frequencies.

The performance of our zero-crossing detection method can still be improved by increasing the output sampling rate from 10 kHz, and by decreasing the nominal sampling period, T_N, from 1 ms. In this case, the length of the FIR filter should be increased proportionally to achieve the same filtering properties as in our example system. Therefore, the selection of these system parameters is a trade-off between the overall performance of our system, and the system cost.

IV. Conclusions

An efficient and flexible digital signal processing system for zero-crossing detection for cycloconverter output phase currents was presented. Our method is flexible because it automatically adapts to wide and rapid alterations of amplitude and frequency, while maintaining delay-constrained filtering properties. Our multistage and multirate filtering system suppresses disturbances efficiently, and the proposed algorithms can be easily implemented in microcontroller or signal processor environments, which are standard components in modern cycloconverter drives. The functional flexibility is achieved by a multistage and multirate filter structure. Each filtering stage performs an individual task, and the filter type and parameters can be selected accordingly.

The proposed method is robust against distortion, other kinds of noise, and both frequency and amplitude alterations. Highly satisfactory performance was achieved for the higher band of frequencies produced by cycloconverters. For the low signal frequencies, the results were worse but, on the other hand, in the low frequencies the torque distortion caused by zero current periods is not as great as in the higher frequencies. The proposed design method can also be adopted for other similar applications, e.g., for Load Commutating Inverters (LCI), where the zero-crossing information is also vital. Another interesting topic for future research is to apply the proposed method in active-filters.

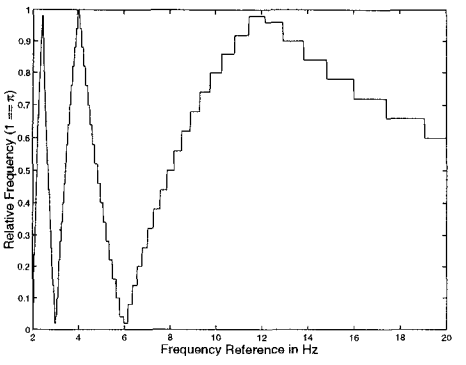

Fig. 14. Relative frequency of 300 Hz frequency component (the sixth harmonic of the line-frequency) as a function of frequency reference.

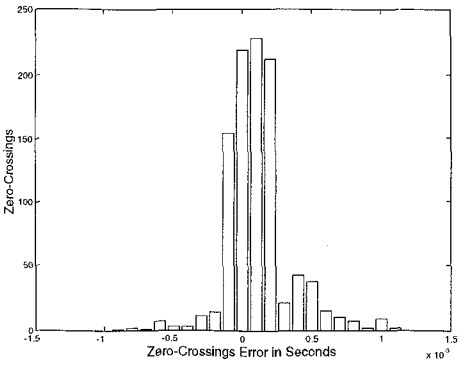

Fig. 15. Misplacements of filtered zero-crossings when the frequency of primary sinusoid was between 8 Hz and 20 Hz. 1000 samples were obtained by repeating the test signal (Fig. 5). Positive values correspond to delay.

References

[1] B. R. Pelly, *Thyristor Phase-Controlled Converters and Cycloconverters: Operations, Control, and Performance.* New York, NY: John Wiley & Sons, Inc., 1971.

[2] J. Niiranen, "Simulation of cycloconverter-fed three- and six-phase synchronous motors during discontinuous stator current," in *Proc. International Conference on the Evolution and Modern Aspects of Synchronous Machines*, pp. 367-372, Zurich, Switzerland, Aug. 1991.

[3] M. S. Arafeen, M. Ehsani, and T. A. Lipo, "Sensorless position measurement in synchronous reluctance motor," *IEEE Trans. Power Electronics*, vol. 9, pp. 624-630, Nov. 1994.

[4] R. Weidenbrüg, F. P. Dawson, and R. Bonert, "New synchronization method for thyristor power converters to weak AC-systems," *IEEE Trans. Ind. Electron.*, vol. 40, pp. 505-511, Oct. 1993.

[5] O. Vainio and S. J. Ovaska, "Noise reduction in zero-crossing detection by predictive digital filtering," *IEEE Trans. Ind. Electron.*, vol. 42, pp. 58-62, Feb. 1995.

[6] O. Vainio and S. J. Ovaska, "Digital filtering for robust 50/60 Hz zero-crossing detectors," *IEEE Trans. Instrum. Meas.*, vol. 45, pp. 426-430, Apr. 1996.

[7] O. Vainio and S. J. Ovaska, "Multistage adaptive filters for in-phase processing of line-frequency signals," *IEEE Trans. Ind. Electron.*, vol. 44, no. 2, Apr. 1997, in press.

[8] B. Widrow and S. D. Stearns, *Adaptive Signal Processing,* Englewood Cliffs, NJ: Prentice-Hall, 1983.

[9] E. Kreyszig, *Advanced Engineering Mathematics,* 7th ed. Singapore: John Wiley & Sons, Inc., 1993.

[10] J. Kyyrä and S. Väliviita, "Simulation method for phase-shift controlled AC - AC converters based on switching vector," in *Proc. Power Conversion Conference*, Nagaoka, Japan, Aug. 1997.

[11] *Matlab: High-Performance Numeric Computation and Visualization Software: User's Guide.* Natick, MA: The MathWorks, Inc., 1993.

[12] J. G. Proakis and D. G. Manolakis, *Digital Signal Processing: Principles, Algorithms, and Applications,* 3rd ed. Upper Saddle River, NJ: Prentice-Hall, 1996.

[13] R. E. Crochiere and L. R. Rabiner, *Multirate Digital Signal Processing.* Englewood Cliffs, NJ: Prentice-Hall, 1983.

Switching-Ripple-Based Current Sharing for Paralleled Power Converters

David J. Perreault Kenji Sato John G. Kassakian

Massachusetts Institute of Technology
Laboratory for Electromagnetic and Electronic Systems
Cambridge, MA 02139 USA

Abstract - **The paper presents the implementation and experimental evaluation of a new current-sharing technique for paralleled power converters. This technique uses information naturally encoded in the switching ripple to achieve current sharing, and requires no inter-cell connections for communicating this information. Practical implementation of the approach is addressed, and an experimental evaluation of the approach based on a 3-cell prototype system is also presented. It is shown that accurate and stable load sharing is obtainable over a wide load range with this approach.**

I. Introduction

Power conversion systems are sometimes constructed by paralleling many quasi-autonomous power converter cells (Fig. 1). Advantages of such a parallel, or *cellular*, converter architecture include high performance and reliability, modularity, and the ability to attain large system ratings [1,2].

One important characteristic of a parallel converter architecture is that the converter cells share the load current equally and stably. Good current-sharing behavior is important for reducing system losses and stresses, for improving system reliability, and for achieving desirable control characteristics. Current sharing is often implemented by interconnecting the cells via a communication bus over which information is shared [3-10]. While this approach is simple and effective, it is undesirable in many applications for reliability reasons, due to the need for additional interconnections among cells. Current sharing is sometimes obtained without additional interconnections using droop methods, in which the voltage drops across the cell output impedances are used to enforce a degree of current sharing [11-13]. Unfortunately, by their nature, droop methods suffer from high output voltage regulation, which is unacceptable in many applications.

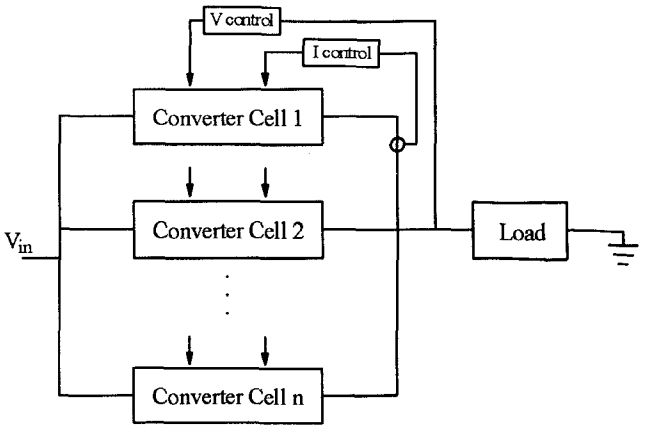

Figure 1 A cellular converter architecture supplying a single load.

The proposed paper presents a current-sharing method which requires no additional interconnections among cells and which does not rely on output droop characteristics. This method, which was proposed but not validated in [14], uses information naturally encoded in the output switching ripple to achieve current-sharing among converter cells. The use of switching ripple to encode current-sharing information leads to performance advantages over other frequency-based approaches such as the output perturbation method of current sharing explored in [14,15]. Section II of the paper describes the operation of the new current-sharing method. Section III details one approach for implementing this method, and presents the design of a low-power prototype system which implements the approach. An experimental evaluation of the current-sharing method using the prototype system is presented in section IV. The final section of the paper presents conclusions and recommendations for further development of the current-sharing approach.

II. The Switching Ripple Method

This paper considers the switching ripple method of current-sharing control proposed in [14] and illustrated in Fig. 2. In this approach, each converter cell is controlled such that its average output current is directly related to its switching frequency. As a result, the frequency content of the aggregate output ripple voltage contains information about the individual cell output currents. Each cell measures the output ripple voltage, and uses the information it contains to achieve current balance with the other cells.

Implementing a relationship between cell output current and switching frequency is typically straightforward, as many conversion approaches yield a natural relationship between them. For example, controlling a buck converter to operate at the edge of discontinuous conduction results in an inverse relationship between switching frequency and average output current (Fig. 3). Conversion approaches which do not exhibit a relationship between output current and switching frequency can often be modified to do so. For example, such a relationship could be achieved in a fixed-frequency PWM converter by adjusting the clock frequency (and PWM ramp slope) as a function of output current.

There are many methods by which the information in the aggregate output ripple voltage can be extracted and used to

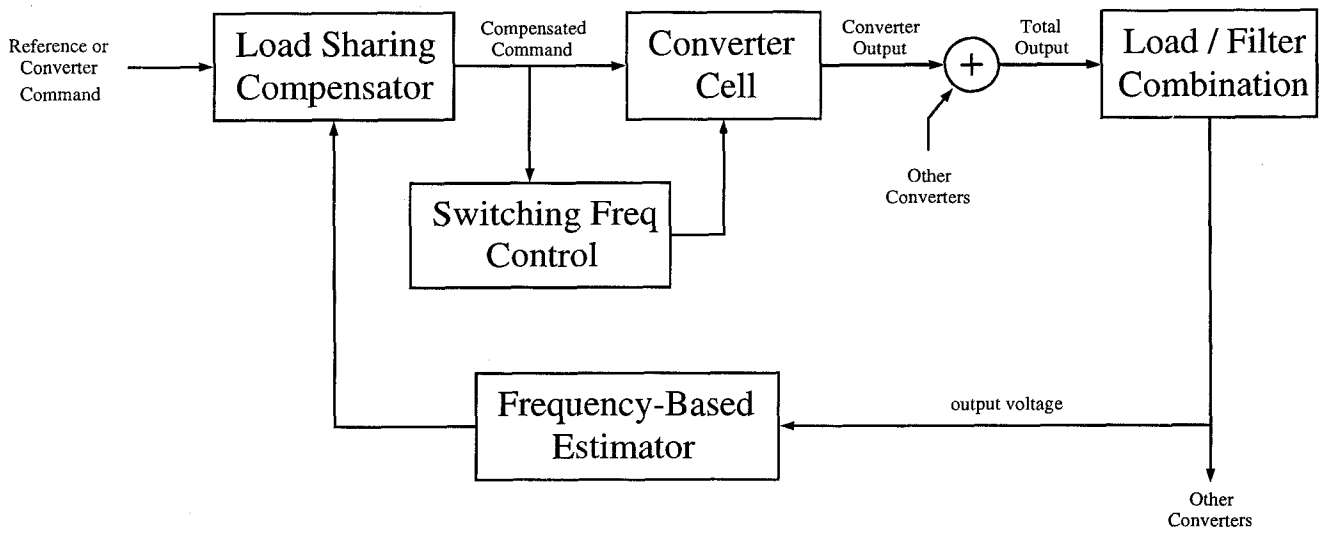

Figure 2 Schematic representation of the switching ripple method of current-sharing control.

achieve current sharing. In the approach considered here, each cell employs a frequency estimator which generates a positive (differential) signal when any other cell is operating at a lower switching frequency. Each cell uses this information to adjust its output such that no other cell is operating at a lower switching frequency. The cells thus converge to operating at the same switching frequency, and achieve current balance as a result. This approach is simple and robust, and is insensitive to the switching ripple harmonic content and waveform shape.

III. Prototype System Implementation

The current-sharing approach is demonstrated using a low-power 3-cell prototype system composed of buck converter cells operating at the edge of discontinuous conduction. Each cell has an inner current control loop, a middle voltage control loop, and an outer current-sharing control loop. The inner current control loop maintains operation of the cell at the edge of discontinuous conduction and inherently enforces a relationship between cell switching frequency and average output current. Current-sharing control is achieved in the prototype system by having each cell adjust its local reference voltage (used by the voltage control loop) if any other cell is operating at a lower switching frequency. Methods and circuits will be described for controlling cell switching patterns, making estimates of switching ripple frequency content based on output voltage measurements, and controlling the output voltage and current balance among cells. A more detailed discussion of the design and implementation of the system can be found in [16,17].

A. Prototype System Power Stage

The prototype system uses low-power buck converter cells operating at the edge of discontinuous conduction under peak current control. Each cell has an inner current control loop which causes the cell output current to ramp between zero and twice the reference current i_{ref}, with an average value of i_{ref}. Each cell is designed to handle a peak current of 20 mA, yielding a per-cell load range of 1 - 10 mA. The system has a total output capacitance, C_f, of 45 μF, and is resistively loaded.

Operation at the edge of discontinuous conduction yields an average output current (equal to one half of the peak output current) that is inversely proportional to the switching frequency. Specifically, for an approximately constant output voltage v_{cf}, we find

$$f_{sw} = \frac{v_{cf}(V_{in} - v_{cf})}{2V_{in}Li_{ref}} \quad . \tag{1}$$

For example, in the prototype system, with L = 125 mH, V_{in} = 10 V, and v_{cf} = 5 V, full load for a cell corresponds to a 1

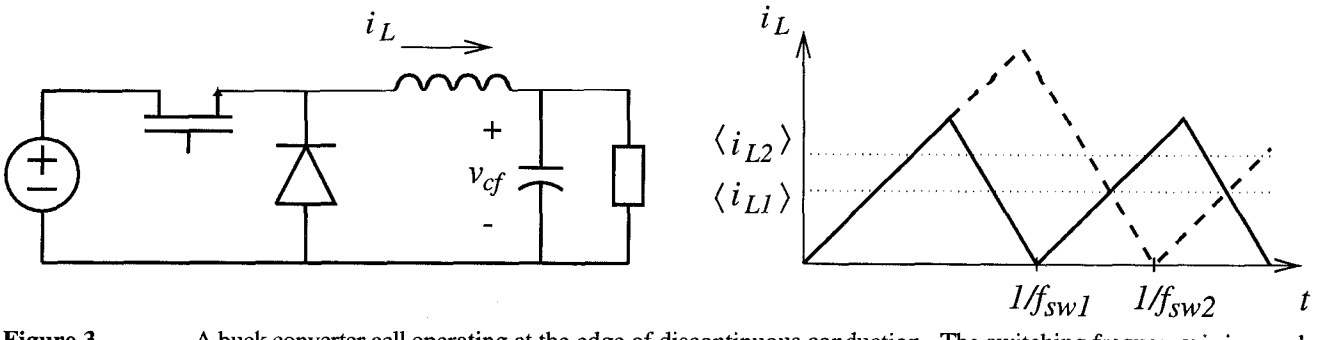

Figure 3 A buck converter cell operating at the edge of discontinuous conduction. The switching frequency is inversely proportional to the average output current.

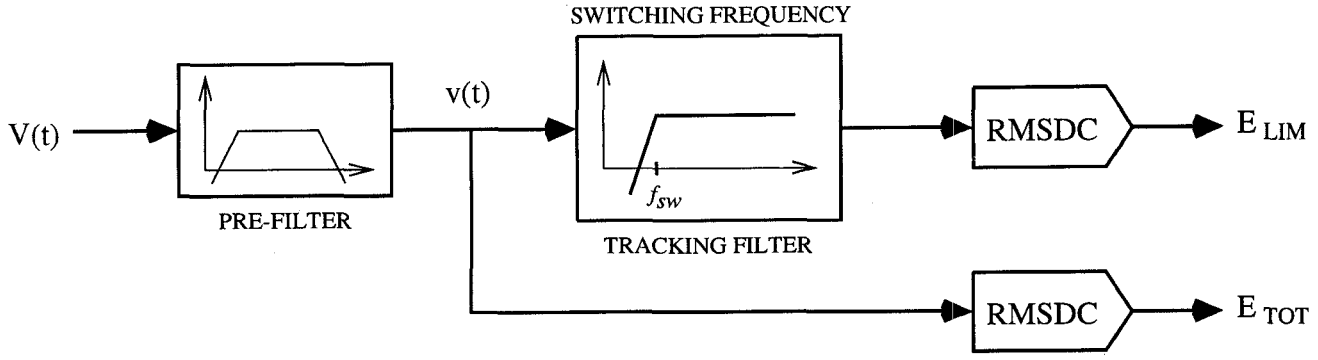

Figure 4 Structure of the frequency estimator used in the prototype system. E_{lim} is the rms of the filtered ripple, E_{tot} is the rms of the total ripple. These signals are used by the current-sharing controller.

kHz switching frequency, while 10% load corresponds to a 10 kHz switching frequency. The cell output current switching ripple causes a very small (<2%) ripple in the output voltage at the same fundamental frequency. It is the frequency content of this output voltage ripple which carries information about the average cell output current.

B. Frequency Estimation

To decode the current-sharing information contained in the output voltage ripple, each cell employs a frequency estimator which detects whether any other cell is operating at a lower switching frequency. The estimator structure used in the prototype system, shown in Fig. 4 , is composed of three stages: (1) a prefilter stage, (2) a frequency-tracking filter stage, and (3) an rms-to-dc conversion stage. The prefilter stage removes the low-frequency and high-frequency (noise) components of the output voltage, while amplifying the switching ripple component. The frequency-tracking filter is a high-pass filter whose cutoff frequency is continuously adjusted to fall just below the local cell switching frequency, in order to attenuate switching ripple components at frequencies below that of the local cell. The rms-to-dc conversion stage measures the rms of the switching ripple signals before and after the tracking filter. If the rms of the filtered switching ripple is lower than that of the unfiltered ripple, it indicates that one or more cells are operating at switching frequencies below that of the local cell. Thus, the estimator structure of Fig. 4 provides enough information to implement the current-sharing approach described previously.

The prefilter stage is a cascade of a second-order Butterworth high-pass filter (f_c = 500 Hz), a second-order Butterworth low-pass filter (f_c = 40 kHz), and a high-gain frequency-dependent amplifier. The frequency-dependent amplifier compensates for the fact that the magnitude of the voltage ripple across the capacitive output filter decreases with increasing frequency. For frequencies below 20 kHz, it acts as a differentiator to amplify ripple components by an amount proportional to their frequency. Above 20 kHz, it acts as an integrator to attenuate high frequency noise. The output of the prefilter stage is thus an amplified and frequency-compensated version of the output switching ripple, with high-order switching harmonics (and high-frequency noise) attenuated.

The frequency-tracking filter stage is a fourth-order Butterworth high-pass filter whose cutoff frequency is continuously adjusted to 0.8 times the local switching frequency. A Butterworth filter is selected because it exhibits no peaking in its response near the cutoff frequency. The tracking filter is implemented using an LMF100 switched-capacitor filter whose clock frequency is derived from the local switching frequency.

To achieve the desired tracking filter cutoff frequency , the LMF100 clock frequency must be 80 times the local switching frequency. A frequency multiplier based on the 74VHC4046 phase-locked loop (PLL) IC is used to generate the LMF100 clock from the local gate drive waveform. A divide-by-eighty counter in the feedback path of the PLL yields a switched-capacitor filter clock frequency of 80 times the (input) switching frequency. This results in a tracking filter cutoff frequency of 0.8 times the switching frequency.

The rms-to-dc conversion stage of the frequency estimator measures the rms of the switching ripple signals before and after the tracking filter. It is implemented using AD637 integrated circuit rms-to-dc converters connected in the two-pole Sallen-Key filter arrangement. The averaging and filter capacitor values (C_{AV} = 0.022 µF, C_2 = C_3 = 0.047 µF) are selected to yield a 1% settling time of 8 ms. This is considered fast enough to track the variations in switching ripple frequency content while still suppressing ripple in the rms-to-dc converter outputs. The two rms-to-dc converter outputs form the output of the frequency estimator stage. Any difference between these signals indicates that another cell is operating at a lower switching frequency. This information is used by the current-sharing controller to achieve load balance with the other cells.

C. Control Design

This section describes the design of the control circuitry used in the prototype converter system. A block diagram of the cell control structure used in the prototype system is shown in Fig. 5. In simplest terms, each cell can be viewed as having an inner current control loop, a middle voltage control loop, and an outer load-sharing control loop. The inner current loop, which maintains cell operation at the edge of discontinuous conduction, causes the average output current i_{out} to accurately track a current reference i_{ref}, and allows the cell power stage to be modeled as a controlled current source of value i_{ref} (yielding $H(s) \sim 1$ in Fig. 5). It also inherently enforces a relationship between the cell switching frequency and average output current, thus encoding current sharing information on the output

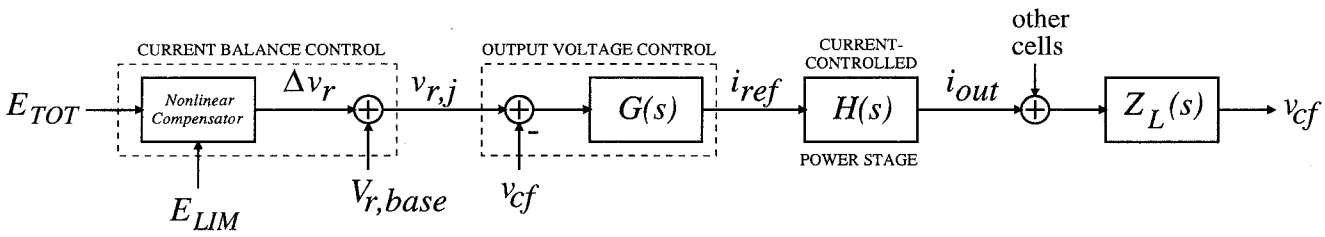

Figure 5 Block diagram of the cell control structure used in the prototype system.

switching ripple.

To regulate the output voltage, each cell has a middle voltage control loop which generates the current reference for its inner loop based on the difference between a local voltage reference and the output voltage. The prototype system employs a lag compensator (τ_p = 0.0159, τ_z = 0.00159, dc gain = 50 mA/V) for this purpose. This yields a voltage control bandwidth on the order of 100 Hz, with less than 5% load regulation over the load range of the cell. The output of the voltage control circuit has a clamp such that the commanded reference current is always within the specified load range of 1 - 10 mA.

To achieve load balance among cells, each cell has a slow outer current-sharing loop which operates by adjusting the local reference voltage v_{ref} over a limited range about a base value $v_{r,base}$. The individual converter references are shifted via integral control based on the difference between the two frequency estimator outputs minus a small offset. That is, the system uses the difference between the rms of the total switching ripple and the rms of the switching ripple components at frequencies of the local cell and higher, minus an additional offset; i.e.

$$\frac{dv_{r,j}}{dt} = K_j[E_{tot} - E_{lim} - \Delta E] \qquad (2)$$

where K_j is the (integral) control gain, E_{tot} and E_{lim} are the two frequency estimator outputs, and ΔE is the offset. The j^{th} reference is adjustable over a small range from a base value $v_{r,j,base}$ to a maximum value $v_{r,j,max}$ (which is about 5% larger than the base value), and is prevented from going outside this range. The offset ΔE guarantees that the reference of the lowest switching frequency (highest current) cell will always be driven down towards its base value so that current sharing can be achieved.

To implement this outer-loop control structure, the prototype system uses the reference adjustment circuitry provided in the UC3907 load-sharing IC. The UC3907 is designed to implement a single-wire current-sharing scheme in which the local voltage reference is adjusted based on the difference between the highest cell current and the local cell current, minus a small offset [10]. By properly scaling and shifting the two outputs of the frequency estimator and using them in place of the local and highest current inputs of the UC3907, the UC3907 can instead be caused to adjust its local reference voltage as previously described. The integrating compensator implemented in the UC3907 yields a current-sharing control bandwidth on the order of a Hertz.

The three control loops operate together to properly regulate the output voltage of the system while maintaining current sharing among cells. While other design approaches are

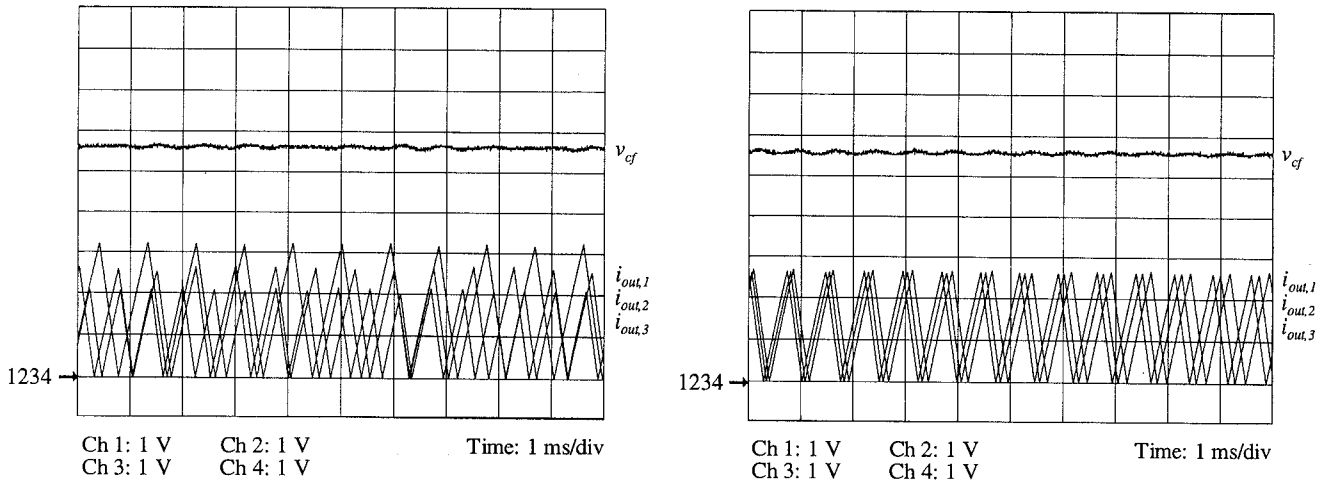

Figure 6 Current-sharing characteristics of the prototype system at approximately 66% of full load ($R_{load} \approx 278\Omega$). (a) Without current-sharing control. (b) With current-sharing control. Current signals are represented at a scale factor of 200 V/A.

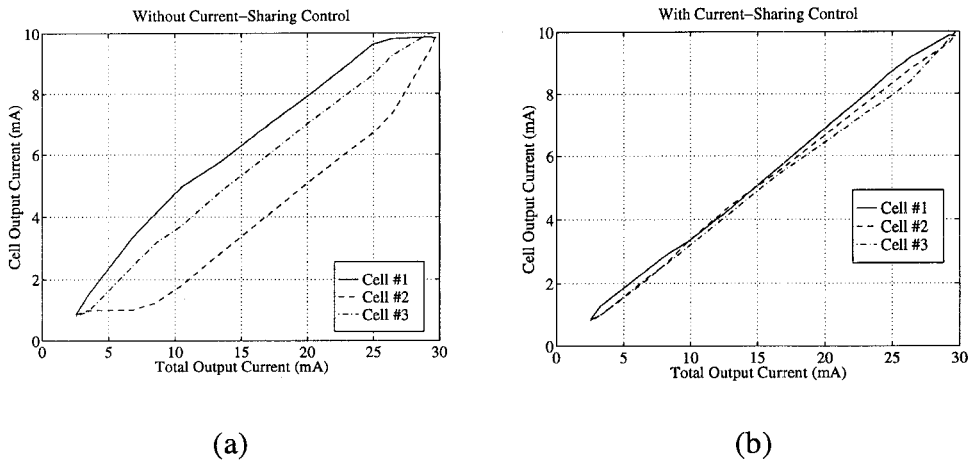

Figure 7 The static current-sharing characteristic of the prototype system. (a) without current-sharing control. (b) with current-sharing control.

possible, this multilayered control strategy has been found to be both simple and effective.

IV. Experimental Evaluation

This section presents an evaluation of the switching ripple method of current-sharing control using a 3-cell prototype system of the design presented in the previous section. Additional results can be found in [16]. It should be noted that the approach is independent of the number of cells in the system, and can be applied to systems with an arbitrary number of cells. Figure 6 shows operation of the prototype system at approximately 66% of full load both with and without current-sharing control. Without current-sharing control, there is a significant imbalance in average output current among the three cells. The inverse relationship between switching frequency and average output current is also apparent. With current-sharing control, the switching frequencies and average cell output currents are almost precisely equal. This high degree of current sharing is achieved by using the information encoded in the frequency content of the output switching ripple, without additional interconnections.

Figure 7 shows the static current-sharing characteristic over the load range of the system both with and without current-sharing control. Without current sharing, there are significant current imbalances over much of the load range, while with current sharing the cells share current to within 5% of the average over the entire load range. This high degree of active current sharing is obtained with less than 5% load regulation over the entire load range.

Current-sharing behavior was also investigated under transient conditions. Figure 8 shows the current-sharing behavior for load steps between 673 Ω and 224 Ω, corresponding to approximately 27% and 83% of full load. The current-sharing behavior is seen to be stable for even large load steps. Figure 9 shows the reference current transient response

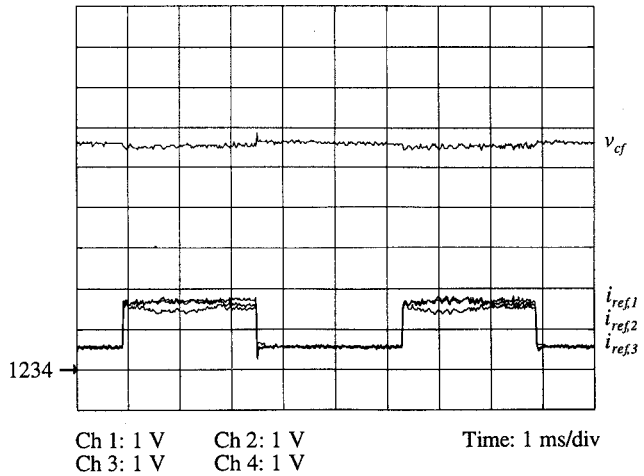

Figure 8 Transient response for load steps between 224 Ω and 673 Ω (approximately 27% and 83 % of full load). Currents are represented at 200 V/A.

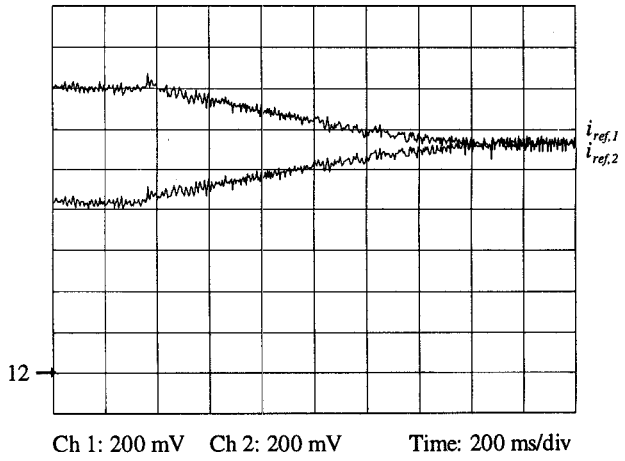

Figure 9 Current reference transient response for two cells when current sharing is turned on with $R_L = 500\,\Omega$. Currents are represented at 200 V/A.

for two cells when current-sharing control is turned on. Again, accurate current sharing is rapidly achieved with stable dynamics. What may be concluded from these results is that the switching ripple method can be used to achieve accurate static and dynamic current sharing without the need for additional interconnections among cells.

V. Conclusions

This paper presents the implementation and experimental evaluation of a new current-sharing approach for paralleled power converters. This approach, which is based on encoding the current-sharing information in the switching ripple of the converter cells, eliminates the need for additional current-sharing interconnections among converters. Practical implementation of the approach is addressed, including methods for controlling the cell switching patterns, decoding the current-sharing information from the output switching ripple, and controlling the output voltage and current sharing. An experimental evaluation of the new current-sharing approach based on a 3-cell prototype system is also presented. It is shown that accurate and stable current sharing is obtainable over a wide load range using this approach.

Acknowledgments

The authors would like to gratefully acknowledge the support for this research provided by the Bose Foundation and the Office of Naval Research. Kenji Sato thanks the Central Japan Railway Company for supporting him during this research.

References

[1] J.G. Kassakian, "High Frequency Switching and Distributed Conversion in Power Electronic Systems," *Sixth Conference on Power Electronics and Motion Control (PEMC 90)*, Budapest, 1990.

[2] J.G. Kassakian and D.J. Perreault, "An Assessment of Cellular Architectures for Large Converter Systems," *First International Conference on Power Electronics and Motion Control*, Beijing, 1994, pp. 70-79.

[3] K.T. Small, "Single Wire Current Share Paralleling of Power Supplies," *U.S. Patent 4,717,833*, 1988.

[4] R. Wu, T. Kohama, Y. Kodera, T. Ninomiya, and F. Ihara, "Load-Current-Sharing Control for Parallel Operation of DC-to-DC Converters," *IEEE Power electronics Specialists Conference*, 1993, pp. 101-107.

[5] T. Kohama, T. Ninomiya, M. Shoyama, and F. Ihara, "Dynamic Analysis of Parallel Module Converter System with Current Balance Controllers," *1994 IEEE Telecommunications Energy Conference Record*, 1994, pp. 190-195.

[6] T. Kohama, T. Ninomiya, M. Wakamatsu, and M. Shoyama, "Static and Dynamic Response of a Parallel-Module High Power-Factor Converter System with Current-Balancing Controllers," *IEEE Power Electronics Specialists Conference*, 1996, pp. 1198-1203.

[7] M. Jovanovic, D. Crow, and L. Fang-Yi, "A Novel, Low-Cost Implementation of 'Democratic' Load-Current Sharing of Paralleled Converter Modules," *IEEE Trans. Power Electron.*, Vol. 11, No. 4, July 1996, pp. 604-611.

[8] V.J. Thottuvelil and G.C. Verghese, "Stability Analysis of Paralleled DC/DC Converters with Active Current Sharing," *IEEE Power Electronics Specialists Conference*, 1996, (in press).

[9] D. Maliniak, "Dense DC-DC Converters Actively Share Stress," *Electronic Design*, Jan. 21, 1993, pp. 39-44.

[10] M. Jordan, "UC3907 Load Share IC Simplifies Parallel Power Supply Design," *Unitrode Application Note U-129*, Unitrode Corp., Merrimack, NH.

[11] J. Bocek and C. Liu, "Determining Current Sharing Criterion for Parallel Operation of Power Converters in Multi-Module Bus Systems," *IEEE Power Electronics Specialists Conference*, 1990, pp. 870-879.

[12] J. Glaser and A. Witulski, "Output Plane Analysis of Load-Sharing in Multiple-Module Converter Systems," *IEEE Transactions on Power Electronics*, Vol. 9, No. 1, Jan. 1994, pp. 43-50.

[13] J. Dixon and B. Ooi, "Series and Parallel Operation of Hysteresis Current-Controlled PWM Rectifiers," *IEEE Transactions on Industry Applications*, Vol. 25, No. 4, July/August 1989, pp. 644-651.

[14] D.J. Perreault, R. Selders, and J.G. Kassakian, "Frequency-Based Current-Sharing Techniques for Paralleled Power Converters", *1996 IEEE Power Electronics Specialists Conference*, Baveno, Italy, pp. 1073-1079.

[15] D.J. Perreault, R.L. Selders, and J.G. Kassakian, "Implementation and Evaluation of a Frequency-Based Current-Sharing Technique for Cellular Converter Systems," *IEEE Africon `96*, Matieland, South Africa, pp. 682-686.

[16] K. Sato, "A Switching Ripple Based Current Sharing Control System for Cellular Converters," S.M. Thesis, *M.I.T. Department of Electrical Engineering and Computer Science*, June 1997.

[17] D. Perreault, "Design and Evaluation of Cellular Power Converter Architectures," Ph.D. Thesis, *M.I.T. Department of Electrical Engineering and Computer Science*, June 1997.

Isolated Three-Phase AC-to-DC Bidirectional Converter with a Small Number of Switches

Akira TAKEUCHI†, Hisahito ENDO, Seiichi MUROYAMA and Satoshi OHTSU
NTT Integrated Information & Energy Systems Laboratories
Musashino-shi, Tokyo 180, JAPAN
Fax: +81-422-59-2172, Phone: +81-422-59-4016,
E-mail: takeuchi@venus.mitaka.ntt-at.co.jp

Abstract - **A bidirectional converter that converts three-phase AC to DC or vice versa by using a high-frequency transformer has been investigated. The main feature of the circuit is that it does not need as many switches as the conventional converter. Suitable operating conditions and design considerations for the circuit were clarified by analyzing the steady-state characteristics and resonant reset of the transformer. Circuit operation was verified by simulation, and it was confirmed that AC currents can be controlled as sinusoidal waveforms by using a simple control circuit.**

I. Introduction

Bidirectional AC-DC converters are useful for such applications as load leveling and providing an uninterruptible power supply. The need of a commercial-frequency transformer makes conventional isolated bidirectional converters large. One way to reduce the converter size is to use a high-frequency transformer and a cycloconverter. However, a three-phase AC-to-DC cycloconverter requires six bidirectional switches, that is, twelve switching devices on the AC side.

This paper proposes a three-phase AC-to-DC bidirectional converter that does not need as many switches. It will enable small low-cost bidirectional converters to be developed. Furthermore, the AC currents can easily be controlled to be sinusoidal waveforms in this converter. We have clarified suitable operating conditions and design considerations by analyzing the steady-state characteristics and resonant reset of the transformer. We have also developed a simplified control method for the converter and verified its circuit operation by simulation.

† Akira Takeuchi is with NTT Advanced Technology Corporation.

II. Circuit Configuration and Principle of Operation

Figure 1 shows the proposed three-phase AC-to-DC bidirectional converter. The switching circuit on the AC side is composed of bidirectional switches (S_a, S_b, and S_c) and capacitors (C_a, C_b, and C_c). The bidirectional switches are composed of two switching devices, such as IGBTs, in series. Although large ripple currents flow in the capacitors, their capacitances are as small as those used as filters to reduce switching ripple.

In the rectifier mode, when one of the switches S_a, S_b or S_c is on, AC current from each phase is supplied to the DC side by synchronizing switches S_{d1} and S_{d2} according to the polarity of the AC voltage. In the inverter mode, when one of switches S_a, S_b or S_c is on, DC current is supplied to each AC phase.

Since the transformer is magnetized only toward the polarity of each three-phase voltage, the magnetizing energy caused by the difference in three-phase voltage magnitudes and polarities must be reset. The switching circuit on the DC side is constructed in order to generate the reset voltage. Circuit operation in the rectifier mode is thus similar to that of a forward converter. In the inverter mode, switch S_{d3} is turned on when all switches on the AC side are turned off, so the reset voltage can be generated.

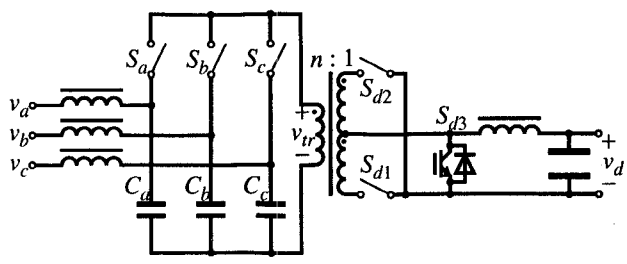

Fig. 1. Three-phase bidirectional converter.

0-7803-3823-5/97/$10.00© 1997 IEEE

Figure 2 shows the control sequence of each switch and the simulated waveforms of the winding voltage and magnetizing current of the transformer. The parameters for simulation are listed in Table I. Either S_{d1} or S_{d2} is turned on selectively according to the polarity of the transformer voltage. To retain the reset periods for the transformer, each on-period of the switches on the AC side is restricted to one-third of the switching period T_s. While various other switching sequences could be used for the converter, we selected the control sequence shown in Fig. 2 because its control circuit is the simplest.

The AC current of each phase is nearly proportional to the duty ratio of each switch. Therefore, the waveforms of the AC current can be controlled without having to detect any AC current. This results in a simplified control circuit for the converter. Control is done using the PWM signals generated from reference sinusoidal signals and a triangular waveform.

Table I Circuit Parameters

V_{ac}	200 V	C_a	2 μF
V_d	100 V	C_{Sa}	2 nF
n	4/3	C_{Sd}	1 nF
f_s	100/3 kHz	L_m	1.6 mH

III. Analysis of Operating Conditions

We clarified the operating conditions best suited for controlling the AC currents to be sinusoidal waveforms so as to reduce the harmonic currents. We analyzed the steady-state characteristics and the resonant reset of the transformer to determine the best circuit design. We ignored the circuit resistances and imbalance between the three-phase voltages.

The following equation was obtained by analyzing the steady-state characteristics in the converter.

$$D_a v_a + D_b v_b + D_c v_c = n v_d , \tag{1}$$

where D_a, D_b, and D_c are the duty ratios of switches S_a, S_b, and S_c. The duty ratios of the switches are controlled in proportion to the AC voltage to create sinusoidal AC currents. The duty ratios are thus expressed as

$$D_a = K_D v_a , \; D_b = K_D v_b , \; D_c = K_D v_c . \tag{2}$$

Therefore, proportional constant K_D is obtained as

$$K_D = \frac{n v_d}{v_a^2 + v_b^2 + v_c^2} = \frac{n v_d}{3 V_{ac}^2} . \tag{3}$$

Consequently, the relationship in the steady-state is

$$\frac{n V_d}{V_{ac}} = \frac{3 T_{on}}{T_s} , \tag{4}$$

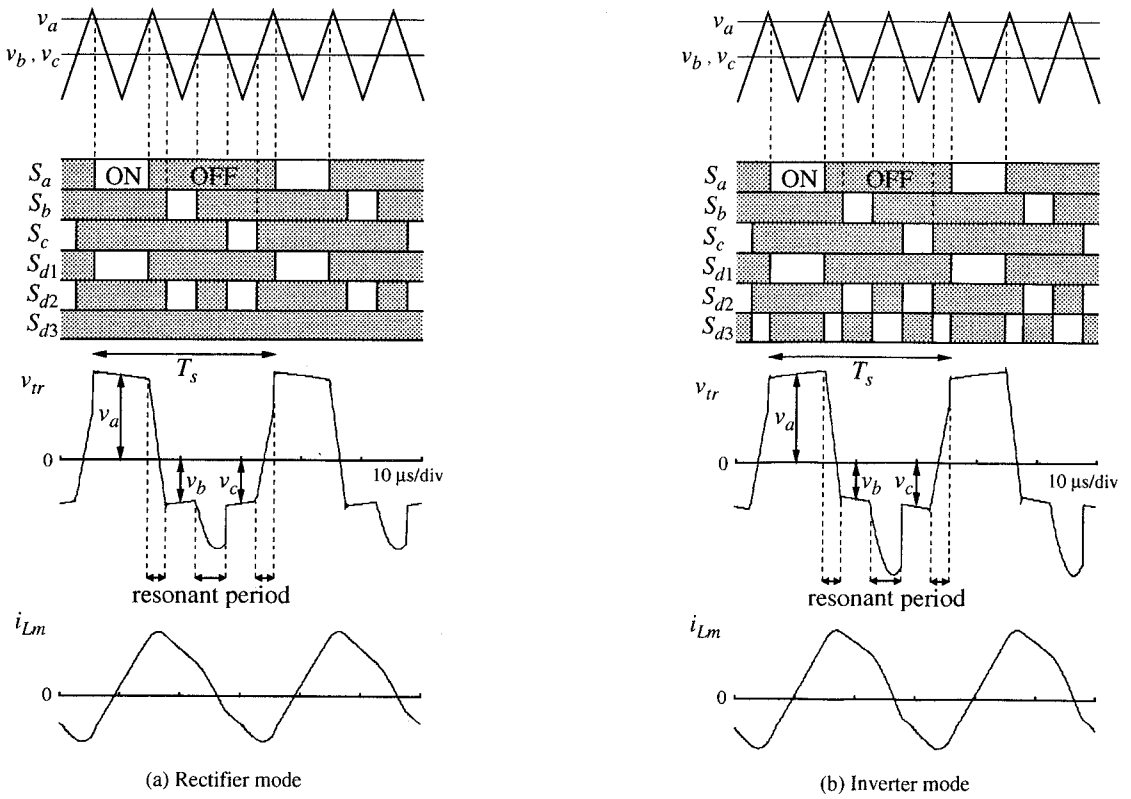

(a) Rectifier mode

(b) Inverter mode

Fig. 2. Switching sequences and simulated waveforms.

where T_{on} is the on-period of the switch on the AC side when each AC voltage is its rms value V_{ac}. Since each on-period is restricted to one-third of the switching period in the control circuit, the operating condition for sinusoidal AC currents is

$$\frac{n V_d}{V_{ac}} < \frac{1}{\sqrt{2}} . \tag{5}$$

When all switches on the AC side are turned off, resonance occurs due to the magnetizing inductance of the transformer and to the parasitic capacitances of the switches and transformer. If the parasitic capacitance of switches S_a, S_b, and S_c is C_{Sa}, and the parasitic capacitance of switches S_{d1} and S_{d2} is C_{Sd}, and assuming that the capacitances of capacitors C_a, C_b, and C_c are large compared with these parasitic capacitances, the circuit is equivalent to that shown in Fig. 3. Therefore, resonant angular frequency ω_r is

$$\omega_r = \frac{1}{\sqrt{L_m\left(3 C_{Sa} + \frac{2}{n^2} C_{Sd}\right)}} . \tag{6}$$

When one of the three-phase voltages is maximum, the magnetizing energy to be reset is also maximum. We analyzed this worst case for the reset.

As the resonant frequency increases, the reset voltage rises. Figure 4(a) shows the winding voltage and magnetizing current of the transformer in a converter with a higher resonant frequency. The resonant voltage rises sharply before S_b turns on. The winding voltage of the transformer in resonant period T_{r1} is expressed as

$$\begin{aligned} v_{tr}(t) &= \sqrt{2} V_{ac} \cos\omega_r (t - t_1) \\ &\quad - \omega_r T_{on} V_{ac} \sin\omega_r (t - t_1) . \end{aligned} \tag{7}$$

When the winding voltage of the transformer at the middle of the resonant period is positive, the resonant voltage is restricted to about the maximum AC phase voltage:

$$\tan\frac{\omega_r T_{r1}}{2} < \frac{\sqrt{2}}{\omega_r T_{on}} , \tag{8}$$

where

$$T_{r1} = \frac{T_s}{3} - \frac{3\sqrt{2}}{4} T_{on} . \tag{9}$$

From Eq. (4), the design consideration for restricting the resonant voltage is

$$\tan\left(\left(1 - \frac{3}{2\sqrt{2}} \frac{n V_d}{V_{ac}}\right) \frac{\omega_r T_s}{6}\right) < \frac{3\sqrt{2}}{\omega_r T_s} \frac{V_{ac}}{n V_d} . \tag{10}$$

In contract, as the resonant frequency decreases, the bias of the magnetizing current increases. Figure 4(b) shows the winding voltage and magnetizing current of the transformer in a converter with a lower resonant frequency. The reset of the transformer has not been completed when S_c turns on. The magnetizing current in resonant period T_{r2} is expressed as

$$\begin{aligned} i_m(t) &= \frac{\omega_r T_{on}}{Z_r} V_{ac} \cos\omega_r (t - t_2) \\ &\quad - \frac{V_{ac}}{\sqrt{2} Z_r} \sin\omega_r (t - t_2) . \end{aligned} \tag{11}$$

To restrain the bias magnetization, the resonant frequency should be designed so that the magnetizing current becomes

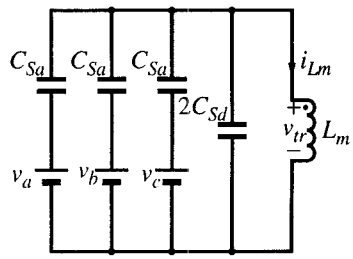

Fig. 3. Equivalent circuit during resonant periods.

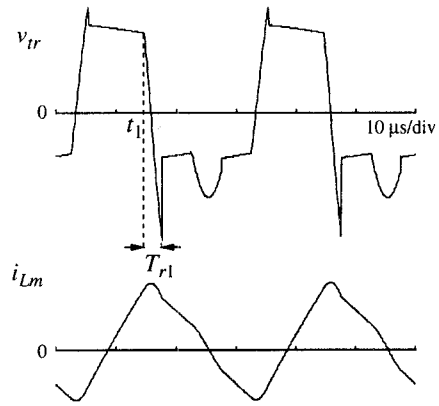

(a) Higher resonant frequency

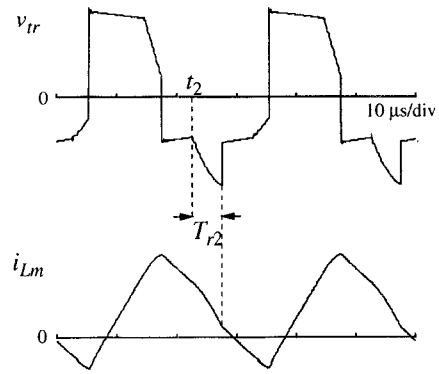

(b) Lower resonant frequency

Fig. 4. Simulated waveforms.

zero before S_c turns on. This reset condition is given by

$$\sqrt{2}\omega_r T_{on} < \tan\omega_r T_{r2}, \quad (12)$$

where

$$T_{r2} = \frac{T_s}{3} - \frac{\sqrt{2}}{2} T_{on}. \quad (13)$$

From Eq. (4), the design consideration for resetting the transformer is

$$\frac{\sqrt{2}\omega_r T_s}{3} \frac{n V_d}{V_{ac}} < \tan\left(\left(1 - \frac{1}{\sqrt{2}} \frac{n V_d}{V_{ac}}\right) \frac{\omega_r T_s}{3}\right). \quad (14)$$

The operating conditions calculated from Eqs. (5), (10), and (14) are shown in Fig. 5. As the ratio on the vertical axis is designed to be larger, the duty ratios of the switches on the AC side can be made wider, thus reducing the conduction loss. The condition for the simulated waveform shown in Fig. 2 falls within the analyzed suitable operating conditions. The conditions for the simulated results shown in Fig. 4 are out side the suitable conditions.

IV. Verification of Control Method

We performed simulation using SIMPLIS to verify the circuit operation and control characteristics of a converter designed to operate under the suitable reset conditions.

A block diagram of the control circuit used for the simulation for the rectifier mode is shown in Fig. 6. It is constructed without a multiplier. The triangular waveform is created by integrating a rectangular pulse whose amplitude is clamped by the output of the error amplifier of DC current i_d. The PWM signal is obtained from comparators whose inputs are the triangular waveform and a sinusoidal signal. The voltages of capacitors C_a, C_b, and C_c are used as the sinusoidal reference. The logic circuit orders the on-periods of switches S_a, S_b, and S_c and generates synchronized gate signals for S_{d1}, S_{d2}, and S_{d3}.

For the inverter mode, the on-periods of each switch are controlled in proportion to the sinusoidal reference signal. The PWM signals are obtained by comparing the sinusoidal reference with a triangular waveform whose amplitude is controlled by the average of the AC voltages.

As shown in Fig. 7, the simulated waveforms of the AC current in the rectifier mode are almost sinusoidal. Consequently, the unity power factor can be achieved in a converter by using the simple control method without having to detect any AC currents.

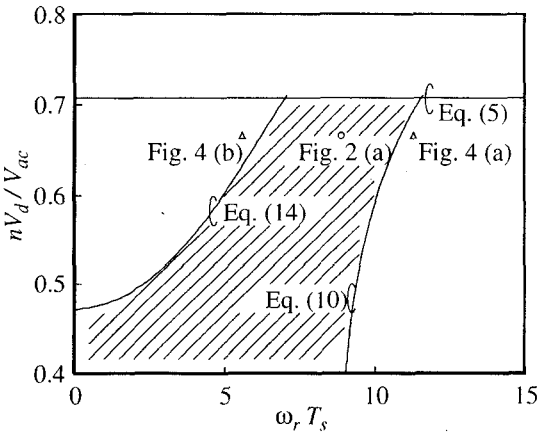

Fig. 5. Operating conditons.

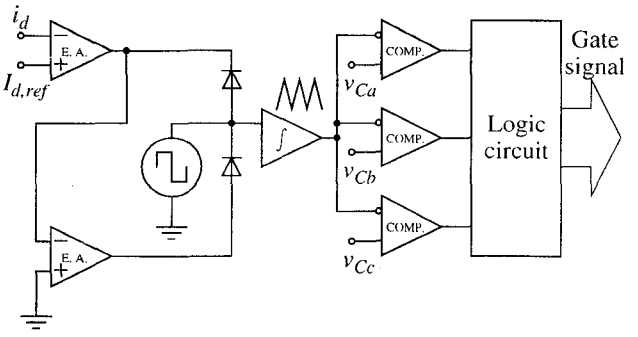

Fig. 6. Control circuit for rectifier mode.

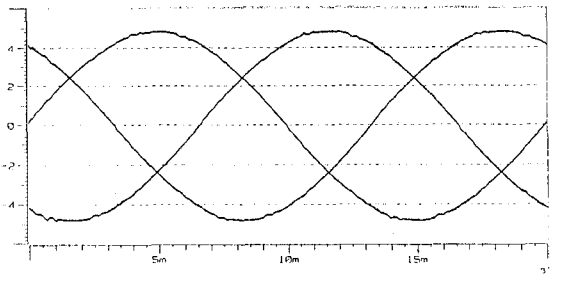

Fig. 7. Simulated AC current waveforms for rectifier mode.

V. Conclusions

Our proposed three-phase AC-to-DC bidirectional converter requires fewer switches. We clarified the suitable operating conditions and design considerations for the circuit by analyzing the steady-state characteristics and the resonant reset. The circuit operation was verified by simulation and it was confirmed that AC currents can be controlled to be sinusoidal waveforms with a simple control circuit.

Acknowledgments

We are grateful to Dr. Ichiro Yamada for his encouragement and support.

Immunity Test Results of a Quick Power Failure Detector of Uninterruptible Secondary Battery System

Satoshi Miyazaki Masaaki Ohshima
Tokyo Electric Power Co., Inc.
4-1, Egasaki-Cho, Tsurumi-ku, Yokohama, Kanagawa 230, Japan

Fuminori Nakamura Yuushin Yamamoto Shinzo Tamai Haruyoshi Mori
Mitsubishi Electric Corp.
8-1-1, Tsukaguchi-Homnachi, Amagasaki, Hyogo 661, Japan

***Abstract*—An Uninterruptible Secondary Battery System (USBS) consists of secondary batteries and a multi-functional power converter having plural operational modes including local load leveling and uninterruptible power supply (UPS). For the USBS, a quick power failure detector is essential for the smooth operational mode changes. However, commercial a.c. line voltage harmonic distortion or voltage unbalance may cause misoperation of the quick power failure detector. In this paper we present immunity test results of the USBS. The test results proved that the proposed detector has sufficient immunity to harmonic distortion and unbalance of the commercial a.c. line voltage.**

I. INTRODUCTION

A steady progress in development of high performance secondary batteries such as NaS enables field tests of large capacity power conversion system (PCS) for local load leveling [1]. For the purpose of uninterruptible electric power supply to critical loads such as computers or communication equipment, we have proposed an uninterruptible secondary battery system (USBS) which has plural operational modes including local load leveling and uninterruptible power supply (UPS). A 3kVA model set of the proposed USBS has been fabricated and its experiment results proved the performance of the proposed USBS is satisfactory [2].

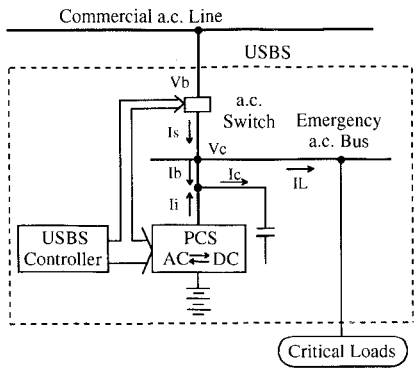

Fig.1. Mains Circuit Configuration of USBS

Fig. 1 shows the main circuit configuration of the USBS. It adopts parallel processing type UPS in order to realize the lower capital investment, smaller occupied space and higher overall efficiency.

In the case of conventional UPS shown in Fig. 2, the overall efficiency is lower because an a.c. power supplied to critical loads is converted twice, that is, the a.c. power is once converted to a d.c. power with a rectifier and the d.c. power is converted to an a.c. power with an inverter again. Additionally, a necessity of a couple of these power converters increases the capital investment and occupied space.

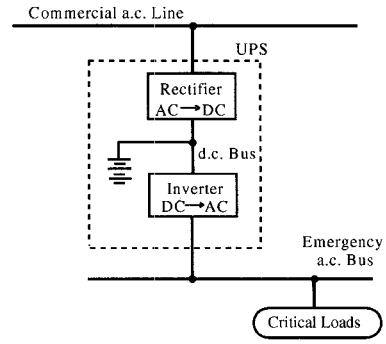

Fig.2. Mains Circuit Configuration of Conventional UPS

Contrarily, in the case of the proposed USBS, the overall efficiency is high because the a.c. power is directly supplied to critical loads through an a.c. switch without any power conversions when the commercial a.c. line voltage is normal. Furthermore, substitution of rectifier of the conventional UPS with the a.c. switch decreases the capital investment and occupied space.

However, in the case of the USBS, the power failure of the commercial a.c. line directly causes the drop of the emergency a.c. bus voltage, because the emergency a.c. bus is directly connected to the commercial a.c. line through the a.c. switch. Therefore, in order to continue to supply critical loads for which no power interruption are permissible with electricity, USBS must detect the power failure quickly and must immediately separate the emergency a.c. bus from the commercial a.c. line by opening the a.c. switch.

0-7803-3823-5/97/$10.00© 1997 IEEE

Although the quick power failure detector is essential to this system, it is difficult to determine the instantaneous amplitude of the sinusoidal signal whose amplitude is different as its phase. Additionally, such severest conditions as harmonic voltage distortions or the voltage unbalance may cause any misoperations of the quick power failure detector. Therefore, it is necessary to develop a quick power failure detector which has immunity to such severest conditions as harmonic voltage distortions or the voltage unbalance and its performance shall be tested.

II . PERFORMANCE OF THE USBS

Fig. 3 shows the control block diagram of the USBS. The USBS has plural operational modes including local load leveling mode and UPS mode.

For the purpose of local load leveling, when the commercial a.c. line voltage is normal, USBS charges its large capacity secondary batteries such as lead-acid or NaS in the nighttime when the supply has some margins, and discharges them in the daytime at the peak of the demand.

For the purpose of UPS, when the power failure occurs, the a.c. switch is opened and USBS changes its operational modes instantaneously to continue supplying the critical loads with electricity.

For these two operational modes, USBS has two independent controller, an a.c. power controller and an a.c. voltage controller. The outputs of these controller are inputted to the current control loop of PCS as a current reference. The control mode of the USBS (Local load leveling mode or UPS mode) is decided by the current reference given to the current control loop and the selection is made by the output signal of the power failure detector.

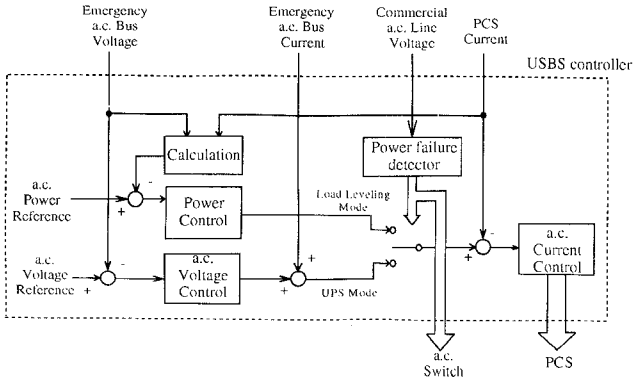

Fig.3. Control Block Diagram of USBS

A. *Load Leveling Mode*

When the commercial a.c. line voltage is normal and USBS is operated in the local load leveling mode, the a.c. switch is closed and the output of the a.c. power controller is selected as the current reference.

In this mode, the PCS generates a.c. power according to the power reference. Namely, the power controller outputs a PCS current reference and controls the output power of the PCS according to the given power reference and the power feedback signal which is calculated from the output current of the PCS and the commercial a.c. line voltage.

B. *UPS Mode*

When the power failure of the commercial a.c. line occurs and USBS is operated in the UPS mode, the a.c. switch is opened and the output of the a.c. voltage controller is selected as the current reference.

In this mode, the PCS keeps the voltage of the emergency a.c. bus constant. The a.c. voltage controller outputs the PCS current reference and controls the emergency a.c. bus voltage according to the rated a.c. voltage reference and the feedback signal of the emergency a.c. bus voltage.

C. *Behavior Under Commercial a.c. Line Fault*

When the power failure occurs and the commercial a.c. line voltage drops, the a.c. switch turned off signal is made by the output signal of the power failure detector, or by the signal of an over current sensors so as to avoid the damage of the a.c. switch caused by an over current. Then operating mode of the USBS is quickly changed to the UPS mode and the a.c. voltage controller regulates the emergency a.c. bus voltage.

D. *Behavior at the Commercial a.c. Line Voltage Recovery*

The USBS recognizes the commercial a.c. power as normal after continuous detection of the commercial a.c. line voltage fluctuation within $\pm 10\%$ of the rated value, and start to adjust phase and amplitude of PCS output voltage within $\pm 1\%$ deference from that of the commercial a.c. line before the a.c. switch is turned on in order to avoid an inrush current. The power reference is also increased gradually with a filter to the set point.

III . QUICK POWER FAILURE DETECTOR

A. *Required Transient Voltage*

Since the parallel processing type UPS is adopted as the main circuit configuration of the USBS, the emergency a.c. bus voltage also drops accordingly when the power failure occurs and the commercial a.c. line voltage drops.

On the other hand, emergency loads have their own permissible transient voltage range and its time period. For example, in the case of the equipment whose internal unit is driven with d.c. voltage such as a computer, the d.c.

voltage is depend on its capacity of filter capacitor which absorb the d.c. voltage ripple.

Therefore, in order to protect any critical loads from interruption, the required transient voltage of the USBS should be set so as to satisfy the permissible transient voltage and its duration and USBS should keep the transient voltage of the emergency a.c. bus within the required level.

We have researched and checked the relations between transient voltage and its duration of various kinds of equipment from principal references in Japan and other countries [3]-[8], and set the required transient voltage of the USBS as fig. 4 so as to meet all the requirements.

Fig. 4 depicts that, for example, the time period during which the emergency a.c. bus voltage is lower than 75% of rated value must be shorter than 2ms.

By setting the required transient voltage of the USBS as fig. 4, almost all sorts of emergency loads are protected from an interruption.

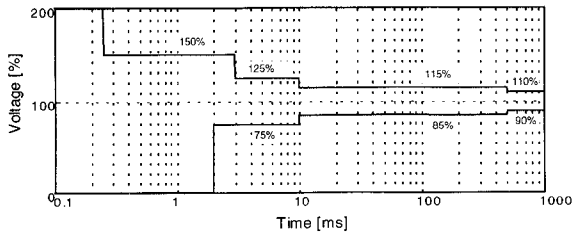

Fig.4. Required Transient Voltage of USBS

B. Specifications of Immunity

Although the loads connected to the commercial a.c. line which generate harmonic currents or unbalanced currents may cause harmonic voltage distortions or voltage unbalance, the power failure detector of the USBS must have an immunity to such severe conditions and the transient voltage of emergency a.c. bus must be kept within the required transient voltage of the USBS.

We have set the immunity specifications to harmonic distortions of the commercial a.c. line voltage as shown in Table I referring to the required value for suppression of voltage distortion [9]-[11], and set the immunity specifications to the commercial a.c. line voltage unbalance as shown in Table II referring to the required value for electromagnetic-resistant environmentality given in [12]-[13]. The unbalance factor F is given by (1).

TABLE I
IMMUNITY SPECIFICATIONS TO HARMONIC VOLTAGE DISTORTIONS

Individual Harmonic Order	3	5	7	THD
Maximam Harmonic Voltage Dsitortion (%)	3.0	4.0	3.0	6.0

TABLE II
IMMUNITY SPECIFICATIONS TO THE VOLTAGE UNBALANCE

Maximam Voltage Unbalance
± 5%

$$F = \frac{Vm - Vave}{Vave} \times 100\% \qquad (1)$$

where Vm : Min. or Max. of line-to-line voltage
Vave : Ave. of line-to-line voltage

In order to examine appropriateness of the immunity specifications to harmonic distortions of the commercial a.c. line voltage, we reviewed the measurement data of harmonic voltage distortions in [14]-[18]. Whereas most of the data fall under the limit of the immunity specification, a few of them show exceeding of the limit.

No measurement data were found which assure appropriateness of the immunity specifications to the voltage unbalance shown in Table II, and the specification stipulates a requirement more moderate than the most severe one in [12].

However, an unnecessarily strict requirement are undesirable for the concept of low cost USBS because it tends to provoke a cost increase in main circuits semiconductors. As we cannot find enough measurement data in the actual distortion system, further research and discussions shall be continued.

C. Problem Under Harmonic Voltage Distortion or Voltage Unbalance

To satisfy the required transient voltage of the USBS, the time period during which the emergency a.c. bus voltage is lower than 75% of the rated value must be shorter than 2 ms.

For this purpose, once a power failure occurs and the emergency a.c. bus voltage drops to under 75% of the rated value, the USBS must quickly detect the power failure, open the a.c. switch, and change its operational mode to UPS mode in order to recover the emergency a.c. bus voltage.

However, when we estimate the amplitude of the commercial a.c. line voltage by the method of calculating the voltage amplitude collectively for the three phase voltages, which is shown in Fig. 5, harmonic voltage distortions and the voltage unbalance may cause a misdetection and the emergency a.c. bus voltage may possibly not satisfy the required transient voltage because it is impossible to calculate the amplitude individually for each phase. Such a misdetection must be avoided,

particularly when the single phase type emergency loads are connected to the emergency a.c. bus.

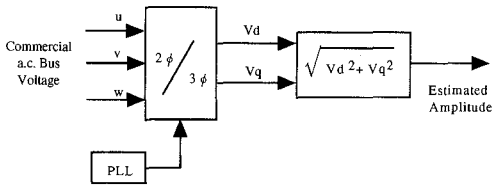

Fig.5. Example of Power Failure Detector

D. Quick Power Failure Detector

In order to attain the required transient voltage of the USBS, we have developed a quick power failure detector shown in Fig. 6, which is effective in detecting power failures exactly and quickly even if the commercial a.c. line voltage includes harmonic distortion and unbalance.

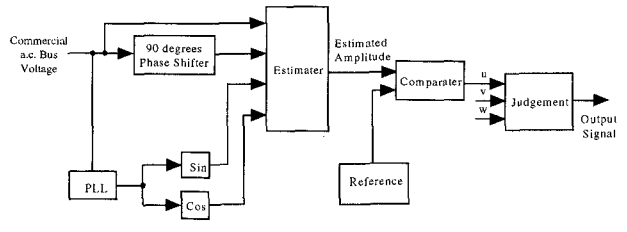

Fig.6. Block Diagram of a Quick Power Failure Detector

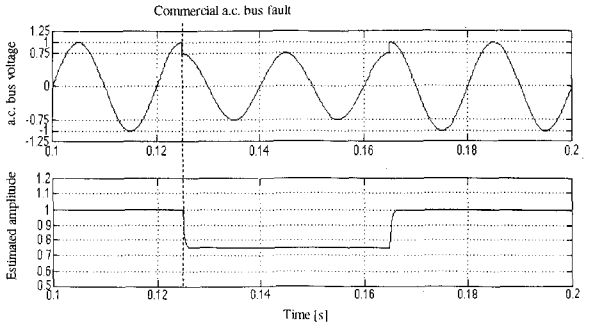

Fig.7. Behavior of Quick Power Failure Detector

This quick power failure detector determine the amplitude at every moment as quickly as within 500 μs using the commercial a.c. line voltage, the 90 degrees shifted signal, the sin and cos signals calculated from the output signal of the PLL. Fig. 7 shows an example of the estimated amplitude, which gives an evidence that a drop of the amplitude to 75% of the rated value is quickly determined. The determined amplitude is compared with a reference which changes in accordance with the required transient voltage in order to judge the power failure.

The advantage of this detector is its capability of determined voltage amplitude in each phase independently, instantaneously and exactly, because it determined the amplitude directly from the input sinusoidal signals. Hence, an exact and quick power failure detection is possible with this detector even when the commercial a.c. line voltage contains harmonic distortions and unbalances such as shown in Tables I and II.

IV . Immunity Test Results

In order to inspect the immunity performance of this quick power failure detector, a 3kVA model set is fabricated and experimented. Table III shows the specifications of the model set. We used popularly obtainable lead-acid batteries in this model set instead of NaS in the actual installation of 50 to 200KW.

TABLE III
SPECIFICATIONS OF THE MODEL SET

Capacity of PCS	3kVA (200V, 50Hz)
Main Cuircuit of PCS	IPM (PM100CSA-60) 100A, 600V
a.c. Switchs	IGBT (CM600HA-24H) 600A, 1200V
Filter Capacitors	1 6 μ F (2 0 % of PCS Capacity) AC600V
Secondary Batteries	Lead-acid (SUC130-12) 180Ah/10Hr

Fig. 8 shows appearance of the model set, and Fig. 9 does its control boards. It employs the direct digital control (DDC), which raises the speed of control computation since the control algorithm is paralleled with multiple DSPs. The control boards are designed compact and high reliable by adoption of a special ASIC. The man-machine interface system adopts a touch panel of color liquid crystal display, which has proved effective to realize easiness both to see and to operate.

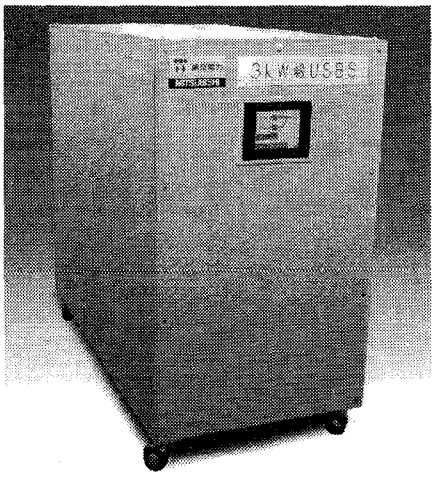

Fig.8. 3kVA Mini Model Set

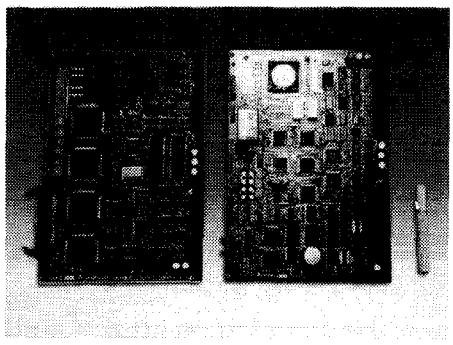

Fig.9. Control Boards

A. Immunity Test to Harmonic Voltage Distortion

In order to clarify the immunity of the quick power failure detector of the USBS to the harmonic distortions of the commercial a.c. line voltage, we examined the emergency a.c. bus voltage in the case where a power failure has occurred at a distant point by adding harmonic distortions to the commercial a.c. line voltage.

Under these conditions, the output signal of the quick power failure detector turns off the a.c. switch and changes the operational mode of the USBS.

Fig. 10 shows the waveforms when the commercial a.c. line voltage includes no harmonic distortion. It indicates that the time duration in which the emergency a.c. bus voltage is lower than 75% of the rated value is 0.86ms, and it satisfies the predefined required transient voltage.

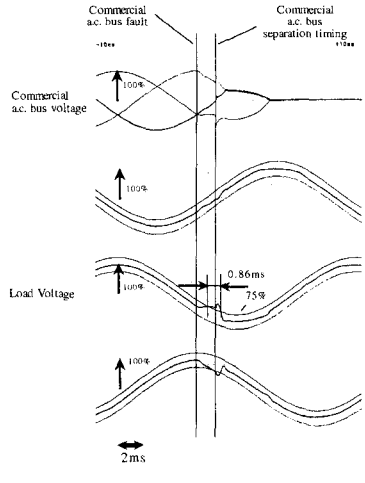

Fig. 10. Waveforms under commercial a.c. line fault
(Without harmonic voltage distortion)

Fig.11, 12 and 13 show waveforms in the case where the commercial a.c. line voltage includes 3% of 3rd, 4% of 5th and 3% of 7th harmonic distortion respectively.

They indicate that the time period during which the emergency a.c. bus voltage is lower than 75% of the rated value are 1.1ms, 0.94ms and 1.1ms respectively, and all of the fluctuation on the emergency a.c. bus are restricted within the predefined level.

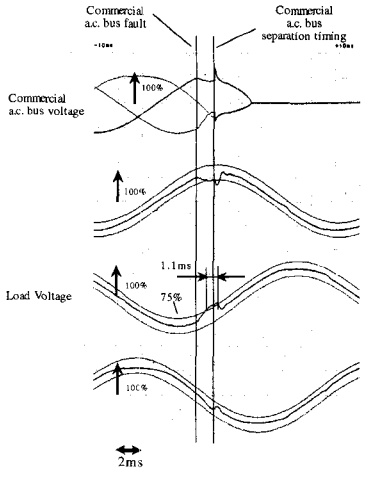

Fig. 11. Waveforms under commercial a.c. line fault
(With 3% of 3rd harmonic voltage distortion)

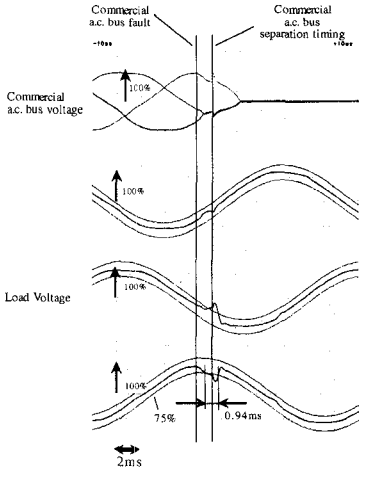

Fig. 12. Waveforms under commercial a.c. line fault
(With 4% of 5th harmonic voltage distortion)

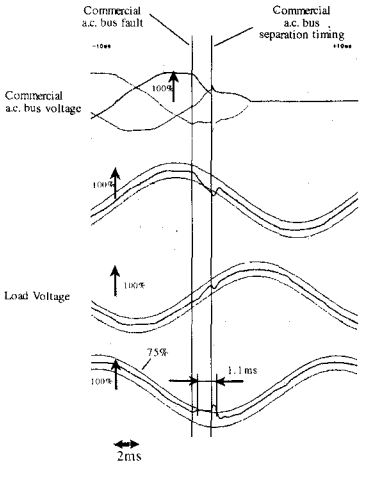

Fig. 13. Waveforms under commercial a.c. line fault
(With 3% of 7th harmonic voltage distortion)

B. Immunity Test to Voltage Unbalance

In order to test the immunity to the commercial a.c. line voltage unbalance, we examined the emergency a.c. bus voltage in the case where a power failure has occurred by unbalancing the three phases of the commercial a.c. line voltage. Unbalance factor of the commercial a.c. line voltage is set at the maximum limit of 5% given in table II.

In this test result also, the duration in which the emergency a.c. bus voltage is lower than 75% of the rated value is 0.92ms, and it satisfies the predefined level.

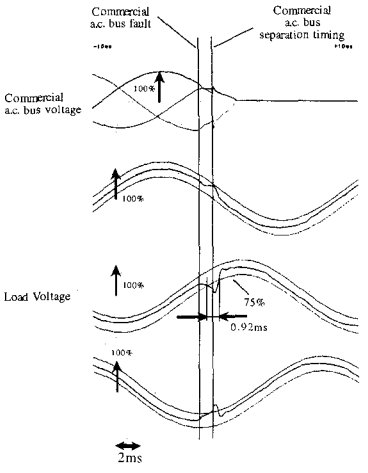

Fig. 14. Waveforms under commercial a.c. line fault (With 5% of voltage unbalance)

V . CONCLUSIONS

USBS has a plural operational modes including local load leveling and UPS and when the power failure occurs, USBS changes its operational mode to the UPS quickly and continue to supply critical load with electricity without interruption.

However, the harmonic voltage distortions of the commercial a.c. line or the commercial a.c. line voltage unbalances may cause any misditection of power failures. Therefore, this demands developing of a quick power failure detector which has immunity to such severest conditions on the commercial a.c. line voltage.

The authors have set the required transient voltage of the USBS as well as the immunity specifications of the commercial a.c. line voltage regarding harmonic voltage distortion and unbalances and in order to meet those requirements and specifications, we have developed a novel quick power detector.

This detector can judge the voltage drop in each single phase instantaneously and exactly by the method of estimating the amplitude directly from input sinusoidal voltage and it can have sufficient immunity to harmonic voltage distortions and the voltage unbalance.

All immunity tests on such a severest conditions as harmonic voltage distortions of the commercial a.c. line or the commercial a.c. line voltage unbalances indicate that the time period during which the emergency a.c. bus voltage is lower than 75% of the rated value is shorter than 2ms and they are restricted within the predefined requirement. This has proved that the USBS has a sufficient immunity to harmonic voltage distortions and the voltage unbalances.

Finally, the authors found that there are few date proving the background for establishing the immunity specification. For the general use of the specifications in the future, it is desirable that studies and discussions are continued further.

REFERENCES

[1] K. Nakaji, Y. Naito, M. Ohshima, S. Sugimoto, "Development and Application of Dispersed Generation Systems," *IEEJ A Publication of Industry Applications Society*, Vol. 115-D, no. 2, 1995, pp. 98-102.

[2] S. Miyazaki, M. Ohshima, S. Tamai, Y. Yamamoto, F. Nakamura, N. Sashida, "Novel Power Conversion System for Uninterruptible Secondary Battery System," *Proceedings of 7th International Conference on Harmonics and Quolity of Power*, October 1996, Session R-5, pp. 655-660.

[3] "Method of specifying the performance and test requirements of uninterruptible power systems including UPS switches," *IEC-146-4*, Deaft, 1993.

[4] "IEEE Recommended Practice for Emergency and Standby Power Systems for Industrial and Commercial Applications, "*ANSI/IEEE Standard* 446-1987.

[5] Mark Waller, "Computer Electrical Power Requirements," Howard W. Sams & Co., 1987.

[6] *NEMA UPS Standard*, Pub. No. PE1-1992.

[7] *JEM-TR* 185, 1993.

[8] *JEM-TR* 186, 1993.

[9] *A Publication of Electric Tecnology Research Association of Japan*, Vol. 46,no.2, 1990, pp.13-16, pp.49-55.

[10] *A Publication of Electric Tecnology Research Association of Japan*, Vol. 37, no.3, 1981, pp88-89.

[11] "IEEE Recommended Practice and Requiremnets for Harmonic Control in Electrical Power Systems, "*ANSI/IEEE Standard* 519-1992.

[12] *JEC*-2410, 1989.

[13] *JEC*-5919, 1990.

[14] K. Oku, O. Nakamura, K. Uemura, "Measurement and Analysis of Harmonics in Distribution Systems and Development of a Harmonics Suppression Method,"*IEEJ A Publication of Power and Energy Society*, Vol. 114-B, no. 3, 1994, pp.234-241.

[15] K. Oku, O. Nakamura, J. Inoue, M. Kohata, "Suppression Effects of Active Power Filter on Harmonics of Distribution System Including Capacitors,"*IEEJ A Publication of Power and Energy Society*, Vol. 115-B, no. 9, 1995, pp.1023-1028.

[16] T. Aizawa, M. Inoue, " The Present Example of the Generation of Higher Harmonics at the High-Tension Customer," *Proceedings of 7th Annual Conference of Power & Energy Society. IEE of Japan*, August 1996, Session II-394, pp.385-386.

[17] E. Ohba, "The Reserch of the Actual Harmonic Voltage Distortions of Power Trasmition Lines,"*OHM*, October 1994, pp.31-36.

[18] D. S. Dorr, " Point of Utilization Power Quality Study Results," IEEE-IAS, 1994, ,Session 873, pp.2334-2344.

Parallel Redundant Operation of UPS with Robust Current Minor Loop

Youichi Ito and Osamu Iyama
SANKEN ELECTRIC Co., LTD.
677 Ohnohara, Shimo-akasaka, Kawagoe-shi, Saitama-ken, 350-11 JAPAN
Phone +81-492-66-8031, Fax: +81-492-66-4230
E-mail: RXQ07536@niftyserve.or.jp

Abstract— **This paper describes a control method of UPS inverters connected in parallel. The UPS output voltage is controlled by an algorithm with an inverter current minor loop using two types of observers. Only following two points are added to the algorithm for realizing parallel operations. 1) Feedback of a common load current instead of the UPS output current. 2) Adjusting the phase of the output voltage to make the reactive component of circulating currents zero. The proposed method has the following features, compared with conventional methods; 1) It dose not need an additional output voltage control for parallel operation. 2) the impedances among UPSs are resistive so that the circulating currents caused by phase difference among UPSs have only reactive components. 3) Increase of software for parallel operation control is little.**

I. Introduction

In recent years, as information societies become higher level in larger scale, the importance of UPSs (Uninterruptible Power Supplies) is increasing and UPSs with high performance, low-price and small size are demanded. The authors have commercialized stand-alone UPSs : SANKEN's SDU-S (30 ~ 200kVA) [1] to satisfy such demands. This time, to establish UPS systems that have higher reliability than stand-alone UPSs, the authors have developed the UPS: SANKEN's SDU-P (30 ~ 200kVA) with the functions of parallel redundant operations and synchronization with the commercial power source.

In the proposed parallel operation method, output impedance of the stand-alone UPS (SDU-S) is considered. The SDU-S or SDU-P adopted the output voltage control algorithm with a robust current minor loop using observers [2]. In this algorithm, the impedance can be changed by adjusting the feedback gain of UPS output current in the minor loop. It is assumed that the impedance is one when 100% of the output current is fed back. The impedance is ten times bigger than that when 0% of the output current is fed back. In parallel operation, when the common load currents is fed back instead of UPS output currents, an output impedance to a load maintains the same as SDU-S's, but an output impedance among SDU-Ps becomes ten times bigger than that among SDU-Ss. Then it is possible for SDU-Ps to operate in parallel connection without additional voltage controller. Voltage phases of each SDU-Ps are adjusted only according to the reactive circulating currents.

Conventional methods [3] [4] provides parallel operation controllers on the outside of the output voltage control loops, and the controllers adjust the characteristics of UPS output impedance. In the proposed method the characteristics are changed in a current minor loop. Because the output impedance among SDU-Ps is high, the controller need not compensate the voltage differences among SDU-Ps, but compensates only the phase differences with a control time constant of several hundred msec. The proposed algorithm impose a light burden on the control processor. Thus, a control processor like TMS320C25 can implements not only the control program for SDU-S but also that for parallel operation. No hardware is added so that a SDU-P control circuit maintains the same cost and reliability.

This paper shows the system configuration, parallel operation control method and experimental results. Experiments show that the circulating current is less than 5% of rated current, and the electric characteristics of UPSs in parallel operation are the same as those when operated stand-alone.

II. System Configuration

Fig. 1 shows a redundant system composed of two SDU-Ps and commercial sources. In this system, usually two SDU-Ps are operating in parallel. Each SDU-P synchronizes its output voltage with the commercial (bypass) voltage and shares fairly the load power. This system has a single redundant UPS. If one of the SDU-Ps fails, it detaches itself from the system and the other one supplies power to the load. If all SDU-Ps have troubles or a over load, the system transfers power supply from SDU-Ps to the bypass sources. Although in this system only two SDU-Ps are shown in parallel, it can have more than two SDU-Ps in parallel.

In the main circuit, the inverter and converter are full-bridge type using IGBTs, and employing PWM control with a switching frequency of 8 kHz. In the control circuit, a DSP: TMS320C25 is used as the control processor. The DSP controls instantaneous waveforms of the inverter and converter, bypass transfer and parallel operation, and detects UPS faults. Main UPS controls are incorporated into the DSP.

There are some signal lines across the SDU-Ps as common signal lines for parallel operation. These lines include the detected output current, the bypass voltage,

0-7803-3823-5/97/$10.00© 1997 IEEE

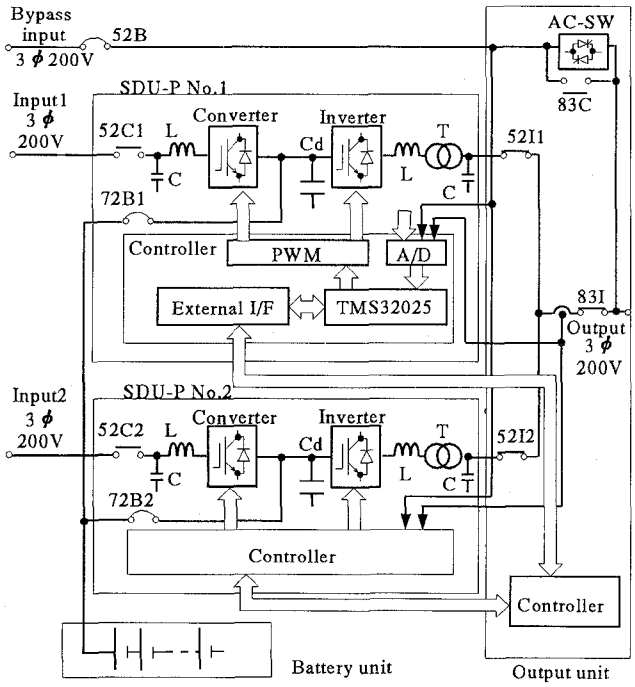

Fig. 1. Configuration of parallel redundant UPS system

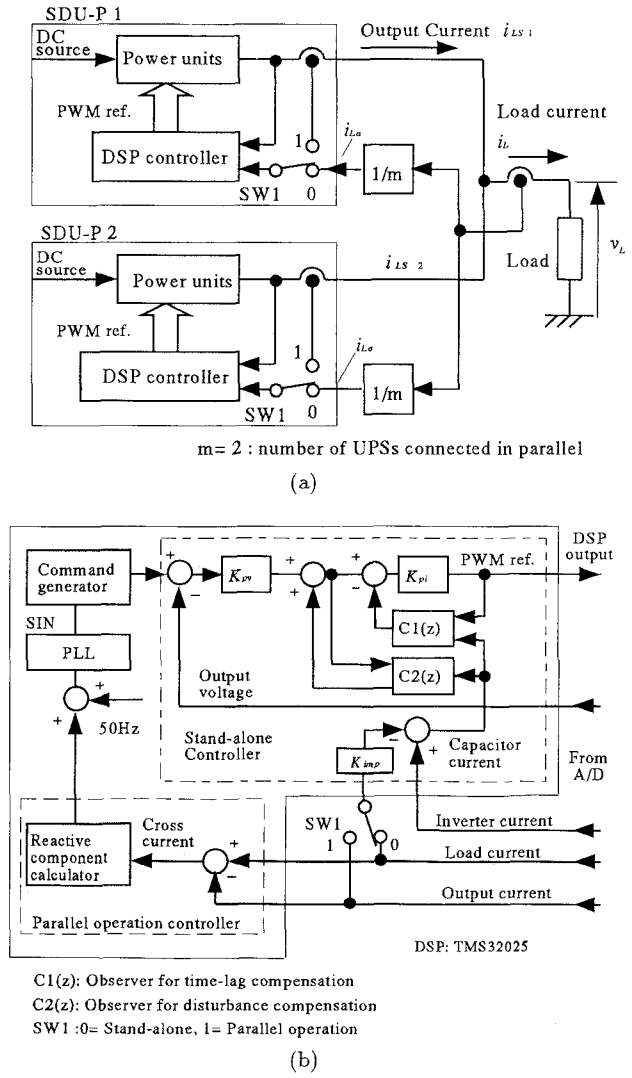

Fig. 2. Output voltage controller of SDU-P (a) Block diagram of inverters connected in parallel (b) Output voltage controller in DSP

and sequence signals. If one of these breaks, SDU-Ps can continue normal operation in steady state. In transient state, the DSP in the broken SDU-P detects the broken line and separates from the system by itself. The other SDU-P supplies power to the load.

III. Principle of Parallel Operation

A. Output voltage controller

Fig. 2 shows the proposed controller for parallel operations, (a) indicates an outline of SDU-Ps connected in parallel. Control of parallel operations needs the common load current i_L. A sensor for the common load current i_L is employed more for parallel operations. In the case of parallel operation, the switch SW1 is at position 0, and the controller feeds back the load current. The SW1 is at position 1 in the case of stand-alone UPS.

In this figure, to clarify the control principle, a load current sensor distributes the sensor signal to each SDU-P. However, in practical use, each SDU-P communicates its output current i_{Ls} using the common signal lines so that the load current sensor as one of the common parts for each SDU-P is not needed. Such common parts decrease the system reliability. Each SDU-P calculates the shared load current $i_{La} = i_L/m$(where m = the number of SDU-P in parallel) using the other SDU-Ps i_{Ls} by hardware [5]. The DSP controller reads the i_{La}.

Figure (b) shows the internal configuration of the DSP controller described in figure (a). The DSP controller contains control algorithms not only for stand-alone operation but also for parallel operation. The stand-alone controller is the same one presented in [1]. Additional blocks for parallel operation are the reactive circulating current controller and the switch SW1 for selecting which currents to be sensed. The circulating current controller detects the reactive component of the circulating current, and regulates the component to be zero through manipulating the phase of sine wave.

B. Relation between UPS output impedance and circulating current

Fig. 3 shows a single-phase generalized equivalent circuit of inverters when two UPSs operate in parallel. The inverter in the circuit is shown as a voltage source with an impedance $Z_{outo\ n}$ (where $n = 1, 2$) connected in series. The circulating current of this circuit $\dot{I}_{cir}$ can be calculated by equation(1)$\sim$ (3) using the phasor vectors.

$$\dot{I}_{cir} = \frac{\dot{V}_{out1} - \dot{V}_{out2}}{Z_{out1} + Z_{out2}} = \frac{V_{m1} - V_{m2}\cos\phi - jV_{m2}\sin\phi}{Z_{out1} + Z_{out2}} \quad (1)$$

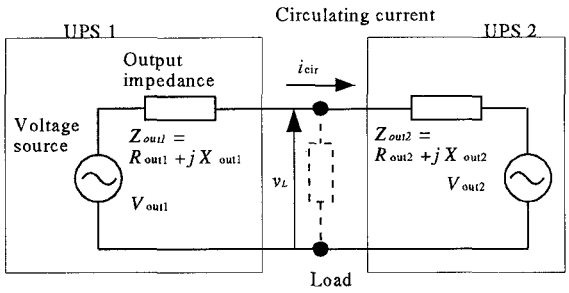

Fig. 3. Generalized equivalent circuit of UPSs connected in parallel

where $\dot{V}_{out1} = V_{m1}\angle 0°$, $\dot{V}_{out2} = V_{m2}\angle \phi°$
In the case that the amplitudes of UPS voltages are different but their phases are same (*i.e.* $\phi = 0°$)

$$\dot{I}_{cirv} = \frac{V_{m1} - V_{m2}}{Z_{out1} + Z_{out2}} \quad (2)$$

On the contrary, if UPS voltages have different phases but same amplitudes (*i.e.* $V_{m1} = V_{m2}$)

$$\dot{I}_{cirp} = \frac{V_{m1}(1 - \cos\phi - j\sin\phi)}{Z_{out1} + Z_{out2}} \quad (3)$$

Components of the circulating current caused by the amplitude and phase differences among UPSs output voltages, active or reactive, are decided by the characteristics of the Z_{outn} being inductive or resistive, and the amplitude of the circulating current depends on the magnitude of the Z_{outn}. The characteristics of the Z_{outn} depend on the control method. It is important to investigate the output impedance of an UPS inverter when UPSs operate in parallel.

C. UPS Output Impedance v.s. Output Current Feedback Gain

In the SDU-S or the SDU-P in the case that SW1 is at position 1, Z_{outn} changes as shown in Fig. 4 as the output current feedback gain K_{imp} changes from 0 to 1. These curved lines are calculated based on the model shown in Fig. 4 of [1]. When K_{imp} is zero, the magnitude of Z_{outn} is 63% and its angle is 180° (resistive). When K_{imp} is one, the magnitude is 6.3% and the angle is 90° (inductive).

Fig. 5 shows a single phase model of the SDU-P inverters when the controller feeds back the load current i_{La} instead of the output current i_{Ls} (SW1 is at position 0 in Fig 2(a)). There are two output impedances, Z_{outo} and Z_{outl}. Z_{outo} is the impedance given by the ratio of the output voltage v_L to the circulating current $i_{cir} = i_{Ls} - i_{La}$. Z_{outl} is the impedance given by the ratio of the v_L to the load current i_{La}. The characteristics of the circulating current depend on the Z_{outo} and UPS output performances are ruled by the Z_{outl}. If Z_{outo} is bigger then the circulating current is smaller, and If Z_{outl} is smaller, the UPS output performances are better.

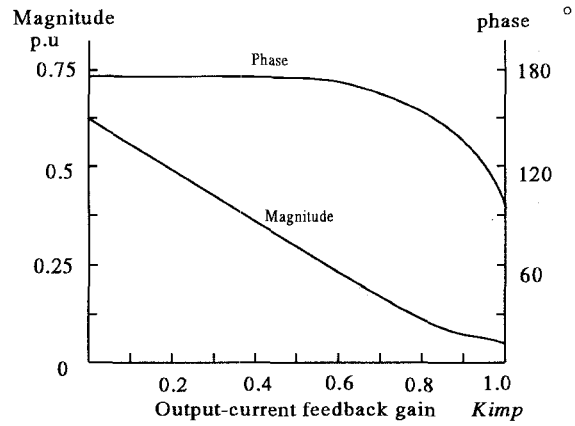

Fig. 4. Output impedance to output current feedback gain K_{imp}

The characteristic of Z_{outl} is different from that of Z_{outo}. Based on Fig. 4, Z_{outo} is 63% because the circulating current is not fed back (same as the case of $K_{imp} = 0$), and $Z_{outl} = 6.3\%$ because of feedback of the load current. Since Z_{outl} is the same for stand-alone or parallel operations (SW1 position = 0 or 1), the UPS output characteristics at parallel operations are not different from those of stand-alone operation. On the other hand, the circulating current flows hard in the case of parallel operations (SW1 position = 0) because the impedance among UPSs Z_{outo} is ten times of Z_{outl}. Z_{outo} is resistive in this case. When there is a small phase difference among UPSs output voltage, the circulating current almost contains reactive component according to equation (3) ($1 - cos\phi \approx 0$).

By calculating the circulating current caused by a voltage difference among UPSs, it is shown that an additional voltage control for parallel operations is not required. Maximum value of the voltage amplitude difference is 1% because the controller can offer output voltage regulation of ±0.5% at stand-alone operation. The circulating current is $\frac{1}{63} = 1.6\%$ with this voltage difference of 1 %. When requirement for load sharing balance among UPSs is ± 5% of the rated current, this circulating current is a sufficient small value for the load balance. Thus additional voltage control for parallel operations is not needed.

Table I indicates a comparison of controlled variables for parallel operation between SDU-P and conventional methods. Output impedance characteristics of SDU-P are different from those of conventional method. Z_{outo} of the SDU-P is resistive while that of conventional is inductive.

IV. Effect of Cable Impedance Among SDU-Ps

The output voltage may have oscillating components due to cable impedances among the SDU-Ps Z_{line} when the SDU-Ps are connected in parallel. Z_{line} is dominated by the inductance L_{line} in the range of UPS control frequency. Resonance among L_{line} , the other

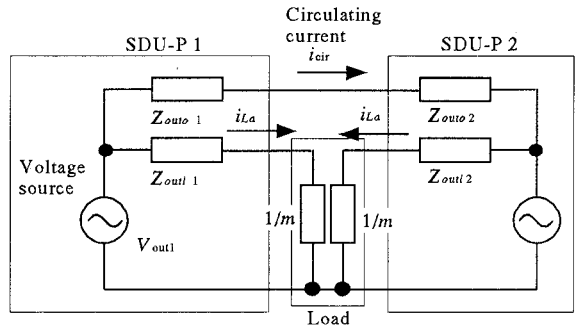

Fig. 5. Equivalent circuit of SDU-Ps connected in parallel in the case that SW1 is at position 0

TABLE I
COMPARISON OF CONTROLLED VARIABLES BETWEEN SDU-P AND CONVENTIONAL METHODS

Compensation for	controlled variables	
	SDU-P	conventional UPS
amplitude difference among UPSs voltage	need not control	reactive component of circulating current
phase difference among UPSs voltage	reactive component of circulating current	active component of circulating current

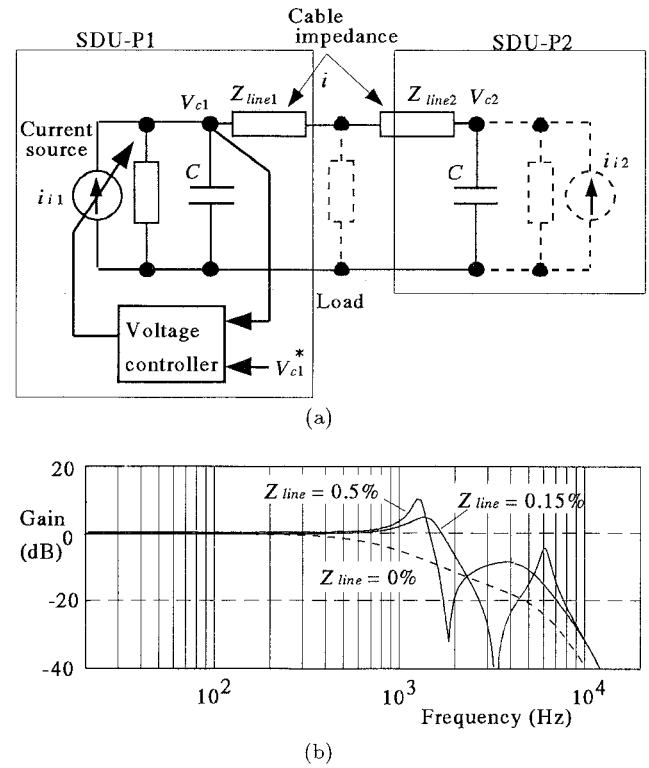

Fig. 6. Effect of cable impedance among SDU-P (a) analysis model (b) frequency characteristics of v_c/v_c^* in (b)

UPS's capacitor C and UPS control system causes this oscillation. To study the effect of L_{line}, it is assumed that L_{line} is 0.15 % as the possible maximum value in practical.

Fig. 6 (a) shows an analysis model. It is assumed that the opposite SDU-P can be modeled as current source with a capacitor C because SDU-P has the current minor loop. This current source can be neglected by the principle of superposition. Its impedance is assumed infinity to simplify the study. In this model, the frequency characteristic of v_c/v_c^* is shown in Fig. 6 (b). The broken line shows the characteristic in the case that Z_{line} is zero. The curves have a resonant point and an anti-resonant point in the case that Z_{line} is not zero. According to these characteristics, as L_{line} increases the oscillation become bigger.

To suppress the oscillation, the gain at the frequency area around the resonant point must be decreased, while maintaining performance of disturbance (UPS output current i_{Ls}) suppression. In this paper, the resonant peak is shaved by increasing the value of C in the L-C filter. Fig. 7 shows the frequency characteristics of v_c/v_c^* (command following performance) and those of v_c/i_{Ls} (disturbance suppression performance) when L_{line} is zero. As the C becomes larger, gain at the frequency area around the resonant point decreases as shown in Fig. 7 (a), while maintaining the performance of disturbance suppression around the fundamental frequency as shown in Fig. 7 (b). Fig. 8 shows the frequency characteristics in the case that C is increased by a factor of 1.5 and L_{line} is 0.15%. The gain curve has little gain peak. When SDU-Ps with this condition are connected in parallel, the output voltage dose not contain oscillating components.

V. ELECTRICAL CHARACTERISTICS

Table II shows the electrical characteristics of SDU-P. The characteristics are the same as those of stand-alone UPS (SDU-S).

Waveforms in steady-state and transient conditions are given in Fig. 9 ~ fig. 12

Fig. 9 represents the output voltage and current waveforms at 100 % non-linear load. THD (Total Harmonic Distortion) of the output voltage is 1.4%.

Fig. 10 shows the output voltage waveforms on sudden change of load, 0%↔100% when three UPSs operate in parallel. A transient voltage regulation is within ±5%(settling time is less than 50msec). The load sharing unbalance is less than ±5%.

Fig. 11 represents the output voltage waveforms in the case that No.3 SDU-P is connected into the system where No.1 and 2 SDU-Ps are supplying the load. The output voltage has no variation and No. 3 SDU-P shares equally the load with the others immediately.

Fig. 12 indicates the output voltage waveforms when one of the SDU-Ps failed. The fault SDU-P is cut off from the system within 50msec, transient voltage regulation is less than ± 5 %.

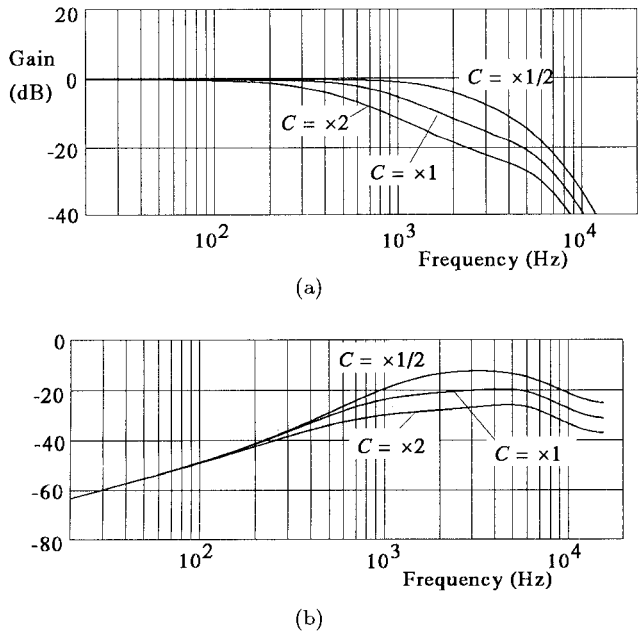

Fig. 7. Frequency characteristics to Capacitance C in $L-C$ filter where $L_{line} = 0\%$ (a) v_c/v_c^* (b) v_c/i_L

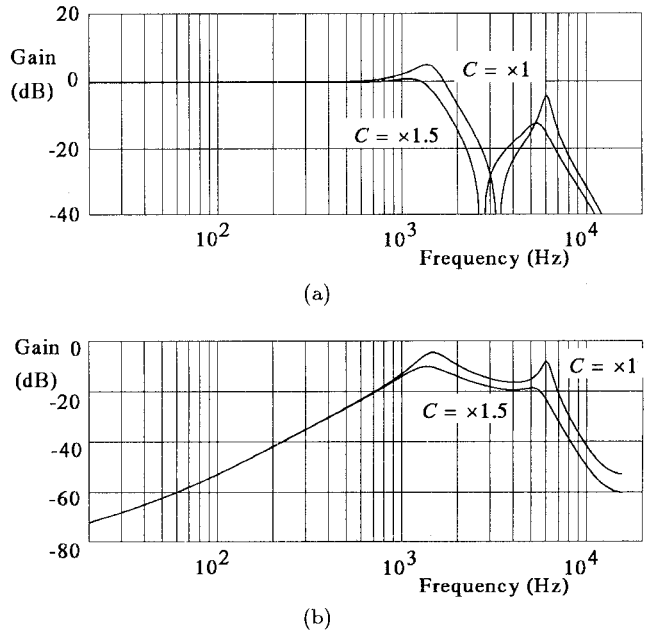

Fig. 8. Compensation for voltage oscillation by increase of capacitance C in $L-C$ filter where $L_{line} = 0.15\%$ (a) v_c/v_c^* (b) v_c/i_L

VI. Conclusion

A control method without a voltage controller for parallel operation of UPSs has been presented. Each SDU-P shares the load power properly, stably and immediately in the case of throwing in parallel or fault detaching operations. The Characteristics of the output voltage THD and the output variation in the case of sudden 100% load change are the same as those of SDU-S. In the case that the cable impedances can not be neglected, the output voltage contains oscillating components. This oscillation is compensated successfully by increasing the capacitance of the L-C filter. The authors are going to consider a compensation method for the oscillation without the increase of C, and to study about methods for decreasing the number of the common signal lines.

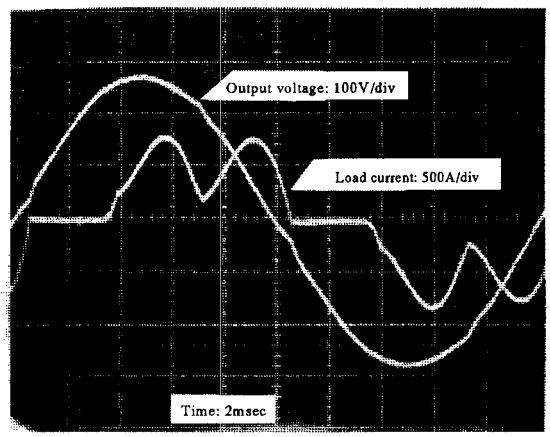

Fig. 9. Output voltage and current waveform (three UPSs in parallel)

Acknowledgments

The authors would like to acknowledge Dr. G. Su, Mr. H. Mikada and Mr. S. Isiguma of SANKEN electric co., ltd.

References

[1] Y. Ito, M. Sgawara, S. Kawauchi, "Robust control of UPS with a Single Microprocessor", in *IPEC '95* Conf. Rec. Vol.2 pp.973

[2] Y. Ito, S. Kawauchi, "Microprocessor-Based Robust Digital Control for UPS with Three-Phase PWM Inverter", in *IEEE Trans. on Power Electron.*, vol. 10. No.2 pp.196-204, March 1995.

[3] Yasuda, Kawakami et al., "Parallel Redundant UPS using IGBT instantaneous control PWM inverter",1991 National Convention Rec. of JIEE, 506 (Japanese)

[4] Yamamoto, Kawai, et al., "Large Capacity Parallel Redundant Using IGBT and Current Minor loop",1991 IAS National Convention Rec. of JIEE 108 (Japanese)

[5] Kawabara, Higashino, "Parallel Operation of Voltage Source Inverters", in *IEEE Trans. on Industrial Applications*, vol. 24, No. 2. pp.281-287, 1988

TABLE II

STANDARD SPECIFICATIONS OF SDU-P IN PARALLEL OPERATION

Input voltage	200V/ 210V ±10%
Input voltage frequency	50Hz/60Hz
Input power factor	1.0
Input current THD	5%
Input capacity	30k /50k /75k /100k /150k /200kVA
Output voltage	200V/ 210V
Output voltage frequency	50Hz/60Hz
Output voltage regulation	
Balanced load	± 1%
Single-phase load	± 1%
Output voltage THD	
linear load	2%
Non-linear load	5%
permitted crest factor	2.5%
Voltage deviation and recovery time for 100% load step change	± 5%, 20msec
Size and weight without batteries	W=600 D=750 H=1,600 600 kg (single 50kVA SDU-P)

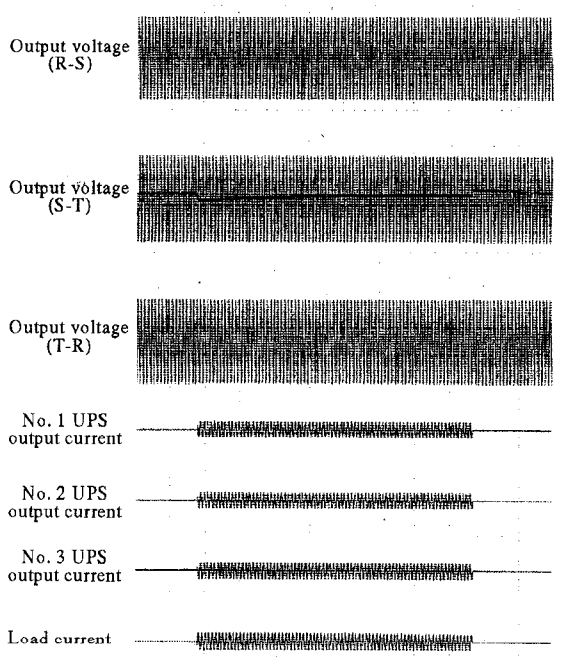

Fig. 10. Dynamic load regulation (0 ↔ 100% load sudden changes, three SDU-Ps in parallel)

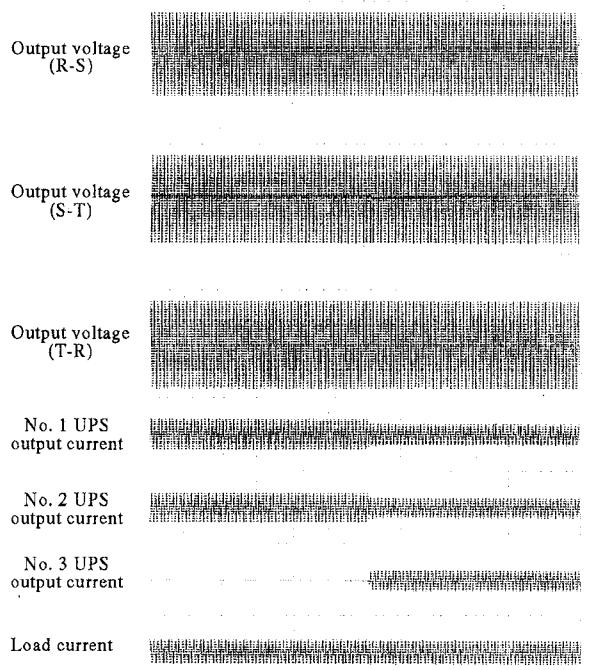

Fig. 11. Waveforms in the case of throwing No.3 SDU-P in parallel (100% load, two SDU-Ps in parallel)

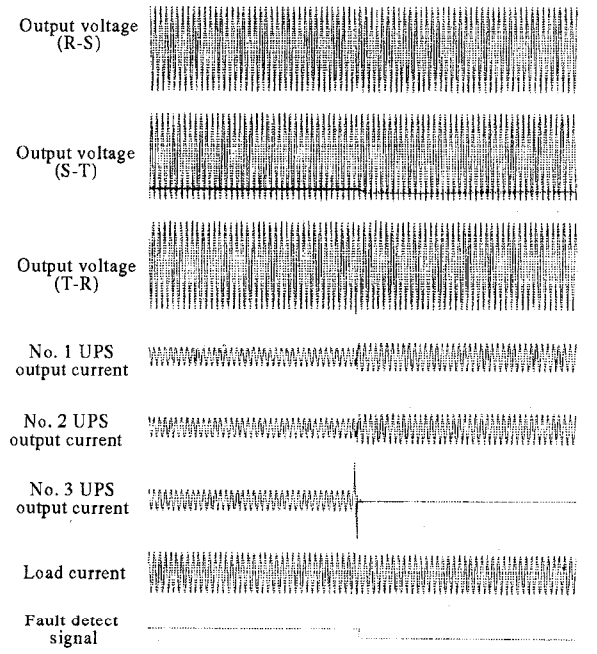

Fig. 12. Waveforms in the case that one faulted and separated from the system (100% load, three SDU-Ps in parallel)

Compensation Method of AC-to-DC Converter Characteristics Under Unbalanced Three-Phase AC side Voltage

Yoshiaki Okui
Sanyo Denki Co., Ltd.
1-1-7 Midorigaoka, Ueda 386, Japan
Fax: +81-268-24-7449, Phone: +81-268-23-8129
E-mail: okui@po.cnet-na.or.jp

Masayuki Mouri, Tsutomu Mizuno, and Hajime Yamada
Shinshu University
500 Wakasato, Nagano 380, JAPAN
Fax: +81-26-223-7754, Phone: +81-26-226-4101
E-mail: Yamadah@gipwc.shinshu-u.ac.jp

Abstract **- The assumption of characteristics analysis of a three-phase AC-to-DC converter is based on a balanced three-phase AC side voltage. When the AC side voltage is unbalanced, the characteristics of the AC-to-DC converter become worse (the AC side currents are distorted and the DC side voltage includes low-order frequency components). Accordingly, compensation method of the AC-to-DC converter characteristics under unbalanced three-phase AC side voltage, is proposed by authors. The compensation method by feed-forward control is investigated by using a new topology AC-to-DC converter in this paper. In both simulated results and experimental results in a laboratory prototype system having the output power of 10kW, it is clear that the proposed compensation method maintains the AC-to-DC converter characteristics whereas the three-phase AC side voltage is unbalanced. However, when a value of an unbalanced rate, *k'*, of each effective value to a three-phase average value is lower than a value of modulation factor of a basic sinusoidal reference signal, both the AC side current distortion and the DC side voltage ripple increase due to over-modulation.**

I . INTRODUCTION

In recent years, serious problems in electric power system have been caused by a harmonic current. It is countermeasure of the problems that an input current of an AC-to-DC converter is controlled both sinusoidal waveform and unity power factor. Such AC-to-DC converters have been much reported [1]. However, the assumption of characteristics analysis of the three-phase AC-to-DC converter is based on a balanced three-phase AC side voltage [2]. If three-phase AC side voltage is unbalanced, characteristics of the three-phase AC-to-DC converter become worse (the AC side currents are distorted and the DC side voltage includes low-order frequency components). Therefore, the compensation method of the AC-to-DC converter characteristics under unbalanced three-phase AC side voltage is investigated by a new topology three-phase AC-to-DC converter. This paper describes the following points:

1) circuit configuration and principle operation of the new topology three-phase AC-to-DC converter, and expression of the AC side current and the DC side voltage (These are presented in section II),

2) proposed compensation method of the AC-to-DC converter characteristics under unbalanced three-phase AC side voltage, and the simulated results of the AC side current distortion and the DC side voltage ripple in the case of using the compensation method (There are discussed in section III), and

3) the experimental results of the AC side current distortion and the DC side voltage ripple in the case of using the compensation method by a laboratory prototype system having the output power of 10kW (There are shown in section IV).

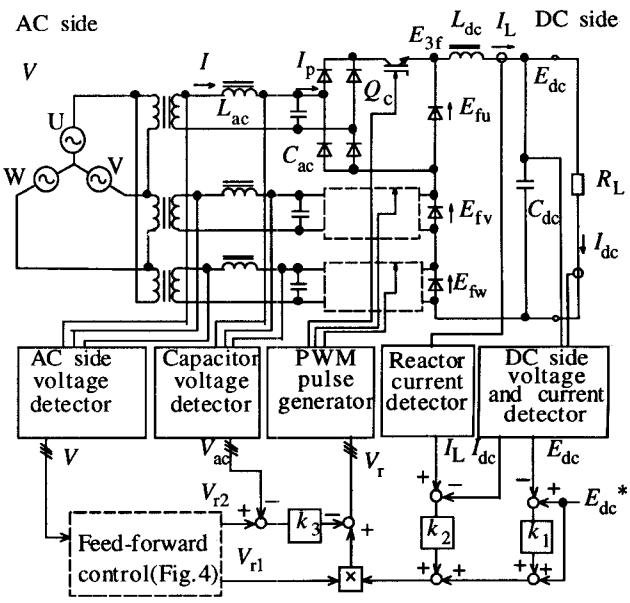

Fig.1 Main circuit and control block diagram of a three- phase high power factor AC-to-DC converter with multiple-connected single phase buck-type choppers.

II . CIRCUIT CONFIGURATION AND PRINCIPLE OPERATION

A. Circuit configuration

Fig.1 shows main circuit and control block diagram of the new topology three-phase high power factor AC-to-DC converter with multiple-connected single-phase buck-type choppers [3]. Each phase of the AC side voltage is isolated by a transformer, and each AC side current, *I*, is controlled sinusoidal waveform by the buck-type chopper using PWM control. The outputs of the buck-type choppers are connected to a DC side *LC* filter (L_{dc},C_{dc}) in a series circuit. The DC side voltage, E_{dc} , is obtained by passing the DC side filter with the composite voltage, E_{3f} , of the output voltage of each chopper. Configuration of the control circuit is simple due to independent control. A number of semiconductor switches of the converter are only three. Therefore, the converter is suited for a large power type converter due to high utilization of switches.

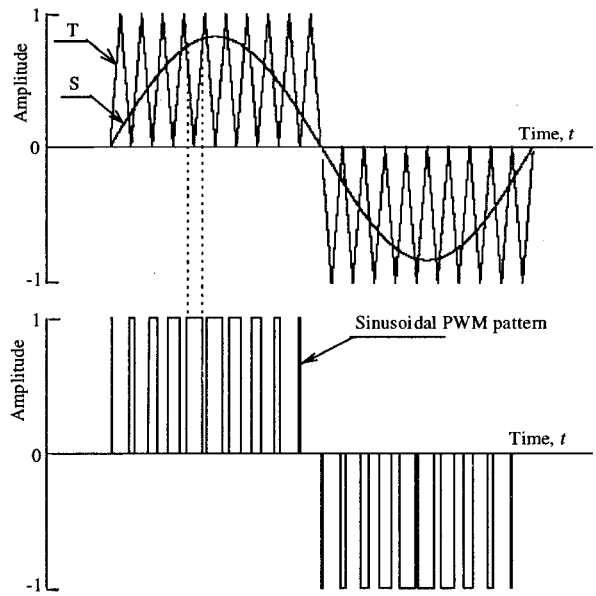

Fig.2 Example of a sinusoidal PWM pattern.

B. Expression of AC Side current

Generally, a sinusoidal PWM pattern is obtained by comparing a sinusoidal waveform, S, with a high frequency chopping waveform, T, as shown in Fig.2. A sinusoidal PWM function, F_p, included fundamental frequency as main component, is defined as following equation [4]:

$$F_P = F_f + F_h, \tag{1}$$

$$F_f = M \sin \omega t, \tag{2}$$

$$F_h = \frac{2}{\pi}\left[\sum_{n=1}^{\infty} \frac{J_0^{(rM\pi/2)}}{n} \sin\left(\frac{n\pi}{2}\right) \sin n\omega_c t + \sum_{n=1}^{\infty}\sum_{m=\pm 1}^{\infty} \frac{J_m\left(\frac{n\pi M}{2}\right)}{n} \sin\left\{\frac{(n+m)\pi}{2}\right\} \sin(n\omega_c t + m\omega t)\right], \tag{3}$$

where F_f : PWM fundamental function, F_h : PWM harmonic function, M : modulation factor, ω : source angular frequency, ω_c : carrier frequency (frequency of chopping waveform,T, in Fig.2), n, m : a natural number (n, m =1,2,3,・・・), J_n : Bessel functions of the first kind of order n .

In Fig.1, if the switches, Q_c, are controlled by the mode of sinusoidal PWM function, F_p, the currents, I_p , become sinusoidal PWM pattern. Amplitudes of the currents, I_p , are determined by the reactor current, I_L , of the reactor, L_{dc} , in the DC side. The currents, I_p , are divided into the fundamental component currents related the PWM fundamental function, F_f , and high frequency component currents related the PWM harmonic function, F_h. Reactance in the electric system and the reactor, L_{ac}, of the AC side LC filter restrain the high frequency components current and the fundamental component currents related the F_f flow from the electric system. The high frequency components currents related the F_h flow from the AC side capacitor, C_{ac} , which have low impedance to high frequency. The fundamental component currents related the F_f are the AC side currents of the converter and the AC side current is given by the follow:

$$I \doteqdot I_L F_f = M I_L \sin \omega t. \tag{4}$$

If the reactor current, I_L , is constant, the AC side current, I, is sinusoidal waveform. When each phase of the AC side current is controlled with the same phase of the each AC side voltage, T.P.F. (Total Power Factor) is nearly 1.0. Amplitudes of the AC side currents are possible to change due to changing the modulation factor, M. Therefore, the converter has drooping characteristic for an over-current in the DC side.

C. Frequency components of input voltage to the DC side LC filter

Each rectified AC side voltage is controlled by switch, Q_c , of the buck-type chopper. The switches are controlled by the mode of sinusoidal PWM function, F_p. Therefore, the switching currents become absolute value of the I_p. The other hand, the output voltage of each buck-type chopper is given by following equation:

$$V = \sqrt{2} E_{ac} \sin \omega t, \tag{5}$$

$$E_f = |V| \times (F_f + F_h) = \sqrt{2} E_{ac} M \sin^2 \omega t + |V| F_h = \frac{\sqrt{2} E_{ac} M (1 - \cos 2\omega t)}{2} + |V| F_h, \tag{6}$$

where E_{ac} is effective values of the AC side voltage.

On above the equation, the output voltage of each buck-type chopper includes two times frequency component to fundamental frequency. The following equation is given by connecting each output voltage of the buck-type chopper in a series circuit:

$$E_{3f} = E_{fu} + E_{fv} + E_{fw} = \frac{\sqrt{2}}{2}\left\{M_u E_{acu} + M_v E_{acv} + M_w E_{acw} - M_u E_{acu} \cos 2\omega t - M_v E_{acv} \cos 2\left(\omega t + \frac{2\pi}{3}\right) - M_w E_{acw} \cos 2\left(\omega t + \frac{4\pi}{3}\right)\right\} + \left\{|V_u| F_{hu} + |V_v| F_{hv} + |V_w| F_{hw}\right\}, \tag{7}$$

where suffix, u,v,w, correspond to U,V,W phase.

If the three-phase AC side voltage is balanced ($E_{ac} = E_{acu} = E_{acv} = E_{acw}$), effective value of each the AC side current is the same. Therefore, each the modulation factor, M, shown in (4) is the same ($M=M_u=M_v=M_w$). Then, the composite voltage, E_{3f} , is given by the following equation:

$$E_{3f} = \frac{3ME_{ac}}{\sqrt{2}} + \left\{|V_u| F_{hu} + |V_v| F_{hv} + |V_w| F_{hw}\right\}. \tag{8}$$

The composite voltage, E_{3f} , includes DC component of the first part and high frequency component related switching frequency of the second part. Fig.3 shows example waveforms of the composite voltage, E_{3f}, (the carrier frequency is comparatively low). The composite voltage becomes stairs-waveform due to connecting the output of buck-type

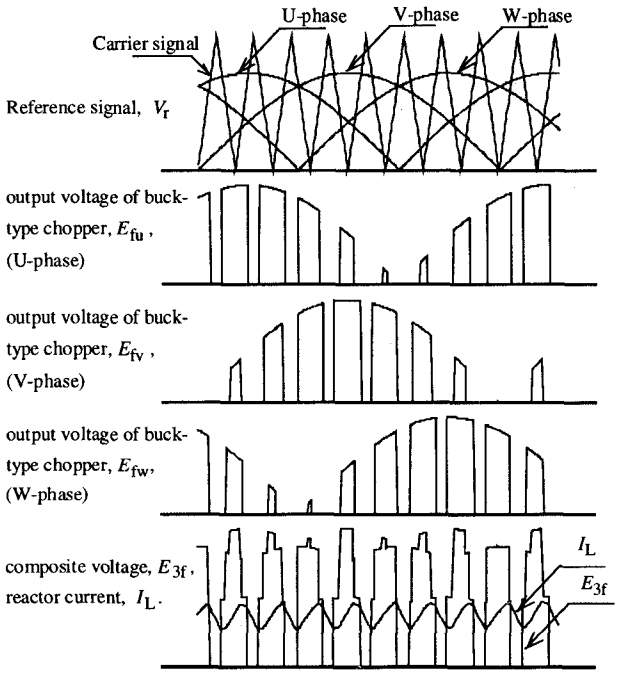

Fig.3 Example waveform of composite voltage, E_{3f}.

choppers in a series circuit. The composite voltage, E_{3f}, which does not include low-order frequency component, passes through the DC side *LC* filter and the high frequency component related the switching frequency is suppressed. Furthermore, the reactor current, I_L, is DC current which does not include low-order frequency component. Therefore, the AC side currents become sinusoidal waveform from (4).

III. Compensation Method under Unbalanced AC Side Voltage and Simulated Results

A. Compensation by feed-forward control

In the case of balanced AC side voltage, the modulation factor, M, of each phase is the same ($M=M_u=M_v=M_w$). However, if the AC side voltage is unbalanced ($E_{ac} \neq E_{acu} \neq E_{acv} \neq E_{acw}$), the terms of cos2ω*t* in (7) can not be omitted. Therefore, the composite voltage, E_{3f}, includes low-order frequency components. Accordingly, in the case of unbalanced AC side voltage, each the modulation factor, $M_{u,v,w}$, changes obeying each effective value of the AC side voltage as follow :

$$M_u \cdot E_{acu} = M_v \cdot E_{acv} = M_w \cdot E_{acw} = M \cdot \overline{E_{ac}} . \quad (9)$$

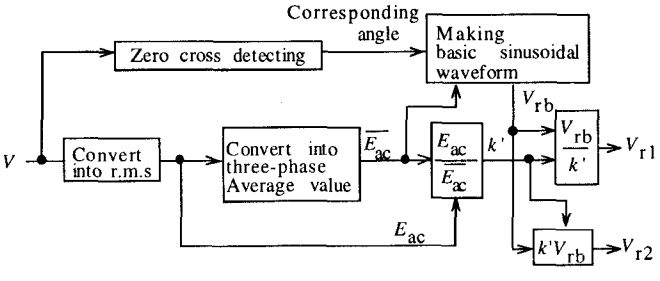

Fig.4 Proposed compensation block diagram with feed-forward control.

Even if the AC side voltage is unbalanced, the terms of cos2ω*t* in (7) can be omitted and the composite voltage, E_{3f}, shown in (7) does not include low-order frequency components. Each modulation factor, $M_{u,v,w}$, is corrected by using an unbalanced rate, k',of each effective value, E_{ac}, to the three-phase average value, $\overline{E_{ac}}$, as follow:

$$\frac{M}{k'_u} k'_u \overline{E_{ac}} = \frac{M}{k'_v} k'_v \overline{E_{ac}} = \frac{M}{k'_w} k'_w \overline{E_{ac}} = M \overline{E_{ac}} , \quad (10)$$

$$k'_u = \frac{E_{acu}}{\overline{E_{ac}}}, \; k'_v = \frac{E_{acv}}{\overline{E_{ac}}}, \; k'_w = \frac{E_{acw}}{\overline{E_{ac}}} , \quad (11)$$

$$M_u = \frac{M}{k'_u}, \; M_v = \frac{M}{k'_v}, \; M_w = \frac{M}{k'_w} . \quad (12)$$

Fig.4 shows proposed compensation block diagram with feed-forward control (FF control) without current sensor. Three-phase average value, $\overline{E_{ac}}$, is calculated by using each effective value which is obtained by detecting the AC side voltage. Moreover, the unbalanced rate, k', is calculated. The signal, V_{r1}, corrected each the modulation factor becomes the reference signals, V_r, and the signal, V_{r2}, becomes basic signals of the AC side state-feed-back control in Fig.1.

B. Low frequency component in the reactor current

The compensation method by the FF control is confirmed by simulation using the Euler's method. Switching devices are assumed to be ideal devices. The circuit condition is shown in Table I. Fig.5 shows the spectrum analysis of the reactor current, I_L, on the condition of unbalanced AC side voltage. The unbalanced condition is as decreasing the W-phase voltage only ($V_u=V_v=200V$, $V_w=140V$). The harmonic current, I_h, with the FF control is restrained compared with the harmonic current without compensation. Main low-order frequencies by decreasing W-phase AC side voltage, are 120Hz and 240Hz. Fig.6 shows the relationship between an unbalanced factor, k, and the harmonic current, I_h, of main low-order frequency components (120 Hz, 240 Hz) in the reactor current, I_L. The unbalanced factor, k, is given by the following equation [5]:

$$k = E_2 / E_1 , \quad (13)$$

where E_1 is a positive sequence component and E_2 is a negative sequence component.

The simulated values with the FF control is compared with the simulated values without compensation. Unbalanced condition is as decreasing W-phase voltage. Main low-order frequency components with the FF control are lower than the components without compensation. The FF control suppresses low-order frequencies at the unbalanced factor, k, within about 15 %. When the DC side voltage is set at 250[V] on the condition of balanced AC side voltage, the modulation factor, M, is 0.58 from the DC component of (8). Moreover, when the unbalanced factor, k, is 16.3%, the W-phase unbalanced rate, k_w', becomes 0.58. The corrected modulation factor is determined by the unbalanced rate, k', and the modulation factor, M, of the basic reference signal, V_{rb}, as shown in Fig.4. If the value of the k' is lower than value of the

Table I
SPECIFICATION OF CIRCUIT CONDITION

Item	Symbol	Value (unit)
Output power	P_o	10 (kW)
AC side voltage (U, V phase)	V_u, V_v	208 (V)
DC side voltage	E_{dc}	250 (V)
Modulation factor	M	0.58
AC side capasitor	C_{ac}	10 (μF)
DC side reactor	L_{dc}	1 (mH)
DC side capasitor	C_{dc}	10 (mF)
Carrier frequency	f_c	15 (kHz)

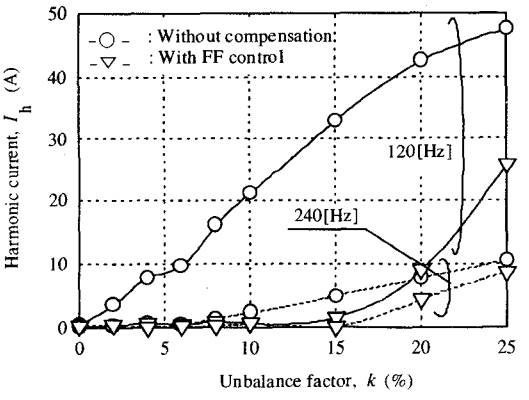

Fig.6 Relationship between harmonic current in the reactor current, I_L, and unbalanced factor, k (simulation, full-load, E_{dc}=250V, k_1=22, k_2=3, k_3=0.25).

modulation factor, M, of the V_{rb} , the corrected reference signal, V_{rl}, becomes over-modulation. Therefore, the reactor current, I_L , includes low-order frequency components at the unbalanced factor, k, above about 15 % due to over-modulation.

C. Harmonic component in the AC side current

Fig.7 shows the relationship between T.H.D. (Total Harmonic Distortion) of the AC side current and the unbalanced factor, k. The simulated values with the FF control is compared with the simulated values without compensation. The FF control suppresses the AC side current distortion at the unbalanced factor within about 15 %. The T.H.D. of the AC side current with the FF control rapidly increase at the unbalanced factor above about 15 % due to over-modulation. Each the AC side voltage at the unbalanced rate, k', within 0.9 is abnormal voltage for the converter in practice. If the unbalanced rate, k', is within 0.9, control of the converter is stopped. Therefore, the maximum DC side voltage which is controlled by the FF control for the unbalanced three-phase AC side voltage is 382V from the DC component of (8).

IV. MEASUREMENT RESULTS OF THE COMPENSATION METHOD

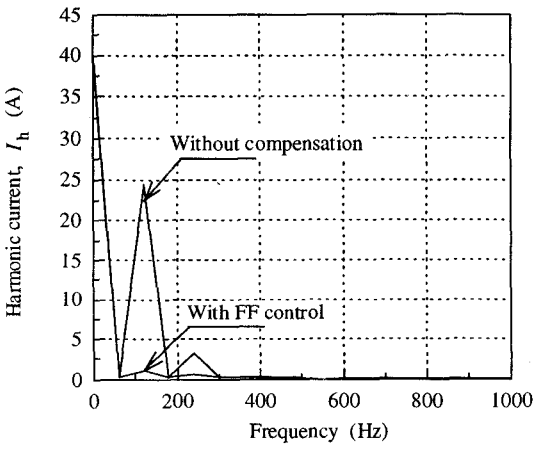

Fig.5 Spectrum analysis of the reactor current , I_L (simulation).

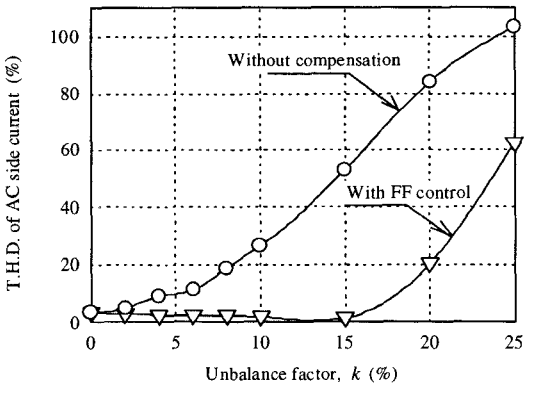

Fig.7 Relationship between T.H.D. of the AC side current and unbalanced factor, k (simulation, full-load, E_{dc}=250V, k_1=22, k_2=3, k_3=0.25).

The FF control is confirmed by a laboratory prototype system having the output power of 10 kW. The measurement condition is the same to the simulation condition as shown in Table I . Fig.8 shows circuit configuration in order to obtain the unbalanced AC side voltage. Each phase of the AC side voltage is isolated by the transformer and each phase voltage in the secondary winding is independence. Therefore, unbalanced condition is obtained by composing an induction voltage regulator (I.V.R) in the W-phase, and the W-phase voltage decreases at desired unbalanced voltage.

Fig.9 and Fig.10 show each waveform without the compensation and with the FF control, respectively. The unbalanced factor is about 10%. The AC side currents in Fig.9(b) are distorted due to the unbalanced AC side voltage as shown in Fig9(a). However, nothing but W-phase voltage decreases

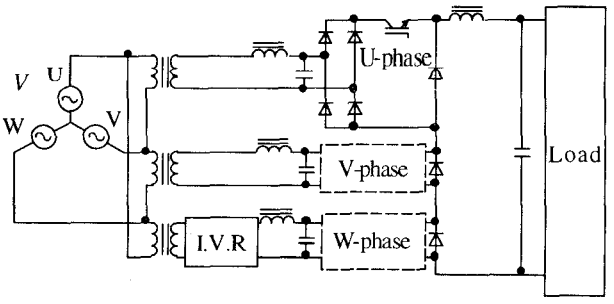

Fig.8 Scheme of the experimental equipment in order to obtain unbalanced AC side voltage.

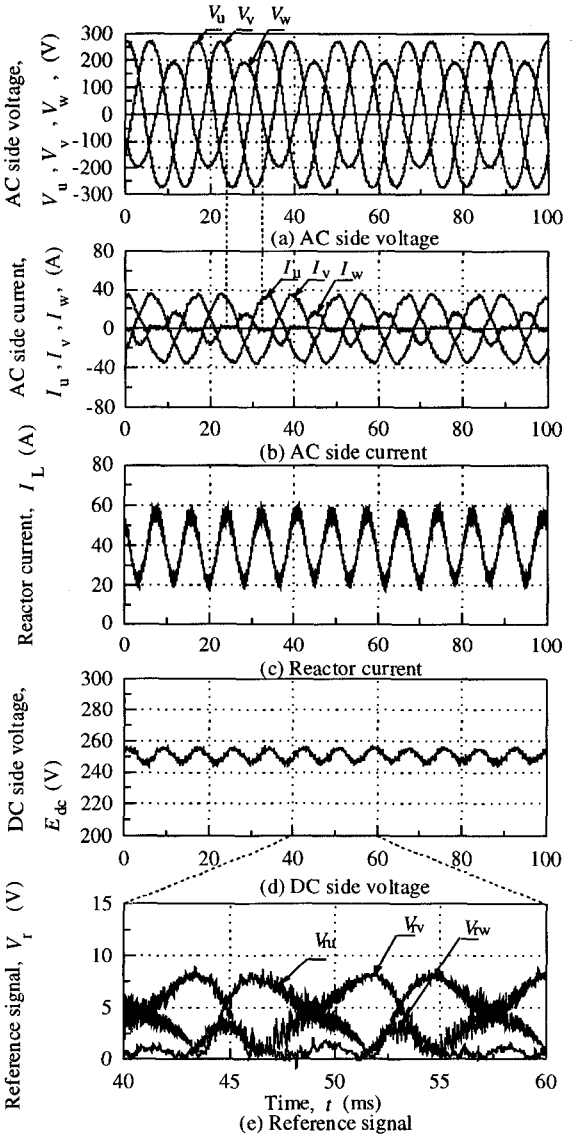

Fig.9 Each waveforms without the FF control in the case of unbalanced factor, k =10% (measured values).

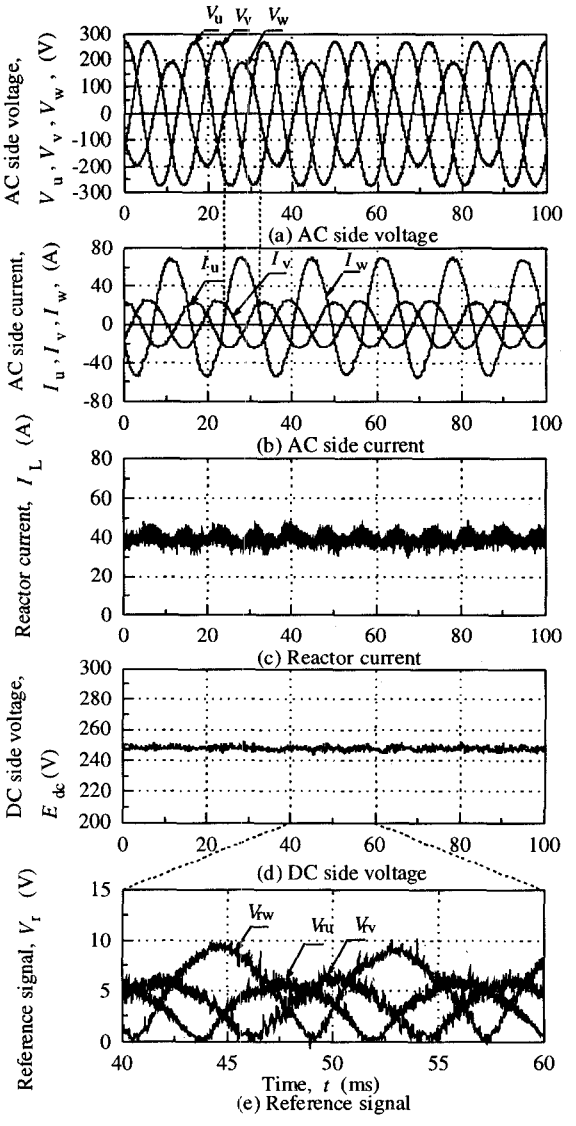

Fig.10 Each waveforms with the FF control in the case of unbalanced factor, k =10% (measured values).

(V_w=140V), each the AC side current with the FF control becomes sinusoidal waveform and obtains unity power factor as shown in Fig.10(b). From Fig.9(c), the reactor current ,I_L, in the DC side LC filter (L_{dc}, C_{dc}) includes low-order frequency components and high frequency component related switching frequency. But, the reactor current, I_L, with the FF control does not includes low-order frequency component as shown in Fig.10(c). Moreover, the DC side voltage with the FF control does not include low-order frequency component as shown in Fig.10(d) compared with Fig9(d).

Fig.11 shows each waveform with the FF control on the condition of the unbalanced factor, k=20% (V_w=100V). The reference signal of Fig.10(e) does not become over-modulation, but the reference signal in Fig.11(e) becomes over-modulation due to setting the peak of the carrier signal at 10V. Therefore, W-phase AC side current shown in Fig.11(b) is distorted at nearby peak. Furthermore, the reactor current, I_L , shown in Fig.11(c) includes low-order frequency components (main component is 120Hz) and the DC side voltage shown in Fig.11(d) also includes low-frequency components.

Fig.12 shows relationship between the harmonic current in the reactor current, I_L, and the unbalanced factor, k. The measured values are compared with the simulated values which are redrawn with the simulated values in Fig.6. Both measured values of 120Hz and 240Hz components agree with the simulated values. Fig.13 shows relationship between the T.H.D. of the AC side current and the unbalanced factor, k. The measured values are also compared with the simulated values which are redrawn with the simulated values in Fig.7. The measured values of U, V-phase and W-phase current distortion agree with simulated values.

It becomes clear by both the simulation and the experiment that both AC and DC side characteristics of the converter using the proposed FF control maintain, whereas the AC side three-phase voltage is unbalanced. However, in the over-modulation range, both the AC and DC side characteristics of the converter become worse. When the value of the un-

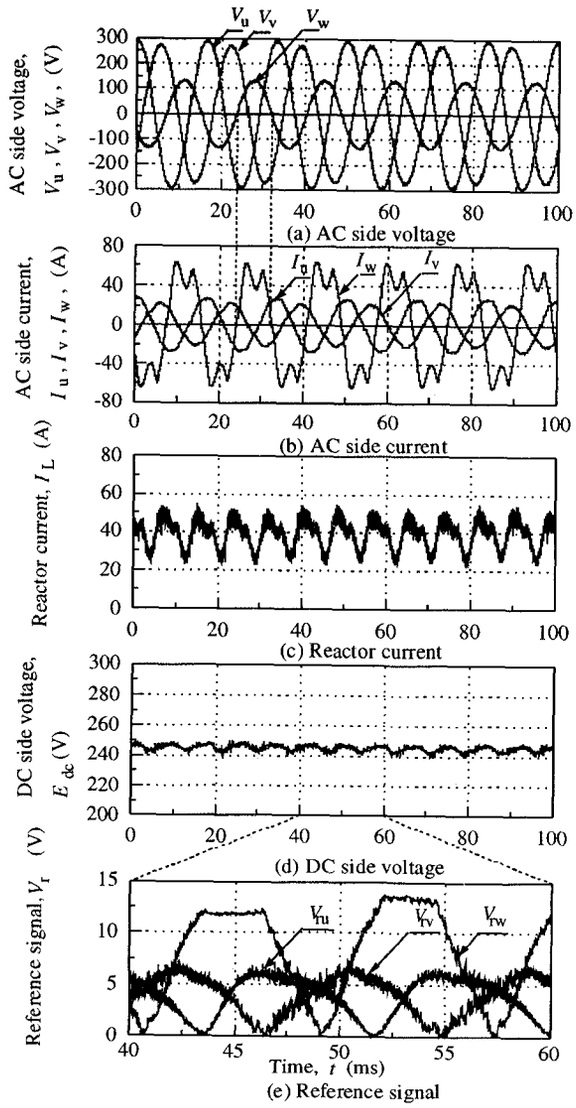

Fig.11 Each waveforms with the FF control in the case of unbalanced factor, k =20% (measured values).

balanced rate, k', is lower than the value of the modulation factor, M, of the basic reference signal, V_{rb}, the corrected reference signal,V_r, become the over-modulation.

Furthermore, it is already known that if third-harmonic component is injected into the reference signal, controllable range can be expand to 1.17 times [6]. If the third-harmonic injection method is used with the FF control, compensable range for the unbalanced AC side voltage can be expand.

V. Conclusion

The compensation method of AC-to-DC converter characteristics under unbalanced AC side three-phase voltage was investigated by using the three-phase high power factor AC-to-DC converter with multiple-connected single-phase buck-type choppers. The following points were clarified :

1) proposed compensation method by the feed-forward control (FF control) without current sensor for unbalanced three-phase AC side voltage was investigated,

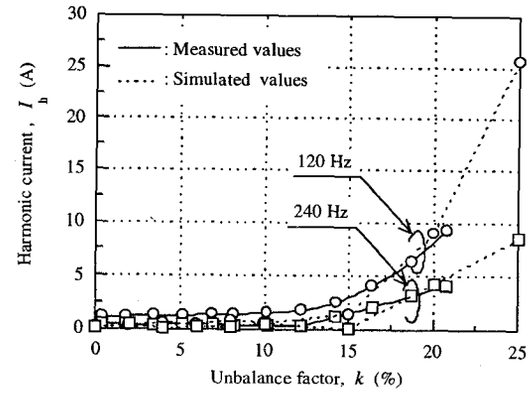

Fig.12 Relationship between harmonic current in the reactor current, I_L, and the unbalanced factor, k (measured values, full-load, E_{dc}=250V)

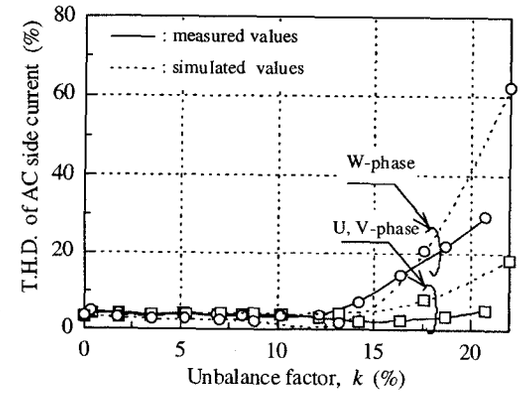

Fig.13 Relationship between T.H.D. of the AC side current and the unbalanced factor, k (measured values, full-load, E_{dc}=250V).

2) in the case of using the FF control, when the value of the unbalanced rate, k', of each effective value, E_{ac} , to the three-phase average value, $\overline{E_{ac}}$, is lower than the value of modulation factor, M, of basic sinusoidal signal, V_{rb}, the corrected reference signal,V_r , was over-modulation ($M_{u,v,w} > 1$),

3) the simulated values agree with the measured values in the laboratory prototype system having the output power of 10kW.

In results, both the low-order frequency components in the reactor current and T.H.D. of the AC side currents with the FF control were suppressed at each the modulation factor, $M_{u,v,w}$, of the corrected reference signal, V_r , within 1.0, whereas the AC side voltage was unbalanced.

References

[1] Akiteru Ueda, Shigeta Ueda, Mitsuyuki Hombu, "Control Method and Characteristics of Current Source GTO Converter with Sinusoidal Input Current ", IEEJ Tras. on Ind, vol. 107-D, No.11, 1987.

[2] Sakutaro Nonaka, Xinmin Jin, "PWM Control Method and Steady-state Characteristics of Novel Current Output Type GTO Converter", IEEJ Tras. on Ind, vol. 109-D, No.2, 1989.

[3] Yoshihiro Sekino, Yoshiaki Okui ,"New unity power factor three-phase converter", IEEJ, SPC94-31, pp.39-46, 1994.

[4] The Institute of Electrical Engineers of Japan, "Basic of Power Electronics", Ohm publication, pp.163-167, 1993.

[5] IEEE , "The New Standard Dictionary of Electrical and Electronics Terms", fifth edition newly revised and expanded, p.1431, IEEE std 100-1992.

[6] M.A. Boost, P.D.Ziogas,"State-of-the-art carrier PWM techniques : a carrier evaluation", IEEE Tras. on Ind. Applic. vol 2, pp.271-280, 1988.

Digital Robust Speed Servo System with Complete Avoidance of Output Saturation Effect

Kiyoshi Ohishi and Tomonori Mashimo
Nagaoka University of Technology
1603-1 Kamitomioka-cho, Nagaoka-city,
NIIGATA, 940-21, Japan
Fax:+81-258-47-9500, Phone:+81-258-47-9525
E-mail:ohishi@vos.nagaokaut.ac.jp

Abstract—**In order to prevent a robust speed servo system from having the saturation effect of controller output, this paper proposes a new anti-windup algorithm for a robust high-order speed controller connected to PI current controller in series. Using the proposed algorithm, a digital speed servo system completely avoids having the effect of output saturation caused by the limitation of motor voltage and motor current. The experimental results show that the proposed digital speed servo system has no output saturation effect caused by the limitation of motor voltage and motor current. The proposed system well keeps the desired speed response for a fast and large speed reference on condition of full load torque.**

I. Introduction

Generally, servo motor is usually driven by the robust speed controller connected to PI current controller in series, and it has an integral element in order to zero a steady output error. A speed controller of servo motor is important for performance improvement of industrial servo systems. For this purpose, the robust servo system based on $\mathcal{H}_\infty$ control theory or two-degrees-of-freedom control design method has been already realized[1][2][3]. The reported servo system well regulate a motor speed robustly, but it often become a high-order system.

Servo motor always has the limit values of motor current and motor voltage. When a speed servo system does not consider these limit values, it often has the windup phenomena caused by the saturation of current and voltage due to a fast and large speed reference. As this result, it has a large overshoot and/or a oscillated response. In order to overcome this problem, the anti-windup algorithm for the ordinary proper system such as PI controller has been already reported[4][5]. The reported anti-windup algorithm is simple, and it can maintain having a stable response. However, the robust servo compensator based on $\mathcal{H}_\infty$ control theory or two-degrees-of-freedom control design method often becomes a strictly proper and high-order system. In this case, the conventional anti-windup algorithm can not be applied to a strictly proper servo compensator. The anti-windup algorithm for a strictly proper control system has never been realized yet.

This paper proposes a new anti-windup algorithm for a strictly proper and high-order control system, and applies the proposed algorithm to the digital robust speed servo system connected to PI current controller in series. In the experimental results, the proposed digital robust speed servo system realizes an anti-windup control and keeps the desired speed response for a large speed reference.

II. Digital robust speed servo system

Recent mechatronics technique requests a realization of robust speed control of servo motor. Generally, the robust speed servo system is constructed as shown in Fig.1. The inner loop system is PI current controller with the voltage limiter. The outer loop system is the speed controller with the current limiter. Those systems have a integral element in order to zero the steady state error.

In order to satisfy both disturbance rejection performance and robust stability condition on parameter variation systematically, this paper designs the robust speed controller by mixed sensitivity $\mathcal{H}_\infty$ design method. The plant system for $\mathcal{H}_\infty$ design method is the servo motor controlled by PI current controller as shown in Fig.2. K_i is the current response gain, $W_1(s)$ and $W_2(s)$ are the weighting function, and $K(s)$ is the robust servo compensator.

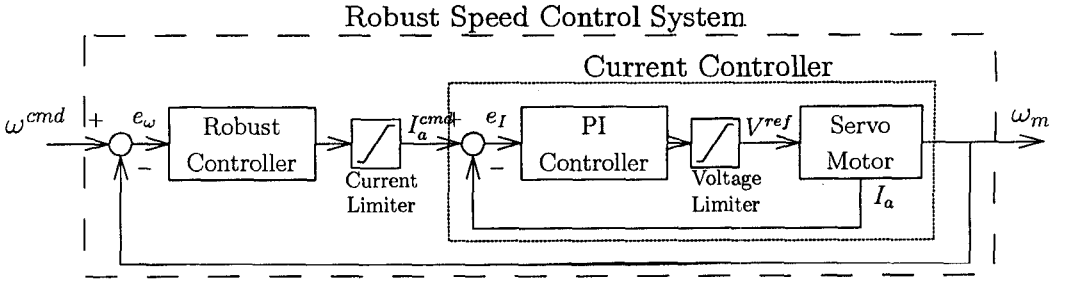

Fig. 1. Robust speed servo system

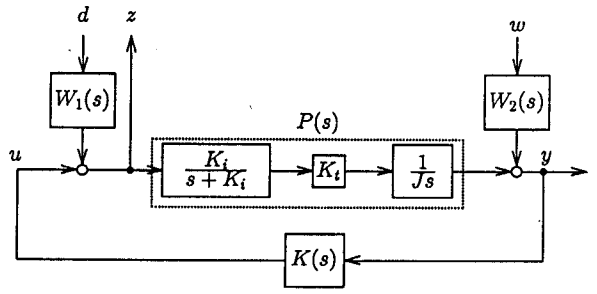

Fig. 2. Servo motor controlled by PI current controller

III. Anti-windup algorithm of PI current controller

PI controller has a simple structure, and it can have a desired response for current control. A digital PI current controller is represented as shown in (1) and Fig.3. Using a discrete state equation, a digital PI current controller is described as shown in (2) and (3). $e_I(k)$ is a current error which is an input of PI current controller. $V^{ref}(k)$ is a voltage reference which is an output of PI current controller.

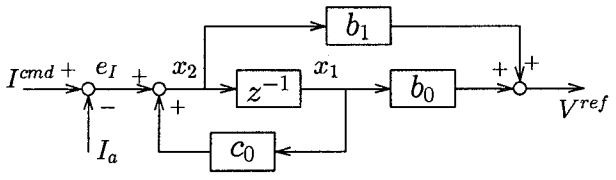

Fig. 3. Digital PI current controller

$$G(z) = \frac{b_1 z + b_0}{z - c_0} \tag{1}$$

$$x_2(k) = c_0 x_1(k) + e_I(k) \tag{2}$$

$$V^{ref}(k) = b_0 x_1(k) + b_1 x_2(k) \tag{3}$$

$$\tilde{e}_I(k) = e_I(k) - \frac{V^{ref}(k) - V_{max}}{b_1} \tag{4}$$

$$\tilde{x}_2(k) = c_0 x_1(k) + \tilde{e}_I(k) \tag{5}$$

When the output $V^{ref}(k)$ of PI current controller is larger than the voltage limit value V_{max}, $V^{ref}(k)$ becomes V_{max}. This is the saturation of controller output. Using the deference between $V^{ref}(k)$ and V_{max}, this paper prevents the windup phenomena caused by the output saturation of PI current controller. The proposed anti-windup algorithm for PI controller corrects the state variable $x_2(k)$ as shown in (4) and (5). The corrected state variable $\tilde{x}_2(k)$ in the current sampling period becomes the state variable $x_1(k)$ in the next sampling period. As the results, PI current controller has no windup phenomena caused by its own output saturation. When $V^{ref}(k)$ is smaller than V_{max}, this anti-windup algorithm is not executed.

IV. Anti-windup algorithm for strictly proper speed servo system

Using $\mathcal{H}_\infty$ design method, the robust servo compensator $K(s)$ often becomes a strictly proper and high-order system. In this paper, $K(s)$ is transformed into the state space expression of the discrete balanced realization $K(z)$ in order to reduce a quantization error. The discrete-state equations of $K(z)$ are represented as shown in (6) and (7), which are state space expression of a strictly proper system. $e_\omega(k)$ is the speed error which is the input of $K(z)$. $I^{cmd}(k)$ is the current command which is the output of $K(z)$. The strictly proper servo compensator $K(z)$ can not be adjusted in the current sampling period, because the output $I^{cmd}(k)$ is determined by only $\boldsymbol{x}(k)$ which is calculated in the last sampling period. Hence, the conventional anti-windup algorithm can not be applied to a strictly proper servo compensator $K(z)$.

This paper proposes a new anti-windup algorithm of state space expression control system for the strictly proper servo compensator $K(z)$. Since both the next output $I^{cmd}(k+1)$ and the next state variables $\boldsymbol{x}(k+1)$ of $K(z)$ are obtained by (6) and (8) in the current sampling period, the proposed anti-windup algorithm corrects the next output $I^{cmd}(k+1)$ and the next state variables $\boldsymbol{x}(k+1)$ in the current sampling period.

$$\boldsymbol{x}(k+1) = \boldsymbol{A}\boldsymbol{x}(k) + \boldsymbol{b}e_\omega(k) \tag{6}$$

$$I^{cmd}(k) = \boldsymbol{c}\boldsymbol{x}(k) \tag{7}$$

$$I^{cmd}(k+1) = \boldsymbol{c}\boldsymbol{x}(k+1) \tag{8}$$

$$\tilde{e}_\omega(k) = e_\omega(k) - \frac{I^{cmd}(k+1) - I_{max}}{\boldsymbol{c}\boldsymbol{b}} \tag{9}$$

$$\tilde{\boldsymbol{x}}(k+1) = \boldsymbol{A}\boldsymbol{x}(k) + \boldsymbol{b}\tilde{e}_\omega(k) \tag{10}$$

When the next output $I^{cmd}(k+1)$ is larger than the current limit value I_{max}, $I^{cmd}(k+1)$ is I_{max}. In this case, the proposed anti-windup algorithm corrects the next state variable $\boldsymbol{x}(k+1)$ by using the deference between $I^{cmd}(k+1)$ and I_{max}, as shown in (9) and (10). The corrected next state variable $\tilde{\boldsymbol{x}}(k+1)$ becomes the current state variable $\boldsymbol{x}(k)$ in the next sampling period. Hence, the proposed anti-windup algorithm for the strictly proper servo compensator $K(z)$ also prevents the windup phenomena caused by its own output saturation completely. Ordinary, as all initial values of the state variables $\boldsymbol{x}(k)$ of $K(z)$ are zero, the strictly proper servo compensator $K(z)$ connecting the proposed anti-windup algorithm always has no saturation effect[6]. Of course, when $I^{cmd}(k+1)$ is smaller than I_{max}, this anti-windup algorithm is not also executed.

V. Avoidance method of output saturation effect of digital robust speed servo system

When both anti-windup algorithms of PI current controller and the strictly proper speed servo compensator $K(z)$ are applied to the digital robust speed servo sys-

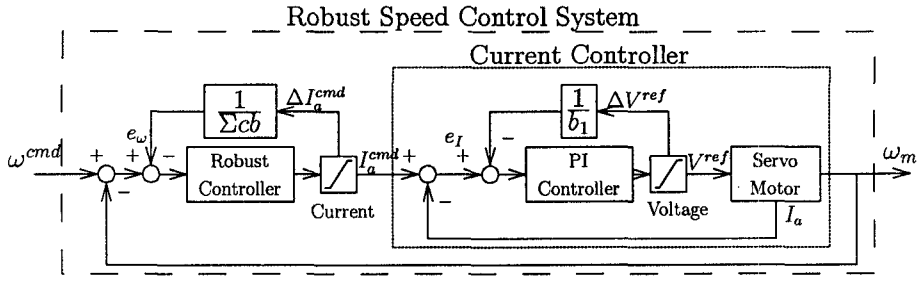

Fig. 4. Robust speed servo system with proposed anti-windup algorithm

tem, the total speed servo system is constructed as shown in Fig.4. On condition that a servo motor has a load torque or a high motor speed, the dynamic range of motor current becomes narrow. In this condition, although the output $I^{cmd}(k)$ of the speed servo compensator $K(z)$ is smaller than I_{max}, PI current controller sometimes has the output saturation effect. This paper thinks that the current limit value I_{max} equivalently changes by a load torque or a high motor speed.

In order to overcome this problem, this paper newly proposes the avoidance method of output saturation effect of digital robust speed servo system, as shown in Fig.5. In Fig.5, the feedback of the deference between $V^{ref}(k)$ and V_{max} is connected to the outer loop of speed control. The proposed complete anti-windup algorithm of digital robust speed servo system is constructed as shown from (11) to (14). It completely prevents the windup phenomena and smoothly regulates the motor speed in any condition.

$$\tilde{I}_{max}(k) = I_{max} - \frac{V^{ref}(k) - V_{max}}{b_1} \tag{11}$$

$$\tilde{e}_\omega(k-1) = e_\omega(k-1) - \frac{I^{cmd}(k) - \tilde{I}_{max}(k)}{cb} \tag{12}$$

$$\tilde{\boldsymbol{x}}(k) = \boldsymbol{A}\boldsymbol{x}(k-1) + \boldsymbol{b}\tilde{e}_\omega(k-1) \tag{13}$$

$$\tilde{\boldsymbol{x}}(k+1) = \boldsymbol{A}\tilde{\boldsymbol{x}}(k) + \boldsymbol{b}e_\omega(k) \tag{14}$$

VI. Numerical simulation and experimental results

The proposed method is applied to the tested DC servo motor as shown in Fig.6 and Table.1. The tested PI current controller and the tested $\mathcal{H}_\infty$ robust speed controller are designed as shown in (15) and (16), respectively. The frequency characteristics of tested robust speed servo system is shown in Fig.7. The sampling time of PI current control is 100[μsec], and the sampling time of robust speed servo controller is 200[μsec]. The tested digital PI current controller and the tested digital $\mathcal{H}_\infty$ robust speed controller are obtained as shown in (17) and (18), respectively. Fig.8 shows the numerical simulation results of large step response of tested speed servo system. In Fig.8, the ideal speed response without each limiter is a quick and smooth response, but the speed response with each limiter has a large overshoot caused by the windup phenomena.

TABLE I
Specification of tested DC servo motor

Armature resistance R_n	1.8 [Ω]
Armature inductance L_n	3.2 [mH]
Counter-e.m.f. constant K_e	0.22 [V·sec/rad]
Torque constant K_{tn}	0.22[N·m/A]
Inertia moment J_n	2.84×10^{-5} [N·m^2]
Mechanical time constant	10.6 [msec]
Electrical time constant	1.78 [msec]
Rated current	4.7 [A]
Rated voltage	75 [V]
Rated speed	314 [rad/sec]
Current Limit value I_{max}	15 [A]
Voltage Limit value V_{max}	75 [V]

$$K_{\mathcal{H}_\infty}(s) = \frac{\begin{array}{l}4.515\times10^5 s^3 + 1.084\times10^7 s^2 \\ +3.776\times10^9 s + 3.065\times10^{11}\end{array}}{\begin{array}{l}s^4 + 5.530\times10^3 s^3 \\ +1.102\times10^7 s^3 + 2.675\times10^9 s\end{array}} \tag{15}$$

$$K_{PI}(s) = \frac{6.4s + 3600}{s} \tag{16}$$

$$K_{\mathcal{H}_\infty}(z) = \frac{0.6608z^3 - 1.711z^2 + 1.457z - 0.407}{z^4 + 3.066z^3 - 3.476z^2 + 1.74z - 0.3308} \tag{17}$$

$$K_{PI}(z) = \frac{6.4z - 6.04}{z - 1} \tag{18}$$

In order to confirm the validity of the proposed avoidance method of output saturation effect of digital robust speed servo system, this paper shows the experimental results of the step response of speed command ω^{cmd}. Fig.9 shows the experimental results of the step responses both from 0 [rad/sec] to 200[rad/sec] and from 200 [rad/sec] to 300[rad/sec], on condition of no load torque. Similarly, Fig.10 shows the experimental results of the step response both from 0 [rad/sec] to 150[rad/sec] and from 150 [rad/sec] to 250[rad/sec], on condition of full load torque. Fig.11 shows the experimental results of the large step response from -300[rad/sec] to +300[rad/sec].

In the experimental results, the proposed avoidance method of output saturation effect of digital robust speed servo system as shown in Fig.5 realizes an anti-

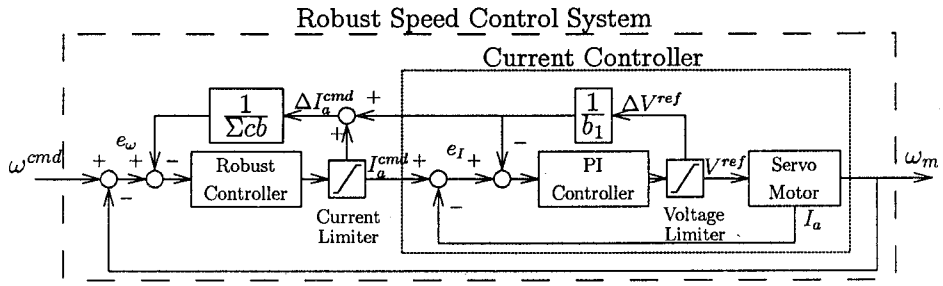

Fig. 5. Robust speed servo system with proposed anti-windup algorithm having the feedback from inner loop to outer loop

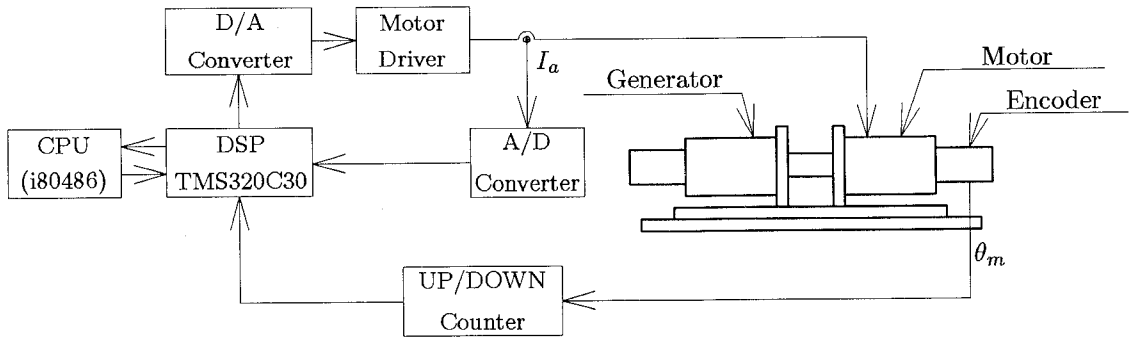

Fig. 6. Tested DC servo motor

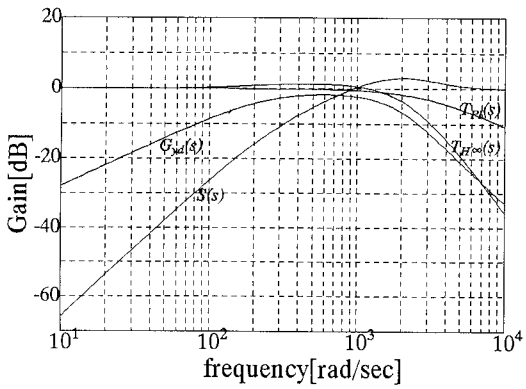

Fig. 7. Frequency characteristics of tested system

windup control and keeps the desired speed response for the large speed command on condition of any load torque. The digital robust speed servo system without the proposed algorithm has the oscillated speed response. Moreover, the digital robust speed servo system as shown in Fig.4 nearly realizes an anti-windup control on condition of any load torque, except for the condition of high motor speed.

VII. Conclusion

This paper proposes a new anti-windup algorithm for a strictly proper and high-order control system, and applies the proposed algorithm to the digital robust speed servo system connected to PI current controller in series. Using the proposed algorithm, a digital speed servo system completely avoids having the output saturation effect caused by the limitation of motor voltage and motor current. The proposed system well keeps the desired speed response for a fast and large speed reference on condition of full load torque.

References

[1] K.Ohishi and M.Ohnishi, "Robust and Easy Realization of Hybrid Control Based on H$^\infty$ Velocity Controller", Proc. of 26th International Symposium on Industrial Robots, pp.197-202, 1995.

[2] T.Umeno and Y.Hori, "Robust Speed Control of DC Servomotors Using Modern Two Degrees-of-Freedom Controller Design", IEEE Trans. on Industrial Electronics, Vol.IE-38, NO.5, pp.363-368, 1991.

[3] K.Ohishi, T.Miyazaki and Y.Nakamura, "High Performance Ultra-Low Speed Servo System Based on Doubly Coprime Factorization and Instantaneous Speed Observer", IEEE Trans. on Mechatronics, Vol.1, No.1, pp.89-98, 1996.

[4] Youbin Peng, Damir Varncic and Raymond Hanus, "Anti-Windup, Bumpless, and Conditioned Transfer Techniques for PID Controllers", IEEE Control Systems Magazine, Vol.16, No.4, pp.48-57, 1996.

[5] R.Hanus, M.Kinnaert and J.-L.Henrotte, "Conditioning Technique, a General Anti-windup and Bumpless Transfer Method", Automatica, Vol.23, No.6, pp.729-739, 1987.

[6] K.Ohishi, K.Akahori and W.Kaewprom, "Robust Manipulator Control Method Cosidering Limit Values of Torque and Controller Output", Proc. of IEEE IES/IECON'96 , Vol.2, pp.1252-1257, 1996.

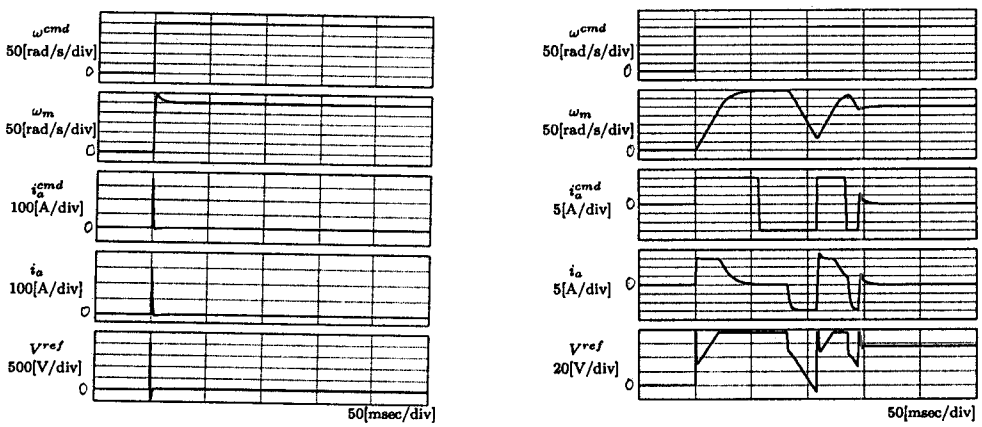

a) without both limitters b) with both limitters

Fig. 8. Numerical simulation results of large step response of tested speed servo system

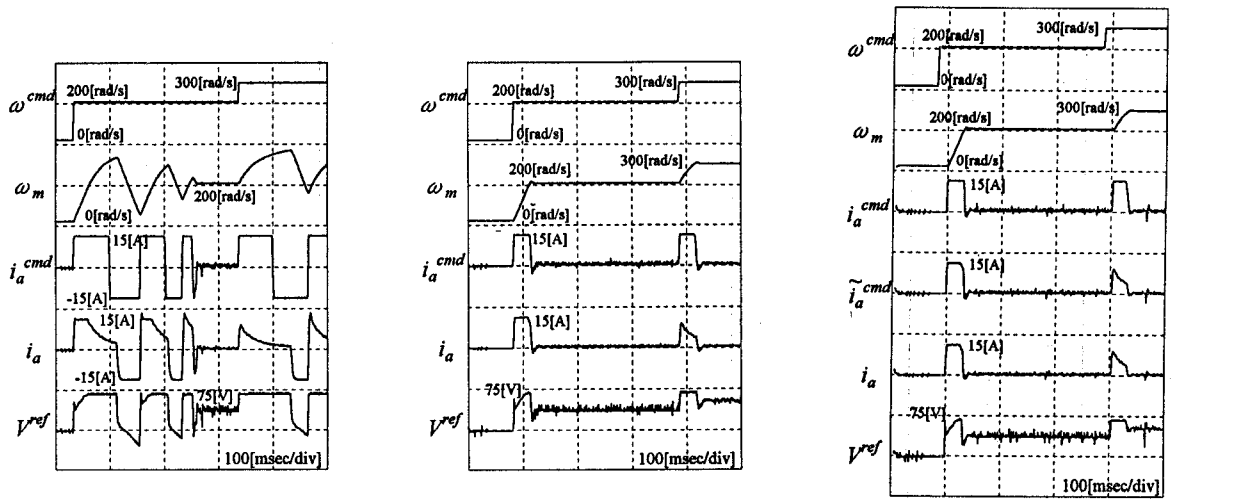

a) without proposed algorithm b) with proposed algorithm c) with proposed algorithm having the feedback form inner loop to outer loop

Fig. 9. Experimental results of the step response on condition of no load torque

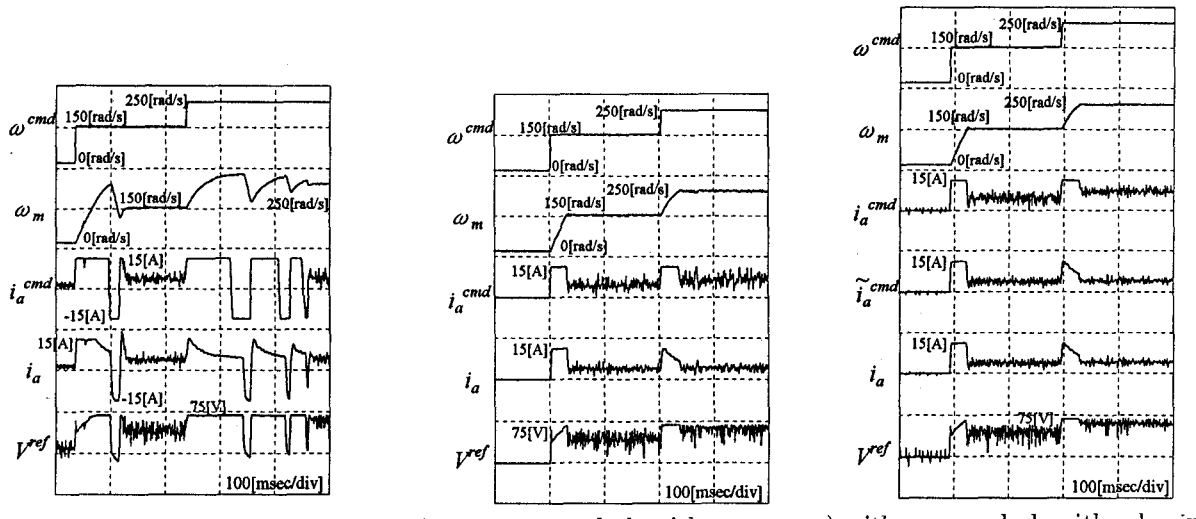

a) without proposed algorithm b) with proposed algorithm c) with proposed algorithm having the feedback form inner loop to outer loop

Fig. 10. Experimental results of the step response on condition of full load torque

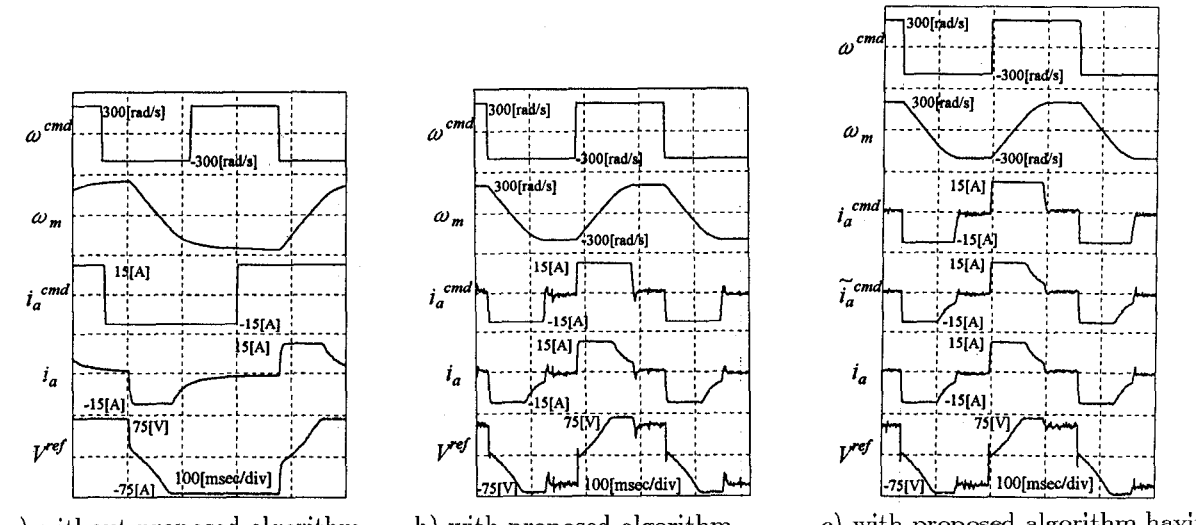

a) without proposed algorithm b) with proposed algorithm c) with proposed algorithm having the feedback form inner loop to outer loop

Fig. 11. Experimental results of the large step response from -300[rad/sec] to +300[rad/sec]

A DSP -based Servo System using Generalized Predictive Control

K. S. Low, K. Y. Chiun and K.V. Ling
School of Electrical and Electronic Engineering
Nanyang Technological University
Blk S2, Nanyang Avenue, Singapore 639798
Republic of Singapore
ekslow@ntu.edu.sg

Abstract - **In this paper, a state space Generalized Predictive Control (GPC) algorithm is developed for a brushless DC servo drive. Both the single rate and multirate input control algorithms have been realized with a DSP to control the position of an experimental motor. The performance and the robustness of the drive have been evaluated. The results show that the drive tracks the reference despite load changes and step changes in the position setpoint. In addition, the multirate input control scheme shows a faster dynamic response and is less sensitive to load disturbance. However, it is less robust against changes in the inertia.**

List of Symbols

θ	rotor displacement
ω	rotor angular velocity
i	motor current
v	output from integrator
L	motor inductance
R	motor resistance
J_m	rotor inertia
B_m	viscous-friction coefficient
K_t	torque constant
K_b	back-emf constant
K_i	integral gain constant
K_p	proportional gain constant

I . INTRODUCTION

Over the last decade, Generalized Predictive Control (GPC) has received increasing attention in many control applications [1]. For example, GPC has been used in an operating theater to control the on-line administration of muscle relaxant drugs [2]. In the process industries, GPC has also proven to be an effective and reliable control methodology. Its applications in process industries include steel casting [3] and glass processing [4]. In motion control, it has been used for the control of an induction motor [5] and machine tool motor drives [6].

GPC is a model-based method which employs the receding horizon approach. Using a plant model, GPC predicts the output of the plant over a time horizon based on the assumption about future controller output sequences. An appropriate sequence of the control signals is then calculated to reduce the tracking error by minimizing a quadratic cost function. After which only the first element of the control signals is applied to the system. This process is repeated for every sample interval. Thus, new information is updated at a regular interval. Due to this approach, GPC gives good rejection against modeling errors or disturbances.

In this paper, we develop a GPC algorithm to control the position of a brushless DC drive. Furthermore, we extend the control scheme to multirate sampling environment such that the input and output sampling rates are not constrained to be the same. The dynamic performance of the drive under inertia load and nonlinear load are studied. The load rejection property of the control schemes is also discussed. The robustness of the approach with respect to parameter changes is also investigated. It is shown that the proposed schemes have good tracking performance and are fairly robust against disturbance.

II . MODELLING OF THE DRIVE

The drive under consideration uses a 160 W, 0.65 Nm, 4 poles brushless DC motor. It is a commercially designed motor and is used as an actuator for application in the linear and rotary stages. Assuming that the commutation is perfect and the converter is supplied from an ideal direct voltage source, then the drive can be modeled as in Fig.1.

As shown in the figure, the drive uses an analog PI current controller in the inner loop. Define the state variables and the output of the system as,

$$\boldsymbol{Z} = \begin{bmatrix} \omega & i & v & \theta \end{bmatrix}^{\mathrm{T}} \tag{1}$$

$$y = \theta . \tag{2}$$

Then the motor dynamics can be described using the following state space equation,

$$\dot{\boldsymbol{Z}} = \boldsymbol{AZ} + \boldsymbol{B}i^{*} + \boldsymbol{F}\mathrm{T}_{\mathrm{L}} \tag{3}$$

$$y = \boldsymbol{CZ} \tag{4}$$

where i^{*} is the control signal , $\mathrm{T_L}$ is the load torque and

$$\boldsymbol{A} = \begin{bmatrix} -\frac{B_m}{J_m} & \frac{K_t}{J_m} & 0 & 0 \\ \frac{-K_b}{L} & -\frac{R+K_p}{L} & \frac{1}{L} & 0 \\ 0 & -K_i & 0 & 0 \\ 1 & 0 & 0 & 0 \end{bmatrix}$$

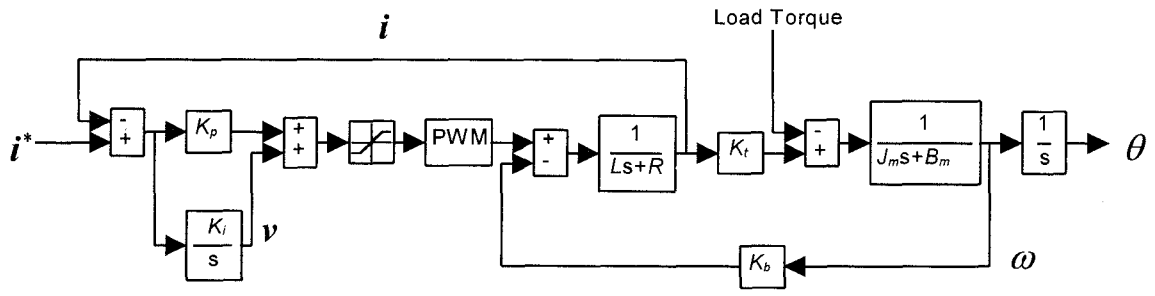

Fig.1. The block diagram of a brushless DC drive.

$$\boldsymbol{B} = \begin{bmatrix} 0 & \dfrac{K_p}{L} & K_i & 0 \end{bmatrix}^{\mathrm{T}}$$

$$\boldsymbol{C} = [0 \quad 0 \quad 0 \quad 1]$$

$$\boldsymbol{F} = \begin{bmatrix} -\dfrac{1}{J_m} & 0 & 0 & 0 \end{bmatrix} .$$

III . DESIGN OF CONTROLLER AND OBSERVER

In this paper, we consider that the dynamics of the motor position is much slower than the motor current. Consequently, the sampling rate of the controller output (i.e. the current command) need not be constrained by the sampling rate of the position output. Fig.2 illustrates the general control scheme. In the system, the controller sampling interval T is referred as the base period. The sampling time T_0 of the position response is referred as the frame period and m is an integer known as the multiplicity. The plant output is only available at the frame period, i.e. $kT_0 + jT$, j = 0, m, $2m$,...etc. In order to incorporate the multirate sampling schemes into the GPC algorithm, we use the m-steps receding horizon control strategy, i.e., applying the first m elements of the control vector calculated at time kT_0 over a frame period $[kT_0, kT_0 + mT)$ and repeat the entire control calculation at time $kT_0 + mT$. When m =1, both the input and the output signals of the drive are updated at the same rate. When m >1, the input of the drive is sampled at a faster rate as compared to the output of the plant. This becomes the multirate input controller (MRIC).

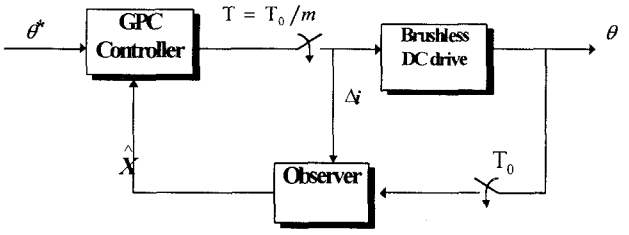

Fig.2. The multirate input control scheme.

A. Controller Design

Assuming that the load torque is varying slowly with respect to the sampling time T_0, then the state space model of the drive (3) and (4) can be expressed in the following incremental discrete time model,

$$\boldsymbol{X}(kT_0 + jT + T) = \boldsymbol{G}\boldsymbol{X}(kT_0 + jT) + \boldsymbol{H}\Delta i^*(kT_0 + jT) \tag{5}$$

$$y(kT_0 + jT) = \theta(kT_0 + jT) \tag{6}$$

where k and j are the discrete time index. j=1,2,...,m-1 and is zero for the single rate case. Δ is the difference operator such that

$$\Delta i^*(kT_0 + jT) = i^*(kT_0 + jT) - i^*(kT_0 + jT - T) . \tag{7}$$

The control law is defined as,

$$\begin{bmatrix} \Delta i^*(kT_0) \\ \Delta i^*(kT_0 + T) \\ \vdots \\ \Delta(i^*(kT_0 + mT - T)) \end{bmatrix} = \mathbf{K}_1\theta^*(kT_0) + \mathbf{K}_2\hat{\boldsymbol{X}}(kT_0) \tag{8}$$

where $\mathbf{K}_1$ and $\mathbf{K}_2$ are the controller gains. They are determined by minimizing the following cost function,

$$J_c = \sum_{j=1}^{N_y} \left\| \theta^*(kT_0 + jT) - \hat{\theta}(kT_0 + jT | kT_0) \right\|^2 + \lambda \sum_{j=1}^{N_u} \left\| \Delta i^*(kT_0 + jT - T) \right\|^2 . \tag{9}$$

with respect to the control increments Δi^* and subject to the constraints that

$$\Delta i^*(kT_0 + jT - T) = 0, \qquad \forall j > N_u .$$

In (9), N_y is known as the prediction horizon. It determines the interval over which the tracking error is to be minimized. N_u is known as the control horizon. It defines the degree of freedom available for minimization. The parameter λ is used to penalize excessive control activity and to ensure a numerically well conditioned algorithm.

B. Observer Design

To design the observer, we consider the following formulation,

$$\hat{X}(kT_0) = E_y Y + E_u U \qquad (10)$$

where

$$Y = \left[\theta(kT_0) \quad \theta(kT_0 - mT) \ldots \theta(kT_0 - (N_e - m)T)\right]^T$$

$$U = \left[\Delta i^*(kT_0 - T) \quad \Delta i^*(kT_0 - 2T) \ldots \Delta i^*(kT_0 - (N_e - 1)T)\right]^T.$$

The state observer feedback gains $\mathbf{E}_y$ and $\mathbf{E}_u$ are obtained by minimizing the following observer cost function,

$$J_e = \sum_{j=0}^{N_e-1} \mu(kT_0 - jT)\left\|\theta(kT_0 - jT) - \hat{\theta}(kT_0 - jT)\right\|^2 \qquad (11)$$

where

$$\mu(kT_0 - jT) = \begin{cases} 1, & j = 0,\ m,\ 2m, \ldots \\ 0, & \text{otherwise} \end{cases}$$

Here, $\mu(kT_0 - jT)$ is a weighting factor which reflects the fact that the output measurements are only available at the frame period while Δi^* is available at every base period. N_e is called the estimation horizon. It determines the number of past samples used in the observer for reconstructing the state vector. N_e is a tuning parameter for the observer dynamics.

IV. Experimental Evaluation

To study the performance of the proposed controller and observer, a prototype system has been developed to investigate the proposed scheme. Fig.3 shows the experimental setup. In the system, the motor is driven by a hardware three phase inverter drive. The inverter receives the current command from a digital signal processing card which uses a 32-bit floating point DSP (TMS 320C31). An optical encoder is mounted onto the motor shaft for position measurement.

In the following study, a position reference of $3\pi/2$ is set initially. To study the drive performance with respect to change of setpoints, the position reference is changed to $\pi/2$ at t=1000ms. The motor position is measured at a frame period of 5 ms. For comparison, we consider six different cases of multiplicities m = 1, 2, 3, 4, 5 and 6, i.e., the base period T= 5 ms, 2.5 ms, 1.667 ms, 1.25 ms , 1 ms and 0.833 ms respectively.

A. Performance of the Drive under Inertia Load

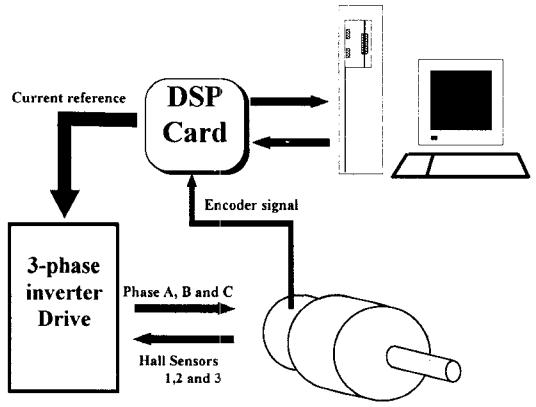

Fig.3. Experimental setup of the position control system.

With the nominal values of motor parameters, the controller and the observer have been designed based on (8) and (10). For the experiment, an inertia load of 6 J_m is used. It is assumed that this additional inertia is known and is included in the design. For comparison of the drive performance with different multiplicities, the prediction horizon N_y is fixed at 50*m i.e. the prediction horizon time is 250 ms (50*m*T). The control horizon N_u is set to 2 * m. The control weighting factor λ is fixed at 10. The estimation horizon is fixed at 6*m i.e. 30ms (6*m*T).

Fig.4 shows the experimental results of the position response for the single rate and the various MRIC schemes. The results show that the drive tracks the position reference despite step changes in the setpoint. It is also observed that there is an improvement in the dynamic response as m increases. Moreover, the overshoot is reduced. When there is a change in the position setpoint, the MRIC scheme corrects the error faster than the single rate control scheme. However, these are achieved with higher motor currents as shown in Fig.5. The velocity response of the MRIC scheme (Fig.6) also shows that it speeds up much faster than the single rate control scheme.

B. Performance of the Drive under Nonlinear Load

To study the performance of the proposed approach in dealing with the unknown load, a cylindrical mass is connected to the motor shaft with a thin rod (Fig.7). The motion of the mass creates a nonlinear load as well as an additional inertia. The equation for the load is

$$T_L = 9.8 \frac{M}{2}(2l\text{-}D)\sin\theta \qquad (12)$$

where M=mass, D=thickness of the cylindrical disc and l=length of rod. The additional inertia is

$$\Delta J = \frac{M}{3}(3l^2 - 3lD + D^2). \qquad (13)$$

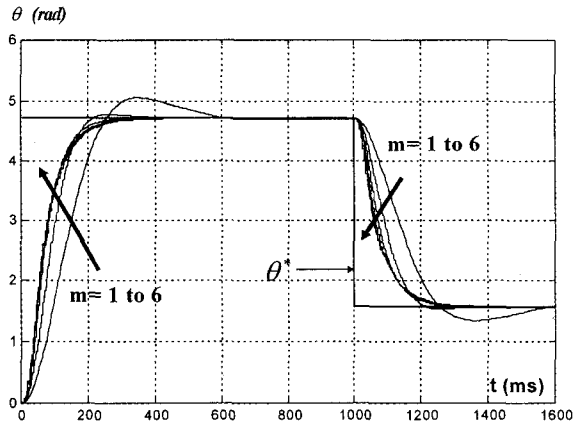

Fig.4. Position Response Under Inertia Load

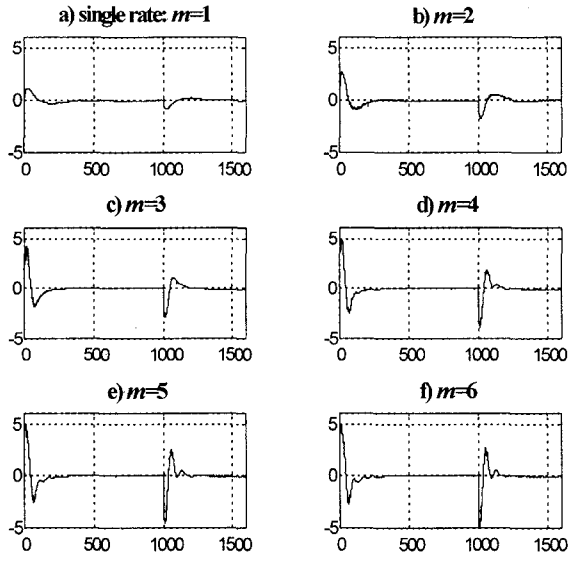

Fig.5. Motor Current (A) versus Time (ms) Under Inertia Load

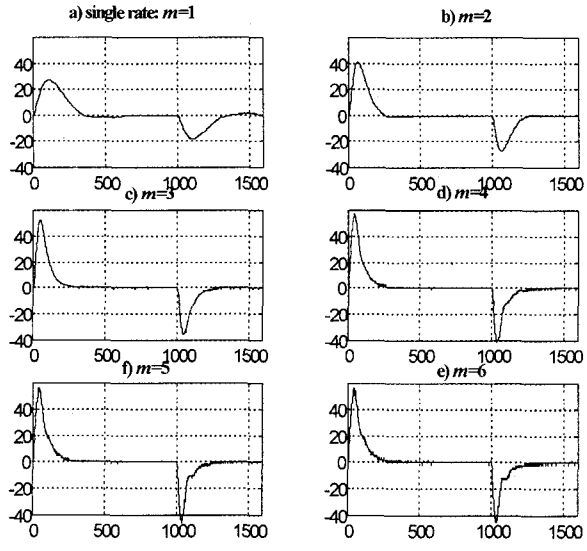

Fig.6. Velocity Response (rad/s) versus Time (ms) Under Inertia Load

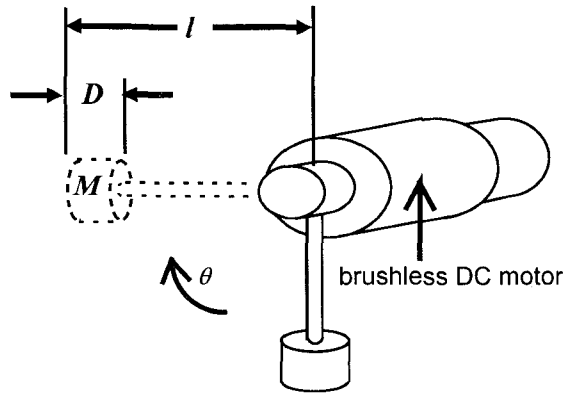

Fig.7. Nonlinear Load Connected to the Motor Shaft.

Consider a load with the following values: M = 0.644 kg, l = 0.086m and D = 0.07m. Substitute these values into (12), the maximum load is 0.32 Nm. This is about half the rated motor torque. The load also yields an addition inertia of 22.5 J_m. To evaluate the effect under nonlinear load only, we consider the case that ΔJ is known and is included in the controller design. Since both the load torque and the inertia are large, λ is set to 1 to reduce the peak current. N_y, N_u and N_e remain unchanged.

Fig.8 shows the position response of the six control schemes with m=1 to 6. In spite of the variation of the load, all the control schemes drive the motor to the position setpoint correctly. The single rate control scheme has the longest setting time and rise time. It also has the highest overshoot. As multiplicity increases, the performance also improves. The corresponding current and speed responses are demonstrated in Fig.9 and Fig.10 respectively. The figures show that the MRIC scheme commanded higher motor current and velocity. This results in a faster dynamic response of the drive. During the setpoint change, the MRIC scheme adjusts to changes much faster than the single rate approach. For multiplicities of 4, 5 and 6, the position response shows similar performance. This is due to the current saturation limits of the drive (Fig.9).

C. Load Disturbance Test

One of the important characteristic of the MRIC scheme is its disturbance rejection property. To illustrate this property, a disturbance load of 0.25 Nm is introduced to the drive when it is at a position of $\pi/2$ holding a load of 0.32 Nm. Fig.11 compares the ability of the various schemes against load disturbance. From the diagrams, single rate case has the deepest dip while m = 6 has the smallest deviation. This shows that the MRIC has good rejection property against load disturbance. Furthermore, the MRIC approach takes a shorter time to return back to the setpoint.

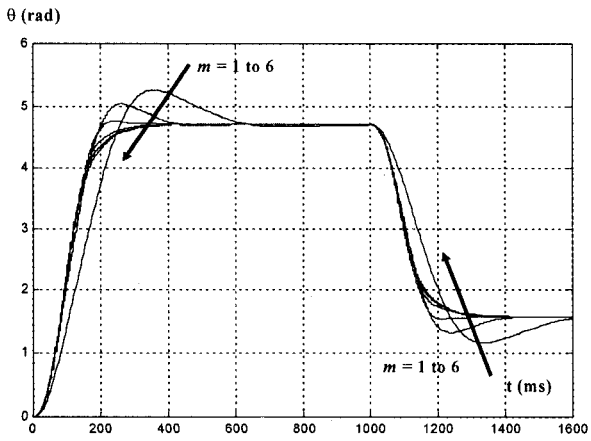

Fig.8. Position Responses Under Nonlinear Load

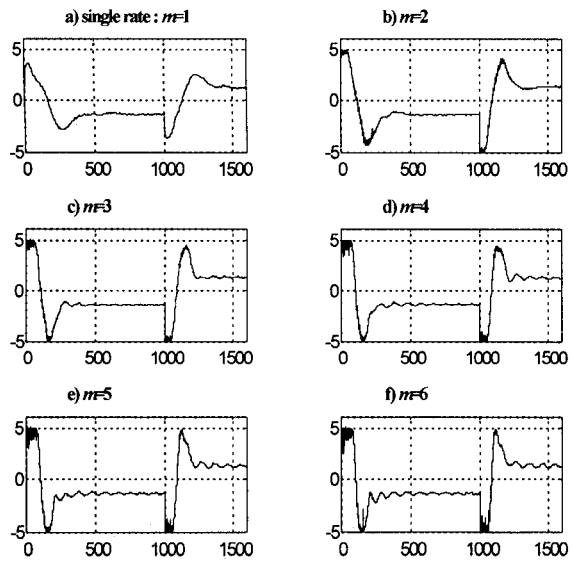

Fig.9. Motor Current (A) versus Time (ms) Under Nonlinear Load

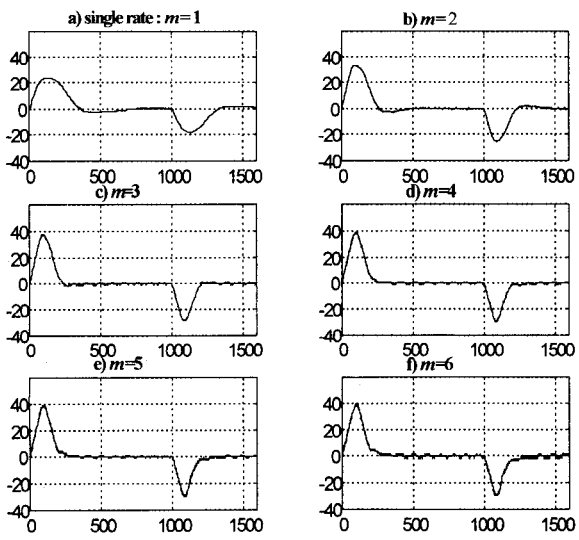

Fig.10. Velocity (rad/s) versus Time (ms) Under Nonlinear Load

D. Robustness of the Drive with respect to Inertia Variations

To investigate the robustness of the drive against changes in inertia, we design the controller based on an inertia of 2 J_m and apply a 600% inertia load to the motor, i.e. a mismatch of three times the inertia.

Fig.12 plots the position response. In the single rate control scheme, the controller tracks the position reference with a slight overshoot (Fig.12a). As m increases to 2, a longer settling time is observed (Fig.12b). Similar observation is also found in m =3. As m increases to 4, 5 and 6, the response becomes more oscillatory. Thus, while the MRIC scheme improves the performance, it is less robust to inertia variation.

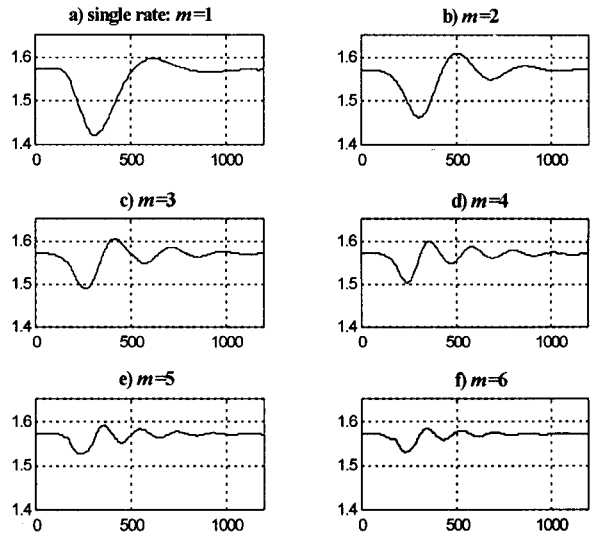

Fig.11. Position (rad) Response Under 0.25 Nm Load Disturbance

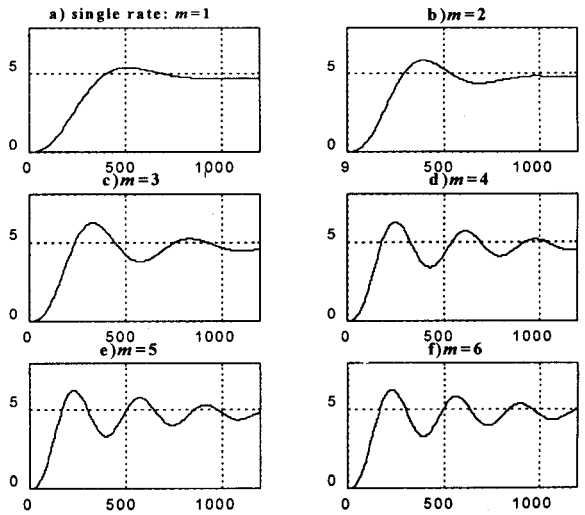

Fig.12. Position (rad) versus Time (ms) with 600% Inertia Load

E. Observer Performance under Parameter Variation

Based on our study, we have observed that there are little variations (less than 5%) in the observer performance by varying the motor winding resistance and inductance to 500% of their nominal values. Moreover, the observer performance is fairly robust with respect to variation in motor inertia. Consider a 600% inertia load is applied to the motor, the performance of the drive under step change in position reference is shown in Fig.13. The figure shows that both the actual and estimated states are close to each other.

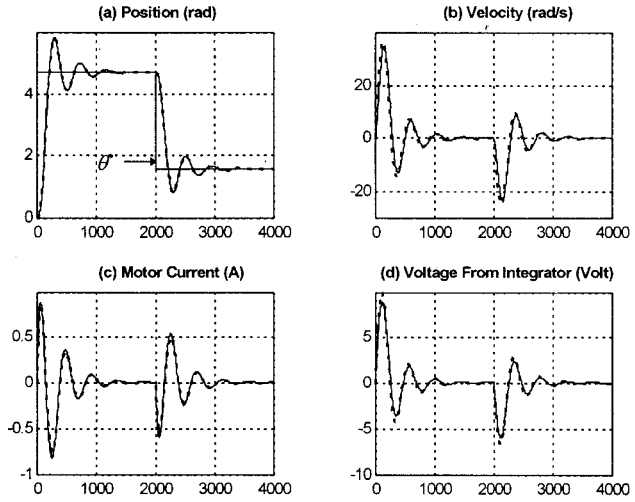

Fig.13. Observer Performance Under 600% inertia load
(.....estimated state, ___actual state.)

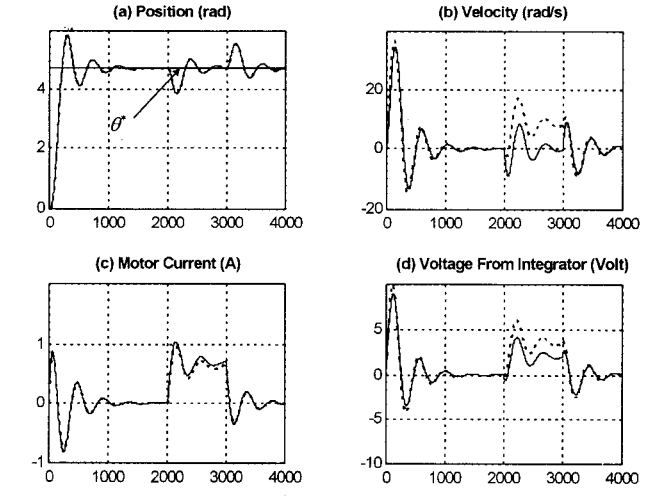

Fig.14. Observer Performance Under 0.15 Nm load
(.....estimated state, ___actual state.)

However, the performance of the state observer is affected by the load torque applied to the motor. This is because the load torque is treated as an unmeasurable variable in the model. To illustrate this occurrence, a constant load of 0.15 Nm is applied to the motor at t = 2000 ms and removed at t = 3000 ms. Fig.14 shows both the actual and estimated states of the drive. Fig.14a shows that the actual position response and the estimated position state are almost identical. This is because the position measurement is updated at every sampling interval. Furthermore, the estimated motor current state also shows little variation from the actual motor current response (Fig.14c). This is due to the feedback of the control signal in the observer. However, the estimated velocity state is affected as shown in Fig.14b. This is also observed in the estimated voltage *v*. Overall, although there is error in two of the observed states when an unknown disturbance is applied to the motor, the closed loop response of the drive is not affected by the error.

V . CONCLUSION

A DSP based servo system using the GPC algorithm has been presented. The performance and the robustness of the drive have been evaluated. With proper tuning, the results show that the drive can perform reasonably well despite load changes and step changes in the position setpoint. Furthermore, the observer is fairly robust against motor parameter changes. Our study shows that the MRIC scheme has improved the dynamic response as compared to the single rate control scheme. It also has good rejection property to the load disturbance. The major drawback of the MRIC is its sensitivity with respect to inertia.

REFERENCES

1. D.W. Clarke, "Advances in Model-based Predictive Control", *Advances in Model-Based Predictive Control*, Oxford Science Publications, 1994, pp.3-21.

2. D.A. Linkens and M. Mahfouf, "Generalized Predictive Control (GPC) in Clinical Anaesthesia", *Advances in Model-Based Predictive Control*, Oxford Science Publications, 1994, pp.429-445.

3. T. Jolly and J. Bentsman, "Generalized Predictive Control with Dynamic Filtering for Process Control Applications", in *Proceedings of American Control Conference, San Francisco, California*, 1993, Vol. 2, pp. 1741-1745.

4. Q. Wang, G. Chalaye, G. Thomas and G. Gilles, "An Industrial Application of Predictive Control to Glass Process - Working Basin and Feeder", in *Proceedings of IEEE Conference on Control Applications*, 1994, Vol. 3, pp. 1891-1896.

5. L. Zhang and H.R. Tayebi, "Field-oriented CSI Induction Motor Drive with Optimal Predictive Current Regulation", in *Proceedings of Power Electronics and Variable-Speed Drives Conference*, 1994, pp. 48-53.

6. Boucher, P. and Dumur, D., "Multirate Polynomial Predictive Cascade Control", in *Proceedings of Second IEEE Conference on Control Application*, Vancouver, 1993, Vol. 2, pp. 613-618.

Analysis and Control of Grasping Motion by Two Cooperative Robots

Kyunghwan Kim and Yoichi Hori
The University of Tokyo
7-3-1, Hongo, Bunkyo-ku, Tokyo 113, JAPAN
E-mail : kim@kaya.t.u-tokyo.ac.jp, hori@kaya.t.u-tokyo.ac.jp

Abstract -- **The grasping motion done by two robot manipulators is analyzed firstly. The analysis makes it clear that the reaction force sensed at each end-effector can be decomposed into two force components, that is, motion-inducing force and object-squeezing force. Based on the force decomposition, two types of robust motion controller for cooperating manipulators are proposed. The proposed controllers track desired contact force and internal force with much strong robustness to object/manipulator dynamics. Finally, some experimental results show the feasibility of robust grasping motion by the proposed controllers.**

1 INTRODUCTION

The cooperative manipulation by using two or more robots has been intensively studied for about a decade. Human has multi-limbed mechanisms and the advantage of using multiple robot manipulators than a single one can be well imagined intuitively. Some robot tasks such as space-based manipulation cannot be performed by a single robot.

The previous researches about cooperative manipulation by multiple robots, have emphasized rigorous analysis of grasping motion. Based on the exact mathematical analysis, elaborate but complicated control schemes for grasping motion have been proposed so far. In most of cases, these schemes require exact dynamic models for a grasped object and manipulators. When implementing these control algorithms into robot system, model uncertainty in the coordinated system was the most critical point for successful manipulation.

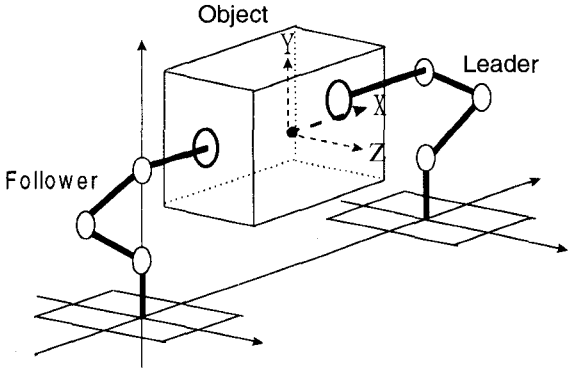

Fig.1. Grasping motion by two cooperative robots

A series of our research tells that the robust controller is quite useful to suppress the effect of model uncertainty on its control performance of robot [1,2,3]. By using the robust controller, robot trajectory and force can be easily controlled even under the circumstance of big model uncertainties such as manipulator dynamics and object dynamics.

In this paper, grasping motion by a dual-arm robot is analyzed firstly. In the analysis, the force exerted to an grasped object by robot arms, can be divided into two components, that is, motion-inducing force and internal force. Based on the analysis, a robust control scheme to control motion and force simultaneously is designed. Finally, some of lab experiments show the effectiveness of our proposed method.

2 ANALYSIS OF GRASPING MOTION

2.1 *Force Decomposition*

When multiple manipulators grasp an object, the force applied by multiple robots can be decomposed into motion-inducing force and internal force. In the proposed cooperative control described in detail later, the internal force to squeeze the grasped object and the contact force sensed at the end-effector, are the controlled variables. In this section, two robot manipulators and a single object are considered as depicted in Fig.1. This analysis may be extended easily to the case for more than two robots. Also, refer to [3] for force analysis in scalar quantity.

When two robots grasp a common object and exert force $\boldsymbol{F}$ to it, the resultant force $\boldsymbol{P}$ at the object frame is determined by grasp matrix G such as

$$\boldsymbol{P} = \boldsymbol{G}\boldsymbol{F} \tag{1}$$

where $\boldsymbol{F} = \left[\boldsymbol{F}_1^T \quad \boldsymbol{F}_2^T\right]^T$ = force applied to the object by two robots, $\boldsymbol{G} = \left[\boldsymbol{G}_1 \quad \boldsymbol{G}_2\right]$ = grasp matrix from the object frame to each end-effector frame. The matrix $\boldsymbol{G}$ is grasp-configuration dependent such as

$$\boldsymbol{G}_i = \begin{bmatrix} \boldsymbol{I}_3 & \boldsymbol{O}_3 \\ \boldsymbol{S}_i & \boldsymbol{I}_3 \end{bmatrix} \tag{2}$$

where s_i is the vector from the object frame to the end-effector frame.

$$S_i = \begin{bmatrix} 0 & -S_{iz} & S_{iy} \\ S_{iz} & 0 & -S_{ix} \\ -S_{iy} & S_{ix} & 0 \end{bmatrix}, \quad s_i = \begin{bmatrix} S_{ix} & S_{iy} & S_{iz} \end{bmatrix}^T \quad (3)$$

In most of control problems, desired motion for the object, P and grasp configuration, G are known. In this case, Eq.(1) may be rewritten as

$$F = G^+P + (I - G^+G)\varepsilon \quad (4)$$

Generally, the above equation is not determined uniquely. G^+ is a generalized inverse of the grasp matrix G and may be defined in general by $G^+ = AG^T(GAG^T)^{-1}$ for some positive definite matrix A. In this paper, a particular pseudoinverse solution is used for calculating G^+ [7]. This solution has the property to decouple the motion-inducing force from the squeez-inducing one. As a result, the force applied to the object by two robots can be decomposed into motion-inducing force F_M and internal force F_I as in the below equation.

$$F = G^+GF + (I - G^+G)F = F_M + F_I \quad (5)$$

where the pseudoinverse matrix is

$$G^+ = \frac{1}{2}\begin{bmatrix} I_3 & O_3 \\ -S_1 & I_3 \\ \hline I_3 & O_3 \\ -S_2 & I_3 \end{bmatrix} \quad (6)$$

In the above equations, internal force can be calculated from the grasp configuration G and the sensed contact force F. Also, F_M and F_I can be transformed from the end-effector frame to the object frame.

2.2 *A Numerical Example*

Consider a simple example to illustrate the results of the previous section. The situation is to manipulate a spherical object of diameter 6 units with center of mass located 3 units in the x direction from the grasp position of arm 1. Arm 2 grasps the object two units further along the line joining arm 1 end-effector and object center of mass.

The inertia matrix of this object is

$$I = \frac{2}{5}\begin{bmatrix} mr^2 & 0 & 0 \\ 0 & mr^2 & 0 \\ 0 & 0 & mr^2 \end{bmatrix} = \begin{bmatrix} 36 & 0 & 0 \\ 0 & 36 & 0 \\ 0 & 0 & 36 \end{bmatrix} \quad (7)$$

in which the mass m is 10 and the radius r is 3. The object trajectory is chosen to have constant acceleration in the x, y and z directions, for example, 0.1 units/s^2 without any rotational motion of the object. Neglecting gravity for simplicity, the net force applied to the object, P is

$$P = \begin{bmatrix} mI_3\ddot{r}^T \\ I\dot{\omega}^T \end{bmatrix} = \begin{bmatrix} 1 & 1 & 1 & 0 & 0 & 0 \end{bmatrix}^T. \quad (8)$$

The grasp matrix G is calculated by Eq.(2) and its pseudoinverse G^+ is also done by substituting the values into (6).

$$G = \left[\begin{array}{c|c|c|c} I_3 & O_3 & I_3 & O_3 \\ \hline \begin{bmatrix} 0 & 0 & -2 \\ 0 & 0 & 0 \\ 2 & 0 & 0 \end{bmatrix} & I_3 & \begin{bmatrix} 0 & 0 & 3 \\ 0 & 0 & 0 \\ -3 & 0 & 0 \end{bmatrix} & I_3 \end{array}\right] \quad (9)$$

Finally, the motion-inducing force at the end-effector is given as in

$$F_{M1} = \begin{bmatrix} 0.5 & 0.5 & 0.5 & 1.0 & 0 & -1.0 \end{bmatrix}^T$$
$$F_{M2} = \begin{bmatrix} 0.5 & 0.5 & 0.5 & -1.5 & 0 & 1.5 \end{bmatrix}^T \quad (10)$$

These forces can be converted to the ones at the object frame such as

$$\overline{F}_{M1} = G_1F_{M1} = \begin{bmatrix} 0.5 & 0.5 & 0.5 & 0 & 0 & 0 \end{bmatrix}^T$$
$$\overline{F}_{M2} = G_2F_{M2} = \begin{bmatrix} 0.5 & 0.5 & 0.5 & 0 & 0 & 0 \end{bmatrix}^T \quad (11)$$

The matrix (11) tells that motion-inducing force does generate no squeezing effect or internal loading. Similarly, the internal force may be derived according to the results in the previous section.

3 DESIGN OF ROBUST CONTROLLER

In the proposed force control scheme, control output of the force controller is the desired position. It is fed into the position controller to track desired internal and contact force. The force control based on position command is said to have the limitation of control resolution compared with the one based on acceleration information. The advantage of this approach, however, is the feasibility of simple implementation in most of commercial robot systems, in which only position command can be designated by users.

3.1 *Internal Force-Based Control*

The relationship between the internal force and the positional displacement, is explicitly described as in

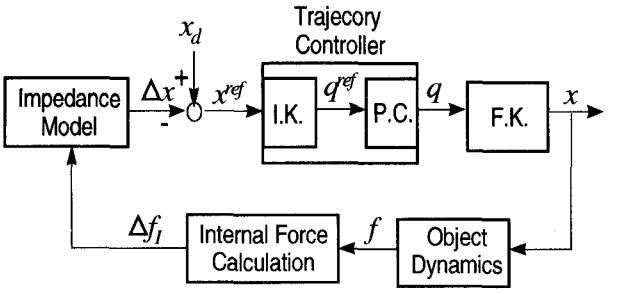

Fig. 2. Internal force-based control

$$M_i \Delta\ddot{x}_i + D_i \Delta\dot{x}_i + K_i \Delta x_i = \Delta F_{Ii} \tag{12}$$

where M_i, D_i and K_i are the impedance parameters of the ith manipulator. The position and internal force displacements are defined as $\Delta x_i = x_{id} - x_i$ and $\Delta F_{Ii} = F_{Ii} - F_{Iid}$ respectively.

The impedance relationship (12) can be rewritten as in

$$\Delta x_i = \frac{1}{M_i s^2 + D_i s + K_i} \Delta F_{Ii} \tag{13}$$

Based on the above model, the block diagram for internal force-based control can be depicted as in Fig.2. Seen from this figure, the position command fed into the position controller, is altered by the impedance relationship.

3.2 *Contact Force-Based Control*

It is a more straightforward grasping strategy to control the contact force at the end-effector than to do internal force. Let me suppose one dimensional motion in which the contact force is controlled to be constant. In this case, the internal force exerted to the object may be less than the contact force, in some cases, very small enough to deteriorate grasp stability.

Despite the global instability of grasp, contact force can be controlled to be constant within a stable motion boundary [3]. In this control scheme, one robot called as leader, determines desired position of the grasped object, and the other robot called as follower, is force-controlled to sustain the contact force at the end-effector constantly.

Seen from the analysis of force decomposition in previous section, a two robot system with a grasped object may be expressed as in

$$P = G_1 F_1^T + G_2 F_2^T \tag{14}$$

Here, suppose that F_2 is controlled to be constant. On the assumption that the grasp configurations, G_1 for robot 1 and G_2 for robot 2, are well known, the resultant motion of the grasped object reflects the change of F_1 imparted by robot 1.

Generally, contact force-based control has much difficulty, since the contact force reacts to the object dynamics expressed as in

$$P_n^f(s) = K_n + D_n s \tag{15}$$

The proposed force controller, however, has strong robustness to changing dynamics of the grasped object. Refer to other papers for details [2,3]. By using the robust force controller, the contact force-based control can be implemented easily without much effort to adjust dynamics parameters of the object.

3.3 *Robust Position controller*

In order to achieve good performance of force control based on position control input, very robust position controller must be designed The dynamic equation for each manipulator in constrained motion, is given by

$$\tau_i = D_i(q_i)\ddot{q}_i + H_i(q_i, \dot{q}_i) + J_i^T(q_i) F_i \tag{16}$$

in which τ_i and F_i are the joint torque of the ith robot, and the force exerted to the object by the ith robot end-effector respectively. Also, D_i and H_i are the inertia matrix and the nonlinear dynamics of the manipulator including Coriolis, centrifugal and gravity forces.

In the proposed position control, constant diagonal matrix for inertia, D_{Ni} is designated in the controller, and the nonlinear dynamics of the manipulators including reaction forces is estimated and canceled by using Two-Degree-Of-Freedom servosystem [1]. The role of disturbance rejection in the TDOF servosystem is depicted in Fig.3. It can be expressed by dynamic equation of robot as in

$$\tau_i = D_{Ni}(q)\ddot{q} + \hat{\tau}_{dis} \tag{17}$$

where $\hat{\tau}_{dis}$ is the estimated quantity of disturbance including robot model uncertainty.

The position command in task space is transformed into the one in joint space by kinematics relationship as in

$$x_i = L_i(q_i) \tag{18}$$

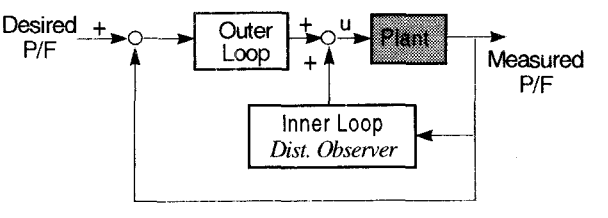

Fig.3. Robust controller including disturbance observer

4 EXPERIMENTAL RESULTS

In this section, the experimental results of contact force-based control will be shown. In coordinated control by multiple robot manipulators, force regulation is most important for sustaining stable grasp.

Fig. 4 shows the experimental setup which consists of two robot manipulators and a grasped object. The simplicity of the proposed algorithm enables PC-based control.

Call two robot manipulators as leader and follower. In the proposed contact force-based control, one 6DOF force sensor is attached only to the follower and the leader performs only position control without force feedback.

Fig.5 depicts the position command applied to the leader. In Fig.6, the contact force between the follower and the object, is regulated to be 30[N] by using PI controller, PI plus feedforward controller and Two Degree Of Freedom(TDOF) controller respectively. Here, the conventional PI controller reveals steady state error in the force regulation. In PI plus feedforward method, the feedforward term, in this case, velocity of the leader, compensates steady state error of the PI controller. Finally, TDOF controller performs good tracking without any steady state error, since it has the property to estimate the disturbance caused from object dynamics and to compensate it almost instantaneously.

Fig. 7 illustrates the robustness of the TDOF force controller against changing dynamics of the grasped object. Almost same accuracy of control can be realized without adjusting dynamics model of the object.

In Fig.8, a hybrid control of position and force is done. Force control is done only in x direction and position control by using the same trajectory with the one of the leader, in y direction. This figure depicts the circular trajectory of the follower. Fig.9 shows its force response.

Fig. 10 draws a circle while the leader determines trajectory of the grasped object and the follower tracks constant contact force at its end-effector. Without any mutual communication between two robots, end-effector of the follower draws a circular trajectory. Fig.11 shows its force response in this case.

Seen from the investigation in section three, contact state between the end-effector and the object is very important in order to determine the grasp matrix, $\boldsymbol{G}$. Imagine the movement of upward and then downward. In a rigid contact as depicted in Fig.12, motion of the grasped object is transmitted well via force sensor. In a soft contact, however, as depicted in Fig. 13, the sensed force does not reflect motion of the grasped object. In coordinated control by multiple robots, the rigid grasping is very important assumption for good control performance.

5 CONCLUSIONS

In this paper, the force applied to a grasped object by a two-armed manipulator is analyzed. Based on the analysis, the force control which aims to control contact force at the end-effector and internal force exerted to the object, has been proposed. By using internal force-based control, two robots can grasp an object without much consideration of robot and object dynamics. Moreover, the contact force-based control is not sensitive to changing object dynamics. It is very difficult to control contact force by using the conventional PI control. Finally, some lab experiments show the effectiveness of the proposed method.

REFERENCES

[1] T. Umeno and Y. Hori, Robust Servosystem Design with Two Degrees of Freedom and its Application to Novel Motion Control of Robot Manipulators, *IEEE Trans. IE*, vol. 40, no. 5, pp. 473-485, Oct. 1990.

[2] K. Shimura, M. Sugai and Y. Hori, Position, collision and force control of robot manipulators based on the robustified joint servo system, *IEEE 2nd IWAMC*, pp. 1-10, 1992.

[3] K. Kim and Y. Hori, Robust Grasping Strategy for Dual-Arm Robot System, *2nd Asian Control Conference*, Seoul, July 1997.

[4] X. Yun, Object Handling Using Two Arms Without Grasping, *Intl. Jour. of RR*, vol. 12, no. 1, pp. 99-106, Feb 1993.

[5] N. Xi, T. J. Tarn and A. K. Bejczy, Intelligent Planning and Control for Multirobot Coordination: An Event-Based Approach, *IEEE Trans. RA, vol. 12, no. 3, Jun* 1996.

[6] R. G. Bonitz and T. C. Hsia, Robust Internal Force-based Impedance Control for Coordinating Manipulators, *IEEE Conf. on Robotics and Automation,* April 1996.

[7] D. Walker, R. A. Freeman and S. I. Marcus, Analysis of Motion and Internal Loading of Objects Grasped by Multiple Cooperating Manipulators, *Intl. Jour. of RR*, vol. 10, no. 4, pp. 396-409, Aug 1991.

[8] D. E. Whitney, Historical Perspective and State of the Art in Robot Force Control, *Intl. Jour. of RR,* vol. 6, no. 1, pp. 3-14, 1987.

[9] O. Khatib, Inertia Properties in Robotic Manipulation : An Object-Level Framework, *Intl. Jour. of RR*, vol. 13, no. 1, pp. 19-35, 1995.

[10] E. Paljug, X. Yun and V. kumar, Control of Rolling Contacts In Multi-Arm Manipulation, IEEE Trans. RA, Vol. 10, No. 4, Aug. 1994.

[11] W. S. Howard and V. Kumar, On the stability of Grasped Objects, IEEE Trans. RA, Vol. 12, No. 6, pp.904-917, Dec. 1996.

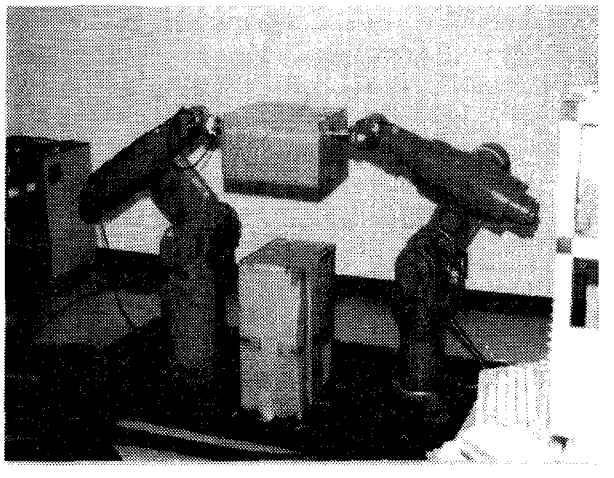

Fig.4. Experimental setup for dual-arm robot system

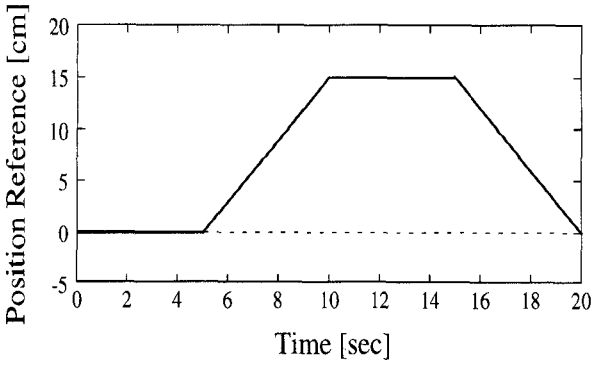

Fig.5. Position command to the leader

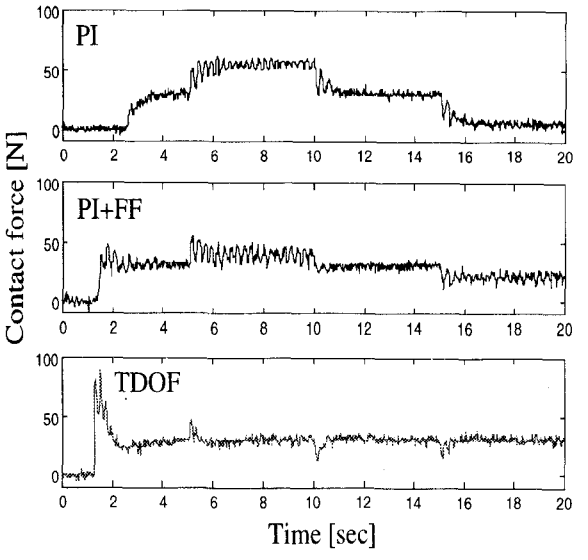

Fig.6. Force response of the follower

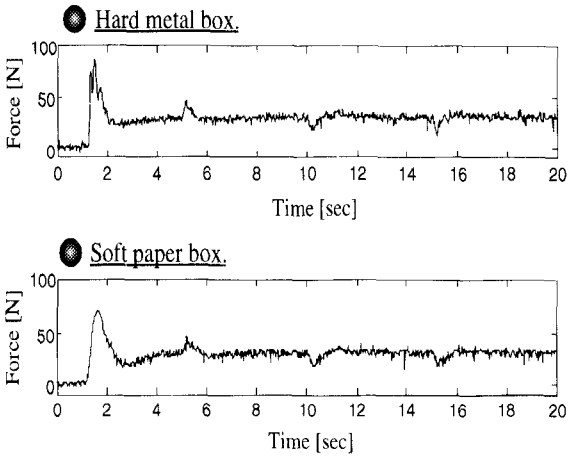

Fig.7. Changing a grasped object

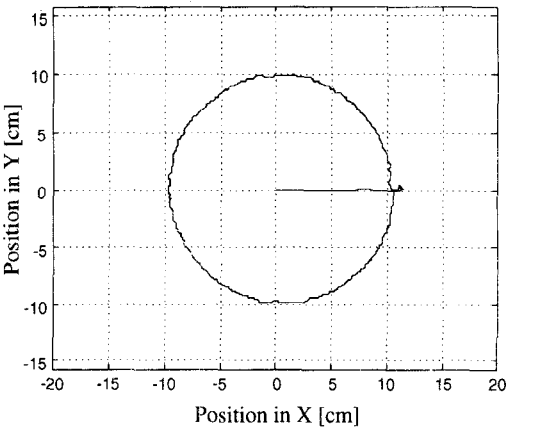

Fig.8. Drawing a circle by using a hybrid force control

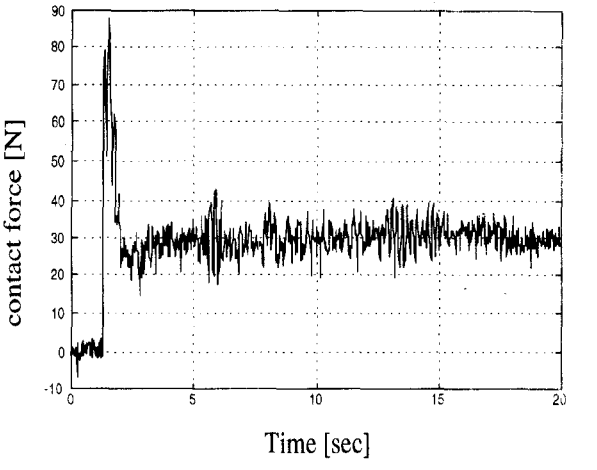

Fig. 9. Force response of the circular motion in Fig.8

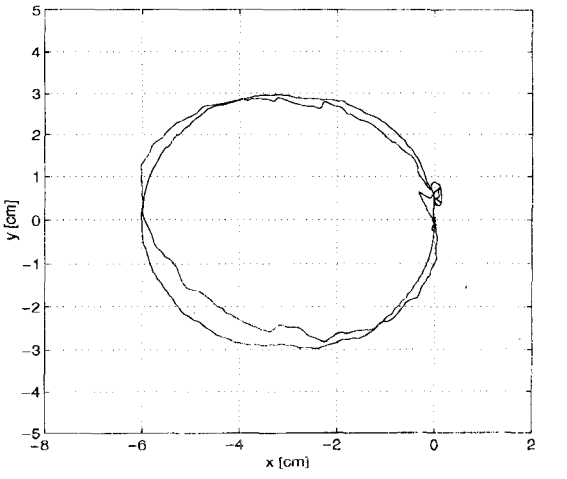

Fig.10. Drawing a circle by contact force-based control

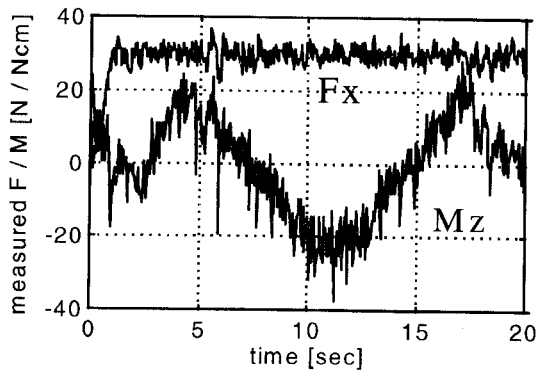

Fig. 11. Force response of the circular motion in Fig.10

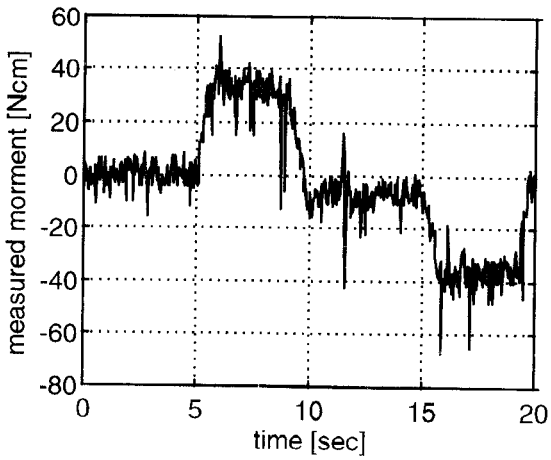

Fig.12. Sensed force in rigid contact

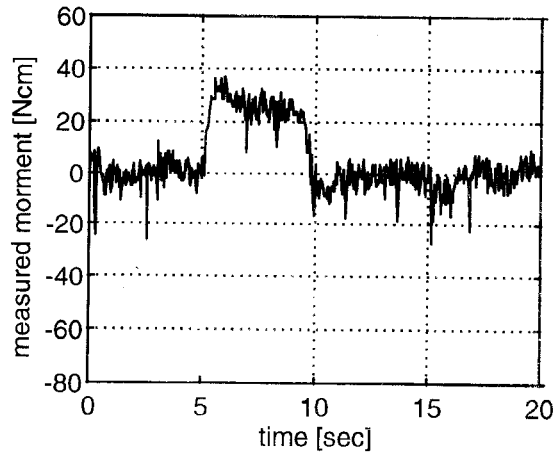

Fig.13. Sensed force in soft contact

Control and Diagnosis for AC Drives and UPS Systems Using Soft Computing

Yasuhiko Dote* and Richard G. Hoft**
* Department of Computer Science and Systems Engineering
Muroran Institute of Technology
Mizumoto-cho 27-1, Muroran 050, Japan
Fax: 0143-47-3374, Phone: 0143-44-4181 (Ext. 2433), 0143-47-3267
E-mail : dote@csse.muroran-it.ac.jp
** Department of Electrical and Computer Engineering
University of Missouri - Columbia
Columbia, Missouri, 65211, U.S.A.

Abstract - **Soft computing was proposed by Dr. L.Zadeh, Director of Berkeley Initiative Soft Computing Center, University of California, Berkeley, U.S.A., in order to solve complicated problems which had not been solved by hard computing with Neumann type computers. It includes neuro (NN), fuzzy computings (FS), chaos computing (CS), genetic algorithms (GA), immune network computing (IN) and others. This paper describes soft computing applied to power electronics and motion control systems which are nonlinear or unmodelled systems. It makes them intelligent systems and gives automated design methods and automated tuning methods by combining the above mentioned soft computing approaches.**

I. Introduction

Human thinking way has both logical and intuitive or subjective (human mind) sides. The logical thinking way has been developed resulting in present advanced Neumann type computers and expert systems as hard computing. However, it is found that hard computing can not solve very complicated problems. In order to cope with this difficulty, the human mind is realized as soft computing which includes neuro and fuzzy computing.

This paper suggests the combination of soft computing methods (NN, FS, CS, GA, IN) for control and diagnosis of AC drives and UPS systems. The advantages of soft computing (combinations of fuzzy logic, neural network, chaos, GA and immune network) used in control and measurement are [1]

1) Nonlinear problems, problems for which mathematical models are not obtained, and complicated problems can be solved (tractability)

2) Human knowledge (recognition, understanding, learning, inference diagnosis) can be introduced to controllers and instrumentations. Therefore distributed and autonomous systems (complicated and symbiosis systems) and intelligent systems can be constructed (Machine Intelligence Quocient). Evolutional and adaptive systems can be also constructed by adding human immune and hormone system behavior to soft computing. Soft computing is also a powerful tool for artificial life science.

3) Automated system design methods can be established.

Recently Dr. Wang proved that any nonlinear mapping obtained by neural networks can be approximated, to any accuracy, by fuzzy logic using the Stone-Weierstrass' approximation theory [2]. Therefore, for example, stability of fuzzy systems which has been difficult can be performed based upon stability analysis of neural networks. This is theoretical relationship between fuzzy systems and neuro systems.

From the application point of view, fuzzy and neuro approaches have their own advantages and disadvantages. It is assumed that they are applied to pattern recognition and function approximation. These applications are considered from knowledge acquisition, inference capability and system tuning points of view [3].

A. Knowledge acquisition

A multi-layered neural network can acquire knowledge by using its learning capability (for example, by using input-output teaching data and backpropagation methods). On the other hand, in fuzzy approaches, knowledge is obtained by having interview with an expert person. Therefore, it may take much time to acquire sufficient knowledge from the expert since the expert may not remember the precise steps used to develop the rules.

B. Inference performance

In multi-layered neural networks their input space can be separated by arbitrary super surface planes. However, the input space in fuzzy systems is only in parallel with its inputs. Therefore, a neural network is more suitable to cluster complicated input variables. In fuzzy systems as the number of input variables is increased, the number of rules becomes tremendously large. It is impossible to construct fuzzy systems in such cases.

C. Tuning

In using neural networks it is difficult to explain logically the cause and the result in the input-output relationships. Therefore, it is difficult to apply fine tunings.

Fuzzy systems which have the same performance as neuro systems have been developed by applying the

0-7803-3823-5/97/$10.00© 1997 IEEE

following techniques.

1) fuzzy rules are deduced from numerical data

2) in order to limit the number of rules, variable fuzzy rules with different magnitudes and shapes are defined.

Fuzzy systems and neuro systems are compared in Table I. Similarities and complement exist between two technologies like these. The combination or fusion of both is suggested.

In this paper, firstly, only the combination of fuzzy technologies and neural networks are considered, then, the application of GA, CS, IN for control and diagnosis of AC drives and UPS systems is described.

II. AC Drive And UPS Neuro Fuzzy Control

A. Neuro Fuzzy Robust Control for AC Drive System

This section proposes a gain scheduling robust controller whose parameters are continuously changed by fuzzy logic such that the controller makes the system respond quickly if the error e is large (signal/noise ratio is large) and vice versa in order to obtain a robust controller which is insensitive to both plant noise and observation noise. Then, the controller is applied to speed control of an induction motor drive. Experiments show that the proposed controller is superior to both a sliding mode controller and a PID controller [4].

A linear robust control block diagram is shown in Fig.1. Fig.2 shows a hardware implementation. This controller consists of an equivalent disturbance observer for cancelling the effect of external disturbance and parameter variation and a feedforward controller to obtain rapid time response. Then, based upon the knowledge of an experienced engineer, To and Kp are changed by using fuzzy logic resulting in a gain scheduling controller which is insensitive to observation noise and plant noise. The fuzzy rules are as follows.

- If e is large (S/N is large), then Kp is large
- If e is small (S/N is small), then Kp is small
- If e is large (S/N is large), then To is small
- If e is large (S/N is small), then To is large.

B. General Parameter Approach for Neuro Fuzzy Control and Diagnosis for AC Drive and UPS Systems

There is a trade-off between approximation ability, structure complexity and convergence rate of any type neural networks to be developed for practical implementations. Therefore, determination of the optimal network structure and development of improving learning feature adjusting procedures are the subject of many investigatons.

A novel neural network structure formation and learning method which has faster training features is proposed based on General Parameter (GP) methodology [5]. Acceleration of convergence rate is achieved by initial reduction of adjusting parameter space dimensionality. The latter is to be increased then during training to improve approximation ability.

TABLE I
COMPARISON OF FUZZY SYSTEM WITH NEURO SYSTEM

	Fuzzy System	Neuro System
Knowledge representation	Membership functions, rules	Distributed patterns
Knowledge acquisition	Interviews with with experts (difficult)	Learning by data
Data processing	Analog and fuzzy logic	Analog
Advantages	Explanations of results, fine tuning	Adaptive by learning, interference capability
Disadvantages	Tolerance for ambiguity	Tolerance for uncertainty

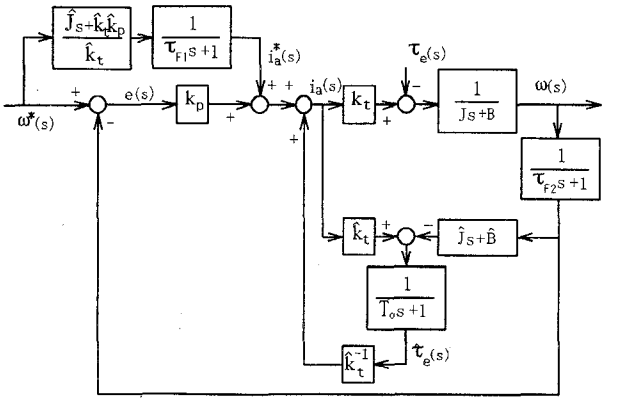

Fig. 1. Overall control block diagram.

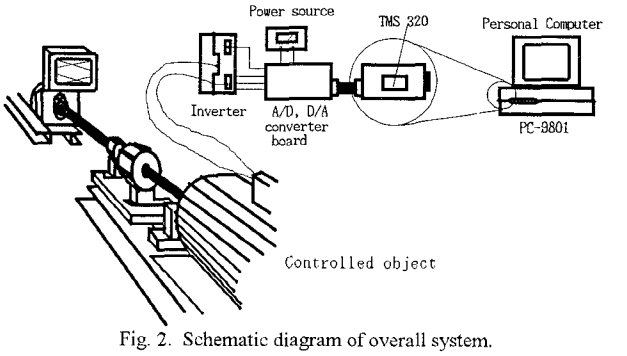

Fig. 2. Schematic diagram of overall system.

Recurrent procedures of process (plant) model reconstruction are based on adjusting model schemes. The structure of the adjusting model is chosen as

$$\hat{x}(t) = \hat{F}\{\tilde{u}(t), \hat{\theta}(t-1)\} \qquad (1)$$

where $\hat{x}(t)$: model output; $\tilde{u}(t)$: input signal; $\hat{F}\{.\}$ is a plant operator estimate; $\hat{\theta}(t) = [\hat{\theta}_1(t)\hat{\theta}_2(t)...\hat{\theta}_N(t)]^T$: model parameter vector that has to be estimated by

using some identification technique; t =0,1,2,...: discrete time; N: plant dimensionality. Using the general parameter approach the model (1) is may be represented by:

$$\hat{x}(t) = \hat{F}\{\tilde{u}(t), \hat{\theta}(0), \tilde{\beta}(t-1)\} \qquad (2)$$

where $\hat{\theta}(0)$: vector of the initial model parameters; $\tilde{\beta}(t) = [\beta_1(t)\beta_2(t)...\beta_M(t)]^T$: general parameter (GP) vector; M: dimensionality of the GP-vector $(1 \le M < N)$. The number of model parameters to be adjusted in the case (2) is reduced to increase the identification algorithm convergence rate. For fixed values of signal/noise ratio the quadratic form $S(t)$ of the general parameter vector error may be considered as an approximation accuracy measure.

The simplest GP-RBFN structure is shown in Fig.3. The equation describing GP-RBFN for a single output network is

$$x = \sum_{j=1}^{K} (w_j^0 + \beta) exp[-\sum_{i=1}^{N} (u_i - c_j)^2 / \delta_j^2] + (w_o^0 + \beta) \qquad (3)$$

where w_j^0 : fixed initial values of network weights; β : scalar general parameter adjusting with the following algorithm

$$\beta = \beta + \gamma_\beta (x^* - x) \times \{\sum_{j=1}^{K} exp[-\sum_{i=1}^{N} (u_i - c_j)^2 / \delta_j^2] + 1\} \qquad (4)$$

where γ_β: adjusting gain; x^*: desired network output.

The steady state expectation and variance of the general parameter provide information about network approximation quality. Both values may be easily calculated and used for decision making purposes. The fuzzy self-organizing network structure determination approach was proposed which results in quasi-optimal structure network with desired approximation ability [6]. The generalized representation of fuzzy rules is as follows

$$R_i : if\ E\{\beta\}\ is\ E_i\ and\ D\{\beta\}\ is\ D_i\ then\ St\ is\ St_i \qquad (5)$$

where i : rule number, $E\{\beta\}$, $D\{\beta\}$: general parameter average and variance correspondingly, St : structure characteristic of neural network to be corrected. In Fig.4 the fuzzy algorithm of GPNN structure determination block-diagram is shown.

The procedure was elaborated for time series model reconstruction and analysis for linear and nonlinear cases. Its background is estimation of general parameter vector statistical characteristics during learning and recall phases. Low memory and computation resources are needed for the procedure realization, especially for diagnosis (recall) stage.

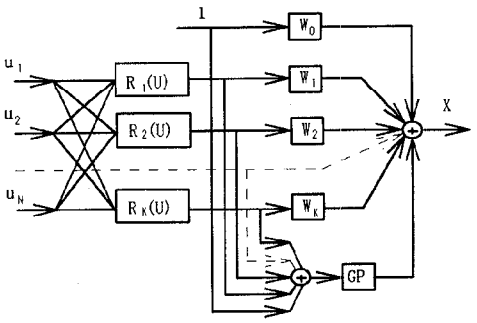

Fig. 3. Simplest GP-RBFN structure.

The block diagram of the time series diagnosis system is shown in Fig.5.

The proposed approach may be considered as a basis of wide class self-organization systems applicable for many AC Drive and UPS control and diagnosis problem solving.

In this section an AC drive controller is presented based on combination of classical state feedback control theory and GP neural network with fuzzy self-organizationof its structure. If the plant or its parts may be

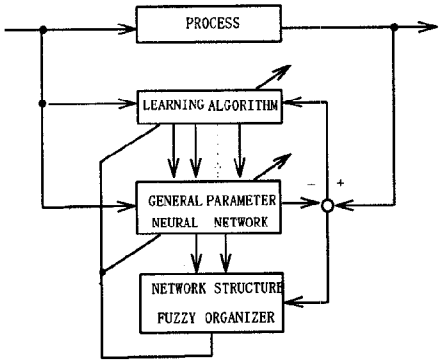

Fig. 4. Fuzzy procedure of GPNN structure determination.

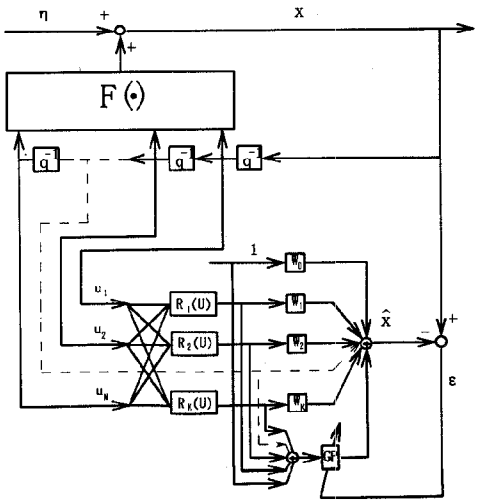

Fig.5. GP-RBFN nonlinear time series identification system.

described in rigorous mathematical form, well formulated and clear analysis and synthesis methods of modern control theory are useful. Meanwhile, specific characteristics of real systems, such us unpredictable load changes, noise and nonlinearities, parameter instability, etc., deteriorate control quality and sometimes make it impossible. Therefore, combined usage of traditional and soft computing approaches may provide advanced control features.

Fig.6 shows an overall servo drive control system which consists of an AC drive, a flexible coupling, a load and controllers [7]. Adaptive state feedback control with a state observer is applied to suppress vibration. A neuro fuzzy feedforward controller with a general parameter adjusting technique and fuzzy logic is designed to cancel the effect of nonlinearities.

C. Waveshape Improvement for UPS Inverter Using Neural Network [8]

In order to obtain less distorted output wave shape for a UPS inverter, various kinds of methods are being developed. As high frequency and large current power semiconductor devices have recently developed, higher carrier frequency can be applied to improve the output waveshape. However, this results in more noise problems.

In this section an improved method to provide better waveforms for a UPS inverter without using a high carrier frequency is proposed by utilizing a neural network based autoregressive moving average model resulting in waveform distortion reduction for nonlinear loads. The network weights are renewed at every sampling instant and also every period for repetitive control (good for periodic external disturbance). The experimental results show that : THD is 5,41% without learning and 2,43% with learning.

D. Adaptive Fuzzy Current Controller with Neural Network for Field-Oriented Induction Machine [9]

Recently, the development of novel control methodology enabled us to improve the performance of AC - machine by using the pulse width modulation (PWM) technique. Usually, the dynamic characteristic of an induction motor (IM) has been represented by a fifth order nonlinear differential equation. The dynamics, however, can be reduced to third order dynamics by applying direct control of IM input current. This methodology shows that it is much easier to control the IM by means of field-oriented methods using the current controller. Therefore precise current control is crucial to achieve a high control performance both in dynamic and steady-state operations.

This section presents an adaptive fuzzy current controller with an artificial neural network (ANN) for the field-oriented controlled IM. This new control structure is able to adaptively minimize a current ripple while maintaning constant switching frequency. The proposed controller uses a neuro-computing philosophy as well as adaptive learning pattern recognizing principles with

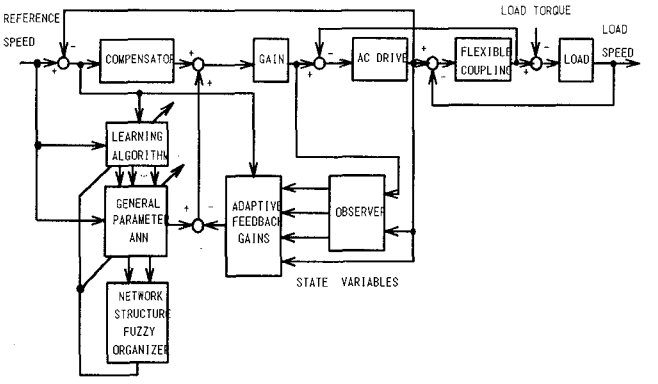

Fig. 6. Neuro fuzzy adaptive vibration suppression control system.

respect to variations of the system parameters. The proposed approach is applied to the IM drive system, and its performance is tested through various simulations. Simulation results show that the proposed system, compared with several known classical methods, has superb performance.

In [10] a neural network is carefully studied. Then it is applied to a model following controller resulting in an excellent controller for drive systems. This is confirmed experimentally.

Reference [11] introduces a neuro induction motor speed observer. Then, it is applied to sensorless speed control for an induction motor. The experimental results are presented. A model reference technique is used to construct the neuro speed observer.

E. Neuro Fuzzy Diagnosis for Induction Motor [12]

Electric motors are exposed to a wide variety of environments and conditions which age the motor and make it subject to incipient faults. These incipient faults, if left undetected, contribute to the degradation and eventual failure of the motors. With proper monitoring and fault detection schemes, the incipient faults can be detected; thus, maintenance and down time expenses can be reduced while also improving safety. Unfortunately, many of the conventional methods used to determine these faults are either very expensive to implement, performed off-line, require the need of an expert, or impractical for small machines.

Artificial neural networks have been proposed and have demonstrated the capability of solving the motor monitoring and fault detection problem using an inexpensive, reliable, and noninvasive procedure. However, the major drawback of conventional artificial neural network fault detection is the inherent black box approach that can provide the correct solution, but does not provide heuristic interpretation of the solution. Engineers prefer the accurate fault detection as well as the heuristic knowledge behind the fault detection process. Fuzzy logic is a technology that can easily provide heuristic reasoning but it is difficult to provide exact solutions. This work introduces the methodology behind a novel hybrid

neural/fuzzy system which merges the neural network and fuzzy logic technologies to solve fault detection problems. This section will also discuss a training procedure for a neural/fuzzy fault detection system. This procedure will be used to determine the correct solutions while providing qualitative, heuristic knowledge about the solutions.

More accurate detection of bearing damage and winding layer shorts for a one-phase induction motor from motor current and motor speed is realized by using a fuzzy neural network. More accurate fault detection is experimentally achieved since the combination of a fuzzy system and a neural network brings effective results as described in the previous section.

III. Genetic Algorithm, Chaos Theory And Immune Network Applied To AC Drives And UPS Systems

A. Fuzzy and Genetic Algorithms Applied to Self-Organizing and Self-Tuning Controllers for Vector-Control Induction Motor Drive [13]

This section proposes a design approach for a self-organizing self-tuning fuzzy logic controller, which is applied to design of a field oriented drive system. The basic structure of a fuzzy logic controller is outlined and the design problems associated with the conventional trial-and-error schemes are addressed. The suitability of the genetic algorithm optimization technique as a means to determine and optimize the fuzzy logic controller design is discussed. In the proposed approach normalization factors and/or membership function parameters and/or the controller policy, are translated into bit-strings. These bit-strings are processed by the genetic algorithm and if the selection process as well as the objective function are chosen properly, a near-optimal solution can be found.

To examine the efficiency of the proposed approach, a self-tuning and self-organizing fuzzy logic controller for an indirect field oriented induction motor drive is designed in both a sequential and a concurrent manner. A particular objective function (i.e. a performance index) is chosen to achieve a high dynamic performance. The simulation results demonstrate a significant enhancement in reducing the development time, and improving system performance over a manually tuned fuzzy logic controller. Fig.7 shows an overall control system. A genetic algorithm is an adaptive method which can be used to solve search and optimization problems. It is based on the biological process of evolution. The starting point is a population of individuals, normally represented as binary strings, that undergoes the operations named after their biological counterparts,such as reproduction, crossover, and mutation. One individual represents one controller design. The given application specifies a fitness value, used to favor the mating of fitter individuals, and thus permitting the most promising areas of search space to be explored. The power of a genetic algorithm comes from the fact that, it does not require the existence of derivatives, it is robust, it can search different areas of space, and consequently it is able

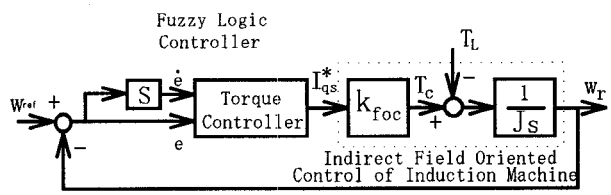

Fig. 7. The Control Block Diagram for the Speed Channel in IFOC of an Induction Motor.

to avoid local minima (if it is properly applied).

To translate the FLC design problem into a genetic algorithm, scaling factors, and/or the membership function parameters, and/or the decision table can be represented by a bit-string, where a field of the bit-string corresponds to a normalization value, or membership function parameter, or table element. In [14] the application of genetic algorithms for optimal induction motor parameter identification is described.

B. Chaos and Fuzzy Computings Applied to Diagnosis of AC Drives and UPS Systems

In [15] short-term prediction of the time series having chaotic behavior is employed to find some deterministic regularity in a phenomenon, which was thought to be noise or to be irregular. For short-term prediction the observed time series is reconstructed in a multi-dimensional state space according to Takens' theorem of embedding and local reconstruction, including the latest observed timeseries.

Proposed methods for this prediction are Gram-Schmidt's orthogonal system method and the tessellation method. However, the former method has a problem that prediction becomes impossible when the selected neighboring vector is not linearly independent. The latter method has a problem that calculation time increases abruptly along with an increase in the dimensions of reconstructed state space. For resolving such problems, Dr. Iokibe proposes the Local Fuzzy Reconstruction method. To verify the effectiveness of this method, he examines the result of its appllication to a short-term prediction of the Lorenz attractor; which has a typical chaotic behavior, and the tap water demand data as used as practical data.

This approach is applied to machine tool breakage and wear prediction for a boring machine resulting in improved accuracy and processing time in comparison with neural network based methods[16]. Reference [17] analyzes PWM Inverter current waveshapes for an induction motor drive by using chaos theory.

C. Immune Network and Neural Network Sensor Failure Detection for Power Electronics Systems

A distributed diagnosis system combining the Immune Network (IN) and Learning Vector Quantization (LVQ) is proposed for accurately detecting faulty sensor outputs in control plants. The system has two execution modes,

namely, its training mode, where the LVQ extracts the correlation between each two sensors from their outputs when they work properly, and its diagnosis mode, where the LVQ contributes to testing each of two sensors using the extracted correlation, and the IN contributes to determining faulty sensors by integrating the local testing results obtained from the LVQ. With the proposed method, faulty sensors can be detected [18,19]. Fig.8 shows an architecture of the developed diagnosis system. This method is applied to sensor failure detection for an induction motor drive [20] and UPS systems [21].

IY. Conclusion

This paper discusses soft computing in power electronics and motion control systems. By using soft computing, intelligent and human friendly power electronics and motion control sytems will be constructed in the future.

Acknowledgement

I thank all members of Emergent Technology Survey Committee on Soft Computing in Industry of the JIEE for providing materials and their research results for this paper. This is the revised paper and is written partly from Chapter 8 of [22]. The original paper was presented at the International Workshop on Soft Computing in Industry, Muroran, Japan, April 27-28, 1996.

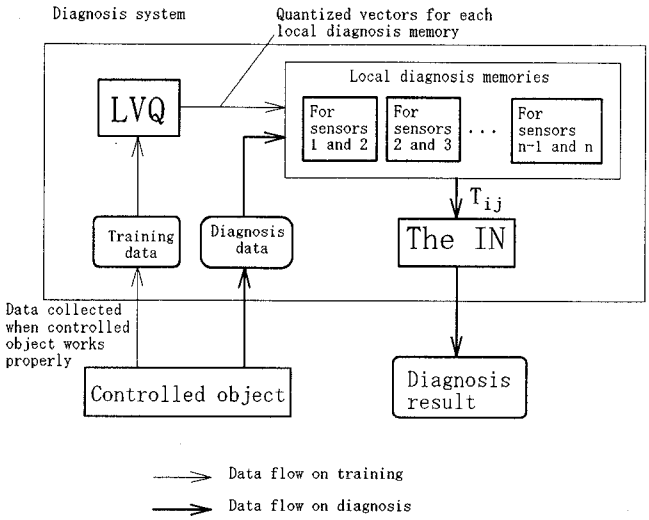

Fig. 8. Architecture of the diagnosis system.

References

[1] Zadeh, L.A.: Fuzzy Logic and Soft Computing, Proc. of the IEEE Int. Workshop on Neuro Fuzzy Control, Muroran, Japan, March 22 - 23, 1993.

[2] Wang, L.X.: Fuzzy Systems are Universal Approximators, Proc. of the IEEE Fuzzy Systems, San Francisco U.S.A., 1992.

[3] Abe, S., 1995, "Fuzzy Systems and Neural Network - Theories and Applications", Kinda: Kagaku-sha, in Japanese.

[4] Strefezza, M., Kobayashi, H., Fujikawa, K., and Dote, Y.: Fuzzy Robust Control for AC Drive System, Journal of Systems Engineering, No.4, 1994.

[5] Akhmetov, D., and Dote, Y.: Novel "on-line" identification procedure using artificial neural network, Proc.of the IFAC Workshop on On-Line Fault Detection and Supervision in the Chemical Process Industries, Newcastle, U.K., June 1995.

[6] Akhmetov, D., and Dote, Y. General parameter neural networks with fuzzy self-organization, Proc. of the Artificial Neural Networks in Eng ineering (ANNIE'96), pp.191-196, St. Louis, Missouri, U.S.A., 1996.

[7] Dote, Y., and Akhmetov, D. : Adaptive vibration suppression control for torsional system driven by fuzzy robust AC drive system, Proc. of the International Conference on Recent Advances in Mechatronics, Istanbul, Turkey, August 14-16, 1995.

[8] Matsuo, H., Haneyashi, T., Miyashita, M., and Haneda, A. : Waveshape improvement for UPS inverter using neural network, Proc. of the JIEE Application Society Conference, Matsuyama Japan, Aug. 1994, in Japanese.

[9] Cho, K.B., and Lee, K.C. : An adaptive fuzzy current controller with neural network for a field-oriented controller induction machine", Journal of Approximate Reasoning, No.1 1994.

[10] El - Sharkawi, M.A. : Neural network application to high performance electric drives systems", Proc. of the IECON, Orland Fl, U.S.A., Nov. 1995.

[11] Ben-Brahim, L., Kudor, T., Shimane, K., and Naito, H. : Implementation of an induction motor speed estimator using neural networks", Proc. of the IPEC, Yokohama Japan, April, 1995.

[12] Goode, P.V., Chow, M.Y. : Using a neural/fuzzy system to extract heuristic knowledge of incipient faults in induction motors: Part I and Part II, IEEE Trans. on IE, Vol.42 No.2, April 1995.

[13] Ashfrazadeh, F., Nowicki, E.P., and Salmov, J.C.: A self-organizing and self-tuning fuzzy logic controller for field oriented control of induction motor drives", Proc. of the IAS, Orland Fl, U.S.A., 1995.

[14] Nollan, R., Pillay, P., and Hague, T. : Application of genetic algorithms to motor parameter detemination, Proc. of the IAS Meeting, 1994.

[15] Iokibe, T., and Ohshima, N. : An application of short-term prediction by local fuzzy reconstruction method to chaotic time series", Proc.of the IEEE Tokyo Section Denshi, Tokyo, No.33 1994.

[16] Nishimura, T., and Dote, Y.: Machine tool breakage prediction by chaos theory", BS Thesis, Muroran Inst. of Tech., March 1996.

[17] Nagy, I., Matakas, L., Jr., and Masada, E. : Application of the theory of chaos in PWM technique of induction motors, Proc. of the IPEC, Yokohama Japan, April 1995.

[18] Kayama, M., Sugita, Y., Morooka, Y., and Fukuoka, S. : Distributed diagnosis system combining the immune network and learning vector quantization", Proc. of the IECON, Orland U.S.A., Nov. 1995.

[19] Ishida, Y. et al. : Learning algorithm on an immune network : Application to sensor diagnosis, Proc. of the IJCNN'92, Beijing, 1992.

[20] Tanno, T., and Dote, Y. : Sensor failure detection with immune network for induction motor drive system", MS Thesis, Muroran Inst. of Tech., March 1996.

[21] Nagano, Y., Akhmetov, D., and Dote, Y. : Sensor failure detection with immune network for UPS systems, BS Thesis, Muroran Inst. of Tech., March 1997 (to appear).

[22] Y.Dote and R.G.Hoft : Intelligent Control of AC Drives and UPS Systems. Oxford Univ. Press, U.K. 1997 to be published (with Dr. L.A.Zadeh's foreword).

New Digital Redesign Method by N-Delay Control and its Application

Hiroshi Fujimoto* Atsuo Kawamura**

Department of Electrical and Computer Engineering, Yokohama National University
79-5 Tokiwadai, Hodogaya-ku, Yokohama 240 Japan
Fax: +81-45-338-1157 Phone +81-45-339-4162
E-mail: * fuji@kawalab.dnj.ynu.ac.jp ** kawamura@kawalab.dnj.ynu.ac.jp

Abstract— **A new digital redesign method is proposed for feedback control systems, by which the states in the continuous-time system are completely reserved in the redesigned sampled-data system. The features of the proposed method are 1) the N-Delay control is employed, and the lth plant input is changed N_l times during one sampling period, 2) the states of the redesigned sampled-data system completely match those of the original continuous-time closed-loop system at every sampling period, and 3) the proposed redesign method can be applicable for a state-feedback and/or a dynamic controller.**

An illustrative example of position control using a DC servo motor is presented. The advantages of the proposed redesign approach are demonstrated both in the time and frequency domains.

I. Introduction

Owing to the recent developments of the computer and interface hardware, digital controllers are always utilized for controlling robots or motors because of cost, reliability, flexibility, compactness, and so on.

The digital redesign is a technique by which an analog controller designed in continuous-time is converted to an equivalent digital controller[1]. It is, in general, very difficult to let the states of digital system match those of the original continuous-time system.

Historically, one of the most popular digital redesign methods is the Tustin (or bilinear) transformation, in which an s-domain analog controller is transformed to a z-domain digital controller by

$$s = \frac{2(z-1)}{T(z+1)} \tag{1}$$

This approach is straightforward, and the stable poles of the controller in s-domain are mapped inside of the unit circle in z-domain. However, the closed-loop stability is not assured. Therefore, in this approach, the feedback system may become unstable if the sampling time is set too large.

In [1][2][3], the digital redesign methods based on the closed-loop characteristics were developed. However, these attempts did not assure the closed-loop stability, because approximations were assumed for obtaining solutions of the digital redesign (see chapter II). In [4], the forward and feedback gains are altered at every sampling period, so that the states of the two systems match at the end of N sampling periods. The method in [4] is similar to the proposed method only in some special cases. However, the number of times of gain alternation, N, is redundant compared to the proposed method in this paper.

The method in [1] was further investigated in [5], and a different approximation was proposed for obtaining a solution of the digital redesign, in which the closed-loop stability was maintained. However, the transition matrices of the original and approximately redesigned systems are not same. Furthermore, the methods in [1][2][3][4][5] have a limitation that the original continuous-time controller must be of state-feedback type and that all of plant state variables must be directly detected.

The other digital redesign methods for a dynamic controller were developed in [6][7][8]. These methods tried to match closed-loop frequency response approximately. However, because of using these approximation, the closed-loop stability could not be assured[6][7], or the solution of the digital redesign could not be obtained in large sampling period[8].

The purpose of the proposed method is to develop a new digital controller from the analog controller so that all of the states of the sampled-data closed-loop system completely match those of the original continuous-time closed-loop system at every sampling instance. Thus, the stability of the closed-loop system is retained, and the transition matrices of the two systems become identical. In the proposed method, the multirate-input digital control is employed, and the lth plant input is changed N_l times during one sampling period[9][10]. We call this method N-Delay control after [11]. The digital redesigned controller can be automatically calculated following the proposed procedure. Moreover, the redesign method for an observer is also presented, in which the multirate-output digital control is employed. Therefore, the proposed method can deal with the system even if a part of plant states are not directly detected. The proposed digital redesign method is applicable both to a continuous-time state-feedback controller and a dynamic controller.

0-7803-3823-5/97/$10.00© 1997 IEEE

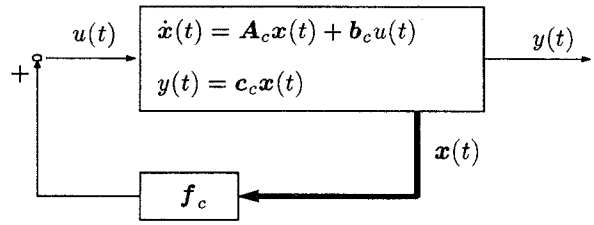

Fig. 1. Continuous-time state-feedback control system.

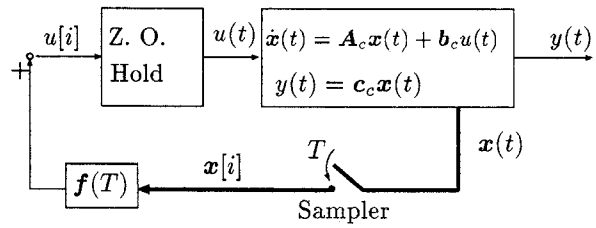

Fig. 2. Discrete-time state-feedback control system.

II. Problem of Digital Redesign by Complete State Matching

In this section, we consider a problem of matching the responses of an existing continuous-time system shown in Fig. 1, with those of the discrete-time system shown in Fig. 2 for the same initial conditions. Consider the linear continuous-time system described by

$$\dot{x}(t) = A_c x(t) + b_c u(t) \tag{2}$$

Also, let the continuous-time state-feedback control law be

$$u(t) = f_c x(t) \tag{3}$$

The continuous-time closed-loop system becomes

$$\dot{x}(t) = (A_c + b_c f_c) x(t) \tag{4}$$

and its sampled-data system with the sampling period T is

$$x((i+1)T) = e^{(A_c + b_c f_c)T} x(iT) \tag{5}$$

Consider the discrete-time system utilizing a zero-order hold described by

$$x[i+1] = Ax[i] + bu[i] \tag{6}$$

where $x[i] = x(iT)$, $A \triangleq e^{A_c T}$, and $b \triangleq \int_0^T e^{A_c \tau} d\tau b_c$. Letting the discrete-time state-feedback control law be $u[i] = f(T)x[i]$, the discrete-time closed-loop system becomes

$$x[i+1] = (A + bf(T))x[i] \tag{7}$$

From (5) and (7), the digital redesign problem is to find the discrete-time gain $f(T)$ from the continuous-time gain f_c so that the equation

$$A + bf(T) = e^{(A_c + b_c f_c)T} \tag{8}$$

is satisfied. If the above condition is satisfied, the states of digitally controlled system in (7) completely match those of continuous-time system in (5) at every sampling period T. The existence of $f(T)$ in (8), however, is not always guaranteed because the dimension of the input is generally less than that of the state. Therefore, in [1][2], (8) is approximately solved for $f(T)$. But, because of the approximation, the stability of the obtained digital closed-loop system is not always assured, and the time response is different from that of the continuous-time feedback system.

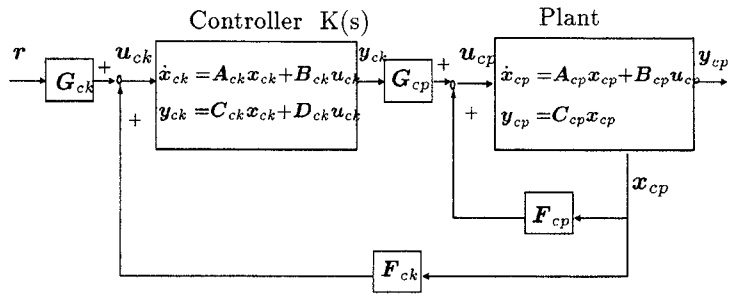

Fig. 3. Continuous-time control system.

III. Digital Redesign by N-Delay Control

In this section, a new digital redesign method by the N-Delay input control is presented, in which the lth plant input is changed N_l times during one sampling period. The introduction of the N-Delay input control causes the increase of the input dimension, thus (8) can be solved without any approximation. Moreover, the proposed method is applicable either to a continuous-time dynamic controller or a state-feedback controller. The proposed method succeeds in this generalization by the introduction of 1) the closed-loop augmented system consisting of the plant and the dynamic controller, and 2) the N-Delay input control.

Consider the continuous-time plant described by

$$\dot{x}_{cp}(t) = A_{cp}x_{cp}(t) + B_{cp}u_{cp}(t) \tag{9}$$

$$y_{cp}(t) = C_{cp}x_{cp}(t) \tag{10}$$

where the plant state $x_{cp} \in R^{n_p}$, the plant input $u_{cp} \in R^{m_p}$, and the plant output $y_{cp} \in R^{p_p}$. As shown in Fig. 3, let the continuous-time control law using a state-feedback and/or dynamic controller be

$$u_{cp}(t) = F_{cp}x_{cp}(t) + G_{cp}y_{ck}(t) \tag{11}$$

where the dynamic controller's output $y_{ck} \in R^{p_k}$. Let the dynamic controller $K(s)$ be represented by

$$\dot{x}_{ck}(t) = A_{ck}x_{ck}(t) + B_{ck}u_{ck}(t) \tag{12}$$

$$y_{ck}(t) = C_{ck}x_{ck}(t) + D_{ck}u_{ck}(t) \tag{13}$$

where the dynamic controller's state $x_{ck} \in R^{n_k}$, input $u_{ck} \in R^{m_k}$. Let the controller's input be given by

$$u_{ck}(t) = F_{ck}x_{cp}(t) + G_{ck}r(t) \tag{14}$$

where the reference input $r \in R^{m_r}$ is piecewise-

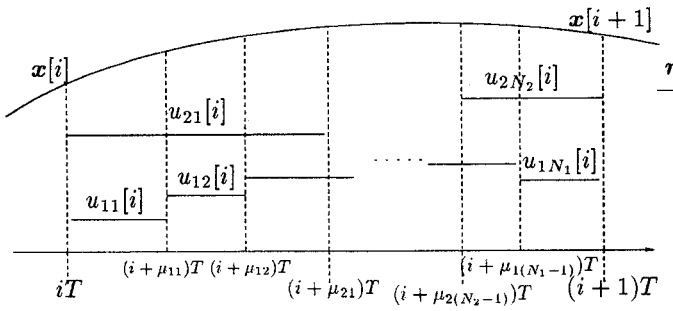

Fig. 4. N-Delay input control.

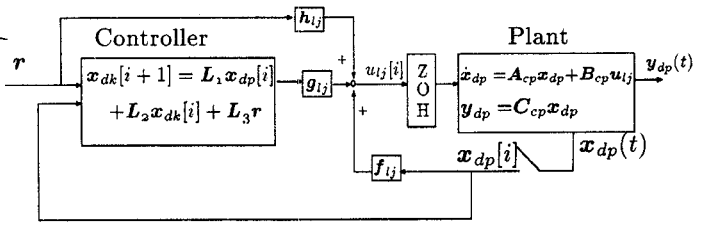

Fig. 5. Discrete-time control system.

constant. i.e. $\boldsymbol{r}(t) = \boldsymbol{r}(iT)$ for $iT \le t < (i+1)T$. From (9) $\sim$ (14), the continuous-time closed-loop augmented system consisting of the plant and the dynamic controller is represented by

$$\dot{\bar{\boldsymbol{x}}}_c(t) = \bar{\boldsymbol{A}}_c\bar{\boldsymbol{x}}_c(t) + \bar{\boldsymbol{B}}_c\boldsymbol{r}(t) \tag{15}$$

where

$$\bar{\boldsymbol{A}}_c \triangleq \begin{bmatrix} \boldsymbol{A}_{cp}+\boldsymbol{B}_{cp}\boldsymbol{F}_{cp}+\boldsymbol{B}_{cp}\boldsymbol{G}_{cp}\boldsymbol{D}_{ck}\boldsymbol{F}_{ck} & \boldsymbol{B}_{cp}\boldsymbol{G}_{cp}\boldsymbol{C}_{ck} \\ \boldsymbol{B}_{ck}\boldsymbol{F}_{ck} & \boldsymbol{A}_{ck} \end{bmatrix}$$

$$\bar{\boldsymbol{B}}_c \triangleq \begin{bmatrix} \boldsymbol{B}_{cp}\boldsymbol{G}_{cp}\boldsymbol{D}_{ck}\boldsymbol{G}_{ck} \\ \boldsymbol{B}_{ck}\boldsymbol{G}_{ck} \end{bmatrix}, \quad \bar{\boldsymbol{x}}_c \triangleq \begin{bmatrix} \boldsymbol{x}_{cp} \\ \boldsymbol{x}_{ck} \end{bmatrix} \tag{16}$$

and the sampled-data system for the sampling period T becomes

$$\bar{\boldsymbol{x}}_c((i+1)T) = \bar{\boldsymbol{A}}\bar{\boldsymbol{x}}_c(iT) + \bar{\boldsymbol{B}}\boldsymbol{r}(iT) \tag{17}$$

where

$$\bar{\boldsymbol{A}} \triangleq e^{\bar{\boldsymbol{A}}_c T} \triangleq \begin{matrix} \\ n_p \\ n_k \end{matrix} \begin{matrix} \begin{matrix} n_p & n_k \end{matrix} \\ \begin{bmatrix} \bar{\boldsymbol{A}}_{11} & \bar{\boldsymbol{A}}_{12} \\ \bar{\boldsymbol{A}}_{21} & \bar{\boldsymbol{A}}_{22} \end{bmatrix} \end{matrix} \tag{18}$$

$$\bar{\boldsymbol{B}} \triangleq \int_0^T e^{\bar{\boldsymbol{A}}_c\tau}\bar{\boldsymbol{B}}_c d\tau \triangleq \begin{matrix} \\ n_p \\ n_k \end{matrix} \begin{matrix} \begin{matrix} m_r \end{matrix} \\ \begin{bmatrix} \bar{\boldsymbol{B}}_1 \\ \bar{\boldsymbol{B}}_2 \end{bmatrix} \end{matrix} \tag{19}$$

The redesigned digital control system is required for the exact matching of the states $\bar{\boldsymbol{x}}_c$ at every sampling instant. In the N-Delay control, the lth ($l = 1, 2, .., m_p$) plant input is changed N_l times during one sampling period as shown in Fig. 4. $(N_1, .., N_{m_p})$ are referred to as input multiplicities[9] [10]. The selections of N_l are made by the following condition.

$$N_l \ge \sigma_l \tag{20}$$

where $(\sigma_1, ..., \sigma_{m_p})$ are a set of controllability indices of $(\boldsymbol{A}_{cp}, \boldsymbol{B}_{cp})$ defined in [9][10].

The discrete-time plant using N-Delay input control is given by

$$\boldsymbol{x}_{dp}[i+1] = \boldsymbol{A}_{dp}\boldsymbol{x}_{dp}[i] + \sum_{l=1}^{m_p}\sum_{j=1}^{N_l}\boldsymbol{b}_{lj}u_{lj}[i] \tag{21}$$

where $\boldsymbol{x}_{dp} \in \boldsymbol{R}^{n_p}$ is the plant state, $u_{lj}[i] \in \boldsymbol{R}^1$ is the lth plant input for $(i+\mu_{l(j-1)})T \le t < (i+\mu_{lj})T$ $(l = 1, .., m_p\ ,\ j = 1, .., N_l)$,

$$\boldsymbol{A}_{dp} \triangleq e^{\boldsymbol{A}_{cp}T}, \boldsymbol{b}_{lj} \triangleq \int_{(1-\mu_{lj})T}^{(1-\mu_{l(j-1)})T} e^{\boldsymbol{A}_{cp}\tau}\boldsymbol{b}_{cl}d\tau \tag{22}$$

$$0 = \mu_{l0} < \mu_{l1} < \mu_{l2} < ... < \mu_{lN_l} = 1 \tag{23}$$

As shown in Fig. 5, let the dynamics of discrete-time controller be

$$\boldsymbol{x}_{dk}[i+1] = \boldsymbol{L}_1\boldsymbol{x}_{dp}[i] + \boldsymbol{L}_2\boldsymbol{x}_{dk}[i] + \boldsymbol{L}_3\boldsymbol{r}[i] \tag{24}$$

where the discrete-time dynamic controller's state $\boldsymbol{x}_{dk} \in \boldsymbol{R}^{n_k}$. Let the discrete-time control law be

$$\boldsymbol{u}_{lj}[i] = \boldsymbol{f}_{lj}\boldsymbol{x}_{dp}[i] + \boldsymbol{g}_{lj}\boldsymbol{x}_{dk}[i] + \boldsymbol{h}_{lj}\boldsymbol{r}[i] \tag{25}$$

From (21) $\sim$ (25), the discrete-time closed-loop augmented system is represented by

$$\bar{\boldsymbol{x}}_d[i+1] = \bar{\boldsymbol{A}}_d\bar{\boldsymbol{x}}_d[i] + \bar{\boldsymbol{B}}_d\boldsymbol{r}[i] \tag{26}$$

where

$$\bar{\boldsymbol{A}}_d \triangleq \begin{bmatrix} \boldsymbol{A}_{dp}+\boldsymbol{B}\boldsymbol{F} & \boldsymbol{B}\boldsymbol{G} \\ \boldsymbol{L}_1 & \boldsymbol{L}_2 \end{bmatrix}$$

$$\bar{\boldsymbol{B}}_d \triangleq \begin{bmatrix} \boldsymbol{B}\boldsymbol{H} \\ \boldsymbol{L}_3 \end{bmatrix}, \bar{\boldsymbol{x}}_d \triangleq \begin{bmatrix} \boldsymbol{x}_{dp} \\ \boldsymbol{x}_{dk} \end{bmatrix} \tag{27}$$

$$\begin{aligned} \boldsymbol{B} &\triangleq [\boldsymbol{b}_{11}, .., \boldsymbol{b}_{1N_1}, \boldsymbol{b}_{21}, .., \boldsymbol{b}_{m_pN_{m_p}}] && (n_p \times N) \\ \boldsymbol{F} &\triangleq [\boldsymbol{f}_{11}^T, .., \boldsymbol{f}_{1N_1}^T, \boldsymbol{f}_{21}^T, .., \boldsymbol{f}_{m_pN_{m_p}}^T]^T && (N \times n_p) \\ \boldsymbol{G} &\triangleq [\boldsymbol{g}_{11}^T, .., \boldsymbol{g}_{1N_1}^T, \boldsymbol{g}_{21}^T, .., \boldsymbol{g}_{m_pN_{m_p}}^T]^T && (N \times n_k) \\ \boldsymbol{H} &\triangleq [\boldsymbol{h}_{11}^T, .., \boldsymbol{h}_{1N_1}^T, \boldsymbol{h}_{21}^T, .., \boldsymbol{h}_{m_pN_{m_p}}^T]^T && (N \times m_r) \\ N &\triangleq N_1 + N_2 + ... + N_{m_p} \ge n_p \end{aligned}$$

Comparing (17) and (26), if the following conditions are satisfied, the states of the digitally controlled system $(\bar{\boldsymbol{x}}_c)$ completely match the states of the continuous-time system $(\bar{\boldsymbol{x}}_d)$ at every sampling period.

$$\begin{bmatrix} \bar{\boldsymbol{A}}_{11} & \bar{\boldsymbol{A}}_{12} \\ \bar{\boldsymbol{A}}_{21} & \bar{\boldsymbol{A}}_{22} \end{bmatrix} = \begin{bmatrix} \boldsymbol{A}_{dp}+\boldsymbol{B}\boldsymbol{F} & \boldsymbol{B}\boldsymbol{G} \\ \boldsymbol{L}_1 & \boldsymbol{L}_2 \end{bmatrix}$$

$$\begin{bmatrix} \bar{\boldsymbol{B}}_1 \\ \bar{\boldsymbol{B}}_2 \end{bmatrix} = \begin{bmatrix} \boldsymbol{B}\boldsymbol{H} \\ \boldsymbol{L}_3 \end{bmatrix} \tag{28}$$

Here, the necessary and sufficient condition for solution of linear matrix equation $(\boldsymbol{A}\boldsymbol{x} = \boldsymbol{b})$ is [12]

$$rank\boldsymbol{A} = rank[\boldsymbol{A}, b] \tag{29}$$

Therefore, the necessary and sufficient conditions for existence of $\boldsymbol{F}, \boldsymbol{G}, \boldsymbol{H}$ in (28) are given by

$$\begin{aligned} rank\boldsymbol{B} &= rank[\boldsymbol{B}, \bar{\boldsymbol{A}}_{11} - \boldsymbol{A}_{dp}] \\ &= rank[\boldsymbol{B}, \bar{\boldsymbol{A}}_{12}] = rank[\boldsymbol{B}, \bar{\boldsymbol{B}}_1] \end{aligned} \quad (30)$$

Concerning the matrix $\boldsymbol{B}$, the next theorem is proved in [13].

Theorem 1: Let $(\boldsymbol{A}_{cp}, \boldsymbol{B}_{cp})$ be an controllable pair. If the input multiplicities satisfy $N_l \geq \sigma_l$ for $(l = 1, 2, .., m_p)$, for almost all $\mu_{lj} (l = 1, 2, .., m_p, j = 1, .., N_l - 1)$ and almost all T, the matrix $\boldsymbol{B}$ has full row rank. i.e.

$$rank\boldsymbol{B} = n_p \quad (31)$$

Because of this theorem, the row rank $\boldsymbol{B}$ in (30) is full, thus, (30) is satisfied. As a result, the existence of $\boldsymbol{F}, \boldsymbol{G}, \boldsymbol{H}$ in (28) is assured. Solving (28), the redesigned parameters are given by

$$\begin{aligned} &\boldsymbol{F} = \boldsymbol{B}^{-}(\bar{\boldsymbol{A}}_{11} - \boldsymbol{A}_{dp}), \boldsymbol{G} = \boldsymbol{B}^{-}\bar{\boldsymbol{A}}_{12}, \boldsymbol{H} = \boldsymbol{B}^{-}\bar{\boldsymbol{B}}_1 \\ &\boldsymbol{L}_1 = \bar{\boldsymbol{A}}_{21} \ , \ \boldsymbol{L}_2 = \bar{\boldsymbol{A}}_{22} \ , \ \boldsymbol{L}_3 = \bar{\boldsymbol{B}}_2 \end{aligned} \quad (32)$$

where $\boldsymbol{B}^{-}$ is generalized inverse of matrix $\boldsymbol{B}$ [12].

Comments 1) if $(\boldsymbol{A}_{cp}, \boldsymbol{B}_{cp})$ is an controllable pair, the system, which is controlled by either a continuous-time dynamic controller or a state-feedback controller, can be always redesigned in this method. 2) If the original continuous-time system is stably designed, the redesigned system is assured to be stable [13] [14]. 3) The states of the redesigned sampled-data system completely match those of the original continuous-time closed-loop system at every sampling period independent of sampling period. Therefore, the proposed method is superior to the conventional method such as Tustin transformation and the other methods [1]–[8].

Furthermore, using the duality of the redesign method mentioned above, it is possible to redesign a new digital observer from an original analog observer. The redesign method for observer is based on the multirate sampling, in which the qth plant output is detected M_q times during one sampling period, and the discrete-time estimation errors completely match the continuous-time estimation errors at every sampling period. Detail will be found in [13].

IV. Illustrative Example

A. Digital redesign of a position control system for a DC servo motor with the disturbance observer

In this section, simulation and experimental results for a position control system for a DC servo motor with the disturbance observer are presented as shown in Fig. 6.

In the experiments, DSP(NEC: μPD77230, 32-b floating point) are used, and the 1/100 gear ratio DC servo motor is driven by a 10-kHz switching frequency MOSFET chopper. The pulse counter generates 1 000 pulse per revolution on the motor shaft (it becomes 100 000 pulse/revolution on the geared shaft), and the speed is detected through a 12-b A/D converter by a tachometer [15].

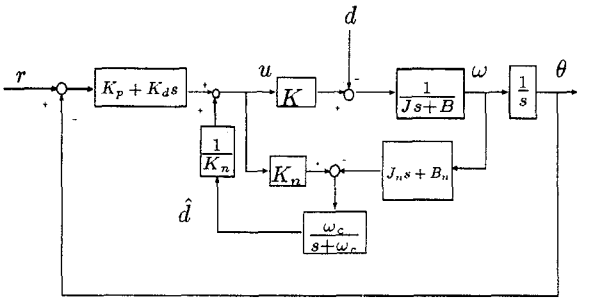

Fig. 6. The position control with the disturbance observer.

In the design of the continuous-time controller, assuming that the disturbance torque d is a step function type, the plant is represented by

$$\dot{\boldsymbol{x}}_{cp}(t) = \boldsymbol{A}_{cp}\boldsymbol{x}_{cp}(t) + \boldsymbol{b}_{cp}u_{cp}(t) \quad (33)$$

$$\boldsymbol{A}_{cp} = \begin{bmatrix} 0 & 1 & 0 \\ 0 & -\frac{B}{J} & -\frac{1}{J} \\ 0 & 0 & 0 \end{bmatrix}, \boldsymbol{b}_{cp} = \begin{bmatrix} 0 \\ \frac{K}{J} \\ 0 \end{bmatrix}, \boldsymbol{x}_{cp} = \begin{bmatrix} \theta \\ \omega \\ d \end{bmatrix}$$

where θ is angular position, ω is angular velocity, and u_{cp} is the DC voltage of the motor terminal. Assuming the command input r to be a step function type, the continuous-time control law is given by

$$\begin{aligned} u_{cp} &= K_p(r - \theta) - K_d\omega + \tfrac{1}{K_n}\hat{d} \\ &= \boldsymbol{f}_{cp}\hat{\boldsymbol{x}}_{cp} + g_{cp}r \end{aligned} \quad (34)$$

where $\boldsymbol{f}_{cp} = [-K_p, -K_d, \frac{1}{K_n}]$, $g_{cp} = K_p$, $\hat{\boldsymbol{x}}_{cp} = [\theta, \omega, \hat{d}]^T$. As shown in Fig. 6, the continuous-time disturbance observer is also given by

$$\begin{aligned} \dot{\hat{v}}_c(t) &= \hat{A}_c\hat{v}_c(t) + \hat{B}_c\omega(t) + \hat{J}_c u_{cp}(t) \\ \hat{d}(t) &= \hat{v}_c(t) + l_c\ \omega(t) \end{aligned} \quad (35)$$

where $\hat{A}_c = -\omega_c$, $\hat{B}_c = -B_n\omega_c + J_n\omega_c^2$, $\hat{J}_c = K_n\omega_c$, and ω_c is the cut-off frequency of low pass filter.

The nominal values of plant constants are $J_n = 0.0730[\text{kg}\cdot\text{m}^2]$,$B_n = 3.26[\text{kg}\cdot\text{m}^2/\text{s}]$,$K_n = 0.388[\text{N}\cdot\text{m/V}]$. Also, the continuous-time control parameters are $K_p = 8.91, K_d = -4.99, \omega_c = 300[\text{rad/s}]$.

First, the control law (34) is redesigned. Although $(\boldsymbol{A}_{cp}, \boldsymbol{B}_{cp})$ in (33) is not controllable, the conditions in (30) are satisfied for input multiplicity $N_1 = 2$. From (32), the redesigned control law for $T = 0.4[ms], \mu_{11} = 0.5$ is obtained, as follows

$$\begin{bmatrix} \boldsymbol{u}_{11}[i] \\ \boldsymbol{u}_{12}[i] \end{bmatrix} = \begin{bmatrix} -33.4 & 3.38 & 2.57 \\ -33.6 & 3.34 & 2.57 \end{bmatrix} \begin{bmatrix} \theta[i] \\ \omega[i] \\ \hat{d}[i] \end{bmatrix} + \begin{bmatrix} 33.4 \\ 33.6 \end{bmatrix} \boldsymbol{r}[i]$$

Second, the disturbance observer in (35) is redesigned. For $T = 0.4[ms], \mu_{11} = 0.5$, the discrete-time observer is obtained [13] by

$$\begin{aligned} \hat{v}_d[i+1] &= \hat{A}_d\hat{v}_d[i] + \hat{B}_d\omega[i] + \hat{J}_{11}u_{11}[i] + \hat{J}_{12}u_{12}[i] \\ \hat{d}[i] &= \hat{v}_d[i] + l_d\ \omega[i] \end{aligned} \quad (36)$$

where $l_d = -20.8, \hat{A}_d = 0.887, \hat{B}_d = 1.99, \hat{J}_{11} = 2.12 \times 10^{-2}, \hat{J}_{12} = 2.21 \times 10^{-2}$.

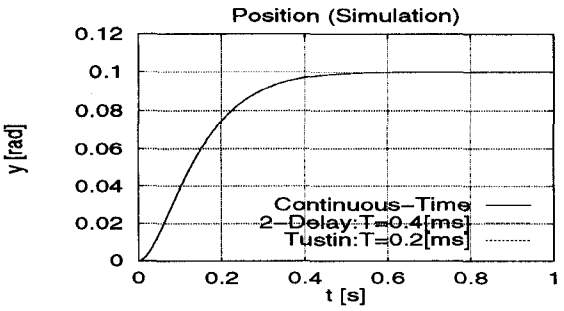

(a) Position responses ($T_u = 0.2[ms]$).

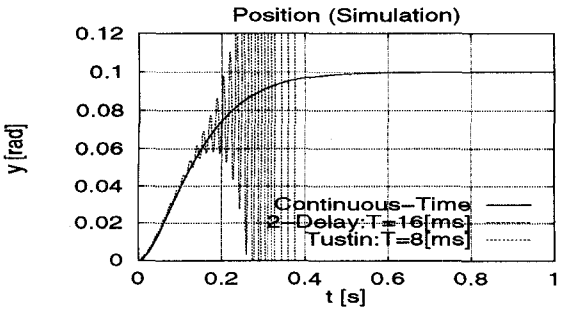

(b) Position responses ($T_u = 8[ms]$).

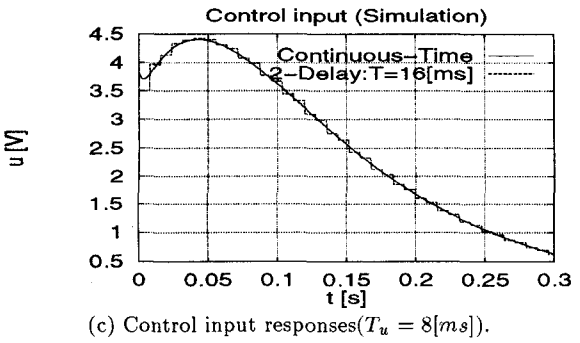

(c) Control input responses($T_u = 8[ms]$).

Fig. 7. Simulation results.

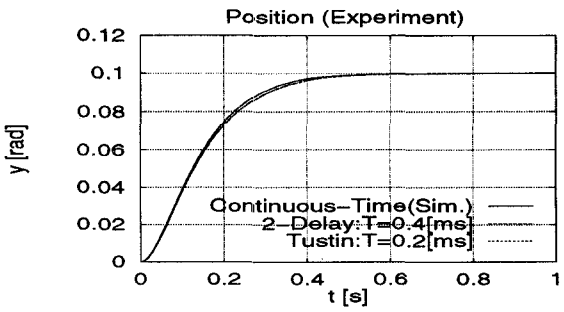

(a) Position responses ($T_u = 0.2[ms]$).

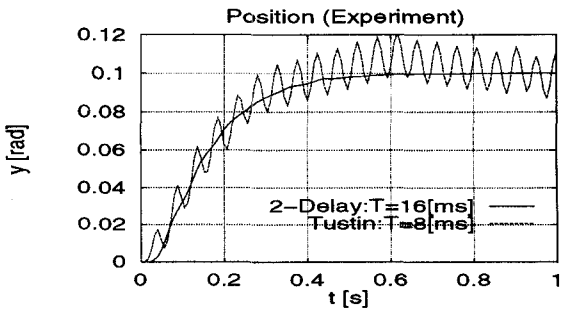

(b) Position responses ($T_u = 8[ms]$).

Fig. 8. Experiment results.

B. Simulations and experiments

Because the redesign system uses the 2-Delay input control, the output sampling period T is twice as long as the input sampling period T_u. In the following simulations and experiments, the proposed method(2-Delay) is compared with the Tustin(bilinear) transformation at same input sampling period so that the calculation costs of two systems may be equal and these comparisons may be fair. Therefore, the output sampling period of proposed method is twice as long as that of Tustin transformation.

Simulated and Experimental results are shown in Fig. 7, 8. In the very short sampling period (0.2 [ms]), we find the Tustin transformation and the proposed transformation have the almost same time response. However, in the long sampling period (8 [ms]), as shown in Fig. 7,8(b), the proposed method gives better performance than the Tustin transformation. While the response of Tustin transformation is unstable, that of the proposed method is stable, and exactly matches the continuous time response.

The simulated time responses of the control input are shown in Fig. 7(c), which indicates that the control input of the proposed method is smooth in spite of using 2-Delay control.

C. Frequency responses of the closed-loop systems

The frequency responses from the command input (r) to the plant state (θ) are shown in Fig. 9(a). In the wide frequency band lower than the Nyquist frequency, the discrete-time response redesigned by the proposed method ($G_{yr}[z]$) matches the continuous-time response ($G_{yr}(s)$). That is guaranteed by (17), (26) and (28).

The frequency responses from the disturbance torque (d) to the plant state (θ) are also shown in Fig. 9(b), which indicates that the longer the sampling period is, the poorer the disturbance rejection performance is. Therefore, Fig. 9(b) tells us the practical limitations of the sampling period for the proposed method.

D. Disturbance responses

The simulation results of the time responses under the step function type disturbances (5 [N · m], t > 1 [s]) are shown in Fig. 10. In the short sampling period (0.4 [ms]), the redesigned system has almost as same performance as the continuous-time system. However, as mentioned above (Fig. 9(b)), the disturbance rejection performance becomes poor in the large sampling period (16 [ms]).

The time responses of the disturbance estimation errors are shown in Fig. 10(b). The estimation error of the discrete-time observer which is obtained by the proposed method[13] completely matches that of the continuous-time observer at every sampling period. Fig.

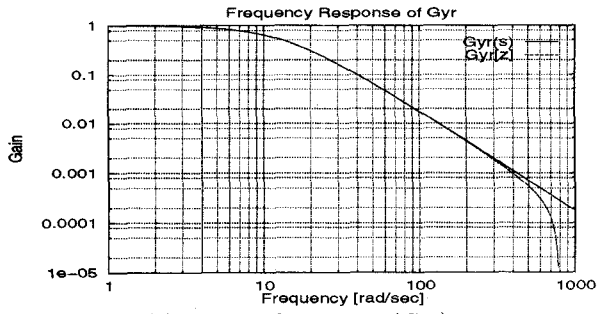

(a) Command responses (G_{yr}).

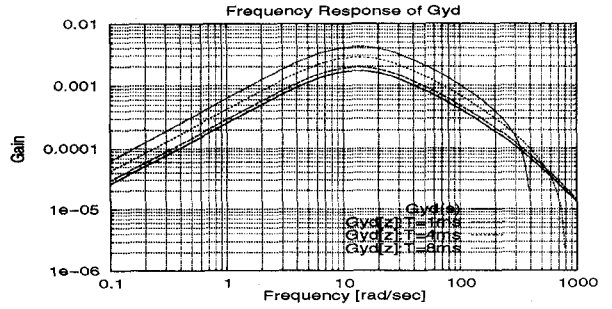

(b) Disturbance responses (G_{yd}).

Fig. 9. Frequency responses.

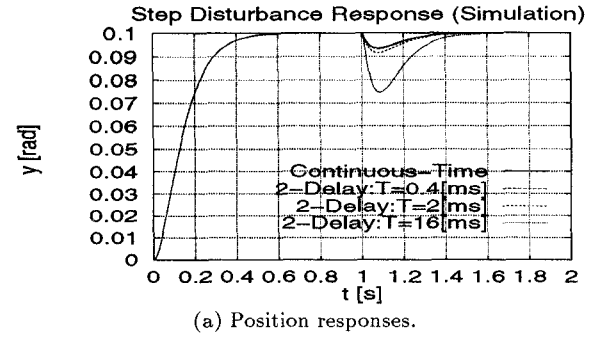

(a) Position responses.

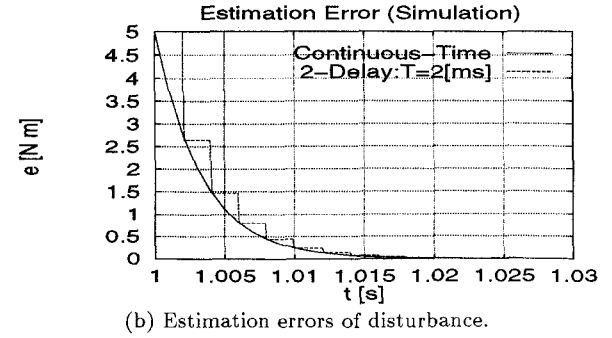

(b) Estimation errors of disturbance.

Fig. 10. Responses under step type disturbance(simulation).

10(b) also assures that there is no offset between the command input (r) and the plant state (θ) [16].

V. Conclusion

A new digital redesign method in use of N-Delay control was proposed. And a position control using a DC servo motor was selected for an example, and simulations and experiments were performed, which indicated that the proposed method had better performance than that of the Tustin transformed digital controller. Moreover, the disturbance rejection performances are considered both in the time and frequency domains.

One of the remarkable advantages of the proposed method is that the states of the sampled-data system completely become equal to those of the continuous-time system independent of sampling period, and as a result, the stability of the redesigned system is assured. The choice of μ_{lj} (a parameter of input sampling period) should be further investigated for the optimal inter-sample time responses and the smoothest control inputs.

References

[1] B. C. Kuo: "Digital Control Systems", Holt Rinehart and Winston Inc. (1980).

[2] B. C. Kuo and D. W. Peterson: "Optimal discretization of continuous-data control system", Automatica, **9**, pp. 125–129 (1973).

[3] L. S. Shieh, J. L. Zhang and S. Ganesan: "Pseudo-continuous-time quadratic regulators with pole in a specific region", IEE Proc. Pt. D, **137**, 5, pp. 297–301 (1990).

[4] R. A. Yackel, B. C. Kuo and G. Singh: "Digital redesign of continuous systems by matching of states at multiple sampling periods", Automatica, **10**, 1, pp. 105–111 (1974).

[5] L. S. Shieh, X. M. Zhao and J. L. Zhang: "Locally optimal-digital redesign of continuous-time systems", IEEE Trans. on Ind. Elec., **36**, 4, pp. 511–515 (1989).

[6] K. S. Rattan: "Digitalization of continuous control systems", IEEE Trans. AC, **29**, 3, pp. 282–285 (1984).

[7] K. S. Rattan: "Compensating for computational delay in digital equivalent of continuous control systems", IEEE Trans. AC, **34**, 8, pp. 895–899 (1989).

[8] J. P. Keller and B. D. O. Anderson: "A new approach to the discretization of continuous-time controllers", IEEE Trans. AC, **37**, 2, pp. 214–223 (1992).

[9] T. Hagiwara and M. Araki: "Time-varying digital controllers (in Japanese)", J. SICE, **27**, 12, pp. 1071–1077 (1988).

[10] M. Araki and T. Hagiwara: "Pole assignment by multirate-data output feedback", Int. J. Control, **44**, 6, pp. 1661–1673 (1986).

[11] T. Mita, Y. Chida, Y. Kazu and H. Numasato: "Two-delay robust digital control and its applications – avoiding the problem on unstable limiting zeros", IEEE Trans. AC, **35**, 8, pp. 962–970 (1990).

[12] S. Kodama and N. Suda: "Matrix Theory for System Control (in Japanese)", SICE (1981).

[13] H. Fujimoto and A. Kawamura: "New digital redesign method in use of N-Delay control (in Japanese)", Trans. IEE of Japan, **117-D**, 5, pp. 645–654 (1997).

[14] H. Fujimoto, A. Kawamura and M. Tomizuka: "Generalized digital redesign method of linear feedback system based on N-delay control", to be presented in American Control Conference (1997).

[15] A. Kawamura, K. Miura and T. Ishizwawa: "Observer based sliding mode CP control of two axis scara robot", Proc. IEEE Int. Workshop Adv. Motion Contr., pp. 197–202 (1990).

[16] H. Fujimoto and A. Kawamura: "Proposal of digital redesign in use of N-Delay control and its application (in Japanese)", IEE of Japan Technical Meeting Record, IIC-96-13, pp. 31–40 (1996).

The Power Conversion Conference-Nagaoka is supported by the following foundations, companies and so on.

The Ministry of Education

Nagaoka-City

Tokyo Electric Power Co., INC.

Kansai Electric Power Co., INC.

Chubu Electric Power Co., INC.

Hitachi, Ltd.

Toshiba Corporation

Mitsubishi Electric Corporation

Tohoku Electric Power Co., LTD.

Electric Power Development Co., Ltd.

Fuji Electric Co., Ltd.

Meidensha Corporation

Sanken Electric Corporation

Nissan Motor Co., LTD.

Eye Lighting Systems Corporation

DAIKIN INDUSTRIES, LTD.

Nissin Electric Corporation

Toyo Electric Mfg. Co., LTD.

TDK Corporation

Sharp Corporation

Shindengen Electric Mfg. Co.

NEMIC LAMBDA K.K.

Neturen Co., LTD.

Yaskawa Electroc Corporation

Research Foundation for the lectrotechnology of Chubu

Shinko Electric CO., LTD.

Nippon Telegraph and Telephone Corporation

Shikoku Research Institute Inc.

Seiko Seiki CO., LTD.

Motor Company, Matsushita Electric Industrial Co., Ltd.

JAPAN STORAGE BATTERY CO., LTD.

Oriental Motor Co., Ltd.

Origin Electric Co., Ltd.

Nippon Steel Corporation

Mitsubishi Heavy Industries Ltd.

NIKON CORPORATION

TOYOTA MOTOR CORPORATION

Sanyo Denki Co., Ltd.

FANUC LTD.

Yuasa Corporation

DENSO CORPORATION

TAKAOKA ELECTRIC MFG. CO., LTD.

Kawasaki Steel Corporation

Railway Technical Research Institute

NSK Ltd.